ACTIVE STRUCTURAL ACOUSTIC CONTROL (ASAC)

APPENDIX C

Published Papers

1 Aug 1995

ONR Grant N00014-92-J-1170

Principal Investigator

Chris R. Fuller

19960618 046

Vibration and Acoustics Laboratories
Department of Mechanical Engineering
Virginia Polytechnic Institute and State University
Blacksburg, VA 24061 - 0238

DISTRIBUTION STATEMENT A
Approved for public release;
Distribution Unlimited

DISCLAIMER NOTICE

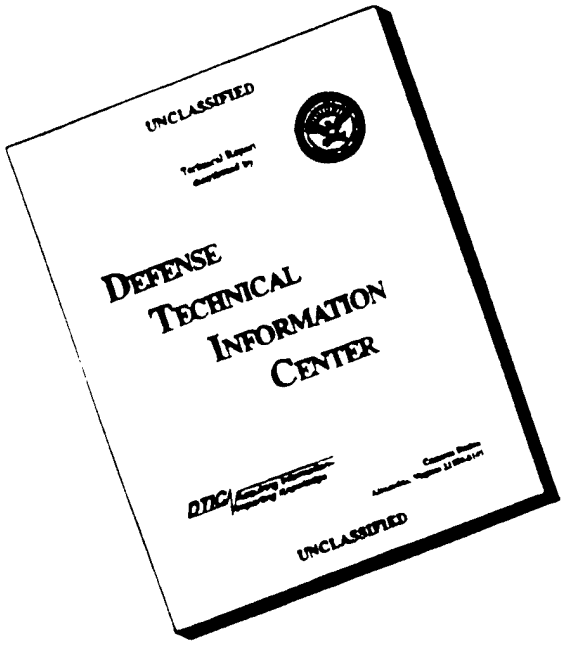

THIS DOCUMENT IS BEST QUALITY AVAILABLE. THE COPY FURNISHED TO DTIC CONTAINED A SIGNIFICANT NUMBER OF PAGES WHICH DO NOT REPRODUCE LEGIBLY.

REPORT DOCUMENTATION PAGE

Form Approved
OMB No. 0704-0188

Public reporting burden for this collection of information is estimated to average 1 hour per response, including the time for reviewing instructions, searching existing data sources, gathering and maintaining the data needed, and completing and reviewing the collection of information. Send comments regarding this burden estimate or any other aspect of this collection of information, including suggestions for reducing this burden, to Washington Headquarters Services, Directorate for information Operations and Reports, 1215 Jefferson Davis Highway, Suite 1204, Arlington, VA 22202-4302, and to the Office of Management and Budget, Paperwork Reduction Project (0704-0188), Washington, DC 20503.

1. AGENCY USE ONLY (Leave blank)	2. REPORT DATE	3. REPORT TYPE AND DATES COVERED
	1 March 1996	Final Report; 8/16/91-8/31/95

4. TITLE AND SUBTITLE
Active Structural Acoustic Control (ASAC)

5. FUNDING NUMBERS
G; N00014-92-J-1170

6. AUTHOR(S)
C. R. Fuller

7. PERFORMING ORGANIZATION NAME(S) AND ADDRESS(ES)
C. R. Fuller
Virginia Tech
Mechanical Engineering Dept.
Blacksburg, VA 24061-0238

8. PERFORMING ORGANIZATION REPORT NUMBER

9. SPONSORING/MONITORING AGENCY NAME(S) AND ADDRESS(ES)
Dr. Kam W. Ng
Office of Naval Research
800 N. Quincy Street; ONR 334
Arlington, VA 22217-5000

10. SPONSORING/MONITORING AGENCY REPORT NUMBER

11. SUPPLEMENTARY NOTES

12a. DISTRIBUTION/AVAILABILITY STATEMENT
Unlimited

12b. DISTRIBUTION CODE

13. ABSTRACT (Maximum 200 words)

This final report for the Office of Naval Research Grant N00014-92-J-1170 concerns further VPI&SU research to develop and refine active structural acoustic control (ASAC) with active/adaptive structures. The focus is on the development and demonstration of advanced system design and optimization techniques for complex structures and disturbances, and realistic system implementations. This required a highly coordinated analytical and experimental research effort in the three areas of structural acoustics, actuators and sensors and control algorithms. These efforts include further development and refinement of promising new directions from a previous Grant. Significant progress and innovations have been made in structural acoustics, actuators, sensors, control approaches, and related design optimization techniques. Due to the coupled nature of the problem, considerable effort has been given to the interaction of these areas with each other, and their integration for realistic disturbances and applications. The investigations have focused on the use of distributed control forces (e.g., distributed piezoelectric strain actuators) and sensors (PVDF), and DSP controllers. Demonstrated technology advancements are highly applicable to acoustic quieting in advanced naval vessel designs in the low frequency range from 10 Hz to 1 kHz.

14. SUBJECT TERMS	15. NUMBER OF PAGES
active structural acoustic control; noise radiation; structural vibration; actuators; sensors; control algorithms	approx. 350
	16. PRICE CODE

17. SECURITY CLASSIFICATION OF REPORT	18. SECURITY CLASSIFICATION OF THIS PAGE.	19. SECURITY CLASSIFICATION OF ABSTRACT	20. LIMITATION OF ABSTRACT
Unclassified	Unclassified	Unclassified	SAR

APPENDIX C

Contents

Invited Papers and Talks

C-1 Active structural acoustic control, C. R. Fuller and R. J. Silcox, Journal of the Acoustical Society of America, Vol 91 No. 1, p. 519, January 1992.

C-2 Active Control of Sound and Vibration with "Intelligent" Structures, C. R. Fuller, International Noise & Vibration Control Conference, St. Petersburg, Russia, 31 May - 3 June 1993, keynote address.

C-3 Transient Electro-Mechanics of Piezoelectric Actuator-Driven Active Mechanical Systems, C. Liang and C. A. Rogers, Journees Numeriques de Besancon on Smart Materials, Besancon, France, 4 January 1994.

C-4 Design of Active Control Systems using Eigenanalysis, C. R. Fuller and R. A. Burdisso, 3rd International Congress on Air- and Structure-Borne Sound and Vibration, Montreal, Canada, 13-15 June 1994, keynote address.

C-5 Recent Developments in Active Control of Vibrations, C. R. Fuller, Nordic Conference on Vehicle and Machine Vibrations, Stockholm, Sweden, 6-8 September 1994, keynote address.

C-6 Active Control of Coupled Wave Propagation and Associated Power in Fluid-Filled Elastic Long Pipes, C. R. Fuller and B. J. Brévart, ACTIVE 95, Newport Beach, CA, July 6-8, 1995, plenary presentation.

Referred Journals

C-7 Control of Sound Radiation with Active/Adaptive Structures, C. R. Fuller, C. A. Rogers and H. H. Robertshaw, Journal of Sound and Vibration, Vol. 157 No. 1, pp. 19-39, 1992.

C-8 Active Control of Sound Radiation from a Fluid-loaded Rectangular Uniform Plate, Y. Gu and C. R. Fuller, Journal of the Acoustical Society of America, Vol. 93 No. 1, pp. 337-345, January 1993.

C-9 Active Control of Sound Radiation from a Simply Supported Beam: Influence of Bending Near-Field Waves, C. Guigou and C. R. Fuller, Journal of the Acoustic Society of America, Vol. 93 No. 5, pp. 2716-2725, May 1993.

C-10 Causality Analysis of Feedforward - Controlled Systems with Broadband Inputs, R. A. Burdisso, J. S. Vipperman and C. R. Fuller, Journal of the Acoustical Society of America, Vol. 94 No. 1, pp. 234-242, July 1993.

C-11 Enhancing Induced Strain Actuator Authority Through Discrete Attachment to Structural Elements, Z. Chaudhry and C. A. Rogers, AIAA Journal, Vol. 31 No. 7, pp. 1287-1292, July 1993.

C-12 Author's Reply, R. A. Burdisso and C. R. Fuller, Journal of Sound and Vibration, Vol. 163 No. 2, pp. 366-371, 1993.

C-13 Active Control of Broadband Structural Vibration Using the LMS Adaptive Algorithm, J. S. Vipperman, R. A. Burdisso and C. R. Fuller, Journal of Sound and Vibration, Vol.166 No. 2, pp. 283-299, 1993.

C-14 An Impedance Method for Dynamic Analysis of Active Material Systems, C. Liang, F. P. Sun and C. A. Rogers, ASME Journal of Vibration and Acoustics, Vol. 116 No. 1, pp. 120-128, January 1994.

C-15 Coupled Electro-Mechanical Analysis of Adaptive Material Systems-Determination of the Actuator Power Consumption and System Energy Transfer, C. Liang, F. P. Sun and C. A. Rogers, Journal for Intelligent Material Systems and Structures, Vol. 5 No. 1, pp. 12-20, January 1994.

C-16 Optimal Placement of Piezoelectric Actuators for Active Structural Acoustic Control, B.-T. Wang, R. A. Burdisso and C. R. Fuller, Journal of Intelligent Material Systems and Structures, Vol. 5, pp. 67-71, January 1994.

C-17 Active Control of Structurally Radiated Sound from an Enclosed Finite Cylinder, R. L. Clark and C. R. Fuller, Journal of Intelligent Material Systems and Structures, Vol. 5, pp. 379-391, May 1994.

C-18 Advanced Time Domain Wave-Number Sensing for Structural Acoustic Systems. I. Theory and Design, J. P. Maillard and C. R. Fuller, Journal of the Acoustical Society of America, Vol. 95 No. 6, pp. 3252-3261, June 1994.

C-19 Advanced Time Domain Wave-Number Sensing for Structural Acoustic Systems II. Radiation Control of a Simply Supported Beam, J. P. Maillard and C. R. Fuller, Journal of the Acoustical Society of America, Vol. 95 No. 6, pp. 3262-3272, June 1994.

C-20 Experiments in piezostructure modal analysis for mimo feedback control, W. R. Saunders, D. G. Cole and H. H. Robertshaw, Smart Mater. Struct., Vol. 3, pp. 210-218, 1994

C-21 Experiments on Active Control of Plate Vibration Using Piezoelectric Actuators and Polyvinylidene Fluoride (PVDF) Modal Sensors, Yi Gu, R. L. Clark, C. R. Fuller and A. C. Zander, ASME Journal of Vibration and Acoustics, Vol. 116, pp. 303-308, July 1994.

C-22 Dynamic Analysis of Piezoelectric Actuator-Driven Circular Rings using an Impedance Approach, A. Rossi, C. Liang, and C. A. Rogers, Journal of the Acoustic Society of America, Vol. 96 No. 3, pp. 1592-1597, September 1994.

C-23 Modeling of Distributed Piezoelectric Actuators Integrated with Thin Cylindrical Shells, S. W. Zhou, C. Liang and C. A. Rogers, Journal of the Acoustic Society of America, Vol. 96 No. 3, pp. 1605-1612, September 1994.

C-24 Design of Active Structural Acoustic Control Systems by Eigenproperty Assignment, R. A. Burdisso and C. R. Fuller, Journal of the Acoustical Society of America, Vol. 96 No. 3, pp. 1582-1591, September 1994.

C-25 Numerical Simulation of Active Structural-Acoustic Control for a Fluid-Loaded, Spherical Shell, C. E. Ruckman and C. R. Fuller, Journal of the Acoustical Society of America, Vol. 96 No. 5, pp. 2817-2825, November 1994.

C-26 The Effect of Distributed or Discrete Pressure and Acceleration Sensors on Active Structural-Acoustic Control Systems, B.-T. Wang and C. R. Fuller, Journal of the Chinese Society of Mech. Eng., Vol. 15 No. 1, pp. 30-39, 1994.

C-27 Modeling of Induced strain actuation of shell structures, Z. Chaudhry, F. Lalande and C. A. Rogers, Journal of the Acoustic Society of America, Vol. 97 No. 5 Part 1, pp. 2872-2877, May 1995.

C-28 A regression approach for simulating feedforward active control, C. E. Ruckman and C. R. Fuller, Journal of the Acoustic Society of America, Vol. 97 No. 5 Part 1, pp. 2906-2918, May 1995.

C-29 Experiments on Active Control of Acoustic Radiation Due to a Clamped Edge on a Semi Infinite Beam, C. Guigou, C. R. Fuller and K. D. Frampton, Journal of Sound and Vibration, Vol. 169 No. 4, pp. 503-526, 1994.

C-30 Adaptive Feedforward Control of Non-minimum Phase Structural Systems, J. S. Vipperman and R. A. Burdisso, Journal of Sound and Vibration, Vol. 183 No. 3, pp. 369-382, 1995.

Published Proceedings

C-31 Active structural acoustic control using fiber sensors and piezoelectric actuators, R. L. Clark, C. R. Fuller, B. R. Fogg, W. V. Miller, A. M. Vengsarkar and R. O. Claus, ADPA/AIAA/ASME/SPIE Active Materials & Adaptive Structures, Arlington, VA, 4-8 November 1991.

C-32 Control of Broadband Radiated Sound with Adaptive Structures, J. P. Smith, C. R. Fuller and R. A. Burdisso, Proceedings of SPIE Conf. on Smart Struct. and Adaptive Materials, Albuquerque, NM, SPIE Vol. 1917 Part I, pp. 587-597, February 1993.

C-33 The impact of piezoelectric sensoriactuators on active structural acoustic control, W. R. Saunders, D. G. Cole and H. H. Robertshaw, Proceedings SPIE Conf. on Smart Structural and Materials, Albuquerque, NM, SPIE Vol. 1917, pp. 578-586, February 1993.

C-34 Power Consumption of Piezoelectric Actuators in Underwater Active Structural Acoustic Control, S. C. Stein, C. Liang and C. A. Rogers, Second Conference on Recent Advances in Active Control of Sound and Vibration, Blacksburg, VA, pp. 189-203, 28-30 April 1993.

C-35 An Evaluation of Feedback, Adaptive Feedforward and Hybrid Controller Designs for Active Structural Control of a Lightly - Damped Structure, W. R. Saunders, H. H. Robertshaw and R. A. Burdisso, Second Conference on Recent Advances in Active Control of Sound and Vibration, Blacksburg, VA, pp. 339-354, 28-30 April 1993.

C-36 Comparison of Various Digital LQ-MIMO Control Laws, D. G. Cole and H. H. Robertshaw, Second Conference on Recent Advances in Active Control of Sound and Vibration, Blacksburg, VA , pp. 355-365, 28-30 April 1993.

C-37 Active Control of Structurally Radiated Sound from an Enclosed Finite Cylinder, R. L. Clark and C. R. Fuller, Second Conference on Recent Advances in Active Control of Sound and Vibration, Blacksburg, VA, pp. 380-402, 28-30 April 1993.

C-38 Optimizing Actuator Locations in Feedforward Active Control Systems Using Subset Selection, C. E. Ruckman and C. R. Fuller, Second Conference on Recent Advances in Active Control of Sound and Vibration, Blacksburg, VA, pp. S122-S133, April 1993.

C-39 Optimum Actuator and Sensor Design for Feedforward Active Structural Acoustic Control, R. A. Burdisso and C. R. Fuller, ASME Winter Annual Meeting - Adaptive Structures & Materials Systems Symposium, 1993.

C-40 The Dynamic Analysis of Piezostructures in Relation to Modal Analysis, D. G. Cole, W. R. Saunders and H. H. Robertshaw, 12th International Modal Analysis Conference, Hawaii, 1-4 February 1994.

C-41 Development of an Actuator Power Factor Meter for Experimental Determination of the Optimal Actuator Location on Complex Structures, C. Liang, P. Sun and C. A. Rogers, Proceedings of SPIE Smart Materials and Structures Conference, Orlando, FL, SPIE Vol. 2190, pp. 262-274, 13-18 February 1994.

C-42 Special Considerations in the Modeling of Induced Strain Actuator Patches Bonded to Shell Structures, Z. Chaudhry, F. Lalande and C. A. Rogers, Proceedings of SPIE Smart Structures and Materials Conference, Orlando, FL, SPIE Vol. 2190, pp. 563-570, 13-18 February 1994.

C-43 Structural Modal Analysis using Collocated Piezoelectric Actuators/Sensors - an Electromechanical Approach, F. P. Sun, C. Liang and C. A. Rogers, Proceedings of SPIE Smart Structures and Materials Conference, Orlando, FL, SPIE Vol. 2190, pp. 238-249, 13-18 February 1994.

C-44 Modeling Considerations for In-Phase Actuation of Actuators Bonded to Shell Structures, F. Lalande, Z. Chaudhry and C. A. Rogers, AIAA/ASME/ASCE/AHS/ASC 35 th Structures, Structural Dynamics and Materials Conference and Adaptive Structures Forum, Hilton Head, SC, pp. 429-437, 18-21 April 1994.

C-45 Control of Sound Radiation/Reflection with Adaptive Foams, C. R. Fuller, M. J. Bronzel, C. A. Gentry and D. E. Whittington, Proceedings of Noise-Con '94, pp. 429-436, Ft. Lauderdale, FL, May, 1994.

C-46 Experimental Modal Testing Using Piezoceramic Patches as Collocated Sensor-Actuators, F. P. Sun, C. Liang and C. A. Rogers, 1994 Spring Conference on Experimental Mechanics and Exhibits, Baltimore, MD, 6-8 June 1994.

C-47 Design of Active Control Systems Using Eigenanalysis, C. R. Fuller and R. A. Burdisso, 3rd International Congress on Air- and Structure-Borne Sound and Vib., Montreal, Canada, 13-15 June 1994.

C-48 Detecting and Analyzing Collinearity in Simulations of Feedforward Active Noise Control, C. E. Ruckman and C. R. Fuller, 3rd International Congress on Air- and Structure-Borne Sound and Vibration, Montreal, Canada, 13-15 June 1994.

C-49 Optimum Design of Feedforward Active Structural Acoustic Control of Complex Structures, H. M. Rodriguez, R. A. Burdisso and C. R. Fuller, Proceedings of ACTIVE 95, The 1995 International Symposium on Active Control of Sound and Vibration, Newport Beach, CA, pp. 335-346, 6-8 July 1995.

C-50 Implementation of Fast Recursive Estimation Techniques for Active Control of Structural Sound Radiation, M. J. Bronzel and C. R. Fuller, Proceedings of ACTIVE 95, The 1995 International Symposium on Active Control of Sound and Vibration, Newport Beach, CA, pp. 359-368, 6-8 July 1995.

C-1 Active structural acoustic control, C. R. Fuller and R. J. Silcox, Journal of the Acoustical Society of America, Vol 91 No. 1, p. 519, January 1992.

Active structural acoustic control [43.40.Vn, 43.50.Ki]

(Received 15 August 1991; accepted for publication 25 August 1991)

Sound fields radiated by vibrating elastic structures often create important noise problems. Previous active control solutions have employed sound sources to control this radiation. This approach typically requires many sources to control the noise from complex structures so that the spatial distributions are reasonably matched and control spillover is minimized. Recently, a more efficient approach has been demonstrated for controlling low to midfrequency structural sound radiation, termed "active structural acoustic control" (ASAC). Instead of using loudspeakers ASAC applies control forces directly to the structure so that the radiated sound-pressure field is minimized. The advantages are that effective control can be implemented with fewer control actuators, and the transducers can be arranged to be reasonably compact.

Early work in ASAC, carried out at NASA Langley and VPI&SU[1] in 1985, demonstrated that sound transmission into cylinders could be controlled by point forces applied to the cylinder wall. The application here was to develop advanced techniques for controlling interior noise within aircraft. It was shown that only certain structural modes couple or radiate to the interior space and thus it was necessary to control only those modes. This effect was termed "modal suppression." As the structural motion that gives rise to the sound-pressure response is being controlled, the interior sound field is reduced globally independent of its modal shape. This principle was applied at Douglas Aircraft to a full-scale DC-9 fuselage. Global control was achieved[2] for structure-borne interior noise transmitted through the engine pylons, using only two point-force control actuators. Weight, mounting considerations, and control spillover effects led to recent cooperative work at NASA and VPI&SU to study the use of piezoceramic actuators bonded to structural members.[3] On a full-scale composite fuselage model a four-actuator, six-sensor system has achieved interior global attenuations of 8 to 15 dB over a range of test conditions.[4] Optimization of the transducer size and distribution is expected to produce further improvement.[5,6]

Controlling marine hull radiated sound is another important application of ASAC, now being investigated in research funded by ONR/DARPA. Previous work in this area studied the control of free field radiation from lightly loaded panels.[7] It showed that sound radiated into a free field could also be globally attenuated by a limited number of control actuators.[8] However another mechanism of control was observed. For the off-resonance cases examined, a reduction in sound radiation occurred with little change in the averaged structural response. It was concluded that the residual or closed-loop structural response has a lower radiation efficiency for the same level of response.[7] This effect was termed "modal restructuring." More recently it was shown that modal suppression corresponds to a decrease in all structural wave-number components while modal restructuring corresponds to a reduction only in the supersonic (radiating) components; the subsonic components are largely unaffected.[9] The significance of modal restructuring is that large attenuations of radiated sound can be achieved by an appropriate change in the controlled structural mode shapes without affecting the overall amplitude. This approach is shown to require significantly less control energy.

Other work on free field application of ASAC has centered on using optimally shaped piezoelectric sensors and actuators bonded or embedded in the structure[10] (an adaptive or "smart" structure). Emphasis has been placed on shaping the sensors so that the radiating components of the structural motions are observed, i.e., the sensor acts as a structural wave-number filter. Good reductions in radiated sound levels were observed for both on and off-resonance conditions. This work has now been extended to include the influence of heavy fluid loading on structural motions.[11] Experiments performed cooperatively by VPI&SU and NRL have shown that the ASAC technique still provides high global attenuations when the radiation loading induces significant modal coupling.

In order to implement the ASAC technique a control strategy is required. Initial work has concentrated on using time domain, multichannel adaptive least means square algorithms.[12] More recent work has utilized state space feedback approaches used in conjunction with radiation filters to model the structural acoustic coupling.[13]

In summary, the ASAC technique has demonstrated much potential in aerospace and marine applications. Future work will center on extending these techniques to broadband disturbances, more complex structures and improved modeling. It is known that optimizing transducer positions is as important as increasing the number of control channels. A multidisciplinary approach is required to synthesize a design procedure that integrates the elements of structural acoustics, transducer, and control technology. The pay off will be in significant cost and weight savings, and in performance improvements for other industrial applications.

C. R. FULLER
Virginia Polytechnic Institute and State University

R. J. SILCOX
NASA Langley Research Center

[1]C. R. Fuller and J. D. Jones, J. Sound Vib. **112**(2), 389 (1987).
[2]M. Simpson *et al.*, AIAA J. Aircraft **28**(3), 208 (1991).
[3]C. R. Fuller *et al.*, AIAA Paper No. 90-3922 (1990).
[4]R. J. Silcox, S. Lefebvre, T. B. Beyer, and V. L. Metcalf, J. Acoust. Soc. Am. Suppl. 1 **90**, S2269 (1991).
[5]V. R. Sonti and J. D. Jones, in *Proceedings of Recent Advances in Active Control of Sound and Vibration, Blacksburg, VA* (Technomic, PA, 1991), p. 27.
[6]H. C. Lester and S. Lefebvre, *Proceedings of Recent Advances in Active Control of Sound and Vibration, Blacksburg, VA* (Technomic, PA, 1991), p. 3.
[7]C. R. Fuller, J. Sound Vib. **136**(1), 1 (1990).
[8]V. L. Metcalf *et al.*, J. Sound Vib. **152**(2), (1992).
[9]R. L. Clark and C. R. Fuller, in Ref. 5, p. 507.
[10]C. R. Fuller, C. A. Rogers, and H. H. Robertshaw, Proc. SPIE Conf. **1170**, 338 (1989).
[11]Y. Gu and C. R. Fuller, J. Acoust. Soc. Am. Suppl. 1 **89**, S1915 (1991).
[12]S. J. Elliott, I. M. Stothers, and P. A. Nelson, IEEE Trans. **ASSP-35**, (10) (1987).
[13]W. T. Baumann, W. R. Saunders, and H. H. Robertshaw, J. Acoust. Soc. Am. Suppl. 1 **88**, S149 (1990).

C-2 Active Control of Sound and Vibration with "Intelligent" Structures, C. R. Fuller, International Noise & Vibration Control Conference, St. Petersburg, Russia, 31 May - 3 June 1993, keynote address.

ACTIVE CONTROL OF SOUND AND VIBRATION WITH "INTELLIGENT" STRUCTURES

Chris R. Fuller
Vibration and Acoustics Laboratories
Mechanical Engineering Department
Virginia Polytechnic Institute and State University
Blacksburg, VA USA 24061-0238

ABSTRACT

This paper is a brief introduction and overview of reduction of sound and vibration with "intelligent" structures. The paper begins with a definition of an intelligent structure and then discusses work in the component areas of actuators, sensors and control approaches. The synthesis of these areas is then illustrated through two example applications; radiation control from vibrating panels and reduction of turbofan inlet noise.

INTRODUCTION

The potential benefits of active control for reducing sound have been convincingly demonstrated [1]. In this paper we discuss a more recent extension of the active control method in which sound and vibration is reduced using "intelligent" structures or systems. Work in this area has been steadily progressing over the last five years as summarized in the review article by Fuller et al. [2]. There are a number of definitions of what are now termed "intelligent, adaptive or smart" structures. (for example, Wada et al. [3]). Here we define an intelligent structure as a system with integrated actuators (corresponding to muscles), sensors (nerves) under the direction of a learning type controller (intelligence). The structure or system thus has the ability to sense and react to its environment in a controllable way by changing its internal properties (either steady state or in a vibrational sense). Further, the controller has the ability to learn how to perform the required control task by "experience" rather than basing its control action on an *à prior* set rule (admittedly the learning procedure has to be prescribed and this in itself is a subject of research).

The advantages of such an approach are many. For instance integration of the actuators and sensors directly into the structure leads to a very compact configuration as opposed to more traditional active noise control methods that, for example, utilize arrays of acoustic sources. This characteristic enables the utilization of a multitude of very small actuators and sensors configured in parallel which, in a collective sense, enables many degrees of freedom of action and thus a wide range of adaptation. Individually each actuator may not impart much control energy but collectively

they can exert much force similar to biological muscle systems. Intelligent structures can thus be seem to be moving towards configurations like natural systems which tend to be non-orthogonal flexible, many degrees of freedom, wet, adaptive, etc. as opposed to conventional engineered structures which generally are orthogonal, dry, rigid, tend to the massive, relatively low number of degrees of freedom and non-adaptive. Like biological systems it is the hope that intelligent systems will sense, adapt and conform with their environment (here environment can mean any chosen external state) rather than act like traditionally engineered structures which are usually designed to "overpower" their environment (and are thus largely "unaware" of their surroundings) by strength, rigidity, etc.

A learning type controller can be seen to have great advantages as well. For these types of control approaches it is not necessary to have an accurate model (mathematical, for example) of the system. The "intelligence" essentially learns what to do in real time using various learning schemes. The implementation of such approaches has been postulated for quite a few years but it is only recently that advances in digital signal processing chips has enabled the "real time" implementation of such schemes. These approaches work well on complex systems where modeling and system identification is extremely difficult if not impossible.

The following paper briefly summarizes work in the component area of an "intelligent" structure. For more detail the reader is referred to the appropriate references. The synthesis of these areas is illustrated through two example applications. At this point the reader is reminded of a key point. Although an intelligent structure can be subdivided into components, the complete system involves the coupled interaction of each part. Thus any investigation or design should also include the interactive nature of the components as well.

ACTUATORS

Actuators are used to impart control energy to the structure. This can be in the form of steady state (i.e. DC) loads or in the form of oscillating loads which excite vibrational response, such as in-plane force, strain, bending moments, etc. Conventional actuators take the form of loudspeakers for sound production and point force actuators for vibrational response. Characteristics of such sources are described in Beranek [4] and Cremer et al. [5], respectively.

Actuators more commonly associated with intelligent structures are described as follows. Surface strain devices are distributed actuators which when bonded or embedded in the structure apply oscillating in-plane strains. As shown by Crawley and deLuis [6] for a 1-D analysis and Dimitriadis et al. [7] in the 2-D case, these devices, when located off the central axis, effectively apply bending moments to the structure (pure bending if arranged in an anti-symmetric fashion). Surface strain devices come in various materials but the two most commonly investigated are piezoceramic and magnetostrictive [3]. Such devices tend to be high force, low displacement transducers and thus impedance matching of the actuator to the system is a critical aspect as illustrated in the work of Liang, et al. [8]. These devices can also be arranged in a "stack" mode where they apply normal forces or displacements to the system similar to conventional shakers; this arrangement is useful for such applications as active isolation, etc.

It is also possible to alter the characteristics of a structure by applying steady loads. The above listed devices can also be used to achieve this function by driving them with the appropriate DC input. This will result in a constant (i.e. non-oscillating), variable (in magnitude) load being applied to the system changing, for example, its resonant frequencies. Shape memory alloy (SMA) has also demonstrated much potential in this area [9]. These materials are configured to utilized

"memory" characteristic by shrinking to their original length when heated, typically by passing a current through them. Composite structures have been configured to have embedded SMA fibers. By applying voltages to the SMA fibers, in-plane loads as well as a change in stiffness is imparted to the system at selected fiber angles and laminate layers thus altering the composite behavior of the system. Thus the mode shapes and resonant frequencies of composite structures can be altered as required [10].

There are other advanced actuators based on materials such as Electro-Rheological fluids and Electrostrictive ceramics and the reader is referred to the paper of Wada et al. [3] for information on these.

SENSORS

Sensors are used to detect the current state of the intelligent system. They provide information which directs the controller to act in a decisive manner, bringing the system to the required response. In intelligent systems, correct sensing is critical to good performance simply from the fact that the learning type controller will try and do everything to bring the output of the sensors to the required values (usually minimize). Sensors must be configured to accurately observe the required variables to be controlled. Conventional sensors are transducers such as microphones, accelerometers, strain gauges, etc. again well described in Beranek [4] and Cremer, et al. [5]. Note that these transducers tend to be point sensors, i.e. very small compared to a wavelength of motion.

The more advanced sensors under study for intelligent systems tend to be of distributed nature covering large parts of the structure and thus observing many wavelengths of motion. The piezoelectric material PVDF has shown much potential in this application [11]. The material can be cut in a required shape and attached to the structural surface where it observes an integral of the surface strain under its area. The PVDF sensor can be cut into various shapes such that, in effect, it carries out an analog wave number transform of the structural response and thus only observes certain wave components. For example, on a simply supported beam, a sensor cut into the shape of $F^{\pm} \sin(\pi x/L)$, where $F^{\pm}$ is the polarization which is flipped through the modal point, will only observe the second mode of motion of the beam while a point sensor such as an accelerometer will observe all motion (unless on a nodal line).

The distributed sensor can thus be seen as a device which through its shape and location can simply and quickly perform spatial filtering. Other transducers such as optical fibers [12] and SMA [2] can also be configured to perform similar sensing capabilities. Current work centers on making the distributed sensor adaptive in shape such that it can change its observability in a required way.

"LEARNING" TYPE CONTROLLERS

The control arrangement provides the "intelligence" of the system. It takes information from the sensors, processes it in order to derive a control decision(s) and sends information to the actuators in order to change the behavior of the structure such that the sensor information is changed to required values. Conventional modern control methods generally use a model of the system to calculate and implement optimal control gains [13].

"Learning type" controllers work on a different approach in which a learning or training rule is used to change the control configuration to minimize a particular performance index. The control arrangements generally have little or no knowledge of the system to be controlled (although some physical knowledge certainly helps in deciding their arrangement). By iteratively changing their

structure over time in a training period they can "learn" to model the system and thus control it. Such approaches have been well known for a number of years. It is only recently that the advent of the digital signal processing chip has made their implementation of adaptive or learning type approaches in "real time" feasible. Here "real time" is meant to imply that the time for training or learning is of the order of the time constants of the system. Generally these controllers are arranged so that a training or reference signal(s) fed through a linear or nonlinear compensator to produce control signals. The configuration of the compensator is adaptively changed in time by the learning or training algorithms in order to minimize the error function derived from the sensors. Such an arrangement is generally known as a "feed-forward" controller [1].

The most popular form of these learning or adaptive type controllers is the Filtered-X LMS algorithm which in multi channel form is well described in the text by Nelson and Elliott [1]. This type of controller is appropriate for linear systems and narrow band or broad band signals which are relatively stationary. Presently the Filtered-X LMS algorithm does not work well on transients since the disturbance is usually much shorter than the time required for the controller to converge or learn.

Artificial Neural Networks (ANN) show much potential for control of nonlinear systems [14,15]. The multi-layered perception arrangement with a back propagation training algorithms can be seen to be related to the Filtered-X configuration. Other advanced learning type control such as genetic algorithms [16] and biologically based systems [17] are presently under investigation.

EXAMPLE APPLICATION OF "INTELLIGENT" STRUCTURES

The following two example applications are meant to illustrate use of an intelligent structure or system in controlling sound and vibration. The reader is reminded that there are many possible applications and arrangements of such systems ; the following two are used to illustrate the synthesis of the above listed component areas.

Control of Sound Radiation from Panels

The work briefly described here was carried out by Clark and Fuller [18]. Figure 1 shows a schematic arrangement of the experimental test rig. A baffled simply supported plate is driven by a point force shaker as a narrowband disturbance or noise input. Control is applied to the plate by three surface mounted piezoceramic actuators configured to produce pure bending [7]. The error information is provided by three piezoelectric PVDF patches mounted on the surface of the plate or by three microphones arranged in the radiated far-field at mid-height. The control aim is to minimize the sound radiation globally (i.e. throughout an extended area in the far-field).

The control arrangement is also shown in Figure 1. The disturbance signal is taken directly as a reference or training signal and passed through three adaptive FIR filters (the controller compensator). The outputs of the compensator are then fed to the piezoceramic actuators as control signals. The output of the error transducers is then fed to the controller where in conjunction with the reference signal it is used by the Filtered-X LMS algorithm to adapt the FIR weights in order to minimize the modulus squared of the time average of the error signals [1].

Figure 2 presents an example result in terms of measured far-field radiation directivities. The disturbance frequency is 550 Hz which is off-resonance for this system. This frequency is between the (1,3) and (4,1) mode of the plate hence the modal density is relatively high [18]. For the results of Figure 2, an optimal procedure was used to locate the actuators and/or the PVDF sensors [19]. The results show that reductions of the order of 15 dB in radiated sound are possible with the

that this approach is not simply active vibration control. Often the plate overall response increases while the sound radiation is reduced [2]. In effect, the controlled plate has a lower radiation efficiency and thus is less well coupled to the radiated field. This mechanism of control is termed "modal restructuring" [2].

The PVDF sensors, although they are attached to the plate surface, are shaped and located so as to observe the plate modal contributions as close as possible to the equivalent modal radiation transfer functions to the far-field error sensors (microphones). Figure 2 also shows results when three microphones were used as sensors and in this case the control performance is improved. This behavior is because of the finite size of the PVDF patches restricts the degrees of freedom in the observability of plate modes, i.e. with more, smaller PVDF patches the curves should be similar.

If the object was to minimize the plate vibration in a controllable way rather than sound radiation then the configuration of the PVDF sensors would be altered. For example work by Gu et al. [20] shows how selected plate modes of vibration can be controlled by using appropriately shaped PVDF sensors.

Control of Turbofan Inlet Radiated Noise

A schematic of the test arrangement for this example is presented in Figure 3. The work described here was carried out by Thomas et al. [21,22]. The object is to minimize the fan noise radiated out of the inlet of a Pratt and Whitney JT15D-F turbofan engine. Figure 4 shows a typical spectrum of the inlet noise which can be seen to be dominated by pure tones associated with the fundamentals and harmonics of the fan noise. In this test arrangement control is achieved with 12 acoustic horn drivers arranged around the circumference of the inlet and wired together in groups of four (i.e. three channels of control). Error signals were taken from three large area PVDF microphones located 3 meters from the inlet. The training signal was derived from a blade passage sensor located in the engine housing. The signal was appropriately filtered to provide individual frequency signals associated with the fundamental and first harmonic of the radiated noise. These individual training signals were then passed through two uncoupled Filtered-X based controllers as shown in Figure 3. The outputs of the Filtered-X controllers were then summed to provide three independent control signals for the acoustic drivers. The error signals were also filtered and fed to the appropriate controller. Such an arrangement enabled implementation of high enough sample rate and choice of independent convergence values to be able to control a frequency of 4.2 kHz [22].

Spectral plots of the radiated noise at the three error microphones with and without control are seen in Figure 4. Attenuations at the fundamental and first harmonic of 18 dB are apparent. An independent traverse of the radiated field shows that attenuation of sound occurs through an arc of 60° centered on the engine axis [22]. This arc is expected to widen with an increase in number of channels of control.

Present work is concerned with replacing the acoustic drivers with compact sound sources designed utilizing piezoelectric technology and located around the inlet periphery [23]. In addition work is being carried out on locating the PVDF sensors in the inlet such that they observe near-field pressure information which is proportional to radiated far-field sound, similar to the work discussed above on plate radiation [19]. The net result will be integrated actuators and sensors in the engine inlet or what could be called an "intelligent" or "adaptive" liner.

CONCLUSIONS

The field of "intelligent" structures or systems shows much potential for innovative, new lightweight compact solutions to controlling radiated sound and vibration. The technique involves the synthesis of knowledge and research in the fields of actuators, sensors and control approaches. Some potential uses have been already demonstrated and market products are being developed. However, before the method is widely applicable, many technical problems need to be investigated and resolved. Although the future of intelligent systems is bright, they should be presently applied with care and a thorough understanding of the physics of the coupled system.

ACKNOWLEDGMENTS

The author gratefully acknowledges the support of most of the work described in this paper by NASA Langley Research Center and the Office of Naval Research. Discussions with Richard J. Silcox of NASA Langley and Prof. R. A. Burdisso of VPI&SU also have been very helpful.

REFERENCES

1. P. A. Nelson and S. J. Elliott, "Active Control of Sound," Academic Press, London, 1992.

2. C. R. Fuller, C. A. Rogers and H. H. Robertshaw, "Control of Sound Radiation with Active/Adaptive Structures," Journal of Sound and Vibration, 157(1), 1992, 14-39.

3. B. K. Wada, J. L. Fanson and E. F. Crawley, "Adaptive Structures," Journal of Intelligent Material Systems and Structures, 1, 1990, 157-174.

4. L. L. Beranek, "Acoustics," AIP Press, N.Y., 1986.

5. L. Cremer, M. Heckel, and E. E. Ungar, "Structure-Borne Sound," Springer-Verlag, Berlin, 1972.

6. E. F. Crawley and J. deLuis, "Use of Piezoelectric Actuator as Elements of Intelligent Structures," AIAA Journal, 25(10), 1987, 1373-1385.

7. E. K. Dimitriadis, C. R. Fuller and C. A. Rogers, "Piezoelectric Actuators for Distributed Vibration Excitation of Thin Plates," ASME Journal of Vibration and Acoustics, 113, 1991, 100-107.

8. C. Liang, F. P. Sun and C. A. Rogers, "Coupled Electro-Mechanical Analysis of Piezoelectric Ceramic Actuator Driven Systems - Determination of the Actuator Power Consumption" Proceedings of the SPIE conference on Smart Structures and Intelligent Systems, Albuquerque, NM, 1993.

9. C. A. Rogers, C. Liang and J. Jia, "Behavior of Shape Memory Alloy Reinforced Composite Plates - Part I: Model Formulations and Control Concepts." Proceedings of 30th SSDM Conference, Mobile, AL, 4, 1989, 1504-1513.

10. C. A. Rogers and D. K. Barker, "Experimental Studies of Active Strain Energy Tuning of Adaptive Composites with Embedded Nitinol Actuators," Proceedings of 31st SSDM Conference, Long Beach, CA, 4, 1990, 2234-2241.

11. C. K. Lee and F. C. Moon, "Modal Sensors/Actuators," ASME Journal of Applied Mechanics, 57, 1990, 434-441.

12. T. Giallorenzi, J. A. Bucaro, A. Danbridge, G. H. Sigel, J. H. Cole, S. C. Rashleigh and R. C. Priest, "Optical Fiber Sensor Technology," IEEE Journal of Quantum Electronics, 18, 1982, 626-665.

13. L. Meirovitch, "Dynamics and Control of Structures" John Wiley, N.Y., 1990.

14. K. S. Narendra and K. Parthasarathy, "Identification and Control of Dynamical Systems Using Neural Networks," IEEE Transactions on Neural Networks, 1(1), 1990.

15. C. R. Fuller, R. H. Cabell, G. P. Gibbs, and D. E. Brown, "A Neural Network Adaptive Controller for Nonlinear Systems," Proceedings of Inter Noise 91, Sydney, Australia, 1991, 169-172.

16. A. R. D. Curtis, "An Application of Genetic Algorithms to Active Vibration Control," Proceedings of Recent Advances in Active Control of Sound and Vibration, Blacksburg, VA, (Technomic Press, PA), 1991, 338-347.

17. C. R. Fuller and J. P. Carneal, "Future Trends in Active Control of Distributed Elastic Systems," Proceedings of Inter Noise 92, Toronto, Canada, 1992, 415-420.

18. R. L. Clark and C. R. Fuller, "Control of Sound Radiation with Adaptive Structures," Journal of Intelligent Material Systems and Structures, 2(3), 1991, 431-452.

19. R. L. Clark and C. R. Fuller, "Optimal Placement of Piezoelectric Actuators and Polyvinylidene Fluoride Sensors in Active Structural Acoustic Control Approaches," Journal of the Acoustical Society of America, 92(3), 1992, 1521-1533.

20. Y. Gu, R. L. Clark, C. R. Fuller and A. Zander, "Experiments on Active Control of Plate Vibration Using Piezoelectric Actuators and Polyvinylidene Fluoride (PVDF) Modal Sensors," submitted to ASME Journal of Vibration and Acoustics, June, 1992.

21. R. H. Thomas, R. A. Burdisso, C. R. Fuller and W. F. O'Brien, "Preliminary Experiments on Active Control of Fan Noise from a JT15D Turbofan Engine," to be published in Journal of Sound and Vibration, 1993.

22. R. H. Thomas, R. A. Burdisso, C. R. Fuller and W. F. O'Brien, "Active Control of Fan Noise from a Turbofan Engine," AIAA Paper 93-0597, 31st Aerospace Sciences Meeting & Exhibit, Reno, NV, 1993.

23. M. E. Dungan, "Development of a Compact Sound Source for the Active Control of Turbofan Inlet Noise," M.S. Thesis, V.P.I.&S.U., Blacksburg, VA, 1992. (Report No. VPI-E-92-23)

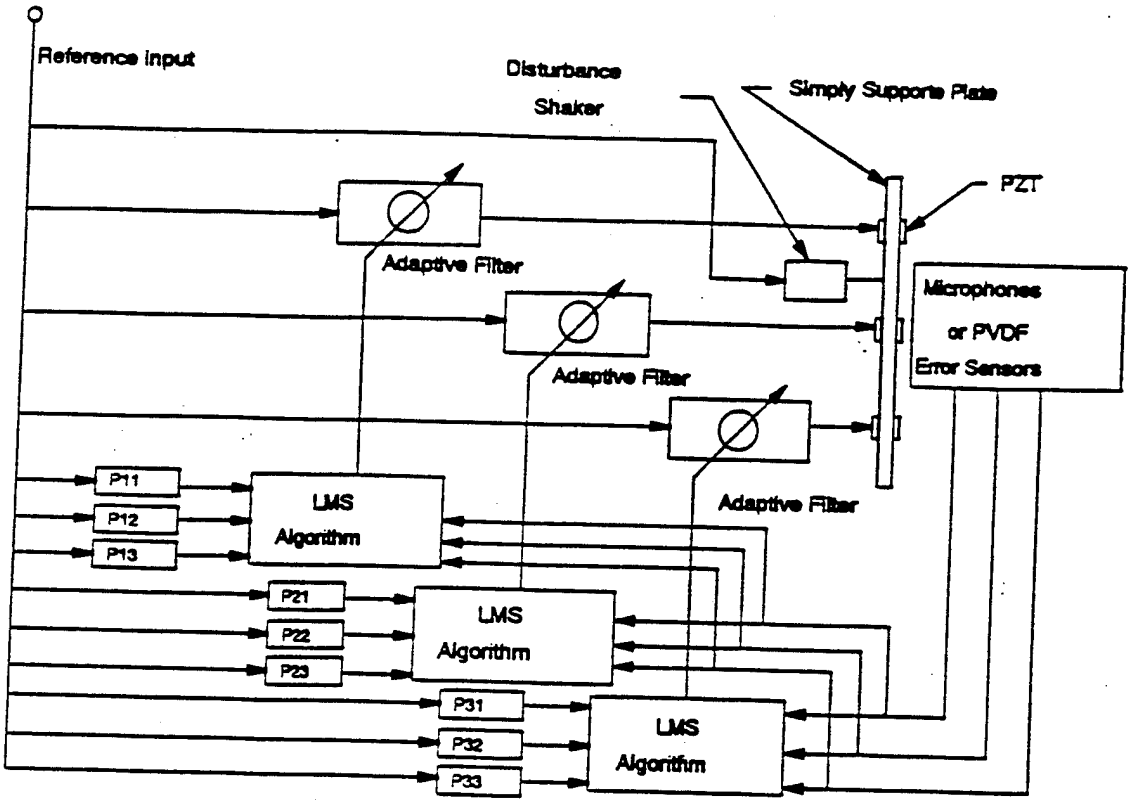

Figure 1.

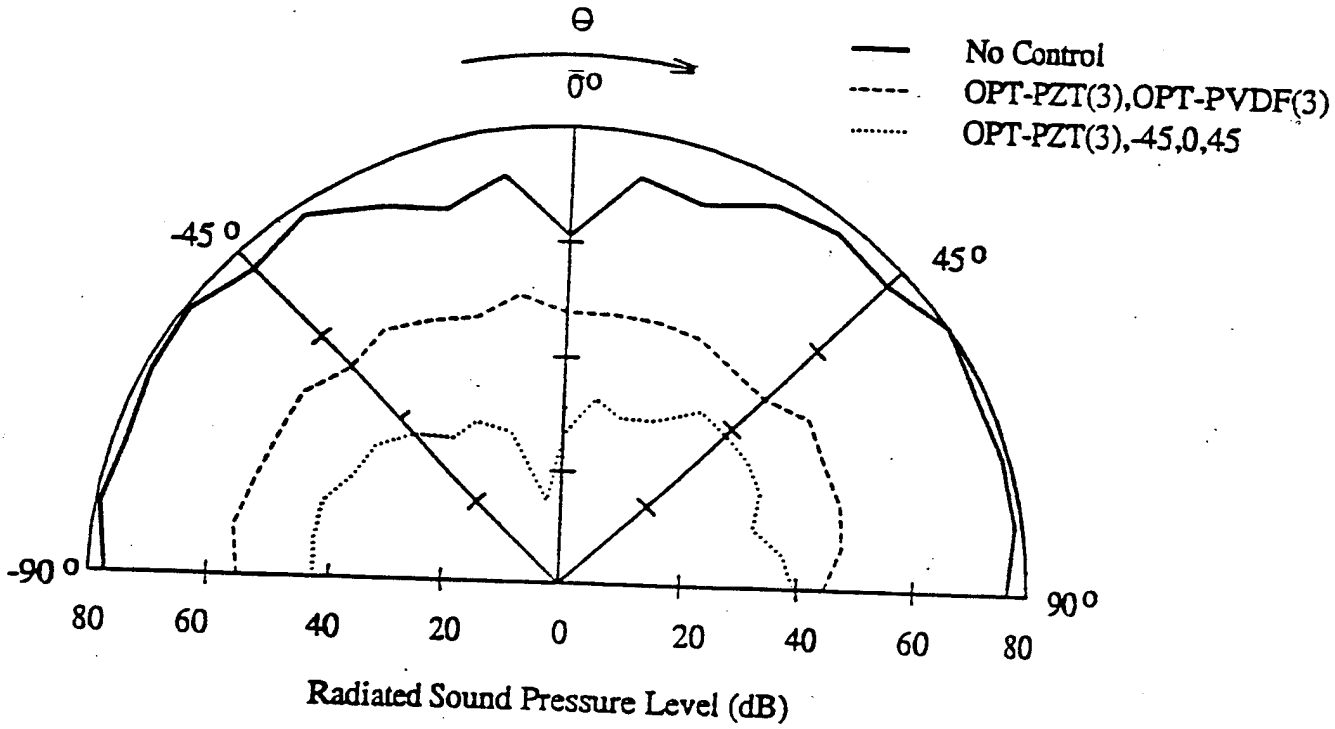

Figure 2.

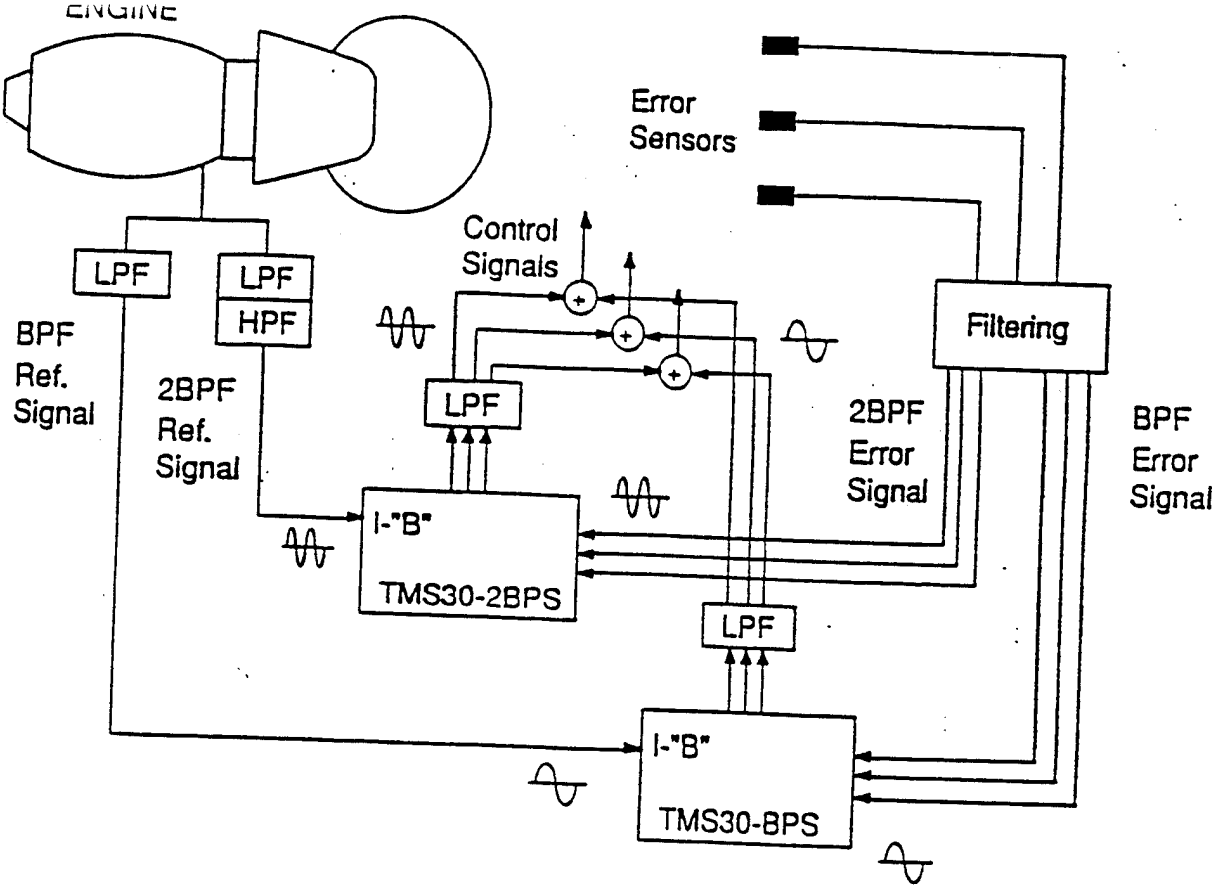

Figure 3.

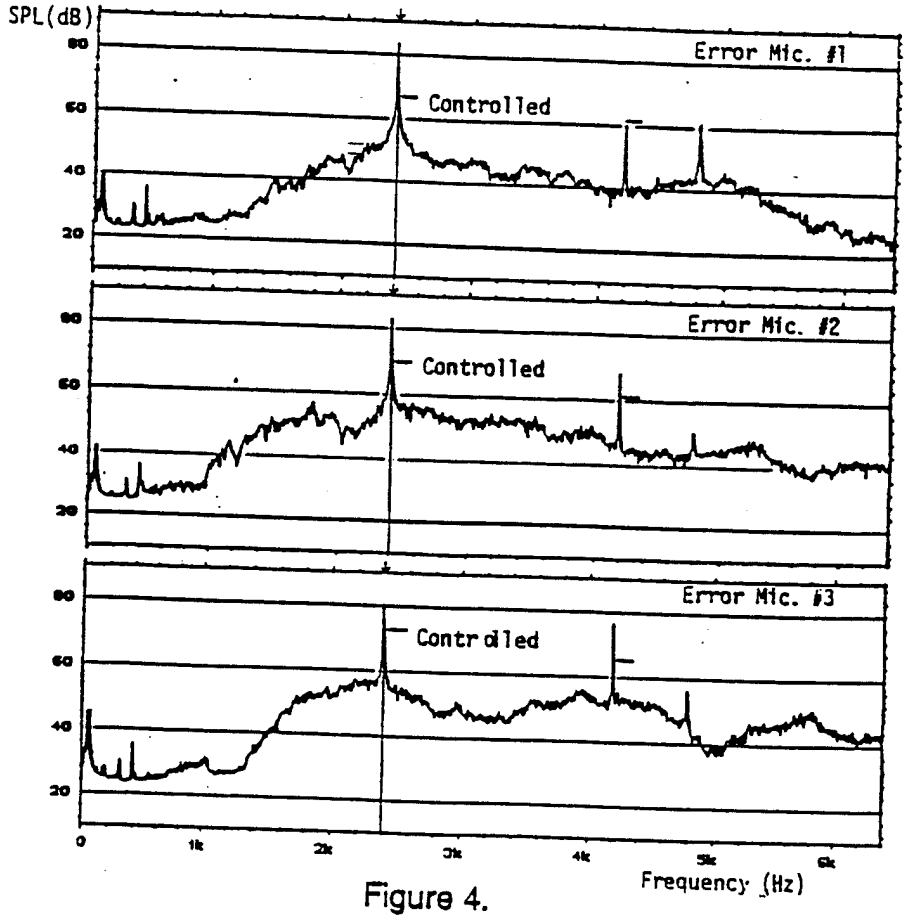

Figure 4.

C-3 Transient Electro-Mechanics of Piezoelectric Actuator-Driven Active Mechanical Systems, C. Liang and C. A. Rogers, Journees Numeriques de Besancon on Smart Materials, Besancon, France, 4 January 1994.

Invited Paper, JOURNEES NUMERIQUES DE BESANCON ON SMART MATERIALS
JAN. 4, 1994, Besancon, France

Transient Electro-Mechanics of Piezoelectric Actuator-Driven Active Mechanical Systems

C. Liang and C. A. Rogers
Center for Intelligent Material Systems and Structures
Virginia Polytechnic Institute and State University
Blacksburg, VA 24061-0261

Abstract

This paper presents a theoretical model to determine the transient electro-mechanical response of active structures driven by piezoelectric (PZT) actuators. The solution is expressed in terms of actuator and structural mechanical impedances, which are the steady state frequency domain dynamic properties and can be characterized theoretically or experimentally. Theoretical case studies have also been presented using a simple example of a PZT actuator-driven one-degree-of-freedom spring-mass-damper system. The solution of the transient response includes the transient electrical current passing through the PZT actuator and the mechanical response of the system (displacement and force). The solution technique may also be applied to active structures driven by other types of induced strain actuators, including electrostrictive and magnetostrictive actuators.

Introduction

Consider an active structure driven by a PZT actuator. If an electrical voltage impulse or step function is applied to the PZT actuator, how will the active structure respond? How much current will pass through the actuator? What are the settling time and over-shoot?

Peter J. Chen and his co-workers (1978 and 1979) have investigated the transient electro-mechanics of ferroelectric materials, including piezoelectric ceramics. Their investigations were only focused on the piezoelectric material itself. For example, Amos and Chen (1978) investigated the transient electro-dynamics of a one-dimensional piezoelectric patch with free-free mechanical boundary conditions under step voltage excitation.

The techniques used to model the transient response of mechanical structures have almost become classical (Thomson, 1950; Meirovitch, 1966). There is no doubt that the modeling techniques discussed in the vibration textbooks can be applied to determine the transient response of active structures. However, since the activation (or excitation) of active structures is caused by integrated induced strain actuators, the dynamic interaction between the actuators and their host structures must be considered in any dynamic modeling of active structures.

In the present modeling of PZT actuator/structure interactions, the static approaches suggested by Crawley and Anderson (1989) and Dimitriadis et al. (1989) are still used. The static

approach assumes that the activation of an induced strain actuator, such as PZT, may be replaced by an equivalent force determined based on the static equilibrium between the actuator and its host structure, as shown in Fig. 1. The equivalent force is determined as:

$$F_e = \frac{K_A K}{K_A + K} x_{in} \qquad (1)$$

where K_A is the actuator stiffness, K the structural stiffness, and x_{in} the free induced displacement.

More accurate dynamic modeling will also include the influence of actuator mass loading and stiffening (Banks et al., 1992), as shown in Fig. 1. However, the force acting on the mass is usually the equivalent force as determined by Eq. (1). In fact, if the actuator stiffening and mass load are considered, the equivalent force acting on the mass, m, should be the blocking force of the actuator, as typically handled using the finite element method (Liang, Sun and Rogers, 1993a).

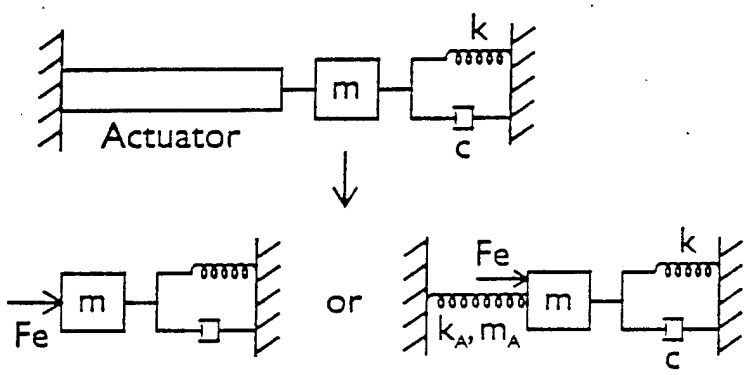

Figure 1. A schematic illustration of active control structures driven by PZT actuator and its dynamic modeling.

When applying the static method to study the transient response of an active structure driven by a PZT actuator, the equivalent force is assumed to be directly proportional to the applied electrical voltage, which ignores the dynamics of the induced strain actuators. The solution techniques discussed in vibration textbooks can then be used to determine the transient structural response.

Liang, Sun, and Rogers (1993a) presented an electro-mechanical impedance model which shows that the interaction between an induced strain actuator and the host structure depends on the dynamic properties of the system. The interaction force between an actuator and its host structure is frequency-dependent and may be expressed as:

$$F = \frac{Z_A Z}{Z_A + Z} \dot{x}_{in} \qquad (2)$$

where Z_A is the short-circuit actuator mechanical impedance, Z is the driving point mechanical impedance of the host structure, and $\dot{x}_{in}$ is the free induced velocity.

The dynamic interaction revealed by Eq. (2) should also be reflected in the modeling of the transient response of active structures driven by induced strain actuators. The first objective of this paper is to include the dynamic interaction between an induced strain actuator and its host structure into the transient response analysis.

This paper will also determine the transient electrical current passing through the PZT actuator. Liang, Sun and Rogers (1993b) have developed a coupled electro-mechanical model to determine the electrical power consumption and transfer of active structures driven by PZT actuators in steady state. The work presented in this paper is an extension of the steady state solutions previously published by the authors.

The transient electro-mechanical model presented in this paper may provide:

- determination of the transient stress within the induced strain actuator during the active control process, which may be much higher than the steady-state stress;
- determination of the transient current (or transient power), which may be higher than the rating of the power supply;
- information regarding the energy conversion between the electrical power system and the mechanical system; and
- determination of the overshoot, settling-time, rise time, and decay-rate of the transient response of the system, which is important in dedicated shape control applications, such as adaptive mirrors.

Transient Analysis

The interaction of a PZT actuator and its host mechanical structure may be represented by a PZT actuator driven general mechanical impedance box, as shown in Fig. 2. The mechanical impedance includes the effect of mass, stiffness, damping and structural boundary conditions, as indicated in Fig. 2. It is assumed that the PZT actuator has only d_{31} effect, i.e., the induced strain is only in the 1-1 (x) direction when an electrical voltage is applied in the 3-3 (y) direction. The length, width, and thickness of the PZT actuator are l, w, and h, respectively.

The transient electro-mechanical interaction of a PZT actuator is governed by the Maxwell relations (Eyges, 1972), the electro-mechanical constitutive relations of the PZT, and Newton's law. The Maxwell relations are not fully included in the analysis. It is assumed that:

$$\frac{\partial E_3}{\partial x} = 0 \qquad (3)$$

where E_3 is the applied electrical field in the 3-3 (y) direction.

The constitutive relation of the PZT actuator is:

$$\begin{cases} S_{11} = s_{11}^{E} T_{11} + d_{31} E_3 \\ D_3 = d_{31} T_{11} + \epsilon_{33}^{T} E_3 \end{cases} \quad (4)$$

where T_{11} is the stress in the 1-1 (x) direction, S_{11} is the strain in the 1-1 direction, D_3 is the electrical displacement in the 3-3 direction, s_{11}^{E} is the mechanical compliance of the PZT in the 1-1 direction under constant electrical field, d_{31} is the piezoelectric constant, and ϵ_{33}^{T} is the dielectric constant of the PZT in the 3-3 direction under constant stress.

The equation of motion for the in-plane vibration of the PZT actuator is:

$$\frac{\partial T_{11}(x,t)}{\partial x} = \rho \frac{\partial^2 u(x,t)}{\partial t^2} \quad (5)$$

where ρ is the mass density of the PZT and u(x,t) is the transient displacement of the PZT in the x (1-1) direction.

Substituting Eqs. (3) and (4, first equation) into Eq. (5) yields:

$$\frac{\partial^2 u(x,t)}{\partial x^2} = \frac{1}{c^2} \frac{\partial^2 u(x,t)}{\partial t^2} \quad (6)$$

where c is the wave speed in the x direction given by $(Y_{11}^{E}/\rho)^{1/2}$. Y_{11}^{E} is the elastic modulus of PZT in the 1-1 direction under constant electrical field.

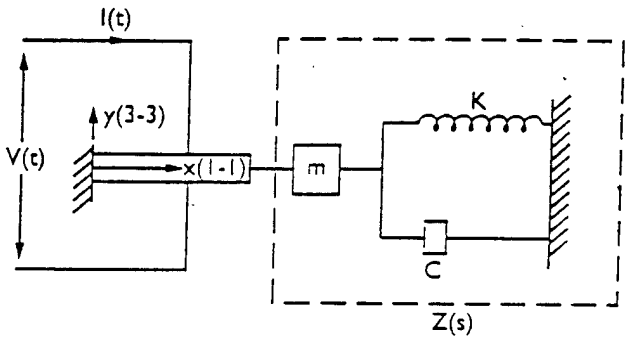

Figure 2. Dynamic modeling of active structures driven by a PZT actuator.

The Laplace transformation of Eq. (6), assuming zero initial displacement and velocity, yields:

$$\frac{d^2 \bar{u}(x,s)}{dx^2} - \frac{s^2}{c^2} \bar{u}(x,s) = 0 \quad (7)$$

(Variables with an overhead bar notation denote their corresponding Laplace transforms.)

The boundary conditions for Eq. (7) are:

$$\bar{u}(0,s) = 0 \quad (8)$$

and

$$Y_{11}^{E} wh\left[\frac{d\bar{u}(x,s)}{dx}\Big|_{x=l} - d_{31}\bar{E}_3(s)\right] = -Z(s)\, s\, \bar{u}(l,s) \qquad (9)$$

Equation (9) indicates the *dynamic* equilibrium between the PZT actuator and its host structure. Z(s) is the generalized structural impedance which is the same as the mechanical impedance, $Z(\omega)$, after replacing s with $i\omega$.

The transformed displacement $\bar{u}(x,s)$ can be solved as:

$$u(x,s) = C_1 e^{kx} + C_2 e^{-kx} \qquad (10)$$

where $k=s/c$. C_1 and C_2 may be solved from the boundary conditions given by Eqs. (8) and (9) as:

$$C_1 = -C_2 = \frac{d_{31} Y_{11}^{E} wh\bar{E}(s)/2}{Y_{11}^{E} whk\cosh(kl) + sZ(s)\sinh(kl)} \qquad (11)$$

The generalized actuator mechanical impedance, $Z_A(s)$, can be determined (Liang et al., 1993a) as:

$$Z_A(s) = \frac{k Y_{11}^{E} wh\cosh(kl)}{s\sinh(kl)} \qquad (12)$$

The transformed displacement $\bar{u}(x,s)$ may be expressed as:

$$\bar{u}(x,s) = \frac{d_{31} Y_{11}^{E} wh\sinh(kx)}{[Z(s)+Z_A(s)]s\sinh(kl)} \frac{\bar{V}(s)}{h} = d_{31} Y_{11}^{E} w\bar{f}(x,s)\bar{V}(s) \qquad (13)$$

where $\bar{V}(s)$ is the Laplace transform of the applied electrical voltage V(t), and

$$\bar{f}(x,s) = \frac{\phi(x,s)}{\Phi(s)} = \frac{\sinh(kx)}{[Z(s)+Z_A(s)]s\sinh(kl)} \qquad (14)$$

The poles of $\bar{f}(x,s)$, which are simple poles based on the physical concept of impedance match, may be determined from $\Phi(s) = 0$:

$$Y_{11}^{E} whk\cosh(kl) + sZ(s)\sinh(kl) = 0 \qquad (15)$$

or

$$Z(s) + Z_A(s) = 0 \qquad (16)$$

The inverse Laplace transform of $\bar{f}(x,s)$, f(x,t), may be expressed as (Meirovitch, 1967):

$$f(x,t)=\sum_{s_m,s_m^*}\frac{\phi(x,s_m)}{\Phi'(s_m)}e^{s_m t} \tag{17}$$

where s_m and s_m^* (s_m^* is the complex conjugate of s_m) are the simple roots of Eq. (15) or Eq. (16). $\Phi'(s)$ is the derivative of Φ with respect to s and is given by:

$$\Phi'(s)=Z(s)kl\cosh(kl)+\frac{klY_{11}^E wh}{c}\sinh(kl)+Z'(s)s\sinh(kl) \tag{18}$$

The transient displacement response of the PZT under an electrical excitation $E_3(t) = V(t)/h$ can then be obtained using Borel's theorem (Thomson, 1950) as:

$$u(x,t)=d_{31}Y_{11}^E w\int_0^t V(\tau)f(x,t-\tau)\,d\tau \tag{19}$$

Once u(x,t) is determined, the strain (S_{11}) and stress (T_{11}) within the PZT may be determined as:

$$\begin{cases} S_{11}=\dfrac{\partial u(x,t)}{\partial x} \\ T_{11}=Y_{11}^E\left[S_{11}-d_{31}E(t)\right] \end{cases} \tag{20}$$

Note: the dynamics of the PZT actuator itself are not fully considered because it is assumed here that the induced strain is expressed as $d_{31}E(t)$. The induced strain has a slight time delay behind the applied electrical voltage as a result of the electrical and mechanical dissipation of the PZT itself. The delay time is on the order of magnitude of 10^{-6} to 10^{-5} second (Amos and Chen, 1978).

The electrical displacement and electrical current may also be determined by substituting Eq. (20) into the piezoelectric constitutive relation (the second equation). The current passing through the PZT actuator and the electrical displacement, D_3, are related by:

$$\begin{aligned}\int_0^t i(\tau)\,d\tau&=\int_0^l D_3(x,t)\,w\,dx=wd_{31}\int_0^l T_{11}(x,t)\,dx+\frac{\epsilon_{33}^T lw}{h}V(t)\\&=d_{31}^2Y_{11}^E wu(l,t)+(\epsilon_{33}^T-d_{31}^2Y_{11}^T)\frac{wl}{h}V(t)\end{aligned} \tag{21}$$

It is assumed here that a free PZT actuator may be considered a perfect capacitor. The electrical damping of PZT is not included.

A PZT actuator-driven single-degree-of-freedom spring-mass-damper system, as illustrated in Fig. 2, is used as an example to demonstrate the utility of the transient electro-mechanical

model. The general impedance Z(s) for the system may be expressed as:

$$Z(s) = m\frac{s^2+\omega_s^2}{s} + C \qquad (22)$$

where ω_s is the resonant frequency of the one-degree-of-freedom system and C is the damping of the system.
The roots of $\Phi(s)=0$ include s_0 and s_n and their complex conjugates s^*_0 and s^*_n:

$$\begin{cases} s_0 \approx -\alpha + i\sqrt{\omega_s^2 + Y_{11}^E wh/lm} \\ s_n \approx -\beta_n + n\pi ci/l \end{cases} \qquad (23)$$

where α and β_n are positive real numbers. β_n is typically much smaller than α (=C/2m).

Equation (19) may be used to determine the transient displacement response of a system for any type of voltage activation V(t). This paper will only discuss the step voltage activation. The displacement field under a step voltage, V_0, activation may be easily determined as:

$$u(x,t) = d_{31} Y_{11}^E w V_0 \sum_{s_m, s_m^*} \frac{\phi(x, s_m)}{\Phi'(s_m)\, s_m} (e^{s_m t} - 1) \qquad (24)$$

The displacement of the mass, u(l,t), the interaction force between the PZT actuator and the mass $T_{11}(l,t)wh$, and the electrical current passing through the PZT actuator can then be determined from Eqs. (24), (20), and (21), respectively.

It is necessary to mention that the current passing through the PZT actuator cannot be accurately determined unless the mechanical loss and dielectric loss of the PZT actuator are included in the analysis. If the system resonance frequency is much below the first resonant frequency of the PZT actuator itself, which for a PZT patch 5 cm long is in the 20 kHz range, the current given by the first term (u(l,t) term) provides acceptable results at $t > 0$. However, further investigation is still needed regarding the influence of actuator mechanical and electrical loss on the transient behavior of PZT actuator-driven active structures.

Numerical Case Studies

Consider a PZT of length l = 5.08 cm (2 in), width w = 2.54 cm (1 in), and thickness h = 0.2 cm (0.079 in) driving a one-degree-of-freedom spring-mass-damper system. The material properties of the PZT used in the theoretical simulation are listed in Table 1. The undamped natural frequency of the spring-mass-damper system, f_s, is 500 Hz. The mass, m, is assumed to be 2 Kg. The damping ratio, ξ, is assumed to be 1%, yielding a damping coefficient C of 125.6 Ns/m ($C=4\pi m\xi f_s$). The stiffness of the spring, K, is given by $m(2\pi f_s)^2$. The voltage excitation is a step function and V_0 is 100 volts.

Table 1: Material Properties of G-1195 PZT (from Piezo Systems, Inc.)

d_{31} (m/volt)	Y_{11}^E N/m^2	ρ kg/m^3	ϵ_{33}^T Farads/m
-180×10^{12}	6.3×10^{10}	7600	1.5×10^{-8}

Figure 3 shows the transient displacement response of the mass, u(l,t), normalized by the steady-state displacement response $u(l,\infty)$. The peak overshoot is almost 100% of the steady-state displacement response which may also be determined based on the static equilibrium as $K_A x_{in}/(K_A+K)$. The oscillation is not at 500 Hz but at the damped resonant frequency of the entire PZT and spring-mass-damper system, which is about 575 Hz as approximated by $[(K_A+K)/m]^{1/2}/(2\pi)$. The settling time for the system is 0.1 second (5% of the steady-state response). The decay rate in this case is apparently governed by the damping of the spring-mass-damper system.

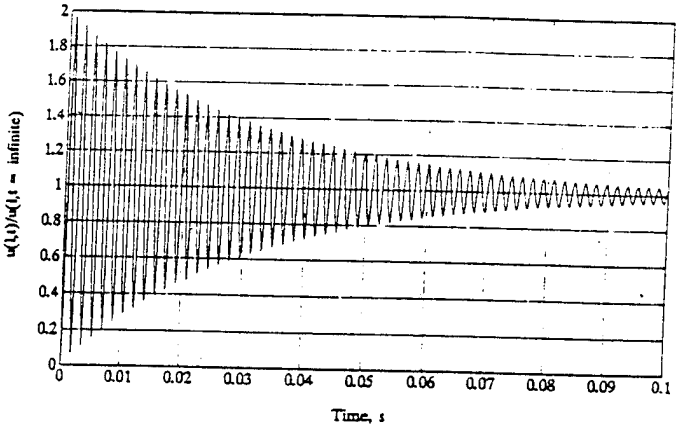

Figure 3. Normalized transient displacement of the mass.

The interaction force between the PZT actuator and the mass is shown in Fig. 4. The result shown in Fig. 4 is also normalized with respect to the steady-state interaction force which may be determined according to Eq. (1). The overshoot is about 30% of the steady-state interaction force. The frequency of the oscillation is also at 575 Hz.

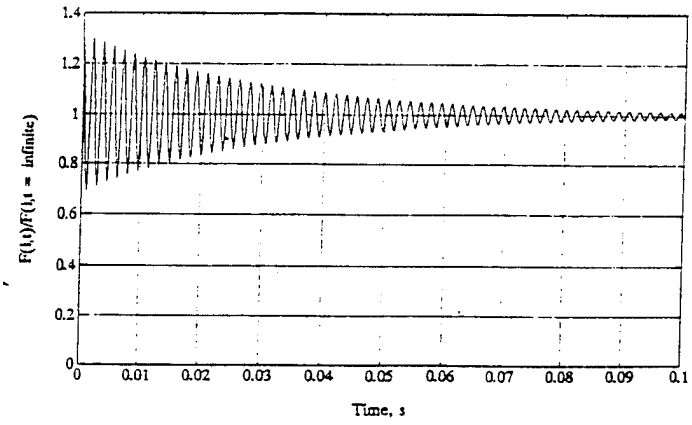

Figure 4. Normalized interaction force between the PZT actuator and the mass.

The electrical current passing through the PZT actuator is plotted in Fig. 5. The current oscillation, as illustrated in Eq. (21), is directly related to the mechanical ring-down of the system.

In the estimation of the transient displacement using Eq. (24), the first 21 terms (42 poles) are used. In fact, it is found that the result predicted using only the s_0 and s_0^* terms is almost the same as that calculated using 21

terms in this case study because the dominant resonant frequency of the entire system (PZT actuator and the spring-mass-damper system) is much below the first resonant frequency of the PZT actuator itself.

Conclusion

A theoretical model to determine the transient electro-mechanical response of active structures driven by PZT actuators is presented in this paper. The dynamic interaction between induced strain actuators and their host structures is incorporated in the model. A simple PZT actuator-driven one-degree-of-freedom spring-mass-damper system is used to demonstrate the utility of the transient electro-mechanical model. Further investigation of this subject includes incorporation of the mechanical and electrical damping of the PZT actuator and its application to complex structures, including beams, plates, and shells.

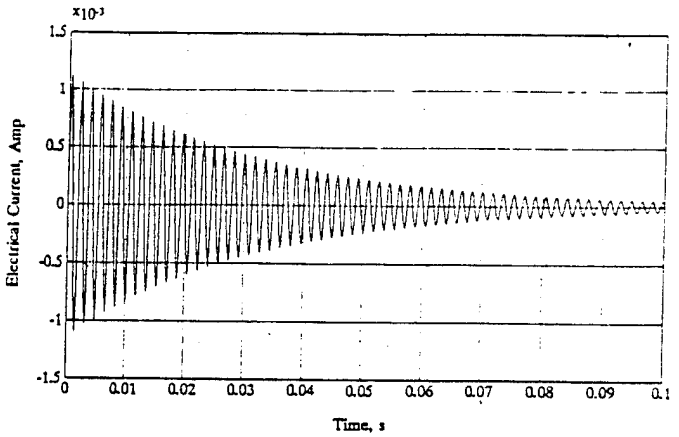

Figure 5. Transient current passing through the PZT actuator.

Acknowledgement

The authors would like to acknowledge the support of Office of Naval Research, Grant No. ONR 00014-92-J-1170, Dr. K. Ng, Technical Monitor.

References

Amos, D. E. and Chen, P. J., 1978, "One Dimensional Linear Dynamic Electromechanical Responses of Ferroelectric Ceramics," *Journal of Applied Mechanics,* Vol. 45, pp. 749-754.

Banks, H. T., Wang, Y., Inman, D. J., and Slater, J. C., 1992, "Variable Coefficient Distributed Parameter System Models for Structures with Piezoceramic Actuators and Sensors", N. C. State University Report, CRSC-TR92-9.

Chen, P. J. and Peerey, P. S., 1979, "One Dimensional Dynamic Electromechanical Constitutive Relations of Ferroelectric Materials", *Acta Mechanica,* Vol. 31, pp. 231-241.

Crawley, E. F. and Anderson, C. R., 1989, Detailed Models for Piezoceramic Actuation of Beams, AIAA Conf. Paper 89-1388-CP, pp. 2000-2010.

Dimitriadis, E. K., Fuller, C. R., and Rogers, C. A., 1989, Piezoelectric Actuators for Distributed Noise and Vibration Excitation of Thin Plates, Proceedings, 8th ASME Conf. on Failure Prevention, Reliability, and Stress Analysis, Montreal, pp. 223-233.

Eyges, L., 1972, "The Classical Electromagnetic Field", Dover Publications, Inc., New York.

Liang, C., Sun, F. P., and Rogers, C. A., 1993a, "An Impedance Method for Dynamic Analysis of Active Material Systems", *ASME Journal of Vibration and Acoustics*, in press. Also in Proceedings, 34th SDM Conference, LaJolla, CA, April 19-21, 1993.

Liang, C., Sun, F. P., and Rogers, C. A., 1993b, "Coupled Electro-Mechanical Analysis of Piezoelectric Ceramic Actuator Driven Systems - Determination of the Actuator Power Consumption and System Energy Transfer", Proceedings, SPIE's 1993 North American Conference on Smart Structures and Materials, Albuquerque, 1-4 February, 1993; in press.

Meirovitch, L., 1967, "Analytical Methods in Vibrations", Macmillan Publishing Co., Inc., New York.

Thomson, W. T., 1950, "Laplace Transformation - Theory and Engineering Applications", Prentice-Hall, Inc., New York.

C-4 Design of Active Control Systems using Eigenanalysis, C. R. Fuller and R. A. Burdisso, 3rd International Congress on Air- and Structure-Borne Sound and Vibration, Montreal, Canada, 13-15 June 1994, keynote address.

DESIGN OF ACTIVE CONTROL SYSTEMS USING EIGENANALYSIS

Chris R. Fuller
Ricardo A. Burdisso
Vibration and Acoustics Laboratories
Mechanical Engineering Department
Virginia Polytechnic Institute and State University
Blacksburg, VA 24061-0238
U.S.A.

ABSTRACT

A design procedure for the location and shape of the control transducers for feedforward controlled active systems is outlined. The procedure is based upon the relationship of the controlled eigenvalues and eigenfunctions of the controlled system to the control load and optimal compensator characteristics. The use of the design procedure is illustrated through modification of dynamics of a beam and radiation control from a plate. The extension of the method to complex structures using numerical techniques such as FEM/BEM and the impact of random broadband disturbances is briefly discussed. The method provides a basis by which feedforward controlled systems can be designed for specified performance requirements in contrast to the largely "ad hoc" methods presently used.

INTRODUCTION

Feedforward active control has shown much potential to alleviate problems in sound and vibration at audio frequencies [1,2]. The design of feedforward controllers is traditionally defined by an "ad hoc" selection of the number and location of actuators and sensors based upon a physical understanding of the behavior of uncontrolled and controlled systems. This empirical design contrasts with the large number of analytical tools available to designers of feedback controllers. Techniques such as pole allocation, various state space design methods, optimal control and so forth, are extensively used in feedback control applications [3]. The lack of mathematically based design formulations in feedforward control stems from the small amount of research carried out on understanding the behavior of feedforward controlled systems. The prevailing view in the feedforward control community is that the control "cancels" the disturbance an observation which is certainly true in a mathematical sense for steady state disturbances. However, it has been demonstrated in a number of different systems that, physically, the disturbance source "sees" a modified input or radiation impedance (see for example the work by Snyder and Hansen [4]).

Recent analytical work by the authors has demonstrated that this change in input impedance is a result of the feedforward controlled structure or system having new eigenvalues and eigenvectors [5,6]. It should be stressed here that these new eigen characteristics only appear for inputs which are coherent with the feedforward disturbance. In contrast to feedback control, the system will respond with

the uncontrolled eigenvalues to any other uncorrelated disturbance. The analysis outlined in reference 5 suggests a design approach for feedforward control systems. That is, given a desired set of modal properties, a feedforward controller can then be designed to force or adapt the controlled system to have those characteristics.

In this paper we summarize work in which a design formulation is developed for a single-input, single-output (SISO) feedforward controller to actively modify the dynamics of a distributed elastic system. Although the formulation is written in terms for a structural system, it is equally applicable to acoustic systems. The design formulation is applied to a problem in dynamics and then the extension to the control of sound radiation is outlined. The paper finishes with a brief discussion of the extension of the method to discretized complex systems, i.e. FEM/BEM analysis, and broadband disturbances.

The work described in this paper is largely a summary and combination of previous work by the authors published in a number of papers [5,7,8,9].

FEEDFORWARD CONTROLLED EIGENPROPERTIES

The structural system is assumed to be an undamped, linear, time invariant, distributed parameter system. Thus, the equations of motion can be written in the form of a partial differential equation as

$$L[W(D,t)] + m(D)\frac{\delta^2 W(D,t)}{\delta t^2} = f(D)\,F(t) + u(D)\,U(t) \qquad (1)$$

where W(D,t) is the displacement in the domain D, L[.] is a self-adjoint linear differential operator, and m(D) is the mass distribution. The disturbance or "primary" input is defined by the time dependent amplitude F(t) and its spatial distribution f(D). The system is controlled by a coherent "secondary" control input defined by the amplitude U(t) and its spatial distribution u(D) as shown in Figure 1. Feedforward control approaches are used in applications where the disturbance excitation is stationary, i.e. single and multiple frequencies as well as random inputs. Then, the disturbance input F(t) is assumed stationary and thus W(D,t) and U(t) are also stationary variables. By taking the Fourier Transform, the analysis can be carried out on the frequency domain. That is,

$$L[W(D,\omega)] - \omega^2 m(D)\,W(D,\omega) = f(D)\,F(\omega) + u(D)\,U(\omega) \qquad (2)$$

Solving for the eigenvalues and eigenfunctions of the homogeneous part of Eq. (2), the response of the system can be written in terms of the mode shape functions by using the expansion theorem as

$$W(D,\omega) = \sum_{n=1}^{N} q_n(\omega)\,\phi_n(D) \qquad (3)$$

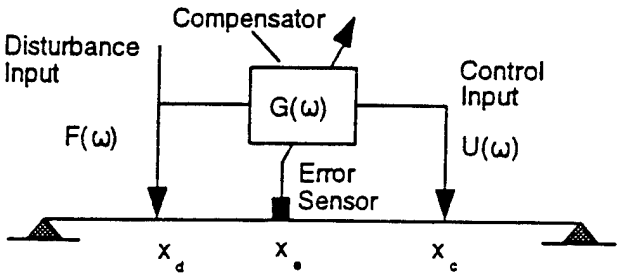

Figure 1--Schematic of a SISO feedforward control system

where $q_n(\omega)$ is the n^{th} generalized coordinate, $\phi_n(D)$ is the n^{th} eigenfunction, and N is the number of modes included in the analysis. The eigenfunctions satisfy the orthogonality conditions

$$\int_D \phi_n(D)\, m(D)\, \phi_m(D) dD = \delta_{nm} \quad ; \quad \int_D \phi_n(D)\, L[\phi_m(D)] dD = \delta_{nm}\, \omega_n^2 \qquad (4a,4b)$$

where δ_{nm} is the Kronecker delta function, and ω_n is the n^{th} natural frequency associated to the eigenfunction $\phi_n(D)$.

The generalized coordinate $q_n(\omega)$ is obtained by replacing Eq. (3) into (2), premultiplying by $\phi_m(D)$ and using the orthogonality conditions of Eq. (4). Then,

$$q_n(\omega) = [f_n F(\omega) + u_n U(\omega)]\, H_n(\omega) \qquad (5)$$

where $H_n(\omega)=(\omega_n^2-\omega^2+j2\beta_n\omega_n\omega)^{-1}$ is the n^{th} modal frequency response function, j is the imaginary number, β_n is the n^{th} modal damping ratio included here to bound the response at resonance, and f_n and u_n are the n^{th} modal disturbance and control forces defined by the inner products

$$f_n = \int_D \phi_n(D)\, f(D) dD \quad ; \quad u_n = \int_D \phi_n(D)\, u(D) dD \qquad (6a,6b)$$

In the SISO feedforward control system considered here, the optimum frequency component of the control input stems from driving to zero, a response of the system which is referred here as the error variable. The error variable can also be represented as the linear contribution of each modal response as follows

$$e(\omega) = \sum_{n=1}^{N} q_n(\omega)\, \xi_n \qquad (7)$$

where ξ_n is the n^{th} modal component of the error variable that is a function of the physical characteristics of the error transducer implemented. The modal error component indicates the relative importance assigned to each mode.

Replacing Eq. (5) into (7), the error signal can then be set to zero to solve for the optimum control input in terms of the modal quantities. That is

$$U(\omega) = -\sum_{n=1}^{N} \xi_n f_n H_n(\omega) \Big/ \sum_{n=1}^{N} \xi_n u_n H_n(\omega)\, F(\omega) = G(\omega)\, F(\omega) \qquad (8)$$

where $G(\omega)$ is the feedforward compensator. In this analysis the control system is assumed to be causal, and thus the compensator $G(\omega)$ is realizable [10]. For noncausal or non-minimum phase control systems, the ideal compensator is not implementable as discussed later. However, the approach presented here can still be used as a design tool. For single frequency and multiple frequencies disturbances, where causality is not an issue, the proposed design formulation is also applicable.

The feedforward compensator, $G(\omega)$, is the transfer function that relates the control input $U(\omega)$ to the disturbance input $F(\omega)$. The controller or compensator $G(\omega)$ in Eq. (8) is defined as the ratio of two transfer functions, where the numerator is the transfer function between the disturbance or "primary" input and the error variable $T_{de}(\omega)$, while the denominator is the transfer function between the "secondary" control input and the error variable $T_{ue}(\omega)$. The controller $G(\omega)$ can provide valuable information as to the performance of the control system. For example, the poles of $G(\omega)$ would indicate

the frequencies at which the control effort would be unbounded if no damping was present in the system.

The traditional view of feedforward control techniques is of "active cancellation" where the uncontrolled modes excited by the "primary" input are canceled by a "secondary" input of appropriate magnitude and phase driving the same uncontrolled modes. This view arises from the fact that the system response can be obtained by superimposing the response of the disturbance and control inputs as suggested by Eq. (2). The unwanted consequence of this view is that the design of feedforward controllers has become an empirical technique based largely on a physical understanding of the uncontrolled system. Recent work has shown that the mechanisms for acoustic control (for example) with stationary disturbances is that, in general, the active source modifies the radiation impedance of the disturbance source, thus leading to less power radiated [4]. For active vibration control (AVC) as well as active structural acoustic control (ASAC), the authors have recently demonstrated that feedforward controlled systems have new eigenvalues and eigenfunctions as in feedback control [6,11]. For the sake of brevity, only the main concepts of the controlled system eigen-analysis are presented here, while a complete description of this formulation can be found in Reference 5.

For this analysis the controlled system is assumed to be undamped. The dynamic behavior of the controlled system is governed by the characteristics of the controller $G(\omega)$. Multiplying and dividing Eq. (8) by the product of the modal frequency response functions $H_n(\omega)$, $G(\omega)$ can be written as the ratio of two polynomials as follows [5,6]

$$G(\omega) = -N(\omega)/P(\omega) \tag{9}$$

with

$$P(\omega) = \sum_{n=1}^{N} \xi_n u_n \prod_{\substack{m=1 \\ m \neq n}}^{N} (\omega_m^2 - \omega^2) \tag{10}$$

The polynomial $P(\omega)$ in the denominator can be shown to be the characteristic polynomial of the controlled system. Thus, the eigenvalues of the controlled system, $(\omega_l)^2$, are obtained by solving for the roots of $P(\omega)$, $P(\omega_l)=0$. It is not difficult to show that $P(\omega)$ is the numerator of the transfer function $T_{oc}(\omega)$ and, thus, the controlled system eigenvalues are the zeros of $T_{oc}(\omega)$ [6]. This implies that we are canceling the zeros of $T_{oc}(\omega)$ with the poles of $G(\omega)$. The order of the polynomial in Eq. (10) is (N-1) in the variable ω^2, and thus the controlled system has (N-1) new eigenvalues. It can be shown that the controller has reduced the dynamic-degree-of-freedom of the system by one through the constraint imposed on the structure by driving the error signal to zero. The controlled system eigenfunction $\phi_l(D)$ associated with the natural frequency ω_l is easily computed once the controlled system eigenvalues have been determined. They are obtained as a linear combination of the uncontrolled modes, since they have been used as an expansion basis. Then,

$$\phi_l(D) = \sum_{n=1}^{N} \Gamma_{ln} \phi_n(D) \tag{11}$$

where the expansion coefficients are

$$\Gamma_{ln} = C_l u_n / (\omega_l^2 - \omega_n^2) \tag{12}$$

The constant C_l in Eq. (12) is included since the controlled mode shapes are arbitrary to a constant multiplier, and it can be computed by requiring $\sum_n (\Gamma_{ln})^2 = 1$. It is worth while mentioning that Eq. (12) is identical to the relationship found in the computation of the modified eigenfunctions in dynamic local modification techniques [12]. Thus, feedforward control can also be used to actively modify the dynamics of a structure without the drawback of the unwanted increase in system mass

generally associated with structural modification methods [12]. Another important observation is that from Eqs. (11) and (12) it can be observed that the eigenproperties of the controlled system are a function of only the control input through u_n and of the error variable to be minimized through the modal error components ξ_n and they are independent of the disturbance input. This conclusions are again similar to those as found in feedback controlled systems.

EIGENVALUE ASSIGNMENT DESIGN APPROACH

The theory in the previous section shows that a system under feedforward control has different modal properties from the uncontrolled system with respect to the excitation $F(\omega)$. This implies that by proper control design a structure could be actively modified to behave with new dynamic properties as required by the analyst. The design of feedback control systems is related to the computation of the feedback gains, where techniques such as eigenvalue assignment, eigenvector assignment, linear optimal control, and others are extensively used to this end. On the other hand, the general design of a SISO feedforward control systems involves the selection of the control input distribution, determined by the modal components u_n, and of the error quantity to be minimized defined by the modal error components ξ_n. In contrast to feedback control where a substantial number of mathematical design formulations are available, analytical feedforward design approaches are effectively non-existent in the literature. In the following, a feedforward control design procedure based on the eigenvalue assignment technique will be presented. Here, it is assumed the control load is fixed and thus the modal control inputs u_n are known. The design approach will then focus on the selection of the proper error sensor, whose output will be minimized, in order to drive the closed loop behavior as required.

In the eigenvalue assignment technique, the controlled system eigenvalues are selected in advance and then the error sensor is designed so as to match the desired controlled system poles. This implies that the (N-1) controlled eigenvalues $(\omega_\ell)^2$ as well as the N modal control forces u_n are known quantities and the modal components of the error variable ξ_n are to be computed. Substituting the selected controlled system eigenvalues into the characteristic polynomial in Eq. (10), we can write

$$P(\omega_\ell) = \sum_{n=1}^{N} \xi_n \, u_n \prod_{\substack{m=1 \\ m \neq n}}^{N} (\omega_m^2 - \omega_\ell^2) = 0 \qquad \ell = 1, \cdots, (N-1) \tag{13}$$

which can also be written in matrix form as follows

$$\begin{bmatrix} S_{11} & S_{12} & \cdots & S_{1N} \\ S_{21} & S_{22} & \cdots & S_{2N} \\ \vdots & \vdots & \ddots & \vdots \\ S_{(N-1)1} & S_{(N-1)2} & \cdots & S_{(N-1)N} \end{bmatrix} \begin{Bmatrix} \xi_1 \\ \xi_2 \\ \vdots \\ \xi_N \end{Bmatrix} = \begin{Bmatrix} 0 \\ 0 \\ \vdots \\ 0 \end{Bmatrix} \quad \text{with} \quad S_{sn} = u_n \prod_{\substack{m=1 \\ m \neq n}}^{N} \left(\omega_m^2 - \omega_\ell^2 \right) \tag{14}$$

The dimension of the matrix in Eq. (14) is (N-1)xN. Careful observation of Eq. (14) shows that if one of the controlled eigenvalues is identical to one of the uncontrolled system eigenvalues, i.e. $\omega_s = \omega_\ell$ only the term S_{sn} in the s^{th} row in the above matrix does not vanish. Therefore, to satisfy the s^{th} equation ξ_n must also be zero. This implies that the s^{th} eigenfunction is unobservable by the error sensor and thus it can not be affected by the control input. The linear system in Eq. (14) is such that any multiple of the vector $\{\xi_1, \xi_2, \ldots, \xi_N\}^T$ is a solution, and therefore the only relevant information is the relative value between the modal error components. Assuming the N^{th} mode is observable, ξ_N is set to unity and by suitably partitioning the matrices in Eq. (14), the modal components can be obtained by solving the reduced linear system of equations

$$\begin{bmatrix} S_{11} & S_{12} & \cdots & S_{1(N-1)} \\ S_{21} & S_{22} & \cdots & S_{2(N-1)} \\ \vdots & \vdots & \ddots & \vdots \\ S_{(N-1)1} & S_{(N-1)2} & \cdots & S_{(N-1)(N-1)} \end{bmatrix} \begin{Bmatrix} \xi_1 \\ \xi_2 \\ \vdots \\ \xi_{N-1} \end{Bmatrix} = - \begin{Bmatrix} S_{1N} \\ S_{2N} \\ \vdots \\ S_{(N-1)N} \end{Bmatrix} \tag{15}$$

The vector $\{\xi_1,\xi_2,...,\xi_{N-1},1\}^T$ defines the error sensor in the modal domain. Thus, this modal information needs to be transformed into a physical sensor on the structure, and to this end two basic approaches can be implemented. One method utilizes an array of discrete point sensors, i.e. accelerometers, strain gages and so forth. The error variable is obtained by summing the weighted discrete sensor signals. Assuming N_s discrete point displacement sensors, the modal error component becomes

$$\xi_n = \int_D \sum_{i=1}^{N_s} b_i \, \delta(D_i - D) \, \phi_n(D) \, dD \tag{16}$$

where b_i is the weight of the i^{th} point sensor located at D_i, and $\delta(D_i-D)$ is the Dirac delta function. Then, Eq. (16) reduces to

$$\xi_n = \sum_{i=1}^{N_s} b_i \, \phi_n(D_i) \qquad n = 1,\cdots,N \tag{17}$$

Equation (17) can also be written in matrix form as

$$[A] \{b\} = \{\xi\} \tag{18}$$

where the components of matrix [A], which relates the error quantity in the physical domain to the modal domain, are $A_{ni}=\phi_n(D_i)$, and $\{b\}=\{b_1,b_2,...,b_N\}^T$ is the weighting vector. Assuming $N \geq N_s$ the solution of Eq. (18) can be obtained by the pseudo-inverse technique [13]. That is,

$$\{b\} = \left([A]^T [A]\right)^{-1} [A]^T \{\xi\} \tag{19}$$

The sum of the output of N_s discrete point sensors is a design approach applicable to any complex structure. However, implementation of this approach could result in considerable signal conditioning effort, particularly in "real-time" digital control where all calculation must be completed in one sampling period. The use of distributed sensors has recently gained acceptance in the control community for their inherent built in filtering capability of the system response. The flexibility, light weight and toughness properties of polyvinylidene fluoride polymer (PVDF) films have found application as distributed structural sensors in active control [14-18]. The PVDF film sensor is mounted on the surface of the structure and yields a response proportional to the integral of the strain over the surface of application. In particular, one dimensional problems are ideally suited for the use of PVDF distributed sensor because any desirable weighted response can be obtained by varying the width and polarity of the sensor as a function of the axial coordinate. The design of a physical PVDF sensor from the modal error components ξ_n will be presented for a beam problem. Thus, the domain D becomes the x coordinate in the following derivation.

Since PVDF film is a strain sensor, the modal error component becomes [7,14]

$$\xi_n = -\alpha h \int_0^L b(x) \frac{d^2\phi_n(x)}{dx^2} dx \tag{20}$$

where h is the distance of the upper beam surface to the neutral axis here assumed constant for the sake of clarity in the presentation; α is a constant of proportionality that relates the film electrical and mechanical properties to the surface strain; and b(x) is the function that weights the strain along the beam, and it is determined by the PVDF film's geometry. This function dictates the width of the film and can take either positive or negative values. The negative effective width can be implemented by segmenting the film with out-of-phase wiring of the negative segments, i.e. inverting the polarity of the sensors. In order to take advantage of the orthogonality conditions of the modes, the weight function b(x) is expanded as follows

$$b(x) = \sum_{m=1}^{N} b_m \, EI(x) \frac{d^2\phi_m(x)}{dx^2} \tag{21}$$

To solve for the unknown expansion coefficients b_m, Eq. (21) is replaced into Eq. (20) and using the orthogonality condition of Eq. (4b) gives

$$b_m = -\frac{\xi_m}{\alpha h \omega_m^2} \tag{22}$$

That yields the weight function in term of the computed modal error components as follows

$$b(x) = \sum_{n=1}^{N} \frac{\xi_n}{\omega_n^2} EI(x) \frac{d^2\phi_n(x)}{dx^2} \tag{23}$$

In this design formulation, the control input was assumed fixed and the error sensor is then configured to achieve the sought controlled system characteristics. However, inspection of the characteristic polynomial in Eq. (13) reveals that the design process could have also been stated as: assuming the error sensor fixed, the control input distribution is then designed to obtain the desired poles. This is simply accomplished by replacing ξ_m by u_n and vice versa in Eqs. (13) through (23). These two eigenvalue assignment design concepts differ only in that the associated controlled eigenfunctions are different since the expansion coefficients Γ_{cn} in Eq. (12) are determined by u_n. Greater design flexibility is possible if both the control load distribution and the weighted error variable are designed simultaneously, as it will be discussed later.

Design Example: Control of motion of a simply supported beam

The applicability of the design formulation presented here is demonstrated for a uniform simply supported beam. The beam is made of steel and has bending stiffness EI=93 N.m^2, mass per unit length m=2.181 N.sec^2/m^2, and beam length L=0.38 m. To compute the response of the system, it is assumed a modal damping ratio of 0.1% in all modes (β_n=0.001), and only the first four modes are included in the analysis. The beam is excited by a concentrated force located at x_d=0.1L, and the response is controlled by another point force placed at x_c=0.65L. In this example, the error sensor, whose output is minimized, is a distributed PVDF shaped film mounted on the beam surface. This sensor is designed to induce the desired dynamic characteristics of the structure. Since the proposed design formulation is based on the modal representation of the system's response, the eigenproperties of the uncontrolled beam to be used in the analysis are given by

$$\omega_n = (n\pi/L)^2 \sqrt{EI/m} \quad ; \quad \phi_n(x) = \sqrt{2/m\,L}\ \mathrm{Sin}(n\pi\, x/L) \qquad (24a,24b)$$

In this example problem, we seek to arbitrarily shift the natural frequencies of the system in the frequency range of the first four modes. As mentioned before, the controlled system has one less dynamic degree of freedom due to the constraint imposed in the system as result of driving the error signal to zero. Thus, the number of controlled modes is three and the desired beam-control system natural frequencies, ω_r, (which are arbitrarily chosen) are shown in Table 1. The uncontrolled natural frequencies are also shown in the same table. These desired natural frequencies are replaced into Eq. (15) to compute the coefficients of the matrix and independent vector. Solving this linear system of equations for the modal error components ξ_n defines the error sensor in the modal space. To convert this into a PVDF distributed sensor, the modal components ξ_n are replaced into Eq. (23) where the weight function b(x) is computed. This function determines the width profile of the PVDF sensor which is shown in Figure 2.

Table 1--Uncontrolled and Controlled System Natural Frequencies

Mode	Natural Frequency [Hz]			
	Uncontrolled, $f_n=\omega_n/2\pi$		Controlled, $f_r=\omega_r/2\pi$	
	Analysis	Experimental	Analysis	Experimental
1	71.0	75	425	424
2	284.1	278	780	750
3	639.3	626	1000	1030
4	1136.5	1120		
5	1775.8	1450		

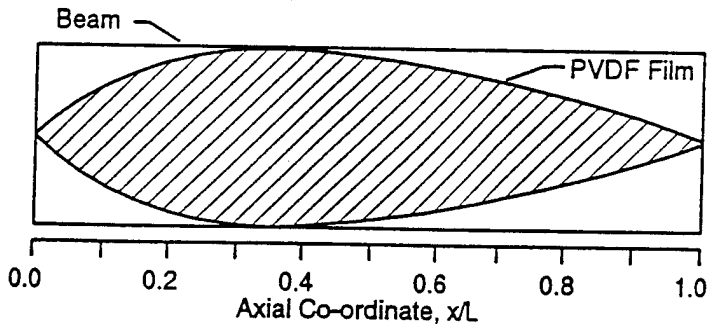

Figure 2--PVDF film sensor geometry

To illustrate the dynamic behavior of the beam before and after control, the acceleration response at the input force location was computed. The acceleration response is obtained by multiplying Eq. (3) by ω^2. Assuming a unit amplitude of the input force, the magnitude of the acceleration before and after control at x_d are shown in Figure 3 as function of the frequency ω. The dashed line is the analytical response of the uncontrolled beam obtained by using Eqs. (3) and (5) and setting $U(\omega)$ to zero. The continuous line corresponds to the controlled system calculated from Eqs. (3), (5) and (8) and shows resonance behavior at the preselected frequencies ω_r. Thus, upon driving the weighted response output from the PVDF sensor to zero, the beam-control system has the desired eigenvalues. Note that the results of Figure 3 were calculated in the frequency domain and the curves were obtained by

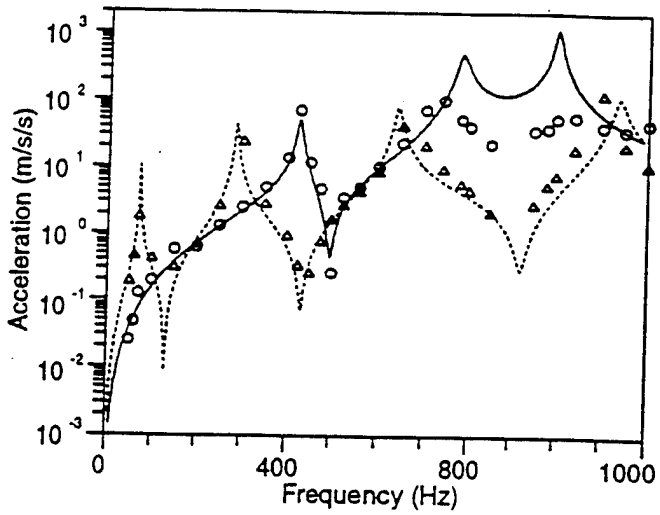

Figure 3--Acceleration at disturbance force location; Uncontrolled --- Analytical, ΔΔΔ Experimental Controlled —— Analytical, ooo Experimental

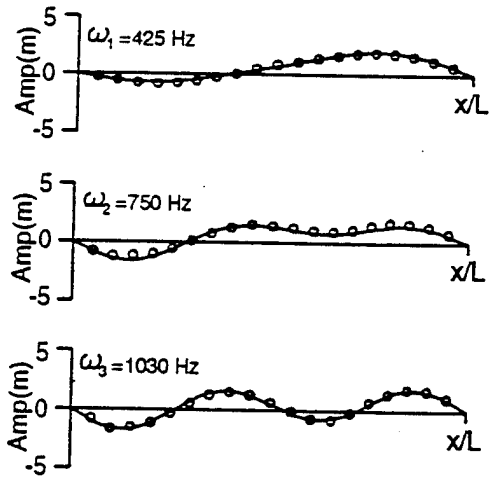

Figure 4--Controlled system eigenfunctions; —— Analytical, ooo Experimental.

evaluating at discrete frequencies. The results, thus, represente the best possible attenuation achievable over the bandwidth. Whether this is physically realizable depends upon the time domain response of the controlled system, i.e. wether it is causal, non-minimum phase etc. The associated controlled eigenfunctions, computed using Eqs. (11) and (12), are shown in Figure 4.

The above numerical example was also experimentally verified as described in reference 7. The experimentally determined values are plotted in Figures 3 and 4 and good agreement with the theory is seen. It should be noted that the computed mode shapes in Figure 5 were calculated from the individual eigenfunction expressions in eq.(11) and (12), rather than the total response of the system at the resonance points. A similar approach has demonstrated how it is possible to design the controller to cause a homogeneous beam to behave exactly as a beam (both eigenvalues and eigenvectors) with an attached mass-spring system [19].

EIGENVALUE-EIGENFUNCTION ASSIGNMENT DESIGN APPROACH

In this case, the controlled system eigenfunctions as well as the eigenvalues are preselected in advance using an eigenvalue-eigenfunction assignment technique. The main application of this approach would be in active structural acoustic control (ASAC) where the radiation efficiency of the controlled mode shapes are as important as the resonance conditions [20].

The main goal in ASAC is for the control system to render a controlled response that poorly couples with the acoustic medium, thus resulting in minimum radiated sound power. This objective can be accomplished if two conditions are met as follows:

(i) Firstly, the resonant frequencies of the controlled structure must lay away from the dominant part of the disturbance input spectrum. In other words, the controlled system resonances should be detuned from the excitation input.

(ii) Secondly and more important, the controlled or residual structural response should be dominated by a linear contribution of weak radiating modes, i.e. the new eigenfunctions.

As mentioned in the previous section, the controlled system has new resonant frequencies and associated eigenfunctions that are only a function of the selected actuator and sensor. Thus, this concept can be merged with the above conditions to yield an efficient design approach. The design formulation proposed here can be stated as to find the optimum actuator and sensor configuration that yields a controlled structure with eigenproperties that satisfied the above two conditions. The work summarized here is reported in detail in reference 9.

We thus seek the optimum expansion coefficients Γ_m that will render the controlled eigenfunctions $\phi_\ell(D)$ to have a minimum radiation efficiency. To achieve this requirement, we minimize the controlled modal radiation efficiency at frequency ω [9]

$$\sigma_\ell(\omega) = \frac{1}{A_r \rho c} \frac{\{\Gamma_\ell\}^T [\Pi(\omega)] \{\Gamma_\ell\}}{\{\Gamma_\ell\}^T [V(\omega)] \{\Gamma_\ell\}} \tag{25}$$

such that $\{\Gamma_\ell\}^T\{\Gamma_\ell\}=1$. In Eq. (25), $[\Pi(\omega)]$ is the uncontrolled power radiated matrix with the (n,m) element is given by

$$\Pi_{nm}(\omega) = \iint_A \frac{p_n p_m^*}{\rho c} dA \tag{26}$$

where p_n is the complex modal pressure computed over the hemisphere A; $[V(\omega)]$ is the uncontrolled mean square velocity matrix with the (n,m) element given by

$$V_{nm}(\omega) = \iint_{A_r} \phi_n(D)\, \phi_m(D)\, dD \tag{27}$$

where A_r is the area of the radiator; and ρc is the impedance of the acoustic medium.

The desired expansion coefficients that yield the lowest radiation efficiency for the controlled modes are obtained by minimizing $\sigma_\ell(\omega)$ in Eq. (25) with respect to the Γ_m with the constraint $\{\Gamma_\ell\}^T\{\Gamma_\ell\}=1$. This constraint minimization problem can be efficiently solved by recognizing that the stationary values of $\sigma_\ell(\omega)$ can be obtained by solving the eigenvalue problem

$$([\Pi(\omega)] - \sigma_\ell [V(\omega)] A \rho_0 c) \{\Gamma_\ell\}_d = \{0\} \qquad \ell = 1, \cdots, N \tag{28}$$

The orthogonality condition

$$\{\Gamma_i\}^T [\Pi(\omega)] \{\Gamma_j\} = \sigma_i \delta_{ij} \tag{29}$$

implies that the controlled modes are uncoupled with each other with respect to the far-field radiation.

As depicted in Eq. (12), the expansion coefficients Γ_m are a function of the modal control forces and both the uncontrolled and controlled natural frequencies. Thus, once the optimum expansion coefficients Γ_m are obtained from the eigensolution in Eq. (28), the modal control forces and the controlled eigenvalues, $(\omega_\ell)^2$, can be determined by solving the least square constrained minimization problem

$$\text{Minimize} \quad F(u_n, \omega_\ell) = \sum_{\ell=1}^{N-1} \sum_{n=1}^{N} \left| (\Gamma_m)_{opt} - c_\ell \frac{u_n}{\omega_\ell^2 - \omega_n^2} \right|^2 \tag{30}$$

$$\text{such that} \quad \sum_{n=1}^{N} u_n^2 = 1$$

$$(\omega_\ell^2)_{lower} \le \omega_\ell^2 \le (\omega_\ell^2)_{upper}$$

where the equality constraint represents the normalization of the modal control forces since the relative controllability of the modes is the only relevant information. The upper and lower limits of the inequality constraints on the values for the controlled system eigenvalues $(\omega_\ell)^2$ are selected based on the characteristic of the spectrum of the disturbance input.

The error sensor modal components ξ_n are determined from the characteristic equation of the controlled system in Eq. (13). Again assuming ξ_N=1, the modal components ξ_n are obtained by solving the linear system of equations in Eq. (15).

The controlled system is completely defined in terms of the optimum modal parameters, u_n and ξ_n. It is then convenient to study the performance of the ASAC system before these modal parameters are translated in realizable actuators and sensors.

Design Example: Radiation control from a plate

As an example calculation, the design formulation is applied to control the sound radiation from a baffled simply supported steel plate of size L_x=0.38m x L_y=0.30m x h=2 mm thick. Thus, the domain D becomes the (x,y) coordinates in this example. The input disturbance is assumed to be a point force acting at the center of the plate with white noise in 0-600 Hz frequency band. In this example, the objective is to control the volumetric modes (1,1), (3,1) and (1,3) modes in the 0-600 Hz bandwidth with a SISO controller. The eigenproperties of the simply supported plate are given by

$$\omega_n = \sqrt{D_p/\rho_p h}\left(\gamma_x^2 + \gamma_y^2\right) \quad ; \quad \phi_n(x,y) = (4/L_x L_y h \rho_p)^{1/2} \sin(\gamma_x x) \sin(\gamma_y y) \tag{31}$$

where $\gamma_x = \pi n_x/L_x$, $\gamma_y = \pi n_y/L_y$, $D = Eh/12(1-\nu^2)$ is the flexural rigidity, ρ_p is the plate density, and (n_x, n_y) are the modal indices traditionally used for rectangular panels that are associated to the n index in the theoretical analysis.

The first step in the design process is to find the desired controlled system eigenfunctions. The

single frequency of 300 Hz was selected to compute the matrices $[\Pi(\omega)]$ and $[V(\omega)]$ to form the eigenvalue problem of Eq. (28). The solution of the eigenvalue problem yielded three eigenvalues and associated eigenvectors. Since the SISO controller reduces the number of dynamic degree-of-freedoms by one, the desired expansion coefficients, $(\Gamma_m)_d$, are the first two eigenvectors. The radiation efficiency at 300 Hz, eigenvalues σ_p and associated expansion eigenvectors, $\{\Gamma_i\}_d$, of the desired controlled eigenfunctions are given in Table 2.

The optimum modal parameters, i.e. modal control and error components, can now be computed. The next step is to find the modal control forces, u_n, and controlled eigenvalues, $(\omega_p)^2$, that yield the desired expansion coefficients of Table 2. This is achieved by solving the minimization problem in Eq. (30) where the controlled eigenvalues $(\omega_p)^2$ are not constrained as in Eq. (30) because the spectrum of the excitation input is white noise. The minimization process was carried out by using the optimization IMSL routine DUNLSF (non-linear least squares problems) which yielded the optimum modal forces u_n shown in Table 3 and two controlled resonant frequencies at 399 and 700 Hz as shown in Table 4. These values yielded the expansion coefficients shown in columns 2 and 3 of Table 4. These coefficients are almost identical to the desired coefficients obtained from the solution of the eigenvalue problem in Eq. (28) and presented in Table 2. The modal control forces and controlled eigenvalues can now be used in the linear system of equations in Eq. (15) to solve for the modal error components, ξ_n, and they are given in Table 4. Note that this procedure could be used with any number of included modes; increasing the number of modes will simply increase the amount of computations required.

Table 2--Radiation efficiency and expansion coefficients of desired eigenfunctions

Radiation Efficiency, $\sigma_p x10^{-3}$		
	.239	1.13
Desired Coefficients, $\{\Gamma_i\}_d$		
(1,1)	-.367	0.128
(3,1)	0.361	-.893
(1,3)	0.857	0.431

Table 3--Modal control and error components.

Mode (n_x,n_y)	Modal Parameters	
	u_n	ξ_n
(1,1)	-.534	0.924
(3,1)	0.479	0.329
(1,3)	0.697	0.192

The resulting modal parameters listed in Table 3 define completely the control system. The controller has modified the eigenstructure of the system in such a way that the controlled structure will respond with two weak radiating modes. To illustrate this fact, the radiation efficiency for the three odd-odd uncontrolled eigenfunctions and the two new controlled eigenfunctions was computed and they are plotted in Figure 5. This figure shows clearly that the controlled modes have substantially lower radiation efficiency than the uncontrolled modes. It is also very interesting to note that, as calculated by numerical integration, the controlled eigenfunctions are nonvolumetric. Since the response is a linear expansion of the modes, this implies that the net volume displaced by the controlled plate is zero at all

frequencies. This same phenomenon was observed by the authors in studying the dynamic behavior of feedforward controlled systems using microphones in the far-field as error sensors [11]. This observation suggest an alternative control approach in which all the closed loop modes are chosen to be non-volumetric. Such a procedure would eliminate the lengthy radiation coupling equations and is the topic of present research.

The sensitivity of the controlled eigenfunctions to the selected frequency used in Eq. (28) is an important issue. Solving the eigenproblem in Eq. (28) for different values of the frequency within the excitation band, showed that the desired expansion coefficients did not vary substantially even though the design frequency and the excitation bandwidth limit is close to the plate critical frequency. This behavior is due to the new eigenvalues being independent of frequency as in all distributed elastic systems. Although this is not a general conclusion, the result suggests that in the proposed design approach the solution of the modal acoustic field could be efficiently carried out at a small number of frequencies. Since this analysis is the most computational intensive process, the proposed design approach has clear computational benefits over direct optimization methods for complex structures and excitations.

Table 4--Controlled system eigenproperties

Resonant Freq. $f_i=\omega_i/2\pi$ [Hz]		
	f_1=399	f_2=700
Expansion coefficients Γ_{in}		
(n_x,n_y)	Γ_{1n}	Γ_{2n}
(1,1)	0.224	-.314
(3,1)	-.877	0.371
(1,3)	0.424	0.874

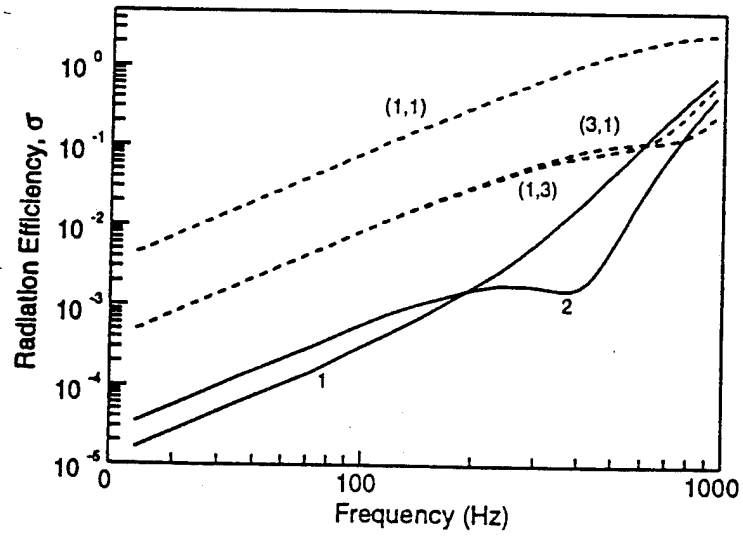

Figure 5--Radiation efficiency of ---- uncontrolled and —— controlled eigenfunctions.

The control system is completely defined in the modal domain in terms of the optimal modal parameters in Table 3. The performance of the controlled structure can be investigated with these basic modal parameters before physical transducers are devised. The effectiveness of the control system was evaluated for a disturbance input consisting of a point force located at $x=0.5L_x$ and $y=0.5L_y$. To illustrate the dynamic behavior of the plate before and after control, the acceleration response of the plate at the disturbance location was computed. The amplitude is shown in Figure 6 as a function of the frequency. The dashed line is the uncontrolled response and shows peaks at the resonant frequencies of the plate. On the other hand, when the control input is applied, the response shows resonance behavior at the two controlled resonant frequencies given in Table 4. The vibration levels of the controlled structure are slightly lower than the uncontrolled system, i.e. amplitude of the second controlled mode is the same as the (1,1) uncontrolled mode. The corresponding the before and after control far-field pressures at $r=(0°,0°,4.5L_x)$ was also computed. The sound pressure level in decibels (dB reference 20μPa) is shown in Fig. 7 as a function of the frequency. This figure shows that the sound levels produced by the

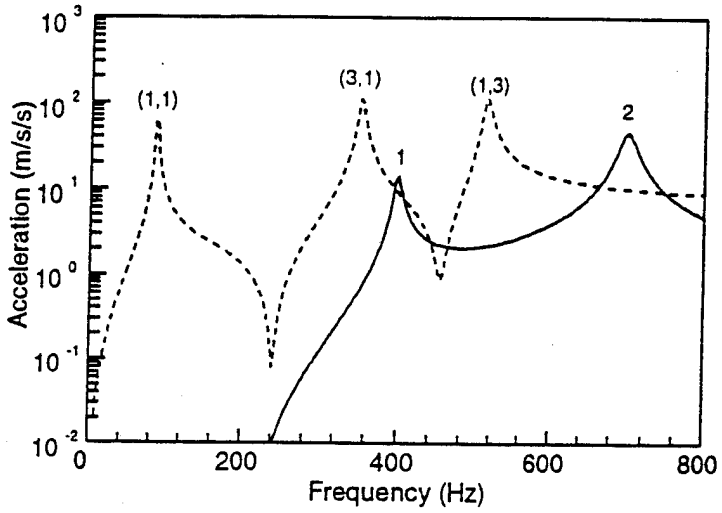

Figure 6--Acceleration at disturbance force location; --- uncontrolled and —— controlled.

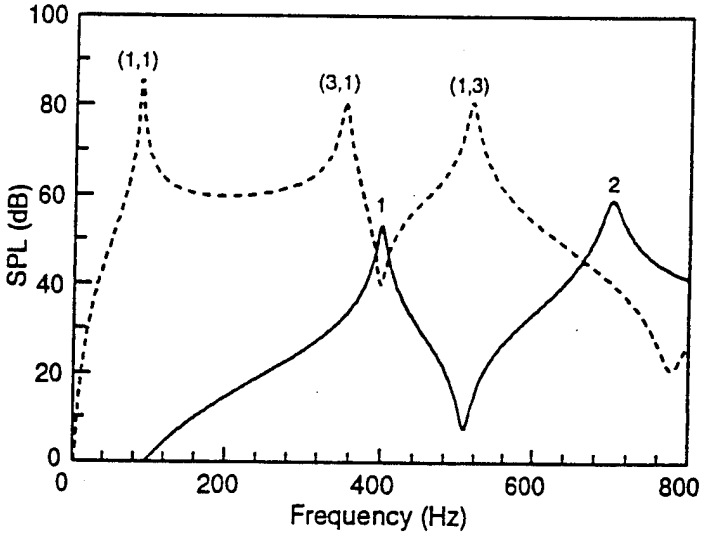

Figure 7--Far-field pressure at $r=(4.5L_x,0,0)$; --- uncontrolled and —— controlled.

controlled structure are well below the level generated by the uncontrolled one. This is due to the low radiation efficiency of the controlled modes that results in a weak coupling of the controlled response with the acoustic medium. This phenomenon takes place in spite of the plate vibration levels being comparable to the uncontrolled response levels.

The results demonstrate that the controller configuration gives good performance. The next step is to translate the optimum modal parameters, u_n and ξ_n, into realizable transducers. Here we assume the actuator and sensor will be rectangular piezoelectric distributed strain devices. Previous work [21] has shown that the modal control forces, u_n, are related to the location and configuration of the patches such that

$$u_n = \sum_{i=1}^{M} P_i \frac{\gamma_x^2+\gamma_y^2}{\gamma_x \gamma_y} \left[\cos(\gamma_x(x_{ci}+p_x)) - \cos(\gamma_x(x_{ci}-p_x))\right] \left[\cos(\gamma_y(y_{ci}+p_y)) - \cos(\gamma_y(y_{ci}-p_y))\right] \tag{32}$$

where $P_i=\pm 1$ is the relative polarity of the N_a patches, (x_{ci},y_{ci}) are the center coordinates of the patch, $2p_x$ and $2p_y$ are the patch dimensions. These can be determined by minimizing the cost function (for fixed sized actuators)

$$F(P_i,x_{ci},y_{ci}) = \sum_{n=1}^{N} \left| (u_n)_{opt} - u_n(P_i,x_{ci},y_{ci}) \right|^2 \tag{33}$$

A similar expression can be written for finding the configuration of the strain sensor [9].

Figure 8(a) shows the optimum PZT actuator which consists of four piezoelectric actuators driven in phase. Figure 8(b) shows the single optimum piezoelectric sensor. Note that these configurations are designed to be optimum across the complete bandwidth of $0 \le f \le 600$ Hz. Experimental testing of such system have recently validated the ASAC design approach and will be reported in the future.

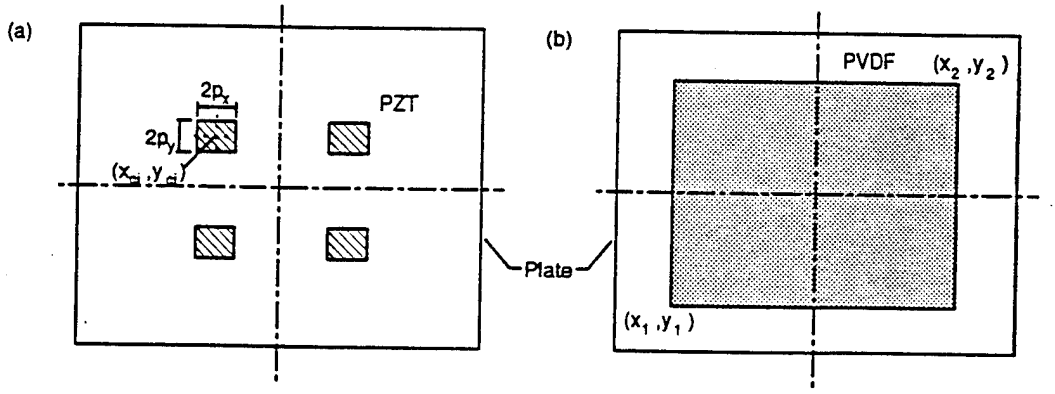

Figure 8--Optimum (a) PZT control actuator and (b) PVDF film error sensor.

EXTENSION TO DISCRETIZED SYSTEMS

The most computationally intensive process in the proposed eigenfunction design approach for

ASAC systems is the evaluation of the matrices $[\Pi(\omega)]$ and $[V(\omega)]$. These matrices will be computed at a few frequencies. A realistic structure will certainly required the numerical prediction of both the structural and the acoustic responses by FEM/BEM techniques. The computation of these matrices using numerical predictions is presented here.

A FEM/BEM model of the structure is first constructed and used to compute the structural eigenproperties, i.e. natural frequencies ω_n and mode shape vectors $\{\phi_n\}$. The (n,m) element of matrix $[V(\omega)]$ given in Eq. (27) can then be approximated as

$$V_{nm}(\omega) = \frac{\omega^2}{2A} \sum_{s=1}^{N_{FE}} \phi_n(s)\, \phi_m(s)\, A_s \tag{34}$$

where $\phi_n(s)$ is the s^{th} component of the mode shape vector; A_s is the area associated to the s^{th} node; A is the total area of the radiator ($A=\Sigma A_s$); and N_{FE} is the number of nodes in the FEM/BEM model.

The acoustic response can be computed by using the mode shape vectors, obtained from the FEM/BEM analysis, in conjunction with an acoustic FEM/BEM code. The velocity profile vector at frequency ω due to the n^{th} mode, $\{v_n(\omega)\}$, is first computed as

$$\{v_n\} = i\omega \{\phi_n\} \tag{35}$$

which in turn is input into an acoustic FEM/BEM code to compute the complex modal far-field radiated pressure over a surface enclosing the structure, i.e. a hemisphere.

The (n,m) component of matrix $[\Pi(\omega)]$ can then be computed using the modal far-field pressure distribution as follows

$$\Pi_{nm}(\omega) = \sum_{s=1}^{N_{BE}} \frac{p_n(s)\, p_m^*(s)}{\rho c} A_s \tag{36}$$

where $p_n(s)$, $s=1,\ldots,N_{BE}$, is the complex pressure computed at the s^{th} node in the far-field; A_s now represents the area associated to $p_n(s)$; and the asterisk denotes the complex conjugate.

The matrices $[\Pi(\omega)]$ and $[V(\omega)]$, evaluated as in Eqs. (34) and (36), are then used to solve the eigenproblem in Eq. (28). From this eigenanalysis, the design process to find the optimum modal control parameters continuous in the same way as presented in the previous section. It is worth to mention that these matrices can also be estimated from experimental measurements carried out on the same system to be controlled.

BROADBAND DISTURBANCES

The previous analysis and design procedure has been based upon a frequency domain approach. This form is appropriate where the disturbance is narrow band, multiple frequencies or the response is dominated by behavior at discrete frequencies (i.e. system resonances). However, in many applications the disturbance is of a random broadband nature. Recently, Alberts and Pota [22] have investigated the broadband implementation of feedforward control to minimize the disturbance response at some point on a vibrating flexible structure. Alberts and Pota have shown that the optimal compensator for the problem of Figure 1 is

$$G(s) = -\frac{T_{de}(s)}{T_{ce}(s)} \tag{37}$$

where $T_{de}(s)$ is the transfer function from the disturbance input to the error point while $T_{ce}(s)$ is from the control to the error point and s is the Laplace variable. Alberts and Pota have extended the previous frequency domain results summarized in this paper and have shown that for broadband excitation (or time domain analysis) the controlled system will have as it's new eigenvalues (to the correlated disturbance force or forces), the zeros of T_{ce} and that all of the original eigenvalues are exactly canceled by the zeros of G(s).

However, many realistic systems have non-minimum phase zeros (for example control systems with non-collocated actuators and sensors) and this implies that the optimum compensator G(s) is unrealizable without leading to control instability. As discussed in the frequency domain approach of this paper, Alberts and Pota show that it is possible to arbitrarily assign the eigenvalues of the compensated system in the time domain and then derive the optimal controller to provide this required behavior. They developed a design technique by which the compensator nearly cancels the original system's poles and simultaneously minimizes the disturbance response at the error point while remaining stable over the complete bandwidth. Through simulations Alberts and Pota demonstrate that using the approach leads to only a slight reduction in control attenuation of the error signal over the bandwidth when compared to the performance calculated using the frequency domain approach (which predicts the maximum possible broadband attenuation).

CONCLUSIONS

A design technique based upon the eigen behavior of feedforward controlled systems has been developed. The technique has been applied to both vibration modification and radiation control of structures. The extension to complex bodies using numerical FEM/BEM techniques and broadband disturbances has been discussed. The method provides a very useful tool for designing the components of feedforward controlled systems based upon a required behavior.

ACKNOWLEDGMENTS

The authors gratefully acknowledge the financial support of a large portion of this work by the Office of Naval Research, Dr. Kam Ng Technical Monitor.

REFERENCES

[1] P.A. Nelson and S.J. Elliott, *Active Control of Sound*, Academic Press, London, 1992.

[2] C.R. Fuller, S.J. Elliott, and P.A. Nelson, *Active Control of Vibration*, Academic Press, London, (in-press).

[3] L. Meirovitch, Baruh, H. and Oz, H., "A Comparison of Control Techniques for Large Flexible Systems," AIAA *J. of Guidance and Control*, **6**(4), July-August 1983, pp. 302-310.

[4] S.D. Snyder and C.H. Hansen, "Active Noise Control in Ducts: Some Physical Insights," *J. Acoust. Soc. Am.* **86**, 1989, pp.184-194.

[5] R.A. Burdisso and C.R. Fuller, "Theory of Feedforward Controlled System Eigenproperties," *J. Sound Vib.* **153**(3), 1992, pp. 437-452.

[6] R.A. Burdisso and C. R. Fuller, "Theory of Feedforward Controlled System Eigenproperties," *J. Sound Vib.* (Letter to the Editor) **163**(2), 1993, pp. 366-371.

[7] R.A. Burdisso and C. R. Fuller, "Feedforward Controller Design by Eigenvalue Assignment," *AIAA J. of Guidance and Control*, 1994 (in press).

[8] R.A. Burdisso and C. R. Fuller, "Actuator and Sensor Design for Active Structural Acoustic Control: Part I - Analysis," *J. Acoust. Soc. Am.*, 1994 (submitted for publication).

[9] R.A. Burdisso and C. R. Fuller, "Optimum Actuator and Sensor Design for Feedforward Active Structural Acoustic Control," *Proceedings of the 1993 ASME Winter Annual Meeting*, Nov.28-Dec.3, New Orleans, pp. 363-370.

[10] R.A. Burdisso, J.S. Vipperman and C.R. Fuller ,"Causality Analysis of Feedforward Controlled Systems with Broadband Inputs," *J. Acoust. Soc. Am.*, **94**(1), 1993, pp. 234-242.

[11] R.A. Burdisso and C.R. Fuller, "Dynamic Behavior of Structural-acoustic Systems in Feedforward Control of Sound Radiation," *J. Acoust. Soc. Am.* **92**(1), 1992, pp. 277-286.

[12] J.T. Weissemburger, "The Effect of Local Modifications on the Vibration Characteristics of Linear Systems," *ASME J. Applied Mechanics*, 1968, pp. 327-332.

[13] T.N Greville, "Some Applications of the Pseudo-Inverse of a Matrix," *SIAM Review*, **2**, 1960, pp. 15-32.

[14] C.K. Lee and Moon F.C., "Modal Sensors / Actuators," *ASME J. of Applied Mechanics*, **57**, June 1990, pp. 434-441.

[15] T. Bailey and J.E. Hubbard, "Distributed Piezoelectric-Polymer Active Vibration Control of a Cantilevered Beam," *AIAA J. of Guidance and Control*, **6**(5), 1985, pp. 605-611.

[16] D.W. Miller, S.A. Collins and S.P. Peltzman, "Development of Spatially Convolving Sensors for Structural Control Applications," *AIAA Paper*, 90-1127-CP, 1990, pp. 2283-2297.

[17] R.L. Clark and C.R. Fuller, "Modal Sensing of Efficient Acoustic Radiators with PVDF Distributed Sensors in Active Structural Acoustic Approaches," *J. Acoust. Soc. Am.*, **91**(6), 1992, pp. 3321-3329.

[18] S.A. Collins, D.W. Miller and A.H. von Flotow, "Sensors for Structural Control Applications Using Piezoelectric Polymer Film," MIT Space Engineering Research Center, Cambridge, MA, SERC 12-90, Oct. 1990.

[19] R.A. Burdisso and C.R. Fuller, "Active Dynamic Modification of Flexible Structures," *Proceedings of the 10th International Modal Analysis Conference (IMAC)*, San Diego, California, Vol. II, Feb. 3-7, 1992, pp. 1159-1166.

[20] R.A. Burdisso and C.R. Fuller, "Design of Feedforward Active Structural Acoustic Control Systems by Eigenfunction Assignment," *126th Meeting of the Acoust. Soc. Am.*, 4-8 October 1993, Denver, Colorado (Abstract only).

[21] E. K. Dimitriadis, C. R. Fuller and C. R. Rogers, "Piezoelectric Actuators for Distributed Vibration Excitation of Thin Plates," *ASME J. Vib. Acoust.*, **113**, 100-107 (1989).

[22] T.E. Alberts and H.R. Pota, "Broadband Dynamic Modification Using Feedforward Control," 1994 (in preparation).

C-5 Recent Developments in Active Control of Vibrations, C. R. Fuller, Nordic Conference on Vehicle and Machine Vibrations, Stockholm, Sweden, 6-8 September 1994, keynote address.

RECENT DEVELOPMENTS IN ACTIVE CONTROL OF VIBRATION

Chris R. Fuller
Vibration and Acoustics Laboratories
Mechanical Engineering Department
Virginia Polytechnic Institute and State University
Blacksburg, VA USA 24061-0238

ABSTRACT

This paper is a brief introduction and overview of new work concerned with the reduction of sound and vibration with "intelligent" structures. The paper begins with a definition of an intelligent structure and then discusses work in the component areas of actuators, sensors and control approaches. The synthesis of these areas is then illustrated through two example applications; reduction of vibration of plates and the development of a hybrid control approach based upon biological systems.

INTRODUCTION

The potential benefits of active control for reducing vibration have been convincingly demonstrated [1]. In this paper we discuss a more recent extension of the active control method in which vibration is reduced using "intelligent" structures or systems. Work in this area has been steadily progressing over the last five years as evidenced by the growing number of publications in which such techniques are used. There are a number of definitions of what are now termed "intelligent, adaptive or smart" structures. (for example, Wada et al. [2]). Here we define an intelligent structure as a system with integrated actuators (corresponding to muscles), sensors (nerves) under the direction of a learning type controller (intelligence). The structure or system thus has the ability to sense and react to its environment in a controllable way by changing its internal properties (either steady state or in a vibrational sense). Further, the controller has the ability to learn how to perform the required control task by "experience" rather than basing its control action on an *à prior* set rule (admittedly the learning procedure has to be prescribed and this in itself is a subject of research).

The advantages of such an approach are many. For instance integration of the actuators and sensors directly into the structure leads to a very compact configuration as opposed to more traditional active control methods that, for example, utilize arrays of shakers. This characteristic enables the utilization of a multitude of very small actuators and sensors configured in parallel which, in a collective sense, enables many degrees of freedom of action and thus a wide range of adaptation. Individually each actuator may not impart much control energy but collectively they can exert much force similar to biological muscle systems. Intelligent structures can thus be seem to be moving towards configurations similar to natural systems which tend to be non-orthogonal, flexible, many degrees of freedom, wet, adaptive, etc. as opposed to conventional engineered structures which generally are orthogonal, dry, rigid, tend to the massive, relatively low number of degrees of freedom and non-adaptive. Like biological systems it is the hope that intelligent systems will sense, adapt and conform with their environment (here environment can mean any chosen external state) rather than act as traditionally engineered structures which are usually designed to "overpower" their environment (and are thus largely "unaware" of their surroundings) by strength, rigidity, etc.

A learning type controller can be seen to have great advantages as well. For these types of control approaches it is not necessary to have an accurate model (mathematical, for example) of the system. The "intelligence" essentially learns what to do in real time using various learning schemes. The implementation of such approaches has been postulated for quite a few years but it is only recently that advances in digital signal processing chips, transputer systems, and ANN chips have enabled the "real time" implementation of such schemes. These approaches work well on complex systems where modeling and system identification is extremely difficult if not impossible.

The following paper briefly summarizes work in the component areas of an "intelligent" structure. For more detail the reader is referred to the appropriate references. The synthesis of these areas is illustrated through two example applications. At this point the reader is reminded of a key point. Although an intelligent structure can be subdivided into components, the complete system involves the coupled interaction of each part. Thus any investigation or design should also include the interactive nature of the components as well.

ACTUATORS

Actuators are used to impart control energy to the structure. This can be in the form of steady state (i.e. DC) loads or in the form of oscillating loads which excite vibrational response, such as in-plane force, strain, bending moments, etc. Conventional actuators usually take the form of point force actuators for vibrational response. Characteristics of such sources are described in Cremer et al. [3].

Actuators more commonly associated with intelligent structures are described as follows. Surface strain devices are distributed actuators which when bonded or

embedded in the structure apply oscillating in-plane strains. As shown by Crawley and deLuis [4] for a 1-D analysis and Dimitriadis et al. [5] in the 2-D case, these devices, when located off the central axis, effectively apply bending moments to the structure (pure bending if arranged in an anti-symmetric fashion). Surface strain devices come in various materials but the two most commonly investigated are piezoceramic and magnetostrictive [2]. Such devices tend to be high force, low displacement transducers and thus impedance matching of the actuator to the system is a critical aspect as illustrated in the work of Liang, et al. [6]. These devices can also be arranged in a "stack" mode where they apply normal forces or displacements to the system similar to conventional shakers; this arrangement is useful for such applications as active isolation, etc.

It is also possible to alter the characteristics of a structure by applying steady loads. The above listed devices can also be used to achieve this function by driving them with the appropriate DC input. This will result in a constant (i.e. non-oscillating), variable (in magnitude) load being applied to the system changing, for example, its resonant frequencies. Shape memory alloy (SMA) has also demonstrated much potential in this area [7]. These materials are configured to utilized their "memory" characteristic by shrinking to their original length when heated, typically by passing a current through them. Composite structures have been configured to have embedded SMA fibers. By applying voltages to the SMA fibers, in-plane loads as well as a change in stiffness is imparted to the system at selected fiber angles and laminate layers thus altering the composite behavior of the system. Thus the mode shapes and resonant frequencies of composite structures can be altered as required [8].

There are other advanced actuators based on materials such as Electro-Rheological fluids and Electrostrictive ceramics and the reader is referred to the paper of Wada et al. [2] for information on these.

SENSORS

Sensors are used to detect the current state of the intelligent system. They provide information which directs the controller to act in a decisive manner, bringing the system to the required response. In intelligent systems, correct sensing is critical to good performance simply from the fact that the learning type controller will try and do everything to bring the output of the sensors to the required values (usually minimize). Sensors thus must be configured to accurately observe the required variables to be controlled. Conventional sensors are transducers such as accelerometers, strain gauges, etc. again well described in Cremer, et al. [3]. Note that these transducers tend to be point sensors, i.e. very small compared to a wavelength of motion.

The more advanced sensors under study for intelligent systems tend to be of distributed nature covering large parts of the structure and thus observing many wavelengths of motion. The piezoelectric material PVDF has shown much potential in this application [9]. The material can be cut in a required shape and attached to the structural surface where it observes an integral of the surface strain under its area. The

PVDF sensor can be cut into various shapes such that, in effect, it carries out an analog wave number transform of the structural response and thus only observes certain wave components (and thus modes for a finite system). For example, on a simply supported beam, a sensor cut into the shape of $F^{\pm} \sin(\pi x/L)$, where $F^{\pm}$ is the sensor material polarization which is flipped through the modal point, will only observe the second mode of motion of the beam while a point sensor such as an accelerometer will observe all motion (unless on a nodal line).

The distributed sensor can thus be seen as a device which through its shape and location can simply and quickly perform spatial filtering. Other transducers such as optical fibers [10] and SMA [11] can also be configured to perform similar sensing capabilities. Current work is concerned with making the distributed sensor adaptive in shape such that it can change its observability in a required and controllable way.

"LEARNING" TYPE CONTROLLERS

The control arrangement provides the "intelligence" of the system. It takes information from the sensors, processes it in order to derive a control decision(s) and sends information to the actuators in order to change the behavior of the structure such that the sensor information is changed to required values. Conventional modern control methods generally use a model of the system to calculate and implement optimal control gains [1].

"Learning type" controllers work on a different approach in which a learning or training rule is used to change the control parameters or configuration to minimize a particular performance index. The control implementation generally have little or no knowledge of the system to be controlled (although some physical knowledge certainly helps in deciding their arrangement). By iteratively changing their parameters and/or structure over time in a training period they can "learn" to model the system and thus control it. Such approaches have been well known for a number of years. It is only recently that the advent of the digital signal processing chip (for example) has made their implementation of adaptive or learning type approaches in "real time" feasible. Here "real time" is meant to imply that the time for training or learning is of the order of or less than the time constants of the disturbance overall variation for example. Generally these controllers are arranged so that a training or reference signal(s) is fed through a linear or nonlinear compensator to produce control signals. The configuration of the compensator is adaptively changed in time by the learning or training algorithms in order to minimize the error function derived from the sensors. Such an arrangement is generally known as a "feed-forward" controller [12].

The most popular form of these learning or adaptive type controllers is the Filtered-X LMS algorithm which in multi-channel form is well described in the text by Nelson and Elliott [12]. This type of controller is appropriate for linear systems and narrow band or broad band signals which are relatively stationary. Presently the Filtered-X LMS algorithm does not work well on transients since the disturbance is usually much shorter than the time required for the controller to converge or learn.

Artificial Neural Networks (ANN) show much potential for control of nonlinear systems [13,14]. The multi-layered perception arrangement with a back propagation training algorithms can be seen to be related to the Filtered-X configuration. Other advanced learning type control such as genetic algorithms [15] and biologically inspired systems [16] are presently under investigation.

EXAMPLE APPLICATIONS OF "INTELLIGENT" STRUCTURES

The following two example applications are meant to illustrate use of an intelligent structure or system in controlling vibration of structures. The reader is reminded that there are many possible applications and arrangements of such systems; the following two are used to illustrate the synthesis of the above listed component areas.

Control of Plate Vibration

The work briefly described here was carried out by Gu, et al. [17]. Figure 1 shows a schematic arrangement of the experimental test rig. A simply supported plate is driven by a point force shaker as a narrowband (i.e. steady state, single frequency) disturbance or noise input. Control is applied to the plate by two surface mounted piezoceramic PZT actuators configured to produce pure bending [5]. The error information is provided by two PVDF distributed sensors or two accelerometers. The arrangement and configuration of the transducers mounted on the surface of the plate are shown in Figure 2. The control aim is to minimize a selected mode of vibration as opposed to attenuation of the response at particular points on the plate.

The control arrangement is also shown in Figure 1. The disturbance signal is taken directly as a reference or training signal and passed through two adaptive FIR filters (the controller compensators). The outputs of the compensators are then fed to the piezoceramic actuators as control signals. The output of the error transducers is then fed to the controller where in conjunction with the reference signal it is used by the Filtered-X LMS algorithm to adapt the FIR weights in order to minimize the modulus squared of the time average of the error signals [12].

Figure 3 presents an example result in terms of plate modal amplitudes. The modal amplitudes were estimated by measuring the plate complex response at a number of points and then using a modal decomposition method as outlines by Hansen, et al. [18]. Three columns are shown for each modal indice; uncontrolled, controlled using the PVDF error sensors and controlled with the accelerometer error sensors.

On examining the shape and position of the PVDF sensors in Figure 2, it is apparent that the sensor denoted PVDF (*,1) is designed to observe only the first modal response in the y direction. However, it will observe all of the modal response in the x direction. Conversely, the sensor PVDF (3,*) will only observe the third mode in

the x direction while observing all motion in the y coordinate. Thus simultaneously minimizing the output of both sensors should lead to selective control of the (3,1) mode of the plate response. In effect, the sensor arrangement of Figure 2 is an approximation of a full 2D distributed modal sensor.

Figure 2 also shows the position of the two accelerometer error sensors and these can be seen to be located in the center of each PVDF sensor for comparison purposes. Due to their small sizes, the accelerometers will observe all motion and are unlikely to provide control of a selected mode.

The test frequency was set at 400 Hz, which is away from any modal resonance point (off-resonance). Figure 3 shows that the uncontrolled response has quite a few modes contributing significantly to the motion. The results of Figure 3 also demonstrate that the use of the PVDF sensors does indeed lead to a reduction of the amplitude of the (3,1) mode, while other modes which were unobserved sometimes increase in amplitude. In contrast, the use of the accelerometers leads to an increase in the amplitude of the (3,1) mode and total plate motion although the signals from each sensor are themselves attenuated by 30 dB. Such an effect is termed control spillover; the motion is attenuated locally but increased globally.

The results illustrate that distributed, shaped structural sensors perform better in controlling selected, global motions than point sensors. On resonance, the performance of each sensor type is comparable since one plate mode will dominate the motion and can be sensed at any discrete point (except nodal lines). Future work is concerned with developing more sophisticated 2D sensors as well as creating adaptive sensors which are able to behave correctly in such situations as a change in control task or broadband disturbances.

Biologically Inspired Control Approaches

The research summarized was carried out by Fuller and Carneal [19]. Recent work has demonstrated the potential of active control of distributed elastic systems using multiple, independent actuators and sensors (the previous section for example). In work concerned with the control of sound radiation from vibrating panels, the importance of number of channels of control and optimization of the transducer position and shape has been demonstrated [20]. However these works were carried out for a fixed frequency and it is apparent that for good control over a bandwidth of frequencies, the control actuators (and sensors) need to be adaptive in shape. At first sight this problem could be solved using an overall transducer broken up into many individual small elements each connected by an individual control channel. In this situation the control transducer will effectively re-optimize its configuration for different conditions by adaptively weighting each transducer segment. Meirovitch and Norris [21] have demonstrated the advantage of such an approach by considering fully distributed control in reducing control spillover. The disadvantage of this approach is that, for systems with a high modal density, the number of actuators and sensors required becomes extremely large. This high number of control channels has a number of

problems mainly associated with memory requirements and computational time in the hardware systems used to implement the control.

This section considers a new approach to the control of the vibrational response of distributed elastic systems using a high number of channels of control. The approach is inspired by biological muscle control where a low number of main signals are transmitted from the brain to a large area of muscle tissue. The signals then stimulate local action which is governed by, for example, chemical interaction of locally connected nerves, etc., resulting in multiple subsequent signals for individual muscle cell elongation or contraction. Put simply, a signal is sent from a central complex processor (the brain) and then is broken into multiple signals by local simplified control rules (muscle cells, etc.) [22].

The work here attempts to mimic such a process. The system to be controlled is a simply supported beam harmonically excited by a point force and controlled by multiple piezoelectric elements bonded to the beam as shown in Figure 4. One actuator is chosen as the "master" actuator (based on some knowledge of the system response) and is under direction of the main, centralized advanced controller. The other "slave" actuators derive their control inputs by localized, simple learning rules related to the behavior of their neighbor actuators and are independent of the main controller direct signal. The overall control configuration is shown in Figure 5 and is termed "biologically inspired" controller although it does have relation to other hybrid, or multilevel control approaches.

In order to carry out the control task a cost function is defined as,

$$\Lambda(\overline{V}) = \int_0^L |\dot{w}_i|^2 \, dx \qquad (1)$$

where *w(x)* is the beam out-of-plane response, *L* is the length of the beam, and $\overline{V}$ is a vector of control inputs to the piezoelectric actuator. The objective is to minimize this cost function thus globally controlling the beam motion by choosing an optimal value of the vector $\overline{V}$. This is accomplished by splitting the control implementation into two steps as in Figure 5. First we optimize the "main" actuator control signal using the centralized processor and then local control rules are used to find the control signals for all the "slave" actuators. The methodology and implementation for controlling the "slave" actuators can be far simpler than the main actuators. As an example implementation of such an approach, the following strategy is implemented.

Main Centralized Controller

Initially the main controller minimizes the vibrational energy density, proportional to Λ, by using linear quadratic optimal control theory [12] to derive the optimal voltage input to the "master" actuator. In practice, this would be achieved with an adaptive LMS control approach. The optimal voltage is given by, for a SISO system,

$$V_{opt} = -\frac{H_{de}(\omega)}{H_{pe}(\omega)} F_d \qquad (2)$$

where *Hde*(ω) is the transfer function between the disturbance force and the error sensor and *Hpe*(ω) is the transfer function between the piezoelectric actuator voltage and the error sensor.

Local Control Approach

Once the optimal voltage to the "master" actuator is found, the control voltages to the "slave" actuators are derived using local learning rules. The following approach is based on the observation that, for a distributed elastic system with low damping, regions are close to either in or 180° out-of-phase with a fixed point. Thus the local learning approach is to take the "master" control voltage and apply it to the neighbor slave actuator (i.e., actuator immediately alongside). The control voltage is tried in-phase (+1), out-of-phase (-1) or turned off (0) while the cost function, Λ, is observed for each change. The condition that causes the cost function to be reduced the most is kept and the process is then applied to the next neighbor "slave" actuator until all elements are progressively tested. By this method, a distributed actuator with a generalized function that drives a response similar to the uncontrolled vibration distribution with low control spillover is constructed.

For an illustrative example, we consider a steel beam of length L = 0.5m, thickness t = 5 mm driven by an input point force disturbance *Fd* of unity magnitude (N) at position *xd* = 0.200m. Ten piezoelectric actuators are used with element lengths of 49.1 mm and spacing gaps of 1 mm. The seventh actuator from the left is chosen as the single "master" actuator. For the first case the input frequency is 552 Hz which is off resonance between the third and fourth mode resonance points of the beam (415.8 and 739.2 Hz). Figure 6 shows the beam rms response for no control, the "master" actuator alone and control using the "master" actuator and localized learning rules to derive "slave" actuator control voltages. Table I also presents the corresponding attenuation of the cost function for both cases as well as the string of control inputs to the slave actuators derived by the localized rules.

As can be seen, the single "master" actuator provides only 2.0 dB of attenuation and leads to significant spillover in the region of the beam 150 - 275 mm. With the use of the multiple "master" and "slave" actuators the attenuation is improved to 9.2 dB. Improved control in the region of largest response is now achieved with little control spillover. The string of control inputs show that many of the control actuators are not implemented at all, while control actuation is centered around the region of largest response.

The input frequency is then lowered to 80 Hz which is off resonance between the first and second mode resonance points (46.2 and 184.8 Hz). Figure 7 shows the beam displacement with and without control and again improved performance is demonstrated using the multiple piezoelectric actuators optimized using local learning rules. Table I also predicts an increase of around 9 dB in attenuation of the cost function when all actuators are used. In this case, it is apparent that more "slave" actuators are required to constrain the control spillover. Note that the optimal inputs are symmetric corresponding to the nearly symmetric uncontrolled response.

For the last case considered the frequency is set to 183 Hz which is close to the second mode resonance point. Table I shows that, as previously pointed out, there is no advantage in using a distributed actuator over a point actuator when the system is on-resonance.

This work has demonstrated the potential of using a hybrid controller based on biological systems. The approach has shown the distinct advantage of the ability to implement a distributed actuator with many degrees of freedom under the direction of a main controller with a low number of control channels. The key to the approach is to take advantage of known system behavior to use localized simple training rules to determine the distributed actuator forcing function. The results of this limited study indicate the procedure works best for off-resonance when modal density is higher. Future work will consider 2D systems, more general local training rules, and hardware implementation of the approach.

CONCLUSIONS

The field of "intelligent" structures or systems shows much potential for innovative, new, lightweight compact solutions to controlling vibration. The technique involves the synthesis of knowledge and research in the fields of actuators, sensors and control approaches. Some potential uses have been already demonstrated and market products are being developed. However, before the method is widely applicable, many technical problems need to be investigated and resolved. Although the future of intelligent systems is bright, they should be presently applied with care and a thorough understanding of the physics of the coupled system.

ACKNOWLEDGMENTS

The author gratefully acknowledges the support of most of the work described in this paper by NASA Langley Research Center and the Office of Naval Research. Discussions with Richard J. Silcox of NASA Langley and Prof. R. A. Burdisso of VPI&SU also have been very helpful. The help of James P. Carneal of VPI&SU in performing some of the analytical calculations and the manuscript preparation has been an integral part of the paper.

REFERENCES

1. L. Meirovitch, "Dynamics and Control of Structures" John Wiley, N.Y., 1990.

2. B. K. Wada, J. L. Fanson and E. F. Crawley, "Adaptive Structures," Journal of Intelligent Material Systems and Structures, 1, 1990, 157-174.

3. L. Cremer, M. Heckel, and E. E. Ungar, "Structure-Borne Sound," Springer-Verlag, Berlin, 1972.

4. E. F. Crawley and J. deLuis, "Use of Piezoelectric Actuators as Elements of Intelligent Structures," AIAA Journal, 25(10), 1987, 1373-1385.

5. E. K. Dimitriadis, C. R. Fuller and C. A. Rogers, "Piezoelectric Actuators for Distributed Vibration Excitation of Thin Plates," ASME Journal of Vibration and Acoustics, 113, 1991, 100-107.

6. C. Liang, F. P. Sun and C. A. Rogers, "Coupled Electro-Mechanical Analysis of Piezoelectric Ceramic Actuator Driven Systems - Determination of the Actuator Power Consumption" Proceedings of the SPIE conference on Smart Structures and Intelligent Systems, Albuquerque, NM, 1993.

7. C. A. Rogers, C. Liang and J. Jia, "Behavior of Shape Memory Alloy Reinforced Composite Plates - Part I: Model Formulations and Control Concepts." Proceedings of 30th SSDM Conference, Mobile, AL, 4, 1989, 1504-1513.

8. C. A. Rogers and D. K. Barker, "Experimental Studies of Active Strain Energy Tuning of Adaptive Composites with Embedded Nitinol Actuators," Proceedings of 31st SSDM Conference, Long Beach, CA, 4, 1990, 2234-2241.

9. C. K. Lee and F. C. Moon, "Modal Sensors/Actuators," ASME Journal of Applied Mechanics, 57, 1990, 434-441.

10. T. Giallorenzi, J. A. Bucaro, A. Danbridge, G. H. Sigel, J. H. Cole, S. C. Rashleigh and R. C. Priest, "Optical Fiber Sensor Technology," IEEE Journal of Quantum Electronics, 18, 1982, 626-665.

11. C. A. Rogers, "Unpublished Results," VPI&SU, Blacksburg, VA, 1990.

12. P. A. Nelson and S. J. Elliot, "Active Control of Sound," Academic Press, London, 1992.

13. K. S. Narendra and K. Parthasarathy, "Identification and Control of Dynamical Systems Using Neural Networks," IEEE Transactions on Neural Networks, 1(1), 1990.

14. C. R. Fuller, R. H. Cabell, G. P. Gibbs, and D. E. Brown, "A Neural Network Adaptive Controller for Nonlinear Systems," Proceedings of Inter Noise 91, Sydney, Australia, 1991, 169-172.

15. A. R. D. Curtis, "An Application of Genetic Algorithms to Active Vibration Control," Proceedings of Recent Advances in Active Control of Sound and Vibration, Blacksburg, VA, (Technomic Press, PA), 1991, 338-347.

16. C. R. Fuller and J. P. Carneal, "Future Trends in Active Control of Distributed Elastic Systems," Proceedings of Inter Noise 92, Toronto, Canada, 1992, 415-420.

17. Y. Gu, R. L. Clark, C. R. Fuller and A. Zander, "Experiments on Active Control of Plate Vibration Using Piezoelectric Actuators and Polyvinylidene Fluoride (PVDF) Modal Sensors," submitted to ASME Journal of Vibration and Acoustics, June, 1992.

18. C. H. Hansen, S. D. Snyder, and C. R. Fuller, "Noise Reduction of a Vibrating Panel by Use of Active Sound Sources and Active Vibration Sources: A Comparison," Proceedings of Noise and Vibration 89, Singapore.

19. C. R. Fuller and J. P. Carneal, "A Biologically Inspired Control Approach for Distributed Elastic Systems," accepted for publication in the Journal of the Acoustical Society of America, 1992.

20. R. L. Clark and C. R. Fuller, "Optimal Placement of Piezoelectric Actuators and Polyvinylidene Fluoride Sensors in Active Structural Acoustic Control Approaches," Journal of the Acoustical Society of America, 92(3), 1992, 1521-1533.

21. L. Meirovitch and M. A. Norris, "Vibration Control," Proceedings of InterNoise 84, 1984, pp 477-482.

22. B. R. Landau, "Essential Human Anatomy and Physiology," Scott, Foresman and Co., Glenview, IN, 1976, pp.191-192.

TABLE I. Control Performance

Freq. (Hz)	Control String	"Master" (dB)	"Master" and "Slaves" (dB)
552	0000-0⊕+00	2.0	9.2
80	-00+00⊕00-	9.6	19.2
183	000000⊕000	55.4	55.4

Note: ⊕= "master" actuator

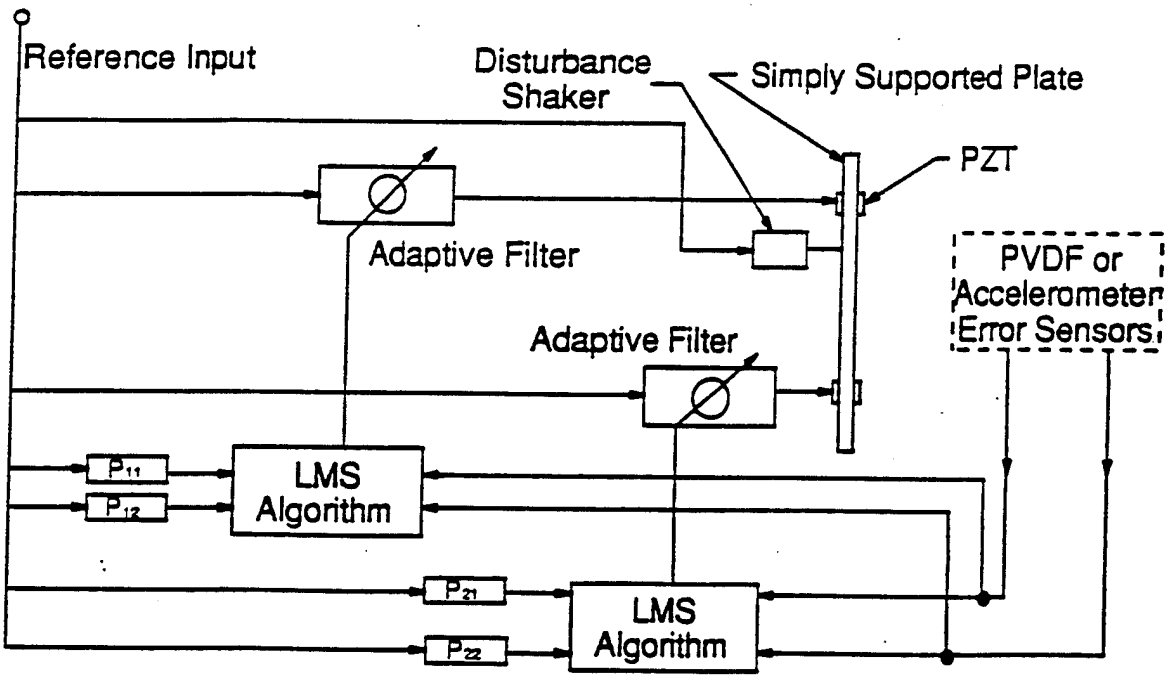

Figure 1.

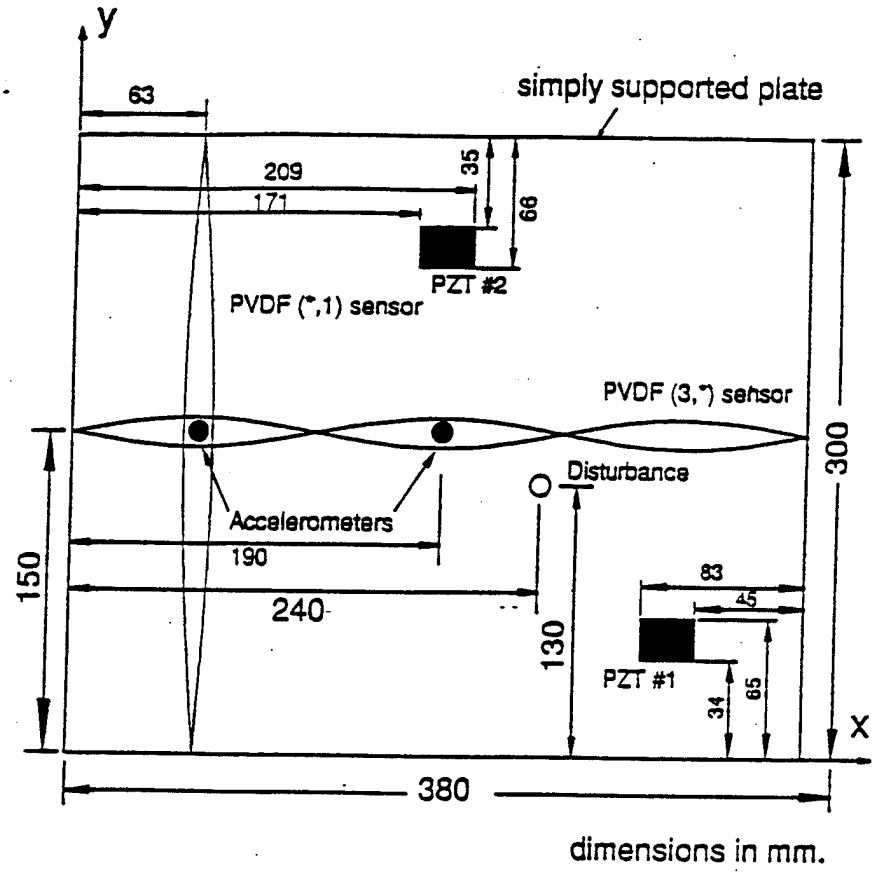

Figure 2.

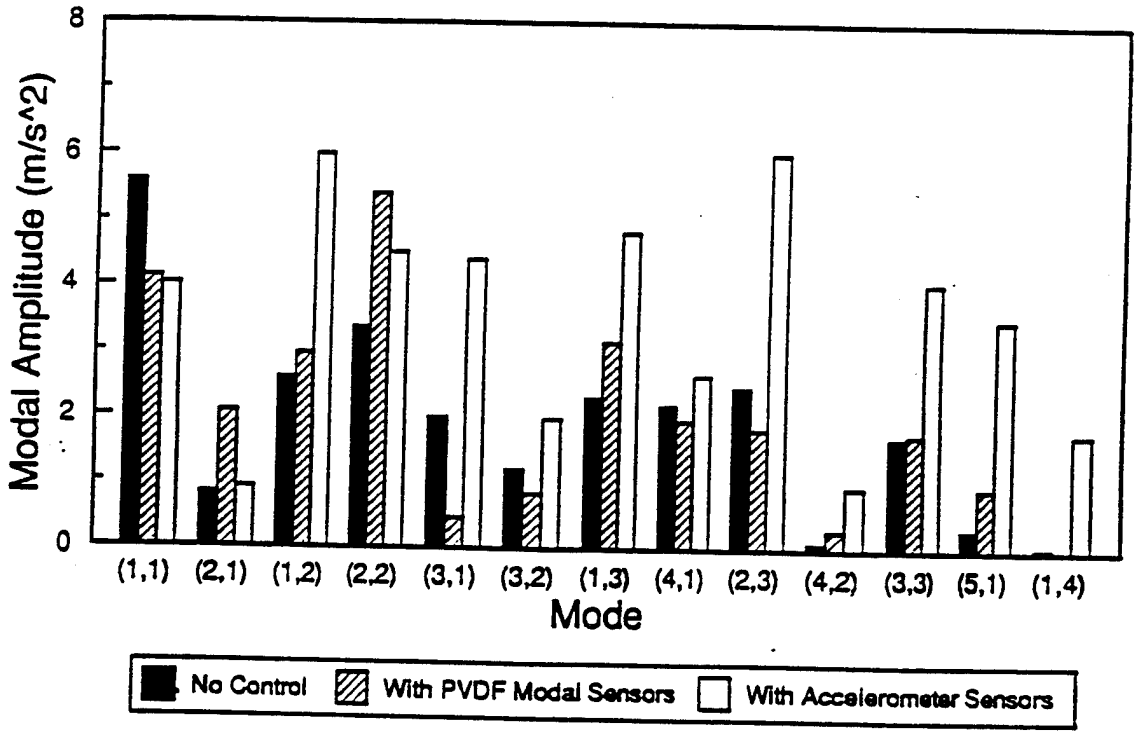

Figure 3.

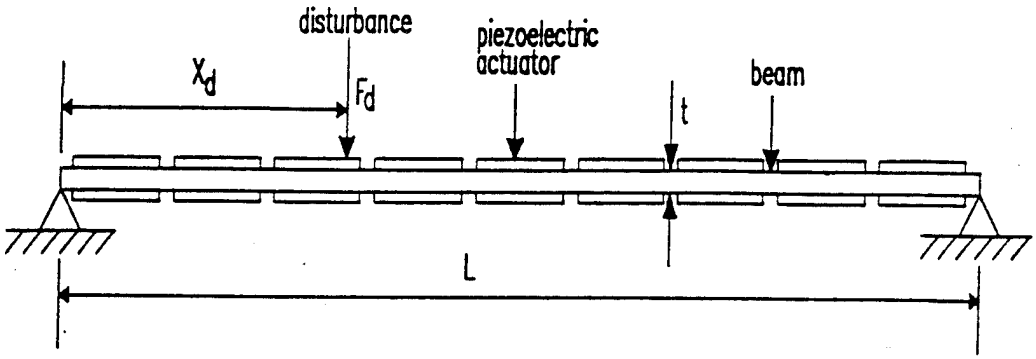

Figure 4.

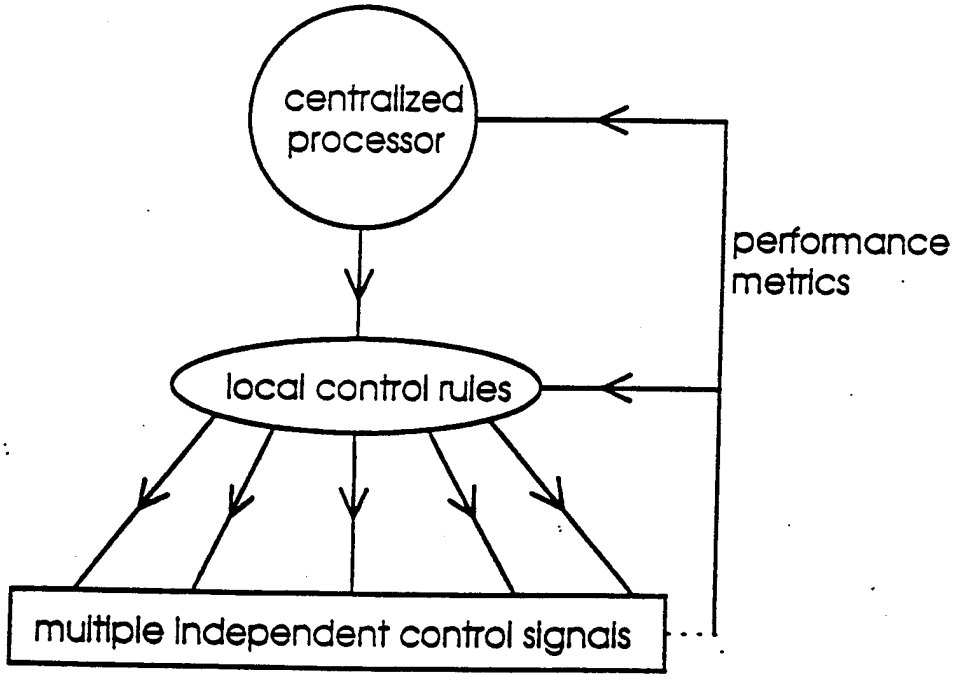

Figure 5.

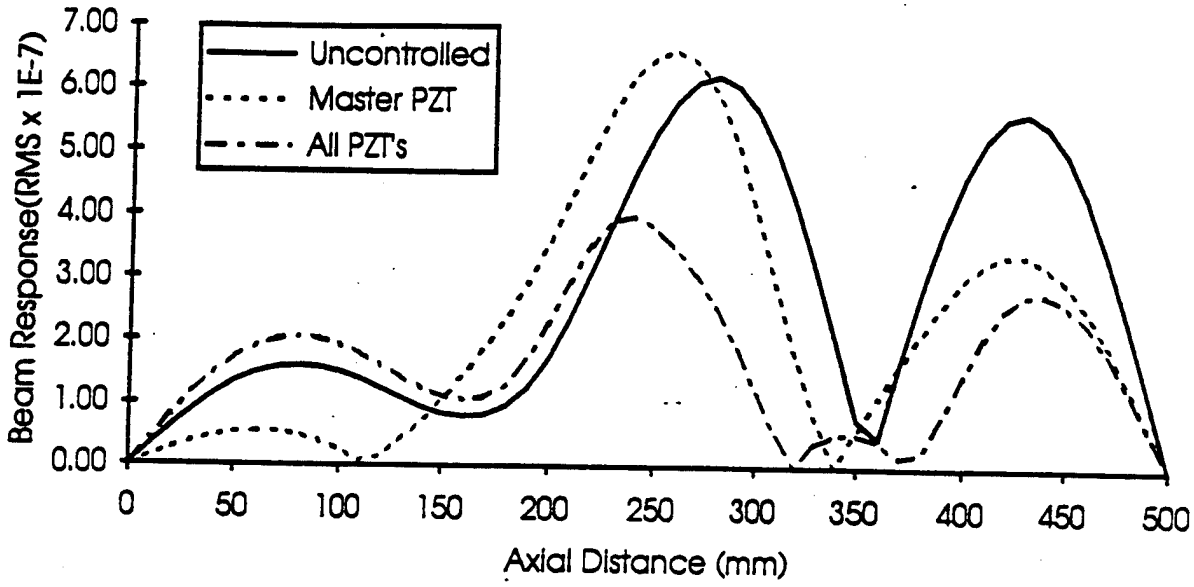

Figure 6.

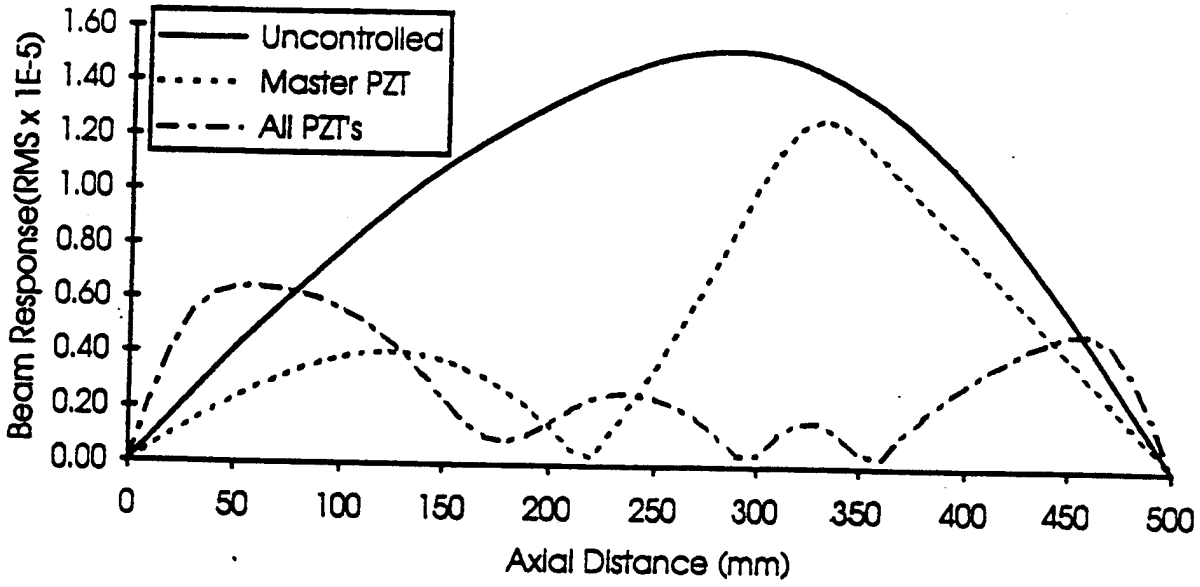

Figure 7.

C-6 Active Control of Coupled Wave Propagation and Associated Power in Fluid-Filled Elastic Long Pipes, C. R. Fuller and B. J. Brévart, ACTIVE 95, Newport Beach, CA, July 6-8, 1995, plenary presentation.

Newport Beach, CA, USA
ACTIVE 95
1995 July 06–08

ACTIVE CONTROL OF COUPLED WAVE PROPAGATION AND ASSOCIATED POWER IN FLUID-FILLED ELASTIC LONG PIPES

Chris. R. Fuller and Bertrand J. Brevart

Vibration and Acoustics Laboratories
Virginia Polytechnic Institute & State University
Blacksburg, Virginia 24061-0238

ABSTRACT

The active control of total power flow in both media of fluid-filled elastic pipes by structurally mounted actuators and sensors is analytically and experimentally studied. The control paradigm used was the feedforward LMS technique. The results indicate that for a 3I30 system, high attenuation of total power is possible for a substantial range of low frequencies. The use of structural actuators and sensors for reducing interior coupled fluid power is thus validated.

INTRODUCTION

Piping systems exist as load and energy carrying structures in many industrial applications and often the vibrations carried by these systems can cause noise and mechanical fatigue problems. Traditionally, passive control has been used to reduce vibrations in pipes but the problem is complicated by the multi-path propagation nature of the system, particularly for fluid-filled pipes where the coupling is strong (i.e., a dense acoustic fluid). Power may be transmitted by the structural and/or the fluid path depending upon the response characteristics of the system. In addition realistic passive control is ineffective at low frequencies where the wavelengths of motion are long.

In this paper we study the use of active control to reduce wave transmission and hence power flow in fluid-filled elastic long cylinders representative of piping systems. The objective is to demonstrate simultaneous control of power flow in both the fluid and the structural path, thereby implying a total reduction of power in the system. A further objective is to achieve this reduction with actuators and sensors attached directly to the outside of the piping system. In other words we intend to demonstrate that the wall of the pipe can be actuated so as to control not only its power but also the power of the coupled fluid medium contained within it. The advantages of this are obvious; many applications preclude the use of actuators located in the fluid due to flow restriction effects, hostile fluid environments, ease of access, etc.

There has been little previous work on the active control of coupled waves in fluid-filled elastic pipes. Brevart and Fuller have analytically studied the active control of waves in infinite elastic steel cylinders *in-vacuo* and filled with water by structural actuators [1,2]. Their results indicated that it is possible to reduce the total power in the system (i.e., in both the fluid and the structure) with point force actuators at frequencies below the ring frequency of the cylinder. More recently Brevart [3] has provided experimental verification of these predictions and some of these results will be presented in this paper. Other related work has been carried out by Harper and Leung [4] in which they experimentally demonstrated the use of an active flexible insert to reduce both structural and fluid vibrations in a water-filled piping system. The active insert consisted of six PVDF piezoelectric polymer cable wire actuators wound helically around a rubber section.

Useful background research on the dynamics of fluid-filled piping systems has also been carried out by White and Sawley [5], Fuller and Fahy [6] and Fuller [7]. Due to the coupled nature of the problem, a good understanding of the dynamics of fluid-filled pipes is essential to the use of active control in such systems and the interested reader is recommended to first read Refs. 5-7.

The paper begins with an analytical investigation of the active control of total power in a fluid-filled elastic infinite cylinder excited by a point force disturbance, using a combination of point force and piezoelectric actuators and sensors. An experimental investigation of a similar active control system applied to a water-filled plexiglass long pipe is also described. The results obtained are discussed and conclusions to the effectiveness of the active control system for vibration and power control in piping systems are made.

ANALYSIS

In this section we analytically study active control of total power flow in fluid-filled elastic infinite cylinders. The cylinder coordinate system and associated circumferential mode shapes are shown in Fig. 1. The Kennard shell equations are used to describe the motion of the cylinder [8]. All disturbances are assumed to be single frequency harmonic. The disturbance is assumed to be a point force applied radially to the shell wall, which is representative of many realistic vibration loads. The active forces are a combination of a ring force and point forces applied to the shell wall downstream of the disturbance as shown in Fig. 2. The error sensors are assumed to be PVDF piezoelectric modal sensors applied around the circumference of the shell as shown in Fig. 2 [9]. These sensors can individually observe the n=0, 1 and 2 circumferential shell modes of vibration.

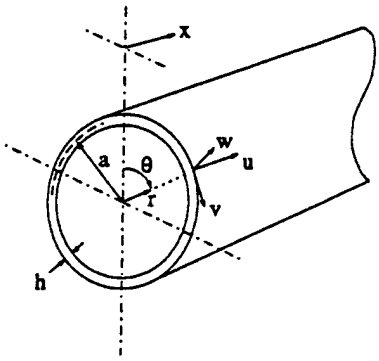

Figure 1a. Coordinate system.

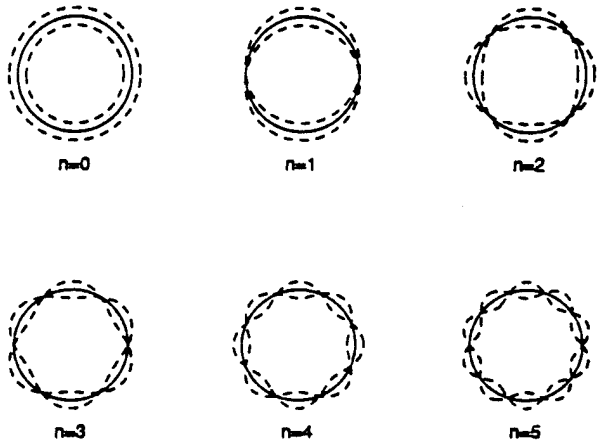

Figure 1b. Circumferential mode shapes.

The cylinder radial displacement response to a point force harmonic disturbance of amplitude F_d located at x_p can be written as (omitting $e^{i\omega t}$ for brevity)

$$w(x,\theta) = \frac{F_d}{4\pi^2 \rho_s c_L^2 (h/a)} \sum_{n=0}^{N} \varepsilon_n \cos(n\theta) \int_{-\infty}^{+\infty} I_{33} e^{ik_n\left(x-x_p\right)} dk_n a \qquad (1)$$

where the matrix term I_{33} is specified in Refs. 3 and 6. Eq. (1) can be rewritten as

$$w(x,\theta) = \sum_{n=0}^{N} w_n(x,\theta) \qquad (2)$$

where $w_n(x,\theta)$ represents the modal radial displacement of the circumferential mode n.

The modal radial displacements of the controlled system, corresponding to the circumferential modes n=0, 1 and 2 at the error sensor locations x_e^0, x_e^1, and x_e^2, respectively, result from the superposition of the displacement fields due to the point force disturbance and the control inputs. Since each circumferential modal distribution is orthogonal, they can be expressed as

$$w_0^t\left(x_e^0,\theta\right)=\frac{1}{2A}\left(F_d\int_{-\infty}^{+\infty}I_{33}e^{ik_0x_e^0}dk_0a+F_c^0\int_{-\infty}^{+\infty}I_{33}e^{ik_0\left(x_e^0-x_c^0\right)}dk_0a\right.$$

$$\left.+F_c^1\int_{-\infty}^{+\infty}I_{33}e^{ik_0\left(x_x^0-x_c^1\right)}dk_0a+F_c^2\int_{-\infty}^{+\infty}I_{33}e^{ik_0\left(x_e^0-x_c^2\right)}dk_0a\right), \tag{3a}$$

$$w_1^t\left(x_e^1,\theta\right)=\frac{1}{A}\left(F_d\cos\theta\int_{-\infty}^{+\infty}I_{33}e^{ik_1x_e^1}dk_1a+F_c^1\cos\theta\int_{-\infty}^{+\infty}I_{33}e^{ik_1\left(x_e^1-x_c^1\right)}dk_1a\right.$$

$$\left.+F_c^2\cos\theta\int_{-\infty}^{+\infty}I_{33}e^{ik_1\left(x_x^1-x_c^2\right)}dk_1a\right), \tag{3b}$$

$$w_2^t\left(x_e^2,\theta\right)=\frac{1}{A}\left(F_d\cos 2\theta\int_{-\infty}^{+\infty}I_{33}e^{ik_2x_e^2}dk_2a+F_c^2\cos 2\theta\int_{-\infty}^{+\infty}I_{33}e^{ik_2\left(x_e^2-x_c^1\right)}dk_2a\right.$$

$$\left.+F_c^2\cos 2\theta\int_{-\infty}^{+\infty}I_{33}e^{ik_2\left(x_x^2-x_c^2\right)}dk_2a\right), \tag{3c}$$

where F_d is the amplitude of the point force disturbance located at $x_p=0$ and A is a constant term equal to $\left(2\pi^2\rho_s c_L^2 h/a\right)$.

It is apparent from eqs. (3a-3c) that the modal radial displacements of the shell, associated with the modes n=1 and n=2, are independent of the control ring force F_c^0. Therefore, they can be expressed in the following matrix form

$$w^t=dF_d+Cf_c, \tag{4}$$

where the vectors and matrices are given by

$$d=\frac{1}{A}\left[\cos\theta\int_{-\infty}^{+\infty}I_{33}e^{ik_1x_c^1}dk_1a \qquad \cos 2\theta\int_{-\infty}^{+\infty}I_{33}e^{ik_2x_e^2}dk_2a\right]^T \tag{5a}$$

$$C=\frac{1}{A}\begin{bmatrix}\cos\theta\int_{-\infty}^{+\infty}I_{33}e^{ik_1\left(x_e^1-x_c^1\right)}dk_1a & \cos 2\theta\int_{-\infty}^{+\infty}I_{33}e^{ik_1\left(x_e^1-x_c^2\right)}dk_2a\\ \cos 2\theta\int_{-\infty}^{+\infty}I_{33}e^{ik_2\left(x_e^2-x_c^1\right)}dk_2a & \cos 2\theta\int_{-\infty}^{+\infty}I_{33}e^{ik_2\left(x_e^2-x_c^2\right)}dk_2a\end{bmatrix} \tag{5b}$$

$$f_c=\left[F_c^1 \quad F_c^2\right]^T \tag{5c}$$

$$w^t=\left[w_1^t\left(x_e^1,\theta\right) \quad w_2^t\left(x_e^2,\theta\right)\right]^T \tag{5d}$$

In order to minimize the modal radial displacements of the shell around the circumference at the axial error positions x_e^1 and x_e^2, corresponding to the location of the n=1 and n=2 modal sensors, the following cost function is defined

$$J = \sum_{i=1}^{2} \int_0^{2\pi} \left| w_i^t \left(x_e^i, \theta \right) \right|^2 d\theta. \tag{6}$$

Eq. (6) assumes that each modal sensor provides an output equal to the integral of the modal displacement around the shell circumference. As discussed in Ref. 3, this is reasonable assuming the width of the sensor is much less than the axial wavelengths of the propagating waves in the system.

The optimal vector of control forces to minimize the quadratic cost function J is given by [10]

$$f_c^{opt} = -[C^H C]^{-1} [C^H d] F_d. \tag{7}$$

Eq. (3a) yields the third optimal control force F_c^0, minimizing the axisymmetric radial displacement at x_e^0, corresponding to the location of the n=0 modal sensor,

$$F_c^0 = \frac{-1}{\int_{-\infty}^{+\infty} I_{33} e^{ik_0 \left(x_e^0 - x_c^0 \right)} dk_0 a} \left(F_d \int_{-\infty}^{+\infty} I_{33} e^{ik_0 x_e^0} dk_0 a \right.$$

$$\left. + F_c^1 \int_{-\infty}^{+\infty} I_{33} e^{ik_0 \left(x_e^0 - x_c^1 \right)} dk_0 a + F_c^2 \int_{-\infty}^{+\infty} I_{33} e^{ik_0 \left(x_e^0 - x_c^2 \right)} dk_0 a \right). \tag{8}$$

In order to evaluate the performance of the active control system we re-substitute the optimal control forces back into the equation for the total system response, eq. (4). We then calculate the total power flow in the shell-fluid system using the relations developed in Refs. 3 and 6 (note these include both the power in the shell and the fluid paths) and use this to study the change in power with and without the control implemented.

Analytical Results. In this section the performance of the control configuration described above for various non-dimensional frequencies, $\Omega = \omega a / c_L$, is presented. The point force disturbance was chosen located at x_p=0 with an amplitude of 100 N/m. The ring control force and the two point control forces were applied at x_c=3a, 4a and 5a, respectively, where a is the radius of the cylinder. The modal error sensors for the n=0, 1 and 2 circumferential modes were located at x_e=7a, 7.5a and 8a, respectively. This configuration was chosen to keep the control implementation as axially compact as possible. As shown below, locating the control and error transducers relatively close to each other limits the achievable performance due to wave near-field effects. The design is thus a compromise between required performance and compactness. Note that Ω=1 corresponds to the *in-vacuo* ring frequency of the cylinder and thus we are considering frequencies well below this value. The power flow in the system was evaluated at x=10a, well downstream of the last modal error sensor. The shell system considered consists of a plexiglass material (to correspond to the experiments discussed later) with properties given in Table 1. The shell was considered either *in-vacuo*, or filled with water, with properties also given in Table 1. The cut-on frequencies for the lowest order circumferential modes in the plexiglass shell system, calculated using the theory of Refs. 3 and 6, are given in Table 2 for the *in-vacuo* and water-filled cases.

The first result we consider is for an *in-vacuo* shell with an excitation frequency of Ω=0.05. Fig. 3 presents the total power flow in the system before and after control, and is also broken down into the circumferential modal components. Results are presented in decibels normalized to 1 Watt. As specified in Table 2, this frequency is below the cut-on frequency of the lowest order n=3 mode and good performance is expected. Fig. 3 shows that the total power reduction is 15.8 dB and the n=1 and 2 modes carry most of the energy. At the frequency of Ω=0.05

only the n=0, 1 and 2 lower order waves are cut-on. Ideally then, with three channels of control, total reduction of power should be achieved. However, due to the relatively close spacing of the control inputs and error sensors, near-field waves are present at the error sensors and consequently the achievable attenuation is reduced. In particular, at Ω=0.05, the n=1 torsional wave is cut-off but has a very small imaginary value of axial wavenumber. This implies that its decay rate is small and of the order of 1dB for the test configuration. Nevertheless, good performance is seen to be still achieved.

Table 1: Plexiglass shell-fluid system characteristics and material properties.

Material	Plexiglass	Water
Thickness ratio to radius, *h/a*	0.0426	---
Young's modulus, *Y* *(N/m^2)*	1.9175×10^9	---
Poisson's ratio, v	0.4	---
Density, ρ *(kg/m^3)*	1109	1000
Free wave speed, c *(m/s)*	1435	1500
Damping Ratio, η	0.036	0

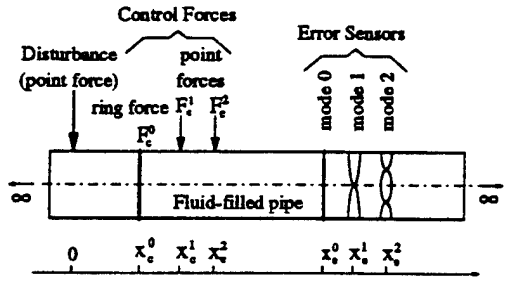

Figure 2. Active control arrangement for a point force disturbance at low frequencies.

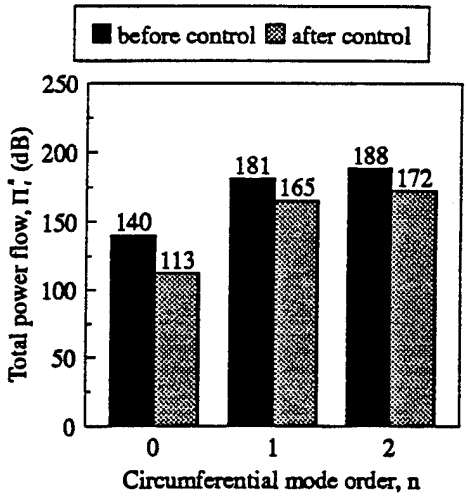

Figure 3. Modal decomposition of the total power flow in an *in-vacuo* plexiglass shell, Ω = 0.05.

Table 2: Cut-on frequencies of higher order circumferential modes for *in-vacuo* and water-filled plexiglass shells.

Mode order† n	*In-vacuo* shell cut-on frequencies Ω	Water-filled shell cut-on frequencies Ω
2	0.033	0.011
3	0.095	0.036
4	0.183	0.074
5	0.294	0.129

†Note the n=0 and n=1 waves cut-on at Ω=0.

We now consider the effect of a contained heavy fluid such as water on the control performance. The main influence of the water is to significantly lower the cut-on frequencies as shown in Table 2. At the frequency of Ω=0.05, the lowest order n=3 mode is now cut-on and hence there are at least four possible waves propagating in the system. The control performance would be expected to decrease with a controller of three degrees of freedom (i.e., three actuators). However, Fig. 4 shows that the total power flow (again normalized to 1 Watt) is attenuated by 13 dB, even though the n=3 shell motion carries most of the energy of vibration. This behavior is most likely due to the n=2 and n=3 shell waves having a nearly identical phase speed at this frequency. The radial displacements induced by the control actuators will be in-phase at the error sensor locations and also at the power evaluation point. Minimization at one location will thus ensure reduction at the other.

When the frequency is increased to Ω=0.1 a different behavior is observed. At this frequency the n=4 mode is cut-on and the n=2 and 3 phase speeds are different. Consequently, while Fig. 5 shows that the n=0, 1 and 2 total power flows are decreased significantly, the higher order modes are increased or only slightly reduced. In fact the total power flow for the system is not changed at all. This behavior is due to control spillover into unobserved modes by the control system and becomes worse as the frequency is increased and more modes (i.e., degrees of freedom) participate in the system response.

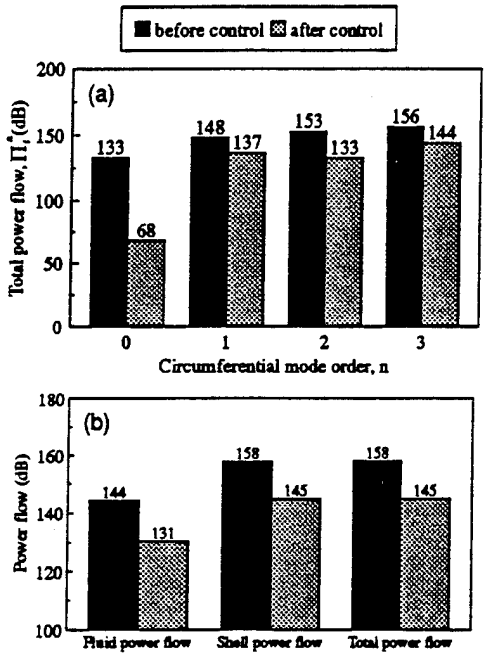

Figure 4. Total power flow in a water-filled plexiglass shell, Ω = 0.05; (a) modal de composition, (b) distribution in the system.

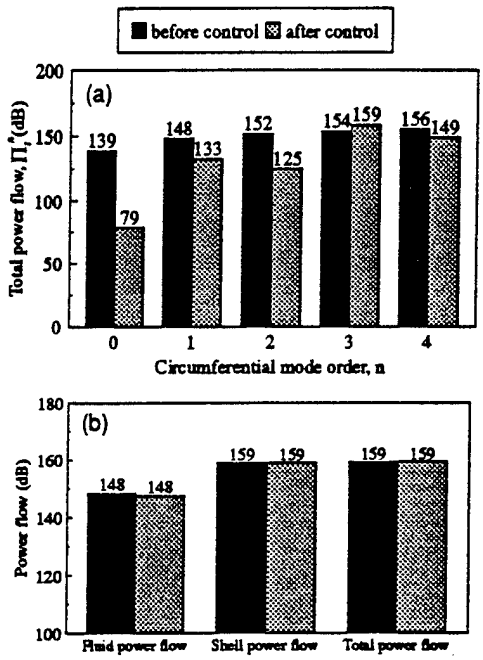

Figure 5. Total power flow in a water-filled plexiglass shell, Ω = 0.1; (a) modal decomposition, (b) distribution in the system.

Nevertheless the analytical results indicate that the total power in the shell and the fluid can be significantly reduced with structural actuators and sensors for a substantial range of low frequencies. The results in particular support the concept of reducing internal fluid power with non-obtrusive actuators attached to the outside shell wall.

EXPERIMENTS

In this section we discuss experiments performed to validate some of the concepts outlined in the previous section. Fig. 6 is a schematic of the experimental setup used to investigate the active control approach. The cylindrical shell studied was manufactured from plexiglass with a length of 1.83m, an outside diameter of 15.2cm and a wall thickness of 3.17mm. Plexiglass was chosen as the shell material for a number of reasons. Firstly, the controller used had an upper frequency limit of around 1kHz and thus for practical cylinder diameters it was preferable to use a material with a small extensional phase speed, thus keeping the ring frequency at relatively

lower values. Secondly, a major concern was to build the shell system to approximate, as best as possible, an infinite system and plexiglass, being a relatively highly damped material, provided natural attenuations of the order of 6-10 dB/m for extensional waves at frequencies of $\Omega \geq 0.3$. Finally, it is extremely important to remove all air bubbles from the fluid field as they significantly alter the dynamics of the coupled system by increasing its compliance, and plexiglass, being transparent, provides a convenient way of checking for this condition.

In order to simulate an infinite pipe as closely as possible, the downstream end of the pipe was treated in a number of ways. An absorbing termination consisting of thin strips of viscoelastic damping material was wrapped around the shell wall. The thickness of the layer was gradually increased towards the end of the shell, as shown in Fig. 6, in order to provide as little structural discontinuity as possible. In addition, an absorptive layer of B. F. Goodrich acoustic rubber tile was bonded on the inner side of the end brass cap in order to minimize reflections in the fluid field. Preliminary tests revealed that while the termination was effective at higher frequencies ($f \geq 500$Hz, or $\Omega \geq 0.17$) there were significant reflections below this frequency mainly due to waves with a dominantly in-plane motion and it is was hoped the natural damping of the plexiglass would help reduce the reflected in-plane waves. The other (source) end of the pipe was supported by a small rubber air tube whose resonance frequency and stiffness were low enough so as to not significantly affect the pipe dynamics. The shell was excited at the right hand end using a point force disturbance.

The internal pressure field for the fluid-filled case was measured using a B&K miniature hydrophone mounted on a movable traverse. The hydrophone could be moved both radially and axially within the contained fluid field, as shown in Fig. 6. The hydrophone leads were routed down the inside of the aluminum axial probe tube so as to minimize leaks and a lowering of the fluid-field compliance.

The shell radial vibration was monitored with a circumferential array of 11 B&K mini-accelerometers attached to the shell wall downstream of the last modal error sensor (see below). The output of the accelerometers were decomposed into circumferential modal amplitudes as described in Ref. 3. For the low frequencies considered in this study, the square of the shell individual radial modal amplitudes is approximately proportional to the total power carried by the shell in each mode (due to the Poisson coupling effects), while the acoustic power in the fluid field is approximately proportional to the square of the pressure amplitude of individual modes. Reduction of either variable at two locations (the error and monitor sensors) with a spacing of less than a wavelength thus indicates reduction of the power in the corresponding modal field (see Ref. 3 for a proof of this).

Extensive preliminary testing was performed on the plexiglass shell as described in Ref. 3. The hysteretic damping constant of the shell plexiglass material was determined to be approximately $\eta = 0.036$. By measuring the transfer mobility of the shell and using the theory of Refs. 3 and 6, the corresponding average extensional phase speed of the plexiglass material was determined to be $c_L = 1435$m/s giving an *in-vacuo* ring frequency of $f = 3061$Hz for the shell used in these experiments. For the following results the frequency will be given in absolute and non-dimensional values ($\Omega = \omega a / c_L$). The theoretically determined cut-on frequencies using these values, and those measured experimentally, are given in Tables 3 and 4 for the *in-vacuo* and water filled cases, respectively. Very good agreement is apparent.

Table 3: Comparison of theoretical and experimental cut-on frequencies of the circumferential modes n=2, 3 and 4, *in-vacuo* plexiglass shell, h/a=0.0426.

Mode order n	Calculated cut-on frequency		Measured cut-on frequency	
	(Hz)	Ω	(Hz)	Ω
2	101	0.034	101.5	0.034
3	285.2	0.094	274	0.091
4	546.7	0.181	564	0.187

The control arrangement of Fig. 6 is very close to that shown in Fig. 2 for the analytical investigation. The disturbance and control point force actuators consisted of Ling 1 lb. mini-shakers attached radially to the shell wall by thin wire stingers at the same angular locations. The ring force actuator was implemented using KYNAR piezoelectric polymer wires wrapped tightly around the circumference of the cylinder. The piezoelectric wires were held in position by double sided sticking tape attached to the shell wall. Although the piezoelectric wire functions by straining in its length when a voltage is applied, it can be shown the above implementation is

equivalent to applying a radial line force to the shell wall [3]. The sensors were implemented using a combination of KYNAR wire and PVDF piezoelectric film. The n=0 mode was observed using a KYNAR cable wrapped completely around the cylinder wall. As demonstrated by Pinnington and Briscoe [11], such a configuration will provide a good transducer for measuring axisymmetric wave motion in pipes. The n=1 and n=2 modes were observed using PVDF film cut to a shape corresponding to each circumferential mode, as described in Refs. 3 and 9, and attached to the shell wall with double side sticking tape. As shown in Ref. 3, the output of each modal sensor is proportional to the integral of the modal displacement around the circumference. In realistic pipes the angular position of the higher circumferential modes is never exactly known (the modes may slightly rotate due to shell inhomogenities, for example). To overcome this problem, each modal sensor consisted of two closely spaced, similarly shaped sensors rotated by 90° and 45° for the n=1 and 2 modes respectively, whose outputs were summed (in other words, one sensor observed the $\cos(n\theta)$ mode while the other observed the $\sin(n\theta)$). Thus, if the sensor is incorrectly positioned in the angular sense, it will still provide information of the corresponding circumferential mode. Table 5 gives the central location of the individual control actuators and error sensors. Note that the residual response is independent of the sensor gains since their outputs are all driven to zero.

Table 4: Comparison of theoretical and experimental cut-on frequencies of the circumferential modes n=2, 3 and 4, water-filled plexiglass shell, h/a=0.046.

Mode order n	Calculated cut-on frequency		Measured cut-on frequency	
	(Hz)	Ω	(Hz)	Ω
2	33.7	0.011	28	0.009
3	110.2	0.037	114	0.038
4	226.5	0.075	213	0.071

Table 5: Spacing between control actuators/sensors and the point force disturbance (shaker)

	Distance from the disturbance x (mm)
Actuator 1	255
Actuator 2	365
Actuator 3	400
Sensor 1 (part 1)	630
Sensor 1 (part 2)	660
Sensor 2 (part 1)	705
Sensor 2 (part 2)	735
Sensor 3	805

The controller used in the experiments was based upon a 3I30 Filtered-x version of the feedforward LMS algorithm, as described in Nelson and Elliott [10]. The control algorithm was implemented on a TMS 320C30 signal processing chip resident in a host personal computer. As the experiments were narrow-band, two coefficients were used in the adaptive and "Filtered-x" filters. The sampling rate was typically chosen at around five times the frequency of interest. Various other standard electronic equipment, such as a signal generator, anti-aliasing filters, amplifiers, etc., were also necessary.

Experimental Results. In this section we present some example results from the experiments for both an air-filled (which corresponds to *in-vacuo*) and a water-filled shell. The axial location of the actuators and the modal sensors are given in Table 5, while the corresponding arrangement is shown in Fig. 6.

For the first experiment an air-filled plexiglass shell was considered. Due to density of air being relatively small, this is extremely close to the *in-vacuo* case discussed previously. The frequency was set to 150 Hz (Ω=0.05) and the controller turned on. The three error signals corresponding to the n=0, 1 and 2 circumferential modes were all attenuated by over 23dB, and this was found to be typical for all the tests performed. Fig. 7 presents the modal decomposition of the shell response obtained from the monitor accelerometers before and after the control

was implemented. The modal acceleration was normalized to the disturbance input voltage of 1 Volt. Note that values from the decomposition for the n=3, 4 and 5 modes are provided even though the waves are not cut-on. These values should be viewed as inaccurate as they are most likely due to slight transducer positioning errors or shell inhomogenities. This observation applies to all the decomposition results. The results, in conjunction with the error sensor outputs, confirm that the control has globally reduced the shell radial vibration (and, hence, the total power). When the frequency was increased to 300Hz (Ω=0.1), the n=3 circumferential lowest order mode becomes cut-on. The decomposition results presented in Fig. 8 again indicate global reduction of wave motion very similar to the theoretical results discussed above. However, when the frequency was increased further to 700Hz (Ω =0.23), Fig. 9 indicates that the overall response has increased. Surprisingly, this increase occurs in the n=1 mode, unlike the theoretical predictions which showed spillover into higher order modes (n>3). This behavior was thought to be due to reflections from the termination causing a standing wave pattern on the shell with a node in the proximity of the n=1 modal sensor, leading this mode to be unobservable. This observation was supported by an axial scan of the shell radial vibration using a movable accelerometer.

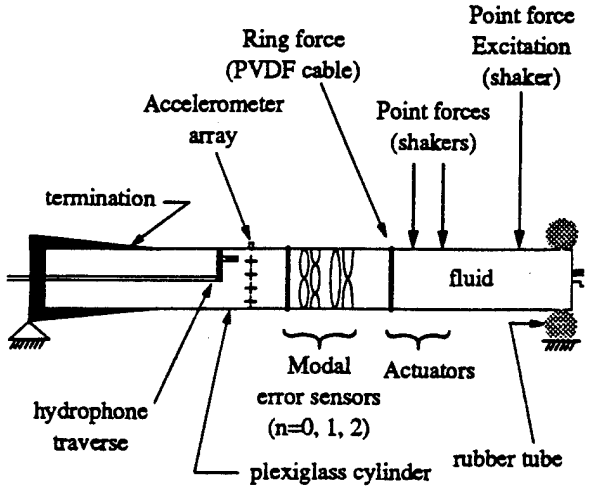

Figure 6. Schematic of the control arrangement and and measurement transducers.

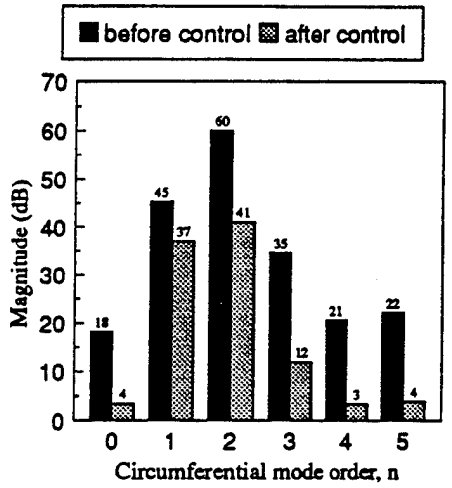

Figure 7. Modal decomposition of the radial acceleration of the shell one diameter beyond the error sensors, *in-vacuo* plexiglass shell, f=150 Hz (Ω=0.05).

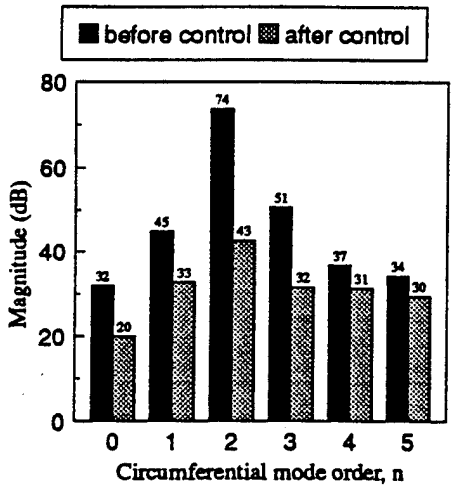

Figure 8. Modal decomposition of the radial acceleration of the shell one diameter beyond the error sensors, *in-vacuo* plexiglass shell, f=300 Hz (Ω=0.1).

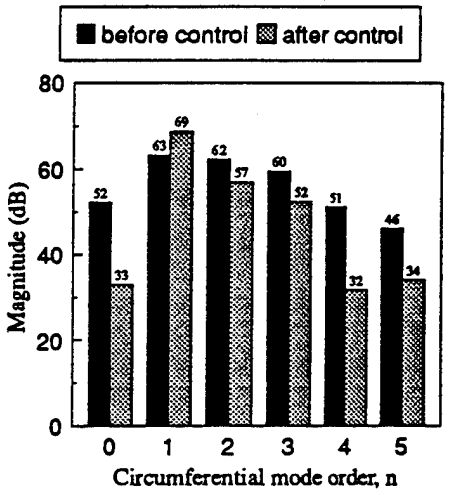

Figure 9. Modal decomposition of the radial acceleration of the shell one diameter beyond the error sensors, *in-vacuo* plexiglass shell, f=700 Hz (Ω=0.23).

For the final tests the plexiglass pipe was filled with distilled water and left to settle in order to remove all air bubbles. The control was turned on and the modal error signals again were attenuated for all tests by over 20dB. Fig. 10 shows the shell modal decompositions for a frequency of 80Hz (Ω=0.026). The decompositions indicate that the n=1 circumferential mode has rotated by θ=-58.8°, demonstrating the necessity of the paired orthogonal sensors discussed previously. The results of Fig. 10 show that all the modes are significantly attenuated with the attenuation of the n=1 mode being the least. Fig. 11 presents the attenuation in fluid pressure amplitude, with control, measured under the accelerometer array using the hydrophone discussed previously. The results demonstrate that the interior pressure field, and hence acoustic power, are also significantly attenuated over the fluid path cross section. The residual pressure distribution resembles an n=1 pattern which corresponds to the shell decompositions discussed above.

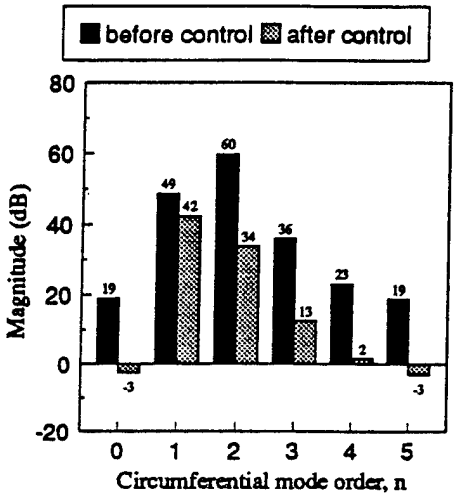

Figure 10. Modal decomposition of the radial acceleration of the shell one diameter beyond the error sensors, water-filled plexiglass shell, f=80 Hz (Ω=0.026).

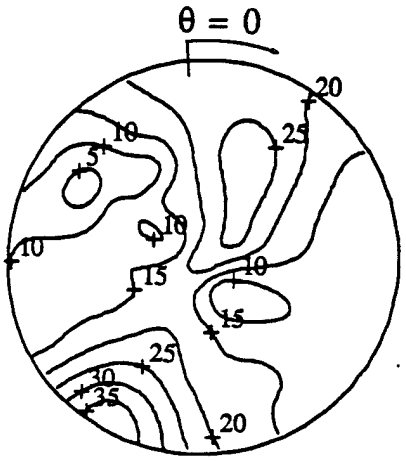

Figure 11. Pressure reduction (dB) with control, one diameter beyond error sensors, f=80 Hz (Ω=0.026).

When the frequency is increased to 150 Hz (Ω=0.05) the n=3 mode is now cut-on. The modal decomposition of Fig. 12 shows that the uncontrolled response is dominated by the n=2 mode, in contrast to the previous theoretical results. This behavior was thought to be again due to reflections from the termination, causing axial resonance in the n=2 motion. The results of Figs. 12 and 13 both confirm that the shell motion and the coupled interior field (and hence, power) were significantly attenuated.

When the frequency was increased further, the amount of reduction in both the shell vibration at the monitor accelerometers and the pressure at the hydrophone plane became increasingly smaller. Fig. 14 presents the shell modal decompositions at frequency of 350Hz (Ω=0.11) and the overall levels are seen, from Fig. 14, to have increased when the control was turned on (even though the error signals were all highly attenuated). An examination of the interior pressure field also reveals an increase with control, implying the total power in the system was increased by the active control. As discussed in the theoretical section, this behavior is due to the increased number of propagating modes at this frequency leading to significant control spillover and degradation in control performance.

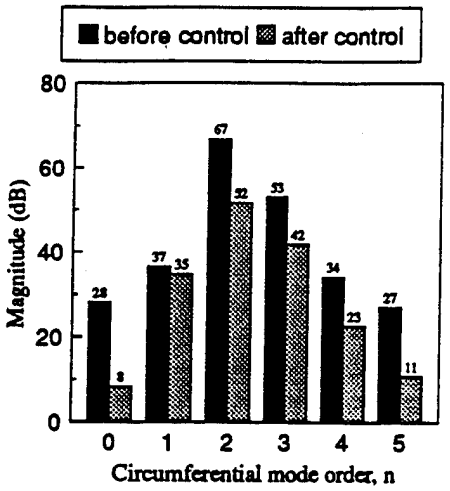

Figure 12. Modal decomposition of the radial acceleration of the shell one diameter beyond the error sensors, water-filled plexiglass shell, f=150 Hz (Ω=0.05).

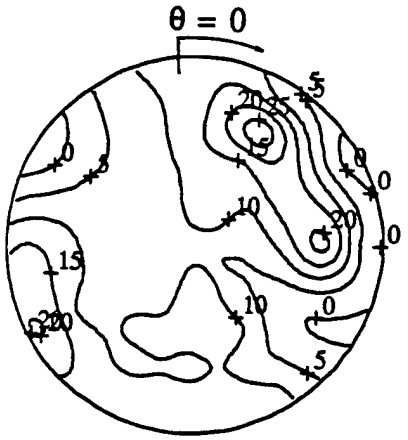

Figure 13. Pressure reduction (dB) with control, one diameter beyond error sensors, f=150 Hz (Ω=0.05).

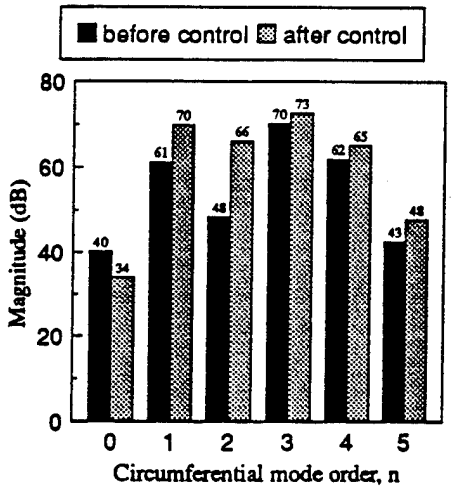

Figure 14. Modal decomposition of the radial acceleration of the shell one diameter beyond the error sensors, water-filled plexiglass shell, f=350 Hz (Ω=0.11).

CONCLUSIONS

An analytical and experimental investigation of the potential of active control of the total power flow in fluid-filled elastic pipes has been completed. The results demonstrate that the power in both the fluid and structural path can be significantly attenuated for a substantial low frequency range using a 3I30 feedforward system of structurally mounted actuators and sensors. At higher frequencies the performance is limited by an increasing number of cut-on waves, and could be improved by increasing the number of control channels. A result of particular importance was the demonstration, both theoretically and experimentally, of the attenuation of the acoustic power in the fluid field with actuators mounted to the exterior of the pipe. This arrangement shows potential when it is not desirable, or possible, to use active acoustic sources in the fluid medium.

In general, the results demonstrate the good potential of using active control to alleviate low frequency power in fluid filled pipes even though the dynamic system is rather complex. To this end, care must be taken to consider the physics of the problem before designing the control arrangement.

REFERENCES

1. Brevart, B. J. and Fuller, C. R., "Active control of axisymmetric wave propagation in fluid filled elastic cylindrical shells", *Journal of the Acoustical Society of America*, **90(4)**, Pt. 2, 2271 (1991).
2. Brevart, B. J. and Fuller, C. R., "Active control of coupled wave propagation in fluid-filled elastic cylindrical shells", *Journal of the Acoustical Society of America*, **94(3)**, Pt. 1, 1467-1475 (1993).
3. Brevart, B. J., "Active control of coupled wave propagation in fluid-filled elastic cylindrical shells", Ph.D. Thesis, Virginia Polytechnic Institute and State University, Blacksburg, Virginia, (1994).
4. Harper, M. and Leung, R., "Active vibration control in pipes", *Proceedings of Inter-Noise 93*, 871-874, (1993)
5. White, P. H. and Sawley, R. J., "Energy transmission in piping systems and its relation to noise control", *Transactions of ASME Journal of Engineering for Industry*, **94**, 746-751 (1972)
6. Fuller, C. R. and Fahy, F. J., "Characteristics of wave propagation and energy distributions in cylindrical elastic shells filled with fluid", *Journal of Sound and Vibration*, **81(4)**, 501-518 (1982)
7. Fuller, C. R., "The input mobility of an infinite circular cylindrical elastic shell filled with fluid", *Journal of Sound and Vibration*, **87**, p409-427 (1983)
8. Leissa, A. W., "Vibration of shells", *NASA SP-288*, Washington, D.C. (1973)
9. Lee, C. K. and Moon, F. C., "Modal actuators/sensors", *ASME Journal of Applied Mechanics*, **57**, 434-441 (1990)
10. P. A. Nelson and S. J. Elliott, *Active Control of Sound*, (Academic Press, London, 1992)
11. Pinnington, R. J. and Briscoe, A. R., "External applied sensor for axisymmetric waves in a fluid-filled pipe", *Journal of Sound and Vibration*, **173(4)**, 503-516 (1994)

ACKNOWLEDGMENTS

The authors gratefully acknowledge the support of this research by the Office of Naval Research, Dr. K. Ng, Technical Monitor, Julien Maillard for help with the graphics and Dee Meier for her patience in typing and manuscript preparation under pressure.

APPENDIX

List of symbols.

w	radial displacement	x	axial coordinate
ρ_s	structural density	ω	frequency
c_L	longitudinal phase speed	J	cost function
h	shell thickness	F_d	force amplitude of disturbance
a	shell mean radius	F_c^n	control amplitude for n'th mode
n	circumferential modal order	Ω	non-dimensional frequency ($=\omega a/c_L$)
θ	angular coordinate	x_e^n	axial location of error sensor for mode n
I_{33}	matrix term	x_c^n	axial location of control actuator for mode n
k_n	axial wavenumber for mode n	ε_n	=1, for n=0, =2 for n>0

C-7 Control of Sound Radiation with Active/Adaptive Structures, C. R. Fuller, C. A. Rogers and H. H. Robertshaw, Journal of Sound and Vibration, Vol. 157 No. 1, pp. 19-39, 1992.

Journal of Sound and Vibration (1992) **157**(1), 19–39

CONTROL OF SOUND RADIATION WITH ACTIVE/ADAPTIVE STRUCTURES†

C. R. FULLER, C. A. ROGERS AND H. H. ROBERTSHAW

Vibration and Acoustic Laboratories, Department of Mechanical Engineering, Virginia Polytechnic Institute and State University, Blacksburg, Virginia 24061, *U.S.A.*

(*Received* 18 *October* 1990, *and in final form* 26 *May* 1991)

This paper is concerned with a discussion of recent research in the area of active structural acoustic control with active/adaptive structures. The material is divided into progress in the areas of structural acoustics, actuators, sensors and control approaches. However, due to the coupled nature of the problem, considerable effort throughout the program has been given to the interaction of these areas with each other. The results presented show that significant progress has been made towards controlling structurally radiated noise by active/adaptive means applied directly to the structure.

1. INTRODUCTION

In many applications the sound fields radiated by vibrating elastic structures are an important noise problem. Examples are machinery noise in factories, marine hull radiated noise and interior noise in aerospace applications. An understanding of the behavior of such systems, with a view to controlling them, involves the field of structural acoustics. Structural acoustics is the study of how elastic structures radiate or receive sound [1] and in its most fundamental form involves the simultaneous solution of the differential equations describing the structure and fluid media with appropriate coupling conditions between the two (a "fully coupled" analysis).

The usual methods of control of such radiated noise fields involve passive techniques such as added mass, damping, stiffness and system modification through re-design. However, these techniques have proved unsatisfactory in many applications for a number of reasons. Passive techniques usually imply a significant mass increase, do not work well at low frequencies and, due to the "coupled" nature of the problem, it is difficult to predict their effect except in the simplest of applications. One approach that shows much potential to overcome these difficulties is active control. Active control has recently re-emerged as a very promising technique to reduce radiated sound fields [2]. The main reason for this have been advances in high speed data acquisition and processing enabling active control to be implemented in "real time". The traditional active approach to the problem of reducing sound radiation from structures is to use a number of secondary acoustic control sources arranged around the structural noise source (see, for example, reference [3]). This technique can be seen to have a number of disadvantages. From an implementation point of view, it is often impracticable to have secondary acoustic sources located away from the structure (as well as error microphones). More importantly, the use of acoustic control sources leads to a generation of additional unwanted noise, termed "control spillover". This situation is overcome by using additional strategically positioned acoustic sources.

†This paper was first presented at SPIE Conference 1170 on Fiber Optic Smart Structures and Skins II, Boston, Massachusetts, 5–8 August 1989.

0022–460X/92/160019+21 $08.00/0

© 1992 Academic Press Limited

Thus, for example, a machine radiating noise requires a large number of active acoustic sources arranged around it to produce global (here global means throughout an extended volume or space) noise reduction [3].

The purpose of this paper is to overview research related to a new technique in which the noise radiated from vibrating structures is reduced by active inputs applied directly to the structure itself. The active inputs may take the form of oscillating forces or strains, adaptive steady state forces or adaptive changes in material properties. While the control inputs are applied directly to the structure, the error information (i.e., the variable to be minimized) is usually taken from the radiated acoustic field. The subtlety of this approach is that one can take advantage of the nature of the natural structural acoustic coupling in order to optimize and reduce the dimensionality of the controller. The discipline thus involves the study of the interaction of controller–structural acoustics. A patent on the technique has recently been awarded [4]. As the aim of the work is to develop structures with embedded actuators and sensors as well as to develop "intelligent" control approaches, the work falls into the domain of what is called adaptive or active structures.

The rapidly emerging field of adaptive structures, and the early work that stimulated it, is well summarized in the review article by Wada *et al.* [5]. In Figure 1, which was based on reference [5], is shown a general framework for adaptive structures. The two most basic systems are the sensory structures in which only information related to the states or parameters of the structure are measured. Adaptive structures are those which include actuators which can alter the system states or parameters in a controllable way. The interaction of these two areas is defined by Wada *et al.* [5] as "controlled structures", and thus includes some degree of control intelligence in dictating the required inputs to the actuators to achieve the required sensed states or parameters. A finer definition on controlled structures is "active structures", in which the actuators and sensors are highly integrated into the structure itself. Due to the fact that the sensors and actuators are directly part of the structure, one may then view the structure itself adapting its properties in an active way to a disturbance. Finally, when the control elements and electronics, and perhaps even power sources, are directly integrated into the structure itself, the structure is defined to be "intelligent" in that it appears to provide its own support energy and cognitive ability (although it admittedly had to be "taught" its process at one stage). For a detailed discussion of the foundation work in sensors, actuators, and applications, the reader is referred to reference [5].

In terms of controlling sound radiation from structures using active or adaptive means applied directly to the structure while sensing some state or parameter of the structural-acoustic system, very little previous work has been done. Knyasev and Tartakovskii [6] demonstrated in a brief experiment that it was possible to reduce sound radiation from a

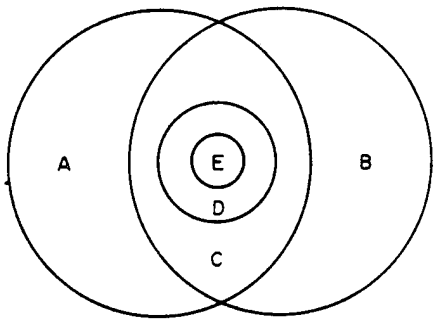

Figure 1. Framework for structures with integrated functions. A, adaptive structures; B, sensory structures; C, controlled structures; D, active structures; E, intelligent structures.

panel using an active damping force. Vylayshev *et al.* [7] analytically considered sound transmission through an one-dimensional plate and showed an increase in the plate transmission loss with one active control force applied to the plate. Fuller and Jones [8] and Jones and Fuller [9] showed both experimentally and analytically that sound transmission into a model elastic fuselage can be globally controlled with a small number of point force control inputs applied to the structure. This early work [8, 9] defined the basis of the research in the present paper; while the control inputs are applied to the structure, the error information is taken from the acoustic field and thus the controlled system includes the natural coupling between the structural response and the acoustic field. This approach will be shown, for low frequency applications, markedly to reduce the dimensions of the controller.

The following sections will detail recent work on this new technique. For clarity, the discussion is divided into four areas: structural acoustics, actuators, sensors and control approaches. However, the research is always a complete synthesis of the above four areas due to the "coupled" nature of the problem. For brevity, the paper is limited to a discussion of the concepts and results; details of the experiments or analyses can be found in the appropriate references. The authors believe that the paper defines a rapidly emerging new field in noise control.

2. STRUCTURAL ACOUSTICS

Structural acoustics is directly concerned with the coupling between the motions of elastic structures and their radiating (or receiving) sound fields. The response of these systems must be solved simultaneously (or in a coupled sense), as in heavy fluids or highly reactive environments the back loading (radiation impedance) of the acoustic field affects the motion of the radiating structure [1]. Obviously this natural "feedback" loop has important implications on the design of active systems for such situations. In this section some of the important characteristics of structural–acoustic coupling and how they relate to the present problem will be discussed. One important aspect of how structures radiate sound is known as radiation efficiency σ, which is defined as the ratio of the acoustic power that a structure radiates to the power radiated by a piston of equivalent area vibrating with an amplitude equal to the time-spatial average of the structure. Obviously the higher σ is, the more sound energy will be radiated for a given structural response. As an example, in Figure 2 is shown the radiation efficiency of various modes of vibration of

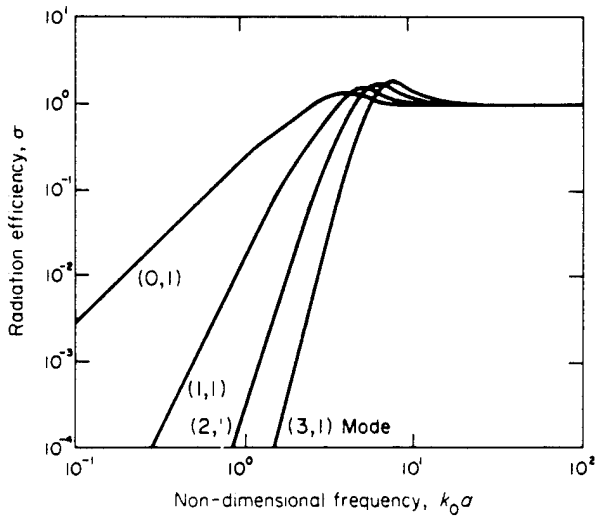

Figure 2. Modal radiation efficiency of clamped circular panel in a baffle.

a baffled circular clamped plate versus the non-dimensional frequency $k_0a = 2\pi fa/c$, where f is frequency of excitation, a is plate radius and c is the speed of sound [10]. For low frequencies, σ is seen to vary strongly with modal order (m, n), where m and n are circumferential and radial mode numbers, respectively. The most efficient mode is the (0, 1) or monopole-like mode. All modally responding structures exhibit behavior related to Figure 2. Thus, if a structure is vibrating in a number of modes of nearly equal amplitude then only a few of these will radiate sound in the low frequency region (which is our frequency region of interest). This implies that only one or two control inputs need be applied to the structure to reduce the radiated field as long as the error information is constructed from radiated acoustic variables.

In Figure 3 are shown results from an experiment in which sound transmitted through an elastic clamped circular panel located in a baffle is reduced by active point force inputs applied to the panel [11]. The error points are two microphones in the radiated acoustic field. In this experiment the aluminum plate was 0·4572 m in diameter and 1·27 mm thick. The incident acoustic wave was planar at an angle of incidence of 45° and was at a single frequency of 112 Hz. Substantial reduction in radiated noise is observed in this off-resonance case where there are many panel modes present in the response. In contrast, the same situation is shown in Figure 4 except that the error information is taken from two accelerometers mounted on the panel (i.e., directly controlling panel vibration). The results

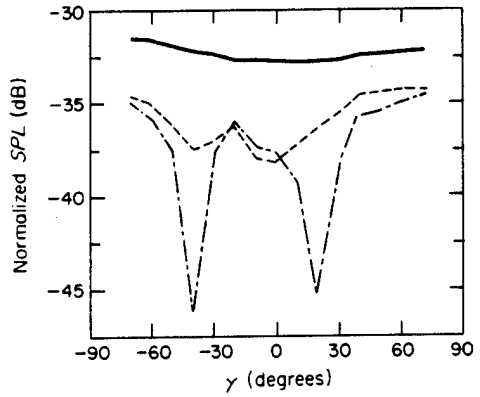

Figure 3. Radiation directivity, microphone error sensors: ——, no control; - - -, one control; — · —, two controls.

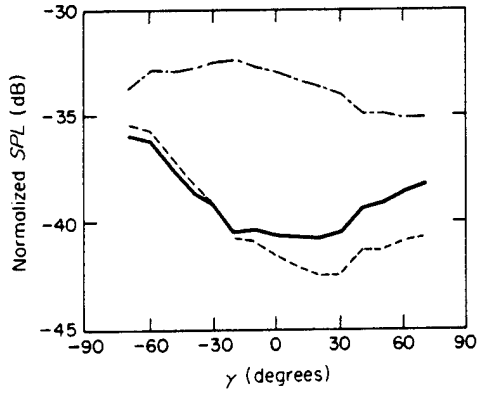

Figure 4. Radiation directivity, accelerometer error sensors: ——, no control; - - -, one control; — · —, two controls.

show that, although panel vibration is attenuated by around 20 dB at the error points, the noise radiation *increases*.

Radiation impedance, a related variable, is also an important characteristic to be considered. Analytical results for a similar situation as discussed above are shown in Figure 5.

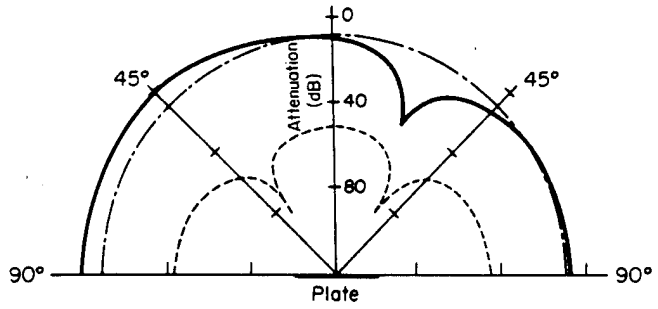

Figure 5. Radiation directivity: ——, no control; — · —, one control; – – –, two controls.

Here the cost function is the total power radiated from the panel rather than minimizing at discrete points and the non-dimensional frequency is $k_0a = 0{\cdot}45$ [12]. Significant increases in sound attenuation are observed when the number of actuators is increased from one to two, while the corresponding panel displacement shown in Figure 6 predicts little change in overall panel amplitude of vibration. In Figures 7 and 8 are given experimental results for radiation directivity and amplitude of panel modes of vibration for control of sound radiation from a vibrating rectangular panel located in a baffle by a single point force [13]. The error sensor is a microphone situated in the radiated acoustic field. The panel is being driven off-resonance. In this case the panel was manufactured from steel with dimensions of $380 \times 300 \times 10$ mm and was excited at a frequency of 1698 Hz, by a non-contacting electromagnetic exciter. Again the results show a significant reduction in radiated sound with relatively little change in panel amplitudes of vibration. What is happening here? The key lies in the results of Figure 8, which show that the relative temporal phases of the uncontrolled modes have changed significantly. Thus the action of the controller has been to alter the relative phases of the modes, with the result that the total residual vibration shape is more complex and has a lower radiation efficiency. More exactly, the modes have been adjusted so that their total radiation impedance is lower, leading to a fall in radiated sound power [14]. We call the first mechanism, where a dominantly radating mode(s) is

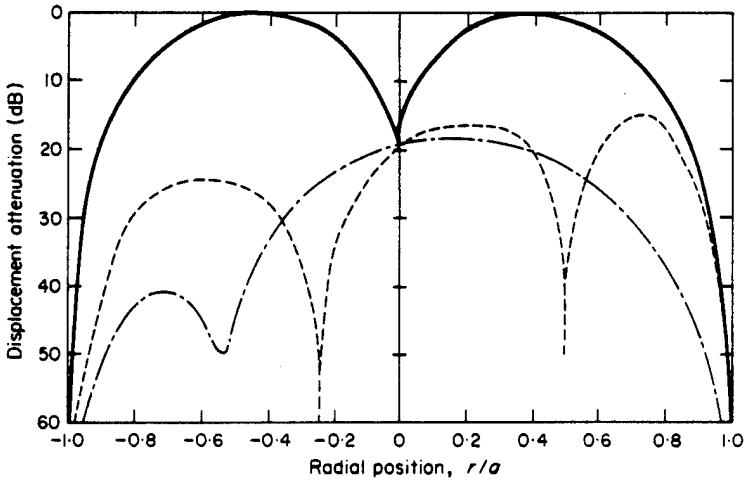

Figure 6. Panel displacement: ——, no control; — · —, one control; – – –, two controls.

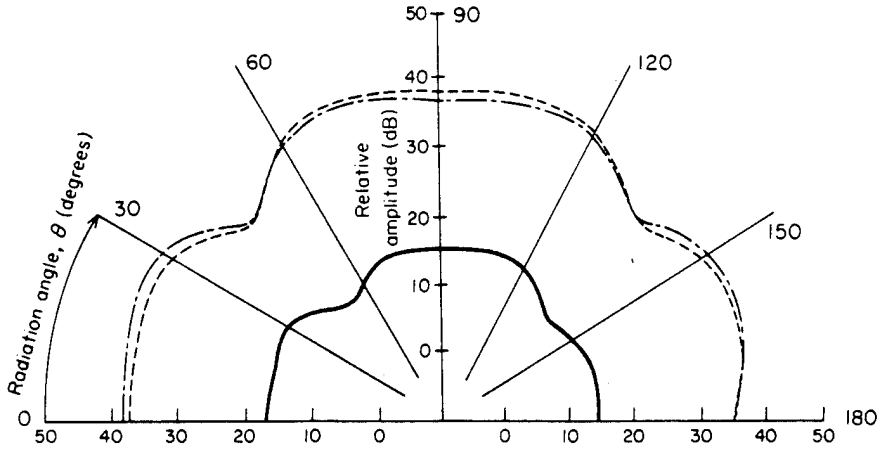

Figure 7. Radiation directivity: — · —, no control; - - -, control field; ——, with control.

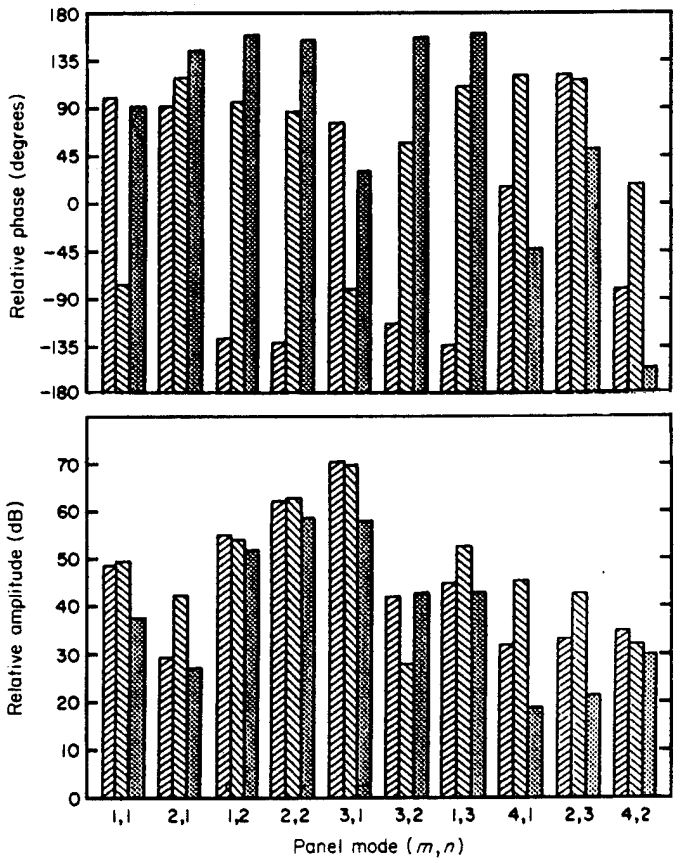

Figure 8. Panel modal response distribution: ▨, no control; ▧, control field; ▩, with control.

reduced in amplitude, control by *modal suppression*; and the second, where the plate response does not reduce but has a lower value of σ, control by *modal restructuring* [13]. Recent work has analyzed this behavior from a wavenumber point of view. By taking the 2-D wavenumber transform of the plate-baffle system one can show that modal suppression corresponds to a general fall in the amplitude of plate response across the complete wavenumber spectrum, while model restructuring correspond to a reduction in supersonic wavenumber components and an increase in subsonic components [15]. As discussed in

reference [1], only supersonic wavenumber components radiate to the far field, and thus although the averaged panel response is approximately the same or possibly greater, the radiated far field sound levels fall globally.

This brief discussion highlights the nature of the structural–acoustic coupling in the control approach. It is apparent that the controlled behavior of these systems can be viewed in a number of ways. These insights, as well as many other aspects of natural sound radiation, can be taken advantage of in such control approaches.

3. ACTUATORS

The above-discussed results pertain to the use of point force actuators as control transducers. There are disadvantages of such devices, mainly that they are cumbersome and require some form of restraining back support. In view of these limitations, much work has been carried out in order to develop actuators bonded to or embedded in the structure itself.

3.1. PIEZOCERAMIC ACTUATORS

Analytical work has shown that piezoceramics can be bonded to the structure surface and used to excite selected modes of vibration [16]. The piezoceramics can be tailored in shape and location in order to selectively excite certain modes of vibration. This has the advantage of reducing control spillover into unwanted structural or acoustic response. In Figure 9 are shown impressive results for control of sound radiation from a baffled circular panel of radius 0·2 m with a radiation from a baffled circular panel of radius 0·2 m with a small piezoceramic patch of dimensions $R_1 = 0{\cdot}15$ m, $R_2 = 0{\cdot}18$ m, $\theta_1 = -15°$, $\theta_2 = 15°$, bonded on the panel [17]. The excitation frequency is 89·1 Hz. Plots of panel displacement under the same conditions across the same diagonal as the radiation pattern are given in Figure 10. Interestingly, this result (and others) predict that the piezoceramic tends to force a node in the panel response near the actuator edge. This result is in line with the analysis of reference [16], which predicts that the piezoceramic effectively exerts a line moment on the structure (for pure bending cases) around its periphery. Thus the above results imply that a good location of the edge of a piezoceramic is near nodal lines and also show possibilities for edge control where structural rotation is high while out-of-plane vibrational motion is low. However, in general, the center of the transducer should be located in regions of high structural surface strain.

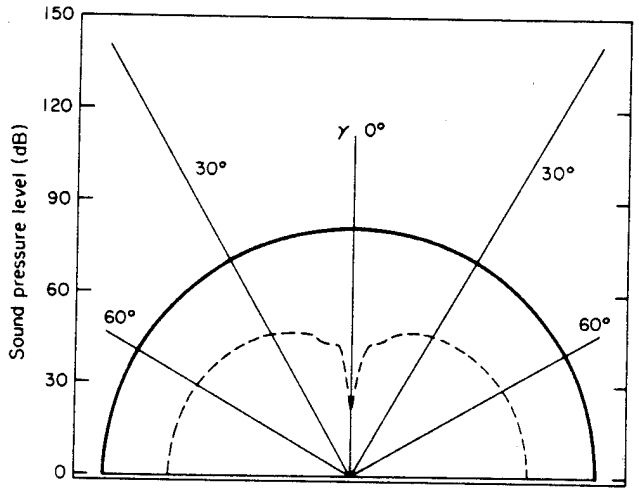

Figure 9. Radiation directivity: ——, no control; – – –, with control. $R_1 = 0{\cdot}15$ m, $R_2 = 0.18$ m, $\theta_1 = -15°$, $\theta_2 = 15°$.

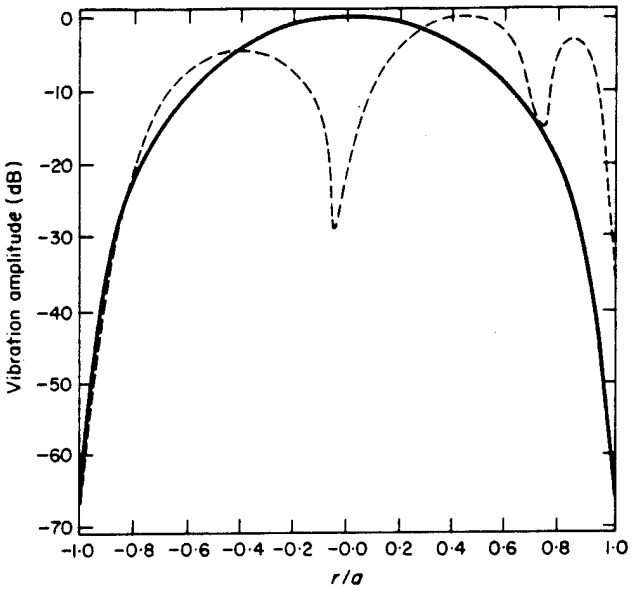

Figure 10. Panel displacement: ——, no control; - - -, with control. $R_1 = 0{\cdot}1$ m, $R_2 = 0{\cdot}18$ m, $\theta_1 = -15°$, $\theta_2 = 15°$.

In Figure 11 are given experimental results for radiation control from a baffled rectangular panel by a single, centrally located, small piezoceramic patch [18]. The panel has the same dimensions as that discussed in Figures 7 and 8, except it has a thickness of 2 mm. The panel is being driven near the resonance of a (3, 1) mode at a frequency of 350 Hz and the error sensor is a single microphone located at 1·8 m from the panel. The results of Figure 11 show excellent global attenuation and panel modal decompositions demonstrate that all panel modes are significantly reduced in amplitude; a surprising result for a single actuator. This effect as well as multi-actuator, multi-sensor (MIMO) systems are presently under investigation [19].

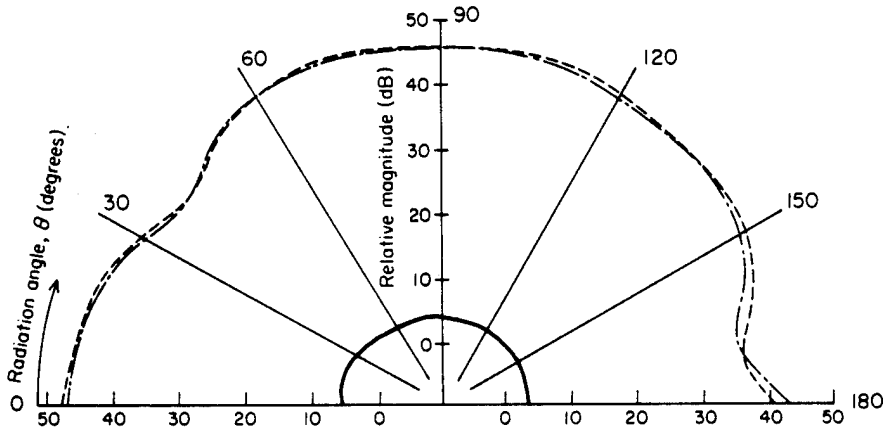

Figure 11. Radiation directivity: — · —, no control; - - -, control field; ——, with control.

3.2. SHAPE MEMORY ALLOY ACTUATORS

Other important work in this area has been concerned with the use of shape memory alloys (SMA) as adaptive inputs. The mechanism by which shape memory alloy fibers (or films) exhibit their characteristic shape memory effect can be described very basically as follows: an object in the low temperature martensitic condition, when plastically deformed

and with the external stresses removed, will regain its original (memory) shape when heated. The process is the result of a martensitic phase transformation taking place during heating. The main aim of the work is the development of adaptive structures utilizing embedded shape memory alloys (SMA). The applications of such "smart" structures are many [20] and much work has been carried out to derive the fundamental equations of motion of such structures [21]. However, the discussion here will be limited to those related to the structural acoustic problem.

Sound radiation has been demonstrated to be related to modal response and shape [1]. Thus if one can alter the mode shapes of a vibrating structure, then the acoustic power radiated by such structures may be reduced (or increased). Analytical work on simply supported panels with embedded SMA fibers of various configurations has shown that, when the fibers are activated (i.e., heated by passing a current through them), significant modification in the radiated acoustic field is achieved. In Figure 12 is shown radiation directivity for an activated SMA panel: activation of the fiber can be seen to cause a significant change in the radiation pattern [22]. This effect has been demonstrated to be due to changes in the panel mode shapes and thus the structural acoustic coupling when the fibers are activated [23]. For the analytical example of Figure 12, the composite plate was of dimension 1·1 m × 0·8 m × 0·008 m, with a quasi-isentropic stacking sequence of [0/-45/45/90] and constructed from equal thickness layers of graphite/epoxy and Nitinol/epoxy. The Nitinol was assumed to be the top and bottom plys of the laminate with a 40% fiber volume percentage, yielding 10% for the entire plate. The Nitinol was also assumed to achieve a recovery stress in the fibers upon activation of 280 MPa. The damping factor δ was set equal to 0·01.

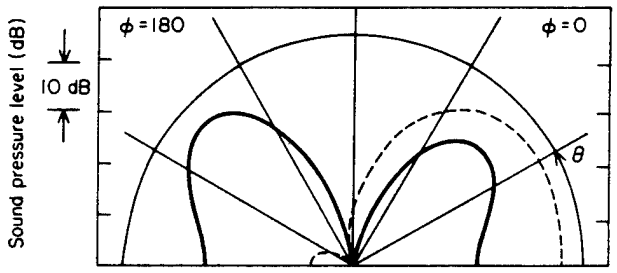

Figure 12. Radiation directivity: - - -, active; ——, inactive.

It should be noted here that, in contrast to the piezoceramic transducer, the active input is not oscillating and what is really being developed here is a truly adaptive (or smart) structure, properties and response of which can be altered by electrical inputs. However, work is progressing on developing a vibrating SMA actuator. In Figure 13 are presented transmission loss (TL) curves for sound transmitting through a SMA panel with and without activation [22] and excited by a plane wave incident at 45°. The main point demonstrated in Figure 13 is that significant modification in the TL curve can be achieved by SMA. Much work is now needed to optimize the layout and activation of the SMA fibers optimally to reduce sound radiation in a required way, based on formulations for the modification in modal shapes and their corresponding radiation efficiency.

Other work of interest concerns control of sound radiation from beams with embedded SMA fibers. In Figure 14 is shown the shift in measured resonant frequency of the fundamental mode of a clamped–clamped beam upon SMA activation [24]. Experiments on controlling radiation from such beams using SMA fibers have also been successful [25]. In this experimental arrangement, the beam has dimensions of 0·822 m × 0·206 m × 0·991 m and was constructed from a Nitinol reinforced graphite/epoxy material with a

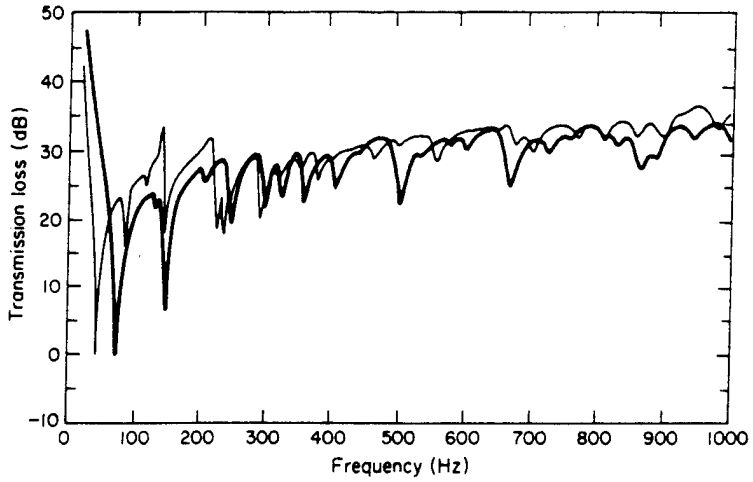

Figure 13. Panel transmission loss: ——, active; ——, inactive.

15% Nitinol volume fraction. The beam was excited into motion by a non-contacting electromagnetic transducer driven by a steady state pure tone frequency. The beam could thus be excited either on or off resonance of required modes by varying the input frequency. In Figure 15 is shown the time history of the sound pressure level of the beam responding to an excitation at the $n=4$ mode (145 Hz). The control strategy uses a pattern search technique, implemented on a mini-computer, to minimize the sound pressure, by adjusting the voltage applied to the embedded SMA fibers. For this case, the effect of the third mode moving close to the excitation frequency is evident at 40 s. The controller then adapted the input so that the disturbance was located at the minimum pressure response (an anti-resonance point) between the third and fourth modes.

4. SENSORS

For any control strategy, observability is an important requirement. Thus, sensing of the plant responses to be minimized is an important part of the research work described here. As stated previously, a key aspect of the approach is to use the radiated acoustic

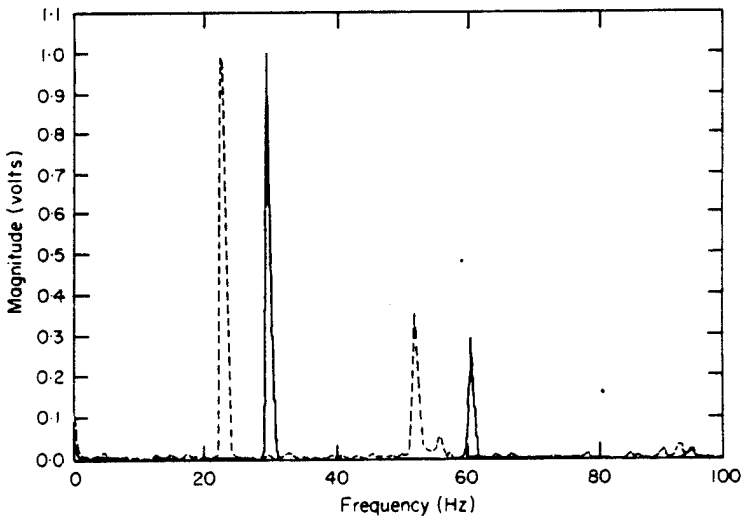

Figure 14. Adaptive SMA beam response: - - -, unactivated; ——, activated.

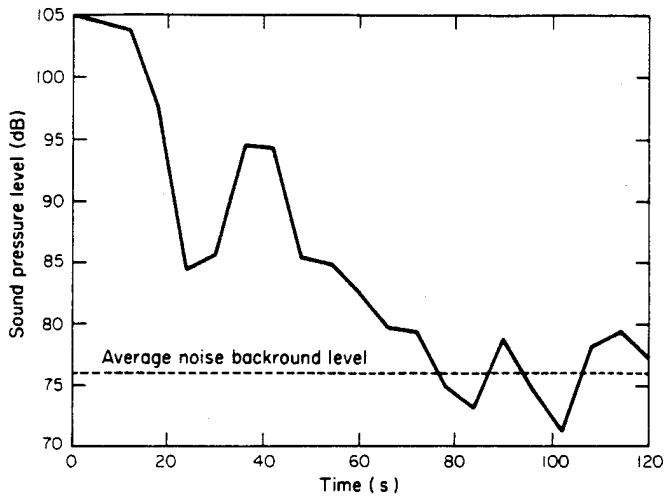

Figure 15. Adaptive control of radiation from SMA beam.

field as direct error information. Most of the previous results discussed here relate to using discrete microphones located in the radiated acoustic field. However, there are many situations in which such an approach is impractical and alternatives have to be sought.

4.1. OPTICAL FIBER SENSORS

Optical fiber waveguides, originally developed for medium distance data communication, have been applied to the sensing of physical observables for the past ten years [26]. By monitoring the intensity, phase, polarization, wavelength, mode and time delay properties of optical signals which propagate in such fiber waveguides, a wide range of physical phenomena relevant to the problem here, including strain, rotation rate, vibrational mode shape amplitudes and acoustic waves, may be measured.

Present work also entails integration of such approaches into the structural acoustic control problem. A spectral estimation of the response of a beam, measured by an accelerometer and an embedded optic fiber [27], is given in Figure 16. It is apparent that the optic

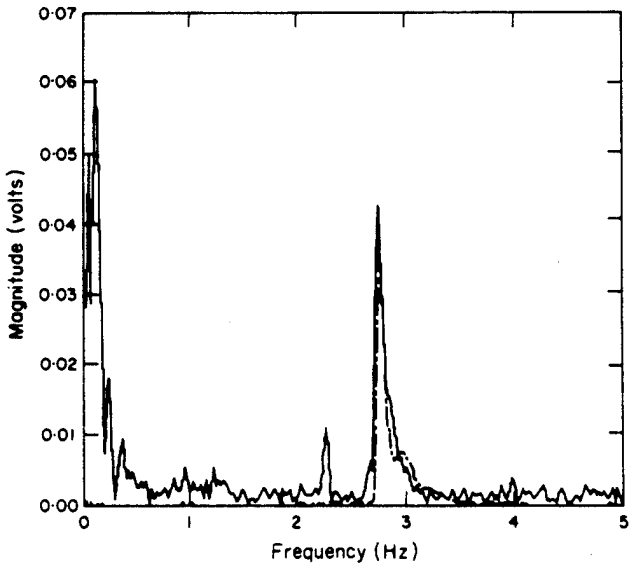

Figure 16. Fiber optic sensing of beam response: ——, fiber optic; — · —, accelerometer.

fiber gives a good estimation of the resonance frequency of the beam. In other applications, optic fibers have been used in conjunction with Kalman filtering to provide modal amplitudes of beam responses required for implementation of control [28]. In Figure 17 are given results of a simulation of such a system on a clamped–clamped beam when excited

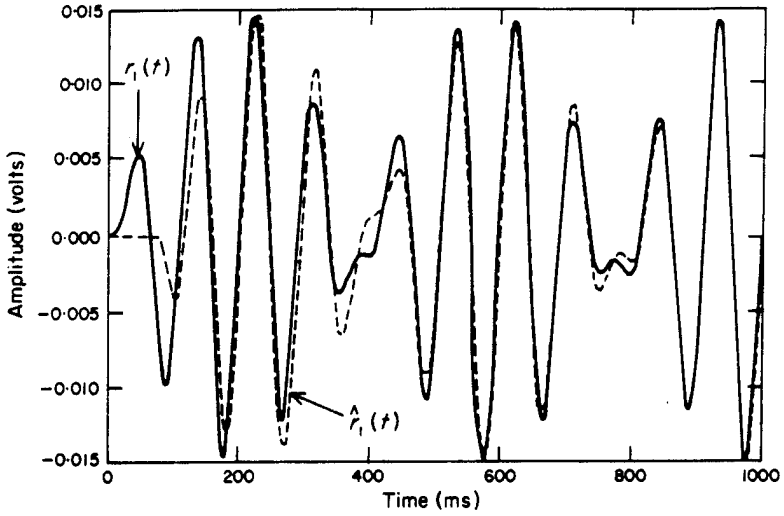

Figure 17. Kalman filtering modal identification.

by a steady state sine wave turned on at $t=0$. There is no damping in the system. The curves are the actual (r_1) and estimated amplitudes ($\hat{r}_1$) of mode 1. The results show that the modal amplitudes can be estimated accurately with a time domain approach. In order to derive a control variable in the radiated acoustic power these modal amplitudes may be weighted by their associated radiation efficiency, thus artificially introducing the structural acoustic coupling characteristic. To fully account for radiated power, the modal cross-interaction terms must also be considered. However, future work will be concerned with direct sensing of near-field acoustic pressures using optic fibers. In conjunction with acoustic holography theory [29], it will then be possible to construct a control cost function in terms of estimated far-field radiated acoustic power, from near-field measurements of pressure.

4.2. NITINOL FIBER SENSORS

Nickel–titanium shape memory alloys (SMA) have many peculiar properties, many of which can be exploited for activation or sensing applications. As is the case with many activator materials, such as piezoceramics and polyvinylidene fluoride (PVDF), Nitinol can be used to perform sensing as well as actuation. However, Nitinol strain sensors differ from Nitinol actuators in that the sensors utilize only one material phase, the austenite phase, whereas Nitinol actuators utilize the reversible transformation between the martensitic and austenitic phase. The distributed (or integrated) Nitinol sensors currently being utilized measure strain. The utility of the integrated strain information has been discussed above in reference to the optical fiber sensors.

The Nitinol fiber strain sensors are simply Nitinol wires with a low transition temperature, so as to assure that the material is always in the austenite phase. In our studies, pseudo-elastic or super-elastic Nitinol has been used. The basic concept is to measure the change in resistance of the Nitinol as a function of integrated strain. This concept allows for very simple processing as the Nitinol sensor is nothing more than a distributed strain gage in a Wheatstone bridge. Nitinol has a high resistivity for a metal, making it well

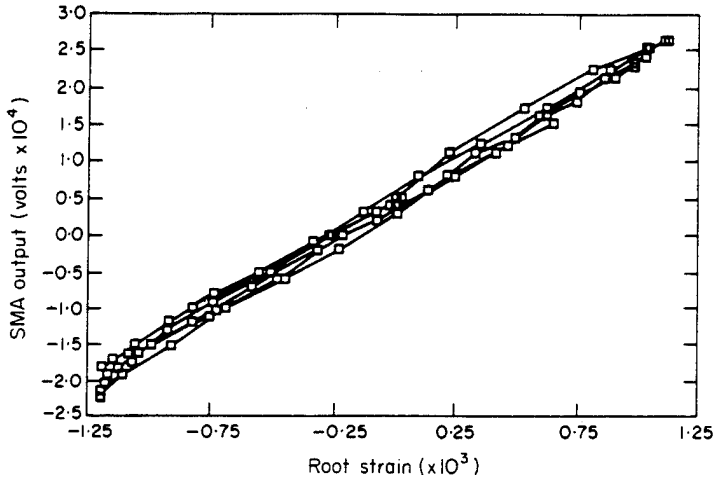

Figure 18. SMA strain sensor.

suited for strain sensing. The super-elastic nature of the Nitinol also means that strains up to 6% can be reliably and repeatedly measured.

Experimental demonstration of the Nitinol sensor was performed by embedding a 0.012 in diameter fiber in a fiberglass cantilever beam off the neutral axis. The Nitinol sensor was then used as the active leg of a Wheatstone bridge. When the embedded Nitinol fiber is strained, the resistance increases and the bridge is no longer balanced, resulting in a voltage across the bridge. The cantilever beam was used to verify the integrated strain capabilities of the fiber in both static and dynamic modes. Static and dynamic tests showed a linear response for root strains (of the fiber) up to 1·2%, the maximum strain tested with the beam. Calibration tests of the Nitinol fiber itself have indicated a linear response greater than 6% strain. However, once the sensing fiber has been strained beyond 6% it becomes plastically deformed. The experimental response of the embedded Nitinol fiber to a freely vibrating cantilever beam at approximately 4 Hz is shown in Figure 18. The primary advantages of Nitinol strain gages is their ease of implementation and large range. Current work involves using the Nitinol fiber as a dual-mode sensor, i.e., to measure temperature and strain simultaneously.

4.3. PIEZOCERAMICS AND POLYVINYLIDENE FLUORIDE (PVDF)

Piezoceramics can also be used as sensors. The advantage of this strategy is that the same devices can be used in some applications in a time sharing mode as actuators and sensors. A comparison of a fast Fourier transform (FFT) of the response of a panel excited by an impulse [18] is shown in Figure 19. The response is measured by a centrally co-located accelerometer and a piezoceramic element bonded to the panel. The estimates of panel resonant frequencies by the piezoceramic can be seen to be good, and thus the information could be used as a control variable for an estimate of the spectral content of the noise input. Other experiments on control of vibrational power flow in beams have also indicated that such piezoelectric devices can be used to sense other control variables [30], such as vibrational response and power flow. Although the above devices can be successfully used to measure structural response, this data must be then manipulated to account for the structural acoustic coupling. A direct measurement of the radiated pressure field would be simpler and it is in this application that PVDF shows much potential. This material has been demonstrated to be of enough sensitivity to be able to measure acoustic pressure fluctuations, and can be easily used as a distributed sensor where averaged effects (i.e., over a distributed control area) are required.

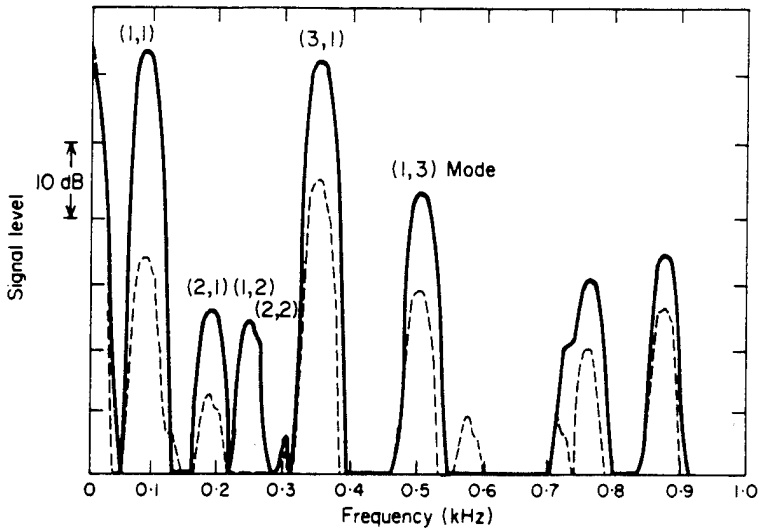

Figure 19. Piezoceramic sensing of panel response: ——, piezoceramic; - - -, accelerometer.

Reference [15] discusses experimental work in which PVDF distributed sensors were directly attached to vibrating panels and used as error sensors in an active structural–acoustic control approach. When the PVDF sensors were shaped to only observe the odd–odd modes of the simply supported panel (i.e, the efficiently radiating modes), high global reductions in far-field sound were measured. This result should be contrasted with the use of point structural sensors such as accelerometers, which often lead to an increase in radiated sound levels [11]. In effect, the shaped PVDF sensor acts as an analog structural wavenumber filter. If the sensor is long compared to the structure, then the PVDF sensor averages the response of high wavenumber, short wavelength inputs (subsonic components) to zero, while retaining information from the low wavenumber, long wavelength inputs (supersonic components). As discussed previously, a structural error sensor with these characteristics is highly desirable, as the controller is only observing the critical radiating components of the motion of the structure. Associated with such approaches is a significant signal processing requirement, in which the sensed data is converted into the required control variables.

5. ACTIVE CONTROL TECHNIQUES

An important aspect of active control of sound radiation from structures is the choice, design and implementation of a suitable control strategy. Ultimate choice of strategy is dependent upon a number of factors, but perhaps the most important is the nature of the noise input; whether it is steady state sinusoidal (including multiple frequencies), random or transient. All of these noise conditions will be encountered in structural acoustic applications.

5.1. STATE FEEDBACK CONTROL TECHNIQUES

Research into the application of state feedback methods has focused on casting the structural acoustics control problem into the paradigms of modern control theory. In one investigation [31], the Linear Quadratic Regulator (LQR) optimal method has been applied to the control of radiation from a subsonic baffled, clamped–clamped beam in air. The approach was to consider the suppression of the transient radiation of the structure when it has been excited by impulsive forces or initial conditions. The structure was

described via an Euler–Bernoulli model of a uniform clamped–clamped beam. This partial differential equation description was then discretized using a Ritz-type expansion in terms of the first three controlled modes of the beam.

The fluid medium, air in this case, was modeled by assuming a harmonic motion input from the beam structure as one argument of a Rayleigh integral written to yield the spatial, far-field pressure distribution. The resulting integral was then treated as a transfer function between the terms of the assumed beam spatial expression (the uncontrolled modes) and the far-field pressure distribution. This study treated only the diagonal terms (the direct terms) of the resulting spectral factorizations of the radiation resistance of the modes. These transfer functions were then implemented as filters in a real-time control analysis. Causality was ensured by using the inverse Laplace transform to derive the filter impulse response functions. This formulation allowed the acoustic radiation to be inferred from the structural motions.

These relations were used as partial state estimators in a LQR optimal control formulation. The performance of the controller designed to reduce radiation (acoustic controller) was compared to the performance of a controller designed to reduce beam vibration. Equal energy was assumed for each case in order to normalize the comparisons. The modal time history of the beam with two force actuators, used to suppress vibration is shown in Figure 20. The result of the acoustic control is shown in Figure 21; the radiation was reduced by 73% as compared to that of the vibration controller. Increased attenuation could be achieved by decreasing the penalty factor on control effort. Note that the acoustic controller allows mode two, an inefficient radiator, to ring much longer than was allowed by the vibration controller; it, instead, puts its energy into the more efficiently radiating third mode. This work is being extended to treatment of the radiation coupling of the modes and to experimental realizations.

Other work with state feedback control of structural acoustic radiation involves the control of SMA-reinforced composite beams [25]. Part of this experimental work, the pattern search minimization, was discussed earlier in section 3.2 of this paper. Another portion of this work was concerned with the closed-loop tuning of the beam radiation response anywhere within an octave bandwidth above the fundamental mode. It has been

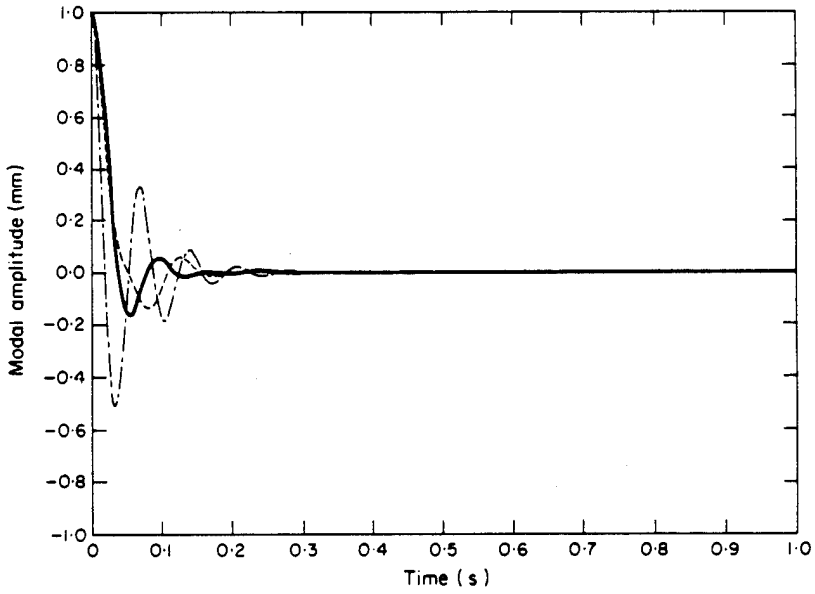

Figure 20. LQR control of beam response: ——, mode 1; ..... mode 2; - · - · - ·, mode 3.

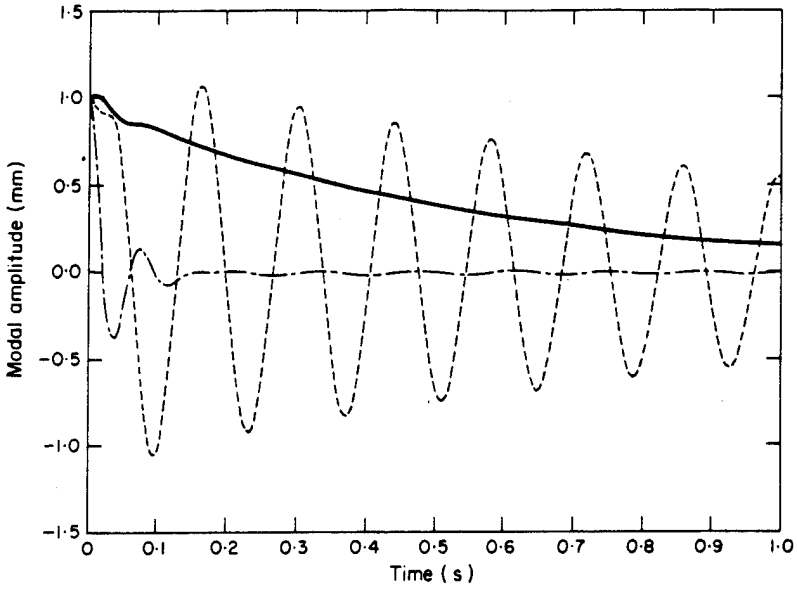

Figure 21. LQR control of beam sound radiation: ——, mode 1; – – –, mode 2; – · – · – · , mode 3.

demonstrated [32] that the frequency of the lower order vibration modes of a clamped–clamped SMA composite beam are linearly related to the bulk temperature of the beam. The control approach was to use the measured temperature as a controlled variable to indirectly control the beam radiation. This experimental and analytical study had as its goal the maximization of the radiation response of the beam subjected to a steady state disturbance.

The beam was modelled with a first-order, thermal capacitance model. The control was accomplished via a minicomputer which adjusted the amount of resistive heating of the SMA filaments in the composite structure to reach and hold a preset temperature. In Figure 22 are shown the results of the control with the beam being driven at 46 Hz, which is off the 35 Hz unactuated fundamental mode frequency. The closed-loop control increased the radiated sound pressure level by 20 dB by moving the fundamental frequency of the adaptive beam close to 46 Hz. This demonstrates the ability of the feedback control scheme to place the beam resonant frequencies at a set point.

5.2. LEAST MEAN SQUARE (LMS) ADAPTIVE ALGORITHMS

For applications in which the noise field is a steady state sinusoidal input (or multiple frequencies) and in some cases random broadband, the feedforward LMS adaptive approach has proved quite successful [33]. In general, this approach relies on constructing a quadratic cost function by squaring the moduli of the error variables and then using various techniques such as steepest descent, pattern search, etc., to find the unique minimum of the cost function. The control approach may be implemented in both the time or frequency domain. An advantage of the LMS approach is that unlike optimal control, little system identification is needed. An important consideration is that a good spectral estimate of the noise signal is needed. However, in many applications this can be either measured or computed directly from the noise input excitation (for example, the fundamental propeller frequency is directly related to shaft speed and number of blades).

Another important aspect of the feedforward LMS control approach is that, in general, as contrasted with the optimal approach, it relies on control inputs to the structure which may be viewed as having all the mass, spring and damper parameters of an attached

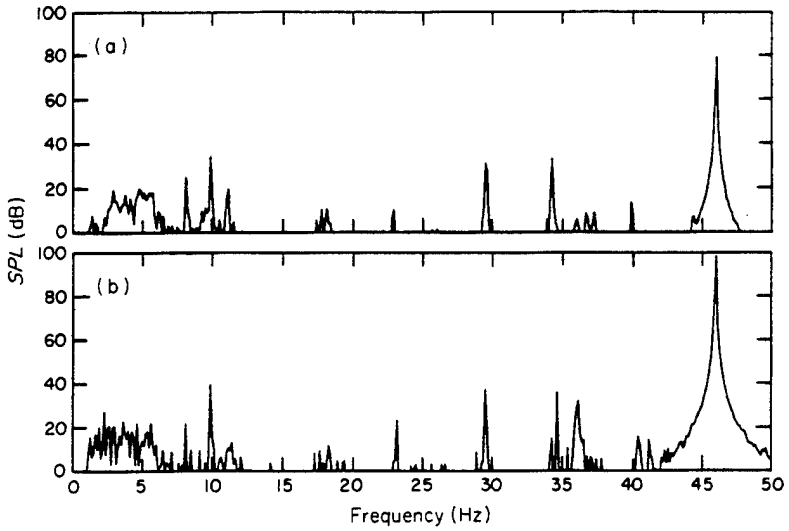

Figure 22. Peak radiation frequency placement: (a) before and (b) after frequency placement control.

substructure. Thus the controller can be viewed as performing "system modification" to lower the structural response by altering the system input impedance to the noise source. The modified input impedance thus generally results in lower noise energy transmitted into the control field. Recent analytical work has also demonstrated that, analogous to feedback controlled systems, the feedforward controlled system has new eigenproperties [34].

In Figure 23 is shown the arrangement of a typical time domain LMS adaptive approach based on the "Filtered X" algorithm [33]. The heart of the system is the adaptive Finite Impulse Response (FIR) filter, the coefficients of which are updated by the control algorithm in order to minimize the signals at the error microphones. In this case the arrangement corresponds to the experiments of reference [11], with corresponding results of Figures 3 and 4. The data acquisition and control algorithm in this application were written in assembly language and down loaded into a TMS320C25 chip in conjunction with three Analog/Digital (A/D) converters and two Digital/Analog (D/A) converters

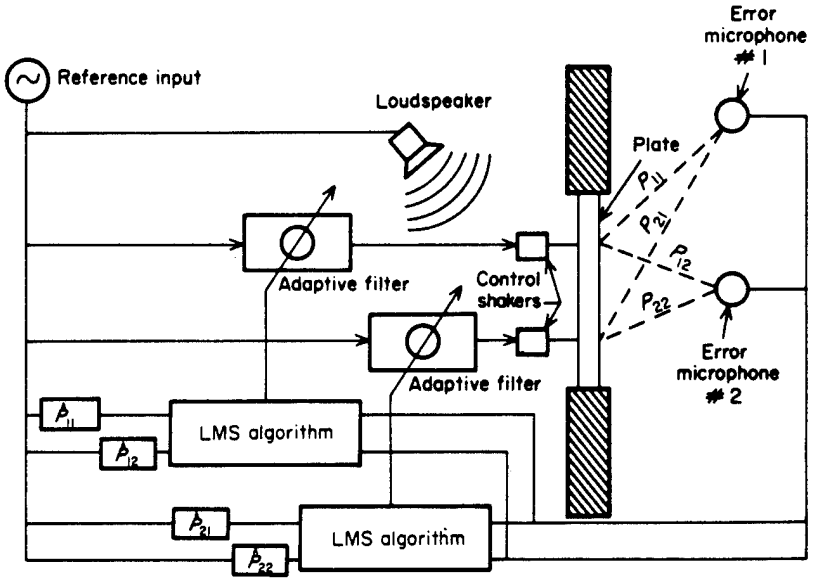

Figure 23. Arrangement of time domain adaptive LMS controller.

for dedicated control implementation. The number of coefficients in each filter was two, thus limiting the application to narrowband. The sample rate was fixed at 2 kHz. This arrangement enabled flexible reprogramming of the control approach as well as high convergence speed. In Figure 24 is shown a typical time history of the error signals, and the system can be seen to converge in approximately 50 ms to approximately 15 dB of attenuation when the control is switched on. Thus, such controllers can effectively adapt and track many structural acoustic inputs (e.g., an aircraft engine) in "real time". Other LMS adaptive approaches rely on constructing a cost function from frequency domain information. In this case it is not necessary to estimate the phase delay between the control inputs and error sensors as this is averaged, and as many error sensors as required can be easily used. However, this approach is generally slower than the time domain due to the higher sampling requirements. In Figure 25 is shown a typical control variable path for a frequency domain LMS adaptive controller as the system searches for the quadratic cost function minimum [35]. This system was used for the control of structure-borne sound in

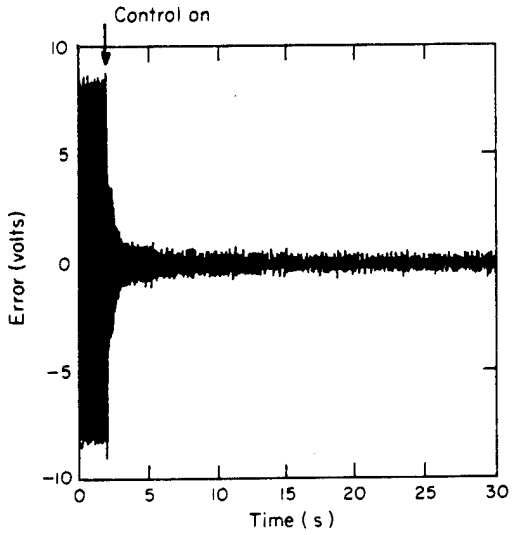

Figure 24. Error signal of adaptive LMS controller.

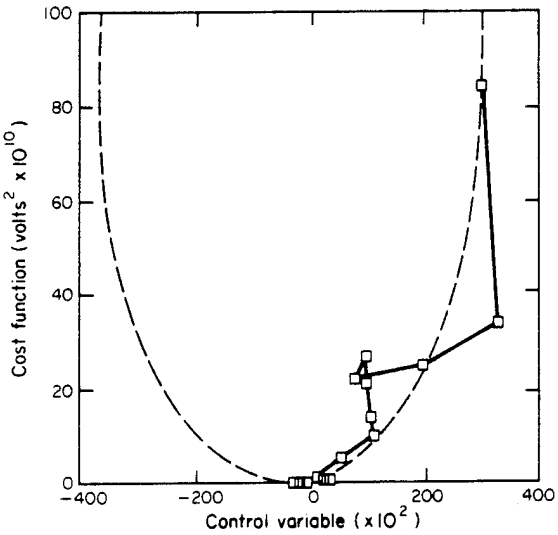

Figure 25. Adaptive controller characteristics: - - -, cost function; —□—, controller path.

aircraft [36] and, while it is slower to converge than the time domain approach, it is easier to implement and more stable with respect to use of multiple sensors.

An interesting aspect of the LMS approach is that there is much similarity between its arrangment and the original Rosenblatt "perceptron" system which is the fundamental basis of artificial neural networks [37]. Thus adaptive LMS filters can also be viewed from the artificial neural network approach as devices which are trained by various methods to model the system plant. When the noise is minimized (for a single input/single output system), the FIR coefficients will contain information related to the plant transfer function. This observation implies that much of the progress presently being achieved in neural networks may be soon implemented to feedforward LMS techniques to create "smart" controllers, particularly for control of non-linear systems.

6. CONCLUSIONS

The results presented here show that significant progress has been made towards both understanding the mechanisms of active structural acoustic control (ASAC) and ultimately implementing the technique in realistic situations. In conjunction with this, new understanding in the individual areas of distributed actuators and sensors as well as control theory and implementation as related to the structural acoustic problem has been achieved. The technique shows much potential for efficiently actively/adaptively controlling structure-borne noise radiation in many situations.

ACKNOWLEDGEMENTS

The authors gratefully acknowledge the support of most of the work performed at VPI&SU by the Office of Naval Research, Grants ONR N00014-88-0721 and ONR N00014-88-0566, and NASA Langley Research Center, Grant NAG1-390. The authors also acknowledge the help of R. J. Silcox, V. L. Metcalf and D. E. Brown of NASA Langley Research Center for performing some of the experiments at NASA Langley.

REFERENCES

1. M. C. Junger and D. Feit 1986 *Sound, Structures and Their Interaction.* Cambridge, Massachusetts: MIT Press.
2. J. E. Ffowcs Williams 1984 *Proceedings of Royal Society of London* **A395**, 63–88. Anti-sound.
3. N. Hesseleman 1978 *Applied Acoustics* **11**, 27–34. Investigation of noise reduction on a 100 kVA transformer tank by means of active methods.
4. C. R. Fuller 1987 *U. S. Patent No.* 4, 715, 599. Apparatus and method of global noise reduction.
5. B. K. Wada, J. L. Fanson and E. F. Crawley 1990 *Journal of Intelligent Materials Systems and Structures* **1**, 157–174. Adaptive structures.
6. A. S. Knyasev and B. D. Tartakovskii 1967 *Soviet Physics—Acoustics* **13**, 115–117. Abatement of radiation from flexurally vibrating plates by means of active local dampers.
7. A. I. Vylayshev, A. J. Dubinin and B. D. Tartakovskii 1986 *Soviet Physics—Acoustics* **32**, 96–98. Active acoustic reduction of a plate.
8. C. R. Fuller and J. D. Jones 1987 *Journal of Sound and Vibration* **112**, 389–395. Experiments on reduction of propeller induced interior noise by active control of cylinder vibration.
9. J. D. Jones and C. R. Fuller 1988 *Proceedings of 6th IMAC Conference*, Orlando, Florida, 315–321. Reduction of interior sound fields in flexible cylinder by active vibration control.
10. C. H. Hansen and D. A. Bies 1976 *Journal of the Acoustical Society of America* **60**, 543–555. Optical holography for the study of sound radiation from vibrating surfaces.
11. C. R. Fuller, R. J. Silcox, V. L. Metcalf and D. E. Brown 1989 *Proceedings of American Control Conference*, Pittsburgh, Pennsylvania, 2079–2084. Experiments on structural control of sound transmitted through an elastic plate.

12. C. R. FULLER 1990 *Journal of Sound and Vibration* **136**, 1–15. Active control of sound transmission/radiation from elastic plates by vibration inputs. I. analysis.
13. C. R. FULLER, C. H. HANSEN and S. D. SNYDER 1991 *Journal of Sound and Vibration* **145**(2), 195–215. Active control of sound radiation from a vibrating rectangular panel by sound sources and vibration inputs: an experimental comparison.
14. P. JIE, S. D. SNYDER, C. H. HANSEN and C. R. FULLER 1992 *Journal of the Acoustical Society of America* **91**(4), 2056–2066. Active control of farfield sound radiated by a rectangular panel—a general analysis.
15. R. L. CLARK and C. R. FULLER 1992 *Journal of the Acoustical Society of America* **91**(6), 3321–3329. Modal sensing of efficient acoustic radiators with polyvinylidene fluoride distributed sensors in active structural acoustic control approaches.
16. E. K. DIMITRIADIS, C. R. FULLER and C. A. ROGERS 1991 *Journal of Vibration and Acoustics* **113**, 100–107. Piezoelectric actuators for distributed vibration excitation of thin plates.
17. E. K. DIMITRIADIS and C. R. FULLER 1991 *AIAA Journal* **29**(11), 1771–1777. Active control of sound transmission through elastic panels using piezoelectric actuators.
18. C. R. FULLER, C. H. HANSEN and S. D. SNYDER 1991 *Journal of Sound and Vibration* **150**(2), 179–190. Experiments on active control of sound radiation from a panel using a piezoceramic actuator.
19. B. T. WANG, E. K. DIMITRIADIS and C. R. FULLER 1991 *AIAA Journal* **29**(11), 1802–1809. Active control of structurally radiated noise using multiple piezoelectric actuators.
20. C. A. ROGERS and H. H. ROBERTSHAW 1988 *Applied Mechanics and Engineering Sciences Conference, University of California-Berkeley, Engineering Science Preprint*-25, ESP25.88027. Shape memory alloy reinforced composites.
21. C. A. ROGERS, C. LIANG and J. JIA 1989 *Proceedings of the 30th SSDM Conference, Mobile, Alabama* **4**, 2011–2017. Behavior of shape memory alloy reinforced composite plates—part I: model formulations and control concepts. (Also *American Institute of Aeronautics and Astronautics Paper* 89–1389.)
22. C. LIANG, C. A. ROGERS and C. R. FULLER 1991 *Journal of Sound and Vibration* **145**(1), 23–41. Acoustic transmission/radiation analysis of shape memory alloy reinforced laminated plates.
23. C. LIANG, J. JIA and C. R. ROGERS 1989 *Proceedings of the 30th SSDM Conference, Mobile, Alabama* **4**, 1504–1513. Behavior of shape memory alloy reinforced plates—part II: results. (Also *American Institute of Aeronautics and Astronautics Paper* 89–1331.)
24. C. A. ROGERS and D. K. BARKER 1990 *Proceedings of 31st SSDM Conference, Long Beach, California.* Experimental studies of active strain energy tuning of adaptive composites with embedded nitinol actuators. (Also *American Institute of Aeronautics and Astronautics Paper* 90–1086.)
25. W. R. SAUNDERS, H. H. ROBERTSHAW and C. A. ROGERS 1990. *American Institute of Aeronautic and Astronautics Paper* 90–1090–CP. Structural acoustic control for a shape memory alloy composite beam.
26. T. GIALLORENZI, J. A. BUCARO, A. DANBRIDGE, G. H. SIGEL, J. H. COLE, S. C. RASHLEIGH, and R. C. PRIEST 1982 *IEEE Journal of Quantum Electronics* **18**, 626–665. Optical fiber sensor technology.
27. C. A. ROGERS 1988 VPI&SU, unpublished results.
28. D. COX, D. THOMAS, K. REICHARD, D. LINDER and R. O. CLAUS 1989 *Proceedings of SPIE Conference* 1170 *on Fiber Optic Smart Structures and Skins II, Boston, Massachusetts*, 372–383. Modal domain fiber optic sensor for closed loop vibration control of a flexible beam.
29. E. G. WILLIAMS, H. D. DARDY and R. G. FUNK 1985 *Journal of the Acoustical Society of America* **78**, 789–798. Nearfield acoustic holography using an underwater, automated scanner.
30. G. P. GIBBS and C. R. FULLER 1992 *AIAA Journal* **30**(2), 457–463. Experiments on active control of vibrational power flow using piezoceramic actuators/sensors.
31. W. T. BAUMANN, A. S. BANACH, W. R. SAUNDERS, and H. H. ROBERTSHAW 1991 *Journal of the Acoustical Society of America* **90**(6), 3202–3208. Active suppression of acoustic radiation from impulsively excited structures.
32. D. K. BARKER 1989 *M. S. Thesis, Department of Mechanical Engineering, Virginia Polytechnic Institute & State University, Blacksburg, Virginia.* Active dynamic response tuning of adaptive composites utilizing embedded nitinol actuators.
33. B. WIDROW and S. D. STEARNS 1985 *Adaptive Signal Processing.* Englewood Cliffs, New Jersey: Prentice-Hall.
34. R. A. BURDISSO and C. R. FULLER 1992 *Journal of Sound and Vibration* **153**(3), 437–451. Theory of feedforward controlled system eigenproperties.

35. C. R. FULLER and J. D. JONES 1987 *American Society of Mechanical Engineers Technical Paper* 87-WA/NCA-9. Influence of sensor and actuator location on the performance of active control systems.
36. M. A. SIMPSON, T. M. LUONG, C. R. FULLER and J. D. JONES 1991 *AIAA Journal of Aircraft* **28**, 208–215. Full scale demonstration tests of cabin noise reduction using active vibration control.
37. R. LIPPMAN 1987 *IEEE ASSP Magazine* **4**, 4–22. An introduction to computing with neural nets.

C-8 Active Control of Sound Radiation from a Fluid-loaded Rectangular Uniform Plate, Y. Gu and C. R. Fuller, Journal of the Acoustical Society of America, Vol. 93 No. 1, pp. 337-345, January 1993.

Active control of sound radiation from a fluid-loaded rectangular uniform plate

Yi Gu and Chris R. Fuller
Department of Mechanical Engineering, Virginia Polytechnic Institute and State University, Blacksburg, Virginia 24061-0238

(Received 2 October 1991; revised 22 April 1992; accepted 4 August 1992)

Active control of sound radiation from a simply supported rectangular fluid-loaded plate is analytically studied. The plate is assumed to be excited by a point force at subsonic frequencies. The solution to the plate motion is based on the admissible functions for an *in vacuo* homogeneous plate, which is also the basis for Fourier decomposition of the fluid loading [B. E. Sandman, J. Acoust. Soc. Am. **61**, 1502–1510 (1977)]. Feed-forward control is carried out by using point forces applied to the plate. The amplitudes of the control forces are determined by the optimal solution of a quadratic cost function that integrates the far-field radiated acoustic pressure over a hemisphere in the radiation half-space. The results show that for subsonic disturbances, a high global reduction in radiated pressure is possible. For on-resonant excitations, a reasonable sound reduction can be achieved with up to two properly located active control forces, and for off-resonant excitations, up to four control forces may be necessary. The results thus indicate that the active structural acoustic control approach will provide large attenuations in radiated sound when edge mode coupling induced by heavy fluid loading is present. The number and location of the control forces are determined so as to suppress the efficiently radiating modes. The far-field directivity pattern, the plate velocity autospectrum in the two-dimensional wave number domain, and the near-field pressure distribution are studied.

PACS numbers: 43.40.Vn, 43.40.Dx, 43.40.Rj

INTRODUCTION

There are many cases of practical interest to the industry and marine engineering in which the control of sound radiation from fluid-loaded plates is important. Much research has been done on the plate vibration response, the modal coupling effects due to the fluid loading, the radiation efficiency, etc. of fluid-loaded plates (Davies, 1977; Sandman, 1977; Lomas and Hayek, 1977; Fahy, 1985; Junger and Feit, 1986). All of the previous work is important in terms of understanding the behavior of sound radiation and dynamic structural response of fluid-loaded plates. On the other hand, active structural acoustic control (ASAC) has been applied recently to many structures such as plates (Fuller, 1988; Fuller *et al.*, 1990a, 1991) and cylinders (Fuller and Jones, 1987; Fuller *et al.*, 1990b) with light fluid loading (i.e., no radiation coupling) as well as to an infinite fluid-loaded plate with discontinuities (Gu and Fuller, 1991, 1992).

The present study is focused on ASAC applied to a simply supported rectangular plate located in an infinite baffle with heavy fluid loading on one side, as shown in Fig. 1. The disturbance is a point force operating at a steady single frequency while control is achieved by point forces applied to the plate. The control objective is to minimize the total radiated power that is a quadratic function of the control force amplitudes. The study focuses on the behavior of the near- and far-field sound radiation as well as the wave-number distribution of the uncontrolled and controlled plate. The investigation is novel because it introduces for the first time the influence of edge mode coupling due to the heavy fluid loading into the ASAC technique. It was not known or understood prior to this work how the modal coupling will affect control performance.

I. ANALYSIS

A. Plate motion analysis

In thin plate theory, the governing equation for the transverse deflection of the plate is

$$D\nabla^4 w + \rho_p h \frac{\partial^2 w}{\partial t^2} = -q(x,y,t) - p_0(x,y,t), \qquad (1)$$

where $D = Eh^3/12(1-\nu^2)$ is the flexural rigidity of the plate, with ν denoting the Poisson ratio, E is the plate material modulus of elasticity, h is the thickness, ρ_p is the mass density, $w(x,y,t)$ is the displacement of point (x,y) at time t, $q(x,y,t)$ is the directly applied external force, which in this case includes the point disturbance force and the control forces, and $p_0(x,y,t)$ is the fluid loading pressure. Combining the wave equation, the Euler equation, and the boundary conditions on the plate and off the plate (Sandman, 1977), the modal amplitudes of the plate vibration can be solved from a complex nondiagonal matrix equation that reveals the coupled fluid-loading effects. The solution of Eq. (1) yields the fluid-loaded plate response $w(x,y,t)$ and the corresponding pressure field $p(x,y,z,t)$. The detailed procedure was described by previous researchers (Davies, 1971; Sandman, 1977; Lomas and Hayek, 1977), and the results are summarized here. The steady-state acoustic pressure is

 0001-4966/93/010337-09$00.80 © 1993 Acoustical Society of America

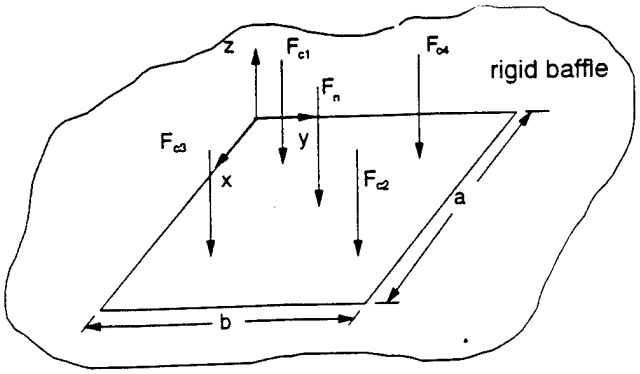

FIG. 1. System arrangement of a simply supported fluid-loaded plate.

$$p(x,y,z) = 12\frac{\rho_f c_f}{\rho_p c_p}\left(\frac{a}{h}\right)^3(i\omega)\frac{ik}{2\pi} \times \sum_{m=1}^{\infty}\sum_{n=1}^{\infty} W_{mn}\int_0^b\int_0^a \sin\frac{m\pi x_1}{a} \times \sin\frac{n\pi y_1}{b}\frac{e^{-ikR}}{R}\,dx_1\,dy_1, \quad (2)$$

where ρ_f and c_f are the fluid density and the sound speed, respectively, c_p is the flexural wave speed, a and b are the plate dimension in the x and y direction, $R = \sqrt{(x-x_1)^2 + (y-y_1)^2 + z^2}$, ω is the nondimensional excitation frequency, and k is the acoustic wave number. Here, W_{mn} are the modal coefficients that can be solved from the coupled matrix equation of

$$\sum_{m=1}^{\infty}\sum_{n=1}^{\infty}(K^p_{rsmn} + i\omega R^f_{rsmn} - M^{f+p}_{rsmn})W_{mn} = a_{rs}, \quad (3)$$

where K^p_{rsmn} is the plate stiffness matrix, $(R^p_{rsmn} + i\omega M^{f+p}_{rsmn})$ is the fluid radiation resistance and combined mass matrix, and a_{rs} are the modal components of the forcing function $q(x,y,t)$, respectively. The detailed definitions of these terms are given by Sandman (1977). To solve Eq. (3), the authors used a truncation of modes of $m = 6$, $n = 6$ for numerical estimation, since the difference is within 1% compared to that achieved by using a truncation of $m = 10$, $n = 10$.

For estimating the radiation pressure, the far-field pressure can be evaluated with the Rayleigh–Ritz method (Sandman, 1977) as given by

$$p_{\text{far}}(R,\theta,\phi) = \frac{6Da\rho_f\omega^3}{\pi R\rho_p h^3}\sum_{m=1}^{\infty}\sum_{n=1}^{\infty} W_{mn}T_{mn}(\theta,\phi), \quad (4)$$

in which

$$T_{mn}(\theta,\phi) = \left(\frac{b}{a}\right)(m\pi)(n\pi) \times \frac{[1-(-1)^m e^{iK_x}][1-(-1)^n e^{iK_y}]}{[(m\pi)^2 - K_x^2][(n\pi)^2 - K_y^2]}, \quad (5)$$

where $K_x = ka\sin\theta\cos\phi$ and $K_y = kb\sin\theta\sin\phi$ are the definitions of the far-field radiation position, and θ and ϕ are defined in Fig. 2.

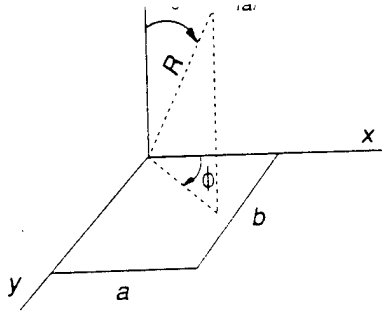

FIG. 2. Spatial coordinate definition.

B. Sound radiation

The total far-field radiated pressure due to the disturbance input and control forces is

$$p^t_{\text{far}}(R,\theta,\phi) = p^n_{\text{far}}(R,\theta,\phi) + p^c_{\text{far}}(R,\theta,\phi) = \sum_{i=1}^{N_s} B_i q_i + \sum_{j=1}^{N_c} A_j p_j = \{B\}^T\{q\} + \{A\}^T\{p\}, \quad (6)$$

in which the total far-field pressure p^t_{far} is the sum of p^n_{far} due to N_s disturbance forces and p^c_{far} due to N_c control forces, while $\{q\}$ is the disturbance force amplitude vector, $\{p\}$ is the control force amplitude vector, $\{B\}$ is the distribution function for the disturbance, and $\{A\}$ is the distribution function for the control force, respectively. Note that both $\{A\}$ and $\{B\}$ are functions of W_{mn}, which are the modal amplitudes of the solution to Eq. (1). Combining Eq. (4) and Eq. (6) results in the following equations:

$$A_j = \frac{6a^4\rho_f\omega^2}{\pi R\rho_p h^3}\sum_{m=1}^{\infty}\sum_{n=1}^{\infty}\frac{W_{mn}}{p_j}T_{mn}(\theta,\phi) \quad (7)$$

and

$$B_i = \frac{6a^4\rho_f\omega^2}{\pi R\rho_p h^3}\sum_{m=1}^{\infty}\sum_{n=1}^{\infty}\frac{W_{mn}}{q_i}T_{mn}(\theta,\phi), \quad (8)$$

where A_j and B_i are the jth element and the ith element of vectors $\{A\}$ and $\{B\}$, respectively, and p_j and q_i are the jth element and the ith element of the control force vector $\{p\}$ and the disturbance forcing vector $\{q\}$, respectively.

C. Optimal control

The objective of the optimal control is to minimize the far-field sound radiation over a hemisphere above the plate in the fluid half-space. The cost function based on the far-field acoustic power is expressed as (Fuller, 1988)

$$\Phi = \frac{1}{R^2}\int_S |p^t_{\text{far}}|^2\,ds = \int_0^{2\pi}\int_0^{\pi/2}|p^t_{\text{far}}|^2\sin\theta\,d\theta\,d\phi, \quad (9)$$

which can be written in matrix form as

$$\Phi = \{p\}^T[A]\{p\}^* + \{q\}^T[B]\{p\}^* + \{p\}^T[B]^H\{q\}^* + \{q\}^T[C]\{q\}^*, \quad (10)$$

where superscript "T" denotes transposition, "*" denotes conjugation, and "H" denotes transposition and conjugation. Matrices $[A]$, $[B]$, and $[C]$ are the results of substituting the vector sum of Eq. (6) into Eq. (9) and can be expressed as follows:

$$[A]_{N_c \times N_c} = \int_0^{2\pi} \int_0^{\pi/2} [\{A\}\{A\}^H] \sin\theta \, d\theta \, d\phi, \quad (11)$$

$$[B]_{N_s \times N_c} = \int_0^{2\pi} \int_0^{\pi/2} [\{B\}\{A\}^H] \sin\theta \, d\theta \, d\phi, \quad (12)$$

and

$$[C]_{N_s \times N_s} = \int_0^{2\pi} \int_0^{\pi/2} [\{B\}\{B\}^H] \sin\theta \, d\theta \, d\phi. \quad (13)$$

In order to minimize the acoustic power expressed in Eq. (9), the cost function is differentiated with respect to the control force amplitude $\{p\}$ and set to zero, as outlined by Nelson *et al.* (1987) and Lester and Fuller (1990). As the optimal solution for the minimization of the cost function defined in Eq. (9), the control force amplitude is

$$\{p\} = -[A]^{-1}[B]^T\{q\}. \quad (14)$$

Equation (14) relates the control force amplitude $\{p\}$ with the disturbance amplitude $\{q\}$. The relationship implies that, given the disturbance, the active feedforward control can be implemented by proper amplitude and phase adjustments of the control forces through Eq. (14) to minimize the sound radiation in the far field. Here, $[A]$ is the distribution matrix of control forces and $[B]$ is the distribution matrix relating the coupling between the control forces and the disturbance.

II. RESULTS AND DISCUSSION

The numerical evaluation is based on an aluminum rectangular plate of which the material properties and dimensions are listed in Table I. The center-point-driven response of the plate depicted in Fig. 3 illustrates the plate resonances with or without heavy fluid loading. For the problem considered here, the excitation frequencies are only those that dominantly excite the low-order modes of the plate and are well below the coincidence frequency, $f_c = c_f^2(m_p/D)^{1/2} = 23\,966$ Hz for the given plate, where c_f is the sound velocity in the sea water and m_p the plate density per area. The disturbance force amplitude is taken as 10 N for all the cases calculated in the following examples.

The presence of fluid loading lowers the resonant frequencies of the plate response but does not significantly change the structural mode shapes (Fahy, 1985). The natural frequencies of the first several modes were estimated numerically from the plate displacement response of Fig. 3 and compared to those results calculated with the approximate expression provided by Fahy (1985). The far-field pressure was calculated using Eq. (6) in which the optimal control forces were based on Eq. (14) for the controlled case. With a harmonic point force applied at the center of the plate as the disturbance, the plate is excited at on- and off-resonant frequencies. The near-field pressure distributions illustrate how the control forces modify the sound radiation sources and change the nature of structural acoustic coupling near the surface of the plate.

TABLE I. Material properties of an aluminum rectangular plate and fluid medium.

System	Phase speed (m/s)	Density (kg/m^3)	Thickness (m)	Size (m)
Aluminum plate	5432	2700	0.009525	0.5588×0.8636
Seawater	1500	1026	...	...

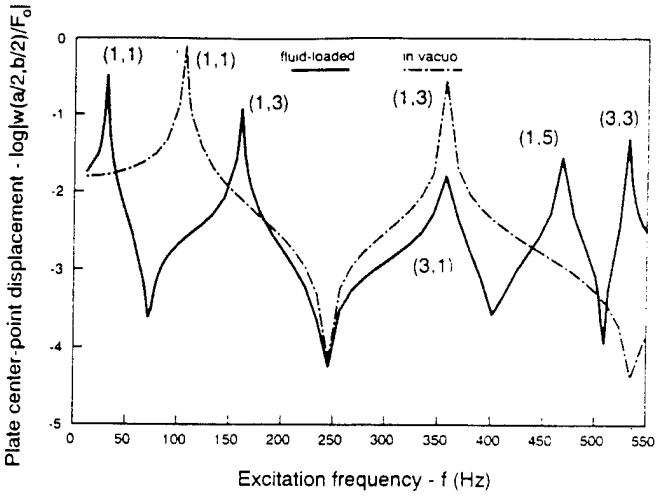

FIG. 3. Frequency response of a rectangular plate.

The two-dimensional wave-number domain (k_x,k_y) analysis demonstrates the change within the supersonic wave-number region $(\sqrt{k_x^2 + k_y^2} \leqslant \omega/c)$. The wave-number spectrum of the plate velocity is given by the Fourier transform of the plate velocity as follows:

$$\begin{aligned}\tilde{V}(k_x,k_y) &= \int_{-\infty}^{\infty} \int_{-\infty}^{\infty} v(x,y) e^{-i(k_x x + k_y y)} \, dx \, dy \\ &= i\omega c_p \sum_{m=1}^{\infty} \sum_{n=1}^{\infty} W_{mn} \\ &\quad \times \left(\frac{m\pi}{k_x^2 - (m\pi/a)^2} [(-1)^m e^{-ik_x a} - 1] \right) \\ &\quad \times \left(\frac{(n\pi/b)}{k_y^2 - (n\pi/b)^2} [(-1)^n e^{-ik_y b} - 1] \right), \end{aligned} \quad (15)$$

where $v(x,y) = i\omega w(x,y)$ and $w(x,y)$ is the solution of Eq. (1). The velocity autospectrum is used to evaluate the wave-number domain energy and its expression is

$$|\tilde{V}(k_x,k_y)|^2 = \tilde{V}(k_x,k_y)\tilde{V}^*(k_x,k_y). \quad (16)$$

It should be noted that the velocity wave-number autospectrum is also a function of the excitation frequency.

A. Resonant frequencies

For a simply supported rectangular plate *in vacuo*, the natural frequencies are estimated as

$$\omega_{mn} = \sqrt{\frac{D}{m_p}}\left[\left(\frac{m\pi}{a}\right)^2 + \left(\frac{n\pi}{b}\right)^2\right], \tag{17}$$

where $m_p = \rho_p h$. For a rectangular plate submerged in heavy fluid, it is assumed that the natural frequencies fall below their *in vacuo* values in proportion to the square root of the ratio of the loaded to unloaded modal masses (Fahy, 1985). According to Fahy, the analysis of reactive loading on structural waves having wave numbers much greater than an acoustic wave number has shown that the effective added mass per unit area is ρ_f/k_{mn}, where ρ_f is the fluid density and k_{mn} is the primary effective wave-number component of the vibration. The approximate expression of the fluid-loaded structure natural frequency is (Fahy, 1985)

$$\omega'_{mn} \approx \omega_{mn}\left[1 + (\rho_f/m_p k_{mn})\right]^{-1/2}, \tag{18}$$

where ω_{mn} is the corresponding *in vacuo* natural frequency defined by Eq. (17) and $k_{mn} = \sqrt{(m\pi/a)^2 + (n\pi/b)^2}$.

Hence, there are two approximate methods to determine fluid-loaded plate natural frequencies: one is to observe the peak values from the frequency response magnitudes such as from Fig. 3,, since the nonlinearity of Eq. (3) makes an explicit solution of eigenvalues unavailable. The other is to use Eq. (18). In the following discussion, the results obtained with these two different methods are compared and found to be very consistent in most cases.

Figure 3 illustrates the center-point displacement magnitude of the plate for center-point excitation. The results are very similar to those previously estimated by Sandman (1977). Because of the location of the drive point, it is seen that even numbered modes can not be excited, so that only odd–odd modes appear on the response diagram. The *in vacuo* resonances are well predicted by Eq. (17). The natural frequencies of the fluid-loaded case evaluated by two different approaches also converge well (referring to Tables II and III). The relative errors between the results are reasonable (8.0% for ω'_{13}, 9.1% for ω'_{31}, 4.6% for ω'_{15}, and 4.3% for ω'_{33}) except for the first mode (30% for ω'_{11}). The comparison of these results suggests that in general Eq. (18) is a fairly good estimate for fluid-loaded plate lower-order modal natural frequencies when $k_{mn} \gg k$ and the discrepancy in estimating the first mode is noted.

B. Fundamental mode excitation

When the disturbance frequency coincides with the first mode (1,1) resonance, a relatively high sound radiation arises. Because of the location and the frequency of the excitation, the fundamental mode dominates the plate vibration and the sound radiation. Since the plate is vibrating in a single efficiently radiating monopole mode, the task is to try to suppress this mode by secondary forces in order to reduce the sound radiation. With one control force located at $(x_1,y_1) = (a/4,b/4)$, the controlled plate is seen to radiate like a dipole (referring to Fig. 4) and the sound radiation is attenuated in the far field by around 65 to 85 dB. From the near-field pressure distribution shown in Fig. 5(a) and (b) it is illustrated that the overall pressure level decreases about 44 dB near the surface of the plate. This indicates that the suppression of the (1,1) mode leads to a global sound reduction. With two control forces located at $(x_1,y_1) = (a/4,b/4)$ and $(x_2,y_2) = (3a/4,3b/4)$, a further 25 to 30 dB of far-field pressure attenuation is achieved as observed in Fig. 4. Comparing Fig. 5(b) and Fig. 5(c) reveals that not only a further 15 to 20 dB reduction of pressure level is achieved in the near field, but the pattern of the radiation source is also changed from a two-lobe type to a three-lobe type. This implies that not only the dominant (1,1) mode is suppressed, but the relations between the residual modes are re-adjusted so as to make their overall contribution to sound radiation less efficient. This phenomenon is known as "modal restructuring". When four control forces are located at one-sixth of the lengths away from the plate edges, even further sound attenuation is observed in the far field (the residual pressure directivity is localized around the origin in Fig. 4). The force amplitudes and locations are listed in Table IV.

The near-field sound pressure magnitude distribution shown in Fig. 5(d) indicates that further modal restructur-

TABLE II. Natural frequencies (Hz) of the fluid-loaded plate estimated with Fahy's approximate formula (Fahy, 1985).

Mode (m,n)	1	3	5
1	40.41	173.8	489.7
3	388.9	555.2	905.7

TABLE III. Natural frequencies (Hz) of the fluid-loaded plate estimated from numerical frequency response evaluation.

Mode (m,n)	1	3	5
1	30.94	160.9	467.8
3	356.4	532.2	···

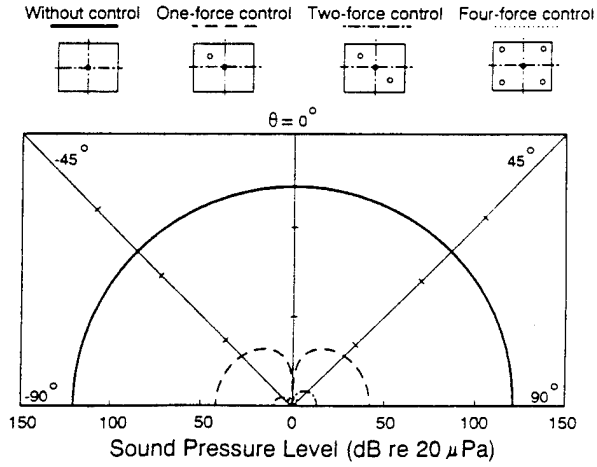

FIG. 4. Far-field directivity pattern: on-resonance excitation, $f = 31$ Hz, $\phi = 0$.

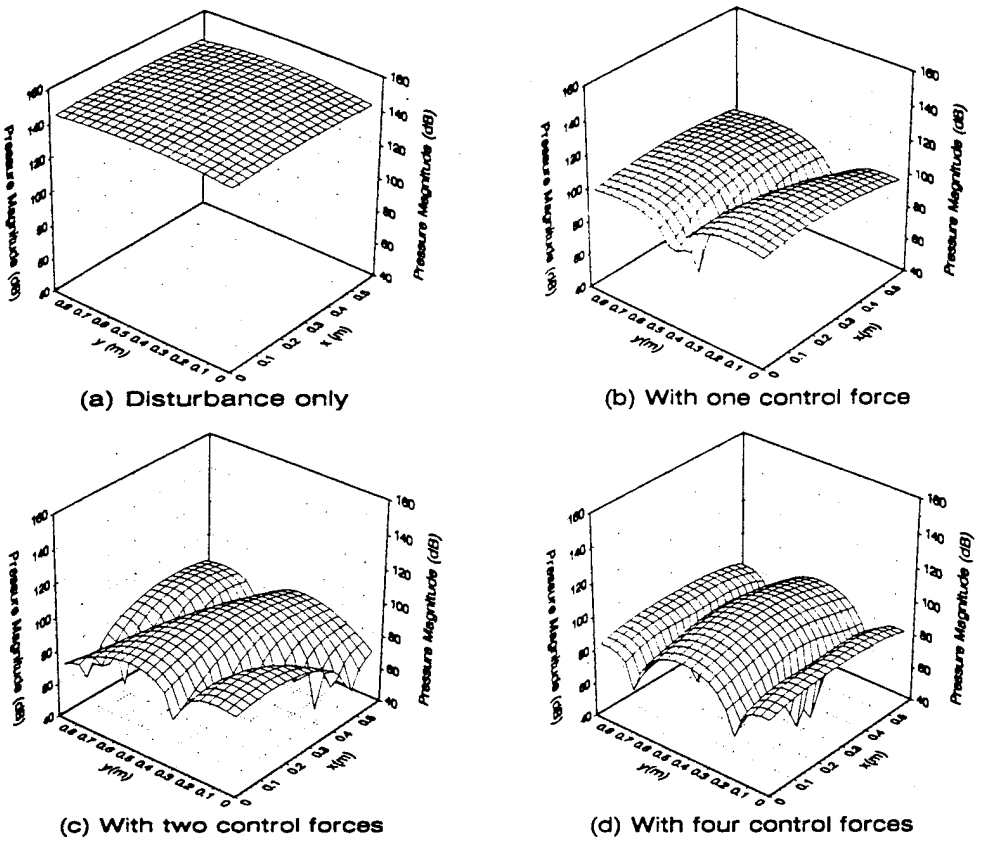

FIG. 5. Near-field sound pressure level at $z = 0.01$ m, $f = 31$ Hz.

ing is performed since the overall pressure level does not seem to be lower than that shown in Fig. 5(c), but different higher-order source patterns are observed in these two controlled cases. Comparing the controlled residual pressure distributions shown in Fig. 5(b), (c), and (d), to the uncontrolled pressure distribution shown in Fig. 5(a), it is noted that the modal suppression, i.e., the suppression of the efficient (1,1) mode, is the dominant cause of the sound reduction. This observation is extendible to those cases when only one efficient mode is dominantly excited to radiate sound.

To better explain the sound power reduction, the plate velocity autospectrum in a two-dimensional wave-number domain is calculated and the results are shown in Fig. 6. (The reference value in Figs. 6 and 9 is arbitrarily taken as 6.36×10^{-9} m^2/s^2 so that the autospectrum represents relative values.) It is observed that the supersonic region of the wave-number spectrum, illustrated by the area within the small circle where $\sqrt{k_x^2 + k_y^2} \leqslant k$, decreases with the increase of number of control forces. This clearly explains that the active control reduces the sound radiation energy through reducing the radiated power in the supersonic region. In addition, it is observed that the reduction in sound radiation is not necessarily accompanied by reduction in plate vibration. For example, the area outside the supersonic region remains almost the same level in Fig. 6(c) and (d), while the supersonic region is reduced. The corresponding far-field pressures demonstrate a fall in magnitude (refer to Fig. 4). The results illustrate the important observation that only the wave-number spectrum within the supersonic region is relevant to the far-field sound radiation and hence reduction. On the other hand, the modal suppression is also confirmed by comparing Fig. 6(b), (c), and (d) with Fig. 6(a), respectively, the velocity autospectrum is reduced within and outside the supersonic region. This indicates that

TABLE IV. Disturbance and control force amplitudes and locations, a—plate length in the x direction, b—plate length in the y direction.

Excitation frequency	Amplitude (N)	Location (x,y)
	$f = 31$ (Hz)	
Disturbance force	$10 + 0\times i$	$(0.5a, 0.5b)$
One control force	$-19.465 - 8.526\times10^{-5}\times i$	$(0.25a, 0.25b)$
Two control forces	$-9.7325 - 4.198\times10^{-5}\times i$	$(0.25a, 0.25b)$
	$-9.7325 - 4.328\times10^{-5}\times i$	$(0.75a, 0.75b)$
Four control forces	$-9.5444 - 3.1253\times10^{-2}\times i$	$(0.1667a, 0.1667b)$
	$-9.5444 - 3.1273\times10^{-2}\times i$	$(0.8333a, 0.8333b)$
	$-9.5448 + 3.1131\times10^{-2}\times i$	$(0.1667a, 0.8333b)$
	$-9.5448 + 3.1149\times10^{-2}\times i$	$(0.1667a, 0.8333b)$
	$f = 434$ (Hz)	
Disturbance force	$10 + 0\times i$	$(0.5a, 0.5b)$
One control force	$5.7973 - 2.8288\times10^{-3}\times i$	$(0.25a, 0.25b)$
Two control forces	$12.981 - 1.3601\times10^{-2}\times i$	$(0.5a, 0.25b)$
	$12.981 - 1.3601\times10^{-2}\times i$	$(0.5a, 0.75b)$
Four control forces	$4.7092 - 3.514\times10^{-3}\times i$	$(0.3333a, 0.3333b)$
	$4.7092 - 3.514\times10^{-3}\times i$	$(0.6667a, 0.6667b)$
	$4.7092 - 3.514\times10^{-3}\times i$	$(0.6667a, 0.3333b)$
	$4.7092 - 3.514\times10^{-3}\times i$	$(0.3333a, 0.6667b)$

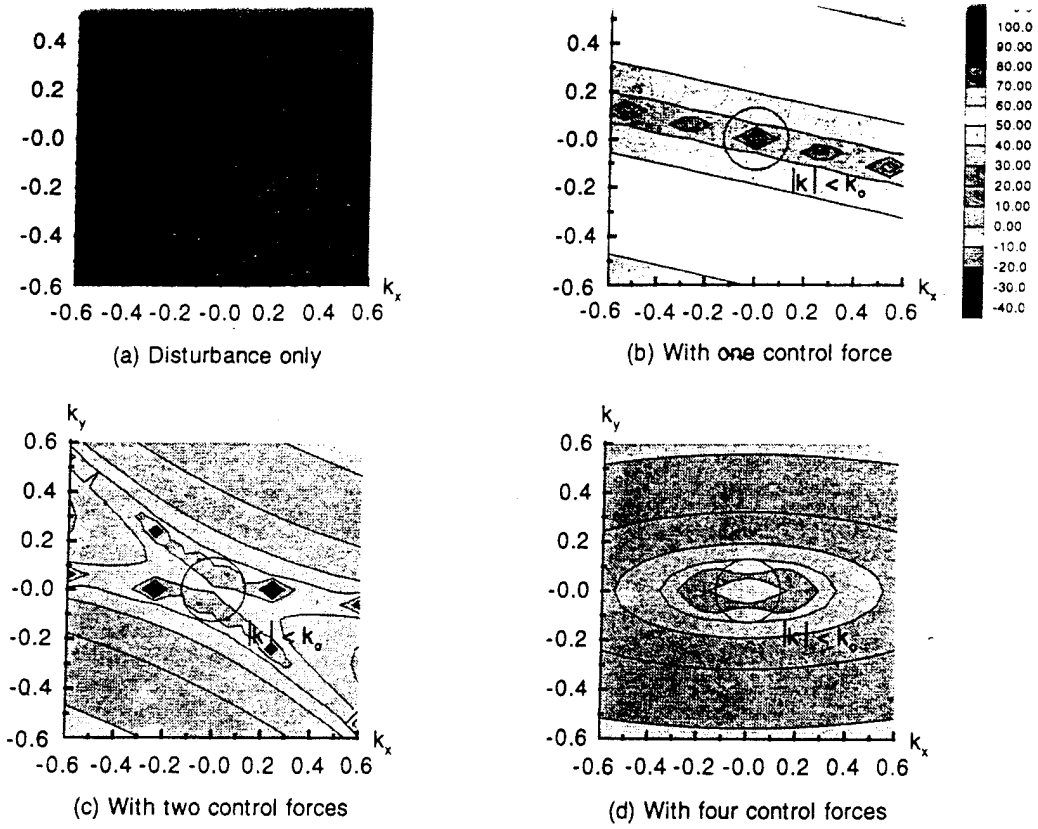

(a) Disturbance only

(b) With one control force

(c) With two control forces

(d) With four control forces

FIG. 6. Wave-number domain plate velocity autospectrum, $f = 31$ Hz.

there is not only a reduction in sound radiation level, but a reduction in plate vibration magnitude level as well.

It is also interesting to examine the optimal control force values that are given in Table IV. For the on-resonant case of $f = 31$ Hz, it is apparent that the control forces are always nearly purely real and 180° out-of-phase with the disturbance force. For a single control force, a much larger magnitude of optimal control force than disturbance is required, although this will depend upon location of the forces. When multiple control forces are used, the control force magnitudes are of the same order as the disturbance and largely independent of location. The results indicate that for the on-resonant case, although multiple control inputs do not significantly increase the sound reduction, they have the advantage of keeping the control force magnitudes lower. This effect, however, needs further investigation before definite conclusions can be made.

C. Off-resonant excitation

The off-resonant example is illustrated with the plate centrally driven at frequency $f = 434$ Hz. From Fig. 3 it can be seen that this frequency is higher than the resonance of mode (3,1) so that more modes are involved in the plate response. The results show that, although the sound radiation level due to the disturbance is relatively lower than that of the on-resonant excitation example, reasonable sound reduction is much harder to obtain. In this case, the (3,1), (1,5), and (3,3) modes combine to contribute to the plate vibration and sound radiation. It is thus difficult to position one control force to couple into all three modes, in such a way as to reduce their respective sound radition properly to achieve a global sound reduction. This is illustrated by the results of Fig. 7 where one control force only reduces the far-field radiation by around 2 to 4 dB. When two or more control forces are employed, reasonable sound reduction is achieved. Figure 7 shows that about 15 to 30 dB of attenuation is obtained in the far field with two control forces and

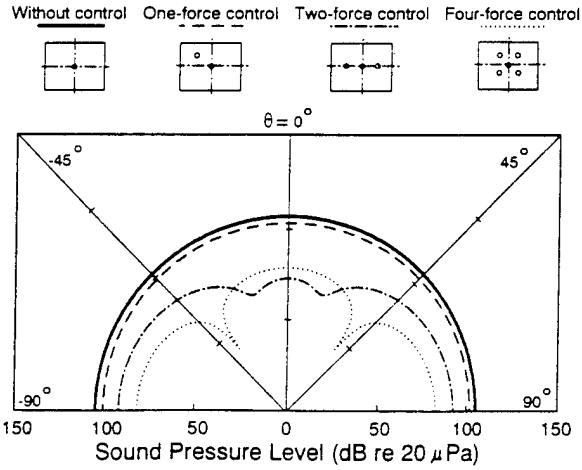

FIG. 7. Far-field directivity pattern: off-resonant excitation, $f = 434$ Hz, $\phi = 0$.

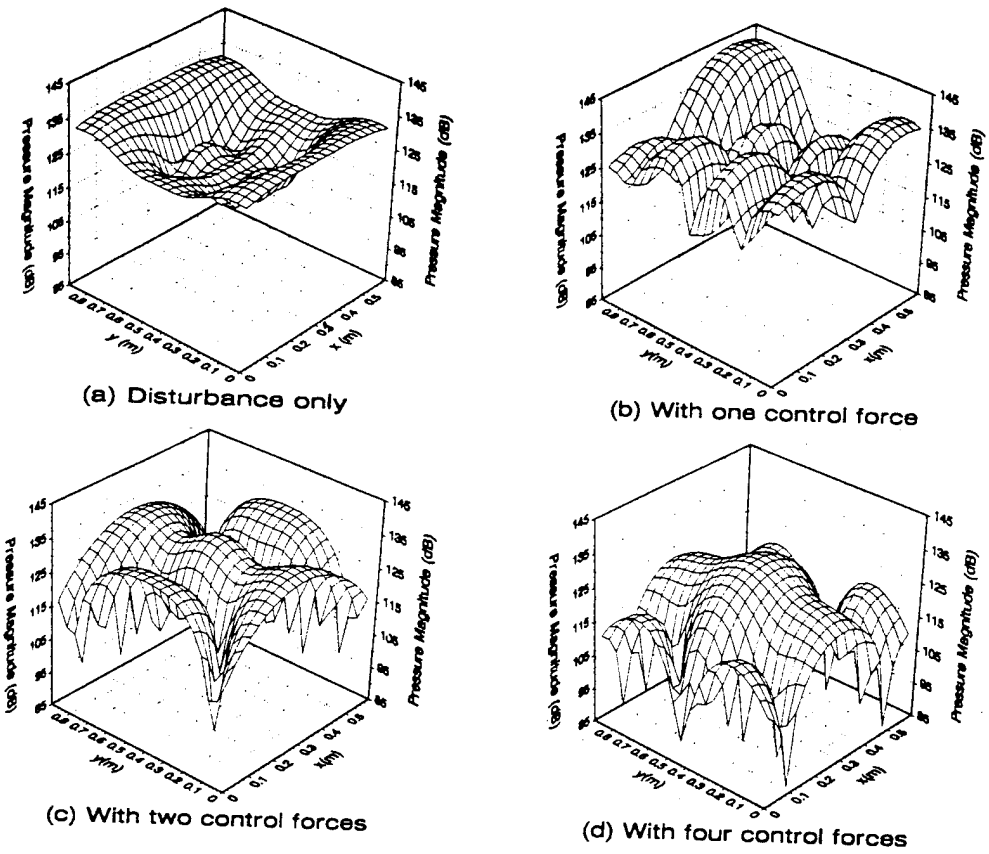

FIG. 8. Near-field sound pressure level at $z = 0.01$ m, $f = 434$ Hz.

the directivity patterns suggest that the radiation source is of multipole type. Four control forces provide a further sound reduction in a global extent of about 10 to 20 dB although in the region from $\theta = -25°$ to $\theta = 25°$ the radiation increases by about 10 to 15 dB over the two-control-force case.

An examination of near-field pressure distribution from Fig. 8(a) to (d) implies that the off-resonant plate source is far more complicated than the on-resonant case and a far-field sound reduction does not always accompany a significant overall pressure level reduction in the near field due to the "modal restructuring" phenomena discussed previously. The near-field pressure distribution in Fig. 8(a) is the result of radiation of the (3,1), (1,5) and (3,3) modes. When one control force is applied, there is no apparent reduction of the pressure level, as shown in Fig. 8(b), but there is some change in the shapes of the source pattern. Meanwhile it is seen in Fig. 9(b) that there is some minor radiation reduction, as illustrated by a decrease of the velocity autospectrum in the upper right area in the supersonic circle. This indicates that ASAC provides some attenuation, although the result is not as good as the on-resonant case when one control force is used. Another interesting phenomenon is that by observing the subsonic regions in Fig. 9(a) and (b), respectively, it is shown that the subsonic region in Fig. 9(b) has a higher level than that in Fig. 9(a), which indicates that the plate vibration level may be higher, when control is applied (this can only be confirmed when the velocity autospectrum is plotted in the full range of $-\infty < k_x < \infty$, $-\infty < k_y < \infty$). This indicates two points: (1) ASAC does not always reduce the structural response; (2) modal restructuring sometimes can play an important role in reducing the sound radiation, particularly for off-resonant cases. When two control forces are applied, it is observed that the overall near-field pressure level is only slight reduced [Fig. 8(c)], but a much better sound reduction is observed in the far field (Fig. 7) as well as in the supersonic region of velocity autospectrum [Fig. 9(c)]. From the near-field pressure distribution shown in Fig. 8(c) it can be concluded that the increase of source order leads to the sound reduction. Finally when four control forces are applied on the plate, the overall near-field pressure level is reduced by about 10 dB and the source order is further modified [Fig. 8(d)]. A further reduction of velocity autospectrum in supersonic is also observed in Fig. 9(d) corresponding to the far-field pressure reduction in Fig. 7. In this four-force-control case, it can thus be concluded that modal suppression as well as modal restructuring is the mechanism of modifying the panel source and reducing the sound radiation. The drop in plate response for the case of Fig. 8(d) is due to the number of control forces being of the order of significant plate modes in terms of sound radiation.

Table IV provides the optimal control force magnitudes for the off-resonant case of $f = 434$ Hz. The control forces are again nearly purely real but are now in phase with the disturbance in contrast to the on-resonant case. When one control force is used, the force magnitude is of the order of the disturbance, but corresponding sound power reduction is small. Using two control forces leads to better sound re-

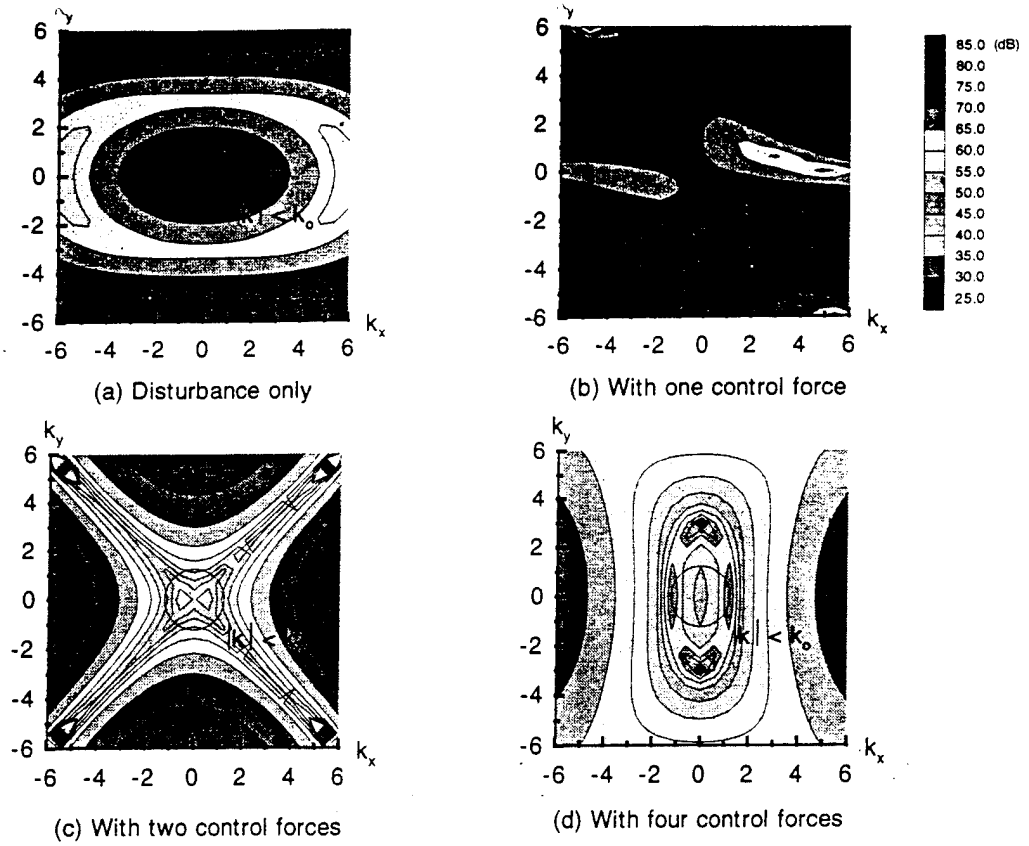

FIG. 9. Wave-number domain plate velocity autospectrum, $f = 434$ Hz.

duction (see Fig. 7) and the control magnitudes are also of the order of the disturbance. Four control forces leads to high sound power reduction and the control magnitudes are now reduced, in line with the on-resonant case.

III. CONCLUDING REMARKS

Active control of sound radiation from a fluid-loaded rectangular plate excited by a centrally located point force at subsonic frequencies has been analytically studied. The control forces are chosen so as to minimize the total acoustic power radiated into a hemisphere in the fluid-loaded half-space. The reduction in sound radiation has been shown to depend on the excitation frequency that determines which modes will contribute dominantly to the total radiation. In general, off-resonant excitations are more difficult to control than on-resonant ones since more modes are involved. In the cases studied in this paper, up to two control forces are needed to control radiation for on-resonant excitation and up to four control forces for off-resonant excitation.

A two-dimensional wave-number domain analysis of the plate response illustrates how the wave-number components in the supersonic region decrease when active control is applied. This approach reveals the cause of sound reduction from the point of view of plate vibration radiating components. It is demonstrated that for plates with heavy fluid loading, sound radiation control occurs by two major mechanisms viz. (1) modal suppression in which dominantly radiating modes are controlled in magnitude and (2) modal restructuring in which the plate averaged response is little changed but has a lower radiation efficiency due to a more complex residual shape. The sound reduction achieved in on-resonant case is mainly through modal suppression, and the sound reduction achieved in off-resonant case is achieved primarily through modal restructuring.

This study adds new understanding to research in controlling the sound radiation from finite fluid-loaded plates. The results indicate that the ASAC feedforward control approach will provide high sound attenuation for vibrating structures submerged in heavy fluids including edge radiation coupling phenomena. Future work will study the effect of localized structural discontinuities as well as experimentally confirm the above conclusions.

ACKNOWLEDGMENT

The authors wish to acknowledge the support of this work to the sponsor, the Office of Naval Research, under Grant No. ONR-N00014-92-j-1170.

Davies, H. G. (**1971**). "Low frequency random excitation of water-loaded rectangular plates," J. Sound Vib. **15**, 107–126.

Fahy, F. (**1985**). *Sound and Structural Vibration: Radiation, Transmission and Response* (Academic, Orlando, FL), pp. 113–142.

Fuller, C. R., and Jones, J. D. (**1987**). "Experiments on reduction of propeller induced interior noise by active control of cylinder vibration," J. Sound Vib. **112**, 389–395.

Fuller, C. R. (**1988**). "Active sound transmission/radiation from elastic plates by vibration inputs. I. Analysis," *Proceedings Internoise '88*, Avignon, France (Noise Control Foundation, Poughkeepsie, NY), pp. 1061–1064.

Fuller, C. R. (**1990a**). "Active control of sound transmission/radiation from elastic plates by vibration inputs. I. Analysis," J. Sound Vib. **136**, 1–15.

Fuller, C. R., Snyder, S. D., Hansen, C. H., and Silcox, R. J. (**1990b**). "Active control of interior noise in model aircraft fuselages using piezoceramic actuators," AIAA Paper 90-3922.

Fuller, C. R., Hansen, C. H., and Snyder, S. D. (**1991**). "Experiments on active control of sound radiation from a panel using a piezoceramic actuator," J. Sound Vib. **150**, 179–190.

Gu, Y., and Fuller, C. R. (**1991**). "Active control of sound radiation due to subsonic wave scattering from discontinuities on fluid loaded plates. I: Far-field pressure," J. Acoust. Soc. Am. **90**, 2020–2026.

Gu, Y., and Fuller, C. R. (**1992**). "Active control of sound radiation due to subsonic wave scattering from discontinuities on fluid loaded plates. II: Plate vibration" (in preparation).

Junger, M. C., and Feit, D. (**1986**). *Sound, Structures, and Their Interaction* (MIT, Cambridge), pp. 235–257.

Lester, H. C., and Fuller, C. R. (**1990**). "Active control of propeller-induced noise fields inside a flexible cylinder," AIAA J. **28**(8), 1364–1380.

Lomas, N. S., and Hayek, S. I. (**1977**). "Vibration and acoustic radiation of elastically supported rectangular plates," J. Sound Vib. **52**, 1–25.

Nelson, P. A., Curtis, A. R. D., Elliott, S. J. and Bullmore, A. J. (**1987**). "The Minimum Power Output of Free Field Point Sources and the Active Control of Sound," J. Sound Vib. **116**, 397–414.

Sandman, B. E. (**1977**). "Fluid-loaded vibration of an elastic plate carrying a concentrated mass," J. Acoust. Soc. Am. **61**, 1502–1510.

C-9 Active Control of Sound Radiation from a Simply Supported Beam: Influence of Bending Near-Field Waves, C. Guigou and C. R. Fuller, Journal of the Acoustic Society of America, Vol. 93 No. 5, pp. 2716-2725, May 1993.

Active control of sound radiation from a simply supported beam: Influence of bending near-field waves

C. Guigou and C. R. Fuller

Vibration and Acoustic Laboratories, Mechanical Engineering Department, Virginia Polytechnic Institute and State University, Blacksburg, Virginia 24061-0238

(Received 21 April 1992; revised 2 November 1992; accepted 4 December 1992)

Active control of sound radiation from a baffled simply supported finite beam is analytically studied. The beam is subjected to a harmonic input force and the resulting acoustic field is minimized by applying a control point force. For a single frequency, the flexural response of the beam subject to the input and control forces is expressed in terms of flexural waves of both propagating and near-field types. The optimal control force complex amplitude is derived by minimizing the acoustic radiated pressure at one point located in the far field. The far-field radiated pressure, the displacement of the vibrating beam, and the one-dimensional wave-number spectrum of the beam velocity are extensively studied. In order to further understand control mechanisms, the radiated pressure due to the flexural propagating wave and the flexural near-field wave, respectively, is investigated at the minimization point before and after the control is involved. The analysis shows that, when the control is applied, the combination of the radiated pressure due to the two different types of waves (as their associated radiation is out-of-phase) at the minimization point causes the large pressure attenuation. These results demonstrate that structural near fields are important in terms of predicting performance in active control of structurally radiated sound.

PACS numbers: 43.40.Vn

INTRODUCTION

Structural vibrations as well as their associated radiated sound fields have always been a problem in industry. If the sound radiation is unacceptable, different passive control approach are traditionally used to attenuate noise. However, passive techniques generally give poor control performances in the low-frequency region. In the last decade, active noise control has emerged as a practical possibility to reduce acoustic noise fields especially at low frequencies. This method usually employs acoustic control sources to attenuate the primary noise field. The active noise control approach and some of its applications have been described in Refs. 1 and 2. The technique has been successfully implemented for one-dimensional sound field. However, for a three-dimensional radiated sound field, there are some disadvantages with using acoustic sources as the control inputs amongst which are the number of sources required, size, and difficulties in implementation.

A new approach for the active control of structurally radiated sound fields has been investigated. Fuller[3] demonstrated that reduction of the far-field acoustic radiation can also be obtained by directly modifying the response of the structure by applying structural inputs rather than by adding a distribution of acoustic sources in the surrounding sound field. The active control of sound radiation can be achieved by either point forces[3] or piezoelectric elements[4] directly applied on the vibrating structure surface, while information is obtained from radiation associated responses.

Most of all previous theoretical and experimental works on beams have been concerned with active control of bending motion and flexural power flow.[5–10] The active control of sound radiation due to a clamped edge discontinuity on a semi-infinite beam has been investigated theoretically by Guigou and Fuller[11] and experimentally by Guigou *et al.*[12] Recently, the dynamic behavior of a controlled simply supported beam has been studied by Burdisso and Fuller.[13,14] They demonstrated that the simply supported beam has new eigenproperties to the disturbance when the control is applied to minimize either the out-of-plane motion at one point on the beam or the radiated pressure level at one point in space.

In the present paper, active control of sound radiation from a finite simply supported beam is studied. The beam is subjected to a harmonic input force and the resulting acoustic field is minimized by applying a control point force (both forces approximating shakers). For a single frequency, the flexural response of the beam subject to the input and control forces is expressed in terms of flexural waves of both propagating and near-field types. The optimal control force complex amplitude is derived by minimizing the acoustic radiated pressure at one point located in the far field. On determining the optimal control force, it can be re-substituted in the constitutive equations for the system and the minimized fields can be evaluated. The main scope of this paper is to investigate how the control of the radiated pressure at the minimization point occurs. It should be noted that all previous analytical studies on ac-

 0001-4966/93/052716-10$06.00 © 1993 Acoustical Society of America

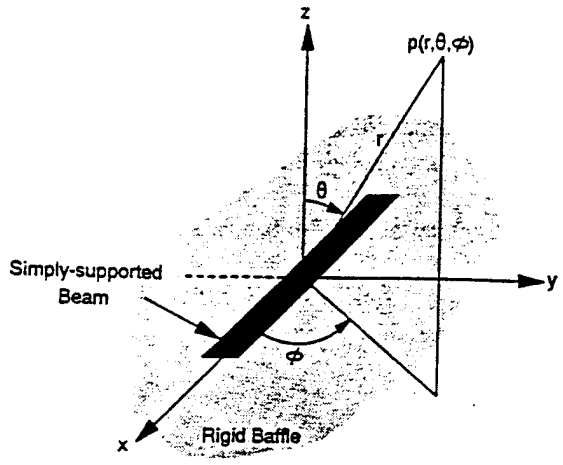

FIG. 1. Coordinate system.

tive structural acoustic control (ASAC), for example Ref. 3, have ignored structural near fields. The main purpose of the present paper is to determine whether these structural near fields, present at discontinuities such as the control and input locations and the boundaries, are important in determining and predicting control performance. To this end, the radiated pressure due to the flexural propagating wave and the flexural near-field wave, respectively, is compared at the minimization point before and after the control is involved and the importance of the wave components is investigated.

I. BEAM DISPLACEMENT

The Cartesian coordinate system used in this analysis and the location of the simply supported beam in the coordinate system are shown in Fig. 1. The beam is taken to be located in an infinite baffle (in the x,y plane) and the simply supported boundary conditions are applied at both ends, i.e., at $x=\pm l/2$, where l is the length of the beam. The time dependence for all the fields is assumed to be $e^{-i\omega t}$, where ω is the angular frequency.

The simply supported beam is first excited by an input shaker, modeled as a point force $\hat{F}_n$ located at $x=\alpha_n$. To achieve active control, a control point force $\hat{F}_c$ located at $x=\alpha_c$, approximating a control shaker, is then applied to the beam. This system is described in Fig. 2(a).

Consider an infinitely long beam. Here, $\hat{F}_1$, $\hat{M}_1$ and $\hat{F}_2$, $\hat{M}_2$ applied on the infinite beam in the manner shown in Fig. 2(b) with the correct complex values will create at $x=-l/2$ and $x=l/2$, respectively, the boundary conditions of a simply supported beam. Hence, the part of the infinitely long beam, which is located between $-l/2<x<l/2$, will behave in every respect as if there were simply supported conditions at both end. Therefore, the response of the beam due to

(i) an input point force $\hat{F}_n$ located at $x=\alpha_n$ (the disturbance),

(ii) a point force $\hat{F}_1$ located at $x=-l/2$ (due to the simply supported condition),

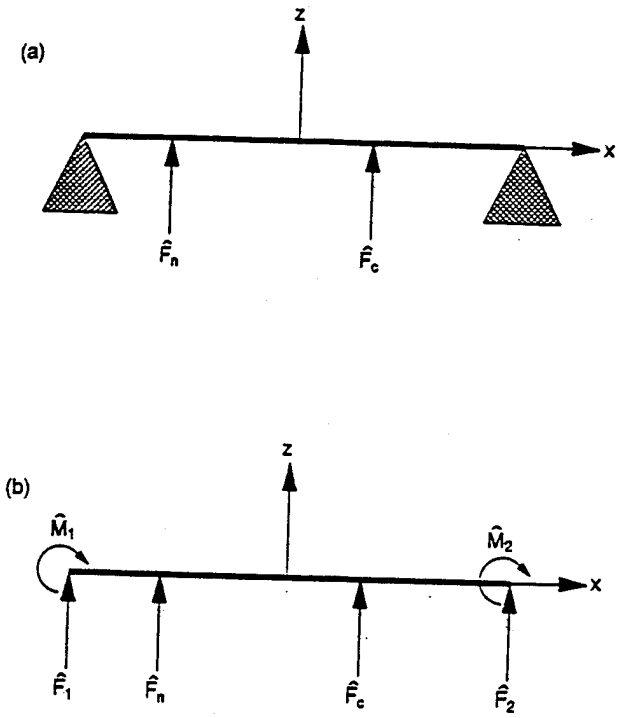

FIG. 2. (a) Schematic of the simply supported beam. (b) Forces and moments applied on the beam.

(iii) a line moment $\hat{M}_1$ located at $x=-l/2$ (due to the simply supported condition),

(iv) a point force $\hat{F}_2$ located at $x=l/2$ (due to the simply supported condition),

(v) a line moment $\hat{M}_2$ located at $x=l/2$ (due to the simply supported condition),

(vi) and a control point force $\hat{F}_c$ located at $x=\alpha_c$, has to be derived.

The flexural displacements of an infinite thin beam due to a point force and a line moment have been fully derived by Guigou.[11] It was found that the out-of-plane displacement due to a point force $\hat{F}$ located at any position $x=\alpha$ on the beam is

$$w(x)=(i\hat{F}/4EIk_f^3)[e^{ik_f|x-\alpha|}+ie^{-k_f|x-\alpha|}], \quad (1)$$

and the out-of-plane displacement due to a line moment located at any position $x=\alpha$ is

$$w(x)=-\frac{\hat{M}\,\mathrm{sgn}(x-\alpha)}{EIk_f^2}[e^{ik_f|x-\alpha|}-e^{-k_f|x-\alpha|}], \quad (2)$$

where the structural wave number is

$$k_f=\sqrt[4]{\omega^2 m/EI}, \quad (3)$$

EI is the flexural stiffness (E is the modulus of elasticity, I is the cross-sectional moment of inertia), m is the density per unit length, both constant throughout the length of the beam, and the function $\mathrm{sgn}(x-\alpha)$ is defined by

$$\operatorname{sgn}(x-\alpha)=\begin{cases}+1, & \text{if } x>\alpha,\\ -1, & \text{otherwise.}\end{cases} \tag{4}$$

It can be observed that a point force or a line moment creates two different flexural waves on each side of the application point: a propagating flexural wave (first term in the bracket) and a nonpropagating near-field flexural wave (second term in the bracket).

In this case, the beam is assumed to be slightly damped. Structural damping is included by using a complex modulus of elasticity defined as follows:

$$\hat{E}=E(1-i\beta), \tag{5}$$

where β is the damping ratio or loss factor. The previous equations are also valid when E is replaced by the complex modulus of elasticity. It can be noted that the structural bending wave number k_f also becomes complex due to the damping.

Thus, using the superposition principle and Eqs. (1) and (2), the flexural displacement of the beam system as shown in Fig. 2(b) is given, for $-l/2<x<l/2$, by

$$w(x)=\frac{i\hat{F}_n}{4\hat{E}Ik_f^3}\left[e^{ik_f|x-\alpha_n|}+ie^{-k_f|x-\alpha_n|}\right]+\frac{i\hat{F}_1}{4\hat{E}Ik_f^3}\left[e^{ik_f(x+l/2)}+ie^{-k_f(x+l/2)}\right]-\frac{\hat{M}_1}{4\hat{E}Ik_f^2}\left[e^{ik_f(x+l/2)}-e^{-k_f(x+l/2)}\right]$$
$$+\frac{i\hat{F}_2}{4\hat{E}Ik_f^3}\left[e^{ik_f(l/2-x)}+ie^{-k_f(l/2-x)}\right]+\frac{\hat{M}_2}{4\hat{E}Ik_f^2}\left[e^{ik_f(l/2-x)}-e^{-k_f(l/2-x)}\right]+\frac{i\hat{F}_c}{4\hat{E}Ik_f^3}\left[e^{ik_f|x-\alpha_c|}+ie^{-k_f|x-\alpha_c|}\right]. \tag{6}$$

Note, in Eq. (6) positive and negative wave components due to the noise and control forces are derivable from the modulus of the spatial variation term.

The forces, $\hat{F}_1$ and $\hat{F}_2$, and the moments, $\hat{M}_1$ and $\hat{M}_2$, are found in such a way that the system satisfies the simply supported boundary conditions at $x=-l/2$ and at $x=l/2$, which are defined by

$$w|_{x=-l/2}=w|_{x=l/2}=0 \tag{7}$$

and

$$\left.\frac{\partial^2 w}{\partial x^2}\right|_{x=-l/2}=\left.\frac{\partial^2 w}{\partial x^2}\right|_{x=l/2}=0. \tag{8}$$

Then, the four unknowns magnitudes are given by a system of four linear equations, which can be written in matrix form as follows:

$$\begin{bmatrix} (1+i) & (e^{ik_fl}+ie^{-k_fl}) & 0 & -ik_f(e^{ik_fl}-e^{-k_fl}) \\ (e^{ik_fl}+ie^{-k_fl}) & (1+i) & ik_f(e^{ik_fl}-e^{-k_fl}) & 0 \\ (-1+i) & (-e^{ik_fl}+ie^{-k_fl}) & -2ik_f & ik_f(e^{ik_fl}+e^{-k_fl}) \\ (-e^{ik_fl}+ie^{-k_fl}) & (-1+i) & -ik_f(e^{ik_fl}+e^{-k_fl}) & 2ik_f \end{bmatrix}\begin{bmatrix}\hat{F}_1\\ \hat{F}_2\\ \hat{M}_1\\ \hat{M}_2\end{bmatrix}$$
$$=\begin{bmatrix} -(e^{ik_f(l/2+\alpha_n)}+ie^{-k_f(l/2+\alpha_n)}) \\ -(e^{ik_f(l/2-\alpha_n)}+ie^{-k_f(l/2-\alpha_n)}) \\ -(-e^{ik_f(l/2+\alpha_n)}+ie^{-k_f(l/2+\alpha_n)}) \\ -(-e^{ik_f(l/2-\alpha_n)}+ie^{-k_f(l/2-\alpha_n)}) \end{bmatrix}\hat{F}_n+\begin{bmatrix} -(e^{ik_f(l/2+\alpha_c)}+ie^{-k_f(l/2+\alpha_c)}) \\ -(e^{ik_f(l/2-\alpha_c)}+ie^{-k_f(l/2-\alpha_c)}) \\ -(-e^{ik_f(l/2+\alpha_c)}+ie^{-k_f(l/2+\alpha_c)}) \\ -(-e^{ik_f(l/2-\alpha_c)}+ie^{-k_f(l/2-\alpha_c)}) \end{bmatrix}\hat{F}_c. \tag{9}$$

Therefore, the four unknowns $\hat{F}_1$, $\hat{F}_2$, $\hat{M}_1$, and $\hat{M}_2$ are determined as functions of the input point force $\hat{F}_n$ and the control point force $\hat{F}_c$. For simplification of the notation, the unknowns are given by

$$\begin{bmatrix}\hat{F}_1\\ \hat{F}_2\\ \hat{M}_1\\ \hat{M}_2\end{bmatrix}=\begin{bmatrix}A_n(1)\\ A_n(2)\\ A_n(3)\\ A_n(4)\end{bmatrix}\hat{F}_n+\begin{bmatrix}A_c(1)\\ A_c(2)\\ A_c(3)\\ A_c(4)\end{bmatrix}\hat{F}_c, \tag{10}$$

where the $A_n(j)$ and $A_c(j)$ for $j=1,4$ can be easily deduced from Eq. (9).

Thus, the flexural displacement of the simply supported beam is given by the following expression, for $-l/2<x<l/2$:

$$w(x)=(i\hat{F}_n/4\hat{E}Ik_f^3)[e^{ik_f|x-\alpha_n|}+ie^{-k_f|x-\alpha_n|}+(A_n(1)+ik_fA_n(3))e^{ik_f(x+l/2)}+(iA_n(1)-ik_fA_n(3))e^{-k_f(x+l/2)}$$

$$+(A_n(2)-ik_fA_n(4))e^{ik_f(l/2-x)}+(iA_n(2)+ik_fA_n(4))e^{-k_f(l/2-x)}]+(i\hat{F}_c/4\hat{E}Ik_f^3)[e^{ik_f|x-\alpha_c|}+ie^{-k_f|x-\alpha_c|}$$

$$+(A_c(1)+ik_fA_c(3))e^{ik_f(x+l/2)}+(iA_c(1)-ik_fA_c(3))e^{-k_f(x+l/2)}+(A_c(2)-ik_fA_c(4))e^{ik_f(l/2-x)}$$

$$+(iA_c(2)+ik_fA_c(4))e^{-k_f(l/2-x)}]. \tag{11}$$

It should be noted at this point that a simply supported boundary condition only transforms an incident (near-field) propagating wave into a reflected propagating (near-field) wave; traveling waves incident on a simple support do not generate a reflected near-field (unlike a clamped boundary condition, which couples an incident propagating wave with a reflected propagating wave and a reflected near-field wave). Thus, in this case, the input force (disturbance) and control force are mainly responsible for the presence of near-field flexural waves, except when located close to a boundary.

In terms of radiation, the simply supported beam system is considered as a 2-D structure and thus the displacement is constant along the width of the beam. Hence, the out-of-plane displacement can be rewritten as

$$w(x,y)=w(x), \tag{12}$$

for $|x|<l/2$ and $|y|<l_y/2$, where l_y represents the width of the beam.

II. FAR-FIELD RADIATED PRESSURE

Using the spherical coordinate system as shown in Fig. 1, it was demonstrated in Ref. 11 that, for any general 2-D system with light fluid loading, the far-field radiated pressure can be closely approximated by the expression, derived using the method of stationary phase

$$p(r,\theta,\phi)=-i\omega\rho_0\tilde{v}(k_0\sin\theta\cos\phi,k_0\sin\theta\sin\phi)\times(e^{ik_0r}/2\pi r), \tag{13}$$

where ρ_0 and k_0 are, respectively, the density and the wave number in the surrounding acoustic medium and $\tilde{v}(k_x,k_y)$ represents the spatial Fourier transform of the velocity of the vibrating structure.

The far-field radiated pressure is a function of the double spatial Fourier transform of the out-of-plane beam velocity for $\sqrt{k_x^2+k_y^2}<k_0$, which is defined as the supersonic region. It can be noticed that a direction of radiation $(\hat{\theta},\hat{\phi})$ in the far field is equivalent to a couple $(\hat{k}_x,\hat{k}_y)$ in the wave-number domain defined by

$$\hat{k}_x=k_0\sin\hat{\theta}\cos\hat{\phi},$$
$$\hat{k}_y=k_0\sin\hat{\theta}\sin\hat{\phi}, \tag{14}$$

which are the points of stationary phase. It is now necessary to find the spectral response of the simply supported beam under study.

The double spatial Fourier transform is defined by

$$\tilde{v}(k_x,k_y)=\int_{-\infty}^{+\infty}\int_{-\infty}^{+\infty}v(x,y)e^{ik_xx}e^{ik_yy}\,dx\,dy, \tag{15}$$

which is reduced to

$$\tilde{v}(k_x,k_y)=\int_{-l/2}^{l/2}\int_{-l_y/2}^{l_y/2}v(x,y)e^{ik_xx}e^{ik_yy}\,dy\,dx, \tag{16}$$

as the beam is located in a rigid infinite baffle, i.e., $v(x,y)=0$ for $|x|>l/2$ and $|y|>l_y/2$.

As the beam displacement is taken to be constant along the width of the beam [see Eq. (12)], the integrals with respect to x and y are separable, i.e.,

$$\tilde{v}(k_x,k_y)=\int_{l_y/2}^{l_y/2}e^{ik_yy}\,dy\int_{-l/2}^{l/2}v(x)e^{ik_xx}\,dx$$
$$=\tilde{v}(k_y)\tilde{v}(k_x), \tag{17}$$

where $v(x)$ can be derived from Eq. (11).

The expression of $\tilde{v}(k_y)$ is easily obtained by integration,

$$\tilde{v}(k_y)=\frac{\sin(k_yl_y/2)}{k_y/2}, \tag{18}$$

and the expression of $\tilde{v}(k_x)$ is found to be

$$\tilde{v}(k_x)=\frac{i\omega\hat{F}_n}{4\hat{E}Ik_f^3}\left(\frac{e^{ik_x a_n}-e^{i(k_f-k_x)(l/2)+ik_f a_n}}{k_f-k_x}+\frac{e^{ik_x a_n}-e^{i(k_f+k_x)(l/2)-ik_f a_n}}{k_f+k_x}+\frac{e^{ik_x a_n}-e^{-(k_f+ik_x)(l/2)-k_f a_n}}{k_f+ik_x}\right.$$
$$+\frac{e^{ik_x a_n}-e^{-(k_f-ik_x)(l/2)+k_f a_n}}{k_f-ik_x}+(A_n(1)+ik_f A_n(3))e^{-ik_x(l/2)}\frac{1-e^{i(k_f+k_x)l}}{k_f+k_x}$$
$$+(A_n(1)-k_f A_n(3))e^{-ik_x(l/2)}\frac{1-e^{-(k_f-ik_x)l}}{k_f-ik_x}+(A_n(2)-ik_f A_n(4))e^{ik_x(l/2)}\frac{1-e^{i(k_f-k_x)l}}{k_f-k_x}$$
$$\left.+(A_n(2)+k_f A_n(4))e^{ik_x(l/2)}\frac{1-e^{-(k_f+ik_x)l}}{k_f+ik_x}\right)+\frac{i\omega\hat{F}_c}{4\hat{E}Ik_f^3}\left(\frac{e^{ik_x a_c}-e^{i(k_f-k_x)(l/2)+ik_f a_c}}{k_f-k_x}\right.$$
$$+\frac{e^{ik_x a_c}-e^{i(k_f+k_x)(l/2)-ik_f a_c}}{k_f+k_x}+\frac{e^{ik_x a_c}-e^{-(k_f+ik_x)(l/2)-k_f a_c}}{k_f+ik_x}+\frac{e^{ik_x a_c}-e^{-(k_f-ik_x)(l/2)+k_f a_c}}{k_f-ik_x}$$
$$+(A_c(1)+ik_f A_c(3))e^{-ik_x(l/2)}\frac{1-e^{i(k_f+k_x)l}}{k_f+k_x}+(A_c(1)-k_f A_c(3))e^{-ik_x(l/2)}\frac{1-e^{-(k_f-ik_x)l}}{k_f-ik_x}$$
$$\left.+(A_c(2)-ik_f A_c(4))e^{ik_x(l/2)}\frac{1-e^{i(k_f-k_x)l}}{k_f-k_x}+(A_c(2)+k_f A_c(4))e^{ik_x(l/2)}\frac{1-e^{-(k_f+ik_x)l}}{k_f+ik_x}\right). \quad (19)$$

The method of separating the double spatial Fourier integral into two single integrals, implies that $\tilde{v}(k_y)$ is independent of the input force and the control force. Thus, only the one-dimensional wave-number spectrum $\tilde{v}(k_x)$ will be studied before and after the control is applied.

III. OPTIMAL CONTROL

In the following control strategy, the sound pressure level is to be minimized at one specified point in the far field. The location of the point in space, where the sound pressure level has to be optimized, is given by (r_e,θ_e,ϕ_e) in the spherical coordinate system. The control point force has to drive the beam such that the sound pressure level is minimum at this location. Thus, the optimum complex amplitude of the control point force $\hat{F}_c$ is obtained by minimizing the square value of the pressure modulus at the point (r_e,θ_e,ϕ_e) in the far field.

The cost function, defined as the square of the pressure modulus is

$$\Lambda=p(r_e,\theta_e,\phi_e)p^*(r_e,\theta_e,\phi_e), \quad (20)$$

where "*" denotes the complex conjugate.

To simplify the notation, the far-field radiated pressure at (r_e,θ_e,ϕ_e) can be rewritten as

$$p(r_e,\theta_e,\phi_e)=N(r_e,\theta_e,\phi_e)\hat{F}_n+C(r_e,\theta_e,\phi_e)\hat{F}_c, \quad (21)$$

where the values of $N(r_e,\theta_e,\phi_e)$ and $C(r_e,\theta_e,\phi_e)$ can be deduced from Eqs. (13), (18), and (19).

Therefore, the cost function Λ to be minimized is rewritten as

$$\Lambda=N(r_e,\theta_e,\phi_e)N^*(r_e,\theta_e,\phi_e)\hat{F}_n\hat{F}_n^*+N(r_e,\theta_e,\phi_e)C^*(r_e,\theta_e,\phi_e)\hat{F}_n\hat{F}_c^*+N^*(r_e,\theta_e,\phi_e)C(r_e,\theta_e,\phi_e)\hat{F}_n^*\hat{F}_c+C(r_e,\theta_e,\phi_e)C^*(r_e,\theta_e,\phi_e)\hat{F}_c\hat{F}_c^*. \quad (22)$$

The cost function is a real quadratic function of the control force. For a given location of the control force, this quadratic cost function has a unique minimum value associated with an optimal control force magnitude. Taking the derivatives of the cost function Λ with respect to the real and imaginary part of the control force leads to the optimal solution for the control force complex amplitude

$$\hat{F}_c=-\frac{N(r_e,\theta_e,\phi_e)}{C(r_e,\theta_e,\phi_e)}\hat{F}_n. \quad (23)$$

It should be noticed that minimizing the radiated pressure in the far field at (r_e,θ_e,ϕ_e) is equivalent to reducing the wave-number spectrum at (k_{xe},k_{ye}), where k_{xe} and k_{ye} are given by Eq. (14) as a function of θ_e and ϕ_e. Wave-number domain control approaches based on this concept have been demonstrated in Ref. 15. Therefore, the control force is independent of the radius r_e if r_e is large enough to place the minimization point in the far field. Thus, this type of control is referred as a directional control, as the radiation is minimized in the direction (θ_e,ϕ_e) in the far field.

IV. INDIVIDUAL FLEXURAL WAVE CONTRIBUTION

Since the out-of-plane displacement of the beam is given in terms of both propagating and nonpropagating near-field waves, it is possible to determine their relative contribution to the radiated far-field pressure.

Width	4.0 cm
Length	38.0 cm
Flexural stiffness	5.33 N m^2
Density	0.6267 kg/m
Damping ratio	0.1%

Equation (11), giving the out-of-plane displacement of the simply supported beam, can be rewritten in the form

$$w(x)=w_{pr}(x)+w_{nf}(x), \tag{24}$$

where w_{pr} and w_{nf} represent, respectively, the propagating (terms in $e^{\pm ik_f x}$) and nonpropagating near-field (terms in $e^{\pm k_f x}$) components of the beam flexural displacement. Upon taking the spatial Fourier transform of each displacement component, the far-field radiated pressure can be then expressed as

$$p(r,\theta,\phi)=p_{pr}(r,\theta,\phi)+p_{nf}(r,\theta,\phi), \tag{25}$$

where p_{pr} and p_{nf} are, respectively, the pressure radiated by the propagating and near-field component of the beam displacement. This decomposition of the pressure into two components respectively due to the propagating waves and to the near-field waves is expected to show the mechanisms by which the control is achieved at the minimization point, as well as enabling a study of the relative contributions of the different wave types.

V. RESULTS

The beam characteristics are presented in Table I. The input point force is taken to have a magnitude of 1N and is located at $x=\alpha_n=-0.4l$. The control force position is fixed at $x=\alpha_c=l/8$. Three different frequencies of excitation are studied: 31.7 Hz, corresponding to the first flexural mode of the system; 126 Hz, corresponding to the second flexural mode of the system; and 600 Hz, corresponding to an off-resonance frequency of the system. The radiated pressure is computed at a radius $r=7.62$ m from the center of the beam, which is well into the far field. The pressure field is minimized at the location ($r_e=7.62$ m, $\theta_e=0$, $\phi_e=0$) in the spherical coordinate system, which is at a distance of 7.62 m above the center of the beam in the x,z plane. By minimizing the radiated pressure in the far field at this location, the one-dimensional wave-number spectrum is minimized at $k_{xe}=0$, as explained previously.

A. On-resonance excitation 31.7 Hz, first mode

Figure 3 shows the far-field pressure radiated in the x,z plane by the simply supported beam for an excitation frequency of 31.7 Hz, corresponding to the first mode. First, it can be noticed that, as expected for this frequency, the radiation from the beam, when no control is involved, is similar to a monopole source corresponding to the structural motion of the first mode. For this particular case, the radiated pressure due to the propagating flexural waves and the near-field flexural waves, respectively, is shown in Fig. 4(a) and is monopolelike for both of them. It can be seen that the radiation is mostly due to the propagating

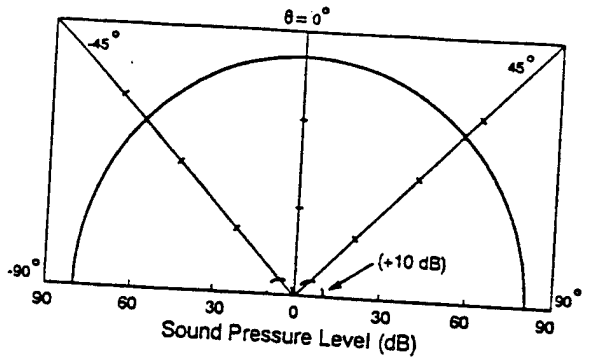

FIG. 3. Far-field pressure radiated in x,z plane at 31.7 Hz: ———, without control; — —, with control.

waves and that the two different types of waves radiate in phase such that their associated radiated fields add coherently (as the total sound pressure level is larger than either each). When the control force is applied to the beam in order to attenuate the pressure at the minimization point, Fig. 3 shows that the pressure field is highly attenuated (more than 80-dB reduction) and dipole like (10 dB were added to the actual pressure levels in order for the pressure field under control to be observable). In Fig. 4(b), it can be observed that the radiated pressure due to the propagating flexural wave has been attenuated by about 65 dB, and that the radiated pressure due to the near-field waves has been reduced by 15 dB. When the control is invoked, the sound pressure levels associated to these two types of waves are almost equal (about 15 dB in all directions).

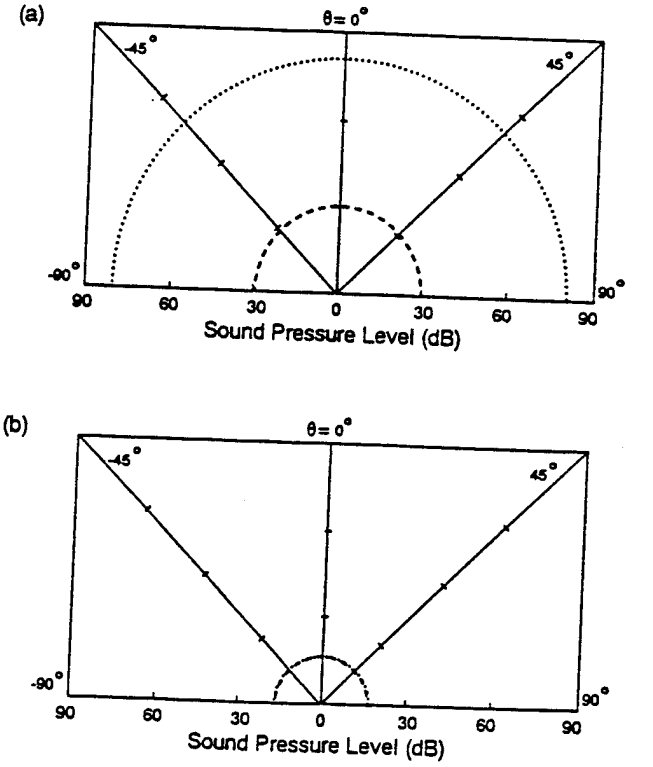

FIG. 4. Components of the far-field pressure radiated in x,z plane at 31.7 Hz: (a) without control; (b) with control. – – –, due to near-field flexural waves; ——, due to propagating flexural waves.

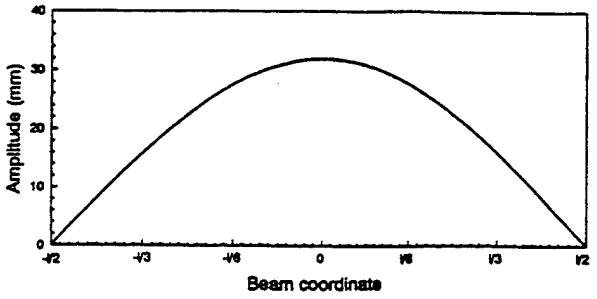

FIG. 5. Out-of-plane displacement at 31.7 Hz: ———, without control; — —, with control.

However, as the total radiated pressure is largely attenuated, it can be deduced that these two different flexural waves now radiate out-of-phase, such that their associated radiated field cancel each other.

Figure 5 shows the out-of-plane displacement without and with control. (The large displacements are due to the slightly damped system being driven very close to resonance.) Before the control force is applied, the displacement corresponds to that expected, i.e., a mode shape corresponding to the first mode of the simply supported beam. When control is applied, the displacement of the beam is reduced to a very low level of vibration (hardly observable on the figure). Therefore, in this case, the attenuation of the radiated pressure is associated with a direct attenuation of the vibratory motion of the beam.

The one-dimensional wave-number spectrum $[\bar{v}(k_x)]$ is shown on Fig. 6. In the case without control, the spectrum corresponds exactly to the one expected for a fundamental mode, with a maximum of amplitude at $k_x=0$. When the control is involved, the wave-number spectrum amplitude is reduced to an amplitude close to zero for all the wave numbers. The extremely small amplitudes in the supersonic region (region defined as the radiating wave-number components) correspond to the fact that the pressure is nearly completely attenuated (as noticed on Fig. 3).

B. On-resonance excitation 126 Hz, second mode

For the second case, the beam is excited with a frequency of 126 Hz near the second mode of vibration. Figure 7 shows the far-field radiated pressure without and

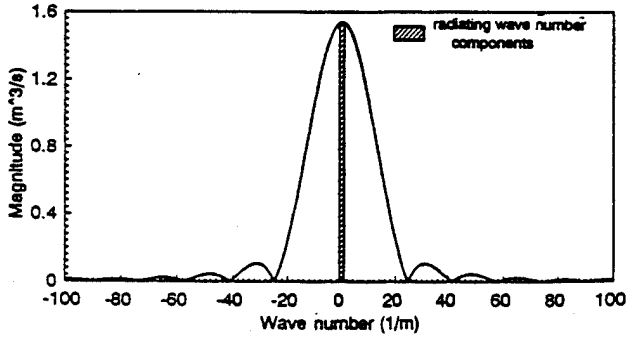

FIG. 6. Wave-number spectrum at 31.7 Hz: ———, without control; — —, with control.

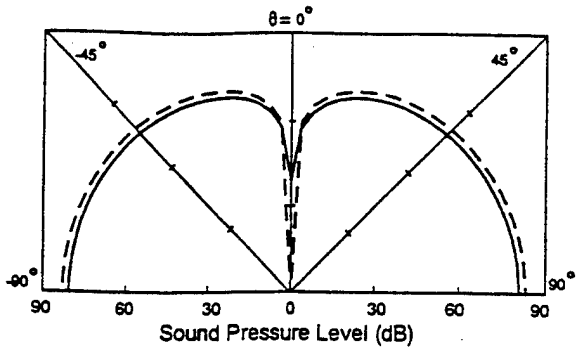

FIG. 7. Far-field pressure radiated in x,z plane at 126 Hz: ———, without control; — —, with control.

with control. For the uncontrolled case, the radiation pattern is similar to that of a dipole radiator, as it is expected for the second mode of vibration. However, the sound pressure level is not zero at $\theta=0$, as the pressure radiated by the second mode should be. This is probably due to the fact that the vibratory motion has small components from other modes and so is not perfectly symmetric with respect to the center of the beam due to the nonsymmetric position of the disturbance force. Figure 8(a) shows that the propagating flexural wave is mostly responsible for the sound radiation in all direction except for θ close to zero. The near-field flexural waves still radiate as a monopole radiator even if the overall motion is dominantly dipole like. At $\theta=0$, these two types of waves radiate in phase. When the control is invoked, the sound pressure level is attenuated at

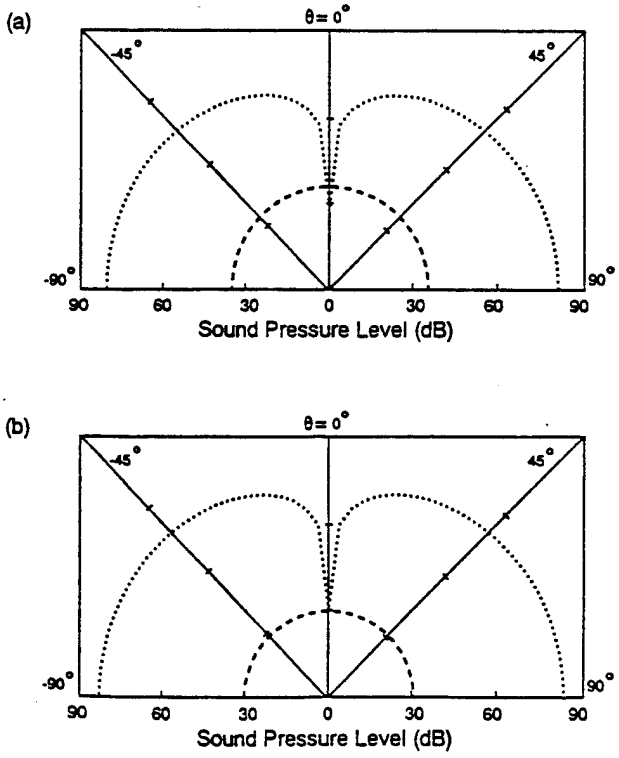

FIG. 8. Components of the far-field pressure radiated in x,z plane at 126 Hz: (a) without control; (b) with control – – –, due to near-field flexural waves; ——, due to propagating flexural waves.

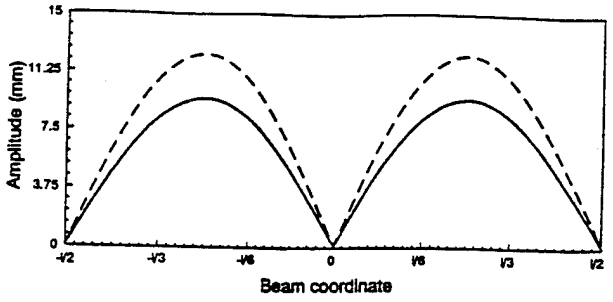

FIG. 9. Out-of-plane displacement at 126 Hz: ———, without control; — —, with control.

the minimization point and for θ very close to zero, elsewhere it is slightly increased (about 2.5 dB). Figure 8(b) shows that the pressure field due to the near-field waves has been decreased by 6 dB; on the other hand, the pressure field due to the propagating waves has been increased by about 2 dB. However, at $\theta=0$, the acoustic pressure radiation due to the propagating waves and the one due to the near-field waves are equal and out-of-phase, such that the total radiated pressure at $\theta=0$ is canceled. This result implies that the attenuation at the error point is due to the interaction of the propagating and near-field waves; a result that stresses the importance of near-field components.

The out-of-plane displacement can be observed on Fig. 9. It corresponds, as expected, to the second mode of vibration, with a node at the center of the beam and a maximum displacement at $x=\pm l/4$. When the control is applied, the mode shape is unchanged but the vibration level is increased. Thus, in this case, the attenuation of the pressure level at the minimization point in the far field leads to an increase of the vibratory motion. Note that near-field terms in the structural response are unobservable. However, being monopolelike, they are more efficient radiators than the propagating component, which increases the near-field structural motion importance in the radiated acoustic field.

The one-dimensional wave-number spectrum for the uncontrolled and controlled cases can be observed on Fig. 10. The shaded region denotes the supersonic region. As expected for the uncontrolled case, the wave-number spectrum peaks for $k_x \simeq \pm |k_f|$, where $|k_f|$ is the modulus of the complex structural wave number. This maximum can

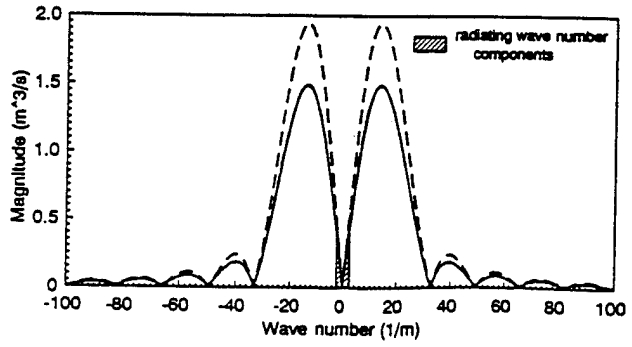

FIG. 10. Wave-number spectrum at 126 Hz: ———, without control; — —, with control.

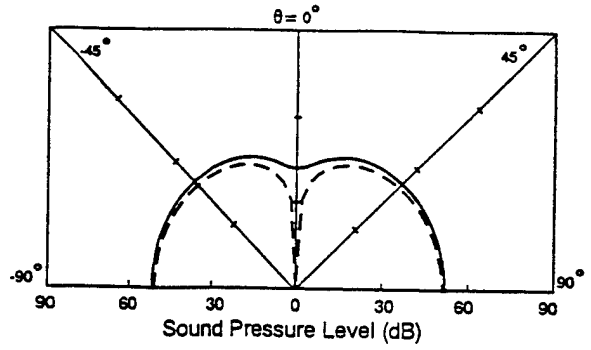

FIG. 11. Far-field pressure radiated in x,z plane at 600 Hz: ———, without control; — —, with control.

also be related to $k_x \simeq \pm 2\pi/l$, corresponding to the second flexural vibrational mode of the simply supported beam determined by modal analysis. When the control is applied, the amplitude of the wave-number spectrum is largely reduced at $k_x=0$ and is slightly increased for all other wave numbers. This increase of magnitude in the supersonic region and the large decrease at $k_x=0$ correspond to the observation made in Fig. 7. The spectrum still presents the same peaks, i.e., the mode shape of the beam is not changed by the control (as noticed previously in Fig. 9).

C. Off-resonance excitation 600 Hz

The last case studied corresponds to an off-resonance excitation of the simply supported beam at 600 Hz. Figure 11 shows the far-field radiated pressure without and with control. The radiation pattern without control is almost like a dipole radiation pattern with only a slight node around $\theta=0$, implying contributions from several modes. In Fig. 12(a), it can be noticed that the near-field flexural waves still radiate as a monopole radiator, and are radiating 12.5 dB more in level than the propagating waves at $\theta=0$. The two wave components radiate in phase and thus add coherently. When the control is applied, the far-field radiation from the beam is reduced to a dipole radiation structural motion, with no radiation in the direction $\theta=0$. The sound pressure levels are also well reduced for the directions close to $\theta=0$ and slightly attenuated elsewhere. It can be noted in Fig. 12(b) that at $\theta=0$, the radiation from the near-field waves has been reduced by 7.3 dB and the one from the propagating waves has been increased by 5 dB. The attenuation of the total sound pressure level at $\theta=0$ again occurs because the two components radiate equally and out-of-phase.

Figure 13 shows the out-of-plane displacement, which is close to that corresponding to the fourth mode (507 Hz). Three node and four antinodes can be observed; however, the displacement distribution is not symmetric with respect to the center of the beam. When the control is invoked, the mode shape is changed as the location of two nodes are moved, and the maximums of amplitude are attenuated. It can also be noticed that the displacement amplitude is attenuated between $x=l/2$ and the location of the input force. In this case, the minimization process leads

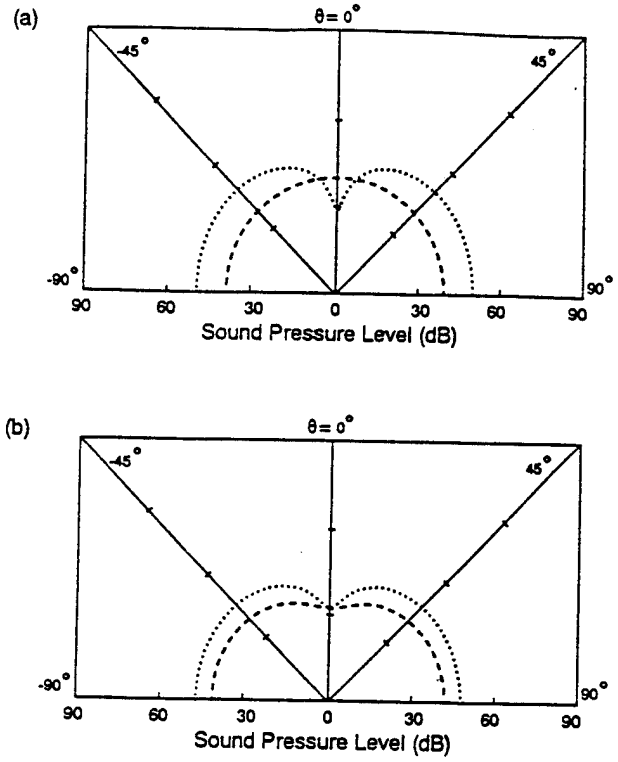

FIG. 12. Components of the far-field pressure radiated in x,z plane at 600 Hz; (a) without control; (b) with control. – – –, due to near-field flexural waves; ——, due to propagating flexural waves.

to a small decrease of radiation for directions not close to $\theta=0$ and to a change of mode shape and a decrease in amplitude of the out-of-plane displacement.

Figure 14 presents the one-dimensional wave-number spectrum with and without control. For the uncontrolled case, two main peaks can be observed close to $k_x \simeq \pm |k_f|$ and two other ones closer to $k_x=0$ located at $k_x=\pm |k_f|/4$. The two main peaks, also corresponding to $k_x \simeq 4\pi/l$ for modal analysis, shows that the fourth flexural vibrational mode is mostly responsible for the response of the beam at this frequency. When the control is invoked, the spectrum amplitude is reduced in all the supersonic region with a large attenuation at $k_x=0$. The general shape of the spectrum is changed (the values of k_x for which the peaks occur are slightly increased), which is related to the change in the mode shape of the vibrating beam noticed previously.

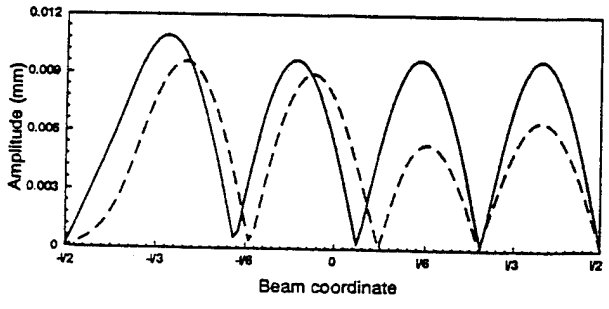

FIG. 13. Out-of-plane displacement at 600 Hz: ——, without control; — —, with control.

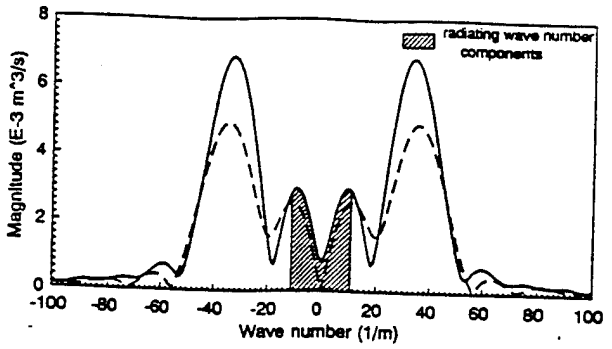

FIG. 14. Wave-number spectrum at 600 Hz: ——, without control; — —, with control.

D. Control comparison with and without near-field waves

It is interesting to investigate the control performance by calculating the optimal forces using only traveling waves and then calculate the minimized field using the expressions that include both near-field and traveling waves. Such calculations should give some insight on the consequences of neglecting the near field when predicting the performance of realistic ASAC system. Table II presents the amplitude and phase of the control forces in order to control, respectively, the total pressure field and the pressure field only due to the propagating waves in the direction $\theta=0$. First, it should be noticed that the control force is for all cases out-of-phase (phase close to 180°) with the input or disturbance force.

For the first mode of the simply supported beam, the control of either the total pressure or the pressure due to the propagating waves leads to almost the same optimal amplitude value for the control force. This was expected, as it was noticed in Fig. 4(a) that the propagating flexural waves are mainly responsible for the sound radiation at this frequency. When the control minimizes the pressure due to only propagating waves at $\theta=0$, the pressure due to the near-field waves is still reduced by half [in the same way observed in Fig. 4(b)] in all directions. However, the pressure due to the propagating waves becomes negligible as highly reduced in all directions. Therefore, the total pressure field under this control situation is approximately equal to the pressure field due to the near-field waves under control, which is about 16.5 dB in all directions.

For the second mode and off-resonance cases, Table II shows that the optimal control forces calculated with the

TABLE II. Optimal control force amplitude and phase.

Condition	Frequency (Hz)	Force to control pressureincl. both wave types	Force to control pressure incl. only propagating waves
1st mode	31.7	0.334435 N, ∠179.99°	0.334232 N, ∠179.99°
2nd mode	126.0	0.252983 N, ∠179.98°	0.112613 N, ∠179.89°
Off-resonance	600.0	0.427298 N, ∠179.86°	0.152152 N, ∠179.30°

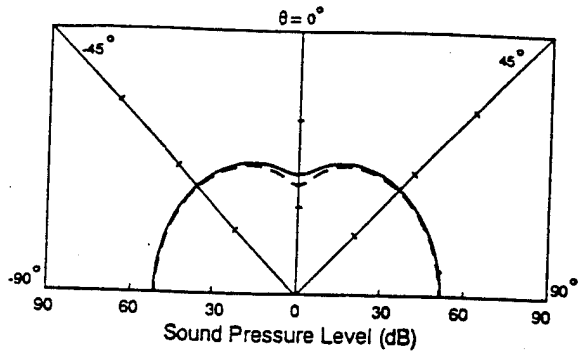

FIG. 15. Far-field pressure radiated in x,z plane at 600 Hz: ———, without control; — —, with control on propagating waves only.

near-field waves neglected are significantly different than when both wave types are included (corresponding to the realistic situation). Figure 15 presents the controlled radiation directivity for the frequency of 600 Hz, corresponding to the optimal gains derived from only propagating wave information. When compared with Fig. 11, it is apparent that the main effect of ignoring the near-field waves on calculating the optimal gain is to markedly reduce the attenuation obtained at the error microphone. At other locations, the residual sound levels are increased by approximately 3 dB. Calculations reveal that the residual value at the error microphone in Fig. 15 is equal to the near-field contribution at this point. This observation agrees with the usual observability requirements in control system performances (i.e., to be controlled, a variable has to be first observed).

VI. CONCLUSIONS

The active control of sound radiation from a simply supported beam has been analytically studied. For excitation on- and off-resonance, a control point force approximating a shaker has been shown to be effective to actively modify the vibrational response of the system in order to obtain directional sound control, i.e., the minimization of the acoustic radiated pressure at one point located in the far field. The large decrease of the radiated pressure at the minimization point has been shown to be caused by the destructive combination of the pressure radiated, respectively, by the propagating flexural waves and the nonpropagating near-field flexural waves (equal and out-of-phase). This phenomenon proves that, even if the near-field flexural waves can be neglected in terms of vibration, they play an important role in terms of radiation and control. This characteristic is due to the high radiation efficiency associated with the monopole source term of the structural near fields. The attenuation of the radiated acoustic pressure at the minimization point in the far field is related to a decrease of the supersonic wave-number component, corresponding to the direction of minimization, in the vibrational response of the system. This attenuation is not necessarily associated with a decrease of the amplitude in the global vibrational response of the system. These results, in general, demonstrate that structural near fields play an important role in active structural acoustic control and should be considered in the design of ASAC systems.

ACKNOWLEDGMENTS

The authors wish to acknowledge the support of the sponsor of this work, the Office of Naval Research under Grant No. ONR-N00014-92-J-1170.

[1] G. E. Warnaka, "Active attenuation of noise- The state of the art," Noise Control Eng. 18(3), 110 (1982).
[2] J. E. Ffowcs-Williams, "Anti-sound," Proc. R. Soc. London Ser. A 395, 63–88 (1984).
[3] C. R. Fuller, "Active control of sound transmission/radiation from elastic plates by vibrational inputs: I. Analysis," J. Sound Vib. 136(1), 1–15 (1990).
[4] R. L. Clark, and C. R. Fuller, "Experiments on active control of structurally radiated sound using multiple piezoceramic actuators," J. Acoust. Soc. Am. 91, 3313–3320 (1992).
[5] W. Redman-While, P. A. Nelson, and A. R. D. Curtis, "Experiments on active control of flexural wave power," J. Sound Vib. 112(1), 181–187.
[6] A. H. Von Flotow and B. Shafer, "Wave absorbing controllers for flexible beam", J. Guidance, Control Dyn. 9(6), 673–680 (1986).
[7] S. J. Elliot, I. M. Stothers, and L. Billet, "Adaptive feedforward control of flexural waves propagating in a beam," Proc. Inst. Acoust. 12(1), 613–622 (1990).
[8] J. Sheuren, "Active attenuation of bending waves in beams," Proc. Inst. Acoust. 12(1), 623–629 (1990).
[9] C. R. Fuller, G. P. Gibbs, and R. J. Silcox, "Active control of flexural and extensional waves in beams," J. Intell. Mater. Syst. Struct. 1(2), 235–247 (1990).
[10] L. O. Gonidou, "Active Control of Flexural Power Flow in Elastic Thin Beams," MS thesis, Department of Mechanical Engineering, Virginia Polytechnic Institute and State University (1989).
[11] C. Guigou and C. R. Fuller, "Active control of sound radiation from a semi-infinite beam with a clamped edge," J. Sound Vib. (to be published).
[12] C. Guigou, C. R. Fuller, and K. D. Frampton, "Experiments on active control of sound radiation from a clamped edge on a semi-infinite beam," J. Sound Vib. (to be published).
[13] R. A. Burdisso and C. R. Fuller, "Theory of feedforward controlled system eigenproperties", J. Sound Vib. 153(3), 437–451 (1992).
[14] R. A. Burdisso and C. R. Fuller, "Dynamic behavior of structural-acoustic systems in feedforward control of sound radiation," J. Acoust. Soc. Am. 92, 277–286 (1992).
[15] C. R. Fuller and R. A. Burdisso, "A wavenumber domain approach to the active control of structure-borne sound," J. Sound Vib. 148(2), 355–360 (1991).

C-10 Causality Analysis of Feedforward - Controlled Systems with Broadband Inputs, R. A. Burdisso, J. S. Vipperman and C. R. Fuller, Journal of the Acoustical Society of America, Vol. 94 No. 1, pp. 234-242, July 1993.

Causality analysis of feedforward-controlled systems with broadband inputs

R. A. Burdisso, J. S. Vipperman, and C. R. Fuller
Vibration and Acoustics Laboratories, Mechanical Engineering Department, Virginia Polytechnic Institute and State University, Blacksburg, Virginia 24061-0238

(Received 14 May 1992; revised 24 November 1992; accepted 23 February 1993)

In recent years adaptive feedforward control algorithms have been successfully implemented to attenuate the response of systems under persistent disturbances such as single and multiple tones as well as random inputs. System causality is not an issue when the excitation is sinusoidal because of its deterministic nature. However, causality is a very important factor in broadband control. Though significant deterioration in the performance of noncausal control systems have been reported in the literature, analytical tools are virtually nonexistent to predict the behavior of broadband controllers. The main objective of this research is to develop an approach to investigate system causality. A formulation is presented to address the effectiveness of a control configuration as a function of the filter size, delay time, and dynamic properties of the structure. The technique is illustrated in a simple numerical example and the results are also corroborated experimentally.

PACS numbers: 43.40.Vn

NOTICE: This material may be protected by copyright law (Title 17, US Code).

INTRODUCTION

Persistent vibrations in elastic structures and their radiated sound fields are problems commonly found in engineering practice. Adaptive feedforward control algorithms have proved to be successful in attenuating stationary disturbances such as single, multiple frequencies, and random inputs. Adaptive feedforward algorithms were first applied to signal noise canceling as demonstrated by Widrow.[1] More recently these techniques have been extended to control one-dimensional,[2] multidimensional acoustic fields,[3] as well as structurally radiated sound using structural control inputs.[4] Feedforward least-mean-square (LMS) and recursive-least-mean-square (RLMS) adaptive algorithms have been applied on active control of bending motion in infinite or semi-infinite thin beams.[5–8] Recently, the simultaneous control of flexural and extensional waves in beams has been demonstrated by a multichannel LMS approach, in conjunction with specialized piezoceramic transducers.[9]

However, most previous theoretical and experimental studies consider only single- and multiple-sinusoidal excitations. Applications of feedforward control for broadband excitation is much more scarce and mostly restricted for attenuating noise in ducts[10–12] and enclosures.[13,14] Active feedforward control of broadband flexural waves in infinite beams have being reported by Elliott.[15] Recently, the authors have developed two new broadband feedforward control configurations for finite structures,[16] which use an adaptive finite impulse response (FIR) filter as a compensator.

A general arrangement of a feedforward control approach applied to a finite system is shown in Fig. 1. The response of the system produced by the offending disturbance $x(t)$ is canceled by a "coherent" control input $u(t)$, which is obtained by tapping the disturbance input and feeding this signal into the compensator W. The compensator is computed such that the mean square value of some system response, i.e., the signal from an error sensor, is minimized. The feedforward control system is said to be causal when the signal fed into the compensator is obtained far enough in advance to allow time for the processing and propagation of the control signal to meet and cancel the disturbance signal at the error sensor. In other words, the propagation time of the disturbance $x(t)$ through the control path should be less than or equal to the propagation time through the disturbance path. System causality is not a constraint when the excitation is sinusoidal because of the deterministic nature of the signal. Future values of the signal are completely predictable under steady-state conditions. On the other hand, causality is a very important issue in broadband control because future values of the excitation cannot be predicted due to the randomness of this type of excitation. The signal is only predictable in some statistical sense. In feedforward broadband control of infinitely long systems, such as ducts and beams where there are no reflected waves from boundaries, the response to the disturbance can always be sensed far enough upstream to yield a causal system. In finite reverberant systems, where standing wave phenomena occur at the natural frequencies, it could be difficult or virtually impossible to configure the control system to render the system causal.

Early broadband control experiments have shown deterioration in the performance due to delays in the control path that results in noncausal control systems. Warner and Bernhard[13] discussed qualitatively the influence of control path delay on the cancellation of nondeterministic sound in acoustic enclosures, while Sutton and his colleagues[14] have experimentally demonstrated significant performance reduction in the control of random sound in enclosures by delaying the signal in the control path. They suggested improvement can be gained by placing the reference sensor close to the disturbance source and the control speaker

 0001-4966/93/94(1)/234/9/$6.00 © 1993 Acoustical Society of America

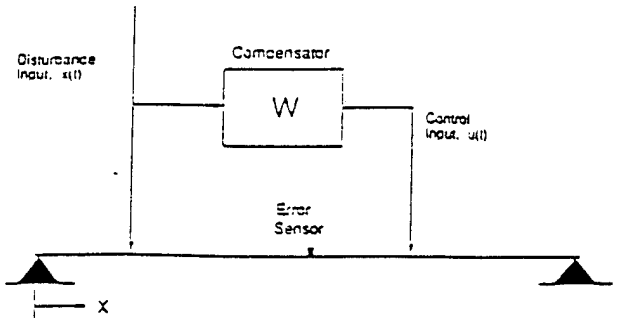

FIG. 1. General arrangement of a feedforward control approach.

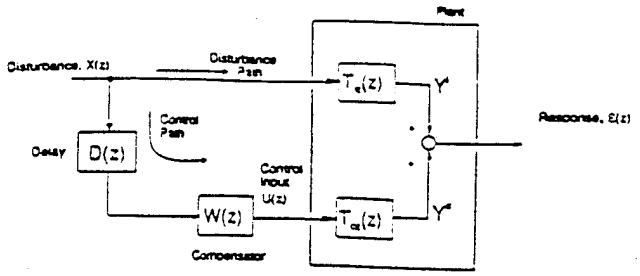

FIG. 2. Discrete time domain feedforward block diagram with a delay in the control path.

close to the error or cancellation transducer. Similar performance degradation has also been observed in broadband structural vibration control experiments.[16] Analytical studies on the performance limits of causally constrained control systems have also been reported in the literature. Nelson *et al.*[17] have developed a time-domain formulation for the case of active control of sound. Joplin *et al.*[18] adopted a numerical scheme to find the optimum causal filter in control of low frequency random sound in enclosures.

In practical implementation of digital controllers, the total control path delay is due to the smoothing filters, the sampling process for the controller, and the physical system itself. A causal controller can often be achieved by carefully choosing the distances between the disturbance and control inputs and the error sensors. This is particularly true in active control of acoustic enclosures where the wave speed is relatively low and the physical dimensions of the system are large. However, a causal system would be difficult to realize in many other situations, i.e., in active control of structural vibrations. Thus, the main goal of this work is to investigate the control performance of noncausal control systems, and to lay out the mathematical foundations to develop design guidelines of noncausal feedforward controllers. In contrast to the work of Nelson *et al.*,[17] the formulation presented here is carried out in the frequency-domain. The analysis demonstrates that some control is always achievable for any degree of "noncausality" in a system. The work also shows that the performance degradation due to delay in the control path can be offset by increasing the compensator filter size. The proposed formulation is then applied to the case of a simply supported beam for illustrative results and also compared to an experimental investigation of the same system.

I. THEORY

The single input, single output feedforward control system shown in Fig. 2 is considered. The analysis is first carried out in the discrete time domain. The disturbance input is assumed to be a zero mean white noise stationary random process. The Z transform of the system response, $Y'(z)$, can be written as follows

$$Y'(z) = T_{ie}(z)X(z), \tag{1}$$

where $T_{ie}(z)$ is the transfer function between the disturbance input and the error output, and $X(z)$ is the Z transform of the input signal.

The system is controlled by feeding forward a reference signal, coherent to the disturbance, through the control filter $W(z)$. The reference signal is obtained by tapping the disturbance input $X(z)$ and passing it through a delay filter $D(z)$ which is given by

$$D(z) = z^{-d}. \tag{2}$$

The time delay produced by the filter $D(z)$ is $\tau = dt_s$, where t_s is the sampling period that is related to the sampling frequency f_s by $t_s = 1/f_s$. The time delay τ represents the difference in propagation time of a pulse through the control and disturbance paths to the error sensor. The control system is causal by selecting the delay $d=0$, i.e., the disturbance takes the same time, in this ideal situation, to propagate through the control and disturbance paths. The control system is made noncausal by setting the delay parameter positive, $d>0$.

The analysis in the discrete time-domain allows us to define a physically realizable causal FIR filter as the compensator $W(z)$. That is

$$W(z) = \sum_{l=0}^{L} w_l z^{-l}, \tag{3}$$

where w_l is the lth weight; and $(L+1)$ is the filter size equal to the number of weights.

The Z transform of the response, $Y^c(z)$, due to the control input is given as follows

$$Y^c(z) = T_{ce}(z)U(z), \tag{4}$$

where $T_{ce}(z)$ is the transfer function between the control input and the error output, and $U(z)$ is the Z transform of the control input.

The response of the system can then be computed as the superposition of the response due to the disturbance and control inputs as follows

$$\epsilon(z) = [T_{ie}(z) + D(z)W(z)T_{ce}(z)]X(z). \tag{5}$$

In feedforward control, the optimum filter weights that define the control input signal are determined by minimizing the mean square value of the error output. The mean square value of $\epsilon(z)$ can be computed as[19]

$$\sigma^2=\frac{1}{2\pi j}\oint \Phi_{\epsilon\epsilon}(z)\frac{dz}{z}, \tag{6}$$

where $\Phi_{\epsilon\epsilon}(z)$ is the discrete power spectral density function (PSDF) of the error sequence; j is the imaginary number; and the path of integration is counterclockwise on a circle centered at the origin on the z plane.

A. Frequency-domain analysis

The integration in Eq. (6) can be conveniently solved in the frequency domain by using the transformation[19]

$$z=e^{j\omega t_s}, \tag{7}$$

which relates the discrete time variable z to the nonnormalized frequency ω. Using Eq. (7), the integral in Eq. (6) becomes[19]

$$\sigma^2=\frac{1}{2\pi}\int_{-\omega_{Ny}}^{\omega_{Ny}} \Phi_{\epsilon\epsilon}(e^{j\omega t_s})\,d\omega, \tag{8}$$

where $\Phi_{\epsilon\epsilon}(\omega)$ is the error signal PSDF defined in the frequency domain, and $\omega_{Ny}=\pi/t_s$ is the Nyquist circular frequency. The same transform, Eq. (7), applied to Eq. (5) gives the frequency content of the error output as

$$\epsilon(\omega)=[T_{i\epsilon}(e^{j\omega t_s})+D(e^{j\omega t_s})W(e^{j\omega t_s})T_{c\epsilon}(e^{j\omega t_s})]x(\omega). \tag{9}$$

Replacing Eq. (7) into Eqs. (2) and (3) and these into Eq. (9) results in:

$$\epsilon(\omega)=[T_{i\epsilon}(e^{j\omega t_s})+e^{-j\omega d t_s}\{W\}^T\{f\}T_{c\epsilon}(e^{j\omega t_s})]x(\omega), \tag{10}$$

where

$$\{W\}=\{w_0,w_1,w_2,\ldots,w_L\}^T \tag{11}$$

is the vector of filter weights, and

$$\{f\}=\{1,e^{-j\omega t_s},\ldots,e^{-j\omega L t_s}\}^T \tag{12}$$

is known as the complex sinusoid vector in digital spectral analysis;[20] and the vector transpose is denoted by the superscript T.

The power spectral density function of the error signal is now defined by

$$\Phi_{\epsilon\epsilon}(\omega)=E[\epsilon(\omega)\epsilon(\omega)^*], \tag{13}$$

where $E[\cdot]$ is the expected value operator; and the asterisk denotes the complex conjugate. Substituting Eq. (10) into Eq. (13) yields

$$\Phi_{\epsilon\epsilon}(\omega)=|T_{i\epsilon}(e^{j\omega t_s})+e^{-j\omega d t_s}\{W\}^T\{f\}T_{c\epsilon}(e^{j\omega t_s})|^2\Phi_{xx}(\omega). \tag{14}$$

Since the disturbance is a zero mean white noise random process, the disturbance PSDF is constant, $\Phi_{xx}(\omega)=\Phi_0$. The mean square value of the error signal as a function of the filter weights can now be computed by replacing Eq. (14) into Eq. (8), and expanding the complex modulus to yield

$$\sigma^2=\sigma_i^2+\{W\}^T[R]\{W\}+\{W\}^T(\{H\}+\{H\}^*), \tag{15}$$

where

$$\sigma_i^2=\frac{1}{2\pi}\int_{-\omega_{Ny}}^{\omega_{Ny}}|T_{i\epsilon}(e^{j\omega t_s})|^2\Phi_0\,d\omega \tag{16}$$

is the variance of the system response due to the disturbance input alone; matrix $[R]$ given by

$$[R]=\begin{bmatrix} R(0) & R(1) & R(2) & \cdots & R(L)\\ R(-1) & R(0) & R(1) & & \vdots\\ R(-2) & R(-1) & R(0) & & \\ \vdots & & & \ddots & R(1)\\ R(-L) & \cdots & & R(-1) & R(0)\end{bmatrix} \tag{17}$$

is a Hermitian Toeplitz matrix that is formed from the $(L+1)$ coefficients

$$R(r)=\frac{1}{2\pi}\int_{-\omega_{Ny}}^{\omega_{Ny}}|T_{c\epsilon}(e^{j\omega t_s})|^2e^{j\omega r t_s}\Phi_0\,d\omega \tag{18}$$

and the vector $\{H\}$ is given by

$$\{H\}=\{H(0),H(1),\ldots,H(L)\}^T \tag{19}$$

with

$$H(r)=\frac{1}{2\pi}\int_{-\omega_{Ny}}^{\omega_{Ny}}T_{i\epsilon}(e^{-j\omega t_s})T_{c\epsilon}(e^{j\omega t_s})\times e^{-j\omega(d+r)t_s}\Phi_0\,d\omega. \tag{20}$$

In adaptive feedforward control the error output mean square value in Eq. (15), referred as the performance surface, is a quadratic function of the filter weights w_l. The optimum weights are those that minimize the mean square value of the error signal. Thus, differentiating Eq. (15) with respect to w_l and setting the result to zero yields the following linear system of equations

$$[R]\{W\}=-\{H_r\}, \tag{21}$$

where $\{H_r\}$ is the real part of the complex vector $\{H\}$.

The properties of matrix $[R]$ will be described in further detail in the next section. Assuming now that the matrix $[R]$ is nonsingular, solving for the optimum vector $\{W\}$ in Eq. (21), and replacing it back into Eq. (15) yields the minimum mean square value as

$$(\sigma^2)_{\min}=\sigma_i^2-\{H_r\}^T[R]^{-1}\{H_r\}. \tag{22}$$

The minimum mean square value of the controlled output response is the difference between the mean square value due to the disturbance alone and the quadratic form $\{H_r\}^T[R]^{-1}\{H_r\}$. Thus, the control system performance will be completely determined by the properties of this quadratic form.

The effectiveness of the control system can be measured by the performance ratio

$$\eta(\text{dB})=10\log_{10}\left(1-\frac{\{H_r\}^T[R]^{-1}\{H_r\}}{\sigma_i^2}\right) \tag{23}$$

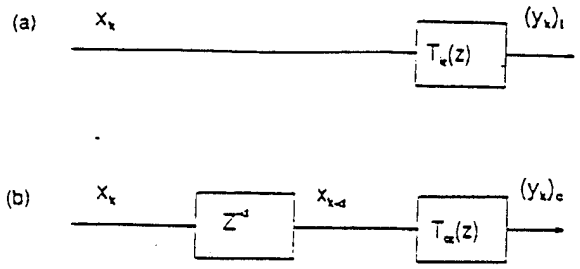

FIG. 3. Random processes associated to the integrals in Eqs. (16), (18), and (20).

that gives the error output power reduction in decibels.

II. CONTROL SYSTEM PERFORMANCE ANALYSIS

A physical interpretation for the terms in matrix $[R]$ and vector $\{H\}$ can be derived by considering the two zero mean random processes depicted in Fig. 3. The process in Fig. 3(a) is the response of the system $(y_k)_i$ when excited at the disturbance location by the sequence x_k, while the process in Fig. 3(b) is the response of the system $(y_k)_c$ when excited at the control location by the delayed sequence x_{k-d}. The term $R(r)$ represents the autocorrelation sequence of the response $(y_k)_c$ as[20]

$$R(r)=E[(y_k)_c(y_{k-r})_c]=\frac{1}{2\pi}\int_{-\omega_{Ny}}^{\omega_{Ny}}\Phi_{y_cy_c}(\omega)e^{j\omega rt_s}\,d\omega, \tag{24}$$

where the PSDF in Eq. (24) is given in terms of the disturbance PSDF and the system dynamics as

$$\Phi_{y_cy_c}(\omega)=|T_{c\epsilon}(e^{j\omega t_s})|^2\,\Phi_0. \tag{25}$$

Since the autocorrelation sequence $R(r)$ is independent of the delay parameter d, the properties of the autocorrelation matrix of the random process $(y_k)_c$ will also be independent of the delay. The properties of $[R]$ are a function of the system dynamics, through the control input and error output transfer function $T_{c\epsilon}(z)$, and the sampling frequency. Since the autocorrelation function of a real stationary random process is an even function $R(r)=R(-r)$, the matrix $[R]$ is real and symmetric. Because of the nonnegative property of the autocorrelation function, the autocorrelation matrix is positive semidefinite.[20]

The term $H(r)$ in Eq. (20) represents the cross-correlation sequence between the random processes $(y_k)_i$ and $(y_k)_c$ as follows[20]

$$H(r)=E[(y_k)_i(y_{k-r-d})_c]$$
$$=\frac{1}{2\pi}\int_{-\omega_{Ny}}^{\omega_{Ny}}\Phi_{y_iy_c}(\omega)e^{-j\omega rt_s}\,d\omega, \tag{26}$$

where the cross PSDF in Eq. (26) is given by

$$\Phi_{y_iy_c}(\omega)=T_{i\epsilon}(e^{-j\omega t_s})T_{c\epsilon}(e^{j\omega t_s})e^{-j\omega dt_s}\Phi_0. \tag{27}$$

Unlike the autocorrelation, the cross-correlation sequence of a real random process is a complex variable. From Eq. (27), $H(r)$ is a function of the system dynamics

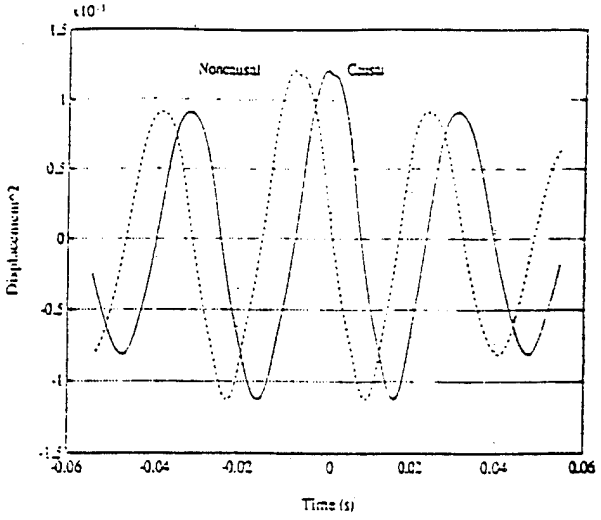

FIG. 4. Real part of cross-correlation sequence $H(r)$ in Eq. (26) for a typical structure.

through the transfer functions $T_{i\epsilon}(z)$ and $T_{c\epsilon}(z)$, the selected sampling frequency and the control path delay d. To graphically illustrate the dependance of $H(r)$ with the delay parameter d, the real part of the cross-correlation sequence is plotted in Fig. 4 as a continuous line for a causal system by setting $d=0$. Assuming the control path has a delay d, the cross-correlation sequence for the noncausal system is the same cross-correlation of the causal system shifted toward the left as shown in Fig. 4 with dashed lines.

Important qualitative conclusions on the controlled system performance can be drawn by considering the special case of sinusoidal random process.[20] In this process, a random sequence is approximated as the sum of M real sinusoids as

$$x_k=\sum_{m=1}^{M}A_m\sin(\omega_m kt_s+\theta_m), \tag{28}$$

where A_m is the real amplitude of the mth sinusoid of circular frequency ω_m, and the associated phase Θ_m is a uniformly distributed random variable on the interval 0 to 2π. The amplitude A_m is related to the magnitude of the PSDF at frequency ω_m. The number and frequency of the sinusoids can be arbitrary. For the sake of clarity in the presentation, we select a uniform distribution for the sinusoid frequencies as $\omega_m=m(\Delta\omega)$ that results in $A_m=2(\Phi_0\Delta\omega)^{1/2}$. In the limiting case that $M\to\infty$ and $\Delta\omega\to 0$ the sequence in Eq. (28) will be a true white noise random sequence.

Replacing Eq. (28) into the process described in Fig. 3(b), it is not difficult to show that the autocorrelation sequence of this sinusoidal process can be easily computed in closed form as[20]

$$R(r)=\Phi_0\Delta\omega\sum_{m=1}^{M}|T_{c\epsilon}(\omega_m)|^2\cos(\omega_m rt_s) \tag{29}$$

and the associated autocorrelation matrix becomes

$$[R]=\Phi_0\Delta\omega\sum_{m=1}^{M}|T_{c\epsilon}(\omega_m)|^2\{S_m\}\{S_m\}^T, \quad (30)$$

where $\{S_m\}$ is

$$\{S_m\}=[1,\cos(\omega_m t_s),\cos(\omega_m 2t_s),\ldots,\cos(\omega_m Lt_s)]^T. \quad (31)$$

Again the autocorrelation matrix $[R]$ is real, symmetric and in general positive semidefinite, or in other words the eigenvalues of matrix $[R]$ are real and non-negative. The rank of the autocorrelation matrix can be shown to be $2M$.[20] The dimension of matrix $[R]$ is equal to the number of filter weights, $(L+1)$. If $2M$ is greater or equal to $(L+1)$, the eigenvalues of $[R]$ are all real and positive and the matrix inverse in Eq. (22) exists. On the other hand, if $(L+1)$ is greater than $2M$, there will be $(L+1)-2M$ zero eigenvalues and matrix $[R]$ is singular. A physical interpretation can be gained by considering the case where the number of weights in the filter is twice the number of sinusoids included in the process, $(L+1)=2M$. Thus, there are enough weights to adjust the phase and magnitude of each sinusoid to drive the output mean square value to zero, $(\sigma^2)_{\min}=0$. Clearly, increasing the number of filter weights provides no further reduction and this is mathematically depicted by the rank of $[R]$ being $2M$.

For the case of $(L+1)<2M$, the positive definite property of $[R]$ and of its inverse allows us to write

$$\{H_r\}^T[R]^{-1}\{H_r\}>0 \quad (32)$$

for any arbitrary vector $\{H_r\}$, which has the important implication that there will always be some degree of reduction in the output variance in Eq. (22) in spite of any delay in the control path. Because of the positive definite property, it is not difficult to show that the quadratic form in Eq. (32) is a monotonically increasing function. That is

$$(\{H_r\}^T[R]^{-1}\{H_r\})_{L+1}\geq(\{H_r\}^T[R]^{-1}\{H_r\})_L. \quad (33)$$

Therefore, the deterioration in the control performance due to the time delay could at least be partially compensated by increasing the filter size. This phenomenon was observed in the numerical and experimental studies of the next section.

III. EXPERIMENTAL AND NUMERICAL RESULTS

Both analytical and experimental investigations of the system causality for broadband structural control were first performed on a simply supported beam. The beam is made of steel and has a length of $L=380$ mm. Two thin, flexible metal shims connect the beam to a rigid frame, providing the simply supported end conditions. The experimentally measured natural frequencies are presented in Table I. Figure 5 shows the location of the error sensor and disturbance and control inputs. The error sensor was a miniaccelerometer located at $x_e=0.626L$. The control actuation was applied by a co-located set of piezoelectric patches mounted on each side of the beam surfaces wired out-of-phase to produce a pair of bending moments applied at $x_{c1}=0.797L$ and $x_{c2}=0.697L$. The disturbance input action was also applied by a piezoelectric patch. The resulting disturbance bending moments are applied at $x_{d1}=0.494L$ and $x_{d2}=0.394L$. The experiment was limited to control the first three bending modes because the location of the control actuator pair rendered the fourth mode uncontrollable. Consequently, the cutoff frequency of the low-pass filters used in the experimental setup was set at 400 Hz.

TABLE I. Simply supported beam natural frequencies.

	Natural frequency (Hz)	
	Analytical	Experimental
1	31.7	32.9
2	127.0	126.9
3	285.6	282.3
4	507.2	505.5

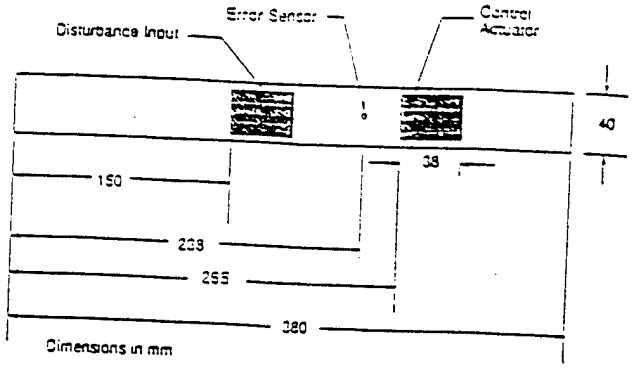

FIG. 5. Sensor and actuator locations on the simply supported experimental beam analysis.

A schematic diagram of the complete experimental setup is shown in Fig. 6. A white noise signal was generated by a Brüel & Kjær 2032 spectrum analyzer, which was low-pass filtered to obtain band-limited random noise from 0 to 400 Hz. This signal was input into a power amplifier whose output drove the disturbance piezoelectric patch. The same input signal was fed into the controller. The control system used in the experiment is a broadband adaptive LMS controller implemented on a Texas Instru-

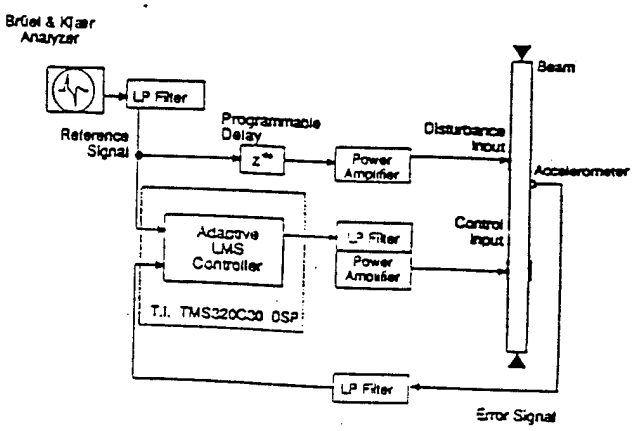

FIG. 6. Experimental setup for testing the feedforward broadband control algorithm.

ment TMS320C30 digital signal processor (DSP).[16] The sampling rate used for the control experiments was $f_s = 2000$ Hz. The control signal from the DSP was low-pass filtered and fed into a power amplifier that in turn drove the control piezoelectric patches.

The propagation time from both the disturbance and control inputs to the error sensor was measured by computing the cross-correlation functions across each path while being excited by white noise. The propagation time for each path is found at the largest peak on the respective cross-correlation function. It was found that the control path has an average delay time of 2.7 ms with respect to the disturbance path, which was introduced mainly by the smoothing filter in the control path. Therefore, the experimental setup yields a noncausal control system. A programmable delay z^{-d_e} was installed in the disturbance path allowing the control system to be made causal by varying the delay d_e. The reader should not confuse this experimental delay parameter d_e with the analytical delay parameter d used in Secs. I and II. The delay in the disturbance path in the experimental setup simply allow us to compare the behavior of the causal with the noncausal control system. On the other hand, the analytical delay parameter d in the control path has the purpose of modeling the actual time delay in a control system whose characteristics are being investigated. It is important to mention that in a real implementation, delaying the disturbance signal as in this experiment is seldom possible. Thus, it is of a paramount importance to address the performance of real noncausal systems.

An analytical model of the experimental setup was also derived by solving the eigenvalue problem of a simply supported beam. The bending stiffness is $EI = 5.329$ NT m^2 and mass per unit length is $m = 0.626$ NT s^2/m^2 that corresponds to the experimental beam properties. The system is assumed to have 0.2% viscous damping in each mode. Again only the three first modes are included in the response analysis. The well known natural frequencies and mass normalized mode shapes are given by

$$f_n = \frac{1}{2\pi}\left(\frac{n\pi}{L}\right)^2\sqrt{\frac{EI}{m}}; \quad \Phi_n(x) = \sqrt{\frac{2}{mL}}\sin\left(\frac{n\pi x}{L}\right). \quad (34)$$

The analytical natural frequencies are also tabulated in Table I and they agree very well with the experimentally measured ones. These eigenproperties are used to compute the transfer functions $T_{ie}(z)$ and $T_{ce}(z)$ needed for the analysis. The derivation of these transfer function is detailed in the Appendix.

A. Causal control system

The behavior of the causal control system was first investigated by implementing a delay of 3 ms ($d_e = 6$) into the disturbance path in the experimental setup. This experimental delay parameter is nearly equivalent to a delay parameter $d = 0$ in the analysis. Figure 7 shows a comparison of the measured error signal before and after control using an adaptive FIR filter with 24 weights. Although the error was not completely canceled, a large amount of vibration attenuation was achieved by the controller. A comparison of the spectrum of the error signal before and after control is shown in Fig. 8, and it gives additional insight into the control mechanism. Despite an increase of the spectrum in some off-resonance frequencies bands, the spectrum at the resonances (32.9, 126.9, and 282.3 Hz) displays a reduction of approximately 20–25 dB. The result was a net reduction of the mean-square error of 19.4 dB. Thus, the controller behaves as a wideband controller rather than broadband controller, attenuating the large frequency components that occur near the structural resonances while adding energy at the antiresonances.

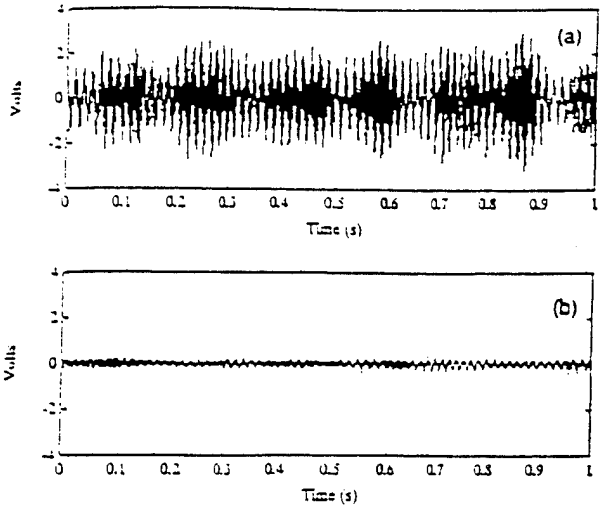

FIG. 7. Error signal from the structure using a FIR filter with 24 weights. (a) Before control; (b) after control.

The influence of the adaptive filter size on the controller performance was then investigated experimentally by varying the filter size $(L+1)$. The reductions in the error signal power was measured for 12, 14, 16, 24, 32, 48, 64, and 80 weights in the FIR filter and they are plotted in Fig. 9. It can be seen that the control performance quickly improves with larger filters to reach a nearly constant reduction of 20 dB. The analytical response of the beam for a causal system is obtained by setting the delay parameter

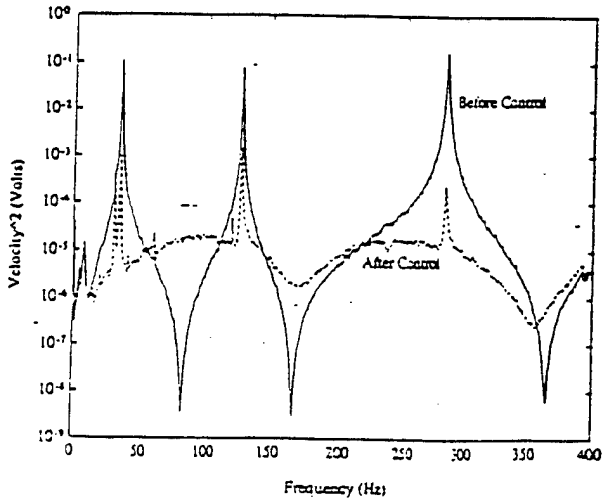

FIG. 8. Spectrum of error signal using a FIR filter with 24 weights.

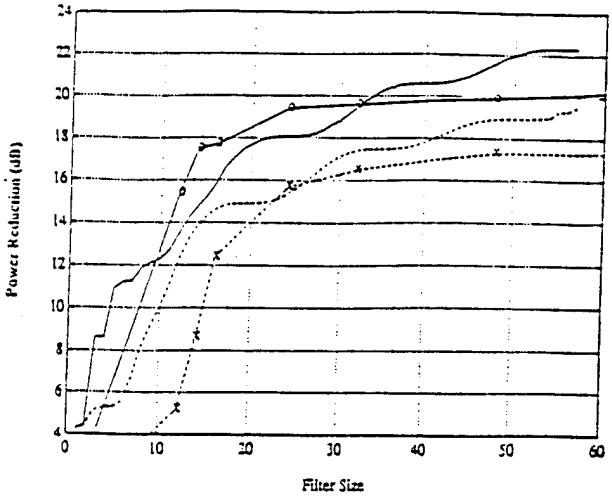

FIG. 9. Power reduction of error signal as a function of the filter size. — Analytical causal; —— analytical noncausal; O—O experimental causal; ×—× experimental noncausal system.

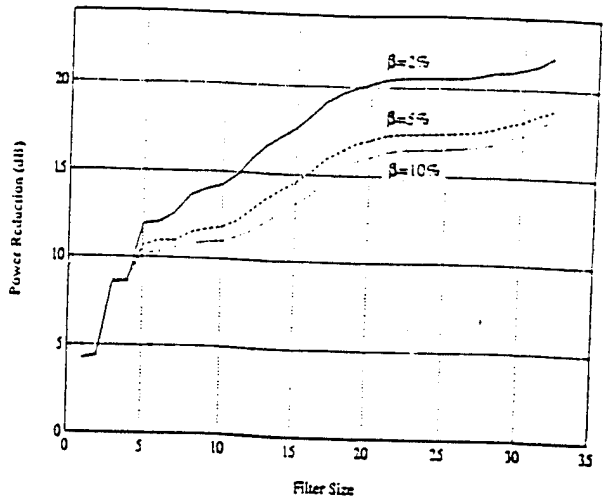

FIG. 10. Power reduction of error signal as function of the filter size and modal damping for a causal system.

$d=0$ in Eq. (2). The integrals in Eqs. (16), (18), and (20) are numerically solved as described in the Appendix. The power reduction at the error sensor location computed from Eq. (23) is plotted in Fig. 9 as a function of the filter size. The analytical prediction shows the same general trend as the experimental observations with two exceptions. Firstly, the analytical curves display some oscillation in the monotonically increasing performance function which is not observed in the experiment. The reason for this discrepancy may lay in the lack of resolution in the experimental results. The period of this oscillation is related to the period of the first natural mode of the beam. The same oscillatory phenomenon was also observed by Nelson *et al.*[17] Secondly, the analytical model displays better control for larger filter sizes than in the experimental observations. This is probably due to the fact that the controller may not have completely converged at the time the response was measured since large filters requires longer convergence times. In addition the convergence parameter was set very small (10^{-7}) for the large filter size, thus increasing the effects of round off error.

B. Noncausal control system

The behavior of the noncausal control system was then studied by setting the programmable delay d_e to zero in the experimental setup of Fig. 6. This is equivalent to setting $d=6$ in the analysis. The experimental error signal time histories and spectrums before and after control show the same features as for the causal system in Figs. 7 and 8, and thus they are not presented here. The reduction in the error signal power in terms of the FIR filter size is again plotted in Fig. 9. The analytically predicted power reduction for the noncausal control system is also plotted in Fig. 9. Both the analytical and experimental results show that the effectiveness of the noncausal controller is severely compromised for filters with less than 24 weights compared with the causal controller. However, for larger filter size, the noncausal controller shows significant reduction of the error variance which is only about 3 dB below the causal controller.

The good agreement between the analytical and experimental results, for both the causal and noncausal control systems, validates the proposed formulation as an analytical tool to predict control system performance. This simple laboratory demonstration shows that the formulation presented here can be used to predict the controller performance as a function of the system parameters such as delay time, sampling frequency, filter size, number of modes to control, etc. As an example, it is useful to predict the minimum filter size to achieve a required degree of reduction of the error signal. The causal controller of the experimental setup needed 12 coefficients to reduce the error variance by 15 dB. On the other hand, the noncausal controller, with a delay of 3 ms, requires 24 filter weights for the same reduction. However, increasing the filter size also slows the adaptive process and increases the computational effort. Thus, careful analysis of the control performance should be considered before a controller is implemented on a particular application.

C. Effect of damping

The effect of damping in a causal system is investigated by varying the modal viscous damping ratio β from 2% to 10%. As shown in Fig. 10 the decrease in damping results in better attenuation of the error output mean square value. This is due to the enhanced notch-filtering effect of the structure that yields the response to resemble the superposition of multiple sinusoids whose frequencies are the natural frequencies of the structure. This behavior is described by Nelson *et al.*[17] as an increase in the "predictability" of the broadband input by the filtering effect of the structure. In the limiting case of the modal damping approaching zero, a filter with the number of coefficients equal to twice the number of modes to control would be sufficient to completely cancel the error signal. Figure 11 presents the parametric study of damping in the noncausal

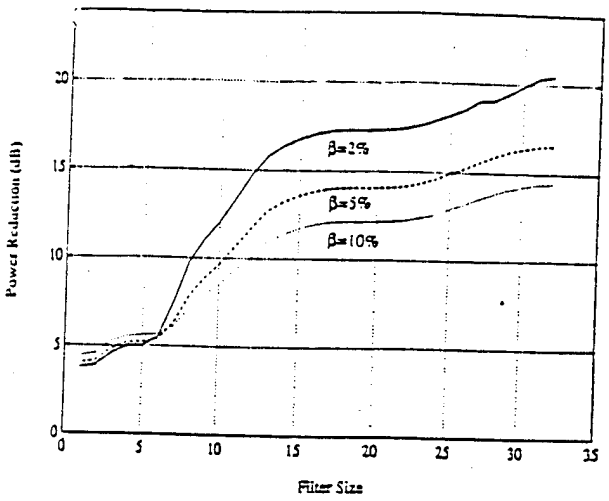

FIG. 11. Power reduction of error signal as function of the filter size and modal damping for a noncausal system.

system. The results shows the same general deterioration in the performance with the increase in damping as for the causal system. The analytical formulation developed here can also be used to investigate the variation in the controller performance with different delays and spectral content of the broadband input disturbance.

IV. CONCLUSIONS

A formulation was developed to carried out causality analysis of feedforward controlled elastic systems subjected to broadband excitations. The control approach used is the feedforward control approach with a FIR filter as compensator. The proposed analytical tool was developed in the frequency-domain and can be used to predict the performance of this type of controllers in terms of system parameters such as delay time, damping, spectral content of the input, filter size, etc... It is demonstrated that reduction in the error signal mean square value is always achievable for any noncausal control system. The analysis also shows that the deterioration in the control performance due to the delay in the control path can be at least partially compensated by increasing the compensator order. The applicability of the formulation is demonstrated on a laboratory model of a simply supported finite beam. The control performance was investigated for both causal and noncausal systems as a function of the compensator size and system damping. The numerical results are also corroborated experimentally. Good agreement is observed between the numerically predicted and measured results, thus validating the proposed formulation.

ACKNOWLEDGMENT

The authors gratefully acknowledge the support of this work by the Office of Naval Research Grant No. ONR-N00014-92-J-1170.

APPENDIX

The integrals in Eqs. (16), (18), and (20) do not have closed form solution. A direct numerical integration poses some difficulties because the peaked nature of the typical structural transfer functions and also due to the oscillatory behavior of the term $e^{j\omega t}$ in Eqs. (18) and (20). Here a detailed description is presented for the numerical evaluation of these integrals.

The transfer function between the control input and error sensor can be written as follows

$$T_{c\epsilon}(z)=\sum_{n=1}^{N} u_n \epsilon_n H_n(z), \tag{A1}$$

the modal control force u_n and the modal error components ϵ_n are given by

$$u_n=\frac{d\phi_n(x_{c2})}{dx}-\frac{d\phi_n(x_{c1})}{dx}; \quad \epsilon_n=\phi_n(x_e). \tag{A2}$$

N is the number of modes included in the analysis; and

$$H_n(z)=\frac{b_{n1}z}{z^2-a_{n1}z+a_{n2}} \tag{A3}$$

is the nth modal frequency response function (FRF) defined in the discrete domain. The coefficients b_{n1}, a_{n1}, and a_{n2} are related to the nth natural frequency ω_n, damping ratio β_n, and the sampling period t_s as[21]

$$\begin{aligned} b_{n1}&=\frac{e^{-\beta_n\omega_n t_s}}{\omega_n(1-\beta_n^2)}\sin(\omega_{nd});\\ a_{n1}&=2e^{-\beta_n\omega_n t_s}\cos(\omega_{nd});\\ a_{n2}&=e^{-2\beta_n\omega_n t_s} \end{aligned} \tag{A4}$$

with $\omega_{nd}=\omega_n(1-\beta^2)^{1/2}$. Solving for the roots of the denominator in Eq. (A3), $H_n(z)$ can be written as

$$H_n(z)=\frac{b_{n1}z}{(z-z_n)(z-z_n^*)}, \tag{A5}$$

where the roots are

$$z_n=e^{-\beta_n\omega_n t_s}\{\cos(\omega_{nd}t_s)+j\sqrt{1-\cos^2(\omega_{nd}t_s)}\}. \tag{A6}$$

The modules square of the transfer function $T_{c\epsilon}(z)$ is computed as

$$\begin{aligned} |T_{c\epsilon}(z)|^2&=T_{c\epsilon}(z)T_{c\epsilon}(z^{-1})\\ &=\sum_{n=1}^{N}\sum_{m=1}^{N} u_n u_m \epsilon_n \epsilon_m H_n(z)H_m(z^{-1}) \end{aligned} \tag{A7}$$

where by replacing z by z^{-1} is equivalent to take the complex conjugate in the frequency domain. Replacing Eq. (A5) into (A7) and using partial fraction expansions, the product of the modal FRFs can be expanded as follows

$$H_n(z)H_m(z^{-1})=\frac{A_{nm}}{z-z_n}+\frac{B_{nm}}{z-z_n^*}+\frac{C_{nm}}{z-1/z_m}+\frac{D_{nm}}{z-1/z_m^*}, \tag{A8}$$

where the coefficients in the partial fractions are easily computed. Replacing Eq. (A8) into (A7) becomes

$$R(r)=\frac{1}{2\pi}\sum_{n=1}^{N}\sum_{m=1}^{N}u_n u_m \epsilon_n \epsilon_m I_{nm}(r), \tag{A9}$$

where

$$I_{nm}(r)=A_{nm}\int_{-\omega_{Ny}}^{\omega_{Ny}}\frac{e^{j\omega r_s}}{e^{j\omega t_s}-z_n}\,d\omega + B_{nm}\int_{-\omega_{Ny}}^{\omega_{Ny}}\frac{e^{j\omega r_s}}{e^{j\omega t_s}-z_n}\,d\omega + C_{nm}\int_{-\omega_{Ny}}^{\omega_{Ny}}\frac{e^{j\omega r_s}}{e^{j\omega t_s}-1/z_m}\,d\omega + D_{nm}\int_{-\omega_{Ny}}^{\omega_{Ny}}\frac{e^{j\omega r_s}}{e^{j\omega t_s}-1/z_m^*}\,d\omega. \tag{A10}$$

Now each integral in Eq. (A9) is better conditioned that the original integral in Eq. (18). The numerical solution of the integrals in Eq. (A9) does not pose any problems for wide range of the parameters r and t_s. Similarly, the integral in Eq. (16) becomes

$$\sigma_d^2=\frac{1}{2\pi}\sum_{n=1}^{N}\sum_{m=1}^{N}f_n f_m \epsilon_n \epsilon_m I_{nm}(0) \tag{A11}$$

and Eq. (20)

$$H(r)=\frac{1}{2\pi}\sum_{n=1}^{N}\sum_{m=1}^{N}f_n u_m \epsilon_n \epsilon_m I_{nm}(d+r), \tag{A12}$$

where the disturbance modal force is given by

$$f_n=\frac{d\phi_n(x_{d2})}{dx}-\frac{d\phi_n(x_{d1})}{dx}. \tag{A13}$$

[1] B. Widrow, J. R. Glover, Jr., J. M. McCool, J. Kaunitz, C. S. Williams, R. H. Hearn, J. R. Zeidler, E. Dong, Jr., and R. C. Goodlin, "Adaptive Noise Canceling: Principles and Applications," Proc. IEEE 63, 1692–1716 (1975).

[2] G. E. Warnaka, "Active Attenuation of Noise: the State of the Art," Noise Control Eng. 18, 100–110 (1982).

[3] R. J. Silcox and H. C. Lester, "An Evaluation of Active Control in a Cylindrical Shell," J. Vib. Stress, Reliability Design 111, 337–342 (1989).

[4] C. R. Fuller, "Active Control of Sound Radiation from a Vibrating Rectangular Panel by Sound Sources and Vibration Inputs: an Experimental Comparison," J. Sound Vib. 145, 195–215 (1991).

[5] W. Redman-White, P. A. Nelson, and A. R. D. Curtis, "Experiments on Active Control of Flexural Wave Power," J. Sound Vib. 112, 187 (1987).

[6] A. H. Von Flowtow and B. Schafer, "Wave-absorbing Controller for a Flexible Beam," J. Guidance, Control Dynam. 9, 673–680 (1986).

[7] J. Scheuren, "Active Attenuation of Bending Waves in Beams," Proc. Inst. Acoust. 12, 623–629 (1990).

[8] G. P. Gibbs and C. R. Fuller, "Experiments on Active Control of Vibrational Power Flow Using Piezoceramics Actuators and Sensors," AIAA paper 90–1132 (1990).

[9] C. R. Fuller, G. P. Gibbs, and R. J. Silcox, "Simultaneous Active Control of Flexural and Extensional Power Flow in Beams," in *Proceedings of International Congress on Recent Developments in Air and Structure-borne Sound and Vibration* (Auburn University, Auburn, AL, 1990), pp. 657–662.

[10] C. F. Ross, "An Algorithm for Designing a Broadband Active Control System," J. Sound Vib. 80, 373–380 (1982).

[11] L. J. Erickson and M. C. Allie, "A Digital Sound Control System for Use in Turbulent Flows," Noise-Con 87, 365–370 (1987).

[12] L. J. Erikson, M. C. Allie, and R. A. Greiner, "The Selection and Application of an IIR Adaptive Filter for Use in Active Control Attenuation," IEEE Trans. Acoust. Speech Signal Process. ASSP-35, 433–437 (1987).

[13] J. V. Warner and R. J. Bernhard, "Digital Control of Sound Fields in Three-dimensional Enclosures," AIAA 11th Aeroacoustics Conference, 1–8 (1987).

[14] T. J. Sutton, S. J. Elliot, P. A. Nelson, and I. Moore, "Active Control of Multiple-source Random Sound in Enclosures," Proc. Inst. Acoust. 12, 689–693 (1990).

[15] S. J. Elliot, I. M. Stothers, and L. Billet, "Adaptive Feedforward Control of Flexural Waves Propagating in a Beam," Proc. Inst. Acoust. 12, 613–622 (1990).

[16] J. S. Vipperman, R. A. Burdisso, and C. R. Fuller, "Active Control of Broadband Structural Vibration Using the LMS Adaptive Algorithm," J. Sound Vib. (to be published) (1993).

[17] P. A. Nelson, J. K. Hammond, P. Joseph, and S. J. Elliott, "Active Control of Stationary Random Sound Fields," J. Acoust. Soc. Am. 87, 963–975 (1990).

[18] P. M. Joplin and P. A. Nelson, "Active Control of Low-frequency Random Sound in Enclosures," J. Acoust. Soc. Am. 87, 2396–2404 (1990).

[19] B. Widrow and S. D. Stearns, *Adaptive Signal Processing* (Prentice-Hall, New York, 1985).

[20] S. L. Marples, Jr., *Digital Spectral Analysis with Applications* (Prentice-Hall, New York, 1987).

[21] R. Isermann, *Digital Control Systems* (Springer-Verlag, Berlin, 1981).

C-11 Enhancing Induced Strain Actuator Authority Through Discrete Attachment to Structural Elements, Z. Chaudhry and C. A. Rogers, AIAA Journal, Vol. 31 No. 7, pp. 1287-1292, July 1993.

AIAA JOURNAL
Vol. 31, No. 7, July 1993

Enhancing Induced Strain Actuator Authority Through Discrete Attachment to Structural Elements

Z. Chaudhry* and C. A. Rogers†
Virginia Polytechnic Institute and State University, Blacksburg, Virginia 24061

In structural control, induced strain actuators are used by bonding them or embedding them in a structure. With bonded or embedded actuators used for inducing flexure, the developed in-plane force contributes indirectly through a locally generated moment. Control authority in this configuration is thus limited by actuator offset distance. In this paper, a new concept of flexural or shape control is presented, whereby induced strain actuators such as piezoelectric ceramic patches or shape memory alloys are attached to a structure at discrete points (as opposed to being bonded). This paper specifically addresses discretely attached induced strain actuators like piezoceramic and electrostrictive actuators which are available in the form of plates or patches, and includes actuator flexural stiffness considerations. This configuration is different from the bonded actuator configuration in two ways. One, because the actuator and the structure are free to deform independently, the in-plane force of the actuator can result in an additional moment on the structure and enhanced control. Second, the actuator can be offset from the structure without an increase in the flexural stiffness of the basic structure. This allows for the optimization of the offset distance to maximize control. Enhanced control is demonstrated by comparing the static response of a discretely attached actuator beam system with its bonded counterpart system. The advantage of this configuration over the bonded configuration is also verified experimentally.

Introduction

In recent years, there has been increased interest in the use of induced strain actuators for various types of structural control. A number of models have been developed to represent the induced strain actuator and substrate coupling. Models of strain actuators coupled with simple beams[1-5] and plates[6,7] have been introduced. Most of this work has focused on the development of accurate models to represent actuator and substrate coupling. In all of these models, however, the actuators are either embedded or bonded to the surface of the structure. No other configuration for mounting the actuator on the structure has been considered.

The focus of this research has been to investigate various configurations for integrating induced strain actuators into structures and to determine an efficient way of utilizing induced strain actuators. The conventional method of bonding induced strain actuators to the surface is certainly the easiest, but may not exploit the full capabilities of the induced strain actuators. By bonding or embedding an actuator in a structure, the actuator becomes part of the structure and as such, deforms along with it. The in-plane force of the actuator, which is the primary force exerted by the actuator on the structure, contributes only indirectly, i.e., in the development of a moment on the structure. This is because of a balancing action between the compression and tension members in the structure.[8] The moment is a product of actuator force and actuator offset distance. Therefore, for a given available force, the actuator offset distance must be increased to increase the moment and consequently the authority of the actuator. Increasing the actuator offset distance poses two problems—it increases the flexural stiffness of the structure and it increases the stroke requirement of the actuator. This is the dilemma regarding structural control with embedded or surface-bonded actuators.

Faced with this dilemma, a new configuration in which the actuator is attached to the structure at discrete points is proposed. This configuration is fundamentally different from the bonded/embedded configuration. In this configuration, the structure and actuator between the two discrete points can deform independently, and the in-plane force of the actuator, which is dormant in the case of the bonded actuator, can cause out-of-plane displacements of the structure. Also, because now the actuator offset distance can be increased without any increase in the basic flexural stiffness of the structure (as seen by the actuator), this distance can be optimized for maximum actuator authority.

Two implementations of this concept are possible. In the first, the actuator (e.g., shape memory alloy actuator wires) does not possess any flexural stiffness and, therefore, force exerted by the induced strain actuator on the structure is directed along a straight line joining the two attachment points. This configuration is the most efficient, and results in much greater control compared to the bonded configuration. The formulation and experimental results for this configuration and its variants have already been investigated and have been reported in an earlier paper.[9] In this paper, the second implementation, where the actuator [like piezoelectric (PZT) and electrostrictive actuators] possesses flexural stiffness, is analyzed. In this configuration, the actuator authority is again enhanced particularly due to correct selection of the actuator offset distance.

Formulation

Consider a simply supported beam with an induced strain actuator attached at two discrete points, as shown in Fig. 1. When the

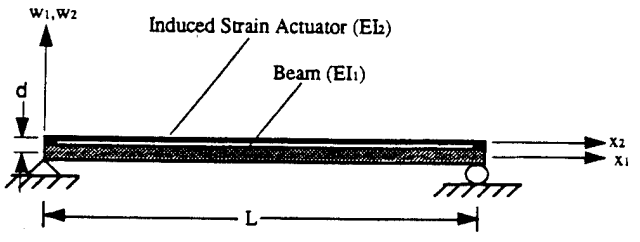

Fig. 1. Geometry of the problem.

Received Aug. 7, 1992; revision received Jan. 15, 1993; accepted for publication Jan. 15, 1993. Copyright © 1993 by Z. Chaudry and C. A. Rogers. Published by the American Institute of Aeronautics and Astronautics, Inc., with permission..

*Graduate Research Assistant, Center for Intelligent Material Systems and Structures. Member AIAA.

†Professor, Center for Intelligent Material Systems and Structures. Member AIAA and ASME.

actuator contracts in response to an applied electric field or temperature gradient, it exerts a compressive force on the beam and the actuator itself goes into tension. The tensile force in the actuator is exactly equal and opposite the compressive force in the beam. The form of the governing equation for both the beam and actuator is:

$$EIw_{,xxxx} \pm Pw_{,xx} = 0 \tag{1}$$

The form of the solution of the previous equation is, of course, different for the actuator and the beam. For the beam, the force P is compressive and for the actuator, the force P is tensile. In general, the flexural stiffnesses EI of the beam and the actuator are also different. The solution of the differential equation for the beam is

$$w_1(x_1) = A_1 \sin kx_1 + B_1 \cos kx_1 + C_1 x_1 + D_1 \tag{2}$$

and for the actuator

$$w_2(x_2) = A_1 \sinh \bar{k}x_2 + B_2 \cosh \bar{k}x_2 + C_2 x_2 + D_2 \tag{3}$$

where

$$k = \sqrt{P/EI_1} \tag{4}$$

and

$$\bar{k} = \sqrt{P/EI_2} \tag{5}$$

The eight constants A_i, B_i, C_i, and D_i (i=1, 2) are solved from the following eight boundary and matching conditions:

at x_1=0, and x_2=0:

$$w_1 = w_2 = 0 \tag{6}$$

$$w_{1,x_1} = w_{2,x_2} \tag{7}$$

$$-EI_1 w_{1,xx} - EI_2 w_{2,xx} = -Pd \tag{8}$$

at $x_1 = l$, and $x_2 = l$:

$$w_1 = w_2 = 0 \tag{9}$$

$$w_{1,x_1} = w_{2,x_2} \tag{10}$$

$$-EI_1 w_{1,xx} - EI_2 w_{2,xx} = -Pd \tag{11}$$

Critical Buckling Load

The true input in such problems is applied electric field or free induced strain of the actuator (e.g., $\Lambda = d_{31}E$), but before addressing the question of the relationship between the free induced strain and the force P, the eigenvalue problem is analyzed. The characteristic equation for the critical buckling load can be obtained by simply setting the actuator offset distance d to zero:

$$2(1 - \cos kl \cosh \bar{k}l) + \frac{\bar{k}^2 - k^2}{k\bar{k}} \sin kl \sinh \bar{k}l = 0 \tag{12}$$

The critical buckling load, as it changes with the flexural stiffness ratio of the actuator and beam (EI_1/EI_2), is shown in Fig. 2. The critical buckling load has been normalized by EI_1/l^2. Also, only flexural stiffness ratios greater than one are considered because in most applications the structure is stiffer than the actuator.

At higher values of flexural stiffness ratios, the value of the critical buckling load is asymptotic to $\pi^2 EI_1/l^2$, which is the critical buckling load of a column with both ends pinned. This is perfectly logical, because as the flexural stiffness ratio increases, the flexural stiffness of the actuator becomes less and less significant compared to the beam, until finally the actuator behaves like a cable (with negligible flexural stiffness) tied to the two ends of the beam.

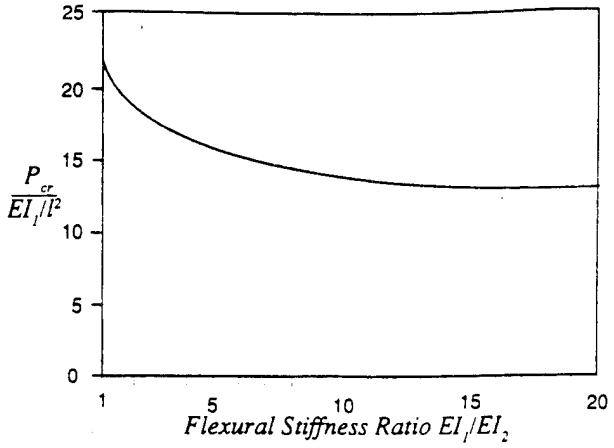

Fig. 2. Critical buckling load vs flexural stiffness ratio EI_1/EI_2.

It is important to realize that buckling in such a configuration is possible, but for most induced strain actuators, which have limited stroke capability, it does not pose any problem. This is because catastrophic buckling (i.e., large displacements) not only requires a force greater than the critical buckling load but also requires that the force remain constant regardless of the displacement of the structure. This is of course not the case with induced strain actuators; they have limited stroke, after which they exert only a negligible force on the structure. Theoretically, buckling can take place with induced strain actuators, but displacements will still depend on the stroke capability of the actuators. Generally speaking, for any significant structural buckling, the actuator strain must be greater than 1%, which is possible only in the case of shape memory alloy (SMA) actuators. But as stated earlier, SMA actuators, which are available in the form of wires, have negligible flexural stiffness and therefore do not fall into this category of problems.

Force-Free Induced Strain Relationship

The free induced strain Λ, which is the true primary input variable, can be computed for a given force P using the following equation:

$$P = EA_2(\varepsilon^0_{x_2} - \Lambda) \tag{13}$$

where

$$\varepsilon^0_{x_2} = \frac{du_2}{dx_2} + \frac{1}{2}\left(\frac{dw_2}{dx_2}\right)^2 \tag{14}$$

Substituting for ε^0_x in Eq. (13) and rearranging,

$$\frac{du_2}{dx_2} = \frac{P}{EA} - \frac{1}{2}\left(\frac{dw_2}{dx_2}\right)^2 + \Lambda \tag{15}$$

Integrating this expression yields the following expression for u_2:

$$u_2 = -\frac{1}{2}\left\{\left(A_2^2\bar{k}^2\left(\frac{\sinh 2\bar{k}x_2}{4\bar{k}} + \frac{x_2}{2}\right) + B_2^2\bar{k}^2\left(\frac{\sinh 2\bar{k}x_2}{4\bar{k}} - \frac{x_2}{2}\right)\right)\right.$$
$$+ C_2^2 x_2 + A_2 B_2 \bar{k}\left(\frac{\cosh 2\bar{k}x_2}{2}\right) + 2A_2 C_2 \sinh \bar{k}x_2$$
$$\left. + 2B_2 C_2 \cosh \bar{k}x_2\right\} + \left(\frac{P}{EA} + \Lambda\right)x_2 + F \tag{16}$$

Two unknowns, Λ and the constant of integration F, can now be evaluated by enforcing the following two boundary conditions on the u_2 displacement at $x_2 = 0$, and $x_2 = l$ (note that at this stage the coefficients A, B, C, and D are all known):

$$u_2(0) = dw_{1,x}(0) \quad (17)$$

$$u_2(l) = dw_{1,x}(l) \quad (18)$$

From these equations, free induced strain Λ can be computed for a given force P. It is noted that the problem could have also been formulated with the free induced strain as the referenced variable instead of the force P. But since in most stability-type problems the primary variable is force, this problem was formulated accordingly.

Beam Response

With the previous equations, it is now possible to examine the beam response as a function of both the actuator-induced force P or the free induced strain Λ. Other variables that influence the response are flexural stiffness ratio EI_1/EI_2, and actuator offset distance d.

The effect of flexural stiffness ratio on the beam response is shown in Figs. 3, 4, and 5. Figure 3 shows the response for $EI_1/EI_2 = 1$, Fig. 4 for $EI_1/EI_2 = 5$, and Fig. 5 for $EI_1/EI_2 = 10$. Although the force has been normalized by the critical buckling load (for the specified flexural stiffness ratio), it is necessary to show a different plot for each of the values of the flexural stiffness ratios because of the nonlinear relationship between force and free induced strain. In all three figures, the normalized force is plotted vs the beam center point displacement, normalized by beam length. The free induced strain corresponding to values of actuator force is plotted on the right vertical axis. For comparison, the response of the beam to a pure moment ($M = Pd$) is also plotted in each figure. Note that the free induced strain on the right vertical axis does not correspond to this linear, moment response curve.

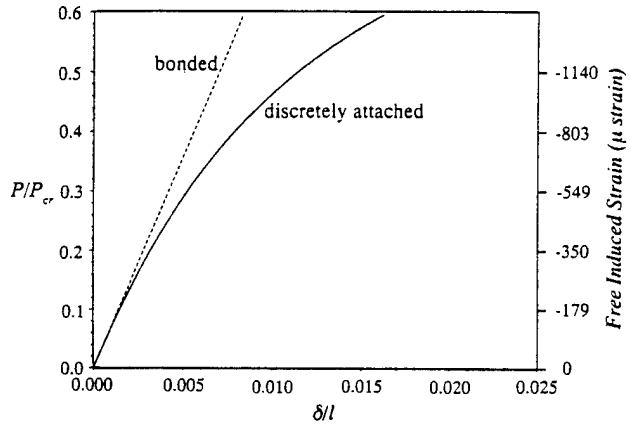

Fig. 3. Beam response for a flexural stiffness ratio = 1 ($d^* = 0.01$). The right vertical axis shows the free induced strain corresponding to the force.

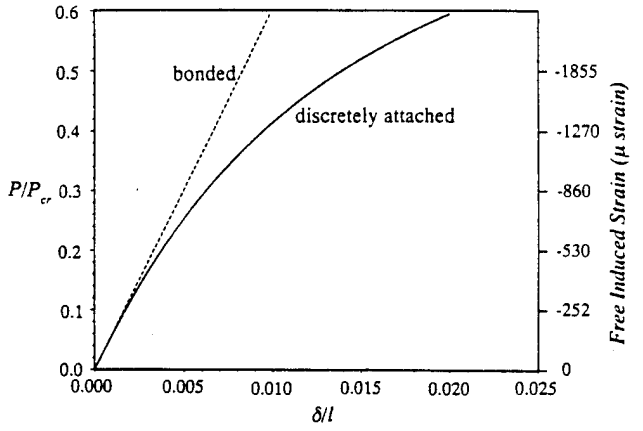

Fig. 4. Beam response for a flexural stiffness ratio = 5 ($d^* = 0.01$). The right vertical axis shows the free induced strain corresponding to the force.

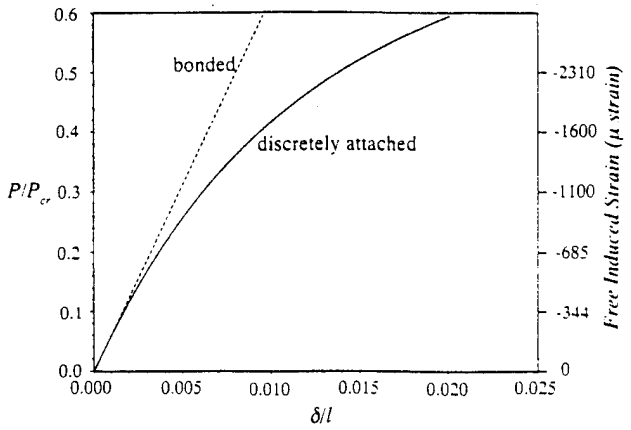

Fig. 5. Beam response for a flexural stiffness ratio = 10 ($d^* = 0.01$). The right vertical axis shows the free induced strain corresponding to the force.

One thing to notice from all three figures is the enhanced bending of the beam with discretely attached actuators compared to the bonded actuator case. But, to take advantage of the nonlinear region of enhanced bending, a certain minimum force and free induced strain are required. For example, in Fig. 3, where the flexural stiffness ratio is 1, a free induced strain greater than 1000 microstrain will result in approximately 70% increase in displacement, compared to that obtained with a bonded actuator.

As the flexural stiffness ratio is increased, the beam becomes stiffer compared to the actuator, and an even greater free induced strain is required to get into the nonlinear region of enhanced bending, as can be seen in Figs. 3 and 4. But, as the flexural stiffness ratio increases beyond 10, the free induced strain required to achieve a certain fraction of the critical buckling load becomes almost a constant. This is consistent with the fact that the normalized critical buckling load becomes insensitive to the flexural stiffness ratio as this ratio becomes greater than 10.

Therefore, for most practical structures, where the flexural stiffness ratio is likely to be higher than 10, an actuator with an induced strain capability of 1000 microstrain can result in a 20–30% increase in bending displacements purely due to the nonlinear effects.

Length of the beam, or distance between the two points where the actuator is attached to the structure, is also an important factor which controls the beam response. In all figures, the force P has been normalized by the critical buckling load, and the critical buckling load is inversely proportional to the length of the beam. Therefore, a longer distance between the two points where the actuator is attached to the structure reduces the critical buckling load and hence the force required to cause nonlinear effects.

Optimization of Offset Distance for Enhanced Control

Within the region of linear response, the most important parameter which influences response is the actuator offset distance. This parameter, as will be shown, if used properly can result in a substantial increase in bending control. As seen in Fig. 6 for a given value of P/P_{cr}, a higher value of the offset distance beneficially decreases the force required (from the actuator) to achieve a certain displacement, but at the same time, as seen in Fig. 7, increasing the actuator offset distance increases the stroke requirement. Mechanically when the actuator is close to the surface, the structure to which it is attached provides a greater constraint to the actuator's expansion and contraction, and in turn a greater force is developed in the actuator and applied to the structure and this leads to force saturation in the actuator. On the other hand if the actuator offset distance is increased, the constraint offered to the actuator by the structure is reduced thereby letting the actuator contract or expand more freely. And in the extreme case where there is no con-

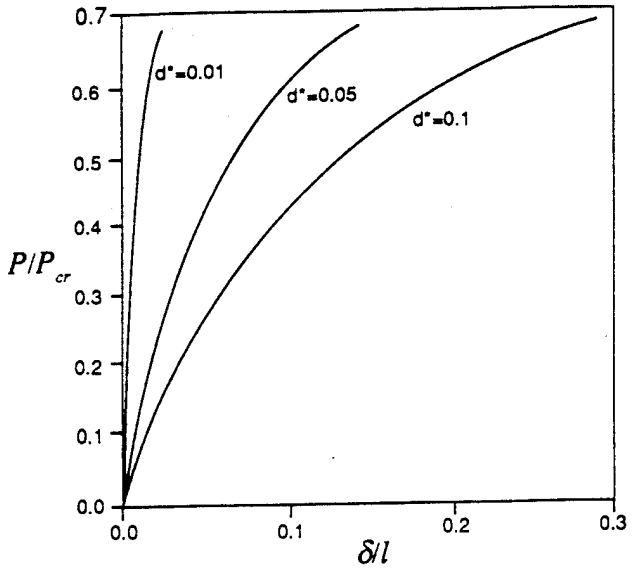

Fig. 6. Beam response for different values of the actuator offset distance d^*.

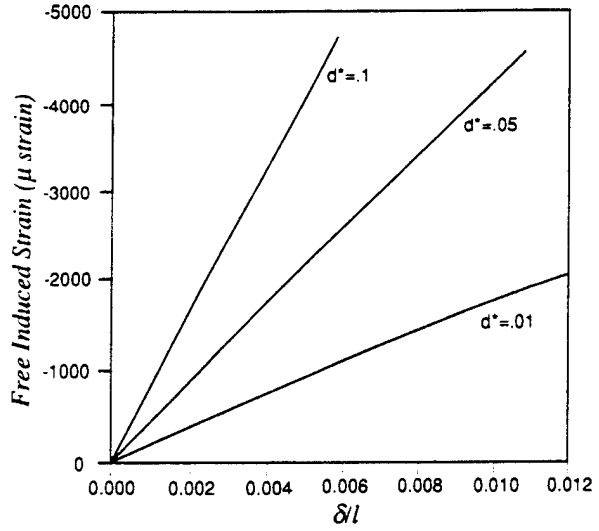

Fig. 7. Beam response for different values of the actuator offset distance d^*, showing the increased stroke requirement for higher values of actuator offset distance.

straint, it will lead to strain saturation. Between the two extremes of force saturation and strain saturation, there is in fact an optimum offset distance that maximizes the moment applied to the substrate.

To study the effect of variation of offset distance on the beam displacements, the offset distance is normalized as follows:

$$\bar{d} = d/(t_b/2)$$

and the beam displacement at the center δ is normalized by the displacement when the offset distance is a minimum, i.e., $\bar{d} = 1$ or $d = t_b/2$.

$$\bar{\delta} = \delta/(\delta)_{\bar{d}=1}$$

This normalizing scheme is physically meaningful and also allows us to study the effect of variation of the offset distance in the most general manner. The minimum value of the normalized offset distance is 1 and this corresponds to when the actuator is on the surface of the beam with minimum offset distance (i.e., $d = t_b/2$). For values higher than 1, it represents the offset distance as a fraction of half of the substrate thickness. Similarly, the normalized beam displacement represents the ratio of the beam displacements with the actuator offset to when the actuator has no offset and lies on the surface.

Figure 8 shows the normalized beam displacement plotted vs the normalized offset distance for two different values of beam-actuator thickness ratio t_b/t_a, and $E_1/E_2 = 1$. Figure 9 shows a similar plot for $E_1/E_2 = 3$. As expected the beam displacement increases with increasing offset distance until it reaches a maximum, after which it begins to decrease again. This behavior is consistent with the physical explanation presented earlier. As seen in Fig. 8, as the substrate becomes thicker relative to the actuator the optimum offset distance also increases. As the thickness ratio is increased from 10 to 20, the normalized optimum offset distance changes from 2 to 2.6. In this figure where the modulus of the beam and the actuator are the same, the beam displacement can be increased by as much as 50% compared to bonded actuator.

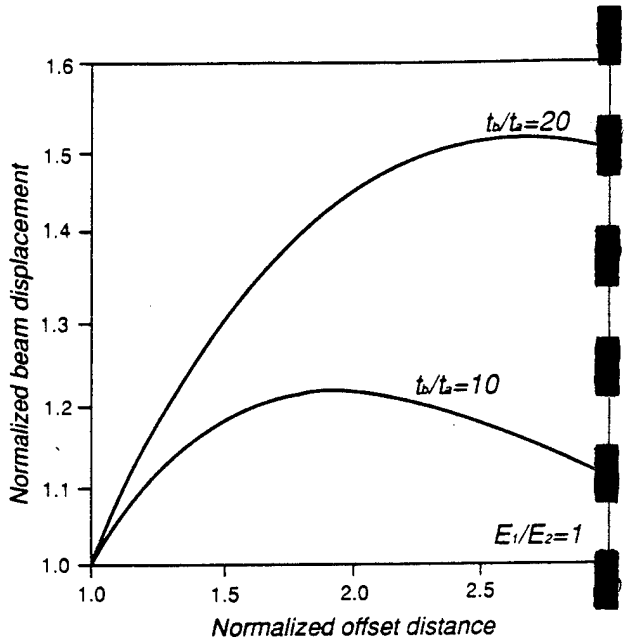

Fig. 8. Normalized beam displacement vs normalized offset distance ($EI_1/EI_2 = 1$) showing 1) the increased displacements with increasing actuator offset distance, and 2) the optimum offset distance.

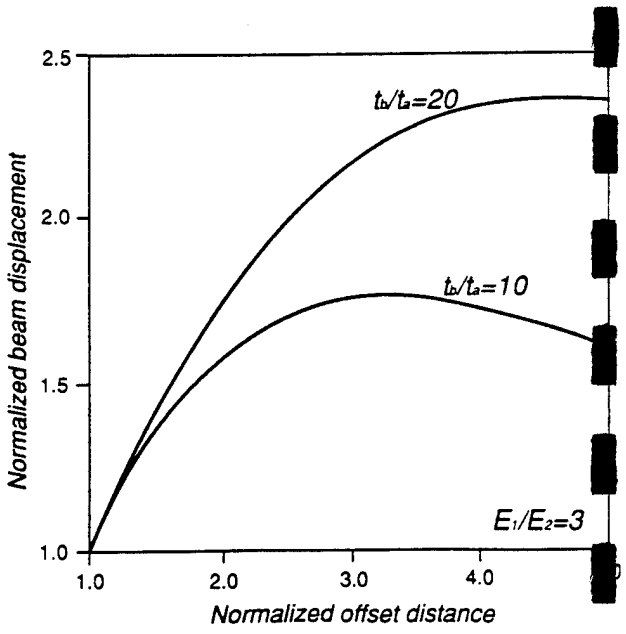

Fig. 9. Normalized beam displacement vs normalized offset distance ($EI_1/EI_2 = 3$) showing 1) the increased displacements with increasing actuator offset distance, and 2) the optimum offset distance.

If the substrate stiffness is greater than the actuator stiffness, the advantage of increasing the offset distance is even greater as seen in Fig. 9 where the beam-actuator modulus ratio is 3. For this stiffness ratio, optimally offsetting the actuator can result in more than 100% increase in displacements compared to bonded actuator. (It will be shown later that the bonded actuator configuration is indeed the degenerate case for this discretely attached actuator configuration.)

It is important to point out that in both Fig. 8 and 9 the beam response is in the linear region and the only factor which is changing with the change in offset distance is the moment applied to the beam (the in-plane force of the actuator does not contribute to the beam's transverse displacements). However, if the distance between the two points where the actuator is attached to the beam is long or if the force of the actuator is a significant fraction of the critical buckling load and the nonlinear effects are prominent, the optimum offset distance also becomes a function of the actuator activation level.

Relationship Between Bonded and Discretely Attached Actuator Configurations

As stated in the discussion on the optimum offset distance, the enhanced displacements in the linear region are due to the increased bending moment and not because of the nonlinear structural response. In the model for the discretely attached actuator, the beam and the actuator are subjected to concentrated moments applied at the two points where the actuator is attached to the beam. For bonded actuators, also, the action of the actuators is represented by concentrated moments applied at two ends of the actuator. Thus, in both cases the response is basically due to end moments. Then how does the discretely attached actuator formulation with minimum offset distance compare with the bonded actuator formulation? The two formulations do in fact give exactly the same response within the linear regime and the bonded configuration is a degenerate case of the discretely attached actuator configuration. In fact, it is possible to derive the Bernoulli-Euler expression for the beam curvature from considerations similar to the one used in the discretely attached formulation.[10]

Thus, the observations regarding the optimum offset distance can be directly applied to bonded actuators with one restriction. The restriction being that increasing the offset distance should not add to the basic flexural stiffness of the structure. This can be done by filling the area created by the offset with a foam or honeycomb type structure which only provides a filler and no increase in flexural stiffness. If the actuator offset distance is increased by increasing the basic thickness of the substrate, obviously none of the advantages mentioned previously apply because it is well known that increasing the substrate thickness increases the flexural stiffness as a square of the offset distance whereas the actuation moment increases only linearly.

The previous discussion also implies that for thinner and softer substrates it would be advantageous to embed actuators below the surface rather than surface mount them.

This problem has been specifically formulated for the case where the actuator is contracting and applying a compressive force to the beam. Within the linear region, where the response is essentially due to the concentrated end moments, all of the observations regarding the optimum offset distance also apply to a situation where the actuator is expanding and applying a tensile force to the beam. In such a situation, however, the discretely attached actuator is likely to bend itself and transmit minimal force to the structure, especially if the substrate is thick. This situation can be alleviated by having a honeycomb type filler between the actuator and the substrate. The honeycomb would ensure that the actuator itself does not bend and transfers all of the force to the substrate.

Experimental Procedure and Results

To demonstrate enhanced control experimentally a relatively thick beam was chosen. As stated earlier, increasing the offset distance is most beneficial for thicker substrates. The actuators used were 0.25-mm-thick (10 mils) Piezoelectric Products G-1195 piezoceramic plates. A PZT patch was attached to a 1/8-in.-thick, 3/4-in.-wide, and 6-in.-long aluminum beam as shown in Fig. 10. Spacers 0.075-in. thick (which provide the optimum offset distance for this case) were placed at the two ends of the PZT to provide the necessary offset. To contrast the response of the discretely attached actuator with the bonded actuator, a second specimen with bonded PZT actuator patch was prepared. Geometric and material properties of the PZT actuator and the beam were identical for both specimen. In preparing the discretely attached actuator specimen, it was important that the actuator be absolutely straight. If there is a slight curvature, the actuator will quickly strain saturate by overcoming the slack due to the initial curvature and very little force will be transmitted to the structure.

Beam displacements were measured in the cantilever configuration at a point 1 in. from the right end of the PZT patch as shown in Fig. 10. A linear variable differential transformer (LVDT)-type miniature displacement transducer type DFg-5 (manufactured by Sangamo Schlumberger Industries), with a sensitivity of 1070 mV/mm, was used. As shown in Fig. 10, the armature of the LVDT transducer rested on the beam, and ensured positive contact between the beam and the armature at all times. The armature of the displacement transducer weighs only 1.14 g and was assumed to have negligible effect on the system response.

The dc voltage applied in the poling direction of the PZT actuator was varied from 0 to 250 V. A personal computer equipped with an analog/digital (A/D) board was used to record the voltage being applied to the actuator and the voltage output from the displacement transducer. The voltage output from the transducer was fed directly to the A/D board, but the voltage applied to the PZT was stepped down through a voltage divider and then fed to the A/D board. The applied voltage and corresponding displacements were recorded at increments of 10 V.

Figure 11 shows the results of the experiment: applied electric field is plotted on the vertical axis and displacement is on the horizontal axis. In the figure there are two sets of experimental data points, for both the bonded and the discretely attached beam-actuator specimen. Agreement between the theoretical response and the experimental data is generally good, except at high field levels, where the theoretical response overpredicts displacements.

A theoretical solution for the bonded beam-actuator specimen is obtained using the pin-force model formulation because for high beam-actuator thickness ratios, as is the case in this experiment, this model is as accurate as the Bernoulli-Euler model and simpler to use. In the computation of the theoretical response for both configurations, a strain-dependent mechanical/electrical coupling coefficient d_{31} is used. The method suggested by Crawley and Lazarus[6] is used to compute d_{31}^* (secant definition of d_{31}). The following second-order curve fit of the reported experimental data was used to compute the value of d_{31}^* iteratively:

$$d_{31}^* = 200 + 0.0012\varepsilon - 2\varepsilon^2$$

It is important to recognize that the nonlinearity in the response in Fig. 2 is not due to structural nonlinearity but is completely due to the nonlinear field-strain behavior of the PZT actuator.

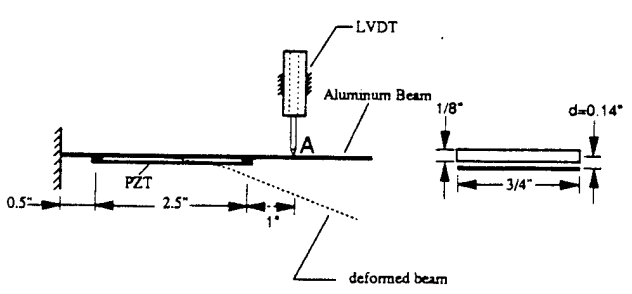

Fig. 10. Schematic representation of discretely attached beam actuator specimen and experimental setup used to measure displacements.

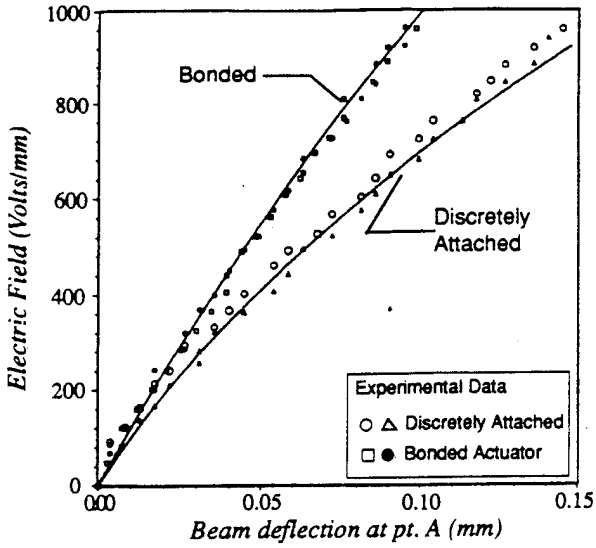

Fig. 11. Experimental results: comparison of bonded and discretely attached actuator configurations.

Table 1 Comparison of experimental and theoretical results

Type	Field, V/mm	d_{31}, pm/V	Displacement, mm		Predicted force, lb	Predicted moment, in. lb
			Predicted	Data		
Discretely Attached	500	273	0.0646	0.0605	4.7	0.611
	1000	349	0.1640	0.1450	11.8	1.534
Bonded	500	223	0.0451	0.0445	6.16	0.3853
	1000	249	0.1000	0.1050	13.767	0.86

It is interesting to note the predicted force in the actuator at different field levels and the resulting moment applied to the beam-actuator structure. Results of the predictions for some representative values are shown in Table 1. At 1000 V/mm, the predicted force in the discrete actuator is 16% less than the bonded actuator, but the moment is 40% greater. The difference in values of d_{31}^* used for predicting the response of the bonded actuator and the discretely attached actuator is also apparent. With an offset piezoelectric actuator, structural control authority is enhanced as a result of the nonlinear field-strain relationship of PZT.

Conclusions

To increase the realm of applications of induced strain actuators beyond vibration control and micropositioning, it is necessary to examine configurations other than the standard bonded/embedded configuration. In this paper, a new configuration of discretely attached induced strain actuators to enhance structural control is developed and verified experimentally. As a first step, a simple beam-actuator system is analyzed. Aside from the distance between the two discrete points where the actuator is attached to the beam, the beam response is basically a function of two variables—the ratio of the flexural stiffnesses of the beam and actuator and the actuator offset distance.

This proposed configuration can enhance the response above that of the bonded actuator configuration by two mechanisms. One is by taking advantage of the geometrically nonlinear enhanced structural response. For most practical structures where the beam actuator flexural stiffness ratio is greater than 10, this would require an actuator with a free induced capability greater than 1000 microstrain. The second mechanism is that of optimally increasing the distance through which the actuator is offset from the structure at the two points of attachment. This mechanism enhances control in both the linear and nonlinear regions of structural response and does not require any minimum stroke capability of the actuator.

The increase in actuator authority achieved by offsetting the actuator depends on the beam-actuator thickness and modulus ratio. For thicker or high modulus substrates, optimal increase in the actuator offset distance results in a substantial increase in flexural control. In experimental work with PZT actuators and aluminum beams, a 40% increase in displacements over the bonded configuration was observed.

The geometry presented in this paper is just one of the possible configurations of discretely attached actuators. Note that as soon as the constraint that the actuator be bonded to the structure everywhere (without significantly modifying the overall geometry of the structure) is relaxed, a whole array of new geometric and kinematic possibilities is opened. The concept can easily be extended to any type of actuator including magnetostrictive and PZT stacks.

Acknowledgments

The support of National Science Foundation through the Presidential Young Investigator Program (Grant MSS-9157080) and the Office of Naval Research (Grant ONR 0014-92-J-1170) is gratefully acknowledged.

References

[1]Forward, R. L., and Swigert, C. J., "Electronic Damping of Orthogonal Bending Modes in a Cylindrical Mast Theory," *Journal of Spacecraft and Rockets*, Vol. 17, No. 1, 1981, pp. 5–10.

[2]Hanagud, S., Obal, M. W., and Calise, A. J., "Optimal Vibration Control by the Use of Piezoceramic Sensors and Actuators," *Proceedings of the 28th SDM Conference* (Monterey, CA), April 1987, AIAA, Washington, DC, pp. 987–997 (AIAA Paper 87-0959).

[3]Crawley, E. F., and de Luis, J., "Use of Piezoelectric Actuators as Elements of Intelligent Structures," *AIAA Journal*, Vol. 25, No. 10, 1987, pp. 1373–1385.

[4]Bailey, T., and Hubbard, J. E., "Distributed Piezoelectric-Polymer Active Vibration Control of a Cantilever Beam," *Journal of Guidance, Control, and Dynamics*, Vol. 8, No. 5, 1985, pp. 605–611.

[5]Lin, M. W., and Rogers, C. A., "Analysis of a Beam Structure with Induced Strain Actuators Based on an Approximated Linear Shear Stress Field," *Proceedings of the Conference on Recent Advances in Adaptive and Sensory Materials and Their Applications*, Virginia Polytechnic Institute and State Univ., Blacksburg, Virginia, Technomic Publishing Co., Inc., Lancaster, PA, April 27-29, 1992, pp. 363–376.

[6]Crawley, E. F., and Lazarus, K. B., "Induced Strain Actuation of Isotropic and Anisotropic Plates," *AIAA Journal*, Vol. 29, No. 6, 1989, pp. 944–951.

[7]Wang, B. T., and Rogers, C. A., "Modelling of Finite Length Spatially Distributed Induced Strain Actuators for Laminate Beams and Plates," *Proceedings of the 32nd SDM Conference* (Baltimore, MD), AIAA, Washington, DC, April 1991, pp. 1511–1520 (AIAA Paper 91-1258).

[8]Chaudhry, Z., and Rogers, C. A., "Response of Composite Beams to an Internal Actuator Force," *Proceedings of the 32nd SDM Conference* (Baltimore, MD), AIAA, Washington, DC, April 1991, pp. 184–193 (AIAA Paper 91-1168).

[9]Chaudhry, Z., and Rogers, C. A., "Bending and Shape Control of Beams using SMA Actuators," *Journal of Intelligent Material Systems and Structures*, Vol. 2, No. 4, 1991, pp. 581–602.

[10]Chaudhry, Z., and Rogers, C. A., "A Mechanics Approach to Induced Strain Actuation of Structures," *Proceedings Third International Conference on Adaptive Structures* (San Diego, CA), Nov. 11–14, 1992, Tech-

C-12 Author's Reply, R. A. Burdisso and C. R. Fuller, Journal of Sound and Vibration, Vol. 163 No. 2, pp. 366-371, 1993.

Journal of Sound and Vibration (1993) **163**(2), 366–371

AUTHORS' REPLY

R. A. BURDISSO AND C. R. FULLER

Vibration and Acoustics Laboratory, Mechanical Engineering Department, Virginia Polytechnic Institute and State University, Blacksburg, Virginia 24061-0238, *U.S.A.*

(*Received* 20 *July* 1992)

The authors wish to thank Professor Yigit [1] for his interest in the paper "Theory of feedforward controlled system eigenproperties" [2]. The notion of a controlled system responding with a new set of eigenproperties, natural frequencies and mode shapes, is well established in feedback control approaches. The control forces are generally expressed in terms of the states of the system and they can be moved to the left side of the equations of motion to recognize easily that the properties of the system have been changed. In other words, the dynamics of the controller is now included with the dynamics of the system. On the other hand, the concept of a linear system under feedforward control responding with a new set of eigenproperties is not widely accepted and is rather controversial. Explanations of dynamic behavior of the feedforward controlled systems in the literature are generally based on physical assumptions and experimental observations. As mentioned in the introduction in reference [2], the traditional view in feedforward control of systems under steady state disturbances is of "active cancellation". The response due to the disturbance exciting the uncontrolled modes is "cancelled" by control force(s) properly driven by the same uncontrolled modes. The experimental work by Snyder and Hansen [3] on active control of sound in ducts demonstrated that the active control input(s) modifies the input impedance of the duct system that the disturbance source is acting upon. This leads to less energy input into the system by the disturbance. Thus, it is clear that the conventional concept of "active cancellation or phase cancellation" may not be appropriate to describe the physical controlled response. Thus, the dynamic behavior of feedforward controlled systems clearly needs to be investigated in strict mathematical terms. The efficient analysis and design of feedforward controlled systems will require a mathematical framework similar to that enjoyed by feedback control techniques. The work in reference [2] is the first effort toward these goals, and outlines a rigorous mathematical formulation to address this issue.

In order to address the comments by Professor Yigit [1], it is first convenient briefly to review the methodology of reference [2]. The response of the uncontrolled system due to the disturbance input F expressed in terms of the modes is given as (equation (9) in reference [2])

$$W_f(D, \omega) = \sum_{n=1}^{N} f_n \phi_n(D) H_n(\omega) F, \tag{1}$$

which can also be written as

$$W_f(D, \omega) = \{n_f(D, \omega^2)/d(\omega^2)\} F = T_{DF}(\omega) F. \tag{2}$$

The uncontrolled transfer function between the response at point D and the disturbance F, $T_{DF}(\omega)$, is the ratio of two polynomials. The denominator $d(\omega^2)$ is common to all transfer functions since the poles of a structure are global properties. On the other hand, the polynomial in the numerator, $n_f(D, \omega^2)$, gives the zeros, and they are local properties

0022-460X/93/110366+06 $08.00/0

© 1993 Academic Press Limited

associated with the particular transfer function. The denominator $d(\omega^2)$ is also the characteristic polynomial of the uncontrolled system: that is, the zeros of $d(\omega^2)$ give the natural frequencies. When the system is excited at those frequencies, the response will be unbounded if there is no system damping.

The equations of motion of the controlled system is traditionally written as follows (equation (12) in reference [2]):

$$W(D, \omega) = \sum_{n=1}^{N} (f_n F + p_n P) H_n(\omega) \phi_n(D). \tag{3}$$

The compensator $G(\omega)$ that relates the control input to the disturbance input, as $P = -G(\omega)F$, is the ratio of two transfer functions. Because of the global characteristic of the poles, $G(\omega)$ is the ratio of two polynomials of order $(N-1)$ in $\omega^2 G(\omega) = N(\omega)/D(\omega)$. The numerator $N(\omega)$ is the zeros of the transfer function between the disturbance input and the displacement response at the error sensor location, $n_f(E, \omega^2)$. The denominator $D(\omega)$ is the zeros of the transfer function between the control input and the displacement response at the error sensor location, $n_c(E, \omega^2)$. Thus, it is clear that the poles of the compensator $G(\omega)$ are the zeros of $D(\omega)$ as Professor Yigit stated in reference [1]. However, as in feedback approaches, in order to analyze the behavior of the *controlled* system it is necessary to include the dynamics of the compensator with that of the plant. Such an approach is what is addressed in reference [2]. To clarify this approach, we expand upon the analysis in more detail.

Equation (3) seems to suggest that the controlled response is simply due to the superposition of the responses by the disturbance and control forces ("active cancellation"). The approach taken in reference [2] to investigate the dynamics of the controlled system is to introduce the compensator, $P = -G(\omega)F$, into the equations of motion in equation (3), as in feedback analysis. Through some mathematical manipulation, equation (3) is shown to become

$$W(D, \omega) = \sum_{l=1}^{N-1} \frac{f_{cl}}{m_{cl}} \phi_{cl}(D) H_{cl}(\omega) F, \tag{4}$$

which can also be written as

$$W(D, \omega) = \{\tilde{n}_f(D, \omega^2)/D(\omega)\}F = (T_{DF}(\omega))_c F. \tag{5}$$

The controlled system response given by equations (4) and (5) has the same structure as that of equations (1) and (3), which represent the uncontrolled system response. The equations of motion in equation (4) state that the composite structure–controller system response is expanded as a linear combination of a new set of modes, $\phi_{cl}(D)$. Each mode will resonate if driven at the excitation frequency ω_{cl} associated with the modal frequency response function $H_{cl}(\omega) = (\omega_{cl}^2 - \omega^2)^{-1}$. Equation (5) shows that the controlled system transfer function between the disturbance input F and the displacement at any arbitrary point D in the structure, $(T_{DE}(\omega))_c$, has as denominator $D(\omega)$. This polynomial is the same for all transfer functions in the controlled system. Also, $D(\omega)$ is the characteristic polynomial of the controlled system, and its zeros give the controlled resonance frequencies: that is, if the system is excited at those frequencies the controlled response will be unbounded. Thus, the poles of the controlled system (zeros of $D(\omega)$) are global properties. The numerators, $\tilde{n}_f(D, \omega)$ (zeros of the controlled system transfer function) are different for each point in the domain D.

The controlled response of the system can be directly written in terms of the uncontrolled transfer functions, as commonly done in control textbooks:

$$W(D, \omega) = \left[\frac{n_f(D, \omega^2)}{d(\omega^2)} + G(\omega) \frac{n_c(D, \omega^2)}{d(\omega^2)} \right] F. \tag{6}$$

where $n_c(D, \omega^2)/d(\omega)$ is the transfer function between the response at point D and the control input P: The response at the error location E due to the disturbance F is given by

$$W(E, \omega) = \left[\frac{n_f(E, \omega^2)}{d(\omega^2)} + G(\omega) \frac{n_c(E, \omega^2)}{d(\omega^2)} \right] F. \tag{7}$$

In traditional control textbooks, various design techniques are developed to obtain the compensator $G(\omega)$. For example, Isermann [4] derived a minimum variance feedforward controller given by $G(\omega) = -(n_f(E, \omega^2) - d(\omega^2))/n_c(E, \omega^2)$. On the other hand, reference [2] is focused upon a very particular compensator $G(\omega)$ that drives the response of the SISO process of equation (7) to zero: i.e., zero dynamics. Moreover, while traditional control textbooks stop the analysis at the design of $G(\omega)$, the work in reference [2] further investigates the dynamic behavior of the response at other locations in the structure given by equation (6). Replacing the compensator found in reference [2] in equation (6) gives

$$W(D, \omega) = \left[\frac{n_f(D, \omega^2)}{d(\omega^2)} - \frac{n_f(E, \omega^2)}{n_c(E, \omega^2)} \frac{n_c(D, \omega^2)}{d(\omega^2)} \right] F. \tag{8}$$

The controlled transfer function becomes

$$\frac{W(D, \omega)}{F} = (T_{DF}(\omega))_c = \frac{1}{d(\omega^2)} \left[n_f(D, \omega^2) - \frac{n_f(E, \omega^2) n_c(D, \omega^2)}{n_c(E, \omega^2)} \right]. \tag{9}$$

This equation seems to suggest that the poles of the system, $d(\omega^2)$, were not affected, while the only change is in the zeros of the transfer functions due to the term in brackets. However, the formulation in reference [2] (by working with the modal expansion of the response) shows that the term in brackets can be reduced to

$$(T_{DF}(\omega))_c = \frac{1}{d(\omega^2)} \left[\frac{\tilde{n}_f(D, \omega^2)\, d(\omega^2)}{n_c(E, \omega^2)} \right] = \frac{\tilde{n}_f(D, \omega^2)}{n_c(E, \omega^2)} = \frac{\tilde{n}_f(D, \omega^2)}{D(\omega)}. \tag{10}$$

In other words, the poles are cancelled by zeros of the numerator in brackets. Therefore, the statement in section 2 of Professor Yigit's letter [1], "... what the authors did in [1] is to consider $G(\omega)$ as the transfer function of the controlled system, and claim that the denominator gives the poles (eigenvalues) of the controlled system", is completely wrong. On the contrary, we have demonstrated that the controlled system has a new resonance behavior given by the poles of the controller $G(\omega)$.

The above discussion can also be used to address the comment in the last paragraph of section 3 in reference [1]. There Professor Yigit states that eigenproperties are independent of any external loading and the feedforward alters the response to a specific input. The formulation in reference [2] (briefly reviewed above) unequivocally shows that the response is altered to the "coherent" disturbance input and the modification is such that the controlled system effectively has new eigenproperties. Simply a careful reading of reference [2] is all that is needed to see that these points were clearly indicated in the last paragraph of section 3 ("The thesis of the present work is that the controlled beam exhibits new eigenvalues and mode shapes to the input disturbance ...") and in the conclusions section

("The analysis presented here shows that feedforward controlled systems have effectively new eigenproperties").

The author of reference [1] again seems to be confused as to how the controlled system eigenfunctions are computed when expressing ". . . develop a method to calculate mode shapes based on the response of the structure to a specific input". Equation (4) shows that the controlled response is expressed in terms of a new set of $(N-1)$ eigenfunctions $\phi_{cl}(D)$. However, these eigenfunctions are *not* computed by evaluating the response, equation (5), at the associated resonance frequency ω_{cl}. The eigenfunctions are computed by conveniently normalizing the controlled eigenfunctions with respect to the mass distribution to take advantage of some well known orthogonality conditions of the uncontrolled modes. The controlled eigenfunctions are shown to be given as a linear combination of the uncontrolled modes, since they have been used as an expansion basis: that is (equation (29) in reference [2]),

$$\phi_{cl}(D) = \sum_{n=1}^{N} \Gamma_{ln}\phi_n(D), \tag{11}$$

where the expansion coefficients are given by

$$\Gamma_{ln} = c_l \frac{p_n}{\omega_{cl}^2 - \omega_n^2}. \tag{12}$$

The constant c_l is included since the controlled mode shapes are arbitrary to a constant multiplier. c_l is computed by requiring

$$\sum_{n=1}^{N} (\Gamma_{ln})^2 = 1 \quad \Rightarrow \quad c_l = \left(\sum_{m=1}^{N} \frac{p_m^2}{(\omega_{cl}^2 - \omega_m^2)^2} \right)^{-1/2}. \tag{13}$$

In reference [1] it was stated that the controlled eigenfunctions are not unique for a given system. However, the controlled eigenfunctions given in equation (11) are *uniquely* defined once the control input and error variable to minimize are specified. It is also very important to mention that the expansion coefficients in equation (12) are identical to the relationship found in the computation of the modified eigenfunctions in dynamic local modification techniques [5]. As shown in references [6, 7], properly selecting the error quantity to be minimized will yield a compensator $G(\omega)$ such that a structure can be actively modified to behave with new dynamic properties. In reference [7] the eigenproperties of the beam-absorber system of Figure 1(a) are computed first. By using the design approach presented in reference [6], an error sensor is designed such that upon cancellation of its output, the controlled system of Figure 1(b) will have eigenproperties (eigenvalues and mode shapes) identical to those of the beam absorber system of Figure 1(a).

In reference [1] the author states that ". . . the peaks appearing in Figure 3 for the controlled case are not because of any change in the system eigenproperties, but simply due to the excitation at those frequencies". This explanation, ". . . simply due to the excitation at those frequencies", of the presence of the peaks in the controlled response, is vague at best. If there is no change in the system dynamics, as Professor Yigit claims, a valid question is "Why does the controlled system not resonate when driven at the natural frequencies of the uncontrolled beam (35, 118, 277 Hz, etc.)?".

It is also stated in reference [1] that the feedforward controller does not reduce the number of degrees of freedom. In reference [2], it is shown that the SISO controlled system has one less resonance frequency due to the constraint imposed by driving the error variable to zero. Further insight into this subject can be gained by considering the simple limiting problem of a structure with N modes that is controlled with N control inputs that

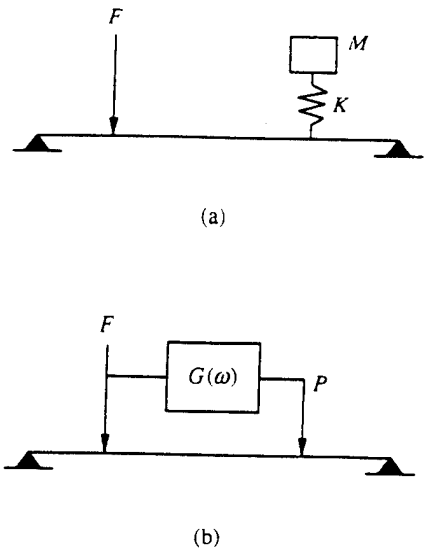

Figure 1. (a) Beam–absorber system and (b) active controlled system, the dynamic properties of which are the same as those of the beam–absorber system.

in turn will drive N error variables to zero. It is an easy exercise to find that the response anywhere in the structure is zero at all frequencies. Thus, it is obvious that the controlled system has eliminated all N dynamic degrees of freedom.

In feedforward control the compensator $G(\omega)$ is computed or derived by minimizing the mean square value of some system response. If the error sensor cannot observe a particular mode (i.e., an accelerometer placed at a node), the component of the response due to the unobservable modes will not be affected by the control input. Similarly, if the control input is orthogonal to a particular mode, that mode cannot be controlled. Thus, contrary to the opinion of the author in reference [1], both issues of observability and controllability are relevant to feedforward control approaches. Furthermore, the concept of observability has been successfully used in active structural acoustic control applications for developing sensors which observe only efficient acoustic radiators modes [8].

Professor Yigit then continues by stating that "... feedforward control neither alters the mass nor the stiffness distribution; therefore there is no new differential equation to be searched for." As we have mentioned before, the system effectively behaves as having new eigenproperties that the input disturbance is acting upon. As mentioned in reference [2], the modal expansion of the controlled response in equation (4) could be represented by a partial differential equation of motion. It was not the main goal of the work in reference [2] to obtain such a differential equation, since is not required to analyze the controlled system. However, such an analytical approach is feasible.

In the last paragraph in reference [1], it is stated that "... the fact that the excitation frequencies chosen were somewhat close to some of the natural frequencies may have been one of the reasons for the mistake ...". The experiments in reference [2] were carried out at 40 excitation frequencies over the range 50–1000 Hz. The very good agreement between the experimental and analytical results is evident over the whole frequency range. Professor Yigit may have not realized that the frequency axis in Figure 3 in reference [2] is in log scale (the third controlled resonance frequency of 631 Hz is separated by 100 Hz from the closest beam natural frequency of 738 Hz). Thus, it is not correct to categorize some of the off-resonance excitation frequencies (60, 70, 80, 190, 230, 800, 830, 1000 Hz etc.) as

being somewhat close to the natural frequencies (Table 2 of reference [2]) and to suggest that this led to misinterpretation of the results.

In conclusion, the theory presented in reference [2] is a new analytical investigation of feedforward controlled systems. The formulation is based on strict mathematical terms and it was, moreover, verified experimentally. The analysis does not have any flaws, nor is it formulated on "wrong transfer functions". Finally, new concepts that depart from the conventional understanding are seldom accepted at once without resistance. However, these same new ideas are the starting point of efficient formulations that can produce significant technological progress. As Don Quijote said, "si ladran, Sancho, es señal que cabalgamos" [9].

REFERENCES

1. A. S. YIGIT 1993 *Journal of Sound and Vibration* **163**, 363–365. Comments on "The theory of feedforward controlled system eigenproperties".
2. R. A. BURDISSO and C. R. FULLER 1992 *Journal of Sound and Vibration* **153**, 437–451. Theory of feedforward controlled system eigenproperties.
3. S. D. SNYDER and C. H. HANSEN 1989 *Journal of the Acoustical Society of America* **86**, 184–194. Active noise control in ducts: some physical insights.
4. R. ISERMANN 1981 *Digital Control Systems*. Berlin, Springer-Verlag.
5. J. T. WEISSEMBURGER 1968 *Journal of Applied Mechanics, Paper No.* 68-APM-17, *ASME*, 327–332. The effect of local modifications on the vibration characteristics of linear systems.
6. R. A. BURDISSO and C. R. FULLER. *Journal of Guidance, Control and Dynamics* Feedforward controller design by eigenvalue assignment (submitted).
7. R. A. BURDISSO and C. R. FULLER 1992 *Proceedings of the 10th International Modal Analysis Conference (IMAC), San Diego, California* 3–7 February **II**, 1159–1166. Active dynamic modification of flexible structures.
8. R. L. CLARK and C. R. FULLER 1992 *Journal of the Acoustical Society of America* **91**(6), 3321–3329. Modal sensing of efficient acoustic radiators with PVDF distributed sensors in active structural acoustic approaches.
9. M. DE CERVANTES SAAVEDRA 1967 *Don Quijote de la Mancha*. Madrid: Editorial Espase-Calpe, S.A.

C-13 Active Control of Broadband Structural Vibration Using the LMS Adaptive Algorithm, J. S. Vipperman, R. A. Burdisso and C. R. Fuller, Journal of Sound and Vibration, Vol.166 No. 2, pp. 283-299, 1993.

Journal of Sound and Vibration (1993) **166**(2), 283–299

ACTIVE CONTROL OF BROADBAND STRUCTURAL VIBRATION USING THE LMS ADAPTIVE ALGORITHM

J. S. VIPPERMAN, R. A. BURDISSO AND C. R. FULLER

Vibration and Acoustic Laboratories, Mechanical Engineering Department, Virginia Polytechnic Institute and State University, Blacksburg, Virginia 24061, *U.S.A.*

(*Received* 27 *November* 1991, *and in final form* 8 *April* 1992)

Two adaptive feedforward control structures based on the filtered-x LMS algorithm have been developed for the active control of broadband vibration in structures. In the first control structure, the conventional filtered-x LMS control configuration is modified such that the transfer function between the control input and the error output is represented by an infinite impulse response (IIR) filter. An IIR filter will most efficiently model the resonances and antiresonances which are characteristic of a structure, but they introduce stability requirements that must be satisfied. In order to remove these stability problems, the equation error control configuration is developed by first filtering the error signal by the system poles before minimizing it. The control signal is obtained in both configurations by filtering the reference signal through an adaptive finite impulse filter (FIR). Both control configurations are experimentally investigated on a simply supported beam, and power reductions of up to 20 dB are observed.

1. INTRODUCTION

Over the past decade, active control methods have become recognized as a viable means of attenuating structural vibration and its associated sound radiation. The principle behind active control is adding "secondary" controlled source(s) in order to "cancel" the response generated by the "primary" or disturbance input. Adaptive feedforward algorithms have proven successful for applications in which the disturbance is stationary, such as single and multiple frequencies, and random inputs. The control inputs are computed by passing a signal which is coherent to the disturbance input through an adaptive filter before being applied to the structure. The coefficients of the adaptive filter are updated in such a way as to minimize a quadratic cost function created from a measurable variable of the system. The sum of the mean-square values of the output of a number of sensors is commonly used as the cost function.

Feedforward control was initially applied to one-dimensional acoustic fields, as summarized in the review article by Warnaka [1]. More recently, the technique has been extended to multi-dimensional acoustic fields [2] as well as control of structurally radiated noise [3]. Feedforward least-mean-square (LMS) and recursive least-mean-square (RLMS) adaptive algorithms have been applied on active control of bending motion in infinite or semi-infinite thin beams [4–8]. Recently, the simultaneous control of flexural and extensional waves in beams has been demonstrated by a multi-channel LMS approach, in conjunction with specialized piezoceramic transducers [9]. Most theoretical and experimental studies consider only single and multiple sinusoidal excitations. Applications of feedforward control for broadband excitation are much more scarce and restricted for attenuating noise in ducts [10–12] and enclosures [13]. Broadband structural control has been demonstrated with feedback and state-space methods, but there is very little reported

0022–460X/93/200283 + 17 $08.00/0

© 1993 Academic Press Limited

implementation of feedforward control in the open literature. The feedforward, broadband structural control that is reported is characterized by infinitely long structures that have no reflected power which occurs from boundary conditions [6]. Consequently, the response to the disturbance can be measured at a location on the structure before the error sensor, providing exact, *a priori* knowledge of the error signal to be cancelled. In addition, the previous implementations of feedforward, broadband controllers for noise and structural vibration have transfer functions between the control input and the error sensor which are relatively flat in magnitude response, allowing them to be easily represented by a fairly low order finite impulse response (FIR) filter.

Here, two adaptive single-input, single-output (SISO) feedforward control configurations for the active control of broadband vibration of a supprted structure are developed. The first controller is based on the filtered-x LMS control algorithm, where the off-line system indentification of the transfer function between the control and error signals is performed by combining an autoregressive moving-average (ARMA) model and variations of the RLMS [14–16] methods to determine the coefficients of an IIR filter. An IIR filter provides an efficient means of representing a structural transfer function which exhibits both poles and zeros, but it complicates the control system because this type of filter must satisfy certain stability requirements. The equation error control configuration provides a means of removing the stability requirements of the IIR filter by incorporating the system identification information into two FIR filters. This configuration is achieved by filtering the error signal with the poles of the plant before minimizing it.

The controllers were implemented in a digital signal processing (DSP) board, and experimental results for a simply supported beam are presented. The delay times through the disturbance and control paths to the error output were measured so that an additional delay could be introduced into the disturbance path to guarantee that the controller would be causal. The control performance of the filtered-x LMS control configuration was evaluated for different size adaptive filters. The same analysis was repeated for an acausal control system, where the disturbance path delay was removed.

2. THEORY

2.1. CONVENTIONAL FILTERED-X LMS CONTROL ALGORITHM

A typical block diagram of a SISO filtered-x LMS [14, 17] control structure is shown in Figure 1. The plant output denoted as the error signal e_k is the combination of the response due to the disturbance input x_k and the control input u_k : that is,

$$e_k = d_k + y_k, \tag{1}$$

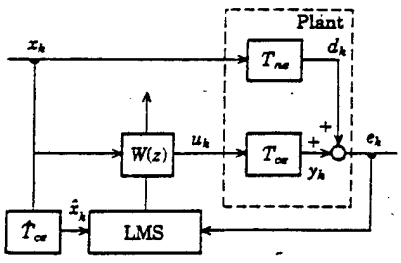

Figure 1. Filtered-x LMS control algorithm for structural vibration control.

where the subscript k indicates a signal sample at time t_k. The response due to the control input in equation (1) can be replaced in terms of the control sequence u_k as

$$e_k = d_k + T_{ce}(z)u_k, \tag{2}$$

where $T_{ce}(z)$ is the z-transform of the transfer function between the control input u_k and its resulting measured beam response y_k.

The control sequence u_k is obtained here by filtering a reference signal that is coherent to the disturbance signal through an adaptive FIR filter. It is assumed here that the reference signal is obtained by directly tapping from the disturbance signal. Thus, the control sequence becomes

$$u_k = W(z)x_k. \tag{3}$$

The adaptive FIR filter, $W(z)$, can be written explicitly in terms of the $(N+1)$ coefficients as

$$W(z) = W_0 + W_1 z^{-1} + W_2 z^{-2} + \cdots + W_N z^{-N} \tag{4}$$

$$= \sum_{i=0}^{N} W_i z^{-i}, \tag{5}$$

where z^{-i} represents a delay of i samples such that $z^{-i}x_k = x_{k-i}$. For the sake of brevity, the adaptive filter coefficients W_i will not be shown as a function of time except in the actual filter update equations. Replacing equation (3) into equation (2), the error output is given as

$$e_k = d_k + T_{ce}(z)W(z)x_k. \tag{6}$$

Since the plant is a linear, time-invariant structure, the transfer function $T_{ce}(z)$ can be efficiently represented by an IIR filter. Such a filter can best represent the resonances and antiresonances typical of a structural frequency response function because it has both poles and zeros:

$$T_{ce}(z) = A(z)/(1 - B(z)), \tag{7}$$

or

$$T_{ce}(z) = \frac{\sum_{i=0}^{N} A_i z^{-i}}{\left(1 - \sum_{j=1}^{N} B_j z^{-j}\right)} \tag{8}$$

where $A(z)$ and $B(z)$ represent polynomials in the complex variable z.

Now, substituting equation (7) into equation (6), the error signal becomes

$$e_k = d_k + [A(z)/(1 - B(z))]W(z)x_k. \tag{9}$$

The LMS algorithm adapts the coefficients $W_i (i = 0, 1, \ldots, N)$ in order to minimize a quadratic cost function of the plant response. The mean square value of the error signal is clearly a quadratic function of the weights of the adaptive filter $W(z)$, and thus there is a unique solution. The cost function is defined as

$$C(W_i) = E[e_k^2], \tag{10}$$

where E[ ] denotes the expected value operator. Substituting equations (5) and (6) into equation (10) gives

$$C(W_i) = E\left[\left\{\left(d_k + T_{ce}(z)\left(\sum_{i=0}^{N} = W_i z^{-i}\right)x_k\right)\right\}^2\right]. \tag{11}$$

The cost function, and thus the error signal, is minimized by computing the gradient of the quadratic performance surface and searching along the negative direction toward the minima. This technique is referred to as the steepest decent method [14]. The algorithm used to update the weights can then be written as

$$W_i(k+1) = W_i(k) - \mu \frac{\partial C}{\partial W_i}, \tag{12}$$

where μ controls the step size and thus the stability and rate of convergence of the minimization process. Information on estimating μ can be found in the literature [14], and will not be presented here.

Differentiating the cost function in equation (10) with respect to the weight W_i yields

$$\partial C/\partial W_i = 2E[e_k\, \partial e_k/\partial W_i], \tag{13}$$

$$= 2E[e_k T_{ce}(z) x_{k-i}], \tag{14}$$

$$= 2E[e_k \hat{x}_{k-i}], \tag{15}$$

where

$$\hat{x}_{k-i} = T_{ce}(z) x_{k-i}. \tag{16}$$

The sequence $\hat{x}_k$ is referred to as the filtered-x signal, and is the predicted response from the plant when the control loop is excited by the reference signal x_k. Therefore, a system identification of the control–error signal path is necessary before the gradient of the performance function can be estimated. The measured transfer function is represented by

$$\hat{T}_{ce} = \hat{A}(z)/(1 - \hat{B}(z)) \tag{17}$$

in Figure 1. Here, we assume that the coefficients of the polynomials $\hat{A}(z)$ and $\hat{B}(z)$ differ by a small amount with respect to the true coefficients in $A(z)$ and $B(z)$, respectively.

The time domain LMS algorithm uses an instantaneous gradient approximation to estimate the deterministic gradient shown by equation (15). Thus, removing the operator E[ ] from equation (15) and placing it into equation (12), the update equation becomes

$$W_i(k+1) = W_i(k) - 2\mu e_k \hat{x}_{k-i}, \qquad i = 1, \ldots, N, \tag{18}$$

where

$$\hat{x}_{k-i} = \hat{T}_{ce}(z) x_{k-i}. \tag{19}$$

For the filtered-x signal $\hat{x}_k$ to be bounded such that the control algorithm will be stable, the filter $\hat{T}_{ce}(z)$ must be stable. The stability of this filter is guaranteed if all of the poles given by the zeros of $(1 - \hat{B}(z))$ in equation (17) remain inside the unit circle in the complex z-plane.

2.2. EQUATION ERROR FILTERED-X LMS CONTROL CONFIGURATION

The fact that the poles of the system represent global system properties can be taken advantage of to develop a second control configuration that will eliminate the stability problems introduced by the IIR filter used in the filtered-x LMS control configuration. As

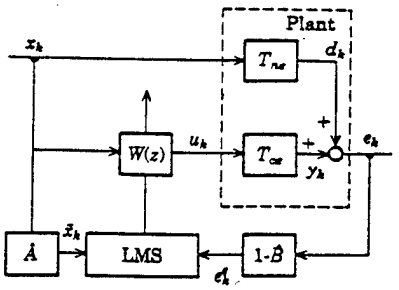

Figure 2. Filtered-x LMS algorithm being used in the equation error control configuration.

shown in Figure 2, the output of the plant is first filtered by the measured poles of the system, $(1-\hat{B}(z))$, and then the LMS algorithm is used to minimize the filtered error signal rather than the error signal itself. Such a filtered version of the error signal is often referred to as equation error—hence the name "equation error filtered-x LMS control configuration". Typically, equation error forms are used to counter stability and convergence problems of adaptive IIR filters in system identification [14–16, 18]. This topic will be addressed in more detail later.

The new error signal to be minimized is then given as

$$e_k^f = (1-\hat{B}(z))e_k, \tag{20}$$

where $(1-\hat{\beta}(z))$ are the poles of the measured system identification. Replacing the error e_k from equation (6) gives

$$e_k^f = (1-\hat{B}(z))(d_k + T_{ce}(z)\,W(z)x_k). \tag{21}$$

The transfer function between the disturbance signal x_k and its contribution y_k to the error signal is

$$T_{ne}(z) = C(z)/(1-B(z)). \tag{22}$$

Thus, equation (21) can be also written as

$$e_k^f = (1-\hat{B}(z))\left[\frac{C(z)}{1-B(z)} + \frac{A(z)}{1-B(z)}\,W(z)\right]x_k. \tag{23}$$

If an exact identification of the system poles is assumed, equation (23) yields

$$e_k^f = [C(z) + A(z)W(z)]x_k. \tag{24}$$

Due to noise in the measurement and variation in the system's properties, an exact cancellation of poles and zeros is rarely possible in practice. However, the resulting response due to the inexact cancellation can be shown to be insignificant unless the zeros and poles are too far off [19]. Furthermore, the adaptive LMS algorithm was shown to tolerate errors in the system identification for harmonic control [17, 20], and a similar error tolerance was observed experimentally when operating the broadband controller. This behavior is attributed to the robust nature of the LMS algorithm, that should be contrasted with feedback control, where an accurate model of the system is generally essential. Equation (24) shows that by forward filtering the output of the plant with $(1-\hat{B}(z))$, the system poles are cancelled in the signal e_k^f. The reader should notice that this control structure is only possible because, again, the system poles $(1-B(z))$ represent global properties.

The update equation for the adaptive filter coefficients is again obtained as in the previous section. The new cost function to be minimized becomes

$$C(W_i) = E[(e_k^*)^2]. \tag{25}$$

Differentiating equation (25) with respect to the weight W_i, and considering equation (24), gives

$$\frac{\partial C}{\partial W_i} = 2E[e_k^* \, \partial e_k^* / \partial W_i] \tag{26}$$

$$= 2E[e_k^* A(z)(z^{-i}) x_k]. \tag{27}$$

Then, using instantaneous values to approximate expected values of the gradient, the updated equation for W_i now becomes

$$W_i(k+1) = W_i(k) - 2\mu e_k^* \tilde{x}_{k-i}, \qquad i = 1, \ldots, N, \tag{28}$$

where

$$\tilde{x}_{k-i} = \hat{A}(z) x_{k-i} \tag{29}$$

is the filtered-x signal required to compute the gradient. This signal is obtained by filtering the disturbance signal with only the zeros of the measured transfer function $\hat{T}_{ce}(z)$. The main advantage of this configuration is that the poles $(1 - \hat{B}(z))$ do not participate in computing the filtered-x signal $\tilde{x}_k$. Thus, the stability requirements of the system identification are removed since the signal $\tilde{x}_k$ will always be stable, even when some or all of the poles of $T_{ce}(z)$ are outside the unit circle. The drawback of this configuration is that a filtered version of the error signal is minimized instead of the error signal itself. It is easy to show that minimizing e_k^* would not necessarily cause e_k to be minimized. However, if the filter $(1 - \hat{B}(z))$ is of adequate size, then minimizing e_k^* also minimizes e_k [14].

3. SYSTEM IDENTIFICATION OF CONTROL LOOP

3.1. LEAST SQUARE SOLUTION OF ARMA MODEL

Recursive filters representing plants with both poles and zeros, as shown in equation (7), are often referred to a autoregressive-moving average (ARMA) models. A time series ARMA model of order N can be written as

$$\hat{y}_k = \sum_{i=0}^{N} A_i x_{k-i} + \sum_{j=1}^{N} B_j y_{k-j}, \tag{30}$$

where $\hat{y}_k$ is the filter output, x_k is the input sequence, and A_i and B_i are, respectively, the coefficients of the MA and AR portions of the IIR filter.

Multiplying each side of equation (30) consecutively by each element from the sequences $\{x_k\}$ and $\{y_k\}$ (e.g., $\{x_k, x_{k-1}, \ldots, x_{k-N}, y_{k-1}, \ldots, y_{k-N}\}$) and taking the expected value, the following linear system of equations results

$$\begin{Bmatrix} \{R_{xy}\} \\ \{R_{yy}\} \end{Bmatrix} = \begin{bmatrix} [R_{xx}] & [R_{xy}] \\ [R_{yx}] & [R_{yy}] \end{bmatrix} \begin{Bmatrix} \{A\} \\ \{B\} \end{Bmatrix}. \tag{31}$$

The components in this equation are defined in terms of the auto- and cross-correlation functions of the sequences $\{x_k\}$ and $\{y_k\}$ as

$$\{R_{xy}\} = \begin{Bmatrix} R_{xy}(0) \\ R_{xy}(1) \\ \vdots \\ R_{xy}(N) \end{Bmatrix}, \qquad \{R_{yy}\} = \begin{Bmatrix} R_{yy}(1) \\ R_{yy}(2) \\ \vdots \\ R_{yy}(N) \end{Bmatrix}, \tag{32, 33}$$

$$[R_{xx}] = \begin{bmatrix} R_{xx}(0) & R_{xx}(-1) & \cdots & R_{xx}(-N) \\ R_{xx}(1) & R_{xx}(0) & \cdots & R_{xx}(-N+1) \\ \vdots & \vdots & \ddots & \vdots \\ R_{xx}(N) & R_{xx}(N-1) & \cdots & R_{xx}(0) \end{bmatrix}, \tag{34}$$

$$[R_{xy}] = \begin{bmatrix} R_{xy}(-1) & R_{xy}(-2) & \cdots & R_{xy}(-N) \\ R_{xy}(0) & R_{xy}(-1) & \cdots & R_{xy}(-N+1) \\ \vdots & \vdots & \ddots & \vdots \\ R_{xy}(N-1) & R_{xy}(N-1) & \cdots & R_{xy}(1) \end{bmatrix}, \tag{35}$$

$$[R_{yx}] = \begin{bmatrix} R_{yx}(1) & R_{yx}(0) & \cdots & R_{yx}(1-N) \\ R_{yx}(2) & R_{yx}(1) & \cdots & R_{yx}(2-N) \\ \vdots & \vdots & \ddots & \vdots \\ R_{yx}(N) & R_{yx}(M-1) & \cdots & R_{yx}(0) \end{bmatrix}, \tag{36}$$

$$[R_{yy}] = \begin{bmatrix} R_{yy}(0) & R_{yy}(-1) & \cdots & R_{yy}(-N+1) \\ R_{yy}(1) & R_{yy}(0) & \cdots & R_{yy}(-N+1) \\ \vdots & \ddots & & \vdots \\ R_{yy}(N-1) & R_{yy}(N-1) & \cdots & R_{yy}(0) \end{bmatrix}, \tag{37}$$

where the correlation functions and some of their properties are defined as

$$\begin{aligned} R_{xx}(m) &= E[x_k x_{k+m}] = R_{xx}(-m), \\ R_{xy}(m) &= E[x_k y_{k+m}] = R_{yx}(-m). \end{aligned} \tag{38}$$

The unknown filter coefficients A_i and B_i are the components of the vectors

$$\{A\} = \begin{Bmatrix} A_0 \\ A_1 \\ \vdots \\ A_N \end{Bmatrix}, \qquad \{B\} = \begin{Bmatrix} B_1 \\ B_2 \\ \vdots \\ B_N \end{Bmatrix}. \tag{39, 40}$$

Solving the system in equation (31) will produce a least square (LS) solution for the IIR filter coefficients, which represents, a complex polynomial in z. This type of solution provides the advantage that the poles do not have to be broken into second order sections and checked for stability during the identification process (in order that the summed filter output remains bounded). Rather, the poles can be factored and stabilized after the parameter estimation is complete and before the filter is implemented in the control system.

The denominator polynomial of the transfer function in equation (7) can be factored into the form

$$1 - B(z) = 1 - b_1 z^{-1} - b_2 z^{-2} \cdots - b_N z^{-N} \tag{41}$$

$$= z^{-N}(z - z_1)(z - z_2)(z - z_3) \cdots (z - z_N), \tag{42}$$

where z_i $(i = 1, 2, \ldots, N)$ are the roots or poles of the structure. They occur in complex conjugate pairs, representing the individual second order sections of the structure. A pole, and therefore the filter is stable when its modulus is less than one. Poles can be made stable by reciprocation, a process where each unstable root is divided into unity in order to reflect it back inside the unit circle [14]. This procedure preserves the magnitude response of the transfer function, but alters the phase response. An accurate estimate of the phase could be needed for response prediction of the control loop when excited by the disturbance input (generation of the filtered-x reference signal). If necessary, the phase corruption can be remedied by using the adaptive IIR configuration for system identification, as explained in section 3.2.

3.2. ADAPTIVE IIR FILTERS FOR SYSTEM IDENTIFICATION

An IIR filter was proposed earlier in equation (7), to represent the transfer function between the control input and the error output, $T_{ce}(z)$. The LMS algorithm can be used to adapt recursive filters [12, 14–16, 18], but left in their conventional form they pose some problems. First, the cost function is not a quadratic function of the filter weights $B(z)$, meaning that the performance surface may be multi-modal. Also, the poles of the filter, $(1 - B(z))$, must remain inside the unit circle for the filter output to remain bounded. One solution to these problems is to use the equation error minimization technique for adapting IIR filters [14, 16, 18]. Shown in Figure 3 is an equation error adaptive IIR filter that will carry out the system identification of the control loop. As with the equation error control configuration, the output error is first filtered with the recursive coeffcients of the IIR, $(1 - B(z))$, before it is minimized, allowing the separation of the feedforward and feedback sections of the filter. Each section is then adapted as independent transversal filters, each having its own quadratic error surface. The output error signal is given as the difference between the plant output d_k, and the predicted plant response from the recursive filter, $\hat{y}_k$: that is,

$$e_k = d_k - \hat{y}_k \tag{43}$$

$$= d_k - T_{ce}(z)x_k$$

$$= d_k - \frac{A(z)}{(1 - B(z))}x_k. \tag{44}$$

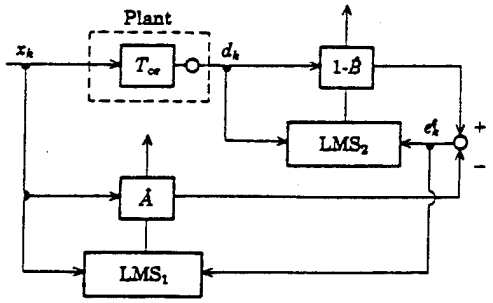

Figure 3. System identification of a plant using an adaptive IIR filter.

Multiplying the above equation by the filter poles $(1 - B(z))$, the desired filtered equation error e_k^e, becomes

$$e_k^e = (1 - B(z))d_k - A(z)x_k. \tag{45}$$

The cost function to be minimized is again the mean square value of e_k^e as

$$C(A_i, B_i) = E[(e_k^e)^2], \tag{46}$$

$$C(A_i, B_i) = E[(d_k - B(z)d_k - A(z)x_k)^2]. \tag{47}$$

Equation (47) can be recognized as a quadratic function of the filter coefficients from both the numerator and denominator of $T_{ce}(z)$. One can now perform a gradient search to update the filter coefficients A_i and B_i, as shown by equation (12). Again, the partial derivatives of the cost function are taken with respect to each filter weight. The gradient and its instantaneous approximation for the coefficient B_i will be

$$\frac{\partial C}{\partial B_i} = 2E[e_k^e \partial e_k^e / \partial B_i] = 2E[e_k^e(-d_{k-i})] \approx -2e_k^e d_{k-i}, \tag{48}$$

where e_k^e is the equation error sequence from equation (45) and d_{k-i} is the measured plant response to the input signal.

Similarly, the gradient for the numerator coefficients can be approximated as follows:

$$\frac{\partial C}{\partial A_i} = 2E[e_k^e \partial e_k^e / \partial A_i] = 2E[e_k^e(-x_{k-i})] \approx -2e_k^e x_{k-i}, \tag{49}$$

where x_k is the input disturbance sequence to the filter and plant, which is zero-mean, band-limited white noise.

Considering equation (12) with equations (48) and (49), we can construct the final form of the LMS coefficient update equations for the system identification as

$$B_i(k+1) = B_i(k) + 2\mu e_k^e d_{k-i}, \qquad A_i(k+1) = A_i(k) + 2\mu e_k^e x_{k-i}. \tag{50, 51}$$

The recursive coefficients B_i, computed using equation (50), must remain inside the unit circle in the z-complex plane for the filter output to be stable. A solution to this problem is to break the polynomial $(1 - B(z))$ into second order filter sections and configure them into cascade form [18]. Then, the stability of each individual filter can be guaranteed by requiring the coefficients to remain inside the region of stability as shown in reference [14, pp. 14, 160 – 1]. However, the cascade form results in a much more complex system identification algorithm, with an associated significant computational effort.

The adaptive IIR configuration can also be used to correct for the phase corruption which may occur during stabilization of the least-squares ARMA solution described in section 3.1. In this case, the coefficients of the stabilized ARMA model provide the first guess to the LMS solution, where only the numerator coefficients of the IIR filter, A_i, are adapted using equation (51).

4. EXPERIMENTAL SET-UP

An experimental investigation of the two broadband control structures from the previous sections was performed in the beam shown in Figure 4. The beam is made of plain carbon steel and its dimensions are 380 × 40 × 2 mm. Two thin, flexible metal shims connect the beam to a heavy support stand, providing the desired simply supported end conditions. The first six natural frequencies which were obtained experimentally are listed in Table 1. The error sensor was a Brüel & Kjær (B&K) mini-accelerator located 238 mm from the

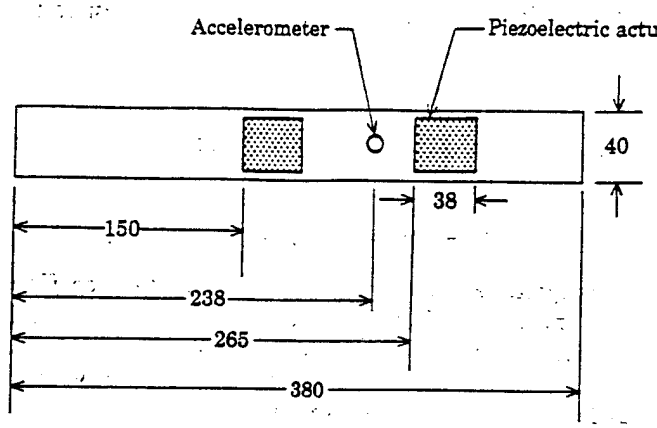

Figure 4. Sensor and actuator locations on the simply supported beam used for the experimental analysis. All dimensions are in mm.

TABLE 1

Experimental natural frequencies

Mode	experimental f_n (Hz)
1	32·9
2	126·9
3	282·3
4	498·6
5	768·7
6	1077·0

left edge of the beam, a location capable of sensing the modes of interest. A B&K type 2635 charge amplifier was used to condition the sensor signal and perform an analog integration of it. It was observed that the controller produced better results when velocity rather than acceleration was used as the error signal. Control action was applied by a co-located set of G1195 piezoelectric strips. The piezoelectric strips measured 38·1 × 32·0 × 0·2 mm and their closest edge was located 265 mm from the left edge of the beam, as shown in Figure 4. The disturbance or input action actuator was also applied by a piezoelectric strip. It measured 38 × 22 × 0·2 mm and was affixed 150 mm from the left edge of the beam, where it is capable of exciting all of the modes of interest.

The two control approaches presented in previous sections were implemented in a Texas Instruments TMS320C30 digital signal processor (DSP) board installed into a host 80386-based personal computer. The system identification and the control codes for the DSP were written in assembly language. Interface programs written in C-language allowed control of the sample rate and convergence parameter from the PC. They also downloaded the compiled assembly codes to the DSP for execution. Three Frequency Devices 9002 low-pass filters were used to filter the input signal, the control signal and the error signal. The propagation time from both the disturbance and control inputs to the error output was measured by computing the cross-correlation functions across each path while being excited by white noise. The propagation time for each path was found at the largest peak on the respective cross-correlation function, and it was discovered that the disturbance

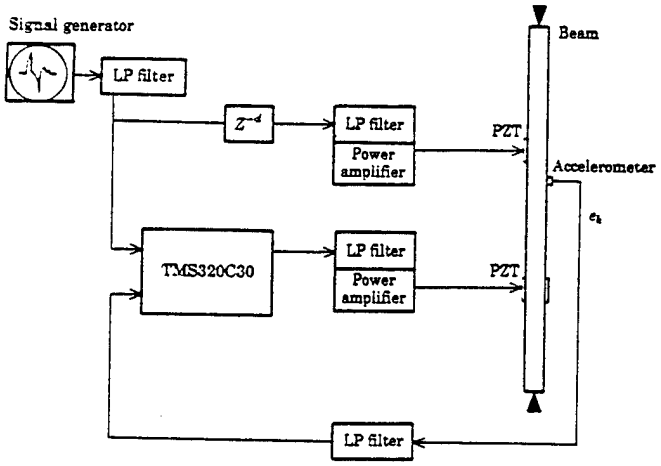

Figure 5. Experimental set-up for testing the feedforward broadband control algorithm.

path had a delay of 3 ms with respect to the control input. Therefore the control system is non-causal. A programmable delay z^{-d} was installed in the disturbance path, allowing the control system to be made causal by varying the delay d to give at least 3 ms of delay. A schematic diagram of the complete experimental set-up is shown in Figure 5.

The experiment was limited to control of the first three bending modes, because the location of the control actuator pair rendered the fourth mode uncontrollable. Consequently, the cut-off frequency of the low-pass filters was set at 400 Hz. The input signal was band-limited random noise from 0 to 400 Hz, which was generated by a B&K 2032 spectrum analyzer. The sampling rate used for the system identification and control experiments was 2000 Hz. Both portions of the IIR filter that represents $T_{ce}(z)$ have 24 coefficients. An IIR filter of any smaller size did not produce accurate estimates of the beam natural frequencies during the system identification.

The first step in operating the control is to perform the off-line system identification. The random input signal was fed into the control actuator, and the error signal was monitored from the excitation. A DSP code measured the two signals and computed the statistics for the ARMA model shown in equation (31). Approximately 30 000 points were used to compute the correlation functions, which were sent back to the PC to form the linear system shown in equation (31), and to solve for the filter coefficients A_i and B_i of $T_{ce}(z)$. The poles were then computed by solving for the zeros of $(1-B(z))$, and the unstable poles were stabilized by reciprocation, as described in the previous section. In the event that the stabilized model has accurately identified the system natural frequencies but does not provide adequate performance for the control system, the phase corruption occurring from the pole reciprocation can be remedied by using the adaptive IIR configuration of Figure 3 to adapt only the numerator coefficients of the filter, A_i. In this case, the coefficients of the stabilized ARMA model provided the first guess to the LMS solution. For this experimental work, the stabilized ARMA model predicted the filtered-x signal well enough that the correction of the phase corruption was not performed. A comparison between the autospectra of the filtered-x signal and the real output error is presented in Figure 6, and they show very good agreement.

The IIR filter coefficients were then stored in the memory of the DSP to be used by the control codes in generating the filtered-x reference signals used for updating the coefficients of the adaptive FIR filter. Next, the random input signal was applied to the disturbance

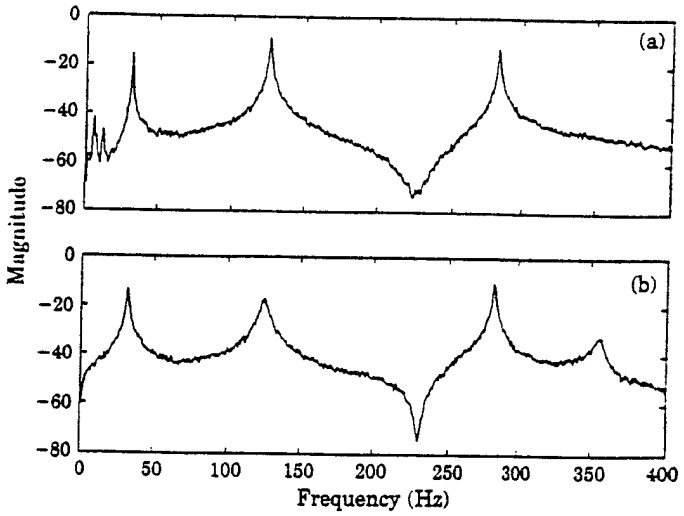

Figure 6. Autospectrum of the control-loop response when excited by white noise: (a) Measured; (b) predicted filtered-x signal.

actuator and the performance of the different control configurations was investigated. Two variables were examined with the filtered-x LMS controller: (a) the effect of adaptive filter size of control performance; and (b) how this performance changes when the system is made non-causal by removing the delay from the disturbance path. The equation error control configuration of Figure 2 was operated with two different sets of coefficients used to filter the error signal. In the first test, the stabilized poles used in the filtered-x controller equation (17) were used to forward filter the errror. The second test filtered the error signal with the same poles after a couple of conjugate pairs had been reflected outside the unit circle. This test was used to demonstrate that when using the equation error configuration, the poles do not have to be stable. A convergence parameter, 5×10^{-4}, was used for all three test cases in which a 24th order adaptive FIR was used. An increase or decrease in convergence parameter was made when the adaptive filter size was decreased or increased, respectively. All time and frequency domain analysis was carried out by the B&K 2032 and was downloaded to a PC via an IEEE-488 interface.

5. RESULTS

The conventional filtered-x LMS control configuration of Figure 1 was studied first. A delay of 5 ms ($d = 59$) was implemented in order to have a causal control system. In Figure 7 is shown a comparison of the steady-state error signal measured from the beam, both before and after the conventional filtered-x LMS control was applied with a 24th order adaptive FIR. Although the error signal was not reduced to zero, a large amount of vibration attenuation was achieved by the controller. A comparison of the graphs of the power spectral density of the two error signals is shown in Figure 8, and it gives additional insight into the control mechanism. Despite an increase of the spectrum in some of the off-resonance frequency bands, the spectrum at the system resonances displays a reduction of approximately 20–25 dB. The result was a net reduction of the mean-square error of 19·4 dB. Thus, the controller behaves as a wide-band controller rather than a true broad-band controller, attenuating the larger frequency components that occur near the structural resonances while adding energy at the antiresonances. The reader should keep in mind

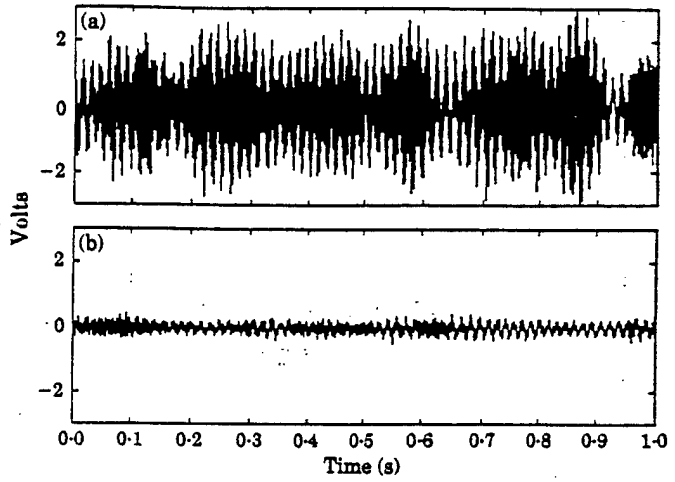

Figure 7. Error signal from the plant: (a) before control; (b) after control.

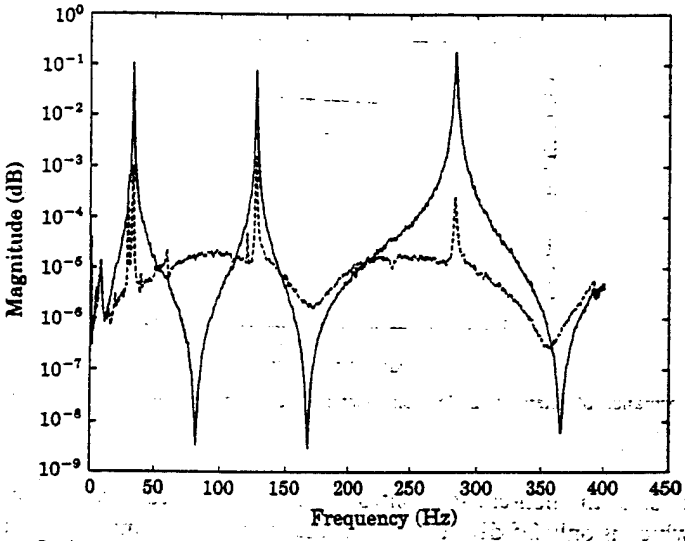

Figure 8. Autospectrum of the error signal: ——, before control; – – –, after control.

that the areas under the two curves can not be compared directly, because of the log scaling. Convergence of the adaptive algorithm occurred in approximately three seconds, as shown by the time histories of the control and error signals in Figure 9.

The influence of the adaptive FIR filter size on the controller performance was then investigated by varying the filter order N from 12 to 80 coefficients. This process was performed for both causal and non-causal control systems. The reduction in the mean square error as function of the filter size is plotted in Figure 10. For the causal system shown by the top curve, it can be seen that the control performance quickly improves with larger filters to reach a nearly constant reduction of 20 dB. The programmable delay d was then set to zero to evaluate the controller when it is non-causal. The results of these tests are shown by the bottom curve in Figure 10. The performance of the non-causal controller is severely compromised for small size adaptive filters compared with the causal controller. However,

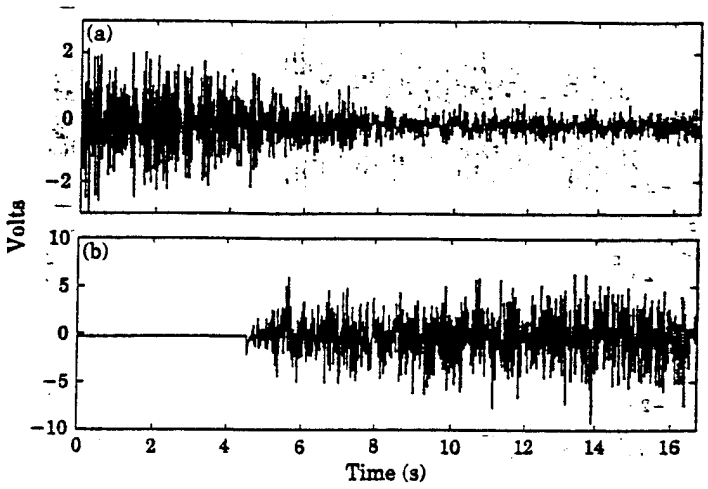

Figure 9. Time histories showing the convergence rate of the adaptive controller: (a) error signal; (b) control input signal.

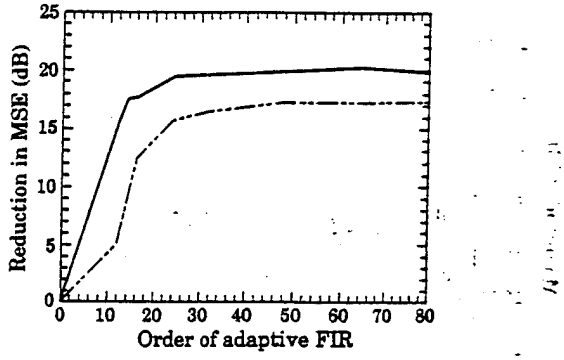

Figure 10. Performance of filtered-x LMS controller as the adaptive filter size is increased: ——, causal; — — —, non-causal.

for larger filter size, the non-causal controller shows significant reduction of the mean-square error, which is only 2·5 dB below the causal controller. Analytical studies are being carried out to characterize this behavior and will be reported in the near future.

Next, the equation error control structure was demonstrated by performing two experiments with a causal control system having 24 adaptive coefficients. In the first test, the error signal was filtered with the same stabilized poles, $(1-\hat{B}(z))$, used for the filtered-x LMS control. This configuration did not produce as much reduction in the error signal as the conventional filtered-x LMS control structure; nor did it converge as quickly. In Figure 11, a comparison of the error signal time histories before and after control is presented. The autospectra of the error signal were similar to those of Figure 8, where the modal amplitudes were reduced while some off-resonance frequency bands increased in energy. A reduction of 10 dB in the power of the error signal was measured in this case. For the second control experiment, some of the poles of $(1-\hat{B}(z))$ were reflected outside the unit circle before being used to filter the error signal with the equation error configuration. This test demonstrates that the equation error control configuration will work even when the IIR filter that is used for the filtered-x LMS control is unstable. Such a result is useful

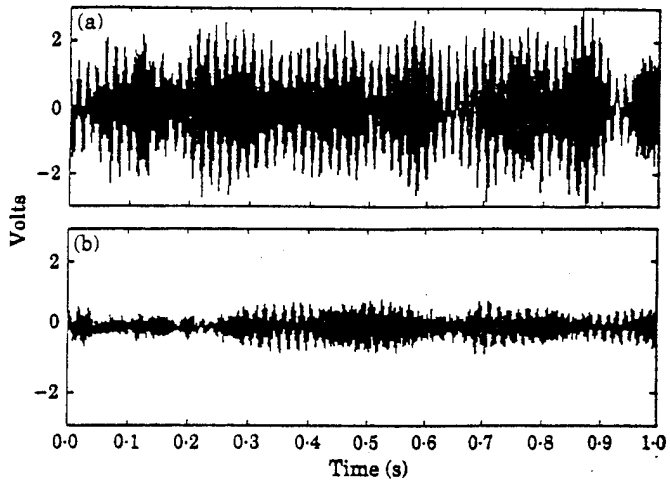

Figure 11. Actual error signal time histories during application of the equation error control form: (a) without control; (b) with equation error control configuration.

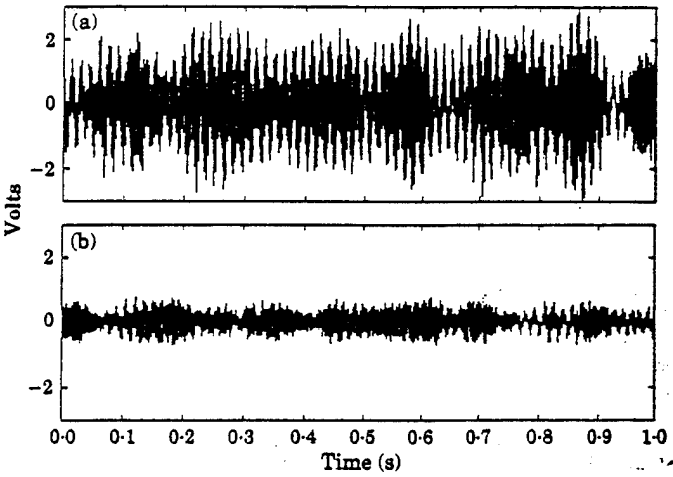

Figure 12. Error signal time histories showing effects of applying the equation error control form with unstable "poles": (a) without control; (b) equation error control configuration.

for systems that apply a simultaneous on-line system identification and control [21–23]. On-line system identification is carried out by injecting an additional, uncorrelated random signal into the control path while operating an LMS or RLMS algorithm in a typical system identification arrangement. After updating the coefficients of $\hat{T}_{ce}(z)$, they are copied to the LMS algorithm and used to create the filtered-x signal. Stabilization of the recursive filter coefficients is not required when emplying the equation error control configuration, reducing both the system complexity and computational overheads. The total power reduction of the error signal for the last experiment was approximately 8·9 dB, which differs slightly from the results of the first equation error control experiment. Again, the before and after control error signals are compared as shown in Figure 12. Both of these experiments displayed much lower power reductions than the corresponding causal, 24th order filtered-x LMS controller, which exhibited 20 dB of attenuation.

TABLE 2

Comparison of three different control structures having a 24th order causal adaptive FIR filter

Control configuration	Reduction (dB)
No control	n/a
Conventional LMS controller	19·4
Equation error LMS controller with stable poles	10·1
Equation error LMS controller with unstable poles	8·91

However, the experiments demonstrate the advantage that a highly accurate system identification with stable poles is not necessary when using the equation error control structure. The penalty for the relaxation on the system identification is a deterioration of the control performance. The difference between the results of the three test cases can be explained simply by the fact that a different cost function is minimized for all three test cases. These test results are summarized in Table 2.

6. CONCLUSIONS

The attenuation of broadband structural vibration using adaptive feedforward control was experimentally demonstrated. Two control configurations based on the filtered-x LMS algorithm were studied, and both used an adaptive FIR filter as a compensator. In the filtered-x LMS control configuration, the measured transfer function between the control input and error output is efficiently represented by an IIR filter, which introduces stability problems into the control system. It is seen that increasing the size of the adaptive filter in the filtered-x LMS controller improves control performance asymptotically for attenuations as large as 20 dB (Figure 10). The same asymptotic behavior was observed when the disturbance path delay was removed ($d = 0$), making the system non-causal. Attenuations for the non-causal control were smaller than those for the causal controller, and yet significant attenuations of up to 17 dB were observed. The equation error control configuration did not achieve as good a control (9–10 dB) as the filtered-x LMS controller, but it demonstrated the advantage that it will work even when the poles of the estimated IIR model for the control-error transfer function are unstable.

ACKNOWLEDGMENTS

The authors gratefully acknowledge the support of this work by DARPA and the Office of Naval Research under grant ONR-00014-88-k-0721.

REFERENCES

1. G. E. WARNAKA 1982 *Noise Control Engineering* **18**, 100–110. Active attenuation of noise: the state of the art.
2. R. S. SILCOX and H. C. LESTER 1989 *Journal of Vibration Stress, and Reliability in Design* **111**, 337–342. An evaluation of active noise control in a cylindrical shell.
3. C. R. FULLER, C. H. HANSEN and S. D. SNYDER 1991 *Journal of Sound and Vibration* **145**, 195–215. Active control of sound radiation from a vibrating rectangular panel by sound sources and vibration inputs: an experimental comparison.

4. W. REDMAN-WHILE, P. A. NELSON and A. R. D. CURTIS 1987 *Journal of Sound and Vibration* **112**, 181–187. Experiments on active control of flexural wave power.
5. A. H. VON FLOWTOW and B. SCHAFER 1986 *Journal of Guidance, Control, and Dynamics* **9**, 673–680. Wave-absorbing controller for a flexible beam.
6. S. J. ELLIOT, I. M. STOTHERS and L. BILLET 1990 *Proceedings of the Institute of Acoustics* **12**(1), 613–622. Adaptive feedforward control of flexural wave propagating in a beam.
7. J. SCHEUREN 1990 *Proceedings of the Institute of Acoustics* **12**(1), 623–629. Active attenuation of bending waves in beams.
8. G. P. GIBBS and C. R. FULLER 1990 *AIAA Paper* 90–1132. Experiments on active control of vibrational power flow using piezoceramics actuators and sensors.
9. C. R. FULLER, G. P. GIBBS and R. J. SILCOX 1990 *Proceedings of International Congress on Recent Developments in Air- and Structure-borne Sound and Vibration, Auburn University, Alabama*, 657–662. Simultaneous active control of flexural and extensional power flow in beams.
10. C. F. ROSS 1992 *Journal of Sound and Vibration* **80**, 373–380. An algorithm for designing a broadband active sound control system.
11. L. J. ERIKSON and M. C. ALLIE 1987 *Noise-Con* 87, 365–370. A digital sound control system for use in turbulent flows.
12. L. J. ERIKSON, M. C. ALLIE and R. A. GREINER 1987 *IEEE Transactions on Acoustics, Speech, and Signal Processing* **ASSP-35**, 433–437. The selection and application of an IIR adaptive filter for use in active sound attenuation.
13. J. V. WARNER and R. J. BERNHARD 1987 *AIAA 11th Aeroacoustics Conference*, 1–8. Digital control of sound fields in three-dimensional enclosures.
14. B. J. WIDROW and S. D. STEARNS 1985 *Adaptive Signal Processing*. Englewood Cliffs, New Jersey: Prentice-Hall.
15. P. L. FEINTUCH 1976 *Proceedings of IEEE* **64**, 1622–1624. An adaptive recursive LMS filter..
16. J. R. TREICHLER, M. G. LARIMORE and J. C. R. JOHNSON 1978 *IEEE Transactions on Acoustics, Speech, and Signal Processing* 118–122. Simple adaptive IIR filtering.
17. S. J. ELLIOTT, I. M. STOTHERS and P. A. NELSON 1987 *IEEE Transactions on Acoustics Speech and Signal Processing* **ASSP-35**, 1423–1434. A multiple error LMS algorithm and its application to the active control of sound and vibration.
18. R. A. DAVID 1982 *Asilomar Conference on Circuits, Systems, and Computers, IEEE*, 182–186. A cascade structure for equation error minimization.
19. B. C. KUO 1982 *Automatic Control Systems*. Englewood Cliffs, New Jersey: Prentice-Hall.
20. J. C. BURGESS 1981 *Journal of Acoustical Society of America* **70**, 715–726. Active adaptive sound control in a duct: a computer simulation.
21. L. J. ERIKSON and M. C. ALLIE 1989 *Journal of Acoustical Society of America* **85**, 797–802. Use of random noise for on-line transducer modeling in an adaptive active attenuation system.
22. L. J. ERIKSON, M. C. ALLIE, C. D. BREMIGAN and J. A. GILBERT 1989 *Sound and Vibration* **23**, 16–21. Active noise control of systems with time-varying sources and parameters.
23. L. J. ERIKSON and M. C. ALLIE 1988 *Proceedings of ISCAS* 88 **3**, 2387–2390. System considerations for adaptive modelling applied to active noise control.

C-14 An Impedance Method for Dynamic Analysis of Active Material Systems, C. Liang, F. P. Sun and C. A. Rogers, ASME Journal of Vibration and Acoustics, Vol. 116 No. 1, pp. 120-128, January 1994.

An Impedance Method for Dynamic Analysis of Active Material Systems

C. Liang

F. P. Sun

C. A. Rogers

Center for Intelligent Material Systems
and Structures,
Virginia Polytechnic Institute
and State University,
Blacksburg, VA 24061-0261

This paper describes a new approach to analyzing the dynamic response of active material systems with integrated induced strain actuators, including piezoelectric, electrostrictive, and magnetostrictive actuators. This approach, referred to as the impedance method, has many advantages compared with the conventional static approach and the dynamic finite element approach, such as pin force models and consistent beam and plate models. The impedance approach is presented and described using a simple example, a PZT actuator-driven one-degree-of-freedom spring-mass-damper system, to demonstrate its ability to capture the physics of adaptive material systems, which is the impedance match between various active components and host-structures, and its utility and importance by means of an experimental example and a numerical case study.

The conventional static and dynamic finite element approaches are briefly summarized. The impedance methodology is then discussed in comparison with the static approach. The basic elements of the impedance method, i.e., the structural impedance corresponding to actuator loading and the dynamic output characteristics of PZT actuators, are addressed. The advantages of using the impedance approach over conventional approaches are discussed using a simple numerical example. A comparison of the impedance method with the static and the dynamic finite element approaches are provided at the conclusion of this paper.

Introduction

There are two approaches currently used in the dynamic analysis of active material systems, one is referred to as a static approach and the other is dynamic finite element approach. Both of these approaches have some drawbacks in analyzing the dynamic response of active material systems resulting from the activation of integrated induced strain actuators, such as PZT patches. A brief review of these two approaches is given below.

Static Approach. The static approach refers to the method of using a statically determined equivalent force or moment as the amplitude of the forcing function to determine the dynamic response due to the activation of integrated induced strain actuators. There are several approaches to determining the equivalent force or moment from bonded PZT actuators. One widely used approach is the pin force model. In the pin force model (Crawley and Deluis, 1989), it is assumed that the mechanical interaction between a bonded actuator and its host structure occurs at the ends of the actuator in the form of concentrated forces. This concentrated force can be determined based on the strain compatibility and *static* force equilibrium between the actuator and structure. This concentrated force or moment is then used to represent the effect of the induced strain actuator in static and dynamic analyses by assuming that the resultant "pin-force" is frequency independent.

Another widely used approach for determining the static equivalent force or moment uses Euler-Bernoulli beam equations (Crawley and Deluis, 1989) or consistent plate equations which are fundamentally the same as the pin force models except for a variation in the assumed strain field. The equivalent force or moment determined from Euler-Bernoulli beam theory is also more accurate than the pin force model because it includes the mechanical stiffening and the bending of the bonded PZT actuators. Once again, the force or moment is calculated based on the stiffness of the structure at the point where the actuators are attached and the resultant induced force or moment is independent of frequency, even for dynamic analysis.

Lin and Rogers (1992) have developed a new model of the equivalent force and moment using an elasticity approach, which shows the nonlinear distribution of the equivalent induced force or moment. This model is very accurate for static analysis, but as described above is a static stiffness approach and does not allow for the actuator performance to vary with frequency and the impedance of the structure.

The static approach, as will be discussed in this paper, should be avoided in the dynamic analysis of active material systems as a result of these obvious shortcomings.

Contributed by the Technical Committee on Vibration and Sound for publication in the JOURNAL OF VIBRATION AND ACOUSTICS. Manuscript received Dec. 1992; Associate Technical Editor: D. J. Inman.

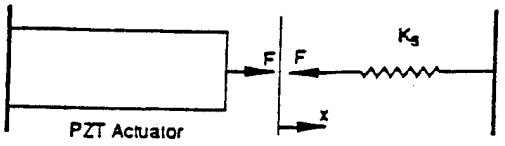

Fig. 1 A spring driven by a PZT actuator

Dynamic Finite Element Approach. The electrically induced strain from any induced strain actuator (i.e., PZT or PMN) has the same effect as thermal expansion on the structural response. When using the dynamic finite element approach to determine the dynamic response of an active material system, the actuators are treated as regular integral structural components with associated mass, stiffness, and damping. The equivalent excitation forces of the actuators (the forcing terms in the finite element equation, $[M]\{\ddot{u}\} + [C]\{\dot{u}\} + [K]\{u\} = \{F_{eq}\}$) are equal to the actuator blocking forces (Liang and Rogers, 1989; Hagood et al.,1990; Sung et al., 1992).

The dynamic finite element analysis can provide correct prediction of the dynamic response. However, there are some drawbacks associated with this approach. For example, extremely fine finite element mesh around an actuator is needed in order to provide satisfactory convergence. It is also difficult to customize a commercially available finite element program to deal with the harmonic dynamic thermal expansion needed to model the induced strain effect of actuators. This approach does not capture the physical essence of the dynamic interaction between the actuator and structures. For example, the forcing terms in the dynamic finite element analysis is frequency independent (blocking forces of the actuators). This may create a false impression that the force exerted on a structure by an actuator is its blocking force, which is not true as will be discussed in this paper.

In this paper, an impedance approach for dynamic analysis of active material systems will be presented. Numerical results of the dynamic response of a beam excited by a PZT actuator based on various approaches discussed will be provided. Experimental validation of the approach will be provided. This paper will also provide a comparison between static, dynamic finite element, and impedance approaches.

Impedance Methodology

The impedance method of analyzing the dynamic response of active material systems can be simply described: the interactions between actuators and structures are governed by the dynamic output characteristics of the actuators and the dynamic characteristics of the structure, i.e., the structural impedance. To begin, we shall study the basic elements of this approach by examining the following example, a PZT actuator-driven one-degree-of-freedom spring-mass-damper (SMD) system and review the static approach as well.

The static response of a PZT/structure interaction (Fig.1) is determined by coupling the constitutive relations of PZT and structure with their equilibrium and compatibility conditions. The force-displacement relation for the PZT actuator can be expressed as:

$$F = K_A (x - x_{in}), \tag{1}$$

where x is the displacement, F is the force exerted by the actuator, and K_A is the static stiffness of the PZT given by $Y_{22}^E w_A h_A / l_A$ where w_A, h_A, and l_A are the width, thickness, and length of the PZT actuator, respectively. x_{in} is the free induced displacement of the actuator given by $d_{32} E l_A$ where d_{32} is the piezoelectric constant and E is the electric field. The force and displacement relation for the spring is given by:

$$F = -K_S x, \tag{2}$$

where K_S is the spring constant. Equations (1) and (2) describe

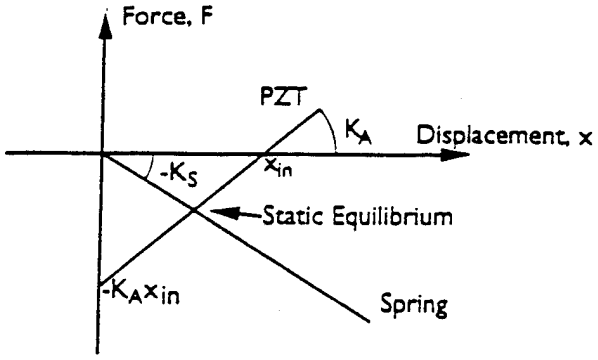

Fig. 2 Determination of static equilibrium

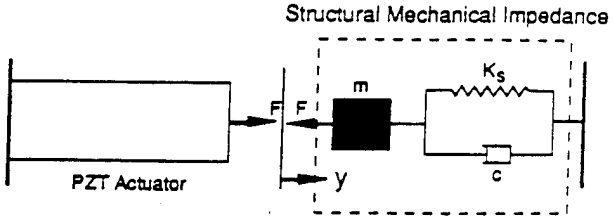

Fig. 3 A schematic representation of the dynamic interaction between an actuator and its host structures illustrated by a PZT actuator-driven one-degree-of-freedom spring-mass-damper system

the force and displacement relations of the PZT actuator and spring. The force given by both equations is the force within the components. The force and displacement sign convention is positive for tension and negative for compression. If the induced displacement of the PZT actuator, x_{in}, is in the positive direction (also positive x direction as shown in Fig. 1), the resulting force in the spring is negative as expressed by Eq. (2).

Figure 2 illustrates the force-displacement relations of both the PZT actuator and spring. The intersection determines the static equilibrium of the actuator and spring system. A so-called "equivalent force" can be determined as:

$$F_{eq} = \frac{K_A K_S}{K_S + K_A} x_{in}. \tag{3}$$

The "equivalent force" is used to represent the presence and activation of the PZT actuator in the static approach. To determine the dynamic response of a mechanical system, as shown in Fig. 3, with the static approach, the governing equation is expressed by: $m\ddot{x} + c\dot{x} + K_S x = F_{eq} \sin(\omega t)$, where F_{eq} is determined from Eq. (3). Notice that the stiffness of the PZT is not included and this "equivalent force" is independent of frequency or constant over the entire frequency range of possible excitation.

The impedance approach will treat the problem differently. As an example of how the impedance approach is used to determine the dynamic response of an actuator-driven system, consider the PZT-driven one-degree-of-freedom spring-mass-damper (SMD) system shown in Fig. 3. In a dynamic scenario, the following relation based on the concept of mechanical impedance should be utilized for the structure (the spring-mass-damper system):

$$F = -Z\dot{x}, \tag{4}$$

where Z is the mechanical impedance of the SMD system given by:

$$Z = c + m\frac{\omega^2 - \omega_n^2}{\omega} i, \tag{5}$$

where i is $(-1)^{1/2}$, c the damping coefficient, m the mass, and

ω the excitation frequency. The reason for the negative sign in Eq. (4) is the same as in Eq. (2). The resonant frequency of the SMD system, ω_n, is given by:

$$\omega_n = \sqrt{K_S/m}. \tag{6}$$

Assuming a harmonic steady state excitation, recall

$$\dot{x} = \omega i x. \tag{7}$$

The force-displacement for the SMD can now be expressed as:

$$F = -K_D x = -[c\omega i - m(\omega^2 - \omega_n^2\}]x, \tag{8}$$

where K_D is called the dynamic stiffness.

In static analysis, the force-displacement relation of PZT, according to the constitutive equations, is given by Eq. (1). In the dynamic analysis, Eq. (1) is no longer adequate, the dynamic output characteristics of PZT actuators must be used, which can be determined based on a coupled electro-mechanical analysis.

Dynamic Output Characteristics of PZT Actuators. Consider the PZT actuator shown in Fig. 3. The electric field is applied in the z-direction, and it is assumed that the PZT expands and contracts only in the y-direction. The constitutive relation of the PZT of the (T, E)-type (stress and electric field as independent variables) may be expressed as follows:

$$S_2 = \bar{s}_{22}^E T_2 + d_{32} E \tag{9}$$

and

$$D_3 = \bar{\epsilon}_{33}^T E + d_{32} T_2, \tag{10}$$

where S_2 is the strain, T_2 the stress, $\bar{s}_{22}^E$ the complex compliance at zero electric field, d_{32} the piezoelectric constant, $\bar{\epsilon}_{33}^T$ the complex dielectric constant at zero stress given by $\epsilon_{33}^T(1 - \delta i)$, δ the dielectric loss factor, and D_3 the electric displacement.

The equation of motion for a PZT vibrating in the y-direction may be expressed as follows:

$$\rho \frac{\partial^2 v}{\partial t^2} = \bar{Y}_{22}^E \frac{\partial^2 v}{\partial y^2}, \tag{11}$$

where v is the displacement in the y-direction, ρ is the density of the PZT, $\bar{Y}_{22}^E = Y_{22}^E(1 + i\eta)$, is the complex modulus of PZT at zero electric field, and η is the mechanical loss factor of PZT.

Solving Eq. (11) by separating the displacement v into time and spatial domain solutions yields:

$$v = \bar{v}e^{i\omega t} = (A \sin ky + B \cos ky)e^{i\omega t}, \tag{12}$$

where

$$k^2 = \omega^2 \rho / \bar{Y}_{22}^E. \tag{13}$$

The PZT is connected to a structure which is represented by its impedance, Z. The equilibrium and compatibility relation between the structure and the PZT can be described by:

$$T_{2_{y=l_A}} = \bar{T}_{2_{y=l_A}} e^{i\omega t} = -\frac{Z\bar{v}_{y=l_A} i\omega}{w_A h_A} e^{i\omega t}. \tag{14}$$

The simplest expression for structural impedance is the one given by Eq. (5) for a one-degree-of-freedom SMD system.

Equation (14) provides one boundary condition for Eq.(12). Another boundary condition is given by $\bar{v}_{y=0} = 0$, which leads to $B = 0$.

Substituting Eq. (14) into Eq. (9) yields:

$$\bar{S}_2 = \frac{d\bar{v}}{dy}\bigg|_{y=l_A} = -\bar{S}_{22}^E \frac{Z\bar{v}_{y=l_A} i\omega}{w_A h_A} + d_{32}\bar{E}. \tag{15}$$

Note: a bar over a variable indicates its spatial component except in the case of complex material properties, such as $\bar{s}_{22}^E$ and $\bar{Y}_{22}^E$. The coefficient, A, in Eq. (12) can be solved from Eq. (15) as:

$$A = \frac{d_{32}\bar{E}}{k \cos (kl_A) + \dfrac{\bar{s}_{22}^E Zi\omega}{w_A h_A} \sin (kl_A)}. \tag{16}$$

In order to further simplify the derivation and help us to explain the physics from a point of view of impedance matching, the mechanical impedance of the PZT actuators is introduced here. If a constant force excitation is applied to a PZT actuator, such as the one shown in Fig. 3, the actuator response can be determined following the same derivation outlined in Eqs. (12) to (16). The mechanical impedance of the PZT actuator defined, as the ratio of the excitation force to the velocity response, may be expressed as:

$$Z_A = -\frac{K_A(1 + \eta i)}{\omega} \frac{kl_A}{\tan (kl_A)} i. \tag{17}$$

Note: the mechanical impedance of the actuator defined above is the short-circuit actuator impedance.

The coefficient, A, given by Eq. (16) can then be simplified as:

$$A = \frac{Z_A d_{32}\bar{E}}{k \cos (kl_A)(Z_A + Z)}. \tag{18}$$

It is necessary to mention here that the second constitutive relation of PZT Given by Eq. (10) is not used. Physically, this indicates that the power supply always satisfies the current requirement of the PZT actuators.

The output displacement of the PZT actuator and the strain and stress field, as well as the electric displacement field can then be solved as follows:

$$\bar{x} = \bar{v}_{y=l_A} = \frac{Z_A d_{32}\bar{E} l_A}{Z_A + Z} \frac{\tan (kl_A)}{kl_A}, \tag{19}$$

and the strain:

$$\bar{S}_2 = \frac{Z_A d_{32}\bar{E}}{Z_A + Z} \frac{\cos (ky)}{\cos (kl_A)}, \tag{20}$$

and the stress:

$$\bar{T}_2 = \left(\frac{Z_A}{Z_A + Z} \frac{\cos (ky)}{\cos (kl_A)} - 1\right) d_{32}\bar{Y}_{22}^E \bar{E}, \tag{21}$$

and the electric displacement field:

$$\bar{D}_3 = \frac{Z_A \bar{Y}_{22}^E d_{32}^2 \bar{E}}{Z_A + Z} \frac{\cos (ky)}{\cos (kl_A)} + (\bar{\epsilon}_{33}^T - d_{32}^2 \bar{Y}_{22}^E)\bar{E}. \tag{22}$$

The force output from the actuator (within the actuator) can be obtained from Eq. (21) as:

$$\bar{F} = w_A h_A \bar{T}_{2_{y=l_A}} = -\frac{Z}{Z_A + Z} d_{32}\bar{E}\bar{Y}_{22}^E w_A h_A. \tag{23}$$

The output characteristics of an excitation device, such as a shaker, are usually expressed in terms of its free stroke and dynamic blocking force. The free stroke of a PZT actuator, $\bar{x}_f$, can be calculated from Eq. (19) by assuming the mechanical impedance, Z, to be zero, yielding:

$$\bar{x}_f = d_{32}\bar{E} l_A \frac{\tan (kl_A)}{kl_A}. \tag{24}$$

The dynamic blocking force, $\bar{F}_b$, can be determined from Eq. (23) by assuming an infinite mechanical impedance, Z, yielding:

$$\bar{F}_b = -\bar{Y}_{22}^E d_{32}\bar{E} w_A h_A. \tag{25}$$

Equations (24) and (25) provide the dynamic output characteristics of PZT actuators. Based on Eq. (25), the dynamic blocking force of a PZT actuator is frequency independent, which is superior to shakers whose dynamic blocking force is constant in only a limited frequency range (Ewins, 1984). However, it is necessary to state that although a PZT actuator has

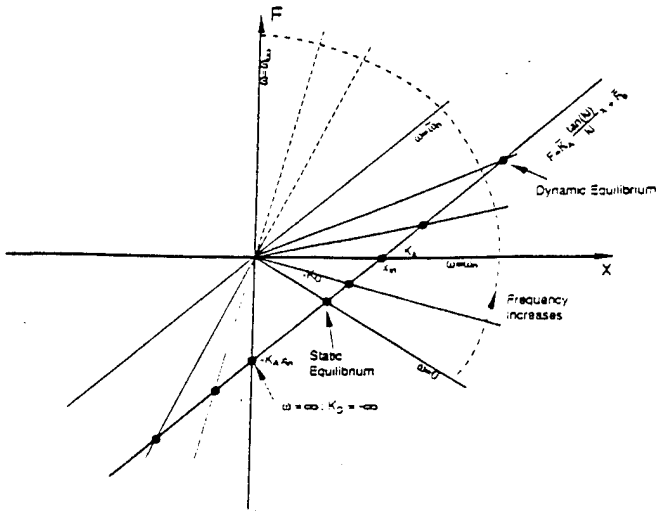

Fig. 4 The dynamic actuator and structure interaction chart (DASIC)

a "constant" dynamic blocking force, the forces acting on a structure from integrated PZT actuators are not necessarily constant. The interaction forces from the integrated actuators are functions of the structural impedance, as will be discussed later.

The free stroke of a PZT actuator is a function of frequency. At the resonance of the PZT actuator corresponding to $kl_A = (n - 1/2)\pi$, where n can be any positive integer, the displacement output for a PZT can be infinite if there is no damping (the tangent function is infinite at these values). However, as a low frequency transducer, the operating frequency range should be far below its first resonant frequency, for example, below 1/5 of the resonant frequency as a rule-of-thumb (Thomson, 1981). Thus, a PZT actuator may be treated as a constant displacement output device ($d_{32}\bar{E}l_A$). This approximation causes less than 3 percent error. For example, if the length of an actuator is 0.05 m, the Suggested Operation Frequency Range (SOFR), which is 1/5 of the first resonant frequency of the PZT actuator, will be from DC to around 2.8 kHz.

If a PZT actuator is driving a mechanical system, the output force and displacement of the PZT actuator are related. This relation can be determined by combining Eq. (19) and (23) to eliminate the structural impedance term, Z, yielding:

$$\bar{F} = K_A(1 + i\eta)\frac{\tan(kl_A)}{kl_A}\bar{x} + \bar{F}_b. \tag{26}$$

Compared with the static force-displacement relation given by Eq. (1), Eq. (26) includes structural damping and the dynamics of the actuator. If the frequency is within the SOFR, $\tan(kl_A)/kl_A$ is about 1. A PZT Actuator may be treated as a linear output device independent of frequency.

Determination of Actuator/Structure Dynamic Interaction. If the dynamic characteristics of the structure and the actuators are known, the dynamic interaction between the structure and actuator can be determined from the Dynamic Actuator/Structure Interaction Chart (DASIC), as shown in Fig. 4. In Fig. 4, the dynamic output characteristics of a PZT Actuator given by Eq. (26) are independent of frequency if the frequency is within the SOFR. The dynamic characteristics of the mechanical system as given by Eq.(8) are represented by a group of rotating lines, as shown in Fig. 4. The intersection of the rotating lines with the output characteristics of the PZT determines the dynamic response, e.g., force and stroke. Note that the damping is not included in the DASIC. When the excitation frequency is zero, the intersection of the dynamic force-displacement lines of the SMD and PZT is the same as the static response determined in Fig. 2. When the frequency increases, the F-D lines of the SMD system rotate counterclockwise around the origin of the coordinate system. The new intersection point of the F-D lines of the SMD system (nonzero frequency) and PZT actuator determines the dynamic response of the system. When the excitation frequency is the same as the resonant frequency of the SMD system, ω_n, the F-D line of SMD is coincident with the displacement axis. This indicates that the PZT actuator is free to expand and contract and the stress inside the actuator is zero, which implies that the induced force of the actuator is zero. When the excitation frequency is greater than ω_n, the mechanical displacement of the PZT actuator is larger than the free stroke, x_{in}. This indicates that the PZT actuator is stressed and deformed by the inertia of the mass and the recovery of the spring. If the excitation frequency is equal to the resonant frequency of the entire system (PZT + SMD), $\bar{\omega}_n$, which corresponds to the line parallel to the F-D relation of the PZT, the force and displacement within the actuator and spring are infinite. $\bar{\omega}_n$ can be approximated from the following expression:

$$\bar{\omega}_n = \sqrt{\frac{K_A + K_S}{m_A + m}}, \tag{27}$$

where m_A is the mass of the actuator.

If the excitation frequency is greater than $\bar{\omega}_n$, the displacement response is out-of-phase with respect to the displacement response before the frequency reaches $\bar{\omega}_n$. The dynamic equilibrium is in the third quadrant as shown in Fig. 4. If the frequency is infinite, the F-D line of the SMD is coincident with the force axis, which means that the SMD is dynamically rigid. The force provided by the actuator is the dynamic blocking force, $\bar{F}_b$. However, it is necessary to remember that the excitation frequency needs to be within the SOFR in order to use this chart. If the excitation frequency is greater than the SOFR, the variation of the actuator output characteristics needs to be considered. This can be done by rotating the F-D line of the PZT actuator clockwise around the point corresponding to the blocking force.

The actuator/structure interaction can also be explained using the concept of mechanical impedance matching in Eq. (23). If the impedance of the mechanical system is at its lowest, which corresponds to its resonance, the force provided by the PZT actuator is at its lowest. This corresponds to the case where the F-D line rotates to coincide with the displacement axis. If the structural impedance matches the actuator impedance, the actuator provides the maximum force and power. In DASIC, actuator and structure impedance matching is represented by parallel F-D lines. It is necessary to state that impedance matching between an output device and its load means that both impedances are complex conjugate.

Calculation of Structural Impedance. In order to use the impedance approach, the structural impedance corresponding to actuator loading must be calculated first. The excitation force provided by integrated actuators can be very complicated. For example, the actuation provided by a PZT actuator bonded on a beam is shear force and its distribution may be expressed with a hyperbolic tangent function (Lin and Rogers, 1992). Determination of the structural impedance corresponding to a distributed force can be very difficult. In this paper, the structural impedance of beams corresponding to two types of actuator excitation will be discussed.

Consider a beam structure with a complex modulus of elasticity $\bar{Y}_B$, mass density ρ_B, and moment of inertia over area K^2. The equation of motion for the transverse deflection $y(x, t)$ is:

$$\frac{\partial^2 y}{\partial t^2} = -\bar{c}^2K^2\frac{\partial^4 y}{\partial x^4} + \frac{p(x,t)}{\rho_B a}, \tag{28}$$

where $p(x, t)$ is the external dynamic loading, a is the cross-

sectional area of the beam, and $\bar{c}$ is the complex wave speed of the beam given by:

$$\bar{c}^2 = \frac{\bar{Y}_B}{\rho_B}. \tag{29}$$

The governing Eq. (28) is solved by expanding the transverse displacements and external loads in terms of the eigenfunctions, $\chi_m(x)$, of the beam. The applied forcing function is harmonic and can be expressed as:

$$p(x,t) = \sum_{m=1}^{\infty} P_m \chi_m(x) \exp(i\omega t), \tag{30}$$

where ω is the driving frequency and $\chi_m(x)$ can be determined based on the boundary conditions of the beam. The transverse displacements can also be expressed in terms of the eigenfunctions of the beam as:

$$y(x,t) = \sum_{m=1}^{\infty} W_m \chi_m(x) \exp(i\omega t). \tag{31}$$

The modal amplitudes, W_m, can then be solved by substituting Eqs. (30) and (31) into Eq. (28). For example, if the boundary condition of the beam is simply-supported, the modal amplitude may be determined as:

$$W_m = \frac{P_m/\rho_B a}{\bar{c}^2 k^2 \left(\frac{m\pi}{L}\right)^4 - \omega^2}, \tag{32}$$

where L is the length of the beam.

Consider a beam with two PZT actuators bonded on top and bottom. The actuators are activated out-of-phase, resulting in a pure bending excitation. The effect of the actuators can be represented by a pair of bending moments, M. If the two ends of the actuators are at ξ_1 and ξ_2, respectively, the internal moment distribution may be expressed as follows using the Delta functions:

$$m(x) = M[H(x-\xi_2) - H(x-\xi_1)] \tag{33}$$

The pressure function, $p(x)$, can be expressed with the following function as:

$$p(x) = \frac{d^2 M(x)}{dx^2} = M[\delta'(x-\xi_2) - \delta'(x-\xi_1)]. \tag{34}$$

The modal amplitudes for the pressure expression, P_m, can be calculated using the following expression:

$$P_m = \frac{\int_0^L p(x)\chi_m(x)dx}{\int_0^L \chi_m^2(x)dx}. \tag{35}$$

The modal amplitudes for the displacement expression can be calculated from Eq. (32). The equivalent rotational structural impedance corresponding to the pure bending moment of the actuators is defined to be:

$$Z_R = M/(\dot{\theta}_2 - \dot{\theta}_1) = M/(\theta_2 - \theta_1)i\omega, \tag{36}$$

where θ_1 and θ_2 are the rotation angles at ξ_1 and ξ_2, respectively, which are found by differentiating the transverse deflection with respect to x:

$$\theta_1 = \sum_{m=1}^{\infty} W_m \chi'_m|_{x=\xi_1}$$

$$\theta_2 = \sum_{m=1}^{\infty} W_m \chi'_m|_{x=\xi_2}. \tag{37}$$

The equivalent structural impedance given by Eq. (36) needs to be modified in order to be used in Eqs. (19) to (23). The interaction between the beam and actuator previously discussed may be represented by a simple system of two actuators creating pure bending moment to drive a rotational mass-spring-damper system having the same rotational impedance as given by Eq. (36), as shown in Fig. 5. The two actuators have the same length l_A, width w_A, and thickness h_A, and they are h_B apart, where h_B is the thickness of the beam. If the rotation of mass is θ, the axial displacement of either of the actuators, x, will be $\theta h_B/2$ (assuming small deformation). The dynamic force equilibrium and geometrical compatibility together may be expressed as:

$$F = [2Z_R/(h_B + h_A)^2]\dot{x} = Z\dot{x}. \tag{38}$$

The equivalent mechanical impedance determined from Eq. (38) can be directly used in Eqs. (19) to (23) to determine the stress, strain, force, displacement, and electric displacement of the PZT actuators.

For an actuator whose effect can be represented with a point loading, such as a stacked PZT actuator used in truss structures and a magnetostrictive actuator, as shown in Fig. 6, the definition of corresponding structural impedance to actuator loading can be expressed as:

$$Z = \frac{F}{\dot{x}}. \tag{39}$$

This impedance is usually determined by calculating the structural response, $\dot{x}$, corresponding to an arbitrary force, F, at the actuator location.

When calculating the structural impedance, the influence of the actuator stiffness and damping should not be included because they have been included in the impedance model through the short-circuit actuator impedance. The mass loading of the actuator, however, needs to be included in the calculation of structural impedance for surface bonded actuator configuration. This requires to solve a set of linear equations to determine the modal amplitude, W_m. The derivation of modal amplitude here, Eq. (28) to Eq.(32), ignores the effect of mass loading on the transverse vibration.

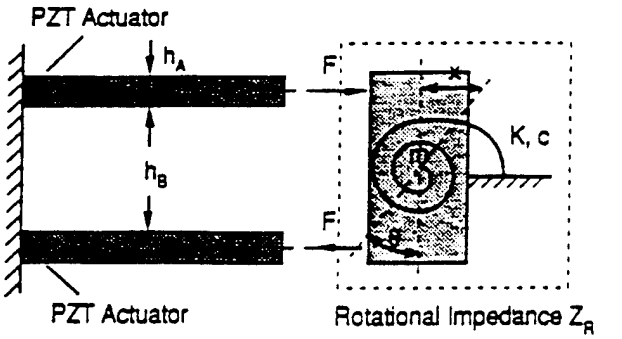

Fig. 5 A simplified model for PZT actuators bonded on beam structures

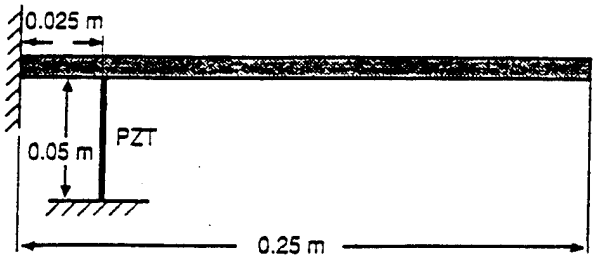

Fig. 6 A cantilever beam excited vertically by a PZT actuator with one end fixed

Table 1 Material properties of G1195 PZT (from Piezo System, Inc.)

d_{31} (m/volt)	Y_{22}^E N/m²	ρ kg/m³	ϵ_{33}^T Farads/m	δ	η
-166×10^{-12}	6.3×10^{10}	7650	1.5×10^{-8}	0.015	0.01

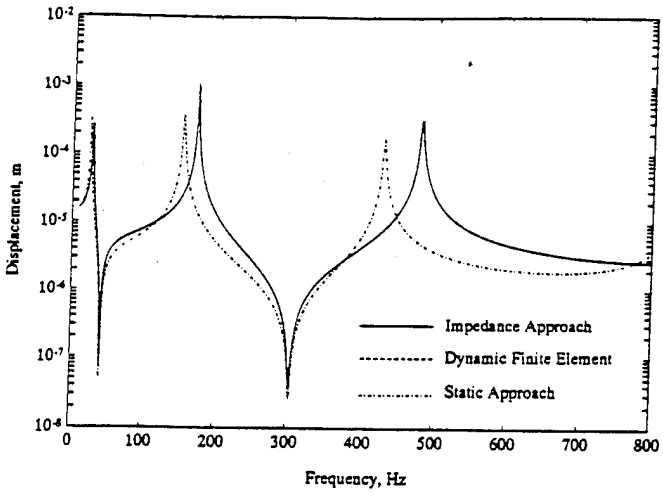

Fig. 7 The dynamic response of a cantilever beam at 0.1 m from its root. The solid line is predicted by the impedance approach. The dashed line, which is completely coincident with the solid line, is predicted by the dynamic finite element approach. The dash-dotted line is predicted by the static approach.

Determination of Structural Dynamic Response

Once the structural impedance corresponding to the actuator load is calculated, the stress within the actuators can be determined form Eq. (21). The actuator excitation, whether it is a moment or force, can then be determined. For example, if the actuators create pure bending, the excitation moment can be determined as:

$$M_A = \overline{T}_2 w_A h_A h_B. \tag{40}$$

If the magnitude of moment in Eq. (33) is assumed to be unity, the corresponding modal amplitudes can be found to be $\overline{W}_m$ from Eq. (32). The actual dynamic response of the beam can then be determined based on the following modal amplitude:

$$W_m = M_A \overline{W}_m. \tag{41}$$

Numerical Example

Figure 6 shows a cantilever beam with a PZT actuator support vertically at 0.025 m away from its root. The d_{32} effect of the actuator is utilized to generate a vertical excitation. The beam is made of aluminum with a density ρ_B = 2700 kg/m^3, elastic modulus Y_B = 60 GPa, length l_B = 0.25 m, width w_B = 0.02 m, and thickness h_B = 2 mm. The loss factor for the aluminum is assumed to be 0.005. The PZT actuator has a width w_A = 2 mm, length l_A = 0.05 m, and thickness h_A = 0.25 mm. The basic material properties for the PZT material (G1195) are listed in Table 1.

Assuming the electric voltage applied to the PZT actuator is 100 volts, the dynamic response of the beam at a point 0.1 m from the root of the beam is calculated using the static, dynamic finite element, and impedance methods, and is illustrated in Fig. 7. The solid line is from the impedance approach, which is completely coincident with the dashed line predicted using the dynamic finite element approach. The response predicted by the static approach is given by the dash-dotted line. It is apparent that the static approach fails to include the stiffening of the PZT actuator, which in this case is significant.

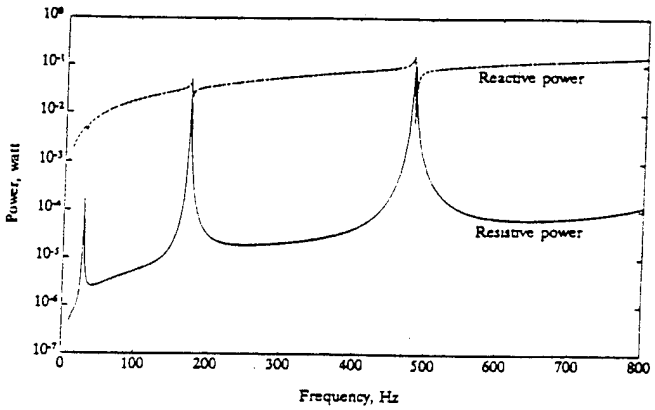

Fig. 8 Resistive (solid line) and reactive power (dashed line) supplied to the PZT actuator

The electro-mechanical power can also be calculated based on the electric displacement given by Eq. (22). The resistive and reactive power of the coupled electro-mechanical system can then be determined, as shown in Fig. 8. The resistive power represents the actuator power consumption due to the mechanical damping of the PZT actuator and the beam, as well as the dielectric loss of the PZT actuator. The reactive power reflects the transfer of the kinetic or potential energy of the entire mechanical system and the reactive electric field energy. Detailed discussion of power consumption and energy transfer can be found in previous work (Liang et al., 1992, 1993).

Experimental Validation

Rossi et al. (1993) have applied the impedance approach presented in this paper to study the dynamic response of one-dimensional cylindrical ring structures. It is very convenient to apply the impedance method to study the structural dynamic response if the structural impedance of the ring, which is similar to the impedance defined by Eqs. (36) and (38), is determined from the equation of motion of cylindrical structures. Experiments have also been conducted to verify the impedance model for shell structures. A brief discussion of the experimental results is provided here.

The test article is an aluminum ring with two bonded curved PZT actuators, as shown in Fig. 9. The out-of-plane displacements at point 1, 2, 3, and 4 are measured using a VPI (vibration pattern image) laser system. The measured velocity response and the theoretical prediction based on the impedance and static approaches at point #4 is plotted in Fig. 10. In Fig. 10, the solid line is the experimental results, the prediction using the impedance approach is given by the dashed line, and the results obtained with the static model similar to the pin-force model given by Crawley and deLuis (1989) are illustrated by the dash-dotted line. It is apparent that the results by the impedance approach agree extremely well with the experimental results while the static approach failed to accurately predict the dynamic resonse around the second and the fourth mode. The physical explanation of this phenomena can be found from the point of actuator mass loading and stiffening. Detailed discussion of these experimental results can be found in the paper by Rossi et al. (1993) as well as in the following discussion.

Discussion of the Numerical Results

What are the mechanics of active material systems? The following discussion of the simple example above will establish an understanding of the dynamic interaction between actuators

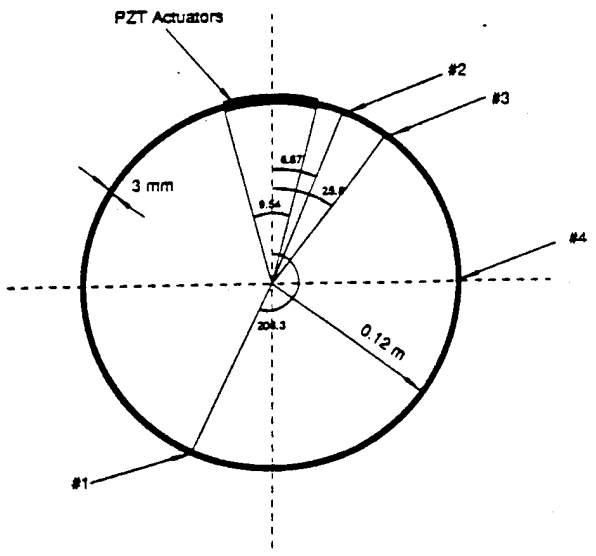

Fig. 9 An aluminum ring excited by two PZT actuators. The velocity response of the ring is measured at point #1, #2, #3, and #4 (Rossi et al., 1993)

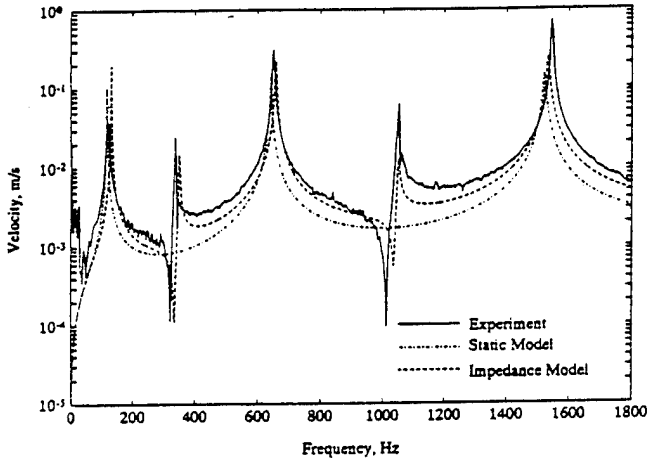

Fig. 10 Experimental measurement and theoretical prediction of the velocity response of the aluminum ring at point #4 (Rossi et al., 1993)

and their host structures. Figure 11 shows the mechanical impedance of the cantilever beam at the point of PZT Actuator support (dashed line). The mechanical impedance of the PZT actuator according to Eq. (14) is also calculated (dash-dotted line). The valleys of the mechanical impedance curve of the beam correspond to the resonances of the cantilever beam, which indicates that at the resonance, the beam is dynamically very soft. This is the reason why the force output from the PZT actuator is the lowest at the resonance of the beam, as shown by the solid line in Fig. 11. When the impedance of the actuator matches the impedance of the beam, the force output of the PZT actuator is maximum. Note: there are two intersections between the mechanical impedance curves of the PZT actuator and the beam around each peak; only the first intersection which corresponds to the complex conjugates of the impedances is physically meaningful. The frequency corresponding to the first intersection is also the resonant frequency of the entire mechanical system (beam and PZT support) as explained in DASIC.

The stiffening effect on the resonant frequency due to the extra stiffness of the PZT actuator can be determined based on the actuator and structural impedance match. If the width

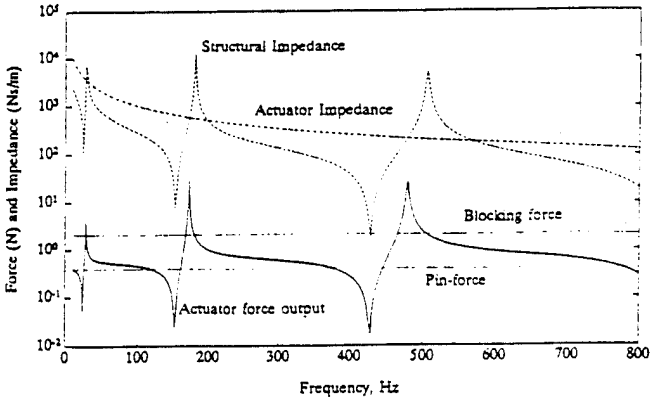

Fig. 11 Mechanical impedance of the beam at 0.1 m from the root (dashed line); mechanical impedance of the PZT actuator (dash-dotted line); force output form the PZT actuator (solid line); equivalent force used by the static approach (lower dotted line); excitation force used by the dynamic finite element approach (upper dotted line)

of the actuator in the above numerical example increases, the mechanical impedance of the PZT actuator also increases. The frequency corresponding to the first intersection around every peak of the beam impedance curve will increase, as can be seen in Fig. 11. A higher resonant frequency indicates more stiffening from the PZT actuator. When the stiffness or impedance of the PZT actuator is so high that the actuator behaves like a rigid support, the resonant frequencies are those corresponding to the peak frequencies of the beam impedance curve. This happens when the actuator impedance curve intersects at the peak or is completely above the beam impedance curve.

The force applied to the beam by the actuator, referred to as the actuator force output in this paper (which is actually the force within the actuator), is apparently not a constant, as illustrated by the solid line in Fig. 11. The lower dotted line is the equivalent force used in static analysis, as determined from Eq. (3). The difference between the two clearly indicates the incorrect physical representation of the static model. The higher dotted line in Fig. 11 is the dynamic blocking force used in the dynamic finite element approach. Using this constant force as the excitation may create confusion in explaining the physics of the dynamic interaction between actuator and structure. Notice that around the resonances of the entire system (PZT actuator and beam), which corresponds to the peaks of the PZT force curve predicted based on the impedance approach, the force inside the actuator (or the force acting on the beam provided by the actuator) can be larger than the dynamic blocking force illustrated by the higher dotted line. This has been observed experimentally and is due to the reactive nature of a vibrating system, and is clearly illustrated in DASIC. Another interesting thing to notice in Fig. 11 is that at the antiresonant frequencies of the beam, the actuator output force is the same as the dynamic blocking force. This is shown in Fig. 11 by the second intersection point between the higher dotted line and the solid line around each peak of the force curve.

The impedance approach to determining the dynamic response is very different from the other two approaches. In experimental modal analysis, the resonance of a system is determined by the frequency response function which is the ratio of the response to the excitation force. This is simply because the excitation force provided by most excitation devices, such as shakers, is not a constant for the same reason stated in this paper. Using a response resulting from a variable force tends to provide misleading results. For example, if the excitation device is a shaker, the frequency corresponding to a peak of the response curve is not the actual resonant frequency of that mode because of the extra mass loading from the shaker.

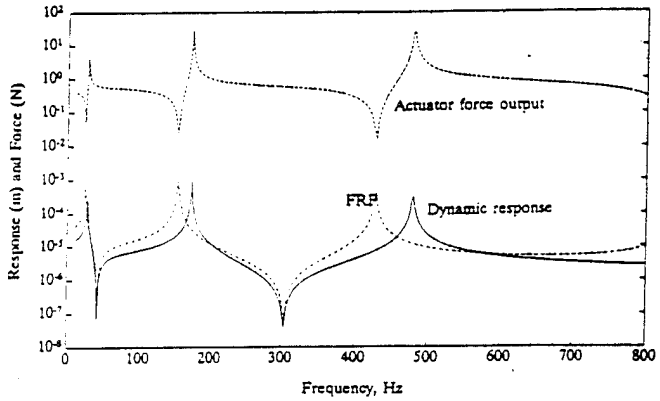

Fig. 12 Determination of the dynamic response based on the frequency response function and actuator force output. Dashed line is the actuator force output, dash-dotted line is the frequency response function (or response under unit force excitation), and the solid line is the true dynamic response predicted by the impedance approach (actuator force output times the frequency response function).

Similarly, if the excitation device is a PZT actuator which has one end fixed as in the numerical example in this paper, the peak frequencies are higher than the corresponding resonant frequencies of the original mechanical system, such as the cantilever beam in the numerical example, because of the stiffening effect. Only when the excitation force is a constant are the resonant frequencies determined from the peak frequencies equal to the true resonance frequency. In the impedance approach, the frequency response function is first calculated by using a constant unit force, the dynamic response is then determined by multiplying the frequency response function and the actual actuator force output determined from the impedance approach. This is why the response predicted by the impedance approach can accurately reflect the mechanical stiffening of the actuators. It is necessary to say that induced strain actuators do not always stiffen the original mechanical system, even in the case where bonded PZT actuators are used to excite a structure. In this case, the impedance approach can still accurately predict the influence of actuator mass loading.

To further illustrate how the impedance approach predicts dynamic response, let us examine Fig. 12 which shows the actuator force output (dashed line), the beam response (dash-dotted line) resulting from a unit force excitation (frequency response function), and the actual dynamic response (solid line) of the entire mechanical system (PZT actuator and cantilever beam). We already know from the force analysis above that the valleys of the force curve correspond to the resonant frequencies of the cantilever beam, while the peaks correspond to the resonant frequencies of the actuator and beam system. It is very clear that when multiplying the dashed line and dash-dotted line to yield the solid line, the peaks of the solid line will represent the resonance of the actuator and beam system.

Conclusions

The contribution of this paper is to introduce the impedance approach, which has been well studied in the modal analysis field, to the area of active material systems. This approach, compared with the static approach and the dynamic finite element approach, has many advantages. The most important advantage of the impedance approach is that it reflects the physical essence of the mechanics of active material systems.

The work presented in this paper provides a methodology for analyzing the dynamics of active material systems with integrated actuators. This methodology can be used with any actuators, any material systems, and any structures as long as the structural impedance corresponding to the actuator loading and the dynamic output characteristics of the actuators can be determined. This paper has also provided an approach to determining the structural impedance corresponding to two types of actuator loading. The concept of DASIC can virtually be used to describe any linear actuator/structure interaction.

This paper has used three approaches to determine the structural response. A comparison of the three approaches, static, dynamic finite element, and impedance, is provided below.

- Static approach

This approach is simple and easy to use, but it can yield very misleading results especially when the dynamic response is sensitive to actuator mass loading or stiffening. More importantly, this approach does not correctly capture the physical essence of the actuator/structure interaction in the dynamic scenario.

- Dynamic finite element approach

The dynamic finite element approach may predict correct dynamic response, but it is difficult to use this approach to explain the physical essence of the mechanics of active material systems. Since most finite element programs do not combine dynamic analysis and thermal analysis together, modifying those programs to model the induced strain actuators can also be very difficult. For large structures with small actuators, fine finite element mesh around an actuator may be needed in order to provide satisfactory convergence, which will make solving the finite element equations time-consuming and costly. It is also very difficult to use the dynamic finite element method to conduct coupled electro-mechanical analysis, such as the determination of actuator power consumption which can be easily determined with the impedance approach.

- Impedance approach

The impedance approach provides a straightforward approach to accurately determining the dynamic response of active material systems. It represents the physical essence of the interaction between actuators and structures. As a discretized method, the impedance approach can provide much more information than the other descretized method, the static approach. This approach can easily be used in the electro-mechanical analysis of an adaptive material system to determine the electrical parameters, such as actuator power consumption and system power requirement. This approach has also provided a window for studying the energy consumption and transfer in an active material system, which is a long-standing issue in the smart material system community. The stress field within a PZT actuator, including the thermal stress resulting from the heat dissipation, can also be accurately calculated using the impedance approach.

Since the actuator dynamics, i.e., the actuator force output, current, etc., are derived from generic structural interaction, the impedance method presented can be easily applied to study complicated structures. The principle of the impedance methodology can also be easily integrated into exiting computer codes. For example, a subroutine can be developed to determine the frequency-dependent force output of the actuators based on the structural impedance calculated from its main program, such as ABAQUS or NASTRAN. The corrected dynamic response can then be determined by multiplying the actuator dynamic force output with the frequency response function prediction from the main program.

Acknowledgment

This work is supported partially by Air Force Office of Scientific Research, Grant # AFOSR-91-0416 and Office of Naval Research, Grant ONR 00014-92-1170. The authors would like to thank Dr. Jim Chang from OFOSR and Dr. K. Ng from ONR for their kind assistance. The authors would also like to thank Dr. Z. Chaudhry for his valuable suggestions.

References

Crawley, E. F., and deLuis, J., 1989, "Use of Piezoelectric Actuators as Elements of Intelligent Structures," *AIAA Journal*, Vol. 25, No. 10.

Ewins, D. J., 1984, *Modal Testing: Theory and Practice*, John Wiley & Sons Inc., NY.

Ha, S. K., Keilers, C., and Chang, F. K., 1992, "Finite Element Analysis of Composite Structures Containing Distributed Piezoelectric Sensors and Actuators," *AIAA Journal*, Vol. 30, No. 3, March, pp. 772-780.

Hagood, N. W., Ching, W. H., and von Flotow, A., 1990, "Modeling of Piezoelectric Actuator Dynamics of Active Structure Control," *Proceedings, 31st SDM Conference*, Long Beach, CA, AIAA-90-697-CP.

Liang, C., and Rogers, C. A., 1989, "Behavior of Shape Memory Alloy Actuators Embedded in Composites," *Proceedings of the 1989 International Composite Conference*, Beijing, China, Aug. 1-4, pp. 475-482.

Liang, C., Sun, F. P., and Rogers, C. A., 1993, "Coupled Electric-Mechanical Analysis of Piezoelectric Ceramic Actuator Driven Systems—Determination of the Actuator Power Consumption," *Proceedings, SPIE Smart Structures and Materials '93*, Albuquerque, NM, Jan 31 to Feb. 4, pp. 286-298.

Liang, C., Sun, F. P., and Rogers, C. A., 1992, "Investigation of the Energy Transfer and Consumption of Adaptive Structures," *Proceedings, IEEE Tucson Conference*, Tucson, AZ, Dec., *in press*.

Lin, M. W., and Rogers, C. A., 1992, "Formulation of a Beam Structure with Induced Strain Actuators Based on an Approximated Linear Shear Stress Field," *Proceedings, 33rd SDM Conference*, Dallas, Texas, April 13-15, pp. 896-904.

Pan, J., Hansen, C. H., and Snyder, S. D., 1991, "A Study of the Response of a Simply-Supported Beam to Excitation by a Piezoelectric Actuator," *Proceedings, Recent Advances in Active Control of Sound and Vibration*, Blacksburg, VA, April 15-17, Technomic Publishing Co., Inc., Lancaster, PA.

Wang, B. T., 1991, "Active Control of Sound Transmission/Radiation from Elastic Plates Using Multiple Piezoelectric Actuators," Ph.D. Dissertation, Dept. of Mech. Eng., Virginia Polytechnic Institute and State University, June.

Rossi, A., Liang, C., and Rogers, C. A.., 1993, "A Coupled Electro-mechanical Analysis of PZT Actuator Driven Structures—An Application to Cylindrical Structures," *Proceedings, 34th SDM Conference*, LaJolla, CA, April 19-21, pp. 3618-3624.

Thomson, W. A., 1981, *Theory of Vibration with Application*, Prentice-Hall, Inc., Englewood Cliffs, NJ.

C-15 Coupled Electro-Mechanical Analysis of Adaptive Material Systems-Determination of the Actuator Power Consumption and System Energy Transfer, C. Liang, F. P. Sun and C. A. Rogers, Journal for Intelligent Material Systems and Structures, Vol. 5 No. 1, pp. 12-20, January 1994.

Coupled Electro-Mechanical Analysis of Adaptive Material Systems—Determination of the Actuator Power Consumption and System Energy Transfer

C. LIANG, F. P. SUN AND C. A. ROGERS
Center for Intelligent Material Systems and Structures
Virginia Polytechnic Institute and State University
Blacksburg, VA 24061-0261

ABSTRACT: This article presents a coupled electro-mechanical analysis of piezoelectric ceramic (PZT) actuators integrated in mechanical systems to determine the actuator power consumption and energy transfer in the electro-mechanical systems. For a material system with integrated PZT actuators, the power consumed by the PZT actuators consists of two parts: the energy used to drive the system, which is dissipated in terms of heat as a result of the structural damping, and energy dissipated by the PZT actuators themselves because of their dielectric loss and internal damping. The coupled analysis presented herein uses a simple model, a PZT actuator-driven one-degree-of-freedom spring-mass-damper system, to illustrate the methodology used to determine the actuator power consumption and energy flow in the coupled electro-mechanical systems. This method can be applied to more complicated mechanical structures or systems, such as a fluid-loaded shell for active structural acoustic control. The determination of the actuator power consumption can be very important in the design and application of intelligent material systems and structures and of particular relevance to designs that must be optimized to reduce mass and energy consumption.

INTRODUCTION

INTEGRATED induced strain actuators provide the energy for intelligent material systems and structures to respond adaptively to internal or external stimuli. The actuator power consumption as well as the energy transfer (from the actuator to the mechanical systems and vice versa), therefore, are very important issues in the application and design of intelligent material systems and structures. However, the research to date on energy transfer and actuator power consumption have been limited. The purpose of this article is to provide a general methodology to study the energy transfer and actuator power consumption in an intelligent material system with integrated induced strain actuators by means of a coupled electro-mechanical analysis.

Considering a plate driven by a piezoelectric ceramic (PZT) actuator powered by an electrical supply, the power consumption can be measured from a power meter connected to the PZT circuit. However, a fundamental question remains: "How is the energy being consumed?" The power consumption is related to the designated function of the plate, i.e., whether it is used for shape control, vibration, or acoustic control, as well as the associated electronic systems, including the power supply itself. In this article, we will not include the power supply system in the coupled electro-mechanical analysis by assuming that the power supply system can always satisfy the current need of the actuators. In vibration control, the energy supplied to the PZT actuators is dissipated by the structural damping in the plate and the internal damping and dielectric loss of the PZT actuator. For acoustic control, some of the energy will be used to radiate sound. In shape control, most of the energy is transferred from reactive electric energy into reactive mechanical energy (strain energy) and still stored in the electro-mechanical system. During the process of maintaining the deformed shape for the plate, the only energy consumed is resulting from the dielectric loss of the PZT actuator.

Why it is important to understand the power consumption of the integrated actuators? We shall examine the following example in active acoustic control of sound from a plate with bonded PZT actuators. In active structural acoustic control with PZT actuators, the sound pressure is linearly related to the induced force or moment from the actuators. Thus, the increase in the sound pressure level in dB is very limited with an increase in the induced force or moment from the actuators. For example, a 50% increase in the induced moment will only increase 3.5 dB in sound pressure level. However, the voltage level and the power consumption for the actuators can be significantly reduced if the original sound pressure level needs to be maintained. A 50% increase in the induced moment can reduce the voltage level by 33% and power consumption by 56%, as will be discussed later. It is clear that the mechanical optimization of an intelligent material system for active control should include minimization of power consumption as one of the primary objective functions.

1045-389X/94/01 0012-09 $6.00/0
© 1994 Technomic Publishing Co., Inc.

This article will also deal with the energy transfer between actuators and their host mechanical systems, which is the basis of active control technology. For example, considering the active vibration control of a beam, the beam is excited by an external force. At steady state, the power supplied by the external excitation force is completely consumed by the damping of the beam. The total mechanical energy of the vibrating beam (reactive in nature) includes the kinetic and elastic potential energy. When PZT actuators are bonded to the beam to change the vibration response of the beam, they will provide mostly a reactive strain energy that changes both the total amount of mechanical reactive energy and its distribution in the PZT and beam system, which is the primary cause of the variation in the dynamic response of the beam. This system energy transfer can be reflected in the reactive electric power supplied, as will be discussed in the article.

Some other benefits for having a fully-coupled model to determine the power consumption of integrated actuators and system energy transfer are:

- determination of the power supply required to operate an intelligent material system
- determination of the energy efficiency of intelligent material systems
- determination of the heat generation from the actuators, which is essential in the thermal stress analysis of induced strain actuators
- as an aid in designing energy-efficient intelligent material systems and structures
- as an aid in understanding the system energy transfer

INTRODUCTION OF THE IMPEDANCE METHOD FOR THE DYNAMIC ANALYSIS OF ACTIVE MATERIAL SYSTEMS

The electro-mechanical modeling of PZT actuator-driven systems is based on the impedance method developed recently by Liang et al. (1993a, 1993b). A brief introduction of the concept of the impedance method is presented below.

The impedance method of analyzing the dynamic response of active material systems can be simply described: the interactions between actuators and structures are governed by the dynamic output characteristics of the actuators and the dynamic characteristics of the structure, i.e., the structural impedance. The structural impedance includes mass, damping, boundary conditions, rigidity, spatial location, and acoustic impedance if fluid coupling effect needs to be included.

The dynamic interaction of a PZT/structure (Figure 1) is determined by coupling one of the constitutive relations (converse effect) of PZT and structure with their equilibrium, compatibility conditions, and the equations of motion for both the PZT actuator and the structure. The force-

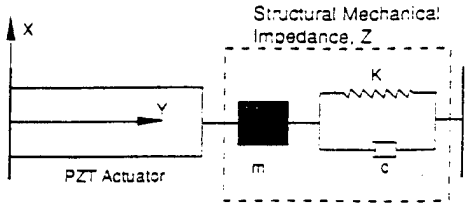

Figure 1. *A schematic illustration of a PZT actuator-driven mechanical system represented by its structural impedance (a one-degree-of-freedom spring-mass-damper system driven by a PZT actuator).*

displacement relation for the PZT actuator can be expressed as:

$$F = K_A(x - x_{in}) \tag{1}$$

where x is the displacement, F is the force exerted by the actuator, and K_A is the static stiffness of the PZT given by $Y_{22}^{E} w_A h_A / l_A$, where w_A, h_A, and l_A are the width, thickness, and length of the PZT actuator, respectively. x_{in} is the free-induced displacement of the actuator given by $d_{32} E l_A$, where d_{32} is the piezoelectric constant and E is the electric field.

In a dynamic scenario, the following relation based on the concept of mechanical impedance should be utilized for the structure (the spring-mass-damper system):

$$F = -Z\dot{x} \tag{2}$$

where Z is the mechanical impedance of the SMD system given by:

$$Z = c + m\frac{\omega^2 - \omega_n^2}{\omega} i \tag{3}$$

where i is $(-1)^{1/2}$, c is the damping coefficient, m is the mass, K_s is the spring constant, and ω is the excitation frequency. The resonant frequency of the SMD system, ω_n, is given by:

$$\omega_n = \sqrt{K_s/m} \tag{4}$$

Assuming a harmonic steady state excitation, recall

$$\dot{x} = \omega i x \tag{5}$$

The force-displacement for the SMD can now be expressed as:

$$F = -K_D x = -[c\omega i - m(\omega^2 - \omega_n^2)]x \tag{6}$$

where K_D is called the dynamic stiffness.

The dynamic interaction force between the actuator and the SMD can be determined from Equations (6) and (1) as:

$$F = -\frac{K_D K_A}{K_D + K_A} x_{in} \tag{7}$$

Since K_D is frequency dependent, the force exerting on a structure by an integrated actuator is also frequency dependent.

COUPLED ELECTRO-MECHANICAL ANALYSIS

Consider the PZT actuator shown in Figure 1. The electric field is applied in the z-direction, and it is assumed that the PZT expands and contracts only in the y-direction. The constitutive relation of the PZT of the (T,E)-type (stress and electric field as the intensive variables) may be expressed as follows:

$$S_2 = \bar{s}^E_{22} T_2 + d_{32} E \tag{8}$$

and

$$D_3 = \bar{\epsilon}^T_{33} E + d_{32} T_2 \tag{9}$$

where S_2 is the strain, T_2 is the stress, $\bar{s}^E_{22}$ is the complex compliance at zero electric field, d_{32} is the piezoelectric constant, $\bar{\epsilon}^T_{33}$ is the complex dielectric constant at zero stress given by $\epsilon^T_{33}(1 - \delta i)$, δ is the dielectric loss factor, and D_3 is the electric displacement.

The equation of motion for a PZT vibrating in the y-direction may be expressed as follows:

$$\varrho \frac{\partial^2 v}{\partial t^2} = \bar{Y}^E_{22} \frac{\partial^2 v}{\partial y^2} \tag{10}$$

where v is the displacement in the y-direction, ϱ is the density of the PZT, $\bar{Y}^E_{22} = \bar{Y}^E_{22}(1 + i\eta)$ is the complex modulus of PZT at zero electric field, and η is the mechanical loss factor of PZT.

Solving Equation (10) by separating the displacement v into time and spatial domain solutions yields:

$$v = \bar{v} e^{i\omega t} = (A \sin ky + B \cos ky) e^{i\omega t} \tag{11}$$

where

$$k^2 = \omega^2 \varrho / \bar{Y}^E_{22} \tag{12}$$

The PZT is connected to a structure which is represented by its impedance, Z. The equilibrium and compatibility relation between the structure and the PZT can be described by:

$$T_{2_{y=l_A}} = \bar{T}_{2_{y=l_A}} e^{i\omega t} = -\frac{Z \bar{v}_{y=l_A} i\omega}{w_A h_A} e^{i\omega t} \tag{13}$$

The simplest expression for structural impedance is the one given by Equation (3) for a one-degree-of-freedom SMD system.

Equation (13) provides one boundary condition for Equation (11). Another boundary condition is given by $\bar{v}_{y=0} = 0$, which leads to $B = 0$.

Substituting Equation (13) into Equation (8) yields:

$$\bar{S}_2 = \left.\frac{d\bar{v}}{dy}\right|_{y=l_A} = -\frac{-\bar{s}^E_{22} Z \bar{v}_{y=l_A} i\omega}{w_A h_A} + d_{32} \bar{E} \tag{14}$$

Note: a bar over a variable indicates its spatial component, except in the case of complex material properties, such as $\bar{s}^E_{22}$ and $\bar{Y}^E_{22}$. The coefficient, A, in Equation (11) can be solved from Equation (14) as:

$$A = \frac{d_{32} \bar{E}}{k \cos(kl_A) + \dfrac{\bar{s}^E_{22} Z i\omega}{w_A h_A} \sin(kl_A)} \tag{15}$$

In order to further simplify the derivation and help explain the physics from a point of view of impedance matching, the mechanical impedance of the PZT actuators is introduced here. If a constant force excitation is applied to a PZT actuator (such as the one shown in Figure 1) in the y-direction, the actuator response can be determined following the same derivation outlined in Equations (11) to (15). The mechanical impedance of the PZT actuator, defined as the ratio of the excitation force to the velocity response, may be expressed as:

$$Z_A = \frac{K_A(1 + \eta i)}{\omega} \frac{kl_A}{\tan(kl_A)} i \tag{16}$$

Note: the mechanical impedance of the actuator defined above is based on the assumption that the PZT actuator behaves like a passive material and has no electric coupling.

The coefficient, A, given by Equation (15) can then be simplified as:

$$A = \frac{Z_A d_{32} \bar{E}}{k \cos(kl_A)(Z_A + Z)} \tag{17}$$

The output displacement of the PZT actuator and the strain and stress field, as well as the electric displacement field, can then be solved as follows:

$$\bar{x} = \bar{v}_{y=l_A} = \frac{Z_A d_{32} \bar{E} l_A}{Z_A + Z} \frac{\tan(kl_A)}{kl_A} \tag{18}$$

the strain:

$$\bar{S}_2 = \frac{Z_A d_{32} \bar{E}}{Z_A + Z} \frac{\cos(ky)}{\cos(kl_A)} \tag{19}$$

the stress:

$$\bar{T}_2 = \left(\frac{Z_A}{Z_A + Z} \frac{\cos(ky)}{\cos(kl_A)} - 1\right) d_{32} \bar{Y}^E_{22} \bar{E} \tag{20}$$

the electric displacement field:

$$\bar{D}_3 = \frac{Z_A \bar{Y}^E_{22} d^2_{32} \bar{E}}{Z_A + Z} \frac{\cos(ky)}{\cos(kl_A)} + (\bar{\epsilon}^E_{22} - d^2_{32} \bar{Y}^E_{22}) \bar{E} \quad (21)$$

The electric current is calculated using

$$I = i\omega \int\int D_3 dx dy \quad (22)$$

which yields:

$$I = \bar{I} e^{i\omega t} \quad (23)$$

where

$$\bar{I} = i\omega \bar{E} w_A l_A \left(\frac{d^2_{32} \bar{Y}^E_{22} Z_A}{Z + Z_A} \frac{\tan(kl_A)}{kl_A} + \bar{\epsilon}^T_{33} - d^2_{32} \bar{Y}^E_{22} \right) \quad (24)$$

Since the electric field is expressed as $E = V/h_A$, the admittance, $Y = I/V$, is then found as

$$Y = i\omega \frac{w_A l_A}{h_A} \left(\frac{d^2_{32} \bar{Y}^E_{22} Z_A}{Z + Z_A} \frac{\tan(kl_A)}{kl_A} + \bar{\epsilon}^T_{33} - d^2_{32} \bar{Y}^E_{22} \right) \quad (25)$$

Because $\tan(kl_A)/kl_A$ is close to one in the frequency range of interest in most applications of intelligent materials, Equation (25) may be further simplified as:

$$Y = i\omega \frac{w_A l_A}{h_A} \left(\bar{\epsilon}^T_{33} - \frac{Z}{Z_A + Z} d^2_{32} \bar{Y}^E_{22} \right) \quad (26)$$

It is clear that the coupled electro-mechanical admittance includes the capacitance of the PZT material and mechanical interaction expressed by the mechanical impedance terms. The resonance of the electro-mechanical system occurs when the actuator impedance, Z_A, and structural impedance, Z, match (complex conjugate).

ELECTRICAL POWER ASSOCIATED WITH AN ACTUATOR-DRIVEN MECHANICAL SYSTEM

If a voltage, $V = v \sin(\omega t)$, is applied to a load, the current measured in the circuit is $I = i \sin(\omega t + \phi)$. The voltage and current are related by the admittance, $Y = \mathrm{Re}(Y) + i\,\mathrm{Im}(Y)$, of the load. There are three types of electric power defined as follows:

The apparent power, W_A:

$$W_A = I_r V_r = \frac{v^2}{2} |Y| \quad (27)$$

where I_r and V_r are the RMS current and voltage, respectively.

The dissipative power, W_D:

$$W_D = W_A \cos\phi = \frac{v^2}{2} \mathrm{Re}(Y) \quad (28)$$

The reactive power, W_R:

$$W_R = W_A \sin\phi = \frac{v^2}{2} \mathrm{Im}(Y) \quad (29)$$

The apparent power is the power supplied to the induced strain actuators. The dissipative power, as implied by its name, is the power transformed into other energy forms, such as heat, sound, and mechanical energy. The reactive power, however, remains and flows within the system. The reactive power consists of mechanical reactive power related to the mass (kinetic energy), spring (potential strain energy), and electric reactive power (electric and magnetic field energy of capacitors and inductors).

The power consumption of an induced strain actuator includes:

- power consumed by the actuator in terms of heat due to the resistive admittance of the actuator materials themselves. The resistive admittance for a PZT actuator comes from the mechanical friction and dielectric loss of PZT materials.
- power dissipated in the mechanical structure. This power is eventually dissipated into heat in the structure. Reflected in the model is the electric power consumption due to the structural damping coefficient.
- power used to radiate sound. This power can be represented in the electric admittance in terms of the resistive part from the acoustic impedance.

The power consumption of an induced strain actuator driven by a constant voltage source is a variable because of the variation of $\mathrm{Re}(Y)$ as a function of frequency. In order to maintain a constant voltage supply for the PZT actuator at various frequencies, the power requirement, i.e., the minimum power rating of the voltage source, should be no less than the following value over the frequency of interest:

$$W_{\text{rating}} = \frac{v^2}{2} \max(|Y|) \quad (30)$$

which represents the maximum power over the frequency range that the actuators are expected to operate.

The real admittance includes two parts: part one is from the damping of the mechanical systems and the other part is from the internal loss of the induced strain actuators (dielectric loss and mechanical loss for a PZT actuator). The power consumption due to the damping of the mechanical systems is useful in driving the mechanical systems, while the power due to the internal loss of the induced strain actuators is dissipated in terms of heat generated in the actua-

tors, an essential quantity in the thermal stress analysis of the system. The energy efficiency of the actuator in driving the system, therefore, should be defined as:

$$\phi = \frac{\mathrm{Re}(Y_s)}{|Y_s|} \tag{31}$$

where Y_s is the coupled electro-mechanical admittance resulting from the mechanical loss of the mechanical system, which may be obtained approximately from Equation (26) by assuming zero dielectric loss and internal damping for the PZT actuators. This energy efficiency of the actuator is similar to the power factor (defined as the ratio of the real power to the total power) in electrics. Similarly, Y_a is defined as the coupled electro-mechanical admittance for the PZT actuator, which can be calculated from Equation (26) by assuming zero structural damping. The heat dissipation of the actuator because of its internal loss can then be expressed as

$$Q = \frac{V^2\,\mathrm{Re}(Y_a)}{2} \tag{32}$$

POWER CONSUMPTION AND SYSTEM ENERGY TRANSFER OF BEAM STRUCTURES DRIVEN BY PZT ACTUATORS

In order to determine the actuator power consumption and system energy transfer of a continuous system, such as a beam, driven by PZT actuators, the structural impedance corresponding to actuator loading must first be calculated. The excitation force provided by integrated actuators can be very complicated. For example, the actuation provided by a PZT actuator bonded on a beam is shear force and its distribution may be expressed with a hyperbolic tangent function (Lin and Rogers, 1992). Determination of the structural impedance corresponding to a distributed actuator loading can be very difficult. In this article, the structural impedance of beams corresponding to two types of actuator excitation will be introduced. Detailed discussion can be found in Liang et al. (1993a).

Consider a beam with two PZT actuators bonded on the top and bottom. The actuators are activated out-of-phase, resulting in a pure bending excitation. The effect of the actuators can be represented by a pair of bending moments, M. If the two ends of the actuators are at ξ_1 and ξ_2, respectively, the equivalent rotational structural impedance corresponding to the pair of the pure bending moment of the actuators is defined to be:

$$Z_R = M/(\dot{\theta}_2 - \dot{\theta}_1) = M/(\theta_2 - \theta_1)i\omega \tag{33}$$

where θ_1 and θ_2 are the rotation angles at ξ_1 and ξ_2, respectively, which are found by differentiating the transverse deflection with respect to x.

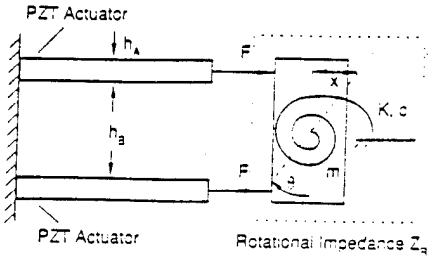

Figure 2. *A simplified model for PZT actuators bonded on a beam structure.*

The equivalent structural impedance given by Equation (33) needs to be modified in order to be used in Equations (17) to (26). The interaction between the beam and actuator previously discussed may be represented by a simple system of two actuators creating a pure-bending moment to drive a rotational mass-spring-damper system having the same rotational impedance as given by Equation (33), as shown in Figure 2. The two actuators have the same length l_A, width w_A, and thickness h_A, and they are h_B apart, where h_B is the thickness of the beam. If the rotation of mass is θ, the axial displacement of either of the actuators, x, will be $\theta h_B/2$ (assuming small deformation). The dynamic force equilibrium and geometrical compatibility together may be expressed as:

$$F = [2Z_R/(h_B + h_A)^2]\dot{x} = Z\dot{x} \tag{34}$$

The equivalent mechanical impedance determined from Equation (34) can be directly used in Equations (17) to (26) to determine the stress, strain, force, displacement, and electric displacement (current) of the PZT actuators, as well as the coupled electro-mechanical admittance of the active material systems.

For an actuator whose effect can be represented with a point loading, such as a stacked PZT actuator used in truss structures and a magnetostrictive actuator used as active mount, the definition of corresponding structural impedance to actuator loading can be expressed as:

$$Z = \frac{F}{\dot{x}} \tag{35}$$

This impedance is usually determined by calculating the structural response, $\dot{x}$, corresponding to an arbitrary force, F, at the actuator location. Note that when calculating the structural impedance, only the influence of the actuator mass needs to be included.

Once the structural impedance corresponding to the actuator loading is determined, it can be substituted into Equation (26) to determine the coupled electro-mechanical admittance and related to the actuator power consumption and

Table 1. Material properties of G1195 PZT (from Piezo System, Inc.)

d_{32} (m/volt)	Y^E_{22} (N/m²)	ϱ (kg/m³)	ϵ^T_{33} (farads/m)	δ	η
-166×10^{-12}	6.3×10^{10}	7650	1.5×10^{-8}	0.012	0.001

system energy transfer if the voltage applied to the PZT actuator is known.

NUMERICAL EXAMPLES AND DISCUSSION

Consider a PZT of length l_A = 5.08 cm (2 in), width w_A = 2.54 cm (1 in), and thickness h_A = 0.2 cm (0.079 in) driving a one-degree-of-freedom spring-mass-damper system. The material properties of the PZT are listed in Table 1.

The natural frequency of the spring-mass-damper system is 500 Hz. Mass, m, is assumed to be 2 kg with a damping, ξ, of 0.01. The damping constant, c, is calculated using $c = 2\xi m\omega_n$ to be 125.7 N/ms^{-1}.

Figure 3 shows the coupled electro-mechanical admittance, including the real, imaginary, and absolute values of the actuator-driven SMD system. The imaginary admittance is almost the same as the absolute value, indicating the strong reactive nature of the coupled electro-mechanical system. However, around the resonance of the system (PZT and spring-mass-damper), its resistive aspect becomes as significant as the reactive aspect of the system.

The absolute value of the mechanical impedance of the SMD system, Z, and the actuator mechanical impedance, Z_A, are plotted in Figure 4. The resonance of the SMD is at

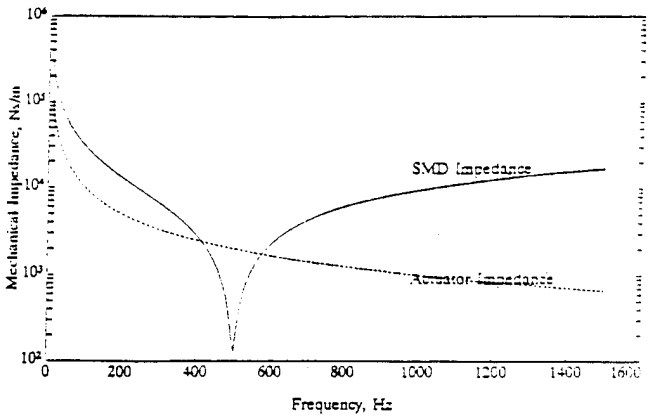

Figure 4. *The mechanical impedance of the PZT actuator and SMD system.*

500 Hz, as indicated by the minimum of its impedance curve. The actuator impedance matches the SMD impedance at two frequencies, but only the one at around 580 Hz is a complex conjugate of the SMD impedance. Therefore, the PZT actuator outputs the maximum current, as well as power, at this frequency as illustrated in Figure 3 and Equations (24) and (25).

The results shown in Figure 5 illustrate how the power supplied to the system is consumed. The real admittance is divided into three parts. One part (dotted line) results from the mechanical loss of the PZT materials. This is calculated by assuming zero structural damping and dielectric loss for the PZT. Since a loss factor of 0.1% represents that 0.62% ($2\pi \times 0.1\%$) of the strain energy being transferred into the thermal energy, the special pattern of the dotted line (minimum at 500 Hz and maximum at 580 Hz) can be explained as follows. From Equations (19) and (20), the strain energy

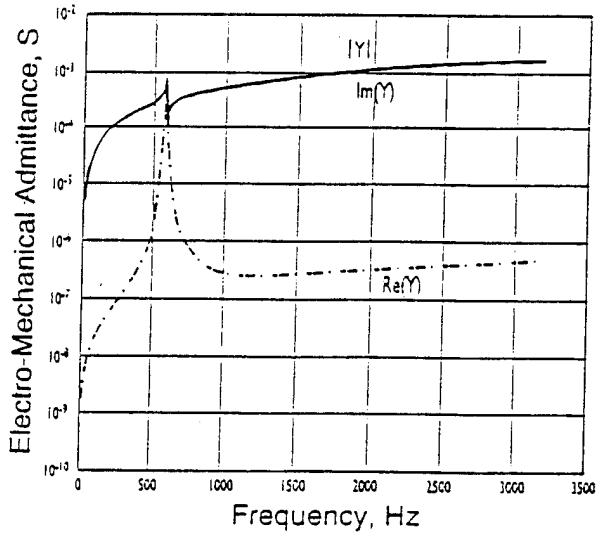

Figure 3. *The coupled electro-mechanical admittance of the PZT actuator-driven spring-mass-damper system.*

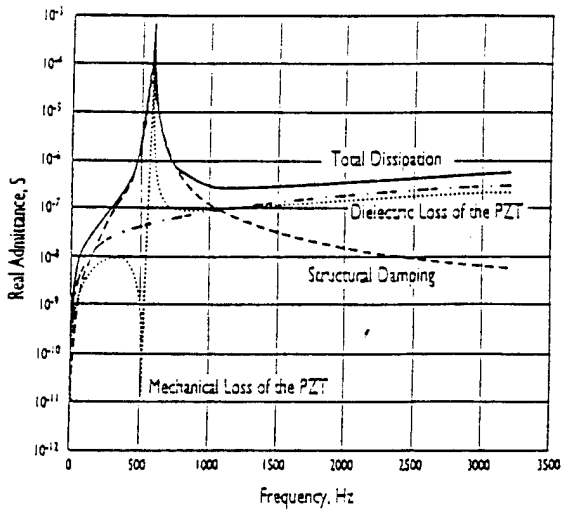

Figure 5. *The real part of the coupled electro-mechanical admittance illustrating how the electrical power is being consumed.*

density, U, of the PZT actuator as a function of frequency can be determined as:

$$U = -\frac{Z_A Z}{(Z_A + Z)^2} d_{32}^2 \bar{Y}_{22}^E \bar{E}^2 \tag{36}$$

Note that $\cos(ky)/\cos(kl_A)$ is assumed to be unity in the above equation if the actuator length is much smaller than the wave length of the PZT actuator oscillating in the y-direction. At the resonance of the SMD system (500 Hz and minimum impedance, Z), the strain energy is minimum, which results in minimum mechanical dissipation of the PZT actuator. When the actuator impedance and SMD impedance matches (580 Hz), i.e., the denominator of the strain energy density, $Z_A + Z$, becomes very close to zero and the actuator stores the maximum amount of strain energy, which inevitably yields more mechanical loss.

The second part (dash-dotted line in Figure 5) results from the dielectric loss. It is calculated by assuming zero mechanical loss for the PZT and the spring-mass-damper system. The third part results from the structural damping, which has a maximum at the resonance of the entire system. The solid line is the entire real admittance as a result of entire dissipation in the mechanical system and PZT actuator. The entire real admittance may also be approximately calculated by summing the individual real admittance.

Figure 6 shows the actuator efficiency according to Equation (31). Piezoelectric materials have an electro-mechanical efficiency which indicates the energy transfer rate between the stored strain and electrical energy; however, it is only a material index and cannot be used to evaluate the effectiveness of piezoelectric actuators integrated in a mechanical material system. The actuator efficiency defined by Equation (31) indicates the amount of the energy dissipated due to the structural damping, i.e., the effectiveness of the actuator to excite the mechanical system. It is always true that the actuator becomes the most efficient when the actuator impedance matches the structural impedance. For a continuous system, there will be many peaks corresponding to

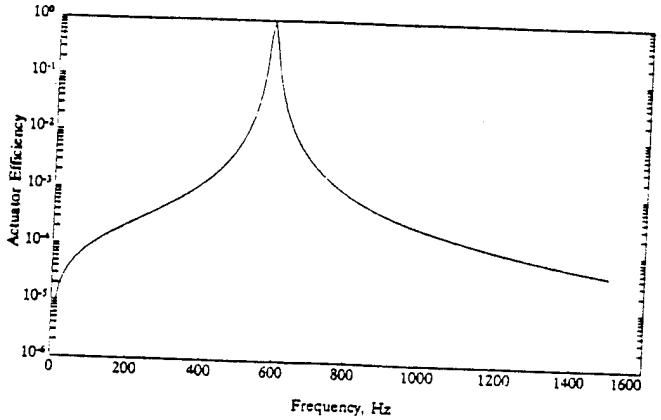

Figure 6. The efficiency of the PZT actuator in driving the spring-mass-damper system.

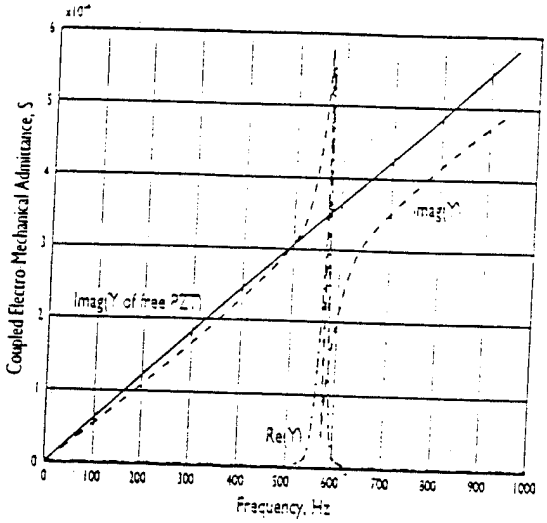

Figure 7. The imaginary part of the coupled electro-mechanical admittance illustrating the energy transfer in the PZT actuator-driven SMD system.

the natural vibration mode of the system. The height of a peak indicates the effectiveness of the actuator to excite that mode. The actuator efficiency defined in this article can be used in the optimal design of actuator configuration (actuator impedance) and location.

How is the energy being exchanged and transferred in a coupled electro-mechanical system? It is necessary to analyze the reactive energy of the system. Figure 7 shows the imaginary part of the coupled electro-mechanical admittance of the system. The solid line is the imaginary admittance of a freely vibrating PZT, which is calculated from Equation (26) by assuming the mechanical impedance, Z, to be zero. It is almost a straight line in the frequency range plotted, which is purely capacitive in nature. The dashed line is the imaginary admittance of the coupled electro-mechanical admittance. It is slightly smaller than that of the free PZT before 500 Hz. At 500 Hz (the resonant frequency of the spring-mass-damper system), the PZT is vibrating "freely" because the spring-mass-damper system has the lowest structural impedance at this frequency. Therefore, the admittance of the PZT + mechanical system is the same as the free PZT at 500 Hz. The imaginary system admittance then increases sharply and reaches its maximum at the system resonant frequency (the resonant frequency of the PZT and SMD system, which includes the stiffening of the PZT, or the frequency at which the strucutral impedance becomes a complex conjugate of the actuator impedance). This sharp increase physically represents the increase of the reactive mechanical energy of the system (kinetic and potential energy) at its resonance at which the kinetic or potential energy is the largest. When the frequency is slightly greater than the system resonant frequency, the reactive power of the system is at its minimum (negative maximum since the force and velocity are out-of-phase) because of the superposition of the reactive admittance of the PZT as a capacitor.

The PZT may have a deformation greater than its maximum induced deformation, or the stress within the PZT can be several times larger than the blocking stress (Liang et al., 1993a, 1993b). These are associated with the reactive energy of the mechanical system, which constantly changes between kinetic and potential energy, but is stored in the system. To maintain this large amplitude vibration around the system resonant frequency, the external power source needs to input more power. This is represented by the increased power consumption (real admittance), as shown by the dash-dotted line in Figure 7. The real admittance reaches its maximum at the system resonant frequency where the mechanical reactive admittance is zero (zero crossing point between the dashed and solid line other than at 500 Hz).

How can the reactive mechanical energy be reflected by the imaginary admittance? To answer this question, we shall examine the second constitutive relation of PZT given by Equation (9). It may be rewritten in the following form:

$$D_3 = \epsilon_{33}^T (E + E_R) \tag{37}$$

where E_R is referred to as the reactive field generated across the PZT actuator as a result of the external stress applied to the PZT, which is given by:

$$E_R = \frac{d_{32}}{\epsilon_{33}^T} T \tag{38}$$

It is because of the reactive field that the reactive mechanical energy is reflected in the coupled electro-mechanical admittance. This strongly suggests that both the piezoelectric and its converse effect are coupled in the actuator application (as well as sensor application) of piezoceramics.

The difference in the solid and dashed lines in Figure 7 represents the electric and strain energy transfer in the PZT actuator. In most cases, the electrical energy of the PZT actuator is converted into the strain energy that interacts with the SMD system (converse piezoelectric effect). However, from 500 to 580 Hz, the SMD operates on the PZT actuator and energy is converted from strain energy into the electrical energy (the piezoelectric effect).

EXPERIMENTAL VERIFICATIONS

Experiments have been conducted to verify the coupled electro-mechanical model presented in this article. A brief introduction of the experiment and its results is provided here. Detailed discussion of the experimental results and the theoretical model will be published later. In this experiment, two PZT actuators are bonded at the end of an aluminum cantilever beam. An HP 4194A Impedance/Gain-Phase Analyzer is used to measure the coupled electro-mechanical admittance, as shown in Figure 8. Theoretical analysis

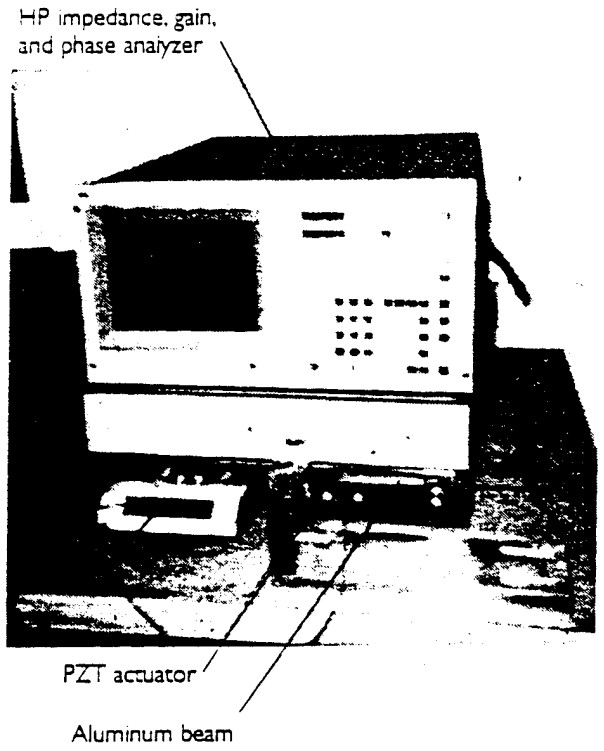

Figure 8. *The experiment apparatus, an aluminum cantilever beam with bonded PZT actuators and an HP Impedance/Gain-Phase Analyzer.*

based on the model presented in this article has also been conducted. The experimental and theoretical coupled electro-mechanical admittance are shown in Figure 9a and 9b. The experimental results (dashed lines) agree with the theoretical predictions (solid lines) well.

The electrical admittance of a plain PZT actuator (same material as used to excite the beam) was measured, which provided the dielectric constant and dielectric loss factor. The dielectric constant of the PZT measured with the HP analyzer is 18% less than the value suggested by the manu-

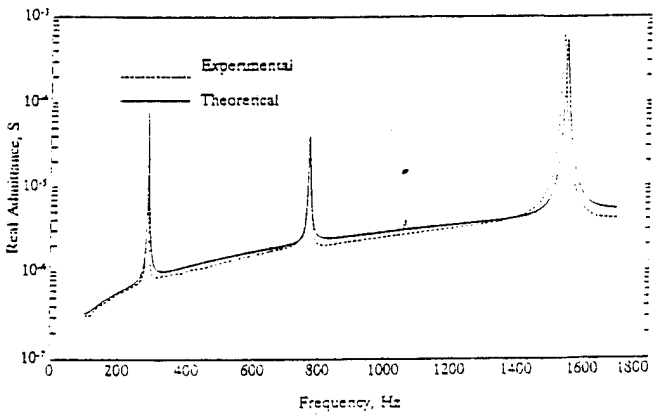

Figure 9a. *The real part of the measured and predicted coupled electro-mechanical admittance.*

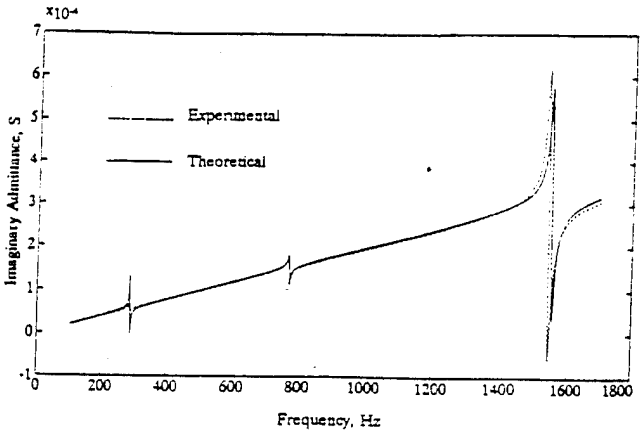

Figure 9b. *The imaginary part of the measured and predicted coupled electro-mechanical admittance.*

facturer. The mechanical loss factor of the PZT was estimated as 0.005. The measured properties of the PZT have been used in the theoretical prediction. Other material properties of the PZT actuators used in the analytical model are the same as those listed in Table 1.

The real part of the coupled electro-mechanical admittance is shown in Figure 9a. The total dissipative power can be obtained from this chart by multiplying the real admittance by the voltage squared over 2. The HP Analyzer cannot distinguish the power consumption due to the internal loss of the actuator and the mechanical loss of the beam, while the theoretical model may provide an approximation of how the energy is being consumed, as shown in Figure 10. The coupled admittance illustrated by the dash-dotted line results from the mechanical loss of the beam. The coupled admittance illustrated by the dashed line is due to the internal loss of the actuator. The solid line represents the total loss of the system, which can also be calculated approximately by summing the dashed and dash-dotted line.

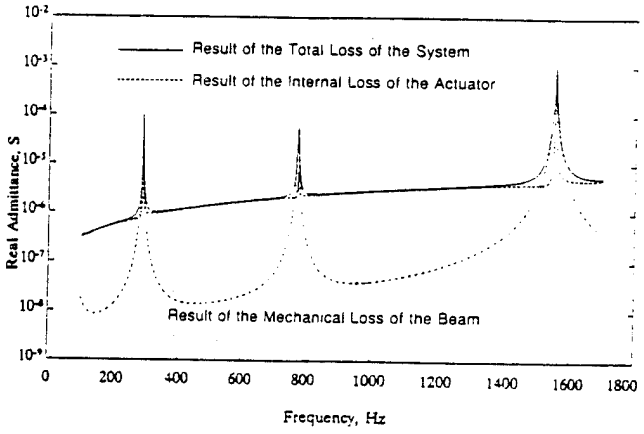

Figure 10. *Theoretical prediction on how the power is consumed by the PZT actuator-driven aluminum cantilever beam.*

SUMMARY

This article describes a coupled electro-mechanical approach to analyze the energy transfer and consumption of active systems using a simple example, a PZT actuator-driven one-degree-of-freedom spring-mass-damper system. The theoretical model has also been validated by experiment. The coupled electro-mechanical model can be applied easily to a continuous mechanical system provided that the structural impedance corresponding to the actuator load is determined. The numerical examples and discussions illustrate the relations of the various types of energy inside the mechanical system, as well as how power is consumed in an active material system. This analysis method can be extended to other types of actuator-driven systems, i.e., systems with integrated magnetostrictive and electrostrictive actuators. This analysis will assist in understanding the mechanisms of active material systems and structures and enable design of energy efficient smart material systems. In summary, this article has

- developed a coupled electro-mechanical analysis methodology to determine the actuator power consumption and energy transfer in an active material system
- demonstrated the utility of this method in the power consumption and energy transfer analysis with a simple PZT actuator-driven spring-mass-damper system

ACKNOWLEDGEMENT

The authors would like to acknowledge the support of the Office of Naval Research, Grant ONR 00014-92-J-1170.

REFERENCES

Carlson and Gisser. 1981. *Electrical Engineering*. California: Addison-Wesley.

Crawley, E. F. and J. deLuis. 1989. "Use of Piezoelectric Actuators as Elements of Intelligent Structures", *AIAA Journal*, 25(10).

Ikeda. 1990. *Fundamentals of Piezoelectricity*. New York: Oxford University Press.

Ha, S. K., C. Keilers and F. K. Chang. 1992. "Finite Element Analysis of Composite Structures Containing Distributed Piezoelectric Sensors and Actuators", *AIAA Journal*, 30(3):772-780.

Liang, C., F. P. Sun and C. A. Rogers. 1993a (in press). "An Impedance Method for Dynamic Analysis of Active Material Systems", accepted by *ASME Journal of Vibration and Acoustics*, also in *Proceedings, 34th SDM Conference, LaJolla, CA, April 19-21, 1993*, pp. 3587-3599.

Liang, C., F. P. Sun and C. A. Rogers. 1993b (in press). "Dynamic Output Characteristics of Piezoceramic Actuators", *SPIE's 1993 North American Conference on Smart Structures and Materials, Albuquerque, NM, February 1-4, 1993.*

Lin, M. A. and C. A. Rogers. 1992. "Formulation of a Beam Structure with Induced Strain Actuators Based on an Approximated Linear Shear Stress Field", *Proceedings, 33rd SDM Conference, Dallas, Texas, April 13-15, 1992*, pp. 896-904.

C-16 Optimal Placement of Piezoelectric Actuators for Active Structural Acoustic Control, B.-T. Wang, R. A. Burdisso and C. R. Fuller, Journal of Intelligent Material Systems and Structures, Vol. 5, pp. 67-71, January 1994.

Optimal Placement of Piezoelectric Actuators for Active Structural Acoustic Control

BOR-TSUEN WANG*
Department of Mechanical Engineering
National Pingtung Polytechnic Institute
Pingtung, Taiwan 91207, R.O.C.

RICARDO A. BURDISSO AND CHRIS R. FULLER
Vibration and Acoustics Laboratories
Department of Mechanical Engineering
Virginia Polytechnic Institute and State University
Blacksburg, VA 24061

ABSTRACT: This paper presents a general formulation of the optimization problem for the placement and sizing of piezoelectric actuators in adaptive LMS control systems. The selection of objective function, design variables and physical constraints are separately discussed. A case study for the optimal placement of multiple fixed size piezoelectric actuators in sound radiation control is presented. A solution strategy is proposed to calculate the applied voltages to piezoelectric actuators with the use of linear quadratic optimal control theory which is to simulate the LMS feedforward control algorithm. The location of piezoelectric actuators is then determined by minimizing the objective function, which is defined as the sum of the mean square sound pressure measured by a number of error microphones. The optimal location of piezoelectric actuators for sound radiation control is determined and shown to be dependent on the excitation frequency. Particularly, the optimal placement of multiple piezoelectric actuators for on-resonance and off-resonance excitation is presented. The results show that the optimally located piezoelectric actuators perform far better sound radiation control than arbitrarily selected ones. This work leads to a design methodology for adaptive or intelligent material systems with highly integrated actuators and sensors. The optimization procedure also leads to a reduction in the number of control transducers.

INTRODUCTION

PIEZOELECTRIC actuators have been widely used in structural sound and vibration control. Wang and Rogers (1991a, 1991b) presented the theoretical analysis of the mechanics of piezoelectric actuators, and Wang et al. (1991) demonstrated their potential as transducers in structural sound control. However, the proper selection of number and location of piezoelectric actuators is critical to efficiently control structural sound radiation. Therefore, the determination of the optimal placement and number of piezoelectric actuators in sound radiation control is an important and interesting issue.

However, previous works on optimal placement of actuators are mostly concerned with vibration control and particularly for feedback control systems with the use of traditional force transducers, such as point force shakers (Norris and Skelton, 1989; Chang and Soong, 1980; Hamidi and Juang, 1981; Juang and Rodriguez, 1979; Chen and Seinfeld, 1975). For state feedback control, a state space equation is first constructed to represent the system model, and a performance index, which is a quadratic form in the state and control effort, can then be defined. Finally, the optimal location is to be determined by minimizing the performance index. Only a few literatures deal with the optimal location of distributed actuators, which are widely used in conjunction with so-called "smart" structures. Jia (1990) studied the optimal position of piezoelectric actuators for beam vibration control by adopting the independent modal space control approach (IMSC). Jia showed that the optimal location and size of piezoelectric actuators can be found by minimizing an objective function which can be either the structural response, control effort, residual response, spillover effect or combinations of all/any of these variables. However, Jia's work is limited to consider only one-dimensional vibration control.

Adaptive feedforward control, on the other hand, has been adopted for structural sound radiation control in recent years (Gibbs and Fuller, 1992; Burdisso and Fuller, 1992; Simpson et al., 1992). The control algorithm is flexible because it is not as crucial as feedback approaches to ac-

*Author to whom correspondence should be addressed.

1045-389X/94/01 0067-11 $6.00/0
© 1994 Technomic Publishing Co., Inc.

curately model the system response. The adaptive feedforward controller can learn the system parameters by itself and converge to the optimal solution using various "training" approaches. However, little work has been discussed on the optimal placement of actuators, particularly distributed in nature, for feedforward control. This paper is thus concerned with the formulation of the optimization problem for the placement of piezoelectric actuators in feedforward control systems, in particular for the ASAC technique.

In this paper, a general formulation for the optimal placement of piezoelectric actuators in a feedforward control approach is first presented and then applied to a typical sound radiation control system using piezoelectric actuators and microphone sensors. A baffled, simply-supported, rectangular plate as shown in Figure 1 is considered as an idealized system. The plate is harmonically excited by a primary source (point force), and piezoelectric actuators are applied to control the plate vibration in order to reduce the associated sound radiation into a free field. The objective here is to determine the optimal location of piezoelectric actuators such that the sound pressure measured from the error microphones can be most efficiently reduced (i.e., with the lowest actuator power and/or number of actuators). A solution strategy is proposed to calculate the applied voltages to piezoelectric actuators with the use of linear quadratic optimal control theory (Wang, 1991). The location of the piezoelectric actuator(s) is then determined by minimizing the objective function, which is defined as the sum of the mean square sound pressure measured by a number of error microphones. The optimal locations for multiple piezoelectric actuators, up to three, were considered. The results show that the optimally placed actuators achieve a far better reduction of sound radiation than actuators whose positions are arbitrarily chosen.

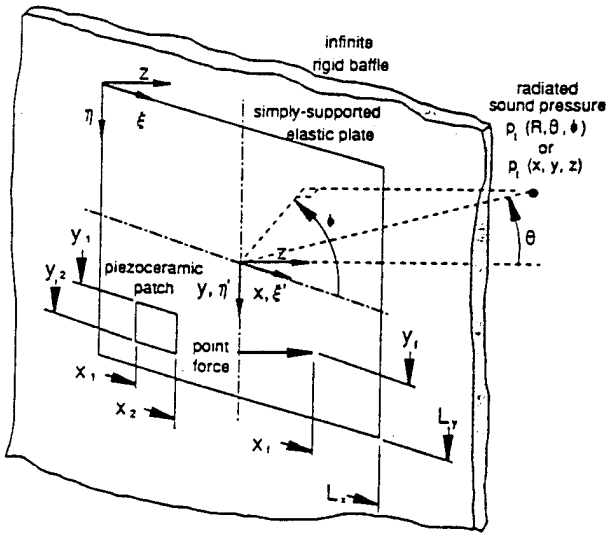

Figure 1. The arrangement and coordinates of the baffled simply-supported plate.

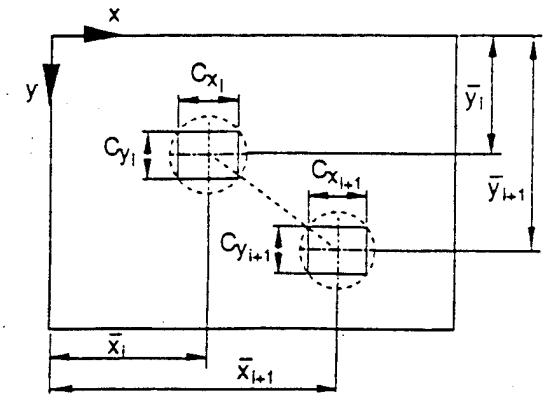

Figure 2. Illustration of design variables.

MATHEMATICAL FORMULATION FOR OPTIMIZATION PROBLEM

Design Variable

As shown in Figure 2, the optimal placement of the jth piezoelectric actuator located inside the boundaries of the plate can contain five variables, $\bar{x}_i$, $\bar{y}_i$, C_{xi}, C_{yi} and V_i. The variables C_{xi} and C_{yi} denote the size of the ith piezoelectric actuator, while $\bar{x}_i$ and $\bar{y}_i$ denote the central location of the actuator, and V_i is the applied voltage to the piezoelectric actuator. If the primary source is known, and piezoelectric actuators are used as control sources, then the total radiated sound pressure into the free field can be shown as follows:

$$P_t = P_t(\bar{x}_i, \bar{y}_i, C_{xi}, C_{yi}, V_i) \quad i = 1,\ldots,N_c \tag{1}$$

The complete derivation of p_t is shown in Wang (1991) and omitted here. As discussed from previous works (Wang et al., 1991), V_i can be calculated from the linear quadratic optimal control theory (LQOCT). The total radiated sound pressure can then be written as follows:

$$P_t = P_t(\bar{x}_i, \bar{y}_i, C_{xi}, C_{yi}, V_i(\bar{x}_i, \bar{y}_i, C_{xi}, C_{yi}))$$
$$i = 1,\ldots,N_c \tag{2}$$

However, if the size of the piezoelectric actuators was first fixed, then the total radiated sound pressure becomes

$$p_t = p_t(\bar{x}_i, \bar{y}_i, v_i(\bar{x}_i, \bar{y}_i)) \quad i = 1,\ldots,N_c \tag{3}$$

The design variables, $\bar{x}_i$, $\bar{y}_i$, C_{xi}, C_{yi} and V_i can be properly selected based upon the concern of the size or location (or both) of the piezoelectric actuator and the control effort (i.e., the voltages or power required for piezoelectric actuators).

Objective Function

There are various choices for the objective function. Wang et al. (1991) chose the integral of the square of radiated

sound pressure over a hemisphere of the radiating field as the cost function. However, such a cost function, in practice, is not useful. Wang and Fuller (1991) constructed a cost function which is the sum of the mean square radiated sound pressures measured by a limited number of microphones. The consideration of the above two types of objective functions is of particular interest in sound radiation control. Since the sound radiation is strongly coupled with the structural vibration, the objective function may also be chosen as the sum of the mean square plate acceleration measured by a limited number of accelerometers, or the integral of the square of the plate acceleration over the vibrating surface. The possible candidates for the objective function used in sound radiation control can be as follows:

1. Distributed pressure sensors

$$\Phi_p = \frac{1}{R^2}\int_s |p_t|^2 ds = \int_0^{2\pi}\int_0^{\pi/2} |p_t|^2 \sin\theta d\theta d\phi \quad (4)$$

2. Discrete pressure sensors

$$\Psi_p = \sum_{i=1}^{N_{mike}} |p_{t_i}(R_i,\theta_i,\phi_i)|^2 \quad (5)$$

6. Distributed accelerometer sensors

$$\Phi_w = \int_A |\ddot{w}_t|^2 dA = \int_0^{L_y}\int_0^{L_x} |\ddot{w}_t|^2 dxdy \quad (6)$$

4. Discrete accelerometer sensors

$$\Psi_w = \sum_{i=1}^{N_{acc}} |\ddot{w}_{t_i}(x_i,y_i)|^2 \quad (7)$$

where N_{mike} and N_{acc} are the number of microphones and accelerometers, respectively. It is noted that Φ_p and Φ_w are measured by ideal distributed sensors, which may not be practical in reality; however, Φ_p and Φ_w represent the power of sound radiation and energy density of out-of-plane structural vibration, respectively. They can be used as an index of control effectiveness. For practical applications, Ψ_p and Ψ_w are the alternative options. A reasonable number and location of sensors shall be selected to reflect the actual system response, such that an optimal solution can be found without losing the global nature of the problem. In effect, the discrete sensors should approach a form of numerical integration of the objective function associated with the distributed sensors to be truly global.

Design Constraints

The design constraints have to be specified to confine the design variables within a reasonable range. These design constraints are necessary for providing a reasonable result by maintaining the rectangular shape of the piezoelectric actuators, locating actuators inside the plate boundaries, avoiding overlapping between actuators, and operating actuators within the working voltage range. It is noted that the constraint set 3 below for avoiding overlapping is conceptually sketched in Figure 2. For the rectangular-shaped piezoelectric actuators, as shown in Figure 2, the constraint sets are listed as follows:

1. To maintain the piezoelectric actuator, a rectangular shape:

$$\begin{aligned} 0 < C_{x_i} \le L_x/2 \\ 0 < C_{y_i} \le L_y/2 \end{aligned} \quad (8)$$

2. To maintain the piezoelectric actuator inside of the plate:

$$\begin{aligned} \bar{x}_i - C_{x_i}/2 \ge 0 \\ \bar{x}_i + C_{x_i}/2 \le L_x \\ \bar{y}_i - C_{y_i}/2 \ge 0 \\ \bar{y}_i + C_{y_i}/2 \le L_y \end{aligned} \quad (9)$$

3. To avoid overlapping between piezoelectric actuators:

$$\begin{aligned} \bar{x}_{i+1} - \bar{x}_i > 0 \\ \bar{y}_{i+1} - \bar{y}_i > 0 \\ [(\bar{x}_{i+1} - \bar{x}_i)^2 + (\bar{y}_{i+1} - \bar{y}_i)^2]^{1/2} - \frac{1}{2}[(C_{x_i}^2 + C_{y_i}^2)^{1/2} \\ + (C_{x_{i+1}}^2 + C_{y_{i+1}}^2)^{1/2}] > 0 \end{aligned} \quad (10)$$

4. To specify the working range of piezoelectric actuators:

$$|V_i| \le 150 \text{ (volt } p - p) \quad (11)$$

Note that the control power to the actuators is not an optimization variable. However, constraint 4 above ensures that the piezoelectric actuator is within a working range.

APPLICATION TO OPTIMAL PLACEMENT OF PIEZOELECTRIC ACTUATORS

For a simple application of the previous theoretical formulation to sound radiation control, the size of the piezoelectric actuators is assumed fixed, i.e., $C_{x_i} = C_{y_i} =$ constant. The applied voltage to the ith piezoelectric actuator, V_i, can be calculated from LQOCT (Wang, 1991).

Only the optimal location of piezoelectric actuators $\bar{x}_i$ and $\bar{y}_i$ will be determined. The objective function is chosen as the sum of the mean square sound pressure measured by a number of microphones in the far-field. Therefore, the optimization problem can be written as:

Objective function:

$$\Psi_p = \Psi_p(\bar{x}_i, \bar{y}_i, V_i(\bar{x}_i, \bar{y}_i)) = \sum_{j=1}^{N_{mike}} |P_{t_j}(R_j, \theta_j, \phi_j)|^2$$

$$i = 1, \ldots, N_c \tag{12}$$

design variables:

$$(\bar{x}_i, \bar{y}_i) \quad i = 1, \ldots, N_c \tag{13}$$

design constraints:

constraint sets 2, 3 and 4 as shown in Equations (9–11).

The design variables are to be determined by minimizing the objective function subjected to a set of design constraints. Now, a suitable optimization algorithm must be adopted to solve the optimal solution.

OPTIMIZATION ALGORITHM

An IMSL subroutine N0ONF (IMSL, 1989) for solving a general nonlinear programming problem using the successive quadratic programming algorithm and a finite difference gradient technique was adopted to calculate the optimal solution. The algorithm requires a high accuracy arithmetic in estimating the gradient. The central finite difference method was then applied to approximate the gradient by adopting the IMSL CDGRD subroutine (IMSL, 1989).

SOLUTION STRATEGY

To solve the above optimization problem, a solution strategy was developed. The flow chart of solution strategy is shown in Figure 3. The procedure to solve the problem is to first set up the initial guess of the optimal central location of the ith actuator, $(\bar{x}_i)_k$, $(\bar{y}_i)_k$, where k denotes the number of iterations. The following steps are then performed:

1. Utilize the linear quadratic optimal control theory (LQOCT) (Wang, 1991) to obtain the applied voltages, $(V_i)_k$, to actuators at the current location, $(\bar{x}_i)_k$, $(\bar{y}_i)_k$.
2. Evaluate the objective function and constraints at the current location, $(\bar{x}_i)_k$, $(\bar{y}_i)_k$.
3. Evaluate the gradients of the objective function and constraints at the current location, $(\bar{x}_i)_k$, $(\bar{y}_i)_k$.
4. Employ an optimization algorithm, N0ONF, to update the optimal location, $(\bar{x}_i)_{k+1}$, $(\bar{y}_i)_{k+1}$.

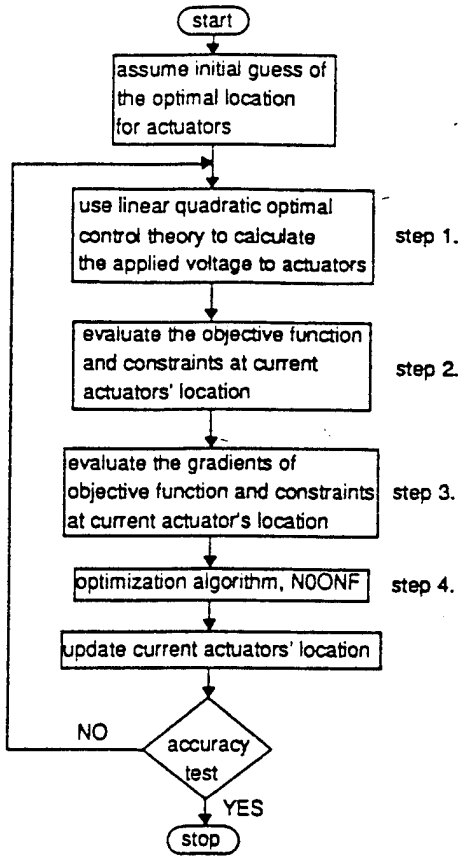

Figure 3. Flow chart of solution strategy.

5. Stop the procedure if the results pass the accuracy test; otherwise, update the current optimal location of actuators and repeat the above steps.

It is noted that the design variables, the central location of the piezoelectric actuators $(\bar{x}_i, \bar{y}_i)$, were normalized by the plate length and width (L_x, L_y), respectively, such that the design variables will be relocated between zero and one. This normalization process will benefit the solution process of the optimization problem.

LQOCT FOR SOLVING APPLIED VOLTAGES TO ACTUATORS

Lester and Fuller (1990) presented an optimization algorithm to obtain the minimum for a linear quadratic function. Wang et al. (1991) had shown the use of linear quadratic optimal control theory (LQOCT) to determine the applied voltages to minimize the selected objective function, which is quadratic. Here, the LQOCT is adopted to solve the voltages independently. One of the advantages is that the optimal voltages can be always determined whenever the location of the actuators is known. The other reason to evaluate the optimal voltage separately is that the order of voltage and the central location of the piezoelectric actuator is

Table 1. Plate specification.

$E = 207 \times 10^9$ (N/m²)	$\nu = 0.292$	$L_x = 0.38$ (m)
$\rho_p = 7870$ (kg/m³)	$h = 1.5875$ (mm)	$L_y = 0.30$ (m)

not consistent mathematically, even after the normalization process. Hence, upon consideration of the numerical difficulty and the number of design variables, it is beneficial to obtain the optimal voltages using LQOCT separately from solving the optimization problem.

ANALYTICAL RESULTS

Table 1 shows the physical properties of the simply-supported plate used for the following simulations. The structural disturbance was assumed to be a point force with magnitude of $F_1 = 1N$ and located at $x_{f1} = 0.08$ m, $y_{f1} = 0.08$ m.

Nine error microphone sensors, whose locations are tabulated in Table 2 and shown in Figure 4, were used; therefore, the objective function defined in Equation (12), which is the sum of mean square measured pressure, can be constructed. This number of microphones is clearly based on the consideration of computing time and a reasonable approximation to the continuous integral of pressure over the complete radiation hemisphere. Too few microphones will not reveal the actual system global radiation response. On the other hand, too many microphones will require excessive computing effort to solve the optimization problem. The microphones located in the far-field are arranged five in a row across the central line of the plate in both the x- and y-directions, as shown in Figure 4. The size of the piezoelectric actuators is fixed, $C_{xi} = 0.06$ m and $C_{yi} = 0.04$ m. The location and applied voltages of the piezoelectric actuators are to be determined.

SUB-REGION SEARCH METHOD

The determination of the optimal location of piezoelectric actuators is dependent on the excitation frequency. A different excitation frequency will lead to a different optimal location. For a particular frequency of excitation, all of the plate modes can be excited; however, only the plate modes near the excitation frequency will contribute significantly to the plate response as well as the sound radiation. It is clear that if the plate was excited near the (1,1) mode, the plate response will be shown as a convex surface. Similar characteristics can be found for the objective function. If the plate was excited at 87 Hz near the (1,1) mode, and the central location of the piezoelectric actuator was varied and moved around the plate, then the objective function and the applied voltage could be calculated from LQOCT and plotted, as shown in Figure 5. Because the objective function is shown as a convex surface, an optimal location for the piezoelectric actuator can always be found to guarantee global minimum. It is also noted from Figure 5 that high control voltages are required for the actuator located near the corner of the plate to achieve sound radiation control. The actuator with the minimum control effort is located at about the same position as the actuator with the minimum objective function.

As shown in Figure 6, for an excitation frequency $f = 357$ Hz near the (3,1) mode, the objective function and the applied voltage reveal a shape close to the (3,1) mode distribution. There is more than one minimum for the objective function; in fact, there is one local minimum at each division separated by nodal lines. This characteristic, related to the plate mode shapes, is similar to what has been shown in Figure 5. If the actuator is located near the nodal line of the plate mode, then sound radiation control is not effective—at least for on-resonance excitation—because of high control voltage and small control authority. The above discussions seem to be contrary to the previous work by Dimitriadis et al. (1991). They claimed that the optimum boundary of the piezoelectric actuators may be along the nodal lines of selected modes to be excited. In the sense of vibration excitation and the characteristic of induced moments by the piezoelectric actuators, their statement may be intuitive. Jia (1990) had also shown that optimal location

Table 2. Location of error microphones.

The ith Microphone	(R, θ, ϕ)
1	(1.8, 75°, 180°)
2	(1.8, 45°, 180°)
3	(1.8, 0°, 0°)
4	(1.8, 45°, 0°)
5	(1.8, 75°, 0°)
6	(1.8, 75°, 90°)
7	(1.8, 45°, 90°)
8	(1.8, 45°, 270°)
9	(1.8, 75°, 270°)

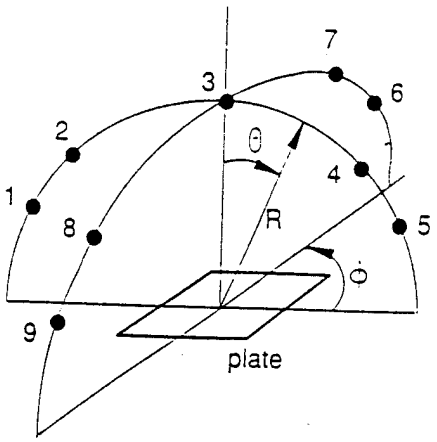

Figure 4. Location of error microphones.

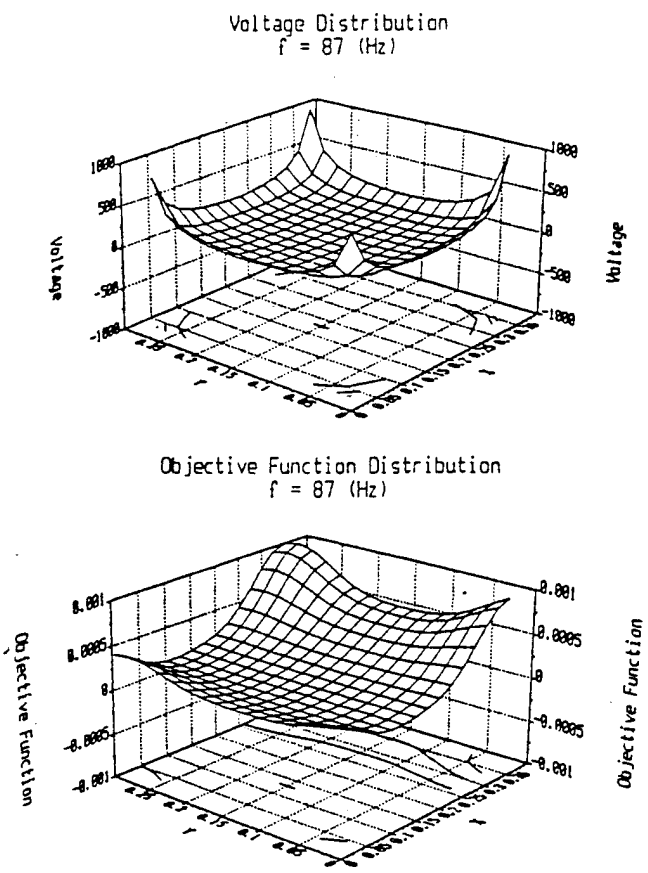

Figure 5. Distribution of objective function and control voltage for f = 87 Hz.

and dimension of piezoelectric actuators to effectively suppress the single mode response of beam vibration is to maximize the length of the piezoelectric actuator covering a whole lobe. Here, in our work, in terms of the attenuation of total sound radiation, the optimal location of "finite" length of piezoelectric actuators is determined upon a compromise to equally reduce several plate modes instead of just one. Therefore, the optimal location of the actuator is found to be away from the nodal line.

Figure 7 shows plots similar to Figures 5 and 6 except that the excitation frequency, $f = 272$ Hz, is between the (2,1) and (3,1) modes. One can see that those distributions become complex and result from the combination of several plate modal responses. Again, there are multiple minima; this makes the global minimum difficult to find using the optimization procedure. However, according to the characteristics shown in Figures 5 and 6, a sub-region search method, which comes from the nature of the objective function distribution similar to that of the plate mode shapes, can be proposed. This search technique involves subdividing the plate into several cells based on the nodal lines of the plate mode shapes, which are set up to be the bound of the locations for the actuators. In other words, in addition to the design constraints illustrated previously, the upper and lower bounds of the locations for actuators can also be specified according to the nodal lines associated with the plate mode shapes.

OPTIMAL LOCATION OF ONE ACTUATOR FOR DIFFERENT EXCITATION

As discussed previously, the optimal location of piezoelectric actuators is dependent on the excitation frequency due to the variation of the modal transfer function in frequencies. The optimal location of the actuator has been of interest for many concerns. As discussed by Juang and Rodriguez (1979), to control a single mode of beam vibration, there are multiple optimal locations for one actuator in high-mode control. If several modes contribute to the response simultaneously, and only a few actuators are applied, then the optimal location will be much different from that for single mode control. The feedforward control approach adopted here is to minimize the objective function, which is the mean square of sound pressure measured by error microphones, and thus to control all of the modal contributions at the same time. Therefore, the optimal location and applied voltage of the actuator are solved under a compromise to eliminate the significant modal responses; however, this compromise will probably incur spillover to other

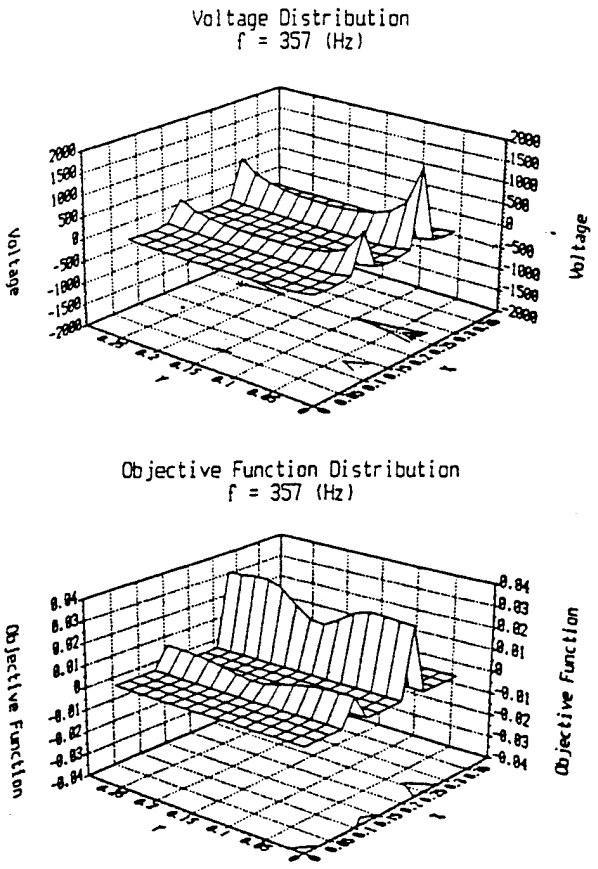

Figure 6. Distribution of objective function and control voltage for f = 357 Hz.

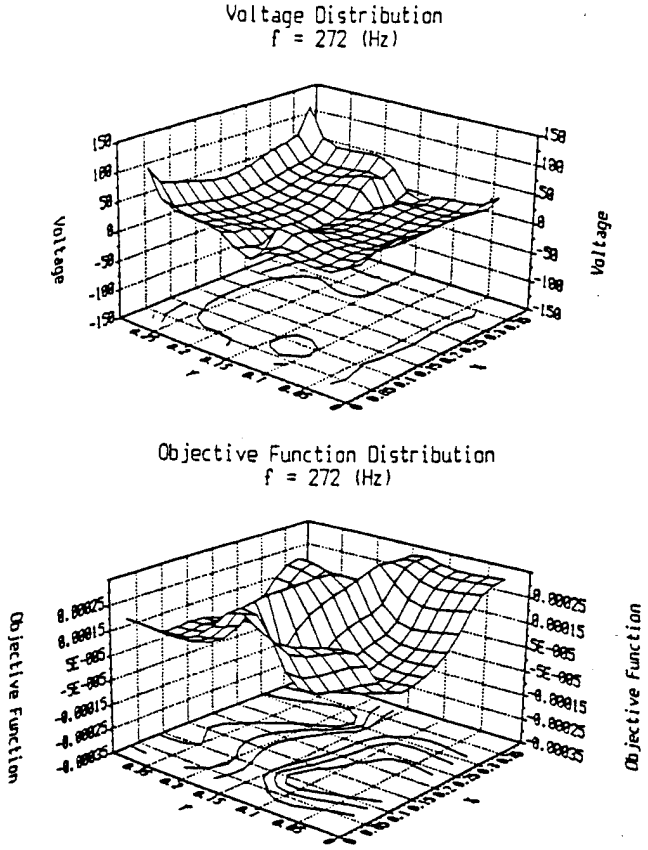

Figure 7. Distribution of objective function and control voltage for f = 272 Hz.

higher modes, which do not radiate efficiently to the error microphones, causing an increase in plate response.

When one piezoelectric actuator is considered, the normalized optimal central location of the piezoelectric actuator and the applied voltage to the actuator can be tabulated (Table 3), as well as the reduction of the objective function, radiated power and pressure modal amplitude. Table 3 is shown for different excitation frequencies varying from 87 Hz to 357 Hz, i.e., between the (1,1) and (3,1) modes. The underlined values are for on-resonance excitation, such as 87 Hz near the (1,1) mode, 190 Hz near the (2,1) mode, and 357 Hz near the (3,1) mode. One can see that the optimal central location of the actuator is located at about one-third of the plate length and width, in the left-bottom quadrant of the plate, i.e., the same quadrant where the point force disturbance is located. The results match well those found in sub-region search methods; therefore, the optimization procedure is suitable to search for the optimal location of piezoelectric actuators. As the excitation frequency increases, the optimal central location of the actuator moves toward the corner of the plate. This can be understood by realizing that when the excitation frequency increases, the contribution of higher modes becomes significant, and thus the optimal location of the actuator is placed where it can couple into all higher mode responses. In applying one actuator—for example, $f = 87$ Hz near the resonance of the (1,1) mode—the actuator attempts to control all of the significant radiating mode responses, including the (1,1) and (2,1) modes, instead of just the (1,1) mode. Therefore, the optimal location is determined under a compromise to eliminate the significant modes; however, as one can see in Table 3, there is spillover to higher modes, such as (3,1), (4,1) and (5,1). This result indicates that the optimal location of a single actuator is such that it eliminates the significant modal response near the excitation frequency; however, this will result in spillover to higher modes, which ultimately limits the amount of attenuation.

On the other hand, when the excitation frequency increases, for example, $f = 357$ Hz near the (3,1) mode excitation, the radiation from the (3,1) mode is controlled, as well as the (1,1) and (2,1) modes, but with less reduction.

Table 3. Results for one actuator with different excitation frequencies.

Excitation Frequency f (Hz)	Normalized Optimal Central Location of Actuator $\bar{x}/L_x$	$\bar{y}/L_y$	Optimal Voltage (volt) V	Reduction of Objective Function Ψ_p (dB)	Reduction of Radiated Power Φ_p (dB)	Reduction of Pressure Modal Amplitude (dB) (1,1)	(2,1)	(3,1)	(4,1)	(5,1)
87	0.3456	0.3933	51.15	171.22	101.51	56:55	12.61	−2.47	−18.94	−27.62
100	0.3442	0.3919	49.89	147.27	59.61	30.94	17.55	−3.53	−18.54	−25.50
120	0.3413	0.3892	47.73	134.37	61.10	22.34	15.54	−1.58	−18.10	−27.45
140	0.3378	0.3861	45.37	128.43	53.33	17.69	18.36	−0.88	−17.63	−27.31
165	0.3324	0.3813	42.26	120.65	46.96	13.87	24.55	0.16	−16.77	−25.24
190	0.3255	0.3757	39.13	138.03	65.11	11.17	50.18	1.47	−15.74	−26.82
220	0.3150	0.3679	35.60	111.69	38.47	8.83	22.61	3.45	−14.52	−26.32
245	0.3043	0.3609	33.08	119.53	46.54	7.41	18.04	5.60	−12.66	−25.83
270	0.2920	0.3541	31.11	99.02	34.11	6.36	15.61	8.46	−10.76	−25.13
300	0.2765	0.3477	29.55	99.69	26.84	5.50	14.02	13.44	−7.94	−23.99
330	0.2631	0.3456	28.67	100.46	29.91	4.99	13.27	21.63	−4.74	−22.68
357	0.2548	0.3416	53.34	148.75	78.26	4.62	12.51	70.28	−1.22	−21.23

Table 4. On-resonance excitation, f = 357 (Hz), near (3,1) mode.

Case	The ith Actuator	Optimal Location $\bar{x}/L_x$	Optimal Location $\bar{y}_i/L_y$	Optimal Voltage V_i (volt)	Reduction of Objective Function Ψ_p (dB)	Reduction of Radiated Power Φ_p (dB)
One Actuator	(1)	0.2548	0.3416	53.34	148.75	78.26
Two Actuators	(1)	0.2511	0.2852	100.54	189.06	66.70
	(2)	0.5504	0.6143	27.97		
Three Actuators	(1)	0.2499	0.2846	56.65	192.78	66.56
	(2)	0.5419	0.6052	50.61		
	(3)	0.8223	0.2198	61.09		
Three Actuators (Lab)	(1)	0.167	0.5	24.11	61.60	60.28
	(2)	0.5	0.833	25.73		
	(3)	0.833	0.167	10.78		

There is still spillover to the higher modes, but there is less than at the lower frequency excitations. This is due to the fact that the (1,1) and (2,1) modes, having high radiation efficiency, can contribute a larger amount of sound radiation to the far-field, even though the (3,1) mode is dominant on the plate due to the excitation frequency. Therefore, the optimal location is determined from a result of compromise to efficiently eliminate the most significant radiating modes, i.e., the (1,1), (2,1) and (3,1) modes in this case. However, this effort causes spillover to higher modes, such as (4,1) and (5,1) modes, which have lower radiation efficiency (Wallace, 1972). It is also noted from Table 3 that for on-resonance excitation, the reduction of radiated power is generally larger, and the control effort (voltage) is higher than for those cases with off-resonance excitation. This result is due to the fact that modes on resonance always contribute considerably more to the modal response and thus require more control effort.

OPTIMAL LOCATION OF MULTIPLE ACTUATORS FOR DIFFERENT EXCITATION FREQUENCIES

On-Resonance Excitation, f = 357 Hz, Near (3,1) Resonant Mode

Table 4 shows the optimal central location and applied voltages of piezoelectric actuators, as well as the reduction of the objective function and radiated power for an excitation frequency of f = 357 Hz. As one can see, although the reduction of objective function increases when more actuators are applied, the amount of attenuation of radiated power is not always increased. This means that the optimization algorithm does work to find a better solution. However, the minimization of the objective function, which is the sum of mean square pressures measured by error microphones, will not guarantee the reduction of radiated power due to the spillover of sound pressure to locations other than the position of error microphones. In terms of the attenuation of radiated power, to properly locate one actuator in controlling sound radiation is more effective than to use two or three actuators when a set of microphones are used as error sensors, as it reduces unnecessary spillover.

Figure 8 shows the radiation directivity pattern for the excitation frequency f = 357 Hz. The point force disturbance input and piezoelectric actuator patches are sketched to scale at the top of Figure 8. The disturbance response, denoted by a solid line, indicates a monopole-like response but is nonuniform, and evidently shows the existence of the (3,1) mode and a significant (1,1) modal contribution. The optimal location of one actuator is at the left-bottom quadrant of the plate, similar to the primary source. The residual pressure field is shown to be a combination of the (3,1) and (1,1) modes.

For two-actuator control as shown at the top of Figure 8, the first optimally located actuator is somewhat near the optimal location for one-actuator control, and the second one

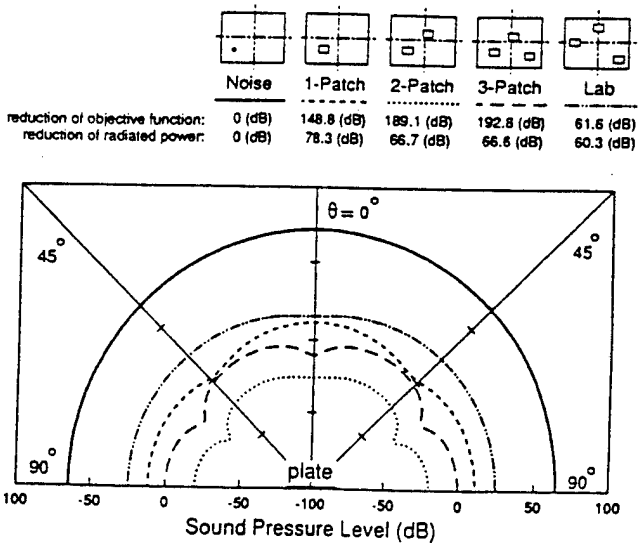

Figure 8. Radiation directivity pattern for f = 357 Hz.

is located at the upper-right quadrant of the plate near the central line. As shown in Table 4, the reduction of objective function is increased, but the reduction of radiated power is decreased. A result such as this implies that more error microphones need to be used due to spillover effects to unobserved radiation points. Nevertheless, the sound pressure level along the central line of the plate in both the x- and y-direction is less than that using one actuator, and it exhibits a combination of the (4,1) and (1,1) modes. It can be seen that there are dips at $\theta = 0°, 75°$ for $\phi = 0°$, and $75°$ for $\phi = 180°$, where the error microphones are located. For three-actuator control, the optimal locations of the first two actuators close to those of two-actuator control, and the third one is located at the bottom-right quadrant of the plate. Again, the objective function has been further minimized. As shown in Figure 8, the dips at $\theta = 0°, 75°$ for $\phi = 0°$ and $75°$ for $\phi = 180°$ are enhanced, but the reduction of radiated power has not increased.

An interesting feature can be observed from the above results, indicating that a one-by-one search method may be used to solve for the location of the successive actuator. The idea is to first find an optimal location for one-actuator control, and then to find a second optimal location for two-actuator control with the same location for the first actuator, and so on. With this searching technique, the computing time can be largely reduced since it costs less to optimize a reduced-parameter problem than a full-parameter problem. This method was attempted; however, the results were not encouraging since the selected objective function cannot be attenuated further due to numerical difficulty (even though a double precision number was used in the program) while an additional actuator was considered. The authors believe that if the objective function is reconstructed as the radiated power rather than the mean square pressure, the one-by-one search method would be appropriate and could reduce significant computing effort for multiple actuator control. Also, it appears that each actuator is optimally configured for separate modes, since their locations stay the same. Hence, an independent optimization procedure for each mode and its associated radiation might be attempted.

Also shown in Figure 8 is an arbitrary selection of multiple actuators located at one-sixth of the plate length or width (denoted lab arrangement). This arrangement is assigned to control the low modal number excitation based upon the nature of the plate mode shapes and was used in companion experiments (Clark and Fuller, 1992). The results show that optimally configured one-, two- or three-actuator control is superior to the arbitrarily chosen actuators for the on-resonance excitation in terms of both objective function and radiated power.

Figure 9 shows the plate displacement distribution along the x-direction at $y = 0$ corresponding to the cases of Figure 8. The solid line depicts the disturbance response and reveals that the (3,1) mode is dominant. With control, the plate displacement has been reduced globally and exhibits a more complex pattern, and the (3,1) mode has been at-

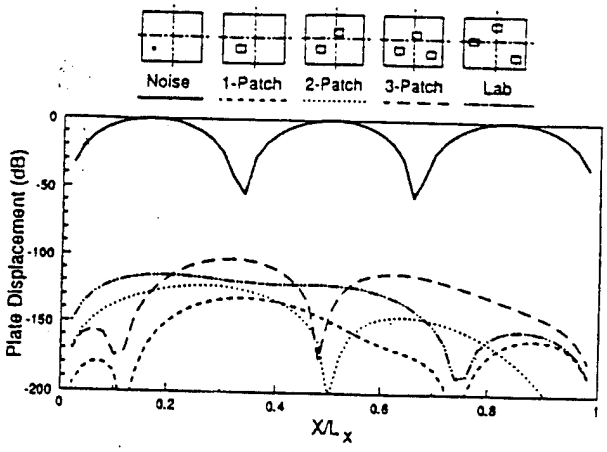

Figure 9. *Plate displacement distribution for f = 357 Hz.*

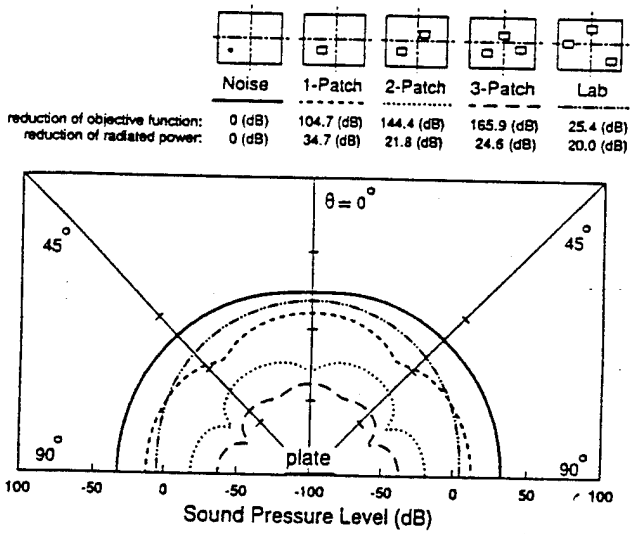

Figure 10. *Radiation directivity pattern for f = 272 Hz.*

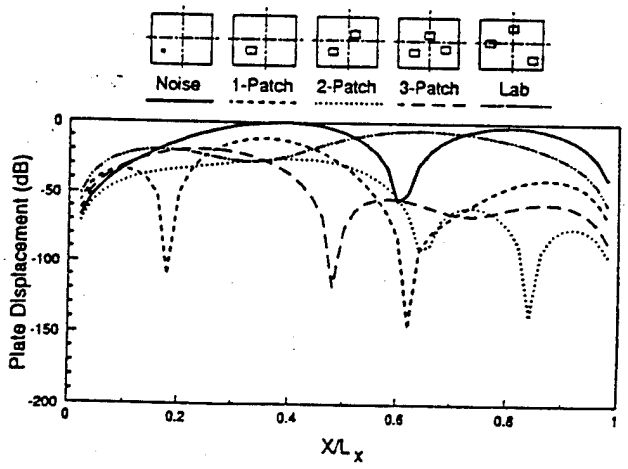

Figure 11. *Plate displacement distribution for f = 272 Hz.*

Table 5. Off-resonance excitation, f = 272 (Hz), between (2,1) and (3,1) modes.

Case	The *i*th Actuator	Optimal Location $\bar{x}/L_x$	Optimal Location $\bar{y}_i/L_y$	Optimal Voltage V_i (volt)	Reduction of Objective Function Ψ_p (dB)	Reduction of Radiated Power Φ_p (dB)
One Actuator	(1)	0.2945	0.3533	59.68	104.73	34.66
Two Actuators	(1)	0.2554	0.2978	100.56	144.38	21.77
	(2)	0.6031	0.6803	33.17		
Three Actuators	(1)	0.2387	0.2762	94.25	165.90	24.55
	(2)	0.5036	0.6353	32.14		
	(3)	0.7701	0.4044	6.70		
Three Actuators (Lab)	(1)	0.167	0.5	39.81	25.43	19.95
	(2)	0.5	0.833	98.24		
	(3)	0.833	0.167	122.64		

tenuated considerably. Further comments on the behavior are as in the previous section.

Off-Resonance Excitation, $f = 272$ Hz, between (2,1) and (3,1) Resonant

Table 5 shows the optimal central location and applied voltages of piezoelectric actuators, as well as the reduction of objective function and radiated power for an excitation frequency $f = 272$ Hz between the (2,1) and (3,1) modes. The control effort (i.e., the control voltages) is not necessarily smaller than that for on-resonance excitation, unlike the previous observation for one-actuator control. In fact, either one of the actuators may require extremely high control voltages; however, others may simultaneously need only a small voltage. The optimal location and required control voltages for multiple actuators are determined in such a way as to not only suppress the disturbance response, but also reduce the interactive spillover effects due to the actuators themselves.

Figures 10 and 11 show the radiation directivity pattern and the plate displacement distribution, respectively, corresponding to the case in Table 5 for the off-resonance excitation. The optimal locations of the piezoelectric actuators, sketched at the top of Figure 10, are very similar to those of the on-resonance excitation. From Figure 10, the primary radiated sound denoted by a solid line shows a small dip at $\theta = 0°$, indicating the strong response of the (2,1) mode. In applying one actuator, the residual response shows a combination of the (3,1) and (1,1) modes, and there are no dips at any location of the error microphones. In applying two and three actuators, the residual response reveals a more complex pattern similar to the (4,1) and (5,1) modes, respectively. Dips can now be seen located at the error microphone locations. It is again shown that increased actuators can further attenuate the pressures at error microphone position; however, the overall radiated power is not necessarily reduced because of spillovers in sound pressure into locations other than the position of the error microphones.

The plate displacement distribution for the case of disturbance, as shown in Figure 11, exhibits the (2,1) mode characteristic shape. With control, the residual plate response reveals a more complex pattern and is not attenuated globally, as was seen in Figure 11 for resonance excitation. This phenomenon is referred to as "modal restructuring" for the off-resonance excitation and "modal suppression" for the on-resonance excitation (Fuller, Hansen and Snyder, 1991).

COMPUTING TIME ANALYSIS

In an optimization procedure, to find the gradient of the objective function is generally the most difficult and the most CPU time-consuming task. Table 6 shows the percentage of CPU time consumed for each step in the optimization procedure. It takes about 20% of CPU time for steps 1 and 2, i.e., the evaluation of the objective function and the applied voltages to actuators, and over 70% (up to 90% for

Table 6. Typical example of CPU time for optimization.

Case	Number of Iteration	CPU Time (sec)	Percentage of Main Program (%) Step 1,2	Step 3	Step 4	Percentage of Optimization Program (%) Step 1,2	Step 3	Step 4
One Actuator	7	181	10.21	28.45	0.004	26.41	73.57	0.01
Two Actuators	27	2787	17.52	65.25	0.003	21.17	78.83	0.003
Three Actuators	7	2285	4.79	57.24	0.001	7.72	92.28	0.002

three actuators) of CPU time for step 3, i.e., the evaluation of the gradients of the objective function and constraints in the optimization procedure. However, it takes only a small percentage of time for step 4 in calculating the update actuator's location in the optimization subroutine. In order to efficiently solve the optimization problem, it is necessary to do a sensitivity analysis. For future work, it could be beneficial to apply an analytical or semi-analytical method rather than the finite difference method to evaluate the gradients so that CPU time can be reduced for solving the optimization problem. Furthermore, the acoustic radiated power could also be considered as the objective function to solve the optimal location of piezoelectric actuators.

SUMMARY

This paper has presented the mathematical formulation for the optimization problem of the placement of piezoelectric actuators in a feedforward control implementation of ASAC. The analysis is applied to an example problem to obtain preliminary information on how the optimization procedure performs. Four different forms of objective functions, which are differentiated by discrete or distributed and by vibrational or pressure sensor, are discussed for sound radiation control. An objective function, which is constructed based on the use of a number of discrete pressure sensors, is applied to the example of sound radiation control. Some significant observations may be summarized as follows:

1. Different excitation frequencies will result in different optimal locations of piezoelectric actuators.
2. The optimally located piezoelectric actuators can provide a large amount of reduction of sound radiated power and are observed to perform better than arbitrarily chosen locations. Properly locating one piezoelectric actuator generally gives a higher reduction of radiated acoustic power than using two or three actuators for the selected objective function, which is the sum of mean square sound pressure measured by a limited number of microphones. This is due to control spillover resulting from driving down the error signals at all error microphones. An alternative would be to limit the attainable attenuation achieved at each error microphone or to use the total radiated power as the objective function.
3. A computing time analysis shows that the evaluation of the gradients of the objective function and constraints consumes most of the CPU time. Sensitivity analysis, which can be used to analytically or semianalytically evaluate the gradients, is required for future research.
4. This work, which lays out the theory for optimal location of piezoelectric actuators, will be the basis for the design of "smart" structures for ASAC with distributed actuators and sensors.

REFERENCES

Burdisso, R. A. and C. R. Fuller. 1992. "Theory of Feed-Forward Controlled System Eigenproperties", *Journal of Sound and Vibration*, 153(3):437–451.

Chang, M. I. J. and T. T. Soong. 1980. "Optimal Controller Placement in Modal Control of Complex Systems", *Journal of Mathematical Analysis and Applications*, 75:340–358.

Chen, W. H. and J. H. Seinfeld. 1975. "Optimal Location of Process Measurements", *International Journal of Control*, 21(6):1003–1014.

Clark, R. L. and C. R. Fuller. 1992. "Modal Sensing of Efficient Acoustic Radiation with PVDF Distributed Sensors in Active Structural Acoustic Control Approaches", *Journal of the Acoustical Society of America*, 91(6):3321–3329.

Dimitriadis, E. K., C. R. Fuller and C. A. Rogers. 1991. "Piezoelectric Actuators for Distributed Vibration Excitation of Thin Plates", *Journal of Vibration and Acoustics*, 113:100–107.

Fuller, C. R., C. H. Hansen and S. D. Snyder. 1991. "Active Control of Sound Radiation from a Vibrating Rectangular Panel by Sound Sources and Vibration Inputs: An Experimental Comparison", *Journal of Sound and Vibration*, 145(2):195–215.

Gibbs, G. P. and C. R. Fuller. 1992. "Experiments on Active Control of Vibrational Power Flow Using Piezoceramic Actuators and Sensors", *AIAA Journal*, 30(2):457–463.

Hamidi, M. and J.-N. Juang. 1981. "Optimal Control and Controller Location for Distributed Parameter Elastic Systems", *Proceedings of the 20th IEEE Conference on Decision and Control*, pp. 502–506.

IMSL. 1989. *IMSL Math/Library*, IMSL Problem-Solving System Software System.

Jia, J. 1990. "Optimization of Piezoelectric Actuator Designs in Vibration Control Systems," Ph.D. Thesis, Department of Mechanical Engineering, VPI&SU.

Juang, J.-N. and G. Rodriguez. 1979. "Formulations and Applications of Large Structure Actuator and Sensor Placements", *Proceedings of the Second VPI&SU/AIAA Symposium on Dynamics and Control of Large Flexible Spacecraft*, Blacksburg, VA, June.

Lester, H. C. and C. R. Fuller. 1990. "Active Control of Propeller Induced Noise Fields Inside a Flexible Cylinder", *AIAA Journal*, 28(8):1374–1380.

Norris, G. A. and R. E. Skelton. 1989. "Selection of Dynamic Sensors and Actuators in the Control of Linear Systems", *Journal of Dynamic Systems, Measurement, and Control*, 111:389–397.

Simpson, M. A., T. M. Luong, C. R. Fuller and J. D. Jones. 1992. "Full Scale Demonstration Tests of Cabin Noise Reduction Using Active Vibration Control", *Journal of Aircraft*, 30(3):624–630.

Wallace, C. E. 1972. "Radiation Resistance of a Rectangular Panel", *Journal of Acoustical Society of America*, 51:946–952.

Wang, B.-T., E. K. Dimitriadis and C. R. Fuller. 1990. "Active Control of Structurally Radiated Noise Using Multiple Piezoelectric Actuators", *AIAA Journal*, 29(11):1802–1809.

Wang, B.-T. and C. R. Fuller. 1991. "Study of the Effect of Distributed or Discrete Pressure and Acceleration Sensors on Active Structural-Acoustic Control Systems", *Proceedings of the Eighth National Conference of the Chinese Society of Mechanical Engineering*, Taipei, Taiwan, R.O.C., pp. 1445–1454.

Wang, B.-T. and C. A. Rogers. 1991a. "Modeling of Finite-Length Spatially Distributed Induced Strain Actuators for Laminate Beams and Plates", *Journal of Intelligent Material Systems and Structures*, 2(1):38–58.

Wang, B.-T. and C. A. Rogers. 1991b. "Laminate Plate Theory for Spatially Distributed Induced Strain Actuators", *Journal of Composite Materials*, 25(4):433–452.

Wang, B.-T. 1991. "Active Control of Sound Transmission/Radiation From Elastic Plates Using Multiple Piezoelectric Actuators", Ph.D. Thesis, VPI&SU.

C-17 Active Control of Structurally Radiated Sound from an Enclosed Finite Cylinder, R. L. Clark and C. R. Fuller, Journal of Intelligent Material Systems and Structures, Vol. 5, pp. 379-391, May 1994.

Active Control of Structurally Radiated Sound from an Enclosed Finite Cylinder

ROBERT L. CLARK*
Duke University
Department of Mechanical Engineering and Materials Science
Durham, NC 27708-0300

CHRIS R. FULLER
Virginia Polytechnic Institute and State University
Department of Mechanical Engineering
Blacksburg, VA 24060

ABSTRACT: A long, thin aluminum cylinder was configured with two rigid end caps and instrumented with piezoceramic actuators and either microphone or polyvinylidene fluoride (PVDF) structural sensors for narrow-band active structural acoustic control. The input disturbance to the cylinder was generated with a shaker attached by a stinger, and all tests were performed in an anechoic chamber. In the first series of tests, the cylinder was driven with a shaker attached to the end cap, exciting the "accordion mode" of the structure. Upon applying control and using PVDF sensors, significant levels of global sound attenuation, approximately 25 dB on-resonance and 15 dB off-resonance, were observed in the acoustic field. In both the on-resonance and off-resonance test cases, three control actuators were required to achieve the stated levels of sound attenuation due to interaction between the accordion modes and the cylinder modes. In the second series of tests, the cylinder was driven radially with a shaker to excite higher order cylinder modes. Control was applied with six piezoelectric actuators wired to control selected circumferential modes in the first test case, and the actuators were chosen in a helical pattern about the cylinder in the second test case. In the latter case, approximately 10 dB of global sound attenuation was observed in the acoustic field when using microphone error sensors, while results obtained when implementing the PVDF error sensors yielded little sound attenuation in controlling the cylinder modes.

INTRODUCTION

PRELIMINARY studies in active structural acoustic control (ASAC) have been applied to beams and plates configured with piezoelectric actuators and polyvinylidene fluoride sensors (Clark and Fuller, 1991; 1992a–e; Clark et al. 1992). In these studies, single frequency control of structure-borne sound was achieved with piezoelectric actuators surface mounted on the structure, and either microphone or polyvinylidene fluoride (PVDF) error sensors were implemented to generate the appropriate cost function in terms of the acoustic response. A preliminary study by Sonti and Jones addressed the operation of piezoelectric actuators for active vibration control of thin, cylindrical shells (Sonti and Jones, 1991). In a later study, Sumali et al. (1991, 1992) considered active vibration control of both an open ended cylinder and one configured with end caps. Piezoelectric actuators and polyvinylidene fluoride sensors were used to control the vibration and thus the coupled acoustic response of the structure on-resonance for a single mode of vibration.

The thrust of the current work is thus to consider more complex structural acoustic response of a cylinder configured with end caps due to off-resonance excitation as well as using an acoustic based cost function. In addition to controlling sound radiation resulting from the vibration response of traditional cylinder modes, the acoustic response due to the accordion modes of the structure is considered in the control approach. Specific goals of this work are:

(a) Choose appropriate configuration of piezoelectric actuators for control of structure-borne sound.
(b) Determine appropriate number of control channels required for global sound attenuation.
(c) Replace microphone error sensors with structural sensors designed from polyvinylidene fluoride.

Details of the experimental configuration are discussed with emphasis on methods of exciting either the accordion modes or the cylinder modes of the structure. In addition, the resonant frequencies of the structure are estimated based upon an approach previously outlined by Blevins (1984) and

*Author to whom correspondence should be addressed.

1045-389X/94/03 0379-13 $6.00/0
© 1994 Technomic Publishing Co., Inc.

Table 1. Theoretical resonant frequencies of accordion modes.

Mode (#)	Predicted Frequency (Hz)
(1)	981
(2)	1804
(3)	4225
(4)	5857

order 1 circumferential mode is denoted the beam-bending mode. The combination of standing waves supported about the circumference of the cylinder and those supported along the axis of the cylinder as illustrated in Figure 2 result in the helical standing wave patterns (Fahy, 1985). A shell with simply supported boundary conditions supports wavenumbers corresponding to the mode shapes of the structure. For example, the structural wavenumbers of a simply supported shell can be expressed as follows:

$$k_r = \sqrt{k_m^2 + k_n^2} \tag{2}$$

where

$$k_m = \frac{m}{a} \qquad m = 0,1,2,\ldots \tag{3}$$

and

$$k_n = \frac{n\pi}{L} \qquad n = 1,2,3,\ldots \tag{4}$$

For the shell constructed in this experimental study, the end caps were machined from aluminum and attached at the cylinder with 1/8" bolts. The boundary conditions corresponding to this method of attachment are somewhere between simply supported and clamped. The assumed-modes method can again be implemented in conjunction with Lagrange's equations to estimate the resonant frequencies of the structure. A torsional spring is included in the model of the cylinder at the boundaries to account for the resistance to motion where the cylinder is attached to the end caps. Details of the analysis are presented in Appendix B and reference is given to previous work by Blevins (1984) as well as that of Sumali (1992) in a similar study.

The stiffness of the torsional spring was chosen such that the first measured resonant frequency of the cylinder matched the predicted resonant frequency. The predicted resonant frequencies for the cylinder are given in Table 2 with the corresponding mode shape numbers. As is apparent from the tabulated values of the resonant frequencies, the structure has high modal density. The term modal density is used in this case to describe structures with resonant frequencies of modes separated by less than 10 Hz. This lack of separation between resonant frequencies results in significant contributions from more than one mode to the structural and acoustic response even for on-resonance excitation. Thus the dimension of the controller must increase to exercise the necessary number of degrees of freedom to control the structural acoustic response of the system.

DETAILS OF THE EXPERIMENT AND CONFIGURATION

The cylinder was configured for active structural acoustic control of sound radiation resulting from cylinder modes as well as the accordion modes. Actuator configurations as well as error sensor arrangements are discussed as they pertain to each specific control experiment. The filtered-x adaptive least mean squares (LMS) algorithm was implemented on a TMS320C30 floating point digital signal processing chip to provide up to six channels of control. A schematic diagram of the controller displaying three output channels and three input channels is illustrated in Figure 3. Experiments were limited to single frequency control, and thus a two coefficient finite impulse response (FIR) filter was utilized as the adaptive filter. The LMS algorithm essentially adapts the coefficients of the FIR filters in the time domain until the control voltage to each piezoelectric actuator is such that the sum of the squares of the chosen error sensors is minimized. This solution has been previously demonstrated to converge to the same result obtained with linear quadratic optimal control (Clark and Fuller, 1992c). Details of the control algorithm are omitted in the discussion; however, further explanation can be found in a variety of references (Widrow and Stearns, 1985; Elliot et al., 1987; Clark and Fuller, 1992a).

General Configuration

All experiments were performed in the anechoic chamber

Table 2. Theoretical resonant frequencies of cylinder modes.

Mode (m,n)	Predicted Frequency (Hz)
(2,1)	228
(3,1)	324
(3,2)	415
(1,1)	492
(2,2)	518
(4,1)	591
(3,3)	602
(4,2)	616
(4,3)	684
(4,4)	807
(3,4)	854
(2,3)	882
(5,1)	951
(0,1)	961
(5,2)	962

center of the cylinder both before and after applying active structural acoustic control.

The out-of-plane vibration response of the cylinder was measured both before and after applying active structural acoustic control with an Ometron VPI scanning laser vibrometer, with a dynamic range of 80 dB and the capability of measuring velocity between 0 and 1 m/s (Barker, 1992). In performing the scan, a grid of 100 points along the axis of the cylinder and 10 points about the circumference was utilized to obtain qualitative and quantitative information about the structural response before and after applying control. These measurements were made to compensate for the lack of detailed information concerning the measured resonant frequencies and mode shapes of the cylinder. In general, agreement between the predicted and measured resonant frequencies of the cylinder were within 5% for the first five modes of the structure. However, the deviation increased with increasing frequency. Deviation between analytical and experimental results might be a result of the assumption made with respect to the boundary conditions in computing the resonant frequencies. Another possible explanation for the observed deviations might be due to the mass loading of the cylinder with respect to the actuators and sensors, or the discontinuities in the cylinder resulting from machining flat positions on the surface for mounting the control actuators. The cylinder was extruded from aluminum, and thus variations in wall thickness and eccentricities in the circumference are factors that also affect the resonant characteristics of the structure.

In all test cases performed, control was achieved with actuators constructed from piezoceramic elements. The specific configurations of each of the piezoceramic elements for controlling the cylinder modes or accordion modes are detailed in the following sections. The positions and dimensions of the corresponding PVDF sensors selected for each specific control application are detailed as well.

Actuators and Sensors for Accordion Modes

A schematic diagram of the cylinder configured with PVDF (Kynar Piezo Film Manual, 1987) sensors for active structural acoustic control of the accordion mode response is presented in Figure 6. As indicated, the input disturbance, which consisted of a shaker attached by a stinger, was mounted on the center of the end cap external to the cylinder. (Measurements of sound radiation from the shaker detached from the cylinder were 40 dB below that of the uncontrolled cylinder at the error microphones and traversing microphone coordinates. Thus, the overall contribution to the global sound radiation was within the noise floor of the control system.) The PVDF sensors were cut in rectangular elements measuring 0.5 m long × 25.4 mm wide × 28 μm thick. The sensors were positioned about the circumference of the cylinder in increments of 120° and were centered between ring 2 and ring 3 of the piezoelectric elements as illustrated in Figure 6. The accordion response of the cylinder

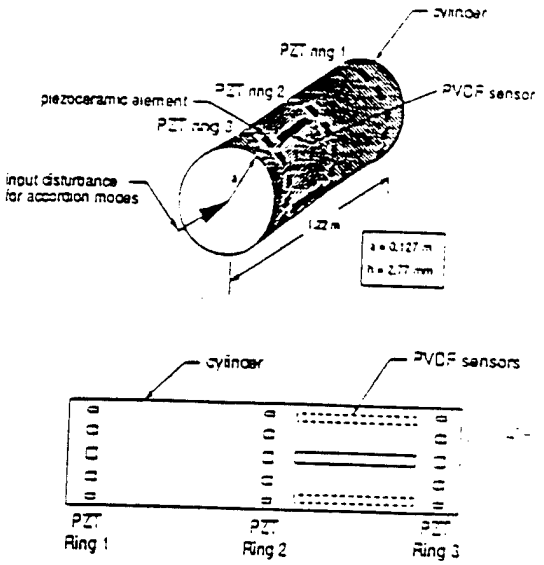

Figure 6. Schematic diagram of cylinder configured for accordion modes.

is dominated by extension and contraction over the length of the cylinder. Thus, the PVDF sensors were positioned to respond primarily to strain along this axis. Only three sensors were implemented since three channels of control proved sufficient for attenuating the global acoustic response of the cylinder when responding in the accordion mode. The cost function for the control algorithm was thus formed from the sum of the squares of the electrical output of each of the PVDF sensors.

The control actuators were arranged as illustrated in the top portion of the schematic diagram of Figure 7. The

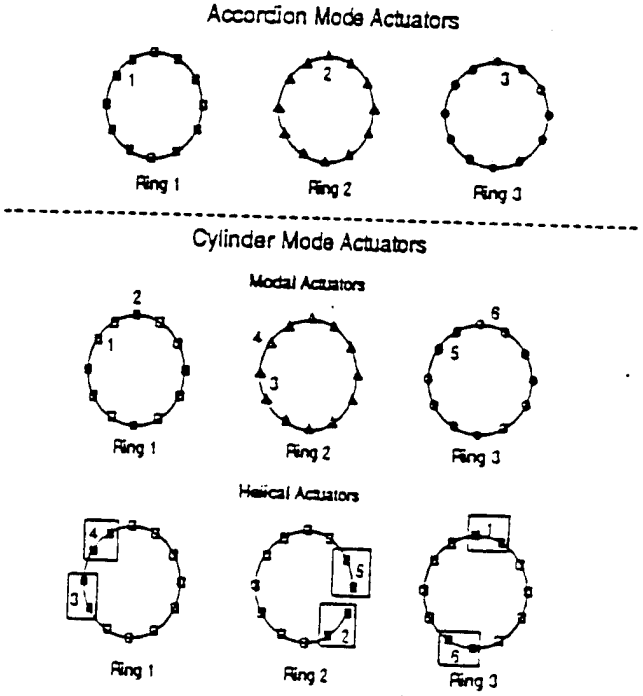

Figure 7. Schematic diagram of control actuator configurations.

since each actuator pair utilized was indexed by 60° along the axis of the cylinder, visually flowing in a helical pattern as illustrated in the bottom portion of Figure 7. The structural response of the cylinder supports helical standing waves, and thus an actuator configuration was chosen which allowed as much flexibility in both the circumferential and axial direction as possible. Piezoelectric elements were wired together in pairs at each respective ring of the cylinder and were alternated as a function of the axial position as is readily observed when visually scanning the lower portion of Figure 7 from right to left (actuators 1–3) and then from left to right (actuators 4–6). The piezoelectric elements represented by the white markers were not utilized in this particular configuration.

The basic configurations for control will be henceforth designated the accordion mode configuration and the cylinder mode configuration. The exception is that in the cylinder mode configuration, two separate actuator arrangements were considered – the modal actuators and the helical actuators. The actuator configurations were selected to reflect two possible schools of thought in the control of the sound radiation from the cylinder – the modal approach as opposed to the wave approach. More extensive research must be conducted to determine the optimal configuration; however, the two configurations selected serve the purpose of this pilot study. All experimental results presented in the next section are based upon the basic configurations discussed here.

RESULTS

Results from active structural acoustic control of the accordion mode are presented first with both on-resonance and off-resonance input disturbances at one of the end caps, as discussed in the previous section. Emphasis is placed upon results for off-resonance excitation due to the interaction of various structural modes. Thus, in the case of active structural acoustic control of the cylinder modes, only off-resonance excitation test cases are presented. Greater demands are placed upon the controller for off-resonance excitation since the number of degrees of freedom required to control the system are proportional to the number of modes contributing to the structural acoustic response if the controller is to be effective over a broad range of frequencies. On the other hand, if the controller is to be designed to operate on a specific frequency of the disturbance, then the number of control channels can be reduced by optimizing the position of the actuator with respect to the structure and thus the controllability of the system increases (Clark and Fuller, 1992b.)

Results from Control of Accordion Mode

The configuration of the cylinder for control of the accordion mode was discussed in the previous section. The first resonant frequency of the accordion mode was observed at an excitation frequency of 958 Hz. Multiple test cases were conducted at various frequencies of excitation; however, two representative sets of results are presented here for both on- and off-resonance excitation. In the case of on-resonance excitation, the end cap of the cylinder was driven at 958 Hz and control was achieved implementing the 6 error microphones and 3 piezoelectric control actuators. The reader is reminded here that "actuator" means an array of hard wired individual piezoelectric elements as described in the previous section. All 6 error microphones were utilized to construct the cost function to ensure global attenuation in the sound field. Results from this test are presented in Figure 9. The acoustic response was assumed symmetric, and thus measurements were obtained between $\theta = 90°$ and $\theta = 180°$ only. The dark solid line represents the acoustic response before control as indicated in the legend, and the dashed line represents the controlled acoustic response when implementing the microphone error sensors, as also indicated in the legend. Observe that the sound pressure was attenuated by approximately 40 dB in the acoustic field near the end cap and by at least 15 dB in the remainder of the acoustic field displayed. (Acoustic attenuation on the order of 15 dB was observed at various other acoustic field points out of the plane of the traversing microphone.) Attenuation at each of the 6 microphone coordinates used as error sensors was on the order of 40 dB.

The dotted line displayed in Figure 9 represents the control case when implementing the 3 PVDF error sensors in the control approach with the same 3 control actuators. The response of each respective PVDF sensor was attenuated by approximately 50 dB upon achieving control, and the acoustic response of the structure was minimized on the order of 25 dB at the end cap and between 5 dB and 10 dB in the remainder of the acoustic field. The discrepancy in performance of the controller when implementing the PVDF sensors as opposed to the microphone sensors is proposed to be an artifact of the interaction between the accordion mode and the cylinder modes at the frequency of excitation. Refer-

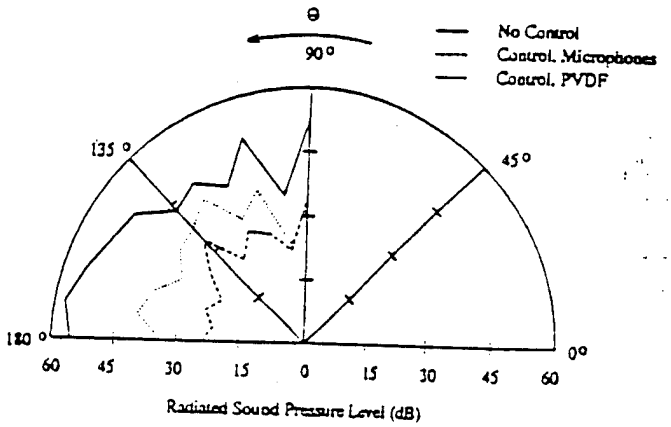

Figure 9. Control of accordion mode on-resonance (958 Hz).

observed in the acoustic field. The sensors were thus ineffective for active structural acoustic control in this case. Lack of control with the chosen PVDF sensors is thought to result from the relatively high modal density and the interaction between modes with the same circumferential modal indice but different axial modal indices. For example, the vibration response of the (5,4) mode, the (5,3) mode and the (5,1) mode can be phased to minimize the response of the PVDF sensors without actually attenuating the total response of each respective mode of vibration.

The velocity contour corresponding to the real part of the uncontrolled and controlled response with the helical actuators and the microphone error sensors is presented in Figure 12. Approximately one quarter of the circumference of the cylinder was scanned, as indicated in Figure 12. This is the largest region that could be accurately scanned since the laser vibrometer measures only the normal velocity of the cylinder. The measured response must be corrected to account for the angle of incidence on the surface of the cylinder with respect to the curvature. The profile of the cylinder is represented by the dark line surrounding the contour plot. Regions characterized by a dark or light rectangular discontinuity result from erroneous measurements obtained when the laser scanned across an electrical wire of one of the actuators or one of the microphone stands that was between the laser and the structure. These data points are out of bounds with respect to the scaled response of the cylinder; however, editing them from the data set was virtually impossible since 1000 data points were scanned. The characteristic most apparent in the plot is that before control, lower order structural modes dominate the response. However, upon applying control, the structural response shifts to higher order structural modes, as is evident upon comparing the contour plots in Figure 12. The surface velocity amplitude also increased by about a factor of 2 upon applying control while the sound radiation decreased. This decrease is acoustic response results from what has

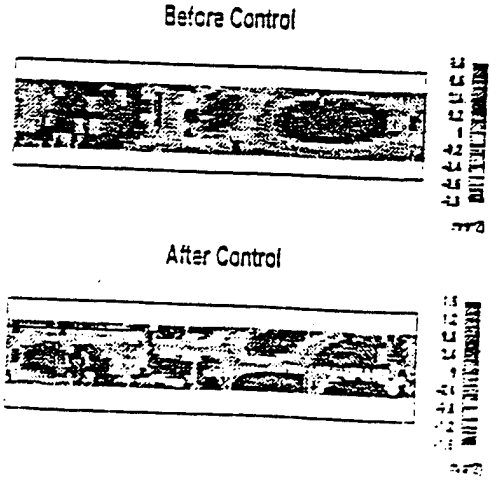

Figure 12. Velocity contour from scanning laser vibrometer (1090 Hz).

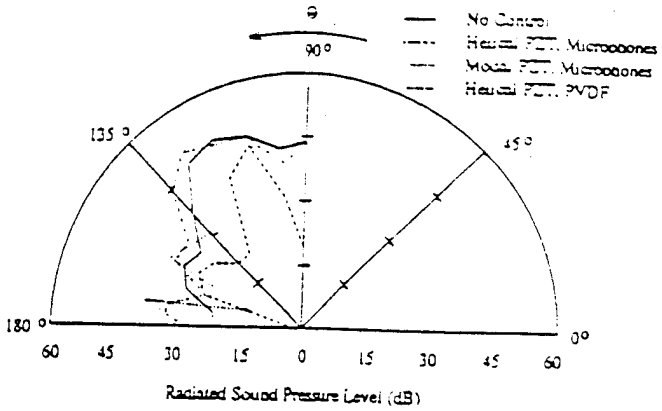

Figure 13. Control of cylinder modes off-resonance (1460 Hz).

previously been termed "modal restructuring" (Clark and Fuller, 1992a, 1992c, 1992d). The higher order structural modes are less efficient acoustic radiators and thus even with an increase in the structural response, the acoustic response of the structure decreased. This important result distinguishes the work presented in this paper, which is devoted to *active structural acoustic control* (ASAC), from previous research devoted to active vibration control (AVC) (Sumali et al., 1991; Sumali, 1992) as a method of controlling sound radiation (Fuller et al., 1991). The plot presented is representative of the results obtained with the scanning laser vibrometer in other off-resonance test cases.

The final test case presented was obtained for an excitation frequency of 1460 Hz. Results from the structural acoustic response are presented in the directivity patterns of Figure 13. The uncontrolled response is represented by the solid line as indicated in the legend, while the controlled response for the helical actuators and modal actuators in conjunction with the microphone error sensors is represented by the dashed line and dotted line, respectively. Between 5 and 10 dB of attenuation in sound pressure was observed when implementing the helical actuators in conjunction with the microphone error sensors. However, when implementing the modal actuators, the acoustic response was observed to increase on the order of 5 dB in the region near the end cap of the cylinder. Due to the high modal density and choice of off-resonance excitation frequency, the level of acoustic attenuation was limited in both test cases. This result is representative of tests performed at arbitrary excitation frequencies in this frequency range. As observed in previous studies conducted with piezoelectric actuators on a simply supported plate, the structural acoustic response can be further attenuated by increasing the number of control channels or by optimizing the positions of the control actuators to reduce the dimension of the controller with similar performance gains (Clark and Fuller, 1992d).

While the response at each of the 6 PVDF sensors was attenuated by approximately 50 dB upon applying control with the helical actuators, the structural acoustic response of the cylinder actually increased as illustrated by the dash-

M_L are the point mass equivalents of the end caps at position 0 and position L, respectively, and EA is the product of the Young's modulus and the area of the cylinder cross-section.

Expressing the system response in modal coordinates,

$$y(x,t) = \sum_{m=1}^{M} \phi_m(x) q_m(t) \tag{7}$$

where $\phi_m(x)$ is the assumed mode shape and $q_m(t)$ are the modal coordinates. Lagrange's equations can be expressed in terms of the modal coordinates as follows:

$$\frac{d}{dt}\left(\frac{\partial T}{\partial \dot{q}_m}\right) - \frac{\partial T}{\partial q_m} - \frac{\partial V}{\partial q_m} = 0 \qquad m = 1,2,\ldots,M \tag{8}$$

Substituting Equation (7) into Equations (5) and (6) and substituting the resulting expressions into Lagrange's equations yields the following expression:

$$\sum_{n=1}^{M} m_{mn}\ddot{q}_n(t) + \sum_{n=1}^{M} k_{mn} q_n(t) = 0 \quad m = 1,2,\ldots,M \tag{9}$$

where

$$q_n(t) = a_n \cos(\omega t - \psi) \tag{10}$$

$$m_{mn} = \int_0^L m(x)\phi_m(x)\phi_n(x)dx + M_0\phi_m(0)\phi_n(0) + M_L\phi_m(L)\phi_n(L) \tag{11}$$

$$k_{mn} = \int_0^L EA \frac{d\phi_m(x)}{dx}\frac{d\phi_n(x)}{dx}dx \tag{12}$$

a_n is a constant coefficient, ω is the circular frequency and ψ is the phase.

If we choose the admissible functions to be that of a structure with free-free boundary conditions, then

$$\phi_m(x) = \cos\left(\frac{m\pi x}{L}\right) \tag{13}$$

Substituting Equation (13) into Equations (11) and (12) results in the following expression for the elements of the mass and stiffness matrix:

$$m_{mn} = \frac{\rho AL}{2}\delta_{mn} + M_0 + M_L(-1)^m(-1)^n \tag{14}$$

$$k_{mn} = EA\frac{mn\pi^2}{2L}\delta_{mn} \tag{15}$$

Solving the following eigenvalue problem yields the resonant frequencies of the system and the mode shapes as a function of the assumed admissible functions.

$$[k]a = \omega^2[m]a \tag{16}$$

A number of numerical routines are available for solving this problem.

APPENDIX B: ASSUMED MODES METHOD FOR CYLINDER MODES

The boundary conditions of the cylinder used in this study range somewhere between that of clamped-clamped and simply supported-simply supported at each end of the cylinder. For such boundaries, the resistance to rotation at the boundaries can be modeled with a torsional spring to approximate the physical boundary conditions realized upon bolting the cylinder to the end caps with small bolts about the circumference of the cylinder. A similar approach was utilized to account for discrepancies between measured and predicted resonant frequencies for a plate with approximate simply supported boundary conditions by the authors (Clark, 1992). The following analysis is based upon a procedure outlined by Blevins (1984) and Gorman (1975) and was previously assembled by Sumali in his thesis (1992). A detailed schematic diagram of the approximate boundary conditions can be found in Sumali (1992). The overall procedure for approximating the resonant frequencies and corresponding mode shapes of the cylinder are reviewed here. However, the reader is referred to the previous references for greater detail.

The Flugge shell theory can be expressed in terms of the following equations of motion:

$$\begin{aligned}
\epsilon_x &= \frac{\partial u}{\partial x} - z\frac{\partial^2 w}{\partial x^2} \\
\epsilon_\theta &= \frac{1}{R}\frac{\partial v}{\partial \theta} - \frac{z}{R(R+z)}\frac{\partial^2 w}{\partial \theta^2} + \frac{w}{R+z} \\
\epsilon_{x\theta} &= \frac{1}{R+z}\frac{\partial u}{\partial \theta} + \frac{R+z}{R}\frac{\partial v}{\partial x} - \frac{\partial^2 w}{\partial x \partial \theta}\left(\frac{z}{R} + \frac{z}{R+z}\right) \\
\epsilon_{xz} &= \epsilon_{\theta z} = \epsilon_{zz} = 0
\end{aligned} \tag{17}$$

where u is the displacement in the x-direction (i.e. along the cylinder length), v is the displacement about the circumference of the cylinder in the θ-direction, w is the displacement in the z-direction, which is normal to the surface of the cylinder, R is the radius of the cylinder in the midplane and ϵ is used to designate strain with subscripts to indicate direction. Greater detail of the equations of motion and coordinate system can be found in Sumali (1992), Blevins (1984), and Gorman (1975).

Clark, R. L. 1992. "Advance Sensing Techniques for Active Structural Acoustic Control." Dissertation for Doctor of Philosophy in Mechanical Engineering, Virginia Polytechnic Institute and State University, pp. 135–136.

Clark, R. L. and C. R. Fuller. 1991. "Control of Sound Radiation with Adaptive Structures." *Journal of Intelligent Material Systems and Structures*. 2(3):431–452.

Clark, R. L. and C. R. Fuller. 1992a. "Modal Sensing of Efficient Acoustic Radiators with Polyvinylidene Fluoride Distributed Sensors in Active Structural Acoustic Approaches." *Journal of the Acoustical Society of America*. 91(6):3313–3320.

Clark, R. L. and C. R. Fuller. 1992b. "Experiments on Active Control of Structurally Radiated Sound Using Multiple Piezoceramic Actuators." *Journal of the Acoustical Society of America*. 91(6):3321–3329.

Clark, R. L. and C. R. Fuller. 1992c. "Active Structural Acoustic Control with Adaptive Structures Including Wavenumber Considerations." *Journal of Intelligent Material Systems and Structures*. 3(2):296–315.

Clark, R. L. and C. R. Fuller. 1992d. "Optimal Placement of Piezoelectric Actuators and Polyvinylidene Fluoride Error Sensors in Active Structural Acoustic Control Approaches." *Journal of the Acoustical Society of America*. 92(3):1521–1533.

Clark, R. L. and C. R. Fuller. 1992e. "A Model Reference Approach for Implementing Active Structural Acoustic Control." *Journal of the Acoustical Society of America*. 92(3):1534–1544.

Clark, R. L., C. R. Fuller and R. A. Burdisso. 1992. "Design Approaches for Shaping Polyvinylidene Fluoride Sensors in Active Structural Acoustic Control." Proceedings of *Recent Advances in Adaptive and Sensory Materials and Their Applications*. C. A. Rogers and R. C. Rogers, eds., Lancaster, PA: Technomic Publishing Company, Inc., pp. 702–728.

Elliott, S. J., I. M. Strothers and P. A. Nelson. 1987. "A Multiple Error LMS Algorithm and Its Application to the Active Control of Sound and Vibration." *IEEE Transaction and Acoustic Speech and Signal Processing* ASSP-35, 1:1423–1434.

Fahy, F. 1985. *Sound and Structural Vibration*. New York: Academic Press, pp. 200–202.

Fuller, C. R., C. H. Hansen and S. D. Snyder. 1991. "Active Control of Sound Radiation from a Vibrating Rectangular Panel by Sound Sources and Vibration Inputs: An Experimental Comparison." *Journal of Sound and Vibration*. 145(2):195–215.

Gorman, D. J. 1975. *Free Vibration Analysis of Beams and Shafts*. New York: Wiley, p. 31.

1987. *KYNAR Piezo Film Technical Manual*. Valley Forge, PA: Pennwalt Corp., pp. 1–65.

Maillard, J. P. and C. R. Fuller. "Advanced Time Domain Sensing for Structural Acoustic Systems. I Theory and Design." *Journal of the Acoustical Society of America*. accepted for publication, 1993.

Meirovitch, L. 1967. *Analytical Methods in Vibrations*. New York: Macmillan Publishing Company, Inc., pp. 233–235.

Sonti, V. R. and J. D. Jones. 1991. "Active Vibration Control of Thin Cylindrical Shells Using Piezo-Electric Actuators." *Recent Advances in Active Control of Sound and Vibration*. Lancaster, PA: Technomic Publishing Co., Inc., pp. 27–38.

Sumali, H., H. Cudney and J. Vipperman. 1991. "Vibration Control of Cylinders Using Piezoelectric Sensors and Actuators." *Proceedings of Conference on Active Materials and Adaptive Structures*. G. Knowles, ed., Philadelphia, PA: Institute of Physics Publishing Company, pp. 467–472.

Sumali, H. 1992. "Demonstration of Active Structural Acoustic Control of Cylinders." Master of Science Thesis, Virginia Polytechnic Institute and State University.

Widrow, B. and S. D. Stearns. 1985. *Adaptive Signal Processing*. Englewood Cliffs, NJ: Prentice-Hall, Inc., pp. 99–116.

C-18 Advanced Time Domain Wave-Number Sensing for Structural Acoustic Systems. I. Theory and Design, J. P. Maillard and C. R. Fuller, Journal of the Acoustical Society of America, Vol. 95 No. 6, pp. 3252-3261, June 1994.

Advanced time domain wave-number sensing for structural acoustic systems. I. Theory and design

J. P. Maillard and C. R. Fuller
Vibration and Acoustics Laboratories, Mechanical Engineering Department, Virginia Polytechnic Institute and State University, Blacksburg, Virginia 24061-0238

(Received 7 December 1992; revised 15 October 1993; accepted 26 January 1994)

This paper discusses new work concerned with developing structural sensors and associated signal processing techniques that provide time domain estimates of far-field pressure or structural wave-number information. The sensor arrangement consists of multiple accelerometers whose outputs are passed through an array of linear filters. The impulse response of each filter is constructed from the appropriate Green's function for the elemental source area associated with each sensor. The outputs of the filter array are then summed in order to predict far-field pressure or wave-number information somewhat analogous to the well-known boundary element technique. A major significance of the approach is that it provides time domain information and can thus be efficiently applied to active structural acoustic control approaches.

PACS numbers: 43.40.At, 43.40.Rj, 43.60.Gk

INTRODUCTION

Structure-borne sound is an important problem in many applications, and it is of prime interest to predict acoustic radiation from vibrating structures. Indeed, the radiation information is often used to develop appropriate control approaches. Acoustic holography[1] has been successfully applied to prediction of far-field radiation from real structures. For example, the technique may involve measurements of the acoustic pressure on a 2-D plane located in the near field using an array of microphones. The measured data are then transformed in the frequency and spatial domains to provide far-field information in a 3-D space. Structural acoustic systems have also been modeled using the boundary element method[2]. In this approach, the structural response, known at discrete locations, is used to construct a solution of the Helmoltz integral by solving a linear system. Both of the above methods allow the study of the radiation behavior of complex structures. However, the use of both methods results in extensive computations (FFT, matrix inversions, etc.) on a large amount of data. Therefore, "real time" prediction cannot be readily achieved. Here, we define "real time" to be in the time domain.

This paper, the first of two companion papers, presents a real time prediction technique using structural sensors. The analytical development will emphasize important aspects for application to the active structural acoustic control (ASAC) technique.[3,4] In this approach, a feedforward adaptive controller minimizes one or several real time error signals representing acoustic radiation information. Traditionally, the error signals are the output of microphones located in the far field. However, the use of microphones is often impractical in real applications and research is now addressing the development of structural sensors to replace error microphones. In that respect, much attention has been focused on new sensing materials (PVDF films, optic fibers) originally used in active vibration control.[3] When applied to acoustic radiation, the sensor should provide information related to the far-field pressure such that only the structural response contributing to radiation is observed. As a result, the controller dimension is reduced and better performances are achieved. Clark and Fuller[4] have discussed the use of PVDF film modal sensors in the feedforward control approach applied to rectangular acoustic radiators. By choosing the appropriate location and shape of the PVDF film, only those structural modes that efficiently radiate to the far field are observed. In related work, Baumann *et al.*,[5] have developed radiation filters for use in state feedback approaches to map structural states to radiation states of the system and demonstrated their use in sound radiation control from impulsively excited structures.

In both of the above works, the sensor output provides global radiation information related to the total acoustic power radiated by the structure. The present work is concerned with estimating far-field pressure radiated in prescribed directions. The approach implements point structural sensors (i.e., accelerometers) in parallel with an array of digital filters to obtain an error signal directly related to the far-field pressure in a prescribed direction. Namely, the sensor output is shown to be proportional to a time-shifted version of the far-field radiated pressure. The present analysis is limited to estimation of radiation from planar surfaces of finite extent. The relation between structural response and far-field pressure becomes more complex in case of nonplanar geometries and will be investigated in future work.

In the first part, the theory underlying the technique is presented. Following the ideas developed in boundary element method, the Rayleigh's integral that gives the far-field pressure radiated from a planar source, is approximated by a finite summation of filtered acceleration signals measured at a number of points on the structure. Two related sensing approaches are analytically outlined. In the first configuration, the filter array is designed to model the

 0001-4966/94/95(6)/3252/10/$6.00 © 1994 Acoustical Society of America

transfer functions between the acceleration and the radiated pressure of the elemental source area associated with each sensor. Then, the same approach is applied to evaluate the acceleration wave-number component in a prescribed direction. The corresponding discrete summation can be referred to as the spatial discrete wave-number transform analogous to the well-known time domain discrete Fourier transform. It is shown that this wave-number domain error information yields the same control performances as the far-field pressure when used in a feedforward control approach. The second part of the paper discusses the practical implementation of the technique. Two design methods are proposed for constructing the digital filters. The first involves frequency domain design algorithms using the analytical transfer functions derived in the first part. The second approach implements time domain optimal filtering techniques that allow the filters to be designed from experimental data.

Results of computer simulations on the sensor design and its application to active control of radiation from a baffled planar radiator excited by broadband disturbances will be discussed in the companion paper in order to illustrate the use of the sensing procedure.

I. THEORY

A. Pressure sensing configuration

Based on Rayleigh's integral, an expression that depends solely on the structural acceleration measured at discrete points on the vibrating surface is derived for the far-field pressure radiated from planar sources.

1. Rayleigh's integral

The Helmoltz integral equation relates the pressure field complex amplitude $P(\mathbf{r})$ at field point $\mathbf{r}$ in terms of the surface pressure $P(\mathbf{r}_0)$ and its gradient defined over the radiating surface $S(\mathbf{r}_0 \in S)$. Assuming a harmonic time dependence of the form $e^{j\omega t}$, where ω is the angular frequency of the source, the Helmoltz integral can be written as[6]

$$P(\mathbf{r}) = \int_S \left(P(\mathbf{r}_0) \frac{\partial g}{\partial \eta}(\mathbf{r}-\mathbf{r}_0) - g(\mathbf{r}-\mathbf{r}_0) \frac{\partial P}{\partial \eta}(\mathbf{r}_0) \right) dS \quad (\mathbf{r} \notin S), \tag{1}$$

where η is the outward normal unit vector and $g(\mathbf{r})$, the free-space Green's function defined in the free field as $g(\mathbf{r}) = (1/4\pi|\mathbf{r}|)\exp(jk_0|\mathbf{r}|)$; $k_0 = \omega/c$ is the acoustic wave number, and c is the speed of sound. Applying the boundary condition prescribed over S,

$$\frac{\partial P}{\partial \eta}(\mathbf{r}_0) = -\rho \ddot{W}(\mathbf{r}_0) \quad (\mathbf{r}_0 \in S), \tag{2}$$

where ρ is the fluid density, the pressure field is expressed in terms of the surface pressure and the fluid particle acceleration over the radiating surface, the latter being equal to the structural normal acceleration distribution $\ddot{W}(\mathbf{r}_0) = -\omega^2 W(\mathbf{r}_0)$. In the above notation, $\ddot{W}(\mathbf{r}_0)$ refers to the complex amplitude of the second time derivative of the normal displacement $w(\mathbf{r}_0,t) = W(\mathbf{r}_0)e^{j\omega t}$.

In the case of an infinite *planar* source, it can be shown that the surface pressure term vanishes when replacing the free-space Green's function $g(\mathbf{r})$ by $G(\mathbf{r}) = 2g(\mathbf{r})$, which satisfies the Neumann boundary condition $\partial G/\partial \eta(\mathbf{r}) = 0$ for $\mathbf{r} \in S$,

$$P(\mathbf{r}) = 2\rho \int_S g(\mathbf{r}-\mathbf{r}_0)\, \ddot{W}(\mathbf{r}_0)\, dS(\mathbf{r}_0). \tag{3}$$

When $\ddot{W}(\mathbf{r}_0)$ is nonzero over a finite surface (i.e., the structure is finite and located in an infinite baffle), analytical evaluation of the above representation becomes possible only in the far field. Removing the denominator of the Green's function from the integral produces the Rayleigh's formula for planar radiators[6]

$$P(\mathbf{r}) = \frac{\rho}{2\pi r} \int_S e^{-jk_0|\mathbf{r}-\mathbf{r}_0|}\, \ddot{W}(\mathbf{r}_0)\, dS(\mathbf{r}_0) \quad (|\mathbf{r}| \gg |\mathbf{r}_0|), \tag{4}$$

where $r = |\mathbf{r}|$. This formulation can be physically interpreted as an infinite sum of monopoles with volume acceleration $\ddot{W}(\mathbf{r}_0)dS(\mathbf{r}_0)$ located on an infinite rigid planar surface (in this case the amplitude of the free point source is multiplied by a factor of 2).

2. Discrete Rayleigh's integral

In practice, the structural response can only be evaluated at a finite number of points by means of point transducers such as accelerometers. Hence, it is necessary to approximate the far-field pressure, expressed in Eq. (4) with continuous coordinates, by an expression involving a finite number, N_d, of discrete coordinates ($\mathbf{r}_i \in S_0$, $i = 1,2,\ldots,N_d$). The resulting approximation will be referred to as the *discrete* Rayleigh's integral. Following the same idea developed in the boundary element method, the surface integral is approximated by a discrete summation over the integrand evaluated at a finite number of points. The surface S is discretized in N_d surfaces $S_i (S = S_1 \cup S_2 \cup \cdots \cup S_{N_d})$ such that a piecewise constant approximation for $\ddot{W}(\mathbf{r}_0)$ can be made over each S_i, i.e., $\ddot{W}(\mathbf{r}_0) \simeq \ddot{W}(\mathbf{r}_i)$ on S_i. Substituting $\ddot{W}(\mathbf{r}_0)$ in Eq. (4), the radiated pressure can then be approximated by

$$P(\mathbf{r}) \simeq \frac{\rho}{2\pi r} \sum_{i=1}^{N_d} \ddot{W}(\mathbf{r}_i) \int_{S_i} e^{-jk_0|\mathbf{r}-\mathbf{r}_0|}\, dS_i(\mathbf{r}_0). \tag{5}$$

The above expression defines the *piston* approximation: the far-field pressure is constructed by summing the radiated pressure of N_d pistons with uniform acceleration distribution $\ddot{W}(\mathbf{r}_i)$ and surface S_i. Assuming $\exp(-jk_0|\mathbf{r}-\mathbf{r}_0|)$ is almost constant over each elemental surface S_i, a simplified expression is obtained by removing the exponential term from the integral in Eq. (5),

$$P(\mathbf{r}) \simeq \frac{\rho}{2\pi r} \sum_{i=1}^{N_d} \ddot{W}(\mathbf{r}_i) e^{-jk_0|\mathbf{r}-\mathbf{r}_i|} S_i. \tag{6}$$

The far-field pressure is now approximated by the acoustic radiation of N_d monopole sources of volume acceleration $\ddot{W}(\mathbf{r}_i)S_i$ located on a rigid baffle. Equation (6) is referred

to as the *monopole* approximation. Both approximations are equivalent in the far field when the acoustic wavelength is much larger than the characteristic dimension a_i of the elemental surfaces $S_i(k_0 a_i \ll 1)$, i.e., in the far field, the rigid piston can be replaced by a monopole source. As the radiation control will be applied in the low-frequency range, the *monopole* approximation is used here.

3. Sensing approach

Introducing the time dependance, $\ddot{w}(\mathbf{r}_i,t)=\ddot{W}(\mathbf{r}_i)e^{j\omega t}$, in Eq. (6), the *discrete* far-field pressure is expressed as the summation of the filtered acceleration signals measured at locations $\mathbf{r}_i$ on the structure,

$$p_d(\mathbf{r},t)=P_d(\mathbf{r})e^{j\omega t}=\sum_{i=1}^{N_d} H_i(\omega)\ddot{W}(\mathbf{r}_i)e^{j\omega t}. \tag{7}$$

The frequency response functions $H_i(\omega)$ are written substituting $k_0=\omega/c$ in Eq. (6) as

$$H_i(\omega)=\frac{\rho S_i}{2\pi r}\exp\left(-j\omega\frac{|\mathbf{r}-\mathbf{r}_i|}{c}\right), \quad i=1,2,...,N_d. \tag{8}$$

The dependence of $H_i(\omega)$ on the field point $\mathbf{r}$ has been omitted for brevity. It is seen from Eq. (8) that the frequency response functions to be modeled present a constant magnitude and a linear phase with a positive acoustic time delay $\tau_i=|\mathbf{r}-\mathbf{r}_i|/c$ making the frequency response functions causal. This important property motivates the use of finite impulse response filters in the sensor implementation.

Now, the sensor is described in the discrete time domain. The signals are sampled with the sampling frequency F_s. FIR filters are commonly represented in terms of their discrete impulse response $\{U_l,\ l=0,1,...,L\}$. In matrix form, the output $y(n)$ of the filter at time t_n is expressed as

$$y(n)=\mathbf{U}^T\mathbf{X}(n)=\sum_{l=0}^{L} U_l x(n-l), \tag{9}$$

where $\mathbf{U}$ is a column vector containing the filter coefficients,

$$\mathbf{U}=[U_0\ U_1\ \cdots\ U_L]^T \tag{10}$$

and $\mathbf{X}(n)$ is a column vector containing the filter input sequence,

$$\mathbf{X}=[x(n)\ x(n-1)\ \cdots\ x(n-L)]^T. \tag{11}$$

Here, T denotes the transpose operator. Using the above representation, the sensor output $e(n)$ at time t_n is expressed as

$$e(n)=\sum_{i=1}^{N_d}\mathbf{U}^{iT}\mathbf{X}^i(n), \tag{12}$$

where $\mathbf{X}^i(n)$ is the ith sampled acceleration signal at time t_n and $\mathbf{U}^i$ the impulse response of the associated FIR filter for the ith accelerometer. The above configuration can be extended to a multiple output sensor involving a set of filter arrays. The jth output becomes

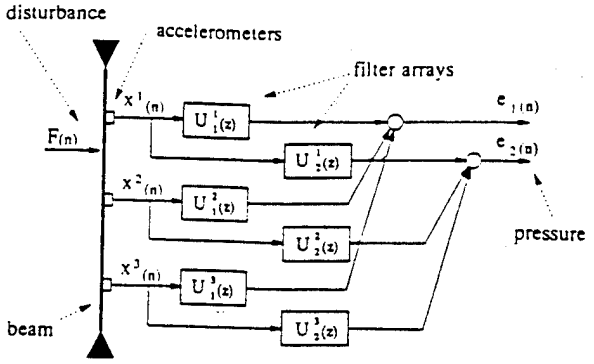

FIG. 1. Sensing configuration applied to a 1-D beam.

$$e_j(n)=\sum_{i=1}^{N_d}\mathbf{U}_j^{iT}\mathbf{X}^i(n), \tag{13}$$

where $\mathbf{U}_j^i(n)$ denotes the ith impulse response of the jth filter array. As an example, Fig. 1 presents the block diagram of the sensing configuration applied to a baffled simply supported beam. In this arrangement, two filter arrays processing the output of three accelerometers give the pressure at two different locations in the far field.

B. Wave-number component sensing configuration

The same approach is now applied to the evaluation of the structural wave-number component. This second sensing configuration is shown to be equivalent to the first method in terms of radiated energy and thus, can be used in a feedforward control approach. Moreover, using the analogy with the time domain discrete Fourier transform, the wave-number transform approach allows for an investigation of spatial sampling and resultant aliasing.

1. Wave-number transform of a 2-D rectangular radiator

Using rectangular coordinates, the spatial response of a 2-D planar source is represented in the wave-number domain in terms of its acceleration distribution $\ddot{W}(x,y)$ and the components k_x and k_y of the structural wave number $\mathbf{k}_f$ in the x and y direction, respectively,

$$\tilde{\ddot{W}}(k_x,k_y)=\int_{-\infty}^{+\infty}\int_{-\infty}^{+\infty}\ddot{W}(x,y)e^{j(k_x x+k_y y)}\,dx\,dy. \tag{14}$$

The time dependence $e^{j\omega t}$ has been omitted for brevity. The above surface integral can be interpreted as the spatial Fourier transform of the acceleration distribution $\ddot{W}(x,y)$. In the case of a finite rectangular radiator with length L_x and width L_y located in an infinite rigid baffle, Eq. (14) simplifies to

$$\tilde{\ddot{W}}(k_x,k_y)=\int_{-L_x/2}^{+L_x/2}\int_{-L_y/2}^{+L_y/2}\ddot{W}(x,y)e^{j(k_x x+k_y y)}\,dx\,dy. \tag{15}$$

The above wave-number domain representation allows the study of the acoustic energy radiated in the far field directly from the structural response. As shown in Ref. 7,

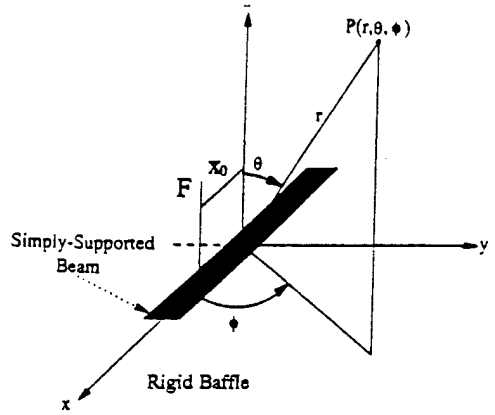

FIG. 2. Coordinate system of the simply supported beam.

the far-field radiated energy is due only to the supersonic wave numbers, k_f, smaller than the acoustic wave number $k_0=\omega/c$,

$$(k_x^2+k_y^2)^{1/2}<k_0. \tag{16}$$

It follows that a wave-number sensor designed for acoustic radiation control will be required to observe only low values of wave numbers.[8]

The relation between the wave-number information and the acoustic radiated pressure is now outlined. The Rayleigh's integral is written in the spherical coordinates (r,θ,ϕ) defined in Fig. 2 using the following approximation:

$$|\mathbf{r}-\mathbf{r}_0|\simeq r-x_0\sin\theta\cos\phi-y_0\sin\theta\sin\phi. \tag{17}$$

Substituting Eq. (17) in Eq. (4) yields

$$P(r,\theta,\phi)=\frac{\rho e^{-jk_0r}}{2\pi r}\int_{-L_x/2}^{L_x/2}\int_{-L_y/2}^{L_y/2}\ddot{W}(x_0,y_0)\times e^{jk_0\sin\theta(x_0\cos\phi+y_0\sin\phi)}\,dx_0\,dy_0. \tag{18}$$

By comparing Eqs. (15) and (18), the far-field pressure can now be expressed in terms of structural information as

$$p(r,\theta,\phi,t)=\frac{\rho e^{-jk_0r}}{2\pi r}\tilde{\ddot{W}}(k_x,k_y)e^{j\omega t}, \tag{19}$$

where k_x and k_y are defined by

$$k_x=k_0\sin\theta\cos\phi,\quad k_y=k_0\sin\theta\sin\phi. \tag{20}$$

Multiplying both sides of Eq. (19) by the complex conjugate quantities yields

$$|P(r,\theta,\phi)|^2=(\rho/2\pi r)^2|\tilde{\ddot{W}}(k_x,k_y)|^2. \tag{21}$$

From Eq. (21), it is seen that the acoustic energy radiated in the direction defined by θ and ϕ is determined solely by the structural wave-number component corresponding to k_x and k_y in Eq. (20). These values of k_x and k_y are always smaller than the acoustic wave number $k_0=\omega/c$; they correspond to the supersonic structural wave numbers that characterize the radiating components of the structural vibration. Therefore, a sensor that evaluates the wave-number component at prescribed values of k_x and k_y defined in Eq. (20) can effectively replace an error microphone located in the far field at angles θ and ϕ. Such a sensor will be referred to as a structural wave-number domain sensor.

2. Discrete wave-number transform

As done previously, the integral in Eq. (15) is approximated using N_d rectangular elements of dimension Δx by Δy by a finite summation in the form

$$\tilde{\ddot{W}}(k_x,k_y)\simeq\Delta x\,\Delta y\sum_{n_x=1}^{N_x}\sum_{n_y=1}^{N_y}\ddot{W}(x_{n_x},y_{n_y})e^{j(k_xx_{n_x}+k_yy_{n_y})}, \tag{22}$$

where $\Delta x=L_x/N_x$ and $\Delta y=L_y/N_y$ (N_x and N_y are the number of elements in the x and the y direction, respectively). The collocation points (x_{n_x},y_{n_y}) are defined by $x_{n_x}=-L_x/2+\Delta x/2(2n_x-1)$ and $y_{n_y}=-L_y/2+\Delta y/2(2n_y-1)$, where $n_x=1,2,\ldots,N_x$ and $n_y=1,2,\ldots,N_y$.

Introducing the time dependence, the *discrete* wave-number component is expressed as the summation of the acceleration signals $\ddot{w}(x_{n_x},y_{n_y},t)=\ddot{W}(x_{n_x},y_{n_y})e^{j\omega t}$ filtered by the frequency response function $H_{n_xn_y}(\omega)$,

$$\tilde{\ddot{w}}_d(k_x,k_y,t)=\tilde{\ddot{W}}_d(k_x,k_y)e^{j\omega t}=\sum_{n_x=1}^{N_x}\sum_{n_y=1}^{N_y}H_{n_xn_y}(\omega)\ddot{W}(x_{n_x},y_{n_y})e^{j\omega t}, \tag{23}$$

where

$$H_{n_xn_y}(\omega)=\Delta x\,\Delta y\exp(j\omega\tau_{n_xn_y}). \tag{24}$$

The above frequency response functions present a constant time delay,

$$\tau_{n_xn_y}=\frac{x_{n_x}\sin\theta\cos\phi+y_{n_y}\sin\theta\sin\phi}{c}. \tag{25}$$

Recalling the time convention $e^{j\omega t}$, the frequency response functions in Eq. (24) can be modeled by causal, linear phase FIR filters only if the time delay defined in Eq. (25) is negative. Since $\tau_{n_xn_y}$ take both positive and negative values, a modified delay must be introduced in order to make the filters realizable.

It is next demonstrated that the above requirement that results in a time-shifted error information can be satisfied in feedforward control. In this case, the controller is defined so as to minimize the mean square value of the sensor output, i.e., $J=E\{e^2(t)\}$ (Ref. 9). After control (after convergence in the case of an adaptive structure), the error signal $e(t)$ can be assumed to be stationary in a steady-state disturbance, i.e., $E\{e^2(t)\}=E\{e^2(t-\Delta t)\}$, where Δt denotes a time delay. This important property implies that a time-shifted version of the actual error signal will result in the same control performances. Also, it is straightforward to show that the error signal $e(t)$ is of arbitrary magnitude: since the optimal solution for the controller is found by setting the partial derivatives of J with

respect to the compensator coefficients to zero, any constant multiplicative factor will cancel. Note that the above result does not apply to model reference control;[10] in that case, the error signal is required to match a prescribed reference signal instead of being minimized. Moreover, when using several error signals, the proportionality constant should be the same for each sensor array. The above results can be verified by plotting the cost functions $J=E\{e^2(t)\}$ and $\bar{J}=E\{\bar{e}^2(t)\}$ versus the weights of the compensator where $\bar{e}(t)=\alpha e(t-\Delta t)$ is a proportional time-shifted version of the original error signal (α constant factor). It is seen that both surfaces have the same minimum but different shapes. Hence, a proportional time-shifted error signal influences the convergence process of the feedforward adaptive controller but does not alter the optimal solution.

The above discussion yields several important results. First, in order to satisfy the causality requirements of the frequency responses in Eq. (24), the time delays $\tau_{n_x n_y}$ can be replaced by $\bar{\tau}_{n_x n_y}=\tau_{n_x n_y}-\Delta t$, where $\Delta t>0$ is such that each modified time delay $\bar{\tau}_{n_x n_y}$ be negative. Second, the equivalence between the pressure and wave-number information can be further analyzed. Recalling Eq. (19), the wave-number component evaluated at k_x and k_y given by Eq. (20) appears to be proportional to the time-shifted acoustic pressure $p(r,\theta,\phi,t+r/c)$ radiated in the direction defined by θ and ϕ. It follows that using the wave-number information as an error signal in a feedforward control approach leads the same optimal solution as the far-field pressure information. This gives a physical interpretation of the wave-number component evaluated in the supersonic region and confirms the validity of its use as error information.

3. Wave-number spectrum

The previous section derived the transfer functions used to evaluate a single wave-number component $\tilde{W}_d(k_x,k_y)$. The approach is now formally extended to provide information over the entire wave-number spectrum.

As shown previously, only the supersonic wave numbers are of interest in radiation control, i.e., $(k_x^2+k_y^2)^{1/2}<k_0$. Physically, they relate to a particular direction of radiation at angles θ and ϕ. Hence, a multiple output structural sensor is built by choosing discrete values of k_x, k_y and constructing for each of them the appropriate transfer functions as given in Eq. (24). In order to obtain a constant time delay over the frequency bandwidth (linear phase), k_x and k_y must also satisfy Eq. (20) where θ and ϕ are fixed. In other words, the structural wave numbers must be proportional to the driving frequency.

The diagram of Fig. 3 shows the *discrete* wave-number spectrum for a 1-D structure ($k_y=0$) at two driving frequencies ω_1 and ω_2. The solid lines represent the modulus of the *discrete* wave-number component defined in Eq. (23). The dots represent the same quantity evaluated by a multiple output sensor at three discrete values of k_x between $-k_0$ and k_0. Each of these discrete values correspond to a fixed direction of radiation ($\theta,\phi=0$) and thus, are located on lines of equation $k_x=\omega/c\sin\theta$ in the (k_x,ω) plane. Therefore, the frequency response of the sensor output in the direction θ is obtained by plotting the wave-number component corresponding to k_x located on this line.

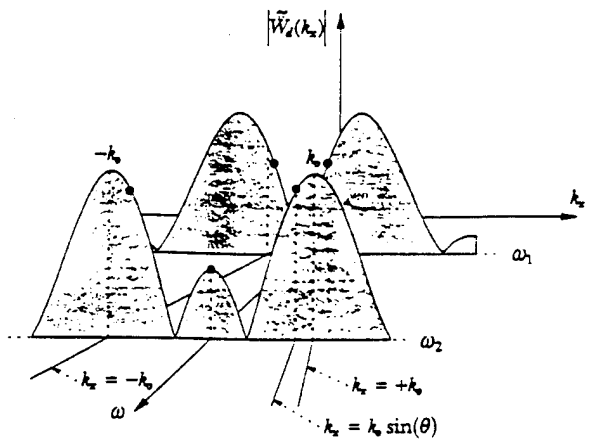

FIG. 3. Typical multiple output wave-number sensor diagram.

As an example, Fig. 4 presents the magnitude and phase of the *continuous* [Eq. (15)] and *discrete* [Eq. (23)] wave-number components evaluated along the direction ($\theta=75°$, $\phi=0$) versus frequency for a simply supported beam. The phase angle is relative to the input disturbance. The closed-form expressions for the *continuous* and *discrete* wave-number components are derived in the appendix. The beam characteristics and natural frequencies are given in Tables I and II, respectively. The model assumed 0.15% damping in the 20 modes included in the beam analytical response [Eqs. (A1) and (A3): $\eta_p=0.0015$,

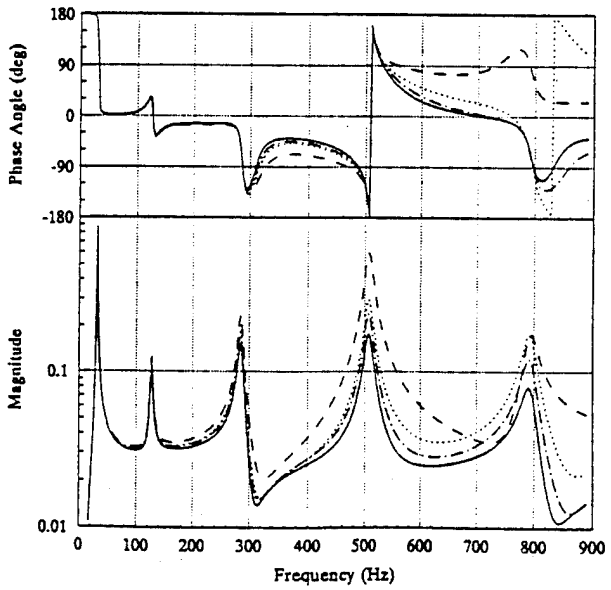

FIG. 4. Wave-number component corresponding to $\theta=75°$ for a simply supported beam; (a) ———, continuous representation; (b) – – –, (c) — —, (d)....., discrete representations using three, four, and five point sensors, respectively.

TABLE I. Beam characteristics.

Length	0.38 m
Width	0.04 m
Section	0.0002 m^2
Mass density	3132 kg/m^3
Bending stiffness	5.3290 N/m^2

$p=1,2,...,20$]. The structure is surrounded by air with density $\rho=1.27$ kg/m^3 and sound velocity $c=343$ m/s. The disturbance point force has magnitude $F=0.35$ N and is located at $x_0=-0.15\times L_x/2$. Three, four, and five accelerometers are used respectively to provide wave-number information over the first five structural modes. As expected, the overall error between continuous and discrete representations decreases when the number of accelerometers is increased. In the three cases [curves (b), (c), and (d)], negligible error is noticed for frequencies up to the third mode. The error becomes significant above the third mode when a three point sensor is used. However, four and five point sensors give good approximation up to the fifth mode, the best result being obtained with $N_d=5$. To summarize, the far-field radiation of the low order structural modes of a simply supported beam is roughly approximated by a small number of monopole sources equally spaced on the beam. Note that other types and locations of excitation would show similar behaviors. The next section discusses how these errors are related to the discrete approximation. Their influence on the control performances will be addressed in the companion paper.

4. Analogy of the discrete wave-number transform with the time domain discrete Fourier transform—Sampling aspects

Analogous to the time domain Fourier transform and its discrete representation (DFT), the discretization mechanism of the wave-number sensing procedure is further investigated. The case of the simply supported beam used previously is considered here for simplicity.

Recalling Eqs. (15) and (23), the *continuous* and *discrete* wave-number components become, respectively,

$$\tilde{\ddot{W}}(k_x)=L_y\int_{-L_x/2}^{+L_x/2}\ddot{W}(x)e^{jk_xx}\,dx, \tag{26}$$

$$\tilde{\ddot{W}}_d(k_x)=L_y\,\Delta x\sum_{i=1}^{N_d}\ddot{W}(x_i)e^{jk_xx_i}, \tag{27}$$

where $x_i=-L_x/2+\Delta x/2(2i-1)$, $i=1,2,...,N_d$. The above representations are analogous to the time domain Fourier transform. The time variable is replaced by the spatial coordinate x, Δx being the sampling period, and the frequency variable by the structural wave number or spatial frequency, k_x. The beam response, $\ddot{W}(x)$, can thus be seen by analogy as a time domain signal of finite duration corresponding to the length L_x and its discretized version, $\ddot{W}(x_i)$, $i=1,2,...,N_d$, as a N_d sample sequence with sampling period corresponding to Δx, where $\Delta x=L_x/N_d$.

TABLE II. Beam analytical natural frequencies.

Mode	Natural frequency (Hz)
1	31.73
2	126.9
3	285.6
4	507.7
5	793.2
6	1142

Applying the properties of the time domain DFT, a fundamental relation between continuous and discrete representations in the wave-number domain is expressed as

$$\tilde{\ddot{W}}_d(k_x)=\tilde{\ddot{W}}(k_x)*\delta_N(k_x), \tag{28}$$

where $*$ denotes the convolution product. The spectral window $\delta_N(k_x)$ solely depends on the sensor arrangement, i.e., location and number of point sensors. In the case of equal spacing, it takes the closed form given by Eq. (A16) of the Appendix. The representation in Eq. (28) is useful since the influence of the sensor arrangement on the wave-number component estimate is solely determined by $\delta_N(k_x)$. As described in the Appendix, the spectral window obtained in the case of equally spaced point sensors has large amplitudes at wave numbers $k_x=nK_s$, where $K_s=2\pi/\Delta x$ is the spatial sampling frequency and n is an integer. It follows that significant contribution to the *discrete* wave-number component $\tilde{\ddot{W}}_d(k_x)$ comes from *continuous* wave-number components that are far removed from the wave numbers of interest, i.e., $\tilde{\ddot{W}}(k_x-nK_s)$. Unless the *continuous* wave-number spectrum has zero amplitude above and below the Nyquist wave numbers $\pm K_s/2$, these aliasing errors will affect the accuracy of the wave-number component estimate. The beam wave-number spectrum extends from $-\infty$ to $+\infty$ since it has finite dimensions [Eqs. (A8) and (A10)]. Therefore aliasing occurs no matter how large K_s is. However, it will be greatly reduced when the Nyquist wave number is above the main peak of all the modes present in the bandwidth of interest, i.e., $K_s/2>p\pi/L_x$ or $N_d>p$, where p is the index of the highest mode found in the response. Also, the use of nonregular sampling is of interest. In this case, the aliasing effects can be reduced by designing some appropriate spectral window associated with a particular sampling scheme. Further investigation of spatial sampling and aliasing aspects will be the topic of a later paper.

II. SENSOR DESIGN

The previous section discussed prediction of sound radiation using analytical expressions for the frequency response functions of the radiation filters. This part addresses the design of the digital filters used to model the frequency response functions in the sensing procedure. Since the earlier sections have shown the equivalence of a Rayleigh's integral and a wave-number-based approach, the following derivations will only consider sensors based on the wave-number information. The transfer functions derived before are first modified in order to optimize the number and length of the FIR filters. Two filter design methods in the frequency and time domains, respectively, are then de-

scribed. The first design method is model-based; it uses the analytical transfer functions in the frequency domain. The second design method allows the use of time-domain experimental data measured on the structural acoustic system.

A. Modified radiation transfer functions

The choice of the time delay $\Delta\tau$ introduced in Sec. I B 2 is first discussed. The case of a 1-D structure ($k_y=0$) is considered for simplicity. The structure is of finite width and its response is assumed to be constant in the y direction (see Fig. 2).

The *discrete* wave-number component corresponding to the direction θ is written as the summation of the structural acceleration measured at a number of points $(x_i,y=0)$ equally spaced and multiplied by the radiation transfer functions $\bar{H}_i(\omega)$ $(i=1,2,...,N_d)$,

$$\tilde{\ddot{W}}_d(k_x)=\sum_{i=1}^{N_d}\bar{H}_i(\omega)\ddot{W}(x_i). \tag{29}$$

Using a unit magnitude factor and a positive time delay $\Delta\tau$ to ensure causality in Eq. (24), the modified frequency response functions for the radiation filters are written as

$$\bar{H}_i(\omega)=\exp(j\omega\bar{\tau}_i),\quad \bar{\tau}_i=\tau_i-\Delta\tau\leqslant 0\quad (i=1,2,...,N_d). \tag{30}$$

The number of coefficients of the ith FIR filter should be at least greater than the time delay $\bar{\tau}_i$ divided by the sampling period $T_s=1/F_s$. Therefore, it is desirable to make $|\bar{\tau}_i|$ as small as possible. An optimal value for $\Delta\tau$ is $\Delta\tau=\max\{\tau_i\}$ where $i=1,2,...,N_d$. For this particular value of $\Delta\tau$, one of the delays $\bar{\tau}_i$ becomes zero while the others are minimum. As a first result, the number of coefficients of the FIR filters is optimized since the set of delays is made minimum. Second, the transfer function corresponding to the largest τ_i becomes equal to unity (zero time delay). Thus, the number of filters used in the sensor is reduced by one. In other words, the optimal $\Delta\tau$ results in a smaller computational effort. A rule of thumb to determine the number of coefficients N_i can be expressed as

$$N_i=R(\bar{\tau}_i/T_s)+\epsilon, \tag{31}$$

where $R(x)$ rounds up the real x (next integer to x), T_s is the sampling period, and ϵ is an integer between 0 and 2.

B. Frequency domain design

In the frequency domain, the filter coefficients are obtained by minimizing, in the least-square sense, the error between the desired and the modeled frequency response functions over the frequency range of interest. The desired frequency response is generated from Eq. (30). The modeled frequency response $H_i^m(\omega)$ can be found from the filter finite impulse response $\{U_l^i, l=0,1,...,N_i-1\}$ as follows:

$$H_i^m(\omega)=\sum_{l=0}^{N_i-1}U_l^i e^{-j\omega lT_s},\quad i=1,2,...,N_d. \tag{32}$$

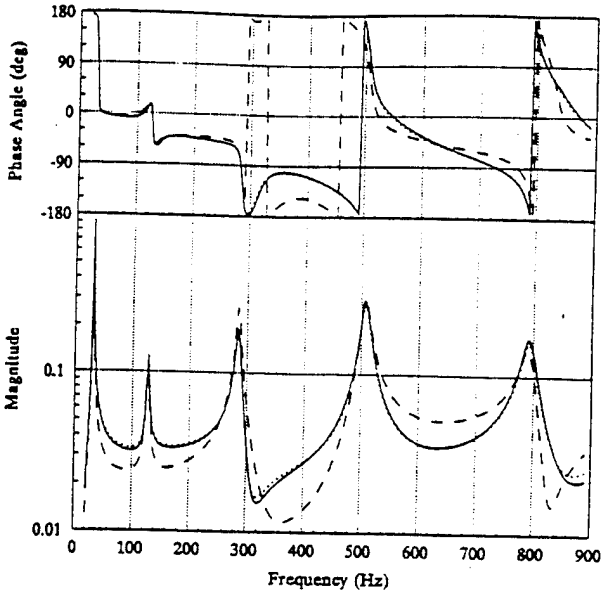

FIG. 5. Analytical and modeled sensor output: (a) ———, analytical discrete representation; (b) —, (c)....., modeled discrete representations with $\epsilon=0$ and $\epsilon=1$, respectively.

Most of the existing frequency domain design algorithms allow the use of a weighting function such that the minimization be only effective over the frequency range of interest. Minimizing over the entire frequency range $[0,F_s/2]$ would reduce the accuracy of the modeled frequency response function. The algorithm implemented in the Matlab function *invfreqz* (software by Math Works[11]) is used here.[12]

To illustrate the design procedure, the *discrete* wave-number component of the beam described earlier is now modeled by an array of filters. The sampling frequency is $F_s=3000$ Hz and the design frequency range extends from 0 to 850 Hz including the first five bending modes. In this example, $N_d=4$ point sensors, i.e., four structural measurement points, are implemented to evaluate the wave-number component corresponding to radiation in the direction $\theta=75°$. Returning to Fig. 4, this case corresponds to the curve (c). The optimal value for $\Delta\tau$ is determined from the time delays τ_i $(i=1,2,3,4)$ as explained in the previous section. This choice implies that only three filters need to be designed, one transfer function being equal to unity. Using the rule of thumb given in Eq. (31) with $\epsilon=0$, the FIR filters have three, two, and one coefficient(s), respectively. A second case uses $\epsilon=1$, i.e., four, three, and two coefficients, respectively, are then determined. The sensor output spectrum is computed from the modeled frequency response functions of Eq. (32) and compared to the analytical *discrete* wave-number component. The results are presented in Fig. 5. The case $\epsilon=0$ (dashed line) gives a relatively good approximation at the resonant frequencies while some error is noticed off-resonance. Very small error is obtained with $\epsilon=1$ (dotted line). Note that since the delays τ_i are replaced by $\bar{\tau}_i=\tau_i-\Delta\tau$, the phase of the analytical and modeled wave-number components in

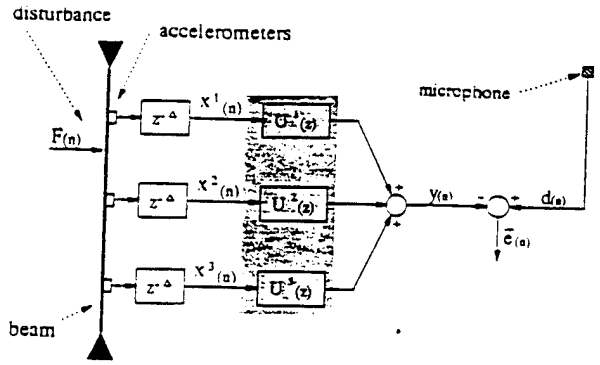

FIG. 6. Time domain sensor design applied to the simply supported beam.

Fig. 5 is different from the phase shown in Fig. 4 by a linear phase factor $\exp(-j\omega\,\Delta\tau/c)$.

C. Time domain design

The time domain design uses adaptive filter theory.[9] It involves the measurements of the time varying structural response at each location (x_{n_x}, y_{n_y}) $(n_x=1,2,...,N_x,$ $n_y=1,2,...,N_y)$ along with the radiated far-field pressure in a prescribed direction. The filter coefficients can be found either on-line using the time domain LMS algorithm or off-line by computing the optimum least-square solution. In this method, the sensor includes the dynamics of the real system along with the response of the measuring instrumentation. This property is an advantage over the first design method, which uses analytical expressions and does not model the dynamics of the instrumentation. However, the time domain design depends on the excitation characteristics, i.e., the filter impulse responses represent the optimal solution over a given bandwidth for a particular type and location of excitation. For example, a sensor based on a particular disturbance input force may be inaccurate when the structure is controlled by the pair of moments induced by a piezoelectric actuator at a different location. However, these variations can be considered small enough compared to the degree of precision required for the sensor.

It has been shown previously that the time-varying wave-number component is proportional to the time-shifted pressure $p(\mathbf{r},t+r/c)$. Thus, the desired sensor output $\bar{e}(t)$ can be expressed in function of the measured acoustic pressure as

$$\bar{e}(t)=p[\mathbf{r},t-\Delta\tau+(r/c)], \tag{33}$$

where $\Delta\tau>0$ accounts for causality. In addition to the causality requirement in Eq. (30), $\Delta\tau$ is required to satisfy $(r/c-\Delta\tau)/T_s=\Delta$, where Δ is an positive integer. The desired sensor output can then be expressed in the discrete time domain as $\bar{e}(n)=p(n+\Delta)$. Figure 6 shows the block diagram of the time domain sensor design in the case of a 1-D simply supported beam. It should be noted that the delay $z^{-\Delta}$ in the *sensor path* makes the system causal and equivalent to the time shift $z^{+\Delta}$ in the *pressure path* since $p(n)=\bar{e}(n-\Delta)=d(n)$. The error to be minimized is the difference between the measured pressure and the sensor output: $e(n)=d(n)-\bar{e}(n)$. The acceleration at time $t_{n-\Delta}$ measured at point x_i is denoted $x^i(n)$. The error signal $e(n)$ can be expressed in matrix form by the following general formula:

$$e(n)=d(n)-\mathbf{X}^T(n)\mathbf{U}=d(n)-\mathbf{U}^T\mathbf{X}(n). \tag{34}$$

The column vector $\mathbf{U}$ contains the N_i coefficients of the filters $\underline{U}^i$ $(i=1,...,N_d)$,

$$\mathbf{U}=\begin{Bmatrix}\{\underline{U}^1\}\\ \vdots\\ \{\underline{U}^i\}\\ \vdots\\ \{\underline{U}^{N_d}\}\end{Bmatrix}, \quad \text{where } \underline{U}^i=\begin{Bmatrix}U_0^i\\ \vdots\\ U_{N_i-1}^i\end{Bmatrix}. \tag{35}$$

The column vector $\mathbf{X}(n)$ is defined as

$$\mathbf{X}(n)=\begin{Bmatrix}\{\underline{x}^1(n)\}\\ \vdots\\ \{\underline{x}^i(n)\}\\ \vdots\\ \{\underline{x}^{N_d}(n)\}\end{Bmatrix}, \quad \text{where } \underline{x}^i(n)=\begin{Bmatrix}x^i(n)\\ x^i(n-1)\\ \vdots\\ x^i(n-N_i+1)\end{Bmatrix}. \tag{36}$$

Here, $\mathbf{X}(n)$ and $\mathbf{U}$ both contain $K=\sum_{i=1}^{N_d}N_i$ elements $X_k(n)$ and $U_k(k=1,...,K)$, respectively. Equation (34) can be rewritten in closed form as

$$\begin{aligned}e(n)&=d(n)-\sum_{i=1}^{N_d}\left\{\sum_{j=0}^{N_i-1}U_j^i x^i(n-j)\right\}\\ &=d(n)-\sum_{k=1}^{K}U_kX_k(n).\end{aligned} \tag{37}$$

The cost function to be minimized is defined as the mean-square value of the error signal,

$$\begin{aligned}J(U_k)&=E\{e^2(n)\}\\ &=E\{d^2(n)\}-2E\{d(n)\mathbf{X}^T(n)\}\mathbf{U}\\ &\quad+\mathbf{U}^TE\{\mathbf{X}(n)\mathbf{X}^T(n)\}\mathbf{U}.\end{aligned} \tag{38}$$

The above expression is a quadratic function of the filter coefficients U_k. Thus there is only one optimal solution. Differentiating $J(U_k)$ with respect to U_k in Eq. (38) produces

$$\frac{\partial J}{\partial U_k}(U_k)=2E\left\{e(n)\frac{\partial e(n)}{\partial U_k}\right\}=-2E\{e(n)X_k(n)\}, \tag{39}$$

where $X_k(n)$ denotes the kth element of $\mathbf{X}(n)$. The optimum solution can be obtained by substituting Eq. (37) in Eq. (39) and setting the partial derivatives with respect to U_k equal to 0 for $k=1,2,...,K$. These K linear equations are rearranged in matrix form as

$$\mathbf{R}_{xx}\mathbf{U}=\mathbf{R}_{dx}. \tag{40}$$

Here, $\mathbf{R}_{xx}$ denotes the autocorrelation matrix of the input signals contained in the vector $\mathbf{X}(n)$ and $\mathbf{R}_{dx}$, the cross-correlation matrix between the input signals and the desired output signal $d(n)$:

$$\mathbf{R}_{xx}=\begin{bmatrix} E\{X_1(n)\mathbf{X}^T(n)\} \\ E\{X_2(n)\mathbf{X}^T(n)\} \\ \vdots \\ E\{X_K(n)\mathbf{X}^T(n)\} \end{bmatrix}, \tag{41}$$

$$\mathbf{R}_{dx}=\begin{bmatrix} E\{d(n)X_1(n)\} \\ E\{d(n)X_2(n)\} \\ \vdots \\ E\{d(n)X_K(n)\} \end{bmatrix}. \tag{42}$$

Alternatively, the LMS algorithm[9] can be used to adapt the coefficients U_k $(k=1,2,...,K)$ in order to minimize the cost function $J(U_k)$ using the steepest descent method,

$$U_k(n+1)=U_k(n)-\mu\frac{\partial J}{\partial U_k}(U_k), \tag{43}$$

where μ controls the stability and rate of convergence. The time domain LMS algorithm uses an instantaneous gradient approximation yielding the following update equation:

$$U_k(n+1)=U_k(n)+2\mu e(n)X_k(n) \quad (k=1,2,...,K). \tag{44}$$

III. CONCLUSIONS

A new sensing technique using point structural sensors has been developed for the prediction of far-field pressure or structural wave-number information in the case of vibrating finite rectangular radiators. The approach is based on the discretization of the Helmoltz integral over the radiating surface. By choosing an appropriate Green's function, the term related to the surface pressure vanishes and the radiated pressure becomes only a function of the radiating surface acceleration. The practical implementation uses accelerometers to measure the structural response and FIR filters to model the transfer functions associated with each elemental area. The summation of the filter outputs gives a good estimate of the far-field pressure radiated in a prescribed direction or its equivalent wave-number expression. When applied to feedforward control approaches, the filter array is optimized to considerably reduce the computational load thus making the technique easy to implement on real structures.

As opposed to the use of distributive sensors that filter the efficient radiating modes in the spatial domain using shaped PVDF films, the present method filters the structural information in the time domain using digital filters. Filters being easier to design and more selective than PVDF films, this real time structural acoustic sensor is believed to yield better control performances in a prescribed direction. In addition, unlike PVDF films that are shaped for a single modal response, the described sensor gives radiation information over a broadband frequency range.

The present approach is only valid for the case of planar radiators. In the case of more complex geometry, the Rayleigh's integral cannot be used and a formulation involving another type of Green's function needs to be derived or the structural diffraction terms accounted for. Further investigation will extend the technique to those cases and experimentally demonstrate its use on real structures.

ACKNOWLEDGMENTS

The authors gratefully acknowledge the support of this work by the Office of Naval Research under Grant No. ONR-N00014-92-j-1170.

APPENDIX

Analytical expressions for the beam response, its continuous and discrete wave-number transforms are derived. The beam shown in Fig. 2 is simply supported with length L_x and width L_y. An harmonic point force $f(t)=Fe^{j\omega t}$ is applied at location $(x=x_0, y=0)$. The beam response is assumed to have constant amplitude of motion in the y direction and the radiated acoustic field is investigated in the x-z plane $(\phi=0)$. The surrounding media is air; it is assumed to have negligible influence on the *in vacuo* structural response.

1. Structural response

The beam out-of-plane displacement complex amplitude $W(x)$ can be expressed as an infinite summation over each modal response

$$W(x)=\sum_{p=1}^{+\infty} q_p(\omega)\psi_p(x), \quad -\frac{L_x}{2}<x<\frac{L_x}{2}, \tag{A1}$$

where $q_p(\omega)$ is the pth modal displacement and $\psi_p(x)$ is the pth eigenfunction. Taking the origin of the coordinate system at the center of the beam, the eigenfunctions corresponding to the simply supported boundary condition are

$$\psi_p(x)=(2/m)^{1/2}\sin[\gamma_p(x+L_x/2)], \tag{A2}$$

where $\gamma_p=p\pi/L_x$. The factor $(2/m)^{1/2}$ results from the normalization chosen for the eigenfunctions, such that they are orthonormal with respect to the mass m of the beam. The modal displacement $q_p(\omega)$ is given by

$$q_p(\omega)=H_p(\omega)\psi_p(x_0)F=\frac{1}{\omega_p^2-\omega^2+2j\eta_p\omega_p\omega}\psi_p(x_0)F, \tag{A3}$$

where $H_p(\omega)$ is the pth modal frequency response function. Here, ω_p and η_p are the pth natural frequency and modal damping ratio, respectively. The analytical natural frequencies are defined as

$$\omega_p^2=\gamma_p^4\frac{EI}{\rho_s S_s}, \tag{A4}$$

where ρ_s is the beam density, S_s the beam section, and EI is the Young's modulus bending inertia product. The acceleration response is obtained by taking the second partial derivative with respect to time of the displacement response,

$$\ddot{w}(x,t)=\ddot{W}(x)e^{j\omega t}=-\omega^2 W(x)e^{j\omega t}. \tag{A5}$$

The beam response is now sampled with N_d points at locations $x_i = -L_x/2 + \Delta x/2(2i-1)$, $i=1,2,\ldots,N_d$, where $\Delta x = L_x/N_d$ is the sampling period. The discrete acceleration response can be expressed using Dirac distributions as

$$\ddot{W}_d(x) = \sum_{i=1}^{N_d} \ddot{W}(x)\Delta x \delta(x-x_i). \tag{A6}$$

This representation will be useful when deriving an alternative expression for the discrete wave-number transform.

2. Wave-number transform

Substituting $k_y=0$ in Eq. (15) yields the following single integral for the one-dimensional acceleration wave-number transform:

$$\tilde{\ddot{W}}(k_x) = L_y \int_{-L_x/2}^{L_x/2} \ddot{W}(x) e^{jk_x x}\, dx. \tag{A7}$$

Equation (A7) can be rewritten in terms of the modal acoustic influence functions as

$$\tilde{\ddot{W}}(k_x) = -\omega^2 \sum_{p=1}^{+\infty} q_p(\omega)\xi_p(k_x), \tag{A8}$$

where

$$\xi_p(k_x) = L_y \int_{-L_x/2}^{L_x/2} \psi_p(x) e^{jk_x x}\, dx. \tag{A9}$$

Here, $\xi_p(k_x)$ is defined as the wave-number transform of the pth eigenfunction. Hence, it can also be referred to as the pth modal wave-number component. Substituting Eq. (A2) in Eq. (A9) yields

$$\xi_p(k_x) = L_y\left(\frac{2}{m}\right)^{1/2} \begin{Bmatrix} \cos(k_x L_x/2) \\ -j\sin(k_x L_x/2) \end{Bmatrix} \frac{2\gamma_p}{(\gamma_p^2 - k_x^2)}, \tag{A10}$$

where $\cos(k_x L_x/2)$ is used when p is odd and $\sin(k_x L_x/2)$ when p is even. As seen in Eq. (A10), $\xi_p(k_x)$ is either purely real (odd mode number) or purely imaginary (even mode number). Its zeros are expressed as

$$k_x = \begin{cases} (2n+1)\gamma_p, & \text{for } p \text{ odd, } n \text{ integer,} \\ & \text{and } 2n+1 \neq \pm p, \\ 2n\gamma_p, & \text{for } p \text{ even, } n \text{ integer,} \\ & \text{and } 2n \neq \pm p. \end{cases} \tag{A11}$$

3. Discrete wave-number transform

Let $\mathcal{K}\{g(x)\}$ denote the wave-number transform operator,

$$\mathcal{K}\{g(x)\} = \int_{-\infty}^{+\infty} g(x) e^{+jk_x x}\, dx. \tag{A12}$$

Using the discrete representation in Eq. (A6), the discrete wave-number transform is expressed as

$$\tilde{\ddot{W}}_d(k_x) = L_y \mathcal{K}\{\ddot{W}_d(x)\} = L_y \mathcal{K}\left\{\ddot{W}(x)\Delta x \sum_{i=1}^{N_d} \delta(x-x_i)\right\}. \tag{A13}$$

An important property of Fourier transforms yields

$$\tilde{\ddot{W}}_d(k_x) = L_y \mathcal{K}\{\ddot{W}(x)\} * \mathcal{K}\left\{\Delta x \sum_{i=1}^{N_d} \delta(x-x_i)\right\} = \tilde{\ddot{W}}(k_x) * \delta_N(k_x), \tag{A14}$$

where * denotes the convolution product and $\delta_N(k_x)$ is a spectral window given by

$$\delta_N(k_x) = \Delta x \sum_{i=1}^{N_d} e^{jk_x x_i}. \tag{A15}$$

Substituting x_i in terms of L_x, Δx, and i, the above expression can be rewritten as

$$\delta_N(k_x) = \Delta x \frac{\sin(k_x N_d \Delta x/2)}{\sin(k_x \Delta x/2)} e^{jk_x(-L_x + N_d \Delta x)/2}. \tag{A16}$$

The magnitude of $\delta_N(k_x)$ takes its maximum value at an infinite set of wave numbers $k_x = nK_s$, where $K_s = 2\pi/\Delta x$ is the spatial sampling frequency and n is an integer. It is symmetric and periodic with period K_s, i.e., $|\delta_N(-k_x)| = |\delta_N(k_x)|$ and $|\delta_N(k_x)| = |\delta_N(k_x + nK_s)|$. In brief, $|\delta_N(k_x)|$ is approximately like an infinite row of sinc functions spaced K_s apart.

[1] J. D. Maynard, E. G. Williams, and Y. Lee, "Nearfield acoustic holography: I. Theory of generalized holography and the development of NAH," J. Acoust. Soc. Am. 78, 1385–1413 (1985).

[2] S. Amini, C. Ke, and P. J. Harris, "Iterative solution of boundary element equations for the exterior Helmoltz problem," J. Vib. Acoust. 112, 257–262 (1990).

[3] C. R. Fuller, C. A. Rogers, and H. H. Robertshaw, "Control of sound radiation with active/adaptive structures," J. Sound Vib. 157(1), 19–39 (1992).

[4] R. L. Clark and C. R. Fuller, "Modal sensing of efficient radiators with PVDF distributed sensors in active structural acoustic approaches," J. Acoust. Soc. Am. 91, 3321–3329 (1990).

[5] W. T. Baumann, W. R. Saunders, and H. H. Robertshaw, "Active suppression of acoustic radiation from impulsively excited structures," J. Acoust. Soc. Am. 90, 3202–3208 (1991).

[6] M. C. Junger and D. Feit, *Sound, Structures and Their Interaction* (MIT, Boston, 1986).

[7] F. J. Fahy, *Sound and Structural Vibration* (Academic, London, 1985).

[8] C. R. Fuller and R. A. Burdisso, "A wavenumber domain approach to the active control of structure-borne sound," J. Sound Vib. 148(2), 355–360 (1991).

[9] B. J. Widrow and S. D. Stearns, *Adaptive Signal Processing* (Prentice-Hall, Englewood Cliffs, NJ, 1986).

[10] R. L. Clark and C. R. Fuller, "A model reference approach for implementing active structural acoustic control," J. Acoust. Soc. Am. 92, 1534–1544 (1992)..

[11] *PC-Matlab for MS-DOS Computers* (The MathWorks, Inc., South Natick, MA, 1989).

[12] J. O. Smith, "Techniques for Digital Filter Design and System Identification, with Application to the Violin," Ph.D. dissertation, Stanford University (1983).

C-19 Advanced Time Domain Wave-Number Sensing for Structural Acoustic Systems II. Radiation Control of a Simply Supported Beam, J. P. Maillard and C. R. Fuller, Journal of the Acoustical Society of America, Vol. 95 No. 6, pp. 3262-3272, June 1994.

Advanced time domain wave-number sensing for structural acoustic systems. II. Active radiation control of a simply supported beam

J. P. Maillard and C. R. Fuller
Vibration and Acoustics Laboratories, Mechanical Engineering Department, Virginia Polytechnic Institute and State University, Blacksburg, Virginia 24061-0238

(Received 9 June 1993; revised 21 October 1993; accepted 4 February 1994)

A real time structural acoustic sensor and associated signal processing is developed and applied to the active control of sound radiated by a simply supported beam. The sensor consists of multiple accelerometers mounted on the structure. An array of FIR filters processes the measured structural information to provide an estimate of the structural wave-number component coupled to acoustic radiation in a prescribed direction. This time domain signal is used as the error information in a feedforward adaptive control approach. The single channel filtered-X LMS algorithm is implemented here. Computer simulations in the discrete time domain demonstrate the ability of the sensor to replace the use of error microphones in the far field. The described sensor represents a significant alternative to the use of distributive structural sensors (for example piezoelectric material) by providing accurate radiation information over a broadband frequency range.

PACS numbers: 43.40.At, 43.40.Cw, 43.40.Vn, 43.60.Gk

INTRODUCTION

Sound radiated by vibrating structures is an important issue in numerous industrial applications and much research has been conducted in the field of noise control. In this respect, active structural active control (ASAC) techniques have been successfully applied in situations where passive methods are inefficient, i.e., in the low-frequency range. Previously, Fuller has demonstrated both theoretically[1] and experimentally[2] that sound radiated from structures can be controlled by applying vibrating point forces directly to the structure, while the error information is taken from microphones in the acoustic far field. More recent work has been devoted to the development of new actuators (piezoelectric ceramics) and distributed structural sensors (PVDF films) designed to eliminate the use of far-field microphones and achieve global control. In particular, Clark and Fuller[3] have demonstrated the use of PVDF film modal sensors in ASAC approaches applied to a simply supported plate under single frequency excitation. Also, Fuller and Burdisso[4] recently suggested the use of wavenumber cost function in ASAC.

In a companion paper,[5] the authors theoretically introduced a sensing approach using point structural sensors in parallel with an array of digital filters. This method provides estimates of the structural wave-number component(s) coupled to acoustic radiation in prescribed direction(s) for finite planar radiators. The sensor implements a number of accelerometers equally spaced on the structure. The accelerometer outputs are passed through finite impulse response (FIR) filters and summed to provide far-field radiation information. This time domain signal can be directly used as the error information in control algorithms. One of the main advantages of the method is that it provides radiation information over a broadband frequency range and can thus be applied to randomly excited structures. It will be referred to as real time structural acoustic sensing.

The present work illustrates structural acoustic sensing applied to the active control of acoustic radiation from a simply supported beam. The control approach is the time domain adaptive filtered-X LMS algorithm and a single control input is applied to the structure in order to minimize the far-field pressure in one direction. Computer simulations are performed in the discrete time domain to demonstrate the use of the sensing procedure.

Recalling the theoretical developments of the companion paper,[5] the sensor is described for the particular case of a simply supported beam in the first part of the paper. The influence of structural acoustic sensing on the control performance is first studied in the frequency domain. In this case, theoretical transfer functions are used to obtain the optimal control input. Therefore, the system does not take into account the causality issue and neglect the errors introduced by the use of digital filters that have a discrete impulse response. To obtain more realistic results, time-domain simulations are performed using discrete impulse responses for the structural acoustic system. In the second part, the filtered-X version of the Widrow–Hoff LMS algorithm[6] is briefly introduced and the computer simulation procedure is discussed along with the design of the filter array for the sensor. Finally, the third part of the paper presents results from the control simulations in the case of broadband excitations encompassing the first four bending modes of the beam.

I. SENSOR DESCRIPTION

The sensing technique presented in the companion paper is applied here to the case of a baffled simply supported

 0001-4966/94/95(6)/3262/11/$6.00 © 1994 Acoustical Society of America

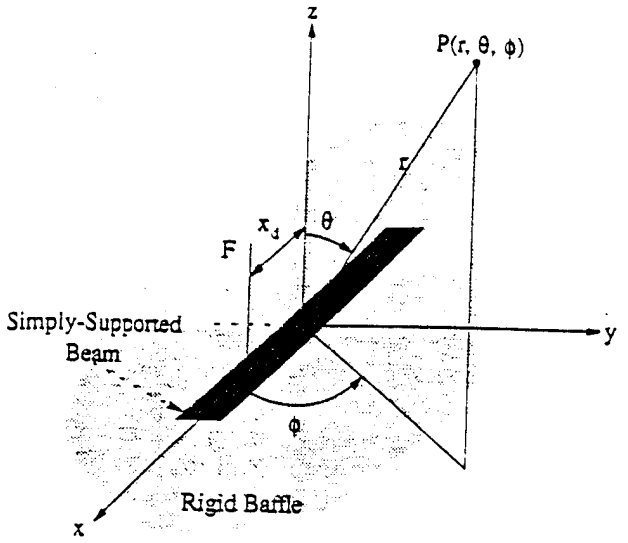

FIG. 1. Coordinate system of the simply supported beam.

beam. With the purpose of establishing basic concepts and notations, the equations governing the beam response and its acoustic radiation in the far field are first recalled along with the desired transfer functions to be modeled in the sensor implementation. The sensor is then further described in the frequency domain in terms of control performance; the acoustic radiation of the beam after control is presented for both cases where continuous and estimated wavenumber components are used as the error information.

A. Simply supported beam system

Figure 1 shows an infinite baffled simply supported beam of length L_x and width L_y excited by a harmonic point force $f^d(t)=F^d e^{j\omega t}$ at point $x=x_d$; ω represents the angular frequency, t is the continuous time, and F^d is the disturbance complex amplitude. The beam response is assumed to have constant amplitude of motion in the y direction and the radiated acoustic field is investigated in the x-z plane ($\phi=0$). The surrounding media is air and is assumed to have negligible influence on the *in vacuo* structural response.

1. Structural response

The beam out-of-plane displacement $w(x,t)$ can be given as a linear combination of the modes as

$$w(x,t)=\sum_{p=1}^{\infty} q_p(\omega)\psi_p(x)e^{j\omega t}, \quad -\frac{L_x}{2}<x<\frac{L_x}{2}, \tag{1}$$

where $q_p(\omega)$ is the pth modal displacement and $\psi_p(x)$ the pth eigenfunction. Using the coordinate system shown in Fig. 1, the eigenfunctions for the simply supported boundary condition are given by

$$\psi_p(x)=(2/m)^{1/2}\sin[\gamma_p(x+L_x/2)], \tag{2}$$

where $\gamma_p=p\pi/L_x$. The factor $(2/m)^{1/2}$ results from the normalization chosen for the eigenfunctions, such that they are orthonormal with respect to the mass m of the beam.

The modal displacement $q_p(\omega)$ is defined as

$$q_p(\omega)=H_p(\omega)\psi_p(x_d)F^d$$

$$=\frac{1}{\omega_p^2-\omega^2+2j\eta_p\omega_p\omega}\psi_p(x_d)F^d, \tag{3}$$

where $H_p(\omega)$ is the pth modal frequency response function; ω_p and η_p are the pth natural frequency and modal damping ratio, respectively. The analytical natural frequencies are

$$\omega_p^2=\gamma_p^4(EI/\rho_s S_s), \tag{4}$$

where ρ_s is the beam density, S_s the beam section area, and EI the bending stiffness.

The beam response due to the input disturbance, $f^d(t)=F^d e^{j\omega t}$, is then controlled with two piezoelectric patches bonded symmetrically to the front and back surface of the beam and driven 180° out-of-phase. The corresponding excitation is modeled by a line bending moment pair with complex amplitude M^c located at the end of the patches.[7] The beam response due to the control input is obtained by replacing in Eq. (3) the point force excitation term $\psi_p(x_d)F^d$ by a bending moment excitation term $m_p M^c$. The control modal force component m_p can be shown to be given by

$$m_p=\frac{d}{dx}\{\psi_p(x_c+c_a)-\psi_p(x_c-c_a)\}, \tag{5}$$

x_c is the coordinate of the center of the actuator, and $2c_a$ is the actuator length. From the superposition principle, the controlled system response is the sum of the response due to the disturbance input and the response due to the control input. The modal displacement of the controlled system $q_p^c(\omega)$ becomes

$$q_p^c(\omega)=H_p(\omega)[\psi_p(x_d)F^d+m_p M^c]. \tag{6}$$

Finally, the acceleration distribution is the second partial derivative with respect to time of the displacement response, i.e.,

$$\ddot{w}(x,t)=\ddot{W}(x)e^{j\omega t}=-\omega^2 W(x)e^{j\omega t}, \quad -\frac{L_x}{2}<x<\frac{L_x}{2}. \tag{7}$$

2. Radiation in the acoustic far field

The far-field pressure $p(r,\theta,t)$ radiated by the beam at point $(r,\theta,\phi=0)$ can be expressed in terms of structural information as[8]

$$p(r,\theta,t)=\frac{\rho e^{-jk_0 r}}{2\pi r}\tilde{\ddot{W}}(k_0\sin\theta)e^{j\omega t}, \tag{8}$$

where $k_0=\omega/c$ is the acoustic wave number, c the speed of sound in the medium, and ρ is its density. In the above expression, $\tilde{\ddot{W}}(k_0\sin\theta)$ denotes the wave-number transform of the beam normal acceleration distribution $\ddot{W}(x)$ defined in Eq. (7). It can be written as the spatial Fourier transform of the beam response. Since the model assumes a constant response versus the y direction, the structural waves travel solely along the x direction and the structural

wave number in the y direction is zero, i.e., $k_y=0$. Therefore, the beam acceleration wave-number transform simplifies as

$$\tilde{\ddot{W}}(k_x)=L_y\int_{-L_x/2}^{L_x/2}\ddot{W}(x)e^{jk_x x}\,dx. \tag{9}$$

Substituting Eqs. (7) and (1), Eq. (9) can be rewritten as

$$\tilde{\ddot{W}}(k_x)=-\omega^2\sum_{p=1}^{\infty}q_p(\omega)\xi_p(k_x), \tag{10}$$

where

$$\xi_p(k_x)=L_y\int_{-L_x/2}^{L_x/2}\psi_p(x)e^{jk_x x}\,dx. \tag{11}$$

Here, $\xi_p(k_x)$ is defined as the wave-number transform of the pth eigenfunction and will be referred to as the pth modal wave-number component. A closed-form expression of the above formulation can be found in the Appendix of the companion paper.[5]

Note that Eq. (8) is only valid in the far field. This representation is equivalent to the stationary phase approximation discussed by Junger and Feit.[8] As seen from Eq. (8), the radiated far-field pressure is solely a function of the wave-number component evaluated at wave numbers $k_x=k_0\sin\theta$ that are smaller than the acoustic wave number k_0 by definition of the sine function. In other words, only the structural motion with supersonic wave numbers $k_x<k_0$ radiates in the far field. Moreover, it is straightforward to show from Eq. (8) that the supersonic wave-number component $\tilde{\ddot{w}}(k_0\sin\theta,t)$ is proportional to the time-shifted far-field pressure $p(r,\theta,t+r/c)$, i.e., it completely describes the system in terms of radiated energy in the far field. The sensor configuration described in the following section is based on the estimate of the wave-number component corresponding to a prescribed direction of radiation θ in the x-z plane.

B. Sensor configuration

The governing equations for the sensor are presented in the case of the above simply supported beam system. The wave-number information is approximated by the summation of the structural acceleration measured at a number of points and multiplied in the frequency domain by complex transfer functions.

1. Discrete wave-number transform

The structural acceleration is measured at locations $x_i=-L_x/2+\Delta x/2(2i-1)$, $i=1,2,\ldots,N_d$ by means of N_d accelerometers. The spacing of the accelerometers is given by $\Delta x=L_x/N_d$. The structural wave-number component in Eq. (9) is approximated by a *discrete* expression defined as

$$\tilde{\ddot{W}}_d(k_x)=L_y\,\Delta x\sum_{i=1}^{N_d}\ddot{W}(x_i)e^{jk_x x_i}. \tag{12}$$

Note that the accuracy of the *discrete* wave-number transform depends on both the number of point sensors N_d and the frequency ω due to the fact that the structural response becomes more complicated at higher frequencies in terms of spatial variation. For instance, results from the companion paper[5] show that a four-point sensor ($N_d=4$) gives a fairly good approximation over the first four bending modes of a simply supported beam. Analogous to the continuous representation, Eq. (12) is expressed in terms of modal contributions as

$$\tilde{\ddot{W}}_d(k_x)=-\omega^2\sum_{p=1}^{\infty}q_p(\omega)\xi_p^d(k_x), \tag{13}$$

where the *discrete* modal wave-number components are given by

$$\xi_p^d(k_x)=L_y\,\Delta x\sum_{i=1}^{N_d}\psi_p(x_i)e^{jk_x x_i}. \tag{14}$$

Introducing the time dependence $e^{j\omega t}$ and the angular frequency $\omega=k_0c$ in Eq. (12) yields

$$\tilde{\ddot{w}}_d(k_x,t)=\sum_{i=1}^{N_d}H_i(\omega)\ddot{w}(x_i,t), \tag{15}$$

where the transfer functions $H_i(\omega)$ to be modeled by the array of filters are written as

$$H_i(\omega)=L_y\Delta x\,e^{j\omega\tau_i},\quad i=1,2,\ldots,N_d, \tag{16}$$

$\tau_i=(x_i/c)\sin\theta$ is a time delay, characteristic of each acoustic path. The transfer functions in Eq. (16) have a constant magnitude and a linear phase term. Therefore, finite impulse response (FIR) filters will be used in the computer simulations discussed in the next part as well as in the practical implementation of the technique. Note that τ_i takes both positive and negative values. Recalling the time convention $e^{j\omega t}$, only negative values of τ_i ensure the transfer function $H_i(\omega)$ to be causal.

2. Modified transfer functions

In order to obtain causal transfer functions and optimize the order of the filters, a time delay $\Delta\tau$ is introduced in Eq. (16). The modified transfer functions become

$$\bar{H}_i(\omega)=L_y\Delta x e^{j\omega\bar{\tau}_i},\quad i=1,2,\ldots,N_d, \tag{17}$$

where $\bar{\tau}_i=\tau_i-\Delta\tau$. The sensor output is now $\bar{e}(t)=e(t-\Delta\tau)=\tilde{\ddot{w}}_d(k_x,t-\Delta\tau)$. It has been shown in the companion paper[5] that this modified error signal yields the same control performances as the error signal without delay, $e(t)=\tilde{\ddot{w}}_d(k_x,t)$, when used in a feedforward control approach. Taking $\Delta\tau=\max\{\tau_i\}$ ensures causal frequency response functions ($\bar{\tau}_i\leq 0$, $i=1,2,\ldots,N_d$) and makes one transfer function equal to unity, i.e., the number of filters to design is now N_d-1. Moreover, the modified delays $\bar{\tau}_i$ are minimized which optimizes the order of the filters. More details on the above discussion can be found in the companion paper.

C. Control performance

As suggested earlier, the *discrete* wave-number component $\tilde{\ddot{w}}_d(k_x,t)$ varies from its *continuous* representation $\tilde{\ddot{w}}(k_x,t)$ depending on the number of point sensors N_d and the driving frequency ω (Ref. 5). In terms of radiation

control, it is of interest to analyze the influence of these variations on the controller performance. In this section, the radiation control of a simply supported beam is analytically investigated in the frequency domain over its first four bending modes using both types of error information, i.e., *continuous* and *discrete* wave-number components corresponding to radiation in a prescribed direction.

1. Optimal control force

For a single channel feedforward control structure, the optimum complex amplitude of the control force M^c is defined so as to minimize a quadratic cost function $J(M^c)$ of the error information. Here, the error information is the time-varying wave-number component associated with the direction of radiation θ. Therefore, the cost function can be expressed as the mean-square value of the error signal, i.e.,

$$J(M^c) = \tilde{\ddot{w}}(k_0 \sin\theta, t)\, \tilde{\ddot{w}}^*(k_0 \sin\theta, t) \tag{18}$$

for the *continuous* representation and

$$J_d(M^c) = \tilde{\ddot{w}}_d(k_0 \sin\theta, t-\Delta\tau)\, \tilde{\ddot{w}}_d^*(k_0 \sin\theta, t-\Delta\tau) \tag{19}$$

for the *discrete* representation, where $\tilde{\ddot{w}}^*$ denotes the complex conjugate of $\tilde{\ddot{w}}$. Both $J(M^c)$ and $J_d(M^c)$ are quadratic functions of the control complex amplitude M^c. Therefore, they present only one minimum. The corresponding optimum control force is found by taking the partial derivatives of the cost function with respect to the real and imaginary parts of the control force. Setting these two equations to zero yields

$$M^c = G(\omega)F^d = -\frac{\sum_{p=1}^{\infty} H_p(\omega)\psi_p(x_d)\xi_p(k_x)}{\sum_{p=1}^{\infty} H_p(\omega) m_p \xi_p(k_x)} F^d \tag{20}$$

for the *continuous* representation and

$$M_d^c = G_d(\omega)F^d = -\frac{\sum_{p=1}^{\infty} H_p(\omega)\psi_p(x_d)\xi_p^d(k_x)}{\sum_{p=1}^{\infty} H_p(\omega) m_p \xi_p^d(k_x)} F^d \tag{21}$$

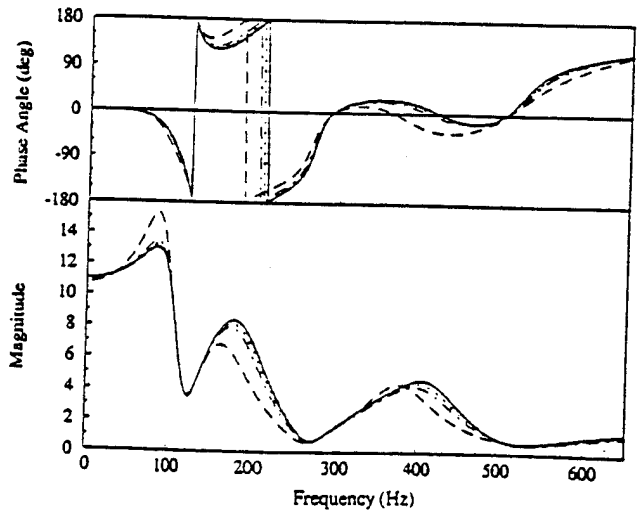

FIG. 2. Optimal controller frequency response function based on (a) ———, continuous wave-number component; (b) – –, three; (c) – – –, five; and (d)....., seven point sensors.

TABLE I. Beam characteristics.

Length	0.38 m
Width	0.04 m
Section	0.0002 m^2
Mass density	3132 kg/m^3
Bending stiffness	5.3290 $N \cdot m^2$

for the *discrete* representation. In the above equations, $G(\omega)$ and $G_d(\omega)$ define the controller transfer functions; $\xi_p(k_x)$ and $\xi_p^d(k_x)$ are the pth *continuous* and *discrete* modal wave-number components, respectively. In both *discrete* and *continuous* cases, they appear as the ratio of the disturbance and control path transfer functions. Substituting the above expressions for the control input in Eq. (6), the far-field pressure is then obtained using Eqs. (8) and (10).

Recalling Eq. (8), it is straightforward to show that using the far-field pressure $p(r,\theta,t)$ as error information would yield the same optimum control force as the *continuous* wave-number component $\tilde{\ddot{w}}(k_0 \sin\theta, t)$. Thus the present analysis can be seen as a comparison between the use of a *discrete* wave-number sensor as described in Sec. I B and a microphone located in the far field.

2. Numerical results

Figure 2 presents the magnitude and phase of the controller transfer function versus frequency obtained for the *continuous* [Eq. (20)] and *discrete* [Eq. (21)] representations. The beam characteristics and its first six natural frequencies are given in Tables I and II. Ten modes are included in the modal series with a constant damping ratio ($\eta_p = 0.01$, $p = 1,2,\ldots,10$). The beam is surrounded by air with density $\rho = 1.27$ kg/m^3 and sound velocity $c = 343$ m/s. The disturbance force is a bandlimited white noise between 0 and 650 Hz, applied at $x_d = 0.43 L_x/2$. The piezoelectric actuator has length $2c_a = 0.1 L_x/2$ and its center is located at $x_c = -0.71 L_x/2$. It is assumed for brevity that the actuator characteristics yield a unity transfer function between the actuator input voltage and the resulting bending moment M^c. The same assumption applies to the other transducer models, i.e., disturbance shaker and sensor accelerometers. The wave-number component to be minimized at $k_x = k_0 \sin\theta$ is associated with the direction of radiation $\theta = 45°$. The solid line corresponds to the *continuous* representation; the dashed, dashdot, and dotted lines correspond to the *discrete* representation using three-, five-, and seven-point sensors, respectively. As expected, the *discrete* representation becomes more accurate as the number

TABLE II. Beam analytical natural frequencies.

Mode	Natural frequency (Hz)
1	31.73
2	126.9
3	285.6
4	507.7
5	793.2
6	1142

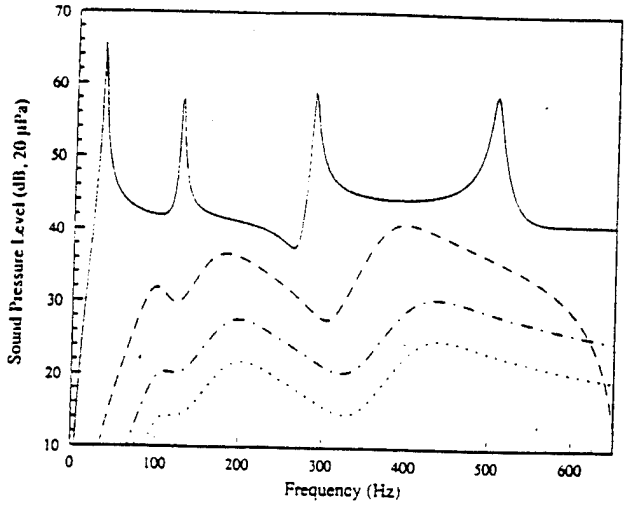

FIG. 3. Far-field pressure for in the direction of minimization: (a) ———, uncontrolled system; (b) – –, (c) – · –, and (d)....., controlled system using three, five, and seven point sensors, respectively.

of point sensors is increased. In all the cases presented here, the error between the *discrete* and *continuous* controller transfer functions is very small at the resonant frequencies due to the fact that the wave-number component is better approximated for the simple modal shapes found on-resonance. A more detailed explanation can be found in Sec. I B 4 of the companion paper.

Figure 3 shows the influence of the errors between *continuous* and *discrete* representations on the controller performances. The modulus of the far-field pressure was computed over the frequency range 0–650 Hz at location ($r=10L_x$, $\theta=45°$, $\phi=0$) for the controlled and uncontrolled system. The solid line represents the pressure for the uncontrolled system. The three dashed lines represent the pressure for the controlled system using the *discrete* controller with three- (dash), five- (dashdot), and seven- (dot) point sensors. Note that the *continuous* controller gives zero pressure over the entire bandwidth at this radiation angle and thus, the corresponding curve is not shown here. The total reduction of the sound pressure level averaged over the frequency range 5–650 Hz is expressed in dB as

$$\Delta_{\text{spl}} = 10 \log\left(\frac{\bar{p}(r,\theta)}{\bar{p}^c(r,\theta)}\right). \tag{22}$$

In the above expression, $\bar{p}(r,\theta)$ and $\bar{p}^c(r,\theta)$ are the mean-square pressure values of the uncontrolled and controlled system averaged over the bandwidth,

$$\bar{p}(r,\theta) = \frac{1}{\omega_{\max}-\omega_{\min}} \int_{\omega_{\min}}^{\omega_{\max}} p(r,\theta,\omega)p^*(r,\theta,\omega)\,d\omega. \tag{23}$$

In all of the three cases, the controlled system presents significant attenuation over the entire bandwidth. Accordingly to Fig. 2, the reduction is more important on-resonance than off-resonance and better results are achieved with a larger number of point sensors. The total reductions averaged over 5–650 Hz are 13.6, 22.7, and 28.5 dB using three, five, and seven point sensors, respectively. Hence, good results are achieved with only a few point sensors.

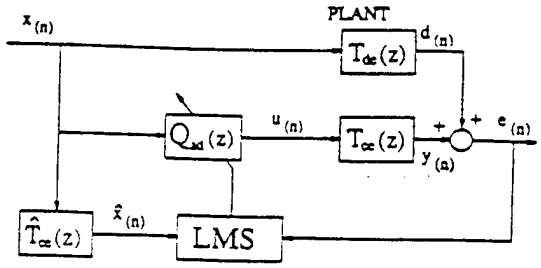

FIG. 4. Feedforward adaptive controller using the filtered-X LMS algorithm.

Recalling Fig. 2, the phase of the controller transfer function is seen to be positive above 300 Hz. In other words, the optimal solution in the frequency domain does not ensure causality for the controller. Therefore, the above results can not be achieved in real situations. The computer simulations described in the next sections will show more realistic results by providing a time domain optimal solution for the controller transfer function.

II. FEEDFORWARD ADAPTIVE CONTROL IMPLEMENTATION

The sensing technique is next implemented in a feedforward adaptive control structure using the filtered-X LMS algorithm.[9] The algorithm is first presented. Then, the design of the filter array is briefly outlined. Finally, the time domain simulation procedure is described for the single channel controller applied to a simply supported beam.

A. Filtered-X LMS algorithm

A conceptual schematic of the single channel feedforward adaptive controller using the filtered-X algorithm is shown in Fig. 4. The plant represents the structural acoustic system, i.e., the inputs are structural excitations (actuators) and the outputs are related to acoustic radiation (sensors). For the SISO system presented here, the plant output $e(n)$ at time t_n is the combination of the response due to the disturbance input $x(n)$ and the control input $u(n)$. This relation can be expressed in the z domain as

$$E(z) = D(z) + Y(z) = D(z) + T_{ce}(z)\,U(z), \tag{24}$$

where the upper case letters refer to the z transform of the associated sequence represented with lower case letters. Here, $T_{ce}(z)$ denotes the z transform of the transfer function between the control input and the resulting sensor output. In a feedforward adaptive structure, the control sequence $u(n)$ is obtained by filtering a reference signal that is coherent to the disturbance $x(n)$ through an adaptive FIR filter $Q_{ad}(z)$, also referred to as compensator,

$$U(z) = Q_{ad}(z)X(z). \tag{25}$$

Taking the inverse z transform of Eq. (25), the control input becomes in the time domain,

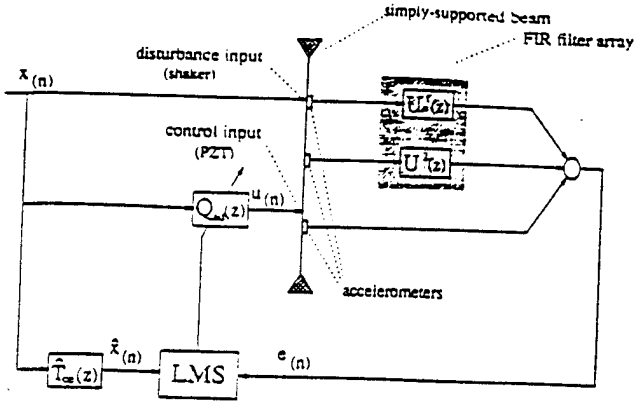

FIG. 5. Sensing configuration applied to the radiation control of a simply supported beam.

$$u(n)=\sum_{l=0}^{N_{ad}-1} Q_l z^{-l} x(n), \tag{26}$$

where z^{-l} denotes a time delay of l samples, i.e., $z^{-l}x(n)=x(n-l)$, and Q_l ($l=0,\ldots,N_{ad}-1$), the compensator coefficients. Substituting Eq. (25) in (24), the error signal becomes

$$E(z)=D(z)+T_{ce}(z)Q_{ad}(z)X(z). \tag{27}$$

The LMS algorithm adapts the coefficients Q_l in order to minimize the cost function $J=E\{e^2(n)\}$, where E denotes the expectation operator. Since this error function is quadratic with respect to the adaptive filter coefficients, only one minimum exists and the steepest descent method can be used to update the coefficients,

$$Q_l(n+1)=Q_l(n)-\mu\frac{\partial J}{\partial Q_l}, \quad l=0,1,\ldots,N_{ad}-1, \tag{28}$$

μ is the convergence parameter that controls the stability of the algorithm. The time domain LMS algorithm uses an instantaneous gradient approximation to estimate $\partial J/\partial Q_l$ at time t_n. Substituting J in the above expression and removing the expectation operator yields

$$Q_l(n+1)=Q_l(n)-2\mu e(n)\hat{x}(n-l), \quad l=0,1,\ldots,N_{ad}-1, \tag{29}$$

where $\hat{x}(n)$ is the filtered-X signal. It is defined in the z domain by $\hat{X}(z)=\hat{T}_{ce}(z)X(z)$. The z-domain transfer function $\hat{T}_{ce}(z)$ represents an estimate of the actual control path $T_{ce}(z)$ and can be modeled by an infinite impulse response (IIR) filter in case of broadband disturbance as discussed in Ref. 10.

Figure 5 presents the feedforward adaptive controller along with the structural acoustic sensor applied to a simply supported beam. The sensor is composed of three accelerometers and two FIR filters. This configuration gives a good estimate of the supersonic wave-number component associated with one direction of radiation for frequencies up to the third bending mode of the beam. A shaker modeled by a point force provides the disturbance input and a single PZT piezoelectric patch modelled by a pair of moments is used as the control input.

B. Filter array design

This section outlines the design of the FIR filters implemented in the sensor. Practically, it involves the calculation of discrete impulse response coefficients such that the modeled frequency response functions match the desired transfer functions in Eq. (17). Two design methods have been introduced in the companion paper. One uses frequency domain design algorithms and the other implements optimal filtering techniques that allow the filters to be design from experimental measurements in the discrete time domain. The first design method is discussed here. It implements the Matlab function *invfreqz* (software by MathWorks[11]).

From Eq. (15), the sensor output sequence is expressed in the z domain as

$$E(z)=\sum_{i=1,i\neq i_0}^{N_d} U^i(z)X_i(z)+X_{i_0}(z), \tag{30}$$

where $X^i(z)$ denotes the z transform of the structural acceleration measured at location x_i and i_0 refers to the direct path (unity transfer function). Here, $U^i(z)$ is the z transform of the finite impulse response for the ith filter modeling $\bar{H}_i(\omega)$ in Eq. (17),

$$U^i(z)=U^i_0+U^i_1z^{-1}+\cdots+U^i_{N^i}z^{-N_i}. \tag{31}$$

In the above expression, $U^i_0,U^i_1,\ldots,U^i_{N^i}$ are the N_i+1 coefficients and N_i the order of the ith filter. The modeled frequency response functions $H^m_i(\omega)$ can be obtained from $U^i(z)$ as

$$H^m_i(\omega)=U^i(e^{j\omega T_s})=\sum_{l=0}^{N_i} U^i_l e^{-j\omega l T_s}, \quad i=1,2,\ldots,N_d, \tag{32}$$

where T_s is the sampling period.

C. Discrete time-domain computer simulation

Unlike simulation in the frequency domain that give the *optimal* control performance (see Sec. I C), a discrete time domain simulation provides more realistic results as it implements the convergence process of the LMS algorithm and ensures causality for the controller. This constraint is a result of the use of physically realizable causal digital filters which cannot model acausal transfer functions. In the frequency domain, the optimal control force is readily obtained using the analytical structural and acoustic responses of the beam as shown in the first section. On the other hand, time domain control simulations require discrete transfer functions expressed in the z domain to provide the beam response in the discrete time domain; in other words, the transient as well as steady state response of the beam is modelled. In order to do this, the beam response is described over the frequency range of interest by using appropriate impulse responses in discrete form as filters.

Figure 6 shows a block diagram of the simulated system corresponding to the configuration of Fig. 5. The discrete transfer functions $T^i_d(z)$ and $T^i_c(z)$ ($i=1,2,\ldots,N_d$)

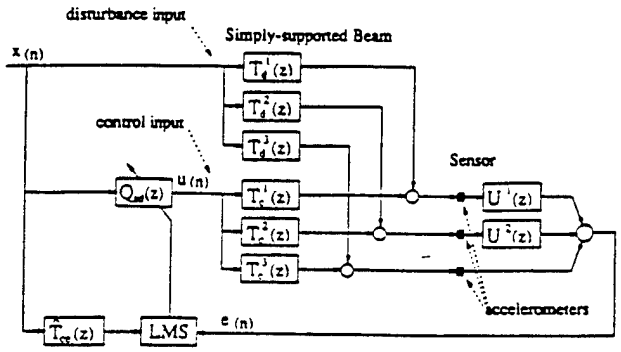

FIG. 6. Simulated system.

model the path between the disturbance input $x(n)$, at location x_d, and the beam acceleration response, at locations x_i, and the path between the control input $u(n)$, at location x_c, and the same acceleration signals. They are obtained as follows.

Recalling Eqs. (1)–(7), the analytical transfer functions between both disturbance and control inputs and the beam acceleration response at $x=x_a$, $H_{de}(x_d,x_a,\omega)$ and $H_{ce}(x_c,x_a,\omega)$, respectively, can be approximated over the bandwidth of interest by the finite summations

$$H_{de}(x_d,x_a,\omega)=\sum_{p=1}^{p_{\max}}\psi_p(x_d)\psi_p(x_a)H_{a,p}(\omega), \tag{33}$$

$$H_{ce}(x_c,x_a,\omega)=\sum_{p=1}^{p_{\max}}\frac{d}{dx}\{\psi_p(x_c+c_a)-\psi_p(x_c-c_a)\}\psi_p(x_a)H_{a,p}(\omega), \tag{34}$$

where $p_{\max}$ is the number of modes included in the representation. Here, $H_{a,p}(\omega)$ is the acceleration frequency response of the pth mode defined as

$$H_{a,p}(\omega)=\frac{-\omega^2}{\omega_p^2-\omega^2+2j\eta_p\omega_p\omega}. \tag{35}$$

Using a ramp invariance approximation, the above second-order modal contribution has the following z-domain representation,[12]

$$H_{a,p}^d(z)=\frac{\alpha z^2-2\alpha z+\alpha}{z^2-2z\exp(-\eta_p\omega_p T_s)\cos(\omega_{p,d}T_s)+\exp(-2\eta_p\omega_p T_s)}, \tag{36}$$

where

$$\alpha=\frac{\sin(\omega_{p,d}T_s)}{\omega_{p,d}T_s}\exp(-\eta_p\omega_p T_s) \tag{37}$$

and $\omega_{p,d}=\omega_p\sqrt{1-\eta_p^2}$. Here, $T_s=1/F_s$ denotes the discrete time sampling period. Note that the above discrete transfer function has poles inside the unit circle which ensures stability. Equation (36) can now be substituted in Eqs. (33) and (34) to obtain the discrete transfer functions for the beam:

$$H_{de}^d(x_d,x_a,z)=\sum_{p=1}^{p_{\max}}\psi_p(x_d)\psi_p(x_a)H_{a,p}^d(z), \tag{38}$$

$$H_{ce}^d(x_c,x_a,z)=\sum_{p=1}^{p_{\max}}\frac{d}{dx}\{\psi_p(x_c+c)-\psi_p(x_c-c)\}\psi_p(x_a)H_{a,p}^d(z). \tag{39}$$

The above expressions can be simplified into a rational transfer function of the form $A(z)/(1-B(z))$, where $A(z)$ and $B(z)$ are obtained by convolving the second-order polynomials in z of Eq. (36). The coefficients of $T_d^i(z)$, $T_c^i(z)$ $(i=1,2,\ldots,N_d)$ are then calculated substituting the input force locations, i.e., x_d and x_c, respectively, and the point sensor locations, i.e., x_i, $i=1,2,\ldots,N_d$, in Eqs. (38) and (39).

The estimated filtered-X control path $\hat{T}_{ce}(z)$ is constructed from the analytical transfer function between the control force and the sensor output,

$$\hat{H}_{ce}(\omega)=\sum_{i=1,i\neq i_0}^{N_d}H_{ce}(x_c,x_i,\omega)\bar{H}_i(\omega)+H_{ce}(x_c,x_{i_0},\omega). \tag{40}$$

In the above expression, $H_{ce}(x_c,x_i,\omega)$ represents the transfer function between the control input force and the beam acceleration at location $x=x_i$ [Eq. (34)], while $\bar{H}_i(\omega)$ is the frequency response of the ith radiation filter [Eq. (17)]. The resulting transfer function, $\hat{H}_{ce}(\omega)$, is modeled by an IIR filter whose coefficients are computed using the Matlab function *invfreqz*.

Another way to design the IIR filter modeling the control path would be to use the beam and radiation filter discrete impulse responses, i.e., $T_c^i(z)$ and $U^i(z)$, as follows:

$$\hat{T}_{ce}(z)=\sum_{i=1,i\neq i_0}^{N_d}T_c^i(z)U^i(z)+T_c^{i_0}(z). \tag{41}$$

This method gives an exact filtered-X path since it is based on the actual simulated system which has discrete sampling. On the other hand, the method chosen here, based on the analytical continuous representation [Eq. (40)], is not exact. This is due to differences between the beam continuous and discrete representations (ramp invariance approximation) as well as between the analytical radiation transfer functions $\bar{H}_i(\omega)$ and the actual filter responses. However, when dealing with real structures and broadband excitation, the filtered-X path modeling also results in errors due to pole instability.[10] Consequently, the first representation appears to be more realistic.

At this point, an important aspect of structural acoustic sensing should be noted. As the sensor is based on wave-number information, the radiation filters do not include the acoustic path time delay r/c. It follows that the above filtered-X path has a much smaller group delay [Eq. (16)], i.e., smoother phase, than the transfer function obtained with a microphone in the far field. In consequence, the order of $\hat{T}_{ce}(z)$ is greatly reduced and better accuracy is achieved for the filtered-X path which is a critical factor in terms of control performances.[10]

The computer simulation is carried out by performing the following sequence of computation during each step through time: (a) compute the disturbance input $x(n)$ and the control input $u(n)$ applied to the beam; (b) compute the sensor output $e(n)$; (c) compute the filtered-X input $\hat{x}(n)$; (d) update the adaptive filter weights according to Eq. (29).

III. SIMULATION RESULTS

The structural acoustic sensing technique is illustrated through computer simulations on sound radiation control for the simply supported baffled beam considered previously. Results are provided for the single channel filtered-X LMS control approach using a band limited broadband disturbance.

A. System characteristics

The beam and surrounding medium have the characteristics presented in Sec. I C. The reference signal is obtained in the discrete time by convolving at each time step a Gaussian white noise with the discrete impulse response $Q_{lp}(z)$ of a low-pass FIR filter. The filter cut-off frequency is $F_c=600$ Hz which allows excitation of the first four bending modes of the beam (see Table II). The resulting band-limited broadband signal is used to model the point force disturbance at location $x=x_d$. As presented earlier, the control input models the excitation of a piezoelectric actuator at location $x=x_c$. It is obtained by filtering the reference signal through an adaptive FIR compensator with a 25 coefficient impulse response ($N_{ad}=25$). The sampling frequency is $F_s=2000$ Hz.

Two different sensing configurations are simulated. The first uses $N_d=3$ accelerometers and the second uses $N_d=5$ accelerometers. In both cases, the N_d-1 radiation FIR filters have three coefficients and the sensor output provides an estimate of the wavenumber component evaluated in the direction ($\theta=45°,\phi=0°$). A 15-order IIR filter is used to model the filtered-X path.

B. Sensor output

Figure 7 presents the structural acoustic sensor output $e(n)$ in the discrete time domain before and after control. This case corresponds to the three point sensor. The sensor output sequence before control [curve (a)] is simply obtained by running the simulation code through a number of iterations with the weights of the compensator $Q_{ad}(z)$ being set to zero. The next step consists of updating the weights of the compensator until convergence has occurred. The sensor output sequence [curve (b)] after control is then obtained by freezing the weights of the compensator. The dominance of the first mode of the beam clearly appears on the time history before control. The wave-number component of this mode, evaluated in the direction of minimization (supersonic region) presents a large magnitude, which explains its high radiation efficiency. About 200 000 iterations were required to reach quasistationarity for the mean-square value of the minimized error signal. A larger value of the convergence parameter μ would result in faster convergence, but stability aspects must be considered. The mean-square value of the sensor output time history before and after control was calculated over 204 800 points. A band averaged reduction of 13.7 dB is achieved. The second case, i.e., $N_d=5$ point sensor, gives a band averaged reduction of 11.5 dB. These results are now further analysed in the frequency domain.

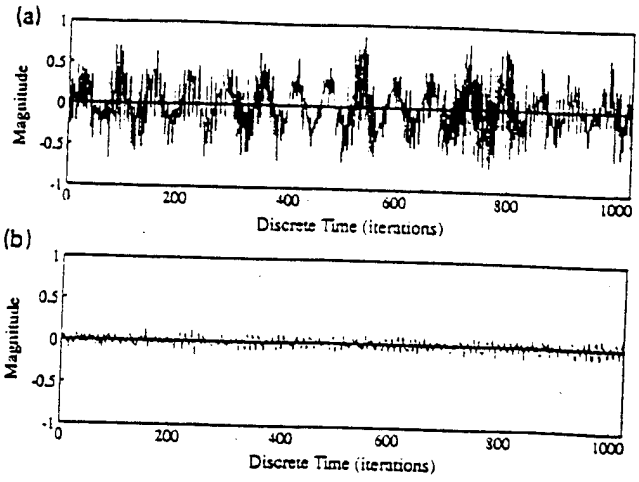

FIG. 7. Structural acoustic sensor output time history before (a) and after (b) control ($N_d=3$).

The sensor output autospectra, shown in Fig. 8 along with the autospectrum of the disturbance input $x(n)$, are computed from the DFT of the discrete time signals before and after control using 50 averages. As expected, the disturbance input (dashed line) is a white noise over the bandwidth 0–600 Hz where the filter cuts in. The sensor output autospectra before control contains the first four modes of the modeled beam. The dominance of the first mode noticed on the time history before control also appears in the frequency domain. After control, the error signal frequency content is significantly reduced over the entire frequency range. Some spill over is noticed off-resonance between the second and third mode resonance

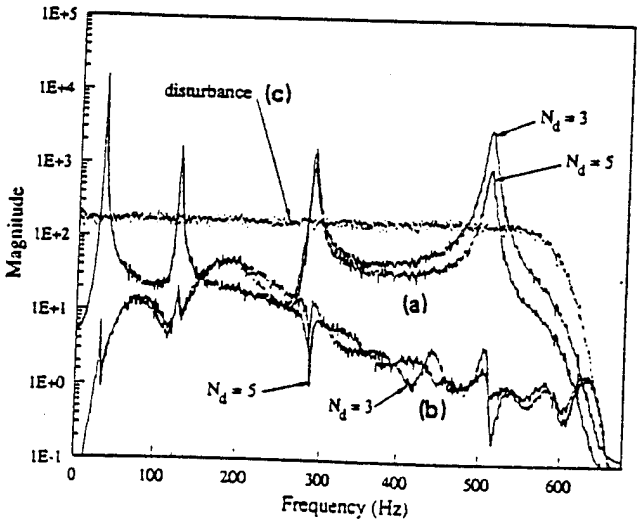

FIG. 8. Structural acoustic sensor output before (a) and after (b) control, and disturbance input (c) auto spectra.

point. The influence of the number of structural measurements N_d is noticeable above the third mode resonant frequency. The error between the actual sensor output (*discrete* wave-number component) and the desired signal (*continuous* wave-number component) is undoubtedly reduced using five measurement points instead of three points. As seen from the two solid lines, the three-point sensor tends to increase the estimate of the wave-number component magnitude before control. After control, the variations between the two sensor configurations also appear before the third mode resonance point. However, the tendency noticed before control, i.e., increase of the magnitude, is replaced by a more complex behavior. Globally, both cases result in the same frequency content after control. It follows that the three-point sensor gives more attenuation of the error signal than the five-point sensor above the third mode resonant frequency. Consequently, the overall reduction obtained for the sensor output is higher for the three-point sensor as found earlier from the time domain histories. However, it should be noted that this result only applies to the sensor output which is an estimate of the radiation information. In other words, it is necessary to analyze the far-field radiation before and after control in order to compare the performance of the three- and five-point sensors in terms of radiation control.

C. Far-field radiation

The far-field pressure information before and after control is now discussed. The calculations use the analytical expressions of Sec. I A. From the impulse response of the low-pass filter $Q_{lp}(z)$ used to generate the input band limited disturbance, the disturbance force complex amplitude $F^d(\omega)$ is computed over the bandwidth [Eq. (32)]. Multiplying $F^d(\omega)$ by the frequency response of the adaptive filter after convergence gives the control input force over the bandwidth $M^c(\omega) = Q_{ad}(e^{j\omega T_s})F^d(\omega)$. Substituting the above quantities in Eqs. (6), (10), (11), and (8), the acoustic pressure in the far field is calculated for each frequency of interest along the half circle ($r=10L_x$, $-\pi/2<\theta<+\pi/2$, $\phi=0$).

The far-field pressure spectrum in the direction of minimization at $\theta=45°$ (Fig. 9) shows significant reduction over the entire frequency range. More than 20-dB reduction is achieved at the four resonant frequencies. The curves before (solid line) and after (dashed and dotted lines) control are relatively close from the sensor output auto-spectra shown in Fig. 8 in the lower frequency range. Again, some spill over is noticed between the second and the third mode resonance points. At higher frequencies (above the third mode frequency point), the sensor accuracy deteriorates. Consequently, the sound reduction in the far field is smaller than the reduction noticed on the sensor output. The best results are obtained with the five-point sensor due to its better accuracy. This is consistent with the results from the frequency domain analysis shown in Fig. 3.

The above results are further interpreted by analysing the compensator frequency response functions, i.e., the transfer function between the reference signal $x(n)$ and the

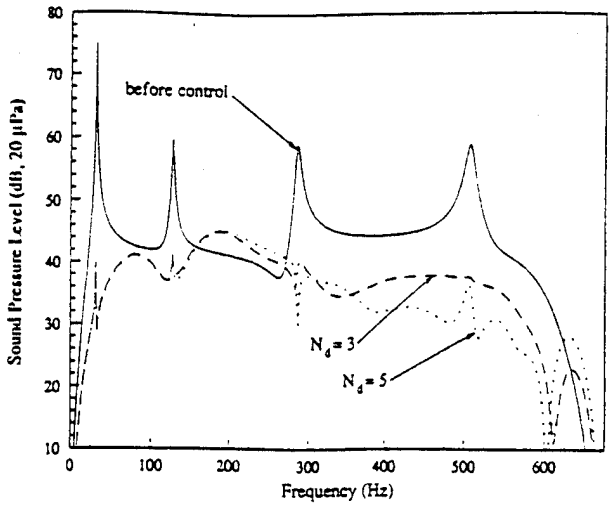

FIG. 9. Far-field pressure at ($\theta=45°$, $\phi=0°$); (a) ———, before control; (b) – – – and (c)....., after control with $N_d=3$ and $N_d=5$, respectively.

control input $u(n)$, shown in Fig. 10. The solid line represents the optimal transfer function found from Eq. (20). As mentioned in Sec. I C, this response results in zero pressure at $\theta=45°$ over the frequency range. The dashed and dotted lines represents the actual compensator frequency response functions using the three- and five-point sensors, respectively. They are obtained from the coefficients of the adaptive filter after convergence using Eq. (32). In both cases, significant variations between the optimal [curve (a)] and actual [curves (b) and (c)] responses are noticed. As expected, the frequency response function of the compensator after convergence is directly related to the control performances. The frequencies at which some spill-over was noticed in Fig. 9, i.e., between 150 and 260 Hz, correspond effectively to the largest variations in Fig. 10. On the other hand, the notch of the far-field pressure noticed around 600 Hz in Fig. 9 is explained by the coincidence at that frequency of the optimal

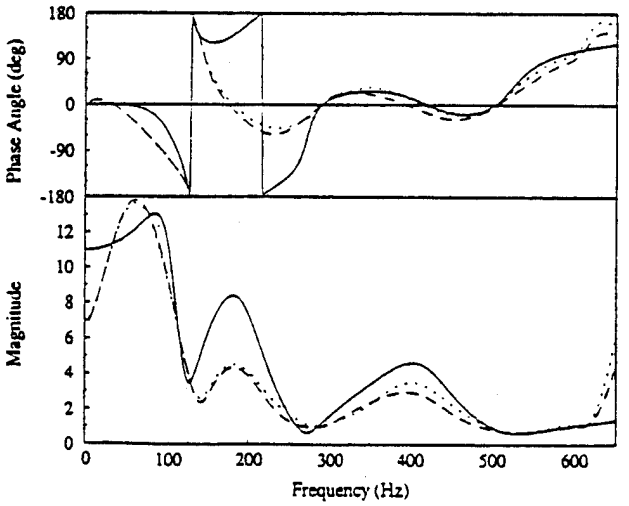

FIG. 10. Compensator frequency response function; (a) ———, optimal response; (b) – – – and (c)....., actual response with $N_d=3$ and $N_d=5$, respectively.

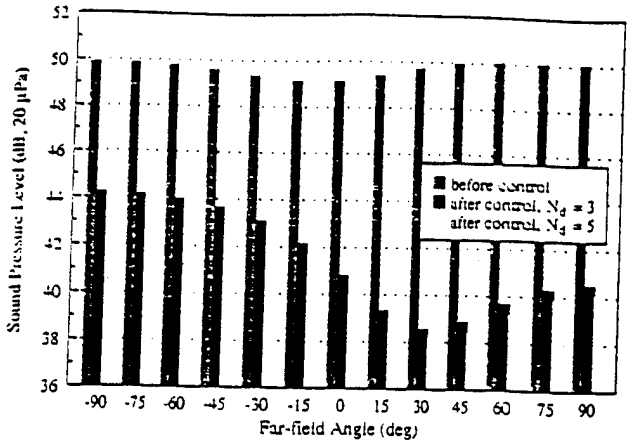

FIG. 11. Total sound pressure level averaged over 5–650 Hz before and after control with $N_d=3$ and $N_d=5$, respectively.

and actual frequency response functions. Moreover, the five-point sensor (dotted line) yields a control transfer function closer to the optimal solution than the three-point sensor (dashed line), especially above the third resonant frequency. This results in larger attenuations at the corresponding frequencies.

The variations between the optimal and actual responses are now further explained. Recalling the discussion of Sec. I C, the optimal solution does not ensure causality. For a system to be causal, the disturbance path must present a longer time propagation delay than the control path. If the above requirement is met over the frequency range of interest, the optimal frequency response of the compensator, defined as the ratio of the disturbance path transfer function over the control path transfer function [see Eq. (20)], has a negative phase response at all frequencies of interest and thus, can be modeled by a digital filter. In the present case, the system appears to be acausal above 300 Hz, i.e., the optimal phase response becomes positive above this frequency [see Fig. 10, curve (a)]. Therefore, the controller compensator is unable to match the optimal response over the entire frequency range, even with an infinite number of coefficients. Consequently, the time domain simulation results in Fig. 9 present smaller attenuation than the corresponding frequency domain results shown in Fig. 3, mainly due to the causality issue discussed above. As seen from Fig. 10, the phase response of the simulated controller after convergence decreases between 120 and 240 Hz whereas the optimal phase response is increasing in the same bandwidth. As mentioned earlier, this phase shift results in spill-over in the frequency range 120–240 Hz. Above 300 Hz, the controller response follows the optimal response with a 360° phase shift that gives good attenuation. One way to make the system causal over the complete frequency range is to add a time delay in the disturbance path. However this solution is often impractical. Burdisso *et al.* have developed analytical formulations to predict reduction in attenuation as the system becomes more acausal.[13]

Figure 11 presents the total sound pressure level averaged over the frequency range 5–650 Hz versus the radiation angle θ,

$$I_{\text{spl}}(\theta) = 10 \log\left(\frac{\bar{p}(\theta)}{2p_{\text{ref}}^2}\right), \tag{42}$$

where $\bar{p}(\theta)$ represents the mean-square pressure value at angle θ averaged over the bandwidth [Eq. (23)]. Global control is achieved over the entire frequency range. The plot shows a reduction of 11 and 11.5 dB in the direction of minimization ($\theta=45°$) for the three-point and five-point sensor, respectively. This result is consistent with the overall reduction obtained from the sensor output (13.7 dB for $N_d=3$ and 11.5 dB for $N_d=5$). Again, note that the five point sensor output gives a more accurate far-field information than the three-point sensor, which yields greater far-field attenuation.

IV. CONCLUSIONS

A real time structural acoustic sensor has been developed for application to active control of sound radiated by rectangular vibrating surfaces. The case of a simply supported baffled beam is considered in this paper. The time domain filtered-X LMS algorithm is implemented to achieve control over a broadband frequency range. Computer simulations show the ability of the technique to replace the use of error microphones in the far field.

For the low-order modes of the beam, only a few point sensors are needed to measure the structural information. Moreover, the FIR filters that process the discretized structural response to provide radiation information have a small number of coefficients due to the constant magnitude and linear phase of the free-space Green's function and the stationary cost function used in feedforward control. The resulting error signal is a fairly good approximation of the supersonic wave-number component associated with a prescribed direction of radiation. Moreover, the computer simulations show that the errors introduced by structural acoustic sensing in the radiation information are not critical in feedforward control compared to other issues such as causality and control authority. Therefore, the proposed structural acoustic sensor presents a important alternative to the use of distributive structural sensors (PVDF films) in ASAC approaches since it provides broadband radiation information.

ACKNOWLEDGMENTS

The authors gratefully acknowledge the support of this work by the Office of Naval Research under Grant No. ONR-N0004-92-j-1170-P00007.

[1] C. R. Fuller, "Active control of sound transmission/radiation from elastic plates by vibration inputs I. Analysis," J. Sound Vib. 136, 1–15 (1990).

[2] C. R. Fuller, R. J. Silcox, V. L. Metcalf, and D. E. Brown, "Experiments on structural control of sound transmitted through an elastic plate," in *Proceedings of American Control Conference*, edited by H. Vincon Poor (Pittsburgh, PA, 1989), pp. 2079–2089.

[3] R. L. Clark and C. R. Fuller, "Modal sensing of efficient radiators with PVDF distributed sensors in active structural acoustic approaches," J. Acoust. Soc. Am. 91, 3321–3329 (1992).

[4]C. R. Fuller and R. A. Burdisso, "A wavenumber domain approach to the active control of structure-borne sound," J. Sound Vib. 148(2), 355–360 (1991).
[5]J. P. Maillard and C. R. Fuller, "Advanced time domain sensing techniques for structural acoustic systems. I. Theory and design," J. Acoust. Soc. Am. 95, 3252–3261 (1994).
[6]S. J. Elliott, I. M. Stothers, and P. A. Nelson, "A Multiple Error LMS Algorithm and Its Application to the Active Control of Sound and Vibration," IEEE Trans. Acoust. Speech Signal Process. ASSP-35 (10), 1423–1434 (1987).
[7]R. L. Clark, C. R. Fuller, and A. L. Wicks, "Characterization of multiple piezoelectric actuators for structural excitation," J. Acoust. Soc. Am. 90, 346–357 (1991).
[8]M. C. Junger and D. Feit, *Sound, Structures and Their Interaction* (MIT, Boston, 1986).
[9]B. J. Widrow and S. D. Stearns, *Adaptive Signal Processing* (Prentice–Hall, Englewood Cliffs, NJ, 1986).
[10]J. S. Vipperman, R. A. Burdisso, and C. R. Fuller, "Active control of broadband structural vibrations using the LMS adaptive algorithm," J. Sound Vib. 166(2), 283–299 (1993).
[11]*PC-Matlab for MD-DOS Computers* (The MathWorks, Inc., South Natick, MA, 1989).
[12]K. J. Åström and B. Wittenmark, *Computer-controlled Systems* (Prentice–Hall, Englewood Cliffs, NJ, 1990).
[13]R. A. Burdisso, J. S. Vipperman, and C. R. Fuller, "Causality analysis of feedforward-controlled systems with broadband inputs," J. Acoust. Soc. Am. 94, 234–242 (1993).

C-20 Experiments in piezostructure modal analysis for mimo feedback control, W. R. Saunders, D. G. Cole and H. H. Robertshaw, Smart Mater. Struct., Vol. 3, pp. 210-218, 1994

Experiments in piezostructure modal analysis for MIMO feedback control

William R Saunders, Daniel G Cole and Harry H Robertshaw

Department of Mechanical Engineering, Virginia Polytechnic Institute & State University, Blacksburg, VA 24061, USA

Received 26 August 1993, accepted for publication 6 December 1993

Abstract. An approximate method for modal analysis of a piezostructure testbed is used to generate a dynamic model for closed-loop, multiple-input–multiple-output (MIMO) feedback controller design. An innovative pole-residue system model for structures instrumented with piezoelectric sensor and actuators is developed which is compatible with existing modal curve-fitting algorithms. This paper examines the use of the new pole-residue model in the absence of truly collocated response information. It is shown that nearly-collocated measurements may be used to estimate a structure's modal parameters; high-precision signal conditioning electronics required for exact drive-point response measurements are thereby avoided. A simply-supported plate is used to demonstrate the approximate piezostructure modal test approach. The test model is then used to design up to a four input, sixteen channel output MIMO feedback control experiment. Closed-loop results are presented which show that more than 10 dB of suppression is achieved near structural resonances within the control bandwidth (10–250 Hz).

1. Introduction

Control design for flexible structures relies on accurate modeling of the system dynamics in the absence of more advanced adaptive or robust design approaches. Typically, test models lead to improved performance over purely analytical models derived from closed-form solutions or finite-element calculations. Numerous approaches are possible for linear, time-invariant test model development, including modal analysis, singular value decomposition analysis, parametric modeling and a number of other on-line and off-line procedures. This paper is concerned with the use of modal analysis for modeling and subsequent vibration control of a *smart structure*—in this case, a plate structure instrumented with piezoelectric sensors and actuators.

The rising popularity of piezoelectric transducers for active structural control has resulted in a decreased role for modal testing methods in the modeling phase of control system design. In fact, the use of piezoelectric transducers for general system identification of structures has lagged far behind when control applications are not intended. This is particularly true for piezoelectric actuator configurations which are not amenable to force measurements or collocation with piezoelectric sensors since traditional modal analysis formulations require both the force and drive-point response information for successful estimation of the structure's modal parameters. A second impediment to modal testing of piezostructures is the estimation of the electromechanical coupling matrix in a manner which is consistent with the estimation of the conventional modal parameters (natural frequency, damping and mode shapes). In this paper, a new method for modal analysis of piezostructures is used to perform preliminary system identification experiments leading to a multi-input–multi-output (MIMO), feedback control demonstration of a simply-supported plate. It is shown that this approach leads to a plate test model with synthesis capabilities for response analysis and control system design.

System identification and control of structures has become a vast technical discipline. Large numbers of reference documents describe the evolution of controlled structures; reports ranging from basic research results to highly sophisticated, engineering applications are now available. The most recent emphasis in structural modeling and control research has been in the area of smart structures. Beginning with the initial descriptions of coupled piezoelectric-structure dynamics by Bailey and Hubbard (1985), Crawley and deLuis (1987) and others, the investigation of smart structures has expanded to include other active materials (Saunders *et al* 1991), shaped-material applications (Burke and Hubbard 1987, Clark and Fuller 1992), and alternative dynamic representations and utilizations of piezoelectric sensors and actuators (Hagood *et al* 1990, Lee *et al* 1991). However, very little research has been reported on practical experimental methods of performing system identification on smart structures.

The element of smart structure system identification which requires unique treatment compared with system identification of conventional structures is the estimation

0964-1726/94/020210+09$19.50 © 1994 IOP Publishing Ltd

of electromechanical dynamic parameters. Several researchers have proposed theoretical approaches to this problem. Tsou and Tseng (1991) investigated a finite-element formulation for structural identification using piezoelectric actuators and sensors. Zharij (1991) developed a modal theory of electromechanical energy conversion which establishes a relation between the electromechanical coupling factor of the displacement field and the partial (modal) electromechanical coupling factors for particular vibration modes. A recent paper by Banks *et al* (1993) included theoretical and experimental parameter identification results for smart structures equipped with piezoelectrics. In that work, a least-squares approach was used to generate estimates of the structure's resonance frequencies, damping, and electromechanical coupling. Unfortunately, none of the approaches presented to date are compatible with broadly available modal analysis algorithms.

Modal testing procedures for smart structures are conspicuously absent in the research literature. It is the authors' opinion that the problems mentioned earlier, specifically the absence of force measurements and drive point response, have created an obstacle to the use of modal analysis for smart structures. Recent overview papers (Leuridan 1992, McConnell and Rogers 1991) on the integration and implementation of modal analysis have no references to the impact or utilization of smart structure technologies. There has been some initial research on the use of piezoelectric elements for dynamic measurements leading to modal analysis. For example, Hanagud *et al* (1991) presented initial results comparing the use of piezoelectrics and conventional transducers for frequency response function (FRF) measurements. These types of analyses and experiments are needed to promote the integration of smart structures in the modal analysis community.

The design of smart structure system identification approaches which are compatible with existing modal analysis methods will bring obvious advantages including availability of algorithms, test-analysis correlation methods etc. A recent paper by Cole *et al* (1994) derived a piezostructure modal analysis approach which utilizes a pole-residue model and is compatible with frequency domain, curve- fit modal analysis algorithms. It was shown that the residue terms of this formulation yield estimates of the electromechanical coupling matrix for the modal displacements or the physical displacements provided that the modal matrix is also available. The important results of the piezostructure pole-residue approach will be explained later in this paper. The piezostructure modal test method strictly relies on simultaneous sensing and actuation of piezoelectric elements; however, it was shown that nearly collocated response measurements will provide estimates with enough accuracy for certain applications. For this paper, a nearly collocated experimental approach will be presented.

In the next section, a modal parametric model is described which can be used in frequency-domain MDOF curve-fitting approaches for modal analysis of piezostructures. A rational fraction algorithm is combined with a pole-residue expression to estimate the modal parameters required to generate state-space model parameters and modal filters for the control experiments presented later. Then, a description of the piezostructure plate testbed is provided and results from the modal testing experiments are presented. Finally, a closed-loop control experiment is described for suppression of persistent, wideband excitation over the modeled system bandwidth. Closed-loop response of the plate is presented for the cases of one, two and four control inputs.

2. A piezostructure pole-residue model for modal analysis

In this section, the theoretical development of a pole-residue model for the simply-supported plate with piezoelectric sensors and actuators is presented. For brevity, it is assumed that the reader is familiar with the general pole-residue form and subsequent frequency-domain, parameter estimation methods. If background information is desired, the reader can refer to technical discussions by Klosterman (1971) or Han and Wicks (1989).

The piezostructure modal parameter model developed in this section is valid for structures which are instrumented with piezoelectric sensors and actuators which are not truly collocated and/or are of different materials and geometries. In this paper, the use of simultaneous sensing and actuation for drive-point response, as previously discussed by Cole *et al* (1994), will not be addressed. To begin, we recall that the usual starting point for the derivation of conventional structure (i.e. force inputs and displacement outputs) pole-residue models is a linear system of equations given by:

$$\mathbf{M}\ddot{x} + \mathbf{C}\dot{x} + \mathbf{K}x = f \qquad (1)$$

where $\mathbf{M}$ is a positive definite, symmetric mass matrix, $\mathbf{C}$ a non-proportional, viscous damping matrix, $\mathbf{K}$ a symmetric stiffness matrix, $x \in R^n$ a vector of surface displacements in physical coordinates, and $f \in R^n$ a vector of structural forces. Note that in practice, there will be many zero elements of f. A finite-dimensional, complex eigenvalue problem results from the q-dimensional model of equation (1). The solution yields n pairs of complex conjugate eigenvalues

$$p_{i,i+n} = -\zeta_i\omega_i \pm j\omega_i\sqrt{1-\zeta_i^2} \qquad i = 1, 2, \ldots, n \quad (2)$$

where p_i is the ith complex eigenvalue of the structure. The solution also yields a corresponding complex modal matrix Φ of eigenvectors ($\Phi_i \in C^n$) which occur in complex conjugate pairs.

For an applied force at a spatial position l and a response measurement at spatial position k, the FRF equation in physical coordinates is

$$\frac{x_k}{f_l} = \sum_{i=1}^{n}\left[\frac{\Phi_{ki}\Phi_{li}}{a_i(s-p_i)} + \frac{\Phi_{ki}^*\Phi_{li}^*}{a_i^*(s-p_i^*)}\right] = \sum_{i=1}^{n}\left[\frac{A_i^{k,l}}{(s-p_i)} + \frac{A_i^{k,l*}}{(s-p_i^*)}\right] \qquad (3)$$

where * refers to the complex conjugate. Here, the residue has been defined as $A_i^{k,l} = \Phi_{ki}/\Phi_{li}a_i$. The pole-residue form in equation (3) underlies a number of modal analysis methods for structural, input–output measurements. Iterative estimates of the system poles, p_i, provide the structure's resonant frequencies and damping values. The structural mode shapes are calculated from the residue terms $A_i^{k,l}$, beginning with the drive-point residue (i.e. $k = l$) which yields the scaled eigenvector $\Phi_{li}/\sqrt{a_i} = \sqrt{A_i^{l,l}}$. This quantity is then used to generate the full modal matrix for locations $l = 1, 2, \ldots, p$ and modes $i = 1, 2, \ldots, n$. When a truly collocated drive point is not available, the residue cannot be used to generate exactly the experimental mode shapes. Next, we will examine the effect of using nearly-collocated piezoelectric sensors and actuators on the modal model given by equation (3).

The equations of motion for piezoelectric structural systems include electromechanical relationships which enter through the actuator and sensor terms in the following second-order MDOF system equation

$$\text{actuator equation} \qquad \mathbf{M}\ddot{x} + \mathbf{C}\dot{x} + \mathbf{K}x = \Theta^a v$$

$$\text{sensor equation} \qquad \Theta^{s^T} x + \mathbf{C}_p v_s = \mathbf{q}$$

as described in Hagood *et al* (1990). Here the traditional force vector, $\mathbf{f}$, is replaced by $\Theta^a v$ where Θ^a is an electromechanical coupling (EMC) matrix associated with the vector of actuator voltages v. The sensor equation indicates that the piezoelectric element charge output vector $\mathbf{q}$ depends on an electrical term $\mathbf{C}_p v_s$ and an electromechanical term $\Theta^{s^T} x$ where $\mathbf{C}_p$ is the piezoelectrics' diagonal capacitance matrix and Θ^s is an EMC matrix associated with the sensor elements. The sensor equation defines the selection of appropriate sensor circuitry, which is chosen as first-order, non-inverting amplifiers for measurements of the open-circuit patch voltage v_s in the experiments presented in this paper.

The EMC matrix $\Theta^{a,(s)}$ describes the interaction between electrical effects, such as voltage and charge, and mechanical effects, such as force and displacement. The matrix values are calculated from the volume integral

$$\Theta = \int_{V_p} \Psi_r^T L_u^T e^T L_\varphi \Psi_\varphi \tag{4}$$

where the integration is over the piezoelectric patch volume V_p, $\Psi_{r\,(3\times n)}$ is the basis of the structure's generalized coordinates x, $L_{u\,(6\times 3)}$ is the differential operator relating displacement and strain, $L_{\varphi\,(3\times 1)}$ is the voltage gradient operator, and $\Psi_{\varphi\,(1\times m)}$ are the voltage modes. The piezoelectric constant $e^T_{(6\times 3)}$ is a function of the piezoelectric properties relating voltage and stress. The EMC matrices Θ^a and Θ^s have two different interpretations: (i) transformation between volts and force (with units of N V^{-1}) and (ii) transformation between displacement and charge (with units of C m^{-1}) respectively.

As mentioned previously, the sensor equation defines the type of piezoelectric output that is selected by the system designer via the appropriate signal conditioning. For this paper, the sensor equation describes the interaction between the structural response x, piezoelectric voltage v_s, the piezoelectric EMC matrix, and the piezoelectric capacitance matrix C_p. By constraining the patch charge to zero with an open circuit (ideally), the voltage output configuration of the piezoelectric sensors is then

$$\mathbf{M}\ddot{x} + \mathbf{C}\dot{x} + \mathbf{K}x = \Theta^a v$$

$$v_s = -C_p^{-1}\Theta^{s^T} x.$$

Noting that only the forcing terms are different for equation (1) and the actuator equation, we can substitute $\Theta_l^a v_l$ for f_l in equation (3) so that the receptance becomes

$$x = \sum_{i=1}^{n}\left[\frac{\Phi_i \Phi_i^T \Theta_l^a}{a_i(s - p_i)} + \frac{\Phi_i^* \Phi_i^{T*} \Theta_l^a}{a_i^*(s - p_i^*)}\right] v_l. \tag{5}$$

Now the sensor equation can be used to determine an input–output relationship from the lth piezoelectric actuator to the kth piezoelectric sensor.

$$\frac{v_{s,k}}{v_l} = -C_p^{-1}\sum_{i=1}^{n}\left[\frac{\Theta_k^{s\,T}\Phi_i\Phi_i^T\Theta_l^a}{a_i(s - p_i)} + \frac{\Theta_k^{s\,T}\Phi_i^*\Phi_i^{T*}\Theta_l^a}{a_i^*(s - p_i^*)}\right]. \tag{6}$$

We can further simplify the above expression by defining

$$\hat{\Theta}_{ij} = \Phi_i^T \Theta_j. \tag{7}$$

The k,lth element of the pole-residue modal model (v_s/v) for sheet piezoelectric transducers can then be written as

$$\frac{v_{s,k}}{v_l} = -C_p^{-1}\sum_{i=1}^{n}\left[\frac{\hat{\Theta}_{ik}^s \hat{\Theta}_{il}^a}{a_i(s - p_i)} + \frac{\hat{\Theta}_{ik}^{s\,*}\hat{\Theta}_{il}^{a\,*}}{a_i^*(s - p_i^*)}\right]$$

$$= -C_p^{-1}\sum_{i=1}^{n}\left[\frac{\hat{A}_i^{k,l}}{(s - p_i)} + \frac{\hat{A}_i^{k,l\,*}}{(s - p_i^*)}\right] \tag{8}$$

where $\hat{A}_i^{k,l} = \hat{\Theta}_{ik}^s/a_i$. In this representation $\hat{\Theta}$ is now

$$\hat{\Theta} = \Phi^T\Theta = \int_{V_p} \Phi^T\Psi_r^T L_u^T e^T L_\varphi \Psi_\varphi \tag{9}$$

$$= \int_{V_p} \hat{\Psi}_r^T L_u^T e^T L_\varphi \Psi_\varphi \tag{10}$$

where $\hat{\Psi}_r$ are the structure's natural (orthogonal) mode shapes and $\hat{\Theta}$ is the EMC matrix in the natural mode basis.

It is apparent from equation (8) that dynamic modeling of a coupled structure piezoelectric system requires knowledge of the system eigenvalues p_i and the EMC matrices $\hat{\Theta}^a$ and $\hat{\Theta}^s$. A comparison of the residues from equations (3) and (8) shows that the distinction

between the pole-residue models for piezostructures and conventional structures is the modified residue term. The traditional residue expression $A_i^{k,l} = \Phi_{ki}/\Phi_{li}a_i$ is a spatial function whose numerical values are determined by the sensor/actuator locations and the boundary conditions of the structure. The residue for the piezostructure $\hat{A}_i^{k,l} = \hat{\Theta}_{ik}^{s}\hat{\Theta}_{il}^{a}/a_i$ exhibits the same functional dependencies, in addition to a functional dependence on the material properties and piezoelectric geometries described by equation (10). This additional dependence on piezostructure parameters is manifested by new zeros for the piezostructure FRFs, even when the sensor and actuator locations are identical for both traditional and piezostructure measurements.

The development of the pole-residue model of equation (8) has important implications in regards to modal testing of piezostructures. First, existing curve-fit software can now be used to estimate the system poles and residues. Extraction of the residues, however, does not generate estimates of the system mode shapes. Instead, the modal electromechanical coupling (MEMC) matrix can be estimated. The procedure to calculate the individual elements of the MEMC is identical to the procedure used for conventional modal matrix calculations. The drive-point residue must be known, as discussed previously, for those calculations to proceed. For piezostructures with patch elements, true drive point measurements must be made using sophisticated circuitry which allows simultaneous sensing and actuation of the piezoelectric element. When a true drive-point measurement is not available, a nearly collocated element may provide adequate results for lower frequency modes. Next, a nearly collocated modal test experiment is described. Test results are then used to design a MIMO feedback control experiment.

3. Modal test of a simply-supported plate using piezoelectric materials

A simply-supported plate was used as a testbed experiment to investigate an approximate piezostructure modal testing method. The approximation refers to the use of nearly collocated drive-point measurements instead of truly collocated actuators and sensors. A description of the modal test experiment and the modal analysis results are presented next.

3.1. Description of the experiment

A steel plate of dimensions 600 × 500 × 2.9 mm was constrained in a steel housing to approximate simply-supported boundary conditions. The details of the plate construction follow the drawings provided by Saunders *et al* (1993) and a schematic of the testbed in shown in figure 1. The (0, 0) coordinate reference is taken at the top left corner of the plate (front view). Sensor and actuator numbers shown on figure 1 refer to the numbers in tables 1 and 2 respectively. The sensor and actuator measurements shown in the tables refer to the center of the patch elements. Notice in the figure that sixteen discrete PVDF sensors were arranged on the plate at the locations described by table 1. The sensor dimensions were 25.40 × 27.94 mm with a thickness dimension of 28 μm. The sensitive axis of the ceramic sensors and actuators were along the x direction. Note that the sensor dimensions are small compared with the wavelengths of the first five plate modes. Five PZT patch actuators were bonded to the plate using the locations shown in table 2. The actuator dimensions were 30.48 × 25.40 mm with a thickness of 254 μm.

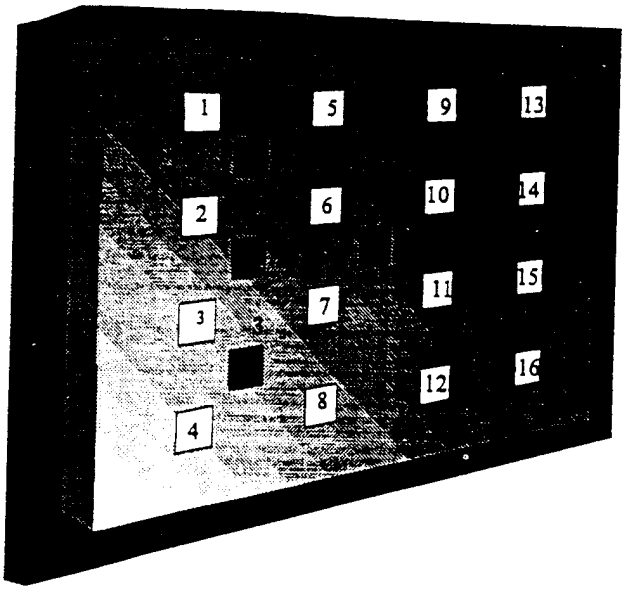

Figure 1. Simply-supported plate testbed sensor and actuator placement

Table 1. Sensor locations (mm).

i	x_0	y_0
1	133.35	64.77
2	133.35	214.78
3	133.35	316.23
4	133.35	413.00
5	253.20	64.77
6	253.20	214.78
7	253.20	316.23
8	253.20	413.00
9	373.06	64.77
10	373.06	214.78
11	373.06	316.23
12	373.06	413.00
13	485.70	64.77
14	485.70	214.78
15	485.70	316.23
16	485.70	413.00

Table 2. Actuator locations (mm).

i	x_0	y_0
1	299.40	254.40
2	149.20	254.40
3	149.20	374.60
4	498.50	374.60
5	165.10	155.60

The signal conditioning and data acquisition hardware components for the modal testing and active control experiments were designed and custom-built at Virginia Tech's Smart Structures Laboratory. A sixteen-channel, variable-gain, filter-amplifier for the PVDF sensors was constructed using JFET op-amps (Burr Brown OPA 602). Bench testing of the sensor amplifier unit was completed to fine-tune the filter settings, ensuring that the low frequency cut-off was sufficiently below the bandwidth of interest for the testing, 5–400 Hz. For PZT actuation, inexpensive power amplifiers were designed using power op-amps and audio transformers. This configuration was bench-tested *in situ* to determine the effective actuator dynamics required for the state space modeling.

The data acquisition and controller hardware were custom-built, Transputer-based components designed by Inmos. The data acquisition hardware, TDACS II, was custom-built at the Smart Structures Laboratory. The system consists of sixteen 12-bit input channels capable of simultaneous sample-hold and sixteen 12-bit DACs with a dynamic range of ±10 V, controlled by a 25 MHz T800 and a 20 MHz T220 processor. For control computations, a B008 motherboard with parallel processing capabilities is installed in a host 80386 computer. The motherboard is equipped with 25 MHz T800 and 30 MHz T800 VLSI processors. The T220 processor has a 16-bit, fixed-point processor and 16-bit external memory interface. The T800 is a floating-point, 32-bit processor with a 32-bit memory interface and four links to other transputers. For this experiment, a single T800 processor was used to implement the control law calculations. A custom-built signal analyzer, TFAS12, was generated to acquire the plate dynamic measurements. The TFAS12 analyzer software provides simultaneous sampling of twelve input channels and subsequent calculations of H1 transfer functions, autospectra, and coherence values. The controller design for the experiments in this paper used a single T800 processor for the computations and the TDACS II hardware for the closed-loop i/o.

Modal testing of the simply-supported plate was performed to estimate the modal parameters necessary for a state-space description of the plate using modal coordinates. H1 frequency response functions (FRFs) were generated for all sixteen PVDF locations. One additional nearly-collocated response measurement was acquired by placing a PVDF sensor adjacent to PZT actuator #5. The nearly-collocated sensor will be referred to as sensor #17. Actuator #5 was used to excite the plate for the FRF measurements. A continuous random signal was chosen for the data acquisition. A large number of averages (200) were acquired for each FRF measurement. The analysis range of the data was 0–400 Hz. This range was chosen because the desired bandwidth for the closed-loop control experiments was 0–250 Hz. The control bandwidth was selected for control of the first five plate modes. The results of the FRF measurements and analysis are discussed in the next section.

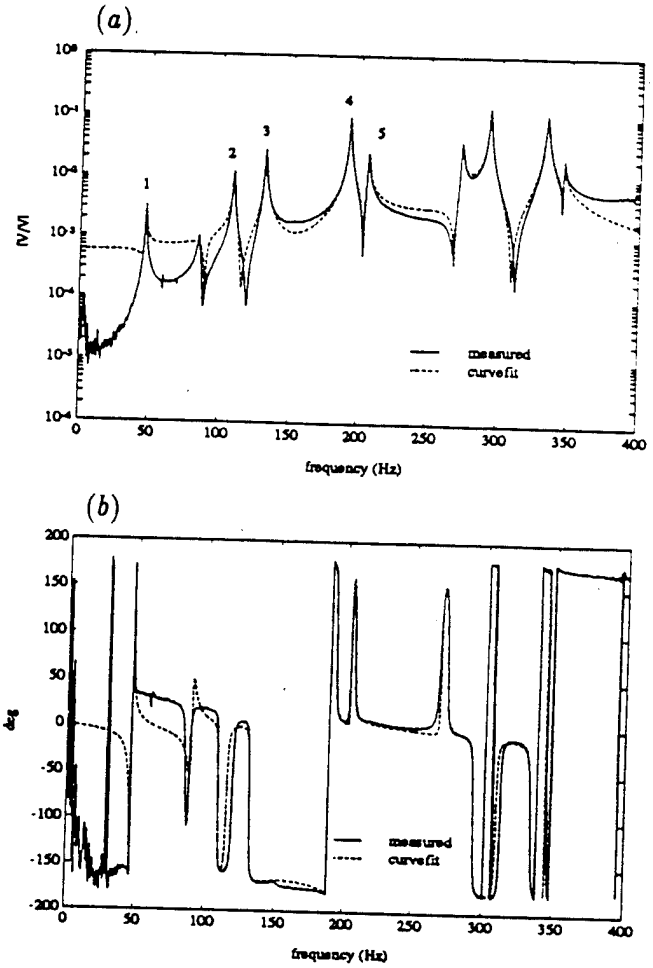

Figure 2. Curve fit and experimental FRFs for sensor #1. (*a*) magnitude, (*b*) phase.

3.2. Modal test and analysis results

The H1 FRF matrix corresponding to actuator #5 was used to estimate the poles and residues of the plate structure. Representative transfer-point FRFs from sensor locations #1 and #13 are shown in figures 1 and 2. The nearly-collocated drive-point response measurement, from sensor #17, is shown in figure 3. The FRFs indicate the moderately light damping and separation of the first five structural modes which are indicated on the figures, making pole estimation a relatively easy task. (A testbed system mode at 89 Hz was evident for certain FRF measurements, including sensor #13. For the control results presented in the next section, the system mode was an unmodeled mode as discussed by Saunders *et al* 1993.) Two curves are shown for each figure, the measured and the curve-fit quantities. The curve-fit quantities shown were synthesized from the generated test model. A brief discussion of the parameter estimation which lead to the curve-fit synthesis follows.

A frequency-domain, modal curve- fit algorithm developed at Virginia Tech was used for the piezostructure modal parameter estimation. The MODHAN code, created by Han and Wicks (1989), is a rational fractions approach which employs orthogonal polynomial basis functions in a least-squares minimization method

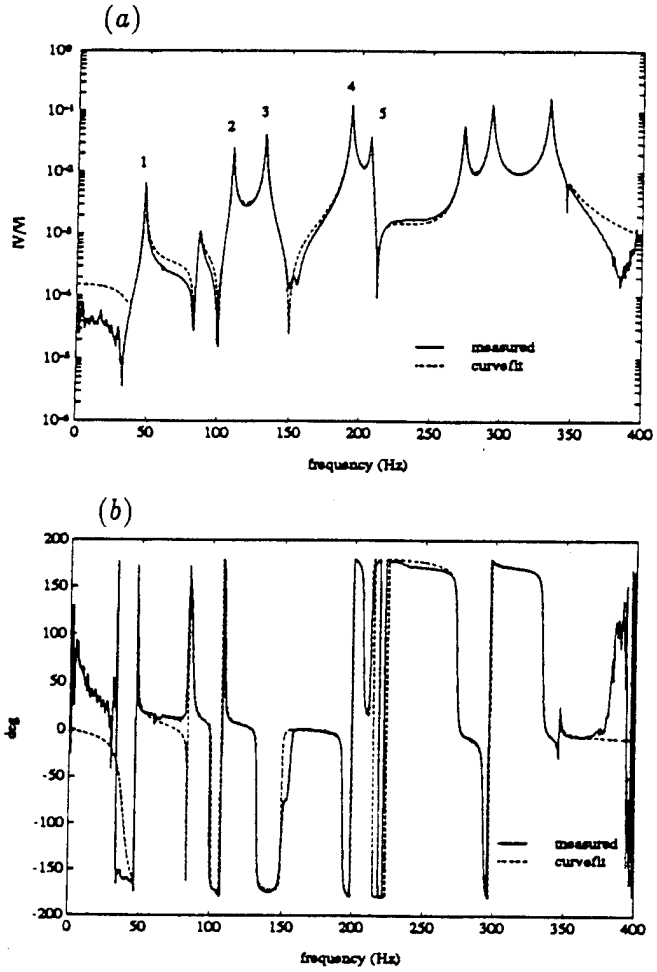

Figure 3. Curve fit and experimental FRFs for sensor #13. (*a*) magnitude, (*b*) phase.

Table 3. Estimated pole parameters.

Mode	Frequency (Hz)	ζ
1	47.7±0.3	0.77±0.10
2	86.9±1.3	2.00±0.90
3	109.4±0.1	0.39±0.03
4	131.5±0.2	0.34±0.04
5	192.7±0.1	0.26±0.00
6	206.4±0.2	0.31±0.04

for pole-residue estimation. The modal analysis of the FRF matrix resulted in the frequency and damping estimates shown in table 3. Frequency and damping estimates for each individual FRF were fairly consistent, agreeing within the shown standard deviations.

An approximation of the EMC values was obtained using the residue quantities defined by equation (8). The source of the approximation is discussed next. Referring back to equation (8), recall that different MEMC values were required for sensor versus actuator elements. Differences between the two values may be caused by different materials for the sensor and actuator piezoelectric materials, differences in the area moments of inertia, and differences in the mounting locations. This is evident in a more explicit expression of Θ_k for the kth piezo element:

$$\theta_k = S_k \int\int \left(e_{31,k} \frac{\partial^2 \Psi_r}{\partial x^2} + e_{32,k} \frac{\partial^2 \Psi_r}{\partial y^2} \right) \mathrm{d}y\,\mathrm{d}x \qquad (11)$$

where e_{31} and e_{32} are properties of the piezoelectric, S is the area moment of inertia, and Ψ are the mode shapes of the simply-supported plate. The field-stress constant e is different for PZT and PVDF materials. The area moment of inertia S changes with different thicknesses of the PZT actuators and PVDF sensors used in the experiment. Finally, the mounting locations affect the integrand through changes in the mode-shape quantities Ψ.

For the experiment, several assumptions were made. First, it was assumed that e_{31} and e_{32} were the same. This allowed removal of the quantity from the integration. (Their values actually differ by a factor of two, so an average quantity was used.) Second, since PVDF sensor #17 was placed very close to the driving patch it was assumed that the evaluation of the integral remained the same for actuator and sensor. These assumptions allowed the product $e_{31}S$ to be factored out of the residuals. Measurements of the diagonal $\mathbf{C}_p$ matrix were then made using a capacitance meter allowing the eigenvectors to be estimated. The quantity $e_{31}S$ was then multiplied back in to yield estimates for $\hat{\Theta}$. Curve fits of the FRFs using the modal parameter estimations are compared to the measured data in figures 2–4. The low-frequency magnitude and phase estimates are wrong because of the filtering characteristics introduced by the sensor amplifier unit. Essentially, the amplifier introduced a real pole to the system dynamics which was difficult to model using the pole-residue approach described earlier. A compensation method for this problem is currently being examined.

4. MIMO feedback control experiments

A state-space, LQG controller was designed using the test model created from the piezostructure modal test results. Active vibration control experiments were performed to suppress the effects of a wideband disturbance on the five lowest plate modes. A brief review of the control law and the test results are presented below.

4.1. Description of the experimental MIMO controller

A state-space model in modal coordinates was developed from the modal test results described in the previous section. The dynamic model was then used in initial MIMO control experiments to demonstrate the potential for closed-loop performance. A linear quadratic Gaussian (LQG) controller, which combines linear quadratic regulator feedback control with an optimal stochastic estimator (Kalman filter), was used for the experiments. This feedback controller minimizes a quadratic cost functional which weighs system states against controller effort (Stengel 1986). A brief description of the control law is shown next.

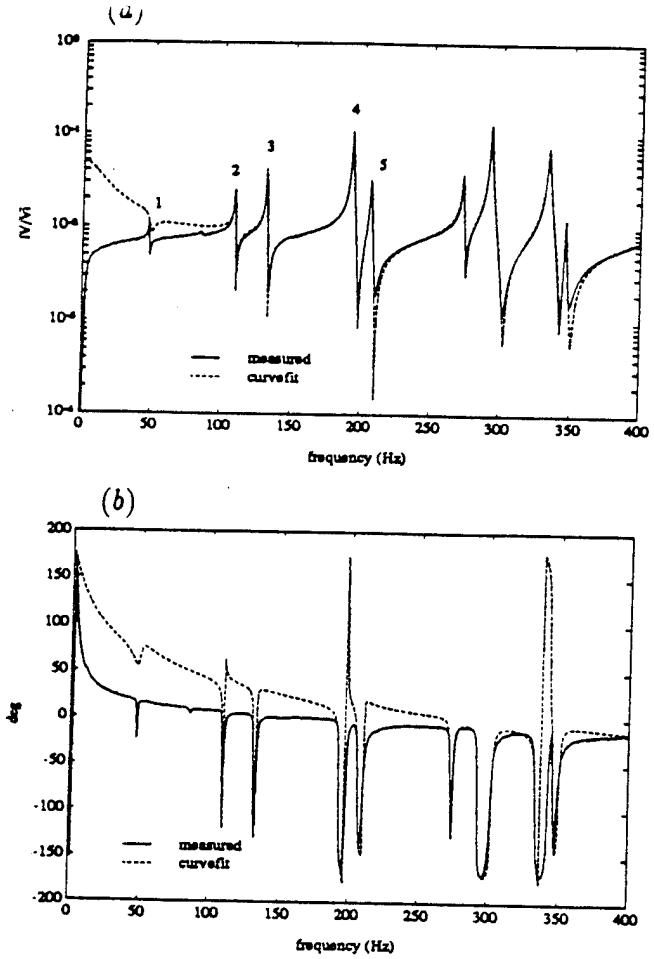

Figure 4. Curve fit and experimental FRFs for sensor #17. (*a*) magnitude, (*b*) phase.

A sampled-data model of the plate dynamics was assumed:

$$\begin{aligned} &\text{state propagation: } x_k = \Phi x_{k-1} + \Gamma u_{k-1} \Phi_{n\times n}\Gamma_{n\times q} \\ &\text{measured output: } y_k = C x_k C_{p\times n} \\ &\text{general output: } \gamma_k = C x_k C_{N\times n} \end{aligned} \tag{12}$$

where the control signal corresponded to state feedback

$$u_k = -K x_k \qquad K_{q\times n}. \tag{13}$$

Second-order actuator dynamics were combined with N modal positions and velocities to form the state vector x. Thus, the system order n depends on the number of inputs q used in each experiment, resulting in $n = 2(N + q)$. Recall that the model was truncated at five modes for this experiment. The state matrix Φ is a series of second-order dynamics for each mode and each actuator. The input matrix Γ is derived from the modal matrix and the output matrix $C = [I_N\ 0]$.

When direct measurements of the modal positions and velocities are not available, as is seldom the case, an estimator structure can be used to create the control signals (Willems 1980). For the control experiments, a predictor–corrector format of the Kalman filter equations were modified for computational efficiency as described previously by Cole *et al* (1994). Beginning with the predictor–corrector equations:

$$\begin{aligned} \hat{x}_k^- &= \Phi \hat{x}_{k-1}^+ + \Gamma u_{k-1} \\ \gamma_k &= \mathrm{M_f} y_k \\ \hat{\gamma}_k &= C \hat{x}_k^- \\ \hat{x}_k^+ &= \hat{x}_k^- + L(\gamma_k - \hat{\gamma}_k) \\ w_k &= K \hat{x}_k^+ \end{aligned} \tag{14}$$

the control w_k becomes a function of the estimated states $\hat{x}$. The operation of the modal filters $\mathrm{M_f}$ is required to convert the measured outputs to modal coordinates. $\mathrm{M_f}$ was created using a pseudo-inverse of the MEMC quantities from the modal analysis discussed above. As discussed by Shelley (1991), calculation of modal filters from modal test data is a potential source of uncertainty in real-time modal filtering. No attempt was made to isolate the effects of modal filtering on the results presented in this paper. Finally, the two gain matrices K and L were calculated using MATLAB's DLQR and DLQE functions, respectively. The quadratic cost function used to generate the control law was

$$Q = [I_N\ I_N\ 0]^{\mathrm{T}}\,[I_N\ I_N\ 0] \tag{15}$$

$$R = \left(\frac{\rho}{q}\right) I_q \tag{16}$$

where $\rho = 5 \times 10^{-8}$ was selected for all cases presented.

The implementation of the digital LQG controller was improved by rearranging terms and performing a change of variables $z_k = \hat{x}_k - L\gamma_k$ to condense equation (14) into

$$\begin{aligned} z_k &= (\Phi - LC\Phi)z_{k-1} + (\Phi - LC\Phi)L\gamma_{k-1} \\ &\quad + (\Gamma - LC\Gamma)u_{k-1} \\ w_k &= Kz_k + KL\gamma_k. \end{aligned} \tag{17}$$

Next, the results of the closed-loop experiments are presented.

4.2. Closed-loop experimental results

Three full-order LQG control experiments were implemented on the simply-supported plate testbed: one SIMO and two MIMO (2 and 4 inputs) experiments. The PVDF sensors were conditioned to measure physical positions and the five PZT actuators were configured to excite bending modes within the plate. PZT actuator #5 was used to provide a broadband, persistent disturbance input. The condensed observer equations discussed above resulted in faster sampling rates than in predictor–corrector implementations as discussed by Cole *et al* (1994) and Saunders *et al* (1993): $\approx$ 2700 Hz versus $\approx$ 2000 Hz using the TDACS II i/o and Transputer control board.

The frequency response functions for the three closed-loop experiments is compared to the open-loop response in figure 5. The sample frequencies and performance metrics for the three controllers are listed in table 4. Each controller added damping to the five modes within the controller bandwidth (25–250 Hz) with

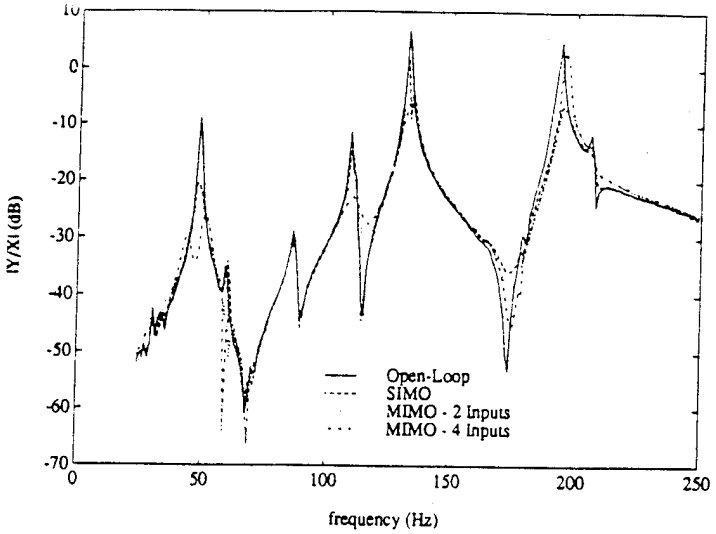

Figure 5. Closed-loop frequency response for MIMO controllers.

Table 4. Controller sample rates and performance ratios.

Inputs	Oper.	f_s (Hz)	$\Pi_{[25,250]}/\Pi_{OL}$	$\Pi_{[25,175]}/\Pi_{OL}$
1	193	2698	0.362	0.443
2	222	2273	0.243	0.213
4	280	1650	0.543	0.191

marginal spillover to unmodeled modes both in and outside of the controller bandwidth. As a metric of performance we define

$$\Pi_{[\omega_a,\omega_b]} = 2\int_{\omega_a}^{\omega_b} |T_{xy}(j\omega)|^2 \, d\omega \qquad (18)$$

which relates to the vibrational energy of the structure over the frequency bandwidth $\omega_a < |w| < \omega_b$. Here T_{xy} is the frequency response function between disturbance x and response y. The performance metrics, normalized by the open-loop response over the same bandwidth, are also listed in table 4.

The loss in performance of the 4-input controller at the fourth mode natural frequency, 206 Hz, is believed to result from poor actuator placement. The 4th mode of the simply-supported plate is a (2, 2) mode and two of the actuators lie on a nodal line of this mode. It is expected that improved actuator placement could improve the performance of all of the controllers.

5. Conclusions

An approximate method for modal testing of a piezostructure was demonstrated using a simply-supported plate structure. A new pole-residue expression was developed to cast the system identification problem for piezoelectric structural measurements in a modal analysis framework. It was shown that simultaneous sensing and actuation of the piezoelectric sheet transducers is strictly required for a successful application of the proposed approach. Although the technology exists for the simultaneous measurement approach, the associated difficulties warrant asking the question whether the nearly-collocated, approximate modal analysis approach used in this paper can generate test models which provide the desired closed-loop behavior.

The approximate modal test results for the simply-supported plate generated test models which synthesized the structural response with sufficient accuracy to allow substantial reductions in vibration response under the action of one, two or four control actuators. For this experiment, three dominant sources of control performance degradation were identified. First, the approximation techniques used to estimate the EMC matrix quantities may be partly responsible for decreased closed-loop performance. Second, the modal filtering process may also contribute to decreased performance. Third, the unmodeled modes in the control bandwidth contribute to less-than-optimal performance of the closed-loop system. Future work is planned to isolate the effects of the different mechanisms of uncertainty.

Finally, the use of existing modal analysis algorithms for piezostructure parameter identification has enormous potential to advance significantly smart structure technology. The modal analysis community is perhaps the largest constituency of scientists who are interested in structural modeling. Development of analysis tools which are compatible with the knowledge-base and methodologies of the modal analysts will encourage their participation in the emerging field of adaptive and intelligent structures.

Acknowledgments

This work was sponsored by ONR Grant No. N00014-92-J-1170

References

Bailey T and Hubbard J E 1985 Distributed piezoelectric polymer active vibration control of a cantilever beam *AIAA J. Guid. Contr.* **6** 605–11

Banks H T, Wang Y, Inman D J and Slater J C 1993 Approximation and parameter identification for damped second order systems with unbounded input operations *Report No. CRSC-TR93-9* (Raleigh, NC: Center for Research in Scientific Computation, NC State University)

Burke S I and Hubbard J 1987 Active vibration control of a simply-supported beam using a spatially distributed actuator *IEEE Contr. Syst. Mag.* **7** 25–30

Clark R L and Fuller C R 1992 Modal sensing of efficient acoustic radiators with PVDF distributed sensors in active structural acoustic approaches *J. Acoust. Soc. Am.* **91** 3313–20

Cole D G, Saunders W R and Robertshaw H H 1994 Modal parameter estimation for piezostructures *ASME J. Vib. Acoust.* at press

Crawley E F and de Luis J 1987 Use of piezoelectric actuators as elements of intelligent structures *AIAA J.* **25** 1373–85

Hagood N W, Chung W H and von Flotow A 1990 Modelling of piezoelectric actuator dynamics for structural control *J. Intell. Mater. Syst. Struct.* **1** 327–54

Han M and Wicks A L 1989 On the application of Forsythe orthogonal polynomials for global modal parameter estimation *7th IMAC (Las Vegas, 1989)* pp 625–30

Hanagud S V, Savanur S G, Nageshbu G L, Won C C and Srinivasan A V 1991 Modal analysis with PVDF films and piezoceramic transducers *ASME Winter Annual Meeting* ADv24 pp19–24

Klosterman A L 1971 On the experimental determination and use of modal representations of dynamic characteristics *PhD Dissertation* University of Cincinnatti

Lee C K, O'Sullivan T C and Chiang W W 1991 Piezoelectric strain rate sensor and actuator designs for active vibration control *AIAA-91-1064, Proc. 32nd AIAA SDM* pp 2197–207

Leuridan J 1992 IMAC 10 Keynote address: modal analysis: a perspective on integration *Int. J. Analyt. Exp. Modal Analy.* **7** 65–73

McConnell K G and Rogers J D 1991 *Int. J. Analyt. Exp. Modal Analy.* **6** 131–45

Saunders W R, Ellis G K and Robertshaw H H 1993 An experimental testbed for sampled data structural control algorithms *ASME J. Dyn. Contr.*

Saunders W R, Robertshaw H H and Togers C A 1991 Structural acoustic control of a shape memory alloy composite beam *J. Intell. Mater. Syst. Struct.* **2** 508–27

Shelley S J 1991 Investigation of discrete modal filters for structural dynamic applications *PhD Dissertation* University of Cincinnatti

Stengel R F 1986 *Stochastic Optimal Control* (New York: Wiley)

Tsou H S and Tseng C I 1991 Distibuted modal identification and vibration control of continua; piezoelectric finite-element formulation and analysis *ASME J. Dyn. Syst. Meas. Contr.* **113** 500–5

Willems J L 1980 Design of state observers for linear discrete-time systems *Int. J. Syst. Sci.* **II** 139–47

Zharij O Y 1991 Modal theory of electrochemical energy conversion in piezoelectric bodies *Priklad. Mat. Mekh.* **55** 330–7

C-21 Experiments on Active Control of Plate Vibration Using Piezoelectric Actuators and Polyvinylidene Fluoride (PVDF) Modal Sensors, Yi Gu, R. L. Clark, C. R. Fuller and A. C. Zander, ASME Journal of Vibration and Acoustics, Vol. 116, pp. 303-308, July 1994.

Experiments on Active Control of Plate Vibration Using Piezoelectric Actuators and Polyvinylidene Fluoride (PVDF) Modal Sensors

Y. Gu

R. L. Clark

C. R. Fuller

Vibration and Acoustics Laboratories,
Department of Mechanical Engineering,
Virginia Polytechnic Institute
and State University,
Blacksburg, VA 24061-0238

A. C. Zander

Department of Mechanical Engineering,
University of Adelaide,
Adelaide, South Australia 5001

An experiment was performed to investigate the implementation of shaped PVDF modal sensors on a simply supported rectangular plate to control specific modes of the vibration. The plate was excited by a steady-state harmonic point force while the control was achieved by two independent piezoelectric actuators bonded to the surface of the plate. A two-channel adaptive controller based on the multi-input multi-output filtered X LMS algorithm was used to provide feed-forward control. Two PVDF modal sensors were shaped such that the (3,1) mode was the dominant structural mode observed by the sensors. With this configuration, the amplitude of the (3,1) mode can be minimized regardless of excitation frequency. A comparative test was performed by using two accelerometers as error sensors. Results indicate that for both on and off-resonance excitations, the shaped PVDF modal sensors are superior to point-error sensors, such as accelerometers for controlling specific structural modes.

1 Introduction

Distributed sensors and actuators constructed from piezoelectric materials such as polyvinylidene fluoride (PVDF) and PZT have been the focus of much research in the last decade. Bailey and Hubbard (1985) introduced a method for controlling vibrational modes of a cantilever beam with a spatially distributed actuator manufactured from PVDF. A later study by Miller and Hubbard (1987) provided the foundation for distributed sensing with PVDF on a one-dimensional structure. Lee and Moon (1986), as well as Lee, Chiang, and Sullivan (1989), developed models for two-dimensional plate structures for distributed sensing. A detailed overview of the diverse applications of piezoelectricity was made by Collins, Miller, and von Flotow (1990). A recent study by Burke and Hubbard (1991) outlined a method of designing "weighted" actuators and sensors for vibration control of thin plates. While the design procedure is relatively simple, achieving the practical design is more involved since the polarization profile (i.e., sensitivity as a function of spatial coordinates) must be varied as a function of two dimensions for a plate structure. This issue has been addressed to some degree by Clark and Fuller (1991, 1992a, 1992b) in previous studies implementing rectangular error sensors constructed from PVDF for active structural acoustic control. However, a modal sensor for two-dimensional structures has not yet been achieved in practice.

Thus, the thrust of the present work is to suggest an alternative method of designing an "approximate" modal sensor for two-dimensional structures. In practice, this is achieved by designing two modal sensors, one for each respective dimension of the structure, positioned such that the response of the desired mode is dominant. In the case to be studied, one sensor is designed to measure the $(3,*)$ modes (here "$*$" denotes all positive integer values) of a simply supported plate in the x-direction, and the other sensor is constructed so as to measure the $(*,1)$ modes of the plate in the y-direction. The combined effort of these sensors is to dominantly measure the (3,1) mode of the plate as an approximation of a 2-D sensor. Hence, the response of the two-dimensional structure must be separable in orthogonal coordinates. This work draws concepts from both the strip rectangular PVDF sensor designs suggested by Clark and Fuller (1991, 1992a, 1992b) and the design approach outlined by Burke and Hubbard (1991).

To evaluate the shaped PVDF sensor design, tests were conducted on a simply supported plate driven harmonically with a shaker. The vibration of the plate was then attenuated using a feed-forward control approach in conjunction with piezoceramic actuators and PVDF sensors. Accelerometer error sensors were implemented as an alternative to the shaped PVDF error sensors to provide a basis for comparison between point sensors and distributed sensors, respectively. The results indicate that the accelerometer error sensors did not achieve the same level of modal control as the shaped PVDF modal sensors at the mode of interest, particularly at off-resonant frequencies.

Contributed by the Technical Committee on Vibration and Sound for publication in the JOURNAL OF VIBRATION AND ACOUSTICS. Manuscript received July 1992; revised June 1993. Associate Technical Editor: L. A. Bergman.

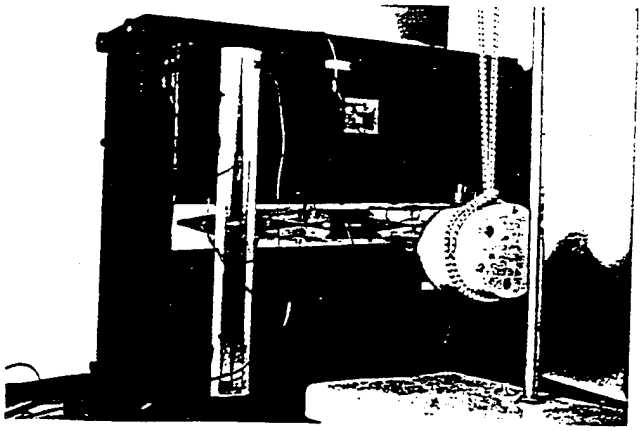

Fig. 1 Experimental setup

2 Experimental Setup

The experimental setup is shown in Fig. 1. The test plate measures $380 \times 300 \times 1.96$ mm and was configured to have simply supported boundary conditions. The implementation of the simply supported boundary was well-explained in previous papers (Hansen et al., 1989; Clark, 1992a). This setup has been tested several times at the Vibration and Acoustic Laboratory of Virginia Tech and the simply supported boundary condition has been proven satisfactory (Clark, 1992a). For comparison, the first 11 measured resonant frequencies of the plate are compared to the first 11 predicted resonant frequencies in Table 1, demonstrating accuracy to within 1.3 percent.

The disturbance input to the plate was provided by a shaker connected to the plate with a stinger. The plate response was measured with two accelerometers, one positioned at a fixed reference point and the other was positioned at 13 independent coordinates on the plate to measure the transfer function between it and the reference under steady-state conditions. The results were recorded, and then a modal decomposition (Hansen et al., 1989) was performed to recover the independent modal amplitudes. The effect of mass loading resulting from the two measurement accelerometers (B & K type 4374) was neglected in the post-processing of the structural response since the mass of each accelerometer was 0.65 grams. The output of these accelerometers was processed with a B & K 2032 dual-channel spectrum analyzer, and the response was measured sequentially at the 13 independent coordinates on the structure.

The control actuators were implemented with two sets of piezoelectric actuators as illustrated in Fig. 2. The mathematical model of the actuator was previously derived by Dimitriadis, et al., (1989). Each actuator consists of two piezoceramic elements of dimension $38 \times 31 \times 0.19$ mm bonded symmetrically to the front and rear of the plate with M-bond 200 adhesive. These two elements were wired out-of-phase such that while one symmetrically located element induced extension, the other induced contraction, and the two elements combine to produce pure bending about the neutral axis of the plate. Because the piezoelectric actuators required high-voltage excitation, the voltage amplification was provided by a transformer connected to the output of a control-signal power amplifier to increased the voltage by 17:1 for each of the PZT actuators.

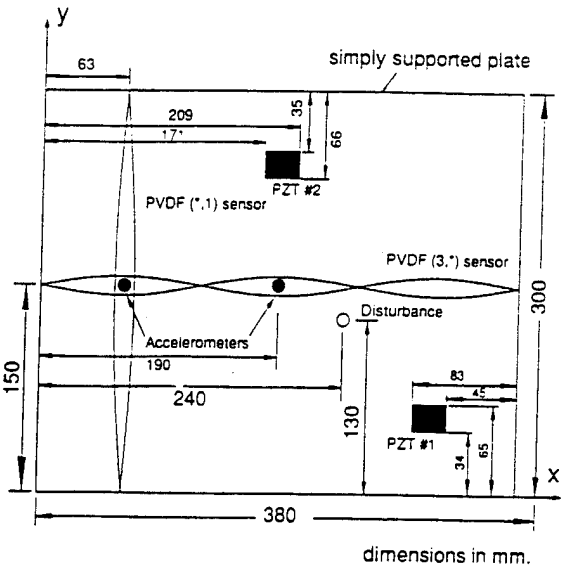

Fig. 2 System schematic

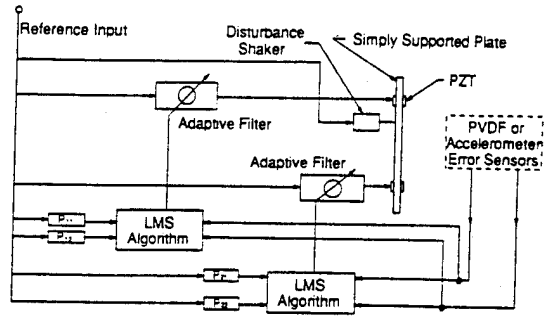

Fig. 3 Block diagram of adaptive LMS controller

Control was achieved with a two-channel adaptive controller based on the multiple-error, filtered X LMS algorithm implemented on a TMS320C25 DSP resident in an AT computer. The control schematic is illustrated in Fig. 3. A more detailed description of the control algorithm can be found in a reference by Elliott, et al., (1987). The harmonic disturbance signal input to the shaker was also fed into the LMS adaptive controller as the reference signal.

As shown in Fig. 2, one PVDF sensor was shaped to sense the family of $(3,*)$ (where '$*$' means a family of modes and is an arbitrary, positive integer) modes of vibration and the other to sense the family of $(*,1)$ modes of vibration (Lee and Moon, 1990). As discussed in Section 1, the combination of these two sensors provides a modal filter for minimizing the

Nomenclature

a = center coordinate in y-direction of PVDF sensor
b = width of PVDF sensor in y-direction
e_{31}^0 = stress per charge constant in x-direction
e_{32}^0 = stress per charge constant in y-direction
e_{36}^0 = stress per charge constant (cross-axis)
$FP_0(x,y)$ = shape and polarization profile as a function of area
h_p = thickness of structure
h_s = thickness of PVDF sensor
j = complex number
L_x = length of the plate in x-direction
L_y = length of the plate in y-direction
M = number of modes for x-direction
N = number of modes for y-direction
m = modal index for x-direction
n = modal index for y-direction
q = sensor response in units of charge
S_s = 1-D modal sensor weights
S_{mn} = 2-D modal sensor weights
W_{mn} = modal amplitudes
w = response of structure
x,y = coordinates of plate
ω = driving frequency

modes (i.e., for example, the (3, *) modes for x-direction sensors or (*,3) modes for y-direction sensors) can be constructed. If these sensors are conveniently placed on nodal lines of the structure, other modes contributing to the sensor response within the desired family of modes can be eliminated or reduced in influence on the sensor output charge.

3.3 Design Sensitivity. In many of the references listed in the Introduction, the studies are primarily theoretical investigations. For those studies involved with experimental implementation of the modal sensors, explanations for response characteristics deviating from that predicted are offered based on the inability to accurately "etch" the metalization or cut the desired shaped sensor. Based on experimental results conducted in this study, the deviation between predicted and measured PVDF modal sensor response appears to be due largely to the inaccuracy in placement of the PVDF sensor on the structure. As demonstrated by Clark and Burke (1993), a small error in positioning the PVDF sensor on the surface of the structure can result in significant response of the sensor near resonance of modes which were supposed to be orthogonal to the spatially distributed sensor. However, for off-resonance response, the frequency-response function of the sensor with respect to the disturbance remains relatively unchanged (Clark and Burke, 1993).

4 Results

Experiments were performed implementing the shaped PVDF modal sensors and accelerometers in active control of plate vibration. Both on- and off-resonance excitations were tested to compare the modal suppression resulting from the control of the PVDF sensors to that of control with the accelerometer error sensors. A two-channel controller was used for both error sensor implementations, whereby the cost function was simply the sum of the error signals squared. The controlled response for all results was compared with the uncontrolled response.

4.1 Sensor Sensitivity Test. Prior to conducting tests with the shaped PVDF modal sensors, each sensor should be individually tested. To evaluate the sensors, a test was performed measuring the frequency response between a force transducer, mounted between the stinger of the shaker and the plate, and the output of each of the PVDF modal sensors, using a random input disturbance.

For the (3, *) sensor, the response is greatest at a driving frequency corresponding to the resonant frequency of the (3,1) mode as illustrated in Fig. 4. The next dominant peak is observed at an excitation frequency corresponding to resonance of the (3,3) mode. The sensor response is predicted, based on the theory outlined in the previous section, and as can be seen, some deviation is noted. In fact, this deviation was shown to be a function of placement error in positioning the sensor on the structure (Clark and Hubbard, 1993). As a result, some unwanted modes are observed, resulting in performance degradation of the modal sensor.

The predicted and measured frequency-response functions for the (*,1) modal sensor are presented in Fig. 5. The dominant response is noted at the (1,1) mode, which was desired. This is achieved by selectively positioning the sensor on the structure such that the response of other (*,1) modes are diminished. As illustrated, the correlation between theory and experiment is excellent. Again, some minor deviations occur as a result of inaccuracy in positioning the PVDF sensor on the structure.

Such deviations in response can be included in an analytical model and are addressed in another publication (Clark and Burke, 1993). The performance of the sensor needs to be carefully examined before any experiment, using the sensor, is performed. In this test, both sensors were periodically evaluated to confirm the desired performance characteristics.

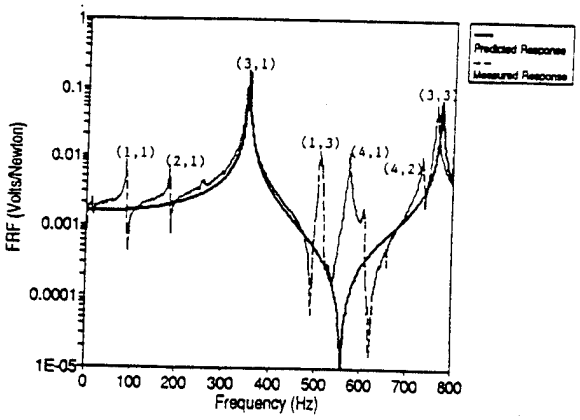

Fig. 4 (3, *) modal-sensor frequency response

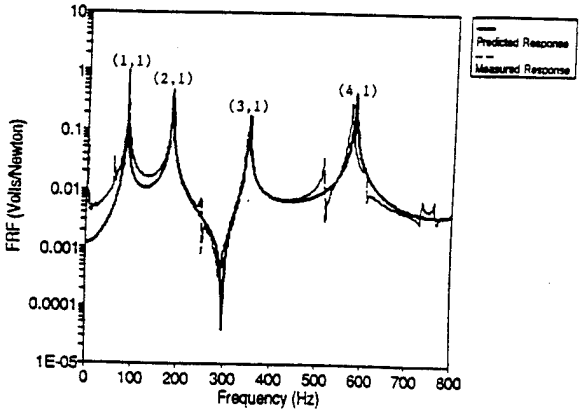

Fig. 5 (*,1) modal-sensor frequency response

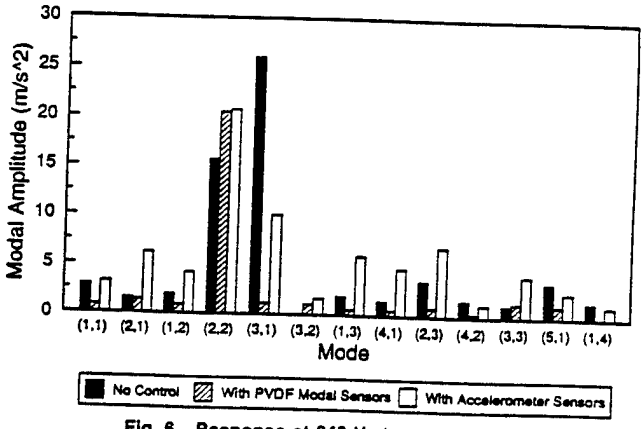

Fig. 6 Response at 348 Hz (on-resonance)

4.2 $f = 348$ Hz, (3,1) Mode Resonance. The first test was conducted on-resonance at an excitation frequency of 348 Hz, corresponding to the resonant frequency of the (3,1) mode of the plate. It should be noted that this resonant frequency was determined by fine tuning the driving frequency before conducting each experiment. A modal decomposition was performed to determine the contribution of each open-loop structural mode to the response of the simply supported plate. A procedure for determining the modal distribution, based on an array of accelerometers, was previously outlined by Hansen et al., (1989) and the reader has referred to this reference for greater detail. As indicated in Fig. 6, the amplitude of the (3,1) mode dominated the response of the system before applying control. Significant response of the (2,2) mode also was observed at this driving frequency; however, this was expected since the resonant frequency of this mode was measured at 346 Hz as indicated in Table 1. The contributions of all other modes were negligible compared with these two modes. With the shaped PVDF sensors, the amplitude of (3,1) mode was

Table 1 Resonant Frequencies of the Plate

Mode	Theoretical f_n (Hz)	Measured f_n (Hz)
(1,1)	87.8	88
(2,1)	189.0	186
(1,2)	250.1	250
(2,2)	351.3	346
(3,1)	357.6	350
(3,2)	519.9	509
(1,3)	520.6	520
(4,1)	593.6	580
(2,3)	621.8	610
(4,2)	755.9	736
(3,3)	790.4	767

reduced by 27 dB, resulting in 2.3 dB of spillover into the (2,2) mode. The spillover results from the implementation of the shaped PVDF error sensors since each sensor was designed to respond to the (3,1) mode and not the (2,2) mode. Hence, the resulting cost function of the LMS algorithm does not constrain the response of the (2,2) mode as a result of the chosen sensor design. The amplitudes of the majority of the other modes also were reduced.

When the error sensors were replaced by accelerometers, the (3,1) mode was reduced by 8.2 dB (i.e., 18.8 dB less than that observed with the PVDF modal sensors). The spillover into all other modes was relatively large compared with the result achieved with the PVDF sensors. The reason for the degraded performance is, of course, that accelerometers are point sensors and as such will observe all wave number or modal responses. The controller tends to achieve minimization in these off-resonance cases by adjusting the phases and amplitudes of the uncontrolled modes so that they "cancel" at the error points. Often this leads to significant control spillover away from the point sensor such that the global properties of the plate (i.e., modes) may be poorly attenuated or even increased. This example serves to demonstrate that the shaped PVDF modal sensors have better performance than the accelerometer sensors for on-resonance excitation. The results obtained with either of the two types of error sensors illustrate that the dominant (3,1) mode was significantly reduced upon applying control, and modal suppression is observed at this mode.

4.3 $f = 320$ Hz, Off-Resonance. The second test was performed at an off-resonance excitation frequency of 320 Hz. Results from the modal decomposition of the uncontrolled and controlled structural response are depicted in Fig. 7. This excitation frequency is between the resonant frequencies corresponding to the (1,2) and (2,2) modes and was chosen to examine the performance of the PVDF sensor off-resonance below the resonant frequency of the (3,1) mode, which the PVDF sensors were designed to observe best. Without control, the plate vibration was dominated by a number of modes instead of one or two modes as in the previous on-resonance test case. When PVDF sensors were implemented, the (3,1) mode was significantly reduced by 6.6 dB, the (1,1) mode decreased slightly by 0.17 dB, and the (2,2) mode decreased by approximately 8.7 dB, while some spillover was observed at other modes. Because the PVDF modal sensors were designed primarily to reduce the structural response of the (3,1) mode, it is not surprising that they did so at the expense of some increase in other modes. However, the point to be emphasized is that the response of the (3,1) mode was reduced even in the off-resonance test case, demonstrating that shaped PVDF modal sensors perform well in off-resonant applications by directly observing the mode to be controlled.

When accelerometer error sensors were implemented in the cost function of the control approach, the (3,1) mode was reduced by only 3.2 dB. Hence, the PVDF modal sensors resulted in a 3.4 dB improvement in reduction of the response

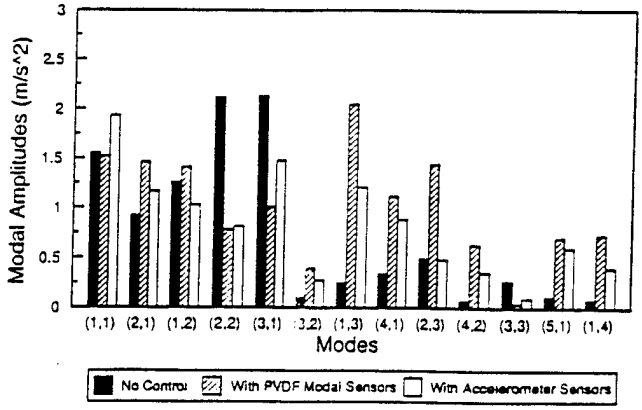

Fig. 7 Response at 320 Hz (off-resonance)

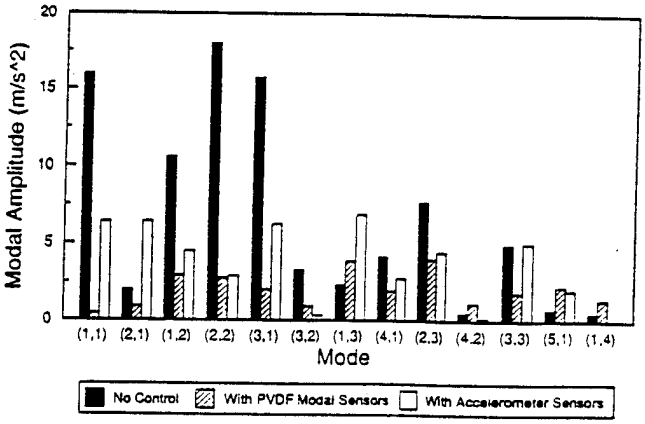

Fig. 8 Response at 375 Hz (off-resonance)

of the (3,1) mode. This illustrates that the distributed PVDF sensors are superior to point accelerometer error sensors for controlling a specific structural mode such as the (3,1) plate mode in both off-resonance and on-resonance test cases in the absence of processing the output of the accelerometers with some modal filter.

4.4 $f = 375$ Hz, Off-Resonance. To further investigate the behavior of the PVDF modal sensors, another off-resonance excitation frequency was chosen at 375 Hz, between resonant frequencies of the (3,1) mode and (3,2) mode. Results from the modal decomposition are presented in Fig. 8 and significant control (18 dB) over the (3,1) mode is achieved when implementing the PVDF modal sensors. While accelerometers also perform well at this frequency, their performance did not match that of the PVDF sensors since a reduction of only 8.0 dB was observed. At the (3,1) mode, the residual controlled amplitude is achieved when implementing the accelerometer errors sensors is more than double that achieved when implementing the PVDF sensors.

4.5 $f = 400$ Hz, Off-Resonance. The final test was conducted to determine how the PVDF error sensors perform under conditions when the (3,1) mode response is small compared with the response of other modes. When the plate was driven at 400 Hz (off-resonance excitation frequency), the (3,1) mode was not dominant and a variety of structural modes contribute to the response of the plate as indicated in Fig. 9. In this case, upon applying control while implementing the PVDF sensors, the modal amplitude of the (3,1) mode was reduced by approximately 12 dB and that of the (1,1) mode was reduced by 2.6 dB. This result is not surprising since the PVDF modal sensors do not respond exclusively to the (3,1) mode. For more complex situations, where the modal response functions are nonorthogonal, it is suggested that a new set of orthogonal basis functions be constructed using, for example, the Gram-Schmidt technique (Morse, 1953). Then the sensor

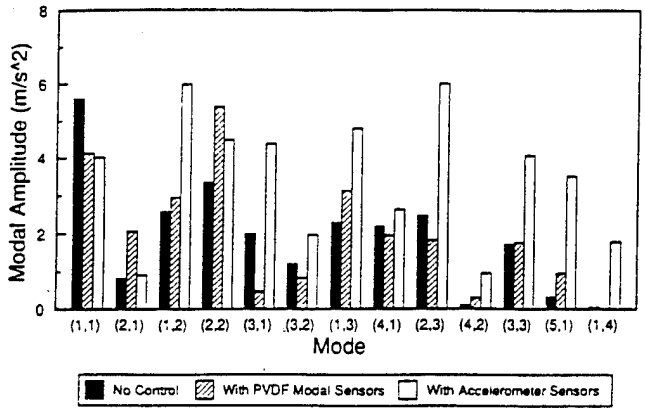

Fig. 9 Response at 400 Hz (off-resonance)

can be shaped to observe these new orthogonal basis functions. Upon comparing the controlled response when implementing the PVDF error sensors to that when implementing the accelerometer error sensors, one observes that the response of the (3,1) mode actually increased upon achieving control as discussed previously. Hence, the PVDF modal sensors were clearly superior in exercising control of the desired structural mode.

5 Conclusions

The emphasis of this work was to develop an approximate method of practically achieving a 2-D modal sensor for plate-type structures. The study presents an alternative of designing two one-dimensional modal sensors to measure certain two-dimensional structural modes. For a simply supported plate, the structural response is separable in two dimensions; thus, it is convenient to implement such a design. It is noted that either of the one-dimensional sensors measured a family of modes in the x- or y-direction, and their combined effort measured dominantly the (3,1) mode of the plate as designed.

Vibration control experiments were performed on a simply supported rectangular plate utilizing the feed-forward filtered X version of the adaptive LMS algorithm to achieve control. Based on the test results, for on- and off-resonant excitations, the PVDF modal sensors consistently proved superior to accelerometers in selectively filtering the desired (3,1) mode. Note that the filtered-x LMS algorithm is a time-domain control algorithm and shaped PVDF sensors are eminently suitable as they provide analog, time-domain filtering of modes. Usual modal (or wave number) filtering occurs in the frequency domain (for example, the modal decomposition method employed in this paper). A comparison between the PVDF and accelerometer sensors indicates that the shaped PVDF distributed sensors have undeniable advantages over the accelerometer error sensors for time-domain vibration control applications. This is because distributed sensors are capable of spatial modal filtering, and accelerometers are incapable of performing the same task in the absence of post-processing.

The results indicate that approximate 2-D PVDF modal sensors perform well for active vibration-control applications and should be investigated in active structural-acoustic-control applications in the future.

Acknowledgment

The authors gratefully acknowledge the support of this work by ONR under Grant ONR-N00014-92-J-1170.

References

Bailey, T., and Hubbard, J. E., 1985, "Distributed Piezoelectric Polymer Active Vibration Control of a Cantilever Beam," *Journal of Guidance, Control and Dynamics*, Vol. 8, pp. 605-611.

Burke, S. E., and Hubbard, J. E., 1987, "Active Vibration Control of a Simply Supported Beam Using a Spatially Distributed Actuator," *IEEE Control. Syst. Mag.*, Vol. 109, pp. 25-30.

Clark, R. L., and Burke, S. E., 1993, "Practical Considerations for Designing Shaped Modal Sensors From Polyvinylidene Fluoride (PVDF)," submitted to *Journal of Intelligent Material Systems and Structures.*

Clark, R. L., and Fuller, C. R., 1992a, "Experiments on Active Control of Structurally Radiated Sound Using Multiple Piezoceramic Actuators," *Journal of the Acoustical Society of America*, Vol. 91(6), pp. 3313-3320.

Clark, R. L., and Fuller, C. R., 1992b, "Optimal Placement of Piezoelectric Actuators and Polyvinylidene Fluoride (PVDF) Error Sensors in Active Structural-Acoustic-Control Approaches (ASAC)," *Journal of the Acoustical Society of America*, Vol. 92(3), pp. 1521-1533.

Clark, R. L., 1992c, *Advanced Sensing Techniques for Active Structural Acoustic Control*, PhD dissertation, Department of Mechanical Engineering, VPI&SU.

Collins, S. A., Miller, D. W., and von Flotow, A. H., 1990, "Sensors for Structural Control Applications Using Piezoelectric Polymer Film," *MIT Report*, pp. 1-83.

Crawley, E. F., and de Luis, J., 1987, "Use of Piezoelectric Actuators as Elements of Intelligent Structures," *AIAA Journal*, Vol. 25(10), pp. 1373-1385.

Dimitriadis, E. K., Fuller, C. R., Rogers, C. A., 1991, "Piezoelectric Actuators for Distributed Vibration Excitation of Thin Plates," ASME JOURNAL OF VIBRATION AND ACOUSTICS, Vol. 113, pp. 100-107.

Elliott, S. J., Stothers, I. M., and Nelson, P. A., 1987, "A Multiple Error LMS Algorithm and Its Application to the Active Control of Sound and Vibration," *IEEE Transaction on Acoustic Speech and Signal Processing*, ASSP-35, 1:1423-1434.

Fanson, J. L., and Chen, J. C., 1986, "Structural Control by the Use of Piezoelectric Active Members," *Proceedings of NASA/DOD Control Structures Interaction Conference*, NASA CP-2447, Part II.

Fuller, C. R., Hansen, C. H., and Snyder, S. D., 1989, "Active Control of Structurally Radiated Noise Using Piezoceramic Actuators," *Proceedings of Inter-Noise*, Vol. 89, pp. 509-511.

Fuller, C. R., Gibbs, G. P., and Silcox, R. J., 1990, "Active Control of Flexural and Extensional Waves in Beams," *Journal of Intelligent Material Systems and Structures*, Vol. 1(2), pp. 235-247.

Fuller, C. R., Hansen, C. H., and Snyder, S. D., 1991, "Active Control of Sound Radiation From a Vibrating Rectangular Panel by Sound Sources and Vibration Inputs: An Experimental Comparison," *Journal of Sound and Vibration*, Vol. 145(2), pp. 195-215.

Hansen, C. H., Snyder, S. D., and Fuller, C. R., 1989, "Noise Reduction of a Vibrating Square Panel by Use of Active Sound Sources and Active Vibration Sources: A Comparison," *Proceedings of Noise and Vibration*, Vol. 89, Singapore.

Lee, C. K., and Moon, F., 1986, "Laminated Piezopolymer Plates for Torsion and Bending Sensors and Actuators," *Journal of the Acoustical Society of America*, Vol. 85(6), pp. 723-726.

Lee, C. K., Chiang, W., and Sullivan, T., 1989, "PVF_2 Modal Sensors and Actuators Achieving Critical Active Damping on a Cantilever Plate," *Proceedings of the AIAA/ASCE/AHS 30th Structures, Structural Dynamics and Materials Conference*, Mobile, AL.

Lee, C. K., 1990, "Theory of Laminated Piezoelectric Plates for the Design of Distributed Sensor/Actuators. Part 1: Governing Equations and Reciprocal Relationships," *Journal of the Acoustical Society of America*, Vol. 87, pp. 1144-1158.

Lee, C. K., and Moon, F. C., 1990, "Modal Sensors/Actuators," *ASME Journal of Applied Mechanics*, Vol. 57, pp. 434-441.

Lefebvre, S., Guigou, C., and Fuller, C. R., 1992, "Experiments on Active Isolation Using Distributed PVDF Error Sensors," accepted by the *Journal of Sound and Vibration*, Vol. 155(1), pp. 177-184.

Miller, S., and Hubbard, J., 1987 "Observability of a Bernoulli-Euler Beam Using PVF_2 as a Distributed Sensor," *Proceedings of Sixth VPI&SU/AIAA Symposium on Dynamics and Control of Large Structures*, Blacksburg, VA, ed. L. Meirovitch, pp. 375-390.

Miller, D. W., Collins, S. A., and Peltzman, S. P., 1990, "Development of Spatially Convolving Sensors for Structural Control Applications," *AIAA Paper, 90-1127-CP*, pp. 2283-2297.

Morse, P. M., 1953, *Methods of Theoretical Physics*, McGraw-Hill, 1953.

Wada, B. K., Fanson, J. L., and Crawley, D. F., 1990, "Adaptive Structures," *Journal of Intelligent Material Systems and Structures*, Vol. 1(2), pp. 157-174.

Wallace, C. E., 1972, "Radiation Resistance of a Rectangular Panel," *Journal of the Acoustical Society of America*, Vol. 51, pp. 946-952.

Wang, B. T., Dimitriadis, E. K., and Fuller, C. R., 1990, "Active Control of Structurally Radiated Noise Using Multiple Piezoelectric Actuators," *AIAA Journal*, Vol. 29, pp. 1802-1809.

C-22 Dynamic Analysis of Piezoelectric Actuator-Driven Circular Rings using an Impedance Approach, A. Rossi, C. Liang, and C. A. Rogers, Journal of the Acoustic Society of America, Vol. 96 No. 3, pp. 1592-1597, September 1994.

Dynamic analysis of piezoelectric actuator-driven circular rings using an impedance approach

Anna Rossi
Aerospace Department, University of Rome, Rome, Italy

Chen Liang and Craig A. Rogers
Center for Intelligent Material Systems and Structures, Virginia Polytechnic Institute and State University, Blacksburg, Virginia 24061-0261

(Received 5 February 1993; revised 28 February 1994; accepted 2 May 1994)

This paper presents a dynamic model for the response of a circular ring excited by piezoelectric transducer (PZT) actuators bonded on the ring surface. The dynamic response is determined based on the dynamic interaction between the PZT actuators and the structure using an impedance approach. Compared with the conventional static approach, in which a statically determined "equivalent force" of the actuator is used as the forcing function in the dynamic analysis, the impedance approach cannot only capture the physics of the actuator/structure interaction, but also accurately predict the structural dynamic response. Experiments have also been conducted to verify the theoretical model. The predicted dynamic response using the impedance approach agrees very well with the experimental results. Comparison of the conventional static approach and the impedance model has also been presented.

PACS numbers: 43.40.Vn

INTRODUCTION

Piezoceramics have often been used as actuators for active structural vibration and acoustic control. The structural behavior (for beams and plates) under the excitation of piezoceramic actuators was modeled by Crawley and de Luis (1987) and Dimitriadis *et al.* (1989). Most dynamic analyses of adaptive structures with integrated actuators have been based on a static approach, namely, using a statically determined transmitting force as the forcing function in the dynamic analysis.

Liang *et al.* (1993) have developed an impedance modeling methodology for the dynamic analysis of adaptive material systems. Unlike the conventional static approach, the impedance approach determines the actuator transmitting force based on actuator and structural impedance, rather than on the static actuator and structural stiffness. The transmitting force depends on the global structural dynamics, including boundary conditions, structural damping, stiffness, and mass. The dynamic response determined with the static approach is a scaled frequency response function (ratio of response to excitation force), not the true response under a variable force excitation.

This paper will apply the general impedance methodology to a circular ring. Experimental results will be presented to validate the theoretical model. Comparison between the impedance approach and the static approach will also be conducted.

I. SYSTEM DYNAMIC MODELING

Consider a ring or a cylinder for which the axial traveling wave is not considered. Two PZT actuators are bonded on the top and bottom of the ring surface to create a pure bending moment, as shown in Fig. 1. The ring is assumed to be "thin" so that the linear Love–Kirchhoff theory (Leissa, 1973; Soedel, 1981) can be used. The actuator is also assumed to be "very thin" so that the stress across the actuator thickness remains constant in order to use the impedance model. To simplify the derivation, the width of the ring is assumed to be unity.

Surface bonded PZT actuators (ideally bonded) interact with their substrate in the form of shear force. However, most of the shear force is concentrated at the end of actuators within two to three actuator thickness distance (Lin and Rogers, 1993). For most cases, the interaction of integrated induced strain actuator (embedded or bonded) and its substrate can be modeled as a concentrated force at the end of the actuator. The interaction of a pair of surface bonded PZT actuators activated out-of-phase may then be modeled as a pair of moments, as shown in Fig. 1. The two concentrated bending moments on the two ends of the actuator can be expressed with the Dirac function as

$$M_{\text{right}} = F(h+s)\,\delta(\theta-\theta_p) \tag{1}$$

and

$$M_{\text{left}} = -F(h+s)\,\delta(\theta+\theta_p), \tag{2}$$

where F is the force exerted on the structure by a PZT actuator at its edge, and s and h are the actuator and ring thicknesses, respectively. Here, θ_p is the angular coordinate of the actuator edge, as shown in Fig. 1. Note that F is the dynamic transmitting force and is presently unknown. The transmitting force F, acting on the ring, also satisfies the following relation:

$$Z = \frac{F}{\dot{v}_{\theta=\theta_p}} = \frac{F}{i\omega v_{\theta=\theta_p}}, \tag{3}$$

where Z is the mechanical impedance of the ring at the actuator edge (ring/actuator interface) corresponding to a force,

 0001-4966/94/96(3)/1592/6/$6.00 © 1994 Acoustical Society of America

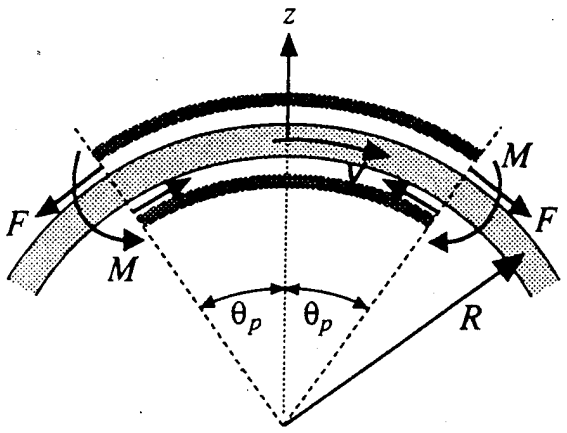

FIG. 1. One-dimensional circular ring with bonded PZT actuators activated out-of-phase.

F, in the circumferential direction, $v_{\theta=\theta_p}$ is the circumferential displacement at the force location, and a dot indicates a function of time derivative.

One PZT actuator (top or bottom) and its interaction with the ring may be represented by a generic system as shown in Fig. 2. The curvature effect has not been considered in the dynamic modeling of the piezoelectric actuators. It is, therefore, necessary to assume that the patch's dimension be kept small relative to the cylinder radius so that the error due to the curvature effect can be neglected. The motion of the piezoelectric will be considered along the d_{32} direction (or in the global y direction).

As an electrical field is applied in the actuator thickness direction, the actuator expands and contracts in the y direction (d_{32} effect). The one-dimensional constitutive equation for the actuator can be written as

$$S_2=\bar{s}_{22}^E T_2+d_{32}E, \tag{4}$$

where S_2 is the strain, T_2 the stress, E the electric field, d_{32} the piezoelectric coefficient, and $\bar{s}_{22}^E$ the complex compliance at a constant electrical field.

The equation of motion of the actuator vibrating in the y direction may be expressed as follows:

$$\rho_p \frac{\partial^2 v}{\partial t^2}=\bar{Y}_{22}^E \frac{1}{R^2}\frac{\partial^2 v}{\partial \theta^2}, \tag{5}$$

where v is the displacement in the y direction, ρ_p is the density of the PZT actuator, $\bar{Y}_{22}^E$ is the complex modulus of the PZT at a constant electrical field and R is the radius of the ring. The thickness of the ring and the PZT actuator is much smaller than the radius and is ignored in the above equation.

Assuming a harmonic excitation and solving Eq. (5) by separating the displacement into time and spatial domain yields:

$$v=\bar{v}e^{i\omega t}=[A\ \sin(kR\theta)+B\ \cos(kR\theta)]e^{i\omega t}, \tag{6}$$

where the wave number k is given by

$$k^2=\omega^2(\rho_p/\bar{Y}_{22}^E), \tag{7}$$

where ω is the excitation frequency.

The boundary condition of the PZT actuator is illustrated in Fig. 2. The interaction between actuator and substructure is taken into account by the equilibrium and compatibility equations which are written in terms of the point impedance of the substructure:

$$T_2|_{\theta=\theta_p} s=-i\omega Z|_{\theta=\theta_p} v|_{\theta=\theta_p} \tag{8}$$

and

$$T_2|_{\theta=-\theta_p} s=-i\omega Z|_{\theta=-\theta_p} v|_{\theta=-\theta_p}. \tag{9}$$

The above equations describe the complex boundary conditions for the PZT actuator, which is given by transmitting force = host structural impedance x driving point velocity.

The two boundary conditions [Eqs. (8) and (9)], together with the constitutive equation of the PZT, provide the necessary conditions to determine A and B. Substituting Eqs. (8) and (9) into Eq. (4), yields:

$$\bar{S}_{22}|_{\theta=-\theta_p}=\frac{1}{R}\left.\frac{\partial v}{\partial \theta}\right|_{\theta=-\theta_p}=-\frac{1}{\bar{Y}_{22}^E}\frac{Z|_{\theta=-\theta_p} v|_{\theta=-\theta_p} i\omega}{s}+d_{32}\bar{E} \tag{10}$$

and

$$\bar{S}_{22}|_{\theta=\theta_p}=\frac{1}{R}\left.\frac{\partial v}{\partial \theta}\right|_{\theta=\theta_p}=-\frac{1}{\bar{Y}_{22}^E}\frac{Z|_{\theta=\theta_p} v|_{\theta=\theta_p} i\omega}{s}+d_{32}\bar{E}, \tag{11}$$

where variables with a bar indicate spatial components except for $\bar{Y}_{22}^E$. Substituting Eq. (6) into Eqs. (10) and (11), a linear equation system in the unknowns A and B is obtained. Considering the symmetry of the ring (impedance at $-\theta_p$ and θ_p are the same and is denoted as Z in the subsequent analysis), B can be determined as zero and A is given by

$$A=\frac{d_{32}\bar{E}}{k\ \cos kR\theta_p+(Zi\omega/\bar{Y}_{22}^E s)\sin kR\theta_p}. \tag{12}$$

The short-circuit actuator mechanical impedance (Liang *et al.*, 1993) for a ring configuration may be derived as

$$Z_p=\frac{\bar{Y}_{22}^E s}{R\theta_p i\omega}\frac{kR\theta_p}{\tan(kR\theta_p)} \tag{13}$$

and the coefficient A can be simplified as

$$A=\frac{Z_p\, d_{32}\bar{E}}{(Z+Z_p)k\ \cos(kR\theta_p)}. \tag{14}$$

The strain and stress within the actuator can be solved as

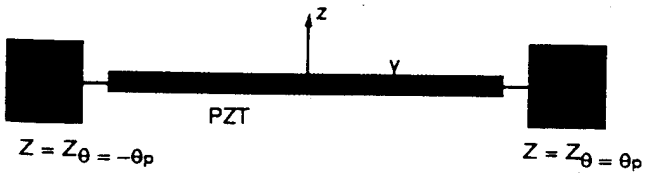

FIG. 2. A generic representation of the dynamic interaction of a surface bonded PZT actuator.

$$\tilde{S}_2 = \frac{Z_p\, d_{32} E}{(Z+Z_p)\cos(kR\theta_p)} \cos(kR\theta) \tag{15}$$

and

$$\tilde{T}_2 = \left(\frac{Z_p\, d_{32} \tilde{E}}{(Z+Z_p)\cos(kR\theta_p)} \cos(kR\theta) - d_{32}\tilde{E} \right) \tilde{Y}^E_{22}. \tag{16}$$

The transmitting force between the actuator and host ring at θ_p can be determined as

$$F|_{\theta=\theta_p} = \tilde{T}_2|_{\theta=\theta_p} S = -\frac{Z\, d_{32}\tilde{E}\, \tilde{Y}^E_{22} S}{Z+Z_p}. \tag{17}$$

It is clear that the transmitting force resulting from the activation of the PZT actuator is governed by the mechanical impedance of the host structure and the actuator. The induced moment of the actuator can then be determined from Eqs. (1), (2), and (17).

II. DETERMINATION OF STRUCTURAL IMPEDANCE

Equation (17) indicates that activation of a PZT actuator-results in a frequency-dependent excitation to the host structure. The transmitting force depends on the structural impedance. This section describes the derivation of structural impedance of the host ring corresponding to the loading of PZT actuator excitation. The impedance calculation will be performed only at position θ_p because of the symmetry of the ring structure. The equation of motion for the ring can be written in matrix form (Soedel, 1981) as

$$\begin{Bmatrix} \frac{D}{R^4}\frac{d^2}{d\theta^2} + \frac{K}{R^2}\frac{d^2}{d\theta^2} & -\frac{D}{R^4}\frac{d^3}{d\theta^3} + \frac{K}{R^2}\frac{d}{d\theta} \\ \frac{D}{R^4}\frac{d^3}{d\theta^3} - \frac{K}{R^2}\frac{d}{d\theta} & -\frac{D}{R^4}\frac{d^4}{d\theta^4} - \frac{K}{R^2} \end{Bmatrix} \begin{pmatrix} v \\ w \end{pmatrix} - \rho_r h \begin{pmatrix} \ddot{v} \\ \ddot{w} \end{pmatrix}$$

$$= \begin{pmatrix} \frac{M_{\text{right}}}{R^2} \\ \frac{1}{R^2}\frac{dM_{\text{right}}}{d\theta} \end{pmatrix}, \tag{18}$$

where

$$D = \frac{h^3 \tilde{Y}_r}{12(1-\mu^2)}, \tag{19}$$

and

$$K = \frac{h\tilde{Y}_r}{(1-\mu^2)}. \tag{20}$$

Here, $\tilde{Y}_r$ is the complex Young's modulus of the ring, ρ_r the density of the ring, and μ the Poisson's ratio. The in-plane displacement v and the transverse displacement w may be expressed as

$$v(t,\theta) = \sum_{n=1}^{\infty} v_n(t)\phi_n(\theta) \tag{21}$$

and

$$w(t,\theta) = \sum_{n=1}^{\infty} w_n(t)\psi_n(\theta). \tag{22}$$

For a one-dimensional ring, the eigenfunctions a $\phi_n(\theta)=\sin(n\theta)$ and $\psi_n(\theta)=\cos(n\theta)$. Substituting Eqs. (2 and (22) into Eq. (18) yields:

$$\begin{Bmatrix} -\frac{D}{R^4}n^2 - \frac{K}{R^2}n^2 & -\frac{D}{R^4}n^3 - \frac{K}{R^2}n \\ -\frac{D}{R^4}n^3 - \frac{K}{R^2}n & -\frac{D}{R^4}n^4 - \frac{K}{R^2} \end{Bmatrix} \begin{pmatrix} v_n \\ w_n \end{pmatrix} - \rho_r h \begin{pmatrix} \ddot{v}_n \\ \ddot{w}_n \end{pmatrix}$$

$$= \begin{pmatrix} \frac{M_{\text{right}} \sin(n\theta)}{\pi R^2} \\ \frac{M_{\text{right}}\, n \sin(n\theta)}{\pi R^2} \end{pmatrix}. \tag{2}$$

To determine structural impedance, the transmitting force the moment acting at θ_p is assumed to have a known mag nitude. Assuming a harmonic excitation, the excitation mo ment may be expressed as $M_{\text{right}}e^{i\omega t}$. The modal amplitude $w_n(t)$ and $v_n(t)$, become

$$w_n(t) = W_n e^{i\omega t} \tag{2}$$

and

$$v_n(t) = V_n e^{i\omega t}. \tag{2}$$

Substituting Eqs. (24) and (25) into Eq. (23) yields a linea system of equations, from which the modal coefficients, V and W_n, can be determined from the following equation:

$$\begin{Bmatrix} -\frac{D}{R^4}n^2 - \frac{K}{R^2}n^2 + \rho_r h\omega^2 & -\frac{D}{R^4}n^3 - \frac{K}{R^2}n \\ -\frac{D}{R^4}n^3 - \frac{K}{R^2}n & -\frac{D}{R^4}n^4 - \frac{K}{R^2} + \rho_r h\omega^2 \end{Bmatrix}$$

$$\times \begin{pmatrix} V_n \\ W_n \end{pmatrix} = \begin{pmatrix} \frac{M_{\text{right}} \sin(n\theta)}{\pi R^2} \\ \frac{M_{\text{right}} \sin(n\theta)}{\pi R^2} \end{pmatrix}. \tag{2}$$

The point impedance of the ring can now be determined onc the driving point velocity is determined. The driving poi (surface of the ring) velocity includes the inplane displac ment and the transverse bending, and may be expressed as

$$\dot{v}|_{\theta=\theta_p} = i\omega \sum_{n=1}^{\infty} \left(V_n + \frac{h}{2R} n W_n \right) \sin(n\theta). \tag{27}$$

The driving point structural impedance from Eq. (3) can the be substituted into Eqs. (15) and (16) to determine the stres and strain within the PZT actuator. The induced moment c the actuators can be determined from Eqs. (1), (2), and (17

When calculating the structural impedance, an arbitrar force (frequency independent) F may be used, which yields structural response, $w(\theta,\omega)$ and $v(\theta,\omega)$. If a unit force is use in the calculation, the structural responses are actually th frequency response functions of the ring. If the frequenc response functions are denoted as

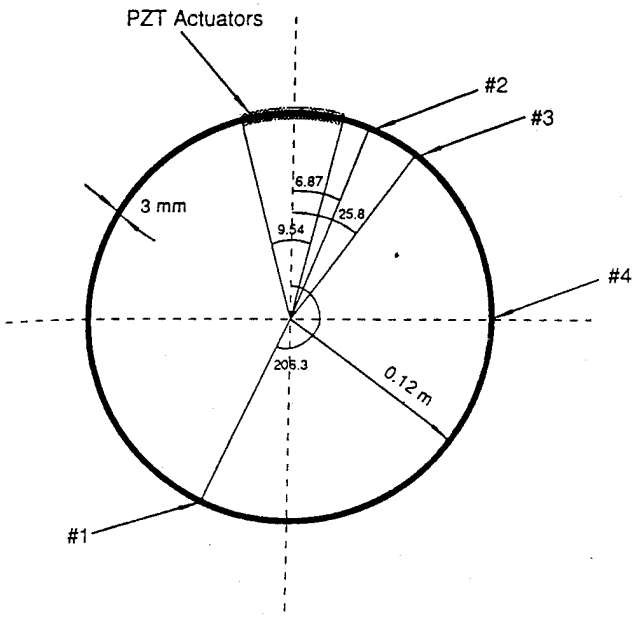

FIG. 3. Dimensions and sensor locations of the circular ring used in the theoretical and experimental investigation.

$$\bar{w} = \sum_{n=1}^{\infty} \bar{W}_n \psi_n \tag{28}$$

and

$$\bar{v} = \sum_{n=1}^{\infty} \bar{V}_n \phi_n . \tag{29}$$

The true structural response under a frequency-dependent actuator excitation can then be obtained by multiplying the transmitting force (or moment) with the above frequency response functions [Eqs. (28) and (29)].

III. THEORETICAL AND EXPERIMENTAL RESULTS

Both experimental and theoretical analyses have been conducted to demonstrate the accuracy and utility of the impedance modeling technique. The results from the static approach have also been presented to illustrate the difference between the two approaches.

Figure 3 shows the aluminum ring with bonded PZT actuators used in the experiments and the theoretical analysis. The material properties and dimensions of the PZT actuator and the aluminum ring are listed in Table I.

TABLE I. Material properties and dimension of the PZT actuators and aluminum ring.

	Aluminum ring	PZT actuator
Young's modulus, Pa	60×10^9	63×10^9
Density, kg/m^3	2647	7600
Loss factor	0.005	0.01
Piezo. Coef., m/v	N/A	-166×10^{-12}
Radius (length), cm	12.48	2.54
Width, cm	2.54	2
Thickness, mm	3	0.23

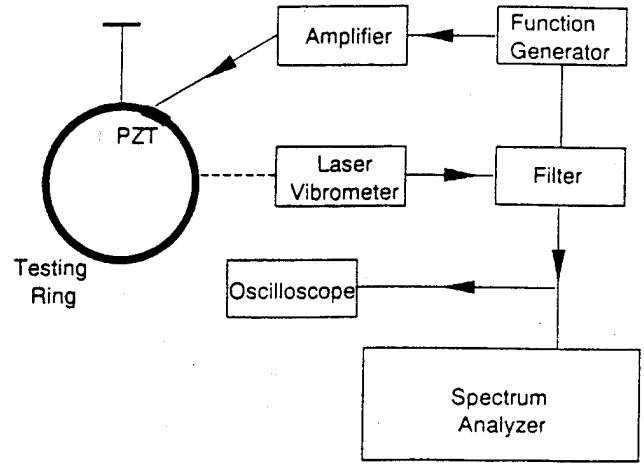

FIG. 4. Experimental setup in the measurement of the ring velocity response. The ring is hung with a fishing line.

The velocity responses of point #1, #2, #3, and #4, as shown in Fig. 3, are calculated using the impedance and static approaches. The ring was hung with a fishing line in the experiment. A laser Doppler measurement system was utilized to measure the velocity response of the ring with bonded PZT actuators. A schematic illustration of the experimental setup is depicted in Fig. 4. The measured and predicted responses of point #2 and #4 are shown in Figs. 5 and 6, respectively.

IV. DISCUSSION

The predicted and measured dynamic responses of point #2 are shown in Fig. 5. The static approach provides reasonably accurate results given by the dash-dotted line. The dashed line from the impedance model agrees well with the experimental results (solid line).

Figure 6 shows the measured and predicted responses at point #4. The experiment results indicate some activities around the second and fourth resonant frequencies, which are

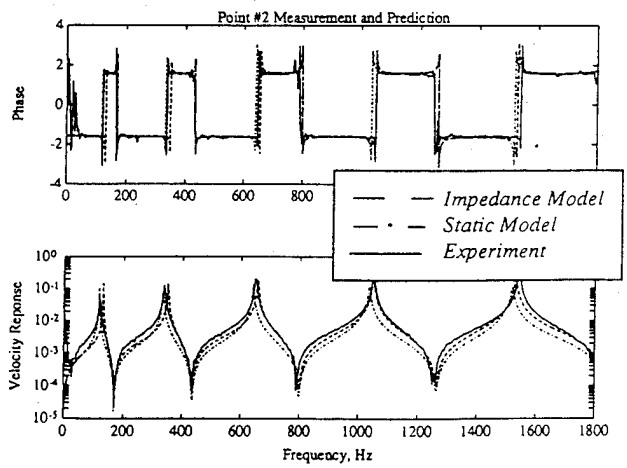

FIG. 5. Measured and predicted velocity and phase response at sensor location #2.

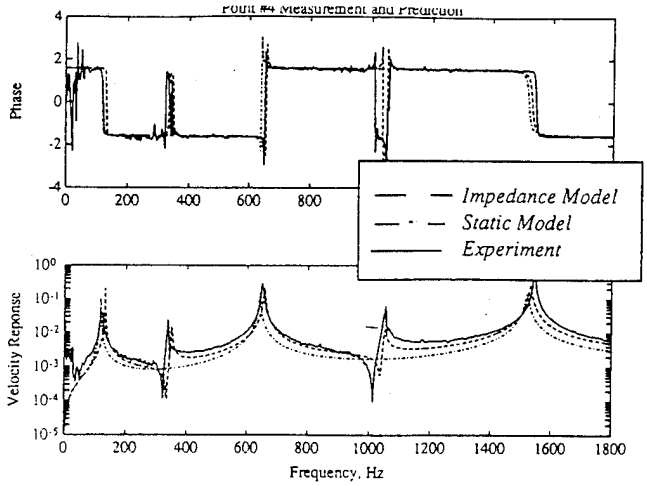

FIG. 6. Measured and predicted velocity and phase response at sensor location #4.

captured by the impedance model. The static model, in this case, does not even predict the response profile around these two resonant frequencies correctly. This is because the static approach does not include actuator stiffening and mass loading effects. Point #4 is the nodal line for the second and fourth mode of the ring itself (without PZT actuators). However, once the PZT actuators are bonded to the ring, point #4 is no longer the nodal line for the new mechanical system (ring and actuators) because of the actuator mass loading and stiffening. The response predicted by the static approach is the frequency response function of the ring itself, while the experimental measurement is the response of the ring and PZT. In this example, the bonding of the actuators may create as much as 45% stiffening within the ring section where the actuators are bonded.

The results in Fig. 6 may be further explained from the perspective of impedance matching and frequency-dependent actuator excitation. Figure 7 shows the structural and actuator impedance, as well as the stress at the edge of the actuator (the transmitting force per actuator cross-sectional area). This figure demonstrates that the physical essence of the dynamic interaction between the integrated induced strain actuators, such as PZT in this case, lies in the match of structural and actuator impedance. At the resonance of the ring (valleys of the structural impedance curve), the actuator transmitting force is at its minimum. The actuator force output reaches a maximum when the actuator impedance matches the structural impedance (complex conjugate). Because the actuators in this case always stiffen the ring, the force output of the actuator demonstrates a repeated valley-peak pattern around each resonant frequency of the ring. It is very clear from this result that the actuator excitation is frequency dependent, which results in the same valley-peak pattern around the second and fourth resonant frequencies for the velocity response of the ring.

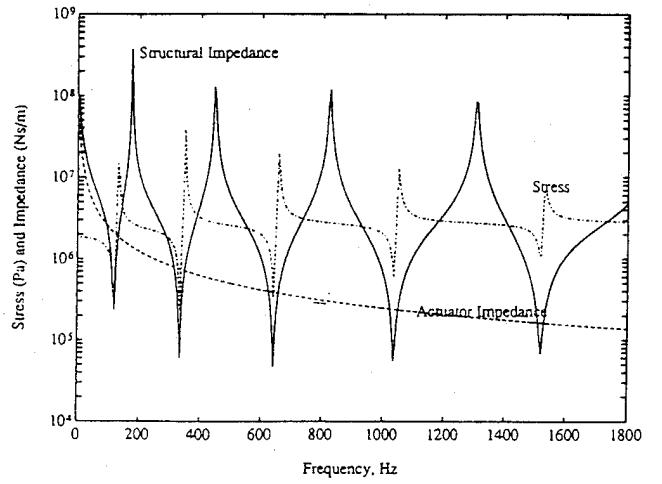

FIG. 7. Structural (solid line) and actuator (dashed line) mechanical impedance, as well as the transmitting force (per actuator cross-sectional area).

The static approach, compared to the impedance method, is simple and can sometimes provide acceptable dynamic response prediction (Clark and Fuller, 1991) if the actuator impedance is much smaller than the structural impedance. The results shown in Fig. 6 also indicate the variation of mode shapes of the ring because of the mass loading and stiffening from the actuators. The impedance model discussed in this paper is more accurate because it considers the stiffening and circumferential mass loading effect (radial direction mass loading effect was not considered) in the analysis. In general, the static model may provide a satisfactory dynamic prediction provided that the actuator is much smaller than the host structure. However, the impedance model can not only provide more accurate results but also reflect the physical essence of the actuator/structure interaction.

V. CONCLUSION

The impedance modeling technique developed by Liang *et al.* (1993) has been utilized to study the dynamic response of circular ring structures. Experiments have been conducted to validate the impedance model. Both experimental and theoretical results indicate that the impedance modeling technique cannot only reflect the physical essence of the dynamic interaction between the integrated induced strain actuators and the host structures, but may also more accurately predict dynamic response than the conventional static approach.

ACKNOWLEDGMENTS

This work was performed while the first author was a visiting graduate student at the Center for Intelligent Material Systems and Structures. The first author would like to express her gratitude to her adviser Professor Paolo Santini of the Aerospace Department of The University of Rome for giving her the opportunity to study at CIMSS. The study visit was made possible by the fellowship program of ALENIA (Italy). The authors would like to acknowledge the funding support of the Office of Naval Research, Grant ONR 00014-92-J-1170, Dr. K. Ng, Program Monitor. The authors would also like to thank Mr. F. P. Sun for his efforts in the experimental work.

Clark, R. L., Jr., and Fuller, C. R. (**1991**). "Characterization of Multiple Piezoelectric Actuators for Structural Excitation," J. Acoust. Soc. Am. **90** (1), 346–357.

Crawley, E. F., and Luis, J. D. (**1987**). "Use of Piezoelectric Actuators as Elements of Intelligent Structures," AIAA J. **25**, 1373–1385.

Dimitriadis, E. K., Fuller, C. R., and Rogers, C. A. (**1989**). "Piezoelectric Actuators for Distributed Noise and Vibration Excitation of Thin Plates," *8th ASME Conference on Failure, Prevention, Reliability and Stress Analysis, Montreal.*

Leissa, A. W. (**1973**). "Vibration of Shells," NASA Rep.

Liang, C., Sun, F. P., and Rogers, C. A. (**1993**). "An Impedance Method for the Dynamic Analysis of Active Material Systems," *Proceedings, 34th SDM Conference, La Jolla, CA, April 19–22*, pp. 3587–3599. Also in ASME J. Vib. Acoust. **116** (1), 120–128 (1994).

Lin, M., and Rogers, C. A. (**1993**). "Modeling of the Actuation Mechanism in a Beam Structure with Induced Strain Actuators," *Proceedings, 34th SDM Conference, La Jolla, CA, 19–21 April*, pp. 3608–3617.

Soedel, W. (**1981**). *Vibrations of Shells and Plates* (Dekker, New York).

C-23 Modeling of Distributed Piezoelectric Actuators Integrated with Thin Cylindrical Shells, S. W. Zhou, C. Liang and C. A. Rogers, Journal of the Acoustic Society of America, Vol. 96 No. 3, pp. 1605-1612, September 1994.

Modeling of distributed piezoelectric actuators integrated with thin cylindrical shells

Su-Wei Zhou, Chen Liang, and Craig A. Rogers
Center for Intelligent Material Systems and Structures, Virginia Polytechnic Institute and State University, Blacksburg, Virginia 24061-0261

(Received 5 August 1993; revised 21 March 1994; accepted 13 May 1994)

The dynamic interaction between induced strain piezoelectric (PZT) actuators and their host structures is often ignored in the modeling of intelligent structures. A more realistic investigation of intelligent material systems must account for the dynamic behaviors of integrated actuator/substrate systems. In this paper, a generic method for the dynamic modeling of distributed PZT actuator-driven thin cylindrical shells has been developed using a mechanical impedance approach. The impedance characteristics of a cylinder corresponding to the excitation of a pair of pure bending moments have been developed, from which the dynamic output moments (or forces) of PZT actuators can be accurately predicted. Direct comparisons have been made between a conventional static modeling approach and the impedance method in order to identify the critical differences between these modeling methods for thin cylindrical structures. The case studies demonstrate that the mechanical impedance matching between PZT actuators and host structures has an impact on the output performance of the actuators. The dynamic essence of integrated PZT/substrate systems has thus been revealed.

PACS numbers: 43.40.Vn, 43.40.Ey, 43.38.Fx

INTRODUCTION

The use of piezoelectric materials (PZT) as actuators and sensors in intelligent structures has drawn much attention in the active controls community. An accurate mathematical description of integrated PZT/substrate systems is indispensable in the development of practical applications of PZT materials in active vibration control and active structural acoustic control. One investigation devoted to the modeling of actively controlled cylinders was based on the layered shell theory (Tzou, 1989); in this study, a completely distinct layer of the piezoelectric material was used to make up a composite cylinder. A more convenient and feasible configuration of PZT actuators in adaptive structures is the use of segmented piezoelectric patches bonded on or embedded in host structures. For the modeling of these PZT actuators locally coupled with shell structures, static approaches have been used to estimate the induced loading. Sonti and Jones (1991) investigated the performance of the controlled cylinder using the piezoactuator control patch and a point force for both on- and off-resonance cases. The output performance of the PZT actuator, however, was not specifically studied. The assumption was made in the modeling that the dimension of the PZT patch in the circumferential direction is kept small relative to the cylinder radius. The curvature effects could then be neglected. The static models developed from thin plate theory (Crawley and Lazarus, 1991; Dimitriadis *et al.*, 1989; Wang and Rogers, 1991) could then be used in smart shell structures. Lester and Lefebvre (1991) applied the same assumption in their study and researched both out-of-plane and in-plane piezoelectric actuation for controlling sound radiation and transmission related to vibrating cylinders. It is typically assumed in the static models that the added mass and stiffness of PZT actuators are insignificant. The dynamic interaction between the PZT actuator and the host structure is ignored. Thus, the input impedance of the actuators and the mechanical impedance of the host structures are not included in the modeling. The static analysis usually leads to the conclusion that the amplitude of the excitation force of the PZT actuator is independent of host structural dynamics and frequency.

A more realistic investigation must account for the dynamic properties of the actuators, the actuators have their own mechanical impedance. When an active force provided by the PZT actuator is applied to a host structure, the PZT itself is driven by the force. Therefore, the mechanical resonance of an integrated PZT/substrate system is the combination of the dynamic behavior of the PZT actuator and that of the actuated structure. Hagood *et al.* (1990) proposed a dynamic model based on Rayleigh–Ritz energy formulation. The parasite mass and stiffness of the integrated PZT patch was included in the governing equation of the system. The actively controlled cantilevered beam was tested and favorable results were obtained. As the active control force needs to be calculated, the blocking force was used. Liang *et al.* (1993) used impedance analysis in modeling of a PZT actuator-driven one-degree-of-freedom spring-mass-damping system. The frequency-dependent output performance of the PZT actuator was predicted. Rossi *et al.* (1993) then applied the impedance approach to model PZT actuator-driven circular rings and performed the experiments for validating the theoretical model. Nevertheless, the previous studies related to the dynamic modeling for shell structures have so far been limited to the one-dimensional systems. For general two-dimensional shell structures, the mechanical impedance coupling in different coordinate directions occurs. An extensive investigation is thus highly required.

The current work is focused on analysis of two-

 0001-4966/94/96(3)/1605/8/$6.00 © 1994 Acoustical Society of America

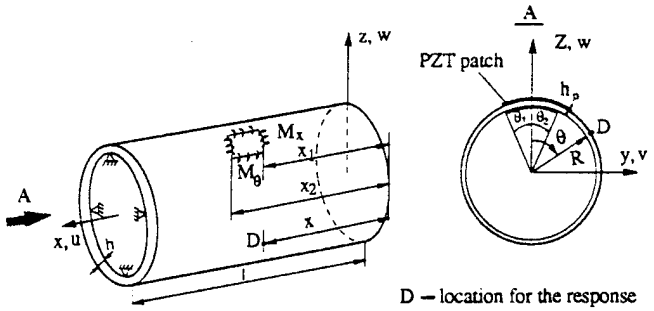

FIG. 1. A thin cylindrical shell with surface-bonded PZT actuators.

dimensional thin cylindrical shells excited by a pair of PZT actuators in a pure bending mode. A generic method for the impedance modeling of integrated PZT/shell systems will be presented. The numerical case studies and comparisons based upon a simply supported cylinder will be performed to demonstrate the significant difference between a conventional static modeling approach and the impedance method. The results will show that the excitation force of the induced strain actuators depends on the mechanical impedance matching between the PZT actuators and the cylinder. The physics of the dynamic interaction between induced strain actuators and host structures will be revealed.

I. IMPEDANCE MODEL OF INTEGRATED PZT/SHELL SYSTEMS

A physical model of a thin cylindrical shell excited by PZT actuators is shown in Fig. 1. The PZT patches are assumed to be perfectly bonded on the internal and external surfaces of the cylinder so that a pure bending moment excitation can be locally created. Figure 2 displays the corresponding impedance model. The dynamic behavior of the cylinder in the x and θ direction is represented by the direct impedance Z_{xx} and $Z_{\theta\theta}$ as well as the cross impedance $Z_{x\theta}$ and $Z_{\theta x}$, respectively. Under the actuation of the moments, M_x and M_θ, the angular velocity response of the cylinder at the edge of the bonded PZT patches may be described by

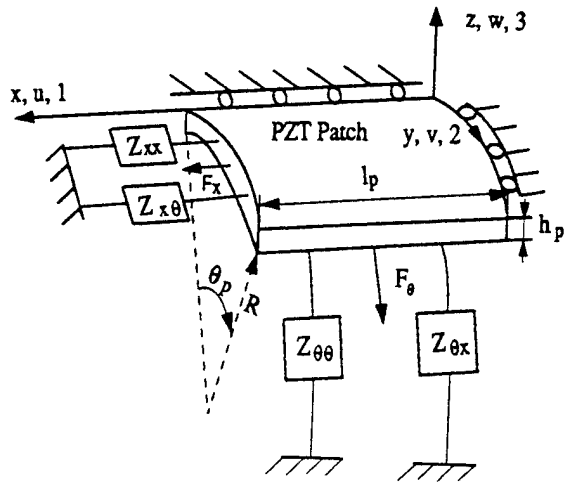

FIG. 2. A physical model of a PZT actuator integrated with a thin shell structure represented by mechanical impedance.

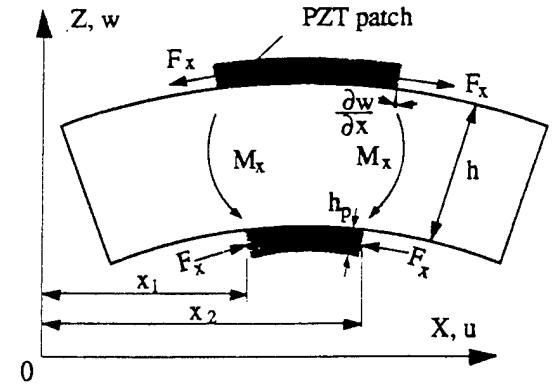

FIG. 3. The angular deformation of a cylinder in the x direction, actuated by a pair of moments.

$$\nabla\beta_x=\left(\frac{\partial\dot{w}}{\partial x}\right)_{x=x_2}-\left(\frac{\partial\dot{w}}{\partial x}\right)_{x=x_1}=-(H_{xx}M_x+H_{\theta x}M_\theta), \tag{1a}$$

$$\nabla\beta_\theta=\left(\frac{\partial\dot{w}}{R\,\partial\theta}\right)_{\theta=\theta_2}-\left(\frac{\partial\dot{w}}{R\,\partial\theta}\right)_{\theta=\theta_1}$$

$$=-(H_{x\theta}M_x+H_{\theta\theta}M_\theta), \tag{1b}$$

where $\nabla\beta$ is the total angular deformation of the cylinder; R is the radius of the cylinder. The minus sign indicates that the structural reactions are equal and opposite to the output forces of the PZT actuator. Here, H_{xx} and $H_{\theta\theta}$ are the direct admittance, $H_{x\theta}$ and $H_{\theta x}$ are the cross admittance of the cylinder and responsible for the coupling of the input moments in the x and θ directions. The moment admittance is defined as

$$H_{lk}=\frac{\nabla\beta_k}{M_l}\quad(l,k=x,y). \tag{2}$$

Figure 3 shows the geometric deformation of the cylinder in the x direction under the actuation of M_x. The similar deformation occurs in the θ direction. Considering the relationship between the translational displacement and the angular deformation of the cylinder, the in-plane displacement, u and v, can be expressed by

$$u=\frac{h+h_p}{2}\left[\left(\frac{\partial w}{\partial x}\right)_{x=x_2}-\left(\frac{\partial w}{\partial x}\right)_{x=x_1}\right], \tag{3a}$$

$$v=\frac{h+h_p}{2}\left[\left(\frac{\partial w}{R\,\partial\theta}\right)_{\theta=\theta_2}-\left(\frac{\partial w}{R\,\partial\theta}\right)_{\theta=\theta_1}\right], \tag{3b}$$

where h and h_p are the thicknesses of the cylinder and the PZT actuator, respectively. The corresponding in-plane velocity, $\dot{u}$ and $\dot{v}$, are then given by

$$\dot{u}=\frac{h+h_p}{2}\left[\left(\frac{\partial\dot{w}}{\partial x}\right)_{x=x_2}-\left(\frac{\partial\dot{w}}{\partial x}\right)_{x=x_1}\right], \tag{4a}$$

$$\dot{v}=\frac{h+h_p}{2}\left[\left(\frac{\partial\dot{w}}{R\,\partial\theta}\right)_{\theta=\theta_2}-\left(\frac{\partial\dot{w}}{R\,\partial\theta}\right)_{\theta=\theta_1}\right]. \tag{4b}$$

Using the relation of the in-plane force and the out-of-plane moment: $M_{x(\theta)}=(h+h_p)F_{x(\theta)}$ and substituting Eq. (4) into Eq. (1) results in

$$\begin{pmatrix} F_x \\ F_\theta \end{pmatrix} = -\frac{2}{(h+h_p)^2}\begin{pmatrix} H_{xx} & H_{\theta x} \\ H_{x\theta} & H_{\theta\theta} \end{pmatrix}^{-1}\begin{pmatrix} \dot{u} \\ \dot{v} \end{pmatrix} = -\begin{pmatrix} Z_{xx} & Z_{x\theta} \\ Z_{\theta x} & Z_{\theta\theta} \end{pmatrix}\begin{pmatrix} \dot{u} \\ \dot{v} \end{pmatrix}, \tag{5}$$

where the structural impedance Z_{lk} $(l,k=x,y)$ can be derived from classic shell theory and will be developed later; $\dot{u}$ and $\dot{v}$ need to be solved so that the output force can be quantitatively predicted.

When an external electric field is applied to PZT patches along the polarization direction (3), the equation of motion of the PZT actuator shown in Fig. 2 may be expressed by

$$\rho_p \frac{\partial^2 u}{\partial t^2} = Y^E_{p11}\frac{\partial^2 u}{\partial x^2}, \tag{6a}$$

$$\rho_p \frac{\partial^2 v}{\partial t^2} = Y^E_{p22}\frac{\partial^2 v}{R\,\partial\theta^2}, \tag{6b}$$

where the subscript p refers to the parameters of the PZT actuator, and 11 and 22 denote the coordinates of PZT materials; ρ is the mass density and Y^E is the Young's modulus. The solution of Eq. (6) is described by

$$u=[A\,\sin(k_{p11}x)+B\,\cos(k_{p11}x)]e^{j\omega t}, \tag{7a}$$

$$v=[C\,\sin(k_{p22}R\theta)+D\,\cos(k_{p22}R\theta)]e^{j\omega t}, \tag{7b}$$

where A, B, C, and D are unknowns and can be determined by the boundary conditions; j symbolizes the imaginary part of a complex number; ω is the input angular frequency. Considering the isotropy of the PZT material in the 1 and 2 directions yields the wave number:

$$k_p^2=k_{p11}^2=k_{p22}^2=\omega^2(\rho_p/Y_p^E). \tag{8}$$

Applying the displacement boundary conditions, $u_{x=0}=0$ and $v_{\theta=0}=0$ to Eqs. (7), leads to $B=D=0$. The unknowns, A and C, can be determined from the constitutive equation of the PZT actuator at $x=l_p$ and $\theta=\theta_p$:

$$\begin{pmatrix} \varepsilon_x \\ \varepsilon_y \end{pmatrix} = \begin{pmatrix} \dfrac{\partial u}{\partial x} \\ \dfrac{\partial v}{R\,\partial\theta} \end{pmatrix} = \begin{pmatrix} \dfrac{1}{Y_p^E R\theta_p h_p} & -\dfrac{\nu_p}{Y_p^E l_p h_p} \\ -\dfrac{\nu_p}{Y_p^E R\theta_p h_p} & \dfrac{1}{Y_p^E l_p h_p} \end{pmatrix}\begin{pmatrix} F_x \\ F_\theta \end{pmatrix} + \begin{pmatrix} d_{31} \\ d_{32} \end{pmatrix}E, \tag{9}$$

where l_p, θ_p, and $d_{31(2)}$ are the length, the angle, and the piezoelectric constant of the PZT actuator, respectively. Note that the Poisson's ratio of the PZT material, ν_p is introduced so that the mechanical coupling of the in-plane motion in different directions (x,θ) of the PZT actuator can be included in the modeling. Substituting Eqs. (5) and (7) into Eq. (9) and taking the algebraic operation to rearrange A and C yield:

$$\begin{pmatrix} C_l\left(1-\dfrac{\nu_p}{\alpha}\dfrac{Z_{x\theta}}{Z_{pxx}}+\dfrac{Z_{xx}}{Z_{pxx}}\right) & C_\theta\left(\alpha\dfrac{Z_{\theta x}}{Z_{p\theta\theta}}-\nu_p\dfrac{Z_{\theta\theta}}{Z_{p\theta\theta}}\right) \\ C_l\left(\dfrac{1}{\alpha}\dfrac{Z_{x\theta}}{Z_{pxx}}-\nu_p\dfrac{Z_{xx}}{Z_{pxx}}\right) & C_\theta\left(1-\nu_p\alpha\dfrac{Z_{\theta x}}{Z_{p\theta\theta}}+\dfrac{Z_{\theta\theta}}{Z_{p\theta\theta}}\right) \end{pmatrix} \times \begin{pmatrix} A \\ C \end{pmatrix} = \begin{pmatrix} d_{31} \\ d_{32} \end{pmatrix}E, \tag{10}$$

where $C_l=k_p\cos(k_p l_p)$ and $C_\theta=k_p\cos(k_p R\theta_p)$; $\alpha=l_p/(R\theta_p)$ is the ratio of the length to the width of the PZT patch; Z_{pxx} and $Z_{p\theta\theta}$ are the input impedances of the PZT actuator in the x and θ directions, defined as

$$Z_{pxx}=K_{px}\frac{k_p l_p}{\tan(k_p l_p)}\frac{1}{j\omega}, \tag{11a}$$

$$Z_{p\theta\theta}=K_{p\theta}\frac{k_p R\theta_p}{\tan(k_p R\theta_p)}\frac{1}{j\omega}, \tag{11b}$$

with the static extension stiffnesses of the actuator in the x and θ directions, $K_{px}=Y^E{}_p R\theta_p h_p/l_p$ and $K_{p\theta}=Y^E{}_p l_p h_p/(R\theta_p)$. Solving for A and C from Eq. (10) and substituting it into Eqs. (7), the displacement and velocity responses of the PZT actuator are obtained. The dynamic force output of the PZT actuator can then be determined from Eq. (5):

$$F_x=\tilde{F}_x e^{j\omega t}=-j\omega(AS_l Z_{xx}+CS_\theta Z_{x\theta})e^{j\omega t}, \tag{12a}$$

$$F_\theta=\tilde{F}_\theta e^{j\omega t}=-j\omega(AS_l Z_{\theta x}+CS_\theta Z_{\theta\theta})e^{j\omega t}, \tag{12b}$$

where $S_l=\sin(k_p l_p)$ and $S_\theta=\sin(k_p R\theta_p)$. Accordingly, the amplitude of the line moments per unit length created by the pair of PZT patches, $\tilde{M}_{x,(\theta)}$ (in N m/m), can be determined as

$$\tilde{M}_x=\frac{\tilde{F}_x(h+h_p)}{R\theta_p}=-j\frac{\omega(h+h_p)(AS_l Z_{xx}+CS_\theta Z_{x\theta})}{R\theta_p}, \tag{13a}$$

$$\tilde{M}_\theta=\frac{\tilde{F}_\theta(h+h_p)}{l_p}=-j\frac{\omega(h+h_p)(AS_l Z_{\theta x}+CS_\theta Z_{\theta\theta})}{l_p}. \tag{13b}$$

The distributed line moments are thus expressed by

$$M_x=\tilde{M}_x[\delta(x-x_1)-\delta(x-x_2)][h(\theta-\theta_1)-h(\theta-\theta_2)]e^{j\omega t}, \tag{14a}$$

$$M_\theta=\tilde{M}_\theta[\delta(\theta-\theta_1)-\delta(\theta-\theta_2)][h(x-x_1)-h(x-x_2)]e^{j\omega t}, \tag{14b}$$

where $\delta(x)$ and $\delta(\theta)$ are the Dirac delta functions; $h(x)$ and $h(\theta)$ are the Heaviside functions; x_1, x_2, θ_1, and θ_2 are the location coordinate of the edge of PZT patches on the cylinder, as illustrated in Fig. 1.

Since the coefficients A and C, as well as the mechanical impedance of the cylinder in Eqs. (13), are functions of the frequency, the moment outputs of the PZT actuator are frequency dependent. If the cross impedance $Z_{x\theta}$ and $Z_{\theta x}$ in Eq. (10) is assumed to be zero and the Poisson's effect of the PZT material is ignored, a decoupled analysis is then ob-

tained for one-dimensional rings. The formulation for the force output of the PZT actuator expressed in Eq. (12) is reduced to

$$F_\theta = -\frac{Z}{Z+Z_p} Y_p^E S_p d_{32} E, \tag{15}$$

where Z is the mechanical impedance of the ring, Z_p is the input impedance of the PZT actuator, and S_p is the cross section area of the PZT actuator. Equation (15) is same as the formulation that was derived from the circular rings by Rossi *et al.* (1993). The two-dimensional impedance analysis, therefore, is applicable to one-dimensional structures.

Thus far, the dynamic forces and moments of the PZT actuator have been obtained based upon the impedance characteristics of the PZT and the cylinder. The input impedance of the PZT actuator is given by Eq. (11). The mechanical impedance of the cylinder is determined by the inverse admittance matrix in Eq. (5), which depends on the location of the actuators, the structural configuration, the boundary condition, and the physical properties. The next section will address the calculation of the admittance of the cylinder actuated by line moments.

II. ADMITTANCE CALCULATION OF A CYLINDER

The general solution of the response of a thin shell excited by line moments can be determined by solving the following Love equations (Soedel, 1981):

$$L_u(u,v,w) - \lambda\dot{u} - \rho h\ddot{u} = -q_u - \frac{1}{2R}\frac{\partial M_n}{\partial \theta}, \tag{16a}$$

$$L_v(u,v,w) - \lambda\dot{v} - \rho h\ddot{v} = -q_v - \frac{1}{2}\frac{\partial M_n}{\partial x}, \tag{16b}$$

$$L_w(u,v,w) - \lambda\dot{w} - \rho h\ddot{w} = -q_w - \frac{1}{R}\left(R\frac{\partial M_x}{\partial x} + \frac{\partial M_\theta}{R\,\partial\theta}\right), \tag{16c}$$

where $q_i (i=u,v,w)$ is the pressure applied along the x, y, and z directions normal to the surface of the shell, respectively. The twisting moment M_n is applied about the normal (z) direction. λ is an equivalent viscous damping factor. The operator L_i $(i=u,v,w)$ can be evaluated from an eigenvalue analysis. Since the transverse modes in a very shallow shell are the dominant modes, it is assumed that the inertial effects in the in-plane directions are neglected and the loading is applied normally to the surface of the shells (Soedel, 1981; Leissa, 1973). In the current case, the ratio of the thickness to the radius of the cylinder is assumed to be 1/100 and the theory for thin shells is thus applied. Only Eq. (16c) is considered in the modeling. The modal expansion series solution of Eq. (16c) is expressed by

$$w = \sum_{m=1}^{\infty}\sum_{n=0}^{\infty} p_{mn} W_{mn}(x,\theta), \tag{17}$$

where m and n refer to the axial and circumferential mode numbers; p_{mn} is the modal participation factor; $W_{mn}(x,\theta)$ is the eigenfunction. The operator L_w is evaluated from the eigenvalue analysis:

TABLE I. Material properties of the PZT (Piezo Systems, Inc., 1987) and aluminum.

	Y^E (N/m^2) ($\times 10^{10}$)	ρ (kg/m^3)	ν	d_{31}, d_{32} (m/V) ($\times 10^{-10}$)	ξ_{mn}
PZT	6.3	7650	0.3	−1.66	0.005
Aluminum	6.9	2700	0.33	N/A	0.005

$$L_w(w_{mn}) = -\rho h\omega_{mn}^2 w_{mn}, \tag{18}$$

where ω_{mn} is the natural frequency of the cylinder. Substituting Eqs. (17) and (18) into Eq. (16c) and assuming $q_w=0$ results in

$$\sum_{m=1}^{\infty}\sum_{n=0}^{\infty} (\rho h\ddot{p}_{mn} + \lambda\dot{p}_{mn} + \rho h\omega_{mn}^2 p_{mn}) W_{mn}(x,\theta) = \frac{1}{R}\left(R\frac{\partial M_x}{\partial x} + \frac{\partial M_\theta}{R\,\partial\theta}\right). \tag{19}$$

For a simply supported cylinder, the eigenfunction $W_{mn}(x,\theta)$ can be described by

$$W(x,\theta) = \sin(m\pi/l)x\,\cos n(\theta-\psi), \tag{20}$$

where ψ is the relative angular location of the input moment with respect to the coordinate system and l is the length of the cylinder. Substituting Eq. (20) into Eq. (19) and using the usual modal expansion technique yields:

$$\ddot{p}_{mn} + 2\xi_{mn}\dot{p}_{mn} + \omega_{mn}^2 p_{mn} = F_{mn} e^{j\omega t}, \tag{21}$$

where the equivalent forcing function, F_{mn}, is of the form

$$F_{mn} = \frac{1}{\rho h N_{mn}} \int_0^l\int_0^{2\pi} W_{mn}(x,\theta) \times\left(R\frac{\partial M_x}{\partial x} + \frac{\partial M_\theta}{R\,\partial\theta}\right) dx\,d\theta, \tag{22}$$

where

$$N_{mn} = \int_0^l\int_0^{2\pi} \sin^2\frac{m\pi x}{l}\cos^2 n(\theta-\psi) R\,dx\,d\theta = \begin{cases} Rl\pi/2 & (n\neq 0), \\ Rl\pi & (n=0). \end{cases} \tag{23}$$

In the case of $\psi=0$, Eq. (22) becomes

$$F_{mn1} = \frac{C_x}{\rho h N_{mn}}\left(\frac{R\pi m}{ln}\bar{M}_x + \frac{ln}{R\pi m}\bar{M}_\theta\right) \times(\sin n\theta_1 - \sin n\theta_2), \tag{24}$$

where $C_x = \cos(m\pi x_1/l) - \cos(m\pi x_2/l)$. In the case of $\psi=\pi/2n$,

$$F_{mn2} = \frac{C_x}{\rho h N_{mn}}\left(\frac{Rm\pi}{ln}\bar{M}_x + \frac{ln}{Rm\pi}\bar{M}_\theta\right) \times(\cos n\theta_2 - \cos n\theta_1). \tag{25}$$

In particular, when $\psi=0$ and $n=0$, the effective force function is reduced to

$$F_{m0}=\frac{C_x}{\rho h}\frac{m}{l^2}(\theta_1-\theta_2)\bar{M}_x. \tag{26}$$

The solution of the governing equation (21) is expressed by

$$p_{mn}(t)=\frac{F_{mn}e^{j(\omega t-\phi_{mn})}}{\omega_{mn}^2\sqrt{(1-(\omega/\omega_{mn})^2)^2+4\xi_{mn}^2(\omega/\omega_{mn})^2}} \tag{27}$$

with the phase shift,

$$\phi_{mn}=\tan^{-1}\frac{2\xi_{mn}(\omega/\omega_{mn})}{1-(\omega/\omega_{mn})^2}, \tag{28}$$

where ξ_{mn} is the modal damping coefficient. The transverse displacement response of the cylinder is thus obtained:

$$w(x,\theta,t)=\sum_{m=1}^{\infty}\sum_{n=0}^{\infty}\frac{(F_{mn1}\cos n\theta+F_{mn2}\sin n\theta)\sin(m\pi/l)xe^{j(\omega t-\phi_{mn})}}{\omega_{mn}^2\sqrt{[1-(\omega/\omega_{mn})^2]^2+4\xi_{mn}^2(\omega/\omega_{mn})^2}}. \tag{29}$$

Substituting Eq. (29) into Eq. (1) and recalling the definition of the admittance in Eq. (2), the direct admittance at the middle point of the edge of the PZT actuator can be determined as

$$H_{xx}=\frac{4\omega\pi}{\rho hR\theta_p l^3}\sum_{m=1}^{\infty}\sum_{n=1}^{\infty}\left(\frac{m^2C_x^2\sin[n(\theta_2-\theta_1)/2]}{n\Delta_{mn}}\right)\times e^{j(\pi/2-\phi_{mn})} \tag{30}$$

and

$$H_{\theta\theta}=\frac{4\omega}{\rho hl_p\pi^2R^3}\sum_{m=1}^{\infty}\sum_{n=1}^{\infty}\left(\frac{n^2C_xS_x[1-\cos n(\theta_1-\theta_2)]}{m\Delta_{mn}}\right)\times e^{j(\pi/2-\phi_{mn})}, \tag{31}$$

where $S_x=\sin[m\pi(x_1+x_2)/(2l)]$ and Δ_{mn} is given by

$$\Delta_{mn}=\omega_{mn}^2\sqrt{(1-(\omega/\omega_{mn})^2)^2+4\xi_{mn}^2(\omega/\omega_{mn})^2}. \tag{32}$$

Similarly, the cross admittances are obtained by

$$H_{x\theta}=\frac{4\omega}{\rho h\theta_pR^2l^2}\sum_{m=1}^{\infty}\sum_{n=1}^{\infty}\left(\frac{mC_xS_x[1-\cos n(\theta_1-\theta_2)]}{\Delta_{mn}}\right)\times e^{j(\pi/2-\phi_{mn})} \tag{33}$$

and

$$H_{\theta x}=\frac{4\omega}{\rho h\pi R^2ll_p}\sum_{m=1}^{\infty}\sum_{n=1}^{\infty}\left(\frac{nC_x^2\sin[n(\theta_2-\theta_1)/2]}{\Delta_{mn}}\right)\times e^{j(\pi/2-\phi_{mn})}. \tag{34}$$

TABLE II. The geometric size of the PZT actuator and the cylinder (unit: mm).

	Length l	Radius R	Angle θ_p(degree)	Thickness
PZT	80	200	6	0.2, 0.5, 1.0
Cylinder	700	200	360	2.0

III. NUMERICAL EXAMPLES AND DISCUSSION

The simply supported thin cylinder used in the case study is made of aluminum and its geometric configuration is shown in Fig. 1. The material properties of aluminum and PZT (G1195) are listed in Table I and their geometric parameters are given in Table II. In the case study, two geometric parameters, the thickness of the PZT (h_p=0.2, 0.5, 1.0 mm) and the location of the PZT on the cylinder (x_1=310, 100 mm) are examined. The purpose is to identify the effect of the input impedance of the PZT and the structural impedance on the moment outputs of the PZT actuator and to determine how they influence the response of the cylinder.

For comparison of modeling approaches, the static line moment calculation is based upon a flat PZT patch, because the dimension of the PZT patch in circumferential direction is kept small relative to the cylinder radius, thus the curvature effects can be neglected (Sonti and Jones, 1991; Lester and Lefebvre, 1991). This is a reasonable approximation from the experimental point of view. In the current numerical examples, the circumferential size of the PZT patch is much smaller than that of the cylinder, $(R\theta_p)/R=1/10$, hence flat PZT patches are used in the static calculations. There are

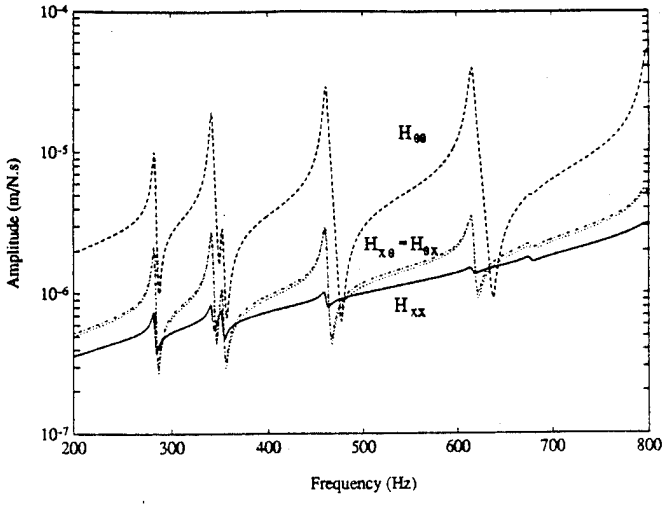

FIG. 4. The admittance characteristics of the simply supported cylinder (h_p=0.5 mm).

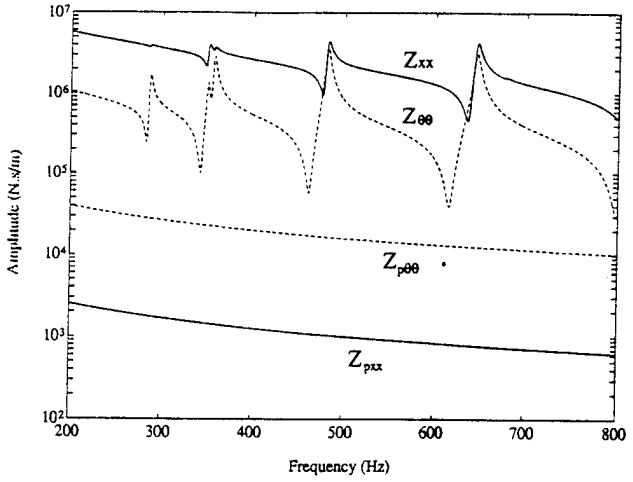

FIG. 5. The direct impedance of the cylinder and the PZT actuator. $h_p=0.2$ mm.

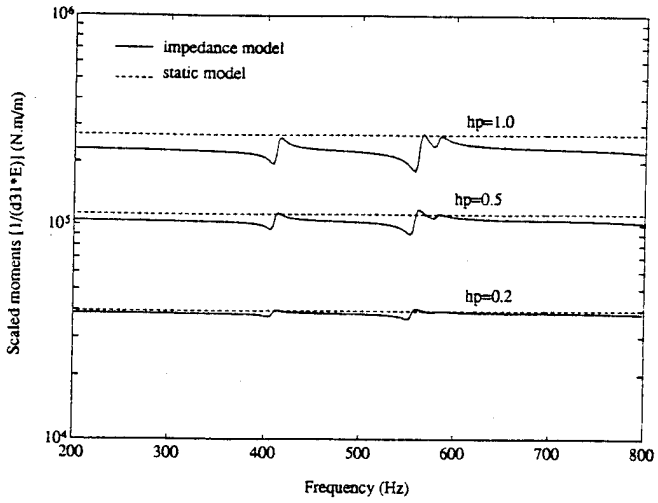

FIG. 7. The moment outputs of the PZT actuator in the axial direction.

several formulas for the actuation of PZT patches on two-dimensional structures (Dimitriadis *et al.*, 1989; Wang and Rogers, 1991; Crawley and Lazarus, 1991). One formula developed from the laminated plate theory (Wang and Rogers, 1991) is used here.

Figure 4 shows the variation of the amplitude of the force admittance with frequency. The peaks of the curves correspond to the resonant frequencies of the original cylinder. When the PZT actuator is much thinner than the cylinder ($h_p=0.2$ mm and $h_p/h=1/10$), the input impedance levels of PZT are much lower than those of the cylinder, as shown in Fig. 5. The corresponding amplitude of the dynamic moments is nearly constant over the whole frequency band, as illustrated in Figs. 6 and 7 ($h_p=0.2$ mm). This result is expected because relatively small PZT patches "planted" in the substrate do not significantly stiffen the cylinder. On the other hand, the host structural dynamics do not yet apply a strong influence on the actuator moment outputs. In this case, the dynamic interaction between the PZT actuator and the cylinder may be ignored. The active moments given by the static model agrees with that predicted by the impedance model.

With increases in the thickness of the PZT actuator up to $h_p=1.0$ mm ($h_p/h=0.5$), the input impedance of the PZT actuator matches with the structural impedance of the cylinder in the circumferential direction, which is displayed in Fig. 8. The moment outputs of the PZT actuator is greatly strengthened at these matching points. Figure 6 demonstrates that the amplitude of the dynamic moments, M_θ, is several times higher than the constant moments predicted by the static approach at some resonance frequencies of the system. The thicker the PZT patches, the greater the increment of the amplitude of the moments. It should be noted that although the axial impedance Z_{xx} in Fig. 8 is not matched by the input impedance $Z_{p\theta\theta}$, the axial moment output $\bar{M}_x$ also goes up, as shown in Fig. 7, because of the coupling effect due to the cross impedance and the Poisson's ratio. In addition, Figs. 5 and 8 show that for the cylinder, the mechanical impedance in the axial direction is different from that in the circumferential direction. This implies that the different actuation is

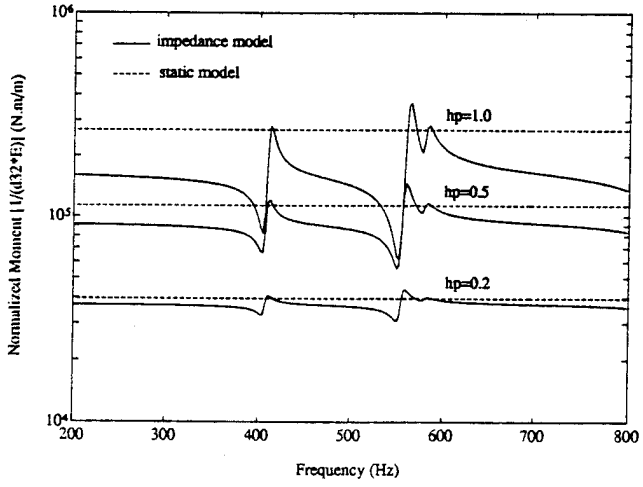

FIG. 6. The moment outputs of the PZT actuator in the circumferential direction.

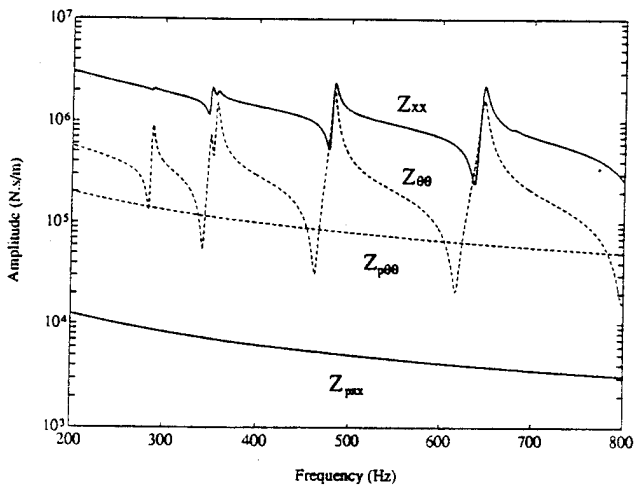

FIG. 8. The direct impedance of the cylinder and the PZT actuator, $h_p=1.0$ mm.

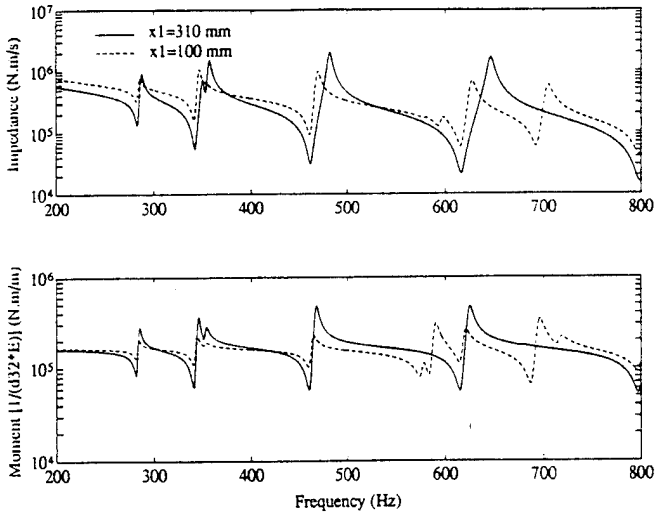

FIG. 9. The effect of the location of the actuator on the circumferential impedance and the moment output (h_p=1.0 mm).

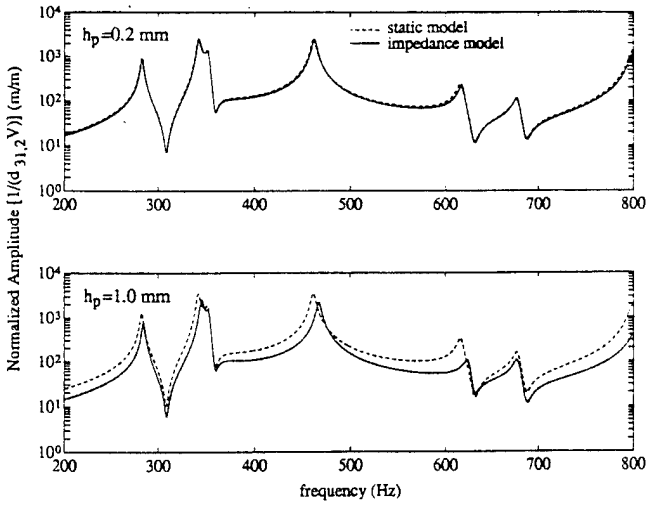

FIG. 10. A comparison of the displacement response of the cylinder predicted by the static model and the impedance model, respectively (x=310 mm and θ=90°).

generated in the axial direction and in the circumferential direction, i.e., $\bar{M}_x \neq \bar{M}_\theta$, as illustrated in Figs. 6 and 7.

The influence of the location of the PZT actuator on the host structure on its dynamic output is examined in Fig. 9. When the location of the excitation points changes, the mechanical impedance of the cylinder varies; accordingly, the moment output of the PZT actuator changes. Since the frequencies corresponding with the peaks of the moments are the resonant frequencies of the entire PZT/shell system, the variation of the peaks due to the location change of the actuator reflects the dynamic performance shifts of the original cylinder. When the PZT actuator is placed on the different locations on the host cylinder, it applies the different stiffening effect on the system. Hence, the location of the PZT actuator is a critical factor affecting the excitation of the actuator on vibrational modes of the system. If the center of the PZT patch is intended to be placed on the nodal line of a certain mode of a host structure, this mode can't be excited. This issue will be further addressed in the following discussion of the dynamic response of the integrated system.

For the convenience of comparing different modeling approaches, a scaled displacement is defined by

$$w_{\text{normal}} = w/d_{1,(2)}V \tag{35}$$

so that the effect of the electric parameters of PZT actuators in the modeling can be eliminated. The displacement response of the cylinder is picked up at x=300 mm and θ=90°. As the thickness of the PZT actuator increases, the natural frequencies of the integrated PZT/cylinder system move up, which is accurately predicted in the impedance model. Figure 10 displays the differences in the displacement responses of the cylinder predicted by the static model and by the impedance model, respectively. The resonant frequencies of the integrated system are shifted to a higher value compared with that of the original cylinder. The corresponding amplitude of the response decreases. It can be explained that thicker PZT patches bonded on the surface of the cylinder stiffen the cylinder, which leads to the variations in the performance of the original structure. The intensity of these changes depends on the extent of the impedance matching between the PZT and the cylinder. When the response happens to be picked up at the nodal line of the 4th mode of the original cylinder (x=310 mm and θ=15°), a significant difference is observed between the different modeling approaches. The static model apparently misses this mode, as shown in Fig. 11. The developed impedance model, however, picks up this mode. In fact, the dynamic performance of the original cylinder has already been shifted by the added PZT actuator and the sensor location (x=310 mm and θ=15°) is not the real nodal line of the 4th mode of the integrated system. The frequency response function of the entire structure thus reflects this 4th mode.

IV. SUMMARY

A theory development using impedance modeling method for the actuation of two-dimensional structures has been performed. The impedance method reveals physics of

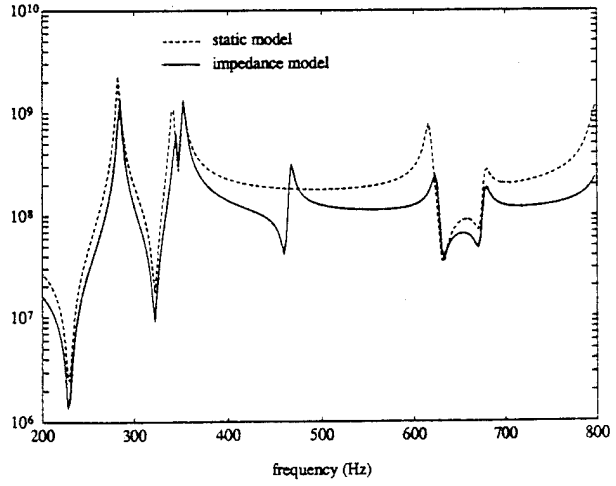

FIG. 11. A comparison of the displacement response of the cylinder predicted by the static model and the impedance model, respectively (x=310 mm and θ=15°, h_p=1.0 mm).

the dynamic interaction between the actuators and host structures, therefore, it gives more accurate prediction of the output moments of induced strain actuators than the conventional static approach.

The output moments (or forces) of induced strain actuators are strongly related to the input impedance of the actuators and the mechanical impedance of the host structure, and they are frequency dependent.

When the actuator input impedance levels approach or match with the host structural impedance levels, the dynamic performance of the original shell structure is altered because of the stiffening effect of the integrated PZT actuators. The intensity of the stiffening effect varies with the location and the thickness of the PZT actuators.

ACKNOWLEDGMENTS

The authors gratefully acknowledge the support of the Office of Naval Research, under Grant No. ONR 00014-92-1170, Dr. K. Ng, Program Manager.

Crawley, E. F. and de Luis, J. (**1987**). "Use of Piezoelectric Actuators as Elements of Intelligent Structures," AIAA J. **25** (10), 1373–1385.

Crawley, E. F., and Lazarus, K. B. (**1991**). "Induced Strain Actuation of Isotropic and Anisotropic Plates," AIAA J. **29** (6), 944–951.

Dimitriadis, E. K., Fuller, C. R., and Rogers, C. A. (**1989**). "Piezoelectric Actuators for Distributed Noise and Vibration Excitation of Thin Plates," ASME Failure Prevent. Reliabil. **16**, 223–233.

Hagood, N. W., Chung, W. H., and von Flotow, A. (**1990**). "Modeling of Piezoelectric Actuator Dynamics for Active Structural Control," in *Proceedings of the 31th SDM* (AIAA, Washington, DC), AIAA-90-1097-CP, pp. 2242–2256.

Leissa, W. (**1973**). *Vibration of Shells* (NASA, U. S. Government Printing Office, Washington, DC), pp. 31–157.

Lester, H. C. and Lefebvre, S. (**1991**). "Piezoelectric Actuator Models for Active Sound and Vibration Control of Cylinders," in *Proceedings of Recent Advances in Active Control of Sound and Vibration* (Technomic, Blacksburg, VA), pp. 3–26.

Liang, C., Sun, F. P., and Rogers, C. A. (**1993**). "Dynamic Output Characteristics of Piezoceramic Actuators," in *Proceedings of Smart Structures and Materials* (SPIE, Albuquerque, NM), Vol. 1917, pp. 286–298.

Piezo Systems, Inc. (**1987**). Piezoelectric Motor/Actuator Kit Manual.

Rossi, A., Liang, C., and Rogers, C. A. (**1993**). "Coupled Electric-Mechanical Analysis of a Piezoceramic Actuator Driven System—An Application to a Circular Ring," in *Proceedings of the AIAA/ASME/ASCE/AHS 34th SDM Conference* (AIAA, Washington, DC), La Jolla, CA, 19–21 April, 3618–3624.

Soedel, W. (**1981**). *Vibrations of Shells and Plates* (Marcel Dekker, New York), pp. 199–228 and 248–260.

Sonti, V. R., and Jones, J. D. (**1991**). "Active Vibration Control of Thin Cylindrical Shells Using Piezo-Electric Actuators," in *Proceedings of Recent Advances in Active Control of Sound and Vibration* (Technomic, Blacksburg, VA), pp. 27–38.

Tzou, H. S. (**1989**). "Theoretical Development of a Layered Shell with Internal Distributed Controllers," ASME Failure Prevent. Reliabil. **16**, 241–249.

Wang, B. T., and Rogers, C. A. (**1991**). "Modeling of Finite-Length Spatially Distributed Induced Strain Actuators for Laminate Beams and Plates," in *Proceedings of the AIAA/ASME/ASCE/AHS 32th SDM Conference* (AIAA, Washington, DC), Baltimore, MD, 8–10 April, pp. 1511–1520.

C-24 Design of Active Structural Acoustic Control Systems by Eigenproperty Assignment, R. A. Burdisso and C. R. Fuller, Journal of the Acoustical Society of America, Vol. 96 No. 3, pp. 1582-1591, September 1994.

Design of active structural acoustic control systems by eigenproperty assignment

Ricardo A. Burdisso and Chris R. Fuller

Vibration and Acoustic Laboratories, Mechanical Engineering Department, Virginia Polytechnic Institute and State University, Blacksburg, Virginia 24061-0238

(Received 9 June 1993; revised 8 March 1994; accepted 22 April 1994)

The traditional design approach of feedforward control systems involves the selection of number and location of the actuators and sensors based on some physical understanding of the system. This empirical methodology yields satisfactory results for simple structures and sinusoidal inputs. However, such a heuristic approach can easily result in an inefficient control system with an unnecessarily large number of control channels for complex structures and more realistic disturbances. In this work an efficient formulation is presented for the design of actuators and sensors for structurally radiated sound reduction. The technique is based on the modification of the eigenstructure such that the system responds with the weakest set of modal radiators. The technique is applicable to both narrow-band and broadband excitations. The formulation is demonstrated for controlling the odd–odd modes of a simply supported plate driven by a point force located at the center of the plate. The radiation due to the first three odd–odd modes is reduced with a single-input, single-output (SISO) controller. The control actuator and error sensor are implemented with piezoelectric (PZT) ceramics and polyvinylidene fluoride (PVDF) films, respectively. It is shown that the design approach yields excellent global sound reduction.

PACS numbers: 43.40.Vn

INTRODUCTION

Sound radiated by vibrating structures is a persistent problem in numerous industrial applications, and it has long been a subject of research interest in the acoustic community. The common practice of using passive techniques often results in heavy systems that are inefficient at low frequencies. In recent years, considerable effort has been devoted to active control techniques to reduce low-frequency structurally radiated sound. The understanding of the physics of the problem has yielded efficient control strategies. One such approach has been proposed by Fuller[1] in which the control inputs are applied directly to the vibrating structure while minimizing radiated sound or related variable. This technique, known as active structural acoustic control (ASAC), has been implemented using both feedback and feedforward control approaches.[2–6] The control approach to be implemented mostly depends on the nature of the disturbance input, i.e., steady-state sinusoid, random, or transient. For applications in which the noise field is due to persistent inputs, the potential of the ASAC technique in conjunction with adaptive feedforward control approaches has been clearly demonstrated.[4–6]

The design of feedforward control systems involves the selection of the type, number, location, and size of the actuators and of the error sensors whose outputs are sought to be minimized. The traditional design approach in feedforward control is to select actuators and sensors based on some physical understanding of the behavior of the uncontrolled system. In general, this empirical methodology yields satisfactory results for ASAC when the error transducers are microphones placed in the acoustic field that directly observe the quantity to be minimized and when the excitation is a single sinusoid. However, this heuristic approach can easily result in an inefficient control system with an unnecessarily large number of control channels even in simple systems and is exacerbated when structural sensors are used. Wang *et al.*[7] investigated the optimum location of actuators to minimize radiation from panels with microphones used as error transducers. It is demonstrated in this work that for single-frequency excitation, both on and off resonance, the optimally located actuators achieved a far better global reduction of sound than actuators whose position are chosen only upon some physical considerations.

As a result of rapid advances in specialized actuator and sensor materials, today research thrust is toward developing smart or adaptive systems with actuators and sensors being an integral part of the structure.[8] The typical transducer to be embedded in a structure will be distributed in nature. In particular, induced strain piezoelectric (PZT) ceramics[9,10] and shape memory alloys[11] as actuators, and polyvinylidene fluoride (PVDF) films[12,13] and fiber optics[14] as sensors have shown potential for ASAC applications. The design of control systems of structures with integrated transducers will be even more critical since these error sensors will not directly measure acoustic pressure which is the quantity to be reduced and not all structural motion is well coupled to the radiation field. Clark *et al.*[15] extended the work of Wang[7] to optimize the location of piezoelectric actuators and both the location and size of PVDF strain sensors on a simply supported plate excited harmonically. Analytical and experimental results showed that a simple single optimally located PZT actuator/PVDF sensor pair rivaled the sound reduction achieved with three arbitrarily located PZT actuators and three error microphones.

These formal optimization approaches[7,15] clearly dem-

 0001-4966/94/96(3)/1582/10/$6.00 © 1994 Acoustical Society of America

onstrate that optimally located actuators and sensors can have a profound impact on the performance of the active control system. Even more important is the fact that significant levels of attenuation can be obtained with far less numbers of properly located transducers, thus reducing the dimensionality and complexity of the controller. Unfortunately, these *direct* optimization techniques require the evaluation of the radiated pressure at each step of the minimization process. The acoustic prediction that will certainly be carried out numerically for real structures is a computationally intensive analysis. Thus, these design optimization techniques cannot be realistically implemented to complex structures and disturbances in the present form because of computational time aspects.

In this paper, a new efficient design formulation for feedforward ASAC systems is proposed. The actuators and sensors are designed such that the controlled structure will respond with a set of poor radiating modes. To this end, the formulation takes advantage of recent work that demonstrated that an active feedforward-controlled structure will respond with a new set of eigenproperties whether vibration or radiation is being attenuated.[16,17] It was demonstrated that for radiation control the controlled eigenfunctions were all nonvolumetric or inefficient (weak) radiators.[17,18] The controlled resonant frequencies and associated eigenfunctions are a function of the selected control actuators and error sensors and are independent of the disturbance input. Thus, the design approach is based on finding the actuators and sensors configuration such that the controlled structure will respond with the weakest set of modal radiators. These weak radiators are defined here as the eigenfunctions with the lowest radiation efficiency and are obtained by solving an eigenvalue problem. The formulation is valid for both narrowband and broadband excitation inputs. The design formulation is demonstrated on a simple supported plate excited with white noise.

I. SYSTEM RESPONSE

The structure is assumed linear and subjected to a stationary disturbance input. Thus the analysis is carried out in the frequency domain by simply taking the Fourier transform of any time-dependent variable. For the sake of clarity, the formulation will be presented for a planar radiator and a single-input, single-output (SISO) control system. However, there is no loss of generality in the design methodology proposed here. A typical SISO feedforward-control arrangement is shown in Fig. 1. In feedforward control the undesirable response of a system due to the "primary" disturbance input is reduced by applying a "secondary" control input. The control input is obtained by feeding a reference signal into the compensator, $G(\omega)$. The compensator is designed such that the output from an error sensor is minimized. In feedforward-control approaches, the reference signal should be "coherent" to the disturbance input signal, and it is assumed here that it is directly obtained by tapping the disturbance input.

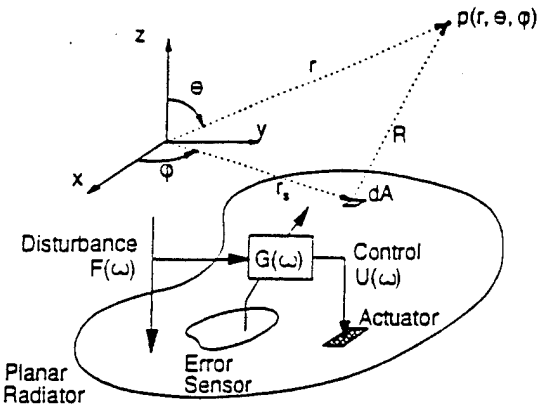

FIG. 1. General arrangement of a SISO feedforward ASAC system.

A. Structural response

The structural response $w(x,y,\omega)$ can be expressed as a linear combination of the modes as

$$w(x,y,\omega)=\sum_{n=1}^{N} q_n(\omega)\phi_n(x,y), \tag{1}$$

where $q_n(\omega)$ is the nth generalized modal coordinate, $\phi_n(x,y)$ is the nth eigenfunction, and N is the number of modes included in the response. The modal displacement can be written as[16]

$$q_n(\omega)=[f_nF(\omega)+u_nU(\omega)]H_n(\omega), \tag{2}$$

where f_n is the nth modal disturbance force, $F(\omega)$ is the Fourier transform of the disturbance input, u_n is the nth unit modal control force, $U(\omega)$ is the Fourier transform of the control input, and $H(\omega)$ is the nth modal frequency response function, given as

$$H_n(\omega)=\frac{1}{\omega_n^2-\omega^2+j2\zeta_n\omega_n\omega}, \tag{3}$$

where ω_n and ζ_n are the nth natural frequency and modal damping ratio, respectively, and j is the imaginary number. Equation (2) assumes that the modes have been normalized with respect to the mass distribution.

The optimum frequency content of the control input stems from minimizing a cost function, which is the mean-square value of a structural response monitored by an error sensor. Since the goal of this work is to design what is termed as adaptive structural systems, actuators and sensors contained within the structure will be the only transducers considered in this study. Then, the Fourier transform of the error sensor output can also be represented as the sum of the linear contribution of each mode as follows:[7]

$$e(\omega)=\sum_{n=1}^{N} q_n(\omega)\xi_n, \tag{4}$$

where ξ_n is the nth modal error component which is a function of the characteristics of the error transducer, i.e., discrete or distributed.

The modal error components ξ_n and the unit modal control forces u_n are a measure of the relative observability and

controllability of the modes by the error sensor and control actuator, respectively. By minimizing the cost function with respect to the control input, it can be shown that the spectrum content of the control input is given by[16,19]

$$U(\omega)=G(\omega)F(\omega)=-\frac{\sum_{n=1}^{N}\xi_n f_n H_n(\omega)}{\sum_{n=1}^{N}\xi_n u_n H_n(\omega)}F(\omega), \quad (5)$$

where $G(\omega)$ is the compensator that relates the control input $U(\omega)$ to the disturbance input $F(\omega)$. For a nonminimum phase control system the optimum compensator $G(\omega)$ is not implementable for broadband disturbances. For single and multiple frequency disturbances, the optimum compensator is always realizable. As discussed later, the design approach presented here will yield a control-error path that is minimum phase and thus the design formulation is applicable to any type of input. The controlled response can now be computed by solving Eq. (5) for the control input $U(\omega)$ and replacing it into Eq. (2) and this into Eq. (1). The uncontrolled response can be computed by simply setting $U(\omega)$ to zero in Eq. (2). In this SISO control configuration, the error output is theoretically driven to zero by the control input at all frequencies.

B. Acoustic response

The far-field pressure radiated by a harmonically vibrating planar structure can be computed from the structural response by using the Raleigh integral[20] as follows:

$$p(\vec{r},\omega)=\frac{i\omega\rho_0}{2\pi}\int_A v(x_s,y_s)\frac{e^{-jkR}}{R}\,dA, \quad (6)$$

where, as shown in Fig. 1, $\vec{r}=(r,\theta,\varphi)$ is the polar coordinate of the observation point in the acoustic field; $r_s=(x_s,y_s)$, where x_s and y_s are the coordinates of the elemental surface dA having normal velocity $v(x_s,y_s)$; A is the area of the radiator; R is the magnitude of the distance from the elementary source and the observation point; ρ_0 is the fluid density; and k is the acoustic wave number given as $k=\omega/c$, where c is the speed of sound in the medium. Here, it is assumed that the acoustic medium is air and thus no feedback of the fluid motion into the structure takes place.

Again the radiated pressure can be expressed as a linear contribution of the modes as

$$p(\vec{r},\omega)=\sum_{n=1}^{N}q_n(\omega)p_n(\vec{r},\omega), \quad (7)$$

where

$$p_n(\vec{r},\omega)=\frac{i\omega\rho_0}{2\pi}\int_A i\omega\phi_n(x_s,y_s)\frac{e^{-jkR}}{R}\,dA \quad (8)$$

is the radiated pressure distribution given by the nth mode with surface velocity $i\omega\phi_n(x,y)$. The controlled acoustic sound field can be computed by replacing Eq. (2) into (7).

It should be noted that typically the computation of the radiated pressure for a complex structure will be performed numerically by finite/boundary element codes.[21] This analysis is a computationally intensive process, and therefore any efficient controller design approach should minimize the number of acoustic evaluations. The following work is directed toward achieving this goal.

II. CONTROLLED SYSTEM EIGENPROPERTIES

The previous analysis provides the tools to compute the controlled structural and acoustic responses. However, it does not give any insight into the control mechanisms. Since the design approach proposed here is founded on the understanding of these mechanisms, the main aspects of the dynamic behavior of feedforward-controlled structures will be described in the sequel, while a full detailed description can be found in Ref. 16. The traditional view of feedforward-controlled systems is of "active cancellation" where the modes of the structure excited by the "primary" disturbance input are canceled by the "secondary" control input of appropriate magnitude and phase driving the same structural modes. This view arises from the fact that the system response can be interpreted as the superposition of the disturbance and control responses as suggested by Eq. (2). However, recent work has shown that the feedforward-controlled system responds effectively with a new set of eigenfunctions and eigenvalues to the disturbance input.[16]

The eigenproperties of the feedforward controlled system are governed by the characteristics of the controller $G(\omega)$ in Eq. (5). Because of the constraint imposed on the structure by driving the error signal to zero at all frequencies, it can be shown that the controller reduces the dynamic degrees of freedom of the system by 1, and thus the controlled system has $(N-1)$ new eigenvalues and associated eigenfunctions. The undamped controlled system eigenvalues, λ_l, are computed such that the following equation is satisfied:

$$\sum_{n=1}^{N}\xi_n u_n\prod_{\substack{m=1\\ m\neq n}}^{N}(\mu_m-\lambda_l)=0, \quad l=1,\ldots,N-1, \quad (9)$$

where $\mu_m=(\omega_m)^2$ is the mth uncontrolled system eigenvalue. This implies that if the structure is excited at a frequency near the control system pole frequency, $f_l=(\lambda_l)^{1/2}/2\pi$, the controlled structural response will be very large (or unbounded for an undamped system, $\zeta_n=0$). This behavior takes place even though the error sensor output vanished at all frequencies.

The controlled system eigenfunction $\phi_l(x,y)$ associated to the eigenvalue λ_l is easily computed once the controlled system eigenvalue has been determined. They can be obtained as a linear combination of the uncontrolled modes. That is,

$$\phi_l(x,y)=\sum_{n=1}^{N}\Gamma_{ln}\phi_n(x,y) \quad (10)$$

and the expansion coefficients are

$$\Gamma_{ln}=C_l u_n/(\lambda_l-\mu_n), \quad n=1,\ldots,N, \quad (11)$$

where C_l is a constant that is included since the controlled mode shapes are arbitrary to a constant multiplier, and it can be computed such that $[(\Gamma_{l1})^2+(\Gamma_{l2})^2+\cdots+(\Gamma_{lN})^2]=1$.

The eigenproperties of the controlled system given by Eqs. (9)–(11) are a function of the control input, through the unit modal control forces u_n, and of the error variable, through the modal error components ξ_n. An important aspect of the eigenproperties are that they are independent of the disturbance input. This implies that once the control actuator and error sensor are selected the eigenstructure of the controlled system is completely determined independently of the nature of the disturbance input including frequency content, location and distribution.

III. DESIGN APPROACH

The main goal in ASAC is for the control system to render a controlled response that poorly couples with the acoustic medium, thus resulting in minimum radiated sound power. This objective can be accomplished if two conditions are met.

(i) The resonant frequencies of the controlled structure must lay away from the dominant part of the disturbance input spectrum. In other words, the controlled system resonances should be detuned from the excitation input.

(ii) More important, the controlled or residual structural response should be a linear contribution of weak radiating modes.

As mentioned in the previous section, the controlled system has new resonant frequencies and associated eigenfunctions that are only a function of the selected actuator and sensor. Thus, this concept can be merged with the above conditions to yield an efficient design approach. The design formulation proposed here can be stated as to find the optimum actuator and sensor configuration that yields a controlled structure with eigenproperties that satisfied the above two conditions.

The first step in the proposed design formulation is to find the desired set of controlled system eigenfunctions with which the controlled structure should respond. The sought eigenfunctions should be weak modal radiator and this can be mathematically formulated by requiring the desired eigenfunctions to have the lowest radiation efficiency possible. Since the controlled eigenfunctions are given as a linear combination of the uncontrolled eigenfunctions, this implies a search for the desired expansion coefficients $(\Gamma_{ln})_d$ in order to achieve this objective.

To compute the radiation efficiency, the ratio of the radiated power to the average mean square velocity of the radiating surface is required. The radiated pressure due to the lth controlled eigenfunction driven harmonically at frequency ω can be computed using the modal surface velocity distribution $v(x,y)=i\omega\phi_l(x,y)$ substituted into the Rayleigh integral,[20] Eq. (6). Considering Eq. (10), the controlled modal pressure distribution is given in terms of the unknown desired coefficients, $(\Gamma_{ln})_d$, and of the uncontrolled modal pressure distribution, $p_n(\vec{r},\omega)$, as

$$p_l(\vec{r},\omega)=\sum_{n=1}^{N}(\Gamma_{ln})_d p_n(\vec{r},\omega). \tag{12}$$

The radiated sound power at frequency ω due to the lth controlled mode over the region D in the acoustic field is computed by integrating the acoustic time average intensity as

$$\Pi_l(\omega)=\int\int_D \frac{|p_l|^2}{\rho_0 c}\,dD \tag{13}$$

and replacing Eq. (12) into (13) gives

$$\Pi_l(\omega)=\sum_{n=1}^{N}\sum_{m=1}^{N}(\Gamma_{ln})_d(\Gamma_{lm})_d\Pi_{nm}(\omega)$$

$$=\{\Gamma_l\}_d^T[\Pi(\omega)]\{\Gamma_l\}_d, \tag{14}$$

where the elements of matrix $[\Pi(\omega)]$ are

$$\Pi_{nm}(\omega)=\int\int_D \frac{p_n p_m^*}{\rho_0 c}\,dD, \tag{15}$$

the desired expansion vector is $\{\Gamma_l\}_d=\{(\Gamma_{l1})_d,\ldots,(\Gamma_{lN})_d\}^T$, and the superscript T denotes the vector transpose.

Matrix $[\Pi(\omega)]$ is symmetric and positive definite because the radiated power is always positive for a nontrivial vector $\{\Gamma_l\}_d$. The term $\Pi_{nn}(\omega)$ represents the radiated power by the nth uncontrolled eigenfunction, while the term $\Pi_{nm}(\omega)$ represents the radiated power due to the acoustic coupling between the nth and mth uncontrolled eigenfunctions. If the cross term $\Pi_{nm}(\omega)$ vanishes, the modes are said to be acoustically uncoupled. The important implication is that the radiation due to the nth mode can not be used to destructively interfere with the radiation due to the mth mode such that the average radiated power over the region D is reduced.

The average mean-square velocity for the controlled mode oscillating at frequency ω can be easily computed as

$$|v_l(\omega)|^2=\frac{\omega^2}{2A}\int\int_A \phi_l^2(x_s,y_s)\,dA. \tag{16}$$

Again, it is straightforward to show that the average mean-square velocity becomes

$$|v_l(\omega)|^2=\{\Gamma_l\}_d^T[V(\omega)]\{\Gamma_l\}_d, \tag{17}$$

where matrix $[V(\omega)]$ is also symmetric and positive definite, and its elements are

$$V_{nm}(\omega)=\frac{\omega^2}{2A}\int\int_A \phi_n(x_s,y_s)\phi_m(x_s,y_s)\,dA. \tag{18}$$

Finally the radiation efficiency of the lth controlled eigenfunction is defined as[22]

$$S_l(\omega)=\frac{1}{A\rho_0 c}\frac{\Pi_l(\omega)}{|v_l(\omega)|^2}=\frac{1}{A\rho_0 c}\frac{\{\Gamma_l\}^T[\Pi(\omega)]\{\Gamma_l\}}{\{\Gamma_l\}^T[V(\omega)]\{\Gamma_l\}}. \tag{19}$$

The desired expansion coefficients $(\Gamma_{ln})_d$ that yield the lowest radiation efficiency for the controlled modes are obtained by minimizing $S_l(\omega)$ in Eq. (19) with respect to the coefficients $(\Gamma_{ln})_d$ with the constraint $(\{\Gamma_l\}_d)^T\{\Gamma_l\}_d=1$. This constrained minimization problem can be efficiently

solved by recognizing that the stationary values of $S_l(\omega)$ can be obtained by solving the eigenvalue problem

$$\{[\Pi(\omega)]-S_l[V(\omega)]A\rho_0 c\}\{\Gamma_l\}_d=\{0\}, \quad l=1,\ldots,N. \tag{20}$$

Because of the symmetry and positive-definite properties of the matrices, the N eigenvalues S_l are all real and positive and they are ordered such that $S_1<S_2<\cdots<S_N$. The eigenvalue S_l represents the radiation resistance at frequency ω of the lth desired controlled eigenfunction that is given as a linear combination of the uncontrolled modes by the coefficients of the eigenvector $\{\Gamma_l\}_d$. Because the SISO control system considered here has $(N-1)$ eigenfunctions, the optimum set of controlled eigenfunctions is that with the $(N-1)$ lowest radiation efficiency. Thus the desired expansion coefficients $(\Gamma_{ln})_d$ are the first $(N-1)$ eigenvectors in Eq. (20). These eigenfunctions form a set of independent basis functions for the controlled system.

The desired eigenfunctions found above are optimum in the sense that they have the lowest radiation efficiency at the single frequency ω. For broadband excitation, the controlled eigenfunctions should have low radiation efficiency in the frequency range of the excitation input. This can be accomplished by solving for the minimum of the weighted radiation efficiency:

$$S_l(\omega)=\frac{1}{A\rho_0 c}\frac{\{\Gamma_l\}_d^T\Sigma_{i=1}^{L}B_i[\Pi(\omega_i)]\{\Gamma_l\}_d}{\{\Gamma_l\}_d^T\Sigma_{i=1}^{L}B_i[V(\omega_i)]\{\Gamma_l\}_d}, \tag{21}$$

where B_i is a weighting constant, and matrices $[\Pi(\omega_i)]$ and $[V(\omega_i)]$ are computed at L frequencies ω_i. The eigenproblem of Eq. (21) will then yield a set of optimum eigenfunctions that have low radiation efficiency, in some weighted sense, at the L frequencies ω_i. Then, the computation of the uncontrolled modes radiated pressure is required at L frequencies. This analysis, in particular if numerical techniques are used, is a computational intensive process and care should be exercised in selecting both the number and values of the frequencies ω_i. Sensitivity analysis of the acoustic pressure with respect to the frequency should be useful here.[23,24]

It should be mentioned that Cunefare[25] developed a similar eigenvalue formulation for obtaining the optimum velocity distribution on a finite beam that minimizes the radiation efficiency of the beam response at a single frequency. It was suggested in this work that the optimum velocity response could be used as the objective function for the design of active control systems. Though similar in concept, the proposed formulation differs markedly from Cunefare's work in a fundamental aspect. Here the formulation searches for controlled eigenfunctions that are weak radiators and that are independent of the frequency.

A. Optimum modal parameters

The expansion coefficients Γ_{ln} are a function of the unit modal control forces u_n, the uncontrolled eigenvalues μ_n, and the controlled eigenvalues λ_l, as depicted by Eq. (11). Thus the unit modal control forces and the controlled eigenvalues can now be determined so they yield the desired expansion coefficients found from the solution of the above eigenproblem. However, the number of expansion coefficients to match is $N\times(N-1)$ while there are $2(N-1)$ design variables, i.e., $(N-1)$ relative modal control forces and $(N-1)$ controlled eigenvalues. Therefore, the desired expansion coefficients can be achieved only in some least-square sense. The controlled eigenvalues λ_l and modal control forces u_n can then be obtained by solving the following least-square constrained minimization problem:
Minimize

$$F(u_n,\lambda_l)=\sum_{l=1}^{N-1}\sum_{n=1}^{N}\left|(\Gamma_{ln})_d-c_l\frac{u_n}{\lambda_l-\mu_n}\right|^2 \tag{22}$$

such that

$$\sum_{n=1}^{N}u_n^2=1, \quad (\lambda_l)_{\text{lower}}\leqslant(\lambda_l)\leqslant(\lambda_l)_{\text{upper}}. \tag{23}$$

The equality constraint represents the normalization of the modal control forces since the relative controllability of the modes is the only relevant information. The upper and lower limits of the inequality constraints on the values for the controlled system eigenvalues λ_l are selected based on the characteristic of the spectrum content of the disturbance input. For example, if the disturbance input consists of multiple sinusoids, the controlled eigenvalues are selected such that they are not coincident with any of the excitation sinusoids. It is also important to remark that the controlled eigenvalues λ_l are restricted to have real positive values. The implication of this constraint is that the optimum compensator $G(\omega)$ is physically realizable. The solution of the minimization problem can be carried out efficiently by a number of optimization routines and yields the unit modal control forces u_n and the controlled eigenvalues λ_l.

Recent work[17] has shown that, given u_n and λ_l, the error modal components ξ_n can be computed from the characteristic equation of the controlled system in Eq. (9). Replacing the optimum controlled eigenvalues λ_l and unit modal control forces u_n found from the solution of the above optimization problem into Eq. (9) gives[17]

$$\begin{bmatrix} A_{11} & A_{12} & \cdots & A_{1N} \\ A_{21} & A_{22} & \cdots & A_{2N} \\ \vdots & & \ddots & \vdots \\ A_{(N-1)1} & A_{(N-1)2} & \cdots & A_{(N-1)N} \end{bmatrix}\begin{Bmatrix}\xi_1\\ \xi_2\\ \vdots\\ \xi_N\end{Bmatrix}=\begin{Bmatrix}0\\0\\\vdots\\0\end{Bmatrix},$$

$$\text{with} \quad A_{ln}=u_n\prod_{\substack{m=1\\ m\neq n}}^{N}(\mu_n-\lambda_l). \tag{24}$$

The homogeneous linear system of equations is such that the only relevant information is the relative observability of the uncontrolled modes by the error sensor. Thus assuming the Nth mode is observable, then by setting ξ_N to 1, the modal error components can be obtained by solving the reduced linear system of equations

$$\begin{bmatrix} A_{21} & A_{22} & \cdots & A_{2(N-1)} \\ \vdots & & \ddots & \vdots \\ A_{(N-1)1} & A_{(N-1)2} & \cdots & A_{(N-1)(N-1)} \end{bmatrix} \begin{Bmatrix} \xi_2 \\ \vdots \\ \xi_{N-1} \end{Bmatrix} = -\begin{Bmatrix} A_{1N} \\ A_{2N} \\ \vdots \\ A_{(N-1)N} \end{Bmatrix}. \tag{25}$$

The optimal modal error ξ_n and control u_n components define completely the control system configuration in the modal domain. The design of the control system in the modal domain as carried out in this formulation offers a number of advantages. The performance of the controller can be investigated with the modal parameters alone before the transducers are selected. Control issues such as number of control channels for a required reduction can be addressed effectively. This approach also allows for the investigation of different kinds of actuators and sensors with minimum additional computational effort.

This modal information needs to be transformed into physical transducers that can then be implemented on the structure. The type of actuator and sensor, i.e., discrete or distributed, to be implemented is an application-dependent problem and beyond the main focus of the proposed design approach. For the sake of completeness, the implementation of physical strain-induced transducers is, however, illustrated in the numerical section.

IV. NUMERICAL EXAMPLE

The applicability of the design formulation presented here is demonstrated for an uniform simple supported plate. This structure was selected because analytical solution of both the structural response and the radiated sound field are available. The plate is assumed made of steel with density $\rho_s = 7833$ N·s^2/m^4, Young's modulus $E = 2.0\times10^{11}$ N/m, Poison's ratio $\nu = 0.3$, thickness $h = 0.002$ m, and dimensions $L_x = 0.38$ m and $L_y = 0.3$ m. The spectrum of the disturbance excitation is assumed to be white noise in the [0–800] frequency band. To compute the response of the system, it is assumed a modal damping ratio of 1.0% in all modes ($\zeta_n = 0.01$), and the number of modes included in the analysis is $N = 8$. Since the proposed design is based on the modal representation of the system's response, the nth natural frequency an eigenfunction of the plate is

$$\omega_n = \sqrt{D_p/\rho_s h}(\gamma_x^2 + \gamma_y^2),$$
$$\phi_n(x,y) = K \sin(\gamma_x x)\sin(\gamma_y y), \tag{26}$$

where $\gamma_x = \pi n_x/L_x$, $\gamma_y = \pi n_y/L_y$, $D_p = Eh^3/12(1-\nu^2)$ is the flexural rigidity, (n_x, n_y) are the modal indices traditionally used for rectangular panels that are associated to the n index used in the theoretical analysis, $n \rightarrow (n_x, n_y)$, and $K = (4/L_x L_y h \rho_s)^{1/2}$.

The plate is assumed baffled to eliminate the acoustic interaction between the back and front radiation and facilitate the analytical predictions. The radiated far-field pressure the Rayleigh integral in Eq. (8). Assuming the observation point to be in the far field ($kL_x \gg 1$ and $kL_y \gg 1$), Eq. (8) has a closed-form solution given by[22]

$$p_n(\vec{r},\omega) = \frac{-\omega^2 \rho_0 L_x L_y K}{2\pi^2 n_x n_y} \frac{e^{-jkr}}{r} \left(\frac{(-1)^{n_x} e^{-jk\alpha} - 1}{(\alpha/n_x\pi)^2 - 1} \right) \times \left(\frac{(-1)^{n_y} e^{-jk\beta} - 1}{(\beta/n_y\pi)^2 - 1} \right), \tag{27}$$

where

$$\alpha = kL_x \sin\theta\cos\varphi, \quad \beta = kL_y \sin\theta\sin\varphi. \tag{28}$$

The uncontrolled modal far-field pressure distribution in Eq. (27) can now be used to compute the auto- and cross-modal radiation power terms in Eq. (15). The aim in this control example is to attenuate the total radiated power. Thus the integration of the local intensity is carried out over one half hemisphere, which for convenience is computed numerically.

The modes of a simply supported plate can be collected in four groups which are the odd–odd, even–odd, odd–even, and even–even modes. Solving Eq. (15) shows that the cross-radiation power terms between modes from different groups vanish. This implies that the modes in a group are acoustically uncoupled from the modes of the other groups. Conversely, the only acoustic coupling takes place between modes of the same group. For example, the (1,1), (3,1), and (1,3) odd–odd modes have nonzero off-diagonal elements. This implies attenuation of sound produced by these modes can be achieved by these modes interacting with each other. In other words the cross-radiated power would balance the direct radiated power. This is the essence of ASAC where sound attenuation can be achieved by restructuring the acoustically efficient modes rather than controlling each one of them. On the other hand, the (1,2) and (3,2) odd–even modes are not acoustically coupled with the odd–odd modes. Thus the radiation over a half-hemisphere due to these modes cannot be canceled by the odd–odd modes. It is evident that for the simply supported plate problem the odd–odd, even–odd, odd–even, and even–even modes should be controlled independently. Thus, a control system design should start by careful identification of not only the strongly radiating modes but also of the acoustic coupling.

The applicability of the design formulation is demonstrated for controlling the radiation due to the (1,1), (3,1), and (1,3) modes with a SISO controller. To this end, it is assumed that these are the only modes excited by both the disturbance and control inputs and observed by the error sensor. This can be expressed mathematically by setting the modal parameters f_n, u_n, and ξ_n to zero for all modes except the odd–odd ones.

A. Desired controlled eigenfunctions

The first step is the design process is to find the desired controlled system eigenfunctions. The single frequency of 300 Hz was selected to compute the matrices $[\Pi(\omega)]$ and $[V(\omega)]$ to form the eigenvalue problem of Eq. (20). The solution of the eigenvalue problem yielded three eigenvalues

TABLE I. Radiation efficiency and expansion coefficients of desired eigenfunctions.

Radiation efficiency, $S_l \times 10^{-3}$		
	0.239	1.13
Desired coefficients, $\{\Gamma_l\}_d$		
(1,1)	−0.367	0.128
(3,1)	0.361	−0.893
(1,3)	0.857	0.431

TABLE III. Controlled system eigenproperties.

Resonant frequency $f_l=(\lambda_l)^{1/2}/2\pi$ (Hz)		
	$f_1=399$	$f_2=700$
(n_x,n_y)	Expansion coefficients Γ_{ln} Γ_{1n}	Γ_{2n}
(1,1)	0.224	−0.314
(3,1)	−0.877	0.371
(1,3)	0.424	0.874

and associated eigenvectors. Since the SISO controller reduces the number of dynamic degrees of freedom by 1, the desired expansion coefficients $(\Gamma_{ln})_d$ are the first two eigenvectors. The radiation efficiency at 300 Hz, eigenvalues S_l, and associated expansion eigenvectors $\{\Gamma_l\}_d$ of the desired controlled eigenfunctions are given in Table I.

B. Optimum modal parameters

The optimum modal parameters, i.e., modal control and error components, can now be computed. The next step is to find the unit modal control forces u_n and controlled eigenvalues λ_n that yield the desired expansion coefficients of Table I. This is achieved by solving the minimization problem in Eqs. (22) and (23) where the controlled eigenvalues λ_l are not constrained as in Eq. (23) because the spectrum of the excitation input is white noise. The minimization process was carried out by using the optimization IMSL routine DUNLSF (nonlinear least squares problems), which yielded the optimum unit modal control forces u_n shown in Table II and two controlled resonant frequencies at 399 and 700 Hz as shown in Table III. These values yielded the expansion coefficients shown in columns 2 and 3 of Table III. These coefficients are almost identical to the desired coefficients obtained from the solution of the eigenvalue problem in Eq. (20) and presented in Table I. The modal control forces and controlled eigenvalues can now be used in the linear system of equations in Eq. (26) to solve for the modal error components ξ_n; they are given in Table III.

The resulting modal parameters listed in Table II define completely the control system. The controller has modified the eigenstructure of the system in such a way that the controlled structure will respond with two weak radiating modes. To illustrate this fact, the radiation efficiency for the three odd–odd uncontrolled eigenfunctions and the two new controlled eigenfunctions was computed and they are plotted in Fig. 2. This figure shows clearly that the controlled modes have substantially lower radiation efficiency than the uncontrolled modes. It is also very interesting to note that, by numerical integration, the controlled eigenfunctions are nonvolumetric. Since the response is a linear expansion of the modes, this implies that the net volume displaced by the controlled plate is zero at all frequencies. This same phenomenon was observed by the authors[18] in studying the dynamic behavior of feedforward-controlled systems using microphones in the far field as error sensors.

The sensitivity of the controlled eigenfunctions to the selected frequency used in Eq. (20) is an important issue. Solving the eigenproblem in Eq. (20) for different values of the frequency within the excitation band showed that the desired expansion coefficients did not vary substantially. Even though this is not a general conclusion, this suggests that in the proposed design approach the solution of the modal acoustic field could be efficiently carried out at a small number of frequencies. Since this analysis is the most computational intensive process, the proposed design approach has clear computational benefits over direct optimization methods for complex structures and excitations.

C. Control system performance

The control system is completely defined in the modal domain in terms of the optimal modal parameters in Table II. The performance of the controlled structure can be investigated with these modal parameters alone before physical transducers are devised. The effectiveness of the control system was evaluated for a disturbance input consisting of a

TABLE II. Modal control and error components.

Mode (n_x,n_y)	Modal parameters u_n	ξ_n
(1,1)	−0.534	0.924
(3,1)	0.479	0.329
(1,3)	0.697	0.192

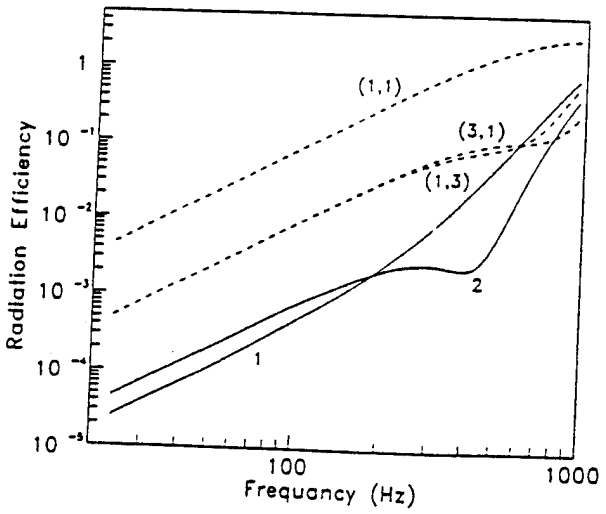

FIG. 2. Radiation efficiency of uncontrolled (----) and controlled (———) eigenfunctions.

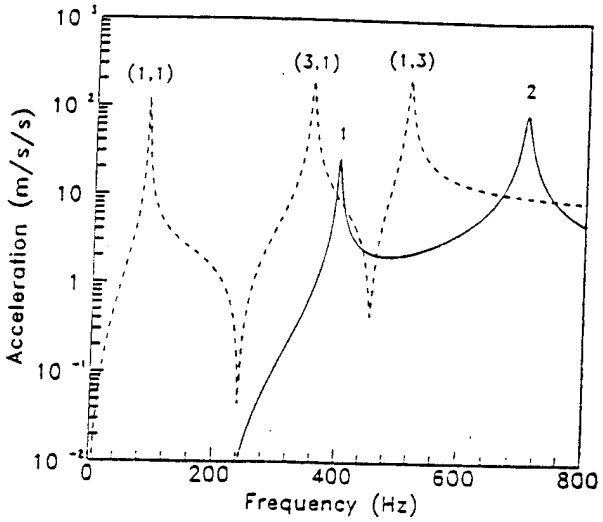

FIG. 3. Acceleration response at disturbance force location before (----) and after (———) control.

point force located at $x=0.5L_x$ and $y=0.5L_y$. To illustrate the dynamic behavior of the plate before and after control, the acceleration response of the plate at the disturbance location was computed. The amplitude is shown in Fig. 3 as a function of the frequency. The dashed line is the uncontrolled response and shows resonant peaks at the frequencies given in Eq. (27). On the other hand, when the control input is applied, the response shows resonance behavior at the two controlled resonant frequencies given in Table III. The vibration levels of the controlled structure are slightly lower than the uncontrolled system, i.e., amplitude of the second controlled mode is the same as the (1,1) uncontrolled mode. Similarly, the before- and after-control far field pressure at $\vec{r}=(0°,0°,4.5L_x)$ was also computed. The sound pressure level in decibels (dB *re*: 20 μPa) is shown in Fig. 4 as a function of the frequency. This figure shows that the sound levels produced by the controlled structure are well below the level generated by the uncontrolled one. This is due to the low radiation efficiency of the controlled modes that results in a weak coupling of the controlled response with the acoustic medium. This phenomenon takes place in spite of the vibration levels being comparable to the uncontrolled response levels.

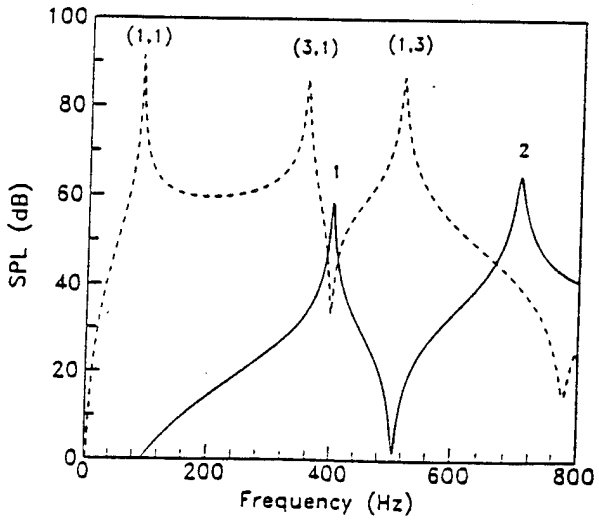

FIG. 4. Far-field pressure at $\vec{r}=(4.5L_x,0°,0°)$: uncontrolled (----) and controlled (———).

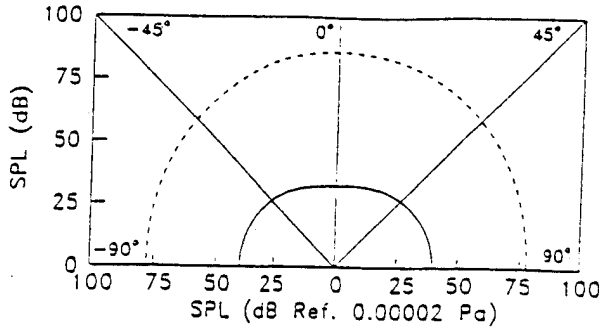

FIG. 5. Radiation directivity on the x-z plane at 352 Hz: uncontrolled (----) and controlled (———).

The radiation directivity in the horizontal x-z planes was then computed at selected frequencies and they are shown in Figs. 5 and 6. In all figures, the dashed and continuous lines represent the uncontrolled and controlled sound radiated pressure at a distance of $4.5L_x$. Figure 5 shows the far-field radiation at 352 Hz, corresponding to the resonance of the uncontrolled (3,1) mode, which shows excellent global reduction. Similar behavior was observed for each of the uncontrolled resonant frequencies. More interesting is to investigate the radiated sound at the controlled system resonance frequencies. Figure 6 shows the far-field radiation at 399 Hz, which is the second resonance of the controlled system. Inspection of this plot demonstrates that even though the response of the plate is very large (because of the resonance) the radiation is not increased significantly. Again this is because the controlled mode has very low radiation efficiency.

To evaluate the overall performance of the control configuration, the sound pressure spectrum was integrated over the bandwidth from 0 to 800 Hz. The integrated spectrum is used to plot the overall radiation directivity in the x-z plane. Total radiation directivities before and after control were computed for the x-z planes and are shown in Fig. 7, respectively. These plots show that an average global sound pressure level reduction of 15 dB is obtained over the whole spectrum, thus attesting to the effectiveness of the design approach presented here.

The process of designing a structural actuator and sensor

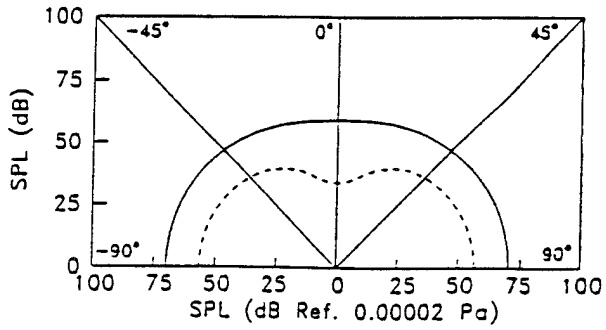

FIG. 6. Radiation directivity on the x-z plane at 399 Hz: uncontrolled (----) and controlled (———).

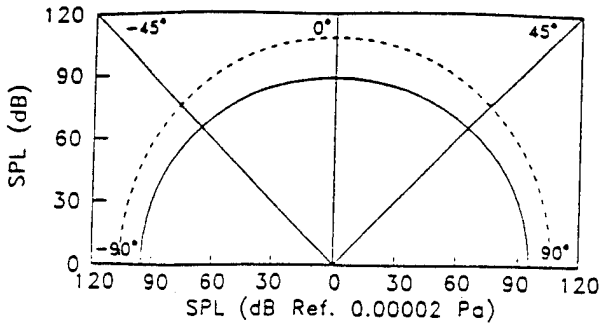

FIG. 7. Total radiation directivity on the x-z and planes: uncontrolled (----) and controlled (———).

that yield the optimum modal parameter is not a key aspect of formulation presented here. However, for the sake of completeness and as well as clarity in the presentation. the design of the strain-induced actuator and sensor is presented in the Appendix.

V. CONCLUSIONS

A formulation has been presented for the design of adaptive structures for ASAC applications. The methodology makes use of the fundamental concept that sound radiation can be effectively reduced by changing the overall radiation efficiency of the structure. The formulation aiso takes advantage of the fact that the feedforward-control system changes the dynamic properties of the structure. The understanding and merging of these two phenomena lead to an efficient method for the design of actuators and sensors. The method is based on the premise that the optimum actuator and sensor will change the eigenstructure of the system such that the controlled response consists of a modal series of weak radiators. The control configuration is first defined in the modal domain by computing the optimum control and error modal parameters. Using this information, the physical actuator and sensor can be then constructed. This particular separation between the modal and physical domain offers the advantage that different transducers and configurations can be investigated with minimum computational effort. The design approach was illustrated for controlling the odd–odd modes on a simply supported plate problem driven by a point force. A SISO controller was designed and the results show excellent reduction over the whole spectrum.

ACKNOWLEDGMENT

The authors gratefully acknowledge the support of this work by the Office of Naval Research Grant No. ONR-N00014-92-J-1170.

APPENDIX: STRAIN-INDUCED ACTUATOR AND SENSOR DESIGN

For the sake of completeness, in this appendix a procedure to design an structural actuator and sensor that yield the desired modal parameters is briefly presented. The actuator and error sensor are implemented with multiple piezoelectric PZT patches and a single PVDF film, respectively. Mechanical models that relate the transducer parameters, i.e., size,

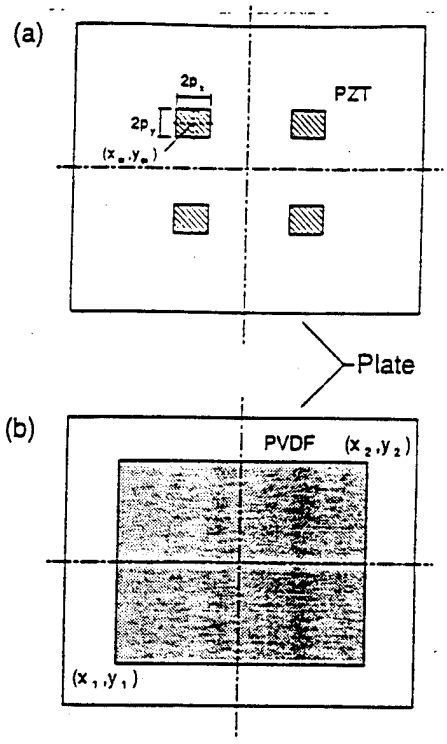

FIG. A1. Optimum (a) PZT control actuator and (b) PVDF film error sensor.

location, etc., to the modal control and error components are required. Assuming the control input consists of M fixed-size PZT patches driven by the same control signal either in- or out-of-phase. Then, the nth modal control force can be shown to be given by[26]

$$u_n=\sum_{i=1}^{M} P_i \frac{\gamma_x^2+\gamma_y^2}{\gamma_x\gamma_y}\{\cos[\gamma_x(x_{ci}+p_x)]-\cos[\gamma_x(x_{ci}-p_x)]\}$$

$$\times\{\cos[\gamma_y(y_{ci}+p_y)]-\cos[\gamma_y(y_{ci}-p_y)]\}, \qquad \text{(A1)}$$

where $P_i=\pm 1$ indicates the relative phase between the PZT patches, (x_c,y_{ci}) are the unknown center coordinates, and $2p_x=0.1L_x$ and $2p_y=0.1L_y$ are the fixed dimensions of the patch. The design variables are the relative phase and coordinates of the patches and are obtained by minimizing the cost function

$$F(P_i,x_{ci},y_{ci})=\sum_{n=1}^{N}|(u_n)_{\text{opt}}-u_n|^2, \qquad \text{(A2)}$$

where the optimum modal control forces $(u_n)_{\text{opt}}$ are the values in Table II for the odd–odd modes and zero for all the others. The optimization process in Eq. (30) is continuous in the variables (x_{ci},y_{ci}) and discrete in the phase indicator P_i and number of patches M. The solution of this optimization. carried out using IMSL routine DUNLSF, is straightforward and leads to the control configuration shown in Fig. A1(a). The control input for the SISO controller consists of four patches driven in phase by the control signal $U(\omega)$.

The error sensor was implemented with a single PVDF film patch. If needed multiple patches, whose electric output

are summed to obtain the error signal, can be considered. The nth error modal component can be shown to be given as[12]

$$\xi_n = \left(e_{31} \frac{\gamma_x}{\gamma_y} + e_{32} \frac{\gamma_y}{\gamma_x} \right) [\cos(\gamma_x x_1) - \cos(\gamma_x x_2)] \times [\cos(\gamma_y y_1) - \cos(\gamma_y y_2)], \quad \text{(A3)}$$

where (x_1, y_1) and (x_2, y_2) are the lower left and upper right corner unknown coordinates, and e_{31} and e_{32} are charge per unit area in the x and y directions, respectively. The coordinates that determine the size and location of the PVDF film are obtained by minimizing

$$F(x_1, y_1, x_2, y_2) = \sum_{n=1}^{N} |(\xi_n)_{\text{opt}} - \xi_n|^2, \quad \text{(A4)}$$

where the optimal modal error components $(\xi_n)_{\text{opt}}$ are again obtained from Table II for the odd–odd modes and zero for all the other modes. The PVDF film error sensor is shown in Fig. A1(b).

[1] C. R. Fuller, "Apparatus and methods for global noise reduction," U.S. Patent No. 4,715,599 (1987).

[2] W. T. Baumann, W. R. Saunders, and H. H. Robertshaw, "Active suppression of acoustic radiation from impulsively excited structures," J. Acoust. Soc. Am. **90**, 3202–3208 (1991).

[3] L. Meirovitch and S. Thangjitham, "Active control of sound pressure," J. Vib. Acoust. **112**, 237–244 (1990).

[4] C. R. Fuller, "Active control of sound transmission/radiation from elastic plates by vibrating inputs—I analysis," J. Sound Vib. **136**, 1–15 (1990).

[5] V. L. Metcalf, C. R. Fuller, R. J. Silcox, and D. E. Brown, "Active control of sound transmission/radiation from elastic plates by vibration Inputs—II experiments," J. Sound Vib. **153**, 387–402 (1992).

[6] J. P. Smith, C. R. Fuller, and R. A. Burdisso, "Control of broadband radiated sound with adaptive structures," in *Proceedings of the SPIE 1993 North America Conference on Smart Structures and Materials*, 31 Jan.–4 Feb. 1993, Albuquerque, NM (SPIE, Bellingham, 1993), pp. 587–597.

[7] B. T. Wang, R. A. Burdisso, and C. R. Fuller, "Optimal placement of piezoelectric actuators for active control of sound radiation from elastic plates," Proc. Noise-Con. **91**, 267–275 (1991).

[8] C. R. Fuller, C. A. Rogers, and H. H. Robertshaw, "Active structural acoustic control with smart structures," Proceedings of the SPIE, Vol. 1170: Fiber Optic Smart Structures and Skins, Boston, MA, 338–358 (1989).

[9] C. R. Fuller, C. H. Hansen, and S. D. Snyder, "Experiments on active control of sound radiation using a piezoceramic actuator," J. Sound Vib. **150**, 179–190 (1991).

[10] R. L. Clark and C. R. Fuller, "Experiments on active control of structurally radiated sound using multiple piezoceramic actuators," J. Acoust. Soc. Am. **91**, 3313–3320 (1992).

[11] W. R. Saunders, H. H. Robertshaw, and C. A. Rogers, "Structural acoustic control for a shape memory alloy composite beam," AIAA paper 90-1090 CP (1990).

[12] R. L. Clark and C. R. Fuller, "Modal sensing of efficient acoustic radiators with polyvinylidene fluoride distributed sensors in active structural acoustic control approaches," J. Acoust. Soc. Am. **91**, 3321–3329 (1992).

[13] R. L. Clark, C. R. Fuller, and R. A. Burdisso, "Design approaches for shaping polyvinylidene fluoride sensors in active structural acoustic control," in *Proceedings of the Conference on Recent Advances in Adaptive and Sensory Materials and Their Applications*, Blacksburg, VA (Technonic, Lancaster, PA, 1992), pp. 702–726.

[14] R. L. Clark, C. R. Fuller, B. R. Fogg, W. W. Miller, W. V. Vengsarkar, and R. O. Claus, "Structural acoustic control using fiber sensors and piezoelectric actuators," in *Proceedings of the International Symposium and Exhibition on Active Materials and Adaptive Structures*, Alexandria, VA (IOP, Philadelphia, 1991), pp. 547–552.

[15] R. L. Clark and C. R. Fuller, "Optimal placement of piezoelectric actuators and polyvinylidene fluoride (PVDF) error sensors in active structural acoustic control approaches," J. Acoust. Soc. Am. **92**, 1521–1533 (1992).

[16] R. A. Burdisso and C. R. Fuller, "Theory of feedforward controlled system eigenproperties," J. Sound Vib. **153**, 437–452 (1992).

[17] R. A. Burdisso and C. R. Fuller, "Feedforward controller design by eigenvalue assignment," AIAA J. Guidance Control 17(3), 466–472 (1994).

[18] R. A. Burdisso and C. R. Fuller, "Dynamic behavior of structural-acoustic systems in feedforward control of sound radiation," J. Acoust. Soc. Am. **92**, 277–286 (1992).

[19] J. T. Post, "Active control of the forced and transient response of a finite beam," Master's thesis, The George Washington University (October 1989).

[20] F. Fahy, *Sound and Structural Vibration* (Academic, Orlando, FL, 1985).

[21] *SYSNOISE: Numerical analysis of acoustical and elasto acoustical problems* (Dynamic Engineering, St. Louis, MO, 1992).

[22] C. E. Wallace, "Radiation resistance of a rectangular panel," J. Acoust. Soc. Am. **51**, 946–952 (1972).

[23] D. C. Smith and R. J. Bernhard, "Computing acoustic design sensitivity information using boundary element methods," in *Proceedings of The Eleventh International Conference on Boundary Element Methods in Engineering*, Cambridge, MA, Vol. 2 (Springer-Verlag, New York, 1989), pp. 369–383.

[24] K. A. Cunefare and G. H. Koopmann, "Acoustic design sensitivity for structural radiators," J. Vib. Acoust. **114**, 178–186 (1992).

[25] K. A. Cunefare, "The minimum multimodal radiation efficiency of baffled finite beams," J. Acoust. Soc. Am. **90**, 2521–2529 (1991).

[26] E. K. Dimitriadis, C. R. Fuller, and C. R. Rogers, "Piezoelectric actuators for distributed vibration excitation of thin plates," J. Vib. Acoust. **113**, 100–107 (1989).

C-25 Numerical Simulation of Active Structural-Acoustic Control for a Fluid-Loaded, Spherical Shell, C. E. Ruckman and C. R. Fuller, Journal of the Acoustical Society of America, Vol. 96 No. 5, pp. 2817-2825, November 1994.

Numerical simulation of active structural-acoustic control for a fluid-loaded, spherical shell

Christopher E. Ruckman
Structural Acoustics and Hydroacoustics Research Branch, Carderock Division, Naval Surface Warfare Center, Bethesda, Maryland 20084-5000

Chris R. Fuller
Vibration and Acoustics Laboratories, Virginia Polytechnic Institute and State University, Blacksburg, Virginia 24061

(Received 10 November 1992; revised 4 November 1993; accepted 14 June 1994)

Numerical methods are used to investigate active structural-acoustic control, a noise control technique in which oscillating force inputs are applied directly on a flexible structure to control its acoustic behavior. The goal is to control acoustic radiation from a thin-walled shell submerged in a dense fluid and subjected to a persistent, pure-tone disturbance. For generality the fully coupled responses are found numerically, in this case using the computer program that combines finite-element and boundary-element techniques. A feedforward control approach uses linear quadratic optimal control theory to minimize the total radiated power. Results are given for a thin-walled spherical shell, and are compared to analytical results. The numerical solution is shown to be suitably accurate in predicting the radiated power, the control forces, and the residual responses as compared to the analytical solution. A relatively small number of control forces can achieve global reductions in acoustic radiation at low frequencies ($k_0a<1.7$). A single point-force actuator reduces the radiated power due to a point-force excitation by up to 20 dB at resonance frequencies; between resonance frequencies, more actuators are required because of modal spillover. With multiple control forces, radiation can be reduced by 6–20 dB over the frequency range $0<k_0a<1.7$.

PACS numbers: 43.40.Vn, 43.40.Rj

INTRODUCTION

The concept of active structural-acoustic control (ASAC) involves controlling the acoustic response of a fluid-structure system by applying oscillating force inputs directly to the structure. Recent theoretical and experimental studies have used ASAC to control radiation from one- and two-dimensional structures including beams, plates, and submerged plates; similar techniques were used to control noise transmitted through flat plates or into infinite cylindrical shells.[1–6] The concept is similar to active vibration control since the actuators are vibrational inputs applied directly on a flexible structure, but the goal of reducing acoustic response often differs from the goal of reducing a purely structural response. ASAC also differs from active noise cancellation (ANC), since ASAC applies vibrational inputs to the structure itself rather than exciting the acoustic medium with loudspeakers.[7] For structure-borne noise, ASAC can often produce widespread far-field reductions with a relatively few actuators as compared to ANC. Also, because vibrational inputs tend to be more compact than loudspeakers, ASAC can be used in certain situations where ANC is impractical.

Submerged shells and other fluid-loaded structures are of significant practical interest, but they also represent a fundamental departure from existing work. Most nonexperimental studies of ASAC have used analytical approaches to obtain the required structural-acoustic quantities. However, for a general, three-dimensional, fluid-loaded shell no such analytical expressions exist. In the present research, dynamic responses are obtained using the computer program NASHUA.[8] NASHUA uses the finite-element method to compute structural quantities, and a boundary-element formulation to solve for the fully coupled structural-acoustic response. A similar study is given by Molo and Bernhard,[9] who used the indirect boundary-element method to formulate active noise cancellation systems for both interior and exterior noise fields. Another related study is by Cunefare and Koopman,[10] which uses a boundary-element approach to examine three-dimensional exterior problems. The main differences from the present work are that the system includes an elastic structure with full fluid–structure coupling, and the control actuators are vibrational inputs rather than acoustic sources.

There are two significant benefits to using an approach based on finite elements/boundary elements. First, altering model geometries involves minimal effort because the boundary-element formulation does not require discretization of the ambient fluid. Second, the approach can treat nearly any structure amenable to finite-element modeling, making it an excellent companion for theoretical and experimental studies of submerged shells.

The present report is an extension to Ref. 11, which outlines some preliminary results obtained by applying these techniques to a thin, spherical shell with fluid loading. A more comprehensive set of results is given, with more emphasis on showing agreement between numerical and analytical results. The aim is to gain confidence in the use of

 0001-4966/94/96(5)/2817/9/$6.00 © 1994 Acoustical Society of America

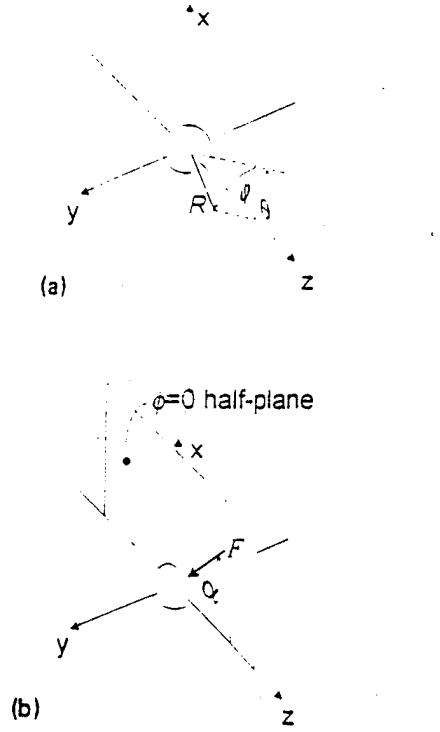

FIG. 1. Coordinate systems for defining (a) sensor locations in the far field, and (b) force locations on the shell. Control forces are restricted to lie within the $\phi=0$ half-plane, thus force locations may be defined by a single angular coordinate α.

numerical techniques for more complex situations.

The following work analyzes steady-state, single-frequency forcing functions. The control algorithm used is a feedforward method which requires *a priori* knowledge of the frequency content and location of the disturbance force. After specifying the number and locations of the control actuators, linear quadratic optimal control theory is used to solve for the complex control forces that minimize a quadratic cost function.

I. THEORETICAL BACKGROUND

This section describes the analytical and numerical models of the structure–fluid system and the feedforward control approach used to find control forces and phases.

A. Analytical and numerical modeling of spherical shell

Figure 1(a) defines the coordinate systems used for the thin-walled spherical shell. The global z axis is defined as the axis along which the disturbance force acts. Far-field locations are defined in global spherical coordinates (R,θ,ϕ), where R is the radial distance, θ the latitudinal angle measured from the global z axis, and ϕ the longitudinal angle measured from the x-z plane. The structure is completely submerged in a dense fluid, with material properties chosen to resemble a steel shell in water. The ratio of shell thickness to radius is 0.01, and the shell radius is $a=1$ m. Frequencies up to $k_0a=1.7$ are examined, where k_0 is the acoustic wave number; this frequency range includes the resonance frequencies of several low-order modes.

To simplify the problem, a restricted set of forcing functions is considered for disturbance and control forces. The forces are concentrated loads (point forces) normal to the shell surface, and are applied only in the $\phi=0$ plane as shown in Fig. 1(b). Force locations are specified by a single angle α. The disturbance is always a single point-force applied to $\alpha=0$. The total far-field response is therefore either axisymmetric (if a single control force is applied at $\theta=\pi$), or symmetric about the $\phi=0$ plane (if a control forces is applied off the z axis.)

Multiforce responses can be found by combining the axisymmetric responses due to each of the individual forces using superposition, even if their combined response is not axisymmetric. Given the restrictions on force locations described above, the coordinate transformation used to find radiation and shell vibration due to any individual force is a simple rotation whose effective rotation angle can be found from the following relation:

$$\cos\theta_{\text{eff}}=(\cos^2\theta+\sin^2\theta\sin^2\phi)^{1/2}\times\cos\left[\alpha+\tan^{-1}\left(\frac{\sin\theta\sin\phi}{\cos\theta}\right)\right]. \tag{1}$$

The analytical model for a thin-walled, fluid-loaded, spherical shell with a radially directed, persistent, point force is due to Junger and Feit.[2] The model includes membrane stresses but ignores bending stresses, and is therefore limited to low frequencies. The far-field pressure due to a force b_i applied on along the z axis is

$$P(R,\theta,b_i)=\sum_{n=0}^{\infty} b_i\Gamma_n(R)\mathbf{P}_n(\cos\theta), \tag{2}$$

where $\mathbf{P}_n$ is the Legendre polynomial of order n, and

$$\Gamma_n(R)=\frac{2n+1}{4\pi a^2}\left(\frac{\rho c}{k_aR}\right)\frac{(-\sqrt{-1})^n}{(Z_n+z_n)h'(k_aa)}. \tag{3}$$

The symbols ρ and c represent the fluid density and acoustic velocity, and h is the spherical Hankel function. The modal acoustic impedance is

$$z_n=j\rho c\frac{h_n(ka)}{h_n'(ka)}, \tag{4}$$

and the modal structural impedance is

$$Z_n=-j\frac{h}{a}\rho_sc_p\frac{\{\Omega^2-(\Omega_n^{(1)})^2\}\{\Omega^2-(\Omega_n^{(2)})^2\}}{\Omega^3-\Omega(n^2+n-1-\nu)}, \tag{5}$$

where $\Omega_n^{(1)}$ and $\Omega_n^{(2)}$ are the two *in vacuo* natural frequencies associated with the roots of

$$\Omega^4-(1+3\nu+\lambda^n)\Omega^2+(\lambda^n-2)(1-\nu^2). \tag{6}$$

For numerical modeling, the computer program NASHUA is used to compute both structural responses and far-field acoustic responses. NASHUA uses the finite-element program NASTRAN to compute mass, damping, and stiffness matrices for the structure. These are used with a discretized form of the Helmholtz surface integral equation to obtain the response of the fully coupled response of the fluid-structure system. Such techniques are well known and are not detailed

here: the interested reader is referred to Ref. 8.

While NASHUA is capable of fully three-dimensional modeling, only axisymmetric models are used here to simplify analysis and reduce computing costs. The finite-element portion of the NASHUA model uses axisymmetric cone elements that include both bending and membrane stresses. The structural mesh contains 129 grid circles. Since NASTRAN does not allow grid circles with zero radius, the poles at $\theta=0$ and $\theta=\pi$ are actually "pinholes" or grid circles of radius $0.001a$. To approximate a point force, a ring force is applied on one of the small-radius grid circles. This approximation casts some doubt on the validity of the model at high frequencies. However, as described below, the agreement between analytical and numerical results is sufficient for the problem at hand.

B. Feedforward control approach

The control approach taken here is a single-frequency, steady-state, feedforward approach based on linear quadratic optimal control theory.[2,3,9] Consider a spherical shell subjected to a total of N_d coherent, persistent, time-harmonic disturbance forces. The *disturbance response* P_d, also known as the *primary response*, is defined as the far-field pressure due to these disturbances forces. Here the disturbance response is axisymmetric to make the development more clear, but any type of disturbance could be used. Suppose the ith disturbance force has strength s_i, and would cause far-field pressure distribution $A_i(\theta)$ if acting alone. Assuming linearity, the disturbance response can be written as a linear sum of the individual disturbance responses:

$$P_d(\theta)=\sum_{i=1}^{N_d} A_i(\theta)s_i. \tag{7}$$

Suppose a total of N control forces are now applied to control the disturbance response, where the ith control force has strength b_i. The control response $\hat{P}$, also known as the secondary response, is defined as the far-field pressure due to only the control forces. Furthermore, suppose that both the control response and the disturbance response must be symmetric about the same axis so that their sum is axisymmetric. Thus the control response $\hat{P}(\theta)$ is a linear sum of the individual control responses $X_i(\theta)$:

$$\hat{P}(\theta)=\sum_{i=1}^{N} X_i(\theta)b_i. \tag{8}$$

The total response is the sum of the disturbance response plus the control response.

Now define a quadratic *cost function* χ^2 as a weighted integral of squared magnitude of the total response over the entire far field which, because of symmetry, is a single integral:

$$\chi^2=\int_0^{\pi} w(\theta)|P_d(\theta)+\hat{P}(\theta)|^2\,d\theta, \tag{9}$$

where $w(x)$ is a weighting function that can be chosen to give physical significance to χ^2 if desired. The feedforward control problem can be restated as an unconstrained quadratic minimization, i.e., seek a set of control forces b_i to minimize χ^2. Since the total radiated power is

$$\Pi=\int_0^{\pi}\frac{\pi R^2\sin\theta}{\rho c}|p(\theta)|^2\,d\theta, \tag{10}$$

a cost function equal to the total radiated power can be found by setting

$$w(\theta)=(\pi R^2/\rho c)\sin\theta. \tag{11}$$

The set of control forces that minimizes χ^2 is the set of control forces for which $\partial\Pi/\partial b_i$ vanishes for each of the N control forces b_i. This requirement produces an $N\times N$ system of complex-valued, simultaneous equations, the so-called *normal equations*, which have as their solution the control forces b_i. The coefficients of the normal equations can be generated in either of two ways, depending on whether $P_c(\theta)$ and $\hat{P}(\theta)$ are given as continuous functions of θ or as discretized functions defined only at discrete values of θ. With continuous expressions for the variables, the integration in Eq. (6) can be performed in closed form. On the other hand, if the variables are defined only at discrete locations, it is necessary to generate discrete (analytical or numerical) transfer functions and integrate Eq. (6) numerically. These two methods are outlined below.

Note that each of the variables A_i and X_i from Eqs. (4) and (5) is merely a transfer function between a unit force somewhere on the structure and the far-field pressure distribution. In the present context these transfer functions are found using either NASHUA or an analytical solution. However, for purposes of simulation they could be obtained from any source such as experimental data or other numerical solutions. Note also that Eq. (6) contains a line integral for a one-dimensional system but could be extended to an integral over an area or through a volume.

1. Obtaining the normal equations from continuous variables

When an analytical solution is available, the problem can be formulated in terms of continuous functions of far-field location θ. It is possible to integrate Eq. (6) in closed form, evaluate the coefficients of the normal equations, and solve for the required control forces. Suppose the control forces and disturbance forces are written in vector form so that

$$B=\{b_1 \quad b_2 \quad \cdots \quad b_N\}^T$$

and (12)

$$S=\{s_1 \quad s_2 \quad \cdots \quad s_N\}^T.$$

Now write the disturbance response as $P_d(\theta)=AS$ and the control response as $\hat{P}(\theta)=XB$, where A and X are row vectors containing the continuous variables $A_i(\theta)$ and $X_i(\theta)$ from Eqs. (4) and (5), respectively. For instance, the form of X is

$$X=\{X_1(\theta) \quad X_2(\theta) \quad \cdots \quad X_N(\theta)\}, \tag{13}$$

and likewise for A. After some algebra, the cost function from Eq. (6) becomes

$$\chi^2 = \int_0^{\pi} B^H X^H X B w(\theta) d\theta - 2\,\mathrm{Re}\left(\int_0^{\pi} S^H X^H A B w(\theta) d\theta \right) + \int_0^{\pi} S^H A^H A S w(\theta) d\theta, \tag{14}$$

where the superscript H denotes the Hermitian transpose. Using the orthogonality of the Legendre polynomials in Eq. (2), Eq. (14) reduces to

$$\chi^2 = B^H C B - 2\,\mathrm{Re}(S^H D B) + S^H E S, \tag{15}$$

where a typical element of the matrix C is

$$C_{ij} = \frac{\pi R^2}{\rho c} \sum_{n=0}^{\infty} \Gamma_n^*(R) \Gamma_n(R) \frac{2}{2n+1} \mathbf{P}_n(\alpha_i) \mathbf{P}_n(\alpha_j), \tag{16}$$

and elements of D and E are similar in form. By differentiating the cost function with respect to each of the control forces f_i and setting all the differentials to zero, it is possible to show that the vector of control forces B_{opt} which minimizes the cost function is the solution to the normal equation

$$C B_{\mathrm{opt}} = S^T D. \tag{17}$$

2. Obtaining the normal equations from discrete variables

Now suppose that the transfer functions are defined only at discrete locations $\mathbf{r}_m$, $m = 1,2,\ldots,M$, where $\mathbf{r}_m$ is a location vector denoting a location in the far field. (This will always be the case with the numerical solution, and the analytical solution can also be used to generate values at discrete locations.) The form of X is

$$X = \begin{bmatrix} X_1(\mathbf{r}_1) & X_2(\mathbf{r}_1) & \cdots & X_N(\mathbf{r}_1) \\ X_1(\mathbf{r}_2) & X_2(\mathbf{r}_2) & \cdots & X_N(\mathbf{r}_2) \\ \vdots & \vdots & & \vdots \\ X_1(\mathbf{r}_M) & X_2(\mathbf{r}_M) & \cdots & X_N(\mathbf{r}_M) \end{bmatrix} \tag{18}$$

and likewise for A. Summing contributions to the cost function at each far-field location θ_m essentially performs a numerical integration of Eq. (6); thus it is possible to evaluate the coefficients of the normal equations and solve for the required control forces. For the numerically computed cost function to closely approximate the radiated power, two conditions must be satisfied. First, there must be enough far-field locations to adequately characterize the response. Second, the weighting function $w(\theta)$ must be discretized to account for the contributions of each location. This is accomplished by defining a diagonal matrix W in which each entry on the diagonal represents a different far-field location. Using the notation of the previous section, the C, D, and E matrices become

$$C = X^H W X, \quad D = A^H W X, \quad E = A^H W A, \tag{19}$$

and the normal equations are identical to Eq. (13).

If the total response is axisymmetric, then X and A contain acoustic pressures at far-field locations θ_m, $m = 1,2,\ldots,M_\theta$ (all at a constant value of ϕ). The row vectors X and B become matrices of column dimension M_θ. For example,

$$X = \begin{bmatrix} X_1(\theta_1) & X_2(\theta_1) & \cdots & X_N(\theta_1) \\ X_1(\theta_2) & X_2(\theta_2) & \cdots & X_N(\theta_2) \\ \vdots & \vdots & & \vdots \\ X_1(\theta_{M_\theta}) & X_2(\theta_{M_\theta}) & \cdots & X_N(\theta_{M_\theta}) \end{bmatrix}. \tag{20}$$

The entries in the diagonal weighting matrix W are weighting coefficients w_i proportional to the areas associated with each of the far-field locations. If the far-field locations are evenly spaced at intervals of $2\Delta\theta$, then

$$w_i = \begin{cases} \dfrac{\pi R^2}{\rho c}(1-\cos\Delta\theta), & i = 1 \text{ or } i = M_\theta \\ \dfrac{\pi R^2}{\rho c}[\cos(\theta_i - \Delta\theta) - \cos(\theta_i + \Delta\theta)], & 1 < i < M_\theta. \end{cases} \tag{21}$$

If the total response exhibits a plane of symmetry, then the variables must be partitioned to contain far-field pressures at θ_m, $m = 1,2,\ldots,M_\theta$ for *each* of the longitudinal locations ϕ_i, $i = 1,2,\ldots,M_\phi$. Thus the row vectors X and A become matrices whose column dimension is the product of M_θ and M_ϕ. The entries in the weighting matrix W must be similarly partitioned, and scaled proportional to the areas associated with each of the far-field locations. If the far-field locations are evenly spaced at intervals of $2\Delta\theta$ in the latitudinal direction and $\Delta\phi$ in the longitudinal direction, then the entries in W are the same as in Eq. (15) but divided by the number of intervals in the ϕ direction.

II. RESULTS AND DISCUSSION

The objectives of this section are (1) to show agreement between the analytical and numerical results, and (2) to discuss results of efforts to control radiation from a point-force disturbance.

The material properties and geometric specifications used for both the analytical and numerical models are summarized below. The model represents an undamped steel shell submerged in water. The shell material has Young's modulus of 1.85×10^{11} Pa, Poisson's ratio of 0.3, and density of 7670 kg/m^3. The shell radius a is 1.0 m, and the wall thickness is 0.01 m. The density and acoustic velocity of the surrounding fluid are 1000 kg/m^3 and 1460 m/s, respectively. All far-field quantities are normalized to a distance of 1.0 m.

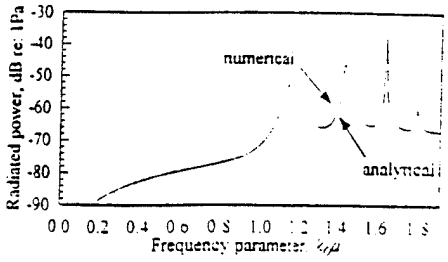

FIG. 2. Comparison of radiated power computed with analytical and numerical (NASHUA) solutions. Frequency regime $0<k_0a<1.7$ contains three peaks; agreement is good between analytical and numerical results. Some frequency shifting occurs at higher frequencies.

A. Analytical and numerical predictions of disturbance response

Figure 2 compares the radiated power spectra obtained using the analytical and numerical models. The response contains sharp peaks at $k_0a=1.14$, 1.44, 1.64, and 1.8, the nature of which are detailed below. The two methods agree well in terms of magnitudes and overall trends, as could be expected for this simple structure. At frequencies above $k_0a>1.7$, the peaks in the numerical model are shifted to slightly lower frequencies. Reasons for this shift could include both modeling simplifications in the analytical solution and discretization approximations in the numerical model. For the purposes of this study, the region below $k_0a=1.7$ contains sufficient features that higher frequencies need not be treated here.

One difference between the analytical and numerical solutions appears in Fig. 3, which shows the distribution of surface velocity at a frequency of $k_0a=1.14$ due to a point-force disturbance without control. The two solutions agree well except near $\theta=0°$, the location at which the force is applied. The numerical solution, which accounts for bending as well as membrane stresses, displays large local deformations near the drive-point location; the analytical solution, which truncates high-order terms and does not account for bending stresses, does not exhibit local deformations. Fortunately, such short-wavelength disturbances do not propagate efficiently to the far field and can be ignored without affecting controller performance. When analytical and numerical velocity distributions are compared to check solution accuracy, one must expect such differences to occur near drive points.

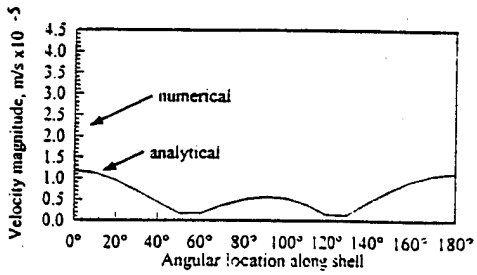

FIG. 3. Sample surface velocity distributions from analytical and numerical solutions ($k_0a=1.14$). Large local deformations near drive point occur in numerical solution but not analytical solution.

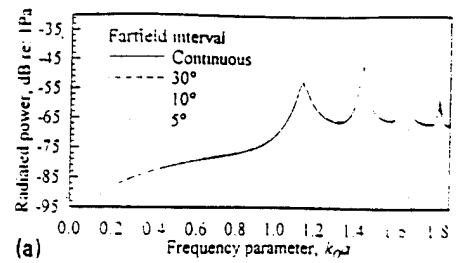

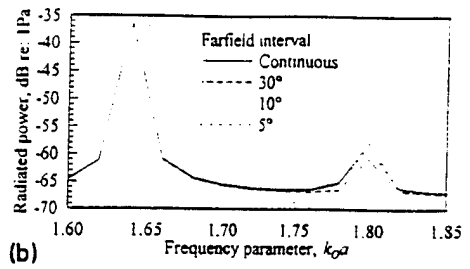

FIG. 4. Effect of far-field discretization on accuracy of radiated power calculations. Solid line represents continuous variables; other lines represent discretized variables with various mesh sizes. (a) Shows entire frequency range; (b) enlarges upper frequencies to show detail. At these low frequencies, 10° far-field interval is sufficient to capture dynamic response.

The solution accuracy also depends on the far-field interval $\Delta\theta$ used to compute radiated power, so it is necessary to verify that the choice of $\Delta\theta$ is sufficiently small to characterize the far-field behavior. (Recall that far-field locations are separated by an angle $2\Delta\theta$.) Since the analytical solution can use either continuous or discrete variables, the radiated power found using continuous variables can be compared to that found using discrete variables with different values of $\Delta\theta$. A small value of $\Delta\theta$ should provide the same radiated power found using continuous variables, and the agreement should deteriorate as $\Delta\theta$ increases. Figure 4(a) and (b) compare the radiated power spectra for continuous variables to that found using far-field intervals of $\Delta\theta=2.5°$, 5°, and 15°. Figure 4(a) shows the frequency range $0<k_0a<1.9$, and Fig. 4(b) shows an enlarged view of the frequency range $1.6<k_0a<1.9$. With $\Delta\theta=2.5°$ and 5°, the agreement with the continuous solution is excellent at all frequencies. Even with $\Delta\theta=15°$ the solution is adequate through $k_0a=1.7$. Results in this paper use a far-field interval of $\Delta\theta=5°$ to decrease computation times.

Figure 5 shows the shapes of the first few vibrational modes, denoted by the number n of nodal circles present. The curves shown are surface velocity distributions obtained using only the nth term from the summation in Eq. (2), and are normalized to unit maxima. The $n=0$ mode is a "breathing" mode, i.e., a uniform radial expansion contraction. The $n=1$ mode is a rigid-body translation, $n=2$ is the first axial mode, and so forth. Each of the modes has an axis of symmetry corresponding to a diameter of the sphere (except for $n=0$ which displays spherical symmetry). For $n>0$ the modes are degenerate because there are infinitely many axes about which different modes occur. For example, the $n=2$ mode that is symmetric about the $\alpha=0°$ diameter is *different*

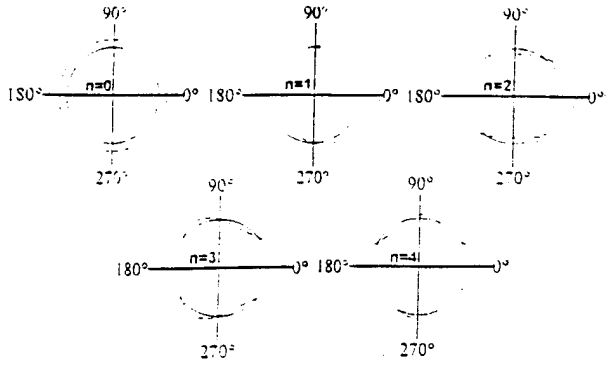

FIG. 5. Mode shapes of first few vibrational modes of the spherical shell, denoted by the number n of nodal circles present.

from the $n=2$ mode that is symmetric about the $\alpha=45°$ diameter (although they occur at the same frequency). On the other hand, the $n=2$ mode that is symmetric about the $\alpha=0°$ diameter is *identical* to the $n=2$ mode that is symmetric about the $\alpha=180°$ diameter. This distinction is important to the discussion given in the next section, because modes that are excited by a point force at $\alpha=0°$ are identical to those that are excited by a point force at $\alpha=180°$.

Figure 6 shows the contributions of individual modes to the radiated power for a single point-force excitation. The modes are orthogonal and are not coupled by the presence of the fluid, so there are no cross terms in the radiated power. Because of high radiation damping, the $n=0$ mode does not display a separate peak in this frequency range, although it does contribute at all frequencies. The $n=1$ mode dominates the radiated power at very low frequencies, which can be considered the "resonant frequency" of the rigid-body mode. The $n=2$, 3, and 4 modes each dominate the response at the frequencies $k_0a=1.14$, 1.44, and 1.64, respectively. These modal contributions are used below to help explain controller performance in terms of modal spillover.

B. ASAC using a single point force

To see whether a single control force can produce significant *global* attenuation, i.e., attenuation throughout the entire radiated field rather than in a localized area, examine how the presence of the control force affects the total radiated power. Figure 7 shows the radiated power spectra due to a unit-magnitude disturbance force at $\alpha=0°$, before and after adding a single control force at $\alpha=180°$ (numerical solution). The control force reduces the radiated power by up to 20 dB at resonance frequencies and at very low frequencies; between resonances the reductions are smaller. There exist several frequencies at which there is no attenuation, a phenomenon that is explored later in this section.

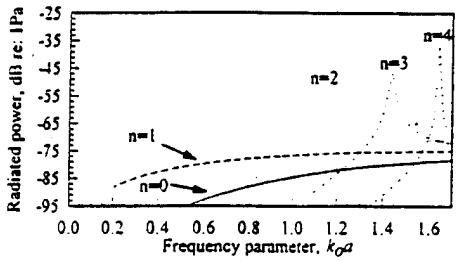

FIG. 6. Modal contributions to radiated power spectrum. The $n=0$ mode does not cause a separate peak in the response because of high radiation damping.

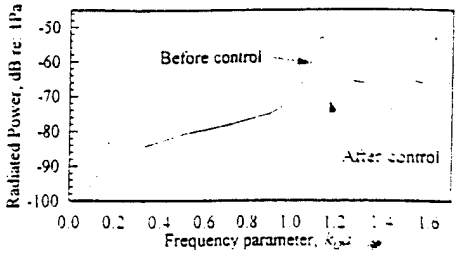

FIG. 7. Radiated power spectrum before and after applying a single control force at $\alpha=180°$. Reductions of up to 20 dB are seen at resonance frequencies and at very low frequencies. Between resonances, little or no attenuation is seen.

Figure 8(a) compares the analytical and numerical solutions for the residual radiated power, that is, the radiated power after the control force has been added. The agreement between the two solutions is excellent, with discrepancies of less than 0.5 dB at frequencies below $k_0a=1.4$. At higher frequencies the levels agree quite well, but exhibit a slight frequency shift consistent with the frequency shift seen in Fig. 2 for the uncontrolled case.

Figure 8(b) compares the analytical and numerical solutions for the control force as a function of frequency. The force varies between $+1$ and -1 for a unit disturbance force; the largest control forces are required at resonance frequencies. Between resonances, the control force drops to zero at frequencies for which there is no reduction in radiated power. The numerical and analytical results agree very closely in levels, although they exhibit the same frequency shift seen in Figs. 2 and 8(a).

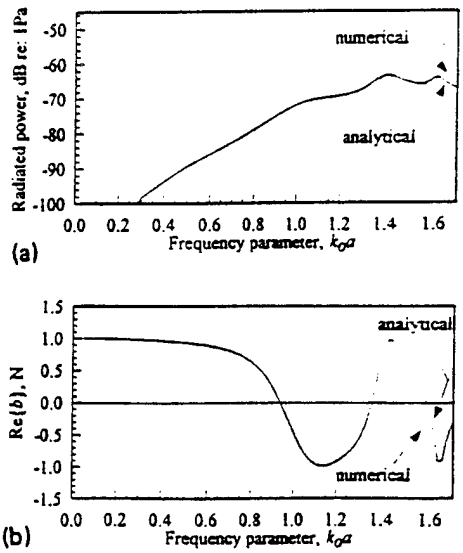

FIG. 8. Comparison of numerical and analytical solutions for (a) radiated power residual vs frequency, and (b) control force. Levels agree well between numerical and analytical solutions; slight frequency shift is observed at higher frequencies. For disturbance force of unit magnitude, control force varies between $+1$ and -1 with extrema occurring at resonance frequencies.

System dynamics can be illustrated by examining the modal components of the radiated power. Recall that the disturbance and control forces are arranged with a spatial separation of 180°, i.e., they act along the same diameter but at opposite poles of the shell. Referring to the earlier discussion of degenerate modes, if equal forces were applied at the disturbance and control locations, they would excite the same modes with the same relative magnitudes. There would, of course, be phase differences as a result of the spatial separation between the two forces. Contributions to even-numbered modes would be in phase with each other, while contributions to odd-numbered modes would be 180° out of phase. Two consequences must be considered in evaluating control performance. First, since all the disturbance modes are either in phase or out of phase with modes excited by the disturbance, the control force will always be purely real for a real disturbance force. Second, if the control force equals the disturbance force, some modal contributions from the disturbance force would be *doubled* in strength by the control force (even-numbered modes) while others would be *cancelled* (odd-numbered modes). If the control force attempted to eliminate the dominant mode, response in other modes could be increased by this "modal spillover."

The column charts in Fig. 9(a)–(c) show the modal contributions to radiated power for $k_0a=1.14$, 0.94, and 1.32, respectively, before and after adding the control force. In Fig. 9(a), the disturbance response is clearly dominated by the $n=2$ mode. The control force, which is out of phase with the disturbance, eliminates the contributions of the $n=2$ mode and, by coincidence, the $n=0$ mode. The response is reduced everywhere both in the far field and on the structure itself, behavior that is often termed "modal suppression" because the dominant radiating mode is cancelled.[7] However, the contributions from the $n=1$ and $n=3$ modes increase by 6 dB. The overall is thus limited because of spillover into modes that happen to be in phase with the control force.

In Fig. 9(b), the frequency is such that the disturbance response contains equal radiated power contributions from the $n=1$ and $n=2$ modes. If the control force attempts to cancel the $n=1$ mode, there is enough spillover into the $n=2$ mode that no net reduction in radiated power takes place. Similarly, the control force cannot achieve net improvements by attempting to cancel the $n=2$ mode. Any nonzero control force only increases the total radiated power, so the optimum solution is to set the control force to zero. Similar situations exist at every frequency for which there is no reduction in radiated power (Fig. 7) and, correspondingly, every frequency for which the control force magnitude is zero [Fig. 8(b)].

In Fig. 9(c) both the $n=2$ and $n=3$ modes contribute, but the larger contribution comes from the $n=2$ mode. The control force partially cancels the $n=2$ mode, but not beyond the balancing point at which spillover into uncontrolled modes would increase the radiated power. The net decrease in radiated power is 3 dB. Interestingly, although the radiated power is reduced, the vibration levels on the shell actually increase slightly. Figure 10 shows the numerically computed surface velocity distribution before and after applying the control force. As in Fig. 3, the solution exhibits relatively

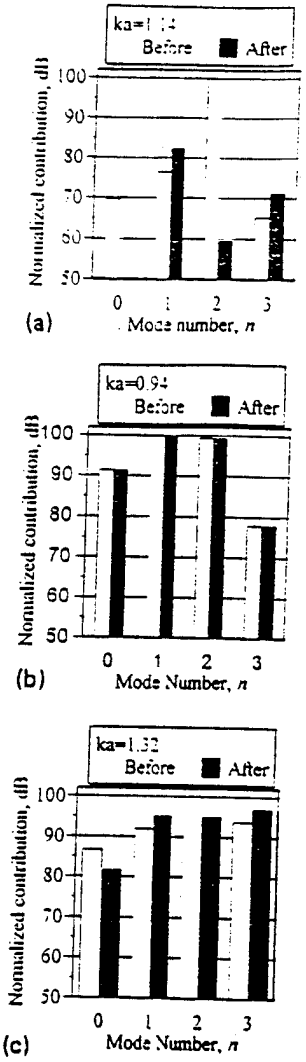

FIG. 9. Modal components of radiated power before and after applying control for (a) $k_0a=1.14$, (b) $k_0a=0.94$, (c) and $k_0a=1.32$. (a) Exhibits modal suppression; the $n=0$ and $n=2$ modes are reduced by 40 dB or more, but the $n=1$ and $n=3$ modes are boosted 6 dB by modal spillover. In (b) no reduction is possible with one control force. In (c) energy is transferred from $n=2$ mode to the less-efficient $n=3$ mode.

large local deformations near the drive points at 0° and 180°. Away from these regions, the surface velocity is actually higher after the control is applied even though the radiated power has decreased. This is similar to "modal restructuring," in which the modal contributions are relatively un-

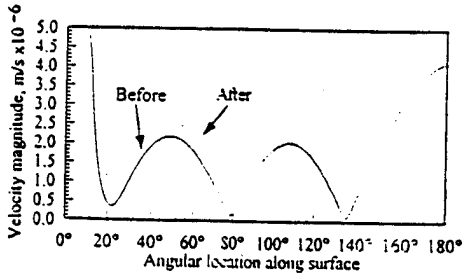

FIG. 10. Surface velocity magnitude before and after applying control force, $k_0a=1.32$. Energy is shifted from $n=2$ mode to less-efficient $n=3$ mode to decrease radiated power, but vibration levels actually increase.

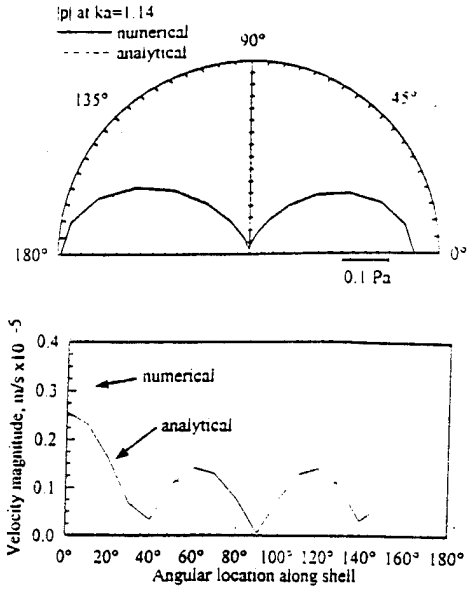

FIG. 11. Comparison of residual response found with analytical vs numerical methods at $k_0a=1.14$ (first resonance frequency). Solid line represents analytical results; the broken line represents numerical results. (a) Shows far-field pressure directivity; (b) shows surface velocity distribution. Far-field solutions agree extremely well. Local deformations near drive points in numerical solution do not propagate to far field, and thus do not affect control behavior.

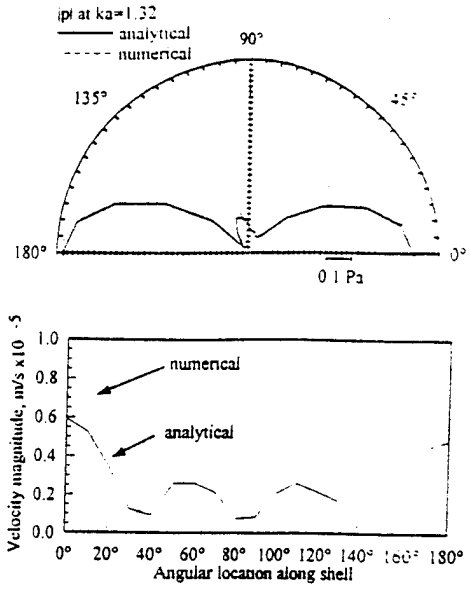

FIG. 12. Comparison of residual response found with analytical vs numerical methods at $k_0a=1.32$. Solid line represents analytical results; the broken line represents numerical results. (a) Shows far-field pressure directivity; (b) shows surface velocity distribution. Far-field solutions agree extremely well. Local deformations near drive points in numerical solution do not propagate to far field, and thus do not affect control behavior.

changed in magnitude but their phases are rearranged to reduce radiation efficiency.[7] In this case, however, energy is merely shifted from a mode that radiates efficiently into another mode with lower radiation efficiency. Modal restructuring cannot take place because the modes, being orthogonal radiators, cannot influence one another.

Numerical accuracy is reflected in part by the agreement between analytical and numerical methods in predicting the residual response, i.e., the response after the control force is applied. Because the controlled radiation levels are small, predicting residuals is often the most stringent test for numerical accuracy, particularly when the residual structural vibration may still be large. Figure 11(a) and (b) show the residual far-field pressure directivity and surface velocity distribution at $k_0a=1.14$, the same frequency examined in Fig. 9(a). Figure 12(a) and (b) show similar plots for $k_0a=1.32$, the same frequency examined in Fig. 9(c). In all cases, the numerical solution reproduces the analytical results to a satisfactory degree, with reasonable agreement on the general character of the residual if not on absolute levels. As seen in Fig. 3, the numerically computed surface velocities near the drive points exhibit significant local deformations that do not appear in the analytical solutions. However, these local surface deformations to not lead to acoustic propagation to the far field, as evidenced by the close agreement between numerically and analytically computed far-field pressure residuals. Overall, the small response levels encountered in predicting residuals to not appear to adversely affect the accuracy of the numerical approach.

C. ASAC using multiple forces

The results of the previous section imply that off-resonance frequencies require multiple control forces, since multiple modes contribute to the radiation. This inference is supported by Fig. 13, which shows numerical predictions of the system performance with multiple actuators. The solid line represents the disturbance response; the other lines represent the controlled response with one, two, four, and seven control forces. Each configuration has one control force at $\alpha=180°$. The configurations with two, four, and seven forces also have control forces evenly spaced at intervals of 90°, 35°, and 25° respectively. Controller performance increases markedly as more control forces are added. This is especially true at off-resonance frequencies where multiple modes are present and thus multiple forces are required to control the radiation. Four control forces can achieve roughly 10 dB attenuation at $k_0a=0.94$, where a single actuator achieves no attenuation. Increasing the number of control forces to seven gives attenuations of 6 dB or more throughout the entire frequency range.

It should be noted here that no attempt has been made to

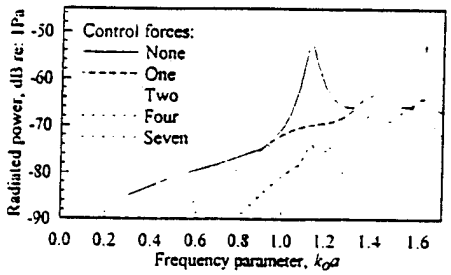

FIG. 13. Radiated power spectrum with multiple control forces. Solid line represents response with no control. Other lines represent response with one, two, four, and seven control forces. Increasing number of control forces improves performance, especially between resonances where multiple modes contribute to the response.

optimize the locations of the control forces. Similar reductions could likely be obtained with a smaller number of optimally placed control forces. The number of control forces needed could be as low as one control force per contributing mode, if control force locations were optimized so that each force could control a separate mode with no spillover into other modes.

III. SUMMARY

The primary research goal is to develop a computer program for investigating active structural-acoustic control (ASAC) of three-dimensional, fluid-loaded structures, and check its performance by investigating an example structure. For generality, a numerical approach is used to calculate structural-acoustic dynamic responses. The feedforward control approach used is based on minimizing the radiated power at a single frequency. The example structure chosen is a thin-walled, fluid-loaded, spherical shell, and numerical results are compared to an analytical solution.

The analytical and numerical models for the spherical shell agree well both in response characterizations and in solutions to the active control problem. Numerical and analytical solutions for the uncontrolled response display excellent agreement below $k_0a=1.4$, with some frequency shifting in the region $1.4<k_0a<1.7$. Predictions of controller performance, including control forces and reductions of radiated power, agree well but are subject to the same frequency shift. Short-wavelength structural responses that appear in the numerical solution but not the analytical solution do not affect the far-field behavior, and therefore do not affect the controller performance. Numerical predictions of residual responses agree with analytical predictions to the same extent that uncontrolled predictions agree. In general, the results give confidence that the methods described could be used to examine other, more complicated structures for which no analytical models exist.

For the spherical shell, ASAC is an efficient method for controlling radiated noise at low frequencies ($0<k_0a<1.7$). At resonance frequencies, radiation due to a point-force disturbance can be reduced by up to 20 dB using only one actuator. The mechanism for reducing radiated power on-resonance is modal suppression, in which the dominant response mode is completely suppressed. Between resonances, multiple actuators are required to obtain large reductions. The main mechanism for reducing radiated power off-resonance is that energy is transferred to less-efficient modes, which can actually increase vibration levels. Increasing the number of control forces improves controller performance. With seven control forces, attenuations of at least 6 dB can be obtained over the entire frequency range $0<k_0a<1.7$.

ACKNOWLEDGMENTS

This project is part of a doctoral program made possible by the Extended-Term Training Program at the Carderock Division, Naval Surface Warfare Center. The work has also been funded by the Office of Naval Research through Grant No. ONR-N00014-92-J-1170.

[1] C. R. Fuller, "Apparatus and method for global noise reduction," US Patent No. 4,715,599 (1987).
[2] C. R. Fuller, "Active control of sound transmission radiation from elastic plates by vibration inputs: I. Analysis," J. Sound Vib. 136, 1–15 (1990).
[3] C. R. Fuller and J. D. Jones, "Experiments on reduction of propeller-induced interior noise by active control of cylinder vibration," J. Sound Vib. 112, 389–395 (1987).
[4] C. Guigou and C. R. Fuller, "Active control of sound radiation from a simply supported beam: Influence of bending near-field waves," J. Acoust. Soc. Am. 93, 2716–2725 (1993).
[5] R. Clark and C. R. Fuller, "Control of sound radiation with adaptive structures," J. Intelligent Mater. Syst. Struct. 2, 431–452 (1991).
[6] Y. Gu and C. R. Fuller, "Active control of sound radiation due to subsonic wave scattering from discontinuities on fluid-loaded plates. I: Far-field pressure," J. Acoust. Soc. Am. 90, 2020–2026 (1991).
[7] C. R. Fuller, C. H. Hansen, and S. D. Snyder, "Active control of sound radiation from a vibrating rectangular panel by sound sources and vibration inputs: An experimental comparison," J. Sound Vib. 145, 195–215 (1991).
[8] G. C. Everstine and A. J. Quezon, "User's guide to the coupled NASTRAN/Helmholtz equation capability (NASHUA) for acoustic radiation and scattering," CDNSWC-SD-92-17, Carderock Division, NSWC, Bethesda, MD (1992).
[9] C. G. Molo and R. J. Bernhard, "Generalized method of predicting optimal performance of active noise controllers," AIAA J. 27, 1473–78 (1989).
[10] K. A. Cunefare and G. H. Koopmann, "A boundary element approach to optimization of active noise control sources on three-dimensional structures," Trans. ASME J. Vib. Acoust. 113, 387–394 (1991).
[11] C. E. Ruckman and C. R. Fuller, "Numerical simulation of active structural-acoustic control for a fluid-loaded spherical shell," Proceedings of the Second International Congress on Recent Developments in Air- and Structure-Borne Sound and Vibration, Auburn University, 1992, edited by M. J. Crocker and P. K. Raju (unpublished), pp. 377–385.
[12] M. C. Junger and D. Feit, *Sound, Structures, and Their Interaction* (MIT, Cambridge, 1986), 2nd ed.

C-26 The Effect of Distributed or Discrete Pressure and Acceleration Sensors on Active Structural-Acoustic Control Systems, B.-T. Wang and C. R. Fuller, Journal of the Chinese Society of Mech. Eng., Vol. 15 No. 1, pp. 30-39, 1994.

中國機械工程學刊第十五卷第一期第 30~39 頁（民國八十三年）
Journal of the Chinese Society of Mechanical Engineers, Vol.15, No.1, pp.30~39 (1994)

The Effect of Distributed or Discrete Pressure and Acceleration Sensors on Active Structural-Acoustic Control Systems

Bor-Tsuen Wang* and Chris R. Fuller**

Keywords: adaptive feedforward control, cost function, structural acoustics, wavenumber, radiation efficiency.

ABSTRACT

This paper presents four types of cost functions, which are based on the use of distributed or discrete pressure and acceleration sensors, for structural sound radiation control in conjunction with the use of the LMS control algorithm. In order to study the influence of cost functions, a system consists of baffled simply-supported plate radiating into a half space is analytically considered. The disturbance input is a harmonic point force, while control is applied by piezoelectric actuators bonded to the structure. The error sensors are either accelerometers, microphones or distributed sensors. To compare the control effectiveness and mechanism of these cost functions, excitation on-resonance and off-resonance was considered. Both the radiation directivity pattern and plate displacement distribution were obtained as well as the average radiation efficiency and radiated power. Additionally, plate wavenumber analysis is also discussed. This work shows that distributed sensors generally perform better than discrete sensors, and pressure sensors are shown to have considerable advantages over acceleration sensors in structural sound radiation control.

INTRODUCTION

Active noise control has been increasingly used and shown to be effective in attenuating low-frequency sound. The LMS adaptive feedforward control approach has also been successfully applied to active structural-acoustic control (ASAC) (Burgess, 1981; Elliott et al., 1987; Erikson et al., 1987). To construct a LMS adaptive controller, a quadratic cost function is generally formulated as the error criterion. Quadratic optimization theory is then applied to minimize the cost function so as to adjust control signals to actuators in order to attenuate the structural sound radiation due to a noise input. The total radiated power is usually chosen as the cost function for theoretical formulations (Fuller, 1988; Dimitriadis and Fuller, 1989; Wang et al., 1990). Although this type of cost function indicates the highest possible attenuation, the total radiated power is not measurable in practice. Fuller et al. (1989) proposed the use of discrete microphones in the radiation far-field as well as accelerometers mounted on the vibrating structure surfaces to serve as error sensors. They experimentally demonstrated the performance of both types of error sensors for active control of sound transmission through an elastic plate by applying vibrational forces directly to the structure. Error microphones in the radiated field which provide acoustic information were shown to be generally advantageous over error accelerometers on the plate.

This paper presents four types of cost functions, which are based on the use of distributed or discrete pressure and acceleration sensors, for ASAC in conjunction with the use of the LMS adaptive control algorithm. In order to study the influence of cost functions, a system consisting of baffled simply-supported plate radiating into a half space is analytically considered. The disturbance input is a harmonic point force, while control is applied by piezoelectric actuators bonded to the structure. The error sensors are either accelerometers, microphones or distributed sensors. To compare the control effectiveness and mechanism inherent in these cost functions, excitation on-resonance and off-resonance was considered. Both the radiation directivity pattern and plate displacement distribution were obtained as well as the average radiation efficiency and radiated power. Additionally, plate wavenumber analysis is also discussed. This

Paper Received October, 1991. Accepted December, 1993. Author for Correspondence: B. T. Wang.

* *Associate Professor, Department of Mechanical Engineering, National Pingtung Polytechnic Institute, Pingtung, Taiwan, ROC.*

** *Professor, Department of Mechanical Engineering, Virginia Polytechnic Institute and State University, Virginia, USA.*

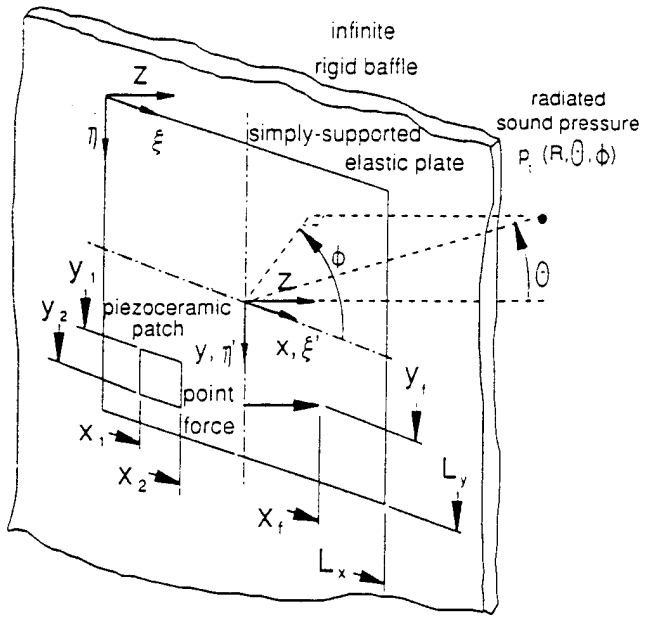

Fig.1. Arrangement and coordinates of the system.

work shows that distributed sensors generally perform better than discrete sensors, and pressure sensors are shown to have considerable advantages over acceleration sensors in ASAC.

THEORETICAL ANALYSIS

Plate Vibration for Noise and Control Inputs

Figure 1 shows the arrangement and coordinates of the system. Point forces considered as noise sources were used to excite the plate, and piezoelectric actuators considered as control sources were applied to control the plate sound radiation. Under the assumption of harmonic excitation, the displacement of the simply-supported plate can be written as:

$$w(\xi,\eta,t)=e^{j\omega t}\sum_{m-1}^{\infty}\sum_{n=1}^{\infty}W_{mn}\sin\left(\frac{m\pi}{L_x}\xi\right)\sin\left(\frac{n\pi}{L_y}\eta\right), \tag{1}$$

where $W_{mn}=P_{mn}/\rho_p h(\omega_{mn}^2-\omega^2)$, ω_{mn} are natural frequencies, ρ_p is the plate density, h the plate thickness, and P_{mn} the modal force which depends on the exact description of the applied external load. The expressions of modal forces corresponding to point force and piezoceramic actuator inputs are given in Wang (1991).

Sound Radiation

The radiated sound pressure can be evaluated from the Rayleigh integral which relates the plate velocity to the transmitted pressure. An approximate closed-form solution for this integral can be obtained in the far-field (Junger and Feit, 1986; Roussos, 1985). For N_s noise sources (point forces) or N_c piezoelectric actuators, the sound pressure radiated to a point, $p(R,\theta,\phi)$, in the far-field for light fluid loading can be derived as follow:

Noise sources:

$$p_n(R,\theta,\phi)=K\sum_{j=1}^{N_s}\sum_{m=1}^{\infty}\sum_{n=1}^{\infty}W_{mnj}^{f}I_mI_n, \tag{2}$$

Control sources:

$$p_c(R,\theta,\phi)=K\sum_{j=1}^{N_c}\sum_{m=1}^{\infty}\sum_{n=1}^{\infty}W_{mnj}^{c}I_mI_n, \tag{3}$$

where the constant K and the quantities I_m and I_n can be found in Roussos (1985) as functions of (R,θ,ϕ). When the noise sources and the piezoelectric actuators act simultaneously, the total sound pressure field can be viewed as a superposition of the above given sound pressures for steady-state harmonic excitation (i.e., $p_t=p_n+p_c$).

Cost Function

The possible candidates of the cost function used in sound radiation control corresponding to different types of sensors can be as follows:

Distributed pressure sensors:

$$\Phi_p=\int_s|p_t|^2R^2\sin\theta d\theta d\phi, \tag{4}$$

Discrete pressure sensors:

$$\Psi_p=\sum_{i=1}^{N_{mic}}|p_{t_i}(R_i,\theta_i,\phi_i)|^2, \tag{5}$$

Table 1. Natural frequency of simply supported plate (Hz).

m\n	1	2	3	4	5
1	87.71	249.81	519.98	898.22	1384.53
2	188.74	350.85	621.02	999.25	1485.56
3	357.13	519.23	789.40	1167.64	1653.95
4	592.88	754.98	1025.15	1403.39	1889.69
5	895.98	1058.08	1328.25	1706.48	2192.79

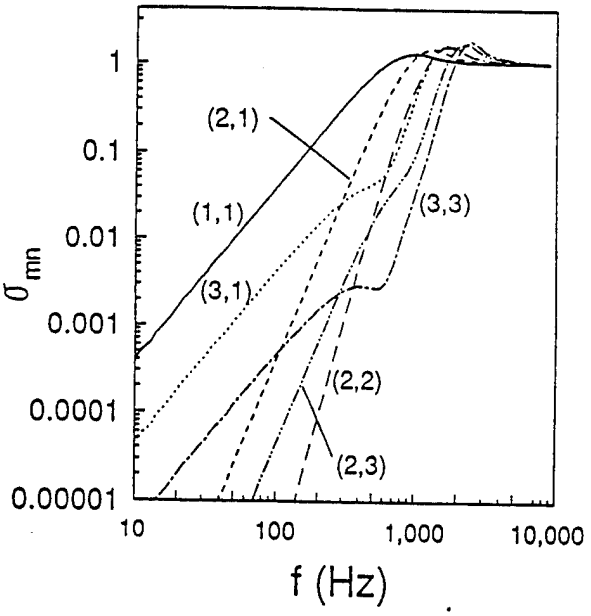

Fig.2. Radiation efficiency vs. frequency.

$y_1 = 0.130m$, $y_2 = 0.170m$. When a single error sensor was used, a microphone at $(R, \theta, \phi) = (1.8m, 0°, 0°)$ in the far-field or an accelerometer at $(x, y) = (0.19m, 0.15m)$ on the plate is considered.

Radiation Efficiency of the (m, n) Mode

Figure 2 shows the (m, n) mode radiation efficiency for the plate under consideration plotted against the excitation frequency. The $(1, 1)$, $(3, 1)$ and $(3, 3)$ modes, (the odd-odd modes), have higher radiation efficiencies than the $(2, 1)$, $(2, 3)$, (the odd-even and even-odd modes), and the $(2, 2)$ modes, (the even-even mode). This indicates that the odd-odd modes are the effective radiating modes with strongly acoustic coupling between sound radiation and mechanical vibration, and the even-even modes, subjected to radiation cancellation, have smaller radiation efficiencies. When the excitation frequency is greater than the modal critical frequency, the radiation efficiencies approach asymptotically to unity. The surprising observation from Fig.2 is that the $(2, 1)$ mode radiation efficiency is greater than the $(3, 1)$ mode radiation efficiency between $300Hz$ and $1000Hz$ which is within our study range ($357Hz$ for the $(3, 1)$ resonance mode). The $(2, 1)$ mode, previously thought to be a less effective radiator, actually has significant contribution.

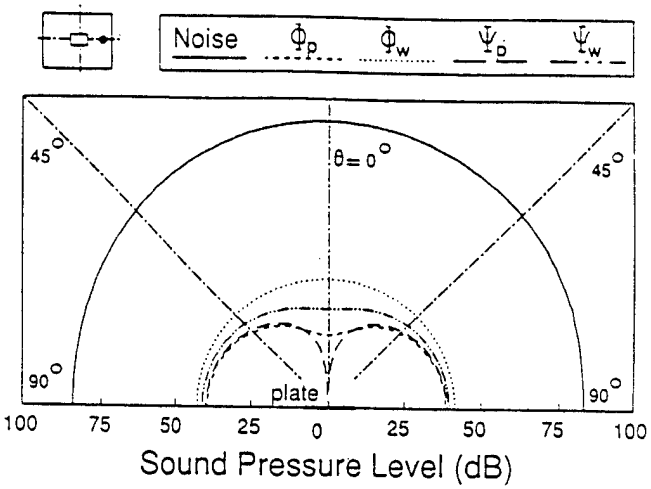

Fig.3. Radiation directivity pattern, $f = 357Hz$.

On-Resonance Excitation

Figure 3 shows the radiation directivity of the noise with a excitation frequency of $357Hz$ near the $(3, 1)$ mode resonance point. The system arrangement is sketched on the top of Fig.3. The noise radiation directivity, denoted by a solid line, can be seen to be fairly constant with radiation angle. This behavior is due to the relatively long wavelength of the acoustic radiation relative to plate size, leading to the higher order plate $(3, 1)$ mode giving a radiating field which is volumetric or monopole like.

If the distributed pressure sensors over a hemisphere of radiating field are used, the corresponding cost function (Φ_p) can be constructed as defined in Eq.(4). The sound pressure level can be thus reduced globally over the radiating field as it is observed at all angles. The residual radiation directivity exhibits a combination of the $(1, 1)$ and $(2, 1)$ mode responses. If a discrete pressure sensor (the corresponding cost function, Ψ_p, defined in Eq.(5)) is used and located at $(R, \theta, \phi) = (1.8m, 0°, 0°)$, the residual radiation directivity reveals a dipole response, because the sound pressure at the location of the error microphone is reduced to zero. Similarly, a distributed or discrete acceleration sensor, located at $(x, y) = (0.19m, 0.15m)$,

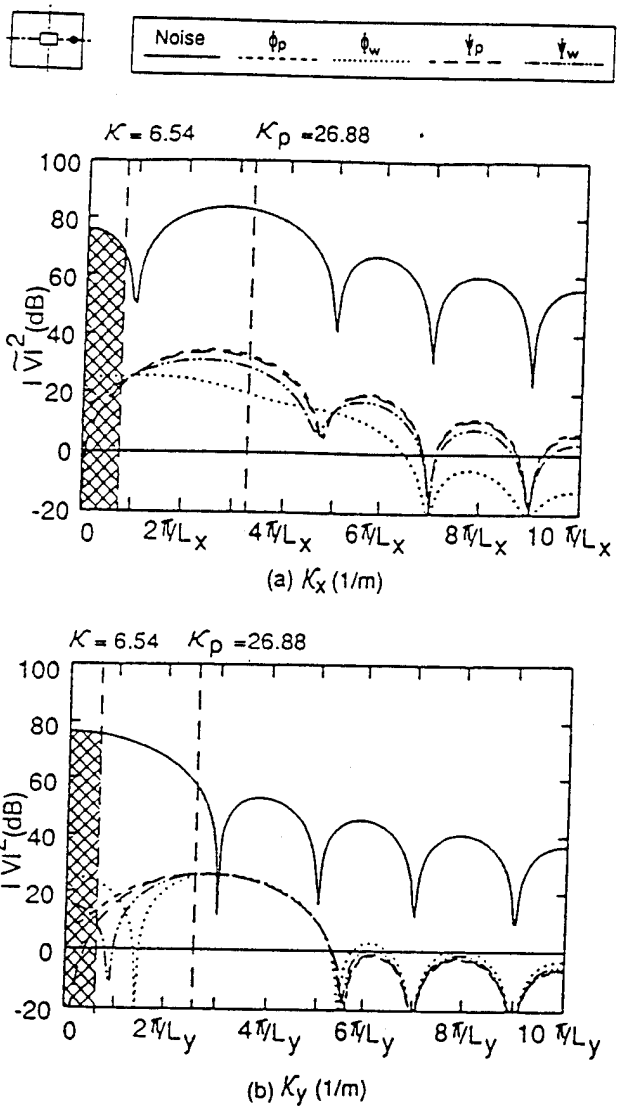

Fig.5. Wavenumber spectra of plate velocity, $f = 357Hz$.

that the oscillations in the spectral distributions at low wavenumbers has been smoothed. This indicates that the residual plate-baffle response is dominated by high wavenumber components or short wavelength, higher modal order motion. Thus two control mechanisms are observed. The first, termed "modal suppression" (Fuller et al., 1991), implies that the plate response falls globally and corresponds to a fall in wavenumber components across the complete spectrum. The second, termed "modal restructuring" (Fuller et al., 1991), implies that the plate residual response becomes more complex (higher modal order) with a lower radiation efficiency. Conversely "modal restructuring" corresponds to a decrease in the supersonic wavenumber components while the subsonic components remain unchanged or even increase. Such

Table 3. Summary of off-resonance excitation case.

cost function form	control voltages V(volts)	average radiation efficiency	reduction of cost function(dB)	reduction of radiated power (dB)
	Off-resonance excitation, f = 272 Hz			
Disturbance		0.01275		
Φ_p	6.3449	0.00885	0.82	0.82
Φ_w	16.573	0.04977	1.03	-4.88
Ψ_p	4.7574	0.00938	152.85	0.77
Ψ_w	17.572	0.05296	153.63	-5.16

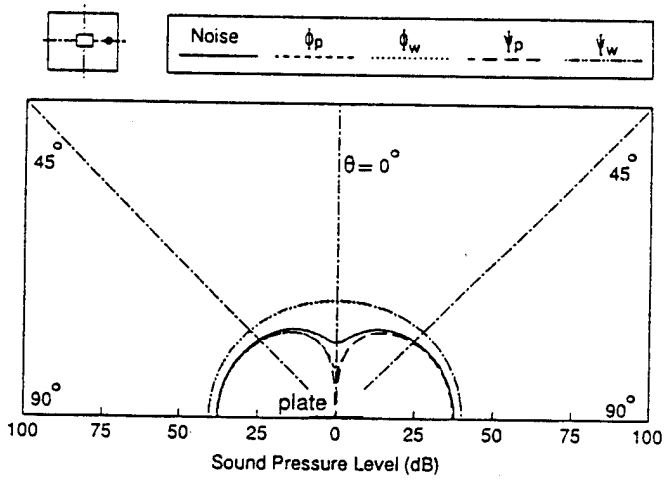

Fig.6. Radiation directivity pattern, $f = 272Hz$.

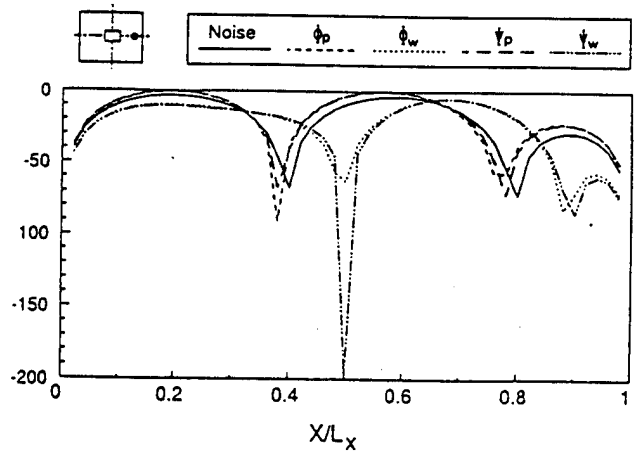

Fig.7. Plate displacement distribution, $f = 272Hz$.

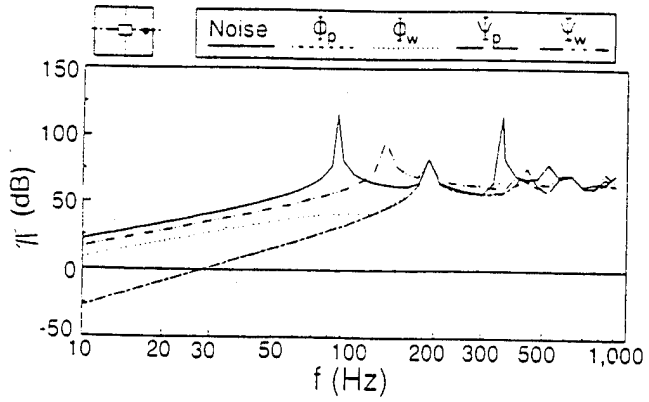

Fig.9. Radiated power vs. frequency.

discussed previously, above this line the wavenumber components recognized as subsonic waves do not contribute to the sound radiation; however, supersonic waves, i.e., wavenumber components below the acoustic wavenumber, do radiate to the far-field. In the case of using pressure sensors, the supersonic components have been reduced while the subsonic components were increased. This results in a small amount of radiated power reduction as shown in Table 3, and the phenomenon is termed "modal restructuring", i.e., the plate vibration pattern becomes close to the $(3,1)$ mode, as seen in Fig.7. In other words, the significant radiation modes have been changed to less efficient mode radiators due to the change of plate vibration pattern, and this change, thus, leads to a reduction or radiated power. In particular, the wavenumber spectrum equals to zero at $\kappa_x = \kappa_y = 0$ (where $\kappa_x = \kappa \cos\theta \sin\phi$ and $\kappa_y = \kappa \sin\theta \sin\phi$), with the discrete pressure sensor located at $(1.8m, 0°, 0°)$. When the pressure is minimized in the far-field at a particular angle, the corresponding wavenumber component to that angle is suppressed. In the case of using acceleration sensors, the subsonic components have been reduced while the supersonic components were increased. The increase at $\kappa_x = \kappa_y = 0$ especially indicates spillover of control energy into the $(1,1)$ mode. This explains why the residual radiation directivity reveals a monopole response in the case of using acceleration sensors as shown in Fig.6. Figure 8(b) shows the similar plot along the κ_y axis. The disturbance denoted by a solid line reveals a $n = 1$ dominant mode pattern, i.e., the $(3,1)$ mode. Again, the analysis of wavenumber spectra also demonstrates that pressure sensors perform better than acceleration sensors. In effect, the distributed far-field pressure sensor acts as distributed structural-wavenumber sensor. They observe every radiating point on the plate and also every supersonic wavenumber component while not observing the subsonic components.

Cost Function Performance Versus Frequency

Figure 9 shows the radiated power for the noise with and without control plotted against the excitation frequency for different forms of cost functions corresponding to the previous case. The solid line denotes the noise and reveals several peaks, such as at 87, 190, 357, 520 and $620Hz$, which are near the natural frequencies of the simply-supported plate. In the case of using pressure sensors, both discrete and distributed sensors have about the same residual radiated power, and a large amount of power reduction is achieved below $180Hz$ near the $(2,1)$ mode. For higher frequency excitation, since more high modal responses contribute to the sound radiation, only a slight reduction can be achieved for using just one actuator. Additionally, there is no improvement at excitation of the even modes, such as the $(2,1)$, $(2,2)$, $(4,1)$ and $(4,2)$ modes, because of the central location of the piezoelectric actuator. Of course, attenuation could be achieved with multiple, appropriately located actuators as shown previously (Wang et al., 1990).

In the case of using acceleration sensors, the radiated power has been attenuated at low frequency range, but the reduction is not as much as that using pressure sensors. The distributed acceleration sensor, located over the plate, generally performs better than the discrete acceleration sensor, located at the center of the plate. For the discrete acceleration sensor, the radiated power increases between 105 and $190Hz$, i.e., between the $(1,1)$ and $(2,1)$ modes, while the radiated power decreases for other selection of sensors. This is because the accelerometer cannot effectively observe the plate response at the central location in this range of excitation frequency, where the $(2,1)$ mode dominates the plate response. The residual radiated power in the case of using distributed acceleration sensors is close to that of using pressure sensors between 110 and $190Hz$, but is higher at frequencies below $110Hz$. This can be explained by the observation that controlling the $(1,1)$ plate modal response is not effective in the reduction of sound radiation within this range. However, controlling the $(2,1)$ plate modal response is effective since the $(2,1)$ mode is the dominant radiator to radiated field in this frequency band.

Figure 10 shows the average radiation efficiency plotted against the frequency corresponding to the cases of Fig.9. The average radiation efficiency generally agrees with the radiated power because of the

Fuller, C. R., Hansen, C. H., and Snyder, S. D., "Active Control of Sound Radiation From a Vibrating Rectangular Panel by Sound Sources and Vibration Inputs: an Experimental Comparison," *Journal of Sound and Vibration*, Vol.14, No.2, pp.195-215 (1991).

Junger, M. C., and Feit, D., *Sound, Structures and their Interaction*, 2nd ed., MIT press, Cambridge, MA (1986).

Lester, H. C., and Fuller, C. R., "Active Control of Propeller Induced Noise Fields Inside a Flexible Cylinder," *AIAA Journal*, Vol.28, No.8, pp.1374-1380 (1990).

Roussos, L. A., "Noise Transmission Loss of a Rectangular Plate in an Infinite Baffle," *NASA Technical Paper 2398* (1985).

Wallace, C. E., "Radiation Resistance of a Rectangular Panel," *Journal of Acoustical Society of American*, Vol.51, pp.946-952 (1972).

Wang, B.-T., Dimitriadis, E. K., and Fuller, C. R., "Active Control of Structurally Radiated Noise Using Multiple Piezoelectric Actuators," *Proceedings of the AIAA/ASME/ASCE/AHS 31st Structures, Structural Dynamics and Materials Conference*, Long Beach, CA, AIAA-90-1172 (1990).

Wang, B.T., "Active Control of Sound Transmission/Radiation from Elastic Plates Using Multiple Piezoelectric Actuators, " PhD Dissertation, VPI & SU, Blacksburg, Virginia, (1991).

均佈或零散之聲壓及加速度感應器在主動結構噪音控制系統之效應

王栢村* Chris R. Fuller**

* 國立屏東技術學院機械工程技術系

** 美國維州理工暨州立大學機械系

摘 要

此篇報告提出四種型態的成本函數用於結構聲音幅射控制，配合最小平方自調式控制法，此成本函數乃基於所使用之均佈或零散的壓力或加速度感應器而定，為研究成本函數的影響，以一阻隔之簡支板的聲音幅射做理論性之分析，以協振點力為干擾源，而以壓電驅動器黏貼在結構上做為控制源，誤差感應器則用加速度感應器，麥克風，或者均佈式感應器。為比較各成本函數的控制效果及其控制形態，激振於共振點和非共振點都同時考慮，而得到聲音幅射方向型譜，板位移分佈，平均聲音幅射效率和聲音幅射能。另外板波數分析也同時探討。此篇報告證明，在結構聲音幅射控制中，均佈感應器通常優於零散感應器，而壓力感應器也有相當程度地優於加速度感應器。

C-27 Modeling of Induced strain actuation of shell structures, Z. Chaudhry, F. Lalande and C. A. Rogers, Journal of the Acoustic Society of America, Vol. 97 No. 5 Part 1, pp. 2872-2877, May 1995.

Modeling of induced strain actuation of shell structures

Zaffir Chaudhry, Frederic Lalande, and Craig A. Rogers
Center for Intelligent Material Systems and Structures, Virginia Polytechnic Institute and State University, Blacksburg, Virginia 24061-0261

(Received 25 May 1994; accepted for publication 17 November 1994)

Based on the thin-shell Donnell theory, a model to represent the action of discrete induced strain actuator patches symmetrically bonded to the surface of a circular cylindrical shell has been developed. The model provides estimates of the bending curvatures due to the out-of-phase actuation and the in-plane strains due to the in-phase actuation of the bonded actuator patches. The magnitudes of the induced curvature and the in-plane strain are found to be identical to those of plates; however, due to the strain-displacement relations in cylindrical coordinates, the in-plane and out-of-plane displacements are coupled. Expressions for the equivalent forces and moments that represent the action of the actuator patches have been developed. Due to the curvature of the shell, the representation of the in-phase actuation with an equivalent in-plane line force applied along the edge of the actuator results in the application of erroneous rigid-body transverse forces. To avoid these rigid body forces, a method to represent the in-phase actuation with a system of self-equilibrating forces is proposed. The action of the actuator is then represented by an equivalent in-plane force and a transverse distributed pressure applied in the region of the actuator patch. Finite element verification of the proposed model is presented. The displacements due to the actual actuator actuation are compared with the proposed model, and very good agreement is found.

PACS numbers: 43.40.Ey, 43.40.Tm

INTRODUCTION

In recent years there has been a great surge of interest in research on shape, vibration, and acoustic control of structures with induced strain actuators like piezoelectric materials and shape memory alloys. What distinguishes induced strain actuators from conventional hydraulic and electrical actuators, and makes them especially attractive for smart structures, is their ability to change their dimensions and properties without utilizing any moving parts. These actuator materials contract and expand just like the muscles in the human body. When integrated into a structure (either through embedding or through surface-bonding), they apply localized strains and directly influence the extensional and bending responses of the structural elements. Because of the absence of mechanical parts they can be easily integrated into the base structure. Integration within the structure ensures an overall force equilibrium between the forcing actuator and the deforming structure, thus precluding any rigid body forces and torques.

Induced strain actuators, like piezoelectric materials when bonded to the surface of a structure, generate a set of forces which are concentrated close to the edges of the actuator. Therefore, their action is often represented by line moments or forces applied along the periphery of the actuator. This representation simplifies analysis because the structure does not have to be discretized (to represent the nonuniform structural properties in the regions of the patches) and global structural equations can be solved with the actuator forces appearing as discretely applied external forces. This analysis method, although approximate (approximate because the actuator mass and stiffness are not represented and actuator forces derived from static and stress-free boundary conditions are used), gives reasonably accurate results for small and thin patches of actuators. Also, for the case of straight structural members like beams and plates, it does not pose any problems such as the equivalent actuator forces producing rigid-body motion. For shell-type structures, however, due to their curvature, this simple representation is not appropriate for the case of in-phase actuation. In-phase actuation refers to the case when the two actuators bonded to the top and bottom surface of the shell are activated to produce strains in the same direction. Because the circumferential forces used to represent the action of the actuator are not colinear they produce rigid-body transverse forces on the shell. Thus certain special modifications must be made to such a representation scheme to accommodate the special characteristics of the shell structures. The modification proposed and verified in this paper is the application of a uniform transverse pressure across the footprint of the actuator.

To date, a number of models to represent the action of actuators on beams and plates have been proposed.[1-5] For shells, the only models that have been developed are based on layered shell theory, i.e., the analytical model assumes that the induced strain actuator material comprises a total, distinct layer of the shell.[6,7] In the work that has been reported on vibration and acoustic control of shells using piezoelectric actuators, plate models are often adapted to shells.[8,9] At first sight, this adaptation seems perfectly reasonable because the shell is thin and r/h is large. This does, however, pose a problem for the representation of in-phase actuation forces because the actuator forces are no longer colinear as in the case of beams and plates, and as stated earlier, this results in a rigid-body force being applied to the shell (see Fig. 1). If this is not recognized, then the action of in-phase actuation of even a small actuator patch will result in an erroneous response and can lead to a totally wrong

 0001-4966/95/97(5)/2872/6/$6.00 © 1995 Acoustical Society of America

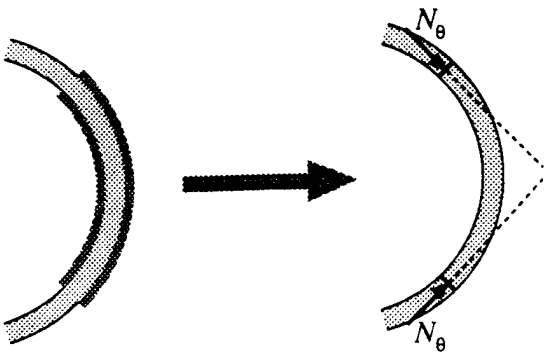

FIG. 1. Nonequilibrium of discrete tangential forces in shell structures.

solution. In a recent model for curved piezoelectric actuators, Sonti and Jones[10] also recognized this fact and showed the necessity of including a uniform transverse pressure, in addition to the axial and tangential forces, to correctly represent the action of in-phase actuation.

A model has been developed to compute the equivalent forces and moments applied by a pair of symmetrically bonded actuator pairs, and is described here. This is followed by a discussion of the special considerations for shell-type structures. The development of the model is similar to the work of Crawley and Lazarus[1] for plates, and relies on classical lamination theory (CLT).

I. MODEL FORMULATION

A model describing the interaction between surface-bonded actuators and a circular cylindrical shell has been developed based on Donnell's theory. For completeness a short derivation of the accompanying equations of motion is also presented. Consider a thin circular cylindrical shell, as shown in Fig. 2. We start with the following Donnell's assumptions $(1+z/R=1,\ r\to R)$ for the kinematics of deformation:

$$u(x,\theta,z)=u^0(x,\theta)-z\,\frac{\partial w^0}{\partial x}, \tag{1}$$

$$v(x,\theta,z)=v^0(x,\theta)-z\,\frac{\partial w^0}{R\ \partial\theta}, \tag{2}$$

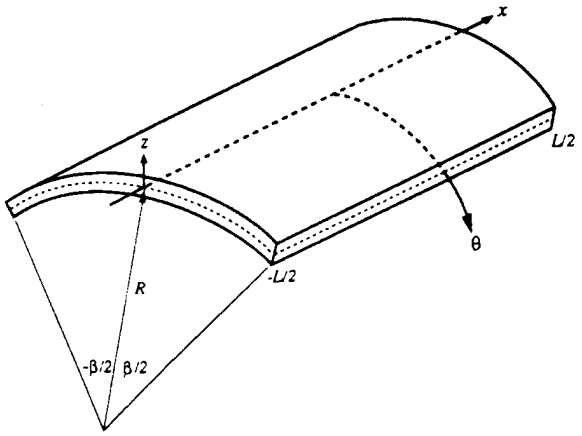

FIG. 2. Thin circular cylindrical shell coordinate system.

$$w(x,\theta,z)=w^0(x,\theta). \tag{3}$$

In the above, z is the local thickness coordinate, measured from the middle surface of the shell. The superscript zero denotes displacements of the cylindrical panel's middle surface. The pertinent strain–displacement relations in cylindrical coordinates are as follows:

$$\epsilon_x=\frac{\partial u}{\partial x}=\epsilon_x^0+z\kappa_x,\quad \epsilon_x^0=\frac{\partial u^0}{\partial x},\quad \kappa_x=-\frac{\partial^2 w^0}{\partial x^2}, \tag{4}$$

$$\epsilon_\theta=\frac{\partial v}{R\ \partial\theta}+\frac{w}{R}=\epsilon_\theta^0+z\kappa_\theta,\quad \epsilon_\theta^0=\frac{\partial v^0}{R\ \partial\theta}+\frac{w^0}{R},$$
$$\kappa_\theta=-\frac{\partial^2 w^0}{R^2\ \partial\theta^2}, \tag{5}$$

and

$$\gamma_{x\theta}=\frac{\partial v}{\partial x}+\frac{\partial u}{R\ \partial\theta}=\gamma_{x\theta}^0+z\kappa_{x\theta},\quad \gamma_{x\theta}^0=\frac{\partial v^0}{\partial x}+\frac{\partial u^0}{R\ \partial\theta},$$
$$\kappa_{x\theta}=-2\,\frac{\partial^2 w^0}{\partial x\ R\ \partial\theta}. \tag{6}$$

The resultant force–strain relations for a layered composite laminate are given by[11]

$$\begin{Bmatrix} N \\ M \end{Bmatrix}=\begin{bmatrix} A & B \\ B & D \end{bmatrix}\begin{Bmatrix} \epsilon^0 \\ \kappa \end{Bmatrix}-\begin{Bmatrix} N_\Lambda \\ M_\Lambda \end{Bmatrix}, \tag{7}$$

where

$$\{N_\Lambda\}=\int [\bar{Q}]\{\Lambda\}dz, \tag{8}$$

$$\{M_\Lambda\}=\int [\bar{Q}]\{\Lambda\}z\ dz \tag{9}$$

are the equivalent of thermal forces in CLT. Note that Λ is the free induced strain developed in the actuator in response to an applied voltage $(\Lambda_x=Ed_{3x}=Vd_{3x}/t_a)$. The three governing equilibrium equations are:

$$\frac{\partial N_x}{\partial x}+\frac{\partial N_{x\theta}}{R\ \partial\theta}-m\ddot{u}=0, \tag{10}$$

$$\frac{\partial N_{x\theta}}{\partial x}+\frac{\partial N_\theta}{R\ \partial\theta}-m\ddot{v}=0, \tag{11}$$

and

$$\frac{\partial^2 M_x}{\partial x^2}+2\,\frac{\partial^2 M_{x\theta}}{\partial x\ R\ \partial\theta}+\frac{\partial^2 M_\theta}{R^2\partial\theta^2}-\frac{N_\theta}{R}-m\ddot{w}=q, \tag{12}$$

with boundary conditions at $x=\pm L/2$ and $\theta=\pm\beta/2$. For an unconstrained symmetric panel with no externally applied forces or moments, i.e., $N,\ M=0$, Eq. (7) reduces to

$$\begin{Bmatrix} \epsilon^0 \\ \kappa \end{Bmatrix}=\begin{bmatrix} A & B \\ B & D \end{bmatrix}^{-1}\begin{Bmatrix} N_\Lambda \\ M_\Lambda \end{Bmatrix}. \tag{13}$$

For a symmetric shell $(B=0)$, the above equations are uncoupled, and

$$\{\epsilon^0\}=[A]^{-1}\{N_\Lambda\}, \tag{14}$$

$$\{\kappa\}=[D]^{-1}\{M_\Lambda\}. \tag{15}$$

To obtain simplified expressions for the induced curvature, we assume that the shell is isotropic and has the same Poisson's ratio as the actuator. For such a case, the $[A]$ and $[D]$ matrices reduce to:

$$[A]=\frac{E_s t_s+2E_a t_a}{(1-\nu^2)}\begin{bmatrix}1 & \nu & 0\\ \nu & 1 & 0\\ 0 & 0 & (1-\nu)/2\end{bmatrix}, \tag{16}$$

$$[D]=\left\{\frac{E_s t_s^3}{12(1-\nu^2)}+\frac{2}{3}\frac{E_a}{(1-\nu^2)}\left[\left(\frac{t_s}{2}+t_a\right)^3-\left(\frac{t_s}{2}\right)^3\right]\right\}\times\begin{bmatrix}1 & \nu & 0\\ \nu & 1 & 0\\ 0 & 0 & (1-\nu)/2\end{bmatrix}. \tag{17}$$

Rewriting in a more convenient way,

$$[A]=\frac{E_a t_a(2+\psi)}{(1-\nu^2)}\begin{bmatrix}1 & \nu & 0\\ \nu & 1 & 0\\ 0 & 0 & (1-\nu)/2\end{bmatrix}, \tag{18}$$

$$[D]=\frac{t_s^2}{12}\frac{E_a t_a}{(1-\nu^2)}\left[6+\psi+\frac{12}{T}+\frac{8}{T^2}\right]\times\begin{bmatrix}1 & \nu & 0\\ \nu & 1 & 0\\ 0 & 0 & (1-\nu)/2\end{bmatrix}. \tag{19}$$

With these assumptions, the following expression for the induced bending strains due to the out-of-phase actuation is obtained from Eq. (15) (t_s=shell thickness, t_a=actuator thickness):

$$\begin{Bmatrix}\kappa_x\\ \kappa_\theta\\ \kappa_{x\theta}\end{Bmatrix}=\frac{6(1+1/T)(2/t_s)}{6+\psi+8/T^2+12/T}\begin{Bmatrix}1\\ 1\\ 0\end{Bmatrix}\Lambda, \tag{20}$$

where

$$\psi=\frac{E_s t_s}{E_a t_a},\quad T=\frac{t_s}{t_a}, \tag{21}$$

and for in-phase actuation, the following expression for induced middle-surface strains is obtained from Eq. (14):

$$\begin{Bmatrix}\epsilon_x^0\\ \epsilon_\theta^0\\ \epsilon_{x\theta}^0\end{Bmatrix}=\frac{2}{2+\psi}\begin{Bmatrix}1\\ 1\\ 0\end{Bmatrix}\Lambda. \tag{22}$$

The above expressions for the middle-surface strains for the case of in-phase actuation and the bending strains for the case of out-of-phase actuation are the same as those obtained for plates; however, the circumferential strain is now coupled with the out-of-plane displacement [Eq. (5)].

To solve a plate or a shell problem, an expression for a set of equivalent forces is often developed. These forces, when applied along the edges of the footprint of the actuator, on the structure result in the same degree of bending strains and in-plane middle-surface strains as those obtained from Eqs. (20) and (22). The equivalent forces and moments are obtained by substituting the bending strains and the in-plane strains from Eqs. (20) and (22) into Eq. (7), with N_Λ and M_Λ set to zero. For out-of-phase actuation, the equivalent moments are found to be:

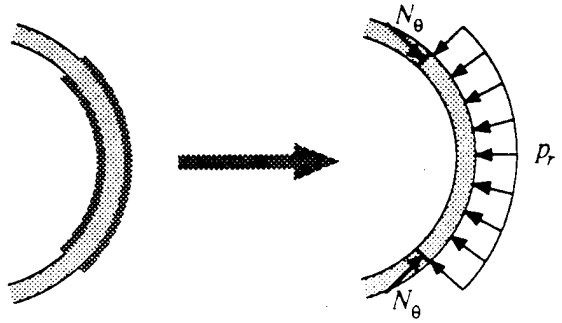

FIG. 3. Adequate equivalent loading to maintain equilibrium.

$$\begin{Bmatrix}M_x\\ M_\theta\\ M_{x\theta}\end{Bmatrix}_{eq}=\frac{E_s t_s^2}{1-\nu}\frac{(1+1/T)}{6+\psi+8/T^2+12/T}\begin{Bmatrix}1\\ 1\\ 0\end{Bmatrix}\Lambda, \tag{23}$$

and for in-phase actuation, the following expression for the equivalent axial and tangential force is obtained:

$$\begin{Bmatrix}N_x\\ N_\theta\\ N_{x\theta}\end{Bmatrix}_{eq}=\frac{E_s t_s}{1-\nu}\frac{2}{2+\psi}\begin{Bmatrix}1\\ 1\\ 0\end{Bmatrix}\Lambda. \tag{24}$$

The tangential force obtained from the above equation, when applied to the shell along the two circumferential edges of the actuator will not be colinear, due to the curvature of the shell, and will have an erroneous component resulting in a rigid body mode. This situation has already been illustrated in Fig. 1. This occurs due to the simplifying assumptions in the above formulation. In actuality, a set of self-equilibrating stresses are developed between the shell and the bonded actuator, and there is no rigid body force developed.

To remedy this situation, we have proposed the application of an equilibrating uniform radial pressure applied across the footprint of the actuator. The magnitude of the uniform pressure is obtained from simple statics and is equal to $-N_\theta/R$ (Fig. 3). This set of forces, i.e., an equivalent tangential force given by Eq. (24) and a uniform radial pressure, now provide a convenient means of representing the action of surface-bonded actuators that are actuated in-phase. To verify whether this set of forces results in approximately the same displacement field as a true actuator bonded to a cylindrical shell (a comparison with a finite element model) a description of which follows, is made.

II. FINITE ELEMENT MODELING AND VERIFICATION

Two finite element models have been constructed to verify the equivalent loading scheme. A 6-in.-radius, 0.032-in.-thick, and 1-in.-deep ring with piezoelectric actuators 1/6 of the ring thickness and covering an arc 10° long (β) have been used. Making use of symmetry, only the top half needs to be modeled. The first model, shown in Fig. 4(a), consists

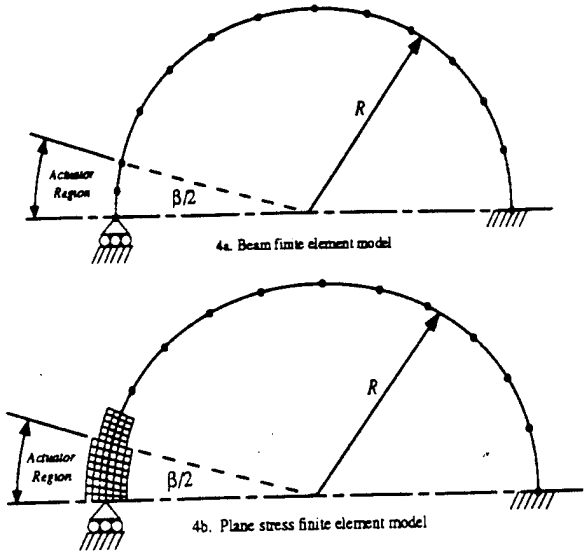

FIG. 4. Finite element models used to verify the theoretical model.

of beam elements. First, the actuation is simulated by specifying a coefficient of thermal expansion for the elements in the actuator region and then applying a known temperature to the model. Second, an equivalent self-equilibrating load, i.e., pressure and tangential force, corresponding to the temperature, is applied [Eqs. (23) and (24)]. The radial and tangential displacements obtained from the above analysis are identical and therefore not shown. It must be noted that the pressure loading must be transformed to nodal forces only (lumped loading). The lumped loading is often better for flat elements representing a curved surface.[12] The second finite element model uses plane stress elements in the actuator region to include the actuator's stiffness and uses beam elements for the rest of the shell [Fig. 4(b)]. A rigid element connecting the five nodes at the end of the plane stress element region is introduced. A constraint equation is then used to ensure the continuity in the rotations between the beam and plane stress elements. Again, thermal expansion is used to simulate the static action of the actuators on the shell.

The radial and tangential displacements are shown in Fig. 5. Discrepancies between the equivalent loading model and the plane stress finite element model exist since no assumptions about the actuator stiffness or about the equivalent loading are made in the latter model. The differences are however greater in the actuator region due to the added structural stiffness of the actuators. Even though displacement differences are present, the plane stress finite element model validates the derived model since it gives results of the same order of magnitude with similar deformed shapes as opposed to when only point tangential forces (without a transverse pressure) are used. The deformed shape of the analytical model and the plane stress finite element model are shown in Fig. 6. Also shown in Fig. 5 are the displacements of the same ring if only discrete tangential forces are applied (without transverse pressure). This model using only tangential forces does not satisfy the ring's self-equilibrium. Major displacement discrepancies between the proposed equivalent loading model and the case using only tangential forces are observed both in shape and magnitude. Using the tangential forces alone over predicts the displacements by a factor of up to 1000, as seen on the right vertical axis of Fig. 5 (note that the scales of the two vertical axis are different). Also, a re-

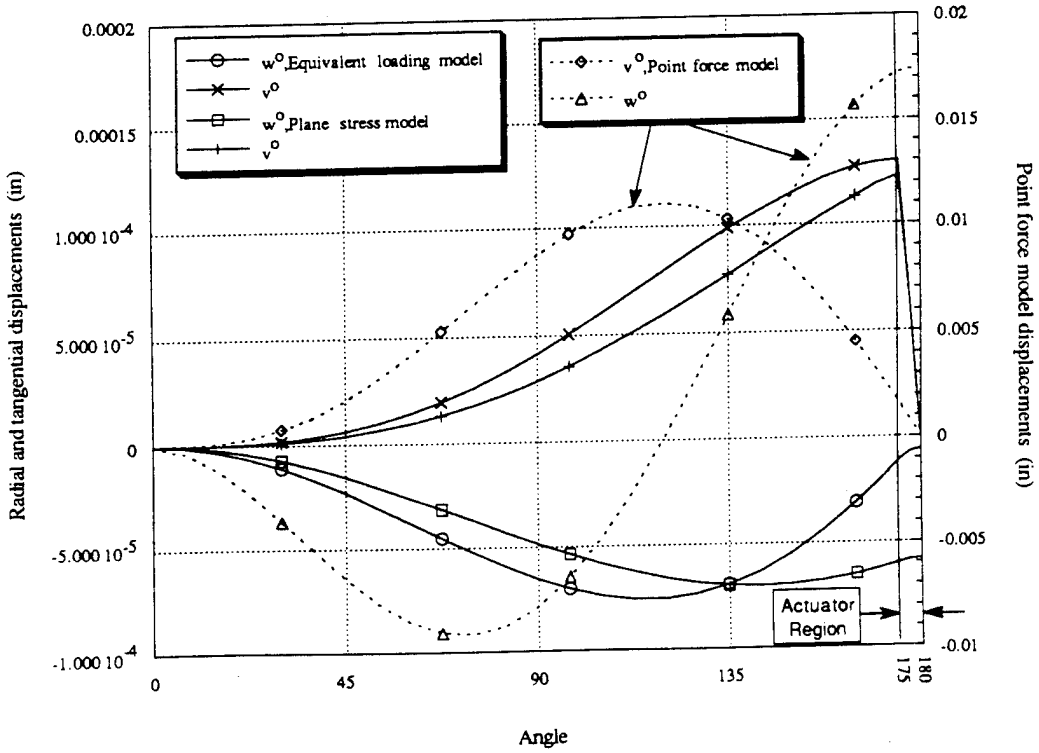

FIG. 5. Comparison of the displacements predicted by the proposed self-equilibrating equivalent forces, the plane stress finite element model, and the tangential force alone (no pressure).

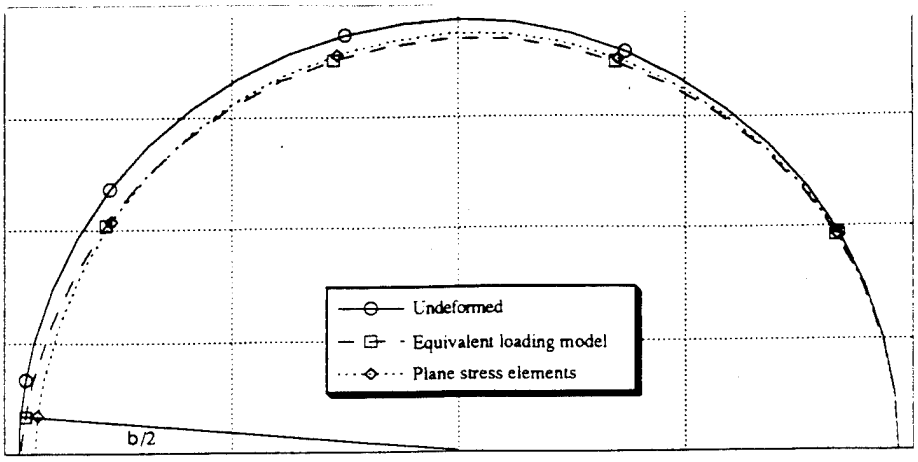

FIG. 6. Deformed shape of the ring using the self-equilibrium loading and the plane stress elements.

action force in the x direction at the clamped boundary is present if uniform pressure is not applied. This reaction force should not be present since the actual ring with bonded actuators is in self-equilibrium. Adequate equivalent loading did not show any reaction force in the x direction at the clamped boundary.

From the finite plane stress element model shown in Fig. 4(b), it is possible to justify the use of a uniform radial pressure on the actuator footprint to maintain the self-equilibrium of the ring. Figure 7 shows the radial stress distribution through the thickness of the actuator and the ring. This stress distribution is virtually constant over the whole actuator region, except at the ends of the actuator, which validates the use of a uniform radial pressure in the analytical model. With the actuators removed, an equilibrating radial pressure applied on both sides of the shell is necessary to produce the same stress distribution on the shell surface ($z/h=1, -1$) shown in Fig. 7. Because the interest is in global shell deformations, the equilibrating pressure can be applied on one side only or on the shell midplane, since it will produce the same shell response.

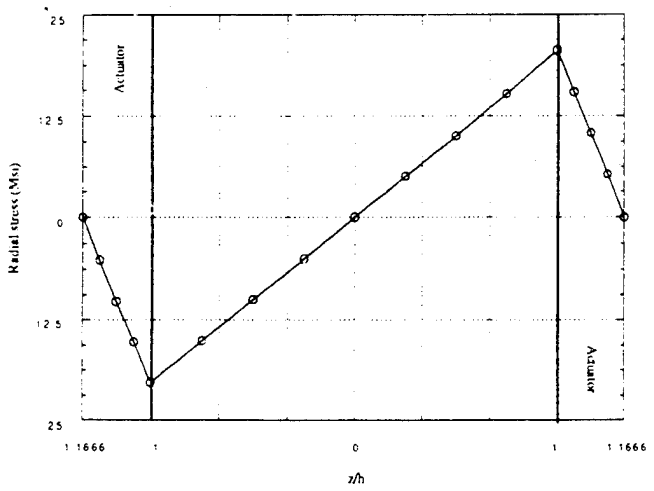

FIG. 7. Radial stress distribution through the thickness in the actuator region.

III. CONCLUSIONS

In this paper, a model to represent the action of discrete induced strain actuator patches bonded to the surface of a circular cylindrical shell is developed based on Donnell's theory. Expressions to represent the actuator forces and moments have been developed for shells and are found to be the same as those obtained for plates. However, this equivalent set of forces and moments produces a rigid body mode resulting from the no-colinearity of the tangential forces due to the shell curvature. To avoid this rigid body mode, uniform pressure is applied in the region of the actuator patch. This solution method is verified using finite element modeling and showed very good agreement.

ACKNOWLEDGMENTS

The authors would like to acknowledge the funding support of the Office of Naval Research, Grant No. ONR N00014-92-J-1170.

[1] E. F. Crawley and K. B. Lazarus, "Induced Strain Actuation of Isotropic and Anisotropic Plates," AIAA J. **29**(6), 944–951 (1989).
[2] C. K. Lee, "Theory of laminated piezoelectric plates for the design of distributed sensors/actuators. Part I: Governing equations and reciprocal relationships," J. Acoust. Soc. Am. **87**, 1144–1158 (1990).
[3] E. F. Crawley and E. H. Anderson, "Detailed Models of Piezoceramic Actuation of Beams," J. Intell. Mater. Syst. Struct. **1**, 4–25 (1990).
[4] B. T. Wang and C. A. Rogers, "Modeling of Finite-Length Spatially Distributed Induced Strain Actuators for Laminate Beams and Plates," J. Intell. Mater. Syst. Struct. **2**, 38–58 (1991).
[5] E. K. Dimitriadis, C. R. Fuller, and C. A. Rogers, "Piezoelectric Actuators for Distributed Vibration Excitation of Thin Plates," J. Vib. Acoust. **113**, 100–107 (1991).
[6] H. S. Tzou, "Theoretical Development of a Layered Thin Shell with Internal Distributed Controllers," Failure Reliability Conference, Montreal, Canada (1989).
[7] J. Jia and C. A. Rogers, "Formulation of a Laminated Shell Theory Incorporating Embedded Distributed Actuators," J. Mech. Design **112**, 596–604 (1990).
[8] V. Sonti and J. D. Jones, "Active Vibration Control of Thin Cylindrical Shells Using Piezoelectric Actuators," in *Proceedings: Recent Advances in Active Control of Sound and Vibration*, Blacksburg, VA (Technomic, Lancaster, PA, 1991), pp. 3–26.

[9]H. C. Lester and S. Lefebvre, "Piezoelectric Actuator Models for Active Vibration Control of Cylinders," in *Proceedings: Recent Advances in Active Control of Sound and Vibration*, Blacksburg, VA (Technomic, Lancaster, PA, 1991), pp. 3–26.

[10]V. R. Sonti and J. D. Jones, "Curved Piezo-Actuator Models for Active Vibration Control of Cylindrical Shells," J. Acoust. Soc. Am. **93**, 2352 (A) (1993).

[11]R. M. Jones, *Mechanics of Composite Materials* (Scripta, Washington, DC, 1975).

[12]G. J. De Salvo and J. A. Swanson, *ANSYS User's Manual* (Swanson Analysis Systems, Houston, PA, 1979).

C-28 A regression approach for simulating feedforward active control, C. E. Ruckman and C. R. Fuller, Journal of the Acoustic Society of America, Vol. 97 No. 5 Part 1, pp. 2906-2918, May 1995.

A regression approach for simulating feedforward active noise control

Christopher E. Ruckman
Structural Acoustics and Hydroacoustics Research Branch, Carderock Division, Naval Surface Warfare Center, Bethesda, Maryland 20084-5000

Chris R. Fuller
Vibration and Acoustics Laboratories, Virginia Polytechnic Institute and State University, Blacksburg, Virginia 24061

(Received 21 April 1994; revised 29 September 1994; accepted 24 November 1994)

Regression analysis is used to examine feedforward active noise control from a statistical point of view. Since numerical techniques for simulating feedforward active noise control in the frequency domain are mathematically similar to linear least-squares regression, two regression-based numerical methods can be applied to control problems. The first uses regression diagnostics such as the F-test, the t-test, and confidence intervals to model the effects of error sensor measurement noise. The second uses collinearity diagnostics to address a form of numerical ill conditioning that can corrupt the results. The regression diagnostics allow realistic modeling of random measurement error; the collinearity diagnostics help avoid numerical difficulties that might otherwise go undetected. Numerical results are given for a structural-acoustic control problem involving a fluid-loaded cylindrical shell.

PACS numbers: 43.40.Vn

INTRODUCTION

This article examines feedforward active noise control from a statistical viewpoint using tools developed for linear least-squares regression. The procedure for simulating feedforward active control using, for example, a finite-element model of the plant, can be conveniently simulated in the frequency domain using a formulation that is essentially identical to regression; the main difference is that the regression variables are complex-valued transfer functions rather than real-valued collections of data observations. Regression diagnostics can be used to assess the effects of error sensor measurement noise, which is analogous to observation error in a regression. Collinearity diagnostics can be used to detect and analyze ill-conditioning problems that might otherwise go unnoticed. Together, these numerical methods provide a unified numerical approach for simulating active control systems.

Consider a single-input, single-output (SISO) feedforward active control system. A primary or disturbance input S injects vibrational or acoustic energy, while one or more actuators (secondary or control inputs) are used to influence system response. The disturbance propagates through the primary path A to form the disturbance response (primary response) P_p. The controller operates on a detection sensor signal to produce the control input b, which propagates through the secondary path X to form the control response P_c. The total response $P_p + P_c$ is measured by the error sensor subject to measurement noise ϵ, and the error sensor output is used in determining the controller gain. Frequency-domain investigations of this type of system have been reported in a variety of contexts.[1–5]

The need for regression diagnostics stems from two facts. First, error sensor outputs in a real control system are contaminated with measurement noise whose properties are known only in a statistical sense. Second, in a MIMO system the error is known only at a finite number of locations (the error sensors) rather than as a continuous function in space. For these two reasons among others, numerical or analytical simulations are usually too optimistic in their predictions of system performance. To make simulations more realistic, regression diagnostics can be used to characterize the effects of measurement noise. This implicit stochastic modeling of measurement noise differentiates the statistical methods outlined below from previous works, which consider the problem from a purely deterministic viewpoint. In keeping with the tutorial nature of the discussion, we discuss only the three most basic regression diagnostics: the F-test, the t-test, and confidence limits on the "estimated model" (a term to be defined below.) Some of the techniques developed here have analogous developments in system identification literature.[6,7] We include them here to provide an expanded, unified development and to emphasize that regression diagnostics are among the many statistical techniques that can be applied to the feedforward active control problem.

The link between regression and feedforward control was first noted by Snyder and Hansen,[8,9] who simulated a feedforward control problem using commercial regression software. Since commercial regression packages operate only on real-valued data, Snyder and Hansen partitioned their problem into separate real and imaginary parts. The present work uses a more general formulation that expresses the regression in the complex domain. The complex formulation allows the use of regression diagnostics and collinearity diagnostics, which were not discussed by Snyder and Hansen. Much of the theoretical development for least-

 0001-4966/95/97(5)/2906/13/$6.00 © 1995 Acoustical Society of America

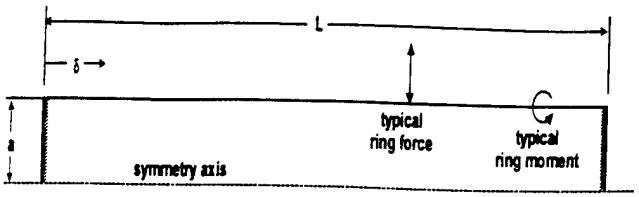

FIG. 1. Geometry of clamped cylindrical shell and typical control inputs.

squares regression of complex variables is taken from Miller.[10,11]

The other major topic of this paper is collinearity, a type of numerical ill conditioning that can corrupt the results of the control simulation. Given that feedforward control in the frequency domain is similar to regression, one might logically assume that numerical difficulties commonly experienced by regressions also appear in feedforward control simulations. This is true of collinearity, the ill conditioning that occurs when one or more transfer functions are not orthogonal. Collinearity is always present to some degree; in fact, control simulations are perhaps more prone to collinearity than other regressions. To simulate a feedforward controller without checking for collinearity is to risk producing meaningless results. The objective is to detect whether the collinearity has serious consequences, and to learn which actuators are causing collinearity problems.

Rosenthal[12] notes that redundancies between the sensors in an active noise filtering system can produce numerical problems limiting the number of sensors that can be used. The issue is also discussed by Nelson and Elliott[1] in the context of iterative gradient descent solution methods. Two references that provide a comprehensive discussion of collinearity diagnostics for real-valued regressions are Belsley *et al.*[13] and Belsley.[14] All of the concepts discussed in this paper are based on the techniques in Ref. 14. The extensions to complex-valued regressions are straightforward, and are based on the work of Miller.[11] The present paper describes how collinearity enters an active control system and how it can affect a feedforward control simulation. Also given is a basic diagnostic procedure for detecting and analyzing collinearity. It is shown that when the sole purpose of the diagnostic is to detect rather than analyze collinearity, the collinearity diagnostic consists of simply examining the condition number of a special scaled design matrix.

While most of the concepts discussed here apply to any feedforward control system, for purposes of illustration we focus on active structural-acoustic control (ASAC). ASAC involves controlling the acoustic response of a fluid–structure system by applying vibrational inputs directly to the structure. Recent theoretical and experimental studies use ASAC to control radiation from one-dimensional and two-dimensional structures including beams, plates, and submerged plates; similar techniques are used to control noise transmitted through flat plates or into infinite cylindrical shells.[15–24]

The example structure used for numerical results (Fig. 1) is a finite-length, fluid-loaded cylindrical shell with clamped, rigid, flat end caps. The entire investigation is conducted in the frequency domain, i.e., using a time-harmonic disturbance whose time dependence $e^{i\omega t}$ is omitted for simplicity of notation. Note that although an axisymmetric example is used here, regression analysis can be applied to three-dimensional problems as well. A three-dimensional case is treated in Ref. 25 by superposing the axisymmetric solutions for a spherical shell to obtain a radiated field with a plane of symmetry. Similar techniques may be used with the procedures outlined here.

I. REGRESSION AND FEEDFORWARD CONTROL

First we review the fundamentals of multiple linear regression as used in general statistics applications. We then discuss how a feedforward active control problem can be expressed as a complex-valued multiple linear regression, paying special attention to the effects of measurement noise. Finally, we discuss the relation between the weighting function and the physical significance of the cost function, and examine some numerical results for the cylindrical shell example problem. Much of the following discussion may be found in textbooks and articles on linear algebra or least-squares approximation; see, for example, Refs. 26–29. The discussion is included here to explicitly define the somewhat confusing nomenclature, and to help illustrate the links between feedforward control and regression.

A. Fundamentals of multiple linear regression

In regression one seeks a model $\bar{Y}(\beta_i, X_i)$, the true model, to approximate a set of measured data Y, also called the dependent variable. The true model is a function of β_i (the true regression coefficients) and a collection of predictor variables X_i, also called independent variables. The data and predictor variables contain M observations, $j=1,2,\ldots,M$, and are written in vector form as $Y=\{y_1 \cdots y_M\}^T$ and $X_i=\{X_{1i} \cdots X_{Mi}\}^T$.

Suppose that each observed value y_i contains a small amount of Gaussian measurement noise ϵ_i. (Note the use of the term "noise" rather than "error." In statistical texts, measurement noise is referred to as "measurement error" or "observation error," whereas in active control literature the term "error" refers to the residual signal that remains after cancellation. To avoid confusion, the term "measurement noise" will refer only to the random component of the measured data y_i.) Assume also that model we seek (the true model) gives a good approximation of the data:

$$y_i=\bar{y}_i+\epsilon_i, \tag{1}$$

where the expected value of the noise is $E[\epsilon_i]=0$. Because we only *assume* the validity of Eq. (1), we must later test whether the data cause us to reject the assumption.

To use regression diagnostics, we must make some assumptions about the measurement noise. These assumptions are *not* needed to perform the regression; we can always use regression to find a set of regression coefficients. However, sometimes we wish to go beyond merely computing the regression coefficients, estimated model, and residuals. The assumptions concern $V(y_i)$, the variance of the ith data measurement. A general form for the variance is

$$V(y_i)=\sigma_Y^2 g^2(\bar{y}_i, w_i), \tag{2}$$

where σ_Y is a variance coefficient and g^2 is the variance function. By including $\bar{y}_i$ in the variance function $g^2(\bar{y}_i, w_i)$, we allow the possibility that measurement noise may depend on the magnitude of the quantity being measured. The weighting coefficients w_i allow us to weight some observations more heavily than others, for example, placing more emphasis on those observations known to be most reliable. Assume that the ϵ_i are normally distributed and pairwise uncorrelated; that is, ϵ_i and ϵ_j are uncorrelated when $i \neq j$. Next we make a simplifying assumption to be scrutinized later: *we assume that $V(y_i)$ is independent of $\bar{y}_i$*. This can be written

$$V(y_i) = \frac{\sigma_Y^2}{w_i}, \quad \text{or, equivalently,} \quad V(Y) = \sigma_Y^2 W^{-1}, \quad (3)$$

where we have defined a weighting matrix $W = \text{diag}(w_1, w_2, \ldots, w_N)$.

Specifying σ_Y^2 is critical. Ideally, σ_Y^2 should come from some *a priori* knowledge of the physical measurement system to be used. For example, we could estimate σ_Y^2 by repeatedly measuring a calibration signal and computing the sample variance of the measurements. In a preliminary investigation such as the present work, however, we might not know σ_Y^2. Lacking a measured value of σ_Y^2, the data itself can be used to estimate σ_Y^2; this approach is used in the present work. The estimated residual variance $s_{Y-\hat{Y}}^2$ [Eq. (23)] is taken as an approximation of σ_Y^2.

Let us now assume a linear regression model of the form

$$\bar{Y} = \sum_{i=1}^{N} \beta_i X_i. \quad (4)$$

Because we do not know the *true* model $\bar{Y}$, we cannot directly find the *true* regression coefficients β_i. But we can use X_i to compute an *estimated* model $\hat{Y}$ with *estimated* regression coefficients b_i:

$$\hat{Y} = \sum_{i=1}^{N} b_i X_i. \quad (5)$$

The objectives are twofold. First, find predictor variables X_i such that the true model $\bar{Y}$ closely approximates the measured data Y. Second, find estimated regression coefficients b_i such that the estimated model $\hat{Y}$ closely approximates the true model $\bar{Y}$. The F test and t test, reviewed in the next section, measure how well we have achieved these objectives.

To simplify notation, we write the estimated regression coefficients in vector form $B = \{b_1 \quad b_2 \quad \cdots \quad b_M\}^T$. Defining a design matrix $X = \{X_1 \quad X_2 \quad \cdots \quad X_M\}$, we can express the estimated model as

$$\hat{Y} = XB. \quad (6)$$

We seek a weighted least-squares solution that minimizes the weighted cost function

$$\chi^2 = \sum_{i=1}^{M} w_i |y_i - \hat{y}_i|^2, \quad (7)$$

ogy.

Statistical regression terminology	Active control terminology
Dependent variable; data	inverse of primary response; inverse of open-loop response
Model; estimated model	secondary response; control response
Independent variable; predictor variable	transfer function
Regression coefficient	control force; control input
Residual	error; closed-loop response; residual response
Observation or measurement	error sensor
Observation or measurement error	error sensor measurement noise

where $y_i - \hat{y}_i$ is the residual. By requiring the derivatives $\partial(\chi^2)/\partial b_i$ to vanish, we obtain the weighted normal equation

$$X^T W X B = X^T W Y, \quad (8)$$

whose solution is the required vector of estimated regression coefficients B.

B. Formulating feedforward active control as a complex-valued regression

First, define the primary response P_p as the vector of error sensor outputs due to the disturbance input. Similarly, define a transfer function X as the vector of error sensor outputs that would result from a single actuator of unit strength acting alone. Finally, define the secondary response $\hat{P}$ as the vector of error sensor outputs that would result from all the actuators acting together but without the disturbance.

To formulate the problem as a multiple linear regression, we must have a linear system as defined by three conditions. The response due to a single actuator alone must equal its transfer function multiplied by its complex strength. The secondary response must be a linear sum of all the actuator transfer functions multiplied by their respective complex strengths. Finally, the total or residual response must equal the sum of the primary response plus the secondary response.

Now we can list one by one the elements of the feedforward control problem and their counterparts in the regression problem, which are listed in Table I. The transfer functions are analogous to the predictor variables. The control forces are analogous to the estimated regression coefficients b_i. The secondary response $\hat{P}$ is analogous to the estimated model $\hat{Y}$. Last, $P = -P_p$ (the *additive inverse* of the primary response) is analogous to the measured data Y. By choosing control forces such that $\hat{P}$ approximates P, we cause the secondary response to "cancel" the primary response, so that the residual response $P + \hat{P} = -P_p + \hat{P}$ is approximately zero.

Recalling that our variables are complex valued, we rewrite the cost function of Eq. (7) as

$$\chi^2 = \sum_{i=1}^{M} w_i (p_i + \hat{p}_i)^* (p_i + \hat{p}_i). \quad (9)$$

After algebra,[28] we can show that the weighted normal equation takes the form

$$X^H W X B = X^H W P, \quad (10)$$

where the superscript H indicates the Hermitian conjugate. Similarly, we must modify how the error sensor measurement noise is characterized. If $\bar{P}$ is the true model approximated by $\hat{P}$, we now assume that

$$p_i=\bar{p}_i+\epsilon, \quad E(p_i)=\bar{p}_i, \quad \text{and } V(|\epsilon_i|)=\sigma_P^2. \tag{11}$$

In other words, we characterize only the variance of the noise magnitude $|\epsilon|$; we do not specify separate variances for the magnitude and phase. Implications of this relationship are discussed later in the paper.

C. Physical significance of the cost function

Often, the cost function approximates a physical quantity. The cost function's physical significance depends on the sensors (predictor variables) and the weighting coefficients. For the example problem in this article, the M sensors are far-field pressure sensors and the predictor variables are vectors of pressure per unit force. The N predictor variables are nothing more than transfer functions between unit actuator forces on the structure and the resulting far-field pressures $P_j(\theta_i)$, $i=1,2,\ldots,M$, $j=1,2,\ldots,N$. Consider the following expressions for the radiated power:[30]

$$\Pi=\oint_{S'}\frac{\pi r^2}{\rho c}|P+\hat{P}|^2\,dS'\cong\sum_{i=1}^{M}\frac{\pi r^2 a_i}{\rho c}|p_i+\hat{p}_i|^2, \tag{12}$$

where S' is a spherical surface of far-field radius r with the origin at its center, and a_i is the area on the surface S' associated with the ith far-field location. If $a_{\max}$ is the largest value of a_i, we can rewrite the estimated radiated power as

$$\hat{\Pi}=\frac{\pi r^2 a_{\max}}{\rho c}\sum_{i=1}^{M}\frac{a_i}{a_{\max}}|p_i+\hat{p}_i|^2. \tag{13}$$

By comparison with Eq. (7), the cost function will be proportional to the radiated power if we specify weighting coefficients of the following form:

$$w_i=a_i/a_{\max}. \tag{14}$$

If there are enough error sensors to completely characterize the radiated field, then the cost function χ^2 is proportional to the radiated power Π; minimizing one minimizes the other. To obtain the radiated power from the cost function, we must use

$$\hat{\Pi}=(\pi r^2 a_{\max}/\rho c)\chi^2. \tag{15}$$

For the remainder of this text, all references to the total radiated power refer to the estimated radiated power in Eq. (15).

The formulation above places no restrictions on the physical configuration of the control system. The present text discusses an axisymmetric example problem for simplicity of notation, since far-field locations may be specified by only one angle rather than two, but the method is not limited to axisymmetric cases. The transfer functions can contain pressures from any number of sensors in any physical locations desired. Assuming the number of sensors is sufficient, and the sensor locations and weighting coefficients are appropriate, the cost function can approximate the radiated power.

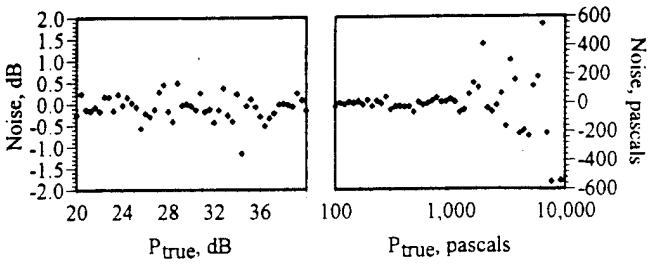

FIG. 2. Example of measurement noise with nonconstant variance. Expressed in decibels, left, the noise variance is independent of signal amplitude. Expressed in linear units, right, the variance is not independent of signal magnitude.

Another important point is that *any* combination of actuators and sensors can be used. Physical interpretation of the cost function, however, will only be possible with certain combinations of actuators, sensors, and weighting coefficients. Also, sensors need not be distributed throughout the entire radiated field; they could be concentrated in one area to reduce radiation in a certain direction. The reduction of radiated power is a specific case of a more general cost function.

D. Assumptions regarding variance of measurement noise

The previous section made some simplifying assumptions about the variance of the measurement noise in a general regression problem; see Eq. (3). Here we examine those assumptions in the context of the ASAC problem to determine whether they represent the type of sensor measurement noise expected in a real control system. Recall that the regression itself does not depend on the distribution of measurement noise, which plays a part only in the regression diagnostics. As discussed below, Eq. (3) may not be entirely appropriate for some types of sensors likely to be used in active noise control systems.

Suppose the error sensors will be hydrophones. Suppose we repeatedly measure a calibration signal P_{true} and find that the measurements, when expressed in decibels, exhibit Gaussian measurement noise with a sample standard deviation of, say, $s_p=0.1$ dB. For real hydrophones, this form of approximation may be reasonable. But what if the measurement noise is Gaussian only when expressed in decibels, while we have defined the regression in linear units of pressure? Consider Fig. 2, which shows a hypothetical set of hydrophone measurements of a "known" pressure P_{true} over a range of pressure levels. The measurement noise is the difference in magnitudes between P_{true} and the measured value. When the measurement noise is expressed decibels, as in the left plot, the noise variance appears to be constant with respect to the magnitude of P_{true}. But when the same data are plotted in units of pressure instead of decibels, the noise is larger at high pressures than at low pressures. In other words, the measurement noise has a nonconstant variance. To describe the variance properly we must use Eq. (2) rather than using the simplified Eq. (3).

Because the primary response varies in space, our supposed hydrophone error sensors will measure different pressure magnitudes depending on their locations. A sensor measuring a large pressure will thus have a larger noise component (in linear units of pressure) than a sensor measuring a small pressure. This highlights an important point: the assumptions used to derive Eq. (3) might not provide an accurate representation of the noise present with real sensors. Perhaps the variance should instead be proportional to the signal magnitude as in Eq. (2). For simplicity in the remainder of this paper, *we shall assume Gaussian measurement noise with a constant variance as in Eq. (3)*. The point of the above discussion is that one must carefully evaluate the mathematical form of measurement noise based on the specific sensors being used, and then formulate the regression diagnostics appropriately.

More sophisticated treatments of variance are available, but they are beyond the scope of the present analysis. Most involve performing a transformation and then using of some form of generalized least squares; see Ref. 29. For example, it may be necessary to convert the transfer functions and error sensor measurements to decibels before using them in a regression. In many cases it will likely be seen that the use of standard constant-variance techniques is well justified, and that more complicated techniques may be of limited benefit.

E. The squared multiple correlation coefficient R^2

The squared multiple correlation coefficient $\mathbf{R}^2$, commonly used to measure the quality of a regression, has a corresponding role in an active control simulation. For a regression that does not include a constant term as one of the predictor variables, $\mathbf{R}^2$ may be written

$$\mathbf{R}^2=\frac{\sum_{j=1}^{M}|\hat{p}_j|^2}{\sum_{j=1}^{M}|p_j|^2}=1-\frac{\sum_{j=1}^{M}|p_j-\hat{p}_j|^2}{\sum_{j=1}^{M}|p_j|^2}, \tag{16}$$

as described in, for example, Appendix II of Ref. 6. A value of $\mathbf{R}^2$ near unity indicates that the estimated model closely fits the measured data. Since p is the open-loop response and $\hat{p}-p$ is the closed-loop response, the controller reduces the open-loop response by an amount expressed in decibels as

$$\Delta_{\mathrm{dB}}=-10\ \log(1-\mathbf{R}^2). \tag{17}$$

F. The role of regression diagnostics

The previous sections describe how a regression predicts control system performance, but do not explicitly consider measurement noise. The regression diagnostics described in this section, which require us to assume a value for the measurement noise variance, provide a more complete picture.

1. Testing the regression for lack of fit: The F-test

The "F-test" measures confidence in the regression as a whole. The other regression diagnostics which follow all assume that the estimated model closely approximates the true model, a condition that cannot be directly verified because we cannot know the true model. However, if we can show via statistical inference that the *variance* of the estimated model *is not drastically different from the variance* of the true model, e.g., that there is no statistically significant lack of fit, then we can proceed with reasonable confidence. The F-test verifies whether this condition is true.

The residual signal sensed by the error sensor contains one or more of the following three components: measurement noise, model error, and uncertainty. Measurement noise is always present because the error sensors are imperfect. Model error is present if the disturbance response contains dynamics that are not contained in the control response, i.e., unmodeled dynamics. Uncertainty is present even when there is no model error, because the control forces (regression parameters) cannot be estimated perfectly in the presence of measurement noise. If the model is nearly perfect, that is, if all modes in the disturbance response are adequately represented in the control response, then the residual contains only measurement noise and uncertainty. There is no lack of fit, and the residual is the smallest residual that can be expected based on the amount of measurement noise introduced by the sensors. On the other hand, if there are significant unmodeled dynamics, there is a lack of fit and the residual will be larger than the minimum possible residual. The F-test gives a statistical measure, *based on the data*, of whether there is a statistically significant lack of fit.

Begin by assuming that there is no lack of fit, and thus the control response $\hat{P}$ is close to the true model $\bar{P}$; call this assumption $H_0:\hat{P}\approx\bar{P}$. One way of verifying $H_0:\hat{P}\approx\bar{P}$ is to show that $\hat{P}$ and $\bar{P}$ have the same variance:

$$V(\bar{P}-\tilde{P})\approx V(\hat{P}-\tilde{P}), \tag{18}$$

where $\tilde{P}$ is the estimated mean of the disturbance response. Since we cannot know $\bar{P}$ directly, we use a relation from regression theory,[27]

$$V(\bar{P}-\tilde{P})=V(P-\hat{P})+V(\hat{P}-\tilde{P}). \tag{19}$$

Loosely speaking, Eq. (19) states that the variance of the true model about $\tilde{P}$ equals the residual variance plus the variance due to the regression. We can rearrange Eq. (19) as

$$V(\bar{P}-\tilde{P})=V(\hat{P}-\tilde{P})\left\{1+\frac{1}{F}\right\},\quad \text{where } F=\frac{V(\hat{P}-\tilde{P})}{V(P-\hat{P})} \tag{20}$$

and F is the so-called *variance ratio*. To satisfy Eq. (18) as closely as possible we must have $F\gg 1$, in which case we do not reject $H_0:\hat{P}\approx\bar{P}$. The F-test is not violated, and there is no significant lack of fit.

To determine whether F is large enough, we compare F to a predetermined value. Let $Q(F,\nu_1,\nu_2)$ be the F-distribution probability function with ν_1 degrees of freedom in the numerator and ν_2 degrees of freedom in the numerator. Then, given X, P, M, and N for the specific problem at hand, $Q(F,\nu_1,\nu_2)$ is the probability of a statistically significant lack of fit, that is, the probability that F could be as large as it is *by chance alone* rather than because of the regression. When $Q(F,\nu_1,\nu_2)$ exceeds some specified risk level, we must reject $H_0:\hat{P}\approx\bar{P}$. In the present context with N actuators and M sensors, we have

$$\nu_1=N \quad \text{and} \quad \nu_2=M-N-1. \tag{21}$$

Values for $Q(F,\nu_1,\nu_2)$ are easily generated by computer or read from tables. The variance ratio can be approximated by the ratio of standard deviations

$$F=s^2_{\hat{P}-\hat{P}}/s^2_{P-\hat{P}}, \tag{22}$$

where

$$s^2_{\hat{P}-\hat{P}}=\frac{1}{\nu_1}\sum_{i=1}^{M} w_i|\hat{p}_i-\bar{p}|^2$$

and (23)

$$s^2_{P-\hat{P}}=\frac{1}{\nu_2}\sum_{i=1}^{M} w_i|p-\hat{p}_i|^2.$$

If F is large enough, that is, if $Q(F,\nu_1,\nu_2)$ does not exceed the specified acceptable risk level, then there is no lack of fit and we can proceed with testing the individual regression coefficients as described in the next section. If F is too small, then it is too likely that we could have chosen regression coefficients at random and still achieved the same fit to the data.

When a regression fails the F-test, it generally means this: Given X, P, M, and N, there is too much variance in the measured data P for us to confidently say that we have modeled the data. In terms of an ASAC problem, one or more of the following conditions exists:

(1) There are too few sensors to confidently say that the response has been adequately modeled, i.e., the data and predictor variables are undersampled. Adding more sensors will provide better estimates of the variances, and may increase F unless other problems are present.

(2) The actuators are decoupled from one or more modes that are present in the disturbance response, i.e., the disturbance response contains unmodeled dynamics that cannot be reproduced by the actuators. Adding more actuators or using different actuators that couple into different modes will improve controllability.

(3) The amount of measurement noise present is much greater than originally thought. Even if the actuators couple into the same modes that appear in the disturbance response, severe measurement noise can have the same effect as unmodeled dynamics.

Generally speaking, a regression will only fail the F test when the control differs substantially from the disturbance response. Any sound cancellation is coincidental and occurs only in localized areas rather than globally.

2. The t-test and confidence limits for individual regression coefficients

The t-test, which examines the individual regression coefficients corresponding to the control inputs in the active control problem, allows us to detect whether any actuators are completely uncoupled from the cost function. If a given actuator has no beneficial effect on the regression, then its regression coefficient vanishes and we could obtain a more reliable regression by reformulating the problem without that actuator. However, determining whether a given coefficient is zero can be difficult because problem scaling may yield arbitrarily small coefficients. To decide whether a coefficient should be removed, we can define a statistical "confidence interval" for the magnitude of that coefficient, and then check whether the confidence interval contains zero.

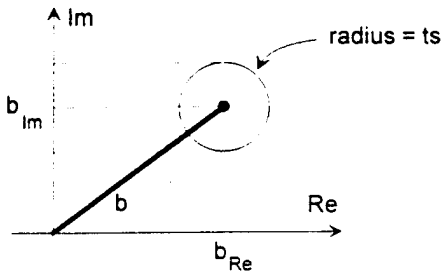

FIG. 3. Circular confidence limit on a regression parameter, where $\mathrm{Re}\{b\}=b_{\mathrm{Re}}$ and $\mathrm{Im}\{b\}=b_{\mathrm{Im}}$. The confidence limit specifies a circular region of radius ts_b centered at $(b_{\mathrm{Re}},b_{\mathrm{Im}})$ such that the true parameter lies within the circle.

Assuming Gaussian measurement noise, the magnitude variance of the ith control force is

$$\sigma_{b_i}=\sqrt{e_i}, \tag{24}$$

where e_i is the ith diagonal of the variance–covariance matrix

$$V(b)=\sigma_p^2(X^HWX)^{-1} \tag{25}$$

and σ_p is the variance of the measurement noise. Since the true error variance σ_p is usually not known, we can use the estimated variance s_p in its place to obtain an estimated variance s_{b_i}.

If an estimated noise variance is available for a specific type of error sensor, that variance may be used in performing a simulation. If no such estimate is available, the residual variance $s_{\hat{P}-\hat{P}}$ may be used instead. Because the present work emphasizes numerical methods rather than results for specific types of hardware, all numerical results in this paper use error variances that are estimated from the data. The reader is reminded that a specific value of the error variance is required only for regression diagnostics, not for the regression itself.

Next we decide on a level of statistical significance α_t, say 90%, and compute a quantity known as *Student's t*, the value of the Student's probability distribution for the chosen level of significance α_t and ν degrees of freedom, where $\nu=M-N-1$. We can then state that *given the data*, the probability of $|b_i-\beta_i|<ts_{b_i}$ is α_t. In other words, there is a 90% probability that the magnitude of the error between the true control input and that computed by the regression is smaller than ts_{b_i}. The confidence interval provides a circular confidence region on b_i in the real–imaginary plane (Fig. 3) such that

$$|b_i|-ts_{b_i}\leq|\beta_i|\leq|b_i|+ts_{b_i}. \tag{26}$$

The largest magnitude inside the confidence region, which represents the largest likely control input magnitude, is $|b_i|+ts_{b_i}$. As noted in Ref. 7, we could also consider the

real and imaginary parts of the problem separately to produce an elliptical confidence region.

A related statistical test is the so-called "t-test," which measures whether a given control input is *significantly* different from zero. If the range $\{|b_i| - ts_{b_i}, |b_i| + ts_{b_i}\}$ contains zero at the specified level of significance, then we cannot conclude that b_i is significantly different from zero. Said another way, if an actuator "fails the t-test," we have no statistically significant indication that control input has nonzero magnitude. Adding sensors for a given number of actuators has the effect of decreasing t, and thus producing tighter confidence intervals and a more reliable model. In terms of the ASAC problem, a control input will only be set equal to zero if the actuator is completely uncoupled from the disturbance response. Therefore any actuator that fails the t test should be removed from the problem.

3. Prediction intervals

The confidence intervals for all the actuators may be condensed into a single quantity, the prediction interval, which provides a confidence interval on the magnitude of the control response $\hat{P}$. The regression provides an estimated residual $P+\hat{P}$ corresponding to the pressure when the control actuators are operating. The control response $\hat{P}$ is based on error sensor outputs that contain measurement noise, and its reliability is therefore related to the accuracy of the error sensors. By applying the appropriate regression diagnostics, we can estimate confidence intervals on $\hat{P}$ and provide a single quantity that reflects the sensitivity to measurement noise for the regression as a whole.

At a given sensor location, the control response is a linear sum:

$$\hat{P}_j = \sum_{i=1}^{n} b_i X_{ij}, \tag{27}$$

where the control inputs b_i have variances as expressed as in the previous section, and the transfer functions X_i are considered constant and completely accurate for the present purposes. If we define the vector $X_{i,1:N} = \{X_{i,1} \quad X_{i,2} \quad \cdots \quad X_{i,N}\}$ as the ith row of the design matrix X, it can be shown that the variance of the estimated model at the location of the jth sensor is

$$V(\hat{P}_j) = \sigma_P^2 X_{i,1:N}(X^H W X)^{-1} X_{i,1:N}^H. \tag{28}$$

This is also equal to the jth diagonal of the variance–covariance matrix

$$V(\hat{P}) = \sigma_P^2 X(X^H W X)^{-1} X^H. \tag{29}$$

Using Student's t for a chosen level of significance, the prediction interval for the estimated model at the jth sensor location is defined by the standard error

$$\pm t\sigma_{\hat{P}+P}\sqrt{V(\hat{P}_j)}. \tag{30}$$

The prediction interval summarizes the sensitivity to measurement noise for the entire regression, whereas the confidence intervals address individual actuators. Prediction intervals can be used to determine whether a given combination of structure, actuators, and sensors is particularly sensitive to noise and, if so, what portions of the radiated field are most likely to be degraded by noise. As with confidence intervals, increasing the number of sensors for a given number of actuators has the effect of decreasing the width of the prediction interval.

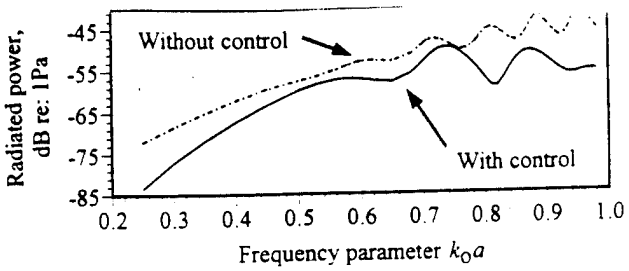

FIG. 4. Radiated power versus frequency. Radiated power without control actuators shown as solid line; with control actuators shown as broken line.

G. Numerical results and discussion

The example structure used for numerical results is a finite-length, fluid-loaded cylindrical shell with rigid, flat end caps (Fig. 1). The points at which the cylinder intersects the end closures are constrained both in translation and in rotation, i.e., the cylindrical section is clamped. The shell length L is $10\times$ the shell radius a, and the ratio of wall thickness to shell radius is 0.005. The global z axis is the shell symmetry axis, with the right-hand end cap intersecting the positive z axis. Far-field locations are described by the global spherical coordinates (R,θ,ϕ) with origin at the midlength of the shell, where the far-field location $\theta=0$ corresponds to the positive z axis. Surface locations are described by a normalized distance coordinate $\delta=z/L$. We examine frequencies as high as $k_0a=0.95$. Material properties are chosen to resemble an undamped steel shell submerged in water: the shell material has Young's modulus of 1.85×10^{11} Pa, Poisson's ratio of 0.3, and density of 7670 kg/m^3. The density and acoustic velocity of the surrounding fluid are 1000 kg/m^3 and 1460 m/s, respectively. All far-field quantities are normalized to a distance of 1.0 m. Numerical solutions for structural-acoustic dynamic response are found using the combined finite-element/boundary-element computer program NASHUA.[31]

The cylinder is disturbed by a unit-magnitude axisymmetric ring force b_d placed near the right-hand end closure at $\delta=0.96$. The two actuators ($M=2$) are axisymmetric ring force b_1 and b_2 placed at $\delta=0.25$ and $\delta=0.50$. The 25 error sensors ($N=25$) are pressure sensors located at 7.5° intervals from 0° to 180° in the far field. The control objective is to minimize the radiated power cost function Π, where Π is the weighted sum of squared pressure magnitudes at the 25 error sensors.

Figure 4 shows the radiated power cost function Π versus nondimensional frequency k_0a for the frequency range $0.2<k_0a<1.0$. The upper curve represents the open-loop case. The lower curve represents the closed-loop case, and the difference between the two is the reduction in the radiated power cost function. The actuator magnitudes and

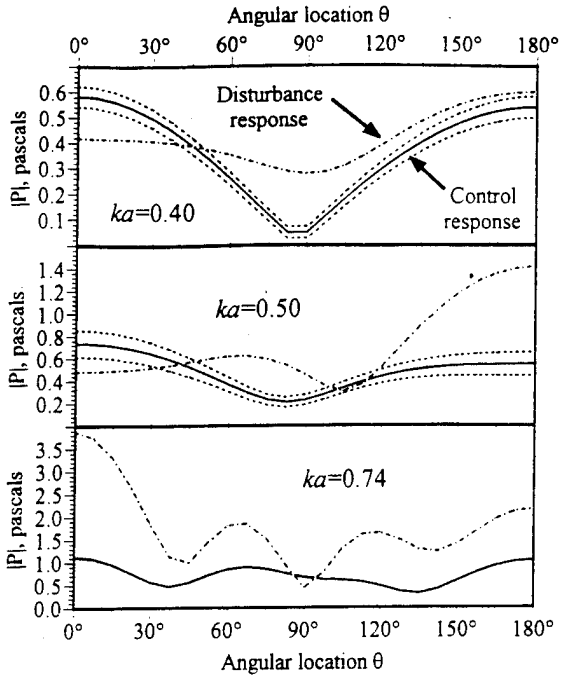

FIG. 5. Confidence limits for estimated control response at three frequencies. Estimated control response pressure magnitude is shown with 90% confidence limits based on estimated error variance. (Confidence limits omitted for $k_0a=0.74$.)

phases have been optimized separately at each frequency in the region, since each regression uses data for a single frequency. The actuators reduce the radiated power cost function by as much as 14 dB depending on the frequency. Detailed analysis of the structural and acoustic responses before and after applying control is not examined here. Since the intent is to illustrate the use of regression diagnostics, we restrict our attention to three specific frequencies as described in the following paragraphs.

At the first frequency, $k_0a=0.40$, the regression predicts that the radiated power cost function will be reduced by 5 dB; the control inputs are $b_1=1.06$ N and $b_2=-1.08$ N. The F-test yields $Q(F,\nu_1,\nu_2)=1.6\times10^{-6}$, which means: *given the data*, there is only a 0.00016% probability of a statistically significant lack of fit. We therefore feel confident enough about the regression to continue with further tests.

To use the t-test and other diagnostics, we must estimate the measurement noise variance; as in previous sections, we estimate the variance from the disturbance response data. Computing confidence intervals at the 90% significance level, we find that the control inputs at this frequency are $b_1=1.06\pm0.27$ N and $b_2=-1.08\pm0.28$ N. Since neither confidence interval contains zero, we can say with 90% confidence that, given the data and our estimate of the error variance, both control inputs are significantly different from zero. The upper plot in Fig. 5 shows the magnitude of the control response as a function of far-field location, with prediction intervals at the 90% significance level; also shown is the disturbance response. The average width of the prediction interval is roughly 0.06 Pa, while the signal levels are on the order of 0.6 Pa.

Next, consider $k_0a=0.50$. The regression indicates that

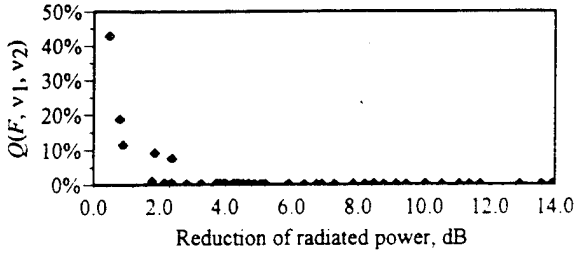

FIG. 6. F-test probability versus reduction of radiated power. Each data point represents a different frequency in the range $0.2<k_0a<1.0$. When $Q(F,\nu_1,\nu_2)$ is greater than a specified acceptable risk level, say, $\alpha_r=1\%$, there is a statistically significant lack of fit.

the control inputs $b_1=0.61$ N and $b_2=0.01$ N reduce the radiated power cost function by about 2 dB. We find that $Q(F,\nu_1,\nu_2)=0.0041$, e.g., there is less than one-half percent probability that this solution arose by chance, so we shall consider the regression statistically significant. However, one of the control forces fails the t-test: we find that the confidence interval $b_2=0.01\pm0.31$ N contains zero, and thus we cannot conclude that $|b_2|$ is significantly different from zero. The middle plot in Fig. 5 shows the prediction interval. At this frequency the average width of the prediction interval is 0.08 Pa, larger than for the frequency discussed above. To improve the reliability of the regression, we could reformulate it without b_2.

Now consider a third single-frequency case with $k_0a=0.74$. At this frequency the regression predicts controller performance of less than 1 dB. Performing the F-test, we find that $Q(F,\nu_1,\nu_2)=0.114$. In other words, there is an 11% chance that the control response is statistically different from the disturbance response. The regression at this frequency fails the F-test by most reasonable standards, and therefore we cannot make use of regression diagnostics such as confidence intervals and prediction intervals. An examination of the data and the estimated model, shown in the lower plot of Fig. 5, confirms that there is little relation between the control response and the disturbance response. Significant cancellation occurs by chance in a localized area near $\theta=90°$, but in general the two curves have very different characteristics.

Figure 6 explores the relationship between the F-test results and controller performance. Each data point represents a regression at a different frequency. The quantity $Q(F,\nu_1,\nu_2)$ is shown on the vertical axis, where $Q(F,\nu_1,\nu_2)$ is the probability that there is a significant lack of fit. Wherever the radiated power cost function is reduced by roughly 2 dB or more, $Q(F,\nu_1,\nu_2)$ is less than 1% and there is no lack of fit. Only when the radiated power cost function is reduced by less than 2 dB does $Q(F,\nu_1,\nu_2)$ rise to appreciable levels. This result is consistent with other force configurations investigated but not shown here. Failing the F-test is *always* accompanied by poor controller performance, meaning that any sound cancellation is coincidental and probably localized. Likewise, excellent controller performance always signals that the regression has passed the F-test. In the present example, a threshold of roughly 2 dB corresponds to passing or failing the F-test. However, it is

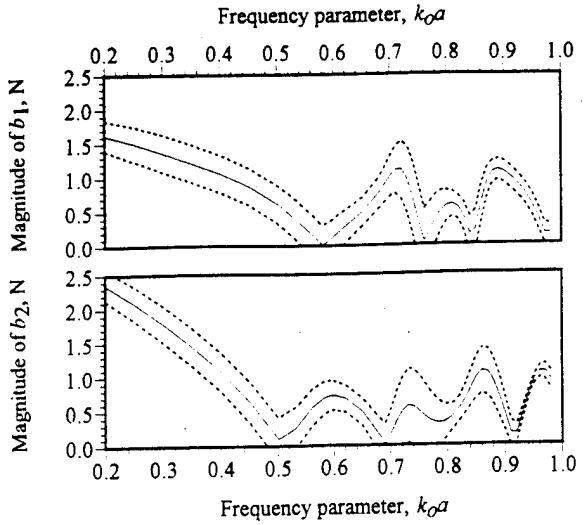

FIG. 7. Magnitude of control forces versus frequency, with 90% confidence limits on control force magnitude.

difficult to make *a priori* assumptions about F-test results: the threshold is problem specific and can only be found by examining F-test results for a number of different frequencies. Other cases not shown here achieved reductions of 4–5 dB but still failed the F-test.

Figure 7 shows the magnitudes and magnitude confidence intervals of the two control forces as a function of frequency. The solid curves represent the control force magnitudes, with the upper and lower 90% confidence limits displayed as broken curves. The upper and lower plots represent b_1 and b_2, respectively. There are several frequency ranges in which one of the control forces fails the t-test, meaning that one of the confidence intervals contains zero. For example, the confidence interval for b_2 contains zero near $k_0a=0.50$, $k_0a=0.69$, and $k_0a=0.91$. When a confidence interval contains zero, the associated control force does not contribute significantly to the regression at that frequency and could probably be removed without significantly affecting the results.

II. COLLINEARITY AND COLLINEARITY DIAGNOSTICS

The previous section describes regression and regression diagnostics, and outlines their relationship to simulating a feedforward control system. The topic of this section is collinearity, a type of numerical ill conditioning that can affect the simulation results. Included is a brief example to show how collinearity can affect the results of a numerical controller simulation.

A. How collinearity occurs in active noise control

Imagine an ASAC problem with two control forces applied at exactly the same location on the structure. In the nomenclature of the previous section, the two transfer functions are identical, the normal equations are singular, and there is no unique solution for the control force magnitudes. Now suppose the two control forces are close together, but not quite collocated. The two transfer functions are not identical, but very similar; the normal equations are not singular, but may be ill conditioned. In fact, the possibility for such near dependencies to cause ill conditioning exists whenever the transfer functions are not all mutually orthogonal.

TABLE II. Effect of simulated measurement noise without collinearity.

	No simulated noise		0.5% simulated noise		5% simulated noise	
	b_i	$\Delta\lvert b_i\rvert$	b_i	$\Delta\lvert b_i\rvert$	b_i	$\Delta\lvert b_i\rvert$
b_1	(−18.1,−0.8)	···	(−18.0,−0.8)	<0.5%	(−17.7,−0.8)	2%
b_2	(−21.3,−2.2)	···	(−21.3,−2.2)	<0.5%	(−21.0,−2.2)	1%
b_3	(131.9,11.4)	···	(131.9,11.4)	<0.5%	(131.8,11.3)	1%

Suppose we plunge ahead and solve the normal equation; what sort of solution can we expect? Often the adjacent (and partially redundant) control forces have opposite phases and very large magnitudes. In some circumstances such results are purely a numerical artifact, the result of ill conditioning of the normal equation. In other circumstances the results could be interpreted as a force couple approximating a concentrated moment, with no indication of whether the solution was genuine or spurious. This disturbing ambiguity motivates the use of collinearity diagnostics.

Note that control forces need not be located next to each other to produce collinearity. If the modal density is low and the structure is very lightly damped, there may be several locations at which applied forces would produce nearly the same response. Control forces applied at two or more such locations would produce collinearity even though they were distant from each other. Another source of collinearity arises when one control force can be replaced by a linear combination of other control forces in the system.

B. An example showing the effects of collinearity

An example shows how collinearity can affect even a relatively simple control simulation. Consider the clamped cylinder of Fig. 1 with a disturbance force b_d acting at a frequency of $k_0a=0.95$. Choose three control actuators b_1, b_2, and b_3, whose locations we shall discuss after performing a brief numerical experiment. The regression predicts controller performance of 23 dB. Since the F-test and t-test results (not shown) appear reasonable, we accept as significant the following complex control inputs:

$$b_1=(-18.1,-0.8),\quad b_2=(-21.3,-2.2),\quad b_3=(131.9,11.4), \tag{31}$$

where, for example, $\mathrm{Re}\{b_1\}=-18.1$ and $\mathrm{Im}\{b_1\}=-0.8$.

A simple numerical experiment can show how measurement noise in the sensor data $Y=\{y_1,y_2,\ldots,y_M\}$ affects the regression results. We simulate measurement noise by artificially injecting random components into Y, recomputing the regression, and examining the control input magnitudes. The results are summarized in Table II. The first pair of columns, labeled "No simulated noise," contains the original regression results given in Eq. (31). Next, each error sensor output y_i is perturbed with 0.5% simulated measurement noise, that is, a noise component with random phase and with random magnitude up to 0.5% of the maximum value in Y, and the regression is recomputed using the perturbed Y. As shown in the second pair of columns in Table II, simulated measure-

TABLE III. Effect of simulated measurement noise with collinearity.

	No simulated noise		0.5% simulated noise		5% simulated noise	
	b_i	$\Delta\lvert b_i\rvert$	b_i	$\Delta\lvert b_i\rvert$	b_i	$\Delta\lvert b_i\rvert$
b_1	(−627.7,−37.0)	···	(−604.5,−49.0)	5%	(−195.1,−78.9)	67%
b_2	(613.5,36.1)	···	(589.7,48.5)	2%	(164.9,78.2)	70%
b_3	(117.3,9.6)	···	(118.1,9.4)	1%	(128.2,9.6)	9%
b_4	(24.1,1.4)	···	(23.2,1.9)	2%	(7.0,3.1)	68%

ment noise of 0.5% does not significantly change the predicted control inputs. Next we increase the simulated measurement noise to 5% and recompute the regression. As shown in the third pair of columns in Table II, the control input magnitudes are changed by less than 2%. In fact, we can increase the simulated measurement noise to 25% or more before the control inputs change substantially. The regression is relatively insensitive to measurement noise.

Now suppose that we add a fourth control input b_4 in an attempt to improve system performance. (For the sake of illustration we choose a particularly bad location for b_4.) For the new configuration with no simulated measurement noise, we predict that the control inputs reduce the radiated power by 29 dB, an improvement of 6 dB over the previous case. Again the F-test and t-test results appear reasonable, so we accept as significant the control inputs shown in the first pair of columns in Table III. But now, simulated measurement noise of only 0.5% produces changes of up to 5% in the predicted control inputs. If we increase the simulated measurement noise to 5%, the control inputs are completely changed. Still, the F-test and t-test show no signs of trouble, and the subroutine used to solve the normal equation gives no warning or error messages. Why is the solution so sensitive to measurement noise? The reason, of course, is collinearity between the particular control forces we chose.

Examining the locations of the control inputs, shown in Fig. 8, we can clearly explain the numerical difficulties. The first two inputs b_1 and b_2 are axisymmetric ring forces and b_3 is a distributed axisymmetric ring force. But the control input used in the second example, b_4, is an axisymmetric ring moment applied exactly between b_1 and b_2. The two ring forces, when combined with opposite phases, produce a force couple that has nearly the same effect as the ring moment. The ring moment is redundant, and in this simple example is easily seen as the cause of the numerical problems. The collinearity diagnostics presented in the next section provide a general method that could be used to detect and analyze collinearities in more complicated systems where relations between actuators might not be so clear.

C. A collinearity diagnostic

Rather than trying to present a comprehensive review of collinearity diagnostics and their possible applications in studying feedforward control, this section presents one diagnostic method with some basic example results. For more detail the reader is referred to Belsley.[14]

Recall the normal equation for a feedforward control system with M sensors and N actuators,

$$(X^H W X)B = X^H W P. \tag{32}$$

As the reader might expect, most collinearity diagnostics involve the condition number of $X^H W X$. Clearly a large condition number announces the presence of ill conditioning, but simply examining the condition number leaves three questions unanswered. First, how can we detect whether more than one near dependency is present? Second, how large a condition number can we tolerate and still have confidence in the regression results? And third, how can we determine which actuators are involved in near dependencies? We will briefly discuss these three questions before presenting the diagnostic method.

The first question, regarding the number of near dependencies present, is answered by examining not just the condition number of $X^H W X$ but the singular values of $X^H W X$. A zero singular value indicates a perfect linear dependency in $W^{1/2}X$; a "small" singular value indicates a near dependency that may cause conditioning problems. In fact, the number of small singular values indicates the number of near dependencies present in the problem.

The second question is, how do we make quantitative comparisons to determine whether the condition number is "large," or equivalently, whether a given singular value is small? The answer is that we must scale the columns of $W^{1/2}X$ before computing the singular values. Column scaling, described in the next section, permits such quantitative comparisons.

To answer the third question of determining which variables are involved in near dependencies, we turn to a result from the least-squares regression. One of the effects of collinearity is variance inflation: when two or more actuators are involved in a near dependency, their variances become large. We can express the variances in terms of the singular

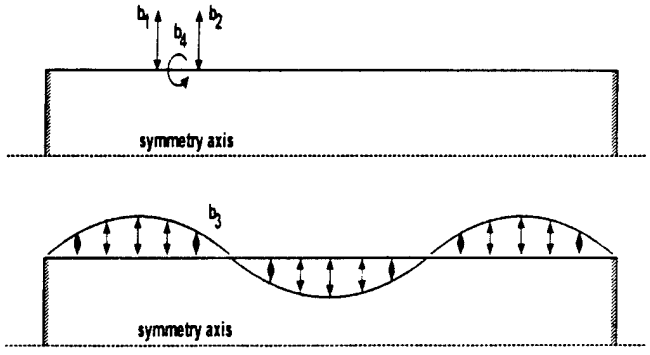

FIG. 8. Example problem for collinearity diagnostics. The first two actuators are axisymmetric ring forces b_1 and b_2 applied at $\delta=0.25$ and 0.31. The third actuator is a axisymmetric distributed force $b_3=\cos(3\pi\delta)$. The fourth actuator is an axisymmetric ring moment b_4 applied at $\delta=0.31$.

values of $W^{1/2}X$. When we find two or more actuators whose variances are primarily associated with a small singular value, then those actuators are involved in a near dependency.

We now describe the diagnostic method in somewhat of a cookbook fashion. The intent is not to present a detailed derivation, but rather to outline the method and show a simple numerical example related to feedforward control. We modify the technique slightly to account for complex-valued variables and weighted least squares, which are not included in the discussion of Ref. 14.

1. Determine $W^{1/2}X$

Each column of $W^{1/2}X$ represents a transfer function between a given control input and the error sensor array. These may be obtained via analytical approximations, numerical calculations, or any other means available. For N actuators and M sensors, X has the form $X=\{X_1\ X_2\ \ldots\ X_M\}$, where each X_j is a complex vector of length M containing the transfer function for the jth actuator. In our example the columns of X are transfer functions between four control inputs ($N=4$) and 25 sensor locations ($M=25$). We obtain the transfer functions by numerical modeling of the structure using a finite-element/boundary-element approach.

2. Apply column equilibration to $W^{1/2}X$

The purpose of column equilibration is to produce a set of singular values that do not depend on the units of the problem. We scale each column in $W^{1/2}X$ to have unit vector length after scaling. This produces a new matrix $\mathbf{Z}$, the scaled weighted design matrix:

$$\mathbf{Z}=\mathbf{\Omega}^{-1/2}W^{1/2}X, \tag{33}$$

where $\mathbf{\Omega}^{-1/2}$ is a diagonal matrix whose diagonals are $\Omega_j^{-1/2}=\{X_j^H\ WX_j\}^{-1/2}$. The relation between $\mathbf{Z}$ and the original problem may be seen from

$$X^HWX=\mathbf{Z}^H\mathbf{\Omega}\mathbf{Z}. \tag{34}$$

3. Obtain scaled condition indexes and variance-decomposition proportions

First we generate the singular-value decomposition of $\mathbf{Z}$,

$$\mathbf{Z}=\mathbf{U}D\mathbf{V}^H, \tag{35}$$

where $\mathbf{U}$ is column orthogonal, $\mathbf{V}$ is column orthogonal and row orthogonal, and D is nonnegative and diagonal. (Note the distinction between the matrix $\mathbf{V}$ and the variance V). The elements of D are the singular values μ_k, $k=1,2,\ldots,N$, which are real and non-negative since $\mathbf{Z}$ is Hermitian. The *scaled condition indexes* are then defined as

$$\tilde{\eta}_k=\mu_{\max}/\mu_k, \quad k=1,2,\ldots,N. \tag{36}$$

If we express the elements of the matrix $\mathbf{V}$ as ν_{kj}, we can write the variances of the regression coefficients in the following useful form:

TABLE IV. Variance decomposition proportions for example problem.

j	$\tilde{\eta}_j$	π_{j1}	π_{j2}	π_{j3}	π_{j4}
1	1.0	0.000	0.000	0.000	0.000
2	1.1	0.000	0.000	0.000	0.000
3	6.3	0.000	0.000	0.871	0.000
4	11 502.1	0.999	0.999	0.129	0.999

$$V(b_k)=\hat{\sigma_P^2}\sum_{j=1}^{N}\frac{\nu_{kj}^2}{\mu_j^2}. \tag{37}$$

The utility of Eq. (37) lies in the fact that each term in the summation is associated with only one scaled condition index $\tilde{\eta}_k$. By noting which of the large scaled condition indexes affect which variances, we can pick out near dependencies among the columns of $W^{1/2}X$. To this end, let us define *variance-decomposition proportions*,

$$\pi_{jk}\equiv\frac{\gamma_{kj}}{\gamma_k}, \quad k=1,\ldots,N,$$

where

$$\gamma_{kj}\equiv\frac{\nu_{kj}^2}{\mu_j^2} \quad \text{and} \quad \gamma_k\equiv\sum_{j=1}^{N}\gamma_{kj}, \quad k=1,\ldots,N. \tag{38}$$

The variance-decomposition proportions are interpreted as follows: π_{jk} is the portion of the variance for the kth regression coefficient that is associated with the jth scaled condition index.

Table IV contains the scaled condition indexes and variance-decomposition proportions for the example problem of Fig. 8. The second column contains the scaled condition indexes ranked by size, with the largest shown in the last row. The remaining four columns contain the variance-decomposition proportions for each of the control forces b_1, b_2, b_3, and b_4. The next sections explain how to interpret Table IV.

4. Determine the number of near dependencies

The method for counting the number of near dependencies involves choosing a threshold $\tilde{\eta}^*$ such that when $\tilde{\eta}_{\max}<\tilde{\eta}^*$, the columns of $W^{1/2}X$ may be said to be free of collinearity. The value suggested by Belsley[14] is $\tilde{\eta}^*=30$, although slightly larger or smaller values could also be argued for. This is the value used for all numerical results in this dissertation. Having chosen a threshold value for $\tilde{\eta}^*$, we now have the most basic collinearity diagnostic: whenever $\tilde{\eta}_{\max}<\tilde{\eta}^*$, at least one near dependency is present and the regression should not be used without further examination of its collinearity properties. Thus $\tilde{\eta}_{\max}$ should be computed as a routine part of every regression, and displayed along with the F-test and t-test results.

If more than one scaled condition index exceeds the threshold $\tilde{\eta}^*$, then multiple near dependencies are present. The number of near dependencies is determined according to the so-called "progression of 10/30:" the first near dependency corresponds to the first $\tilde{\eta}>30$, the second near depen-

dency corresponds to $\tilde{\eta}>100$, the third to $\tilde{\eta}>300$, the fourth to $\tilde{\eta}>1000$, and so forth. For example, the sequence of scaled condition indexes (1,9,33,35) indicates only one near dependency, while the sequence (1,9,33,105,108) indicates two near dependencies.

Referring to the first column of Table IV, it is evident that only one scaled condition index exceeds $\tilde{\eta}^*$, so we conclude that only one near dependency is present in the example.

5. Determine actuator involvement

To determine which actuators are affected by a near dependency, we examine the variance-decomposition proportions π_{jk}. Having associated a particular $\tilde{\eta}$ with a near dependency, we examine the π_{jk} in that row of the table. If two or more actuators have π_{jk} in that row larger than some threshold value π^*, then those actuators are involved in the near dependency. The value of π^* suggested by Belsley[14] and used in our example is $\pi^*=0.5$. In Table IV we examine the last row since that row is associated with a near dependency. Noting that the π_{jk} for b_1, b_2, and b_3 are all well above π^*, we can clearly see that these actuators are involved in the near dependency. (Recall that b_1 and b_2 are the ring forces and b_4 is the ring moment.) The third actuator, with $\pi_{jk}=0.129$, is not involved in the near dependency.

The rules for determining actuator involvement when multiple near dependencies are present are somewhat more complicated and need not be discussed here to illustrate the basic technique. Again, the interested reader is invited to examine Belsley.[14]

6. Examine auxiliary regressions

Once we know which actuators are involved in a near dependency, we can regress the individual transfer functions against each other to clarify the relationships between them. For example, we have determined that b_1, b_2, and b_4 are involved in a near dependency. If we set up a new regression using b_4 as the disturbance input with b_1 and b_2 as control inputs, we can see that the combination of b_1 and b_2, if given equal magnitudes and opposite signs, reproduces b_4 almost exactly (as suspected.) Thus the control input b_4 could be removed to obtain a more stable regression result.

7. Determine unaffected actuators

When an actuator associates most of its variance with small values of $\tilde{\eta}$, we can consider that actuator to be uninvolved with any near dependency. To be more precise, when the total proportion of variance associated with small $\tilde{\eta}^*$ is less than π^*, that actuator is uninvolved with any near dependency. In the example problem, the variance of b_3 is associated almost entirely with the first three small $\tilde{\eta}^*$, and therefore we conclude that it is not involved in any near dependency. This is supported by the fact that b_3 was the least affected by the simulated measurement noise introduced in the example discussed earlier.

III. SUMMARY

Multiple linear least-squares regression provides a numerical approach for simulating feedforward active control in the frequency domain. Solving the regression for a given frequency provides the complex control inputs and the amount by which the cost function is reduced. The squared multiple correlation coefficient $\mathbf{R}^2$ provides the amount of attenuation possible in the absence of measurement noise. In some cases, particularly where the effects of error sensor measurement noise are a concern, these quantities alone do not adequately characterize the regression. To help model the effects of measurement noise, one may consider the F-test, the t-test, and prediction intervals. The F-test measures the integrity of one the regression as a whole. When the regression fails the F-test, as in the example problem whenever the controller performance falls below 2 dB, other regression diagnostics may not be used for that particular frequency. The t-test measures the reliability of the estimated control input magnitudes. Prediction intervals combine the information from all the actuators to help describe the sensitivity to noise for the regression as a whole.

Before using regression diagnostics, it is important to carefully examine the statistical properties of the measurement noise present in the proposed error sensors. Strictly speaking, the noise must be normally distributed for the F-test, t-test, and prediction intervals to be valid. Furthermore, the noise should have constant variance. For some types of sensors, measurement noise may be neither normally distributed nor independent of signal magnitude.

Collinearity problems can produce numerical ill conditioning. Without proper collinearity diagnostics, numerical problems can go undetected and produce results that are very sensitive to measurement noise in the error sensors. Collinearity diagnostics can detect and analyze numerical ill conditioning. Collinearity diagnostics for complex-valued regressions follow directly from their real-valued counterparts, which are developed in considerable detail in the statistics literature. The primary collinearity diagnostic is the scaled condition number. Even when no other collinearity diagnostics are performed, the analyst may compute the scaled condition number for each regression and compare it to the threshold value in a somewhat mechanical fashion. If the scaled condition number exceeds the threshold, the regression should be discarded because of collinearity. More detailed diagnostics are also available for determining the number of near dependencies and which control forces are involved.

ACKNOWLEDGMENTS

The authors gratefully acknowledge financial support from Carderock Division, Naval Surface Warfare Center and from the Office of Naval Research (Grant No. ONR-N00014-88-K-0721). The authors also thank Dr. Alan Miller (CSIRO) and Dr. Kenneth White (University of British Columbia) for generously providing advice concerning regression and general statistical considerations. Felix Rosenthal provided helpful input concerning singular-value decomposition.

[1] P. A. Nelson and S. J. Elliott, *The Active Control of Sound* (Academic, London, 1992).
[2] P. A. Nelson, A. R. D. Curtis, S. J. Elliott, and A. J. Bullmore, "The active minimization of harmonic enclosed sound fields, Part I: Theory," J. Sound Vib. **117**, 1–13 (1987).
[3] A. J. Bullmore, P. A. Nelson, A. R. D. Curtis, and S. J. Elliott, "The active minimization of harmonic enclosed sound fields, Part II: A computer simulation," J. Sound Vib. **117**, 15–33 (1987).
[4] C. G. Mollo and R. J. Bernhard, "Generalized method of predicting optimal performance of active noise controllers," AIAA J. **27**, 1473–78 (1989). Note: author's name misspelled as "Molo."
[5] L. Song, G. H. Koopmann, and J. B. Fahnline, "Active control of the acoustic radiation of a vibrating structure using a superposition formulation," J. Acoust. Soc. Am. **89**, 2786–2792 (1991).
[6] L. Ljung, *System Identification: Theory for the User* (Prentice-Hall, Englewood Cliffs, NJ, 1987).
[7] B. Wahlberg and L. Ljung, "Hard frequency-domain model error bounds from least-squares like identification techniques," IEEE Trans. Autom. Control **37**, 900–912 (1992).
[8] S. D. Snyder, "A fundamental study of active noise control system design," unpublished Dissertation, Department of Mechanical Engineering, University of Adelaide, 1991.
[9] S. D. Snyder and C. H. Hansen, "Using multiple regression to optimize active noise control system design," J. Sound Vib. **148**, 537–542 (1990).
[10] K. S. Miller, "Complex Gaussian processes," SIAM Rev. **11**, 544–567 (1969).
[11] K. S. Miller, "Complex linear least squares," SIAM Rev. **15**, 707–726 (1975).
[12] F. Rosenthal, "A new technique for the active cancellation of wide-band noise using multiple sensors," Proceedings of the Second International Congress on Recent Developments in Air- and Structure-borne Sound and Vibration, March 1992 (unpublished), Vol. 1, pp. 337–344.
[13] D. A. Belsley, E. Kuh, and R. E. Welsch, *Regression Diagnostics: Identifying Influential Data and Sources of Collinearity* (Wiley, New York, 1980).
[14] D. A. Belsley, *Conditioning Diagnostics: Collinearity and Weak Data in Regression* (Wiley, New York, 1991).
[15] C. E. Ruckman, "Method and example application for least squares regression of complex-valued variables," Appl. Statistics (submitted 1994).
[16] C. E. Ruckman, "A regression-based approach for simulating active noise control in the frequency domain, with application to fluid–structure interaction problems," Doctoral dissertation, Virginia Polytechnic Institute and State University, May 1994.
[17] C. R. Fuller and J. D. Jones, "Experiments on reduction of propeller-induced interior noise by active control of cylinder vibration," J. Sound Vibr. **112**, 389–395 (1987).
[18] H. C. Lester and C. R. Fuller, "Active control of propeller induced noise fields inside a flexible cylinder," AIAA J. **28**, 1374–1380 (1989).
[19] R. L. Clark and C. R. Fuller, "Control of sound radiation with adaptive structures," J. Intelligent Mater. Syst. Struct. **2**, 431–45 (1991).
[20] C. R. Fuller and R. A. Burdisso, "A wavenumber domain approach to the active control of structure borne sound," J. Sound Vib. **148**, 355–360 (1991).
[21] C. R. Fuller, C. H. Hansen, and S. D. Snyder, "Active control of sound radiation from vibrating rectangular panel by sound sources and vibration inputs: An experimental comparison," J. Sound Vib. **145**, 195–215 (1991).
[22] C. R. Fuller, "Active control of sound transmission/radiation from elastic plates by vibration inputs: I. Analysis," J. Sound Vib. **136**, 1–15 (1990).
[23] Y. Gu and C. R. Fuller, "Active control of sound radiation due to subsonic wave scattering from discontinuities on fluid-loaded plates. I: Far-field pressure," J. Acoust. Soc. Am. **90**, 2020–2026 (1991).
[24] C. Guigou and C. R. Fuller, "Active control of edge sound radiation from a semi-infinite elastic beam with a clamped edge: Influence of bending near-field waves," J. Acoust. Soc. Am. **93**, 2716–25 (1992).
[25] C. E. Ruckman and C. R. Fuller, "Numerical simulation of active structural-acoustic control for a fluid-loaded, spherical shell: Formulation and validation," J. Acoust. Soc. Am. **96**, 2817–2825 (1994).
[26] A. M. Neville and J. B. Kennedy, *Basic Statistical Methods for Engineers and Scientists* (International Textbook, Scranton, PA, 1964).
[27] N. R. Draper and H. Smith, *Applied Regression Analysis* (Wiley, New York, 1966).
[28] C. L. Lawson and R. J. Hanson, *Solving Least Squares Problems* (Prentice-Hall, Englewood Cliffs, NJ, 1974).
[29] R. J. Carroll and D. Ruppert, *Transformation and Weighting in Regression* (Chapman and Hall, New York, 1988).
[30] M. C. Junger and D. Feit, *Sound, Structures, and Their Interaction* (MIT, Cambridge, 1986), 2nd ed.
[31] G. C. Everstine and A. J. Quezon, "User's guide to the coupled NASTRAN/Helmholtz equation capability (NASHUA) for acoustic radiation and scattering," CDNSWC-SD-92-17, Carderock Division, NSWC, Bethesda, MD, 1992.

C-29 Experiments on Active Control of Acoustic Radiation Due to a Clamped Edge on a Semi Infinite Beam, C. Guigou, C. R. Fuller and K. D. Frampton, Journal of Sound and Vibration, Vol. 169 No. 4, pp. 503-526, 1994.

Journal of Sound and Vibration (1994) 169(4), 503–520

EXPERIMENTS ON ACTIVE CONTROL OF ACOUSTIC RADIATION DUE TO A CLAMPED EDGE ON A SEMI-INFINITE BEAM

C. GUIGOU, C. R. FULLER AND K. D. FRAMPTON

Vibration and Acoustic Laboratories, Mechanical Engineering Department, Virginia Polytechnic Institute and State University, Blacksburg, Virginia 24061-0238, *U.S.A.*

(*Received* 15 *April* 1992, *and in final form* 22 *July* 1992)

Active control of acoustic radiation from a "semi-infinite" beam clamped at one end is studied experimentally. The beam is excited by subsonic flexural travelling waves which "scatter" (or produce reflected travelling and near-field waves) when they encounter the clamped discontinuity. The main purpose of these experiments is to demonstrate control of the acoustic radiation from the beam by actively changing the characteristics of the "scattered" waves with control actuators. The beam is disturbed by a harmonic input from a point force shaker. Control actuators, in the form of shakers or piezoelectric actuators, are attached to the beam near the clamped discontinuity. An error microphone is positioned in the acoustic field which supplies an error signal to a digital controller. The digital controller employed is the Filtered-X version of the adaptive LMS algorithm. An array of accelerometers is attached to the beam in order to obtain the out-of-plane displacement amplitude of the vibrating system. Applying a spatial Fourier transform, the wavenumber spectrum is calculated and used to describe the far-field radiated pressure. Experimental results are compared with related theoretical predictions. Experimental and theoretical results show that large attenuation at the error microphone is possible along with global attenuation of the acoustic field. Control is shown to be associated with reductions and changes in the shape of the vibration distribution near the discontinuity; the vibrational magnitudes away from the discontinuity are left largely unchanged.

1. INTRODUCTION

Many structures in use today incorporate beams as integral components. Structural elements such as aircraft and maritime vessel infrastructures, buildings frames and heavy machinery mounts can all include various forms of beams in their designs. As these structures are excited by machinery, noise and other environmental effects, vibrational waves propagate through these systems. When subsonic vibrational waves, travelling along structural components such as beams, encounter a discontinuity (such as a joint), sound is produced in this area. This emission of sound is caused by the scattering of travelling subsonic waves into reflected/transmitted near-field and reflected/transmitted propagating waves, which in turn produce supersonic wavenumber components in the vibrational response. These supersonic wavenumber components are responsible for acoustic radiation to the far field. The efficient control of this type of noise source is desirable in many applications.

In the last decade, active noise control has emerged as a practical method of reducing acoustic noise fields, especially at low frequencies [1, 2]. However, there are some disadvantages with using acoustic sources as control inputs. One such disadvantage, for example, is the number of acoustic sources required for the control. It has been

0022–460X/94/040503 + 24 $08.00/0

© 1994 Academic Press Limited

demonstrated by Fuller [3] that reduction of the far-field acoustic radiation can also be obtained by directly modifying the response of the structure by applying structural inputs rather than by adding a distribution of acoustic sources. This type of control has been termed Active Structural Acoustic Control (ASAC), as opposed to Active Noise Control (ANC).

A typical active control system, such as the one presented by Widrow *et al.* [4], requires three basic components: error sensors, which produce an electrical signal proportional to the signal to be controlled (in the present case, the sound pressure amplitudes); a control system, which calculates the control signals to be applied based on the error signal; control actuators, which apply inputs to the system in order to minimize the signal from the error sensors.

The error sensor can be any transducer which converts the signal to be controlled into an electrical signal. Microphones in the acoustic field were used by Fuller *et al.* [5] and by Clark and Fuller [6] to sense, respectively, sound transmitted through a plate and acoustic radiation from plates. Shaped piezoelectric films, recently utilized as sensors, were used by Clark and Fuller [7] to sense radiating modes on a simply supported plate. In the experiments presented in this paper, microphones located in the acoustic near field are used as error sensors.

In many of the previously conducted active control experiments, the control system is in the form of a digital signal processing (DSP) board hosted by a personal computer. The DSP board samples the signal from the error and, based on this information, calculates a control signal to send to the control actuators. The method used by Fuller *et al.* [5] and Clark and Fuller [6, 7] for calculating the control signals is based on a narrow-band form of the Filtered-X version of the adaptive least mean square (LMS) algorithm. This method is also used in the experiments. The algorithm uses a steepest gradient descent method which minimizes the least mean square of the error signals by converging on the set of optimal weighting coefficients for the adaptive filters. Elliot, Stothers and Nelson [8] describe this algorithm in detail.

The last components of a typical active control system are the control actuators. The purpose of the control actuators is forcibly to change the structure vibrational characteristic such that error signals are minimized. Two different kinds of actuators are usually utilized in ASAC: shakers [5] and, recently, piezoelectric actuators [6, 7]. In the experiments presented in this paper, both previously mentioned actuator types are applied to the beam near the clamped discontinuity, in order to minimize the error microphone signal.

Experiments were conducted by Frampton [9] with the intention of demonstrating the feasibility of active control of acoustic radiation due to subsonic wave scattering by discontinuities on thin beams. The "semi-infinite" beam studied in these experiments had a clamped discontinuity at one end (wave reflection only); the other end was placed in an anechoic termination which made the beam appear infinite to waves propagating in that direction by preventing their reflection. All experiments were performed in a 5·6 m × 2·8 m × 2·1 m anechoic chamber. The goal was actively to affect the scattered structural waves in such a manner as to minimize the acoustic radiation at particular points in the acoustic field. A semicircular array of microphones was used to obtain information about the acoustic field associated with the discontinuity. Due to space limitations in the anechoic chamber, the microphone array was located in a region which was the border between the far and near fields for the operating frequencies. For the purpose of this paper, we term this region the "radiation field". By comparing the two sets of microphone data (before and after control), the effectiveness of the control on the acoustic field was established. In addition, an array of accelerometers was used to measure the

acceleration of the beam at several points. From these accelerometer data points, the complex coefficients of an assumed beam displacement equation were calculated using a least squares regression method. A spatial Fourier transform was then taken in order to determine the wavenumber spectrum of the beam response. The wavenumber spectrum was then used to predict the far-field radiated pressure and to indicate whether the far-field levels were attenuated.

In addition, analytical models of the beam response and the optimal control input were developed. A comparison of the analytical and experimental results was then presented.

2. EXPERIMENTAL SET-UP

This section describes the set-up for the experiment. A schematic of the entire system is presented in Figure 1(a), while a photograph of the rig is shown in Figure 1(b). Each component of the system is described below.

The beam used in the experiments was made of 6061 aluminum and was 3·66 m long, 0·102 m wide and 0·00318 m thick. The properties of the beam are summarized in Table 1.

The beam was arranged such that one end was outside of the anechoic chamber. This end of the beam was placed in an anechoic termination and passed through a hole in the wall of the anechoic chamber. The anechoic termination was a pyramid-shaped wooden box filled with sand. This configuration caused flexural waves which encountered the termination to experience a gradual increase in impedance. Therefore, the flexural waves were absorbed by the anechoic termination and no reflected waves were created. This served to make the beam appear infinite in this direction (the positive x-direction). The effectiveness of the anechoic termination was verified experimentally by calculating its power reflection ratio, which is defined as the ratio of the reflected vibrational power to the incident vibrational power. This was accomplished by exciting the beam with broadband noise delivered to a shaker. By taking the autospectra and the cross-spectra from the signals of two accelerometers on the beam, the power reflection ratio was calculated using the expression found in reference [10],

$$\Phi = \frac{S_1 + S_2 - 2C_{12}\cos(k_f \Delta) + 2Q_{12}\sin(k_f \Delta)}{S_1 + S_2 - 2C_{12}\cos(k_f \Delta) - 2Q_{12}\sin(k_f \Delta)}, \tag{1}$$

where S_1 and S_2 are the autospectra of the accelerometer signals, C_{12} and Q_{12}, respectively, the real and imaginary parts of their cross-spectrum, k_f is the structural wavenumber, and Δ is the distance between the accelerometers. The results showed that the reflected power was less than 10% of the incident power for all frequencies above 180 Hz, and was 4% less than for the frequencies of interest of this paper.

TABLE 1

Beam properties

Total length	3·66 m
Baffled length	2 m
Width	0·102 m
Thickness	0·00318 m
Young's modulus	$7{\cdot}1 \times 10^{10}$ N/m^2
Density	2700 kg/m^3

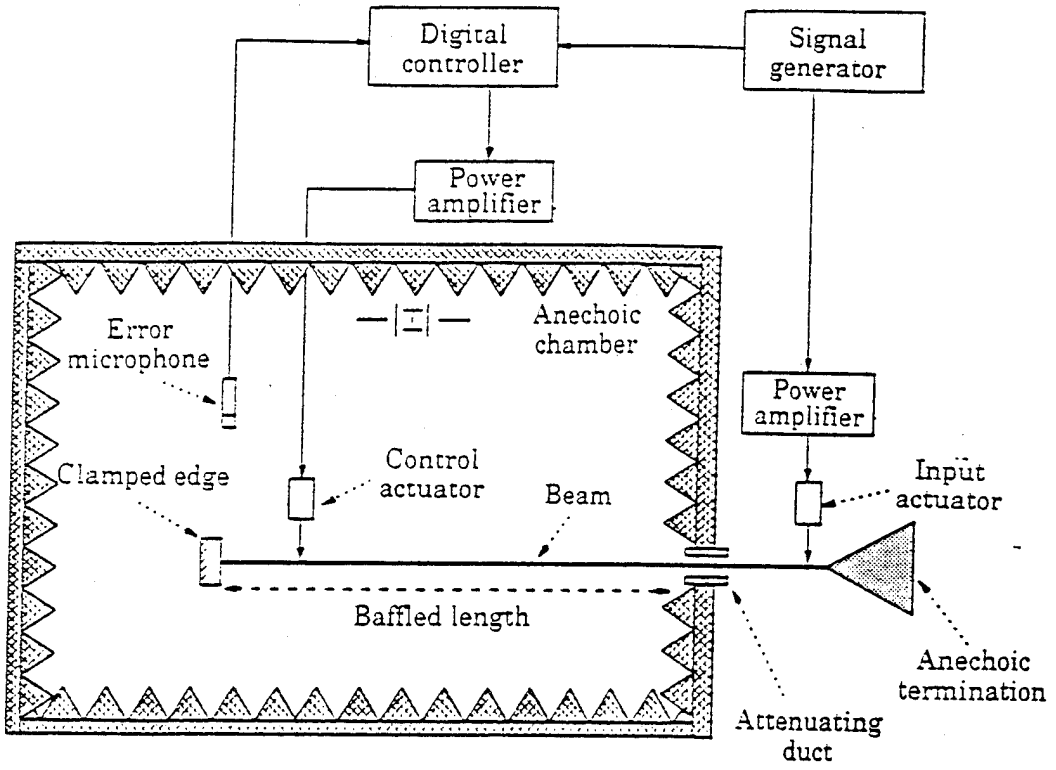

(a)

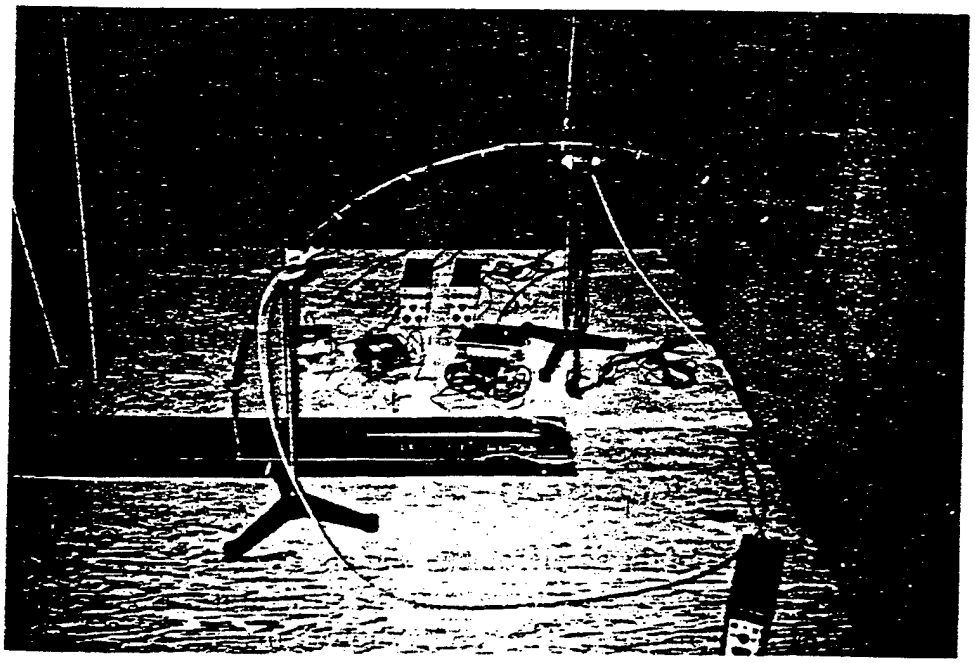

(b)

Figure 1. (a) Schematic of the experimental set-up: (b) photograph of the rig.

Along with the anechoic termination, the input disturbance shaker was fastened to the beam outside of the anechoic chamber by a point attachment and stringer. Since the input shaker produces a significant amount of noise, it could have affected the outcome of the experiments. By attaching the input shaker to the beam outside of the anechoic chamber, passing the beam through a narrow (1 cm) slit in the wall of the chamber and then through an attenuation duct (a rectangular duct 25 cm long, made of plywood and lined with fiberglass insulation), the amount of noise produced by the input shaker that entered the anechoic chamber was minimized. To quantify the

effect of the input shaker acoustic radiation on the experiments. the shaker was driven at the experimental operating frequencies, while disconnected form the beam. Microphone measurements were taken for these frequencies inside the chamber, and all levels due to the disconnected input shaker were less than 10 dB (*re* 2×10^{-5} Pa). Since the operating levels for the experiments were the order of 50–60 dB, the effects of the input shaker were negligible.

For the purpose of studying the radiation from the beam in the half-plane and for facilitating comparison with theoretical models, the beam was surrounded by a plywood baffle in the horizontal x–y plane. Since the theoretical model assumes an infinite baffle, some differences between the infinitely baffled theory and the finitely baffled experiments were expected. However, it should be noticed that the scattering noise source is at the clamped end which was close to the center of the baffle. In addition, the assumption is made in the theoretical model that none of the air near the surface of the beam is able to move back and forth across the baffle. Since it would be impossible to achieve a perfect seal between the edge of the baffle and the edge of the beam without interfering with the vibrational response of the beam, some differences between theoretical and experimental results were expected. These differences are manifested as a decreased acoustic radiation efficiency by the experimental beam, as compared to the theoretical model caused by losses associated with the air near the surface of the beam moving back and forth across the baffle, particularly along the small gap between the beam and baffle edges. However, a great deal of effort was made to adjust the gap to be no greater than 2 mm and, since wavelengths associated with the radiated field are much longer, this effect was considered to be negligible.

The beam was supported at three axial locations by elastic tubing fastened to the ceiling of the anechoic chamber. The tubing was of sufficient length and stiffness such that their natural frequencies were well below the operating frequencies of the experiments. Independent tests confirmed that the tubing had little effect on the propagation of waves in the beam.

The clamped discontinuity was constructed from a large (10 cm × 7 cm × 20 cm) block of aluminum and a steel clamping plate (10 cm × 7 cm × 0·5 cm). By placing 2 cm of the end of the beam between the clamping plate and the block and tightening three clamping screws, an approximate clamped end condition was achieved. An illustration of the clamp is shown in Figure 2. In order to determine the effectiveness of the clamped discontinuity, a test was run to determine its power reflection ratio. This test was performed similarly to the one run to examine the performance of the anechoic termination, and described previously. For an ideal clamp, the power reflection ratio would be unity for all frequencies. Results from this test showed that, for all frequencies above 280 Hz, the power reflection coefficient was greater than 0·95.

Thirteen miniature 1/4 inch microphones were used in the experiments. They were attached to a semicircular, steel array with a radius of 0·86 m, centered over the discontinuity and suspended from the anechoic chamber ceiling, as shown in Figure 1(b). The angular positions of each microphone in the array is shown in Table 2. In each case, the array could be situated in either a perpendicular or axial position. While, in the perpendicular position, the semicircular array is perpendicular to the long axis of the beam, in the axial position the microphone array is parallel to the long axis of the beam, as shown in Figure 3. The array was made as large as the space in the anechoic chamber would allow, so that the array could be rotated from the axial position to the perpendicular position. These two array positions allowed a global selection of acoustical data to be taken in each experiment.

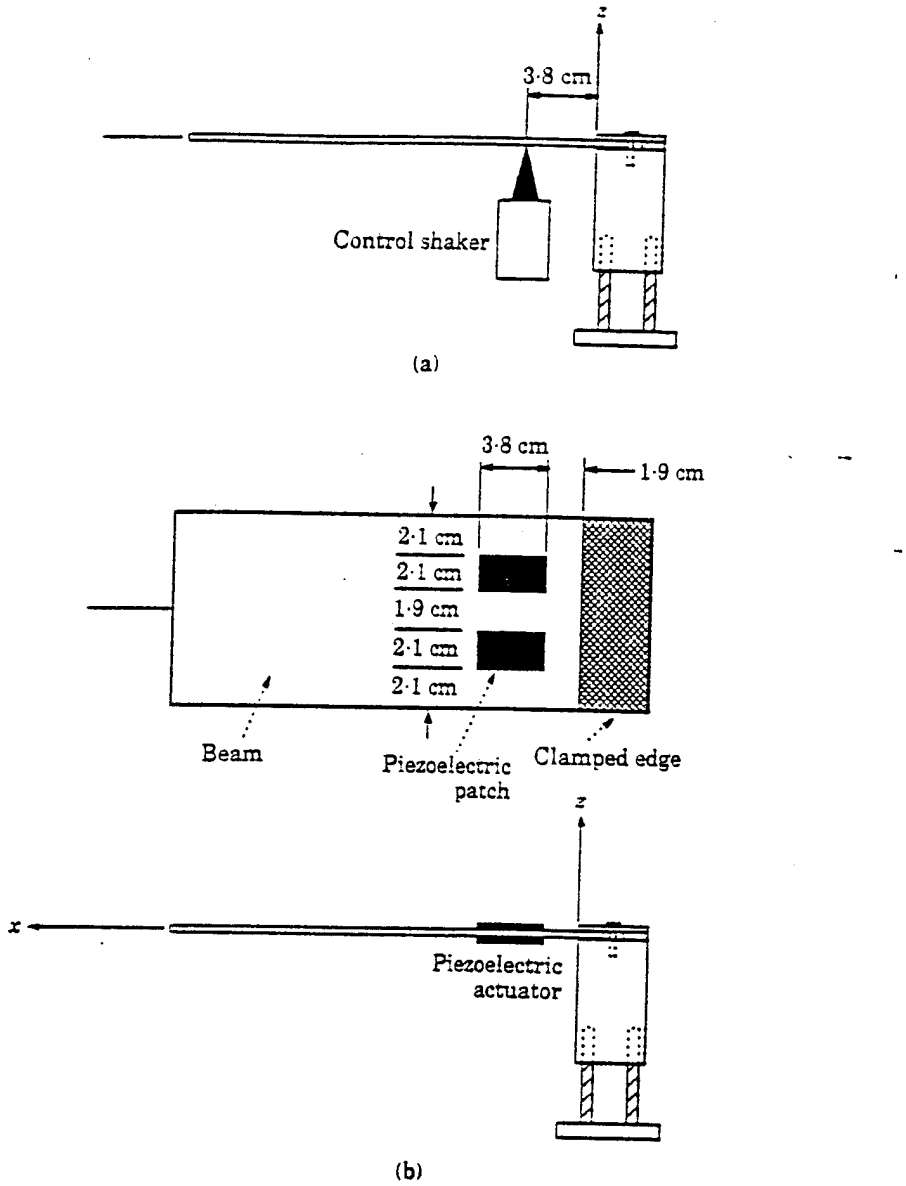

Figure 2. Position of (a) the control shaker and (b) the piezoelectric actuator.

Since the microphone array was moved (perpendicular and axial position) during each experiment, it was necessary to have a stationary error microphone so that pressure data could be collected from the array while the digital controller was operating. For this reason, a Bruel & Kjaer type 4166 condenser microphone was used as an error sensor. The Bruel & Kjaer microphone also has a superior signal-to-noise ratio which allows improved attenuation by the controller.

Ten Bruel & Kjaer type 4374 accelerometers along with two Bruel & Kjaer type 2635 charge amplifiers were used to sense the beam acceleration in each experiment, as shown in Figure 1(b). The positions of each of the accelerometers are listed in Table 3. One accelerometer was used as a reference and the other nine were run through a switching box. The reference accelerometer signal was run through one charge amplifier, while the switching box output was run through the other. The switching box was operated remotely from outside of the anechoic chamber. When taking vibrational data, the magnitude of the reference accelerometer was measured and then the transfer function between the reference accelerometer and each of the other accelerometers was collected. All experiments were performed at a steady state single frequency, enabling measurement of transfer functions in the above manner.

TABLE 2

Microphone positions on semicircular array of radius 0·86 m

Microphone	Position (degrees)
1	77·1
2	64·3
3	51·4
4	38·6
5	25·7
6	12·9
7	0·0
8	−12·9
9	−25·7
10	−38·6
11	−51·4
12	−64·3
13	−77·1

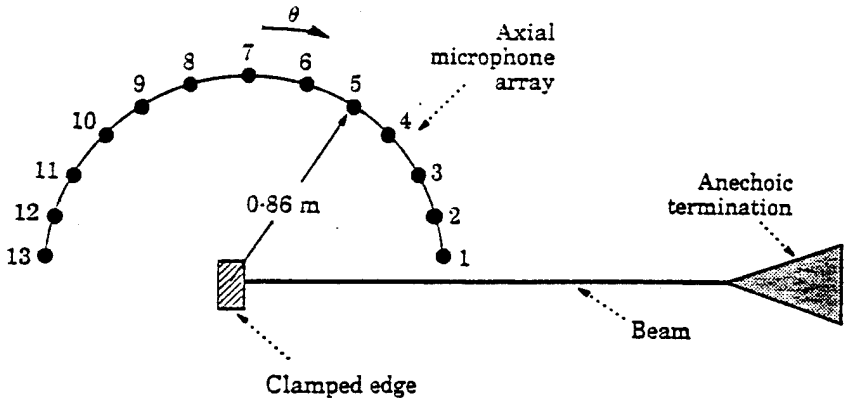

(a)

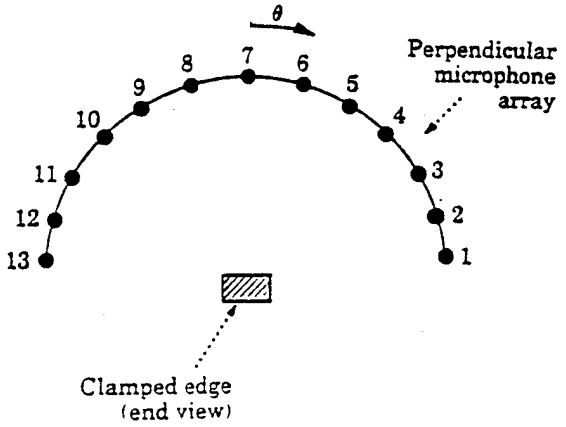

(b)

Figure 3. Position of the microphone array: (a) axial; (b) perpendicular.

TABLE 3

Accelerometer positions

Accelerometer	Position (m)
1	0·005
2	0·01
3	0·02
4	0·03
5	0·08
6	0·11
7	0·17
8	0·20
9	0·29
10	0·31

The data received from the accelerometers were used to decompose the complex amplitudes of the assumed displacement equations. From the displacement equation, an analysis of the beam response allowed a detailed examination of the mechanism by which control of the acoustic field was achieved.

Two types of control actuators were used in these experiments, a shaker and a set of piezoelectric patches. The shaker was attached to the underside of the beam and baffle, 3·8 cm from the discontinuity. The control actuators were located close to the discontinuity, as the analytical work of reference [11] demonstrated that this was the best location for control of the acoustic field due to wave scattering. The noise produced by the control shaker was also minimized by wrapping it in fiberglass insulation. A schematic of the beam and control shaker is shown in Figure 2(a).

The piezoelectric actuators were bonded to the beam, using cyanoacrylate strain gage glue, in the positions shown in Figure 2(b). It is important to note that four individual piezoelectric patches were operating dependently as one actuator. This method of creating a piezoelectric actuator (four patches for one actuator) has also been used by Crawley and de Luis [12]. One actuator consisted of two pairs of piezoelectric patches, while each pair consisted of two individual patches bonded directly opposite each other on the beam. Two patches on the same side of the beam operated in phase; patches on opposite sides of the beam were driven 180° out of phase. This allowed the piezoelectric actuator to produce pure bending moments on the beam [12, 13]. The reason for having two dependent pairs placed symmetrically about the central long axis of the beam was that the beam central axis needed to be accessible for connection of the shaker and positioning of the accelerometer array.

A multiple channel Filtered-X LMS algorithm was used in these experiments. It was implemented from a digital signal processing board hosted on a Swan 286 PC. Experimental uses of this control algorithm are discussed by Gonidou [10] for vibrational control and by Clark and Fuller [6, 7] for noise control. This type of control system implements a variable coefficient FIR filter. The coefficients of the FIR filter are updated by the LMS algorithm, which employs a steepest gradient descent method for minimizing the least mean square error. A complete description of this algorithm is given by Elliot *et al.* [8]. The output of the lth error sensor can be represented at the nth time step by

$$e_l(n) = d_l(n) + \sum_{m=1}^{M} \sum_{j=0}^{N-1} P_{lmj} \sum_{i=0}^{N-1} w_{mi}(n-j)x(n-i-j), \tag{2}$$

where $d_l(n)$ is the lth error sensor output due to the input excitation alone, $x(n)$ is the input reference source, w_{mi} are the coefficients of the adaptive FIR filters and P_{lmj} is the jth coefficient of the transfer function between the output of the mth adaptive filter and the lth error sensor. M and N are, respectively, the number of control actuators and filter coefficients. In the LMS algorithm, the error function is defined by the mean square error signal; i.e.,

$$J = E\left[\sum_{l=1}^{L} e_l^2(n)\right], \tag{3}$$

where E is the expectation operator and L is the total number of error sensors utilized to implement the control. Since this error function is quadratic, only one minimum solution exists. At each sample time n, the outputs of the compensating filters P_{lmj} are used by the LMS algorithm to minimize J by individually updating each of the adaptive filter coefficients according to the relation

$$w_{mi}(n+1) = w_{mi}(n) - \mu \sum_{l=1}^{L} e_l(n) r_{lm}(n-i), \tag{4}$$

where the outputs of the compensating filters P_{lmj} are

$$r_{lm}(n-i) = \sum_{j=0}^{N-1} P_{lmj} x(n-i-j), \tag{5}$$

and μ is the stability parameter. Since the disturbance is narrow-band only, two coefficients are needed in each adaptive FIR filter. Note that this control method can easily be extended to multi-frequency excitation by increasing the number of coefficients in each adaptive FIR filter.

3. EXPERIMENTAL PROCEDURE

This paper presents only two cases among all the experiments which have been performed in reference [9]. The first case involves a shaker as control actuator, and an error microphone located at position 4 on the axial microphone array (see Figure 3 and Table 2) for an excitation frequency of 510 Hz. The second case uses a piezoelectric actuator as control actuator, and an error microphone at the same location as in the previous case, for an excitation frequency of 320 Hz. These two frequencies correspond to subsonic flexural waves, and have also been chosen in such a way that the anechoic termination and the clamped discontinuity have good performance. It should be noticed that, because the two different actuators were used for control at two different frequencies, their relative merits cannot be compared. However, the analytical analysis showed that for this type of control (minimization of the radiated pressure at one point), the force actuation and the moment actuation lead to almost the same performances and that, at low frequencies, the control performance is dependent on the position rather than on the type of actuator.

For each experiment, the same procedure, as described below, was followed. Before applying the control, data from the accelerometer array and the microphone array in the axial and perpendicular positions were measured to determine both the response of the structure and the acoustic field when no control is applied. This served as a baseline to evaluate the effectiveness of the control. After obtaining measurements for the uncontrolled case, the controller was started and allowed to converge to the optimal weighting coefficients which minimized the error microphone signal. Then, data were again collected from the accelerometer and microphone arrays to provide information on the acoustic field

and structural response under control. After obtaining these measurements, the uncontrolled and controlled responses could be compared.

4. THEORETICAL ANALYSIS

4.1. DISPLACEMENT OF THE BEAM

Full details about the derivation of the displacement of the beam can be found in reference [11]. The Cartesian co-ordinate system used in this analysis is shown in Figure 4. The beam is taken to be located in an infinite baffle corresponding to the x–y plane and is infinite in the x-positive direction. The time dependence is assumed to be $e^{-i\omega t}$ for all of the fields. Since in the experiments the input shaker was located outside the anechoic chamber, only the propagating wave travelling in the x-negative direction was taken into account (from the input shaker, the propagating waves travelling in the x-positive direction were absorbed by the anechoic termination and the disturbance produced non-propagating near-field waves were negligible at distances well away from the disturbance).

The shaker used in these experiments can be analytically approximated as a point force. The displacement of the beam subjected to an incident flexural wave of magnitude $\hat{W}_n$ (due to the input shaker) and one control force of magnitude $\hat{F}^c$ located at $x = x^c$ (due to the control shaker) can be found to be [11]

$$\begin{aligned} w(x) = \hat{W}_n[e^{-ik_f x} + i\,e^{ik_f x} - (1+i)\,e^{-k_f x}] \\ + (i\hat{F}^c/4EIk_f^3)[e^{ik_f|x-x^c|} + i\,e^{-k_f|x-x^c|} \\ + (i\,e^{ik_f x^c} - (1+i)\,e^{-k_f x^c})\,e^{ik_f x} - ((1+i)\,e^{ik_f x^c} - e^{-k_f x^c})\,e^{-k_f x}], \end{aligned} \tag{6}$$

where k_f is the structural wavenumber, defined by

$$k_f = \sqrt[4]{(\rho S\omega^2/EI)}. \tag{7}$$

In equation (7), ρ is the density, S is the cross-sectional area, EI is the flexural stiffness of the beam, and ω is the angular frequency of excitation.

In the first and second square brackets of equation (6), the two last terms correspond, respectively, to the propagating waves ($e^{ik_f x}$) and near-field flexural waves ($e^{-k_f x}$) reflected

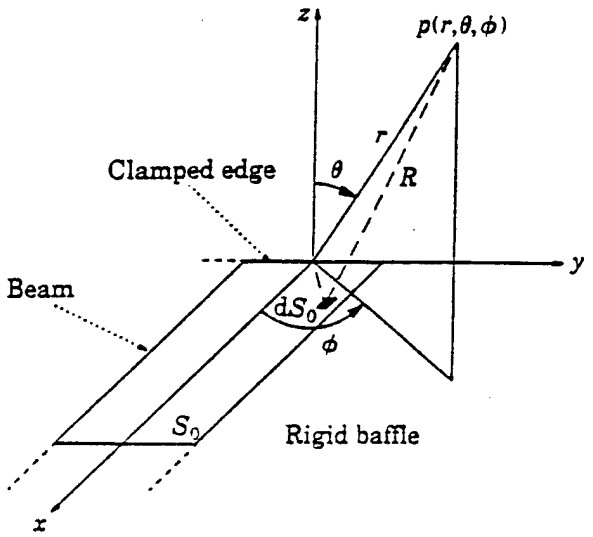

Figure 4. Co-ordinate system.

by the clamped end discontinuity. Also notice that the control force creates two different flexural waves on each side of the application point; a propagating flexural wave ($e^{ik_f|x-x^c|}$) and a non-propagating near-field flexural wave ($e^{-k_f|x-x^c|}$).

The piezoelectric patches described previously were also used as control actuators. These can be modelled as two out-of-phase moments acting at each edge of the piezoelectric patch. The displacement of the beam submitted to an incident wave of magnitude $\hat{W}_n$ and one pair of control moments, approximating the piezoelectric actuator, can be written as [11]

$$\begin{aligned} w(x) = \hat{W}_n[&e^{-ik_f x} + i\,e^{ik_f x} - (1+i)\,e^{-k_f x}] \\ &+ (\hat{M}^c/4EIk_f^2)[\operatorname{sgn}(x-(x^c+L_a))(e^{ik_f|x-(x^c+l_a)|} - e^{-k_f|x-(x^c+L_a)|}) \\ &- \operatorname{sgn}(x-x^c)(e^{ik_f|x-x^c|} - e^{-k_f|x-x^c|}) \\ &+ (-i\,e^{ik_f(x^c+L_a)} - (1-i)\,e^{-k_f(x^c+L_a)} + i\,e^{ik_f x^c} + (1-i)\,e^{-k_f x^c})\,e^{ik_f x} \\ &+ ((1+i)\,e^{ik_f(x^c+L_a)} - i\,e^{-k_f(x^c+L_a)} - (1+i)\,e^{ik_f x^c} + i\,e^{-k_f x^c})\,e^{-k_f x}], \end{aligned} \tag{8}$$

where

$$\operatorname{sgn}(x-x^c) = \begin{cases} +1, & \text{if } x \geqslant x^c, \\ -1, & \text{if } x < x^c, \end{cases} \tag{9}$$

and L_a is the length of the piezoelectric actuator (the piezoelectric actuator is actually located between $x = x^c$ and $x = x^c + L_a$).

4.2. RADIATED PRESSURE IN THE NEAR FIELD

In the co-ordinate system as shown in Figure 4, the radiated acoustic pressure is given by the so-called Rayleigh's integral [14]

$$p(r,\theta,\phi) = \int_{S_0} 2i\omega\rho_0 v(x_0,y_0) g(R)\,dS_0, \tag{10}$$

where ρ_0 is the density of the acoustic medium, $v(x_0, y_0)$ is the out-of-plane velocity of the vibrating surface S_0, and R is the distance between the elementary source dS_0 and the observation point. The free-space Green's function is defined by

$$g(R) = -e^{ik_0 R}/4\pi R, \tag{11}$$

where k_0 is the wavenumber in the acoustic medium, given as $k_0 = \omega/c_0$, and c_0 represents the speed of sound in the acoustic medium. Then, the Rayleigh's integral can be rewritten as

$$p(r,\theta,\phi) = -i\omega\rho_0 \int_{S_0} (e^{ik_0 R}/2\pi R) v(x_0,y_0)\,dS_0, \tag{12}$$

where $R = [r^2 + x_0^2 + y_0^2 - 2r\sin\theta(x_0\cos\phi + y_0\sin\phi)]^{1/2}$.

It can be noted that, since $v(x_0, y_0)\,dS_0$ is the volume velocity of an elementary area of the surface S_0, the planar source located in an infinite baffle is equivalent to a distribution of point sources.

In the acoustic field corresponding to radial locations of this study (i.e., not completely in the far field), the integral in equation (12) has no closed form solution. Therefore, it

was numerically computed over the surface S_0 of the vibrating beam located in the anechoic chamber, in order to compare theoretical and experimental results. The surface S_0 is defined by $0 \leqslant x_0 \leqslant l_b$ and $-l_y/2 \leqslant y_0 \leqslant l_y/2$, where l_b is the length of the baffled portion of the beam and l_y is the beam width.

It is apparent that the pressure in the near field can also be written as a function of the incident wave and the control force or control moment as

$$p(r, \theta, \phi) = A(r, \theta, \phi)\hat{W}_n + B(r, \theta, \phi)\hat{C}^c, \tag{13}$$

where the values of $A(r, \theta, \phi)$ and $B(r, \theta, \phi)$ can be deduced from the previous equations and are obtained by numerical integration. $\hat{C}^c$ can be either the control force or a pair of control moments. (Note that the value of the coefficient $B(R, \theta, \phi)$ is different for a control force and a pair of control moments.) The first term in equation (13) is the near-field pressure radiated before the control is applied to the beam structure.

4.3. OPTIMAL CONTROL

For optimal control, the square of the pressure modulus was minimized at the location of the microphone, defined by (r^c, θ^c, ϕ^c). It is given by

$$|p(r^c, \theta^c, \phi^c)|^2 = |A(r^c, \theta^c, \phi^c)|^2 |\hat{W}_n|^2 + \hat{W}_n A(r^c, \theta^c, \phi^c) B^*(r^c, \theta^c, \phi^c)\hat{C}^{c*}$$
$$+ \hat{C}^c B(r^c, \theta^c, \phi^c) A^*(r^c, \theta^c, \phi^c)\hat{W}_n^* + |B(r^c, \theta^c, \phi^c)|^2 |\hat{C}^c|^2, \tag{14}$$

which is a real quadratic function of the control input. For a given magnitude of the incident wave and a given location of the control input, this quadratic function has only one minimum value associated with an optimal control input. A general solution for this type of optimization problem has been developed by Nelson *et al.* [15] which is, in this particular case, given by

$$\hat{C}^c = -\frac{A(r^c, \theta^c, \phi^c) B^*(r^c, \theta^c, \phi^c)}{|B(r^c, \theta^c, \phi^c)|^2}\hat{W}_n. \tag{15}$$

The value of the optimal control input is then substituted back into the displacement and near-field pressure equations in order to find the different fields with control.

4.4. WAVENUMBER SPECTRUM

The far-field radiated pressure has been shown in reference [11] to be proportional to the wavenumber spectrum of the beam velocity in the supersonic region. As the experiments were performed at locations which did not fulfil far-field radiation conditions, it is instructive to use the beam-measured wavenumber spectrum to predict and study actual far-field radiation without and with control. This technique overcomes the physical limitations of the anechoic chamber used in this set of experiments.

As explained in reference [11], the one-dimensional wavenumber spectrum $\tilde{v}(k_x)$ is related to the far-field pressure radiated in the x–z plane and is defined by

$$\tilde{v}(k_x) = \int_0^{+\infty} -i\omega w(x)\, e^{-ik_x x}\, dx. \tag{16}$$

Using the expression developed by Keltie [16] from the distribution theory

$$\int_0^{+\infty} e^{iux}\, dx = \pi\delta(u) + i/u, \tag{17}$$

the spectral response of the system with control forces is

$$\tilde{v}(k_x) = -i\omega\hat{W}_n\Bigg[\pi\delta(-k_x-k_f) - \frac{i}{k_x+k_f} + i\pi\delta(k_f-k_x) - \frac{1}{k_f-k_x}$$

$$-(i+1)\pi\delta(ik_f-k_x) + \frac{(1-i)}{ik_f-k_x}\Bigg]$$

$$+\frac{\omega\hat{F}^c}{4EIk_f^3}\Bigg[i\frac{e^{-ik_x x^c} - e^{ik_f x^c}}{(k_x+k_f)} - \frac{e^{-ik_x x^c}}{i(k_f-k_x)} + e^{-ik_f x^c}\pi\delta(k_f-k_x) - \frac{e^{-ik_x x^c} - e^{-k_f x^c}}{(k_x+ik_f)}$$

$$-\frac{e^{-ik_x x^c}}{(ik_f-k_x)} + i\,e^{k_f x^c}\pi\delta(ik_f-k_x) + (i\,e^{ik_f x^c} - (1+i)\,e^{-k_f x^c})\left(\pi\delta(k_f-k_x) + \frac{i}{k_f-k_x}\right)$$

$$+(-(1+i)\,e^{ik_f x^c} + e^{-k_f x^c})\left(\pi\delta(ik_f-k_x) + \frac{i}{ik_f-k_x}\right)\Bigg], \tag{18}$$

and the spectral response of the system with piezoelectric actuator control is

$$\tilde{v}(k_x) = -i\omega\hat{W}_n\Bigg[\pi\delta(-k_x-k_f) - \frac{i}{k_x+k_f} + i\pi\delta(k_f-k_x) - \frac{1}{k_f-k_x}$$

$$-(i+1)\pi\delta(ik_f-k_x) + \frac{(1-i)}{ik_f-k_x}\Bigg]$$

$$+\frac{-i\omega\hat{M}^c}{4EIk_f^2}\Bigg[-i\frac{e^{-ik_x(x^c-L_a^c)} - e^{ik_f(x^c+L_a^c)}}{k_x+k_f} + i\frac{e^{-ik_x(x^c+L_a^c)}}{k_f-k_x} + e^{-ik_f(x^c+L_a^c)}\pi\delta(k_f-k_x)$$

$$+\frac{e^{-ik_x(x^c+L_a^c)} - e^{-k_f(x^c+L_a^c)}}{k_f-ik_x} - \frac{e^{-ik_x(x^c+L_a^c)}}{ik_x+k_f} - e^{k_f(x^c+L_a^c)}\pi\delta(ik_f-k_x)$$

$$+i\frac{e^{-ik_x x^c} - e^{ik_f x^c}}{k_x+k_f} - i\frac{e^{-ik_x x^c}}{k_f-k_x} - e^{-ik_f x^c}\pi\delta(k_f-k_x)$$

$$-\frac{e^{-ik_x x^c} - e^{-k_f x^c}}{k_f-ik_x} + \frac{e^{-ik_x x^c}}{ik_x+k_f} + e^{k_f x^c}\pi\delta(ik_f-k_x) + (-i\,e^{ik_f(x^c+L_a^c)} - (1-i)\,e^{-k_f(x^c+L_a^c)}$$

$$+i\,e^{ik_f x^c} + (1-i)\,e^{-k_f x^c})\left(\pi\delta(k_f-k_x) + \frac{i}{k_f-k_x}\right) + ((1+i)\,e^{ik_f(x^c+L_a^c)} - i\,e^{-k_f(x^c+L_a^c)}$$

$$-(1+i)\,e^{ik_f x^c} + i\,e^{-k_f x^c})\left(\pi\delta(ik_f-k_x) + \frac{i}{ik_f-k_x}\right)\Bigg]. \tag{19}$$

The wavenumber spectrum is usually divided in two regions; the supersonic region defined by $k_x \leqslant k_0$, and the subsonic region defined by $k_x > k_0$. As explained in reference [11], only the supersonic region of the wavenumber spectrum of the beam velocity contributes to the far-field radiated pressure. Since the flexural waves travelling along the beam are assumed to be subsonic, i.e., $k_f > k_0$, the Dirac delta functions associated with them do not contribute to the far-field radiated pressure. Consequently, the far-field radiated pressure is due to the flexural near-field components and also to the distributed spectra associated with the one-sided propagating waves. It can be noted that the shape of the wavenumber spectrum in the supersonic region describes the far-field radiation pattern of the source under study.

4.5. BEAM DISPLACEMENT FROM ACCELEROMETER DATA

The acceleration data are used to decompose the unknown complex amplitude in an assumed displacement equation by means of a least mean square regression method.

The assumed equation for the beam with point force control (approximating a shaker) is

$$w_a(x) = \hat{A}\, e^{-ik_f x} + \hat{B}\, e^{-k_f|x-\alpha^c|} + \hat{C}\, e^{ik_f|x-\alpha^c|} + \hat{D}\, e^{-k_f x} + \hat{E}\, e^{ik_f x}, \tag{20}$$

which is a reduced form of equation (6).

For the beam with a piezoelectric actuator, the assumed equation is

$$\begin{aligned} w_a(x) = {} & \hat{A}\, e^{-ik_f x} + \hat{B}[\operatorname{sgn}(x - (\alpha^c + L_a))\, e^{ik_f|x-(\alpha^c+L_a)|} - \operatorname{sgn}(x-\alpha^c)\, e^{ik_f|x-\alpha^c|}] \\ & + \hat{C}[\operatorname{sgn}(x - (\alpha^c + L_a))\, e^{-k_f|x-(\alpha^c+L_a)|} - \operatorname{sgn}(x-\alpha^c)\, e^{-k_f|x-\alpha^c|}] \\ & + \hat{D}\, e^{-k_f x} + \hat{E}\, e^{ik_f x}, \end{aligned} \tag{21}$$

which is a reduced form of equation (8).

In order to find the unknown complex amplitudes for the assumed displacement equation, a set of dependent equations has to be solved. Since ten accelerometers are used and only three (in the situation without control) or five (in the situation with control) complex amplitudes have to be calculated, the system of equations is overdetermined. Therefore, a least mean square regression method is used to decompose these complex amplitudes. With ten data points, up to ten equations could be obtained (one for each data point). The method of least mean square, as described by Draper and Smith [17], is derived as follows.

We define

$$\mathbf{Y} = \begin{bmatrix} z_1(x_1) \\ \vdots \\ z_n(x_n) \end{bmatrix}, \tag{22}$$

where $z_i(x_i)$ is the displacement measured at x_i and n is the number of data points (ten in this case),

$$\mathbf{X} = \begin{bmatrix} X_1^a & X_1^b & X_1^c & X_1^d & X_1^e \\ \vdots & \vdots & \vdots & \vdots & \vdots \\ X_n^a & X_n^b & X_n^c & X_n^d & X_n^e \end{bmatrix} \tag{23}$$

where, for the control force case,

$$X_i^a = e^{-ik_f x_i}, \qquad X_i^b = e^{-k_f|x_i-\alpha^c|}, \qquad X_i^c = e^{ik_f|x_i-\alpha^c|},$$

$$X_i^d = e^{-k_f x_i}, \qquad X_i^e = e^{ik_f x_i}, \tag{24a–e}$$

for the piezoelectric actuator case,

$$X_i^a = e^{-ik_f x_i},$$

$$X_i^b = \operatorname{sgn}(x_i - (\alpha^c + L_a))\, e^{ik_f|x_i-(\alpha^c+L_a)|} - \operatorname{sgn}(x_i-\alpha^c)\, e^{ik_f|x_i-\alpha^c|},$$

$$X_i^c = \operatorname{sgn}(x_i - (\alpha^c + L_a))\, e^{-k_f|x_i-(\alpha^c+L_a)|} - \operatorname{sgn}(x_i-\alpha^c)\, e^{-k_f|x_i-\alpha^c|},$$

$$X_i^d = e^{-k_f x_i}, \qquad X_i^e = e^{ik_f x_i}, \tag{25a–e}$$

and

$$\mathbf{U} = \begin{bmatrix} \hat{A} \\ \hat{B} \\ \hat{C} \\ \hat{D} \\ \hat{E} \end{bmatrix}. \tag{26}$$

The set of n linear equations can then be written in matrix form as

$$\mathbf{XU} = \mathbf{Y}. \tag{27}$$

Pre-multiplying each side by $\mathbf{X}^{\mathrm{T}}$, the least mean square equation is then given by

$$\mathbf{X}^{\mathrm{T}}\mathbf{XU} = \mathbf{X}^{\mathrm{T}}\mathbf{Y}. \tag{28}$$

The unknown vector of complex amplitudes $\mathbf{U}$ can be then determined:

$$\mathbf{U} = (\mathbf{X}^{\mathrm{T}}\mathbf{X})^{-1}\mathbf{X}^{\mathrm{T}}\mathbf{Y}. \tag{29}$$

It is now possible to decompose the beam displacement from the experimental data of the accelerometer array into travelling and near-field structural waves. The previous derivation was done for the case where five coefficients have to be determined. For the uncontrolled case, only three coefficients have to be calculated, as $\hat{B}$ and $\hat{C}$ are set to zero in equations (20) and (21). The derivation is similar, except that the rectangular matrix $\mathbf{M}$ has only three columns and the vector $\mathbf{U}$ three rows.

It should be noted that the theoretical model developed uses the value of the coefficient $\hat{A}$, determined as previously described from the uncontrolled experimental case, as the value for the magnitude $\hat{W}_n$ of the incident propagating wave.

4.6. WAVENUMBER SPECTRUM FROM ACCELEROMETER DATA

Now that the complex coefficients of the assumed displacement equations are known (equations (20) and (21)) the wavenumber spectrum of the beam velocity can be calculated. The same approach used to obtain the theoretical wavenumber spectrum (equations (16) and (17)) can be utilized. Therefore, the wavenumber spectrum of the system with point force control is

$$\begin{aligned}
\tilde{v}_a(k_x) = &-\mathrm{i}\omega\hat{A}\left[\pi\delta(-k_x-k_f) - \frac{\mathrm{i}}{k_x+k_f}\right] \\
&-\mathrm{i}\omega\hat{B}\left[\mathrm{i}\frac{\mathrm{e}^{-\mathrm{i}k_x x_c} - \mathrm{e}^{-k_f x_c}}{(k_x+\mathrm{i}k_f)} + \mathrm{i}\frac{\mathrm{e}^{-\mathrm{i}k_x x_c}}{(\mathrm{i}k_f-k_x)} + \mathrm{e}^{k_f x_c}\pi\delta(\mathrm{i}k_f-k_x)\right] \\
&-\mathrm{i}\omega\hat{C}\left[-\frac{\mathrm{e}^{-\mathrm{i}k_x x_c} - \mathrm{e}^{\mathrm{i}k_f x_c}}{\mathrm{i}(k_x+k_f)} - \frac{\mathrm{e}^{-\mathrm{i}k_x x_c}}{\mathrm{i}(k_f-k_x)} + \mathrm{e}^{-\mathrm{i}k_f x_c}\pi\delta(k_f-k_x)\right] \\
&-\mathrm{i}\omega\hat{D}\left[\pi\delta(\mathrm{i}k_f-k_x) + \frac{\mathrm{i}}{\mathrm{i}k_f-k_x}\right] \\
&-\mathrm{i}\omega\hat{E}\left[\pi\delta(k_f-k_x) + \frac{\mathrm{i}}{k_f-k_x}\right],
\end{aligned} \tag{30}$$

and the wavenumber spectrum of the system with piezoelectric actuator control is

$$\begin{aligned}\tilde{v}_a(k_x) = &-i\omega\hat{A}\left[\pi\delta(-k_x-k_f)-\frac{i}{k_x+k_f}\right]\\
&-i\omega\hat{B}\left[-i\frac{e^{-ik_x(x^e+L_a)}-e^{ik_f(x^e+L_a)}}{k_x+k_f}+i\frac{e^{-ik_x(x^e+L_a)}}{k_f-k_x}\right.\\
&+e^{-ik_f(x^e+L_a)}\pi\delta(k_f-k_x)+i\frac{e^{-ik_x x^e}-e^{ik_f x^e}}{k_x+k_f}\\
&\left.-i\frac{e^{-ik_x x^e}}{k_f-k_x}-e^{-ik_f x^e}\pi\delta(k_f-k_x)\right]\\
&-i\omega\hat{C}\left[-\frac{e^{-ik_x(x^e+L_a)}-e^{-k_f(x^e+L_a)}}{k_f-ik_x}+\frac{e^{-ik_x(x^e+L_a)}}{ik_x+k_f}\right.\\
&+e^{k_f(x^e-L_a)}\pi\delta(ik_f-k_x)+\frac{e^{-ik_x x^e}-e^{-k_f x^e}}{k_f-ik_x}\\
&\left.-\frac{e^{-ik_x x^e}}{ik_x+k_f}-e^{k_f x^e}\pi\delta(ik_f-k_x)\right]\\
&-i\omega\hat{D}\left[\pi\delta(ik_f-k_x)+\frac{i}{ik_f-k_x}\right]\\
&-i\omega\hat{E}\left[\pi\delta(k_f-k_x)+\frac{i}{k_f-k_x}\right]. \qquad (31)\end{aligned}$$

5. RESULTS

5.1. FREQUENCY OF EXCITATION 510 HZ

For the first case considered here, the beam system is excited at a frequency of 510 Hz. The error microphone is located at a position identical to position 4 on the axial microphone array (see Figure 3(a) and Table 2) and the control actuator is a shaker located at 3·8 cm from the clamped end of the beam, as shown on Figure 2(a).

The experimentally measured acoustic field without and with control in the axial and perpendicular position is shown in Figure 5. It can be noticed that the radiation from the beam system without control is related to a monopole radiation structural motion, mainly due to the back reaction force applied by the constraint. When control is invoked, an attenuation of 36 dB at the error microphone is achieved. Although the rest of the acoustic field does not experience such dramatic attenuation, sound pressure levels are globally attenuated. This implies that controlling the acoustic field at one point is not at the expense of increasing levels elsewhere in the acoustic field.

The theoretically predicted acoustic field for the same situation and co-ordinates is presented in Figure 6. These values are calculated assuming the same parameters that were used in the experimental set-up. First, the complex amplitude of the incident propagating wave is determined from the displacement experimental data without control. Then, this actual value is used in the theoretical model. The sound pressure levels are computed at the same locations as the experimental microphone array in the axial and perpendicular positions. Before the control is applied, the results agree very well with those obtained experimentally. The analytical sound pressure levels were expected to be higher

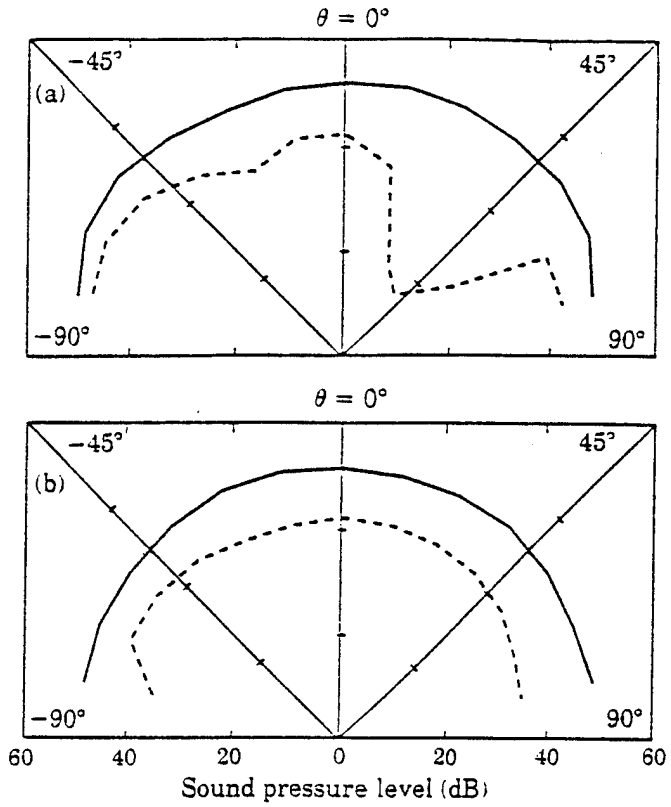

Figure 5. Experimental pressure directivity at 510 Hz: (a) axial array: (b) perpendicular array. ——, Without control; —, with control shaker.

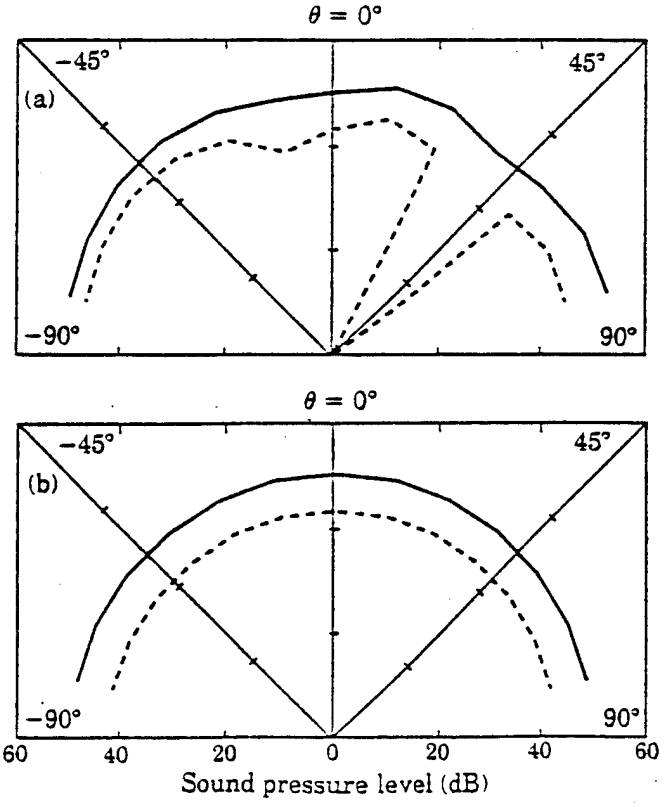

Figure 6. Theoretical pressure directivity at 510 Hz: (a) axial array; (b) perpendicular array. ——, Without control; --, with control shaker.

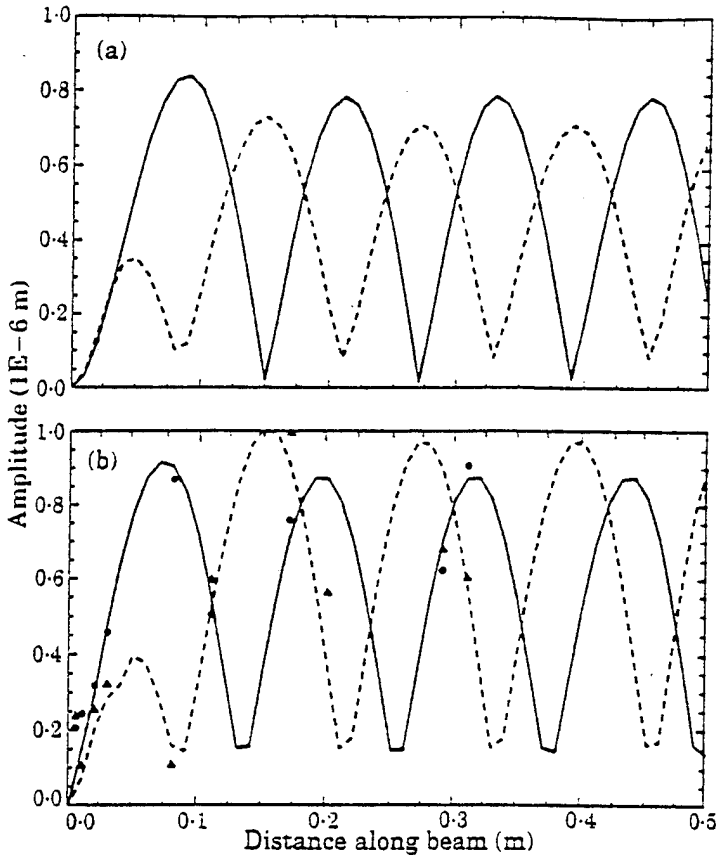

Figure 7. Beam displacement at 510 Hz: (a) theoretical; (b) experimental. ——, Without control; —, with control shaker; •, point experimental data without control; ▲, point experimental data with control.

than the experimental ones due to the fact that the baffle is not infinite and perfect in the experiments, allowing some of the air near the surface of the beam to move back and forth across it. However, the theoretical model showed that the pressure levels were dependent on the beam length considered to be located inside the anechoic chamber. This length was difficult to determine due to the attenuation duct, used to minimized the noise produced by the input shaker outside the anechoic chamber, and to the absorbing elements of the anechoic chamber. The length was assumed to be equal to the length of the baffle surrounding the beam (in the x-direction), which was 2 m ($l_b = 2$ m). When the control is applied, theory predicts a large attenuation at the error microphone and slight attenuation throughout the rest of the acoustic field. The most noticeable difference between analytical and experimental results is that theory predicts an extremely low pressure level at the error microphone location while, experimentally, the sound pressure level was about 17 dB. This is due to the noise floor associated with the error microphone used in the experiments, which is about 15–18 dB.

The theoretical and experimental beam displacements for the 510 Hz case are shown in Figure 7. The experimental waves are a result of determining wave amplitudes from the wave decomposition and then calculating the overall beam vibration using equation (20). The actual point measurement values are also included for comparison. The theoretical and experimental results do not agree as well for the displacement as for the acoustic field results. Although the general shape of the standing waves both with and without control are similar, theory predicts decreasing vibrational amplitudes with control, while experimental results show the opposite. This is probably due to two factors. First of all, the clamped end condition used in the experiments is assumed to be perfect in the theoretical analysis. Although the clamped edge showed good characteristics, it was by no

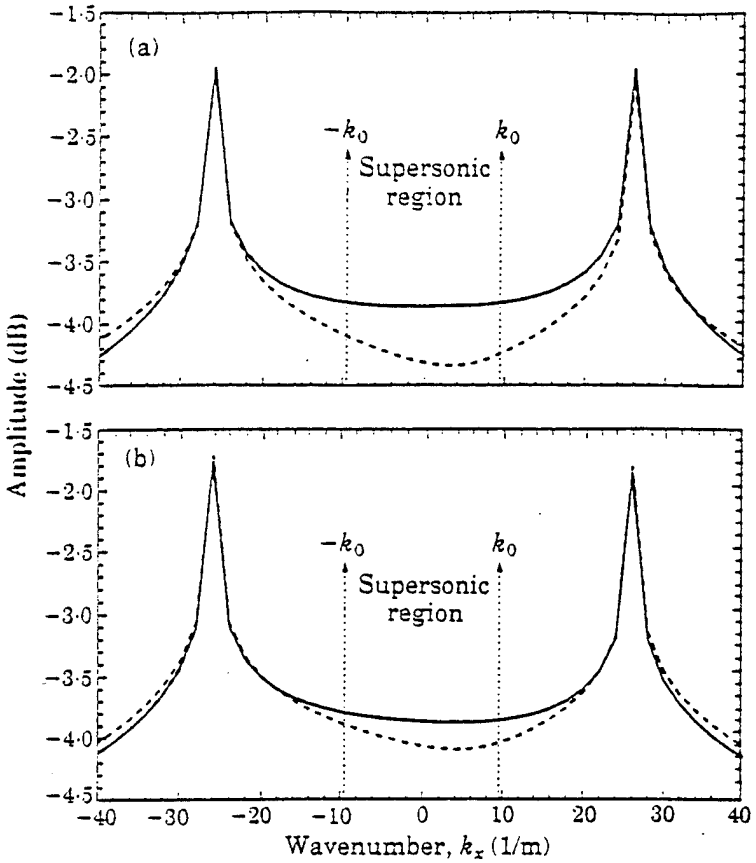

Figure 8. Wavenumber spectrum at 510 Hz: (a) theoretical; (b) experimental. ——, Without control; – –, with control shaker.

means perfect. Note that, in the case without control, the ratio $\hat{A}/\hat{E}$ provides information about the performance of the clamped edge. For a perfect clamped boundary condition, this ratio magnitude is equal to unity. In the experiments, the ratio was found to be greater than 0·9 in magnitude. Second, when the control actuator was turned on, the input impedance seen by the input shaker changed, which caused the amplitude of the incident wave to change (i.e., the disturbance source is not of infinite input impedance and $\hat{A}$ is not the same before and after control). In this particular case, the magnitude of $\hat{A}$ was found to be increased by about 10% under control. In the theoretical analysis, it is assumed that the incident wave amplitude is the same with and without control. However, it should also be noted that both theory and experiments demonstrate that the most important changes in the beam vibrational displacement under control are localized close to the clamped edge discontinuity. Thus, it is apparent that the control is effective in reducing sound radiation by modifying the scattered wave motion near the discontinuity. This control mechanism was also theoretically shown by Guigou and Fuller in reference [11].

The wavenumber spectrum of each spectural displacement function, shown in Figure 7, is shown in Figure 8. Even though the theoretical and experimental displacements do not agree well, the resulting wavenumber spectra do in the range presented in Figure 8. That means that theoretical and experimental results agree well on the wavenumbers composition of the structure motion. The errors in actual displacement are, thus, associated with large axial wavenumbers which are not important in terms of radiation. It was shown in reference [11] that the far-field acoustic pressure is a function of the wavenumber spectrum in the supersonic region. Without control, both spectra are almost constant in magnitude in the supersonic region. This is related to a monopole radiation pattern in the far field.

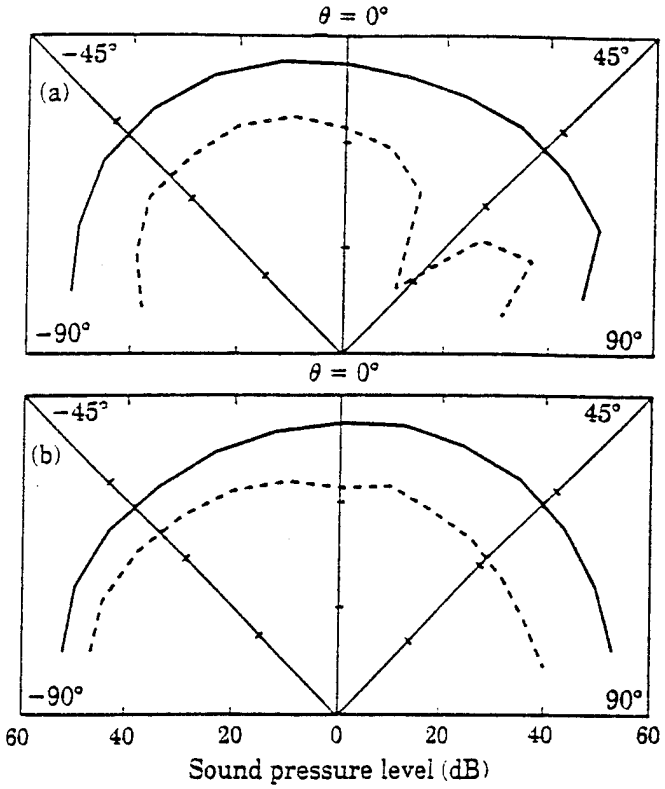

Figure 9. Experimental pressure directivity at 320 Hz: (a) axial array; (b) perpendicular array. ——, Without control; – –, with piezoelectric actuator.

When the control is applied, the theoretical model predicts larger attenuation in the supersonic region than the experiments. However, the theoretical and experimental spectra are at a minimum in the wavenumber region directly corresponding to the directions close to the direction defined by the error microphone ($\theta^e = 38{\cdot}6°$ and $\phi^e = 0°$ correspond to $k_x^e \simeq 5{\cdot}8\ \mathrm{m}^{-1}$, see reference [11]). Therefore, while applying control to the acoustic field of this experiment, the supersonic wavenumber components are attenuated. This implies that the acoustic far-field radiation is attenuated as well. Considering the method of obtaining the beam response, these results are considered to be very good.

5.2. FREQUENCY OF EXCITATION 320 HZ

For the second case, the beam system is excited at 320 Hz. The error microphone is located at the same position as in the first case. The control actuator is a piezoelectric actuator located at 1·9 cm from the clamped end and 3·8 cm long (see Figure 2(b)).

The acoustic field for the experimental case without and with control is shown in Figure 9 for the axial and perpendicular array positions. When no control is applied, the sound radiation again has a monopole radiation pattern, as expected, since the clamp exerts a reaction force component on the beam which will lead to monopole radiation. When the control is activated, an attenuation of 32 dB is obtained at the error microphone, while the rest of the acoustic field is again globally attenuated. Thus, as in the previous case, the control of the acoustic field at the error microphone leads to a reasonable decrease in the pressure levels in both axial and perpendicular directions.

The analytical acoustic field for the same situation is shown in Figure 10. Before the control is applied, the predicted results agree well with those obtained experimentally. When the control is invoked, large attenuation is achieved at the microphone location. A slight increase of the pressure level can be observed for the microphone located at

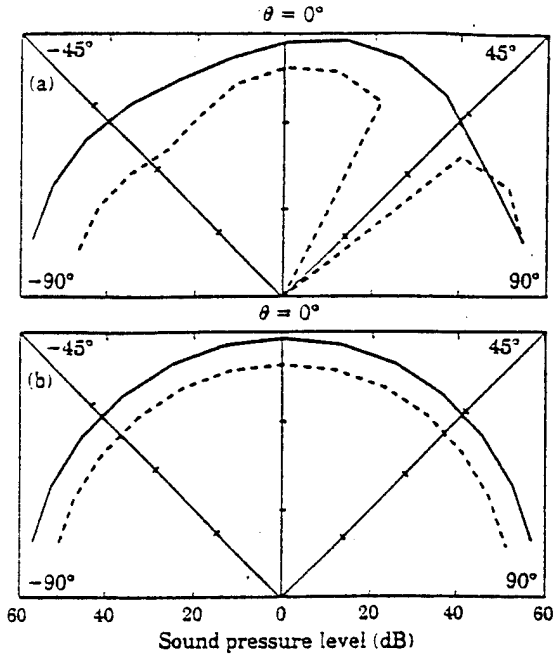

Figure 10. Theoretical pressure directivity at 320 Hz: (a) axial array; (b) perpendicular array. ——, Without control; --, with piezoelectric actuator.

position 2 on the axial array. Elsewhere in the acoustic field, the sound pressure levels are attenuated.

The theoretical and experimental displacement amplitudes without and with control are shown in Figure 11. While the two agree fairly well without control, they do not agree

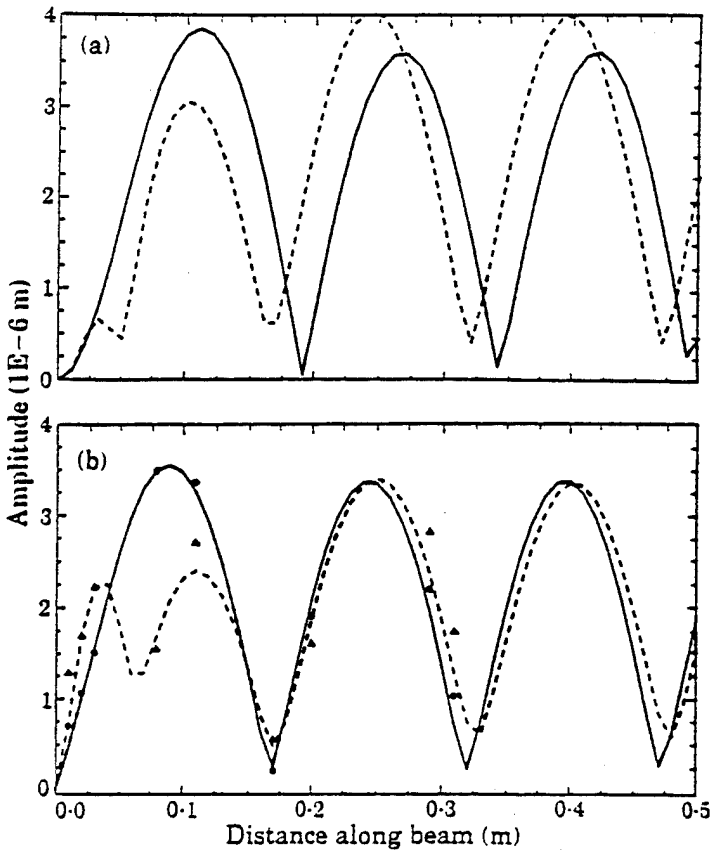

Figure 11. Beam displacement at 320 Hz: (a) theoretical; (b) experimental. ——, Without control; —, with piezoelectric actuator; •, point experimental data without control; ▲, point experimental data with control.

well with control. This is especially evident for positions close to the clamped end of the beam. This may be due, as mentioned previously, to the fact that the experimental clamped end is not perfect and that the piezoelectric actuator, when the control is invoked, causes a back reaction, changing the amplitude of the incident wave. Note that, in this case, the magnitude of $\hat{A}$ was also found to be increased by around 10% under control. The accuracy of the decomposition method, used for the experimental results, may also have caused these differences, as the method is sensitive to the phase and amplitude from the accelerometer signals and the position of these accelerometers. Also, the theoretical model makes the assumption that the piezoelectric patches are perfectly bonded on the beam (a thin and constant layer of glue), which may not have been the case in the experiments. However, as in the previous case, the most important changes in beam displacement can be observed for both results, under control close to the clamped edge discontinuity.

The resulting theoretical and experimental wavenumber spectra are shown on Figure 12. Both agree very well for the case without control, predicting a monopole radiation pattern in the far field (as the spectra are almost constant in the supersonic region). When the control is applied, the theoretical model predicts a minimum of radiation in the directions close to the direction defined by the error microphone (as observed in the previous case with the control shaker). For the experimental case under control, the dip in the spectrum occurs outside the supersonic region. This may be due to some measurement errors for the accelerometer array, which could also explain the differences in the two displacements with control, as observed previously in Figure 11. However, these results also demonstrate that controlling the pressure level at one point in the acoustic field of these experiments

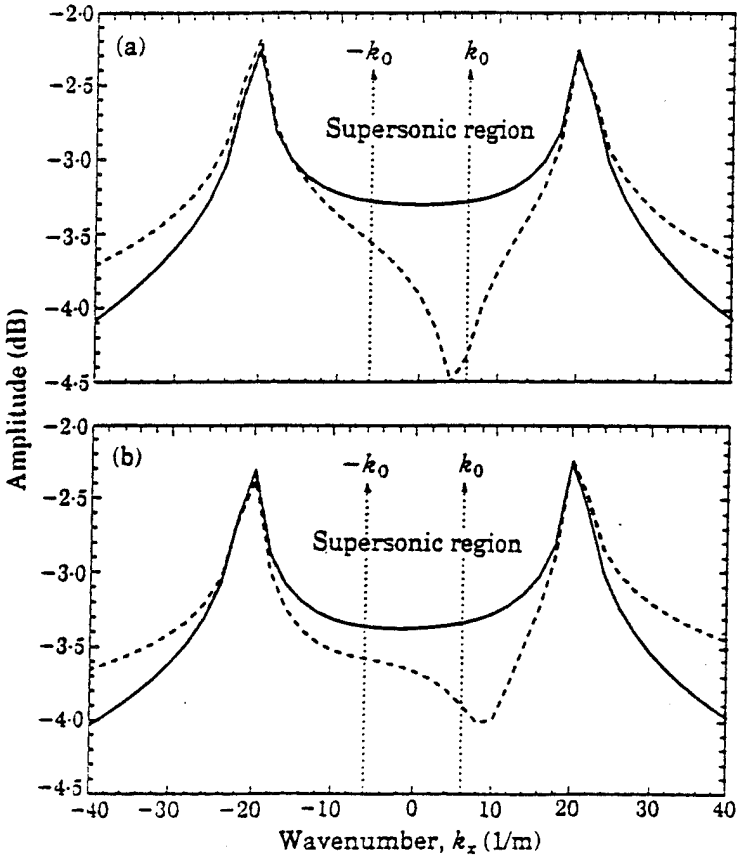

Figure 12. Wavenumber spectrum at 320 Hz: (a) theoretical; (b) experimental. ——, Without control; —, with piezoelectric actuator.

(i.e., not completely in the far field) results in attenuation in the acoustic far field, as all the supersonic wavenumber components are reduced.

6. CONCLUSIONS

Active control of acoustic radiation due to subsonic flexural waves on a "semi-infinite" beam with a clamped end has been experimentally and analytically studied. A control shaker and a piezoelectric actuator located near the discontinuity have been shown to be effective in actively modifying the vibration response of the system, in order to obtain large pressure attenuation at the error microphone along with a global decrease of the pressure levels in the acoustic field in both axial and perpendicular directions. The attenuation of the radiated acoustic field was not related to a decrease in amplitude of the global vibrational response of the system. However, it was demonstrated that control reduced and changed the beam vibration distribution close to the clamped edge discontinuity, i.e., control was effective in modifying scattered wave motion near the discontinuity. This can also be interpreted as changing the one-sided window of the beam response from a sharp rectangular to closer to a smoother exponential, which is known to have fewer associated supersonic wavenumber components. It was also inferred from the wavenumber spectra of the beam vibrational responses that, while controlling the pressure level at one point (microphone location) in the acoustic field of these experiments, the acoustic far-field radiation was also attenuated. When control was applied, this was demonstrated by an observed decrease of the wavenumber spectrum in the supersonic region.

ACKNOWLEDGMENT

The authors wish to acknowledge the support of the sponsor of this work, the Office of Naval Research, under Grant ONR-N00014-92-J-1170.

REFERENCES

1. G. E. WARNAKA 1982 *Noise Control Engineering* **18**, 100–110. Active attenuation of noise—the state of the art.
2. J. E. FFOWCS WILLIAMS 1984 *Proceedings of the Royal Society of London* **A395**, 63–88. Anti-sound.
3. C. R. FULLER 1990 *Journal of Sound and Vibration* **136**, 1–15. Active control of sound transmission/radiation from elastic plates by vibrational inputs, I: analysis.
4. B. WIDROW, J. R. GLOVER, J. M. MCCOOL, J. KAUNITZ, C. S. WILLIAMS, R. H. HEARN, J. R. ZEIDLER, E. DONG and R. C. GOODLIN 1975 *Proceedings of the IEEE* **63**, 1692–1716. Adaptive noise cancelling: principles and applications.
5. C. R. FULLER, R. J. SILCOX, V. L. METCALF and D. E. BROWN 1989 *Proceedings of the American Control Conference* **3**, 2079–2084. Experiments on structural control of sound transmitted through an elastic plate.
6. R. L. CLARK and C. R. FULLER 1992 *Journal of the Acoustical Society of America* **91**, 3313–3320. Experiments on active control of structurally radiated sound using multiple piezoceramic actuators.
7. R. L. CLARK and C. R. FULLER 1990 in *Proceedings of the First Joint U.S. Japan Conference on Adaptive Structures, Maui, Hawaii* (B. K. Wada, J. L. Fanson and K. Miura, editors), 227–245. Technomic Press. Control of sound radiation with adaptive structures.
8. S. J. ELLIOT, I. M. STOTHERS and P. A. NELSON 1987 *IEEE Transactions on Acoustics, Speech, and Signal Processing* **ASSP-35**, 1423–1434. A multiple error LMS algorithm and its application to the active control of sound and vibration.

9. K. D. FRAMPTON 1991 *Master of Science Thesis, Department of Mechanical Engineering, Virginia Polytechnic Institute and State University*. Active control of acoustic radiation due to discontinuities on thin beams.
10. L. O. GONIDOU 1988 *Master of Science Thesis, Department of Mechanical Engineering, Virginia Polytechnic Institute and State University*. Active control of flexural power flow in elastic thin beams.
11. C. GUIGOU and C. R. FULLER 1991 *Journal of Sound and Vibration* (in press). Active control of sound radiation from a semi-infinite beam with a clamped edge.
12. E. F. CRAWLEY and J. DE LUIS 1987 *American Institute of Aeronautics and Astronautics Journal* **25**, 1373–1385. Use of piezoelectric actuators as elements of intelligent structures.
13. E. K. DIMITRIADIS, C. R. FULLER and C. A. ROGERS 1991 *Journal of Vibration and Acoustics* **113**, 100–107. Piezoelectric actuators for distributed vibration excitation of thin plates.
14. M. C. JUNGER and D. FEIT 1972 *Sound, Structures and their Interaction*. Cambridge, Massachusetts: MIT Press, second edition, 1986 re-issue.
15. P. A. NELSON, A. R. D. CURTIS, S. J. ELLIOTT and A. J. BULLMORE 1987 *Journal of Sound and Vibration* **116**, 397–414. The minimum power output of free field point sources and the active control of sound.
16. R. F. KELTIE 1990 *Journal of the Acoustical Society of America* (in press). Sound radiation from simple structural discontinuities.
17. N. DRAPER and H. SMITH 1966 *Applied Regression Analysis*. New York: John Wiley, second edition.

C-30 Adaptive Feedforward Control of Non-minimum Phase Structural Systems, J. S. Vipperman and R. A. Burdisso, Journal of Sound and Vibration, Vol. 183 No. 3, pp. 369-382, 1995.

Journal of Sound and Vibration (1995) **183**(3), 369–382

ADAPTIVE FEEDFORWARD CONTROL OF NON-MINIMUM PHASE STRUCTURAL SYSTEMS

J. S. VIPPERMAN AND R. A. BURDISSO

Vibration and Acoustics Laboratory, Mechanical Engineering Department, Virginia Polytechnic Institute and State University, Blacksburg, Virginia 24061-0238, *U.S.A.*

(*Received* 2 *August* 1993, *and in final form* 6 *April* 1994)

Adaptive feedforward control algorithms have been effectively applied to stationary disturbance rejection. For structural systems, the ideal feedforward compensator is a recursive filter which is a function of the transfer functions between the disturbance and control inputs and the error sensor output. Unfortunately, most control configurations result in a non-minimum phase control path; even a collocated control actuator and error sensor will not necessarily produce a minimum phase control path in the discrete domain. Therefore, the common practice is to choose a suitable approximation of the ideal compensator. In particular, all-zero finite impulse response (FIR) filters are desirable because of their inherent stability for adaptive control approaches. However, for highly resonant systems, large order filters are required for broadband applications. In this work, a control configuration is investigated for controlling non-minimum phase lightly damped structural systems. The control approach uses low order FIR filters as feedforward compensators in a configuration that has one more control actuator than error sensors. The performance of the controller was experimentally evaluated on a simply supported plate under white noise excitation for a two-input, one-output (2I1O) system. The results show excellent error signal reduction, attesting to the effectiveness of the method.

1. INTRODUCTION

The past decade has seen many advancements in the active control of sound and vibration. Feedback control algorithms have proven useful in achieving narrowband or wide-band disturbance rejection for both sound and vibration [1–4]. They work by modelling the unwanted persistent signal and feeding it back, through a gain matrix and into the system to cancel it. Additional benefits are obtained by augmenting the system natural properties, e.g., damping can be increased to minimize the "ring" time caused by transient excitations. More recently, feedforward control methods have also been successfully applied to stationary disturbance rejection. One and three-dimensional acoustic fields have been controlled, whereby an undelayed reference signal coherent to the disturbance signal is used to create "antinoise" to cancel the primary disturbance through superposition [5–11]. Feedforward control of structurally radiated noise has been demonstrated through vibrational inputs and showed that decreasing the sound radiation does not necessarily correspond to a reduction of the vibration energy [12]. Feedforward vibration control has also been used in finite and infinite structures under harmonic and broadband excitations [13–17].

Because of their inherent stability, adaptive finite impulse response (FIR) or all-zero filters as compensators are extensively employed in adaptive feedforward control. Control of a harmonic signal can be achieved by an FIR filter having only two coefficients. The two coefficients provide a frequency response which matches the optimal solution in phase

0022-460X 95 230369 + 14 $08.00 0

© 1995 Academic Press Limited

and magnitude at that particular excitation frequency. Additional filter coefficients can be added at the rate of two per frequency to control multiple sinusoids. Relatively small size FIR filters work well for broadband applications where the controlled plant has an approximately linear-phase transfer function [18], such as damped three-dimensional acoustic rooms, long ducts and infinite beams, which can all be essentially modelled as a pure delay. Large FIR filters give acceptable results for broadband control of finite structures. Vipperman *et al.* [17] used a combination of adaptive FIR and fixed IIR filters for the compensator and system identification, respectively, for controlling the broadband vibration of beams. However, some applications have proven better suited for the use of adaptive infinite impulse response (IIR) filters [20–22]. These filters have both poles and zeros, and thus it is much easier to shape the frequency response using an IIR filter. Eriksson discussed a technique of removing feedback from systems which obtain the reference signal directly from the plant by using IIR filters that are adapted by a variation of the recursive least-mean-square (RLMS) algorithm [23].

Perfect feedforward broadband cancellation in structural systems is typically not possible because the ideal compensators are non-realizable IIR filters. This problem is due to the fact that in most control configurations the control path transfer functions have non-minimum phase, and thus the optimal control solution will consequently have unstables poles. Furthermore, adapting IIR filters has proven difficult for a number of reasons. Typically, the stability of the filter must be checked and preserved during the adaptation process. This task is easier if the filter is in a cascade structure [20]. In addition, gradient search methods prove difficult because error surfaces associated to IIR filters are non-quadratic and may have many local minima [19–22, 23]. An equation error minimization technique will rectify this problem, usually at the expense of biasing the solution [33].

Recently, a method for determining the inverse of reverberant room acoustics as well as for controlling noise in them was presented by Miyoshi *et al.* [24–26]. In this technique, denoted as the multiple input/output inverse filter theorem (MINT), the exact system inverse at M locations can be achieved by using $M + 1$ FIR filters. Since feedforward control inherently contains an inverse modelling element, the MINT theory could prove valuable when applied in this context. Thus, MINT filter theory offers a possible solution to the above problems previously associated with feedforward control, by simply using $M + 1$ FIR compensators to cancel the response of a structural system at M points.

In this paper, a two-input, one-output (2I1O) MINT control system is developed to experimentally investigate the potential of the approach in attenuating structural vibrations. The testbed consists of a simply supported steel plate excited with band-limited white noise. Performance of a 2I1O MINT control system is compared to that of the conventional single-input, single-output (SISO) controllers while keeping the total number of adaptive coefficients the same. The results show excelled performance of the MINT controller.

2. THEORY

For simplicity, a 2I1O MINT control system is considered, as shown in Figure 1. Here, the two compensators are represented by $W_1(z)$ and $W_2(z)$. The plant dynamics between the inputs (disturbance and actuators) and the error sensor are represented by the discrete transfer functions $T_{de}(z)$, $T_{c1e}(z)$ and $T_{c2e}(z)$, where the subscripts de represents the disturbance error path, $c1e$ represents the control 1 error path, and $c2e$ represents the control 2 error path. It is assumed that an undelayed, coherent reference signal can be obtained by directly tapping the disturbance input signal, x_k.

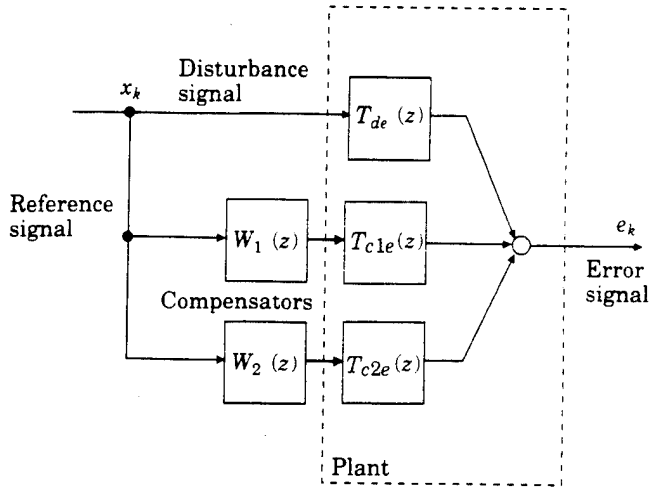

Figure 1. A block diagram of a 2IIO MINT feedforward control system.

For a lightly damped linear structure, the displacement transfer functions will take the form

$$T_{de}(z) = \frac{D(z)}{1 - A(z)}, \qquad T_{c1e}(z) = \frac{C_1(z)}{1 - A(z)}, \qquad T_{c2e}(z) = \frac{C_2(z)}{1 - A(z)}, \tag{1a–c}$$

where the roots of the polynomial $(1 - A(z))$ are the poles of the system. This polynomial is the same for any transfer path in a structural system [27], since the poles represent global system properties. The roots of the polynomials in the numerators are the zeros and they are unique to each transfer path. The order of the polynomial $(1 - A(z))$ is $2N$, where N is the number of modes in the structure. On the other hand, the order of $D(z)$, $C_1(z)$ and $C_2(z)$ is generally $2(N - 2)$ for a displacement transfer function and $2N$ for an accelerance transfer function. From Figure 1, the response of the system, e_k, can be written in terms of the plant transfer functions and input sequence x_k as

$$e_k = Z^{-1}[(T_{de}(z) + W_1(z)T_{c1e}(z) + W_2(z)T_{c2e}(z))X(z)], \tag{2}$$

where $W_1(z)$ and $W_2(z)$ are the control compensators and Z^{-1} denotes the inverse Z-transform. In feedforward control the objective is to drive the plant output e_k to zero, thus achieving perfect disturbance rejection. From inspection of equation (2), the optimum compensators $W_1^*(z)$ and $W_2^*(z)$ will have to satisfy

$$T_{de}(z) + W_1^*(z)T_{c1e}(z) + W_2^*(z)T_{c2e}(z) = 0. \tag{3}$$

Substituting equations (1) into equation (3) and multiplying by $1 - A(z)$ yields

$$-D(z) = W_1^*(z)C_1(z) + W_2^*(z)C_2(z). \tag{4}$$

The order of the compensators as well as the coefficients of $W_1^*(z)$ and $W_2^*(z)$ should be selected such that equation (4) is satisfied. To this end, it is convenient to first investigate the case in which $W_2(z) = 0$, which is the conventional SISO controller [17]. In this case, only one polynomial, $W_1(z)$, can be manipulated in order to make the following equation valid:

$$W_1(z)C_1(z) = -D(z). \tag{5}$$

That leads to the optimum compensator to become

$$W_1^*(z) = \frac{-D(z)}{C_1(z)}. \tag{6}$$

Note that the compensator $W_1(z)$ is modelling the disturbance loop, $D(z)$, while simultaneously inverse modelling the control loop, $C_1(z)$. Implementing $W_1^*(z)$ with a finite impulse response (FIR) filter would generally have a remainder filter or polynomial $R(z)$ associated with the polynomial division in equation (6). The exception is the rare case in which $D(z)$ is proportional to $C_1(z)$, indicating a collocated or symmetrical spacing of the disturbance and control actuator. Thus, the optimal solution for $W_1(z)$ requires an IIR filter with the order and coefficients defined by equation (6). However, the following requirements must be met in order to realize this solution. First, the delay associated with $D(z)$ must be larger than or equal to that associated with $C_1(z)$ in order for the solution to be causal. Secondly, the order of the numerator and denominator must be equal to the order of $D(z)$ and $C_1(z)$, which is defined by the truncated system model. Lastly, and most importantly, $C_1(z)$ must have minimum phase such that $W_1(z)$ as defined by equation (6) will be stable, i.e., the poles of the compensator all lie inside of the unit circle centered about the origin of the complex z-plane. In the continuous domain, a minimum phase system can be achieved by collocating the control actuator and error sensor. Unlike poles, there is no direct mapping of zeros from the continuous to the discrete domain, making it difficult to guarantee minimum phase in discrete systems. To complicate matters further, stable zero locations are independent of the sampling rate in the sense that very fast sampling (to approximate a continuous system) will not necessarily produce a minimum phase discrete transfer function either. In fact, non-minimum phase continuous systems can even produce a minimum phase transfer function when discretized [28]. Needless to say, a discrete minimum phase transfer function is extremely difficult to achieve, in particular for structural systems, and one cannot depend on obtaining one in order to realize the control solution represented by equation (6).

If all of the conditions to implement an IIR solution to the SISO control problem cannot be met, the solution to the rational expression in equation (6) can be approximated by a finite, causal FIR filter. Because of their inherent stability, the use of FIR filters is very convenient in adaptive control approaches. However, Miyoshi and Kaneda [24] showed that even a theoretically infinite-length FIR will have a modelling error when inverting a non-minimum phase plant. This may lead to poor error reduction even for large filter sizes. Thus, it will be desirable to devise a control configuration that makes use of the simple low order FIR filter that still renders acceptable control performance. A control approach that satisfies the above requirements is the MINT configuration. This control configuration was first developed and used by Miyoshi *et al.* in controlling 3-D acoustic fields [24–26].

Let us consider the 2I1O MINT control case of Figure 1, where now $W_2(z) \neq 0$. In the MINT technique, complete cancellation of the error signal is theoretically possible using simple FIR filters as

$$W_1(z) = \sum_{l=0}^{L} w_{1l} z^{-l}, \qquad W_2(z) = \sum_{l=0}^{L} w_{2l} z^{-l}, \tag{7}$$

if the following conditions are met: (1) the two control paths do not have common zeros; (2) actuators and sensors are located to ensure a causal optimal solution; and (3) the order of the compensator is less than the order of the plant ($L < 2N$).

The first condition can be achieved by careful positioning of the actuators with respect to the error sensor such that the modal control forces of each actuator are different. Thus, $C_1(z)$ and $C_2(z)$ will not have common roots and they are said to be relatively prime [29]. To satisfy the third condition requires that the physical dimensions between the control actuators and the error sensor must be less than that between the disturbance input and the error sensor. Further details can be found in the literature

[8, 11, 30]. That the last condition above is satisfied will be evident after the following discussion.

The two polynomials $W_1(z)$ and $W_2(z)$ can now be designed such that equation (4) is true. By definition of relatively prime, there exist two polynomials $W_1(z)$ and $W_2(z)$ with orders less than that of $C_1(z)$ and $C_2(z)$ that will make equation (4) true. This solution exists even if the control paths are non-minimum phase, i.e., $C_1(z)$ and $C_2(z)$ have roots outside the unit circle in the z-plane. Physically, the zeros of the control path represent the uncontrollable frequencies since the response for an input at that frequency will be zero. These are often referred to as transmission zeros for multi-input, multi-output (MIMO) systems. Since both control paths are excited with the same broadband input signal, x_k, and since $C_1(z)$ and $C_2(z)$ are relatively prime, each path is able to compensate for the uncontrollable frequencies that are present in the other path.

It is possible to find a unique solution for $W_1(z)$ and $W_2(z)$ by setting up the following linear system of equations as described in reference [26]:

$$[C]\{w\} = \{n\}, \tag{8}$$

where

$$\{w\} = \{w_{10}, \ldots, w_{1L}, w_{20}, \ldots, w_{2L}\}^{\mathrm{T}} \tag{9}$$

is the vector of compensator coefficients.

$$[C] = \begin{bmatrix} c_{10} & 0 & \cdots & 0 & c_{20} & 0 & \cdots & 0 \\ c_{11} & c_{10} & \ddots & 0 & c_{21} & c_{20} & \ddots & 0 \\ \vdots & & & \vdots & \vdots & & & \vdots \\ c_{1L} & & \cdots & c_{10} & c_{2L} & & \cdots & c_{20} \\ 0 & c_{1L} & \ddots & & 0 & c_{2L} & \ddots & \\ \vdots & & & \vdots & \vdots & & & \vdots \\ 0 & 0 & \cdots & c_{1L} & 0 & 0 & \cdots & c_{2L} \end{bmatrix} \tag{10}$$

is the matrix based on the coefficients of the control path numerators $C_1(z)$ and $C_2(z)$, and

$$\{d\} = \{d_0, d_1, \ldots, d_L, 0, \ldots, 0\} \tag{11}$$

is based on the disturbance loop numerator, $D(z)$.

The linear system in equation (8) is created by expanding the products of the polynomials in equation (4) and equating like powers of z.

It is assumed here that equation (1) represents accelerance transfer functions. Thus, the orders of $D(z)$, $C_1(z)$ and $C_2(z)$ are $2N$. Note that matrix $[C]$ is square when the order of $W_1(z)$ and $W_2(z)$ are chosen to be one less than the order of $D(z)$, $L = 2N - 1$, thus satisfying condition (3). Given that all three conditions have been met, then there exists an exact set of optimal filter weights to the control problem given by the solution of equation (8).

An advantage of using the MINT control approach is that there is now a criterion for selecting the length of the adaptive FIR filters, a parameter which has not been extensively investigated in previous broadband feedforward designs [31, 32]. Usually, there is a trade-off between accuracy and computational effort. Since the control is limited to a finite bandwidth, the system models, $T_{de}(z)$, $T_{c1e}(z)$ and $T_{c2e}(z)$, will be truncated as well, in accordance with the system order within a specified bandwidth. To yield an exact solution of equation (4), the adaptive filters should then be one tap smaller than the system models.

If the FIR filters have less or more coefficients, i.e. an under or over-determined system, then a least-squares method will be required to find an approximate solution. A method for finding the MINT solution on line by means of an adaptive algorithm is described in the next section.

3. ADAPTIVE ALGORITHM

Typically, the parameters of the control compensators, $W_1(z)$ and $W_2(z)$, are determined by minimizing a quadratic cost function, C, which is the mean square value of the error signal, e_k, as follows:

$$C = \mathrm{E}[(e_k)^2], \tag{12}$$

where E[.] represents the expected value operator. The optimal solutions $W_1^*(z)$ and $W_2^*(z)$ correspond to the point where C is minimum, and they are found using an adaptive algorithm. Such a system has the advantage of being able to change with time to varying system parameters and environments.

The simplest method for finding the optimum weight is the steepest descent method [33], which has the following weight update equation at time $k+1$:

$$W_{jl}(k+1) = W_{jl}(k) - \mu \frac{\partial C}{\partial W_{jl}}, \qquad j = 1,2, \quad l = 0, \ldots, L, \tag{13}$$

where μ is the step size and governs the stability and rate of convergence of the minimization process.

Physically, equation (13) finds the optimal solution by marching down the bowl-shaped quadratic cost function in opposite direction to the gradient vector until finding the minimum point. The gradient of the cost function with respect to the filter coefficients needed in equation (13) can be easily shown to be

$$\partial C / \partial W_{jl} = 2E[e_k (x_j)_{k-l}], \tag{14}$$

where e_k is the kth sample of the error signal and $(\bar{x}_j)_k$ is the disturbance signal filtered by an estimate of the transfer function between the jth control input and the error sensor, $\hat{T}_{cje}(z)$: that is,

$$(x_j)_k = Z^{-1}[T_{cje}(z) X(z)]. \tag{15}$$

The expected value in equation (14) is further approximated with instantaneous values of e_k and x_k:

$$\partial C / \partial W_{jl} \approx 2 e_k (x_j)_{k-l}. \tag{16}$$

Equation (16) can now be substituted into equation (13) to yield

$$W_{jl}(k+1) = W_{jl}(k) - 2\mu e_k (x_j)_{k-l}, \tag{17}$$

which is widely known as the filtered-x LMS equation (33).

It is clear from equation (15) that knowledge of the control path transfer functions is required before implementing the update equation (17). As seen from equation (15), the disturbance sequence, x_k, will be filtered by estimates of the transfer functions, $\hat{T}_{c1e}(z)$ and $\hat{T}_{c2e}(z)$ in order to update the compensator weights. For structural systems, these transfer functions are modelled with IIR filters [17].

TABLE 1

Measured plate natural resonant frequencies

Resonance number	Modal indices (n, m)	Resonant frequency (Hz)
1	(1, 1)	92
2	(2, 1)	189
3	(1, 2)	252
4	(3, 1)	338
5	(2, 2)	357

4. EXPERIMENTAL SET-UP

The control algorithm was tested on a simply-supported steel plate measuring 11·8 × 15 in and 0·08 in in thickness. This two-dimensional structure provided a stringent test bed due to the relatively high modal density. The first five experimentally measured natural resonant frequencies are listed in Table 1.

The input disturbance was implemented with a collocated set of piezoelectric (PZT) patches measuring 38 × 32 × 0·2 mm and was configured to produce a bending moment input [34]. The input disturbance signal, x_k, was a 0–400 Hz band-limited white noise signal generated by a B&K 2032 spectrum analyzer. The disturbance input is labelled as "$(PZT)_D$" in the diagram of the plate shown in Figure 2. A B&K accelerometer marked "Accel." in Figure 2 was used to measure the plate response, which will be the error signal to be minimized by the controller. An additional pair of bending moment inputs, identical to the disturbance actuator, were used to control the plate response. These were labeled as control 1 and control 2 and are indicated by "$(PZT)_1$" and "$(PZT)_2$" in Figure 2.

Frequency Devices 9002 elliptic low-pass filters were used in the set-up. One filter band-limited the input signal, x_k, and had the cut-off frequency set to 400 Hz. A second filter served as an anti-aliasing filter for the error signal, which was set to remove signal

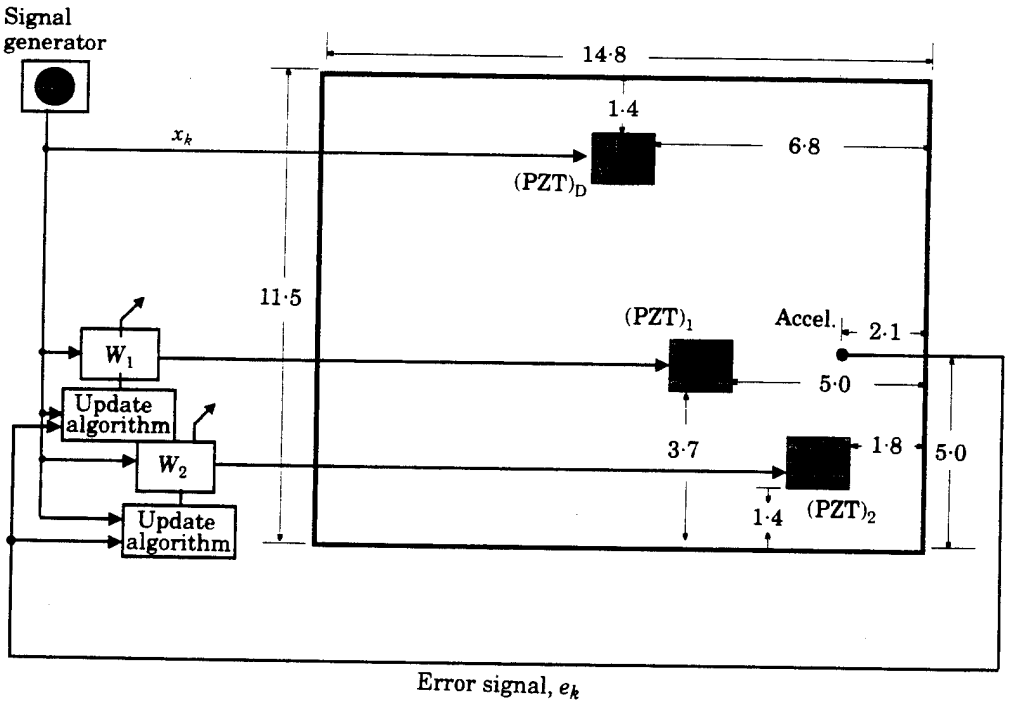

Figure 2. The arrangement of the plate sensors and actuators. Dimensions in inches.

content above the Nyquist frequency of the control system (800 Hz). Lastly, two filters smoothed the higher harmonics from the control signal, which were produced by the zero order hold from the digital controller. The cut-off frequencies of these filters were set equal to the Nyquist frequency as well.

The error signal output of the accelerometer was conditioned with a B&K 2635 charge amplifier. Three channels of NAD 2700 power amplifiers were used to amplify the signals for the two control actuators and disturbance inputs. In addition, the output from the amplifiers was sent through transformer with a 1:16 ratio, in order to boost the voltage sent to the piezoelectric actuators. The control algorithms were implemented on a TMS320C30-based DSP board manufactured by Spectrum Signal Processing. A 80386 PC was used to host the DSP board. All time and frequency domain analysis was performed by the B&K 2032 spectrum analyzer as well.

5. EXPERIMENTAL PROCEDURE

Before implementing the control algorithms, a system identification of both control paths must be performed. IIR filters are required to most efficiently model lightly damped structural systems [17]. Each control actuator was driven with white noise and the frequency response function (FRF) between the actuator and the error sensor was measured. The parameters of the IIR filters were estimated from the FRF using the Matlab INVFREQZ.M routine [35]. This routine performs a curve fit in the frequency domain by minimizing a Hankel norm. The coefficients of the IIR model are then downloaded to the DSP prior to operating the control system. A comparison of the measured and modelled FRF's for both of the control channels is shown in Figures 3 and 4 out to the Nyquist frequency of the control system. The measured transfer functions are shown by the solid line while the IIR filter transfer functions are shown by the dashed line. Note that the frequency response of the filters matches the plant FRF both in phase and magnitude very well, with the exception of the 0–20 Hz range where measured FRF's are typically quite noisy. The phase has been "unwrapped" so that the reader can see that the phase does not remain within a $(0, \pi)$ boundary (ignoring the linear trend), and therefore control loops

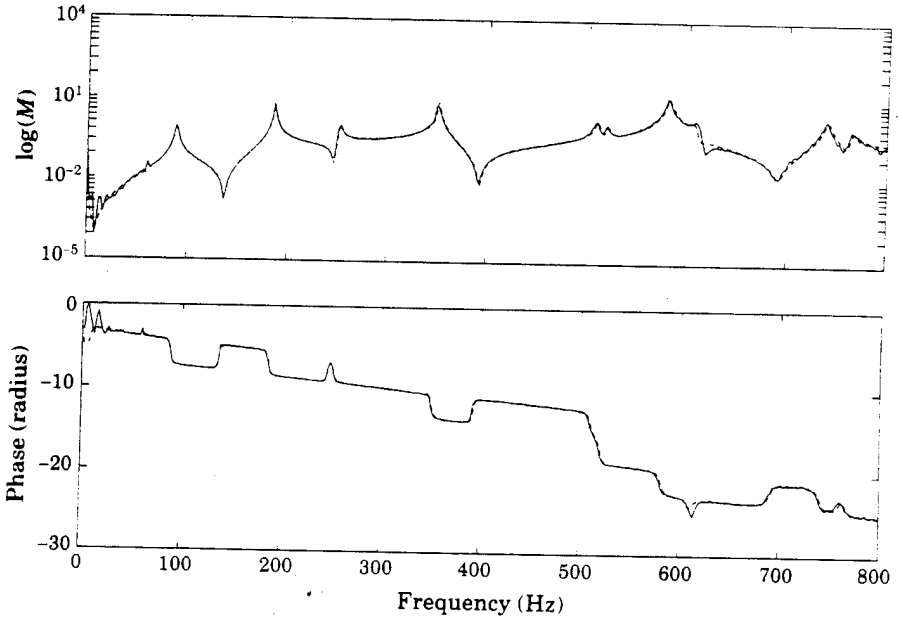

Figure 3. A comparison of the measured (——) and modelled (– – –) transfer functions between control actuator 1 and the error sensor.

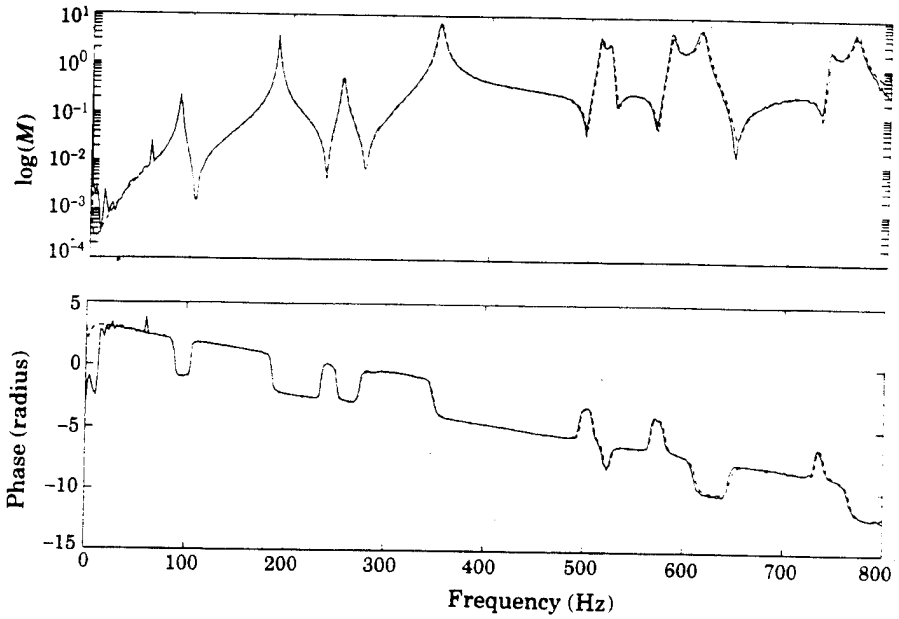

Figure 4. Measured (——) and modelled (– – –) transfer functions between control actuator 2 and error sensor.

are indeed non-minimum phase in the bandwidth of interest [36]. The resulting nearly linear, decreasing trend in the phase is due to a combination of the unit sample delay from the DSP, the dispersive propagation of the flexural wave between the actuator and sensor, and the phase of the analog smoothing filters.

The control system was operated in the three separate configurations presented in Table 2. Using each control actuator with the error sensor, two conventional SISO Filtered-x LMS (FXLMS) controllers can be devised. The SISO-1 in Table 2 indicates that only the control actuator 1 is used to minimize the response of the error sensor. Similarly, SISO-2 indicates that only the second control actuator is used to reduce the error signal. The last configuration corresponds to the 2I1O MINT controller, in which both control actuators, $(PZT)_1$ and $(PZT)_2$, are used to minimize the error sensor response. By operating in these different configurations, the performance of the two conventional SISO FXLMS control systems (SISO-1 and SISO-2) was compared to that of the 2I1O MINT control algorithm. Several experiments were performed using each of the three configurations where different sizes of the adaptive filter were used and they are again summarized in Table 2. For a valid comparison the number of adaptive filter weights was the same for all three configurations. For example, if a filter size of ten was used for both $W_1(z)$ and $W_2(z)$ in the 2I1O MINT control configuration, the corresponding FXLMS conventional controllers used a filter size of 20.

TABLE 2

Summary of all plate experiments

Control configuration	Set-up (actuator, sensor)		Number of adaptive coefficients					
SISO-1	PZT_1	Accel.	10	20	30	40	50	60
SISO-2	PZT_2	Accel.	10	20	30	40	50	60
2I1O MINT	PZT_1 and PZT_2	Accel.	2×5	2×10	2×15	2×20	2×25	2×30

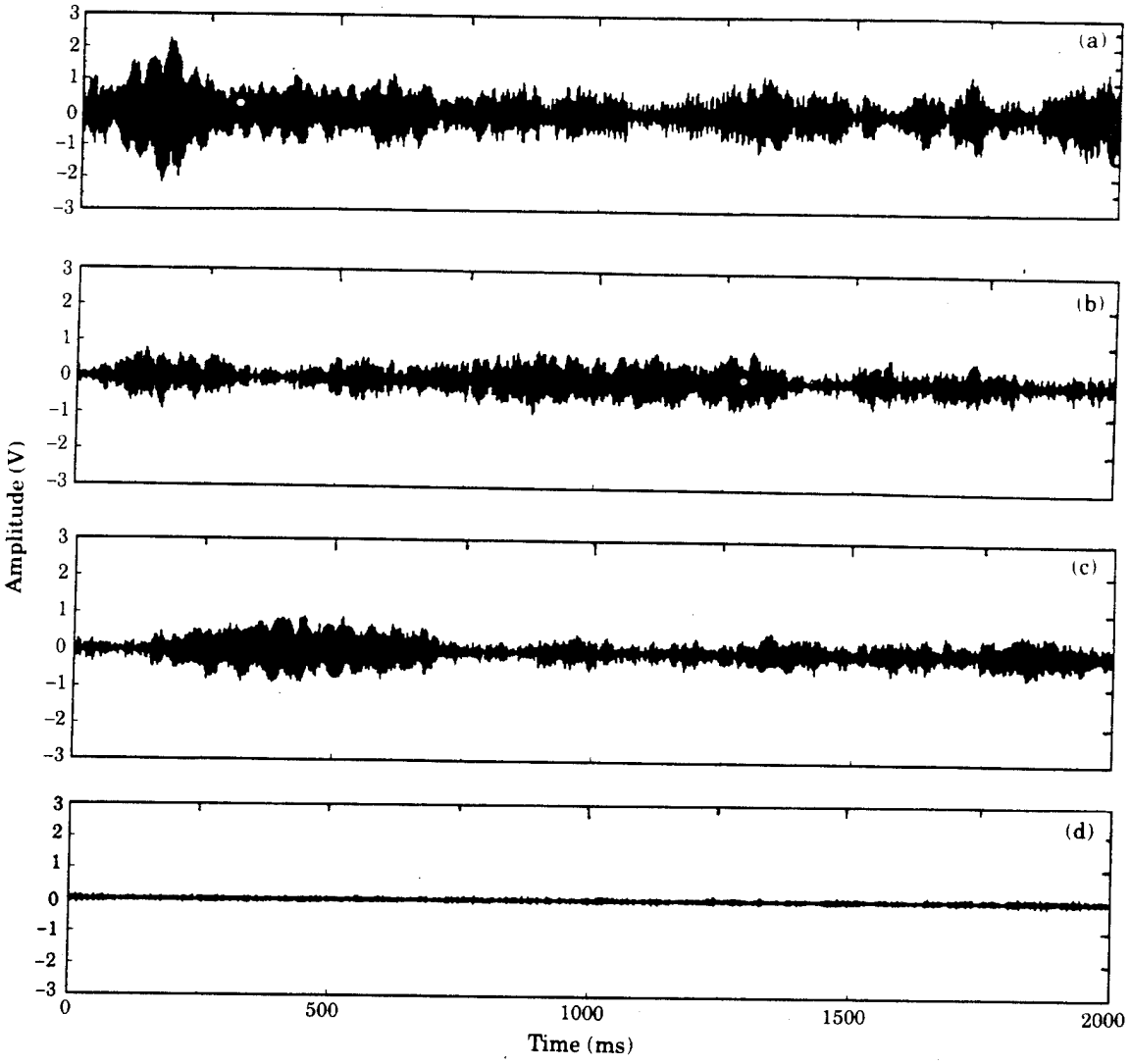

Figure 5. The error signal (a) before and (b) after convergence of SISO-1; (c) SISO-2 and (d) MINT control configurations with 50 adaptive coefficients.

6. EXPERIMENTAL RESULTS

All controlled measurements have been obtained after convergence of the adaptive algorithms to the optimum weights. The time histories before and after convergence of the three control configurations having 50 adaptive coefficients are shown in Figures 5(a)–(d), which correspond to no control, SISO-1, SISO-2 and MINT control configurations, respectively. It is observed that the MINT arrangement is superior to both SISO controllers, achieving nearly complete attenuation of the error signal. The power reductions in the error signals achieved in each of the three configurations (Figures 5(b)–(d) are 8, 6 and 22 dB, respectively. A reduction of 15 dB was observed after 5 s, but the large filters were allowed to adapt for several minutes before recording the data. In Figures 6–8 are shown the averaged autospectrums of the error signal corresponding to the error signals represented in Figure 5. Note that for the two SISO systems, the power was reduced at the system resonances, but energy was often added between the peaks. In contrast, the MINT system provided a true broadband reduction across the entire bandwidth, with three minor exceptions. The increase in

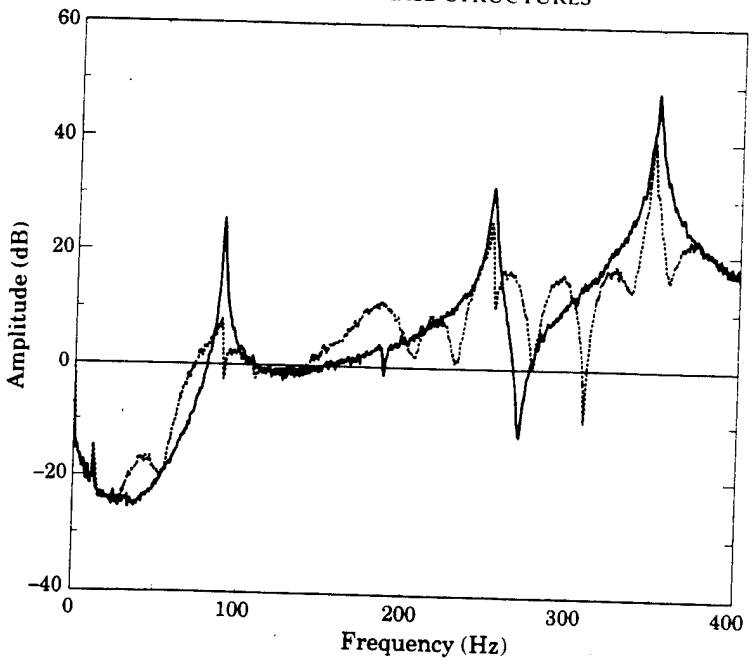

Figure 6. The autospectrum of the error signal before (——) and after (– – –) application of the SISO-1 control configuration with 50 adaptive coefficients.

energy below 50 Hz results from the error signal being below the noise floor of the DSP. The 12-bit resolution provides about 65 dB of dynamic range. The increase at 189 Hz, the natural frequency of the (2, 1) mode which was not excited by the disturbance, is the result of energy spill-over by the control inputs. Finally, the system zero that occurred at 285 Hz before control was shifted to the right after the control system was applied.

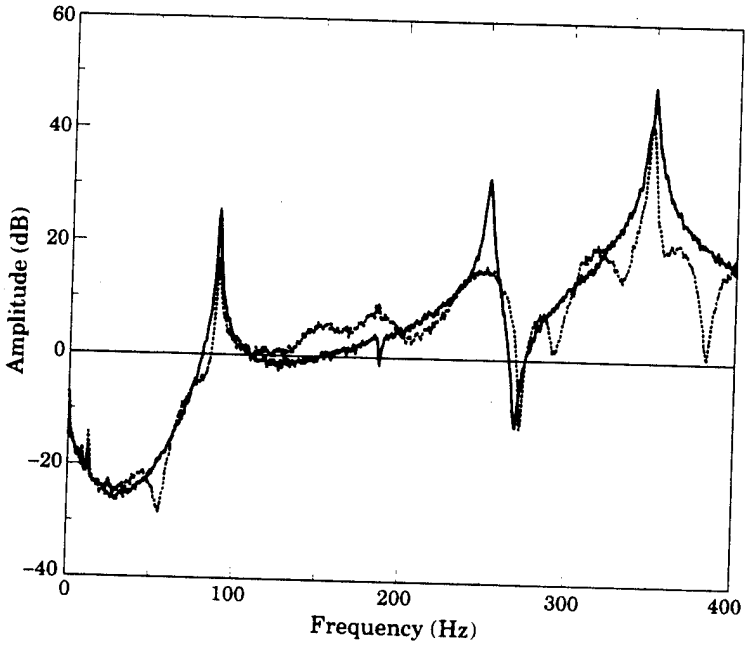

Figure 7. The autospectrum of the error signal before (——) and after (– – –) application of the SISO-1 control configuration with 50 adaptive coefficients.

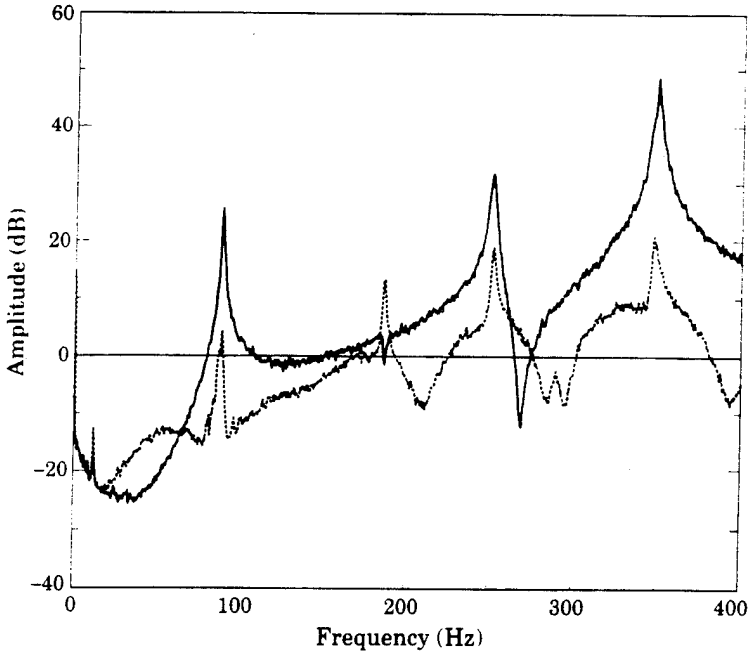

Figure 8. The autospectrum of the error signal before (——) and after (– – –) application of the MINT control configuration with 50 adaptive coefficients.

The performance of the controllers was next investigated as a function of the filter size. The total power reduction of the error signal as a function of the total number of adaptive coefficients shown in Figure 9. The MINT controller obtained an additional 4–14 dB reduction as compared to either SISO FXLMS controller as the adaptive filter coefficients were increased. For 60 coefficients (30 coefficients in each compensator), the MINT system reduced the measured plate acceleration by 22 dB, while the SISO control configurations were limited to 6 and 8 dB reductions. The peak in the performance of the MINT control system between 50 (2×25) and 60 (2×30) adaptive coefficients was expected, since within the Nyquist interval there are six to eight plate antiresonances (see Figures 3 and 4) and two low-pass filters (each with eight poles and six zeros). Since each plate zero is of second order [27], the ideal filter size is expected to be $2 \times 8 + 2 \times 6 = 28$ coefficients.

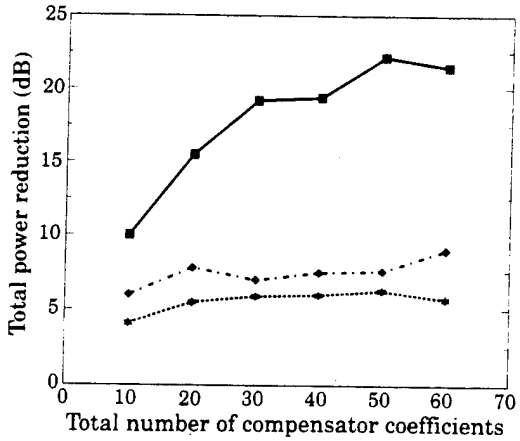

Figure 9. The performance of the three experimental configurations MINT (——), SISO-1 (– . – .), and SISO-2 (– – –) for differing numbers of adaptive coefficients.

7. CONCLUSIONS

An adaptive implementation of the two-input, one-output (2I1O) multiple inverse input/output filter theorem (MINT) was presented and then demonstrated experimentally on a non-minimum phase structural system. The filtered-x LMS (FXLMS) algorithm implemented on a TMS320C30 DSP was used to find the MINT filter parameters. Experiments on a simply supported plate revealed that, for the same number of adaptive parameters in the control system, the performance of the 2I1O MINT configuration was significantly superior to the SISO implementations of the FXLMS algorithm, with little increase in control system complexity. The best performance of the MINT control system was 22 dB of power reduction as compared to 6 and 8 dB of reduction for SISO FXLMS control systems. The autospectra of the error signal before and after control revealed that MINT reduces the power across almost the entire control bandwidth, indicating a true "broadband" control. In contrast, the conventional FXLMS SISO controllers attenuated the system response at the resonance frequencies, while often increasing the response at off-resonance. Lastly, through the use of the MINT filter theorem, one can determine an adequate length for the control compensators.

ACKNOWLEDGMENT

The authors gratefully acknowledge the Office of Naval Research for funding of this research with grant number N00014-92-J-1170.

REFERENCES

1. A. H. VON FLOTOW and B. SCHAFER 1986 *Transactions of the American Society of Mechanical Engineers, Journal of Guidance, Control, and Dynamics* **9**, 673–680. Wave-absorbing controller for a flexible beam.
2. L. MEIROVITCH and H. BARUH 1981 *Journal of Guidance and Control* **4**, 157–163. Optimal control of damped flexible gyroscopic systems.
3. J. S. BURDESS and A. V. METCALFE 1985 *Transactions of the American Society of Mechanical Engineers, Journal of Vibration, Acoustics, Stress, and Reliability in Design* **107**, 33–37. The active control of forced vibration produced by arbitrary disturbances.
4. S. LEE and A. SINHA 1986 *Journal of Sound and Vibration* **109**, 347–352. Design of an active vibration absorber.
5. L. J. ERIKSSON and M. C. ALLIE 1987 in *Noise-Con* 87, 365–370. A digital sound and control system for use in turbulent flows.
6. R. J. SILCOX and H. C. LESTER 1989 *Transactions of the American Society of Mechanical Engineers, Journal of Vibration, Acoustics, Stress, and Reliability in Design* **111**, 337–342. An evaluation of active noise control in a cylindrical shell.
7. C. F. ROSS 1982 *Journal of Sound and Vibration* **80**, 373–380. An algorithm for designing a broadband active sound control system.
8. J. V. WARNER and R. J. BERNHARD 1987 in *AIAA Paper* 87-2706 *11th Aeroacoustics Conference*, 1–8. Digital control of sound fields in three-dimensional enclosures.
9. J. V. WARNER and R. J. BERNHARDT 1990 *American Institute of Aeronautics and Astronautics Journal* **28**, 284–289. Digital control of local sounds fields in an aircraft passenger compartment.
10. L. A. POOLE, G. E. WARNAKA and R. C. CUTTER 1984 *Proceedings of IEEE ICASSP-84, San Diego, U.S.A.* **2**, 2171–2174. The implementation of the Widrow-Hoff algorithm for the adaptive cancellation of acoustic noise.
11. T. J. SUTTON, S. J. ELLIOT, P. A. NELSON and I. MOORE 1990 *Proceedings of the Institute of Acoustics, Southampton*, 689–693. Active control of multiple-source random sound in enclosures.
12. C. R. FULLER 1991 *Journal of Sound and Vibration* **145**, 195–215. Active control of sound radiation from a vibrating rectangular panel by sound sources and vibration inputs: an experimental comparison.
13. W. REDMAN-WHILE, P. A. NELSON and A. R. D. CURTIS 1987 *Journal of Sound and Vibration* **112**, 181–187. Experiments on active control of flexural wave power.

14. S. J. ELLIOT, I. M. STOTHERS and L. BILLET 1990 *Proceedings of the Institute of Acoustics, Southampton*, 613–622. Adaptive feedforward control of flexural wave propagating in a beam.
15. J. SCHEUREN 1990 *Proceedings of the Institute of Acoustics, Southampton*, 623–629. Active attenuation of bending waves in beams.
16. C. R. FULLER, G. P. GIBBS and R. J. SILCOX 1990 *Journal of Intelligent Material Systems and Structures* **1**, 236–247. Simultaneous active control of flexural and extensional power flow in beams.
17. J. S. VIPPERMAN, R. A. BURDISSO and C. R. FULLER 1993 *Journal of Sound and Vibration* **166**, 283–299. Active control of broadband structural vibration using the lms adaptive algorithm.
18. L. B. JACKSON 1991 *Digital Filters and Signal Processing*. Boston: Kluwer Academic: second edition.
19. P. L. FEINTUCH 1976 *Proceedings of the IEEE*, 1622–1624. An adaptive recursive lms filter.
20. R. A. DAVID 1982 *Asilomar Conference on Circuits, Systems, & Computers, IEEE*, 182–186. A cascade structure for equation error minimization.
21. M. G. LARIMORE, J. R. TREICHLER and C. R. JOHNSON, JR. 1980 *IEEE Transactions on Acoustics, Speech, and Signal Processing, ASSP-28* 428–440. Sharf: an algorithm for adapting IIR digital filters.
22. J. R. TREICHLER, M. G. LARIMORE and C. R. JOHNSON JR. 1978 *IEEE Transactions on Acoustics, Speech, and Signal Processing, ICASSP* 118–122. Simple adaptive IIR filtering.
23. L. J. ERIKSSON, M. C. ALLIE and R. A. GREINER 1987 *IEEE Transactions on Acoustics, Speech, and Signal Processing* **ASSP-35**(4), 433–437. The selection and application of an IIR adaptive filter for use in active sound attenuation.
24. M. MIYOSHI and Y. KANEDA 1988 *IEEE Transactions on Acoustics, Speech, and Signal Processing* **36**(2), 145–152. Inverse filtering of room acoustics.
25. M. MIYOSHI and Y. KANEDA 1990 *Noise Control Engineering Journal* **36**(2), 85–90. Active control of broadband random noise in a reverberant three-dimensional space.
26. M. MIYOSHI and Y. KANEDA 1988. *Proceedings of Inter-noise* 88, 983–986. Active noise control in a reverberant three-dimensional sound field.
27. D. J. EWINS 1986 *Modal Testing: Theory and Practice*. Letchworth, Hertfordshire, England: Research Studies Press.
28. K. J. ÅSTRÖM, P. HAGANDER and J. STERNBY 1980 *Proceedings of IEEE Conference on Decision and Control, Sweden* 1077–1081. Zeros of sampled systems.
29. M. BÔCHER 1924 *Introduction to Higher Algebra*. New York: Macmillan.
30. R. A. BURDISSO, J. S. VIPPERMAN and C. R. FULLER 1993 *Journal of Acoustical Society of America* **94**, 234–242. Causality analysis of feedforward controlled systems with broadband inputs.
31. L. J. ERIKSSON and M. C. ALLIE 1988 *Proceedings IEEE ISCAS* 88, *Espoo, Finland* **3**, 2387–2390. System considerations for adaptive modeling applied to active control.
32. L. J. ERIKSSON, M. C. ALLIE, C. D. BREMIGAN and J. A. GILBERT 1989 *Proceedings ICASSP '89, Glasgow, Scotland* **3**, 2029–2032. Weight vector analysis of an RLMS filter with on-line auxiliary path modeling.
33. B. J. WIDROW and S. D. STEARNS 1985. *Adaptive Signal Processing*. Englewood Cliffs, New Jersey: Prentice-Hall.
34. E. K. DIMITRIADIS, C. R. FULLER and C. A. ROGERS 1991 *Journal of Vibration and Acoustics* **118**, 100–107. Piezo-electric actuators for distributed vibration excitation of thin plates.
35. ANONYMOUS 1989 *PC-Matlab for MS-DOS Computers*. South Natick, Massachussetts: The Math Works.
36. B. WIE and A. E. BRYSON, JR 1981 in *Proceedings of the 3rd VPI&SU/AIAA Symposium on Dynamics and Control of Large Flexible Spacecraft*, 153–174. Modeling and control of flexible space structures.

C-31 Active structural acoustic control using fiber sensors and piezoelectric actuators, R. L. Clark, C. R. Fuller, B. R. Fogg, W. V. Miller, A. M. Vengsarkar and R. O. Claus, ADPA/AIAA/ASME/SPIE Active Materials & Adaptive Structures, Arlington, VA, 4-8 November 1991.

Paper presented at the ADPA/AIAA/ASME/SPIE Conf. on Active Materials and Adaptive Structures – Session 29

Active structural acoustic control using fiber sensors and piezoelectric actuators

Robert L. Clark and Chris R. Fuller
Vibration and Acoustics Laboratory
Mechanical Engineering Department

Brian R. Fogg, William V. Miller, Ashish M. Vengsarkar, and Richard O. Claus
Fiber & Electro-Optics Research Center,
Bradley Department of Electrical Engineering

Virginia Polytechnic Institute and State University
Blacksburg, Virginia 24061

ABSTRACT: We present a novel closed loop adaptive control system employing fiber optic strain sensors. The discussion and results in this paper will be based on preliminary experimental studies of sound radiation from a simply supported plate residing in a baffle. The filtered-x version of the adaptive LMS algorithm is implemented on a TMS320C25 DSP board resident in an AT computer. The disturbance is created with a shaker, and control is achieved with a single piezoceramic actuator. All tests conducted are based on a narrow band, stationary disturbance.

1. INTRODUCTION

Interest in adaptive structure development for active structural acoustic control (ASAC) has prompted many theoretical and experimental investigations (Clark *et al* 1990a, Dimitriadis *et al* 1989, Fuller *et al* 1989, Fuller *et al* 1990a, Wang *et al* 1990). Much has been documented concerning the modeling and application of piezoelectric actuators for control of structural vibration as well as sound radiation from structures (Clark *et al* 1990b, Crawley *et al* 1989, Fanson *et al* 1986). To implement control of structure-borne sound, error information related to far-field sound radiation must be supplied to the controller. Since the goal is to develop an adaptive structure with sensing capabilities embedded within the structure, many different types of sensors come to mind. Previous studies by Clark and Fuller (Clark *et al* 1990c,d) have been devoted to developing sensors from polyvinylidene fluoride (PVDF), which can be attached directly to the surface of the structure. An alternative sensing technique with similar response characteristics can be constructed from two-mode, elliptical-core (e-core) optical fibers (Murphy *et al* 1991, Vengsarkar *et al* 1991). Many previous studies have been devoted to vibration control of structures by implementing e-core optical fibers as error sensors (Cox *et al* 1991). The goal of this preliminary study is to demonstrate that optical fibers can also be used as error sensors for controlling structure-borne sound radiation.

© 1992 IOP Publishing Ltd

2. DESCRIPTION OF CONTROLLER

To achieve control, an adaptive controller based on the multi-channel version of the Widrow-Hoff Filtered-X control algorithm was implemented. This algorithm is described in detail by Elliott, *et al* (1987). The output of an error sensor can be modeled at the nth time step as

$$e_f(n) = d_f(n) + \sum_{m=1}^{M} \sum_{j=0}^{N-1} P_{fmj} \sum_{i=0}^{N-1} \omega_{mi}(n-j)\, x(n-i-j) \,. \tag{1}$$

where $d_f(n)$ is the the fth error sensor, $x(n)$ is the input reference source, ω_{mi} are the coefficients of the adaptive finite impulse response (FIR) filters and P_{fmj} is the jth coefficient of the transfer function between the output of the mth adaptive filter and the fth error sensor. The number of control actuators and filter coefficients are designated by M and N respectively. The outputs of the fixed filters, $\hat{P}_{fmj}$, at each time step *n*, were used by the LMS algorithm to minimize the mean square error signal by modifying the coefficients of the adaptive filter as follows:

$$\omega_{mi}(n+1) = \omega_{mi}(n) - \mu \sum_{f=1}^{L} e_f(n)\, r_{fm}(n-i) \,, \tag{2}$$

where

$$r_{fm}(n-i) = \sum_{j=0}^{N-1} \hat{P}_{fmj}\, x(n-i-j) \,. \tag{3}$$

Rather than computing the expectation of the squared error signal, the square of the error signal was simply taken as an estimate of the desired expectation in the LMS algorithm. As a result, the gradient components contain a large contribution of noise; however, the noise is attenuated with time due to the adaptive process (Widrow *et al* 1985). In Equation (2), L is the total number of error sensors utilized, and $L \geq M$. The coefficients $r_{fm}(n)$ are the outputs of the compensating filters $\hat{P}_{fmj}$ which are estimates of the actual coefficients, P_{fmj} measured prior to starting the control algorithm. This procedure is necessary since the LMS algorithm assumes that the error $e_f(n)$ is the instantaneous result of the control input for which the signal $r_{fm}(n)$ is a better estimate than $x(n)$ (Elliot *et al* 1987). The factor μ in Equation (2) is the gain constant that regulates the speed and stability during convergence.

3. EXPERIMENTAL SETUP

Experiments were performed in an anechoic chamber with dimensions 4.2 × 2.2 × 2.5 meters and a cut-off frequency of 250 Hz. The test plate, which was mounted in a rigid steel frame, was cut from steel and measured 380 × 300 × 1.96 mm. The simply supported boundary conditions were achieved by attaching thin shim spring steel to the boundaries of the plate with small set screws and a sealing compound. Previous testing has shown that this arrangement adequately models the simply supported boundary conditions (Ochs *et al* 1975). The test rig was then placed in the chamber where it was rigidly supported on a structure configured with a 4.2 × 2.2 × 19 mm wooden baffle.

To achieve a steady state sinusoidal noise input, the plate was driven with a shaker attached to the structure with a stinger. Control was achieved with a single piezoceramic actuator for narrow band applications by way of the filtered-x version of the adaptive LMS algorithm implemented on a TMS320C25 digital signal processing board. The shaker used to create the disturbance was located at plate coordinates of (240 mm, 130 mm). The piezoelectric actuator was constructed from two piezoceramic elements of dimensions 38.1 × 21 × 0.19 mm bonded symmetrically (front and back). The symmetrically located patches were wired in a bimorph configuration, resulting in uniform bending about the neutral axis of the plate (Dimitriadis *et al* 1989). The optical fiber for sensing strain on the plate is oriented symmetrically about the vertical centerline of the plate. The sensor was configured such that response from odd-odd plate modes [i.e. (1,1), (3,1), etc.] would be most dominant.

The plate was instrumented with nine Bruel and Kjaer mini accelerometers and the output of these accelerometers was analyzed by solving a set of simultaneous equations to recover the amplitudes of independent modes on the panel (Fuller *et al* 1990b). The directivity pattern of the acoustic field along the plate mid-plane was quantified with a Bruel and Kjaer microphone situated on a traversing system. The radius of the traverse was approximately 1.6 m and measurements were taken in nine degree increments to map the sound radiation directivity with and without control. In addition, a few microphones were randomly located in the chamber to provide a measure of the global attenuation.

4. RESULTS

Three tests were conducted using optical fiber sensors to provide error information for controlling sound radiating from vibrating structures. More emphasis should be placed on results from the off-resonance test cases since both the structural and acoustic response of the plate depend on interaction from multiple structural modes.

4.1 On-Resonance Test Case

The first test case was conducted at an excitation frequency of 88 Hz, corresponding to the resonance condition of the (1,1) mode of the simply supported plate. The directivity pattern for the acoustic response is presented in Figure 1(a) and modal amplitudes for the structural response are illustrated in Figure 1(b). As indicated in Figure 1(a), the sound radiation was attenuated by approximately 25 dB along the mid-plane of the plate. (Similar levels of attenuation were observed throughout the acoustic field.) Control was achieved by suppressing the response of the (1,1) mode as is evident in Figure 1(b). In addition, the residual modes (i.e. modes other than the resonant mode) were attenuated as well. This method of control has been previously termed "modal reduction", since all modes observed were attenuated during the control process (Fuller *et al* 1990b).

4.2 Off-Resonance Test Cases

For the second test case the plate was driven at 320 Hz. corresponding to off-resonance excitation between the (1,2) and (2,2) modes of the plate. The radiated sound was attenuated by approximately 10 dB as illustrated in Figure 2(a). Upon achieving control, all of the modal amplitudes were observed to decrease as depicted in Figure 2(b). The dominant (3,1) mode, which is an efficient acoustic radiator, was reduced by approximately 40 dB. The remaining modes were attenuated to lesser degrees; however, all modes were reduced, thereby subscribing to the "modal reduction" method of control.

The final test case was conducted at an excitation frequency of 349 Hz. which is an off-resonance frequency lying between the (2,2) and (3,1) mode of the plate. Acoustic attenuation on the order of 10 dB was observed as depicted in Figure 3(a). The modal response for this particular case is more complex than that of the previous test cases as can be seen in Figure 3(b). Before applying control, the (3,1) mode is dominant in response; however, significant response is observed in the (1,1), (2,1), (2,2), and (2,3) modes of the structure. Upon achieving control all modes were attenuated except the (2,2) mode. The most significant attenuation was again observed in the (3,1) mode of the structure as in the previous test case. Since the modal response of the (2,2) mode increased upon achieving control, the method of control is termed "modal restructuring" (i.e. the modal response was rearranged as opposed to being reduced).

5. CONCLUSIONS

Results from this preliminary study suggest that two-mode e-core optical fibers can be used as error sensors for controlling sound radiation from the surface of vibrating structures. Sound radiation was attenuated for both on-resonance and off-resonance operating conditions for a narrow band disturbance. In the on-resonance case, approximately 25 dB of acoustic attenuation was achieved, while off-resonance control resulted in approximately 10 dB of attenuation for the cases studied. The optical fiber was oriented on the plate such that the sensor response was most sensitive to modes with a high radiation efficiency. Since the response of the optical fiber is proportional to the integral of strain over the path of the fiber, the sensor can be oriented on a structure for specific applications.

ACKNOWLEDGMENTS

The authors gratefully acknowledge the support of this work by DARPA and the Office of Naval Research under grant ONR-N00014-88-K-0721.

REFERENCES

Clark R L and Fuller C R 1990a *Submitted to J. of Acoustical Society of America*, (also presented at the 120th ASA meeting, Nov. 1990)

Clark R L, Fuller C R, and Wicks A L 1990b Accepted for publication in the *J. of Acoustical Society of America*, (also presented at the 119th ASA meeting, April 1990)

Clark R L and Fuller C R 1990c Presented at *First Joint U.S./Japan Conf. on Adaptive Structures* November 13-15 Maui Hawaii
Clark R L and Fuller C R 1990d Submitted to *J. of Acoustical Society of America*, (also presented at the 120th ASA meeting, Nov. 1990)
Cox D E and Lindner D K 1991 Accepted for publication in the *Journal of Sound and Vibration*
Crawley E F and de Luis J 1989 *AIAA Journal* 25 (10) pp 1373-85
Dimitriadis E K, Fuller C R and Rogers C A 1989 *Proc. of ASME 8th BiennialConf. on Failure Prevention and Reliability* Montreal Canada pp 223-33
Elliott S J, Stothers I M, and Nelson P A 1987 *IEEE Transaction on Acoustic Speech and Signal Processing*, ASSP-35 (1) pp 1423-34
Fanson J L and Chen J C 1986 *Proc. of NASA/DOD Control-Structures Interaction Conf.* NASA CP-2447 Part II
Fuller C R, Hansen C H and Snyder S D 1989 *Inter-Noise* 89 pp 509-11
Fuller C R, Gibbs G P, and Silcox R J 1990a *J. of Intelligent Material Systems andStructures*]
1 (2) pp 235-47
Fuller C R, Hansen C H, and Snyder S D 1990b Accepted for publication in the *J. of Sound and Vibration*
Murphy K A, Miller M S, Vengsarkar A M. and Claus R O 1991 *J. Composites Tech. & Res.*
13 (1) pp 29 - 35
Ochs J and Snowdon J 1975 *J. of the Acoustical Society of America* 58 pp 832-40
Vengsarkar A M, Fogg B R, Miller W V, Murphy K A, and Claus R O 1991 *Electronics Letters* 27 (17) pp 931 - 32
Wang B T, Dimitriadis E K, and Fuller CR 1990 *Proc. of AIAA SDM Conf.*, AIAA Paper 90-
1172-CP Long Beach California
Widrow B and Stearns S D 1985 *Adaptive Signal Processing*, (Englewood Cliffs, N. J.: Prentice Hall Inc)

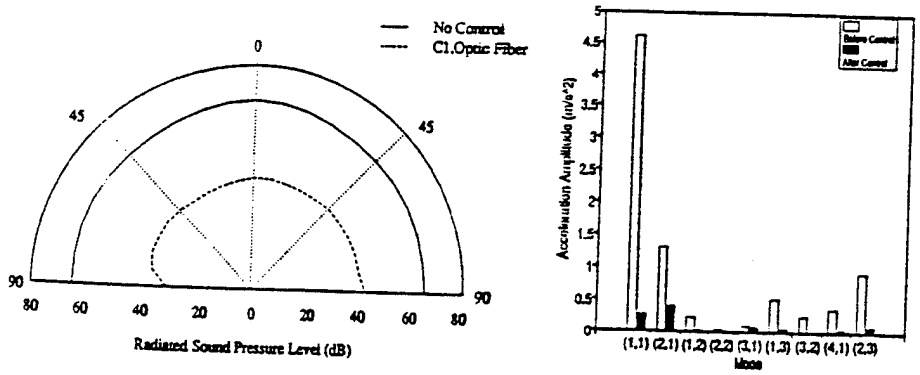

(a) Acoustic Directivity Pattern of Plate/Baffle System

(b) Modal Response of Plate

Figure 1: Excitation of (1,1) at 88 Hz

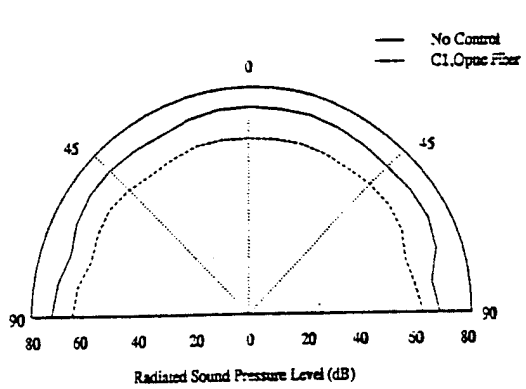

(a) Acoustic Directivity Pattern of Plate/Baffle System

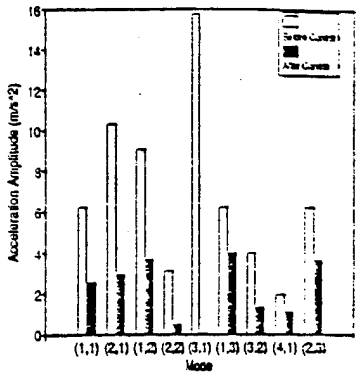

(b) Modal Response of Plate

Figure 2: Off-Resonance Excitation at 320 Hz

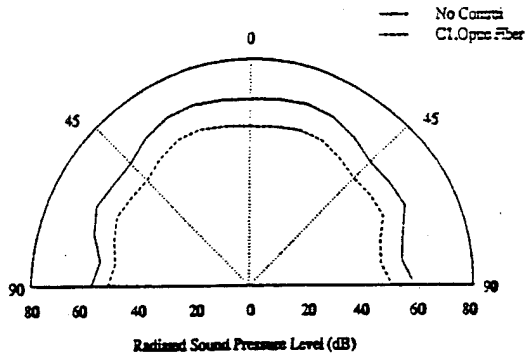

(a) Acoustic Directivity Pattern of Plate/Baffle System

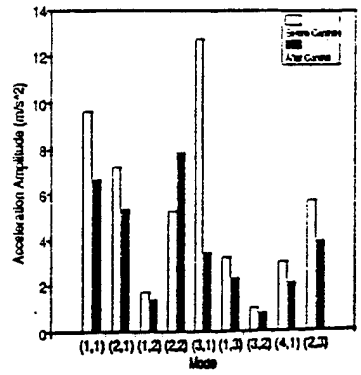

(b) Modal Response of Plate

Figure 3: Off-Resonance Excitation at 349 Hz

C-32 Control of Broadband Radiated Sound with Adaptive Structures, J. P. Smith, C. R. Fuller and R. A. Burdisso, Proceedings of SPIE Conf. on Smart Struct. and Adaptive Materials, Albuquerque, NM, SPIE Vol. 1917 Part I, pp. 587-597, February 1993.

Control of broadband radiated sound with adaptive structures

Jerome P. Smith, Chris R. Fuller and Ricardo A. Burdisso

Vibration and Acoustics Laboratories
Department of Mechanical Engineering
Virginia Polytechnic Institute and State University
Blacksburg, VA 24061

ABSTRACT

Active structural acoustic control using adaptive structures has been demonstrated for harmonic disturbances. This paper presents an extension of this work to the attenuation of acoustic radiation from structures subject to broadband disturbances. An adaptive, multi-input multi-output (MIMO), feedforward broadband acoustic control system has been developed based on the least mean squares (LMS) algorithm. The compensators are adaptive finite impulse response (FIR) filters. The control inputs are implemented with piezoelectric ceramic actuators. Both far-field microphones and polyvinylidene fluoride (PVDF) structural sensors designed to observe the efficient acoustic radiating modes are used as error sensors. The disturbance is band-limited zero mean white noise and is implemented with a point force shaker. In the control of harmonically excited systems, satisfactory attenuation is possible with a single-input single-output (SISO) controller. In contrast, for systems excited with broadband disturbances, a MIMO controller is necessary for significant acoustic attenuation. Experimental results for the control of a simply supported plate are presented.

1. INTRODUCTION

In recent years, active control has become a viable means of attenuating sound radiation from structures. Active Structural Acoustic Control[1] (ASAC) involves implementing the "secondary" control input forces directly to the offending structure vibrating under the excitation of the "primary" disturbance force input. The control inputs are designed such that the total acoustic response, which is the sum of the radiation due to the primary and secondary inputs, is minimized. Thus the control inputs serve to "cancel" the effect of the primary input on the structure.

The technique of ASAC has been implemented using both feedback and feedforward control approaches. Meirovitch used a standard LQR feedback control design to attenuate sound radiation from plates[2]. Baumann et. al. developed a state-space feedback method which implemented the acoustic radiation dynamics directly into the control compensator[3]. ASAC has also been demonstrated using adaptive feedforward control techniques for structures excited by single frequency harmonic disturbances[4]. Fuller and others have shown that using feedforward control approaches, global attenuation of sound transmission and radiation from harmonically excited panels can be achieved with only one or two control inputs[5-7]. Structurally mounted vibration error sensors have also been successfully developed and implemented for harmonic ASAC[8].

Substantial control of sound radiation from structures subject to harmonic disturbances both on and off-resonance can be achieved without optimally designing the sensors and control actuators[9]. In cases of control of radiation due to a harmonic disturbance, the after control modal analysis exhibits a forced modification of the structural response. The structural response modification can be characterized as "modal suppression" or "modal restructuring"[5,10,11]. In on-resonance harmonic disturbance excitation, where the disturbance frequency corresponds to a natural mode of the structure, the structural response is usually dominated by that mode, depending on the degree of modal density. In these cases, the controlled system often exhibits "modal suppression" identified by an after control decrease in the vibrational amplitude of the dominating mode. In the control of off-resonant harmonic disturbances, the controlled system generally shows an increase in the vibrational amplitudes of the inefficient radiating modes. Thus, the residual response is not attenuated but rather the structure is forced to behave like an inefficient radiator, i.e. "modal restructuring". In modal restructuring, the vibrational energy is spilled over into inefficient radiating modes. In the case of broadband excitation, all modes on the bandwidth are being excited both on-resonance and off-resonance simultaneously, since the disturbance contains content at all frequencies on the bandwidth. Thus control spill over energy is much harder to restructure into inefficient, unexcited mode shapes when dealing with broadband disturbances. This implies that the control system configuration is then critical

in the control of broadband radiation.

This paper is an experimental study into the potential of controlling broadband acoustic radiation from structures using the adaptive feedforward control approach. The experimental test structure consists of a simply-supported plate with the first five natural modes on the bandwidth of interest. The control inputs are implemented with piezoceramic actuators, and both far-field microphones and PVDF structural sensors are used as error transducers. The control approach used in this work is the Filtered-x LMS algorithm and is briefly described, follow by a description of the experimental setup. Results for a simply-supported plate are presented for SISO and MIMO control systems. Finally, conclusions are drawn on some of the aspects of controlling broadband acoustic radiation.

2. CONTROL ALGORITHM

Adaptive feedforward control techniques have been successfully applied to the control of broadband structural vibration[12]. The algorithm implemented here is a feedforward filtered-x LMS control approach. For simplicity, a block diagram of the control system for the SISO case is shown in Figure 1. The control signal time sequence u_k is obtained by filtering a reference signal, which is coherent to the disturbance signal x_k, through an adaptive finite impulse response (FIR) filter, W(z). It is assumed here that the reference signal is obtained by directly tapping into the disturbance signal and that there is no feedback of the control input into the reference signal. That is,

$$u_k = \sum_{j=0}^{L} W_{j,k}\, x_{k-j} \qquad (1)$$

where $W_{j,k}$ is the j^{th} filter coefficient at the k^{th} time step, L is the FIR filter order and the subscript k indicates a signal sample at time t_k. Since the transfer function of an FIR filter contains only zeros and no poles, the FIR is inherently stable.

The filter coefficients $W_{j,k}$ are updated at each time step in order to minimize a cost function. The cost function is formed as the mean square value of the error signal as follows

$$C(W_j) = E[e_k^2] \qquad (2)$$

where E[.] is the expected value operator.

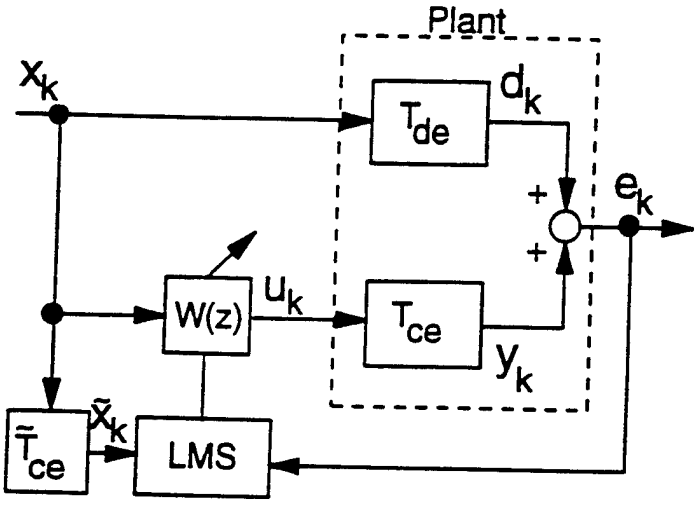

Fig. 1. Block diagram of SISO adaptive feedforward control system.

The result of deriving the Least Mean Square (LMS) algorithm to minimize the cost function yields a set of recursive equations to update the filter coefficients at each time step. The derivation can be found in detail in Reference 12 and is not presented here for brevity. The filter update equation for the SISO case is

$$W_{j,k+1} = W_{j,k} - 2\mu e_k \tilde{x}_{k-j} \qquad ; j = 0, 1, \ldots L \tag{3}$$

where the signal $\tilde{x}_k$ is known as the filtered-x signal, and μ is a convergence parameter which controls the rate of convergence and stability of the minimization process. Thus, the LMS algorithm requires a knowledge of both the error and the filtered-x signal.

The filtered-x signal $\tilde{x}_k$ is the predicted response of the structure to the disturbance signal echoed through the control path transfer function $T_{ce}(z)$. Thus an estimate of the control path transfer function $T_{ce}(z)$ is necessary to obtain the filtered-x signal. In practice, the control path transfer function is commonly measured directly from the system. The control actuator is driven with white noise and the transfer function between the control input and the error sensor output is measured in the frequency domain. An infinite impulse response (IIR) filter is designed to model this transfer function so that it yields the same frequency response function. The IIR filter is expressed as

$$T_{ce}(z) = \frac{B(z)}{1+A(z)} = \frac{b_0 + b_1 z^{-1} + \ldots + b_m z^{-m}}{1 + a_1 z^{-1} + \ldots + a_p z^{-p}} \tag{4}$$

which has m zeros and p poles. The IIR filter is designed by a curve-fit technique which solves a system of equations for the coefficients a_n and b_n of the IIR filter[13]. Since the IIR filter has both poles and zeros, potential for instability exists if any of the poles are located outside of the unit circle in the z-plane. In the event that the IIR filter design yields unstable poles, the poles are "reciprocated" across the unit circle into the stable region. The process of reciprocation involves dividing each unstable root by its modulus in order to reflect it across the unit circle into the stable region[14]. This distorts the phase response of the model somewhat, but inversion of a small number of slightly unstable poles in a large model still yields a model with a satisfactory match of both magnitude and phase response.

For a MIMO controller, the reference signal is fed forward to an array of FIR adaptive filters whose outputs drive N_c control actuators. The filter coefficients are updated to minimize a cost function that is now defined as the sum of the mean square value of the error signals. That is

$$C = \sum_{s=0}^{N_s} E\left[(e_s)_k^2 \right] \tag{5}$$

where $(e_s)_k$ is the s^{th} error sensor signal, and N_s is the number of error sensors.

The update equation for the filter coefficients can be shown to be as follows

$$W_{rj}(k+1) = W_{rj}(k) - 2\mu \sum_{s=1}^{N_s} (e_s)_k (\tilde{x}_{rs})_{k-j} \qquad j = 0, 1, \cdots, L \qquad r = 1, \cdots, N_c \tag{6}$$

where $(\tilde{x}_{rs})_k$ is the disturbance signal filtered by the transfer function between the r^{th} control actuator and the s^{th} error sensor. Thus, it is clear from equation (6) that there are $N_s x N_c$ transfer functions that need to be measured and modelled with IIR filters.

3. EXPERIMENTAL SETUP

The structure used for the experiments was a simply-supported steel plate with dimensions 380 x 300 x 2 mm. Thin, flexible metal shims connect the edges of the plate to a heavy support stand to provide the simply-supported boundary conditions. The experimentally measured natural frequencies for the first 5 modes of the plate are presented in Table 1. The well known modal indices are also given in Table 1. The disturbance signal is zero mean white noise with frequency content from 0 to 400 Hz. The disturbance is applied with a point force shaker actuator, which is located at x= 65 mm and y= 225 mm. The shaker can then effectively excite all 5 natural plate modes on the bandwidth of interest. The control inputs were applied by co-located pairs of G1195 piezoelectric ceramic patches (PZT), each patch measuring 38.0 x 32.0 x 0.2 mm. Each pair of PZT actuators were oppositely mounted, one on each side of the plate, and actuated 180° out of phase. The forcing function associated to this arrangement is a line moment along the actuator edges[15]. The locations of the actuators were designed using an optimization routine developed for narrowband disturbances[16]. In this optimization routine, the actuator locations are optimized to minimize the total sound radiated power at a number of excitation frequencies. The (1,1) and (3,1) modes, corresponding to 88 Hz and 331 Hz respectively, are the most efficient acoustic radiators below the critical frequency[17]. Therefore, the system was assumed to be excited at 88 and 331 Hz and the optimum locations for the piezoceramic actuators was determined and they are shown in Figure 2.

TABLE 1: Simply supported plate natural frequencies.

Mode	Modal Indices	Frequency - Hz
1	(1,1)	86
2	(2,1)	182
3	(1,2)	248
4	(3,1)	331
5	(2,2)	350

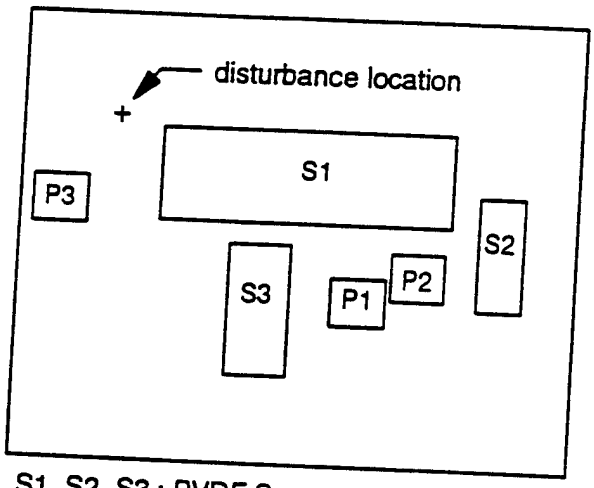

Fig. 2. Diagram of experimental plate configuration.

Since the goal of this work is to attenuate the acoustic radiation, the fundamental choice for error transducers are microphones placed at various locations in the acoustic far-field. Brüel & Kjær type 4134 microphones were used as error transducers. The microphone signals were conditioned with a Brüel & Kjær multi-channel type 228 power supply. Microphones located in the far-field may not be suitable in some practical implementation. Moreover, the design of "adaptive" structures will require sensors and actuators that are embedded in the same structure. Thus, the performance of structurally mounted vibration error sensors was also investigated. These structural sensors should provide signals that upon

their minimization result in attenuation of sound radiation. One type of distributed structural sensor which has recently received much attention is polyvinylidene fluoride (PVDF) film. PVDF error sensors provide an output signal proportional to the integral of the rate of strain over the surface of application. Thus, a structurally mounted film of PVDF material provides a "window" which observes the vibration over the area of the plate on which the PVDF is mounted. However, simply attenuating the signal from a PVDF sensor may not necessarily result in significant acoustic attenuation. The development of optimal PVDF sensors for broadband radiation is a topic of current research. The geometry and location of the PVDF error sensors used in these experiments were again designed to achieve optimum reduction of sound radiation at the frequencies of the (1,1) and (3,1) modes[17]. Figure 2 shows the shape and locations of the PVDF sensors.

The disturbance signal was generated by a Brüel & Kjær 2032 spectrum analyzer, and was low-pass filtered through an Ithaco 4032 24 dB/octave filter with cutoff frequencies set to 400 Hz. Both the control inputs and the error signals were filtered through Frequency Devices 9002 low-pass filters set with a 400 Hz cutoff frequency. Filtering the control inputs allowed "smoothing" of the signal from the DSP after the zero order hold. The error signals were filtered to reduce noise and the high frequency content which was out of the range of the bandwidth of interest. The plate was mounted in a rigid baffle and the data was taken in an anechoic chamber with a cutoff frequency of 250 Hz. The radiation directivity data before and after control was taken with a Brüel & Kjær microphone traversing the horizontal plane passing through the center of the plate at a radius of 1.83 m.

Three control systems were developed for these experiments. A SISO, a two-input, two-output (2I2O) and a three-input, three-output (3I3O) controller. The adaptive feedforward control systems were implemented on a Texas Instruments TMS320C30 digital signal processing (DSP) board. The sample rate used for the experiments was 1500 Hz. The adaptive FIR filters, used as compensators, each contained 100 coefficients. The IIR filters used for system identification of the control path transfer functions had 50 coefficients in the numerator and 49 coefficients in the denominator, which corresponded to 50 zeroes and 50 poles. This yielded an accurate model of both phase and magnitude response on the bandwidth of interest.

4. EXPERIMENTAL RESULTS

Experiments were conducted for SISO, 2I2O and 3I3O control systems using both far-field microphones and PVDF structural sensors as error transducers. Extensive data was collected and put into different formats for presentation. Error signal power spectral density plots before and after control showed the ability of the controller to reduce the error signals, and revealed information about modal controllability and observability. Plots of total radiation directivity, obtained by integrating the sound pressure spectrum over the bandwidth from 0 to 400 Hz, provided a representation of the global reduction obtained. They were used as a basis of comparison to evaluate the performance of each experimental configuration. Radiation directivity plots before and after control at each of the plate resonant frequencies revealed the effect of control on the radiation at each of the individual modes. To quantify with a single numerical estimate the performance of the controlled system, the sound power reduction was computed by integrating the radiation directivity data in the horizontal plane passing through the center of the plate. All sound pressure levels are reported in decibels with reference pressure of 20 μPa.

4.1. Microphone Error Sensor Results

The first test involved the SISO controller with the error microphone located at 0° in the far-field (on the axis perpendicular to the plate and passing through the center of the plate) and the piezoceramic actuator P1 (See Figure 2). The reduction in overall sound level at the error microphone was 5.95 dB. However, the total attenuation tapered off to zero in the directivity field moving away from the location of the error microphone. The total sound power reduction in the horizontal plane was only 2.26 dB. It was observed that the radiation at 182 Hz, corresponding to the (2,1) mode, is not controlled, and there is actually an increase (spill over effect) in the acoustic radiation at this frequency. The directivity at this frequency is dominated by the radiation of the (2,1) mode that is similar to that of a dipole with relatively little radiation at 0°. Then, the error microphone does not observe the radiation due to the (2,1) mode and therefore control at this frequency is not achieved.

To observe all radiating modes in the horizontal plane, the error microphone was moved to 30° in the far-field and the

experiment repeated. The total sound reduction at the microphone was 5.55 dB. The radiation directivities at the first four natural frequencies are plotted in Figure 3. The radiation plot for the (2,2) mode was omitted for brevity. Since all modes are now observed by the error microphone, global sound reduction at all the resonant frequencies is observed.

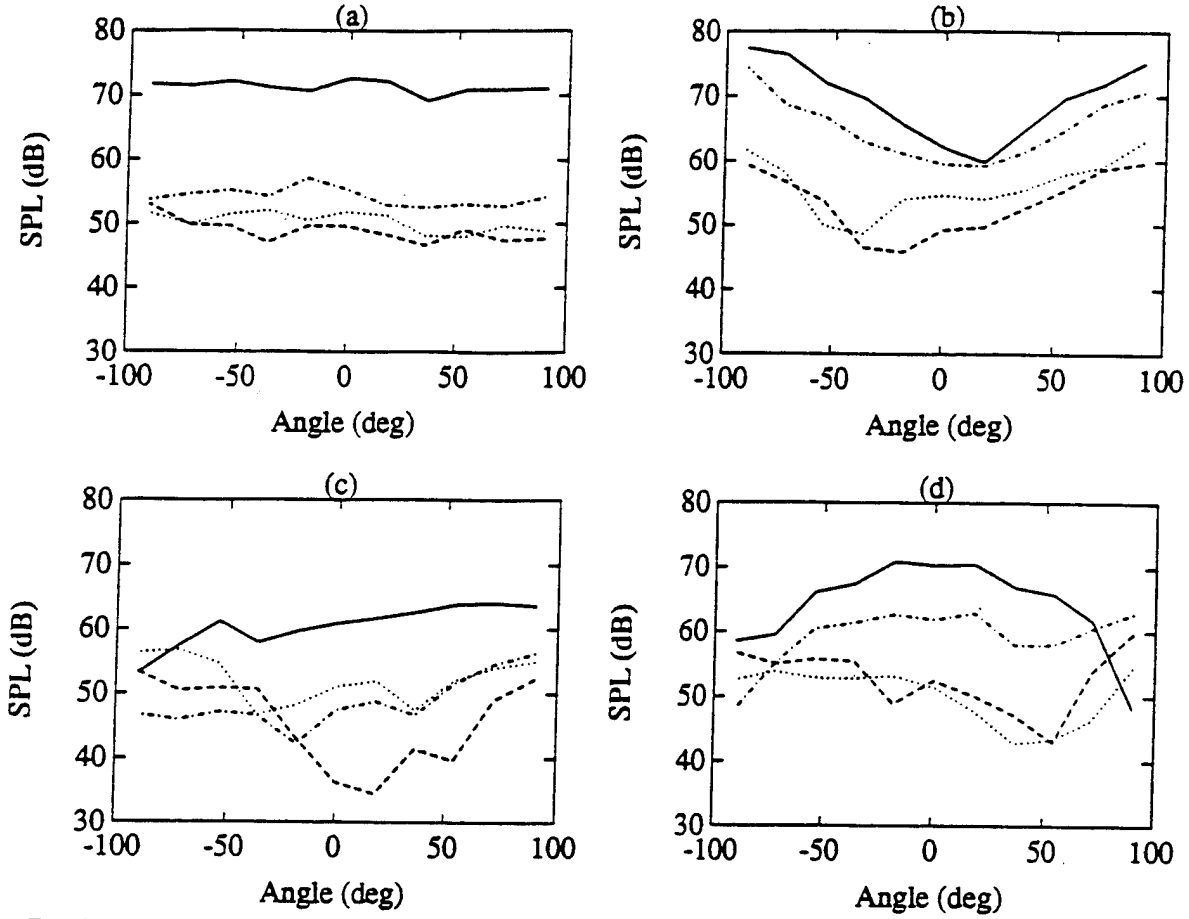

Fig. 3. Radiation directivity at (a) 86 Hz, (b) 182 Hz, (c) 248 Hz and (d) 331 Hz using microphones.
——— No control, ------ SISO, ····· 2I2O, —— 3I3O

The sound radiation of the (1,1) mode in Figure 3a shows the best reduction of nearly 16 dB, while the reduction from the (2,1) in Figure 3b shows the least reduction. The before and after control total sound radiation directivities are shown in Figure 4. Global attenuation, ranging from 3 to 8 dB, was obtained at all directions in the far-filed even though the total reduction at the error microphone at 30° was slightly less than with the error microphone at 0°. This is due to the fact that the radiation from all the modes was observed and controlled. A total sound power reduction of 3.79 dB was obtained in the horizontal plane. This demonstrates the importance of observing all modes, good and poor radiators, on the bandwidth in order to achieve global reduction with broadband inputs.

The results with the 2I2O control system were significantly better than with the SISO configuration. The two actuators used for 2I2O control were P2 and P3 in Figure 2. The two error microphones were placed at +30° and -30°. The error microphones signals were reduced by 8.91 and 7.91 dB, respectively. The radiation directivity at the frequency of the plate modes are plotted in Figure 3. This figure shows that significant improvement in sound reduction was obtained in the radiation due to the (2,1) and (3,1) modes. This yields considerably more global reduction as shown in Figure 4. Attenuation of 7 to 12 dB with are now observed in the directivity field. The total sound power in the horizontal plane was reduced by 6.36 dB. The increase in the number of control channels resulted in a better observability and controllability of all the plate mode radiation. This is an important issue in broadband radiation control because to obtain significant global sound reduction, attenuation of all radiating modes is necessary. This should be contrasted to control of harmonic disturbances where only the efficient acoustic modes need to be controlled to obtain global attenuation.

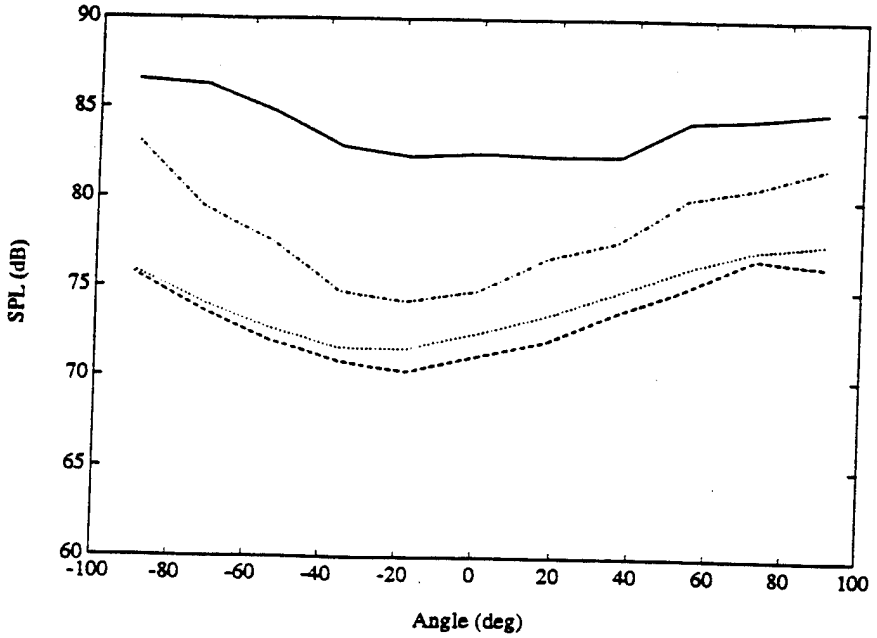

Fig. 4. Total radiation directivity using microphones as error sensors.
——— No control, ------ SISO, ····· 2I2O, —— 3I3O

The 3I3O control system was implemented with actuators P1, P2 and P3 in Figure 2. The error microphones were located at +30°, 0° and -30°. The error microphones signals were reduced by 10.8, 11.1, and 10.4 dB, respectively. To illustrate the reduction at the error microphones, the before and after control sound spectra for the error sensor at -30° is presented in Figure 5. Again the radiation directivity at the plate resonance frequencies are plotted in Figure 3, while the overall radiation directivity is shown in Figure 4. The total sound power attenuation in the horizontal plane was 7.37 dB.

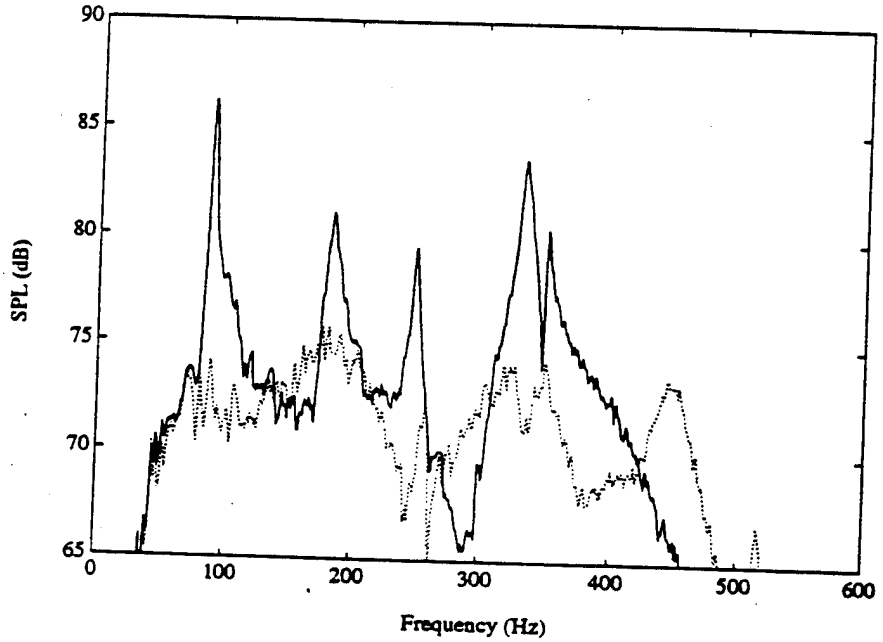

Fig. 5. Spectra of error microphone at -30° for 3I3O control system.
——— before control, ····· after control

Though the 3I3O control system yields better reduction than 2I2O control as expected, the improvement was only marginal. This is probably due to the fact that there are two modes that dominate the radiation on the bandwidth of interest, the (1,1) and (3,1) modes. Then, good control can be obtained with only two actuators and two error sensors. However, the significance of the inefficient radiating modes in broadband acoustic control should not be understated, since energy spillover into these modes can result in little global reduction. Increasing the number of actuators limits the spill over and allows more modes to be controlled.

4.2. Results with PVDF Error Sensors

Results with PVDF error transducers were obtained for SISO, 2I2O and 3I3O control configurations. The radiation directivities at the plate resonant frequencies are shown in Figure 6, while the overall radiation directivities are presented in Figure 7 for all three control configurations. For the SISO configuration, actuator P1 was used in conjunction with PVDF sensor S1 as shown in Figure 2. The geometry and location of the PVDF sensor S1 is such that it observes only the (1,1), (1,2) and (3,1) modes. Therefore, reduction in the radiation of these modes is observed in Figure 6. Again the fundamental mode shows the best attenuation with 20 dB while the reduction of the (3,1) mode was small. The (2,1) mode is unobserved by the error sensor and thus no reduction is observed at the 182 Hz frequency as shown in Figure 6b. This yielded an overall radiation directivity that shows 6.4 dB at 0° tapering off to about 2.5 dB at the edges of the directivity field ±90° as observed in Figure 7. The total sound power reduction was only 2.62 dB, even though the total reduction of the PVDF signal was 5.55 dB. Thus, the PVDF sensor design had the same observability drawback as the error microphone located at 0°, and yielded similar results. Spillover into the unobserved (2,1) mode increased the radiation at this frequency and prohibited good global control.

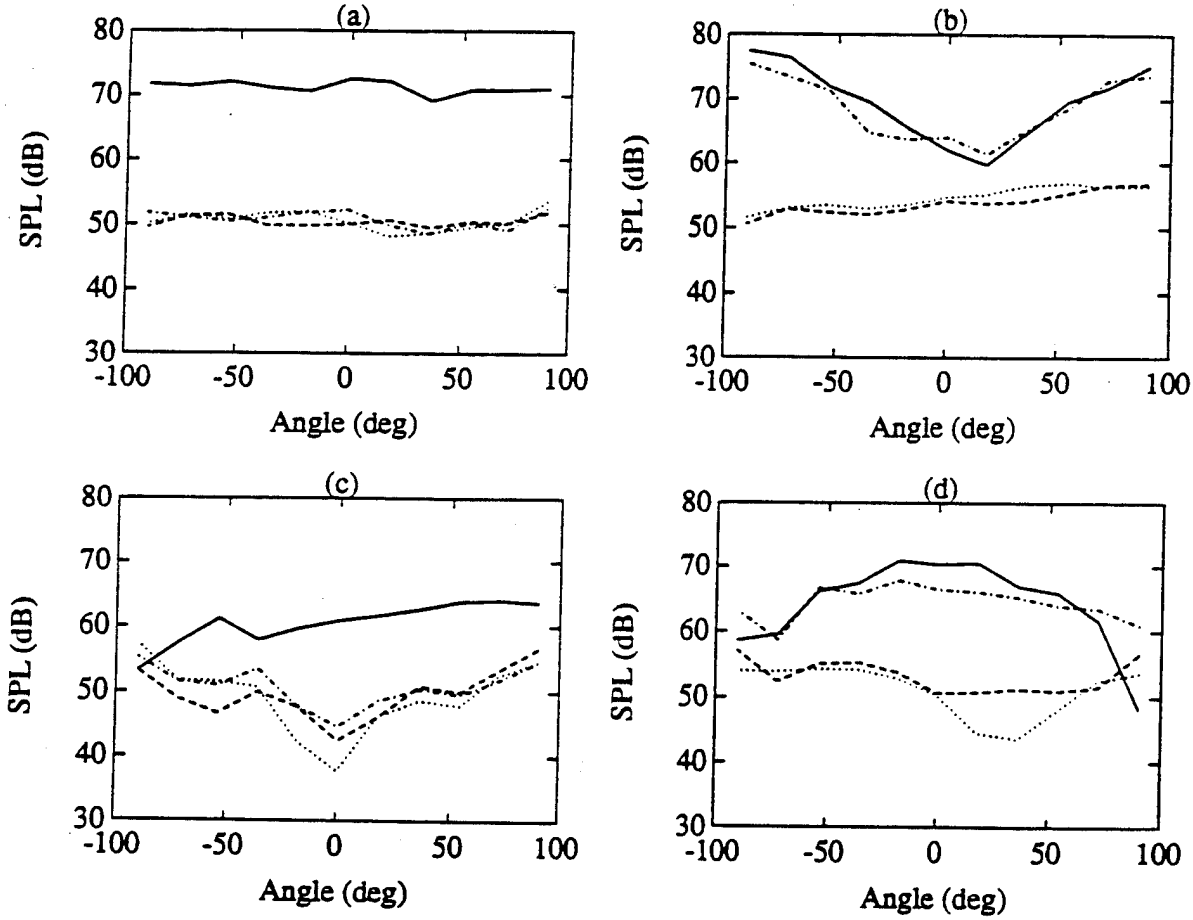

Fig. 6. Radiation directivity at (a) 86 Hz, (b) 182 Hz, (c) 248 Hz and (d) 331 Hz using PVDF sensors.
——— No control, ------ SISO, ····· 2I2O, —— 3I3O

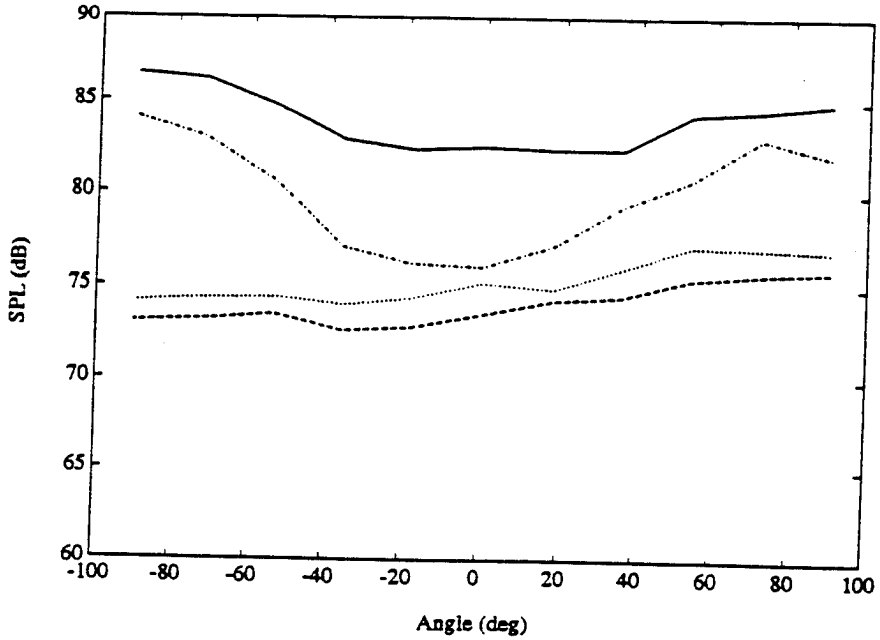

Fig. 7. Total radiation directivity using PVDF as error sensors.
——— No control, ------- SISO, ····· 2I2O, —— 3I3O

The next experiment involved the S2 and S3 PVDF sensors in conjunction with the P2 and P3 piezoceramic actuators as shown in Figure 2. With this configuration all five modes in the bandwidth are observed and controlled. The reduction of PVDF sensor P2 and P3 signals were 11.5 and 7.45 dB, respectively. This resulted in total sound attenuation of 6 to 12 dB in the directivity field as shown in Figure 7. The sound power reduction in the horizontal plane was 5.13 dB. Figure 6 shows that acoustic attenuation was achieved at all of the plate resonant frequencies.

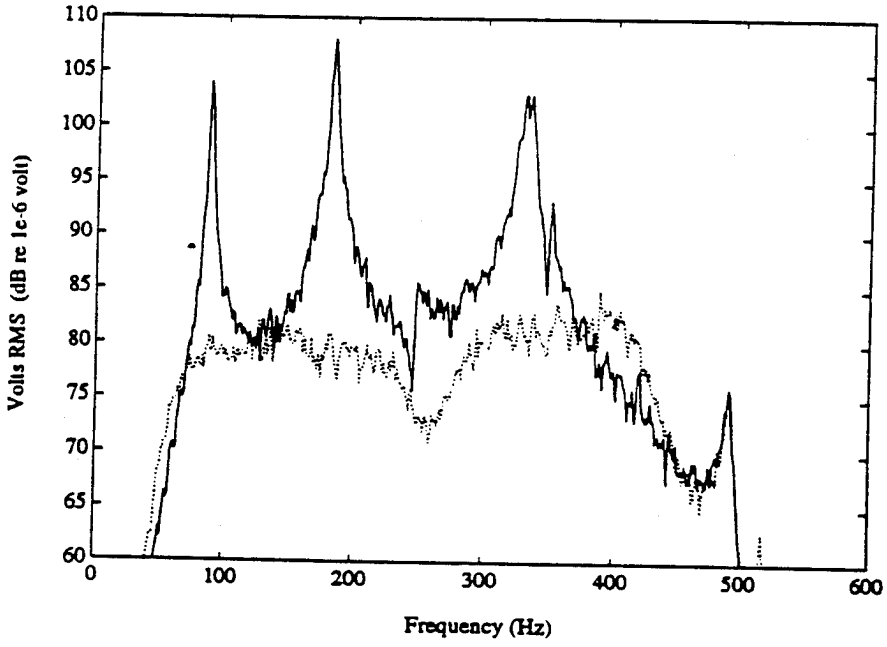

Fig. 8. Spectra of PVDF error sensor P2 for 3I3O control system.
——— before control, ····· after control

The last test was for the 3I3O control system using actuators P1, P2, and P3 and PVDF error sensors S1, S2, and S3 in Figure 2. The PVDF error signals were attenuated by 13.3, 12.9, and 7.47 dB, respectively. Figure 8 shows the spectra of the PVDF sensor P2 before and after control and indicates reduction at both on and off resonance frequencies. The radiation directivies at the resonant frequencies and the overall are again plotted in Figures 6 and 7, respectively. The sound power reduction in the horizontal plane was 6.6 dB. The trends are similar to the error microphone results, with a significant increase in the obtained attenuation when changing from SISO to 2I2O control, and only a slight increase in attenuation going from 2I2O to 3I3O control.

5. CONCLUSIONS

Active Structural Acoustic Control has been demonstrated on a simply-supported plate subject to a broadband disturbance with random frequency content on a bandwidth of 0 to 400 Hz. An adaptive feedforward filtered-x LMS control algorithm was developed with up to three control and three error sensor channels. Both microphones placed in the acoustic far-field and distributed PVDF structural transducers were investigated as error sensors. The control actuation was implemented with piezoceramic patches. Five plate modes were excited in the excitation frequency band that includes the (1,1) and (3,1) modes which are efficient acoustic radiators. The first set of tests were conducted using microphones as error sensors. The experimental results show that for the SISO control configuration limited global reduction in radiated sound is obtained. This is because the SISO control system is unable to observe and control all radiating modes irrespective of the their radiation efficiency. This should be compared with control of narrowband disturbances, where attenuation of only the efficient acoustic modes is necessary for global sound reduction. When the control system was extended to 2I2O, an average sound reduction of 11 dB at all directions in the acoustic sound field was obtained. Further extension to the 3I3O improved the attenuation by an average of 1 dB. This is because good control of both the efficient and poor acoustic radiating modes was achieved with the 2I2O control configuration. The second set of experiments involved the use of distributed PVDF structural transducers as error sensors. The design and implementation of these type of sensors is fundamental for the development of "adaptive" system. The results using PVDF sensors show similar performance as for the error microphone configuration. Thus, the potential of using structural sensors for ASAC subjected to broadband disturbances was demonstrated. Moreover, this experimental investigation illustrates the importance of optimal actuator and sensor design for efficient broadband radiation control.

6. ACKNOWLEDGEMENTS

The authors wish to gratefully acknowledge the financial support of this work by the Office of Naval Research under Grant N00014-92-J-1170.

7. REFERENCES

1. C. R. Fuller, "Apparatus and methods for global noise reduction," U.S. Patent No. 4,715,599 (1988).

2. L. Meirovitch and S. Thangjitham, "Active control of sound radiation pressure," ASME J. Vib. Acoust. 112, pp 237-244 (1990).

3. W.T. Baumann, W. R. Saunders and H. H. Robertshaw, "Active suppression of acoustic radiation from impulsively excited structures," J. Acoust. Soc. Am. 90(6), pp 3202-3208 (1991).

4. R. L. Clark and C. R. Fuller, "Experiments on active control of structurally radiated sound using multiple piezoceramic actuators, " J. Acoust. Soc. Am. 91(6), pp 3313-3320 (1991).

5. C. R. Fuller, "Active control of sound transmission/radiation from elastic plates by vibrating inputs-I analysis," J. Sound Vib. 136(1), pp 1-15 (1990).

6. V. L. Metcalf, C. R. Fuller, R. J. Silcox, and D. E. Brown, "Active control of sound transmission/radiation from plates by vibration inputs-II experiments," J. Sound Vib. (accepted for publication) (1991).

7. C. R. Fuller, C. H. Hansen, and S. D. Snyder, "Experiments on active control of sound radiation using a piezoceramic actuator," J. Sound Vib. 150(2), pp 179-190, (1990).

8. R. L. Clark and C. R. Fuller, "Optimal placement of piezoelectric actuators and polyvinelidene fluoride (PVDF) error sensors in active structural acoustic control approaches (ASAC)," J. Acoust. Soc. Am. 92(3), pp 1521-1533, (1992).

9. R. L. Clark and C. R. Fuller, "Experiments on active control of structurally radiated sound using multiple piezoceramic actuators," J. Acoust. Soc. Am. (to appear) (1990).

10. R. A. Burdisso and C. R. Fuller, "Dynamic behavior of structural-acoustic systems in feedforward control of sound radiation," J. Acoust. Soc. Am. 92(1), July 1992 pp 277-286. (1992)

11. R. A. Burdisso and C. R. Fuller, "Theory of Feedforward Controlled System Eigenproperties," J. Sound Vib. 153(3), 437-452 (1992)

12. J. S. Vipperman, R. A. Burdisso and C. R. Fuller, "Active control of broadband structural vibration using the LMS adaptive algorithm," J. Sound Vib. (to appear) (1991).

13. J. O. Smith, "Techniques For Digital Filter Design and System Identification with Application to the Violin," 1983 Ph.D. Dissertation, Stanford University.

14. B. Widrow and S. D. Stearns 1985 Adaptive Signal Processing. Englewood Cliffs, NJ: Prentice-Hall.

15. E. K. Dimitriadis, C. R. Fuller and C. R. Rogers, "Piezoelectric actuators for distributed vibration excitation of this plates," J. Vib. Acoust. 113, pp 100-107, (1989).

16. T. Song, C. R. Fuller, "Optimization of Actuator Location and Controller Robustness Analysis for Active Structural Acoustic Control," J. Acoust. Soc. Am. (to appear) (1992).

17. C. E. Wallace. "Radiation Resistance of a Rectangular Panel," J. Acoust. Soc. Am. vol 51 number 3(Part 2) 1972 pp 946-952

C-33 The impact of piezoelectric sensoriactuators on active structural acoustic control, W. R. Saunders, D. G. Cole and H. H. Robertshaw, Proceedings SPIE Conf. on Smart Structural and Materials, Albuquerque, NM, SPIE Vol. 1917, pp. 578-586, February 1993.

The impact of piezoelectric sensoriactuators on active structural acoustic control

William R. Saunders, Daniel G. Cole, Harry H. Robertshaw

Virginia Polytechnic and State University, Department of Mechanical Engineering, Blacksburg, VA 24061

Abstract

The development of simultaneous sensing and actuation for a single piezoelectric element, called a sensoriactuator in this paper, provides the opportunity for truly collocated control in adaptive structures. Issues related to collocation are discussed in terms of their effects on active structural acoustic control (ASAC). A variation on earlier feedback ASAC methods, direct radiation feedback (DRFB), is suggested for the sensoriactuator adaptive structure. The DRFB method relies on a discrete-point formulation of the associated radiated energy norm. The influence of the acoustic dynamics on proven sufficient conditions for globally stable collocated velocity feedback is discussed for the first time. Selection of an appropriate Lyapunov function for the stability analysis of collocated DRFB is discussed and compared to previous results for direct velocity feedback in active vibration control.

1. INTRODUCTION

An important application of adaptive structures is the active suppression of radiated structural acoustic energy. Dynamic structural loading initiates the propagation of acoustic waves into the surrounding fluid medium. Control of the radiated acoustic energy can be approached using both passive and active strategies. For adaptive structures, numerous combinations of active control methods and active materials can be designed to provide the structure with the ability to adjust to changing load conditions. The closed-loop response of the structure is then tailored to conform to various system specifications. This paper examines one specific configuration of adaptive structures, simultaneous sensing and actuation of PZT elements, for active structural acoustic control (ASAC) implementations.

Simultaneous sensing and actuation using a single PZT element, referred to as a *sensoriactuator* in this paper, was recently discussed by two different groups of researchers.[1,2]. One of the clearest advantages of sensoriactuators is the ability to design adaptive structures with truly collocated sensor-actuator configurations. Collocated piezoelectric transducers can provide more accurate system identification [3] and have the potential to improve the stability properties of feedback, active control strategies. Many researchers have discussed the stability of various collocated vibration control strategies but there are virtually no comparable analyses for ASAC implementations. Design of a direct radiation feedback controller and the inherent stability of the collocated ASAC design is the main focus of this paper.

Earlier research showed that collocated active vibration control (AVC) provided some guarantees on the closed-loop stability. Balas demonstrated that direct velocity feedback control (DVFB) provided a closed-loop stability margin which was never lower than that of the open-loop system.[4] Subsequent work by Caughey and Goh discussed the effect of actuator dynamics on such stability results.[5] Their analyses led to the development of positive position feedback (PPF) which exhibited good stability and spillover properties in the presence of actuator dynamics.[6,7] Bar-Kana et.al. proved the feasibility of shape control and active damping using collocated sensors and actuators with a direct position-plus-velocity feedback approach.[8] All of the existing literature on stability of closed-loop structural control systems has been associated with minimization of the structure's vibrational energy norm, $E_v(t) = \| (w, \dot{w}) \|$ where w and $\dot{w}$ are the structural position and velocity vectors. Examination of stability for collocated ASAC requires a slightly different analysis approach.

The primary distinction between active vibration control (AVC) and ASAC is the inclusion of structural acoustic dynamics in the ASAC solution.[9] Generically, two different approaches underly various ASAC designs. First, output control introduces the acoustic process mechanisms directly by minimizing a cost function consisting of microphones (hydrophones) located at a field point in the fluid domain. This approach is used more successfully by adaptive feedforward controllers because of the added complexity which the acoustic wave propagation introduces to feedback control paradigms. The second approach employs various weighted-norm minimizations where the cost function

is synthesized through acoustic modelling. The weighted-norm representation refers to a linear mapping from the structural state vector $x \in R^n$ to some acoustic output vector $Z \in R^m$, so that the control cost functional becomes

$$J = \int_0^{t_f} Z^T(t)\, Z(t) + u^T(t)\, R\, u(t)\, dt. \tag{1}$$

Different images of x under varying matrix transformations $Z = G\, x$ can be developed. Numerous researchers have reported on the effects of weighted-norm ASAC controllers. Baumann et.al. introduced the radiation filter concept for feedback ASAC where the filter output represented the modal contribution to the farfield radiated power.[10] Suppression of radiated sound from light fluid-loaded structures subject to transient and persistent structural disturbances was demonstrated for this approach.[11] ASAC of a heavy fluid-loaded plate was reported by Saunders using a weighted-norm of the in-vacuo structural states.[9] Clark and Fuller proposed wavenumber weighting of the surface velocities for minimization of steady-state, radiated pressure in specific subdomains.[12] Their adaptive feedforward controller, like adaptive feedforward control approaches in general, was not developed for transient disturbances. In fact, *a survey of the most recent ASAC research results indicates that feedback control strategies must be used if the performance goal is suppression of transient disturbances.* This important design consideration motivates our analysis.

As discussed earlier, many researchers investigated the performance of direct, collocated feedback for AVC. Their results identified conditions for guaranteed stability and examined the performance of various feedback schemes (DVFB, PPF, etc.). The success of these analyses prompts an important question for ASAC research: are there similar advantages for direct feedback ASAC approaches relative to closed-loop stability and system performance? It is important to question whether collocated ASAC control performs better, relative to some metric, than collocated AVC strategies. Stated otherwise, can direct feedback ASAC controllers provide comparable stability margins and increased performance over direct feedback AVC methods? The remainder of this paper develops a direct feedback ASAC method and formulates the stability analysis to help answer these questions.

In this paper we formulate the DRFB approach using sensoriactuators and examine the closed-loop stability. We begin with dynamic descriptions of the coupled piezoelectric-structural plant, followed by the development of discrete-point radiation filters which model the linear transformation from surface velocity to acoustic farfield pressure. The discrete-point radiation filters, presented here for the first time, are compatible with finite-element model (FEM) representations of the structure. This FEM approach eliminates the requirement for spatial (modal) filtering required by previous feedback ASAC control laws. A Lyapunov function for the controlled structural acoustic plant, corresponding to the radiated energy norm, is examined and conclusions about sufficient conditions for closed-loop stability are presented.

2. DYNAMIC REPRESENTATION OF THE STRUCTURAL ACOUSTIC PLANT

A state-space formulation of the structural acoustic plant dynamics is presented for the purpose of examining the stability of DRFB control. The coupled piezoelectric-structural dynamics are reviewed, followed by a development of the discrete-point radiation filters. It is shown that DRFB is a type of weighted-norm ASAC control which results in a frequency shaped cost functional (FSCF) as discussed by Gupta.[13] A transformation of the FSCF problem to an augmented state vector with a constant weighting matrix is reviewed in this section to prepare for analysis of the closed-loop structural acoustic plant's asymptotic stability properties.

2.1. Structural dynamics

Consider the state-space representation of a flexible structure in a light fluid, where we adopt Crighton's criteria for fluid loading.[14]

$$\dot{w}(t) = A\, w(t) + B\, u(t) \tag{2}$$

$$y(t) = C\, w(t) + D\, u(t) \tag{3}$$

where $w(t) \in R^{2n}$ are the generalized positions and velocities, $u(t) \in R^m$ is a vector of control inputs, $y(t) \in R^p$ is the vector of measured output signals at a sensoriactuator location and the n modes of the structure are assumed to be truncated at some very large, finite number. (The time dependence notation will be dropped for the remainder of the paper unless desired for clarity.) We will assume that the structure is equipped with PZT sensoriactuators so that $m = p$ and the matrices of equations 2 and 3 are $A = \begin{bmatrix} 0 & I \\ -\lambda & -2\zeta\lambda^{\frac{1}{2}} \end{bmatrix}$, $B = \begin{bmatrix} 0 \\ \Psi^T \end{bmatrix}$, $C = [\alpha\,\Psi \;\; \beta\,\Psi]$ and the feedthrough matrix D is assumed to be zero for this analysis. The coefficient matrices $\alpha = diag\,[\alpha_1, \alpha_2, \ldots, \alpha_p]$ and $\beta = diag\,[\beta_1, \beta_2, \ldots, \beta_p]$ isolate the position and velocity signals generated by the p'th sensoriactuator location. Note that Ψ is the discrete modal matrix for the structure with elements $\psi_i(z_k)$ where $i = 1, 2, ..., n$ and z_k is the sensoriactuator location $k = 1, 2, ..., p$. The mode frequencies are $\omega_i = \lambda^{\frac{1}{2}}$ and we have assumed a viscous damping model. It will be helpful to define notation for the state vector $w = \begin{bmatrix} w_1 \\ w_2 \end{bmatrix}$ so that the output

$$\begin{aligned} y &= y_1 + y_2 \qquad (4) \\ &= \alpha\,\Psi\,w_1 + \beta\,\Psi\,w_2 \qquad (5) \end{aligned}$$

can be distinguised as some combination of structural position and velocity measurements. Equations 2 and 5 formulate the description of the plant's structural dynamics for unspecified actuator and sensor designs. Next, the sensoriactuator equations are reviewed to show the effect on the plant state equations.

2.2. Coupled structure-sensoriactuator equations

The equations of motion of a piezoelectric system are derived in Hagood et al.[15] resulting in two equations which describe the electromechanically coupled system.

$$\text{Actuator Eqn.} \qquad M\ddot{w} + C\dot{w} + Kw = \Theta v \qquad (6)$$

$$\text{Sensor Eqn.} \qquad \Theta^T w + C_p v = q \qquad (7)$$

The mass matrix M, damping matrix C and stiffness matrix K are related to the quantities of the state matrix A by a similarity transformation. The sensoriactuator voltage v corresponds to the control signal u of equation 2 and the charge q can be made proportional to the induced mechanical strain (i.e. position) at the sensoriactuator location.

The Sensor equation further describes the electromechanical coupling between a structure and electronics via piezoelectrics. The Sensor equation is important when designing sensor circuitry and/or passive control schemes. Electromechanical coupling is described in the electromechanical coupling matrix Θ which describes the interaction between electrical effects, such as voltage and charge, and mechanical effects, such as force and displacement. Notice that the Sensor equation converts the modal position (velocity) vector to a charge (current) which is proportional to the physical strain (strain rate) at the sensoriactuator location.

Sensoriactuators use a single piezoelectric element to provide both measurement and control and take advantage of being able to measure current and/or charge on a piezoelectric actuator as described by the Sensor equation. It is apparent that the patch current is directly related to structural velocities through the relationship

$$i_{total} = \dot{q} = \underbrace{\Theta^T \dot{w}}_{i_{mech}} + \underbrace{C_p \dot{v}}_{i_{elec}} \qquad (8)$$

If the *electrical current*, corresponding to the capacitor electrodynamics, is correctly compensated for then the *mechanical current*, corresponding to the structural dynamics, directly relates to structural velocities.

Compensation can easily be achieved using a simple analog circuit as shown in figure 1. The compensation circuit proposed by Anderson and Hagood uses a reference capacitor, which is ideally equal to the sensoriactuator capacitance, to create a current equal to i_{elec}. This reference current is then subtracted from the measured current yielding the desired mechanical information.

$$i_{mech} = \Theta^T \dot{w} + (C_p - C_r)\dot{v} \qquad (9)$$

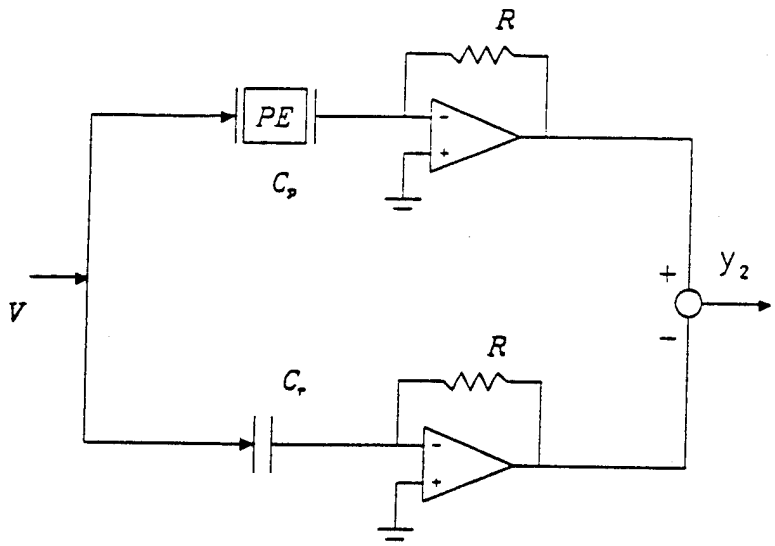

Figure 1: Compensating transresistance amplifier for strain rate measurement

It should be noted that it may be difficult, in practice, to exactly match the patch capacitance. Also, due to differences in sensitivity of a piezoelectric to structural and electrical excitation there may be large differences in the magnitudes of i_{mech} and i_{elec} requiring the reference capacitor to be exact to several decimal places. This paper will assume that the compensation can be performed accurately.

The state equations of the structural plant with sensoriactuator transducers then become

$$\begin{bmatrix} \dot{w}_1 \\ \dot{w}_2 \end{bmatrix} = \begin{bmatrix} 0 & I \\ -\lambda & -2\zeta\lambda^{\frac{1}{2}} \end{bmatrix} \begin{bmatrix} w_1 \\ w_2 \end{bmatrix} + \begin{bmatrix} 0 \\ \Theta \end{bmatrix} v \tag{10}$$

$$\begin{bmatrix} q \\ \dot{q} \end{bmatrix} = [\alpha\,\Theta^T \;\; \beta\,\Theta^T] \begin{bmatrix} w_1 \\ w_2 \end{bmatrix} + (C_p - C_r)\,\dot{v} \tag{11}$$

The essential difference between the state equations for the sensoriactuator-equipped structure is the substitution of the patch voltage v for the control signal u and the substitution of the electromechanical coupling matrix Θ for the modal matrix Ψ. We will assume that the sensoriactuator conditioning circuits are designed for velocity (strain rate) measurements and that $C_p = C_r$ so that the output equation can be written

$$y_2 = [0 \;\; \beta\,\Theta^T] \begin{bmatrix} w_1 \\ w_2 \end{bmatrix} \tag{12}$$

2.3. Discrete-point radiation filters

The acoustic dynamics are introduced to the plant equations by the synthesis of radiation filters. As mentioned earlier, Baumann et.al. presented the development of modal radiation filters for transient control and suppression of broadband, persistent disturbances.[10,11] Next, we introduce the design of discrete-point radiation filters to facilitate the minimization of the radiated energy norm using sensoriactuator elements in adaptive structures.

The discrete-point radiation filters derive from Rayleigh's equation for planar sources. This approach assumes the planar source is located in an infinite baffle. As discussed by Junger and Feit, [16] the Rayleigh equation is

$$p(t,\vec{R}_f) = -2j\omega \int_S g(|\,\vec{R}_f - \vec{R}_s\,|)\, y_2(t,\vec{R}_s)\, dS(\vec{R}_s) \tag{13}$$

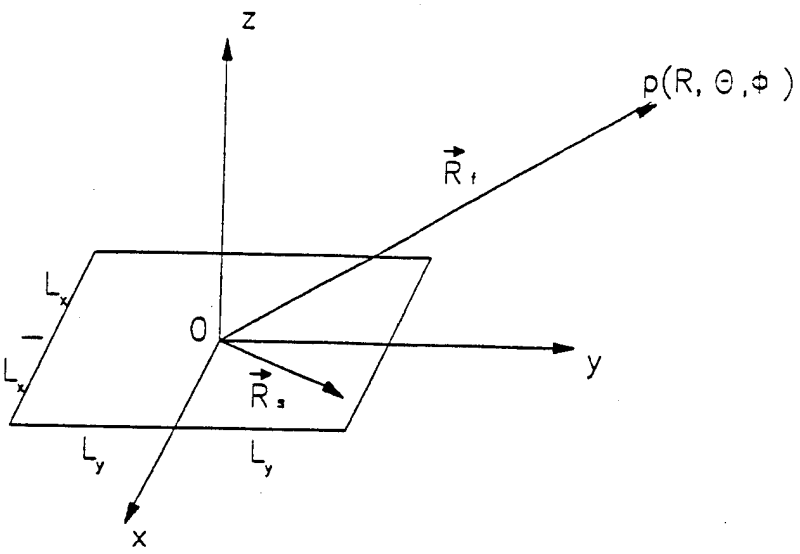

Figure 2: Coordinate system for elemental piston radiators

where $\vec{R}_f$ and $\vec{R}_s$ are the position vectors in the fluid and on the structure and $g(|\ \vec{R}_f - \vec{R}_s\ |)$ is the free-space Green's function. Referring to figure 2, the coordinate origin can be chosen such that equation 13 becomes

$$p(t,R,\theta,\phi) \;=\; \frac{j\omega\rho e^{jkR}}{2\pi R}\int_{-L_x}^{L_x}\int_{-L_y}^{L_y} y_2(t,x,y)exp[-jksin\theta(xcos\phi + ysin\phi)]dxdy \tag{14}$$

The physical interpretation of equation 14 is that the pressure at a field point can be perceived as the pressure due to a distribution of point velocity sources of elemental area $dx\ dy$. The exponential term describes the relative phasing between the effective sources which is caused by the differences in path length to the field point. For low wavenumber acoustic radiation ($\frac{kr}{k} << 1$), this model adequately describes the farfield pressure in the hemisphere adjacent to the baffled structure.

Next, we assume that the velocity is prescribed by $y_2(t) = y_2 exp[j\omega t]$. Utilizing the Fourier transform, we can write a transfer function between the velocity measured by the k'th sensoriactuator and the resulting pressure in the farfield $p_k(R,\theta,\phi)$ as

$$\hat{p}_k(R,\theta,\phi,\omega) \;=\; y_2(\omega)\,\frac{\hat{h}_k(\theta,\phi,\omega)exp[jkR]}{R} \tag{15}$$

where $\hat{}$ denotes Fourier transformed variables. Defining $H^T(\theta,\phi,\omega) \;=\; \left[\hat{h}_1(\theta,\phi,\omega)\ \hat{h}_2(\theta,\phi,\omega)\ \ldots\ \hat{h}_p(\theta,\phi,\omega)\right]$ and

$y_2(\omega) \;=\; \begin{bmatrix} \hat{y}_{2,1}(\omega) \\ \hat{y}_{2,2}(\omega) \\ \vdots \\ \hat{y}_{2,p}(\omega) \end{bmatrix}$ we can write the total farfield pressure as

$$\hat{p}(R,\theta,\phi,\omega) \;=\; y_2^T(\omega)\,H(\theta,\phi,\omega)\,\frac{exp[jkR]}{R}. \tag{16}$$

Note that the general form of equation 16 is identical to the corresponding quantity in the development of modal radiation filters.[10] The difference is the absence of the spatial components Ψ in the transfer function matrix $H(\theta,\phi,\omega)$ because the velocity inputs are in the physical coordinate space for this derivation. At this stage in the radiation filter development, $H(\theta,\phi,\omega)$ is a matrix of linear phase, constant magnitude filters as discussed recently by Maillard and Fuller.[17] For a prescribed wavenumber k and radius R, the $H \in C^{p\times 1}$ filter matrix simply tracks the phase of acoustic particle velocity from the elemental source associated with each sensoriactuator location z_k to the field

point (R, θ, ϕ).

The remaining steps in the development of the discrete-point radiation filters follow nearly identically to Baumann et.al. and will only be summarized here. Using the real-valued pressure and fixing R, the total energy per unit area radiated into the farfield in direction (θ, ϕ) is given by the integration of the instantaneous power per unit area with respect to time, that is

$$\frac{1}{\rho\, c} \int_o^\infty \left[\sum_{i=1}^{P} p_k(R, \theta, \phi, t) \right]^2 dt. \tag{17}$$

By Parseval's theorem and substitution of equation 16, the radiated energy becomes

$$\int_0^\infty y_2^T(\omega)\, M(\omega)\, y_2(\omega)\, d\omega \tag{18}$$

where

$$M(\omega) = \frac{1}{\pi\, \rho\, c} \int_0^{2\pi} \int_0^{\pi} H(\theta, \phi, \omega)\, H^*(\theta, \phi, \omega)\, sin\theta\, d\theta\, d\phi \tag{19}$$

is the 'radiated power operator matrix'. $M(\omega) \in R^{p \times p}$ will generally be of larger dimension than the corresponding matrix in a generalized coordinate system. The conjugate transpose matrix is a positive definite matrix whose elements are rational transfer functions which describe the dynamics of the linear transformation from elemental source velocities to farfield radiated energy. When evaluated at a specific frequency ω, the singular values represent the contribution of each elemental source to the farfield radiated energy. Finally, it is possible to approximately factor $M(\omega)$, to some desired accuracy, as

$$M(\omega) \approx G^*(\omega)\, G(\omega). \tag{20}$$

The total radiated energy can thus be expressed as

$$\Pi = \int_0^\infty y_2^T(\omega)\, G^*(\omega)\, G(\omega)\, y_2(\omega)\, d\omega \tag{21}$$

and by Parseval's theorem this is equivalent to

$$\Pi = \int_0^\infty Z^T(t)\, Z(t)\, dt \tag{22}$$

where $Z(t) = \mathcal{L}^{-1}[G(s)\, y_2(s)]$. As discussed earlier, $Z \in R^p$ is the image of y_2, created by passing the vector of sensoriactuator velocity measurements through a filter with transfer function $G(s)$.

2.4. The augmented state description

The dynamics of the radiation filter matrix can be written in state-space form as follows:

$$\dot{r} = A_f\, r + B_f\, y_2 \tag{23}$$

$$Z = C_f\, r + D_f\, y_2 \tag{24}$$

$$= C_f\, r + D_f\, \beta\, \Theta^T\, w_2 \tag{25}$$

where the filter state-vector is $r \in R^s$, y_2 is the input to the radiation filter matrix, Z is the filter output and we have used equation 11. Using equations 10, 23 and 25 we can write the state and output equations for the structural acoustic plant for the augmented state vector $x_a = \begin{Bmatrix} w_1 \\ w_2 \\ r \end{Bmatrix}$ as

$$\dot{x}_a = \begin{bmatrix} 0 & I & 0 \\ -\Lambda & -2\,\zeta\,\Lambda^{\frac{1}{2}} & 0 \\ 0 & B_f\,\beta\,\Theta^T & A_f \end{bmatrix} x_a + \begin{bmatrix} 0 \\ \Theta \\ 0 \end{bmatrix} v \tag{26}$$

$$Z = [0 \quad D_f \beta \Theta^T \quad C_f] \, x_a \tag{27}$$

Closed-loop plant equations can be now be designed using direct radiation state feedback. The DRFB method refers to the control law $v = -K Z$. This control law represents partial state feedback of plant velocities w_2 and acoustic filter states r. Next, we pose the stability analysis of the closed-loop system which minimizes the cost functional given by equation 1.

3. DIRECT RADIATION FEEDBACK CONTROL: STABILITY ISSUES

Suppression of structural velocity will result in suppression of the radiated acoustic energy. However, it is intuitive (but not proven) that forcing the radiation to the zero state is more advantageous for the ASAC problem. Direct radiation feedback is examined relative to the closed-loop stability in this section. We begin with a dialogue on previous stability results from the AVC literature.

The following criteria due to Lyapunov are used to show stability of a linear system

$$\dot{x}(t) = A \, x(t) \tag{28}$$

Theorem 1: If there exists a Lyapunov function, $V(t) = x^T P \, x(t)$ with a positive definite, Hermitian matrix P and the function $\dot{V}(t) < 0$, i.e. is negative definite, then the system of equation 28 is aysmptotically stable.

A less restrictive corollary also exists requiring that P be positive semidefinite and the pair (A, C) be observable, where $y = C \, x$. Next, we assume that DVFB generates the control signal and examine the corresponding Lyapunov function used for a vibration cost function.

Previous AVC researchers showed that controlling the structural velocity provided nice stability features. For the vibration control system, the energy norm is a sufficient Lyapunov function given by

$$E_v(t, w) = [w_1^T \quad w_2^T] \begin{bmatrix} \Lambda & 0 \\ 0 & I \end{bmatrix} \begin{bmatrix} w_1 \\ w_2 \end{bmatrix} \tag{29}$$

The choice of the weighting matrix in equation 29 provides an estimate of the total energy in the system. Then it was shown that the derivative of $E_v(t, w)$ was a dissipatory function, continuously decreasing with time.[4] Physically, the total energy for the vibratory system forms a monotonically decreasing function along the quadratic because of the interaction of the position and velocity terms in the energy norm.

For the DRFB design, we wish to examine the stability of the system of equation 26, with the substitution $v = -K \, Z$, such that we can write the closed-loop equation $\dot{x}_{a,c} = A_c \, x_{a,c}$

$$\dot{x}_{a,c} = \begin{bmatrix} 0 & I & 0 \\ -\Lambda & -2\,\zeta\,\Lambda^{\frac{1}{2}} - \Theta \, K \, D_f \, \Theta^T & -\Theta \, K \, C_f \\ 0 & B_f \, \Theta^T & A_f \end{bmatrix} x_{a,c} \tag{30}$$

The radiated energy norm is given by

$$E_r(t, x_a) = (Z^T(t) \, Z(t)) \tag{31}$$

$$= [w_2^T \quad r_T] \begin{bmatrix} \Theta \, D_f^T \, D_f \, \Theta^T & \Theta \, D_f^T \, C_f \\ C_f^T \, D_f \, \Theta^T & C_f^T \, C_f \end{bmatrix} \begin{bmatrix} w_2 \\ r \end{bmatrix} \tag{32}$$

where we have used equation 27 to expand $Z^T \, Z$. The description of the radiated energy does not depend on the full state; position is not required. However, if we are to design a Lyapunov function for the system, we need to provide a PD weighting matrix on the full augmented state. Our first selection weights the positions as follows to generate a Lyanpunov function $V_r(t, x_{a,c}) = x_{a,c}^T \, P \, x_{a,c}$ for the system, where P is given by

$$P = \begin{bmatrix} \epsilon \, \Lambda & 0 & 0 \\ 0 & \Theta \, D_f^T \, D_f \, \Theta^T & \Theta \, D_f^T \, C_f \\ 0 & C_f^T \, D_f \, \Theta^T & C_f^T \, C_f \end{bmatrix} \tag{33}$$

Taking the derivative,

$$\dot{V}_r(t, x_{a,c}) = x_{a,c}^T \left[A_c^T P + P A_c\right] x_{a,c} \tag{34}$$

where the matrix quantity must be expanded before we can make conclusions about the stability. Defining $N = \left[A_c^T P + P A_c\right]$, we can expand the matrix using equations 30 and 33. However, the terms in the matrix are quite lengthy. Using general notation for A_c and P we will show only the general result of the expansion

$$N = \begin{bmatrix} 0 & P_{1,1} - \Lambda^T P_{2,2} & -\Lambda^T P_{2,3} \\ -(P_{2,2} + \epsilon)\Lambda & P_{2,2}A_{2,2} + A_{2,2}^T P_{2,2} + P_{2,3}A_{2,3} + A_{3,2}^T P_{3,2} & P_{2,2}A_{2,3} + A_{2,2}^T P_{2,3} + P_{2,3}A_{3,3} + A_{3,2}^T P_{3,3} \\ -P_{3,2}\Lambda & P_{3,2}A_{2,2} + A_{2,3}^T P_{2,2} + P_{3,3}A_{2,3} + A_{3,3}^T P_{3,2} & P_{3,2}A_{2,3} + A_{2,3}^T P_{2,3} + P_{3,3}A_{3,3} + A_{3,3}^T P_{3,3} \end{bmatrix} \tag{35}$$

The matrix is not positive definite, as required by the Lyapunov criteria, and it is not possible to determine easily whether the matrix is in fact positive semidefinite.

The selection of the Lyapunov function must be made using some other criteria than the radiated energy of the system. This may be explained physically by noting that the radiated energy of the system, as defined earlier through equation 32, is expected to be an oscillatory function as the state decays to zero. We feel that through proper selection of the terms in the Lyapunov function, it should be possible to show asymptotic stability of the closed-loop system. This will be the focus of future work.

5. Conclusions

Collocated ASAC control approaches are facilitated by the use of PZT sensoriactuators in adaptive structures. A direct radiation feedback approach was suggested here for the first time, where the output of discrete-point radiation filters are fed back by the control law. The discrete-point radiation filters are a new contribution, also. The DRFB, weighted-norm ASAC approach was evaluated for its stability using the radiated energy norm. It was concluded that, unlike the vibrational energy norm, the radiated energy norm provides a positive definite Lyapunov function but does not exhibit continuously decreasing radiated energy. Specifically, it was not possible to demonstrate that the derivative of the Lyapunov function was positive semidefinite. Our conclusions are that the radiated energy of the system, as formulated here, is not guaranteed to be monotonically decreasing. Physically, this is related to the oscillatory behavior of the function in time. However, it is also intuitive that the radiated energy of the system should exhibit asymptotic stability under certain controller gains. We feel that it remains to select an appropriate Lyapunov function to demonstrate this stability and this will be the focus of future work.

6. Acknowledgements

The authors gratefully acknowledge many helpful discussions with Bill Baumann throughout the preparation of this paper. We also acknowledge the funding support of the Office of Naval Research, contract number N00014-92-J-1170.

7. References

1. N.W. Hagood and E.H. Anderson, "Simultaneous sensing and actuation using piezoelectric materials," *SPIE Conf. on Active and Adaptive Optical Components*, SPIE 1543-40, July 1991.
2. J.J. Dosch, D.J. Inman, and E. Garcia, "A self-sensing actuator for collocated control," *ADPA Intl. Symp. on Active Materials and Adaptive Structures*, Alexandria, VA, Nov. 1991.
3. D.G. Cole, W.R. Saunders and H.H. Robertshaw, "Methods for collocated piezostructure modal parameter estimation," In Preparation.
4. M.J. Balas, "Direct velocity feedback control of large space structures," J. Guidance and Control, Vol.2, No.3, pp.252, 1978.
5. T.K. Caughey and C.J. Goh, Dynamics Laboratory Report DYNL-82-3, California Institute of Technology, 1982.
6. C.J. Goh and T.K. Caughey, "On the stability problem caused by finite actuator dynamics in the collocated control of large space structures," Int. J. Control, Vol.41, No.3, pp.787, 1985.

7. T.K. Caughey and J.L. Fanson, "An experimental investigation of vibration suppression in large space structures using positive position feedback", Dynamics Laboratory Report DYNL-87-1, Cal Tech, Jan. 1987.
8. I. Bar-Kana, R. Fischl and P. Kalata, "Direct position plus velocity feedback control of large flexible structures," IEEE Trans. Aut. Cont., Vol.36, No.10, pp.1186, 1991.
9. W.R. Saunders, "On the use of modern control theory for active structural acoustic control", Ph.D. Dissertation, VPI&SU, Blacksburg, VA, Dec., 1992.
10. W.T. Baumann, W.R. Saunders and H.H. Robertshaw, "Active suppression of acoustic radiation from impulsively excited structures," J. Acoust. Soc. Am., Vol., 1992.
11. W.T. Baumann, Ho Fu-Sheng and H.H. Robertshaw, "Active structural acoustic control of broadband disturbances", accepted for publication in J. Acoust. Soc. Am.
12. R.L. Clark and C.R. Fuller, "Control of sound radiation with adaptive structures," J. Intell. Mat. Sys. and Struct., 2(3), pp.431, 1991.
13. N.K. Gupta, "Frequency-shaped cost functionals: extension of linear-quadratic-gaussian design methods,"J. Guid. Cont., Vol.3, No.6, 1980.
14. D.G. Crighton and D. Innes, "The modes, resonances and forced response of elastic structures under heavy fluid loading," Proc. R. Soc. Lond. A312, pp.295, 1984.
15. Hagood, N. W., Chung, W. H., and von Flotow, A., 1990. "Modelling of Piezoelectric Actuator Dynamics for Structural Control," AIAA-90-1087-CP.
16. M.C. Junger and D. Feit, *Sound, Structures, and Their Interaction*, The MIT Press, 1986.
17. J.P. Maillard and C.R. Fuller, "Advanced time domain sensing techniques for active structural acoustic control," Presented at the 124th Meeting of the Acoustical Society of America, New Orleans, LA, Oct31-Nov4, 1992.

C-34 Power Consumption of Piezoelectric Actuators in Underwater Active Structural Acoustic Control, S. C. Stein, C. Liang and C. A. Rogers, Second Conference on Recent Advances in Active Control of Sound and Vibration, Blacksburg, VA, pp. 189-203, 28-30 April 1993.

POWER CONSUMPTION OF PIEZOELECTRIC ACTUATORS IN UNDERWATER ACTIVE STRUCTURAL ACOUSTIC CONTROL

S. C. Stein,[1] C. Liang,[2] C. A. Rogers[3]

ABSTRACT

A power consumption model of piezoelectric actuators inducing vibration in an underwater structure which radiates sound has been developed. The one-dimensional model based on structural impedance (termed the impedance model) has been applied to the case of a simply supported beam in an infinite rigid baffle with a fluid medium on one side. The effects of the fluid medium are included in the impedance analysis by considering the fluid-structure interaction. Power consumption results in air are compared with those in water to illustrate the effect of the fluid-structure interaction on the actuator power consumption and requirements.

INTRODUCTION

Active structural acoustic control (ASAC) using induced strain actuators has recently gained attention as a possible means of controlling low-frequency noise (< 1000 Hz). ASAC has been demonstrated experimentally for composite beams with embedded shape memory alloy (SMA) actuators (Rogers, 1989; Saunders et al., 1990), beams with bonded piezoelectric (PZT) actuators (Fuller et al., 1990) and plates with bonded PZT actuators (Clark and Fuller, 1992). Other research has focused on optimization of multiple PZT actuators for ASAC of plates (Wang, 1990) and ASAC of cylindrical shells using PZT actuators (Lester and Lefebvre, 1991; Jones and Sonti,1991). These efforts have been useful in identifying the significant design parameters for an induced strain actuator utilized in an ASAC system (i.e., size, location, thickness, phasing, etc.).

In most, if not all, of the research related to ASAC with induced strain actuators, the investigation of energy consumption has been ignored. A recent paper by Liang et al. (1992) considers actuator power consumption in vibration control. For thin beam, plate and shell structures, the energy consumption may not be a concern; however, for larger,

[1]Graduate Research Assistant, Center for Intelligent Material Systems and Structures (CIMSS), Virginia Polytechnic Institute and State University, Blacksburg, VA 24061-0261, U.S.A.
[2]Research Scientist, CIMSS, Virginia Polytechnic Institute and State University, Blacksburg, VA 24061-0261, U.S.A.
[3]Director, CIMSS, and Associate Professor, Department of Mechanical Engineering, Virginia Polytechnic Institute and State University, Blacksburg, VA 24061-0261, U.S.A.

complicated structures, such as marine vessels, which may require a great number of relatively large actuators, the power consumed by the actuators may be very significant. Large actuator power consumption signifies large power supplies which are expensive and massive. Reducing the power consumption of intelligent material systems, therefore, will reduce both the cost and mass of such systems, two of the aims of intelligent material systems for active control.

In ASAC with PZT actuators, the sound pressure is linearly related to the applied forces and moments. Increasing the sound pressure level in dB is therefore limited by the amount of induced force/moment the actuator can deliver. The voltage level and power consumption, however, can be significantly reduced by increasing the force/moment output of the actuator for a set electric field. One way of increasing the moment over the moment from a bonded actuator without changing the applied electric field is to offset the actuator from the structure (Chaudhry and Rogers, 1992). As an example, consider an actuator configured in such a way as to obtain a 100% increase in induced moment. This increase in moment increases the sound pressure level by only about 3 dB. However, the voltage level needed to maintain the original sound pressure level will drop by 50% and the power consumption can be reduced by up to 75%. Thus, power consumption of actuators should be included as a primary variable in the objective function for optimization of intelligent material systems for active control. This paper uses the general impedance method, developed by Liang et al. (1992,1993), for determining the power consumed by PZT actuators in underwater ASAC.

INTRODUCTION TO IMPEDANCE AND ACTUATOR POWER CONSUMPTION MODEL

The impedance and actuator power consumption model, introduced by Liang et al. (1992,1993), describes the interactions between actuators and structures using the dynamic output characteristics of the actuators and the dynamic characteristics of the structure, i.e., the structural impedance. Mass, damping, rigidity, boundary conditions and acoustic fluid loading all contribute to the impedance of a structure. The model may be used to determine the dynamic response and power consumption for actuators used in active material systems. This section introduces the impedance and power consumption model by using a simple one-degree-of-freedom spring-mass-damper system as an example.

Liang et al. (1992,1993) used a PZT actuator driving a one-degree-of-freedom spring-mass-damper system, shown in Figure 1, to arrive at general equations for dynamic response and power consumption of PZT actuators. For the system shown, the electric field is applied in the z-direction and the actuator expands and contracts only in the y-direction. The force output from the actuator varies as a function of frequency and is related to the mechanical impedances of the actuator and the structure by (Liang et al., 1992):

$$\bar{F} = w_A h_A \bar{T}_{2_{y=l_A}} = -\frac{Z}{(Z_A + Z)} d_{32} \bar{E} \bar{Y}_{22}^{E} w_A h_A \qquad (1)$$

where $\bar{T}_2$ is the stress in the actuator, w_A the width, h_A the thickness, d_{32} the piezoelectric coefficient, $\bar{E}$ the applied electric field, $Y_{22}^{E} = Y_{22}^{E}(1+i\eta)$ the complex elastic modulus at

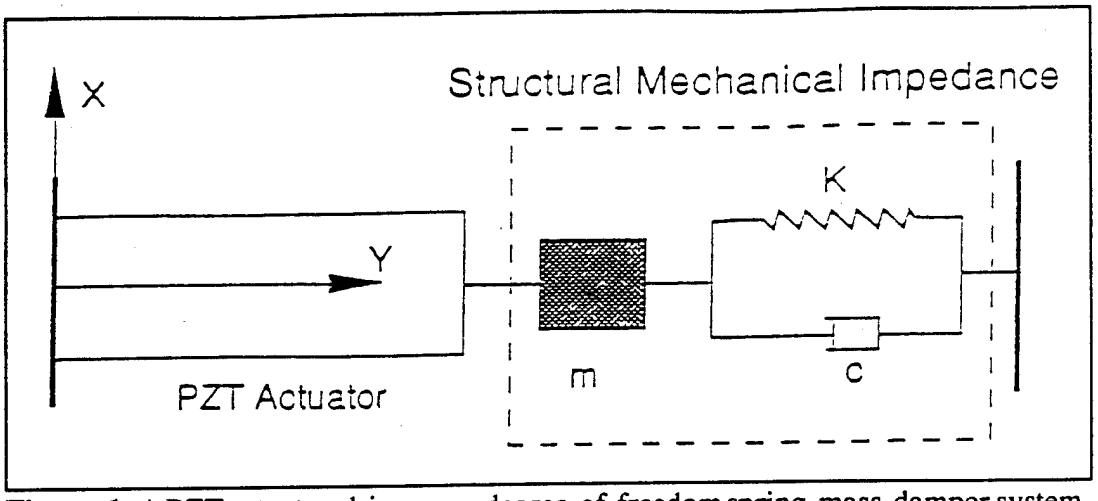

Figure 1. A PZT actuator-driven one-degree-of-freedom spring-mass-damper system.

zero electric field, η the mechanical loss factor for the PZT and Z the mechanical impedance of the structure. The short circuit actuator mechanical impedance, Z_A, is (Liang et al., 1992):

$$Z_A = \frac{K_A}{i\omega}\frac{kl_A}{\tan(kl_A)}, \tag{2}$$

where K_A is the dynamic stiffness of the PZT actuator given by $Y_{22}^E w_A h_A / l_A$ and $k^2 = \omega^2\rho / Y_{22}^E$. The structure impedance varies depending on the type of structure. The force output of the PZT is used to determine the dynamic response of the integrated actuator/structure system which will be discussed later in this section.

From the constitutive relation of piezoelectricity (charge as a function of applied stress), the electric displacement of a PZT actuator, which is frequency dependent, may be determined. The electric current passing through the PZT actuator can be determined by integrating the charge over the actuator surface. The coupled electro-mechanical admittance, defined as current over voltage, provides the link between the actuator and structure impedances and the electronics of the actuator. The admittance (defined as $Y = I/V$) is:

$$Y = i\omega\frac{w_A l_A}{h_A}\left[\epsilon_{33}^T - \frac{Z}{Z_A + Z} d_{32}^2 \bar{Y}_{22}^E\right]. \tag{3}$$

The influence of the structure and the actuator impedance is clear in the equation. The actuator electrical power is related to the admittance through the following:
the apparent power, W_A:

$$W_A = \frac{V^2 |Y|}{2}, \tag{4}$$

the dissipative power, W_D:

$$W_D = \frac{V^2 \mathrm{Re}(Y)}{2} , \tag{5}$$

and the reactive power, W_R:

$$W_R = \frac{V^2 \mathrm{Im}(Y)}{2} . \tag{6}$$

Only the dissipative power is considered herein since it is the power consumed by the actuator. For a mechanical system vibrating in vacuo, the power consumed includes three parts: the first two result from the mechanical and dielectric losses in the PZT itself and the third results from the damping in the mechanical system. For a system with fluid loading, the additional impedance from the interaction of the structure with the fluid medium causes an increase in the power consumption of the actuator.

Everything in Eqs. (1) and (3) is known except for the structure's mechanical impedance, Z. The other terms in the equations are functions of the electrical and mechanical properties of the PZT actuator. By determining the structural impedance, the dynamic response and power consumption of the actuator may be found. For the spring-mass-damper system of Figure 1, the mechanical impedance is:

$$\bar{Z} = c + m\left[\frac{\omega^2 - \omega_n^2}{\omega}\right] i , \tag{7}$$

where c is the damping coefficient and ω_n is the natural frequency of the spring-mass-damper system. The expression for admittance in Eq. (3) is general and holds for any system, thus the equations for the one-degree-of-freedom system can be applied to a continuous system simply by replacing the impedance of the spring-mass-damper system with the structural impedance of a continuous system at the actuator location. Therefore, the admittance and power consumption relations shown above can be appropriately applied to beams, plates and shells. The structural impedance for a simply-supported beam excited with a single, vertical PZT actuator support and radiating acoustic energy into a fluid medium is developed in the subsequent section.

SIMPLY SUPPORTED BEAM FORMULATION

This section develops the structural impedance for a continuous system, namely a beam radiating sound into an acoustic fluid. The emphasis is on the effect of the fluid loading on the structural impedance of the actuator/beam system and, subsequently, the effect on the power consumption of the actuator. Consider a simply-supported beam with a vertical PZT actuator support as shown in Figure 2. The beam is surrounded by an infinite rigid baffle and radiates sound into an acoustic fluid on one side. The beam has a modulus of elasticity E, mass density ρ, and moment of inertia over area k_i^2. Damping is included in the model through the use of a complex modulus, $E(1+i\delta)$, where δ is about 1/2%.

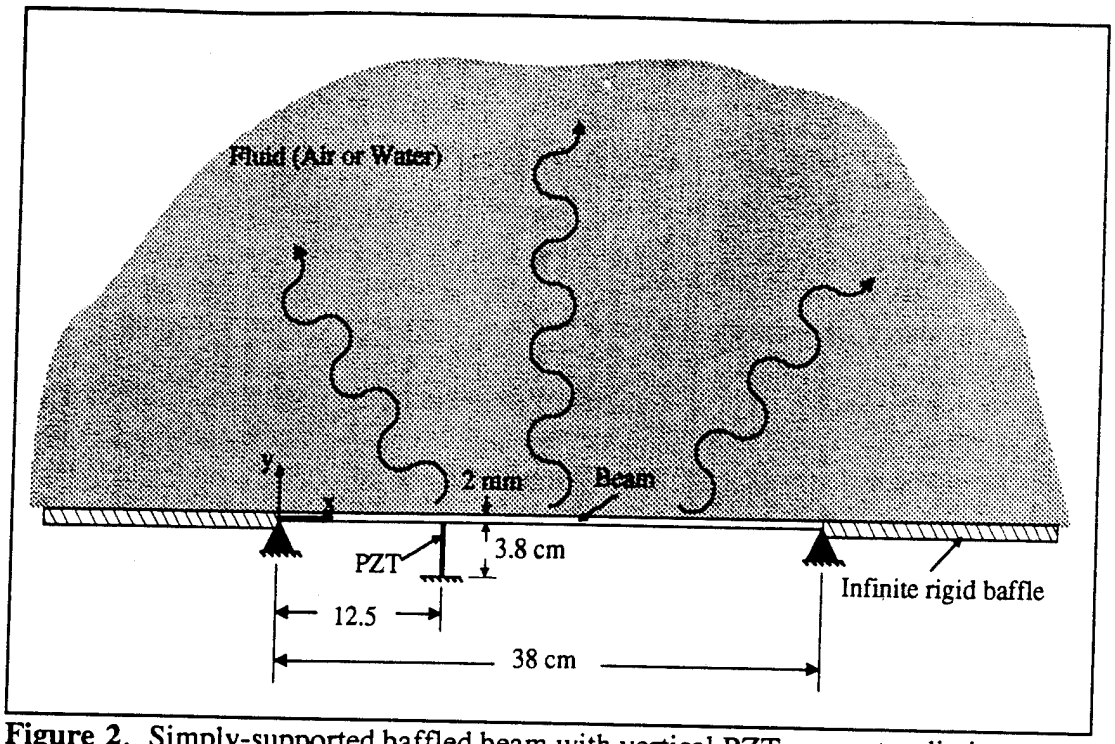

Figure 2. Simply-supported baffled beam with vertical PZT support radiating sound into an acoustic fluid on one side.

The equation of motion for the transverse deflection y(x,t) in the presence of an acoustic fluid is:

$$\rho \frac{\partial^2 y}{\partial t^2} = -(1+i\delta) E k_i^2 \frac{\partial^4 y}{\partial x^4} + p(x) + p_i \ , \tag{8}$$

where p(x) is the external dynamic loading term and pressure p_i is induced as a result of the acoustic radiation into the fluid. The pressure, p_i, is determined from (Sandman, 1977):

$$p_i(x,y,t) = -\rho_f \left[\frac{\partial \Psi}{\partial t} \right]_{z=0} , \tag{9}$$

where ρ_f is the mass density of the fluid and Ψ is the velocity potential which is governed by the wave equation:

$$\nabla^2 \Psi = \frac{1}{c_f^2} \frac{\partial^2 \Psi}{\partial t^2}, \qquad z > 0 \tag{10}$$

with boundary conditions:

$$\left[\frac{\partial \Psi}{\partial z}\right]_{z=0} = \frac{\partial w}{\partial t} \qquad \text{on the plate}$$

and

$$\left[\frac{\partial \Psi}{\partial z}\right]_{z=0} = 0 \qquad \text{off the plate.}$$

The solutions to Eqs. (5) and (7) provide the complete displacement and fluid pressure response.

The governing Eq. (5) is solved by expanding the transverse displacements and external loads in terms of the eigenfunctions of the system without fluid loading. The applied forcing function is harmonic and can be expressed as:

$$p(x,t) = \sum_{m=1}^{\infty} P_m \chi_m(x) \exp(i\omega t) \ , \tag{11}$$

where ω is the driving frequency and:

$$\chi_m = \sin\left[\frac{m\pi x}{L}\right] \tag{12}$$

are the normal modes of a simply-supported beam of length L. The transverse displacements can be expressed in terms of the normal modes of the beam as:

$$y = \sum_{m=1}^{\infty} W_m \chi_m(x) \exp(i\omega t) \ . \tag{13}$$

A detailed derivation of the steady-state acoustic pressure from a flat, elastic plate is given by Sandman (1977). Following a similar derivation, the pressure from a fluid-loaded beam can be expressed as:

$$p_i(x,y,t) = -\frac{\rho_f k \omega}{2\pi} \sum_{m=1}^{\infty} W_m \int_0^b \int_0^L \chi_m(x_1) \frac{\exp(-ikR)}{R} dx_1 dy_1 \exp(i\omega t) \ , \tag{14}$$

where k is the acoustic wavenumber ω/c and

$$R = \sqrt{(x-x_1)^2+(y-y_1)^2+z^2} \ . \tag{15}$$

Substituting Eqs. (8), (10) and (11) into Eq. (5), multiplying by χ_n and integrating over the surface of the beam gives:

$$A_m W_m + B \sum_{n=1}^{N} \gamma_{mn} W_n = \frac{1}{\rho} P_m \ , \tag{16}$$

where

$$A_m = c^2k^2\left[\frac{m\pi}{L}\right]^4 - \omega^2 \tag{17}$$

and

$$B = \frac{\rho_f\omega^2}{2\pi\rho} . \tag{18}$$

The fluid loading terms are:

$$\gamma_{mn} = \int_0^b\int_0^L\int_0^b\int_0^L \sin\left[\frac{n\pi x_1}{L}\right] \sin\left[\frac{m\pi x}{L}\right] \frac{\exp(-ikR)}{R} dx_1 dy_1 dx dy , \tag{19}$$

and P_m are the piezoelectric loading terms:

$$P_m = \frac{F_{eq}}{\rho AL}\sin\left[\frac{m\pi\xi_1}{L}\right] , \tag{20}$$

where F_{eq} is a unit actuation force and ξ_1 is the x coordinate of the actuator support. Equation (13) can be written in matrix form as

$$\left([A] + B[\gamma]\right)\{W\} = \frac{1}{\rho}\{P\} , \tag{21}$$

which describes a set of linear equations that can be solved for the modal amplitudes, W_m. For a beam in air, the fluid density, ρ_f, is approximately zero (thus the coefficient B is zero). Since matrix [A] is diagonal, the modal amplitudes W_m can easily be solved as:

$$W_m = \frac{P_m}{\rho A_m} . \tag{22}$$

For a beam with fluid loading, $[\gamma]$ must be obtained using numerical integration and W_m is found using:

$$\{W\} = \frac{1}{\rho}\left([A] + B[\gamma]\right)^{-1}\{P\} . \tag{23}$$

At this point, the displacement frequency response function corresponding to the unit excitation force is determined by substituting the modal amplitudes, W_m, into the modal series expansion of Eq. (10). The acoustic power frequency response function corresponding to the unit excitation force, Π, is found by integrating the acoustic intensity over the semi-infinite hemisphere. For both the uncoupled and fluid-coupled analyses, the structural impedance is the ratio of the unit force amplitude over the velocity amplitude at

ξ_1:

$$Z = \frac{1}{i\omega y_1} , \tag{24}$$

where y_1 is the displacement at ξ_1.

Once the structural impedance is known, the force output of the actuator, the electro-mechanical admittance of the actuator and the power consumption of the actuator are computed from the expressions given in Eqs. (1) and (3). Since the acoustic power is proportional to the square of the force, the actual acoustic power can be found by multiplying the acoustic power found from a unit excitation force, Π, by the square of the force output from the actuator,

$$\Pi = \bar{\Pi} F^2 . \tag{25}$$

COMPARISON OF IMPEDANCE AND STATIC APPROACHES

The static approach refers to the method of using a statically equivalent set of forces and moments as the amplitude of the forcing function in determining the dynamic response of actuation from integrated actuators.

Figure 3 compares the radiated acoustic power, from the beam described above, calculated using both the impedance approach and the static approach. The figure also shows the force output of the actuator. For the static model, the force output is the static force and is independent of frequency; however, for the impedance model, the force varies with frequency. It is evident from the curves that the force behavior is reflected in the radiated acoustic power. The correlation occurs as a result of the direct relationship between the square of the force and the radiated sound power. The radiated sound power predicted by the impedance model is calculated using Eq. (22).

Figure 3 shows that the force output from the static model simply becomes a frequency independent scaling factor by which the radiated sound power amplitudes at all frequencies are multiplied. The radiated sound power results calculated from the impedance model can be obtained from the static model results using

$$\Pi_{\text{impedance}} = \Pi_{\text{static}} \frac{F(\omega)^2_{\text{impedance}}}{F^2_{\text{static}}} . \tag{26}$$

Clearly, the impedance model provides more physical insight into the dynamic actuator-structure interaction than do static models. The use of a static model for predicting dynamic behavior is ill-advised as attested by the results of Figure 3. While the results show a general correlation in shape, the natural frequencies differ, as do the sound power amplitudes which are off by about an order of magnitude. Static models, therefore, should be avoided when calculating dynamic and acoustic responses for active material systems, especially when the actuator impedance is close to the structural impedance.

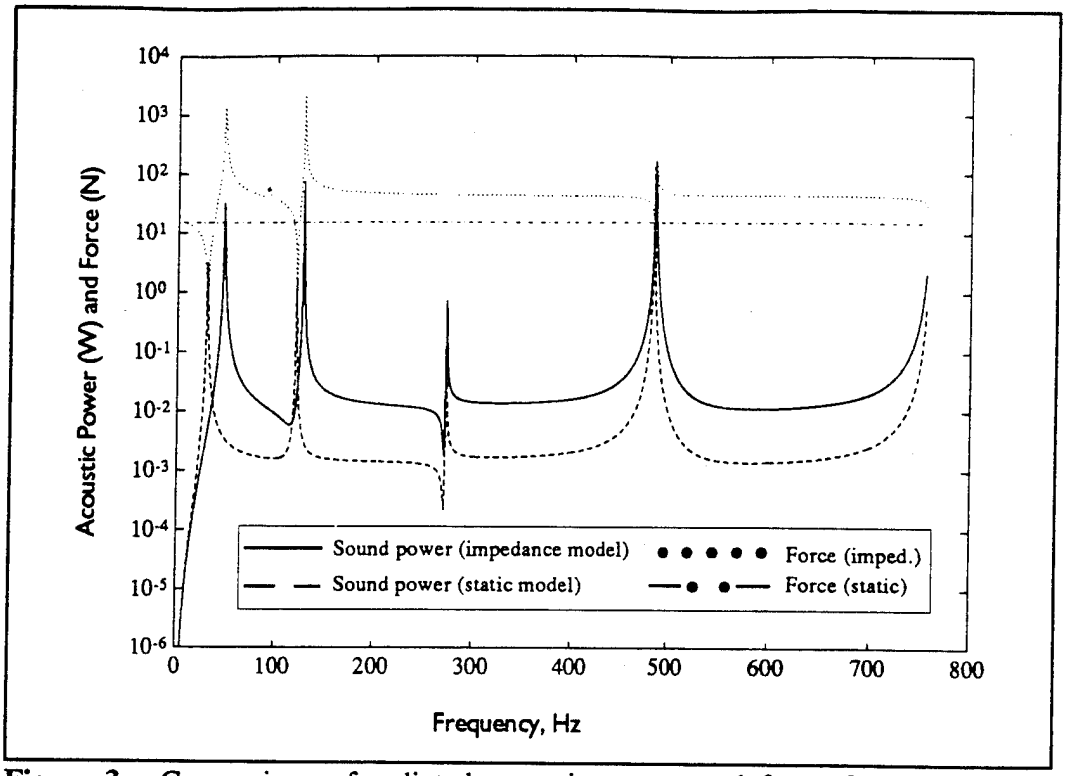

Figure 3. Comparison of radiated acoustic power and force from the power consumption model and the static model.

EXPERIMENTAL VERIFICATION OF THE ACTUATOR POWER CONSUMPTION MODEL

An experiment was performed to demonstrate the usefulness of the impedance model for predicting the dynamic actuator-structure interaction and actuator power consumption. The experiment consisted of a cantilever beam with bonded actuators close to its fixed end. The real part of the admittance was measured using an HP Impedance Analyzer. Figure 4 compares the measured data with the electro-mechanical admittance calculated using the power consumption model. The actuator electrical and mechanical properties (G1195 PZT) used in the impedance model calculations are shown in Table 1. The actuator power consumption model accurately predicts the admittance measured experimentally both on and off-resonance. Interested readers may refer to Liang et al. (1993) for more information regarding the experimental results and theoretical model.

Table 1. Electrical and mechanical properties of a PZT actuator (G1195).

d_{32} (m/volt)	Y_{22}^E (N/m^2)	ρ (kg/m^3)	ϵ_{33}^T (Farads/m)	δ	η
-166×10^{-12}	6.3×10^{10}	7650	1.5×10^{-8}	0.0015	0.001

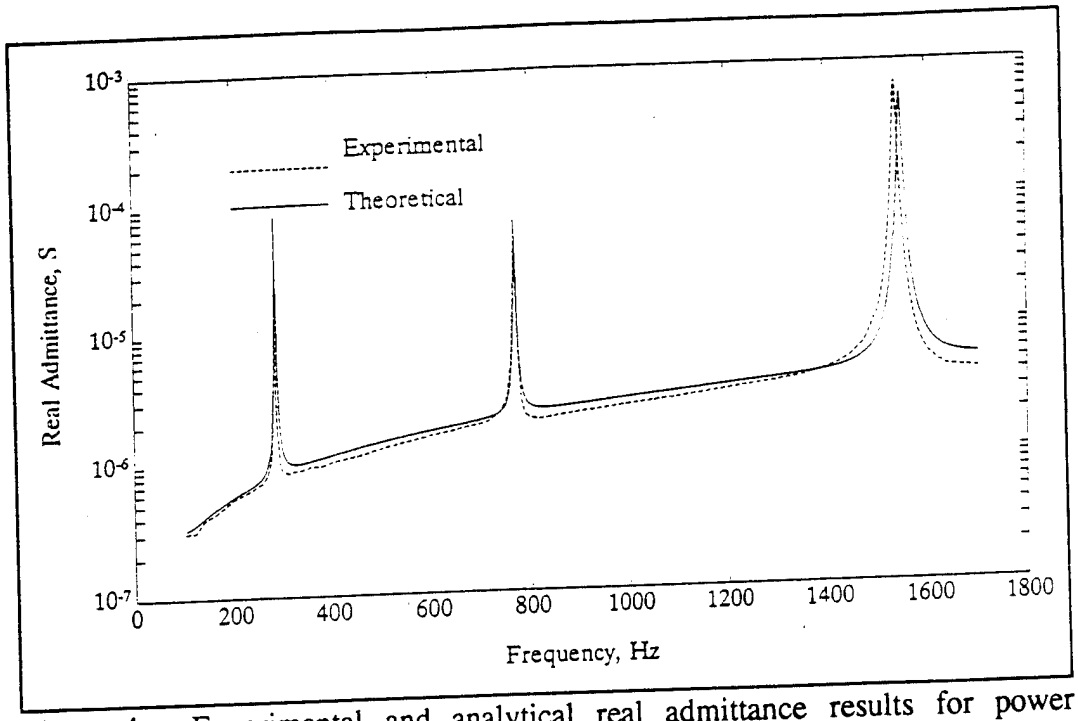

Figure 4. Experimental and analytical real admittance results for power consumption model verification.

NUMERICAL EXAMPLE

Figure 2 shows a simply-supported beam with a vertical PZT actuator support at x=12.5 cm which imparts a transverse excitation to the beam. The beam is 38 cm long, 4 cm wide and 2 mm thick with modulus of elasticity 63 GPa and Poisson's ratio 0.3. The beam is enclosed by an infinite rigid baffle and radiates acoustic energy into a fluid medium on one side. The PZT actuator support is 3.8 cm long, 4 cm wide, .2 mm thick and has the same mechanical and electrical properties as those given in Table 1. The PZT is located at 12.5 cm along the span of the beam.

A FORTRAN code was written to perform the necessary numerical integrations and modal summations to compute the structural impedance of the beam. Ten modes are used in the modal expansion to provide reasonable accuracy. Power consumption is computed using fluid densities of 1.21 kg/m^3 and 1000 kg/m^3 for air and water fluid loading respectively.

RESULTS AND DISCUSSION

As previously discussed, the impedance model is useful for calculating the power consumed by actuators in an active control system. Power consumption of PZT actuators was discussed for vibration control in a previous paper by Liang et al. (1993). Here, the focus is on actuator power consumption in active acoustic control systems. The main

differences are that the radiated sound is an additional energy sink for which the PZT actuator must continually supply energy.

Figure 5 shows the real part of the mechanical impedance, which represents the mechanical energy dissipation, for the beam with air and water fluid loading. In calculating the results in Figure 5, dielectric and mechanical losses in the PZT and damping in the structure were not considered, allowing the effects of fluid loading to be examined independently. The water fluid loading has two effects on the structural impedance: the natural frequencies shift due to the mass loading effects of the water which is much more dense than air, and the water creates a two to three order of magnitude increase in the real part of the off-resonance impedance over the case of air fluid loading.

The change in impedance created by the heavier fluid loading causes a corresponding variation in power consumption, as demonstrated by Figure 6a. The figure compares the power consumption of the actuator for the beam loaded by water with that of the beam loaded by air. Figure 6b quantifies the power consumed by the four various mechanisms of power dissipation: dielectric loss of the PZT, mechanical loss of the PZT, damping of the structure, and acoustic radiation. To determine the individual effect of a single parameter, models were run with the other parameters set to zero. For example, to determine the power consumed by structural damping of the beam, the dielectric loss and mechanical loss factors of the PZT were set to zero as was the density of the acoustic medium. It is apparent from Figures 6a and 6b that the on-resonance

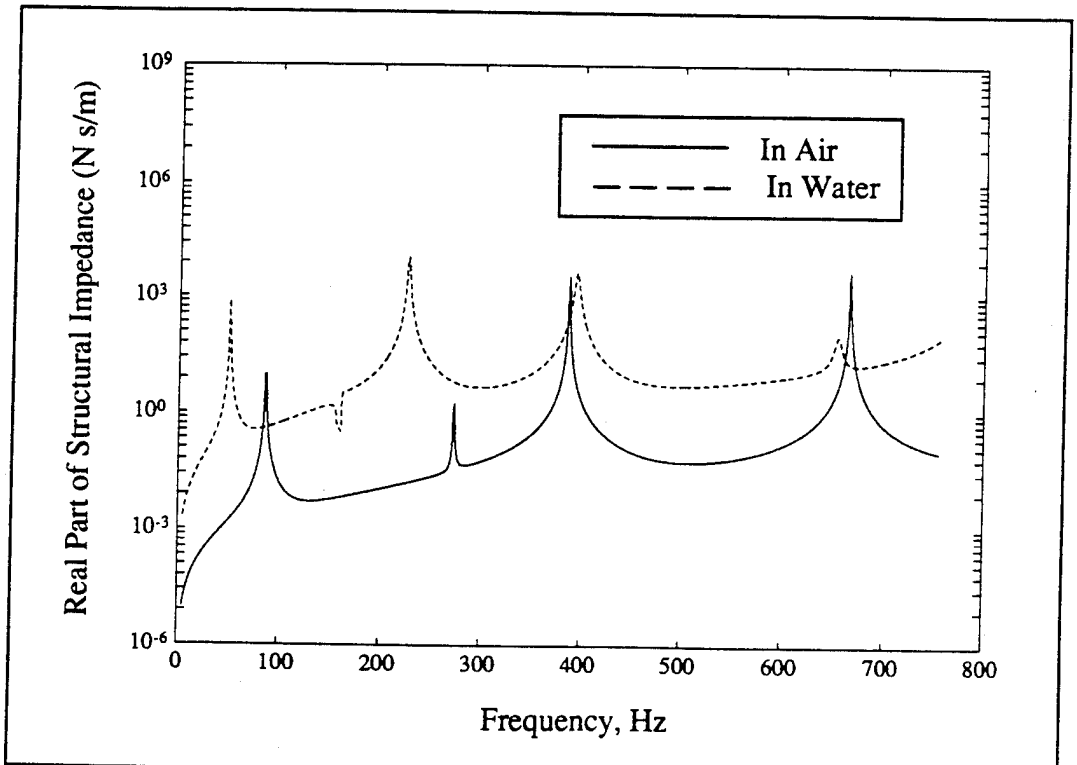

Figure 5. Comparison of the real part of the beam structural impedance with air and water fluid loading.

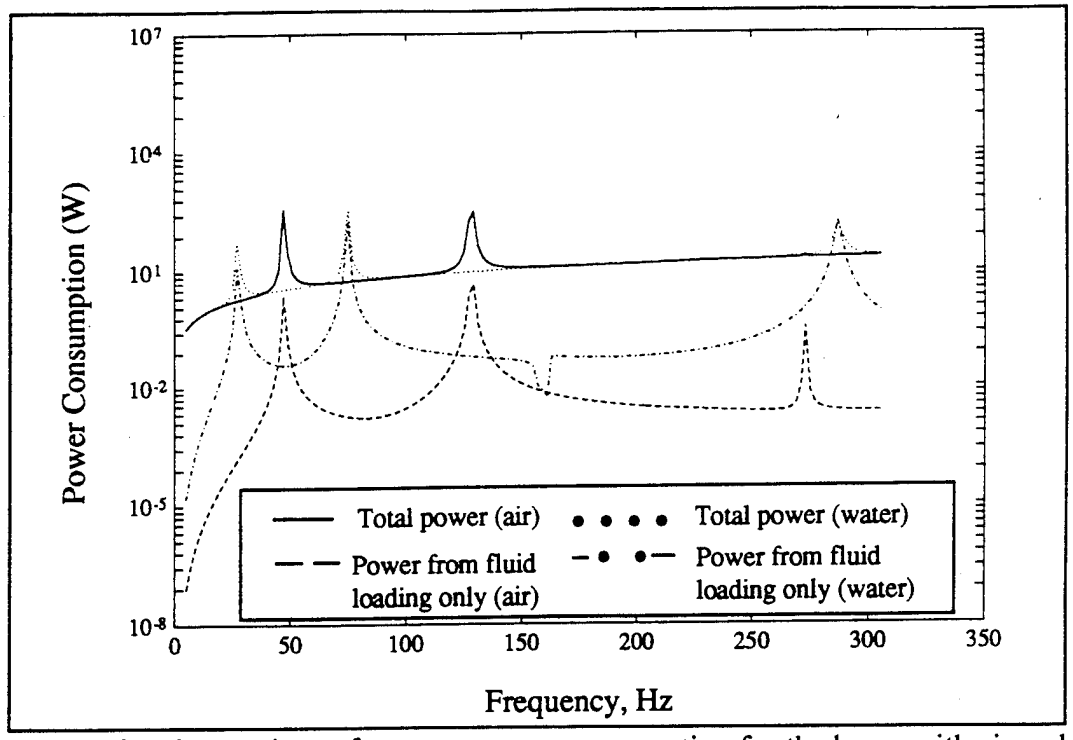

Figure 6a. Comparison of actuator power consumption for the beam with air and water fluid loading.

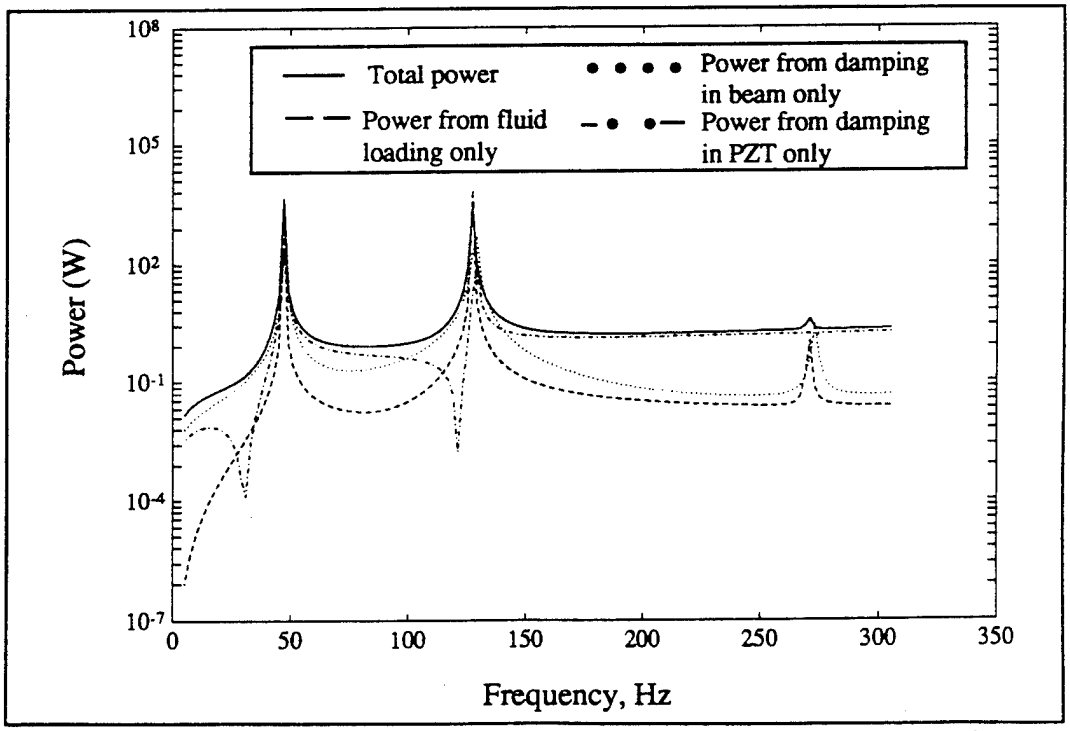

Figure 6b. Breakdown of power consumption by mechanism of dissipation.

power consumption is governed mainly by damping in both the PZT and structure as well as by acoustic radiation. Off-resonance, the effect of the fluid loading is negligible and the primary mechanisms of power consumption are structural damping at low frequencies and mechanical loss in the PZT actuator at higher frequencies. Figure 6a shows that the power consumed by the actuator caused by the acoustic radiation in air does not even contribute significantly to the total power consumed by the actuator on-resonance. Therefore, for an actuator/structure system in air, power consumed due to acoustic radiation need not be accounted. However, when the structure is loaded by a heavy fluid such as water, the power consumed by the actuator due to acoustic radiation is significant both on-resonance and off-resonance and must be included in the power consumption analysis.

An interesting potential application exists for the impedance model along with the power consumption analysis. Figure 7 plots the actuator power consumption and radiated sound power in air. The dielectric loss in the PZT, mechanical loss in the PZT and damping in the beam are all zero. The dissipative acoustic power should, in theory, be identical to the power consumed by the actuator. In Figure 7, the sound power and actuator power consumption show a good correspondence in terms of profile and magnitude but do not correspond exactly as expected. The close correlation suggests that there may be a way to obtain an experimental estimate for the radiated sound power by experimentally measuring the power consumed by the PZT actuator and then calculating and subtracting from it the power consumed in the system by dielectric and mechanical losses.

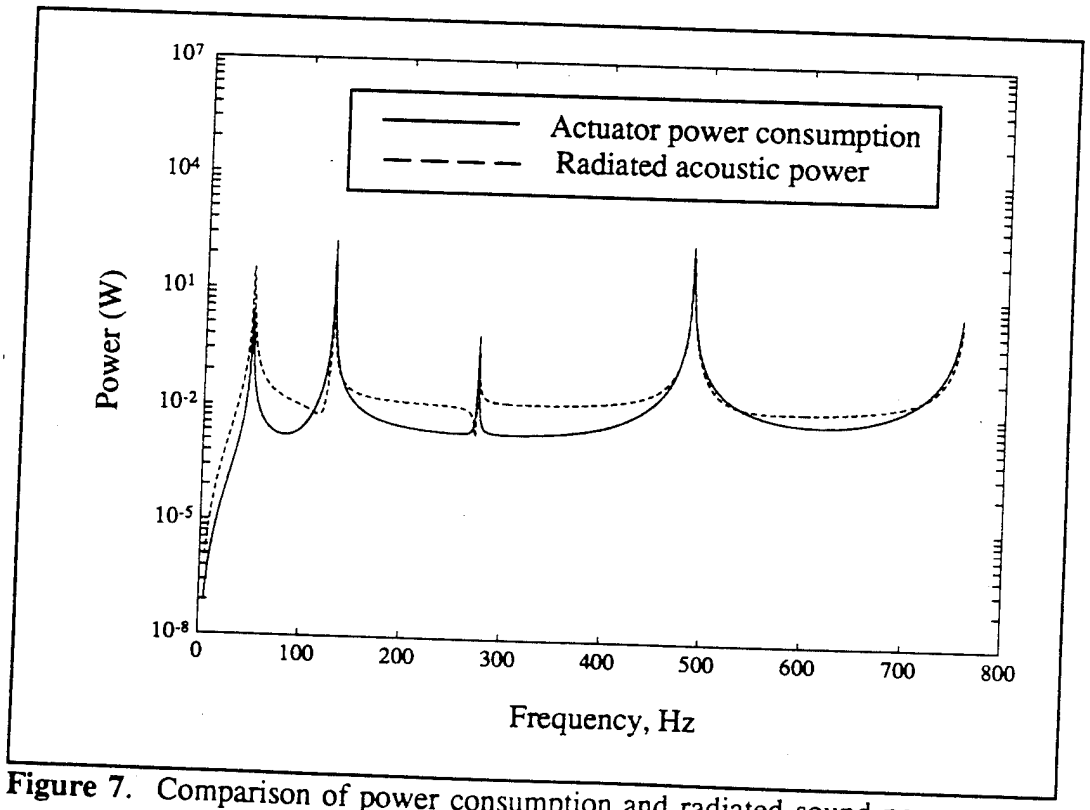

Figure 7. Comparison of power consumption and radiated sound power.

CONCLUSIONS

This paper extends the coupled electro-mechanical approach for analyzing the energy transfer and power consumption in active material systems, developed by Liang et al. (1993), to the case where acoustic radiation in the presence of a fluid is considered. The approach uses a structural impedance method to find radiated acoustic power and power consumption. The numerical results demonstrate the significance of accounting for fluid coupling when determining the structural impedance of systems and power consumption of actuators used in intelligent material systems. In addition, the numerical results show the inadequacy of static models for predicting dynamic response and power consumption. The capability to analyze the power consumption and energy transfer of actuators utilized in underwater acoustic control will enable the design of more energy efficient active control systems.

ACKNOWLEDGEMENTS

The authors gratefully acknowledge support from the Office of Naval Research, Grant ONR-00014-92-J-1170.

REFERENCES

Z. Chaudhry and C.A. Rogers, "Enhanced Structural Control with Discretely Attached Induced Strain Actuators", AIAA 92-2404-CP, Proceedings of the 33rd SDM Conference, 548-555, Dallas, TX, (1992).

R.L. Clark and C.R. Fuller, "Experiments on Active Control of Structurally Radiated Sound Using Multiple Piezoceramic Actuators", J. Acoust. Soc. Am. **91**(6), 3313-3320, (1992).

E.F. Crawley and J. deLuis, "Use of Piezoelectric Actuators as Elements of Intelligent Structures", AIAA J. **25**(10), 1373-1385, (1989).

E.K. Dimitriadis, C.R. Fuller and C.A. Rogers, "Piezoelectric Actuators for Distributed Vibration Excitation of Thin Plates", J. Vib. Acoust. **113**(1), 100-107, (1991)

C.R. Fuller, G.P. Gibbs and R.J. Silcox, "Simultaneous Active Control of Flexural and Extensional Waves in Beams", J. Intell. Mater. Syst. and Struct. **1**(2), 235-247, (1990).

C. Liang, F. Sun and C.A. Rogers, "Coupled Electric-Mechanical Analysis of Piezoelectric Ceramic Actuator Driven Systems - Determination of the Actuator Power Consumption and System Energy Transfer", SPIE Conference on Smart Structures and Materials '93, 31 Jan - 4 Feb, Albuquerque, NM, (1993); in press.

C. Liang, F. Sun and C.A. Rogers, "An Impedance Method for Dynamic Analysis of Active Material Systems", submitted to the J. of Vib. and Acoustics, (1993).

C. Liang, F. Sun and C.A. Rogers, "Investigation of the Energy Transfer and Consumption of Adaptive Structures", Proceedings, IEEE Conference, Tucson, AZ, Dec. (1992), in press.

C.A. Rogers, "Active Vibration and Structural Acoustic Control of Shape Memory Alloy Hybrid Composites : Experimental Results", J. Acoust. Soc. Am. **90**(1), 2803-2811, (1990).

B.E. Sandman, "Fluid-loaded Vibration of an Elastic Plate Carrying a Concentrated Mass", J. Acoust. Soc. Am. **61**(6), 1503-1510, (1977).

W.R. Saunders, H.H. Robertshaw and C.A. Rogers, "Experimental Studies of Structural Acoustic Control for a Shape Memory Alloy Composite Beam", AIAA-90-1090-CP, Proceedings of the 31st SDM Conference, 2274-2282, Washington D.C., (1990).

C. E. Wallace, "Radiation Resistance of a Baffled Beam", J. of the Acoustical Society of America, V.51 No.3 (Part 2), 936-945, (1972).

B.T. Wang, "Active Control of Sound Transmission/Radiation from Elastic Plates Using Multiple Piezoelectric Actuators", PhD Dissertation, Dept. of Mech. Eng., Virginia Polytechnic Institute and State University, June (1991).

B.T. Wang, E.K. Dimitriadis and C.R. Fuller, "Active Control of Structurally Radiated Noise Using Multiple Piezoelectric Actuators", Proceedings of the AIAA SDM Conference, AIAA 90-1172-CP, 2409-2416, Long Beach, CA (1990).

C-35 An Evaluation of Feedback, Adaptive Feedforward and Hybrid Controller Designs for Active Structural Control of a Lightly - Damped Structure, W. R. Saunders, H. H. Robertshaw and R. A. Burdisso, Second Conference on Recent Advances in Active Control of Sound and Vibration, Blacksburg, VA, pp. 339-354, 28-30 April 1993.

AN EVALUATION OF FEEDBACK, ADAPTIVE FEEDFORWARD AND HYBRID CONTROLLER DESIGNS FOR ACTIVE STRUCTURAL CONTROL OF A LIGHTLY-DAMPED STRUCTURE*

William R. Saunders,[1] Harry H. Robertshaw,[1] Ricardo A. Burdisso[1]

ABSTRACT

Effective active control strategies can be designed for lightly damped structures using feedback, adaptive feedforward or hybrid control laws. This study begins with analytical and numerical descriptions of three different controller designs for the problem of vibration suppression on a lightly-damped, simply-supported plate. The applicability of each approach is investigated for harmonic and transient mechanical disturbances on the plate. It is shown that in the absence of modelling uncertainty, all three controllers perform equally well for persistent disturbances. The feedback and hybrid designs provide comparable performance for impulsive disturbances. Next, structured modelling uncertainties are introduced to investigate the effect on the closed-loop response for the different control laws. Advantages of the hybrid controller in the presence of modelling uncertainties are illustrated. Finally, numerical simulations and experimental results are presented for the Virginia Tech plate testbed.

INTRODUCTION

The control strategy for active vibration suppression of an adaptive structure can be stated as a general design approach: select a control architecture which is closed-loop stable and minimizes the structural response due to transient and persistent external disturbances. It is assumed that the designer has both feedback control laws and adaptive signal processing methods available. This paper shows that it is advantageous to use blended feedback and adaptive feedforward control to generate a unique hybrid control architecture for structural vibration control.

BACKGROUND

Active control of flexible systems was initiated during the 1960's. Early motivation for active control research was related to the design specifications for space platform vibration levels. It was predicted that precise communication and observation tasks would be compromised by the dynamic response of the necessarily lightweight, lightly-

*This work was supported under ONR Grant No. N00014-92-J1170.

[1]Department of Mechanical Engineering, Center for Intelligent Material Systems and Structures, Virginia Polytechnic Institute and State University, Blacksburg, VA 24061, U.S.A.

damped space structure systems. Active vibration suppression strategies were developed to reduce the additional mass and volume which accompany traditional passive damping mechanisms. Early concepts were mostly active damping methods, including direct velocity feedback [1,2], independent modal space control (IMSC) [3], and collocated position feedback [4].

Design of control laws for flexible structures has matured during the past fifteen years. It is now quite common that suppression of persistent disturbances is included as a design requirement. Several multi-input, multi-output (MIMO) feedback control laws were developed which provided both active damping and disturbance rejection. Stochastic, multivariate control theory was employed to develop Linear Quadratic Gaussian (LQG) regulation for plants subject to process (input) and measurement noise [5]. By including the dynamics of external disturbance processes in the plant model, the LQG disturbance model (LQG-DM) approach was designed for simultaneous transient and steady-state disturbance suppression. During the mid-1980's, an optimal controller was designed for minimization of the H_∞ norm. Application of the H_∞ controller to structural vibration suppression was investigated by Ellis [6]. The performance of the H_∞ controller was shown to be comparable to the discrete LQG-DM controller using the Virginia Tech plate testbed experiment.

The goal of suppressing steady-state disturbances on structural systems has been addressed by the adaptive signal processing community, also. The pioneering work by Widrow [7] was applied to the active noise control problem by Elliott et.al.[8]. Their implementation of a MIMO filtered-X LMS (FXLMS) algorithm proved to be a robust control approach for minimization of steady-state, harmonic disturbances. The adaptive controller was then applied to the structural acoustic control problem by Fuller and Jones [9]. Their method was one of the first applications of adaptive feedforward for reduction of harmonic structural vibration. Subsequent research in this area has shown that the adaptive feedforward controllers can be extended to rejection of wideband disturbance inputs [10].

MOTIVATION

Selection criteria for feedback versus adaptive feedforward structural control algorithms has received relatively little attention in the literature. Generally, there appears to be two nearly distinct categories of vibration control research dedicated to either adaptive feedforward control or modern control theory methods. The focus of this research is to generate hybrid control architectures which utilize both approaches.

Table I summarizes some advantages and disadvantages of feedback control versus adaptive feedforward control. For adaptive feedforward vibration control, the error signal is adaptively minimized to zero. The FXLMS algorithm is a widely-studied adaptive algorithm which exhibits high stability and performance robustness. A particularly important advantage is that apriori modelling is not required. Successful implementation requires that a correlated reference signal be available. An additional constraint is that the reference signal be uncontrollable from the actuator input(s). In other words, there must be no feedback path from the actuator to the reference signal if the system is truly characterized as adaptive feedforward. One disadvantage for this approach is that the suppression of transient signals is not presently within the capabilities of adaptive feedforward control architectures, although increasing success with wideband adaptive controllers may lead to breakthroughs in this area.

Table I - Comparison of Adaptive Feedforward and Feedback Control

Control Approach	Advantages	Disadvantages
Adaptive Feedforward Control	error signal is typically driven to zero.	Transient suppression is difficult
	large stability bounds	coherent reference required
	no modelling required	
Feedback Control	active damping provides transient suppression	modelling uncertainty leads to robustness problems

Active vibration suppression using feedback control is structured into two distinct mechanisms: active damping and disturbance compensation. The active damping results from the eigenvalue modification which occurs in the presence of feedback signals. This effective increase in structural damping provides substantial reductions in structural response caused by completely arbitrary temporal and spatial distributions of disturbance waveforms. The suppression provided by active damping is highest near the resonance frequencies of the structure. Disturbance compensation, sometimes called disturbance rejection, refers to the effective cancellation of the system response caused by external disturbances on the structure. An excellent discussion of the relationship between different disturbance compensation methods was provided by Sievers and vonFlotow [11]. The most significant disadvantage associated with the two feedback suppression mechanisms, for fixed-gain controllers like the LQG-DM and H_∞ control laws, is their dependence on apriori system modelling. Modelling uncertainty can degrade closed-loop performance and lead to stability problems for the closed-loop system, particularly for high-gain disturbance compensation methods.

This paper demonstrates advantages which accompany the blended use of feedback control and adaptive feedforward control for the suppression of persistent disturbances. We propose a hybrid control law which uses an optimal formulation for the feedback gains and the FXLMS algorithm to minimize the effect of persistent disturbances on the structure. The presence of a closed-loop around an adaptive feedforward path is very new in the general control literature. The earliest reference we found on the use of combined feedback and adaptive feedforward is by Alcone et.al. [12]. Their application involved adaptive noise cancellation (ANC) to reduce jitter in laser beam control systems. They showed the feasibility of introducing a feedback loop around the nonlinear, ANC system. For active noise control, there have been successful cancellation methods which incorporate adaptive feedforward control *with* feedback compensation [13,14].

However, the purpose of the feedback in those situations was for the compensation of feedback introduced to the reference signal by the action of the controller. A comprehensive discussion of those system architectures, which are not of the type we will discuss in this paper, was given by Swanson [15].

A review of the structural control literature indicates that the combined use of feedback and adaptive feedforward control was first implemented by Finefield [16]. He concluded that the combined control approach was very effective when the structure was excited over a broad frequency range. We have not discovered any additional structural control applications which incorporate hybrid control approaches.

This paper examines three different controller designs applied to the problem of vibration suppression on a lightly-damped, simply-supported plate. A discrete LQG stochastic compensator with internal Disturbance Modeling (DLQG-DM), the Filtered-X LMS adaptive algorithm and a hybrid controller will be evaluated. The impact of modelling uncertainty on the different controllers will be demonstrated. Implementation issues are discussed and demonstrated using the simply-supported plate testbed. The remainder of the paper provides brief descriptions of the three control laws, followed by a discussion of each compensator's frequency response. Structured uncertainty is introduced in the form of multiplicative perturbations on the nominal plant to clarify the favorable properties of FXLMS control for a harmonic disturbance. Finally, the hybrid control law is used to demonstrate robust suppression of simultaneous transient and harmonic disturbances.

Description of Control Laws

This section will summarize the relevant equations which describe the DLQG-DM, FXLMS and hybrid control laws. It is assumed that the reader is familiar with the development of the stochastic optimal feedback approach and the adaptive gradient search algorithm. If a more detailed discussion of the two control approaches is desired, the previously cited material by Ridgely [5] and Widrow [7] can be reviewed, respectively.

DLQG-DM Control

The sampled-data, LQ regulator is combined with state reconstruction by a Kalman filter to form the DLQG stochastic control law. When dynamics of any external disturbances are included in the estimated state vector, i.e. internal disturbance modelling, the DLQG-DM controller results. The optimal, stochastic, output linear regulator results from the solution to the following problem:

$$x_{k+1} = \Phi\, x_k + \Gamma\, u_k + \Lambda\, v_k \tag{1}$$

$$y_k = C\, x_k + D_c\, u_k + D_d\, v_k + \Theta_k \tag{2}$$

$$z_k = H\, x_k \tag{3}$$

where we have assumed that Φ, Γ, Λ, C, D_c,and D_d are time-invariant, $u_k \in R^m$ is the control vector, y_k is the output measurement, z_k is the controlled variable and $x_k \in R^n$, $v_k \in R^s$, and $\Theta_k \in R^p$ are random variables described by Gaussian distributions

$$E[x_k] = \mu_k \qquad E[\Theta_k] = 0$$
$$E\left[(x_k - \mu_k)(x_k - \mu_k)^T\right] = P_k \qquad E\left[\Theta_k \Theta_k^T\right] = R_k^{\Theta}$$
$$E[v_k] = 0 \qquad E\left[v_k \Theta_k^T\right] = 0$$
$$E\left[v_k v_k^T\right] = R_k^v$$

Subscripted variables such as x_k refer to the k'th sample. We wish to minimize the value function

$$J = \frac{1}{2} E\left\{ \sum_{k=0}^{k_f - 1} \left[\hat{x}_{k/k}^T \, u_k^T\right] \begin{bmatrix} Q & M \\ M & R \end{bmatrix} \begin{bmatrix} x_{k/k} \\ u_k \end{bmatrix} \right\} \tag{4}$$

subject to the state equations 1, 2 and 3. The control law which results from this problem is

$$u_{fb_k} = -K_c \, \hat{x}_{k/k} \tag{5}$$

where $K_c \in R^{m \times n}$ is the regulator feedback gain matrix and $\hat{x}_{k/k}$ is the estimate of the state at the k'th sample given output measurements of y_k. The k/k or $k + 1/k$ notation comes from the predictor-corrector form of the Kalman filter. Bender [17] provides an in-depth discussion of the various forms for the discrete Kalman filter equations. We choose to use the *a posteriori* compensator for sampling compatibility between the feedback and adaptive feedforward components of the control signal in the hybrid development presented later. A summary of the complete discrete compensator equations will be postponed until after a review of the disturbance modelling approach.

External disturbances on the plant can often be modelled sufficiently for estimation purposes. In the problem statement above, we supposed the existence of a white (process) noise disturbance v_k on the plant. The disturbance model technique is to design shaping filters, driven by the process noise, whose output directly influences the structural states. For the correlated disturbances, we can write a state variable description using $s \in R^t$. For this paper, we assume a second-order ($t = 2$), Gauss-Markov process as shown:

$$\begin{Bmatrix} s_{1_{k+1}} \\ s_{2_{k+1}} \end{Bmatrix} = exp\left\{ \begin{bmatrix} 0 & 1 \\ -\omega_n^2 & -2\zeta\omega_n \end{bmatrix} T \right\} \begin{Bmatrix} s_{1_k} \\ s_{2_k} \end{Bmatrix} + [B_d] \, v_k \tag{6}$$

$$w_k = C_d \begin{Bmatrix} s_{1_k} \\ s_{2_k}. \end{Bmatrix} \tag{7}$$

When these dynamics are augmented to the estimated state vector, the Kalman filter generates an estimate of the colored-noise disturbance w_k, along with the estimate of its effect on the structural plant states. The augmented state vector then becomes $x_{a_k} = \begin{Bmatrix} x_k \\ s_k \end{Bmatrix}$ so that the final t states in x_{a_k} are associated with the disturbance w_k.

Finally, we can summarize the DLQG-DM controller using the predictor-corrector format for the augmented system variable:

$$\hat{x}_{a_{k/k-1}} = A_a \hat{x}_{a_{k-1/k-1}} + G_a u_{fb_k} \tag{8}$$

$$\hat{x}_{a_{k/k}} = \hat{x}_{a_{k/k-1}} + K_f(y_k - \hat{y}_{k/k-1}) \tag{9}$$

$$u_{fb_k} = -K_c \hat{x}_{a_{k/k}} \tag{10}$$

Two remarks about subtle features of the *a posteriori* DQLG-DM equations 8 to 10 will be made for clarification. First, the disturbance states are uncontrollable from the control input. This means that there is no feedback path between the control input and the disturbance estimate. Since the estimator has knowledge of the control input and the plant dynamics, it estimates the proper value of the disturbance for open-loop or closed-loop situations. Second, the DLQG-DM compensator has poles which coincide with the sampled-data poles of the disturbance model. Since the zeros of the closed-loop system are the sum of the zeros of the open-loop plant and the poles of the compensator, the DLQG-DM controller places closed-loop zeros at the disturbance frequencies. This well-known fact will be important in understanding the performance of the hybrid control law.

FXLMS Control

The FXLMS algorithm is a gradient search algorithm which trades off an instantaneous estimate of the signal statistics for fast implementation. The principle behind the FXLMS control is the cancellation of a "primary" response through the action of "secondary" control sources. Operation of the adaptive control requires passing a correlated reference signal (i.e. coherent with the disturbance source) through an adaptive filter, whose coefficients are determined on-line via minimization of a quadratic cost function of some chosen error signal. We choose not to elaborate the details of the controller development but show the final weight update equation which comprises the FXLMS algorithm:

$$W_{i_{k+1}} = W_{i_k} - 2\,\alpha\, y_k\, x_{fr_{k-i}} \quad i = 1, 2, \ldots N \tag{11}$$

where the filtered-x signal x_{fr_k} is generated by passing the input x_{r_k} through the plant model $G_{fx}(z)$. The gain parameter α controls the rate of convergence and stability of the algorithm. Note that $G_{fx}(z)$ must be a stable representation to guarantee a bounded reference signal.

The control signal is generated by passing the reference signal through an FIR filter whose weights are those of equation 11. After convergence, the adaptive feedforward control signal can be written

$$u_{ff_k} = W_0 x_{r_k} + W_1 x_{r_{k-1}}. \tag{12}$$

The selection of the reference signal is critical to the analysis of the FXLMS algorithm. In the next section, we pose a hybrid control law which uses the estimated disturbance of equation 7 as the reference signal.

Hybrid Control

The two previous sections summarized an optimal, fixed-gain, feedback control law and an adaptive feedforward gradient search algorithm which can both be used for disturbance compensation. In this section, we summarize a blend of the two approaches such that we retain the active damping provided by the feedback control but design the hybrid control law to deliver disturbance rejection through the exclusive action of the

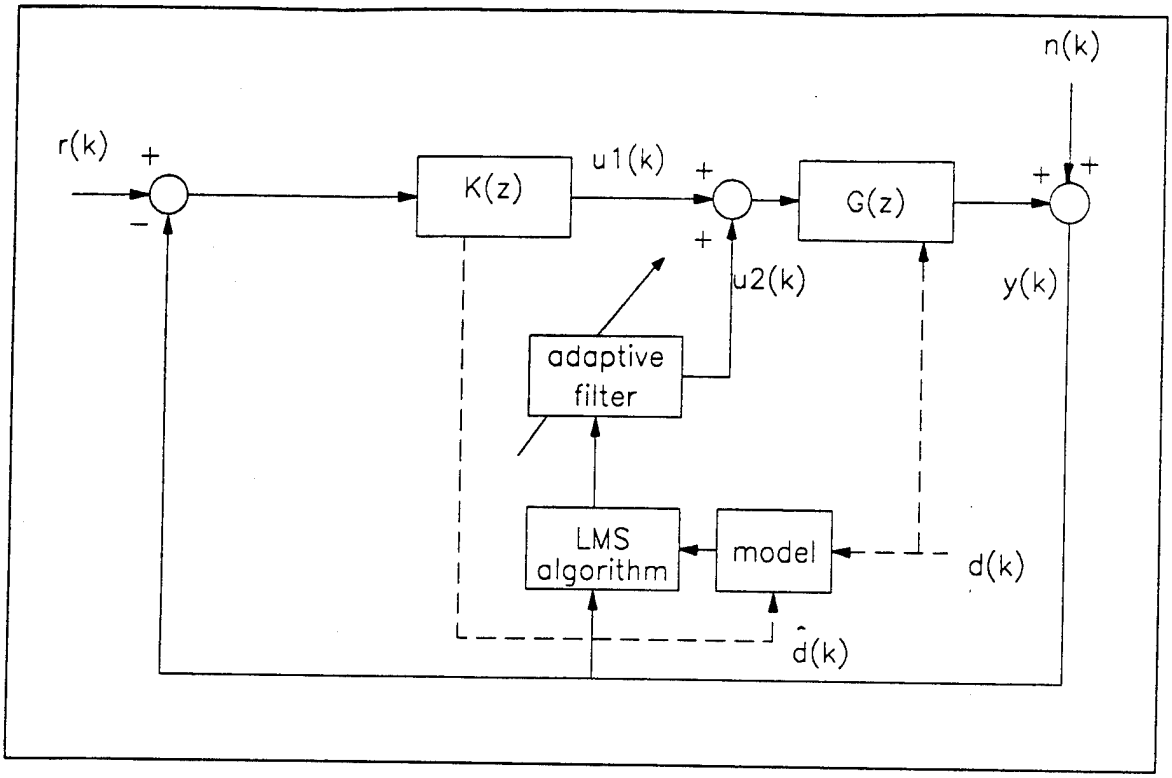

Figure 1: Hybrid control architecture

FXLMS control law. The concept is simply linear superposition of the two controllers, so that the control signal consists of the feedback component and the adaptive feedforward segment:

$$u_{h_k} = u_{fb_k} + u_{ff_k} \tag{13}$$

$$= -K_h \hat{x}_{k/k} + W_0 x_{r_k} + W_1 x_{r_{k-1}} \tag{14}$$

where the two components follow from equations 10 and 12, with the exception of a modified feedback gain matrix K_h. Dimensions of the previous feedback gain matrix $K_c \in R^{m \times (n+t)}$ have been reduced such that $K_h \in R^{m \times n}$ no longer feeds back the disturbance model states. The implication of this change will be discussed in the next section. A block diagram of the proposed hybrid control architecture is shown in Figure 1. The schematic shows that the hybrid control consists of a feedback loop around an adaptive feedforward control path. The block diagram has been manipulated to present the DLQG compensator in the forward path with unity feedback. The feedback gain matrix is part of the compensator, as discussed in the next section. A coherent reference signal is supplied to the adaptive controller from a measurement of the disturbance $d(k)$ or from the estimate of the disturbance $\hat{d}(k)$ in the Kalman filter. The selection of the controlled (error) signal is arbitrary for this formulation. Because of the system linearity, each control law operates independently of the other. However, there is some interaction since the adaptive controller "sees" a different plant during open-loop versus closed-loop feedback control. The performance of the hybrid compensator can best be described by examining the form of the compensators for the three cases: DLQG-DM

control, FXLMS control and hybrid control.

Compensator Comparison

The frequency response of the three compensators described above will be discussed in this section. It is well-known that compensators designed for narrowband disturbance rejection share a common feature, as discussed by Sievers and vonFlotow [11]. Each compensator includes a pair of complex poles at the disturbance frequency such that the magnitude of the loop gain is high over the disturbance bandwidth. It is precisely this high loop gain which provides the desirable, low sensitivity to plant disturbances. It will be shown that the feedback gains on the disturbance model states generate the high loop gain for the DLQG-DM compensator. When these states are not fed back, the disturbance rejection is not present. It will also be demonstrated that the action of the FXLMS control signal is equivalent to feedback gains on the disturbance model states when those disturbance dynamics are used for the reference signal to the algorithm.

For the following comparison, we will use the plate testbed model discussed by Rubenstein, et.al. [18]. The operating frequency of the disturbance and the selection of the error signal must be specified for the compensator design. For the following cases, we choose to suppress the response of the first plate mode to a 55 Hz disturbance. The frequency response of the discrete LQG-DM compensator is derived from the control law $u_{fb_k} = -K_c \hat{x}_{a_{k/k-1}}$. Substituting from equations 2, 8 and 9, we can solve for $u(z) = G_{fb}(z)\, y(z)$ where

$$G_{fb}(z) = \left[-K_c \left(zI - (A_a + A_a K_f D_a K_c - A_a K_f C_a - G_a K_c)\right)^{-1} A_a\, K_f\right]. \qquad (15)$$

A bode plot of the DLQG-DM compensator magnitude and phase is shown in Figure 2. Notice the expected pole at 55 Hz which coincides with the disturbance frequency. When there are no feedback gains on the disturbance states, the loop gain does not exhibit the peak at the disturbance bandwidth. Active damping is still present but the disturbance rejection capability is removed in that situation.
The discrete transfer function for the SISO FXLMS compensator was discussed by Elliott, et.al. [8]. We can write $u_{ff}(z) = G_{ff}(z)\, y(z)$ where

$$G_f f(z) = -\frac{C\mu\bar{Y}}{2}\left\{\frac{z\cos(\omega_d T - \phi) - \cos\phi}{1 - 2z\cos(\omega_d T) + z^2}\right\} \qquad (16)$$

and the plant model has been evaluated at the disturbance frequency, $\bar{G}(j\omega_d) = \bar{Y}e^{j\phi}$. A bode plot of this compensator is shown in Figure 3. As mentioned earlier, complex poles which coincide with the disturbance poles are present in the compensator. Thus, the adaptive FXLMS compensator can be used to perform the disturbance rejection instead of the feedback disturbance modelling approach. A comparison of the DLQG-DM, FXLMS and hybrid compensators is developed next for the situation where the estimated disturbance dynamics are used for the reference signal input to the FXLMS algorithm.

A direct comparison of the hybrid compensator to the individual DLQG-DM and FXLMS compensators follows after a transformation of the disturbance state space

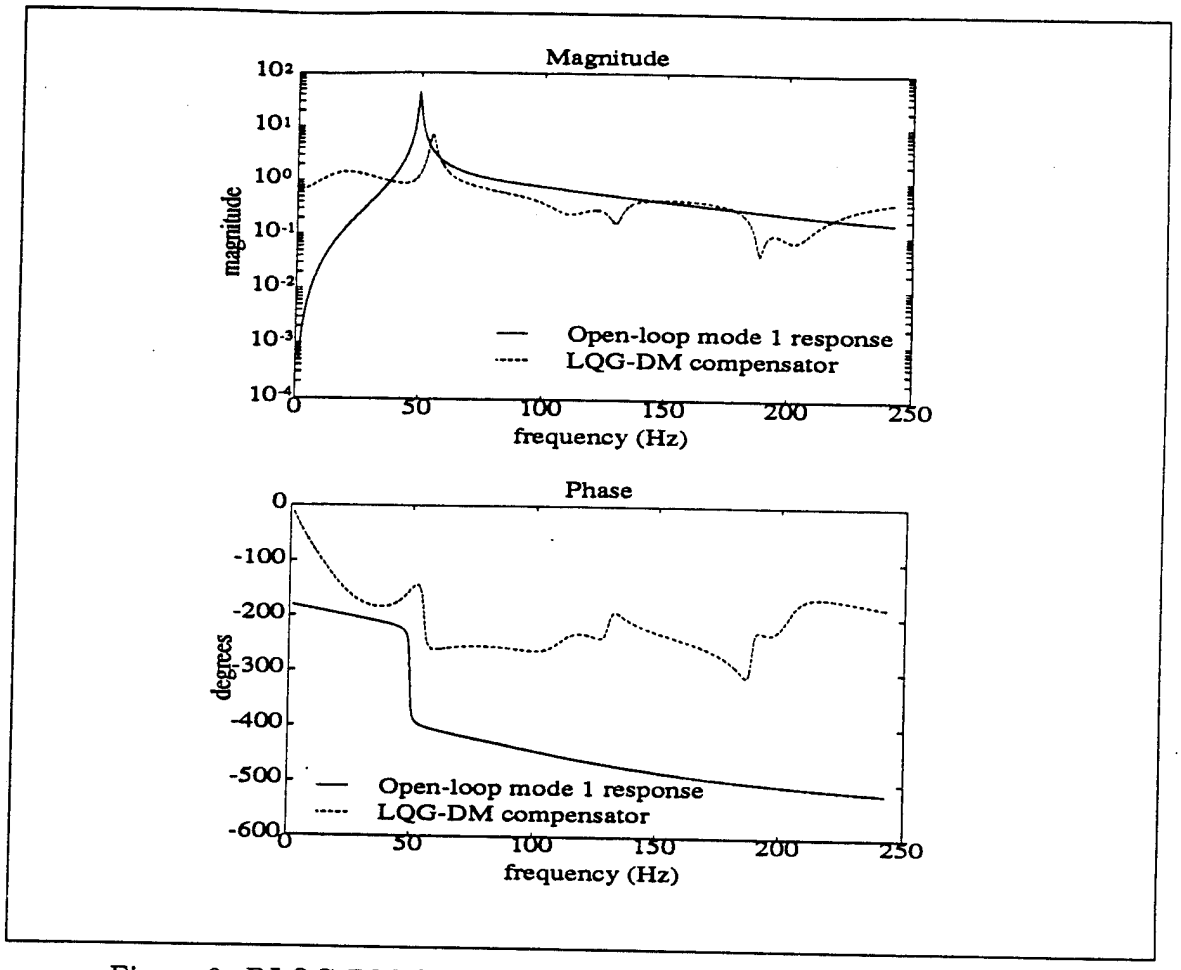

Figure 2: DLQG-DM Compensator and Mode 1 Open-loop Response

model to phase variable canonical form. Discrete-time phase variables are equivalent to tapped-delays in adaptive signal processing applications. Using the appropriate transformation, the disturbance dynamics in phase variable form are such that $s_{1_{k+1}} = s_{2_k}$. Then, we observe that the adaptive feedforward component of the control signal becomes

$$\begin{aligned} u_{ff}[k] &= W_0\, s_{2_k} + W_1\, s_{2_{k-1}} && (17)\\ &= W_o\, s_{2_k} + W_1\, s_{1_k} && (18)\\ &= W^*\, s_{k/k} && (19) \end{aligned}$$

where we define W^* as the optimal weights of the converged adaptive filter. Referring back to the augmented state, we can write

$$\begin{aligned} u_{h_k} &= -K_h\, \hat{x}_{k/k} + W^* s_{k/k} && (20)\\ &= -\acute{K}_h\, x_{a_{k/k}} && (21) \end{aligned}$$

Thus the converged hybrid compensator can be evaluated as if the control law were state feedback, once again. (Recall that the gains on the disturbance states had been zeroed for the feedback component of the hybrid control u_{h_k}.) Several observations can

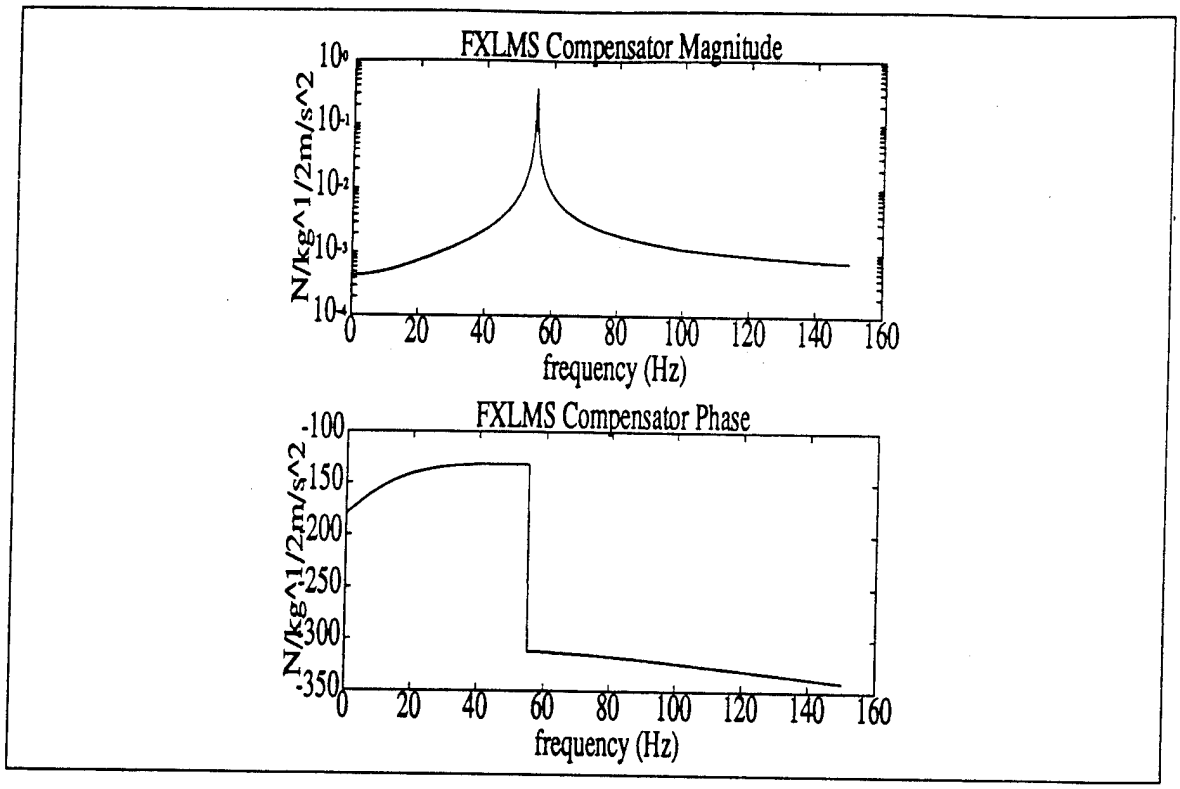

Figure 3: FXLMS SISO Discrete Compensator Frequency Response

be made about equation 21. First, the adaptive filter gains on the disturbance states are the converged values. Second, it is not possible to calculate the values of these weights *a priori*. Real-time simulations or experimental results are required. Finally, we have assumed that the t'th disturbance state is used as the reference signal for the FXLMS algorithm.

An important distinction of the hybrid controller is that it adaptively estimates the disturbance feedback gains, thereby ensuring disturbance rejection regardless of the degree of modelling uncertainty. Next, we examine the effect of modelling uncertainty on the performance robustness of the three control approaches.

Effect of Modelling Uncertainty on Performance Robustness

We are concerned with the performance robustness of the closed-loop structure. Performance robustness is defined here as the maintenance of a satisfactory level of performance in the presence of modelling errors (uncertainties). For this analysis, we assume highly structured perturbations of the nominal plant, which refer to magnitude bounds on individual elements of some perturbation matrix which is compatible with a given model structure. The second assumption is that we have a stable system to begin with. Next, a structured perturbation matrix is proposed to represent probable uncertainties and a numerical investigation of the effect on the controller performance is presented.

Performance robustness analysis is typically carried out either in the frequency domain or in the time domain. For this paper, we choose perturbations on the state space input weighting matrices Γ and Λ which correspond to a time domain analysis approach.

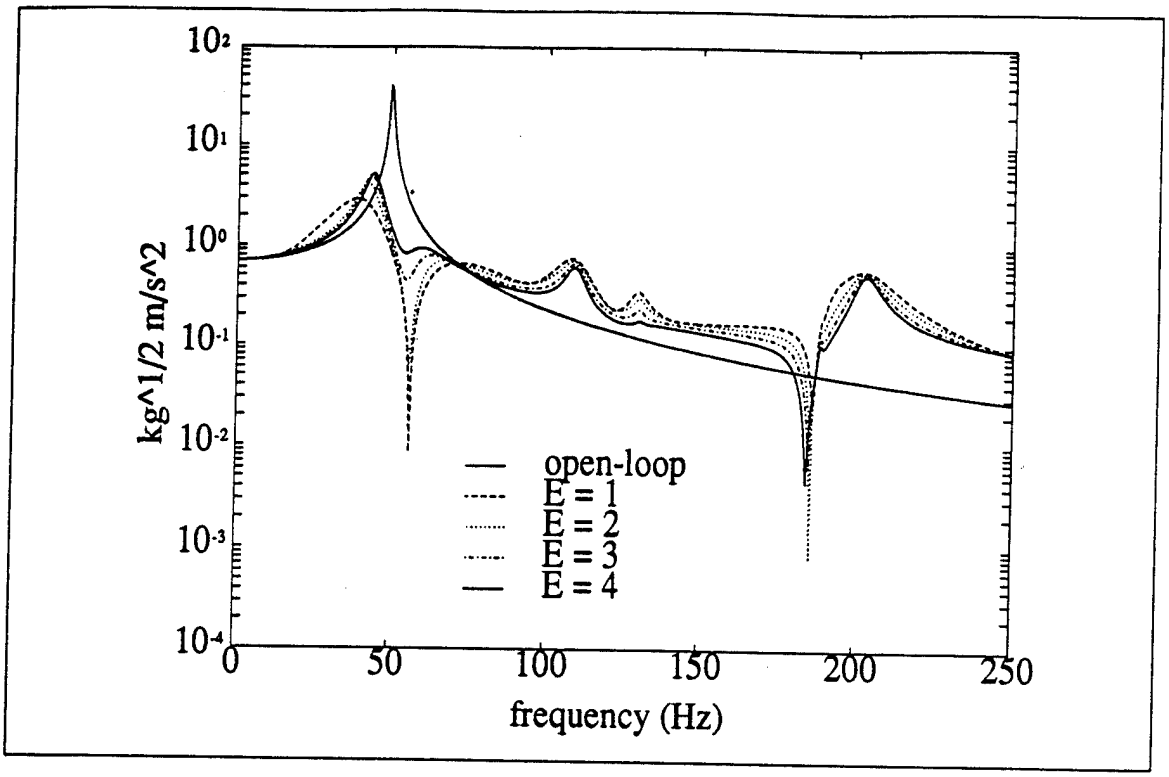

Figure 4: Effect of Model Uncertainty on DLQG-DM Closed-Loop Response

For a general state space system, we can write

$$\dot{x}(t) = (F + \Delta F)x(t) + (G + \Delta G)u(t) + (L + \Delta L)w(t) \tag{22}$$

where the matrices ΔF,ΔG and ΔL represent the maximum perturbations on an elemental basis. For the following calculations, the perturbation matrices are defined by

$$\Delta G = [I + E]G \tag{23}$$

$$\Delta L = [I + E]L. \tag{24}$$

where E is a diagonal matrix which scales the desired uncertainty and G and L are the continuous-time weighting matrices on the control input and disturbance input. Hence, the uncertainties are introduced before the transformation to the sampled-data system. Next, the effect of different values of E on the DLQG-DM closed-loop performance is examined.

It is clear that a fixed-gain control law, such as DLQG-DM cannot sustain the desired closed-loop performance in the face of increasing modelling uncertainties. The closed-loop response in Figure 4 confirms this fact. The excellent performance of the closed-loop system is degraded as the uncertainty is increased to 300 percent. Although this seems like a large uncertainty, the values in the weighting matrices G and L are derived from the modeshapes of the structure. These numbers are typically small and difficult to accurately measure. We suggest that these levels of uncertainties are probable for many structural models.

The hybrid control law and the adaptive control law are not affected by the uncertainty because the adaptive feedforward path finds the gains on the disturbance states

adaptively. In essence, the FXLMS algorithm adapts to the optimal gains for the *actual* plant as opposed to the *nominal* plant. This adaptation process eliminates the performance degradation which occurs for fixed-gain, feedback control approaches. It is this excellent performance robustness which provides the motivation for the present work.

Simulation and Experimental Results

Examples of the hybrid compensator's closed-loop performance are presented in this section. Disturbance compensation of a 60 Hz harmonic disturbance is demonstrated numerically and experimentally for the Virginia Tech plate testbed. The effect of a transient disturbance on the closed-loop system is also demonstrated. Results indicate that hybrid control architectures will be beneficial for active vibration control of structures subject to transient and persistent disturbances.

The plate configuration for the simulation and experiment was arranged to conform with the setup described by Rubenstein et.al. [18]. To summarize, the control was a SISO implementation using an accelerometer array in conjunction with modal filters to produce an output vector of modal accelerations. The first mode was chosen as the error signal for this evaluation. A time-domain simulation of the hybrid control, closed-loop response is presented in Figure 5. The results shown are for the hybrid control with the estimated disturbance reference signal. The controller was initiated at $t = 2$ seconds on the plot. Reduction of the first modal acceleration response to the 60 Hz disturbance is fast and complete. A comparison of the hybrid controller performance to the DLQG-DM controller is shown in the figure. Notice that the minimization performance is less for this case, even though this is a simulated result for no modelling uncertainty. This is to be expected because minimization of the LQ cost function was based on equal penalties for the states. As a result, the controller attempts to minimize more than the single mode one response. Of course, if the actual plant were significantly different from the nominal plant, the results would be degraded accordingly for the DLQG-DM control, as indicated in the previous section.

Experimental results are shown for the hybrid controller in Figure 6. The compensation of a 60 Hz disturbance was performed for a SISO control law. The experimental hybrid controller used the estimated disturbance as the reference signal. A good agreement between the simulated and experimental results for this control example was observed.

Finally, simulated time histories of mode 1 shown in Figure 7 are for the identical conditions of the previous case except a transient pulse, duration of 0.1 seconds, was applied to the structure at t = 3 seconds. The hybrid controller is able to recover quite quickly because of the active damping component of the control signal. The FXLMS controller shows less ability to maintain performance in the presence of the transient disturbance.

Conclusions

Performance of a hybrid control law, which blends an optimal, stochastic, feedback control law with an adaptive signal processing technique, has been evaluated. Simulation and experimental results for the Virginia Tech plate testbed experiment demonstrated

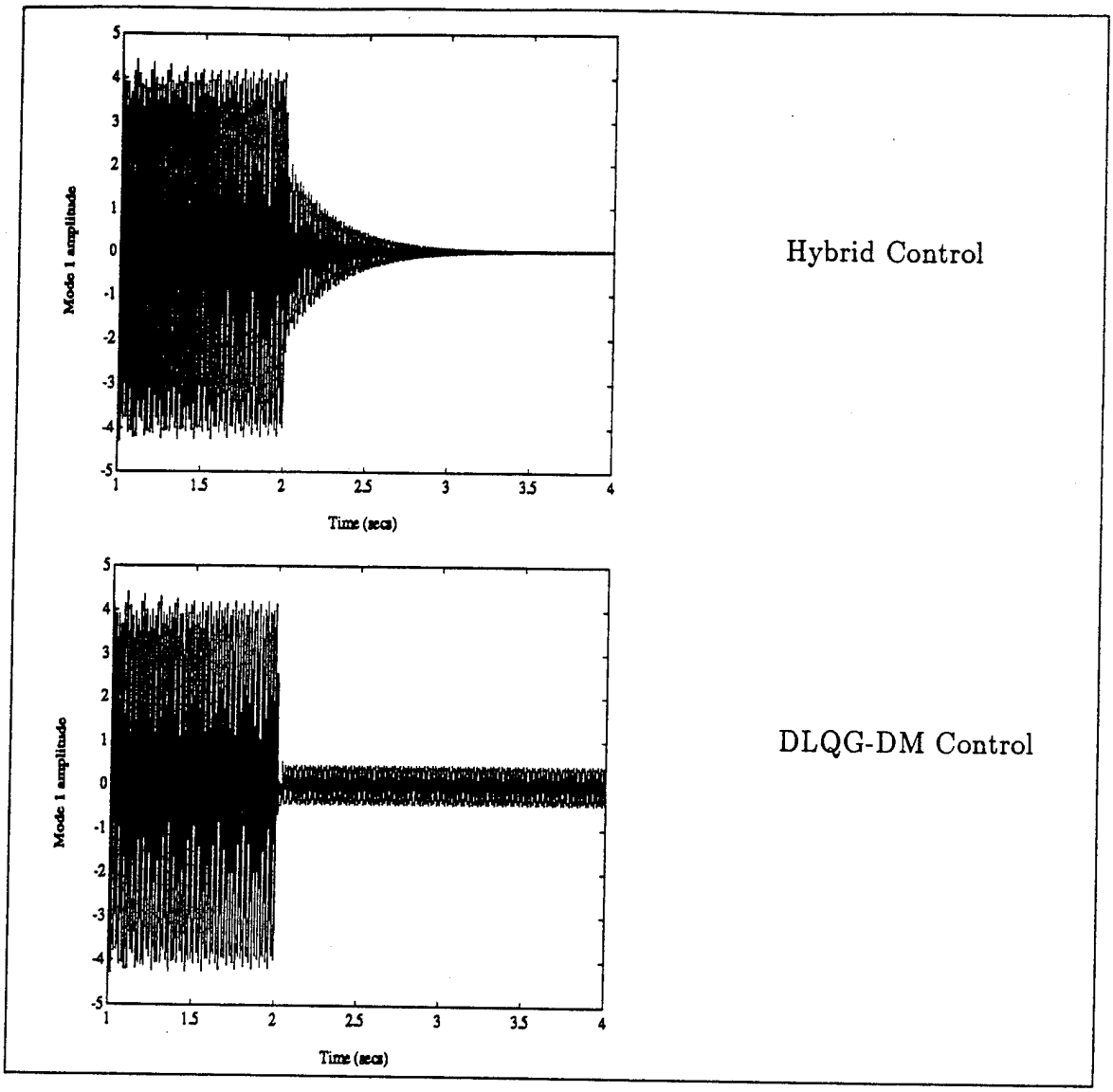

Figure 5: Disturbance Rejection Simulation: 60 Hz Disturbance

that the hybrid control combines the performance robustness of the FXLMS algorithm with the active damping provided by the DLQG feedback control law. It was shown that the hybrid compensator can use the estimated disturbance, available from a Kalman filter estimator, for an uncontrollable reference signal input to the adaptive feedforward path. Analysis of the hybrid compensator illustrated a direct analogy to the full state feedback structure of the DLQG-DM compensator, provided the model dynamics were in phase variable form. It was shown that the essential difference in the two cases was the adaptive versus fixed-gain nature of the feedback gains on the augmented disturbance states. Numerical and experimental results showed that combining the adaptive feedforward and feedback properties of the hybrid controller produced faster convergence times compared to the solitary FXLMS implementation. Future work will address this more clearly. This research indicates that hybrid control architectures will be beneficial for active vibration control of structures subject to transient and persistent disturbances.

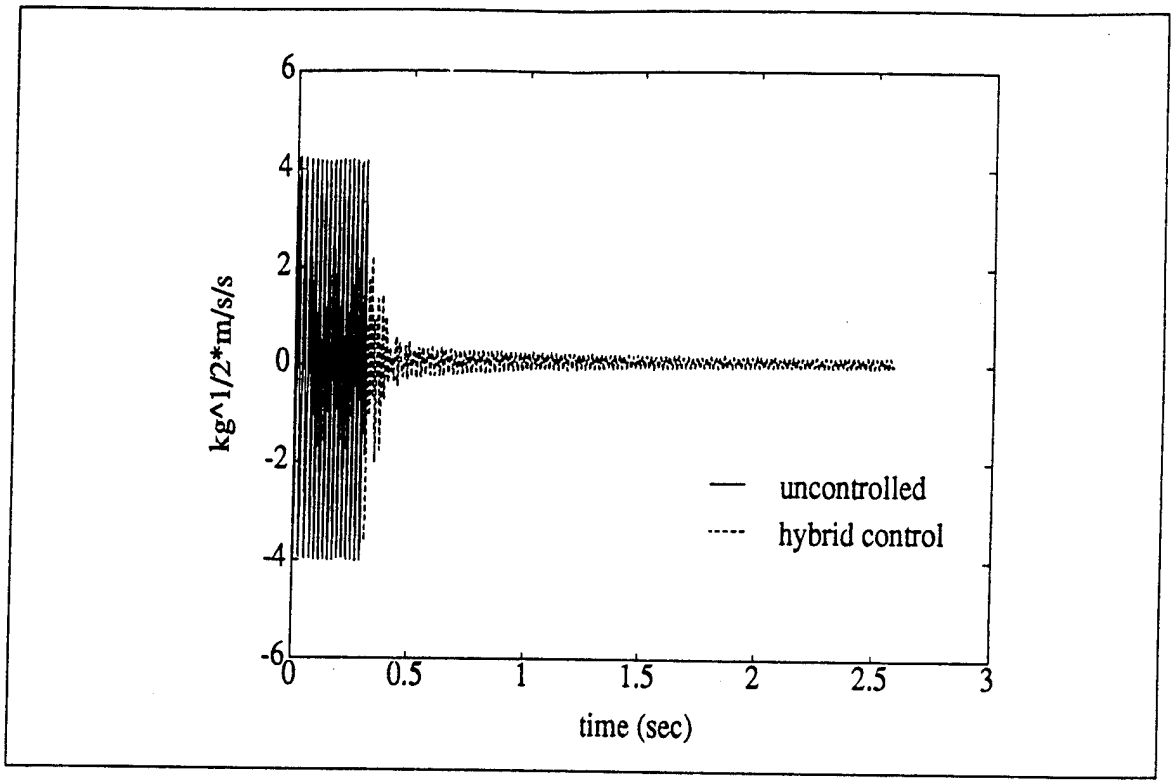

Figure 6: Experimental Hybrid Disturbance Rejection: 60 Hz Disturbance

REFERENCES

1. Balas, G.J., 1978. "Direct Velocity Feedback Control of Large Space Structures." J. Guidance and Control, Vol.2, No.3, pp.252-265.

2. Aubrun, J.N. 1980. "Theory of the Control of Structures by Low-Authority Controllers." J. Guidance and Control, Vol.3, No.5, pp.444-451.

3. Meirovitch, L. and H. Oz, 1980. "Modal Space Control of Distributed Gyroscopic Systems." J. Guidance and Control, Vol.3, pp.140-150.

4. Caughey, T.K. and J.L. Fanson, 1987. "An Experimental Investigation of Vibration Suppression in Large Space Structures Using Positive Position Feedback." Dynamics Laboratory Report DYNL-87-1, Cal Tech.

5. Ridgely, D.B. and S.S. Banda, 1986. "Introduction to Robust Multivariable Control", AFWAL-TR-85-3102, Wright-Patterson AFB, OH.

6. Ellis, G.K. 1992. "H_∞ and LQG Optimal Control for the Rejection of Persistent Disturbances: Analysis, Design and Experiment." Ph.D. Dissertation, Dept. of Mech. Eng. VPI&SU, Blacksburg, VA.

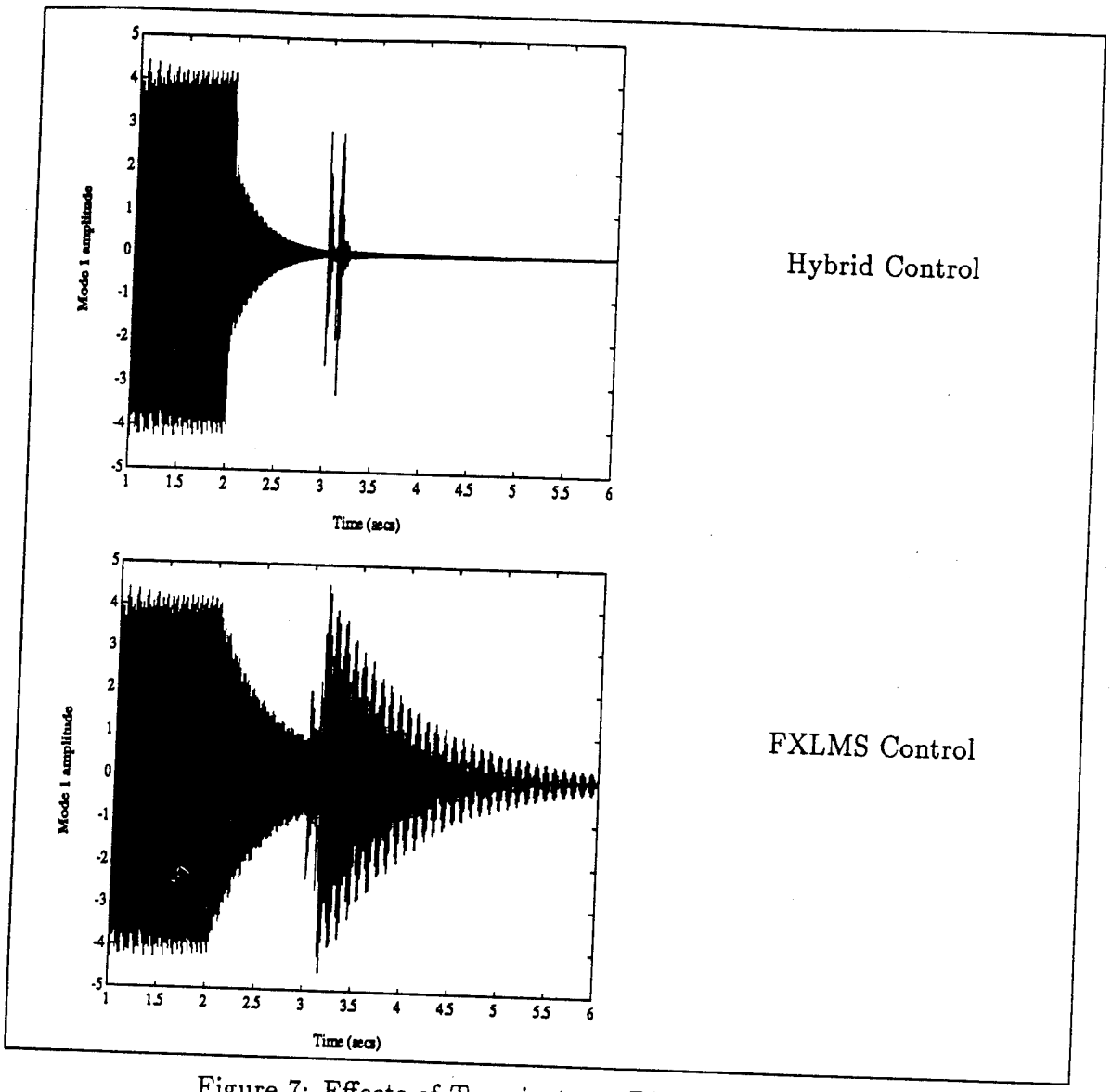

Figure 7: Effects of Transients on Disturbance Rejection

7. Widrow B. and S.D. Stearns, 1985. Adaptive Signal Processing, Englewood Cliffs, NJ, Prentice-Hall.

8. Elliott, S.J., I.M. Stothers and P.A. Nelson, 1987. "A Multiple Error LMS Algorithm and Its Application to the Active Control of Sound and Vibration." IEEE Trans. on Acoust., Speech and Sig. Proc., Vol.ASSP-35, No.10, pp.1423-1434.

9. Fuller, C.R. and J.D. Jones, 1987. "Experiments in Reduction of Propeller Induced Interior Noise by Active Control of Cylinder Vibration." J. Sound and Vib., 112(2), pp.389-395.

10. Vipperman, J.S., R.A. Burdisso and C.R. Fuller, 1992. "Active Control of Broadband Structural Vibration Using the LMS Adaptive Algorithm.", accepted for

publication J. Sound. Vib

11. Sievers, L. and A.H. vonFlotow, 1990. "Comparison and Extensions of Control Methods for Narrowband Disturbance Rejection." Proceedings of the 1990 ASME Winter Annual Meeting in Dallas, TX.

12. Alcone, J.M., L.R. Ebbesen, B. Widrow, P.H. Merritt, M.E. Meline, K.E. Bardwell and S.D. Monaco, 1987. "Analysis and Design of Adaptive Noise Cancellation for Closed Loop Applications." Hughes Aircraft Company, Albuquerque Engineering Laboratory, NM.

13. Warnaka, G.E., L.A. Poole and J. Tichy, 1984. "Active Acoustic Attenuator," US Patent No. 4,473,906.

14. Eriksson, L.J. 1987. "Active Sound Attenuation System With On-line Adaptive Feedback Cancellation." US Patent No. 4,677,677.

15. Swanson, D.C. 1991. "A Stability Robustness Comparison of Adaptive Feedforward and Feedback Control Algorithms." in Proceedings of Recent Advances in Active Control of Sound and Vibration, VPI&SU, Blacksburg, VA, pp.754-767.

16. Finefield, J.K. 1992. "Investigation of Combined Feedback and Adaptive Digital Control of Cylinder Vibrations." Master's Thesis, VPI&SU, Blacksburg, VA.

17. Bender, D.J. 1985. "Frequency Response with Estimators", Int. J. Cont., Vol.41, No. 5, pp.1093-1127.

18. Rubenstein, S.P., W.R. Saunders, G.K. Ellis, H.H. Robertshaw, and W.T. Baumann, 1991. "Demonstration of a LQG Vibration Controller for a Simply-Supported Plate" in Proceedings of Recent Advances in Active Noise and Vibration Control Conference Blacksburg, VA, VPI & SU.

C-36 Comparison of Various Digital LQ-MIMO Control Laws, D. G. Cole and H. H. Robertshaw, Second Conference on Recent Advances in Active Control of Sound and Vibration, Blacksburg, VA , pp. 355-365, 28-30 April 1993.

COMPARISON OF VARIOUS DIGITAL LQ-MIMO CONTROL LAWS

D. G. Cole,[1] H. H. Robertshaw[1]

ABSTRACT

Multi-Input/Multi-Output (MIMO) control strategies produce improved performance over Single-Input/Multi-Output (SIMO) methods when applied to the Active Vibration Control (AVC) and Active Structural Acoustic Control (ASAC) problems. However, digital MIMO control is limited due to a higher computational load resulting from an increased system order, more control gain calculations, etc. The decrease in sample speed results in a decrease in controller bandwidth and can affect closed-loop stability criteria (i.e. gain margin and phase margin). In addition, the observer structure can effect both bandwidth and closed-loop stability. This work investigates the application of digital MIMO control approaches to real structures. Considerations such as computational load, system model order, and control law complexity are evaluated for a variety of MIMO control methods. Experimental results are shown for LQR-MIMO control laws implemented using full-order observers. Considerations for the implementation of reduced-order observers are discussed; in particular, the relationship between the measurement variable and estimator state, and the effect sample speed has on estimator gains.

INTRODUCTION

Active Vibration Control (AVC) and Active Structural Acoustic Control (ASAC) strategies are being applied to flexible structures with multiple modes of vibration and resultant acoustic radiation. In the search for increased controller bandwidth and performance, AVC and ASAC strategies are incorporating a large number of sensors and actuators to control the ever-increasing system order. Such Multi-Input/Multi-Output (MIMO) control strategies are easily implemented using digital controllers which offer increased flexibility over similar analog approaches, where control laws can be easily

This work supported under ONR Grant No. N00014-92-J-1170

[1]Department of Mechanical Engineering, Center for Intelligent Material Systems and Structures, Virginia Polytechnic Institute and State University, Blacksburg, VA 24061-0238, U.S.A.

adjusted to account for improved system models. Digital control schemes also include adaptive approaches, such as LMS, which can be coupled with feedback control schemes to provide improved system transient response and disturbance compensation [1].

While MIMO control strategies do provide improved performance over similar SISO and SIMO strategies, they are limited due to a higher computational load resulting from increased system order, more control gain calculations, etc. These effects can decrease the sampling speed of the controller which results in a decrease of controller bandwidth and can affect closed-loop stability. However, this is in contradiction to initial reasons for implementing MIMO control schemes. Some of the problems can be alleviated by using high speed digital processing or parallel computation schemes, resulting in a faster sampling speed, but this alternative is often costly. The implementation of MIMO control schemes is possible using conventional personal computers (PC's) provided the design of the digital compensator accounts for computational load and is optimized to maximize controller speed.

One method for reducing controller complexity is through model reduction. By limiting system models to only those modes which can or need to be controlled, compensator size can be reduced accordingly. Frequently, however, no system model dynamics can be eliminated and the system order is sufficiently large to cause problems with closed-loop properties. In addition, model reduction may not provide sufficiently accurate results in closed-loop behavior. A design which may be robust and provide excellent performance in one frequency range may not be acceptable in another. In such situations other approaches need to be considered.

Other methods seek to limit controller size by searching for controllers which perform as well or almost as well as a full-order design. Full-order designs can be approximated by compensators of lower order (e.g. frequency weighting, reduction via fractional representations) or controller design can be begun initially (*ab initio*) with compensator order constraints in mind (e.g. reduced-order and functional observers, velocity feedback, positive position feedback). Methods which pursue this last alternative will be considered here [2].

The sampling speed of a computer controlled system can have a large influence on system performance. Faster sampling speeds may provide improved performance, due to improved estimates of the system state, as well as an increase bandwidth. Notwithstanding speed limitations of the controller hardware, the sampling speed is directly related to the number of operations that must be performed within the sampling period. Multiplication operations are the most costly and an accounting of the number of multiplies for a given compensator can provide a reasonably accurate estimate of controller speed.

Controller speed and performance is compared here for single- and multi-input plants using full-order observers which implement similar AVC control laws. Similar results are expected for reduced-order observers; however, reduced-order estimators can be difficult to implement due to large feedback gains within the estimator structure. The relationship between measurement variable and estimator state has a large effect on estimator gains. System natural frequencies and the sampling frequency affect the structure of the discrete-time model which in turn affects the ability to place the poles of the reduced-order observer. An analysis of a single-mode second-order system is shown to demonstrate this point.

COMPENSATOR FORMULATION

Given a structure described by a discrete time model.

$$\begin{array}{lrcll} \text{State Propagation:} & x_k & = & \Phi x_{k-1} + \Gamma u_{k-1} & \Phi_{n\times n} \quad \Gamma_{n\times q} \\ \text{Measured Output:} & y_k & = & Cx_k & C_{p\times n} \\ \text{General Output:} & \gamma_k & = & \mathcal{C}x_k & \mathcal{C}_{\mathcal{N}\times n} \end{array} \tag{1}$$

Actuator and sensor dynamics may be included in the system model; therefore, the system order is typically greater than twice the number of modes modelled ($n > 2\mathcal{N}$). The reader is referred to Åström & Wittenmark [3] and Franklin et al. [4] for the formulation of the sampled-data system.

Often it is desired to control the plant by a feedback control law (controllability assumed).

$$u_k = r_k - Kx_k \qquad K_{q\times n} \tag{2}$$

where the closed-loop poles are the eigenvalues of $\Phi - \Gamma K$. However it is usually the case that not all of the plant states are available for feedback. In such situations an observer can be implemented which provides an estimate of plant states (observability assumed).

For discrete-time systems there are two different kinds of estimates of the state variable x:

1. *Current:* x_k is reconstructed from the measurements $y_k, y_{k-1}, \ldots, y_0$.

2. *Predictor:* x_k is reconstructed from the measurements $y_{k-1}, y_{k-2}, \ldots, y_0$.

Both estimates could be used for control but the current estimate is preferred since it is based on the most recent measurement. A disadvantage of using the current estimate is that the estimate is old (by no more than one time step) when implemented in the control law creating a delay not accounted for in the design process and usually resulting in reduced performance. The predictor estimate could be used, eliminating the time delay; in general, however, the current estimate provides the faster response to disturbances and measurement errors and thus better system regulation. Inadequate system response due to the latency from the computational lag can be improved by additional iterations on the controller design or accounted for by introducing the time delay in the plant model [4]. Current estimators for both the full- and reduced-order observers will be used here.

The inputs to the observer are the plant control u and plant output y, and the output of the observer w asymptotically approaches a linear combination of the plant states, very often the desired state feedback control ($w_k \to Kx_k$ as $k \to \infty$).

$$\begin{array}{rcll} z_{k+1} & = & Fz_k + Gy_k + Hu_k & F_{m\times m} \quad G_{m\times p} \quad H_{m\times q} \\ w_k & = & Mz_k + Ny_k & M_{q\times m} \quad N_{q\times p} \end{array} \tag{3}$$

A block diagram of the above observer is illustrated in figure 1. The observer is realized

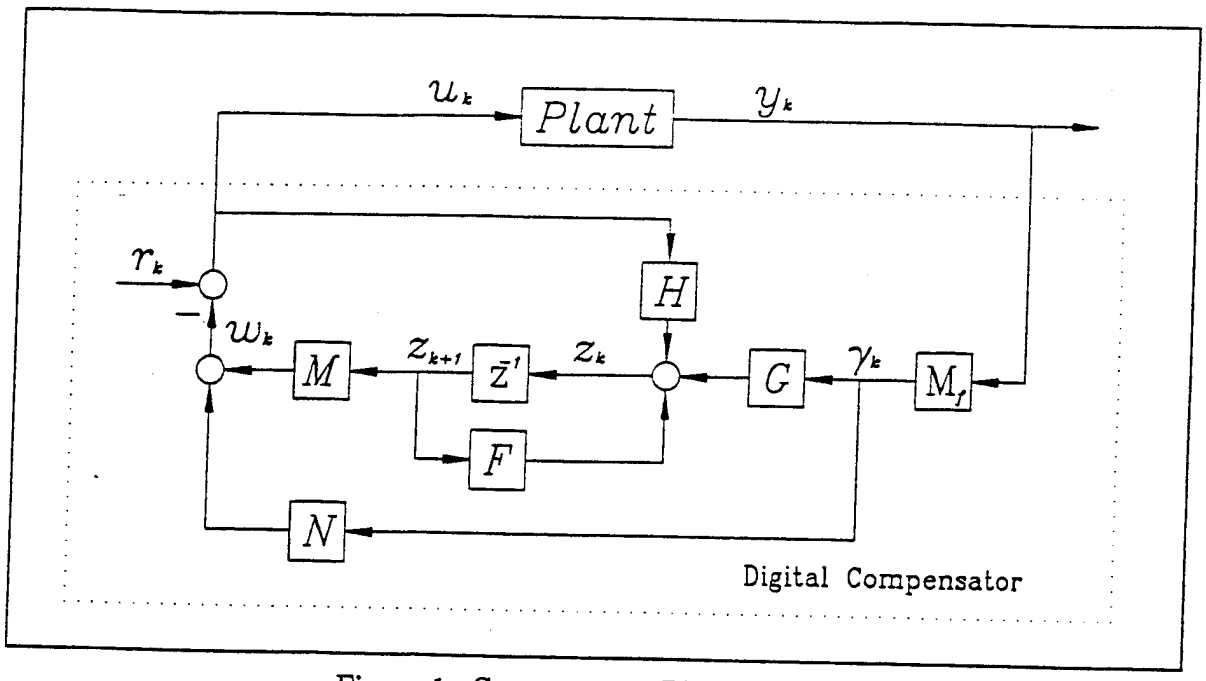

Figure 1: Compensator Block Diagram

as a system of first- and second-order systems in parallel. This is a block-diagonal representation with the i^{th} block of the form:

1^{st} Order

$$z_{ik+1} = \sigma_i z_{ik} + G_i y_k + H_i u_k \tag{4}$$

2^{nd} Order

$$\begin{bmatrix} z_i \\ z_{i+1} \end{bmatrix}_k = \begin{bmatrix} \sigma_i & \omega_i \\ -\omega_i & \sigma_i \end{bmatrix} \begin{bmatrix} z_i \\ z_{i+1} \end{bmatrix}_{k-1} + \begin{bmatrix} G_i \\ G_{i+1} \end{bmatrix} y_{k-1} + \begin{bmatrix} H_i \\ H_{i+1} \end{bmatrix} u_{k-1} \tag{5}$$

Here the complex poles are represented as real numbers, a prerequisite for computer application [3]. It will be assumed that all observer representations here will be in block-diagonal form.

Since the speed of operation (i.e. the time required for one multiply) is machine dependent, a comparison of the number of operations will provide a suitable performance ratio. The above observer format has the following operations count:

Step 1: State Propagation	$z_{k-1} = Fz_{k-1} + G\gamma_{k-1} + Hu_{k-1}$	$m(2+\mathcal{N}+q)$
Step 2: Modal Filter	$\gamma_k = \mathrm{M}_f y_k$	$\mathcal{N}p$
Step 3: Estimator Output	$w_k = Mz_k + N\gamma_k$	$mq+\mathcal{N}q$
Total Operations ($\times$)	$m(2+\mathcal{N}+2q)+\mathcal{N}(p+q)$	

(6)

It might be expected that, since the control law is defined as a function of the states, the control input term, Hu_k, could be included in the state transition matrix; however,

implementation of the controller results, at times, in saturated control inputs and these saturated values should be used in the observer to provide a more accurate estimate of the system state.

It is often advantageous to use modal representations of structural dynamics within both AVC and ASAC control schemes. Modal parameters can be measured experimentally and very often, in the control of structures, the plant output is the structural position, velocity, or acceleration. In such situations it may be advantageous to extract modal information directly from measurements. The measured response output $y_{p\times 1}$ is related to the modal response output $\gamma_{\mathcal{N}\times 1}$ through the modal eigenvector matrix, $\Psi_{p\times\mathcal{N}}$. It is often necessary to oversample modes ($p > \mathcal{N}$) in order to extract sufficiently accurate modal information. The modal filter, which maps the structural domain to the modal domain, is then formed by the pseudoinverse [6].

$$\gamma = [\Psi^T\Psi]^{-1}\Psi^T y = \mathrm{M}_f y \tag{7}$$

It is not apparent at this point that the use of a modal filter can reduce the computation load, since it most assuredly is fully populated and would require $p\mathcal{N}$ operations. By including the modal filter in the observer, the measurement input matrix, G, can be reduced in size thus eliminating operations, provided $\mathcal{N} < mp/(m+p)$. No attempt will necessarily be made to preserve modal states in the estimator formulation; instead, estimator realizations will be in block diagram form discussed previously to minimize operations and other consequences due to roundoff and quantization.

COMPENSATOR IMPLEMENTATION

Three SIMO and MIMO control laws were experimentally implemented on a simply-supported plate testbed [5]. This testbed implements piezoelectric sensors and actuators with 16 outputs and up to 5 control inputs. The measured outputs, for this analysis, are directly related to the structure's modes and are spatially filtered, with a modal filter, to produce signals proportional to modal positions or (with changes in transducer preprocessing) modal velocities, so that

$$\gamma = Cx = \begin{bmatrix} \mathrm{I}_{\mathcal{N}} & 0 \end{bmatrix} x \tag{8}$$

Here γ can be related to either the structure's modal positions or modal velocities.

The only actuator dynamics included in the model are in the form of a smoothing filter-amplifier-transformer combination which is represented by a nearly critically damped second-order model. Thus the system order n is directly related to the number of modes included in the model, $\mathcal{N}$, and the number of inputs to the plant, q.

$$n = 2(\mathcal{N} + q) \tag{9}$$

The modal plant model is truncated at the 5^{th} mode (bandwidth: 25-250 Hz).

The control law ($u_k = r_k - Kx_k$) was chosen to regulate the state, $r_k \equiv 0$, and minimize a quadratic cost function with the weighting matrices

$$\begin{aligned} Q &= \begin{bmatrix} \mathrm{I}_{\mathcal{N}} & \mathrm{I}_{\mathcal{N}} & 0 \end{bmatrix}^T \begin{bmatrix} \mathrm{I}_{\mathcal{N}} & \mathrm{I}_{\mathcal{N}} & 0 \end{bmatrix} \\ R &= (\rho/q)\,\mathrm{I}_q \end{aligned} \tag{10}$$

In all cases $\rho = 5 \times 10^{-8}$ and the control law was calculated using MATLAB's `dlqr` function.

FULL-ORDER KALMAN FILTER

The Kalman filter has been used in AVC and ASAC control schemes as both a state estimator for feedback control laws and as a disturbance estimator for disturbance cancellation [5,6,7]. The Kalman filter is very often presented in predictor-corrector format.

$$\begin{aligned} \hat{x}_k^- &= \Phi \hat{x}_{k-1}^+ + \Gamma u_{k-1} \\ \gamma_k &= \mathrm{M}_f y_k \\ \hat{\gamma}_k &= C\hat{x}_k^- \\ \hat{x}_k^+ &= \hat{x}_k^- + L(\gamma_k - \hat{\gamma}_k) \\ w_k &= K\hat{x}_k^+ \end{aligned} \tag{11}$$

Here the observer state $\hat{x}$ directly estimates the plant state x, that is $\hat{x}_k \rightarrow x_k$ as $k \rightarrow \infty$. As mentioned earlier, the desired output of the estimator is a control signal used to regulate the plant states. It is possible to reduce the apparent complexity by collapsing the predictor-corrector format into just two equations. Combining equations, rearranging terms, and omitting the explicit predictor-corrector notation the estimator has the following structure.

$$\begin{aligned} \hat{x}_k &= (\Phi - LC\Phi)\hat{x}_{k-1} + Ly_k + (\Gamma - LC\Gamma)u_{k-1} \\ w_k &= K\hat{x}_k \end{aligned} \tag{12}$$

This provides a current estimate of the plant state x. The modal filter equation has been dropped since it will be implemented each iteration of the controller regardless of controller size or representation. This representation of the Kalman Filter is related to the observer format shown in equation 3 through a change of variable, $z_k = \hat{x}_k - L\gamma_k$, with the following result.

$$\begin{aligned} z_k &= (\Phi - LC\Phi)z_{k-1} + (\Phi - LC\Phi)L\gamma_{k-1} + (\Gamma - LC\Gamma)u_{k-1} \\ w_k &= Kz_k + KL\gamma_k \end{aligned} \tag{13}$$

and the matrices F, G, H, M, N of equation 3 are described accordingly. This observer representation is faster than the other full order observers reported in Cole and Rubenstein [5,6]: ~2700 Hz vs. ~2000 Hz. Also, it is easy to implement and requires fewer variable assignments and addition operations, both of which improve controller efficiency.

Three full-order LQG estimators were implemented on the simply supported plate testbed: one SIMO and two MIMO (2 & 4 inputs). The PVDF sensors were conditioned to provide position measurements and the five PZT actuators were configured to excite bending modes within the plate [5]. A PZT actuator provided a broadband disturbance

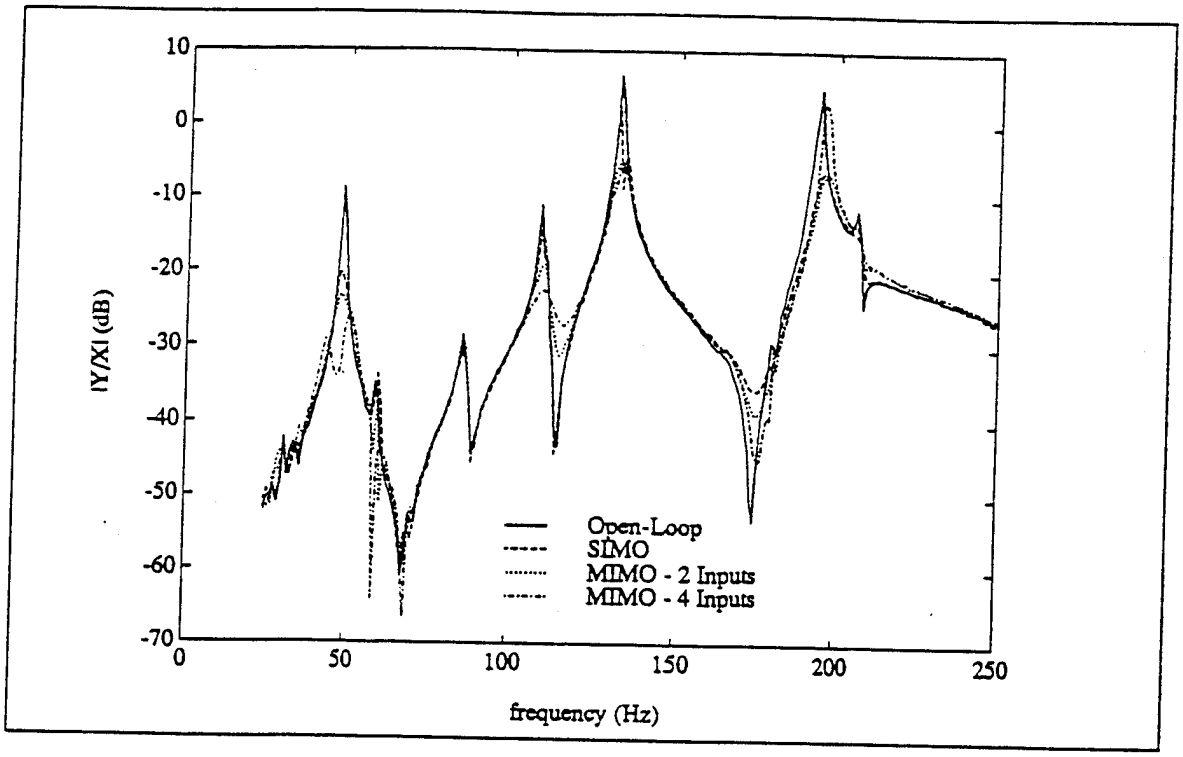

Figure 2: Frequency Response Function

and figure 2 shows the frequency response functions between the disturbance and an arbitrary sensor location.

The sample frequencies and performance metrics for the four controllers are listed in table 1. Each controller added damping to the five modes within the controller bandwidth (25-250 Hz) with marginal spillover to unmodelled modes both in and outside of the controller bandwidth. As a metric of performance we define

$$\Pi_{[\omega_a,\omega_b]} = 2\int_{\omega_a}^{\omega_b} |T_{xy}(j\omega)|^2 d\omega \tag{14}$$

which relates to the vibrational energy of the structure over the frequency bandwidth $\omega_a < |w| < \omega_b$. Here T_{xy} is the frequency response function between disturbance x and response y. The performance metrics, normalized by the open-loop response over the same bandwidth, are also listed in table 1.

The loss in performance of the 4-input controller at the 4^{th} mode natural frequency, 206 Hz, is believed to result from poor actuator placement. The 4^{th} mode of the simply-supported plate is a (2,2) mode and two of the actuators lie on a nodal line of this mode. It is expected that improved actuator placement could improve the performance of all of the controllers.

At this point the estimator structure shown in equation 11 has been simplified as much as possible by collection of terms and state realization. Further reduction in the number of operations can only be achieved through the reduction in the number of estimator states by using reduced-order observers. Implementation of a reduced-order is not as

Table 1: Controller Sample Rates and Performance Ratios

# Inputs	# Oper.	f_s (Hz)	$\Pi_{[25,250]}/\Pi_{OL}$	$\Pi_{[25,175]}/\Pi_{OL}$
1	193	2698	0.362	0.443
2	222	2273	0.243	0.213
4	280	1650	0.543	0.191

straightforward as the Kalman filter. By design, the Kalman filter provides an optimal least-squares estimate of the system state; that is, process and measurement noise are filtered out through the Kalman filtering process. Reduced-order observers only estimate unmeasurable states, thus any noise in the measurements is fedthrough directly. This result is undesirable particularly for estimators with high feedback gains. As will be shown, the magnitude of the feedback gain in a reduced-order observer strongly depends upon the type of measurement (position or velocity) and the states to be estimated.

REDUCED-ORDER OBSERVER

Since the output γ can be used to determine at least $\mathcal{N}$ of the state variables, thus only the remaining $m = \mathcal{N} + 2q$ system states need be estimated.

Consider again the structure described by the discrete time system.

$$\begin{aligned} x_{k+1} &= \Phi x_k + \Gamma u_k \\ \gamma_k &= C x_k \end{aligned} \tag{15}$$

which can be partitioned

$$\begin{aligned} \begin{bmatrix} \tilde{x}_k \\ \bar{x}_k \end{bmatrix} &= \begin{bmatrix} \Phi_{11} & \Phi_{12} \\ \Phi_{21} & \Phi_{22} \end{bmatrix} \begin{bmatrix} \tilde{x}_{k-1} \\ \bar{x}_{k-1} \end{bmatrix} + \begin{bmatrix} \Gamma_1 \\ \Gamma_2 \end{bmatrix} u_k \\ \gamma_k &= \begin{bmatrix} \mathrm{I}_{\mathcal{N}} & 0 \end{bmatrix} \begin{bmatrix} \tilde{x}_{k-1} \\ \bar{x}_{k-1} \end{bmatrix} \end{aligned} \tag{16}$$

Since $\tilde{x}$ is identical to the output γ only the state $\bar{x}$ need be reconstructed. The reader is referred to Willems [7] for a proper derivation of reduced-order observers and the result is shown here without detail.

$$\begin{aligned} z_k &= (\Phi_{22} - L\Phi_{12}) z_{k-1} + \\ &\quad (\Phi_{21} - L\Phi_{11} + \Phi_{22}L - L\Phi_{12}) L\gamma_{k-1} + (\Gamma_2 - L\Gamma_1) u_{k-1} \\ \hat{\bar{x}}_k &= z_k + L\gamma_k \end{aligned} \tag{17}$$

If we partition the state feedback matrix

$$w_k = Kx_k = \begin{bmatrix} K_1\tilde{x}_k & K_2\bar{x}_k \end{bmatrix} \tag{18}$$

then the output equation for the estimator becomes

$$w_k = K_2 z_k + (K_1 + K_2 L)\gamma_k \tag{19}$$

The observer poles can be placed arbitrarily through proper choice of the estimator feedback gain matrix L.

It should be pointed out that the reduced-order observer is, in effect, a full-order observer with $\mathcal{N}$ poles located at the origin and can be achieved by appropriate selection of observer gain matrix.

Consideration should be placed on the type of measurement (position or velocity) that is going to be fed back within the estimator. Initial investigations, using the simply-supported plate testbed, indicated that reduced-order state estimation using position-type measurements (i.e. velocity estimation) requires large feedback gains, L. Conversely, estimation of positions using velocity measurements is better suited to reduced-order estimation. While analysis of general multi-mode structures is quite complicated, an example using a single-mode model is shown here without loss of generality.

Consider the continuous time model of a single-mode system.

$$\frac{d}{dt}\begin{bmatrix} r \\ \dot{r} \end{bmatrix} = \underbrace{\begin{bmatrix} 0 & 1 \\ -\omega_n & -2\zeta\omega_n \end{bmatrix}}_{A}\begin{bmatrix} r \\ \dot{r} \end{bmatrix} \tag{20}$$

This system has complex conjugate poles

$$\begin{gathered} \lambda = \lambda_{1,2^*} = \sigma + j\omega = -\zeta\omega_n + j\omega_n\sqrt{1-\zeta^2} = \omega_n e^{j\theta} \\ \theta = \tan^{-1}\frac{\sqrt{1-\zeta^2}}{-\zeta} \end{gathered} \tag{21}$$

The above system is described in discrete-time as a zero-order-hold discrete-time model (equation 1) through the following relationship.

$$\Phi = e^{Ah} = \frac{-1}{\lambda - \lambda^*}\begin{bmatrix} e^{\lambda h}\lambda^* - e^{\lambda^* h}\lambda & -(e^{\lambda h} - e^{\lambda^* h}) \\ |\lambda|^2(e^{\lambda h} - e^{\lambda^* h}) & -(e^{\lambda h}\lambda - e^{\lambda^* h}\lambda^*) \end{bmatrix} \tag{22}$$

where h is the sampling period and * denotes complex conjugation. Let

$$\bar{\lambda} = \lambda h = \sigma h + j\omega h = \bar{\sigma} + j\bar{\omega} \tag{23}$$

The above expression for Φ can be simplified to give

$$\Phi = \frac{-1}{\omega}\begin{bmatrix} \omega_n e^{\bar{\sigma}}\sin(\bar{\omega} - \theta) & -e^{\bar{\sigma}}\sin\bar{\omega} \\ \omega_n^2 e^{\bar{\sigma}}\sin\bar{\omega} & -\omega_n e^{\bar{\sigma}}\sin(\bar{\omega} + \theta) \end{bmatrix} \tag{24}$$

For a lightly damped system $\theta \simeq \frac{\pi}{2}$ and $\omega \simeq \omega_n$ thus

$$\Phi \simeq e^{\bar{\sigma}} \begin{bmatrix} \cos\bar{\omega} & -\frac{1}{\omega_n}\sin\bar{\omega} \\ \omega_n \sin\bar{\omega} & -\cos\bar{\omega} \end{bmatrix} \tag{25}$$

As $h \to 0$ (increasing sample frequency) $\bar{\omega} \to 0$ and $\Phi \to \mathrm{I}$.

In the formulation for the reduced order observer (equation 17)

$$\begin{aligned} \Phi_{22} &= -\cos\bar{\omega} \\ \Phi_{12} &= -\frac{1}{\omega_n}\sin\bar{\omega} \end{aligned} \tag{26}$$

thus it takes a large gain, L, to place the pole of a reduced-order observer, $\Phi_{22} - L\Phi_{12}$. This problem is aggravated for a high natural frequency. In addition, the estimator gain L is a feedthrough term in the estimator output equation which amplifies measurement noise. These affects are undesirable, particularly in the face of unmodelled dynamics, modelling uncertainties, and system disturbances.

If instead measurements relate to modal velocities and estimates of modal positions are required then

$$\begin{aligned} \Phi_{22} &= \cos\bar{\omega} \\ \Phi_{12} &= \omega_n \sin\bar{\omega} \end{aligned} \tag{27}$$

and considerably smaller gains, on the order of $\frac{1}{\omega_n^2}$ are required in the estimator with a correspondingly smaller feedthrough term.

This result is could be expected since it is usually difficult to numerically determine rates from process information, even if process dynamics are known. This correspond, in some sense, to numerical differentiation. However, using rate information to determine a process is considerably easier since noise is, in effect, filtered out through integration.

CONCLUSION

While the application of digital feedback control schemes to multi-mode structures seems limited due to computation complexity and the accompanying reduction in bandwidth for systems of high order, digital MIMO control methods can be applied with reasonable success and improved performance over similar single-input methods. Experiments shown here demonstrated reductions in a vibrational-energy metric to as much as 20% of open-loop values over a bandwidth. Reductions in performance were noted and believed to relate to actuator placement. Further improvements in sample speed should improve the state estimate and provide better control and can be achieved by reducing the number of multiplies executed each time step. Reduced-order observers can be implemented but considerations should be placed on the type of measurement (position or velocity) that is going to be used in the feedback compensator. Position measurements used to determine velocity states typically require large gains to place observer poles and subsequently amplify noise through the estimator feedthrough term.

Velocity measurements used to determine position states are better suited to reduced-order observers and require smaller gains (on the order of the natural frequency squared for a single-mode system) than the previous case.

REFERENCES

1. William R. Saunders, Harry H. Robertshaw, and Ricardo Burdisso, 1993. "An Evaluation of Feedback, Adaptive Feedforward and Hybrid Controller Design for Active Structural Control of Lightly-Damped Structures," 2nd Conference on Recent Advances in Active Control of Sound and Vibration, April 1993.

2. Brian D. O. Anderson and John B. Moore, 1990. *Optimal Control: Linear Quadratic Methods*, Englewood Cliffs, NJ: Prentice-Hall.

3. Karl J. Åström and Björn Wittenmark, 1990. *Computer Controlled Systems: Theory and Design*, Englewood cliffs, NJ: Prentice-Hall.

4. Gene F. Franklin, J. David Powell, and Michael L. Wortman, 1990. *Digital Control of Dynamic Systems*, Reading, MA: Addison-Wesley.

5. Daniel G. Cole, 1992. "Design of, and Initial Experiments with, a MIMO Plate Control Testbed," Master's Thesis, Virginia Polytechnic Institute and State University, Blacksburg, VA.

6. Stephen P. Rubenstein, 1991. "An Experiment in State-Space Vibration Control of Steady Disturbance on a Simply-Supported Plate," Master's Thesis, Virginia Polytechnic Institute and State University, Blacksburg, VA.

7. J. L. Willems, 1980. " Design of State Observers for Linear Discrete-Time Systems," *Int. J. Systems Sci.*, vol. II, no. 2, pp. 139–147.

C-37 Active Control of Structurally Radiated Sound from an Enclosed Finite Cylinder, R. L. Clark and C. R. Fuller, Second Conference on Recent Advances in Active Control of Sound and Vibration, Blacksburg, VA, pp. 380-402, 28-30 April 1993.

ACTIVE CONTROL OF STRUCTURALLY RADIATED SOUND FROM AN ENCLOSED FINITE CYLINDER

Robert L. Clark,[1] Chris R. Fuller[2]

1 2

ABSTRACT

A long, thin aluminum cylinder was configured with two rigid end caps and instrumented with piezoceramic actuators and either microphone or polyvinylidene fluoride (PVDF) structural sensors for narrow-band active structural acoustic control. The input disturbance to the cylinder was generated with a shaker attached by a stinger, and all tests were performed in an anechoic chamber. In the first series of tests, the cylinder was driven with a shaker attached to the end cap, exciting the "accordion mode" of the structure. Upon applying control and using PVDF sensors, significant levels of global sound attenuation, approximately 25 dB on-resonance and 15 dB off-resonance, were observed in the acoustic field. In both the on-resonance and off-resonance test cases, three control actuators were required to achieve the stated levels of sound attenuation due to interaction between the accordion modes and cylinder modes. In the second series of tests, the cylinder was driven radially with a shaker to excite higher order cylinder modes. Control was applied with six piezoelectric actuators wired to control selected circumferential modes in the first test case, and the actuators were chosen in a helical pattern about the cylinder in the second test case. In the latter case, approximately 10 dB of global sound attenuation was observed in the acoustic field when using microphone error sensors, while results obtained when implementing the PVDF error sensors yielded little sound attenuation in controlling the cylinder modes.

INTRODUCTION

Preliminary studies in active structural acoustic control (ASAC) have been applied to beams and plates configured with piezoelectric actuators and polyvinylidene fluoride sensors [1-7]. In these studies, narrow-band control of structure-borne sound was achieved with piezoelectric actuators surface mounted on the structure, and either microphone or polyvinylidene fluoride (PVDF) error sensors were implemented to generate the appropriate cost function in terms of the acoustic response. A later study conducted by Sumali *et al.*, [8,9] considered active vibration control of both an open ended cylinder and one configured with end caps. Piezoelectric actuators and polyvinylidene fluoride sensors were used to control the vibration and thus the coupled acoustic response of the structure on-resonance for a single mode of vibration.

The thrust of the current work is thus to consider more complex structural acoustic response of a cylinder configured with end caps due to off-resonance excitation as well as

[1]Department of Mechanical Engineering and Materials Science, Duke University, Durham, NC 27708-0300, U.S.A.
[2]Department of Mechanical Engineering, Virginia Polytechnic Institute and State University, Blacksburg, VA 24061, U.S.A.

use an acoustic based cost function. In addition to controlling sound radiation resulting from the vibration response of traditional cylinder modes, the acoustic response due to the accordion modes of the structure is considered in the control approach. Specific goals of this work are:

a. choose appropriate configuration of piezoelectric actuators for control of structure-borne sound.

b. determine appropriate number of control channels required for global sound attenuation.

c. replace microphone error sensors with structural sensors designed from polyvinylidene fluoride.

Details of the experimental configuration are discussed with emphasis on methods of exciting either the accordion modes or the cylinder modes of the structure. In addition, the resonant frequencies of the structure are estimated based upon an approach previously outlined by Blevins [10] and Gorman [11] and also used by Sumali [9]. The control approach is based upon the feedforward, filtered-x, adaptive least mean squares (LMS) algorithm. Details of the algorithm are briefly reviewed. Results from the control approach are discussed as pertains to both the accordion modes and the cylinder modes of the structure. Up to six channels of control were employed with significant levels of attenuation in sound radiation observed when controlling either the accordion modes or the cylinder modes, 30 dB and 10 dB respectively.

BASIC CONCEPTS

A shell configured with two rigid end caps responds to forced excitation in two basic manners. If the end caps are much thicker than the shell wall (i.e. an order of magnitude), then a radial disturbance results in vibration response from classical shell modes similar to that observed with simply supported boundary conditions. On the other hand, if the shell is driven normal to one of the end caps, the vibration response is dominated by the accordion modes of the structure. Vibration resulting from either type of disturbance can result in significant levels of structure-borne sound, and thus both methods of response must be considered for active structural acoustic control.

ACCORDION MODES

The accordion modes of a finite shell with end caps can be very simply modeled by considering two point masses connected by a single spring as illustrated in Figure 1. The spring stiffness of the shell can be crudely approximated based upon the Young's modulus of the material, the area of the cross section and the length of the shell.

$$k_s = \frac{EA}{L}, \tag{1}$$

where k_s is the equivalent spring stiffness, E is the Young's modulus of the shell material, A is the area of the cross-section and L is the length of the cylinder. The mass of each respective end cap is computed from the density of the material and the corresponding volume.

$$M_{cap} = \rho_{cap} V_{cap}, \tag{2}$$

where M_{cap} is the equivalent mass of the end cap, ρ_{cap} is the density of the end cap material and V_{cap} is the volume of the end cap. Other than the rigid body mode, the first mode of vibration appears to oscillate in a similar manner to that of an accordion. Considering the circular shape of the end caps, sound radiation resulting from this method

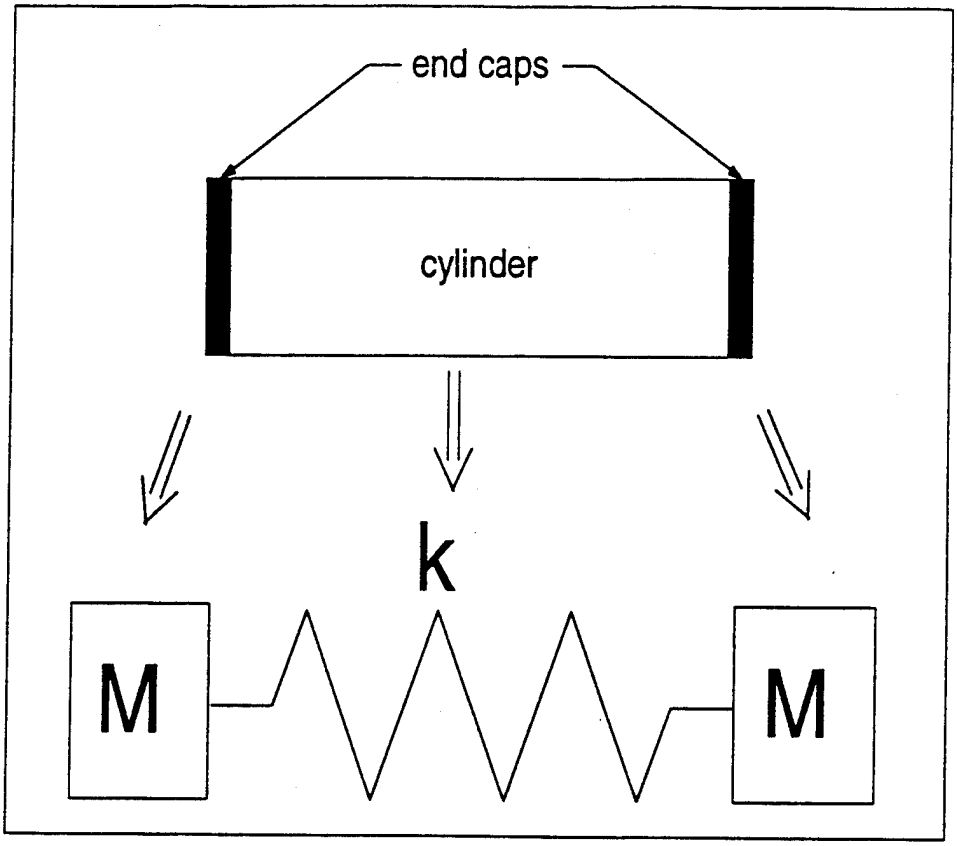

Figure 1: Schematic of simplified mass-spring system

of vibration can be modeled by two circular disks or pistons mounted in each end of a cylindrical baffle.

A more rigorous approach based upon the assumed-modes method [12] and Lagrange's equations was used to approximate the resonant frequencies of the distributed system. Details of the approach are outlined in Appendix A. The shell used in this study was extruded from aluminum having a length of 1.28 m, an outside diameter of 0.254 m and a wall thickness of 2.77 mm. The end caps were machined from aluminum and measured 27.4 mm thick. The first four resonant frequencies of the accordion modes are tabulated below. The resonant frequencies of the first 20 modes were computed to increase the accuracy of the solution; however, only the first four are presented as higher order modes are not relevant in active structural acoustic control since the resonant frequency of the fourth mode is predicted at 5857 Hz.

CYLINDER MODES

The classical cylinder modes of a finite shell with simply supported boundary conditions are illustrated in Figure 2. The circumferential indice is designated with m while the axial indice is designated with n. The order 0 circumferential mode is typically denoted the breathing mode, and the order 1 circumferential mode is denoted the beam-bending mode. The combination of standing waves supported about the circumference of the cylinder and those supported along the axis of the cylinder as illustrated in Figure 2 result in the helical standing wave patterns. A shell with simply supported boundary conditions supports wavenumbers corresponding to the mode shapes of the structure. For example, the structural wavenumbers of a simply supported shell can be expressed

Table 1: Theoretical resonant frequencies of accordion modes.

Mode (#)	Predicted Frequency (Hz)
(1)	981
(2)	1804
(3)	4225
(4)	5857

as follows:

$$k_s = \sqrt{k_m^2 + k_n^2}, \tag{3}$$

where

$$k_m = \frac{m}{a}; \quad m = 0, 1, 2, ... \tag{4}$$

and

$$k_n = \frac{n\pi}{L}; \quad n = 1, 2, 3... \tag{5}$$

For the shell constructed in this experimental study, the end caps were machined from aluminum and attached at the cylinder with 1/8″ bolts. The boundary conditions corresponding to this method of attachment are somewhere between simply supported and clamped. The assumed-modes method can again be implemented in conjunction with Lagrange's equations to estimate the resonant frequencies of the structure. A torsional spring is included in the model of the cylinder at the boundaries to account for the resistance to motion where the cylinder is attached to the end caps. Details of the analysis are presented in Appendix B and reference is given to previous work by Blevins [10] as well as that of Sumali [9] in a similar study.

The stiffness of the torsional spring was chosen such that the first measured resonant frequency of the cylinder matched the predicted resonant frequency. The predicted resonant frequencies for the cylinder are given in Table 2 with the corresponding mode shape numbers. As is apparent from the tabulated values of the resonant frequencies, the structure is modally dense. The term modal density is used in this case to describe structures with resonant frequencies of modes separated by less than 10 Hz. This lack of separation between resonant frequencies results in significant contributions from more than one mode to the structural and acoustic response even for on-resonance excitation. Thus the dimension of the controller must increase to exercise the necessary number of degrees of freedom to control the structural acoustic response of the system.

DETAILS OF THE EXPERIMENT AND CONFIGURATION

The cylinder was configured for active structural acoustic control of sound radiation resulting from cylinder modes as well as the accordion modes. Actuator configurations as well as error sensor arrangements are discussed as pertains to each specific control experiment. The filtered-x adaptive least mean squares (LMS) algorithm was implemented on a TMS320C30 floating point digital signal processing chip to provide up to six channels

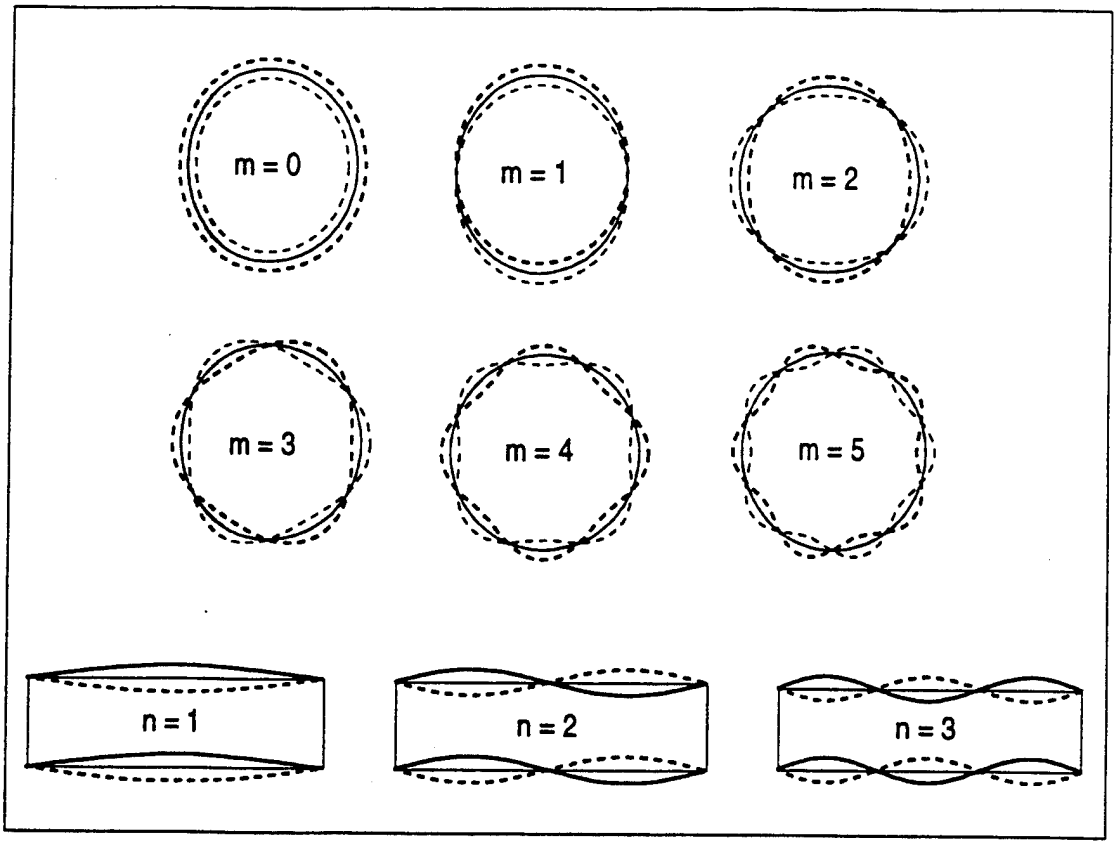

Figure 2: Schematic of shell mode shapes

of control. A schematic diagram of the controller displaying three output channels and three input channels is illustrated in Figure 3. Experiments were limited to narrow band (i.e. single frequency) control, and thus a two coefficient finite impulse response (FIR) filter was utilized as the adaptive filter. The LMS algorithm essentially adapts the coefficients of the FIR filters in the time domain until the control voltage to each piezoelectric actuator is such that the sum of the squares of the chosen error sensors is minimized. This solution has been previously demonstrated to converge to the same result obtained with linear quadratic optimal control [4]. Details of the control algorithm are omitted in the discussion; however, further explanation can be found in a variety of references [13,14,6].

GENERAL CONFIGURATION

All experiments were performed in the anechoic chamber at the Vibration and Acoustics Laboratories at VPI&SU. The chamber measures 4.2 m × 2.2 m × 2.5 m and has a cut-off frequency of 250 Hz. The cylinder was suspended from the ceiling of the chamber with bungee cord, and a picture of the cylinder configured with piezoelectric actuators and circumferential polyvinylidene fluoride (PVDF) sensors is presented in Figure 4. The cylinder was extruded from aluminum and measured 1.28 m long with an outside diameter of 0.254 m and a wall thickness of 2.77 mm. Each end cap was machined from aluminum stock, measuring 27.5 mm thick, and the diameter was machined to match the inner diameter of the cylinder except for a 6 mm shoulder, which had a diameter consistent with the outer diameter of the cylinder. Control actuators were constructed from the 36 piezoelectric elements illustrated on the surface of the cylinder in Figure 3. As indicated in Figure 3, the elements were configured in rings about the circumference

Table 2: Theoretical resonant frequencies of cylinder modes.

Mode (m,n)	Predicted Frequency (Hz)
(2,1)	228
(3,1)	324
(3,2)	415
(1,1)	492
(2,2)	518
(4,1)	591
(3,3)	602
(4,2)	616
(4,3)	684
(4,4)	807
(3,4)	854
(2,3)	882
(5,1)	951
(0,1)	961
(5,2)	962

of the cylinder and 12 elements were placed in ring 1, ring 2 and ring 3 respectively. Each piezoelectric element was equally spaced in 30° increments about the circumference and was wired independently such that the arrangement of the elements could be altered for different actuator configurations. Ring 2 was positioned in the center of the cylinder, and ring 1 and ring 3 were positioned 63.5 mm from each end cap respectively. Each piezoelectric element measured 21.5 mm by 18.5 mm with a thickness of 1.96 mm. The surface of the aluminum cylinder was machined flat at the location of each piezoelectric element. The depth of cut was such that the actuator mounted flat against the cylinder, and the actuator was attached with M-bond 200 adhesive as previously outlined by Clark [15].

Microphone error sensors were implemented in the initial experiments to determine the appropriate number of control channels required for global sound attenuation for an off-resonance disturbance. A schematic diagram of the cylinder is presented in Figure 5 with a coordinate system and corresponding details of the position of each microphone error sensor. As indicated in Figure 5, the microphones were restricted to one sector of the cylinder primarily due to the finite dimension of the chamber with respect to the cylinder dimension. Three of the microphones were placed in the x-y plane of the cylinder, and the other three were placed out of the plane of the cylinder as indicated in the table of Figure 5 for $90° < \theta < 180°$. The acoustic directivity pattern was measured in 9^0 increments in the x-y plane of the cylinder over the same region ($90° < \theta < 180°$) to evaluate the level of sound pressure attenuation. The traversing microphone was controlled with a stepper motor, and the sound pressure was measured at a radius of 1.65 m from the center of the cylinder both before and after applying active structural acoustic control.

The out-of plane vibration response of the cylinder was measured both before and after applying active structural acoustic control with an Ometron VPI scanning laser vibrometer, having a dynamic range of 80 dB and capability of measuring velocity between 0 and

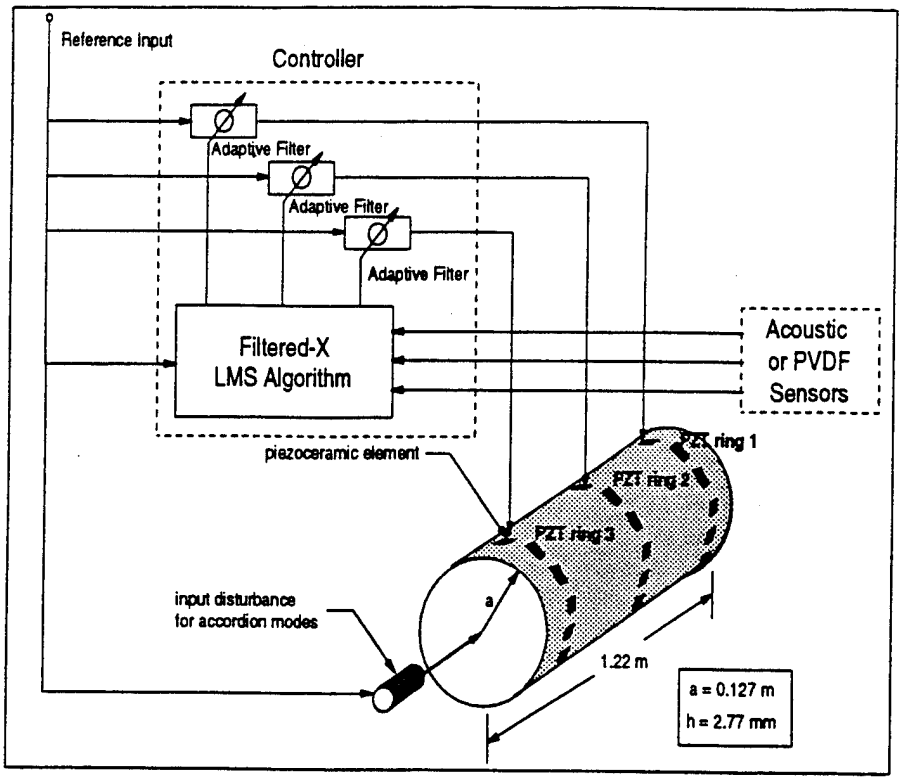

Figure 3: Schematic of filtered-x LMS control approach

1 m/s [18]. These measurements were made to compensate for the lack of detailed information concerning the measured resonant frequencies and mode shapes of the cylinder. In general, agreement between the predicted and measured resonant frequencies of the cylinder were within 5% for the first five modes of the structure. However, the deviation increased with increasing frequency. This deviation is a result of the mass loading of the cylinder due to the actuators and sensors as well as the discontinuities in the cylinder resulting from machining flat positions on the surface for mounting the control actuators. In addition, the cylinder was extruded from aluminum, and thus variations in wall thickness and eccentricities in the circumference were observed. In performing the scan, a grid of 100 points along the axis of the cylinder and 10 points about the circumference was utilized to obtain qualitative and quantitative information about the structural response before and after applying control.

In all test cases performed, control was achieved with actuators constructed from piezoceramic elements. The specific configurations of each of the piezoceramic elements for controlling the cylinder modes or accordion modes are detailed in the following sections. The positions and dimensions of the corresponding PVDF sensors selected for each specific control application are detailed as well.

ACTUATORS AND SENSORS FOR ACCORDION MODES

A schematic diagram of the cylinder configured with PVDF [16] sensors for active structural acoustic control of the accordion mode response is presented in Figure 6. As indicated, the input disturbance, which consisted of a shaker attached by a stinger, was mounted on the center of the end cap external to the cylinder. (Measurements of sound

Figure 4: Picture of cylinder in anechoic chamber

radiation from the shaker detached from the cylinder were 40 dB below that of the uncontrolled cylinder at the error microphones and traversing microphone coordinates. Thus the overall contribution to the global sound radiation was within the noise floor of the control system.) The PVDF sensors were cut in rectangular elements measuring 0.5 m long $\times$ 25.4 mm wide $\times$ 28 μm thick. The sensors were positioned about the circumference of the cylinder in increments of 120° and were centered between ring 2 and ring 3 of the piezoelectric elements as illustrated in Figure 6. The accordion response of the cylinder is dominated by extension and contraction over the length of the cylinder. Thus the PVDF sensors were positioned to respond primarily to strain along this axis. Only three sensors were implemented since three channels of control proved sufficient for attenuating the global acoustic response of the cylinder when responding in the accordion mode. The cost function for the control algorithm was thus formed from the sum of the squares of the electrical output of each of the PVDF sensors.

The control actuators were arranged as illustrated in the top portion of the schematic diagram of Figure 7. The shaded markers are utilized to represent the piezoelectric elements at ring 1, ring 2 and ring 3 which were electrically wired in phase at each respective ring to elicit extension and contraction of the cylinder. The entire ring of piezoelectric elements can be electrically wired in phase to create a control actuator if so desired; however, no discernible performance advantage was observed with either actuator configuration. The actuator arrangement illustrated in the top portion of Figure 7 was chosen since it was based upon one of the configurations used in controlling the cylinder modes. In light of the fact that actuators will likely be configured for multiple applications (i.e. control of accordion modes or cylinder modes), one of the actuator arrangements used in control of the cylinder modes was implemented for control of the

Microphone	r (m)	θ (deg.)	z (m)
1	1.67	90	0.000
2	1.67	108	0.286
3	1.67	126	-0.413
4	1.67	135	0.000
5	1.67	171	0.273
6	1.67	180	0.000

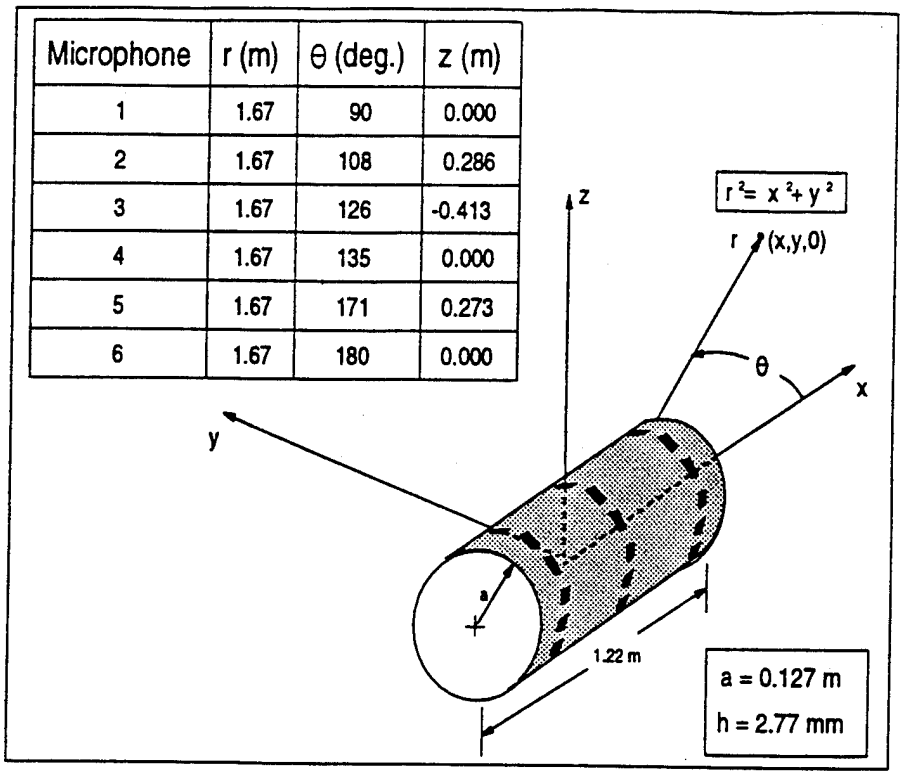

Figure 5: Schematic diagram of cylinder with microphone coordinates

accordion modes to demonstrate that the configuration could serve a dual purpose.

ACTUATORS AND SENSORS FOR CYLINDER MODES

A schematic diagram of the cylinder configured with PVDF sensors and piezoelectric actuators for active structural acoustic control of the cylinder modes is presented in Figure 8. As illustrated in the figure, the input disturbance was positioned in the x-y plane of the cylinder and was located 0.343 m from the end cap nearest ring 3 with respect to the coordinate system illustrated in Figure 5. The radial input disturbance was achieved with a shaker attached by a stinger and suspended from the ceiling of the chamber with a bungee cord external to the cylinder. The acoustic response of the shaker was 40 dB below that of the uncontrolled cylinder response and was thus in the noise floor of the instrumentation with respect to the controller. The PVDF sensors were shaped with respect to the dominant circumferential modes of the cylinder illustrated in the top portion of Figure 1. The sensors were designed in pairs corresponding to $m = 3$, $m = 4$ and $m = 5$ modal indices. The structural response of the cylinder resulting from modes with these circumferential indices were dominate over the chosen frequency range for testing (i.e. between 900 Hz and 1500 Hz). One each of the $m = 3$, $m = 4$ and $m = 5$ PVDF sensors was positioned such that a spatial anti-node of the sensor was located on the top surface of the cylinder with respect to Figure 5. The matching sensor was positioned adjacent to each respective circumferential mode sensor and was shifted spatially by 90° to eliminate rotation of the modes with respect to the cylinder under control conditions. The sensors were located 0.152 m from the end cap nearest ring 1 as illustrated in Figure 8 and measured 19 mm wide each. The number above each respective sensor illustrated in Figure 8 is used to designate the circumferential modal

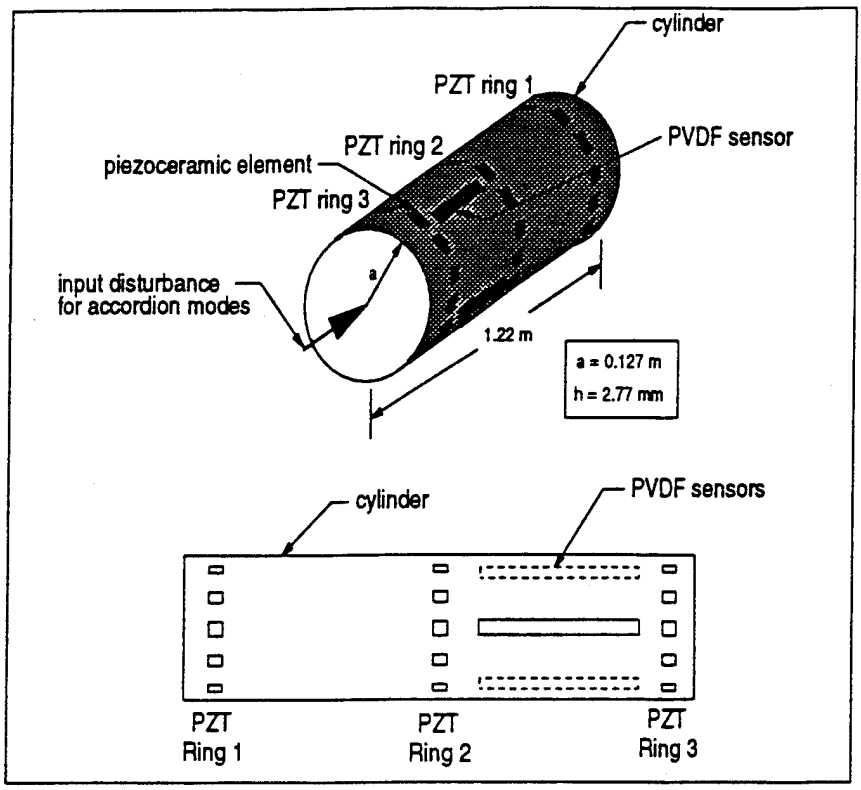

Figure 6: Schematic diagram of cylinder configured for accordion modes

indice that the sensor was designed to observe. The sensors were placed side by side but were electrically isolated from each other except for a common ground which was necessary to reduce noise due to electric fields. The cost function was thus the sum of the squares of the electrical response of all 6 PVDF sensors in the control approach. The output of each sensor was conditioned such that the electrical response was of the same order of magnitude for each of the sensors implemented. An important aspect of this approach is that the sensor design does not account for modal coupling between cylinder modes with common circumferential modal indices, and thus coupling between modes with the same circumferential indices but different axial indices can result.

The control actuators for active control of the cylinder modes are illustrated in the bottom portion of Figure 7. Two sets of actuators were compared in the experiment. The first set of 6 actuators, denoted the "modal actuators", were configured to control the third, fourth and fifth circumferential modes of the cylinder as illustrated in Figure 7. Piezoelectric elements at each ring were electrically wired together to create a single actuator and these elements are illustrated with black markers and white markers at each respective ring. The numbers at each ring of the modal actuators presented in Figure 7 are used to define each of the 6 independent control actuators implemented. The number is positioned by a dark marker or a light marker, and all like colored markers at each respective ring were electrically wired in phase to form a single actuator.

The second set of control actuators are denoted the "helical actuators" due to the chosen arrangement. The actuators were not electrically wired to specifically drive the helical waves on the cylinder. The term "helical" was chosen since each actuator pair utilized was indexed by 60° along the axis of the cylinder, visually flowing in a helical pattern

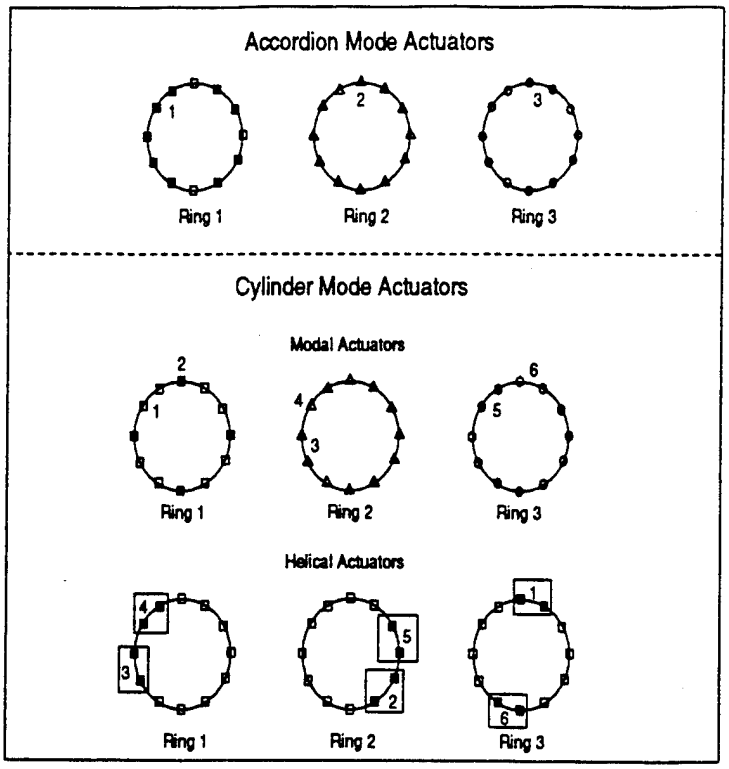

Figure 7: Schematic diagram of control actuator configurations

as illustrated in the bottom portion of Figure 7. The structural response of the cylinder supports helical standing waves, and thus an actuator configuration was chosen which allowed as much flexibility in both the circumferential and axial direction as possible. Piezoelectric elements were wired together in pairs at each respective ring of the cylinder and were alternated as a function of the axial position as is readily observed when visually scanning the lower portion of Figure 7 from right to left (actuators 1-3) and then from left to right (actuators 4-6). The piezoelectric elements represented by the white markers were not utilized in this particular configuration.

The basic configurations for control will be hence forth designated the accordion mode configuration and the cylinder mode configuration. The exception being that in the cylinder mode configuration, two separate actuator arramgememts were considered, the modal actuators and the helical actuators. All experimental results presented are based upon the basic configurations discussed in this section.

RESULTS

Results from active structural acoustic control of the accordion mode are presented first with both on-resonance and off-resonance input disturbances at one of the end caps as discussed in the previous section. Emphasis is placed upon results for off-resonance excitation due to the interaction of various structural modes. Thus, in the case of active structural acoustic control of the cylinder modes, only off-resonance excitation test cases are presented. Greater demands are placed upon the controller for off-resonance excitation since the number of degrees of freedom required to control the system are proportional to the number of modes contributing to the structural acoustic response if

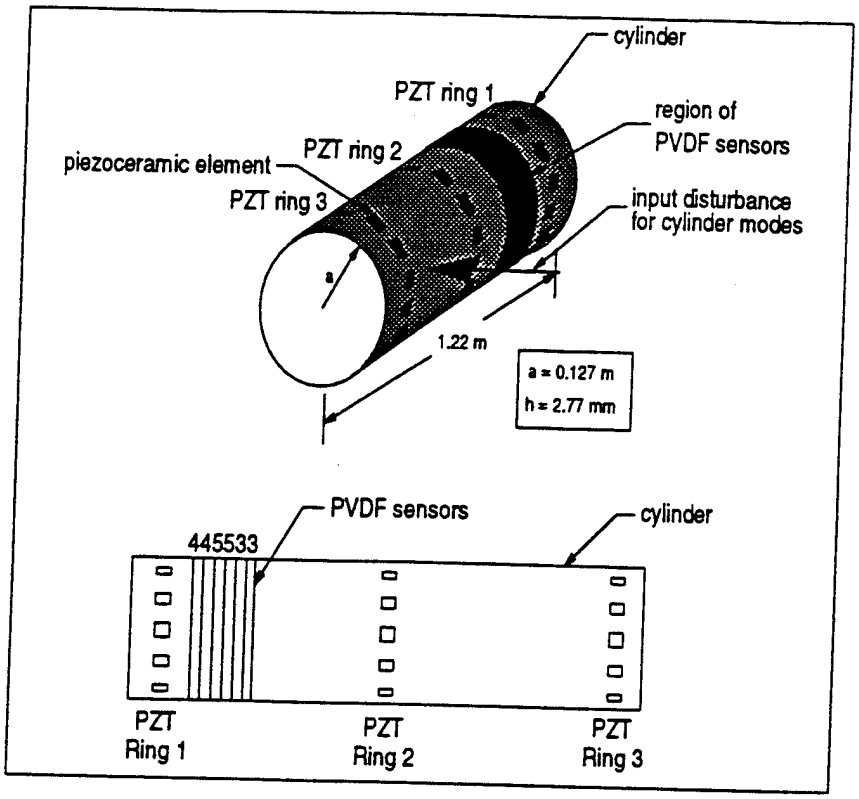

Figure 8: Schematic diagram of cylinder configured for cylinder modes

the controller is to be effective over a broad range of frequencies. On the other hand, if the controller is to be designed to operate on a specific frequency of the disturbance, then the number of control channels can be reduced by optimizing the position of the actuator with respect to the structure and thus increase the controllability of the system [5].

RESULTS FROM CONTROL OF ACCORDION MODE

The configuration of the cylinder for control of the accordion mode was discussed in the previous section. The first resonant frequency of the accordion mode was observed at an excitation frequency of 958 Hz. Multiple test cases were conducted at various frequencies of excitation; however, two representative sets of results are presented here for both on and off-resonance excitation. In the case of on-resonance excitation, the end cap of the cylinder was driven at 958 Hz and control was achieved implementing the 6 error microphones and 3 piezoelectric control actuators. The reader is reminded here that "actuator" means an array of hard wired individual piezoelectric elements as described in the previous section. All 6 error microphones were utilized to construct the cost function to ensure global attenuation in the sound field. Results from this test are presented in Figure 9. The acoustic response was assumed symmetric, and thus measurements were obtained between $\theta = 90°$ and $\theta = 180°$ only. The dark solid line represents the acoustic response before control as indicated in the legend, and the dashed line represents the controlled acoustic response when implementing the microphone error sensors as also indicated in the legend. Observe that the sound pressure was attenuated by approximately 40 dB in the acoustic field near the end cap and by at least 15 dB in the remainder of the acoustic field displayed. (Acoustic attenuation on the order of 15 dB was observed at various

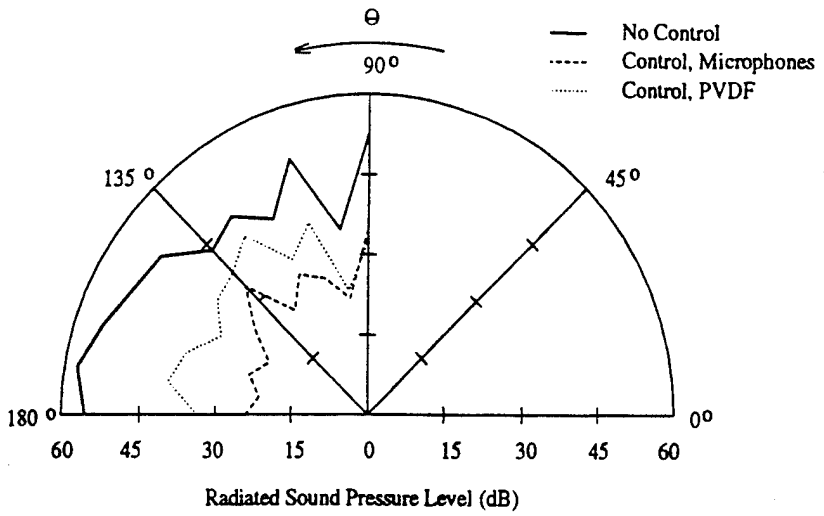

Figure 9: Control of accordion mode on-resonance (958 Hz)

other acoustic field points out of the plane of the traversing microphone.) Attenuation at each of the 6 microphone coordinates used as error sensors was on the order of 40 dB.

The dotted line displayed in Figure 9 represents the control case when implementing the 3 PVDF error sensors in the control approach with the same 3 control actuators. The response of each respective PVDF sensor was attenuated by approximately 50 dB upon achieving control, and the acoustic response of the structure was minimized on the order of 25 dB at the end cap and between 5 dB and 10 dB in the remainder of the acoustic field. The discrepancy in performance of the controller when implementing the PVDF sensors as opposed to the microphone sensors is proposed to be an artifact of the interaction between the accordion mode and the cylinder modes at the frequency of excitation. Referring back to table 2, the resonant frequencies of the (5,1), (0,1) and (5,2) cylinder modes were all within 7 Hz of the excitation frequency. Results obtained from the scanning laser vibrometer for this test case were suppressed since the radial response of the cylinder was in the noise floor of the instrumentation when driving the accordion modes of the cylinder. However, the vibration response of the end cap was monitored with an accelerometer and levels of attenuation were proportional to that observed in the acoustic field.

The off-resonance test case for the accordion mode excitation was conducted at an input disturbance frequency of 930 Hz. The acoustic directivity patterns for the uncontrolled and controlled acoustic response are presented in Figure 10. Again the uncontrolled response is represented by the dark solid line in Figure 10. The dashed line represents control of the structural acoustic response with the 6 error microphones discussed previously and the 3 piezoelectric control actuators. The dotted line illustrates the acoustic directivity pattern achieved upon minimizing the response at the 3 PVDF error sensors with the same three control actuators. In this test case, the performance of the two control approaches was very similar with between 15 dB and 20 dB of attenuation in the acoustic field near the end cap and between 5 dB and 10 dB in the remainder of the acoustic field. (Acoustic attenuation on the order of 6 dB was observed at various other acoustic field points out of the plane of the traversing microphone.) The vibra-

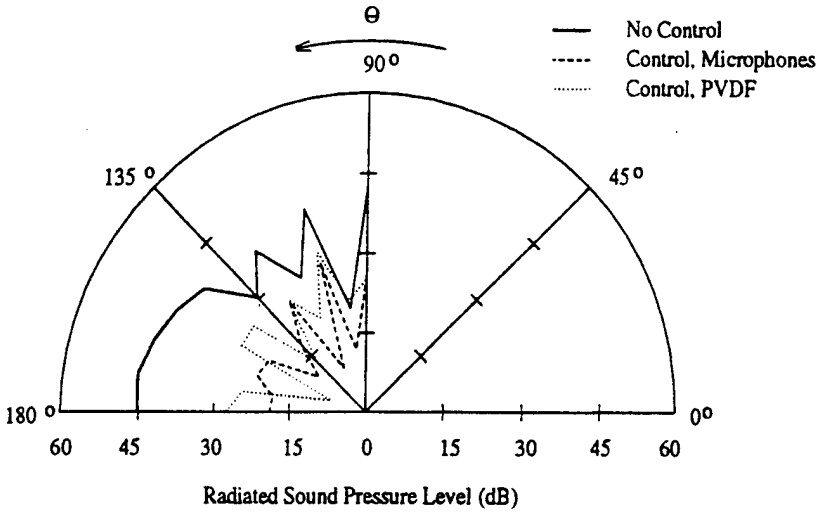

Figure 10: Control of accordion mode off-resonance (930 Hz)

tion response of the end cap was again monitored with an accelerometer and levels of attenuation were proportional to levels of sound attenuation measured at the end cap. The consistency between the controlled response when implementing either microphone or PVDF error sensors in this test case stems from the observation that the excitation frequency is well away from any resonant frequencies corresponding to the cylinder modes of the structure as can be observed in Table 2. Thus very little interaction occurs between the accordion mode of the structure and the cylinder modes at the chosen frequency of excitation.

RESULTS FROM CONTROL OF CYLINDER MODES

The structural acoustic response of the cylinder modes was controlled with two different actuator configurations. As discussed earlier, one configuration was denoted the modal actuators and the other was denoted the helical actuators. The two configurations were based upon the physics of the structural response which can be represented in modal coordinates or in terms of traveling waves. The helical actuator configuration was observed to yield better results when implemented with microphone error sensors in terms of the controlled structural acoustic response and thus were utilized in conjunction with the PVDF sensors for active structural acoustic control. Results from two representative off-resonance test cases are presented below.

In the first test case, the cylinder was driven at an excitation frequency of 1090 Hz, which is between the predicted resonant frequencies of the (1,2) and (4,6) modes of the cylinder. The acoustic directivity pattern for the uncontrolled and controlled response is presented in Figure 11. The dark solid line represents the acoustic response before applying control while the dashed line represents the structural acoustic control with the 6 helical actuators and the 6 microphones outlined in the previous section. As illustrated in Figure 11, very little attenuation was obtained in the vicinity of the end caps; however, between 15 dB and 20 dB of sound attenuation was observed in the remainder of the acoustic field. (Acoustic attenuation at field points out of the plane of the traversing microphone was on the order of 15 dB in general.) The "notches" in the directivity pattern correspond

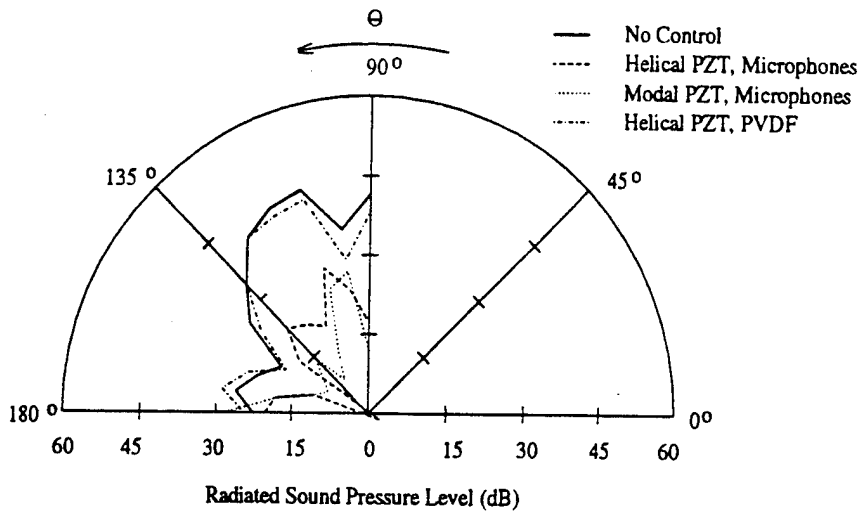

Figure 11: Control of cylinder modes off-resonance (1090 Hz)

to coordinates where error microphones were positioned.

Similar results were obtained when implementing the modal actuators as is illustrated by the directivity pattern represented by the dotted line in Figure 11. The last test case at this excitation frequency was conducted implementing the helical actuators in conjunction with the 6 modal PVDF sensors discussed in the previous section. The structural response at the PVDF error sensors was minimized by approximately 50 dB; however, little if any attenuation was observed in the acoustic field. The sensors were thus ineffective for active structural acoustic control in this case. Lack of control with the chosen PVDF sensors is thought to result from the relatively high modal density and the interaction between modes with the same circumferential modal indice but different axial modal indices. For example, the vibration response of the (5,4) mode, the (5,3) mode and the (5,1) mode can be phased to minimize the response of the PVDF sensors without actually attenuating the total response of each respective mode of vibration.

The velocity contour corresponding to the real part of the uncontrolled and controlled response with the helical actuators and the microphone error sensors is presented in Figure 12. Approximately one quarter of the circumference of the cylinder was scanned as is indicated in Figure 12. This is the largest region that could be accurately scanned since the laser vibrometer measures only the normal velocity of the cylinder. The measured response must be corrected to account for the angle of incidence on the surface of the cylinder with respect to the curvature. The profile of the cylinder is represented by the dark line surrounding the contour plot. Regions characterized by a dark or light rectangular discontinuity result from erroneous measurements obtained when the laser scanned across an electrical wire of one of the actuators or one of the microphone stands which were between the laser and the structure. These data points are out of bounds with respect to the scaled response of the cylinder; however editing them from the data set was virtually impossible since 1000 data points were scanned. The characteristic most apparent in the plot is that before control, lower order structural modes dominate the response. However, upon applying control, the structural response shifts to higher order structural modes as is evident upon comparing the contour plots in Figure 12. The

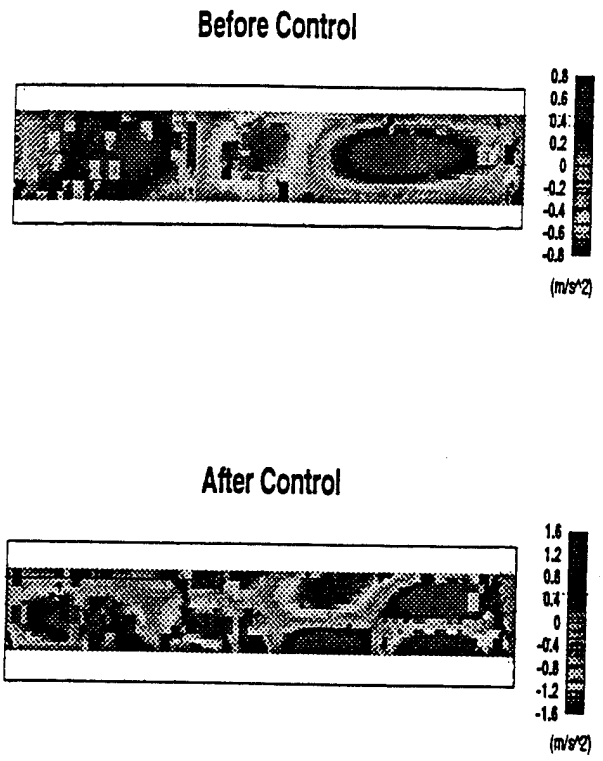

Figure 12: Velocity contour from scanning laser vibrometer (1090 Hz)

surface velocity amplitude also increased by around a factor of 2 upon applying control while the sound radiation decreased. This decrease in acoustic response results from what has previously been termed "modal restructuring" [2,4,5]. The higher order structural modes are less efficient acoustic radiators and thus even with an increase in the structural response, the acoustic response of the structure decreased. This important result distinguishes the work presented in this paper, which is devoted to *active structural acoustic control* (ASAC), from previous research devoted to active vibration control (AVC) [8,9] as a method of controlling sound radiation. The plot presented is representative of the results obtained with the scanning laser vibrometer in other off-resonance test cases.

The final test case presented was obtained for an excitation frequency of 1460 Hz. Results from the structural acoustic response are presented in the directivity patterns of Figure 13. The uncontrolled response is represented by the solid line as indicated in the legend, while the controlled response for the helical actuators and modal actuators in conjunction with the microphone error sensors is represented by the dashed line and dotted line respectively. Between 5 and 10 dB of attenuation in sound pressure was observed when implementing the helical actuators in conjunction with the microphone error sensors. However, when implementing the modal actuators, the acoustic response was observed to increase on the order of 5 dB in the region near the end cap of the cylinder. Due to the high modal density and choice of off-resonance excitation frequency, the level of acoustic attenuation was limited in both test cases. This result is representative of tests performed at arbitrary excitation frequencies in this frequency range. As observed in previous studies conducted with piezoelectric actuators on a simply supported plate, the structural acoustic response can be further attenuated by increasing the number of control channels or by optimizing the positions of the control actuators to reduce the

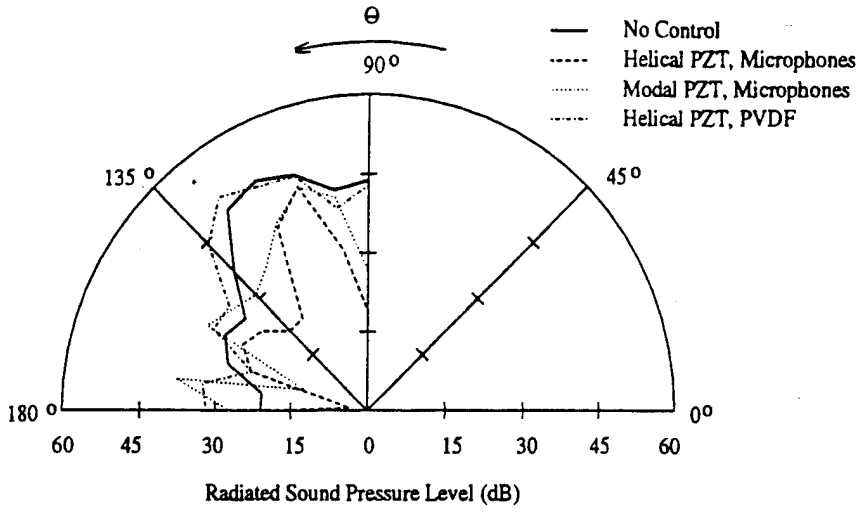

Figure 13: Control of cylinder modes off-resonance (1460 Hz)

dimension of the controller with similar performance gains [5].

While the response at each of the 6 PVDF sensors were attenuated by approximately 50 dB upon applying control with the helical actuators, the structural acoustic response of the cylinder actually increased as illustrated by the dash-dotted line in Figure 13. Based upon the high modal density and the interaction between structural modes, this result is not surprising. The modes were simply rearranged to minimize the response at the PVDF error sensor locations without actually attenuating the magnitude of the desired circumferential modes. As previously discussed, two or more modes with the same circumferential modal indice and different axial modal indices, for example the (3,3) and the (3,4) modes, can be appropriately phased to minimize the response of the sensors designed for the respective circumferential modes without actually attenuating the vibration response and resulting acoustic response of each respective mode.

CONCLUDING DISCUSSION

Results from this study demonstrate that the exterior acoustic response of an enclosed cylinder excited by a point force disturbance is dependent upon both the accordion modes of the structure and the cylinder modes. Significant levels of sound attenuation (between 15 dB and 30 dB) were observed upon controlling the fundamental accordion mode. The structural acoustic response of this mode is relatively easy to control with piezoelectric actuators and PVDF error sensors in conjunction with a feedforward controller, even with very little a-priori design other than a basic understanding of the physics of the problem. Success in this control case results from the fact that there is very little interaction between each of the accordion modes since the resonant frequency of the first and second mode are separated by approximately 820 Hz. Some interaction between the accordion mode and the cylinder modes occurs, explaining the necessity of three control channels for the on-resonance and off-resonance test cases.

The cylinder modes of the structure were in general more difficult to control than the accordion modes, primarily due to the high modal density in the region of excitation (1000

Hz to 1500 Hz). Theory predicts 16 distinct modes within this region of excitation. When implementing microphone error sensors in conjunction with the piezoelectric actuators configured in the helical pattern on the structure, the structural acoustic response was attenuated between 5 dB and 10 dB in the residual field for a six-input/six-output controller. Results when implementing piezoelectric actuators configured to couple with selected circumferential modes were not as promising, suggesting that the actuator positions should be designed from a wave approach as opposed to a modal approach.

The modal PVDF sensors which were designed to observed the primary circumferential modes dominant in the structural response over the frequency range of excitation were totally ineffective for active structural acoustic control. Thus the emphasis of future work should be devoted to methods of designing more sophisticated structural sensors for active structural acoustic control. Some preliminary work in this area is currently underway and shows much promise for such applications [17]. In terms of the control actuators, one is faced with the decision of design optimization or increasing the dimensionality of the controller. This question is ultimately determined by the speed of the control system and the general complexity in modeling the structural acoustic response of the system. If the necessary throughput of the control system is not compromised for the desired application by increasing the number of control channels, then this is obviously the easiest solution. However, if system throughput is a constraint, then optimal design is a viable alternative for increasing the overall performance gains without sacrificing the frequency range of operation.

ACKNOWLEDGEMENTS

The authors gratefully acknowledge the support of this work by the Office of Naval Research under grant ONR-N00014-92-J-1170. The authors acknowledge Jeff Vipperman for implementing the control algorithm on the TMS320C30 digital signal processor, and Al Wicks for providing the Ometron scanning laser vibrometer.

APPENDIX A: ASSUMED MODES METHOD FOR ACCORDION MODES

The resonant frequencies of the accordion modes of the cylinder configured with two end caps were estimated based upon the assumed modes method in conjunction with Lagrange's equations. Expressions for the kinetic energy and potential energy including the mass of each respective end cap are presented as follows:

$$T(t) = \frac{1}{2}\int_0^L m(x)\left[\frac{\partial y(x,t)}{\partial t}\right]^2 dx + \frac{1}{2}M_0\left[\frac{\partial y(0,t)}{\partial t}\right]^2 + \frac{1}{2}M_L\left[\frac{\partial y(0,t)}{\partial t}\right]^2, \tag{6}$$

and

$$V(t) = \frac{1}{2}\int_0^L EA\left[\frac{\partial y(x,t)}{\partial x}\right]^2 dx \tag{7}$$

where $m(x)$ is the mass of the cylinder per unit length, $y(x,t)$ is the displacement of the cylinder along the axis, M_0 and M_L are the point mass equivalents of the end caps at position 0 and position L respectively and EA is the product of the Young's modulus and the area of the cylinder cross-section.

Expressing the system response in modal coordinates,

$$y(x,t) = \sum_{m=1}^{M} \phi_m(x) q_m(t), \tag{8}$$

where $\phi_m(x)$ is the assumed mode shape and $q_m(t)$ are the modal coordinates. Lagrange's equations can be expressed in terms of the modal coordinates as follows:

$$\frac{d}{dt}\left(\frac{\partial T}{\partial \dot{q}_m}\right) - \frac{\partial T}{\partial q_m} - \frac{\partial V}{\partial q_m} = 0; \quad m = 1, 2, ..., M \tag{9}$$

Substituting equation (8) into equations (6) and (7) and substituting the resulting expressions into Lagrange's equations yields the following expression:

$$\sum_{n=1}^{M} m_{mn}\ddot{q}_n(t) + \sum_{n=1}^{M} k_{mn}q_n(t) = 0; \quad m = 1, 2, ...M \tag{10}$$

where

$$q_n(t) = a_n \cos(\omega t - \psi), \tag{11}$$

$$m_{mn} = \int_0^L m(x)\phi_m(x)\phi_n(x)dx + M_0\phi_m(0)\phi_n(0) + M_L\phi_m(L)\phi_n(L), \tag{12}$$

$$k_{mn} = \int_0^L EA\frac{d\phi_m(x)}{dx}\frac{d\phi_n(x)}{dx}dx, \tag{13}$$

a_n is a constant coefficient, ω is the circular frequency and ψ is the phase.

If we choose the admissible functions to be that of a structure with free-free boundary conditions, then

$$\phi_m(x) = cos(\frac{m\pi x}{L}). \tag{14}$$

Substituting equation (14) into equations (12) and (13) results in the following expression for the elements of the mass and stiffness matrix:

$$m_{mn} = \frac{\rho AL}{2}\delta_{mn} + M_0 + M_L(-1)^m(-1)^n. \tag{15}$$

$$k_{mn} = EA\frac{mn\pi^2}{2L}\delta_{mn}. \tag{16}$$

Solving the following eigenvalue problem yields the resonant frequencies of the system and the mode shapes as a function of the assumed admissible functions.

$$[k]a = \omega^2[m]a. \tag{17}$$

A number of numerical routines are available for solving this problem.

APPENDIX B: ASSUMED MODES METHOD FOR CYLINDER MODES

The boundary conditions of the cylinder used in this study range somewhere between that of clamped-clamped and simply supported-simply supported at each end of the cylinder. For such boundaries, the resistance to rotation at the boundaries can be modeled with a torsional spring to approximate the physical boundary conditions realized upon bolting the cylinder to the end caps with small bolts about the circumference of the cylinder. A similar approach was utilized to account for discrepancies between measured and predicted resonant frequencies for a plate with approximate simply supported boundary conditions by the authors [15]. The following analysis is based upon a procedure outlined by Blevins [10] and Gorman [11] and was previously assembled by Sumali in his thesis [9]. The overall procedure for approximating the resonant frequencies and corresponding mode shapes of the cylinder are reviewed here. However, the reader is referred to the previous references for greater detail.

The Flugge shell theory can be expressed in terms of the following equations of motion:

$$\begin{aligned}
\epsilon_x &= \frac{\partial u}{\partial x} - z\frac{\partial^2 w}{\partial x^2} \\
\epsilon_\theta &= \frac{1}{R}\frac{\partial v}{\partial \theta} - \frac{z}{R(R+z)}\frac{\partial^2 w}{\partial \theta^2} + \frac{w}{R+z} \\
\epsilon_{x\theta} &= \frac{1}{R+z}\frac{\partial u}{\partial \theta} + \frac{R+z}{R}\frac{\partial v}{\partial x} - \frac{\partial^2 w}{\partial x \partial \theta}\left(\frac{z}{R} + \frac{z}{R+z}\right) \\
\epsilon_{xz} &= \epsilon_{\theta z} = \epsilon_{zz} = 0,
\end{aligned} \tag{18}$$

where u is the displacement in the x-direction (i.e. along the cylinder length), v is the displacement about the circumference of the cylinder in the θ-direction, w is the displacement in the z-direction which is normal to the surface of the cylinder, R is the radius of the cylinder in the mid-plane and ϵ is used to designate strain with subscripts to indicate direction. Greater detail of the equations of motion and coordinate system can be found in the references [9-11].

The assumed solution for the above set of equations of motion are as follows:

$$\begin{aligned}
u &= A\tilde{\phi}_n'(x/L)cos(m\theta)cos(\omega t) \\
v &= B\tilde{\phi}_n(x/L)cos(m\theta)cos(\omega t) \\
w &= C\tilde{\phi}_n(x/L)cos(m\theta)cos(\omega t)
\end{aligned} \tag{19}$$

where $m = 0, 1, 2, ..., M$ and $n = 1, 2, 3, ..., N$ with M and N dictating the number of modes included in the solution. The x-direction mode shape, $\tilde{\phi}_n(x/L)$, is dependent upon the boundary conditions of the structure. Gorman [11] previously demonstrated that a torsional spring could be included in the assumed mode shape if the following expression was applied:

$$\begin{aligned}
\tilde{\phi}_n(x/L) = {} & \sin(\gamma_n x/L) - \sinh(\gamma_n x/L) + \Lambda_n[\cos(\gamma_n x/L) - \cosh(\gamma_n x/L) \\
& -\frac{2\gamma_n}{T_1}\sinh(\gamma_n x/L)],
\end{aligned} \tag{20}$$

where

$$\Lambda_n = \frac{\sinh(\gamma_n) - \sin(\gamma_n)}{\cos(\gamma_n) - \cosh(\gamma_n) - \frac{2}{T_1}\sinh(\gamma_n)}, \tag{21}$$

$$T_1 = \frac{k_T L}{EI} \tag{22}$$

and k_T is the torsional spring stiffness used in the model. The characteristic equation for the above assumed solution can be expressed as follows [9]:

$$T_1^2 + 2T_1 \frac{\sin(\gamma_n)\cosh(\gamma_n) - \cos(\gamma_n)\sinh(\gamma_n)}{1 - \cos(\gamma_n)\cosh(\gamma_n)} + \frac{2\gamma_n^2 \sin(\gamma_n)\sinh(\gamma_n)}{1 - \cos(\gamma_n)\cosh(\gamma_n)} = 0. \tag{23}$$

By choosing a value for T_1, the roots of the characteristic equation, γ_n, can be computed and thus the corresponding mode shape. This mode shape can then be utilized to solve for the eigenvalues of the cylinder with the chosen torsional spring constant by substituting the assumed solutions for the response into the equations of motion and solving the following characteristic equation which results from the determinant of the equations expressed in matrix form.

$$\begin{aligned}\alpha_2\lambda^6 - \lambda^4(a_{11} + \alpha_2(a_{22} + a_{33})) - \lambda^2(a_{12}^2 + a_{13}^2 + \alpha_2(a_{23}^2 - a_{22}a_{33}) - a_{11}a_{33} - a_{11}a_{22}) \\ + a_{12}^2 a_{33} + a_{23}^2 a_{11} + a_{13}^2 a_{22} - a_{11}a_{22}a_{33} - 2a_{12}a_{23}a_{13} = 0\end{aligned} \tag{24}$$

where

$$\lambda = \omega R[\mu(1 - \nu^2)/E]^{1/2}, \tag{25}$$

$$a_{11} = \beta_n^2 + \frac{1}{2}(1 + k)(1 - \nu)m^2\alpha_2, \tag{26}$$

$$a_{12} = -\nu m\beta_n\alpha_1 - \frac{1}{2}(1 - \nu)m\beta_n\alpha_2, \tag{27}$$

$$a_{13} = -\nu\beta_n\alpha_1 + k\beta_n[-\beta_n^2 + \frac{1}{2}(1 - \nu)m^2\alpha^2], \tag{28}$$

$$a_{22} = m^2 + \frac{1}{2}(1 + 3k)(1 - \nu)\beta_n^2\alpha_2, \tag{29}$$

$$a_{23} = m + km\beta_n^2[\nu\alpha_1 + \frac{3}{2}(1 - \nu)\alpha_2], \tag{30}$$

$$a_{33} = 1 + k[\beta_n^4 + (m^2 - 1)^2 + 2\nu m^2\beta_n^2\alpha_1 + 2(1 - \nu)m^2\beta_n^2\alpha_2], \tag{31}$$

$$\beta_n = \gamma_n R/L, \tag{32}$$

$$k = \frac{h^2}{12R^2}, \tag{33}$$

$$\alpha_1 = \frac{-1}{L}\int_0^L \tilde{\phi}_n''(x)\tilde{\phi}_n(x)dx, \tag{34}$$

$$\alpha_2 = \frac{1}{L}\int_0^L [\tilde{\phi}_n'(x)]^2 dx \tag{35}$$

and the $'$ indicates a derivative with respect to $\gamma_n x/L$. The solution of the previous set of equations yields the corresponding eigenvalues of the system. The torsional spring stiffness constant T_1 can be adjusted until the resonant frequency of the first mode matches that measured for the real structure.

REFERENCES

1. Clark, R.L. and C.R. Fuller, 1991. "Control of Sound Radiation with Adaptive Structures," *Journal of Intelligent Material Systems and Structures*, **2**(3):431-452.

2. Clark R.L. and C.R. Fuller, 1992. "Modal Sensing of Efficient Acoustic Radiators with Polyvinylidene Fluoride Distributed Sensors in Active Structural Acoustic Approaches," *Journal of the Acoustical Society of America*, **91**(6):3313-3320.

3. Clark R.L. and C.R. Fuller, 1992. "Experiments on Active Control of Structurally Radiated Sound Using Multiple Piezoceramic Actuators," *Journal of the Acoustical Society of America*, **91**(6):3321-3329.

4. Clark, R.L. and C.R. Fuller, 1992. "Active Structural Acoustic Control with Adaptive Structures Including Wavenumber Considerations," *Journal of Intelligent Material Systems and Structures*, **3**(2):296-315.

5. Clark, R.L. and C.R. Fuller, 1992. "Optimal Placement of Piezoelectric Actuators and Polyvinylidene Fluoride Error Sensors in Active Structural Acoustic Control Approaches," *Journal of the Acoustical Society of America*, **92**(3):1521-1533.

6. Clark, R.L. and C.R. Fuller, 1992. "A Model Reference Approach for Implementing Active Structural Acoustic Control," *Journal of the Acoustical Society of America*, **92**(3):1534-1544.

7. Clark, R.L., C.R. Fuller and R.A. Burdisso, 1992. "Design Approaches for Shaping Polyvinylidene Fluoride Sensors in Active Structural Acoustic Control," proceedings of *Recent Advances in Adaptive and Sensory Materials and their Applications*, C.A. Rogers and R.C. Rogers, ed. Lancaster, Technomic Publishing Company, Inc., pp. 702-728.

8. Sumali, Hartono, H. Cudney and J. Viperman, 1991. "Vibration Control of Cylinders Using Piezoelectric Sensors and Actuators," proceedings of *Conference on Active Materials and Adaptive Structures*, Gareth Knowles, ed., Philadelphia, PA, Institute of Physics Publishing Company, pp. 467-472.

9. Sumali, Hartono, April, 1992. "Demonstration of Active Structural Acoustic Control of Cylinders," Master of Science Thesis, Virginia Polytechnic Institute and State University.

10. Blevins, R.D., 1984. *Formulas for Natural Frequency and Mode Shape*, Krieger Publishing Company, Florida, pp. 291-336.

11. Gorman, D.J., 1975. *Free Vibration Analysis of Beams and Shafts*, Wiley, New York, p. 31.

12. Meirovitch, L., 1967. *Analytical Methods in Vibrations*, Macmillan Publishing Company, Inc., New York, pp. 233-235.

13. Widrow, B. and S.D. Stearns, 1985. *Adaptive Signal Processing*, Prentice-Hall, Inc., Englewood Cliffs, New Jersey, pp. 99-116.

14. Elliott, S.J., I.M. Strothers and P.A. Nelson, 1987. "A Multiple Error LMS Algorithm and Its Application to the Active Control of Sound and Vibration," *IEEE Transaction on Acoustic Speech and Signal Processing* ASSP-35, 1:1423-1434.

15. Clark, R.L, 1992. "Advance Sensing Techniques for Active Structural Acoustic Control," Dissertation for Doctor of Philosophy in Mechanical Engineering, Virginia Polytechnic Institute and State University, pp. 135-136.

16. *KYNAR Piezo Film Technical Manual*, 1987. Pennwalt Corp., Valley Forge, Pennsylvania, pp. 1-65.

17. Mailard, J.P. and C.R. Fuller, 1992. "Advanced Time Domain Sensing for Structural Acoustic Systems. I Theory and Design," submitted to the *Journal of the Acoustical Society of America.*

18. Barker, A.J., 1992. "Rapid Full Field Vibration Pattern Imaging Using a Laser Doppler Vibration Sensor," proceedings of *The 10th International Modal Analysis Conference*, San Diego, California, Society for Experimental Mechanics, Inc., Bethal Conneticut, pp. 650-655.

C-38 Optimizing Actuator Locations in Feedforward Active Control Systems Using Subset Selection, C. E. Ruckman and C. R. Fuller, Second Conference on Recent Advances in Active Control of Sound and Vibration, Blacksburg, VA, pp. S122-S133, April 1993.

OPTIMIZING ACTUATOR LOCATIONS IN FEEDFORWARD ACTIVE CONTROL SYSTEMS USING SUBSET SELECTION

C. E. Ruckman and C. R. Fuller

ABSTRACT

This numerical simulation uses multiple linear regression with subset selection to optimize the locations of control actuators in a feedforward active noise control system. Actuator locations can have a profound impact on controller performance, but a complex system may defy intuition. Numerical optimization approaches can be impractical for complex structures or systems with large numbers of actuators because of computation costs. By formulating the feedforward control approach as a regression, subset selection can find the actuator locations that provide the best system performance. The technique is general enough for use on complex structures that cannot be modeled analytically, and is efficient enough to allow comprehensive studies involving large numbers of actuators. Numerical results are given for a simple system in which radiation from a cylindrical shell is controlled by oscillating forces applied on the shell surface. [Work supported by Carderock Division, NSWC, and by Office of Naval Research.]

INTRODUCTION

With active control techniques becoming increasingly popular for solving low- to mid-frequency noise problems, there is a growing need for more formal ways of optimizing actuator layouts. Implementing an active noise control solution for a well-posed problem has become quite practical, if not yet routine, given recent advances in control algorithms and microprocessor technology. However, the performance bottleneck for some systems involves not controller or processor technology but poor coupling between the actuators and system response (poor controllability). For simple systems the designer can rely on intuition and experience, but problem complexity has increased as software and hardware have become more sophisticated. Geometrically complex systems require multiple actuators whose optimal placement may defy intuition, and optimization by trial and error can be costly and time-consuming. This research seeks a more general method for optimizing the locations of multiple actuators in feedforward control in frequency-domain numerical simulations.

Christopher E. Ruckman, Acoustics Technology Dept., Carderock Div., NSWC, Bethesda, MD 20084-5000
Chris R. Fuller, Mechanical Eng. Dept., Virginia Polytechnic Institute & State Univ., Blacksburg, VA 24061

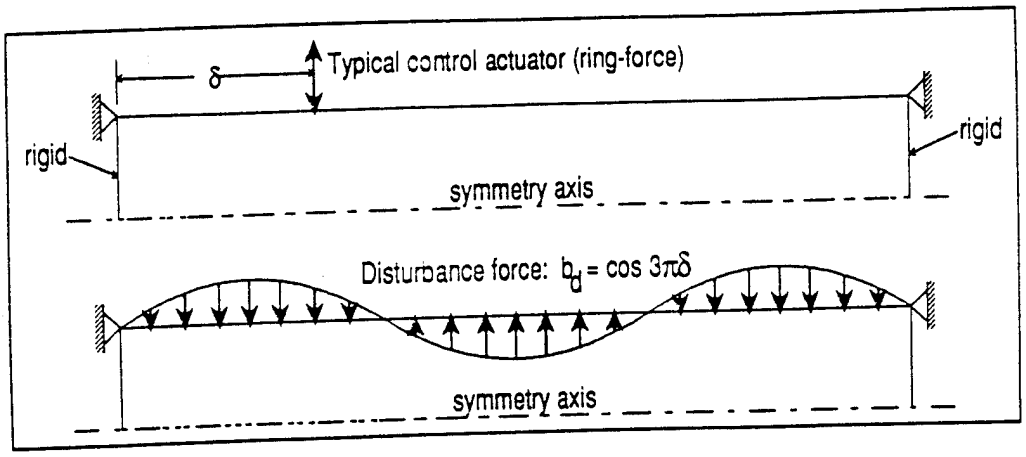

Figure 1: Geometry of example problem.

Two types of approaches are possible, the first of which can be used when the permissible actuator locations are a continuous function in space. This approach generally involves some type of numerical optimization in which the actuator locations are included as optimization parameters [1,2,3]. For example, Wang *et. al.* [3] optimize the locations of piezoelectric actuators used to control acoustic radiation from a rectangular plate. Such studies are instructive, but the high computational expense of repeated response evaluations limits the approach to relatively small problems with analytical solutions. Also, minimization routines can become trapped by local minima and fail to find global minima.

Anther possible approach can be used for discrete problems, those in which only certain actuator locations are permissible (see, for example, [4]). This approach is based on discrete optimization, also referred to as integer programming. It is usually applied to truss structures or other systems for which the permissible actuator locations are naturally discrete, and to the authors' knowledge has not been used for optimizing structural-acoustic systems.

Subset selection combines some capabilities of both of the above methods, and overcomes some of their limitations. The method begins with an analogy between feedforward active control and complex-domain multiple linear regression [5]. The main benefit of subset selection over other methods is its extreme computational efficiency, which allows more comprehensive studies with larger numbers of actuators. Since the method is based on discretized transfer functions, it is quite general and is ideal for simulations involving numerical models or experimental data. Perhaps more importantly, the language and concepts of multiple linear regression and subset selection provide new physical insights and a better understanding of why and how control systems work. Indeed, once the analogy between multiple regression and feedforward control is understood, many concepts from statistical science (including the concept of subset selection) can be applied more or less directly to the feedforward control problem.

To help explain subset selection, we examine active structural-acoustic control (ASAC) for a finite-length cylindrical shell, shown in Figure 1. The shell has flat, rigid end caps that are constrained against translation along the symmetry axis. In ASAC, acoustic radiation from a vibrating, elastic structure is controlled by applying "control forces" directly on the

structure while minimizing a radiation-related variable [6-10]. Here, the shell is disturbed into steady-state vibration by an oscillating distributed axial force applied on the shell surface. Control is achieved by applying axial ring-forces at other locations on the shell, with the objective of reducing the total radiated power. The structure is a thin-walled steel shell submerged in water, and therefore exhibits significant coupling between acoustic and structural responses. The dynamic response is computed numerically using a finite-element approach coupled with a boundary-element formulation [11]. A similar numerical simulation of feedforward active control is described by the authors in [10] for a fluid-loaded spherical shell, and is shown by comparison with analytical findings to produce accurate results.

THEORETICAL BACKGROUND

We first review the fundamentals of multiple linear regression to introduce terminology that may not be familiar to a general acoustics-oriented or controls-oriented audience. Then we explain how a feedforward active control problem can be expressed as a complex-valued regression, and describe how subset selection can optimize actuator locations. The section concludes with a brief discussion of potential numerical difficulties. Much of the following discussion may be found in textbooks and articles on linear algebra or least-squares; see, for example, [12] or [13]. We include the discussion to introduce terminology not normally associated with active noise control, and to better illustrate the analogy between and regression feedforward control.

Fundamentals Of Multiple Linear Regression

In multiple linear regression, also known as curve fitting or parametric data modeling, one typically seeks a model $\hat{y}$ to approximate a dependent variable y. The model takes the form of a weighted sum of *independent variables* X_i, also called *predictor variables*. Suppose the dependent and independent variables contain M observations, and we write them as vectors

$$y \equiv \begin{Bmatrix} y_1 \\ y_2 \\ \vdots \\ y_M \end{Bmatrix} \quad \text{and} \quad X_i = \begin{Bmatrix} X_{i1} \\ X_{i2} \\ \vdots \\ X_M \end{Bmatrix}, \tag{1}$$

A model of human body weight, for example, would have the body weights of a group of people as the data variable y, while the predictor variables X_i might be other measurable characteristics such as height, age, etc. The general form of the linear multiple regression problem is to find a set of *regression coefficients* b_i such that

$$\hat{y} = \sum_{i=1}^{N} b_i X_i \approx y, \tag{2}$$

If we also write the regression coefficients as a vector $B=\{b_1 \;\; b_2 \;\; \ldots \;\; b_M\}^T$, then we can define a *design matrix* $X=\{X_1 \;\; X_2 \;\; \ldots \;\; X_M\}$ and express the model as

$$\hat{y} = BX \approx y. \tag{3}$$

Note that the design matrix X generally has many more rows than columns, that is, there are many more observations of each variable than there are variables, though this need not be the case.

The most commonly used solution technique is least squares, in which we seek regression coefficients that minimize a weighted sum of the squared deviations between y and $\hat{y}$ at all of the M observation points. In other words, we require that the b_i minimize a *cost function*

$$\chi^2 = \sum_{i=1}^{M} w_i |y_i - \hat{y}_i|^2 \tag{4}$$

where the w_i are weighting coefficients, usually set to unity. The cost function is also known as the residual sum of squares (RSS). By defining a diagonal weighting matrix W containing the weighting coefficients w_i and requiring that $\partial\chi^2/\partial b_i$ vanish for all i, we obtain the $N \times N$ set of *normal equations* , whose solution is the vector of regression coefficients B.

$$X^T W X B = X^T W y . \tag{5}$$

Formulating Feedforward Active Control as a Complex-Valued Regression

In feedforward control, we assume that we know the *disturbance response* P, that is, the error sensor outputs that would result from the disturbance force acting alone. We also assume that the system is linear: the total response equals the disturbance response plus the *control response* $\hat{P}$, defined as the error sensor outputs that would result from the actuators acting together but without the disturbance. The path between each individual actuator and the error sensor outputs is represented as a transfer function, so that the control response is a linear sum of all the transfer functions weighted by the associated actuator strengths or *control forces*. Once we specify the physical locations of the actuators on the structure, we must find the control forces that minimize a cost function, often taken to be the total radiated power.

The direct analogies between feedforward control and multiple linear regression are as follows. The transfer functions between the actuators and error sensors are analogous to the predictor variables, X_i. The control forces are analogous to the regression coefficients, and the desired control response is analogous to the model $\hat{y}$. Finally, dependent variable y equals the *negative* of the disturbance response. By choosing control forces such that $\hat{y}$ approximates $-y$, we cause the control response to "cancel" the disturbance.

Since most quantities of interest in vibrations and acoustics problems are complex-valued, we must reformulate the regression using complex variables. This is accomplished by defining a new cost function

$$\chi^2 = \sum_{i=1}^{M} w_i (y_i - \hat{y}_i)(y_i - \hat{y}_i)^* \tag{6}$$

where the superscript * indicates the complex conjugate. After some algebra [14], we can show that the normal equations take the form

$$X^{T*} W X B = X^{T*} W y . \tag{7}$$

The physical significance of the cost function depends on how the variables and weighting coefficients are defined. In this paper the disturbance response being canceled is the farfield pressures $P=P(\theta_i)$, i=1, 2, ... M, where the number of observations M is the number of farfield points at which pressure is monitored. The predictor variables are transfer functions between unit forces in various locations and farfield pressures $P_j(\theta)$, j=1, 2, ... N. Consider the following expression for the radiated power:

$$\Pi = \oint_S \frac{\pi R^2}{\rho c}\left|P+\hat{P}\right|^2 dS \equiv \sum_{i=1}^{M}\sum_{j=i}^{N}\frac{\pi R^2 a_i}{\rho c}\left|P_j(\theta_i)+\hat{P}_j(\theta_i)\right|^2 \qquad (8)$$

where S is a spherical surface of farfield radius R with the structure at its center, and a_i is the area on the surface S associated with the ith farfield location. By comparison with Eq. (6), we see that the cost function will approximate the radiated power if we specify weighting coefficients of the following form.

$$w_i = \frac{\pi r^2}{\rho c}a_i \qquad (9)$$

Using Subset Selection To Optimize Actuator Locations

In the statistical sciences, one often has access to many more variables than are necessary (or prudent) to include in a model. One might be tempted to include all available variables in hopes of devising the most complete model, but practical concerns often prevent this approach. Some variables are more expensive than others to measure; others might duplicate information already contained in other variables, or might not contribute any new information to the fit. For these reasons and others, statisticians have developed a considerable body of literature describing the concept of *subset selection* or *variable reduction* (see [15] for detailed discussion and a bibliography). The idea is to pick out, from among a large set of candidate variables, some optimal subset of variables that provides an adequate fit to the data.

Similarly, in the feedforward control problem, there are usually many possible locations for the actuators. Unfortunately, cost and complexity preclude covering the entire structure with actuators at every possible location. Since it is neither necessary nor practical to use a large number of actuators, subset selection lets us choose an optimal subset of actuator locations from among all the candidates, in effect optimizing their locations for the given disturbance and frequency. To do this we must compute many transfer functions (one per candidate actuator location for each frequency of interest.) A numerical approach based on finite elements is ideally suited for this: when we compute the transfer function for one actuator location, we can compute transfer functions for all the other candidate actuator locations at almost no additional cost.

The various approaches to subset selection have different strengths and different levels of complexity; the most straightforward methods are the *exhaustive search* technique. In an exhaustive search, we compute χ^2 for every possible combination of actuator locations, and keep track of which combinations produce the smallest residual χ^2 values. An exhaustive search is guaranteed to find the global minimum rather than becoming trapped in a local minimum. However, the method is not feasible for more than approximately 20 variables

because of long computation times. The present work uses a variation of exhaustive search which examines only subsets of n or fewer variables where n is specified by the analyst. For example the analyst might examine all subsets of 10 or fewer variables out of 25 candidates. The method is orders of magnitude faster than examining all subsets of all sizes, and allows the use of many more variables.

Other types of subset selection include forward selection, backward elimination, sequential replacement, and various "stepwise" methods. These are faster than exhaustive searches, but bring into question whether the solutions found are global minima. For purposes of demonstration, only exhaustive searching is used in this article.

Before describing the mechanics used to perform subset selection on complex-valued regressions, a few words of caution are in order. As with most forms of numerical optimization, one should not treat subset selection as a "black box" technique that will produce the single best configuration of actuators. The analyst should examine a large number of the better-fitting subsets over a range of frequencies looking for actuator locations that appear again and again. This point cannot be overstated; one must vigilantly guard against putting too much confidence in a numerical technique without a good understanding of the physics involved.

Subset selection is related to integer programming, that is, numerical optimization using discretized parameters. It is instructive to note the different approaches used in the subset selection literature as opposed to the integer programming literature. Specifically, studies that use integer programming usually make no mention of examining a number of near-optimal solutions; they tend to take a single solution as the absolute optimum. Also, there is often no mention of the possibility of collinearity or other numerical difficulties.

Subset Selection Using Exhaustive Search

Subset selection techniques examine many different combinations of variables to find which combination(s) produce the lowest RSS (cost function). This suggests two ways of reducing computation time. First, we should compute only the RSS and not spend the extra effort required to solve for the regression coefficients. Second, we should choose a solution technique that allows us to remove or add variables without regenerating the entire computation. Both goals are accomplished by using a QR factorization as described below.

Gentlemen [16,17] gives an efficient computational method for QR factorization of real-valued systems of normal equations. After performing the factorization and including the effects of weighting coefficients, the normal equations may be written

$$\overline{R}B = Y \tag{10}$$

where $\overline{R}$ is an N by N upper triangular matrix and Y is a vector of length N. Solving for B is trivial by back-substitution.

A general set of routines for weighted least-squares regression is presented by Miller [18]. However, these routines are for real-valued variables only. The routines can easily be

modified to operate on complex-valued variables; the modifications and a sample application are described in Ruckman [19]. For further details on exhaustive search using *QR* decomposition, the interested reader is referred to [15].

All regression and subset selection computations for this paper were performed on a desktop computer, and none required more than a few minutes of computing time. (The transfer functions were computed separately, before performing subset selection.) The high computational efficiency of the *QR* decomposition allows large systems to be investigated economically.

Collinearity (Ill-Conditioning)

Numerical ill-conditioning of the design matrix is referred to in the statistics literature as *collinearity*. Collinearity occurs whenever (or actually, *to the extent that*) one or more transfer functions are not mutually orthogonal. For example, if two actuators in a regression are located too close together, they will have nearly identical transfer functions which are not mutually orthogonal. Since the transfer functions for a realistic structure will rarely be perfectly orthogonal to each other, collinearity will always be present to some degree.

Collinearity degrades the accuracy of the regression, and if severe can completely destroy the results. A common result is *bias error*, that is, an erroneously low or high RSS which is actually no more than a numerical artifact. Thus we see the impact of collinearity on subset selection: if we merely record the subsets with the lowest RSS values, many of them may actually be contaminated by collinearity. We must test a number of near-optimal subsets to see which, if any, exhibit collinearity; those that do should be discarded or treated separately.

Detecting collinearity is not difficult, and the subject of collinearity is treated at great length in the statistics literature [20]. Many different diagnostics are available for detecting, analyzing, and remedying collinearity. Most diagnostics stem from examining the condition number of the design matrix, but their details are beyond the scope of this paper. For the present purpose, we use a three-step procedure whose derivation we omit for brevity. First, we normalize each column of the design matrix by the magnitude of its largest component. Second, we estimate the condition number of the normalized design matrix. Third, if the condition number is greater than 30, we discard the regression being considered. The cutoff value of 30 is, as the reader may guess, subject to some interpretation. For more details, see [20].

Even with collinearity present, we could still find a solution if needed; many approximate methods are available for solving ill-conditioned equations. Most notably, singular-value decomposition (SVD) provides an approximate solution that minimizes the length of the solution vector [13]. However, SVD and other approaches are not suitable for use with subset selection because of the computing time involved. Unlike *QR* decomposition, normal equations solved with SVD must be completely regenerated and solved from scratch each time the variables are rearranged.

RESULTS AND DISCUSSION

The example problem consists of a finite-length, fluid-loaded cylindrical shell with rigid, flat end caps as shown in Figure 1. The shell length L is ten times the shell radius a, and the ratio of wall thickness to shell radius is 0.005. The disturbance is an oscillating distribution of axial ring-forces b_d. The set of candidate actuator locations, shown in Figure 2, includes 25 axisymmetric ring forces evenly spaced along the length of the cylinder. They are numbered sequentially, with actuator 1 at δ=0.02, actuator 13 at δ=0.50, and actuator 25 at δ=0.98. To illustrate the subset selection technique, we will investigate the frequency $k_a a$=0.59, where k_a is the acoustic wavenumber.

Figure 3 shows the distribution of normal surface velocity due to the disturbance force, which helps in explaining later results. The horizontal axis shows the location coordinate δ on the shell, where the end caps have been omitted and $0.0 \leq \delta \leq 1.0$. The vertical axis shows the magnitude of the normal surface velocity. The surface velocity has local maxima at δ of approximately 0.1, 0.5, and 0.9.

After finding the 75 best subsets of one, two, three, four, and five actuators, we must examine the different combinations of actuators for collinearity. For subsets of one actuator, obviously only 25 different subsets are possible (one for each candidate actuator location). Subsets of one actuator cannot display collinearity, which requires at least two actuators. In this case no collinearity appears in any of the subsets of two, three, or four actuators. However, all of the first 75 subsets of five actuators are contaminated by collinearity and must be discarded.

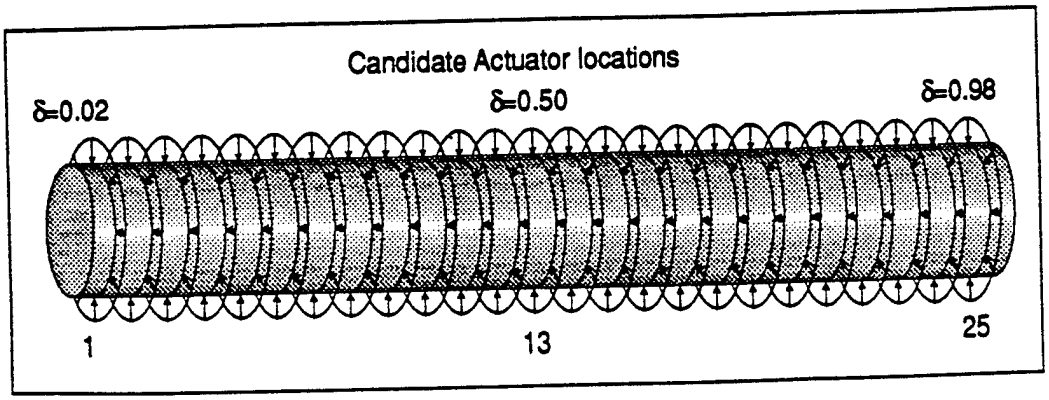

Figure 2: Locations of candidate actuators

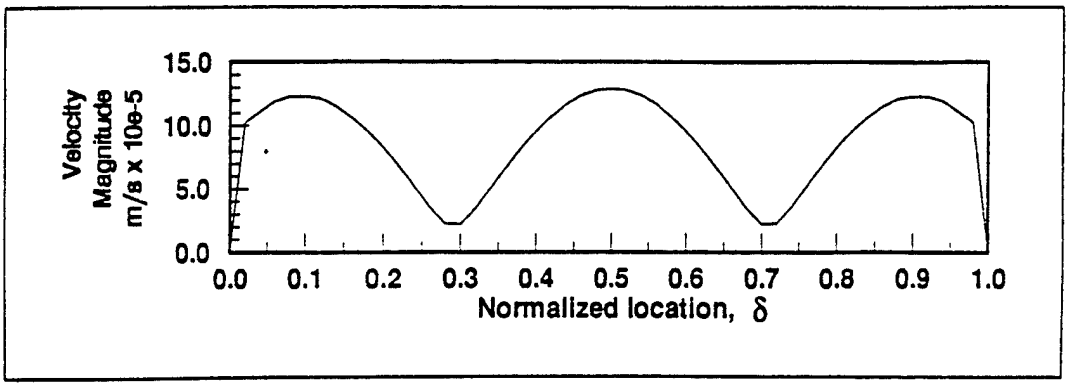

Figure 3: Operating shape at $k_a a$=0.59.

Residual Radiated Power Levels With Optimized Actuator Locations

Figure 4 shows the extent to which radiated power is lowered by one, two, three, or four optimally located actuators. The horizontal axis shows the rank among subsets: the best subset of a given size has rank one, the second best has rank two, etc. With one actuator, the reduction ranges from 12 dB to less than 1 dB depending on which actuator is used. With multiple actuators reductions of over 70 dB are possible. In general, each additional actuator brings a substantial improvement on the order of 10 dB or more.

Within a given subset size, many near-optimal subsets are available that perform almost as well as the "best" subset. (One notable exception occurs when using three actuators, in which case the best subset performs much better than the second-best subset.) The designer therefore has some freedom in choosing actuator locations. This is important in designing systems for broadband control; one would seek subsets that are near-optimal at several or many frequencies, rather than subsets that are exactly optimal for one specific frequency.

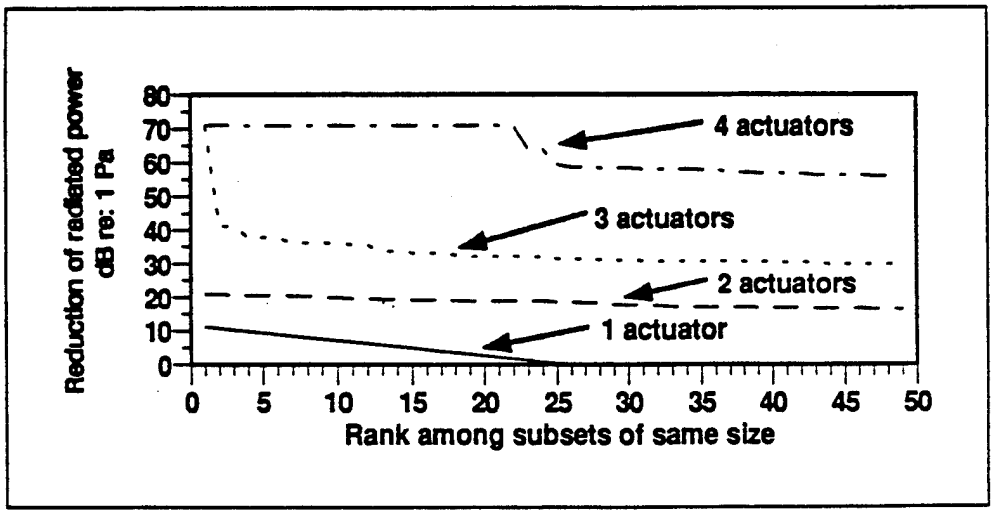

Figure 4: Reductions in radiated power.

Optimal Locations For Actuators

Figure 5 shows the actuator locations for the 15 best subsets of one, two, three, or four actuators at $k_a a$=0.59. The horizontal axis shows where each actuator is located on the cylinder, with δ=0 being the left end cap and δ=1 being the right end cap. Each row on the chart represents a different subset, with actuator locations for that row appearing as squares in the appropriate locations. The reduction in radiated power for each subset is shown in decibels at the left side. The best subset is shown in the top row, second-best in the second row, etc.

For the case of a single actuator, Fig. 5a, the optimal location corresponds to what a designer might anticipate from prior knowledge of the system dynamics. Judging from the distribution of surface velocity shown in Figure 3, one could guess that the most effective location for a single control force would be near one of the "antinodes" at δ=0.1, 0.5, and 0.9. But optimizing for two or more actuators leads to configurations that are less intuitive. In past studies [3], a single optimally located actuator generally retained its location when a second actuator was added and both locations were optimized. In the present example, there appears to be little relation between actuator locations for different subset sizes. With two actuators (Fig. 5b) the optimal placement does not require actuators at the antinodes; instead, they are placed in opposed pairs on either side of a nodal circle. With three actuators (Fig. 5c), the optimal actuator placement again calls for actuators near the antinodes.

With four actuators (Fig. 5d), all of the best 15 subsets call for actuators to be placed at δ=0.08, 0.50, and 0.92. The location of the fourth actuator varies, but has almost no effect on system performance. This can also be seen in Fig. 4, where the reduction achieved with four actuators is nearly unchanged over the first 22 subsets. Only in subsets 24 through 75, not shown here, do the locations begin to affect the performance.

The results of this particular example are less important than the fact that even this relatively simple structure provides results that are not immediately obvious. For more realistic and complicated systems, it may be difficult or impossible to guess the best actuator locations. The more complicated the physical system is, the more important it is to have formal, general methods for optimizing the system configuration.

SUMMARY

This report discusses a numerical method for optimizing actuator locations in a feedforward active control system to provide the best system performance. The method formulates the feedforward controller as a complex-valued multiple linear regression, and uses subset selection to choose the most effective subset of actuators from a set of candidates. Computational efficiency and a logical, general approach make this method ideal for analyzing complex systems with large numbers of actuators. Although presented here for an axisymmetric structure, the method can be extended to more general situations including three-dimensional structures.

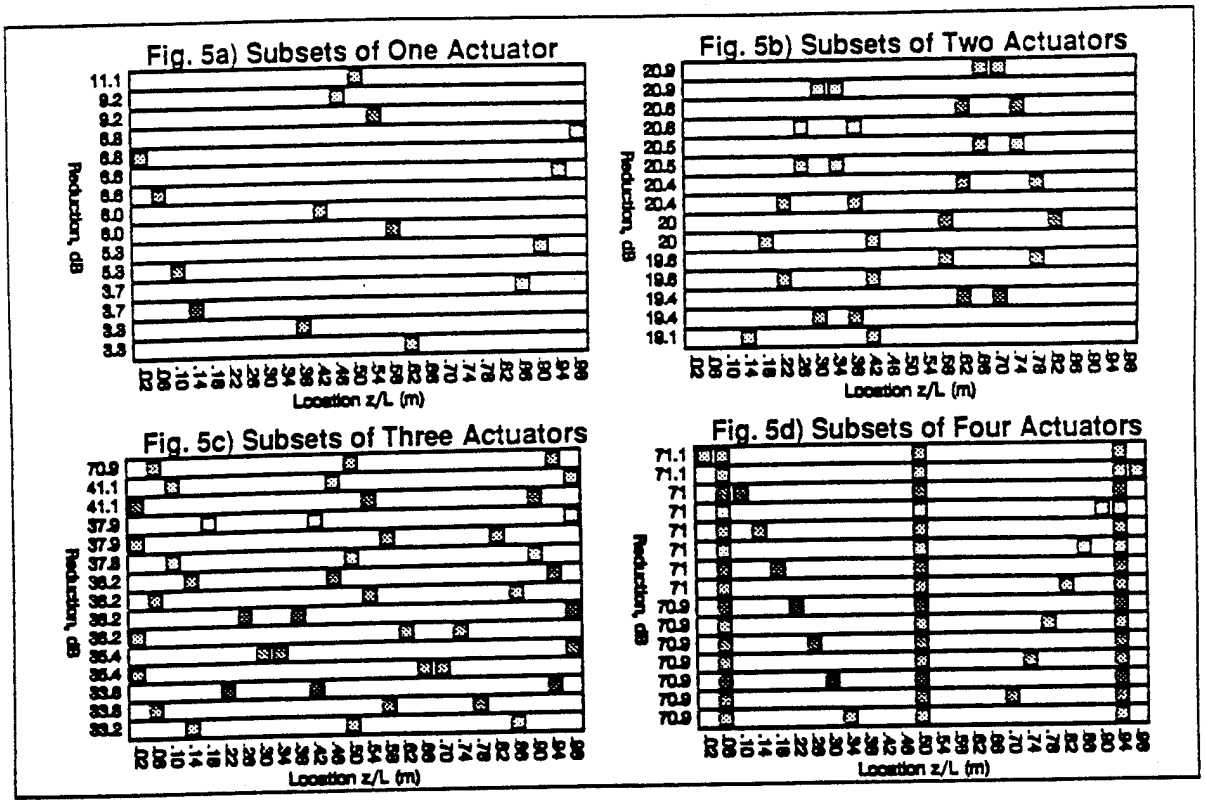

Figure 5: Optimized actuator locations for subsets of four or fewer actuators.

The method is illustrated by optimizing a simple active structural-acoustic control system consisting of a finite-length, fluid-loaded cylindrical shell with flat, rigid, clamped end caps. The locations of control forces on the cylinder are optimized to reduce the total radiated power caused by a harmonic, distributed force. It is shown that while the optimal location of a single actuator can be predicted from examining system dynamics, multi-force configurations can be difficult to predict from intuition alone.

Subset selection provides an efficient, versatile, general way to optimize actuator locations. However, the analyst must be sure to test the results for collinearity, the numerical ill-conditioning that can result from poor choice of actuator locations. In the example problem all subsets of more than four actuators were discarded because of collinearity.

ACKNOWLEDGMENTS

The authors gratefully acknowlege Dr. Alan Miller for providing computer programs and valuable advice. This project was funded by Carderock Division, NSWC, and by the Office of Naval Research through Grant ONR-N00014-92-J-1170.

REFERENCES

1. Chen, G.-S., R. J. Bruno, and M. Salama, 1991. "Optimal placement of active/passive

members in truss structures using simulated annealing." AIAA Journal, 29(8).
2. Skelton, R.E. and M.L. DeLorenzo, 1983. "Selection of noisy actuators and sensors in linear stochastic systems." Journal of Large Scale Systems, Theory, and Applications, 4:109-136.
3. Wang, B.-T., R.A. Burdisso, and C.R. Fuller, 1991. "Optimal placement of piezoelectric actuators for active control of sound radiation from elastic plates." Proceedings of NOISE-CON '91, Tarreytown, NY, pp. 267-274.
4. Haftka, R.T. and H.M. Adelman, 1985. "Selection of actuator locations for static shape control of large space structures by heuristic integer programming." Computers & Structures, 20(1-3): 575-582.
5. Snyder, S.D. and C.H. Hansen, 1990. "Using Multiple Regression to Optimize Active Noise Control System Design." Journal of Sound and Vibration, 148(4):537-542.
6. Fuller, C.R., 1990. "Active control of sound transmission/radiation from elastic plates by vibration inputs: I. Analysis." Journal of Sound and Vibration, 136(1):1-15.
7. Gu, Y. and C.R. Fuller, 1991. "Active control of sound radiation due to subsonic wave scattering from discontinuities on fluid-loaded plates. I: Far-field pressure." Journal of the Acoustical Society of America, **90**(4-1):2020-2026.
8. Clark, R. and C.R. Fuller, 1991. "Control of sound radiation with adaptive structures." Journal of Intelligent Material Systems and Structures, 2:431-452.
9. Ruckman, C.E. and C.R. Fuller, 1992. "Numerical simulation of active structural-acoustic control for a fluid-loaded spherical shell." Proceedings of the Second International Congress on Recent Developments in Air- and Structure-borne Sound and Vibration, Auburn Univ., eds. M.J. Crocker and P.K. Raju, Vol. 1, pp. 377-385.
10. Ruckman, C.E. and C.R. Fuller, 1993. "Numerical simulation of active structural-acoustic control for a fluid-loaded, spherical shell: Formulation and validation." Submitted for publication in Journal of the Acoustical Society of America.
11. Everstine, G.C. and A.J. Quezon, 1992. "User's guide to the coupled NASTRAN/Helmholtz equation capability (NASHUA) for acoustic radiation and scattering." CDNSWC-SD-92-17, Carderock Division, NSWC, Bethesda, MD.
12. Lawson, C.L. and R.J. Hanson, 1974. Solving Least Squares Problems. Prentice-Hall, New Jersey.
13. Press, W.H., B.P. Flannery, S.A. Teukolsky, and W.T. Vetterling, 1989. Numerical Recipes: The Art of Scientific Computing. Cambridge University Press, Cambridge.
14. Miller, K.S., 1975. "Complex linear least squares." SIAM Review, **15**(4):707-726.
15. Miller, A.J., 1990. Subset Selection in Regression. Chapman and Hall, New York.
16. Gentleman, W.M., 1973. "Least squares computations by Givens transformations without square roots." Journal of the Institute of Mathematics Applications, 12:329-336.
17. Gentleman, W.M., 1974. "Algorithm AS75: Basic procedures for large, sparse, or weighted linear least squares problems." Applied Statistics, 23(3):448-454.
18. Miller, A.J., 1991. "Algorithm AS274: Least squares routines to supplement those of Gentleman." Applied Statistics, 38:458-478.
19. Ruckman, C.E., 1993. "Method and example application for least squares regression of complex-valued variables." To be submitted to Applied Statistics.
20. Belsley, D.A., E.Kuh, and R.E. Welsch, 1980. Regression Diagnostics: Identifying Influential Data and Sources of Collinearity. Wiley, New York.

C-39 Optimum Actuator and Sensor Design for Feedforward Active Structural Acoustic Control, R. A. Burdisso and C. R. Fuller, ASME Winter Annual Meeting - Adaptive Structures & Materials Systems Symposium, 1993.

OPTIMUM ACTUATOR AND SENSOR DESIGN FOR FEEDFORWARD ACTIVE STRUCTURAL ACOUSTIC CONTROL

Ricardo A. Burdisso
Vibration and Acoustics Laboratories
Mechanical Engineering Department
Virginia Polytechnic Institute and State University
Blacksburg, Virginia 24061-0238

Chris R. Fuller
Vibration and Acoustics Laboratories
Mechanical Engineering Department
Virginia Polytechnic Institute and State University
Blacksburg, Virginia 24061-0238

ABSTRACT

An efficient feedforward control system design is presented for attenuation of low frequency structurally radiated sound. The technique is based on the modification of the eigenstructure such that the system responds with the weakest set of modal radiators. The approach is applicable to both narrowband and broadband excitations and it is insensitive to the disturbance input location. The formulation is demonstrated on a simply-supported plate driven by a point force with white noise spectral content. The sound radiation due to the first three odd-odd modes is attenuated with single-input, single-output (SISO) control system. The optimum control configuration yields an average overall global sound reduction of up to 24 dB.

INTRODUCTION

In recent years, considerable effort has been devoted to active control techniques to reduce low frequency structurally radiated sound. The understanding of the physics of the problem has yielded efficient control strategies. One such approach has been proposed by Fuller (1987) in which the control inputs are applied directly to the vibrating structure while minimizing radiated sound or related variable. This technique is known as active structural acoustic control (ASAC). For applications in which the noise field is due to persistent inputs, the potential of the ASAC technique in conjunction with adaptive feedforward control approaches has been clearly demonstrated (Fuller, 1990, Metcalf, 1992, Smith, 1993).

The design of feedforward control systems involves the selection of the type, number, location and size of the actuators and of the error sensors whose outputs are sought to be minimized. The traditional design approach in feedforward control is to select actuators and sensors based on some physical understanding of the behavior of the uncontrolled system. In general, this empirical methodology yields satisfactory results for ASAC when the error transducers are microphones placed in the acoustic field that directly observe the quantity to be minimized and when the excitation is a single sinusoid. However, this heuristic approach can easily result in an inefficient control system with an unnecessarily large number of control channels even in simple systems and is exacerbated when structural sensors are used. (Wang, 1991). Due to rapid advances in specialized actuator and sensor materials, today research thrust is toward developing smart or adaptive systems with actuators and sensors being an integral part of the structure (Fuller, 1989). The design of control systems of structures with integrated transducers will be even more critical since these error sensors will not directly measure acoustic pressure which is the quantity to be reduced and not all structural motion is well coupled to the radiation field.

Formal optimization approaches (Wang, 1991, Clark, 1992) clearly demonstrated that optimally located actuators and sensors can have a profound impact on the performance of the active control system. Even more important is the fact that significant levels of attenuation can be obtained with far less numbers of properly located transducers, thus reducing the dimensionality and complexity of the controller. Unfortunately, these *direct* optimization techniques require the evaluation of the radiated pressure at each step of the minimization process. The acoustic prediction, that will be certainly carried out numerically for real structures, is a computationally intensive analysis. Thus, these design optimization techniques can not be realistically implemented to complex structures and disturbances in the present form due to computational time aspects.

Here an efficient design formulation for feedforward ASAC systems is proposed. The optimum actuators and sensors are determined such that the controlled structure will respond with a set of weakly coupled sound radiating mode shapes. To this end, the formulation takes advantage of recent work that demonstrated that an active feedforward controlled structure will respond with a new set of eigenproperties whether vibration or radiation is

being attenuated (Burdisso, 1992a and 1992b). The controlled resonant frequencies and associated eigenfunctions are a function of the selected control actuator(s) and error sensor(s) and are independent of the disturbance input. Thus, the design approach is based on finding the actuator(s) and sensor(s) configuration such that the controlled structure will respond with the weakest set of modal radiators. These weak radiators are defined here as the eigenfunctions with the lowest radiation efficiency and are obtained by solving an eigenvalue problem. The formulation is valid for both narrow and broad band excitation inputs. The design formulation is demonstrated on a simple supported plate excited with band limited white noise.

SYSTEM RESPONSE

The structure is assumed linear and subjected to a stationary disturbance input and the analysis is, thus, carried out in the frequency domain. For the sake of clarity, the formulation will be presented for a planar radiator and a SISO control system. However, there is no loss of generality in the design methodology proposed here for multiple channels, complex structures and disturbances. A typical SISO feedforward control arrangement is shown in Fig. 1. In feedforward control the undesirable response of a system due to the "primary" disturbance input is reduced by applying a "secondary" control input. The control input is obtained by feeding a reference signal into the compensator, $G(\omega)$. The compensator is designed such that the output from an error sensor is minimized. In feedforward control approaches, the reference signal should be "coherent" to the disturbance input signal, and it is assumed here that it is directly obtained by tapping the disturbance input.

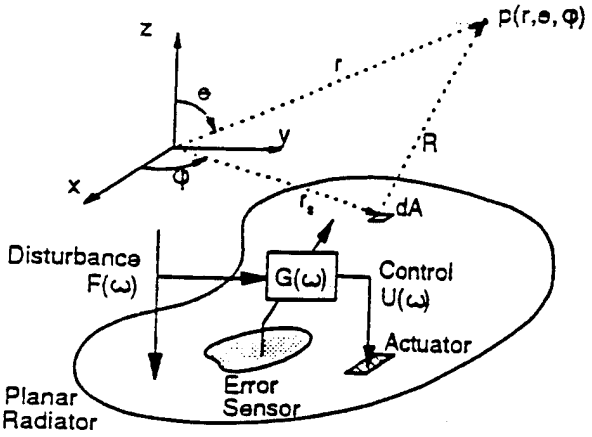

Fig. 1: Arrangement of a SISO feedforward ASAC system.

Structural Response

The structural response $w(x,y,\omega)$ can be expressed as a linear combination of the modes as

$$w(x,y,\omega) = \sum_{n=1}^{N} q_n(\omega)\,\phi_n(x,y) \qquad (1)$$

where $\phi_n(x,y)$ is the n^{th} mass normalized eigenfunction, N is the number of modes, and the $q_n(\omega)$ is the modal displacement

$$q_n(\omega) = [\,f_n F(\omega) + u_n U(\omega)\,]\,H_n(\omega) \qquad (2)$$

where f_n is the n^{th} modal disturbance force, $F(\omega)$ is the Fourier Transform of the disturbance input, u_n is the n^{th} modal control force, $U(\omega)$ is the Fourier Transform of the control input, $H(\omega)=(\omega_n^2-\omega^2+j2\xi_n\omega_n\omega)^{-1}$ is the n^{th} modal frequency response function, where ω_n and ζ_n are the n^{th} natural frequency and modal damping ratio, respectively; and j is the imaginary number.

The optimum frequency content of the control input stems from minimizing a cost function, which is the mean square value of the error sensor output. The error sensor output, in particular for distributed transducers, is a weighted response of the system and can be expressed as

$$e(\omega) = \int_S b(x,y)\,R[w(x,y,\omega)]\,ds \qquad (3)$$

where R[.] is a linear differential operator that relates the system displacement to any quantity of interest, b(x,y) is a weighting function related to the properties of the sensors, and S is the area of application of the distributed sensor.

Replacing eq.(1) into (3), the error variable can also be represented as the sum of the linear contribution of each mode as follows

$$e(\omega) = \sum_{n=1}^{N} q_n(\omega)\,\xi_n \qquad (4)$$

where ξ_n is the n^{th} modal error component given by

$$\xi_n = \int_S b(x,y)\,R[\phi_n(x,y)]\,ds \qquad (5)$$

The modal error components, ξ_n, and the modal control forces, u_n, are a measure of the relative observability and controllability of the modes by the error sensor and control actuator, respectively. For a SISO control configuration, the error output is theoretically driven to zero by the control input at all frequencies. Thus, the spectrum content of the control input is

$$U(\omega) = G(\omega)\,F(\omega) = -\frac{\sum_{n=1}^{N} \xi_n f_n H_n(\omega)}{\sum_{n=1}^{N} \xi_n u_n H_n(\omega)}\,F(\omega) \qquad (6)$$

where $G(\omega)$ is the compensator that relates the control input $U(\omega)$ to the disturbance input $F(\omega)$. The controlled response can now be computed by solving eq.(6) for the control input $U(\omega)$ and replacing it into eq.(2) and this into eq.(1). The uncontrolled response is computed by setting $U(\omega)$ to zero in eq.(2).

Acoustic Response

The far-field pressure radiated by a harmonically vibrating planar structure can be computed from the structural response by using the Raleigh integral (Fahy, 1985) as follows

$$p(\bar{r},\omega) = \frac{i\omega\rho_0}{2\pi}\int_A v(x_s,y_s)\,\frac{e^{-jkR}}{R}\,dA \qquad (7)$$

where, as shown in Fig. 1, $\bar{r}=(r,\theta,\varphi)$ is the polar coordinate of the observation point in the acoustic field; $r_s=(x_s,y_s)$ are the coordinates of the elemental surface dA having normal velocity $v(x_s,y_s)$; A is the area of the radiator; R is the magnitude of the distance from the elementary source and the observation point; ρ_0 is the fluid density; and k is the acoustic wave number given as $k=\omega/c$, where c is the speed of sound in the medium. Here, it is assumed that the acoustic medium is air and thus no feedback of the fluid motion into the structure takes place.

Again the radiated pressure can be expressed as a linear contribution of the modes as

$$p(\bar{r},\omega) = \sum_{n=1}^{N} q_n(\omega)\,p_n(\bar{r},\omega) \qquad (8)$$

where

$$p_n(\bar{r},\omega) = \frac{i\omega\rho_0}{2\pi}\int_A i\omega\phi_n(x_s,y_s)\,\frac{e^{-jkR}}{R}\,dA \qquad (9)$$

is the radiated pressure distribution given by the n^{th} mode with surface velocity $i\omega\phi_n(x,y)$. The controlled acoustic sound field can be computed by replacing eq.(2) into (8).

It should be noted that typically the computation of the radiated pressure for a complex structure will be performed numerically by Finite/Boundary element codes. This analysis is a computationally intensive process, and therefore any efficient controller design approach should minimize the number of acoustic evaluations. The following work is directed towards achieving this goal.

CONTROLLED SYSTEM EIGENPROPERTIES

The previous analysis provides the tools to compute the controlled structural and acoustic responses. However, it does not give any insight into the control mechanisms. Since the design approach proposed here is founded on the understanding of these mechanisms, the main aspects of the dynamic behavior of feedforward controlled structures will be described here, while a full detailed description can be found in the work by Burdisso (1992a). The traditional view of feedforward controlled systems is of "active cancellation" where the modes of the structure excited by the "primary" disturbance input are canceled by the "secondary" control input of appropriate magnitude and phase driving the same structural modes. This view arises from the fact that the system response can be interpreted as the superposition of the disturbance and control responses as suggested by eq.(2). However, recent work has shown that the real mechanism is that the feedforward controlled system responds effectively with a new set of eigenfunctions and eigenvalues to the disturbance input (Burdisso, 1992a).

The eigenproperties of the feedforward controlled system are governed by the characteristics of the controller $G(\omega)$ in eq.(6). Because of the constraint imposed on the structure by driving the error signal to zero at all frequencies, the controller reduces the dynamic DOF of the system by one ,and thus the controlled system has (N-1) new eigenvalues and associated eigenfunctions. The undamped controlled system eigenvalues, λ_ℓ, are computed such that the following equation is satisfied

$$\sum_{n=1}^{N} \xi_n u_n \prod_{\substack{m=1\\ m\neq n}}^{N} (\mu_m - \lambda_\ell) = 0 \quad ; \quad \ell = 1,-,N-1 \qquad (10)$$

where $\mu_m=(\omega_m)^2$ is the m^{th} uncontrolled system eigenvalue.

The controlled system eigenfunction $\phi_\ell(x,y)$ associated to the eigenvalue λ_ℓ is easily computed once the controlled system eigenvalue has been determined. They can be obtained as a linear combination of the uncontrolled eigenfunctions. That is,

$$\phi_\ell(x,y) = \sum_{n=1}^{N} \Gamma_{\ell n}\,\phi_n(x,y) \qquad (11)$$

and the expansion coefficients are

$$\Gamma_{\ell n} = C_\ell \frac{u_n}{(\lambda_\ell - \mu_n)} \quad ; \quad n = 1,-,N \qquad (12)$$

where C_ℓ is a constant that is included since the controlled eigenfunction are arbitrary to a constant multiplier, and it can be computed such that $\{(\Gamma_{\ell 1})^2+(\Gamma_{\ell 2})^2+...+\Gamma_{\ell N})^2\}=1$.

The eigenproperties of the controlled system given by eqs.(10) through (12) are a function of the control input, through the modal control forces u_n, and of the error variable, through the modal error components ξ_n. An important aspect of the eigenproperties are that they are independent of the disturbance input. This implies that once the control actuator and error sensor are selected the eigenstructure of the controlled system is completely determined independently of the nature of the disturbance input including frequency content, location and distribution.

DESIGN APPROACH

The main goal in ASAC is for the control system to render a controlled response that poorly couples with the acoustic medium, thus resulting in minimum radiated sound power. This objective can be accomplished if two conditions are met. They are

(i) Firstly, the resonant frequencies of the controlled structure must lay away from the dominant part of the disturbance input spectrum. In other words, the controlled system resonances should be detuned from the excitation input.

(ii) Secondly and more important, the controlled or residual structural response should be a linear contribution of weakly radiating modes.

As mentioned in the previous section, the controlled system has new resonant frequencies and associated eigenfunctions that are only a function of the selected actuator and sensor. Thus, this concept can be merged with the above conditions to yield an efficient design approach. The design formulation proposed here can be stated as to find the optimum actuator and sensor configuration that yields a controlled structure with eigenproperties that satisfy the above conditions.

The first step in the proposed design formulation is to find the

desired set of controlled system eigenfunctions with which the controlled structure should respond. The sought eigenfunctions should be weak modal radiator and this can be mathematically formulated by requiring the desired eigenfunctions to have the lowest radiation efficiency possible. Since the controlled eigenfunctions are given as a linear combination of the uncontrolled eigenfunctions, this implies a search for the desired expansion coefficients $(\Gamma_m)_d$ in order to achieve this objective.

To compute the radiation efficiency, the ratio of the radiated power to the average mean square velocity of the radiating structure is required. The radiated pressure due to the ℓ^{th} controlled eigenfunction driven harmonically at frequency ω can be computed using the modal surface velocity distribution $v(x,y)=i\omega\phi_\ell(x,y)$ substituted into the Rayleigh integral, eq.(7). Considering eq.(11), the controlled modal pressure distribution is given in terms of the unknown desired coefficients, $(\Gamma_m)_d$, and of the uncontrolled modal pressure distribution, $p_n(\bar{r},\omega)$, as

$$p_\ell(\bar{r},\omega) = \sum_{n=1}^{N} (\Gamma_m)_d \, p_n(\bar{r},\omega) \qquad (13)$$

The radiated sound power at frequency ω due to the ℓ^{th} controlled mode over the region D in the acoustic field is computed by integrating the acoustic time average intensity as

$$\Pi_\ell(\omega) = \iint_D \frac{|p_\ell|^2}{\rho_0 c} \, dD \qquad (14)$$

and replacing eq.(13) into (14) gives

$$\Pi_\ell(\omega) = \{\Gamma_\ell\}_d^T [\Pi(\omega)] \{\Gamma_\ell\}_d \qquad (15)$$

where the elements of matrix $[\Pi(\omega)]$ are

$$\Pi_{nm}(\omega) = \iint_D \frac{p_n p_m^*}{\rho_0 c} \, dD \quad ; \qquad (16)$$

the desired expansion vector is $\{\Gamma_\ell\}_d=\{(\Gamma_{\ell 1})_d,\ldots,(\Gamma_{\ell N})_d\}^T$, and the superscript T denotes the vector transpose.

Matrix $[\Pi(\omega)]$ is symmetric and positive definite because the radiated power is always positive for a non-trivial vector $\{\Gamma_\ell\}_d$. The term $\Pi_{nn}(\omega)$ represents the radiated power by the n^{th} uncontrolled eigenfunction, while the term $\Pi_{nm}(\omega)$ represents the radiated power due to the acoustic coupling between the n^{th} and m^{th} uncontrolled eigenfunctions. If the cross term $\Pi_{nm}(\omega)$ vanishes, the modes are said to be acoustically uncoupled. The important implication is that the radiation due to the n^{th} mode can not be used to destructively interfere with the radiation due to the m^{th} mode such that the average radiated power over the region D is reduced.

The average mean square velocity for the controlled mode oscillating at frequency ω can be easily computed as

$$|v_\ell(\omega)|^2 = \frac{\omega^2}{2A} \iint_A \phi_\ell^2(x_s,y_s) \, dA \qquad (17)$$

where A is the area of the planar radiator. Again, it is straight forward to show that the average mean square velocity becomes

$$|v_\ell(\omega)|^2 = \{\Gamma_\ell\}_d^T [V(\omega)] \{\Gamma_\ell\}_d \qquad (18)$$

where matrix $[V(\omega)]$ is also symmetric and positive definite with

$$V_{nm}(\omega) = \frac{\omega^2}{2A} \iint_A \phi_n(x_s,y_s) \, \phi_m(x_s,y_s) \, dA \qquad (19)$$

Finally, the radiation efficiency of the ℓ^{th} controlled eigenfunction is defined as (Wallace, 1972)

$$S_\ell(\omega) = \frac{\Pi_\ell(\omega)}{A\rho_0 c V_\ell(\omega)} = \frac{\{\Gamma_\ell\}^T [\Pi(\omega)] \{\Gamma_\ell\}}{A\rho_0 c \{\Gamma_\ell\}^T [V(\omega)] \{\Gamma_\ell\}} \qquad (20)$$

The desired expansion coefficients $(\Gamma_m)_d$ that yield the lowest radiation efficiency for the controlled modes are obtained by minimizing $S_\ell(\omega)$ in eq.(20) with respect to the coefficients $(\Gamma_m)_d$ with the constraint $\{\Gamma_\ell\}_d^T\{\Gamma_\ell\}_d=1$. This constrained minimization problem can be efficiently solved by recognizing that the stationary values of $R_\ell(\omega)$ can be obtained by solving the eigenvalue problem

$$([\Pi(\omega)] - \sigma_\ell [V(\omega)]) \{\Gamma_\ell\}_d = \{0\} \; ; \; \ell = 1, \ldots, N \qquad (21)$$

Because of the symmetry and positive definite properties of the matrices, the N eigenvalues σ_ℓ are all real and positive such that $\sigma_1<\sigma_2<\ldots<\sigma_N$. The eigenvalue σ_ℓ represents the radiation efficiency at frequency ω of the ℓ^{th} desired controlled eigenfunction that is given as a linear combination of the uncontrolled modes by the coefficients of the eigenvector $\{\Gamma_\ell\}_d$.

Because the SISO controlled system has (N-1) eigenfunctions, the optimum set of controlled eigenfunctions is that with the (N-1) lowest radiation efficiency. Thus, the desired expansion coefficients, $(\Gamma_m)_d$, are the first (N-1) eigenvectors in eq.(21).

The desired eigenfunctions found above are optimum in the sense that they have the lowest radiation resistance at the single frequency ω. For broad band excitation input, the controlled eigenfunctions should have low radiation resistance in the frequency range of the excitation input. This can be accomplished by solving for the minimum of the weighted radiation efficiency

$$S_\ell(\omega) = \frac{1}{A\rho_0 c} \frac{\{\Gamma_\ell\}_d^T \sum_{i=1}^{L} B_i [\Pi(\omega_i)] \{\Gamma_\ell\}_d}{\{\Gamma_\ell\}_d^T \sum_{i=1}^{L} B_i [V(\omega_i)] \{\Gamma_\ell\}_d} \qquad (22)$$

where B_i is a weighting constant, and matrices $[\Pi(\omega_i)]$ and $[V(\omega_i)]$ are computed at L frequencies ω_i. The eigenproblem of

eq.(21) will then yield a set of optimum eigenfunctions that have low radiation resistance, in some weighted sense, at the L frequencies ω_l. Then, the computation of the uncontrolled modes radiated pressure is required at L frequencies.

Optimum Modal Parameters

The expansion coefficients, Γ_m, are a function of the modal control forces, u_n, the uncontrolled eigenvalues, μ_n, and the controlled eigenvalues, λ_p as depicted by eq.(12). Thus, the modal control forces and the controlled eigenvalues can now be determined so they yield the desired expansion coefficients found from the solution of the above eigenproblem. However, the number of expansion coefficients to match is Nx(N-1) while there are 2(N-1) design variables, i.e (N-1) relative modal control forces and (N-1) controlled eigenvalues. Therefore, the desired expansion coefficients can be achieved only in some least square sense. The controlled eigenvalues, λ_p and modal control forces, u_p can then be obtained by solving the following least square constrained minimization problem

$$\text{Min.} \quad F(u_n, \lambda_l) = \sum_{l=1}^{N-1} B_l \sum_{m=1}^{N} \left| (\Gamma_m)_d - c_l \frac{u_n}{\lambda_l - \mu_n} \right|^2$$

$$\text{such that} \quad \sum_{n=1}^{N} u_n^2 = 1 \qquad (23)$$

$$(\lambda_l)_{lower} \le \lambda_l \le (\lambda_l)_{upper}$$

where B_l is a weighting factor and the equality constraint represents the normalization of the modal control forces since the relative controllability of the modes is the only relevant information. The upper and lower limits of the inequality constraints on the values for the controlled system eigenvalues, λ_p are selected based on the characteristic of the spectrum content of the disturbance input. For example, if the disturbance input consists of multiple sinusoids, the controlled eigenvalues are selected such that they are not coincident with any of the excitation sinusoids. The solution of the minimization problem in eq.(22) yields the modal control forces, u_p and the controlled eigenvalues, λ_p.

Recent work (Burdisso, 1992c) has shown that given u_n and λ_p the error modal components, ξ_m, can be computed from the characteristic equation of the controlled system in eq.(10). Replacing the optimum controlled eigenvalues, λ_p and modal control forces, u_n, found from the solution of the above optimization problem into eq.(10) gives

$$\begin{bmatrix} A_{11} & A_{12} & \cdots & A_{1N} \\ A_{21} & A_{22} & \cdots & A_{2N} \\ \vdots & & \ddots & \vdots \\ A_{(N-1)1} & A_{(N-1)2} & \cdots & A_{(N-1)N} \end{bmatrix} \begin{Bmatrix} \xi_1 \\ \xi_2 \\ \vdots \\ \xi_N \end{Bmatrix} = \begin{Bmatrix} 0 \\ 0 \\ \vdots \\ 0 \end{Bmatrix} \qquad (24)$$

where the elements of matrix [A] are

$$A_{mn} = u_n \prod_{\substack{n=1 \\ n \neq n}}^{N} (\mu_n - \lambda_l) \qquad (25)$$

and $\{\xi\}=\{\xi_1,\ldots,\xi_N\}^T$ is the vector of modal error components.

The homogeneous linear system of equations is such that the only relevant information is the relative observability of the uncontrolled modes by the error sensor. Thus, assuming the N^{th} mode is observable, then by setting ξ_N to one, the modal error components can be obtained by solving the reduced linear system of equations

$$\begin{bmatrix} A_{11} & A_{12} & \cdots & A_{1(N-1)} \\ A_{21} & A_{22} & \cdots & A_{2(N-1)} \\ \vdots & & \ddots & \vdots \\ A_{(N-1)1} & A_{(N-1)2} & \cdots & A_{(N-1)(N-1)} \end{bmatrix} \begin{Bmatrix} \xi_1 \\ \xi_2 \\ \vdots \\ \xi_{N-1} \end{Bmatrix} = - \begin{Bmatrix} A_{1N} \\ A_{2N} \\ \vdots \\ A_{(N-1)N} \end{Bmatrix} \qquad (26)$$

The optimal modal error, ξ_m, and control, u_n, components define completely the control system configuration in the modal domain for N modes. The design of the control system in the modal domain as carried out in this formulation offers a number of advantages. The performance of the controller can be investigated with the modal parameters alone. Before the transducers are selected, control issues such as number of control channels for a required reduction can be addressed effectively. This approach also allows for the investigation of different kinds of actuators and sensors with minimum additional computational effort.

This modal information needs to be transformed into physical transducers that can then be implemented on the structure. The type of actuator and sensor, i.e. discrete or distributed, to be implemented is an application dependent problem and beyond the main focus of the proposed design approach. The implementation of physical strain induced transducers is the subject of another paper.

NUMERICAL EXAMPLE

The applicability of the design formulation is demonstrated for controlling the radiation due to the (1,1), (3,1) and (1,3) odd-odd modes of an uniform simply supported plate. To this end, it is assumed that these are the only modes excited by both the disturbance and control inputs and observed by the error sensor. This implies that $f_n=u_n=\xi_m=0$ for all modes except the odd-odd ones. The plate has density $\rho=7833\ N.s^2/m^4$, Young's modulus $E=2.0\times10^{11}$ N/m, Poison's ratio $\nu=0.3$, thickness $h=0.002$ m, and dimensions $L_x=0.38$ m and $L_y=0.3$ m. The disturbance input is a point force located at the center of the plate. The spectrum of the disturbance is assumed to be white noise in the [0-600] frequency band. A modal damping ratio of 1.0% is assumed for all modes ($\zeta_n=0.01$). The n^{th} natural frequency of the plate is

$$\omega_n = \sqrt{D/\rho h}\left(\gamma_x^2 + \gamma_y^2\right) \qquad (27)$$

where $\gamma_x=\pi n_x/L_x$, $\gamma_y=\pi n_y/L_y$, $D=Eh^3/12(1-\nu^2)$ is the flexural rigidity, and the eigenfunction is

$$\phi_n(x,y) = K \sin(\gamma_x x)\, \mathrm{Sin}(\gamma_y y) \qquad (28)$$

where (n_x,n_y) are the modal indices traditionally used for rectangular panels that are associated to the n index used in the theoretical analysis, $n \rightarrow (n_x,n_y)$, and $K=(4/L_xL_y\rho h)^{1/2}$. is a normalization constant.

Desired Controlled System Eigenfunctions

The plate is assumed baffled to eliminate the acoustic interaction between the back and front radiation and facilitate the analytical predictions. The radiated far-field pressure due to each of the plate modes was first computed by solving the Rayleigh integral in eq.(9). Assuming the observation point to be in the far-field ($kL_x>>1$ and $kL_y>>1$), eq.(9) has a closed form solution given by (Wallace, 1972)

$$p_n(\bar{r},\omega) = \frac{-\omega^2 \rho L_x L_y K}{2\pi^3 n_x n_y} \frac{e^{-jkr}}{r} \xi_n(\alpha,\beta) \qquad (29)$$

where

$$\xi_n(\alpha,\beta) = \left[\frac{(-1)^{n_x} e^{-jk\alpha}-1}{(\alpha/n_x\pi)^2-1}\right]\left[\frac{(-1)^{n_y} e^{-jk\beta}-1}{(\beta/n_y\pi)^2-1}\right] \qquad (30)$$

$$\alpha = kL_x \sin\theta \cos\varphi \quad ; \quad \beta = kL_y \sin\theta \sin\varphi \qquad (31)$$

Since the excitation input is white noise from 0 to 600 Hz, the center frequency of 300 Hz was used to solve for the eigenproblem in eq.(21). The modal far-field pressure distribution in eq.(29) can now be used in eq.(16) to compute the auto and cross modal radiation power terms. The aim in this control example is to attenuate the total radiated power. Thus, the numerical integration of the local intensity in eq.(16) is carried out over one half hemisphere. The auto and cross modal mean square velocity are computed by replacing eq.(28) into (19) and integrating over the surface of the plate.

The eigenvalue problem in eq.(21) was then solved to find the set of desired expansion coefficients that yield the desired controlled eigenfunctions. Since the SISO controller reduces the number of dynamic DOF by one, the desired expansion coefficients, $(\Gamma_m)_d$, are the first two eigenvectors of the eigenvalue problem in eq.(21). Table I shows the desired expansion coefficients that define the two controlled eigenfunctions.

TABLE I: Desired expansion coefficients, $(\Gamma_m)_d$.

(n_x,n_y)	$(\Gamma_{1n})_d$	$(\Gamma_{2n})_d$
(1,1)	-.128	-.366
(3,1)	0.894	0.357
(1,3)	-.427	0.858

Optimum Modal Parameters

The optimum modal parameters, i.e. modal control force u_n and error ξ_m components, can now be computed. The first step is to find the modal control forces and controlled eigenvalues that yield the desired expansion coefficients from Table I. This is achieved by solving the minimization problem in eq.(23) where the controlled eigenvalues λ_r are not constrained because the spectrum of the excitation input is white noise. The minimization process was carried out by using the optimization IMSL routine DUNLSF (non-linear least squares problems) which yielded the optimum modal forces u_n shown in Table II and the two controlled eigenvalues shown in Table III. Using these values in eq.(12) resulted in the expansion coefficients shown in Table III, which are almost identical to the desired coefficients in Table I. The modal control forces and controlled eigenvalues can now be used in the linear systems of equations in eq.(26) to solve for the modal error components ξ_m, and they are given in Table II.

TABLE II: Modal control and error components.

(n_x,n_y)	(1,1)	(3,1)	(1,3)
u_n	-.522	0.485	0.702
ξ_m	0.929	0.319	0.188

TABLE III: Controlled system eigenproperties.

Controlled natural frequencies, $f_r=(\lambda_r)^{1/2}/2\pi$		
	f_1=399 Hz	f_2=701 Hz
(n_x,n_y)	Γ_{1n}	Γ_{2n}
(1,1)	-.217	-.305
(3,1)	0.880	0.374
(1,3)	-.423	0.875

The control system configuration is completely determined by the modal parameters in Table II and it has modified the eigenstructure of the system in such a way that the controlled structure will respond with two weak radiating modes. To illustrate this phenomena, the radiation efficiency for the uncontrolled and controlled eigenfunctions was computed and it is plotted in Fig. 2. This figure clearly demonstrates that the controlled modes have substantially lower radiation resistance than the uncontrolled modes in the bandwidth of interest. It is also very interesting to note that, by numerical integration, the controlled eigenfunctions are nonvolumetric. Since the response is a linear expansion of the modes, this implies that the net volume displaced by the controlled plate is zero at all frequencies. This same phenomenon was observed by Burdisso (1992b) in studying the dynamic behavior of feedforward controlled systems using microphones in as error sensors.

$$\phi_n(x,y) = K \sin(\gamma_x x) \sin(\gamma_y y) \qquad (28)$$

where (n_x,n_y) are the modal indices traditionally used for rectangular panels that are associated to the n index used in the theoretical analysis, $n \rightarrow (n_x,n_y)$, and $K=(4/L_xL_yhp)^{1/2}$, is a normalization constant.

Desired Controlled System Eigenfunctions

The plate is assumed baffled to eliminate the acoustic interaction between the back and front radiation and facilitate the analytical predictions. The radiated far-field pressure due to each of the plate modes was first computed by solving the Rayleigh integral in eq.(9). Assuming the observation point to be in the far-field ($kL_x>>1$ and $kL_y>>1$), eq.(9) has a closed form solution given by (wallace, 1972)

$$p_n(\vec{r},\omega) = \frac{-\omega^2 \rho L_x L_y K}{2\pi^3 n_x n_y} \frac{e^{-jkr}}{r} \left[\frac{(-1)^{n_x} e^{-jk\alpha} - 1}{(\alpha/n_x\pi)^2 - 1} \right] \left[\frac{(-1)^{n_y} e^{-jk\beta} - 1}{(\beta/n_y\pi)^2 - 1} \right] \qquad (29)$$

where

$$\alpha = kL_x \sin\theta \cos\varphi \quad ; \quad \beta = kL_y \sin\theta \sin\varphi \qquad (30)$$

The modal far-field pressure distribution in eq.(29) can now be used to compute the auto and cross modal radiation power terms in eq.(16). The aim in this control example is to attenuate the total radiated power. Thus, the numerical integration of the local intensity in eq.(16) is carried out over one half hemisphere.

Since the excitation input is white noise from 0 to 600 Hz, the center frequency of 300 Hz was used in eq.(21). Matrix $[\Pi(\omega)]$ was computed for the (1,1), (3,1) and (1,3) odd-odd modes laying in the excitation bandwidth of interest. The auto and cross modal mean square velocity are computed by replacing eq.(28) into (19) and integrating over the surface of the plate.

The eigenvalue problem in eq.(21) was then solved to find the set of desired expansion coefficients that yield the desired controlled eigenfunctions. Since the SISO controller reduces the number of dynamic DOF by one, the desired expansion coefficients, $(\Gamma_m)_d$, are the first two eigenvectors of the eigenvalue problem in eq.(21). Table I shows the desired expansion coefficients that defines the two controlled eigenfunctions.

TABLE I: Desired expansion coefficients, $(\Gamma_m)_d$.

(n_x,n_y)	$(\Gamma_{1n})_d$	$(\Gamma_{2n})_d$
(1,1)	-.128	-.366
(3,1)	0.894	0.357
(1,3)	-.427	0.858

Optimum Modal Parameters

The optimum modal parameters, i.e. modal control force u_n and error ξ_m components, can now be computed. The first step is to find the modal control forces and controlled eigenvalues that yield the desired expansion coefficients from Table I. This is achieved by solving the minimization problem in eq.(23) where the controlled eigenvalues λ_q are not constrained because the spectrum of the excitation input is white noise. The minimization process was carried out by using the optimization IMSL routine DUNLSF (non-linear least squares problems) which yielded the optimum modal forces u_n shown in Table II and the two controlled eigenvalues shown in Table III. Using these values in eq.(12) resulted in the expansion coefficients shown in Table III, which are almost identical to the desired coefficients in Table I. The modal control forces and controlled eigenvalues can now be used in the linear systems of equations in eq.(26) to solve for the modal error components ξ_m, and they are given in Table II.

TABLE II: Modal control and error components.

(n_x,n_y)	(1,1)	(3,1)	(1,3)
u_n	-.522	0.485	0.702
ξ_m	0.929	0.319	0.188

TABLE III: Controlled system eigenproperties.

Controlled natural frequencies, $f_i=(\lambda_i)^{1/2}/2\pi$		
	f_1=399 Hz	f_2=701 Hz
(n_x,n_y)	Γ_{1n}	Γ_{2n}
(1,1)	-.217	-.305
(3,1)	0.380	0.374
(1,3)	-.423	0.875

The control system configuration is completely determined by the modal parameters in Table II and it has modified the eigenstructure of the system in such a way that the controlled structure will respond with two weak radiating modes. To illustrate this phenomena, the radiation efficiency for the uncontrolled and controlled eigenfunctions was computed and it is plotted in Fig. 2. Three dimensional perspectives of these eigenfunctions are also shown in the figure. Figure 3 clearly demonstrates that the controlled modes have substantially lower radiation resistance than the uncontrolled modes in the bandwidth of interest. It is also very interesting to note that, by numerical integration, the controlled eigenfunctions are nonvolumetric. Since the response is a linear expansion of the modes, this implies that the net volume displaced by the controlled plate is zero at all frequencies. This same phenomenon was observed by Burdisso (1992b) in studying the dynamic behavior of feedforward controlled systems using microphones in as error sensors.

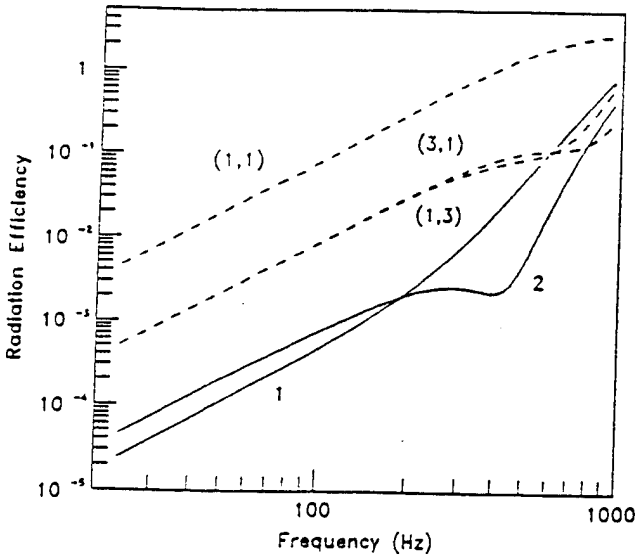

Fig. 2: Radiation efficiency of — uncontrolled and —— controlled eigenfunctions.

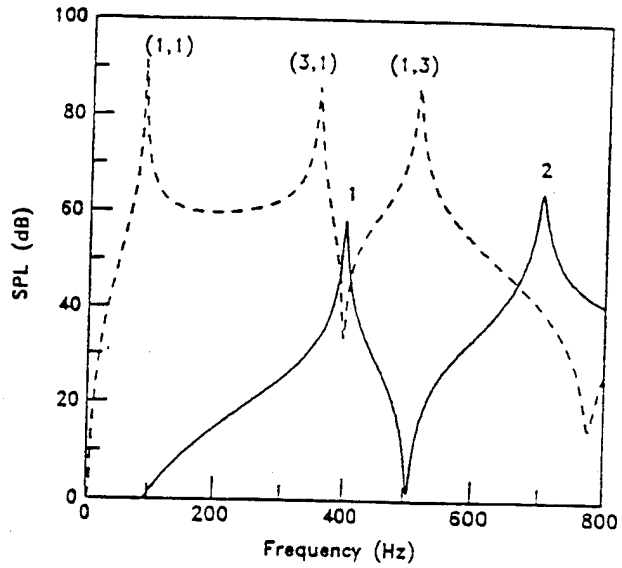

Fig. 3: Far-field pressure at $\bar{r}=(0°,0°,4.5L_x)$; — uncontrolled and —— controlled.

Control System Performance

The control system is completely defined in the modal domain in terms of the optimal modal parameters in Table II. The performance of the controlled structure can be investigated with these modal parameters alone before physical transducers are devised. To illustrate the dynamic behavior of the plate before and after control, the far field pressure at $\bar{r}=(0°,0°,4.5L_x)$ was computed using eqs.(8) and (2). The sound pressure level (dB reference 20μPa) is shown in Fig. 3 as a function of the frequency. The dashed line is the uncontrolled response that shows resonant peaks at the frequencies of the odd-odd modes given by eq.(27). On the other hand, when the control input is applied the response shows resonance behavior at the two controlled resonant frequencies of 399 and 701 Hz. It can be seen that the sound levels produced by the controlled structure over the bandwidth are well below the levels generated by the uncontrolled structure at the natural frequencies of the odd-odd modes.

The radiation directivity on the horizontal x-z plane at a distance of $4.5L_x$ was computed at selected frequencies. Figure 4 shows the far-field radiation at 352 Hz, corresponding to the uncontrolled (3,1) mode resonance frequency, which shows excellent global reduction. Similar behavior was observed for each of the uncontrolled resonant frequencies. More interesting is to investigate the radiated sound at the controlled system resonance frequencies. Figure 5 shows the far-field radiation at 399 Hz which is the first resonance of the controlled system. Inspection of this plot demonstrates that even though the response of the plate is very large (because of the resonance) the radiation is not increased significantly and is well below the levels at the uncontrolled resonance frequencies. This is because the controlled mode is non-volumetric and has very low radiation efficiency or in other words the mode does not strongly couple into the acoustic medium even when it is excited near resonance.

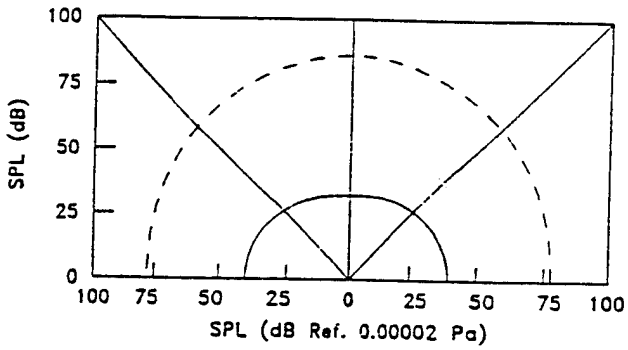

Fig. 4: Radiation directivity on x-z plane at 352 Hz; — uncontrolled and —— controlled.

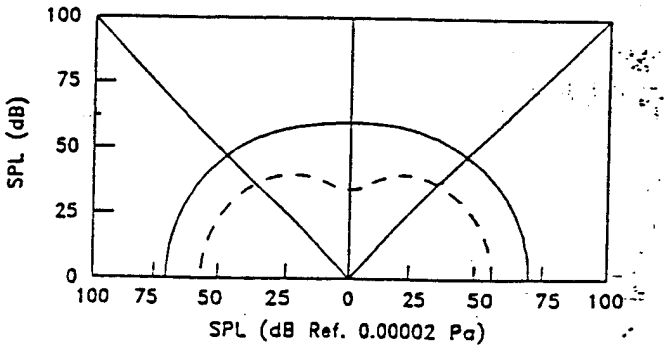

Fig. 5: Radiation directivity on x-z plane at 399 Hz; — uncontrolled and —— controlled.

The overall radiation directivity was obtained by integrating the sound pressure spectrum over the bandwidth from 0 to 600 Hz. Total radiation directivities before and after control were computed for the x-z, Fig. 6. The plot shows that an average global sound pressure level reduction of 24 dB is obtained over the complete spectrum, thus attesting to the effectiveness of the design approach presented here.

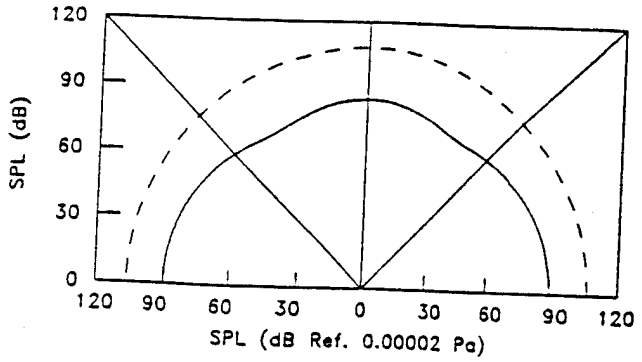

Fig. 6: Overall radiation directivity on x-z plane; ---- uncontrolled and —— controlled.

The process of designing structural actuators and sensors that yield the optimum modal parameter is not a key aspect of formulation presented here. However, the interested reader is referred to the work by Burdisso (1993) in the design of strain induced PZT actuators and PVDF sensors.

CONCLUSIONS

A formulation has been presented for the design of adaptive structures for ASAC applications. The methodology makes use of the fundamental concept that sound radiation can be effectively reduced by changing the overall radiation efficiency of the structure. The formulation also takes advantage of the fact that the feedforward control system changes the dynamic properties of the structure. The understanding and merging of these two phenomena leads to an efficient method for the design of actuators and sensors. The method is based on the premise that the optimum actuators and sensors will change the eigenstructure of the system such that the controlled response consists of a modal series of weak radiators. The control configuration is first defined in the modal domain by computing the optimum control and error modal parameters. Using this information, physical actuators and sensors can be then constructed. This particular separation between the modal and physical domain offers the advantage that different transducers and configurations can be investigated with minimum computational effort. The design approach was succesfully illustrated on a simply supported plate problem. The technique is general and could be extended to multi-input, multi-output systems and complex structures using FEM/BEM techniques to define the modal parameters

ACKNOWLEDGEMENT

The authors gratefully acknowledge the support of this work by the Office of Naval Research Grant No. ONR-N00014-92-J-1170.

REFERENCES

Burdisso,R.A., and Fuller,C.R., 1992a, "Theory of Feedforward Controlled System Eigenproperties," J. Sound Vib. 153(3), pp. 437-452.

Burdisso,R.A., and Fuller,C.R., 1992b, "Dynamic Behavior of Structural-acoustic Systems in Feedforward Control of Sound Radiation," J. Acoust. Soc. Am. 92(1), pp. 277-286.

Burdisso,R.A., and Fuller,C.R., 1992c, "Feedforward Controller Design by Eigenvalue Assignment," AIAA Journal of Guidance and Control (Accepted).

Burdisso,R.A., and Fuller,C.R., 1993, "Actuator and Sensor Design for Active Structural Acoustic Control: Part I - Analysis," J. Acoust. Soc. Am. (Submitted for publication).

Clark,R.L., and Fuller,C.R., 1992, "Optimal Placement of Piezoelectric Actuators and Polyvinylidene Fluoride (PVDF) Error Sensors in Active Structural Acoustic Control Approaches," J. Acoust. Soc. Am. 92(3), pp. 1521-1533.

Fahy,F., 1985, *Sound and Structural Vibration*, Academic Press, Orlando, FL.

Fuller,C.R., 1987, "Apparatus and Methods for Global Noise Reduction," U.S. Patent No. 4,715,599.

Fuller,C.R., Rogers,C.A., and Robertshaw,H.H., 1989, "Active Structural Acoustic Control with Smart Structures," Proceedings of the SPIE, Vol. 1170, Fiber Optic Smart Structures and Skins, Boston, MA, pp. 338-358.

Fuller,C.R., 1990, "Active Control of Sound Transmission / Radiation from Elastic Plates by Vibrating Inputs-I Analysis," J. Sound Vib. 136(1), pp. 1-15.

Metcalf,V.L.,Fuller,C.R.,Silcox, R.J., and Brown, D.E., 1992,"Active Control of Sound Transmission/Radiation from Elastic Plates by Vibration Inputs-II Experiments," J. Sound Vib. 153(3), pp. 387-402.

Smith,J.P.,Fuller,C.R., and Burdisso,R.A., 1993, "Control of Broadband Radiated Sound with Adaptive Structures," Proc. of the SPIE 1993 North America Conference on Smart Structures and Materials, 31 Jan.- 4 Feb., Albuquerque, New Mexico.

Wallace,C.E., 1972, "Radiation Resistance of a Rectangular Panel," J. Acoust. Soc. Am., 51(3), pp. 946-952.

Wang,B.T., Burdisso,R.A., and Fuller,C.R., 1991, "Optimal Placement of Piezoelectric Actuators for Active Control of Sound Radiation from Elastic Plates," Proceedings of Noise-Con 91, pp. 267-275.

C-40 The Dynamic Analysis of Piezostructures in Relation to Modal Analysis, D. G. Cole, W. R. Saunders and H. H. Robertshaw, 12th International Modal Analysis Conference, Hawaii, 1-4 February 1994.

The Dynamic Analysis of Piezostructures in Relation to Modal Analysis.

D. G. Cole, W. R. Saunders and H. H. Robertshaw
Department of Mechanical Engineering
Virginia Polytechnic Institute and State University
Blacksburg, Virginia 24061-0238

Abstract

The paper develops fundamental relationships between modal analysis techniques for traditional structures and piezostructures. The estimation of frequency domain modal parameters for piezostructures is formulated in a format similar to those traditionally considered for structures. This enables the modal testing of piezostructures to take place within the existing framework of modal analysis and enables piezostructure parameters to be measured experimentally. A transformation between the pole-residue model for traditional structures and piezostructures is shown which relates the structures modal matrix and its electromechanical coupling (EMC) matrix. Piezostructure modal tests yield experimental measurements of the EMC matrix, previously unmeasurable. It is also suggested that a piezostructure modal test can produce the modal parameters without the need for a shaker and corresponding input force measurements.

Nomenclature

a_i	modal constant
f	force vector
i	modal index
k	sensor index
l	actuator index
m	number of structural forces
n	number of modes
p	number of structural displacements
p_i	eigenvalue
q	charge vector
s	Laplace variable
v	voltage vector
x	displacement vector
ω	angular frequency
ω_i	natural frequency
ζ_i	damping coefficient
$A_i^{k,l}$	structural residue
$\hat{A}_i^{k,l}$	electromechanical residue
$\mathbf{M}$	mass matrix
$\mathbf{C}$	damping matrix
$\mathbf{C_p}$	capacitance matrix
$\mathbf{K}$	stiffness matrix
$\mathbf{\Theta}$	EMC matrix
$\hat{\mathbf{\Theta}}$	modal EMC matrix
$\mathbf{\Phi}$	modal (eigenvector) matrix
B_i	i^{th} column of matrix $\mathbf{B}$
B_{ki}	(k,i) entry of matrix $\mathbf{B}$
$()_s$	sensor vector
$()^a$	actuator matrix
$()^s$	sensor matrix
$()^T$	transpose

1 Introduction

Modal analysis is a system identification technique used to determine the dynamic behavior of elastic structures. The frequency domain method utilizes the well known, second-order differential equation for a single degree-of-freedom response and assumes

a linear superposition of the responses according to

$$x = \sum_{i=1}^{n} \frac{\Phi_i \Phi_i^T}{m_i \left[(\omega_i^2 - \omega^2) + 2\, j\, \zeta_i\, \omega\, \omega_i\right]} f \qquad (1)$$

with the assumptions of general viscous damping, modal coordinates and where ω_i is the undamped natural frequency, ζ_i is the i^{th} modal damping coefficient and Φ_i is the natural basis for the vibrating system. A vast area of research has developed in the process of both analytical and experimental validation of various forms of Equation 1. A variety of parameter estimation methods are available such that the "modal parameters" (resonant frequencies, damping coefficients, and modal shape functions) can be estimated from experimental frequency response function (FRF) measurements on a vibrating structure [1]. The techniques of modal analysis comprise a significant percentage of practical system ID approaches for linear, elastic structures.

This paper is motivated by the need for consistency between piezostructure measurements and existing modal analysis approaches. The rapid progress in the field of intelligent material systems and structures has led to the permanent establishment of piezoelectric actuators and sensors as important elements for noise and vibration monitoring and control. However, the recent emphasis on the use of piezoelectric transducers in the control of structures has resulted in some confusion about the role that modal testing system identification can play in the smart structure field. The apparent lack of force measurements and collocated *drive-point* measurements for piezostructures has diminished the emphasis on traditional modal testing methods.

The subject of this paper is the unique approach required for modal testing of general piezostructures. An important contribution is contained in the development of fundamental relationships which reveal that the existing framework of traditional modal analysis approaches can be used to estimate modal parameters which describe the piezostructure dynamics within the statistical accuracy of the experimental methods. The long-range benefits of this work include generation of experimental piezostructure models for active control, test-model correlation, dynamic analysis and a variety of other important applications.

A comparison of the governing dynamic equations for a traditional test structure and a piezostructure highlights the unique characteristics of the piezostructure.

Traditional structure:

$$\left[-\omega^2 \mathbf{M} + j\omega \mathbf{C} + \mathbf{K}\right] x = f \qquad (2)$$

Piezostructure:

$$\text{Actuator Eqn.} \quad \left[-\omega^2 \mathbf{M} + j\omega \mathbf{C} + \mathbf{K}\right] x = \Theta v \qquad (3)$$

$$\text{Sensor Eqn.} \quad \Theta^T x + \mathbf{C_p} v = q \qquad (4)$$

Two essential concepts are embodied in the comparison of the equations for the different structures. First, the poles of the two structural systems are identical. Second, the zeros of the two systems are vastly different because of the electromechanical coupling (EMC) between the electrical input and output vectors v and q and the structural response x in Equations 3 and 4. In this paper, a derivation of an appropriate analog to Equation 1 is presented so that piezostructure FRF representations are compatible with existing modal analysis curve-fitting algorithms. This is accomplished by using collocated, piezoelectric *sensoriactuators* in combination with conventional piezoelectric transducers. *Sensoriactuators* refer to piezoelectric transducers which are designed to perform simultaneous sensing and actuation using a single element. It will be shown that the inherent collocation of the sensoriactuator configuration leads to fully-populated FRF matrices, thereby circumventing the characteristic absence of true drive-point response measurements.

The feedthrough effect, $\mathbf{C_p} v$, shown in the Sensor equation (Equation 4) may be eliminated through appropriate analog circuitry [2,3]. It is important to realize that the existence of the feedthrough capacitance has drastic effects on the zeros of the piezostructure and therefore influences the evaluation of residues and EMC coefficients. For the remainder of this paper, we will assume that the capacitance can be effectively eliminated from the output measurements, such that $q = \Theta^T x$.

The following sections of the paper will highlight the use of piezostructure system measurements

such that compatibility with general modal analysis techniques is maintained. First, the pole-residue parametric model for conventional structures is reviewed to establish a baseline for comparison to the subsequent derivation of the piezostructure pole-residue parametric model. Then, fundamental relationships between the new residue expression, the structural modal matrix, and the piezostructure's EMC matrix are illuminated. Finally, piezostructure modal analysis is demonstrated numerically for a cantilever beam using a generic viscous damping curvefitter developed at Virginia Tech.

2 Modal Analysis Methods Using Piezoelectric Transducers

The purpose of this section is to develop the modal parameter model for a piezostructure. To begin, we will briefly review a common form of the elastic equation of motion which is used for parametric modal analysis [4]. Next, the modeling results for piezoelectric sensing and actuation will be presented without detail. The interested reader is referred to Crawley & de Luis [5], Hagood et al. [6], and Cole [7].

We start with the usual equation of motion for a MDOF system with general, viscous damping:

$$\mathbf{M}\ddot{x} + \mathbf{C}\dot{x} + \mathbf{K}x = f \qquad (5)$$

where $\mathbf{M}$ is a positive definite, symmetric mass matrix, $\mathbf{C}$ is a non-proportional, viscous damping matrix, $\mathbf{K}$ is a symmetric stiffness matrix, $x \in R^p$ is a vector of surface displacements in physical coordinates, and $f \in R^p$ is a vector of structural forces. Note that in practice, there will be many zero elements of f. A finite-dimensional, complex eigenvalue problem results from the n-dimensional model of Equation 5. The solution yields n pairs of complex conjugate eigenvalues

$$p_{i,i+n} = -\zeta_i\omega_i \pm j\omega_i\sqrt{1-\zeta_i^2} \qquad i = 1,2,\ldots,n \qquad (6)$$

where p_i is the i^{th} complex eigenvalue of the structure. The solution also yields a corresponding complex modal matrix Φ of eigenvectors ($\Phi_i \in C^n$) which occur in complex conjugate pairs.

For an applied force at a spatial position l and a response measurement at spatial position k, the FRF equation in physical coordinates is

$$\begin{aligned}\frac{x_k}{f_l} &= \sum_{i=1}^{n}\left[\frac{\Phi_{ki}\Phi_{li}}{a_i(s-p_i)} + \frac{\Phi_{ki}^*\Phi_{li}^*}{a_i^*(s-p_i^*)}\right] \\ &= \sum_{i=1}^{n}\left[\frac{A_i^{k,l}}{(s-p_i)} + \frac{A_i^{k,l\,*}}{(s-p_i^*)}\right] \qquad (7)\end{aligned}$$

Here, the residue has been defined as $A_i^{k,l} = \frac{\Phi_{ki}\Phi_{li}}{a_i}$. The pole-residue form in Equation 7 underlies a number of modal analysis methods for structural, input-output measurements. Iterative estimates of the system poles, p_i, provide the structure's resonant frequencies and damping values. The structural mode shapes are calculated from the residue terms $A_i^{k,l}$. When a drive-point FRF (i.e. $k = l$) is available, the residue yields the scaled eigenvector $\frac{\Phi_{li}}{\sqrt{a_i}} = \sqrt{A_i^{l,l}}$ at the drive-point location. This quantity is then used to generate the full modal matrix for locations $l = 1,2,\ldots,p$ and modes $i = 1,2,\ldots,n$. When the drive point is not available, the residue cannot be used to directly generate the experimental mode shapes. Next, we will examine the effect of using piezoelectric sensors and actuators on the modal model given by Equation 7.

A comparison of Equation 5 and the Actuator Equation shows that only the forcing terms are different. Substituting $\Theta_l^a v_l$ for f in Equation 5, the receptance becomes

$$x = \sum_{i=1}^{n}\left[\frac{\Phi_i\Phi_i^T\Theta_l^a}{a_i(s-p_i)} + \frac{\Phi_i^*\Phi_i^{T*}\Theta_l^a}{a_i^*(s-p_i^*)}\right] v_l \qquad (8)$$

Using charge output ($q_s = \Theta^{s\,T}x$), the Sensor Equation can be used to determine an input-output relationship from the l^{th} piezoelectric actuator to the k^{th} piezoelectric sensor.

$$\frac{q_k}{v_l} = \sum_{i=1}^{n}\left[\frac{\Theta_k^{s\,T}\Phi_i\Phi_i^T\Theta_l^a}{a_i(s-p_i)} + \frac{\Theta_k^{s\,T}\Phi_i^*\Phi_i^{T*}\Theta_l^a}{a_i^*(s-p_i^*)}\right] \qquad (9)$$

We can further simplify the above expression by defining

$$\hat{\Theta}_{ij} = \Phi_i^T\Theta_j \qquad (10)$$

The k,l^{th} element of the pole-residue modal model (q/v) for conventional piezoelectric transducers can

then be written as

$$\frac{q_k}{v_l} = \sum_{i=1}^{n}\left[\frac{\hat{\Theta}^s_{ik}\hat{\Theta}^a_{il}}{a_i(s-p_i)} + \frac{\hat{\Theta}^{s*}_{ik}\hat{\Theta}^{a*}_{il}}{a^*_i(s-p^*_i)}\right] = \sum_{i=1}^{n}\left[\frac{\hat{A}^{k,l}_i}{(s-p_i)} + \frac{\hat{A}^{k,l*}_i}{(s-p^*_i)}\right] \quad (11)$$

where $\hat{A}^{k,l}_i = \frac{\hat{\Theta}^s_{ik}\hat{\Theta}^a_{il}}{a_i}$. In this representation $\hat{\Theta} = \Phi^T\Theta$ is the EMC matrix in the natural mode basis.

It is apparent from Equation 11 that the description of a coupled structure-piezoelectric system requires knowledge of the system eigenvalues p_i and the EMC matrices $\hat{\Theta}^a$ and $\hat{\Theta}^s$. A comparison of the residues from Equation 7 and Equation 11 shows that the influence of the piezostructure on the modal model is to modify the residue term. The traditional residue expression $A^{k,l}_i = \frac{\Phi_{ki}\Phi_{li}}{a_i}$ is a spatial function whose numerical values are determined by the sensor/actuator locations and the boundary conditions of the structure. The residue for the piezostructure $\hat{A}^{k,l}_i = \frac{\hat{\Theta}^s_{ik}\hat{\Theta}^a_{il}}{a_i}$ exhibits the same functional dependencies, in addition to a functional dependence on the material properties and piezoelectric geometries. The important advantage for modal testing is that $\Theta^a = \Theta^s$ for sensoriactuators, resulting in a truly collocated sensor/actuator pair of similar material properties. Evaluation of the scaled EMC coefficient is

$$\frac{\hat{\Theta}_{il}}{\sqrt{a_i}} = \sqrt{\hat{A}^{l,l}_i} \quad (12)$$

where $\hat{A}^{l,l}_i$ is the residue for the l^{th} sensoriactuator location. This quantity can then be used to generate the full EMC matrix for locations $l = 1, 2, \ldots, p$ using residues found from non-collocated piezoelectric measurements.

3 Relationships between $\hat{\Theta}$, Φ and Θ.

The residue expressions of Equations 7 and 11 indicate the striking similarity between the roles which the Φ and Θ matrices fill in modal descriptions of the traditional and piezoelectric structures. The modal matrix Φ relates the structural

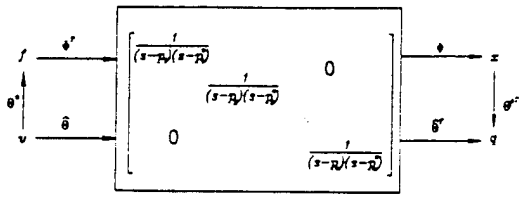

Figure 1: Relationships between $\hat{\Theta}$, Φ and Θ

forces and displacements while the modal EMC matrix $\hat{\Theta}$ relates the applied piezoelectric voltage and developed charge. Both quantities relate the respective input-output variables to the structural modes. More importantly, $\hat{\Theta}$ contains information of how the piezoelectric charge q relates to structural physical response x via Θ and how those x relates to the structure's modal response r via Φ. These important transformation relationships for the piezostructure are summarized in the flow diagram of Figure 1.

The previous analysis and the relationships highlighted in Figure 1 lead to three linear transformation equations which will provide the framework for conducting modal analysis on piezostructures. The first expression follows from the definition of the modal EMC matrix:

$$\hat{\Theta} = \Phi^T\Theta. \quad (13)$$

The second expression is from the Sensor Equation

$$q = \Theta^{s^T}x. \quad (14)$$

The third expression is simply the modal expansion theorem

$$x = \Phi r \quad (15)$$

where r is the modal coordinate vector. The most important of the three relationships is Equation 13. It contains the three parameters necessary to define the zeros of either the mechanical or electromechanical structural systems. From this expression, it is clear that if any two of the three parameters are known, then the third parameter can be found. The remaining equations indicate additional transformations which can be used to generate experimental measurements of Θ or Φ. From this point, the designer has a large degree of flexibility in designing the structural system identification procedure. In particular, note that the use of non-intrusive motion measurements (e.g. laser) via Equation 14,

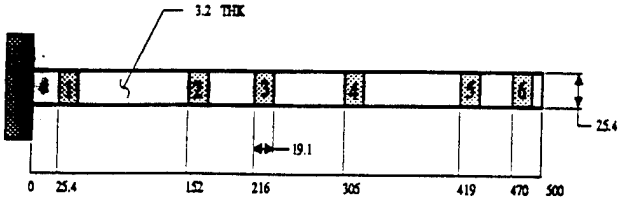

Figure 2: Cantilever beam arrangement for numerical experiment

combined with piezostructure modal analysis for $\hat{\Theta}$, yields estimates of all piezostructure modal parameters without using externally attached sensors or actuators.

Beam	*Value*
Young's modulus	70×10^{9} Pa
density	2710 kg/m^3
area moment of inertia	8.4683×10^{-12} m^4
PZT	*Value*
Young's modulus	6.3×10^{10} Pa
density	7600 kg/m^3
coupling coefficient (d_{31})	190×10^{-12} m/V
thickness	0.25 mm

Table 1: Piezobeam material properties

4 Numerical Example: A Cantilever Beam

A numerical demonstration of a proposed dual-test modal analysis approach is presented in this section. The objectives of the numerical experiment include estimation of the conventional modal parameters (p_i, Φ) and the EMC matrix $\hat{\Theta}$ for the piezostructure. Recall that estimation of these variables yields any desired input-output information for the piezostructure system (see Figure 1). A simple cantilever beam was used for the following analysis. The conceptual approach remains the same for more complex piezostructures.

4.1 Description of Experiment

A description of the aluminum cantilever beam used for the modal test is provided in Table 1 and Figure 2. The material properties of the beam and piezoelectric transducers listed in Table 1 were used to generate a finite-dimensional model using MATLAB software. Six PZT elements were spaced along the beam as shown in Figure 2. Element one, configured as a sensoriactuator, was used to excite the beam for the piezostructure test measurements. The remaining elements were configured for charge response measurements only ($q_s = \Theta^{s^T} x$). Additionally, it was assumed that position sensors were available at the beam locations coinciding with the mid-point of each PZT element. Note that the position measurements do not have to be made at the same coordinates as the PZT elements. We also make the assumption that the position measurements were obtained without changing the mass or stiffness of the structure; laser scanning would be one approach to accomplish this. A point force excitation was placed at the location corresponding to sensor six for acquisition of traditional force-displacement data. Analysis results for the receptance FRFs will be referred to as the mechanical modal test results and the electrical FRF analysis will be called the piezostructure modal test results.

Truncated modal models (six modes) of the beam's mechanical and electromechanical response were used to generate two different sets of H1 FRF estimates. The two sets of FRF measurements were used to generate the mechanical modal test results and the piezo modal test results, respectively. The frequency range was 0-500 Hz for the modal analysis. This bandwidth included five of the six modes. Next, the analysis results are presented for each approach.

Actual		*Mech. Test Estm.*		*Piezotest Estm.*	
f_i	ζ_i	f_i	ζ_i	f_i	ζ_i
7.2	.01	7.2	.00998	7.2	.00102
45.8	.01	45.8	.01003	45.8	.00105
129.3	.01	129.3	.00995	129.3	.00990

Table 2: Piezotest pole estimates: dual-test approach

4.2 Results

The MODHAN modal analysis software was used to generate estimates of the structural poles and residues from the two FRF matrices described above. Table 2 is a comparison of the actual and estimated poles for both modal test approaches. The curvefit quantities are essentially identical to the values used for the simulation. This is to be expected for the lightly damped beam structure.

Estimates of the Φ matrix are shown in Table 3. As discussed earlier, the quantities were extracted from the residues generated by the curvefits of the mechanical test data. All of the mode vector entries were estimated with less than 2 percent error as indicated by the comparison to the modal matrix used for the beam FRF calculations. Finally, estimates of $\hat{\Theta}$ are shown in Table 4. The modal EMC quantities were extracted from the residues generated by the curvefits of the piezostructure test data. Again, the errors in the estimated quantities are generally very low.

Least squares solutions can be used to generate the EMC matrix Θ, if desired. The issues associated with those calculations is not within the focus of this paper and will be addressed in future work.

5 Conclusion

This paper has developed a technique for the modal analysis of piezostructures and was motivated by the need for consistency between piezostructure

i	k	*Curvefit* Φ	*Actual* Φ	*Error* (%)
1	1	5.647×10^{-2}	5.684×10^{-2}	6.488×10^{-1}
	2	1.191	1.192	7.882×10^{-2}
	3	2.156	2.169	6.202×10^{-1}
	4	3.805	3.798	1.944×10^{-1}
	5	6.139	6.141	3.803×10^{-2}
	6	7.204	7.213	1.226×10^{-1}
2	1	-3.681×10^{-1}	-3.669×10^{-2}	3.304×10^{-1}
	2	-4.348	-4.351	9.154×10^{-2}
	3	-5.555	-5.557	5.012×10^{-2}
	4	-4.281	-4.285	1.020×10^{-1}
	5	2.147	2.149	9.245×10^{-2}
	6	5.869	5.861	1.346×10^{-1}
3	1	1.037	1.049	1.073
	2	5.731	5.741	1.894×10^{-1}
	3	2.321	2.333	5.175×10^{-1}
	4	-4.450	-4.464	3.185×10^{-1}
	5	-1.000	-9.974×10^{-1}	2.781×10^{-1}
	6	4.789	4.774	3.273×10^{-1}

Table 3: Mechanical test modal matrix estimate

measurements and existing modal analysis approaches. The fundamental approach has been the identification of dynamic equations which allow the piezostructure system identification problem to be cast within the existing framework of modal analysis. While the location of system zeros is different for traditional structures and piezostructures, a careful analysis of the pole-residue models of the two structures shows them to have similar forms. The residues of the traditional structure FRFs yield weighted estimates of the system eigenvector matrix Φ. Similarly, the residues obtained from piezoelectric FRF measurements yield the piezostructure's modal EMC matrix $\hat{\Theta}$. For piezostructures, $\hat{\Theta}$ is of similar importance as the eigenvalue matrix, although not as fundamental in its origin.

The relationship between the modal matrix and the EMC matrix has been discussed, $\hat{\Theta} = \Phi^T\Theta$. This transformation relationship forms the basis for a variety of different modal testing approaches, which not only include the estimate of Φ and $\hat{\Theta}$ from their respective modal tests but also the estimation of Φ from a piezostructure modal test in combination with structural displacement measurements (i.e. laser). This approach provides the experimen-

i	k	*Curvefit* $\hat{\Theta}$	*Actual* $\hat{\Theta}$	*Error (%)*
1	1	1.003×10^{-3}	1.011×10^{-3}	8.029×10^{-1}
	2	7.321×10^{-4}	6.244×10^{-4}	1.724×10^{1}
	3	4.049×10^{-4}	4.190×10^{-4}	3.372
	4	2.645×10^{-4}	2.478×10^{-4}	6.710
	5	4.699×10^{-5}	4.589×10^{-5}	2.400
	6	5.191×10^{-6}	5.361×10^{-6}	3.162
2	1	4.739×10^{-3}	4.722×10^{-3}	3.406×10^{-1}
	2	-2.475×10^{-3}	-2.489×10^{-3}	5.571×10^{-1}
	3	-4.675×10^{-3}	-4.703×10^{-3}	5.926×10^{-1}
	4	-4.818×10^{-3}	-4.833×10^{-3}	3.099×10^{-1}
	5	-1.475×10^{-3}	-1.477×10^{-3}	1.117×10^{-1}
	6	-1.720×10^{-4}	-1.739×10^{-4}	1.128
3	1	9.378×10^{-3}	9.396×10^{-3}	1.840×10^{-1}
	2	-1.229×10^{-2}	-1.228×10^{-2}	4.773×10^{-2}
	3	-5.329×10^{-3}	-5.338×10^{-3}	1.732×10^{-1}
	4	1.243×10^{-2}	1.246×10^{-2}	2.321×10^{-1}
	5	8.354×10^{-3}	8.297×10^{-3}	8.871×10^{-1}
	6	9.435×10^{-4}	9.763×10^{-4}	3.366

Table 4: Piezotest modal electromechanical coupling matrix estimate

tal measurement of parameters which previously could only be calculated analytically.

There has been an increasing dichotomy between smart structures research and modal analysis research. Two perceived roadblocks to modal testing of piezostructures have been addressed in this paper: drive-point measurements and input force measurements. It has been shown that piezostructure electrical FRFs can be generated so that drive-point measurements and input force measurements are available from knowledge of the driving voltage. In addition, the coupled electromechanical dynamic equations allow a relatively easy transformation between traditional modal parameters and the piezostructure modal parameters whether or not a customary shaker-loadcell modal test approach has been completed. Thus, the proposed piezostructure modal test methods introduce a significant shift in previous philosophies for modal testing. Modal parameter estimation for smart structures can be accomplished without the addition of shaker and sensor mass which traditionally accompanies modal test methods. Hopefully, the implications of such an approach, especially for lightweight, flexible structures, will lead to increased research in modal testing of smart structures.

References

1. Brown, D.L., Allemang, R.J. and Zimmerman, R., 1979, "Parameter Estimation Techniques for Modal Analysis," SAE paper 0148-7191/79/0226-0221.

2. Dosch, J. J. and Inman D. J., 1992, "A Self-Sensing Piezoelectric Actuator for Collocated Control," J. of Intell. Mater. Syst. and Struct., Vol 3.

3. Anderson, E. H. and Hagood, N. W., 1992, "Self-Sensing Piezoelectric Actuation: Analysis and Application to Controlled Structures," AIAA-92-2465-CP.

4. Klosterman, A.L., 1971, "On the Experimental Determination and Use of Modal Representations of Dynamic Characteristics," PhD Dissertation, U. of Cinn.

5. Crawley, E.F. and de Luis, J., 1987, "Use of Piezoelectric Actuators as Elements of Intelligent Structures," AIAA J., **25**, 10, pp.1373-1385.

6. Hagood, N.W., Chung, W.H. and von Flotow, A., 1990, "Modeling of Piezoelectric Actuator Dynamics for Structural Control," J. Intell. Mater. Syst. and Structures, 1, 3, pp.327-354.

7. Cole, D.G., 1992, "Design of, and Initial Experiments with, a MIMO Plate Control Testbed," Master's Thesis, VPI&SU, Blacksburg, VA.

C-41 Development of an Actuator Power Factor Meter for Experimental Determination of the Optimal Actuator Location on Complex Structures, C. Liang, P. Sun and C. A. Rogers, Proceedings of SPIE Smart Materials and Structures Conference, Orlando, FL, SPIE Vol. 2190, pp. 262-274, 13-18 February 1994.

Development of an Actuator Power Factor Meter for Experimental Determination of the Optimal Actuator Location on Complex Structures

C. Liang, F. P. Sun, and C. A. Rogers

Center for Intelligent Material Systems and Structures
Virginia Polytechnic Institute and State University
Blacksburg, VA 24061

ABSTRACT

Actuator power factor, defined as the ratio of structural dissipative mechanical power to apparent supplied electrical power, describes the effectiveness of the integrated actuators to convert supplied electrical power to mechanical power which creates the intended structural response. A large actuator power factor in the frequency range of application indicates that the corresponding actuator (position) has a higher authority to excite its host structure in that frequency range than positions with a lower power factor. The use of actuator power factor provides an alternate tool in the determination of the optimal actuator locations and dimensions to theoretical calculations. More importantly, the power factor can be experimentally measured on large-scale complex structures, thereby eliminating the need for sophisticated theoretical modeling.

The concept of an actuator power factor was first introduced by the authors (Liang et al., 1993a) and will be briefly described herein. The utility of using the actuator power factor in optimizing an actuator system will then be illustrated using a numerical case study. The hardware development of the actuator power factor meter will be presented. The application of actuator power factor meter for optimal experimental actuator placement will be discussed.

1. INTRODUCTION

The optimal actuator location for an active control application depends on the type of objective functions, the nature and magnitude of the disturbance force, control frequency or frequency ranges, and certainly the structure itself. Such theoretical analysis have been conducted on simple structures, such as simply-supported plates (Wang et al., 1994; Wang, 1991; Song et al., 1992a; 1992b), but extending such analyses technique to complex structures is almost impossible because of the difficulty involved in quantifying the disturbance and structural dynamic characteristics.

The underlying philosophy of the method proposed by the authors is that, if one needs to use actuators to create a controllable response to minimize the overall vibration or structural acoustic radiation, the structural response resulting from the actuators must be comparable (at the same magnitude level) to the structural response created by the disturbance force alone. Therefore, the objective function for selecting the optimal actuator locations for active control in this proposed technique is to maximize the structural response resulting from the actuator activation. In other words, to maximize the energy conversion efficiency from the actuators to the host structures.

The energy conversion between an integrated actuator and its host structure is a very delicate issue. Several parameters may be used to represent the conversion efficiency (Liang et al., 1994). The easiest and, most importantly, the measurable

0-8194-1485-9/94/$6.00

index, is the actuator power factor.

The current approaches to determining the optimal induced strain actuator position for active control application may be categorized into two categories. One involves theoretical modeling, while the other approach uses an experimental trial-and-error method. An example of the latter approach is described in the following discussion regarding active vibration control of plate structures. To reduce the vibration of a plate structure, the first step is to determine the control frequency or control frequency range and select the type of actuator, e.g., a PZT actuator. To determine where to place the actuator, several of them may be bonded to the plate and activated individually to excite the plate at the frequency or in the frequency range determined during the first step. Whether this actuator position is good or bad can be determined based on the magnitude of the structural response. A large response indicates the actuator is at a good position. This means that it is also necessary to measure the response of the structure, sometimes the response of the entire structure. Several actuator positions may need to be tested in order to find the most effective actuator location. However, if the active vibration control is to be applied in a frequency range rather than at a single frequency, the structural responses in that frequency range resulting from individual actuators at different positions will then be compared to determine the most effective actuator position. In summary, to determine the effective actuator position based on current techniques, one would need to bond the actuators at several locations on the structure, activate individual actuators, measure the structural response, and compare the structural response. Comparing the structural response at different locations and in a frequency range can sometimes be very frustrating.

The technique introduced herein to experimentally determine the actuator locations and dimensions is based on the concept of the actuator power factor (Liang, Sun, and Rogers, 1993a). The actuator power factor, defined as the ratio of structural dissipative mechanical power to apparent supplied electrical power, describes the effectiveness of integrated actuators to convert supplied electrical power to mechanical power which creates the intended structural response. A large actuator power factor in the frequency range of application indicates that the corresponding actuator position has a higher authority to excite the host structure in that frequency range than positions with a lower power factor. The actuator power factor can be easily measured from actuators integrated in large-scale complex structures. The use of the actuator power factor concept provides an experimental tool in the design of the optimal actuator locations and dimensions and is an alternative to theoretical modeling and the present trial-and-error experimental approach. This paper discusses the development of a piece of electronic hardware, an actuator power factor meter, which can be used to conveniently determine the optimal actuator locations.

Consider the following scenario where an actuator power factor meter is used to locate the optimal PZT actuator locations on a plate. The meter is connected to both of the electrodes of an actuator to measure the actuator power factor. This is done by essentially measuring the current through the actuator which is governed by the structural impedance at the actuator location. Moving the actuator to another position will yield another power factor curve (vs. frequency), depending on whether the actuator is to be operated at a particular frequency or in a frequency range. For example, the power factor of an identical actuator at three different locations in a frequency range can be measured, as shown in Fig. 1. The best actuator position, which provides the highest power factor overall, can be easily determined from the results shown in Fig. 1 as the second location.

2. INTRODUCTION TO ACTUATOR POWER FACTOR

If a voltage, $V = v \sin(\omega t)$, is applied against a load (electrical or electro-mechanical), the current measured in the circuit is $I = i \sin(\omega t+\phi)$. The voltage and current are related by the electrical admittance, $Y=Re(Y)+iIm(Y)$, of the load, i.e., $I = YV$. A measured electrical admittance of an integrated actuator, such as a PZT, a PMN, a Terfenol, and a shaker actuator, (referred to as electro-mechanical admittance) includes structural dynamic characteristics and physical and material properties of the integrated actuator. There are three types of electric power defined as follows (Hammond, 1970):

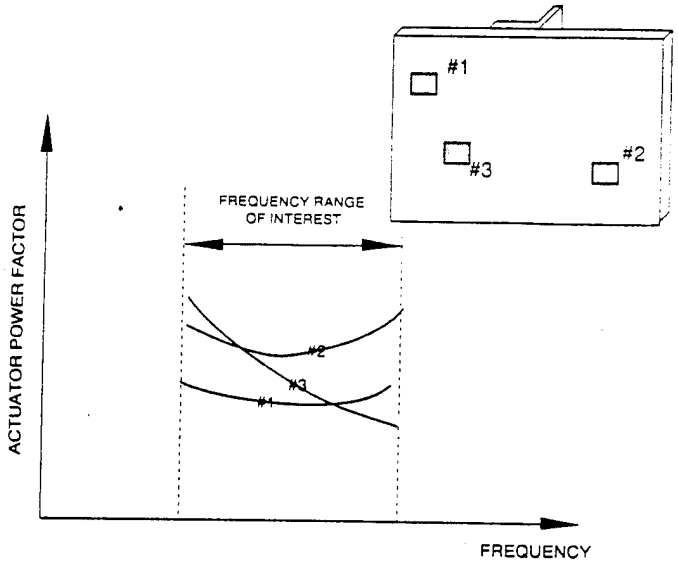

Figure 1: Schematic diagram of actuator power factor measured from an actuator at three locations.

The apparent power, W_A:

$$W_A = I_e V_e = \frac{V^2}{2} |Y| , \tag{1}$$

where I_e and V_e are the RMS current and voltage, respectively.

The dissipative power, W_D:

$$W_D = W_A \cos\phi = \frac{V^2}{2} Re(Y) . \tag{2}$$

The reactive power, W_R:

$$W_R = W_A \sin\phi = \frac{V^2}{2} Im(Y) . \tag{3}$$

The apparent power is the power supplied to the induced strain actuators. The dissipative power, as implied by its name, is the power transformed into other energy forms, such as heat and acoustic radiation. The reactive power, however, remains and circulates within the electro-mechanical system, including power source, mechanical structures, and actuators. The reactive power consists of mechanical reactive power related to the mass (kinetic energy), stiffness (potential strain energy), and the electrical reactive power (electric and magnetic field energy associated with the capacitors and inductors).

The real admittance includes two parts: part one is from the damping of the mechanical systems, and the other part from the internal loss of the induced strain actuator (dielectric loss and mechanical loss for a PZT actuator). The power

tion due to the damping of the mechanical system, or the structural dissipative mechanical power, is associated with ctural vibration. The power due to the internal loss of the induced strain actuators is dissipated in terms of heat generated the actuators, which is an important parameter to quantify for the thermal stress analysis of the system. The energy cy of the actuator (actuator power factor) in driving the system, therefore, may be defined as:

$$\psi = \frac{Dissipative\ Mechanical\ Power}{Supplied\ Electric\ Power} = \frac{Re(Y_s)}{|Y|}, \qquad (4)$$

Y_s is the coupled electro-mechanical admittance which does not include the electrical loss of the actuators.

The actuator power factor defined in Eq. (4) indicates the percentage of the electrical energy converted into mechanical and dissipated within the structure as a result of the structural damping, acoustic radiation, etc. Consider the structural tor which may be defined as (Harris, 1988):

$$\eta = \frac{U_{MD}}{2\pi U_M}, \qquad (5)$$

U_{MD} is the dissipative mechanical energy and U_M is the total mechanical energy or the total of the mechanical kinetic potential energy. A larger dissipated power, therefore, indicates a larger vibrational energy (or a larger response). A higher tor power factor means that more electrical power has been converted into mechanical power, resulting in a larger tural response and, consequently, a higher dissipative mechanical power. Therefore, the actuator power factor can be used present the actuator effectiveness or control authority.

The concept of actuator power factor is similar to the electric power factor used in the theory of electricity, which is ined as the ratio of total dissipative electrical power to apparent electrical power for an electrical network (Hammond, 1970). tuator power factor discussed herein is derived based on a coupled electro-mechanical model of induced strain actuators and impedance method as discussed in Liang, Sun, and Rogers (1993a and 1993b). A brief introduction to the actuator power tor is presented below. PZT actuators are used as an example in this paper, however, the algorithm and experimental device lined herein can also be applied to determining the optimal actuator locations for other types of actuators, including ctrostrictive, magnetostrictive, electro-magnetic actuators, etc.

3. INTRODUCTION OF PZT ACTUATOR POWER CONSUMPTION

The dynamic interaction of a PZT actuator and its host structure can generally be simplified as shown in Fig. 2 (PZT assumed to operate in its 3-2 mode). Using the constitutive relations of PZT (both piezoelectric effect and its converse effect), the equation of motion of PZT (the dynamic characteristics of PZT actuator), and a mixed boundary condition at $x=l_A$, which is described by force = impedance·velocity, the stress, strain, and electric displacement field within the PZT actuator can be written as (Liang et al., 1993a):

$$\bar{S}_2 = \frac{Z_A d_{32} \bar{E}}{Z_A + Z} \frac{\cos(ky)}{\cos(kl_A)}, \qquad (6)$$

the stress:

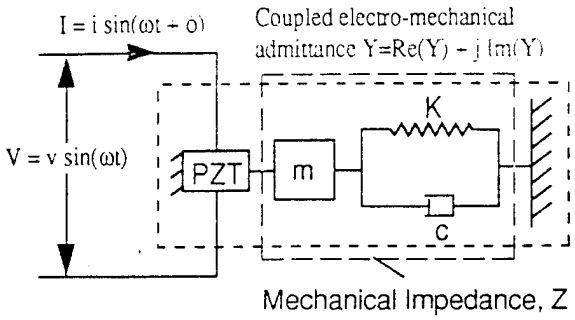

Figure 2: A schematic electro-mechanical representation of a PZT actuator driven mechanical system.

$$\overline{T}_2 = \left(\frac{Z_A}{Z_A + Z} \frac{\cos(ky)}{\cos(kl_A)} - 1 \right) d_{32} \overline{Y}_{22}^E \overline{E}, \tag{7}$$

and the electric displacement field:

$$\overline{D}_3 = \frac{Z_A \overline{Y}_{22}^E d_{32}^2 \overline{E}}{Z_A + Z} \frac{\cos(ky)}{\cos(kl_A)} + (\overline{\epsilon}_{22}^E - d_{32}^2 \overline{Y}_{22}^E) \overline{E}, \tag{8}$$

where $\overline{S}_2$ is the strain, $\overline{T}_2$ the stress, $\overline{E}$ the electric field, $\overline{s}_{22}^E$ the complex compliance at a constant electric field, d_{32} the piezoelectric constant, $\overline{\varepsilon}_{33}^T$ the complex dielectric constant at a constant stress given by $\varepsilon_{33}^T(1-\delta i)$, δ the dielectric loss factor, and $\overline{D}_3$ the electrical displacement. ρ is the density of the PZT, $\overline{Y}_{22}^E = Y_{22}^E (1+i\eta)$, is the complex modulus of PZT at a constant electrical field, and η is the mechanical loss factor of PZT. The complex wave number k is given by:

$$k^2 = \omega^2 \rho / \overline{Y}_{22}^E . \tag{9}$$

The short-circuit mechanical impedance of the PZT actuator, Z_A, is given by Liang et al. (1993a):

$$Z_A = -\frac{K_A(1+\eta i)}{\omega} \frac{kl_A}{\tan(kl_A)} i, \tag{10}$$

where K_A is the static stiffness of the PZT actuator.

The electric current is calculated using

$$I = i\omega e^{i\omega t} \int\int \overline{D}_{dx} dy = \overline{I} e^{i\omega t}, \tag{11}$$

yielding:

$$\bar{I} = i\omega \bar{E} w_A l_A \left(\frac{d_{32}^2 \bar{Y}_{22}^E Z_A}{Z + Z_A} \frac{\tan(kl_A)}{kl_A} + \bar{\epsilon}_{33}^T - d_{32}^2 \bar{Y}_{22}^E \right), \tag{12}$$

where w_A is the width of the PZT actuator.

Since the electric field, $\bar{E} = \bar{V}/h_A$, (h_A is the thickness of the actuator) the electro-mechanical admittance, $Y = \bar{I}/\bar{V}$, is then found as:

$$Y = i\omega \frac{w_A l_A}{h_A} \left(\frac{d_{32}^2 \bar{Y}_{22}^E Z_A}{Z + Z_A} \frac{\tan(kl_A)}{kl_A} + \bar{\epsilon}_{33}^T - d_{32}^2 \bar{Y}_{22}^E \right). \tag{13}$$

Because $\tan(kl_A)/kl_A$ is close to one in the frequency range of interest in most active vibration control applications, Eq. (13) may be further simplified as:

$$Y = i\omega \frac{w_A l_A}{h_A} \left(\bar{\epsilon}_{33}^T - \frac{\dot{Z}}{Z_A + Z} d_{32}^2 \bar{Y}_{22}^E \right). \tag{14}$$

It is clear that the coupled electro-mechanical admittance includes the capacitance of the PZT material and mechanical interaction represented by the mechanical impedance terms. The resonance of the electro-mechanical system occurs when the actuator impedance, Z_A, and the structural impedance, Z, match (are complex conjugate).

There are two possible power factor definitions: one is referred to as system power factor defined by:

$$\psi_s = \frac{total\ dissipative\ power}{total\ supplied\ power} = \frac{Re(Y)}{|Y|} \tag{15}$$

where the admittance, Y, is given by Eq. (14). The definition given by Eq. (4) is different from the definition of the system power factor because it does not include the electrical dissipation of the induced strain actuators, which is the dielectric loss in the case of PZT materials.

The electro-mechanical admittance used in Eq. (4), Y_s, may be calculated from Eq. (14) by assuming a zero dielectric loss factor for the PZT actuator. The direct measurement is the system power factor, ψ_s, defined by Eq. (15). However, since the dissipation associated with the electrical loss of an induced strain actuator is linearly related to the total dissipation and can be quantified beforehand, its influence may be subtracted directly from the measured electrical admittance, Y, to obtain Y_s in order to calculate the true actuator power factor defined by Eq. (4).

4. NUMERICAL CASE STUDIES

In this case study, the influence of actuator location on the actuator power factor is investigated. The structure is a simply-supported beam with two actuators bonded on its top and bottom surfaces, as shown in Fig. 3. The beam is made of aluminum with a density $\rho_B = 2700$ kg/m^3, elastic modulus $Y_B = 69$ GPa, length $l_B = 0.6$ m, width $w_B = 25.4$ mm, and thickness $h_B = 3$ mm. The loss factor for the aluminum is assumed to be 0.005. The PZT actuator has a width $w_A = 25.4$ mm, length

l_A =40 mm, and thickness h_A = 0.2 mm. Four actuator locations have been examined. The basic material properties for the PZT material (G1195) are listed in Table 1. A detailed discussion on this case study can be found in Liang et al. (1993c).

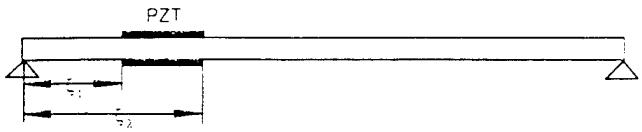

Figure 3: A schematic of the simply-supported beam used in the numerical case study.

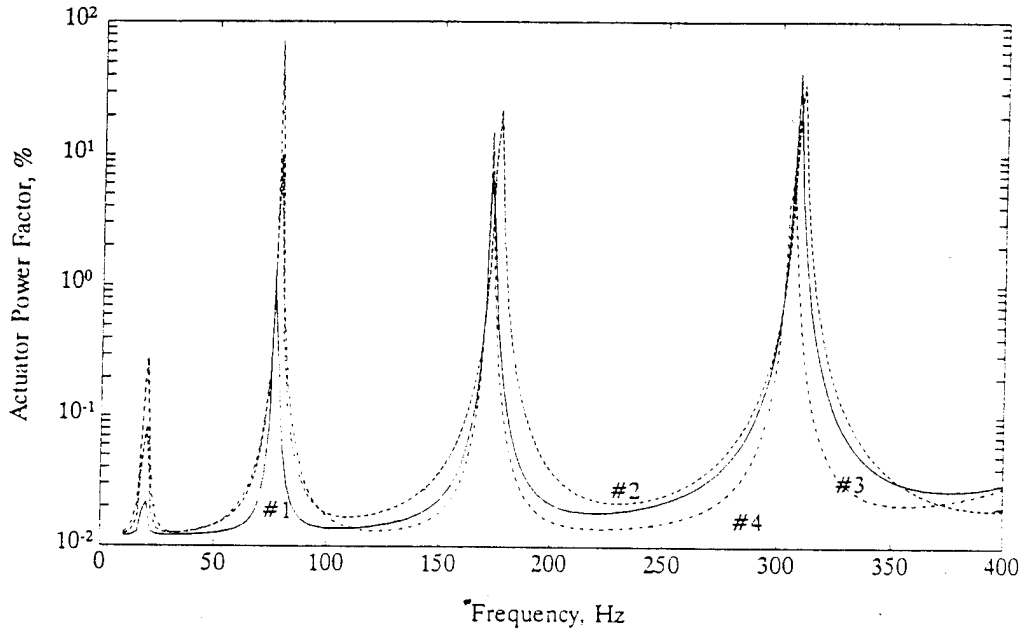

Figure 4: Actuator power factors vs. frequency for four actuator positions. Position #1 (solid line) is 20 mm from the left end (to the left end of the actuator) of the beam, #2 (dashed line) is 80 mm, position #3 (dash-dotted line) is 150 mm, and position #4 is 280 mm.

Table 1: Material Properties of G1195 PZT (from Piezo System, Inc.)

d_{32} (m/volt)	Y_{22}^E N/m^2	ρ kg/m^3	ε_{33}^T Farads/m	δ	η
-166×10^{-12}	6.3×10^{10}	7650	1.5×10^{-8}	0.012	0.001

Four actuator locations, 20 mm, 80 mm, 150 mm, and 280 mm (ξ_1) from the left end of the beam to the left end of the actuator (listed as location 1, 2, 3, and 4), have been examined. The actuator power factors corresponding to these four

cations are plotted in Fig. 4. The actuator power factor for position 1 (20 mm from the left end) given by the solid line has lowest resonance power factor (power factor at system resonance) at the first mode. This indicates that an actuator at this cation is not effective for exciting the first mode. This conclusion is the same as what has been obtained from the modal domain optimization approach (Juang and Rodriguez, 1981; Jia, 1990) which shows that actuator at anti-nodal line (curvature mode for bonded PZT actuators) has the highest authority (or excites the most of vibration for a given voltage), while actuator at nodal line has the lowest authority to excite the corresponding mode. The power factor of the actuator at location 4 (dotted line in Fig. 4) also demonstrates that a PZT actuator at the curvature anti-nodes can effectively excite their corresponding modes. Note: in the case of simply-supported boundary condition, curvature modes coincide with the normal modes. Since the position 4 is the antinode of the odd modes and the node of the even modes, actuator at this location has the highest authority on the odd modes but almost zero effect on the even modes. The results in Fig. 4 show that the resonance actuator power factor (position 4) is the maximum at the first and third mode and very small at the second and fourth mode. The small peak at the fourth mode is caused by the mass loading of the actuator.

If active vibration control is to be applied to the on-resonance response, the design of actuator location based on actuator power factor provides identical results as that determined based on modal domain optimization approach. However, the power factor approach can provide much better options for the actuator location for off-resonance vibration control. Although the results shown in Fig. 4 indicate that the actuator power factor generally is much smaller than unity except on-resonance, it is still meaningful to compare the small off-resonance actuator power factor to determine the most energy-efficient actuator location. For example, if the frequency range is limited from 200 to 250 Hz, position 3 (dash-dotted line) is definitely the worst of the four locations. Position 2 (dashed line) seems to be the most efficient position of the four locations considered. If, for some reason, the actuator can only be bonded at position 3, other approaches, such as changing the actuator length and thickness, need to be explored to increase the actuator authority.

It is very important to recognize that a higher actuator power factor only indicates a higher energy conversion efficiency for the actuator. Whether the actuator is capable of generating enough response to suppress what caused by disturbance is dependent on the capability of actuator to deliver force or stroke.

5. DEVELOPMENT OF ACTUATOR POWER FACTOR METER

A commercial electrical impedance analyzer may be used to determine the actuator power factor. The impedance analyzer applies an AC voltage across an actuator and measures the current passing through the actuator at the same time. The electrical (or electro-mechanical) admittance or impedance can be determined from the current and voltage. However, a commercial impedance analyzer costs more than $10,000 dollars and has extra functions which are not needed for the specific application discussed in this paper. A commercial impedance analyzer is also heavy and not convenient to transport. One of the most important drawbacks of the commercial impedance analyzer currently available is that the voltage supplied to an actuator is very low (below 2 volts RMS) and is not enough to sufficiently activate the actuators on very large structures, especially the PZT actuators which need high driving electrical field, resulting in a low signal-to-noise ratio in some frequency ranges for large structures.

The technique of using an actuator power factor meter to experimentally determine the optimal actuator location will rely on two major hardware components: the actuator power factor meter and re-attachable actuator/sensors. Re-attachable actuator/sensors can be easily attached to the surface of complex structures and have the authority to generate an excitation similar to the actuators of interest. For example, a re-attachable PZT actuator/sensor can be made by bonding two PZT actuator patches to both sides of a larger thin steel piece (base), as shown in Fig. 5. The actuators generate in-plane excitation when

activated. The steel base can be attached to a structural surface through mechanical fastening, adhesive bonding, or even magnetic attraction, which allows it to be removed easily to put at other locations without damaging the PZT patches. An actuator of such design similar to the one shown in Fig. 5 is now being investigated.

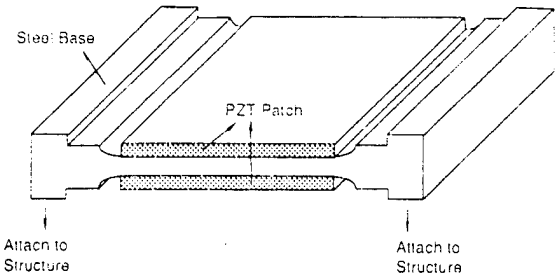

Figure 5: A schematic of a re-attachable PZT actuator.

The power factor meter being developed is a self-contained unit, as shown in Fig. 6. It consists of a signal generator capable of frequency sweeping, a power amplifier, power factor calculation module, a data display, and a PC RS-232 interface. When measuring the power factor, the power factor meter is connected to an actuator (PZT, Terfenol, PMN actuator, and even an electro-magnetic shaker), and the function generator is set at a particular frequency or allowed to sweep a particular frequency range. The display screen of the meter will then plot the power factor vs. frequency curve. The power factor meter will also be able to transfer data to a personal computer for further data processing and printing.

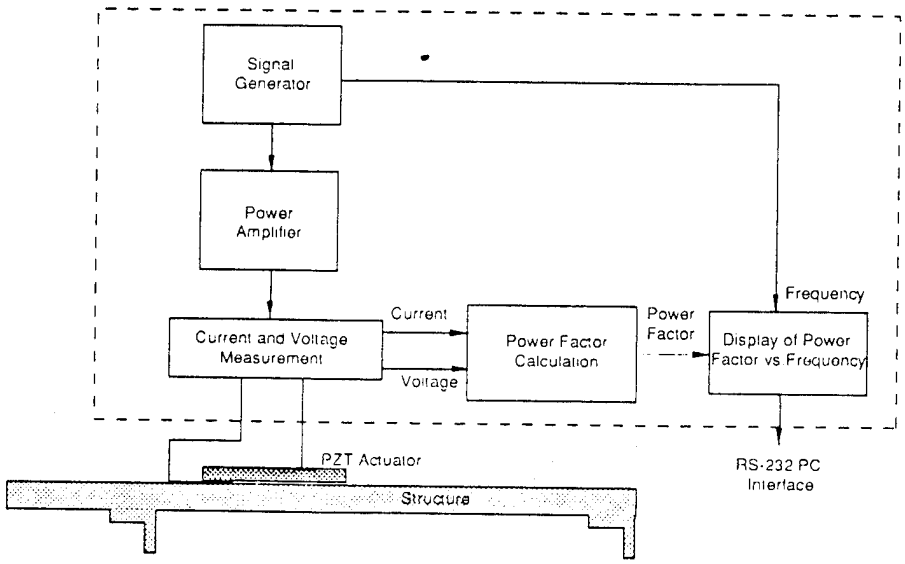

Figure 6: A schematic of the design of the actuator power factor meter.

Figure 7 shows the block diagram of the circuit used to determine the system power factor, ψ_s. The electrical voltage across and the current passing through an actuator (or a re-attachable actuator/sensor) are measured first. The voltage is measured as $V = v \sin(\omega t) = I/Y = I Z$. The current is $I = i \sin(\omega t+\phi)$. The measured voltage and current are fed to a multiplier (commercial chips available) which outputs a signal $y = i^2|Z| \cos(\phi) - i^2|Z| \cos(2\omega t)$. This output, y, consists of a DC and an AC component. The DC component can be obtained using a low-pass filter. The amplitude of the AC component can also be obtained using a combination of high-pass filter and peak detector circuit. The DC component represents the real or dissipative power (dissipated within the structure and actuator) (Clayton, 1977). The amplitude of the AC component provides the apparent electrical power. The signals obtained after the low-pass filter and peak detector, i.e., the real and apparent power, are fed to a divider to determine the system power factor or $\cos(\phi)$. The analog output of the actuator power factor can then be processed to display or to an RS-232 board to transfer the data to a personal computer.

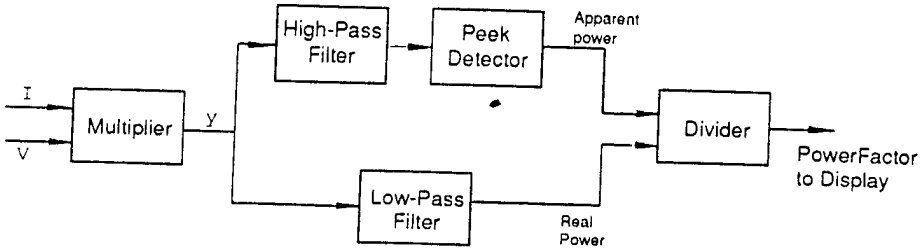

Figure 7: A schematic of the circuit diagram to determine system (actuator) power factor.

Theoretical prediction of the actuator power factor may distinguish the dissipative power resulting from the actuator electrical loss and structural mechanical loss. A direct experimental measurement of the power factor will include the influence from the energy loss of the actuator (its dielectric loss), which causes a slight increase in the power factor, especially at off-resonance. Circuit compensation must be made to isolate the influence of the loss of the actuator itself. For example, a simple circuit may be added to compensate the DC component of the signal y so that the actuator electrical loss can be subtracted. This can be easily performed if the measured electrical voltage and current are processed digitally, which is the next goal of this research.

6. MEASUREMENT RESULTS

Figure 8 shows a power factor meter prototype which contains the calculation module illustrated in Fig. 7. An external function generator and power amp are used with the power factor meter. A LCD panel is used to display the measured actuator power factor value. Shown in Fig. 8 also includes a simply-supported aluminum panel bonded with a PZT actuator of which the actuator power factor (in this case system power factor, ψ_s) is measured.

The measured actuator (system) power factor is plotted in Fig. 9. The dashed line is the theoretical prediction which is documented in detail in Zhou et al., (1994). The theoretical prediction generally agrees with the power meter measurement except at the fifth and seventh mode. The difference is caused by the use of ideal simply-supported boundary conditions in the theoretical predictions.

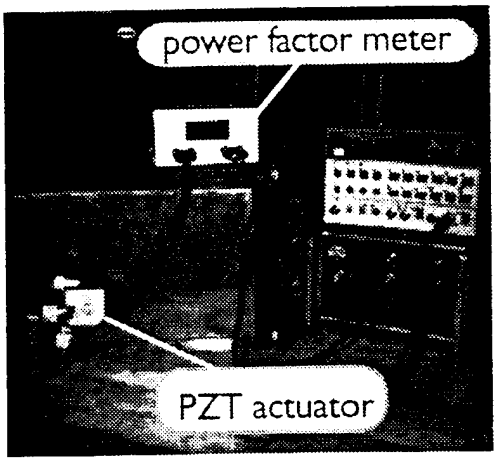

Figure 8: Measurement of actuator (system) power factor of a PZT actuator bonded on a plate.

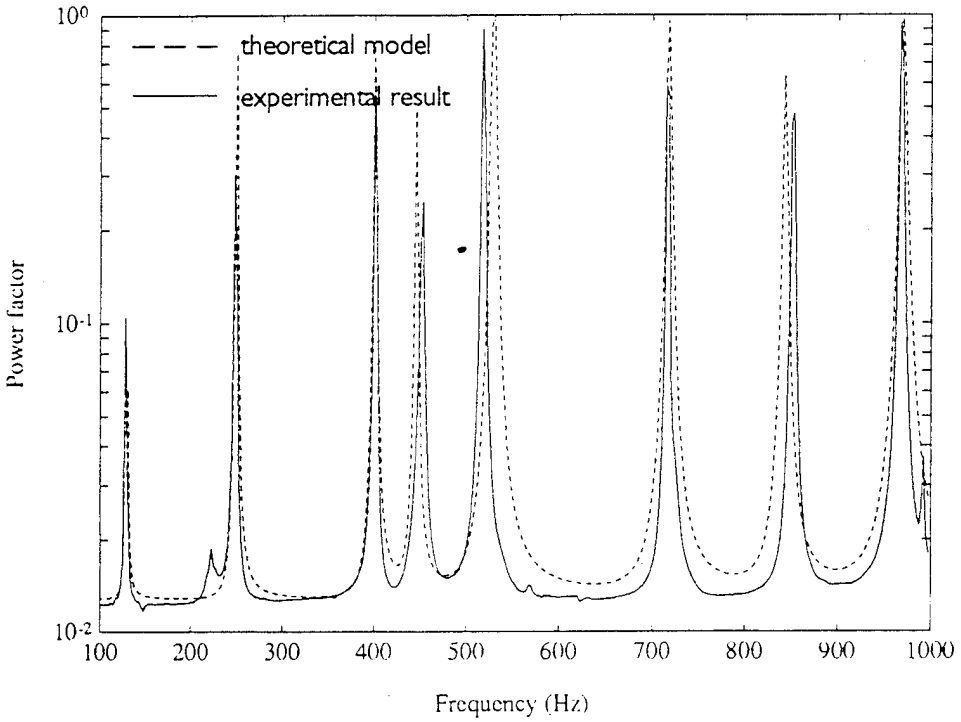

Figure 9: Measured and predicted system (actuator) power factor (Zhou et al., 1994).

7. SUMMARY

This paper presents a technique and associated hardware devices to experimentally determine the optimal actuator locations for structural vibration and acoustic control. The proposed technique and devices can be used with any types of actuators, including PZT, Terfenol, PMN, and even electro-magnetic shakers. The proposed technique has a clear advantage for locating the optimal actuator positions on complex structures where vibration testing and theoretical modeling are difficult.

Besides further hardware development, one of the major issues to be addressed in the future is to develop an algorithm to help locate multiple optimal actuator positions. If the multiple actuator system is driven by one control channel, the multiple actuator system may be treated as one single actuator and the technique presented in this paper can still be applied. If the multiple actuator system is to be controlled by several channels, more investigation is still needed in order to quantify the optimal actuator locations using the proposed technique and hardware devices.

8. ACKNOWLEDGEMENT

The authors would like to express their gratitude to the Office of Naval Research, Grant ONR N00014-92-J-1170, Dr. Kam Ng, the program monitor.

9. REFERENCES

Clayton, G. B., 1977, Linear Integrated Circuit Applications, Blue Ridge Summit, PA.

Hammond, S. B., 1970, Electrical Engineering, McGraw-Hill, NY.

Harris, C. M., 3rd Edition, 1988, Shock and Vibration Handbook, McGraw-Hill Inc., NY.

Juang, J. N. and Rodriguez, G., 1981, "Formulation and Application of Large Structure Actuator and Sensor Placements," Proceedings of 3rd VPI and SU/AIAA Symposium on Dynamics and Control of Large Flexible Spacecraft, Blacksburg, 1981.

Jia, J. H., 1990, "Optimization of Piezoelectric Actuator Systems for Vibration Control of Flexible Structures", Ph.D. Dissertation, Department of Mechanical Engineering, Virginia Polytechnic Institute and State University, Blacksburg.

Liang, C., Sun, F. P., and Rogers, C. A., 1993a "Coupled Electric-Mechanical Analysis of Piezoelectric Ceramic Actuator Driven Systems - Determination of the Actuator Power Consumption and System Energy Transfer," Proceedings of Smart Structures and Materials'93, Albuquerque, NM, Jan. 31 to Feb. 4, 1993, pp. 286-298.

Liang, C., Sun, F. P., and Rogers, C. A., 1993b, "An Impedance Method for the Dynamic Analysis of Active Material Systems," Proceedings of 34th SDM Conference, LaJolla, CA, April 19-21, 1993, pp. 3587-3599.

Liang, C., Sun, F. P. and Rogers, C. A., 1993c, "Determination of the Optimal Actuator Location and Configurations Based on Actuator Power Factor," Proceedings, Fourth International Conference on Adaptive Structures, Cologne, Germany, Nov. 2-4, 1993, in press.

Liang, C. Sun, F. P., and Rogers, C. A., 1994, " An Investigation of the Energy Consumption and Conversion of Piezoelectric Actuators Driving Active Structures," an invited paper to the Second International Conference on Intelligent Materials, Williamsburg, Virginia, June 5-8, 1994, in press.

Song, T., Fuller, C. R., and Burdisso, R. A., 1992a, "Optimization of Actuator Locations for Active Control of Sound Radiation from Structures Under Multiple-Frequency Excitation," submitted to Journal of Acoustical Society of America.

Song, T., Burdisso, R. A., and Fuller, C. R., 1992b, "Optimization of Actuator Location and Controller Robustness Analysis for Active Structural Acoustic Control", submitted to Journal of Acoustical Society of America.

Wang, B. T., 1991, "Active Control of Sound Transmission/Radiation from Elastic Plates Using Multiple Piezoelectric Actuators", Ph.D. Dissertation, Dept. of Mech. Eng., Virginia Polytechnic Institute and State University, June.

Wang, B. T, Burdisso, R. A., and Fuller, C. R., 1994, "Optimal Placement of Piezoelectric Actuators for Active Structural Acoustic Control", Journal of Intelligent Material Systems and Structures, No. 1, Vol. 5, pp. 67-77.

Zhou, S. W., Liang, C., and Rogers, C. A., 1994, "An Electro-Mechanical Impedance Analysis to Predict Power Consumption of Piezoelectric Actuators Integrated with Thin Plates", Proceedings of 35th SDM Conference, in press.

C-42 Special Considerations in the Modeling of Induced Strain Actuator Patches Bonded to Shell Structures, Z. Chaudhry, F. Lalande and C. A. Rogers, Proceedings of SPIE Smart Structures and Materials Conference, Orlando, FL, SPIE Vol. 2190, pp. 563-570, 13-18 February 1994.

Special considerations in the modeling of induced strain actuator patches bonded to shell structures

Z. Chaudhry, F. Lalande and C. A. Rogers
Center for Intelligent Material Systems and Structures
Virginia Polytechnic Institute and State University
Blacksburg, Virginia 24061-0261

ABSTRACT

Based on the thin-shell Donnel theory, a model to represent the action of discrete induced strain actuator patches bonded to the surface of a circular cylindrical shell has been developed. The model provides estimates of the curvature due to the out-of-phase actuation and the in-plane strains due to the in-phase actuation of the bonded actuator patches. The magnitudes of the induced curvature and the in-plane strain are found to be identical to those of plates; however, due to the cylindrical strain-displacement relations, the in-plane and out-of-plane displacements are coupled. Expressions for the equivalent forces and moments that represent the action of the actuator patches have been developed. Due to the curvature of the shell, the representation of the in-phase actuation with an equivalent in-plane line force applied along the edge of the actuator results in the application of erroneous rigid-body transverse forces. To avoid these rigid body forces, a method to represent the in-phase actuation with a system of self-equilibrating forces is proposed. The action of the actuator is then represented by an equivalent in-plane force and a transverse distributed pressure applied in the region of the actuator patch. Finite element verification of the proposed model is presented. The displacements due to the actual actuator actuation are compared with the proposed model, and very good agreement is found.

INTRODUCTION

In recent years there has been a great surge of interest in research on shape, vibration and acoustic control of structures with induced strain actuators like piezoelectrics and shape memory alloys. What distinguishes induced strain actuators from conventional hydraulic and electrical actuators, and makes them especially attractive for smart structures, is their ability to change their dimensions and properties without utilizing any moving parts. These actuator materials contract and expand just like the muscles in the human body. When integrated into a structure (either through embedding or through surface-bonding), they apply localized strains and directly influence the extensional and bending responses of the structural elements. Because of the absence of mechanical parts they can be easily integrated into the base structure. Integration within the structure ensures an overall force equilibrium between the forcing actuator and the deforming structure, thus precluding any rigid body forces and torques.

Induced strain actuators, like piezoelectrics when bonded to the surface of a structure, generate a set of forces which are concentrated close to the edges of the actuator. Therefore, their action is often represented by line moments or forces applied along the periphery of the actuator. This representation simplifies analysis because the structure does not have to be discretized (to represent the non-uniform structural properties in the regions of the patches) and global structural equations can be solved with the actuator forces appearing as discretely applied external forces. This analysis method, although approximate (approximate because the actuator mass and stiffness are not represented and actuator forces derived from static and stress-free boundary conditions are used), gives reasonably accurate results for small and thin patches of actuators. Also, for the case of straight structural members like beams and plates, it does not pose any problems such as the equivalent actuator forces producing rigid-body motion. For shell-type structures, however, due to their curvature, this simple representation is not appropriate for the case of in-phase actuation. In-phase actuation refers to the case when the two actuators bonded to the top and bottom surface of the shell are activated to produce strains in the same direction. Because the circumferential forces used to represent the action of the actuator are not co-linear they produce rigid-body transverse forces on the shell. Thus, certain special modifications must be made to such a representation scheme to accommodate the special characteristics of the shell structures. The modification proposed and verified in this paper is the application of a uniform transverse pressure across the footprint of the actuator.

To date, a number of models to represent the action of actuators on beams and plates have been proposed.[1-5] For

shells, the only models that have been developed are based on layered shell theory, i.e., the analytical model assumes that the induced strain actuator material comprises a total, distinct layer of the shell.[6,7] In the work that has been reported on vibration and acoustic control of shells using piezoelectric actuators, plate models are often adapted to shells.[8,9] At first sight, this adaptation seems perfectly reasonable because the shell is thin and r/h is large. This does, however, pose a problem for the representation of in-phase actuation forces because the actuator forces are no longer co-linear as in the case of beams and plates, and as stated earlier, this results in a rigid-body force being applied to the shell (see Fig. 1). If this is not recognized, then the action of in-phase actuation of even a small actuator patch will result in an erroneous response and can lead to a totally wrong solution. In a recent model for curved piezoelectric actuators, Sonti and Jones[10] also recognized this fact and showed the necessity of including a uniform transverse pressure, in addition to the axial and tangential forces, to correctly represent the action of in-phase actuation.

A model has been developed to compute the equivalent forces and moments applied by a pair of symmetrically-bonded actuator pairs, and is described here. This is followed by a discussion of the special considerations for shell-type structures. The development of the model is similar to the work of Crawley and Lazarus[1] for plates, and relies on classical lamination theory (CLT).

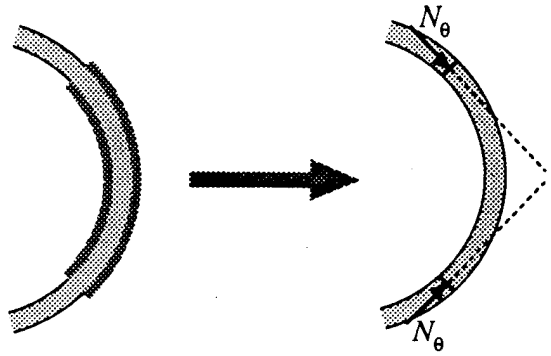

Fig. 1. Non-equilibrium of discrete tangential forces in shell structures.

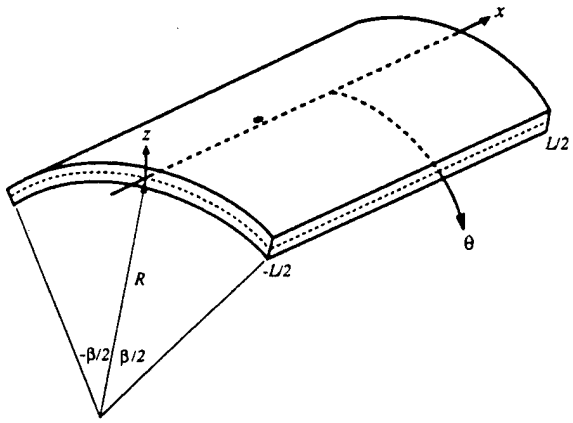

Fig. 2. Thin circular cylindrical shell coordinate system.

MODEL FORMULATION

A model describing the interaction between surface-bonded actuators and a circular cylindrical shell has be developed based on Donnel's theory. For completeness a short derivation of the accompanying equations of motion also presented. Consider a thin circular cylindrical shell, as shown in Fig. 2. We start with the following Donn assumptions $(1+\frac{z}{R}=1, \quad r \to R)$ for the kinematics of deformation:

$$u(x,\theta,z) = u^{o}(x,\theta) - z\frac{\partial w^{o}}{\partial x} \ , \tag{1}$$

$$v(x,\theta,z) = v^{o}(x,\theta) - z\frac{\partial w^{o}}{R\partial\theta} \ , \tag{2}$$

$$w(x,\theta,z) = w^{o}(x,\theta) \ . \tag{3}$$

In the above, z is the local thickness coordinate, measured from the middle surface of the shell. The superscript zero denotes displacements of the cylindrical panel's middle surface. The pertinent strain-displacement relations in cylindrical coordinates are:

$$\varepsilon_x = \frac{\partial u}{\partial x} = \varepsilon_x^{o} + z\kappa_x; \quad \varepsilon_x^{o} = \frac{\partial u^{o}}{\partial x}; \quad \kappa_x = -\frac{\partial^2 w^{o}}{\partial x^2} \ , \tag{4}$$

and

$$\varepsilon_\theta = \frac{\partial v}{R\partial\theta} + \frac{w}{R} = \varepsilon_\theta^{o} + z\kappa_\theta; \quad \varepsilon_\theta^{o} = \frac{\partial v^{o}}{R\partial\theta} + \frac{w^{o}}{R}; \quad \kappa_\theta = -\frac{\partial^2 w^{o}}{R^2\partial\theta^2} \ , \tag{5}$$

$$\gamma_{x\theta} = \frac{\partial v}{\partial x} + \frac{\partial u}{R\partial\theta} = \gamma_{x\theta}^{o} + z\kappa_{x\theta}; \quad \gamma_{x\theta}^{o} = \frac{\partial v^{o}}{\partial x} + \frac{\partial u^{o}}{R\partial\theta}; \quad \kappa_{x\theta} = -2\frac{\partial^2 w^{o}}{\partial x R\partial\theta} \ . \tag{6}$$

The resultant force-strain relations for a layered composite laminate are given by Jones[11]:

where

$$\begin{Bmatrix} N \\ M \end{Bmatrix} = \begin{bmatrix} A & B \\ B & D \end{bmatrix} \begin{Bmatrix} \varepsilon^{o} \\ \kappa \end{Bmatrix} - \begin{Bmatrix} N_\Lambda \\ M_\Lambda \end{Bmatrix} \tag{7}$$

$$\{N_\Lambda\} = \int [\overline{Q}]\{\Lambda\} dz \tag{8}$$

$$\{M_\Lambda\} = \int [\overline{Q}]\{\Lambda\} z\, dz \tag{9}$$

are the equivalent of thermal forces in CLT. Note that Λ is the free induced strain developed in the actuator in response to an applied voltage ($\Lambda_x = Ed_{3x} = Vd_{3x}/t_a$). The three governing equilibrium equations are:

$$\frac{\partial N_x}{\partial x} + \frac{\partial N_{x\theta}}{R\partial\theta} - m\ddot{u} = 0 \ , \tag{10}$$

and

$$\frac{\partial N_{x\theta}}{\partial x} + \frac{\partial N_\theta}{R\partial\theta} - m\ddot{v} = 0 \ , \tag{11}$$

$$\frac{\partial^2 M_x}{\partial x^2} + 2\frac{\partial^2 M_{x\theta}}{\partial x R\partial\theta} + \frac{\partial^2 M_\theta}{R^2\partial\theta^2} - \frac{N_\theta}{R} - m\ddot{w} = q \ , \tag{12}$$

with boundary conditions at $x=\pm L/2$ and $\theta=\pm\beta/2$. For an unconstrained symmetric panel with no externally applied forces or moments, i.e., $N, M=0$, Eq. (7) reduces to:

$$\begin{Bmatrix} \varepsilon^{o} \\ \kappa \end{Bmatrix} = \begin{bmatrix} A & B \\ B & D \end{bmatrix}^{-1} \begin{Bmatrix} N_\Lambda \\ M_\Lambda \end{Bmatrix} . \tag{13}$$

For a symmetric shell ($B=0$), the above equations are uncoupled, and

$$\{\varepsilon^o\} = [A]^{-1}\{N_\Lambda\} \tag{14}$$

$$\{\kappa\} = [D]^{-1}\{M_\Lambda\} . \tag{15}$$

To obtain simplified expressions for the induced curvature, we assume that the shell is isotropic and has the same Poisson's ratio as the actuator. For such a case, the *[A]* and *[D]* matrices reduce to:

$$[A] = \frac{E_s t_s + 2E_a t_a}{(1-\nu^2)} \begin{bmatrix} 1 & \nu & 0 \\ \nu & 1 & 0 \\ 0 & 0 & \frac{1-\nu}{2} \end{bmatrix} , \tag{16}$$

$$[D] = \left\{ \frac{E_s t_s^3}{12(1-\nu^2)} + \frac{2}{3}\frac{E_a}{(1-\nu^2)}\left[\left(\frac{t_s}{2} + t_a\right)^3 - \left(\frac{t_s}{2}\right)^3 \right] \right\} \begin{bmatrix} 1 & \nu & 0 \\ \nu & 1 & 0 \\ 0 & 0 & \frac{1-\nu}{2} \end{bmatrix} .. \tag{17}$$

Rewriting in a more convenient way,

$$[A] = \frac{E_a t_a (2+\psi)}{(1-\nu^2)} \begin{bmatrix} 1 & \nu & 0 \\ \nu & 1 & 0 \\ 0 & 0 & \frac{1-\nu}{2} \end{bmatrix} , \tag{18}$$

$$[D] = \frac{t_s^2}{12}\frac{E_a t_a}{(1-\nu^2)}\left[6 + \psi + \frac{12}{T} + \frac{8}{T^2} \right] \begin{bmatrix} 1 & \nu & 0 \\ \nu & 1 & 0 \\ 0 & 0 & \frac{1-\nu}{2} \end{bmatrix} . \tag{19}$$

With these assumptions, the following expression for the curvature induced due to the out-of-phase actuation is obtained from Eq. (15) (t_S = shell thickness, t_a = actuator thickness):

$$\begin{Bmatrix} \kappa_x \\ \kappa_\theta \\ \kappa_{x\theta} \end{Bmatrix} = \frac{6\left(1+\frac{1}{T}\right)\frac{2}{t_s}}{6+\psi+\frac{8}{T^2}+\frac{12}{T}} \begin{Bmatrix} 1 \\ 1 \\ 0 \end{Bmatrix} \Lambda , \tag{20}$$

where

$$\psi = \frac{E_s t_s}{E_a t_a}, \quad T = \frac{t_s}{t_a} , \tag{21}$$

and for in-phase actuation, the following expression for induced middle-surface strains is obtained from Eq. (14):

$$\begin{Bmatrix} \varepsilon_x^o \\ \varepsilon_\theta^o \\ \varepsilon_{x\theta}^o \end{Bmatrix} = \frac{2}{2+\psi} \begin{Bmatrix} 1 \\ 1 \\ 0 \end{Bmatrix} \Lambda . \tag{22}$$

The above expressions for the middle-surface strains for the case of in-phase actuation and the curvatures for the case of out-of-phase actuation are the same as those obtained for plates; however, the circumferential strain is now coupled with the out-of-plane displacement (Eq. (5)).

To solve a plate or a shell problem, an expression for a set of equivalent forces is often developed. These forces, when applied along the edges of the footprint of the actuator, on the structure result in the same degree of curvatures and in-plane middle-surface strains as those obtained from Eqs. (20) and (22). For out-of-phase actuation, the equivalent moments are found to be:

$$\begin{Bmatrix} M_x \\ M_\theta \\ M_{x\theta} \end{Bmatrix}_{eq.} = \frac{E_s t_s^2}{1-\nu} \frac{\left(1+\frac{1}{T}\right)}{6+\psi+\frac{8}{T^2}+\frac{12}{T}} \begin{Bmatrix} 1 \\ 1 \\ 0 \end{Bmatrix} \Lambda \ , \tag{23}$$

and for in-phase actuation, the following expression for the equivalent axial and tangential force is obtained:

$$\begin{Bmatrix} N_x \\ N_\theta \\ N_{x\theta} \end{Bmatrix}_{eq.} = \frac{E_s t_s}{1-\nu} \frac{2}{2+\psi} \begin{Bmatrix} 1 \\ 1 \\ 0 \end{Bmatrix} \Lambda \ . \tag{24}$$

The tangential force obtained from the above equation, when applied to the shell along the two circumferential edges of the actuator will not be co-linear, due to the curvature of the shell, and will have an erroneous component resulting in a rigid body mode. This situation has already been illustrated in Fig. 1. This occurs due to the simplifying assumptions in the above formulation. In actuality, a set of self-equilibrating stresses are developed between the shell and the bonded actuator, and there is no rigid body force developed.

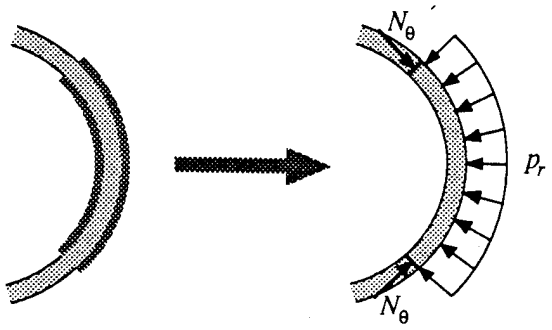

Figure 3. Adequate equivalent loading to maintain equilibrium.

To remedy this situation, we have proposed the application of an equilibrating uniform radial pressure applied across the footprint of the actuator. The magnitude of the uniform pressure is obtained from simple statics and is equal to $-N_\theta / R$ (Fig. 3). This set of forces, i.e., an equivalent tangential force given by Eq. (24) and a uniform radial pressure, now provide a convenient means of representing the action of surface-bonded actuators which are actuated in-phase. To verify whether this set of forces results in approximately the same displacement field as a true actuator bonded to a cylindrical shell (a comparison with a finite element model) a description of which follows, is made.

FINITE ELEMENT MODELING AND VERIFICATION

Two finite element models have been constructed to verify the equivalent loading scheme. A 6" radius, 0.032" thick and 1" deep ring with piezoelectric actuators 1/6 of the ring thickness and covering an arc 10° long (β) have been used. Making use of symmetry, only the top half needs to be modeled. The first model, shown in Fig. 4a, consists of beam elements. First, the actuation is simulated by specifying a coeffiecient of thermal expansion for the elements in the actuator region and then applying a known temperature to the model. Second, an equivalent self-equilibrating load, i.e., pressure and tangential force, corresponding to the temperature, is applied. The radial and tangential displacements obtained from the above analysis are identical and therefore not shown. It must be noted that the pressure loading must be transformed to nodal forces only (lumped loading). The lumped loading is often better for flat elements representing a curved surface (De Salvo and Swanson, 1979). The second finite element model uses plane stress elements in the actuator region to include the actuator's stiffness and uses beam elements for the rest of the shell (Fig. 4b). Again, thermal expansion is used to simulate the static action of the actuators on the shell.

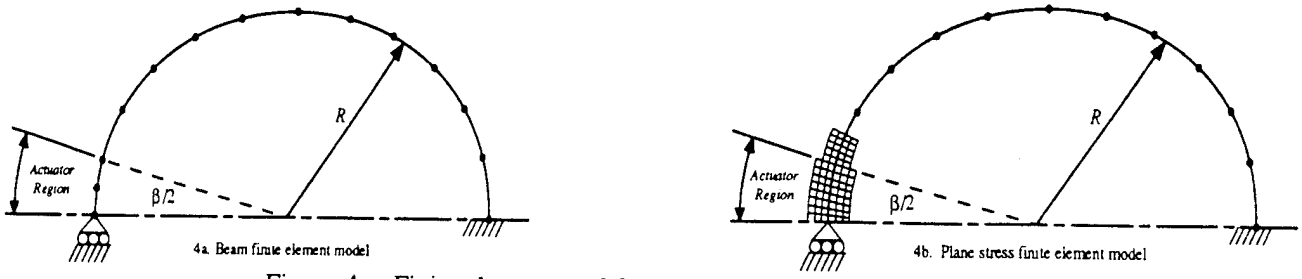

Figure 4. Finite element models used to verify the theoretical model.

The radial and tangential displacements are shown in Fig. 5. Discrepancies between the equivalent loading model and the plane stress finite element model exist since no assumptions about the actuator stiffness or about the equivalent loading are made in the latter model. Even though displacement differences are present, the plane stress finite element model validates the derived model since it gives results of the same order of magnitude with similar deformed shapes as opposed to when only point tangential forces (without a transverse pressure) are used. The deformed shape of the analytical model and the plane stress finite element model are shown in Fig. 6. Also shown in Fig. 5 are the displacements of the same ring if only discrete tangential forces are applied (without transverse pressure). This model using only tangential forces does not satisfy the ring's self-equilibrium. Major displacement discrepancies between the proposed equivalent loading model and the case using only tangential forces are observed both in shape and magnitude. Using the tangential forces alone overpredicts the displacements by a factor of up to 1000, as seen on the right vertical axis of Fig. 5 (note that the scales of the two vertical axis are different). Also, a reaction force in the x-direction at the clamped boundary is present if uniform pressure is not applied. This reaction force should not be present since the actual ring with bonded actuators is in self-equilibrium. Adequate equivalent loading did not show any reaction force in the x-direction at the clamped boundary.

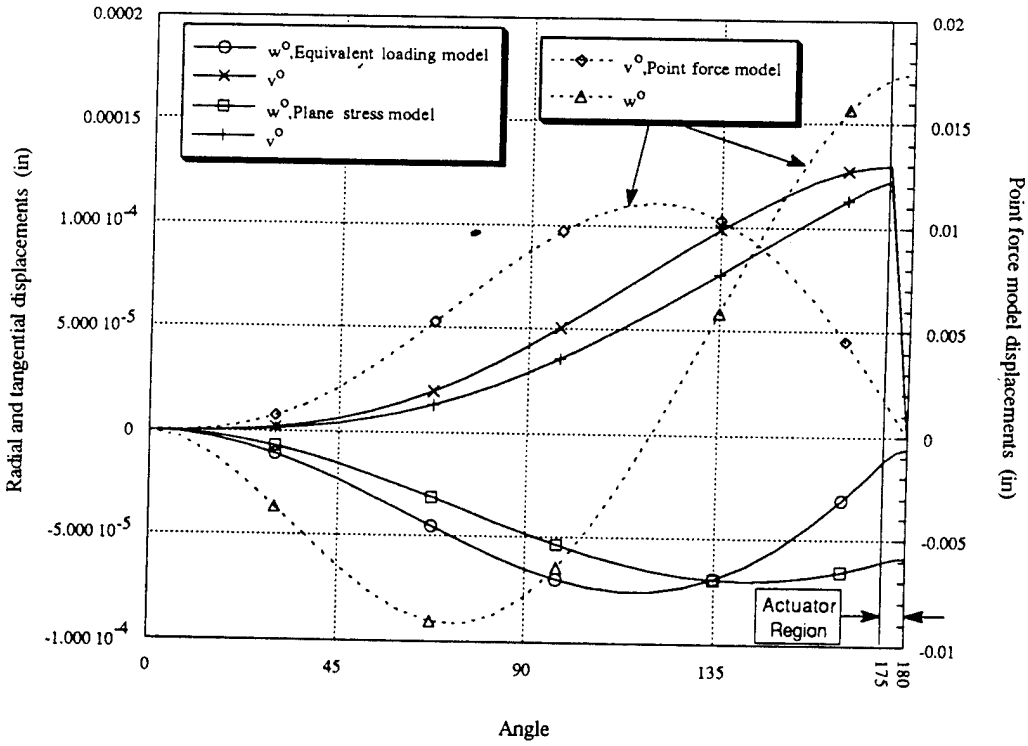

Figure 5. Comparison of the displacements predicted by the proposed self-equilibrating equivalent forces, the plane stress finite element model and the tangential force alone (no pressure).

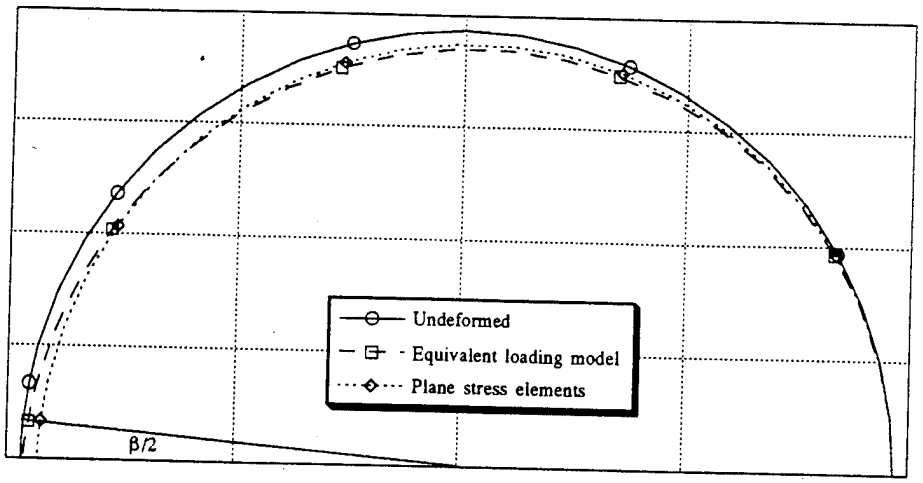

Figure 6. Deformed shape of the ring with and without the self-equilibrium loading using plane stress elements.

From the finite plane stress element model shown in Fig. 4b, it is possible to justify the use of a uniform radial pressure on the actuator footprint to maintain the self-equilibrium of the ring. Figure 7 shows the radial stress distribution through the thickness of the actuator and the ring. This stress distribution is virtually constant over the whole actuator region, except at the ends of the actuator, which validates the use of a uniform radial pressure in the analytical model. From the radial stress distribution, the ring is in self-equilibrium since the integral of the radial stress through the thickness is zero. Also, if the actuators are removed, the radial stress distribution will be dramatically changed due to the stress-free state of free surfaces. In order to retrieve the actual stress distribution, a radial pressure has to be applied on the shell to maintain self-equilibrium.

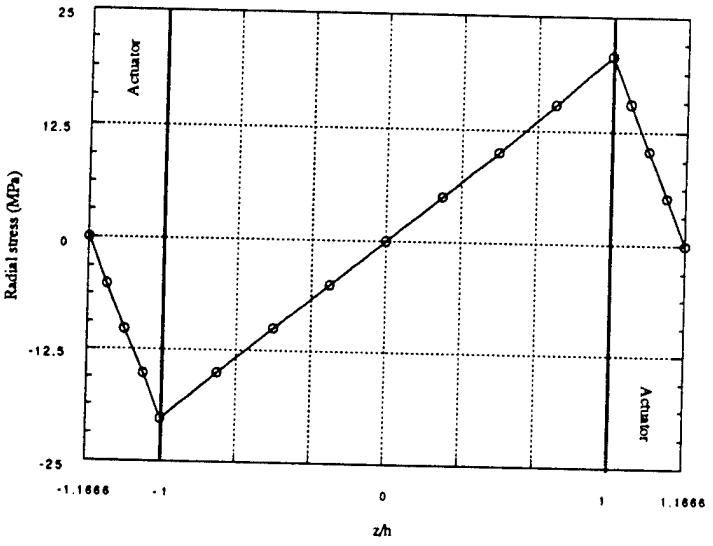

Figure 7. Radial stress distribution through the thickness in the actuator region.

CONCLUSIONS

In this paper, a model to represent the action of discrete induced strain actuator patches bonded to the surface of a circular cylindrical shell is developed based on Donnel's theory. Expressions to represent the actuator forces and moments have been developed for shells and are found to be the same as those obtained for plates. However, this equivalent set of forces and moments produces a rigid body mode resulting from the no-colinearity of the tangential forces due to the shell curvature. To avoid this rigid body mode, uniform pressure is applied in the region of the actuator patch. This solution method is verified using finite element modeling and showed very good agreement.

ACKNOWLEDGMENTS

The authors would like to acknowledge the funding support of the Office of Naval Research, Grant ONR N00014-92-J-1170.

REFERENCES

1) Crawley, E. F. and Lazarus, K. B., 1989, "Induced Strain Actuation of Isotropic and Anisotropic Plates," *AIAA Journal*, Vol. 29, No. 6, pp. 944-951.

2) Lee, C. K., 1990, "Theory of laminated piezoelectric plates for the design of distributed sensors/actuators. Part I: Governing equations and reciprocal relationships," *Journal of Acoustic Society of America*, Vol. 87(3), pp. 1144-1158.

3) Crawley, E. F. and Anderson, E. H., 1990, "Detailed Models of Piezoceramic Actuation of Beams," *Journal of Intelligent Material Systems and Structures*, Vol. 1, pp. 4-25.

4) Wang, B. T. and Rogers, C. A., 1991, "Modeling of Finite-Length Spatially Distributed Induced Strain Actuators for Laminate Beams and Plates," *Journal of Intelligent Material Systems and Structures*, Vol. 2, pp. 38-58.

5) Dimitriadis, E. K., Fuller, C. R. and Rogers, C. A., 1991, "Piezoelectric Actuators for Distributed Vibration Excitation of Thin Plates," *Journal of Vibration and Acoustics*, Vol. 113, pp. 100-107.

6) Tzou, H. S., 1989, "Theoretical Development of a Layered Thin Shell with Internal Distributed Controllers," *Failure Reliability Conference*, 1989.

7) Jia, J. and Rogers, C. A., 1990, "Formulation of a Laminated Shell Theory Incorporating Embedded Distributed Actuators", *Journal of Mechanical Design*, Vol. 112, pp. 596-604.

8) Sonti, V. and Jones, J. D., 1991, "Active Vibration Control of Thin Cylindrical Shells Using Piezoelectric Actuators," *Proceedings, Recent Advances in Active Control of Sound and Vibration*, Blacksburg, VA, pp. 3-26.

9) Lester, H. C. and Lefebvre, S., 1991, "Piezoelectric Actuator Models for Active Vibration Control of Cylinders", *Proceedings, Recent Advances in Active Control of Sound and Vibration*,, Blacksburg, VA, pp. 3-26.

10) Sonti, V.R. and Jones, J.D., 1993, "Curved Piezo-Actuator Models for Active Vibration Control of Cylindrical Shells", *Proceedings 125th meeting of the Acoustical Society of America*, Ottawa, Canada, May 17-21; abstract published in *J. of Acoustical Society of America*, 93 (4) part.2, pp. 2352, April 1993.

11) Jones, R.M., 1975, *Mechanics of Composite Materials*, Scripta book company, Washington.

12) De Salvo, G.J. and Swanson, J.A., 1979, *ANSYS User's Manual*, Swanson analysis systems, Houston, PA.

C-43 Structural Modal Analysis using Collocated Piezoelectric Actuators/Sensors - an Electromechanical Approach, F. P. Sun, C. Liang and C. A. Rogers, Proceedings of SPIE Smart Structures and Materials Conference, Orlando, FL, SPIE Vol. 2190, pp. 238-249, 13-18 February 1994.

Structural modal analysis using collocated piezoelectric actuator/sensors - an electromechanical approach

F. P. Sun, C. Liang and C. A. Rogers

Center for Intelligent Material Systems and Structures
Virginia Polytechnic Institute and State University
Blacksburg, Virginia 24061-0261

Abstract

A single piezoceramic (PZT) patch bonded to a structure may be used as a collocated actuator/sensor for structural modal analysis. When activated by a voltage signal, the PZT element excites the structure as a result of its induced strain. The interaction between PZT and its host structure is governed by the mechanical impedance of the structure. If the applied electrical voltage and resulting electrical current (or the electrical transfer function) of the collocated PZT actuator/sensor are known, the mechanical impedance of the structure can be determined through an appropriate electromechanical model.

This paper presents a modal analysis technique based on the measurement of electric admittance of collocated actuator/sensors. The technique utilizes thin piezoelectric patches bonded on structures as both sensor and actuator. A commercial electrical impedance analyzer is used to measure the electrical admittance of the PZT patch. An SDOF model governing the electromechanical interaction is derived and then used to extract the mechanical impedance of the structures from the measured electrical admittance. Two corresponding algorithms, revised inverse Nyquist plane curve fitting and admittance matching-half power bandwidth approaches are presented for the extraction of modal parameters. Both approaches exclude the stiffening effect of PZT on structure yielding better estimations of extracted structure natural frequencies. The placement of PZT on structure is also studied. An experimental example is given on a small flexible beam. The results show the advantages of this technique in modal test of light-weight and flexible structures whose modal parameters are extremely sensitive to the stiffening of the transducers and shaker.

1. Introduction

Experimental modal test has now become a mature and standard technique in structure dynamic analysis. It usually consists of several independent stages: structure excitation, measurement of driving force and vibrational response, formation of Frequency Response Function (FRF), and modal parameter extraction. The entire process needs a set of sophisticated equipment, such as a multi-channel signal analyzer, force and response transducers, shakers, and various types of signal conditioners. Typical transducers used in a modal test are piezoceramic force gauges, accelerometers and shakers. The attachment of conventional transducers onto a testing structure may result in considerable errors in the extracted system parameters, especially with light-weight and flexible structures. The use of Laser Doppler Vibrometer and eddy current sensor provide a non-contact measurement technique, but they still need attachment of force gauge and shaker to the structure.

A piezoceramic patch, on the other hand, may serve as both sensor and actuator [1,2] at the same time as a result of piezoelectric effect and its converse. When bonded to a structure and driven by an alternating voltage, it imposes a bending moment on the structure through its longitudinal expansion and contraction, causing the structure to vibrate. This vibration then in turn "modulates" the current flowing through the patch. Consequently, the electric admittance of the bonded patch, defined as the ratio of the current to the voltage, is physically in a same position as its mechanical counterparts, such as compliance and mobility, in representing the transfer characteristics of a structure between the excitation and the response. As a pure electric quantity, the electric admittance is much easier to measure than a mechanical transfer function. Because of the light weight and the low flexural stiffness of a PZT patch, the mass loading effect can usually be neglected and its stiffening effect can be easily compensated.

This paper presents a technique of structure modal test using surface-bonded piezoceramic patch as a collocated sensor-actuator. The electric admittance or impedance of the bonded piezoceramic patch versus frequency is measured with a sine-sweeping impedance analyzer. A generic model governing the electromechanical interaction of the actuator and the structure is derived and used to extract the structure admittance, or mobility at the position where the PZT is bonded. Two algorithms of modal parameter extraction associated with the technique are presented. One uses electric admittance match / half-power band width

In Proceedings, SPIE Smart Structures and Materials Conference,
Orlando, FL, 13-18 February, 1994, in press.

method, and the other employs inverse Nyquist plane curve fitting. Both algorithms can extract a structure's modal damping coefficients, natural frequencies and curvature mode shapes of the structure. The model has considered the stiffening effect of the actuator on the structure, yielding refined estimations of extracted structure natural frequencies. This is important when the test piece is flexible and small. In addition, the influence of the location and size of the sensor/actuator on the results is also discussed. The method is proven to be effective in conducting modal test on a structure extremely sensitive to the stiffening of transducers.

2. Modeling of electromechanical interaction of piezoelectric sensor-actuator

A piezoceramic, most commonly known as PZT, short for Lead (Pb) Zirconate Titanate, exhibits a bi-directional "piezoelectric" effect. When motion in only one direction is considered and the stress T and the electric field E are chosen as the intensive variables, the electromechanical interaction between the stress, strain, the electric field and flux density is governed by the following constitutive equations :

$$S_2 = s_{22}^E T_2 + d_{32} E_3 \tag{1}$$

$$D_3 = d_{32} T_2 + \varepsilon_{33}^T (1 - i\delta) E_3 \tag{2}$$

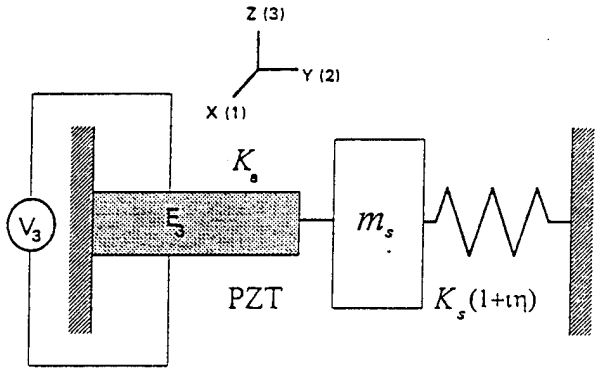

Figure 1 SDOF model of electromechanical interaction of PZT with structure

where, as shown in Figure 1, S_2 is the strain and T_2 the stress in PZT along the y-axis, E_3 the electric field and D_3 electric flux density along the z-axis between two parallel surfaces. s_{22}^E the complex mechanical compliance at zero electric field, d_{32} the piezoelectric constant at zero stress, ε_{33}^T the dielectric constant at zero stress and δ the dielectric loss tangent of PZT. Assume that the PZT actuator is fixed at one end and the other end is connected to a structure represented by a mass-spring-damper, the velocity of the moving end under voltage V_3 may be expressed as

$$v = \frac{F_{2b}}{Z_a + Z_s} \tag{3}$$

and the driving force on the mechanical system

$$F_2 = Z_s v = \frac{Z_s}{Z_a + Z_s} F_{2b} \tag{4}$$

where Z_S is the mechanical impedance of the structure and Z_a the short-circuit mechanical impedance of PZT actuator, respectively. F_{2b} is the force when PZT is blocked, which can be obtained from Eq. (1) by simply letting $S_2 = 0$ as

$$F_{2b} = -\frac{d_{32} E_3}{s_{22}^E} w_a h_a = -d_{32} E_3 Y_{22}^E w_a h_a \tag{5}$$

where $Y_{22}^E = 1/s_{22}^E$ is the complex modulus of PZT, and w_a and h_a are the width and thickness of PZT, respectively. Differentiating the electric flux density with respect to time and integrating it over the electroded area yields the total electric current flowing through the PZT

$$I_3 = i\omega \iint_{\sigma} D_3 dx dy \tag{6a}$$

Substituting Eqs.(2), (4) and (5) in it and using the relation $E_3 = V_3 / h_a$ and $T_2 = F_2 / (w_a h_a)$ result in

$$I_3 = i\omega \frac{w_a l_a}{h_a} [\varepsilon_{33}^T (1 - i\delta) - \frac{Z_s}{Z_s + Z_a} (d_{32})^2 Y_{22}^E] V_3 \tag{6b}$$

or the coupled electric admittance of PZT

$$Y = \frac{I_3}{V_3} = i\omega \frac{w_a l_a}{h_a} [\varepsilon_{33}^T (1 - i\delta) - \frac{Z_s}{Z_s + Z_a} (d_{32})^2 Y_{22}^E] \tag{7a}$$

where l_a is the length of PZT. Note that a uniform distribution of electric flux density in PZT is assumed in the integration. It is obvious that the first term in Eq.(7a) is the capacitance admittance and the second term is the result of the electromechanical interaction of PZT with the structure. The mechanical frequency response function of the structure, or the mobility, defined as the ratio of velocity response to excitation force (the reciprocal of the mechanical impedance Z_s) may then be easily solved from Eq. (7a) as

$$FRF = \frac{1}{Z_s} = \frac{1}{Z_a} \left(\frac{d_{32}^2 Y_{22}^E}{\varepsilon_{33}^T (1 - i\delta) - Yh_a / i\omega l_a w_a} - 1 \right) \tag{7b}$$

The significance of Eq.(7b) lies in that a pure mechanical parameter of a structure can be determined from the electric admittance of the actuator/sensor bonded to the structure. This provides a convenient alternative to the shaker-impedance head approach for determining a frequency response function of a mechanical structure, which constitutes the basis of experimental modal analysis. Although most modal analysis approaches are applicable to Eq.(7b), the extraction algorithms presented in this paper are different due to the involvement of the actuator impedance Z_a in the structure impedance expression.

3. Modal parameter extraction with SDOF model

To demonstrate the application of this electromechanical approach to modal analysis, an SDOF model for extraction is developed. The mechanical impedance of the PZT element in Fig. 1 may be expressed as

$$Z_a = -\frac{i}{\omega} k_a \tag{8}$$

where k_a is the short-circuit stiffness of PZT along the y-axis. The effect of PZT's mass along the y direction is neglected, assuming that the stress wavelength is much larger than PZT's characteristic dimension under normal operating frequency [3]. The mechanical impedance of an SDOF system with a structure damping is given by

$$Z_s = i(m_s \omega - \frac{k_s (1 + i\eta)}{\omega}) \tag{9}$$

where m_s is the modal mass, k_s the modal stiffens and η the modal damping. Substituting Eqs.(8) and (9) in Eq. (7) yields the electric admittance in term of the modal parameters

$$Y = \omega a [\varepsilon\delta + \frac{c k_a k_s \eta}{(k_s \eta)^2 + (k_s + k_a - m_s \omega^2)^2} + i(\varepsilon - c + \frac{c k_a (k_s + k_a - m_s \omega^2)}{(k_s \eta)^2 + (k_s + k_a - m_s \omega^2)^2})] \tag{10}$$

where a = $w_a l_a / h_a$ and c = $(d_{32})^2 Y_{22}^T$. The real and imaginary parts of the mechanical compliance (reciprocal of the mechanical impedance) can then be deduced as:

$$Y_{mr} = (\frac{\mathrm{Re}(Y)}{\omega a} - \varepsilon\delta)/c = \frac{k_a k_s \eta}{(k_s\eta)^2 + (k_s + k_a - m_s\omega^2)^2} \tag{11}$$

$$Y_{mi} = (\frac{\mathrm{Im}(Y)}{\omega a} - \varepsilon - c)/c = \frac{k_a(k_s + k_a - m_s\omega^2)}{(k_s\eta)^2 + (k_s + k_a - m_s\omega^2)^2} \tag{12}$$

As a PZT actuator usually has a size much smaller than that of the host structure, its mechanical damping can be ignored. Equations.(11) and (12) traces out a non-closing circle in Nyquist plane as

$$(Y_{mr} - \frac{k_a}{2k_s\eta})^2 + Y_{mi}^2 = (\frac{k_a}{2k_s\eta})^2 \tag{13}$$

This is the locus of the mechanical compliance of an SDOF system with proportional damping connected in parallel with a massless spring K_a.

3.1 Inverse Nyquist plane curve fitting (INPCF)

As Eqs. (11) and (12) are highly nonlinear functions of the modal parameters, it is much easier to conduct the curve fitting in inverse Nyquist plane than to do direct parameter extraction with the mobility.The mechanical impedance of SDOF with structural damping takes simple form [4] as

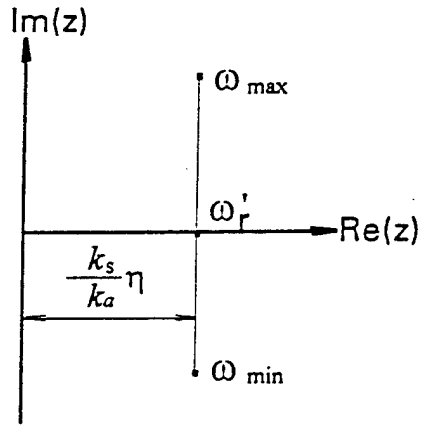

Figure 2 Mechanical Impedance of SDOF in inverse Nyquist plane

$$Z = \frac{1}{Y_{mr} + iY_{mi}} = \frac{k_s}{k_a}\eta - i\frac{k_s + k_a - m_s\omega^2}{k_a} \tag{14}$$

It traces out a straight line on the inverse Nyquist plane as shown in Fig. 2. Note that due to the stiffening effect of PZT to structure, the intersection of the line with the real axis determines the natural frequency of the joint system rather than that of SDOF system alone. Curve fitting the measurement data to the imaginary part of Eq. (14) generates two quantities k_s/k_a and m_s/k_a. Note that they are the structure modal stiffness and mass normalized to the actuator modal stiffness, and none of them has a physical meaning. However, structural natural frequency can be determined as

$$\omega_r = \sqrt{\frac{k_s}{m_s}} = \sqrt{\frac{k_s/k_a}{m_s/k_a}} \tag{15}$$

Another independent curve fitting to the real part of the measurement data yields a refined estimation of Re(Z), and from it the structural modal damping can be calculated

$$\eta = \frac{\mathrm{Re}(Z)}{k_s/k_a} \tag{16}$$

Equations (14), (15) and (16) constitute the revised inverse Nyquist plane curve fitting approach which will be referred to as INPCF later.

3.2.Admittance match/ half power bandwidth (AM/HPB)

Equation(12) provides an alternative approach to the determination of η and ω_r. Take the partial derivative of Eq.(12) with respect to ω and let it be zero

$$\frac{\partial(Y_{mi})}{\partial\omega} = \frac{-2k_a m_s[(k_s\eta)^2 - (k_s + k_a - m_s\omega^2)]}{[(k_s\eta)^2 + (k_s + k_a - m_s\omega^2)^2]^2} = 0 \tag{17}$$

This leads to

$$k_s\eta = (k_s + k_a - m_s\omega_1^2) \tag{18}$$

$$k_s\eta = -(k_s + k_a - m_s\omega_2^2) \tag{19}$$

where ω_1 and ω_2 correspond to the peak and valley of Y_{mi} ,respectively. Addition of Eqs.(18) and (19) results in the modal damping

$$\eta = \frac{1}{2\omega_r^2}(\omega_2^2 - \omega_1^2) \tag{20}$$

where

$$\begin{aligned} \omega_r^2 &= k_s / m_s \\ \omega_1^2 &= (k_s(1-\eta) + k_a)m_s \\ \omega_2^2 &= (k_s(1+\eta) + k_a)m_s \end{aligned} \tag{21}$$

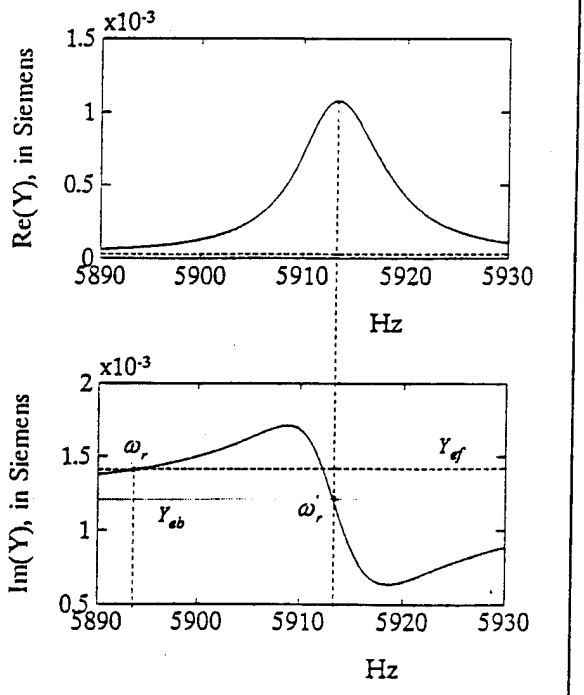

Figure 3 Determination of structure natural frequency by electric admittance matching

Equation (20) is very similar to, but different from, conventional half power band width approach in the determination of the natural frequency ω_r. As the mechanical impedance of the structure Z_S drops nearly to zero at structure resonance, Eq.(7) presents the electric admittance of the free PZT sensor/actuator (a capacitor without piezoelectric effect)

$$Y_{ef} = \omega\alpha\varepsilon_{33}^T\ (\delta + i) \tag{22}$$

and the electric admittance of a blocked actuator is obtained by letting Z_S be ∞

$$Y_{eb} = \omega\alpha\ (\varepsilon_{33}^T\delta + i(\varepsilon_{33}^T - c)) \tag{23}$$

The imaginary parts of both admittance intersect with Im(Y), as is illustrated in Fig. 3. It is apparent by definition that it is the intersection of *Im* (Y_{ef}) with *Im* (Y) that determines the natural frequency of the structure (impedance match). By checking Eq.(10), it is not difficult to see that the intersection of *Im* (Y_{eb}) with *Im(Y)* happens to correspond to the natural frequency of the joint system of PZT and SDOF

$$\omega_r' = \sqrt{\frac{k_s + k_a}{m_s}} \tag{24}$$

at which *Re(Y)* peaks and *Im(Y)*'s interaction term vanishes. The physical interpretation of this seeming coincidence is that at ω_r', there is no mechanical reactive power going into the joint system from PZT. For PZT, this is as if it is blocked by a still structure. Note that in Eq.(20), ω_r is a characteristics of the structure alone and ω_1, ω_2 are those of the joint system. This distinguishes it from the conventional half power band method and it will be referred to as Admittance Match / Half Power Band (AM/HPB) approach later.

3.3.Modal shapes

Equations.(11) and (12) also provide a way of eigenvector extraction when applied to a multi-degree-of-freedom or continuum system. At the system resonance ω_r', $Y_{mi} = 0$ and

$$Y_{mr} = \frac{k_a}{k_s \eta} = \frac{k_a}{\eta} y \tag{25a}$$

where y is the modal displacement response to a unit force excitation ($y = 1/k_s$). For a continuum structure, this modal displacement is a function of measurement coordinate and mode. However, PZT's modal stiffness k_a and structure modal damping η for a particular mode is independent of the coordinate. When measurements of Y_{mr} are made at *m* coordinates along the structure for each of its *n* modes, the eigenvector is obtained and its element takes the form of

$$Y_{mr}(i,j) = \frac{k_a(i)}{\eta(i)} y(i,j) \tag{25b}$$

where i = 1,2,...m and j = 1,2...n. This can also be directly deduced from the fact that $k_a / k_s \eta$ is the diameter of the modal circle in Nyquist plane. However, it should be understood that this is an approximation with an acceptable accuracy only when PZT is trivial in size to the structure.

4. Placement of sensor/actuator on structure

Modal test requires appropriate placement of transducer and shaker on a structure to ensure accurate results. The placement of a surface-bonded collocated sensor-actuator requires special considerations because high activation and detection sensitivity are desired simultaneously. Unlike electromagnetic shaker, a surface-bonded PZT patch excites, and senses the structure's in-plane motion rather than the transverse motion. In addition, a PZT patch is a distributed actuator and sensor. Its measured electric admittance reflects the overall vibration response over the area of the structure underneath the PZT patch. From Eq.(2) through (6a), a more general form of a PZT's electric admittance can be found as

$$Y = \frac{i\omega w_a l_a}{h_a} \varepsilon_{33}^T (1 - i\delta) + \frac{i\omega}{V} \iint_\sigma d_{32} T_2 dx dy \tag{26}$$

As mentioned previously, the second integration is the result of electromechanical interaction. In the SDOF model, a uniform stress and strain distribution is assumed. It is correct when PZT is attached to the structure only at its end and the wavelength of stress is much larger than the PZT geometry. However, a PZT is actually bonded on a flexurally deflected surface with a distributed area. The stress amplitude and sign, and then the resultant local electric current density is a function of location and mode shape of the structure. For a PZT bonded to a beam, this stress can be related to the beam's curvature by

$$T_2 = -Y_{22}^E \left(\frac{t_s + h_a}{2} \kappa(x) - d_{32} E_3\right) \tag{27}$$

where the $\kappa(x)$ is the curvature of the structure at location x and t_s the thickness of the structure. Equation (26) may then be expressed

$$Y = \frac{i\omega w_a l_a}{h_a}\left[\varepsilon_{33}^T (1 - i\delta) - (d_{32})^2 Y_{22}^E\right] - \frac{i\omega w_a Y_{22}^E d_{32} (t_s + h_a)}{2V} \int_{x_s}^{x_s + l_a} \kappa(x) dx \tag{28}$$

Obviously, if a PZT happens to straddle on or near the "curvature node" of certain modes, as is the case of mode 3 and 6 shown in Fig. 6, the coupling term vanishes, the influence of these particular modes virtually disappears in the admittance (Fig.4). In contrast, a mode will be detected with a maximum sensitivity when PZT is placed in the middle of a convex or concave where the curvature peaks, as illustrated by mode 2, 4, 5 and 7 in the same figures. Similarly, the activation of PZT is also a function of its location. The effective moment applied to structure are nearly zero for mode 3 and 6, and reaches maximum for mode 2, 4, 5 and 7. This compatibility of the two opposite functions of PZT simplifies its placement as a collocated sensor-actuator. As a consequence, a collocated PZT actuator/sensor should always be placed away from "curvature node" of all modes of interest when it is used to determine natural frequencies and damping of a structure. This differs from a conventional modal test in which shakers and out-of-plane motion transducers are often placed away from the flexural deflection node lines.

In contrast to the location, the length of PZT affects its behavior as a sensor differently than as an actuator. Generally, a longer PZT provides larger activation and higher detection sensitivity. However, the measured admittance always represents the average strain of the structure underneath the PZT patch. It may be biased lower or higher than the central strain depending on the shape of the curvature as long as PZT's length is not zero. This will reduce the spatial resolution of modal analysis and affect accuracy of the extracted natural frequencies and damping. Therefore, as a sensor, a shorter PZT is preferable, especially when measuring high vibration modes. But as an actuator, a longer one always provides larger moment as long as it is in a region of constant strain sign. This is important in measuring a relatively large structure with medium damping when a measurable structure response is a major issue and the activation needs to be as large as possible. However, in practice, the decision is usually compromised to cope with both requirements.

5. Modal test of a free-free beam

System identification of a small size and lightly damped structure is usually a challenge as the extracted structure's modal parameters are extremely sensitive to the stiffening and mass loading of the attachment of sensor and actuator. As an example, a test of proof-of-concept-is conducted on a aluminum beam of 153.0 × 25.7 × 0.8 mm. A thin PZT patch (32×19× 0.19 mm) is bonded on the beam 52.3 mm from its end and the beam is suspended in air by very thin wires to simulate a free-free boundary condition and to avoid introducing external damping. The electric impedance of the PZT is measured over a broad frequency band by an HP 4194A Impedance Analyzer.

Figure 4 is the electric admittance spanning from 100 Hz to 7000 Hz, in which the beam's first 9 flexural vibration modes are clearly identifiable except mode 6. Note that each mode is well separated from the others. This qualifies the application of the SDOF model to the data. For the actual parameter extraction, each mode is zoomed in to obtain a much higher frequency resolution and amplitude accuracy. Figures 5a through 5d are examples of several typical modes. Table 1 shows the natural frequencies and modal damping of the beam extracted respectively by the two algorithms previously discussed. To verify the algorithms' capability of eliminating the stiffening effect, the original PZT patch is replace by a tiny one (4 × 6 × 0.19 mm) at the same center location. It is assumed that the stiffening is negligible as its length is less than 1/6 of the original one. Therefore, the frequencies of the beam thus measured are considered as the "true" structure natural frequencies. Table 2 lists these true structure natural frequencies verses the natural frequencies of the beam-PZT joint system. Table 3 is the relative errors of the extracted and predicted frequencies with respect to the structure natural frequencies. Table 4 shows the material constants of the actuator used.

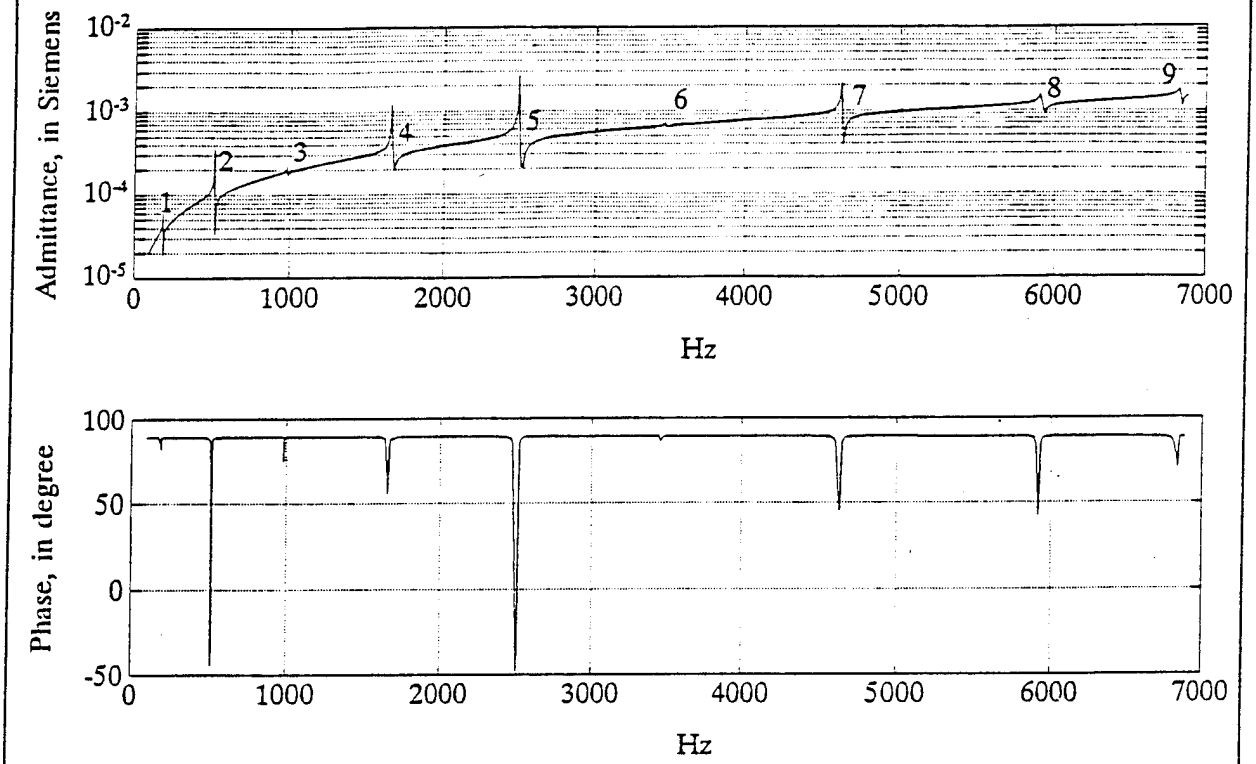

Figure 4 Electric admittance of PZT bonded on beam (first 9 flexural modes)

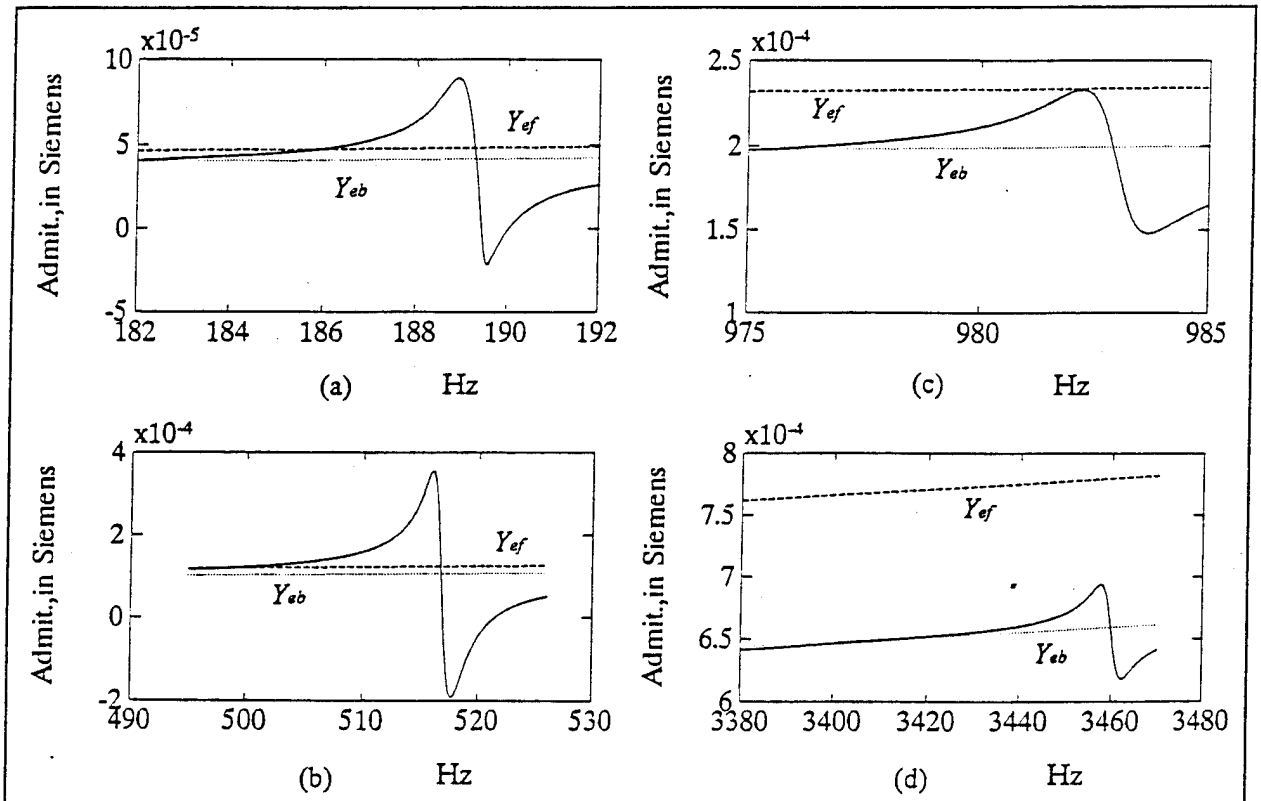

Figure 5 Four typical cases of the stiffening effect

Table 1 Natural frequencies and modal damping of the beam extracted with the two algorithms

Mode	1	2	3 *	4	5	6 *	7	8	9
f_{r1}(Hz)	185.9	498.3	982.0	1628.4	2437.5	3457.6	4588.5	5893.8	6820.0
η_1 (%)	0.37	0.37	0.15	0.20	0.22	0.13	0.16	0.17	0.17
f_{r2}(Hz)	187.6	497.2	982.2	1628.0	2439.9	3456.0	4588.2	5891.7	6813.8
η_2 (%)	0.21	0.31	0.095	0.15	0.18	0.064	0.15	0.17	0.16

Subscript 1----AM/HPB and Subscript 2---- INPCF

Table 2 Natural frequencies of the beam-PZT system, the structure natural frequencies and their relative difference

Mode	1	2	3 *	4	5	6 *	7	8	9
f_{rj} (Hz)	189.3	516.7	983.0	1656.8	2493.1	3459.9	4622.5	5913.3	6830.3
f_{rs}(Hz)	183.3	494.7	982.5	1621.8	2437.5	3455.2	4580.6	5863.4	6786.4
E_{js} (%)	+3.2	+4.4	+0.05	+2.2	+2.3	+0.14	+0.9	+0.85	+0.65

where : f_{rj} --- PZT- beam joint system resonance frequencies
f_{rs} --- The measured natural frequencies of the beam alone.
$E_{js} = (f_{rj} - f_{rs}) / f_{rs}$, E_{js} max. = 4.4 % and E_{js} average = 1.62 %.

Table 3 The relative errors of the extracted and predicted frequencies with respect to the structure natural frequencies

Mode	1	2	3 *	4	5	6 *	7	8	9
E_1(%)	+1.40	+0.67	-0.05	+0.33	0	+0.07	+0.17	+0.51	+0.49
E_2(%)	+2.30	+0.51	+0.03	+0.38	+0.10	+0.02	+0.17	+0.48	+0.41
f_{rc}(Hz)	180.3	497.0	974.2	1610.4	2405.7	3360.1	4474.4	5745.9	7177.5
E_c(%)	+1.64	+0.46	-0.48	-0.76	-1.30	-1.79	-2.32	-2.33	+5.50

where :
$E_1 = (f_{r1} - f_{rs}) / f_{rs}$, E_1max = +1.40 % and E_1average = 0.41 %
$E_2 = (f_{r2} - f_{rs}) / f_{rs}$, E_2max = +2.30 % and E_2average = 0.49 %
$E_c = (f_{rc} - f_{rs}) / f_{rs}$, $E_c$max = +5.50 % and $E_c$average = 0.16 %

* Two special modes that are not stiffened by PZT.

Table 4 Material constants and geometry of PZT

d_{32}	y_{22}	ε_{33}^T *	δ *	w_a	l_a	h_a
m/v	N/m^2	F/m		mm	mm	mm
-166e-12	6.30e10	1.50e-8	0.02	19.0	32.0	0.19

* nominal values published by the manufacturer

In order to obtain the curvature mode mode shape, a tiny (4 × 6×0.19 mm) PZT was bonded to 5 uniformly spaced locations on the beam respectively (see Fig.6b.). It was removed after each measurement of the electric impedance so that the impact on the shape is minimized. Due to the limited spatial resolution, only the first 5 mode shapes are meaningful. Figure 6c is the normalized curvature shapes of these 5 modes and Figure 6d is their mountain plot.

6. Analysis of Results

Figure 4 shows an overall electric admittance of the PZT covering the first 9 modes of the beam. It gives approximate estimations of the natural frequencies. However, they are consistently higher than the true natural frequencies of the beam alone

as listed in Table 2. This bias can be up to 4.4 % with an average of 1.62 % for the first 9 flexural modes. Obviously, the stiffening, rather than mass load, of PZT to the beam dominates within this frequency range, and it generally introduces more impact on low modes than high modes in term of the relative shift in natural frequencies. This demonstrates the need of correction for the stiffening effect when using surface-bonded PZT for a precision modal test of structure.

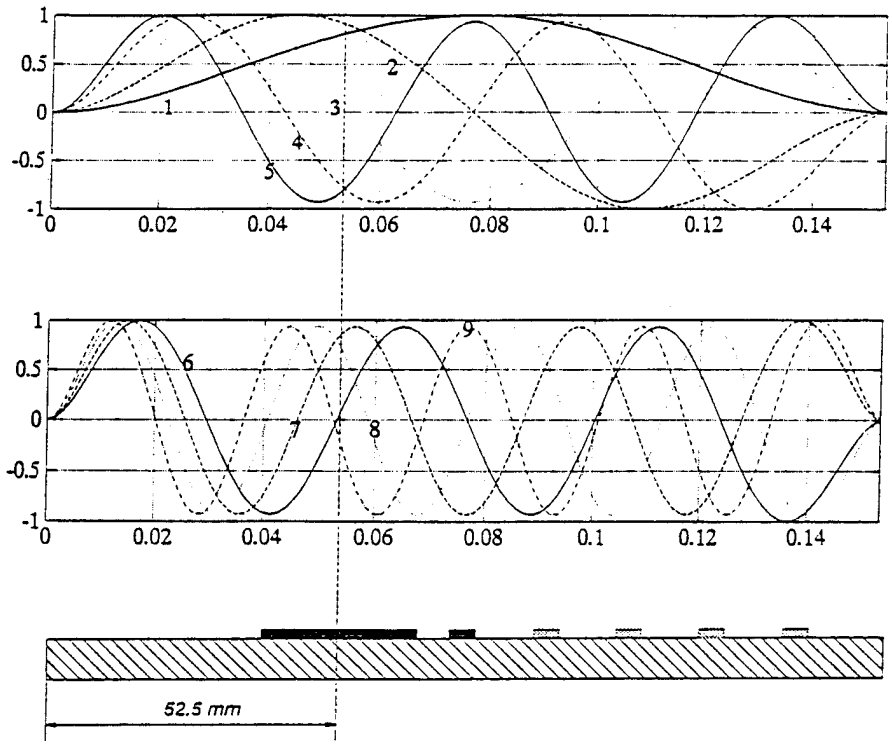

a. Analytical curvature shapes of the beam b. Locations of sensor/actuator on the beam

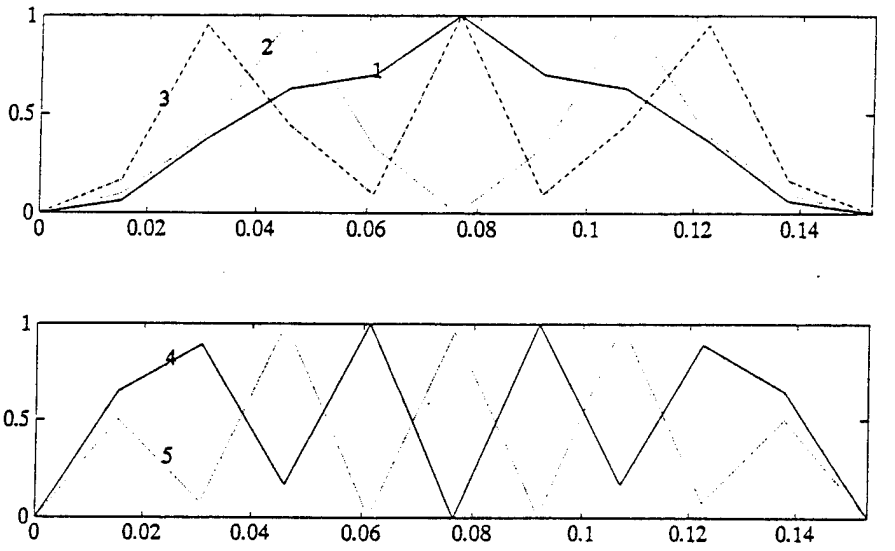

c Normalized curvature shapes of the first 5 modes

Figure 6a-c Placement of PZT and the curvature mode shapes of the beam

Table 1 shows the beam's natural frequencies and modal damping extracted using the two algorithms. Table 3 lists the relative errors of these natural frequencies with respect to the measured data. Note that the maximum errors reduce to 1.4 % and 2.3 % at the first mode, and average errors reduce to 0.41 % and 0.49 %, respectively. Although the results from two algorithms vary slightly, both of them produce better estimations of the true values of the beam's natural frequencies in the sense that average error decreases by 75 %.

The demand for this frequency correction varies with each mode at a particular PZT location. As one can see in Fig. 4, the strength of each mode varies significantly. Figure 5 lists four typical modes of the nine. For mode 1 and mode 2 (Fig.5a and 5b), $Im(Y_{ef})$ intersects with $Im(Y)$ before the system resonance, which implies the motion of the beam is stronger than that of a free PZT. In other words, PZT is constraining or stiffening the beam. There is substantial stiffening. For mode 3 (Fig. 5c), the two motions are completely compatible, neither of them imposes constraint on the other. This is indicated by the tangency of the two curves. As for Fig.5d, mode 6 is marginally activated. The motion of PZT for this particular mode is nearly being blocked by the beam, or in other words, the PZT is "stiffened" by the beam rather than vice-versa. This variation of the stiffening with mode is also shown in Table 2 where the relative frequency errors for mode 3 and mode 6 are much smaller than the other modes. Obviously, there is no need for frequency correction at all for those modes. Therefore, the application of algorithms should be selective.

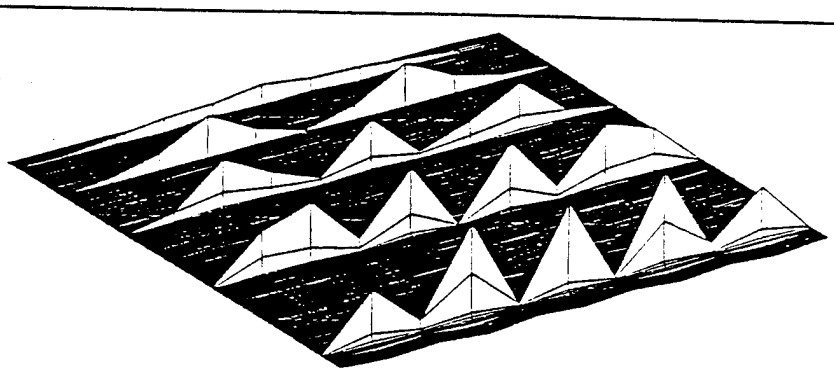

Figure 6d Mountain plot of the first 5 curvature mode shapes

Figure. 6c is the normalized curvature shapes of the first 5 modes extracted from the mechanical mobility. They are in good agreement in the amplitudes with the analytical results obtained using transfer matrix method. They can be integrated twice with respect to the spatial link to obtain the flexural mode shapes. However, due to limited spatial resolution, higher modes are not identifiable in this case.

SDOF modal parameter extraction algorithm is based on the assumption that each mode of the structure is well separated from the others. Thus, its utility is usually limited to structures such as a slender beam. However, the two algorithms presented might be applicable to an extended category despite their SDOF nature. It is due to the fact that modal coupling have little effect on the extracted natural frequencies and damping coefficients, and the fact that real part of the mechanical compliance is less subject to the modal pollution [5].

Table 3 also lists the first 9 natural frequencies of the beam analytically obtained by transfer matrix method. They are all close to but statistically biased lower than the measured ones. This is probably due to the imperfection of the specimen's geometry and shape, such as a slight bow of the beam, which usually increases the natural frequencies.

There are several inherent limits of this approach when used for experimental modal analysis. First of all, as a collocated sensor-actuator, the deduced mechanical mobility is a "point transfer function". Therefore, its real part is always positive. This creates difficulty in determination of the sign of curvature mode shapes. Second, due to its in-plane sensing and actuation, a proper placement of PZT on a structure relies on the knowledge of the curvature mode shapes, rather than the flexural shapes, which are generally less straight forward even with a simple structure. In the beam example, the PZT location is deliberately selected by referring to the curvature mode shapes analytically predicted (see Fig. 6a). Third, the involvement of the modal stiffness of the actuator k_a in Eq. (14) makes the individual extraction of the modal stiffness k_s and mass m_s very difficult, not to say impossible. Finally, because of the limits of the energizing voltage of the impedance analyzer (typically 1 volt rms for HP 4194A) and the high electric impedance of PZT, this approach may be less effective for a highly-damped structure than a lightly damped one, as for a high damping case, a much larger power is required to obtain Y_{mr} with an acceptable signal to noise ratio at each mode.

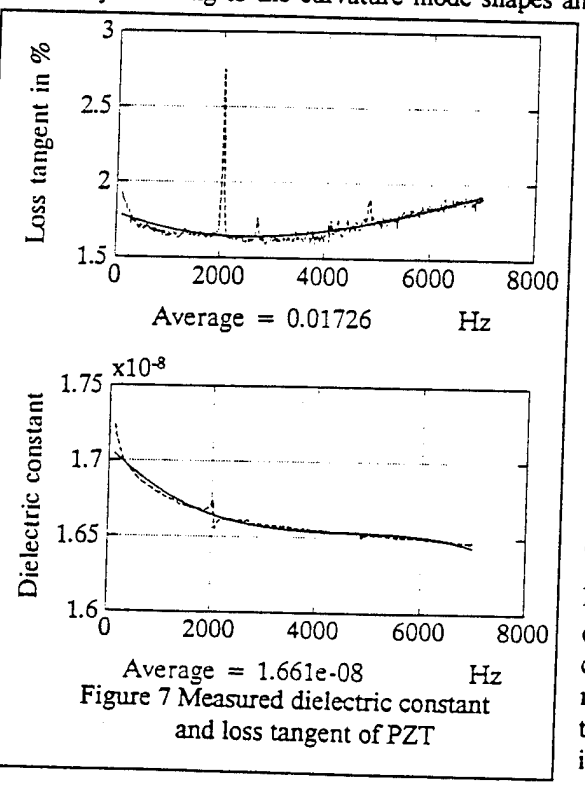

Figure 7 Measured dielectric constant and loss tangent of PZT

It has been noted during the beam test that both INPCF and AM/HPB approaches are sensitive to the dielectric constant of PZT in the modal damping and, especially, frequency extraction. From Eqs.(11) and (12), one can see that deviation of ε_{33}^T from its true value may considerably shift the mechanical mobility from its SDOF characteristics, making the curve fitting with INPCF marginal . For AM/HPB, the impact of this deviation on the extracted frequencies can be easily seen from Fig. 3. Figure 7 shows ε_{33}^T and δ deduced from measured electric admittance of a free PZT (G1195) based on Eq.(22). They are, instead of a constant as claimed, functions of frequency, and can be perfectly represented by third order polynomial. Therefore, it is preferable to use the curve fitting data of the same PZT (before bonded to structure) to improve the extraction accuracy.

It should be understood that applying the two algorithms to the modes which are not stiffened by PZT will introduce error rather than improve the accuracy. Modes 3 an 6 are the example in which an underestimation of the natural frequencies may be obtained if imposing the algorithms to the measured data. Generally, for these "tiny modes", the resonant frequencies of the joint system f_{rj} may be considered as the structure's natural frequencies without correcting.

Conclusion

A complete modal analysis of structure can be conducted with surface bonded piezoceramic patch as a collocated sensor-actuator. The measurement of electric admittance of PZT is quicker, more convenient and needs less experience and skill than that of mechanical frequency response function. Applying either of the extraction algorithms to the measurement data leads to refined estimations of modal damping and structure natural frequencies free of the stiffening effect of PZT. The curvature mode shapes of structure can also be extracted with this technique. The beam example demonstrates the effectiveness of the approaches in removal of the impact of PZT on the natural frequencies. This makes it an alternative approach to the noncontact modal test of small structure sensitive to the stiffening and mass loading of the transducers. The techniques, despite their SDOF nature, may also be applicable to more complicated structures. The identification of the sign of curvature mode shape needs to be addressed in the future work. The effect of mass loading of PZT sensor/actuator may also need to be considered.

Acknowledgment

The authors would like to express their gratitude to the Office of Navy Research, Grant ONR N00014-92-J-1170.

References

1 Dosch, J.J., Inman, D.J., and Garcia, E., "A Self-Sensing Actuator for Collocated Control," *ADPA Intl. Symposium. on Active Materials and Adaptive Structures,* Alexandria, VA, Nov. 1991.

2 Hagood, N.W. and Anderson, E.H., "Simultaneous Sensing and Actuation Using Piezoelectric Materials," *SPIE Conference on Active and Adaptive Optical Components,* July 1991, SPIE 1543-40.

3 Liang, C, Sun, F.P. and Rogers, C.A., "Dynamic Output Characteristics of Piezoelectric Actuators", *Proceedings of SPIE Conference on Smart Structures and Materials*, February 1-4, 1993, Albuquerque, NM.

4 Ewins, D.J, "*Modal Test: Theory and Practice*," Research Studies Press LTD., Letchworth, 1984, Hertfortshire, England.

5 Sun, F.P., Mitchell, L.D. and Arrudar, J.R.F., "Mode Decoupling Considerations in Mode Shape Measurement of a Plate with Monoexcitation and Laser Doppler Vibrometer," *Proceedings of SEM VII International Congress*, June 8-11, 1992, Las Vegas, Nevada.

C-44 Modeling Considerations for In-Phase Actuation of Actuators Bonded to Shell Structures, F. Lalande, Z. Chaudhry and C. A. Rogers, AIAA/ASME/ASCE/AHS/ASC 35 th Structures, Structural Dynamics and Materials Conference and Adaptive Structures Forum, Hilton Head, SC, pp. 429-437, 18-21 April 1994.

MODELING CONSIDERATIONS FOR IN-PHASE ACTUATION OF ACTUATORS BONDED TO SHELL STRUCTURES

Frédéric Lalande, Zaffir Chaudhry and Craig A. Rogers
Center for Intelligent Material Systems and Structures
Virginia Polytechnic Institute and State University
Blacksburg, VA 24061-0261

AIAA/ASME/ASCE/AHS/ASC 35th Structures, Structural Dynamics, and Materials Conference and Adaptive Structures Forum, April 18-22, 1994, Hyatt Regency, Hilton Head, South Carolina

Abstract

A model to represent the in-phase actuation of induced strain actuators bonded to the surface of a circular shell is developed. Due to the inherent shell curvature, the equivalent discrete tangential forces generally used to represent the in-phase actuation of the actuators (such as in pin-force models) are not co-linear and result in the application of rigid body forces on the shell. This non-equilibrium state violates the principle of self-equilibrium of fully integrated structures, such as piezoelectrically actuated shells. The solution to this non-equilibrium problem is to apply a uniform transverse pressure over the actuator region to maintain equilibrium. Using this adequate equivalent loading scheme for in-phase actuation, a deformation model for a circular ring is derived based on shell governing equations.

To verify the deformation model, finite element analysis is performed. A perfect match between the in-phase actuation deformation model and the finite element results, when the actuator mass and stiffness are neglected, validates the derived analytical model. A deformed shell comparison between the point force model, often used to represent the actuator in-phase actuation, and the derived analytical model showed major displacement disparities. Thus, by simply applying a uniform transverse pressure along with the discrete tangential forces in order to maintain the self-equilibrium of the shell, the shell deformation can be modeled accurately.

Introduction

Piezoelectrics actuators have been used for active shape, vibration and acoustic control of structures because of their adaptibility and light weight. Their ability to be easily integrated into structures makes them very attractive in structural control since all moving parts encountered with conventional actuators are eliminated. Structural control is implented by simply embedding PZT actuators in the structure or bonding them on the structure. In structural control, the desired deformation in the structure is obtained by the application of localized line forces and moments generated by the expanding or contracting bonded or embedded PZT actuators. In the case of vibration and acoustic control, the piezoelectric actuators will change the impedance of the structure to reduce the unwanted dynamic effects at given frequencies.

Previous research performed on PZT-actuated beam and plate structures has led to models describing their response (Crawley and de Luis, 1987; Crawley and Anderson, 1990; Wang and Rogers, 1991; Dimitriadis et al., 1991; Zhou et al.., 1994; Liang et al., 1993). Simple but efficient models were proposed to describe the response of a plate structure to the piezoelectric actuators (Crawley and Lazarus, 1989). By simply replacing the PZT actuator with line forces and moments on its edges, very accurate results are produced even though this type of model is approximate since the mass and stiffness of the actuator is not considered. However, much less research has been performed on structures with curvature. Some experimental work (Fuller, 1990) and adaptations of flat structure models to curved structures have been made (Sonti and Jones, 1991; Lester and Lefebvre, 1991). Models based on shell equations have also been proposed (Rossi et al., 1993; Sonti, 1993; Zhou et al., 1993; Larson and Vinson, 1993).

In a recent paper, Chaudhry, Lalande and Rogers (1994) considered the modeling of piezoelectric actuator patches on circular cylinders. When the piezoelectric actuators are actuated in-phase, it is found that the point force model used to represent the actuator creates a rigid body motion since the equivalent line forces are not collinear due to the curvature of the shell. Since the PZT actuators are integrated within the structure, self-equilibrium must be satisfied. This equilibrium discrepancy between the actual structure and the equivalent loading scheme will produce serious errors when the shell deformation, based on the line force representation of the actuator, is calculated. Until now, no models take account of this non-equilibrium application of the equivalent line forces. The solution proposed to solve this problem is to apply a uniform transverse pressure over the actuator location to eliminate the rigid body mode. Good agreement between the equivalent loading model and the actual deformation of the piezoelectrically-actuated structure was found.

In this paper, an analytical deformation model of a piezoelectrically-actuated circular ring, which takes into account the non-collinear equivalent line forces, is proposed.

Copyright© 1994 by
Center for Intelligent Material Systems and Structures.
Published by the AIAA inc. with permission.

Shell equivalent loading model

The first step in this paper is to repeat the conclusions established by Chaudhry, Lalande and Rogers (1994). In that paper, an equivalent loading scheme for shell structures was presented. It was shown that in the case of in-phase actuation, a rigid body mode was present due to the fact that the equivalent line forces L_θ are not collinear (Fig. 1).

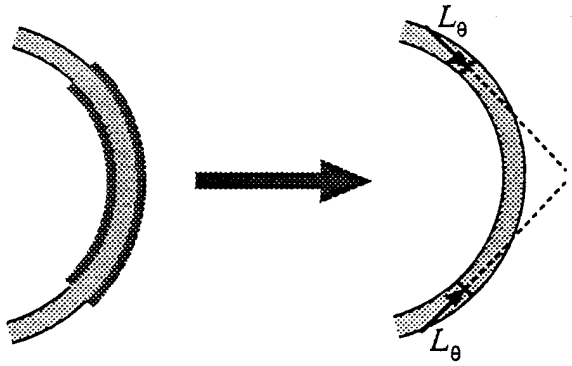

Figure 1. Non-equilibrium of discrete tangential forces in shell structures.

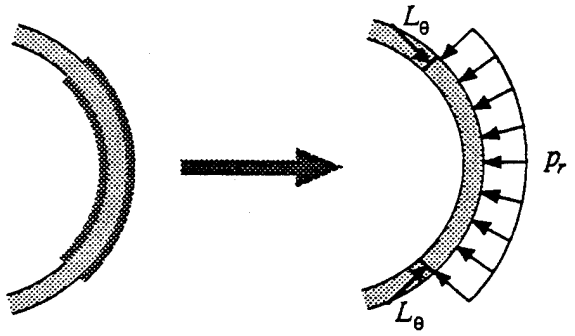

Figure 2. Adequate equivalent loading to maintain equilibrium.

To eliminate this non-equilibrium state of the structure, a transverse uniform pressure is added (Fig. 2). The magnitude of the transverse pressure from simple statics is then:

$$\bar{p}_r = -\frac{\bar{L}_\theta}{a}, \tag{1}$$

where

$$\bar{L}_\theta = \frac{E_s t_s}{1-\nu}\frac{2}{2+\psi}\Lambda \tag{2}$$

and

$$\psi = \frac{E_s t_s}{E_a t_a}, \tag{3}$$

when the Poisson's ratio of the shell and the piezoelectric actuator are assumed to be the same. E, t, L and a are the Young's modulus, the thickness, the free induced strain and the radius of the ring, respectively, while the subscripts s and a stand for shell and actuator, respectively. If a circular ring is considered, the Poisson's effect disappears since there are no constraints in the axial direction. Thus, for the case of a ring, the Poisson's ratio in Eq. (2) is set to zero. Based on this equivalent loading scheme, a deformation model for a circular ring with two discrete tangential forces and a uniform radial pressure will be derived.

Derivation of governing equations

In the current literature (Soedel, 1981; Flugge, 1973), the governing shell equations are limited to shells subjected to external pressure loading only. Since the proposed equivalent loading model involves discrete tangential forces, the available shell equations are not adequate. To simplify the governing equations, the added mass and stiffness of the actuators are neglected. Thus, the governing equations of a uniform stiffness circular ring subjected to radial pressure and discrete tangential loading will be derived using the approach proposed by Soedel (1981). In the case of a thin circular ring, only the in-plane stress resultants N_θ, M_θ and $Q_{\theta r}$ are present. The stress resultants in the axial direction, N_x, M_x, the shear stress resultant $N_{x\theta}$, the twisting moment resultant M_{xq} and the transverse shear force Q_{xr} are all zero since the displacements are constant in the axial direction and the axial displacements are zero.

Starting with the classical theory of elasticity, the polar strain-displacement relations are given by Timoshenko and Goodier (1951):

$$\varepsilon_r = \frac{\partial w}{\partial r} \tag{4a}$$

$$\varepsilon_\theta = \frac{w}{r} + \frac{\partial v}{r\partial\theta} \tag{4b}$$

$$\gamma_{\theta r} = \frac{\partial w}{r\partial\theta} + \frac{\partial v}{\partial r} - \frac{v}{r}. \tag{4c}$$

A neutral surface system of coordinates is used instead of the global polar coordinates to simplify the equations. Thus, the change of variable is:

$$r = a + z = a\left(1 + z/a\right), \tag{5}$$

where a is the radius of the ring. Combining the polar strain-displacement relations Eq. (4) and the change of coordinate system Eq. (5), the strain-displacement relations in the neutral surface coordinate system become:

$$\varepsilon_r = \frac{\partial w}{\partial z} \tag{6a}$$

$$\varepsilon_\theta = \frac{1}{a\left(1+z/a\right)} w + \frac{\partial v}{\partial \theta} \tag{6b}$$

$$\gamma_{\theta r} = \frac{1}{a\left(1+z/a\right)}\left[\frac{\partial w}{\partial \theta} - v + a\left(1+z/a\right)\frac{\partial v}{\partial z}\right]. \tag{6c}$$

Since the ring is thin, a linear variation in the tangential direction and a constant radial displacement through the thickness are assumed (Kirchhoff's assumption; Soedel, 1981):

$$v = v^o + z\beta \tag{7a}$$

$$w = w^o, \tag{7b}$$

where β is the rotational displacement and v^o and w^o are the neutral surface tangential and radial displacements, respectively. If the shear deflection is neglected ($\gamma_{\theta r}$ = 0), the expression of β is obtained from Eqs. (6c) and (7):

$$\beta = \frac{1}{a}\left(v^o - \frac{\partial w^o}{\partial \theta}\right). \tag{8}$$

Even though we assumed the shear strain $\gamma_{\theta r}$ to be zero, this does not imply that the transverse shear force $Q_{\theta r}$ is neglected. When the ring is thin, the z/a term can be neglected since it is much less than one. Thus, the strain-displacement relations become:

$$\varepsilon_r = 0 \tag{9a}$$

$$\varepsilon_\theta = \frac{1}{a}\left(\frac{\partial v^o}{\partial \theta} + w^o\right) + \frac{z}{a^2}\left(\frac{\partial v^o}{\partial \theta} - \frac{\partial^2 w^o}{\partial \theta^2}\right) \tag{9b}$$

$$\gamma_{\theta r} = 0. \tag{9c}$$

The membrane force, bending moment and transverse shear force resultants are obtained by integrating through the thickness of the ring:

$$N_\theta = \int_{-t_s/2}^{t_s/2} \sigma_\theta dz = \int_{-t_s/2}^{t_s/2} E\varepsilon_\theta dz = \frac{K}{a}\left(\frac{\partial v^o}{\partial \theta} + w^o\right) \tag{10a}$$

$$M_\theta = \int_{-t_s/2}^{t_s/2} \sigma_\theta z\, dz = \int_{-t_s/2}^{t_s/2} E\varepsilon_\theta z\, dz = \frac{D}{a^2}\left(\frac{\partial v^o}{\partial \theta} - \frac{\partial^2 w^o}{\partial \theta^2}\right) \tag{10b}$$

$$Q_{\theta r} = \int_{-t_s/2}^{t_s/2} \sigma_{\theta r}\, dz, \tag{10c}$$

where the membrane stiffness is:

$$K = Et_s, \tag{11a}$$

and the bending stiffness is:

$$D = \frac{Et_s^3}{12}. \tag{11b}$$

It must be noted that the Poisson's ratio is not present in the stiffnesses expressions Eq. (11) since the ring is free to deform in the axial direction.

The equilibrium equations derivation is based on the energy method. Using Hamilton's principle, the Love ring equations for the equivalent loading scheme will be developed. Hamilton's principle is given by:

$$\int_{t_o}^{t_1}\left[\delta\left(U - E_b - E_L\right) - \delta K\right]dt = 0, \tag{12}$$

where $\delta(U-E_b-E_L)$ is the total variational potential energy and δK is the variational kinetic energy. Since the ring is subjected to static loading, the kinetic energy term is equal to zero.

The first term involved in the total potential energy is the strain energy. The infinitesimal ring element is subjected to tangential stress σ_θ and to $\sigma_{\theta r}$ only. Thus, the strain energy stored in this infinitesimal element is:

$$dU = \frac{1}{2}\left(\sigma_\theta \varepsilon_\theta + \sigma_{\theta r}\gamma_{\theta r}\right) a d\theta\, dx\, dz. \tag{13}$$

The transverse shear term is retained in order to obtain an expression for b, even though it was assumed that $\gamma_{\theta r} = 0$ Eq. (9c). The previous equation is integrated over the volume of the ring to obtain the total strain energy:

$$U = \iiint_{x\,\theta\,z} \frac{1}{2}\left(\sigma_\theta \varepsilon_\theta + \sigma_{\theta r}\gamma_{\theta r}\right) a d\theta\, dx\, dz. \tag{14}$$

The free body diagram of the ring is shown in Fig. 3. The possible externally applied boundary forces and moment resultants introduce energy into the ring. This second type of potential energy is given by:

$$E_b = \int_x \left(N_\theta^* v^o + Q_{\theta r}^* w^o + M_\theta^* \beta\right) dx. \tag{15}$$

The term of potential energy introduced in the ring due to external loading is due to a radial pressure and a

discrete tangential load (Fig. 4). The external loading energy is given by:

$$E_L = \iint_{x\,\theta} p_r w^o \, a d\theta \, dx + \int_x \bar{L}_\theta v^o \, dx. \tag{16}$$

Rewriting the previous equation under a unique double integral by introducing a Dirac function:

$$E_L = \iint_{x\,\theta} \left(\frac{\bar{L}_\theta}{a} \delta(\theta - \theta_p) v^o + p_r w^o \right) a d\theta \, dx, \tag{17}$$

where θ_p is the location of the applied line load. The loads are assumed to be applied on the neutral surface of the ring.

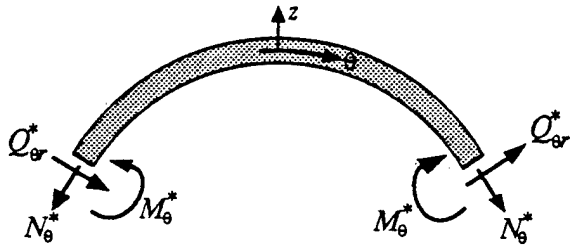

Figure 3. Ring free-body diagram.

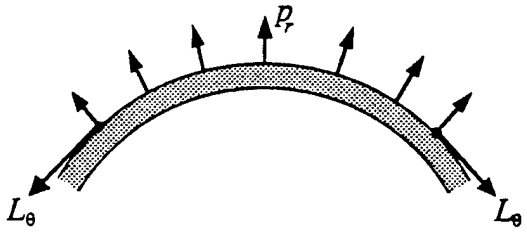

Figure 4. External loading applied to the ring.

Introducing the variational operator in the potential energy expressions, one can obtain the variational strain energy:

$$\delta U = \iiint_{x\,\theta\,z} \left[\sigma_\theta \, \delta\varepsilon_\theta + \sigma_{\theta r} \, \delta\varepsilon_{\theta r} \right] a d\theta \, dx \, dz. \tag{18}$$

Substituting the strain-displacement relationships Eq. (9) and using the zero normal shear strain Love simplification, Eq. (18) is rewritten as:

$$\delta U = \iiint_{r\,x\,\theta} \begin{bmatrix} \sigma_\theta \left(\dfrac{\partial \delta v^o}{\partial \theta} + z \dfrac{\partial \delta\beta}{\partial \theta} + \delta w^o \right) + \\ \sigma_{\theta r} \left(\delta\beta \, a - \dfrac{\partial \delta v^o}{\partial \theta} - \dfrac{\partial \delta w^o}{\partial \theta} \right) \end{bmatrix} d\theta \, dx \, dr. \tag{19}$$

Integrating by parts, the above expression for the variational strain energy becomes:

$$\delta U = \left\{ \begin{array}{c} \displaystyle\iint_{x\,\theta} \left[\left(-\frac{\partial N_\theta}{\partial \theta} - Q_{\theta r} \right) \delta v^o + \left(N_\theta - \frac{\partial Q_{\theta r}}{\partial \theta} \right) \delta w^o \right. \\ \left. + \left(-\frac{\partial M_\theta}{\partial \theta} + Q_{\theta r} a \right) \delta\beta \right] d\theta \, dx \\ + \displaystyle\int_x \left[N_\theta \, \delta v^o + M_\theta \, \delta\beta + Q_{\theta r} \, \delta w^o \right] dx \end{array} \right\} \tag{20a}$$

The variational form of the energy introduced by the external boundary forces is:

$$\delta E_b = \int_x \left(N_\theta^* \delta v^o + Q_{\theta r}^* \delta w^o + M_\theta^* \delta\beta \right) dx, \tag{20b}$$

and the variational external loading energy is:

$$\delta E_L = \iint_{x\,\theta} \left(\frac{\bar{L}_\theta}{a} \delta(\theta - \theta_p) \delta v^o + p_r \delta w^o \right) a d\theta \, dx. \tag{20c}$$

Substituting the expressions of the different types of energy involved in the total variational potential energy Eq. (20) in Hamilton's principle Eq. (12), we obtain

$$\int_{t_o}^{t_1} \left\{ \begin{array}{c} \left\{ \displaystyle\iint_{x\,\theta} \left[\left(-\frac{\partial N_\theta}{\partial \theta} - Q_{\theta r} \right) \delta v^o + \left(N_\theta - \frac{\partial Q_{\theta r}}{\partial \theta} \right) \delta w^o + \left(-\frac{\partial M_\theta}{\partial \theta} + Q_{\theta r} a \right) \delta\beta \right] d\theta \, dx + \int_x \left[N_\theta \, \delta v^o + M_\theta \, \delta\beta + Q_{\theta r} \, \delta w^o \right] dx \right\} - \\ \left\{ \displaystyle\int_x \left[N_\theta^* \delta v^o + Q_{\theta r}^* \delta w^o + M_\theta^* \delta\beta \right] dx \right\} - \left\{ \displaystyle\iint_{x\,\theta} \left[\frac{\bar{L}_\theta}{a} \delta(\theta - \theta_p) \delta v^o + p_r \delta w^o \right] a d\theta \, dx \right\} \end{array} \right\} dt = 0 \tag{21}$$

Rewriting the previous equation:

$$\int_{t_o}^{t_1}\iint_{x\,\theta}\left[\left(\frac{\partial N_\theta}{\partial\theta}+Q_{\theta r}+\bar{L}_\theta\delta\left(\theta-\theta_p\right)\right)\delta v^o+\left(\frac{\partial Q_{\theta r}}{\partial\theta}-N_\theta+a\,p_r\right)\delta w^o+\left(\frac{\partial M_\theta}{\partial\theta}-Q_{\theta r}a\right)\delta\beta\right]d\theta\,dx\,dt+$$
$$\int_{t_o}^{t_1}\int_{x}\left[\left(N_\theta{}^*-N_\theta\right)\delta v^o+\left(Q_{\theta r}{}^*-Q_{\theta r}\right)\delta w^o+\left(M_\theta{}^*-M_\theta\right)\delta\beta\right]dx\,dt=0 \tag{22}$$

To be satisfied, each integral term of Hamilton's principle must be individually zero. Since the variational displacements cannot be zero due to their arbitrariness, the Love circular ring equations are:

$$\frac{\partial N_\theta}{\partial\theta}+Q_{\theta r}+\bar{L}_\theta\delta\left(\theta-\theta_p\right)=0, \tag{23a}$$

$$\frac{\partial Q_{\theta r}}{\partial\theta}-N_\theta+a\,p_r=0, \tag{23b}$$

and

$$\frac{\partial M_\theta}{\partial\theta}-Q_{\theta r}a=0. \tag{23c}$$

Substituting Eq. (23c) in Eqs. (23a) and (23b), the equilibrium equations of the circular ring are found to be:

$$a\frac{dN_\theta(\theta)}{d\theta}+\frac{dM_\theta(\theta)}{d\theta}+a\bar{L}_\theta\,\delta\left(\theta-\theta_p\right)=0, \tag{24a}$$

$$\frac{d^2M_\theta(\theta)}{d\theta^2}-aN_\theta(\theta)+a^2p_r(\theta)=0. \tag{24b}$$

The derived equilibrium equations Eq. (24) are very similar to those obtained by Soedel (1981) and Flugge (1973). The difference appears in the tangential loading term $a\bar{L}_\theta\,\delta\left(\theta-\theta_p\right)$ which replaces the $a^2\,p_\theta(\theta)$ term when tangential pressure loading is considered.

By setting the line integrals to zero in Eq. (22), the necessary boundary conditions for the ring are:

$$N_\theta=N_\theta{}^*\ \text{or}\ v^o=v^{o^*}, \tag{25a}$$

$$M_\theta=M_\theta{}^*\ \text{or}\ \beta=\beta^*, \tag{25b}$$

and

$$Q=Q^*\ \text{or}\ w^o=w^{o^*}. \tag{25c}$$

Derivation of the In-Phase Actuation Deformation Model

With the governing equations now derived, the next step is to apply them to the particular problem shown in Fig. 5. To simplify the analytical model derivation, the actuator stiffness will be neglected.

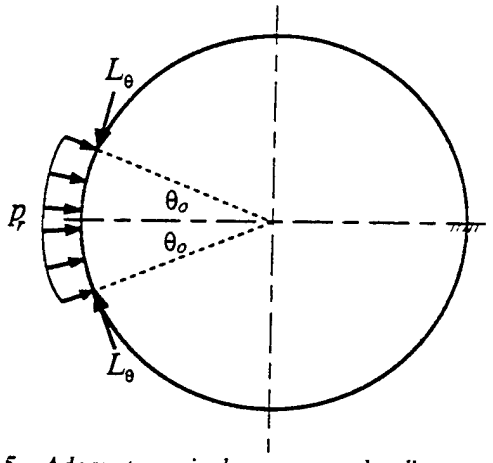

Figure 5. Adequate equivalent actuator loading on the ring.

As established previously, the ring is subjected to discrete tangential forces at the end of the modeled actuator and to a uniform radial pressure of magnitude $(\frac{\bar{L}_\theta}{a})$ Eq. (1), to ensure equilibrium of the ring. The loading of the ring is expressed using Dirac and Heaviside functions:

$$L_\theta(\theta)=\bar{L}_\theta\left[\delta^--\delta^+\right] \tag{26}$$

$$p_r(\theta)=\bar{p}_r\left[H^--H^+\right]=-\frac{\bar{L}_\theta}{a}\left[H^--H^+\right], \tag{27}$$

where

$$\theta^-=\theta-(\pi-\theta_o) \tag{28a}$$

$$\theta^+=\theta-(\pi+\theta_o) \tag{28b}$$

$$\delta^-=\delta\left[\theta^-\right] \tag{29a}$$

$$\delta^+=\delta\left[\theta^+\right] \tag{29b}$$

$$H^-=H\left[\theta^-\right] \tag{30a}$$

$$H^+=H\left[\theta^+\right]. \tag{30b}$$

The integration constants will be determined from the continuity conditions at $\theta = 0, 2\pi$:

$$w^o(0) = w^o(2\pi) \tag{31a}$$

$$v^o(0) = v^o(2\pi) \tag{31b}$$

$$\beta(0) = \beta(2\pi). \tag{31c}$$

From the rotational displacement expression Eq. (8), it is possible to rewrite the continuity conditions of Eq. (31c), by making use of Eq. (31a), as:

$$w'^o(0) = w'^o(2\pi). \tag{31d}$$

Combining the equilibrium equations Eq. (24), the differential equation for the moment in the ring is obtained as follows:

$$\frac{d^3 M_\theta(\theta)}{d\theta^3} + \frac{dM_\theta(\theta)}{d\theta} = -a^2\left[\frac{L_\theta(\theta)}{a} + p_r'(\theta)\right] = 0. \tag{32}$$

Substituting the loading expressions Eqs. (26) and (27) in the previous equation (Eq. (32)), it can be seen that the right hand side of the equation will be zero. Solving the differential equation (Eq. (32)), an expression of the moment distribution in the ring is obtained:

$$M_\theta(\theta) = C_1 + C_2 Sin\theta + C_3 Cos\theta. \tag{33}$$

Combining the two stress-displacement equations Eq. (10), the following differential equation is obtained:

$$w^o(\theta) + \frac{d^2 w^o(\theta)}{d\theta^2} = \frac{a^2}{D}\left(\frac{N_\theta(\theta) D}{Ka} - M_\theta(\theta)\right). \tag{34}$$

Rewriting the second equilibrium equation (Eq, (24b)):

$$N_\theta(\theta) = \frac{1}{a}\frac{d^2 M_\theta(\theta)}{d\theta^2} + a\, p_r(\theta). \tag{35}$$

Substituting the expression of the moment Eq. (33) and the tangential force Eq. (35) into Eq. (34), the following differential equation in $w^o(\theta)$ is obtained:

$$w^o(\theta) + \frac{d^2 w(\theta)}{d\theta^2} = -\frac{a^2}{D}\left[\begin{array}{l} C_1 + C_2\left(1 + \dfrac{D}{K a^2}\right) Sin\theta + \\ C_3\left(1 + \dfrac{D}{K a^2}\right) Cos\theta - \dfrac{D}{K} p_r(\theta) \end{array}\right]. \tag{36}$$

For thin rings, the $\frac{D}{K a^2}$ term is neglected since its value is much less than one. The radial displacement equation is obtained using Laplace transform:

$$w^o(\theta) = \frac{a^2}{D}\left\{\begin{array}{l} C_1(1 - Cos\theta) + \dfrac{C_2}{2}(Sin\theta - \theta Cos\theta) \\ + \dfrac{C_3}{2}(\theta Sin\theta) + w^o(0) Cos\theta + w^{o'}(0) Sin\theta \\ + \dfrac{D\,\bar{p}_r}{K}\left[\left(1 - Cos\theta^-\right)H^- - \left(1 - Cos\theta^+\right)H^+\right] \end{array}\right\} \tag{37}$$

Introducing Eq.(37) in Eq. (10a), the tangential displacement differential equation is

$$\frac{dv^o(\theta)}{d\theta} = \frac{a^2}{D}\left\{\begin{array}{l} -C_1(1 - Cos\theta) - \dfrac{C_2}{2}(Sin\theta - \theta Cos\theta) \\ - \dfrac{C_3}{2}(\theta Sin\theta) - w^o(0) Cos\theta - w^{o'}(0) Sin\theta \\ + \dfrac{D\,\bar{p}_r}{K}\left[Cos\theta^- H^- - Cos\theta^+ H^+\right] \end{array}\right\} \tag{38}$$

Solving this equation using Laplace transformation and applying continuity conditions Eq. (31), the equations of the radial and tangential displacements are found to be:

$$v^o(\theta) = \frac{a^2\,\bar{p}_r}{K}\left\{\begin{array}{l} -\dfrac{Sin\theta_o}{\pi}(Sin\theta - \theta Cos\theta) \\ +\left[Sin\theta^- H^- - Sin\theta^+ H^+\right] \end{array}\right\}, \tag{39}$$

and

$$w^o(\theta) = \frac{a^2\,\bar{p}_r}{K}\left\{\begin{array}{l} \dfrac{Sin\theta_o}{\pi}\theta Sin\theta + \\ \left[\left(1 - Cos\theta^-\right)H^- - \left(1 - Cos\theta^+\right)H^+\right] \end{array}\right\}. \tag{40}$$

Finite Element Verification

The developed in-phase actuation deformation model is verified using finite element analysis. A ring of 6" radius, 0.032" thickness and 1" deep, and piezoelectric actuators 1/6 of the ring thickness and covering an arc 30° long ($2\theta_o$), are used. Making use of symmetry, the finite element model consists of beam elements only in the upper half, as shown in Fig. 6. Two loading cases are considered: i) temperature contraction equivalent to 1000 μstrain of the beam elements modeling the actuator region; and ii) equivalent discrete forces and uniform pressure loading from Eqs. (1) and (2). The finite element analysis results are shown in Fig. 7, as well as the in-phase actuation deformation model results. A single

curve can be observed since the curves match perfectly. Also shown in Fig. 7 are the displacements of the same ring if only discrete tangential forces are applied (point force model). The point force model does not satisfy the ring's self-equilibrium. Major displacement discrepancies between the in-phase actuation deformation and the point force model occur both in shape and magnitude. The point force model overpredicts the displacements by a factor up to 1000. Fig. 8 shows the deformed shape of the self-equilibrium loading and the non-equilibrium loading with the displacements magnified by a 500 and 2 factor, respectively. It can be seen again that when a uniform pressure is not applied to maintain equilibrium, the deformed shape is erroneous. Also, a reaction force in the x-direction at the clamped boundary condition is present if the uniform pressure is not applied. This reaction force should not be present since the actual ring with bonded actuators is in self-equilibrium. The adequate equivalent loading did not show any reaction force in the x-direction at the clamped boundary condition. The verification of the results also have been made with 10° and 60°-long piezoelectric patches, and the coincidence is still perfect between the in-phase actuation deformation model and the finite element analysis.

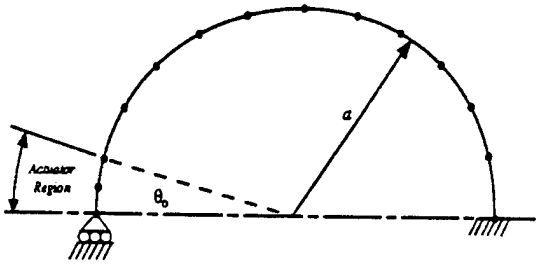

Figure 6. Beam finite element model.

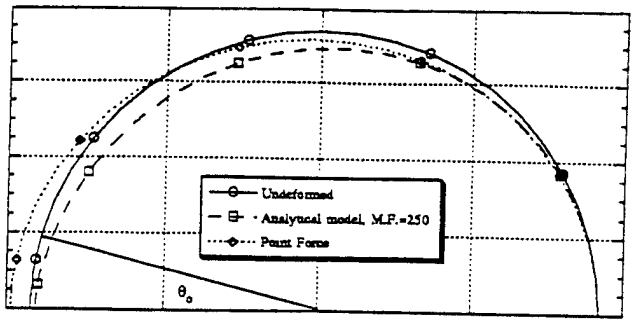

Figure 8. Deformed shape of the ring with and without self-equilibrium loading.

However, it must be mentionned that the deformation of the ring is very sensitive to the applied load in the finite element model. An error of 0.1% in the magnitude of the applied equivalent line force will completely change the response of the ring. This sensitivity of the nodal displacements is due to the low stiffness of the ring (0.032" thick only). The application of a tangential line force of 0.1% magnitude of the applied equivalent line force on the ring will produce nodal displacements of the same order as the self-equilibrium loading nodal displacements.

Also, the pressure loading must be transformed to nodal forces only (lumped loading). The lumped loading is often better for flat elements representing a curved surface (De Salvo and Swanson, 1979).

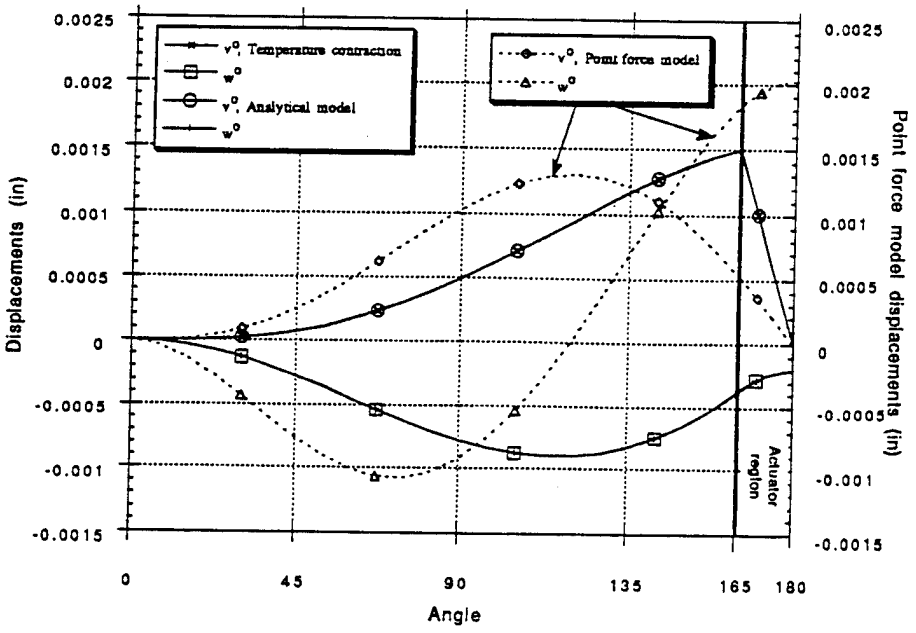

Figure 7. Match of displacements between the analytical model and the beam finite element model.

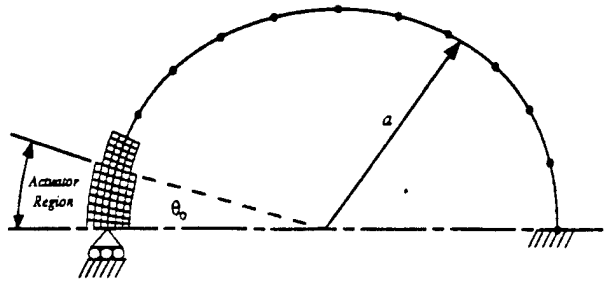

Figure 9. Plane stress finite element model.

Up to this point, the added stiffness of the actuators has been neglected both in the analytical model and the finite element analysis. A second finite element model, using plane stress elements in the actuator region to include the actuator's stiffness, is made to compare the actual behavior of the system to the derived analytical model (Fig. 9). To keep the FE model small, the actuator size is reduced to 10° ($2\theta_o$). The radial and tangential displacements are shown in Fig. 10. Disparities between the analytical model and the plane stress finite element model are present since no assumptions on the actuator stiffness or on the equivalent loading are made on the latter one. Even though displacement differences are present, the plane stress finite element model validates the derived analytical model since it gives results of the same order of magnitude with similar deformed shapes as opposed to the point force model previously discussed. The deformed shape of the analytical model and the plane stress finite element model is shown in Fig. 11.

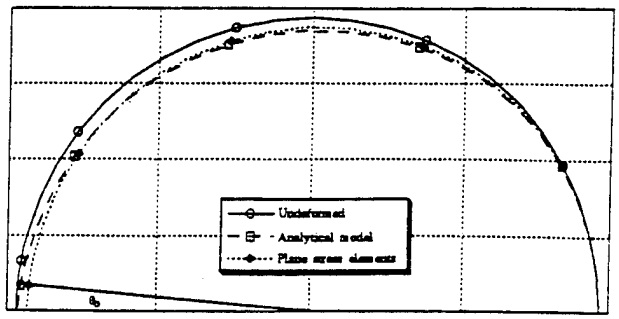

Figure 11. Deformed shape of the ring with and without self-equilibrium loading using plane stress elements.

The discussion of in-phase actuation of induced strain actuators symmetrically bonded on shells can be extended to unsymmetric actuation. Unsymmetric actuation is obtained when the actuators on each side of the shell are submitted to voltages of different magnitudes, or when a single actuator is bonded on one side of the shell. Unsymmetric actuation is a combination of extension and bending of the shell and can be solved using simple superposition. Thus, for unsymmetric actuation, the equivalent loading will consist of discrete tangential forces and moments at the ends of the actuator(s) and a distributed transverse pressure over the actuator(s) footprint to maintain the self-equilibrium of the shell.

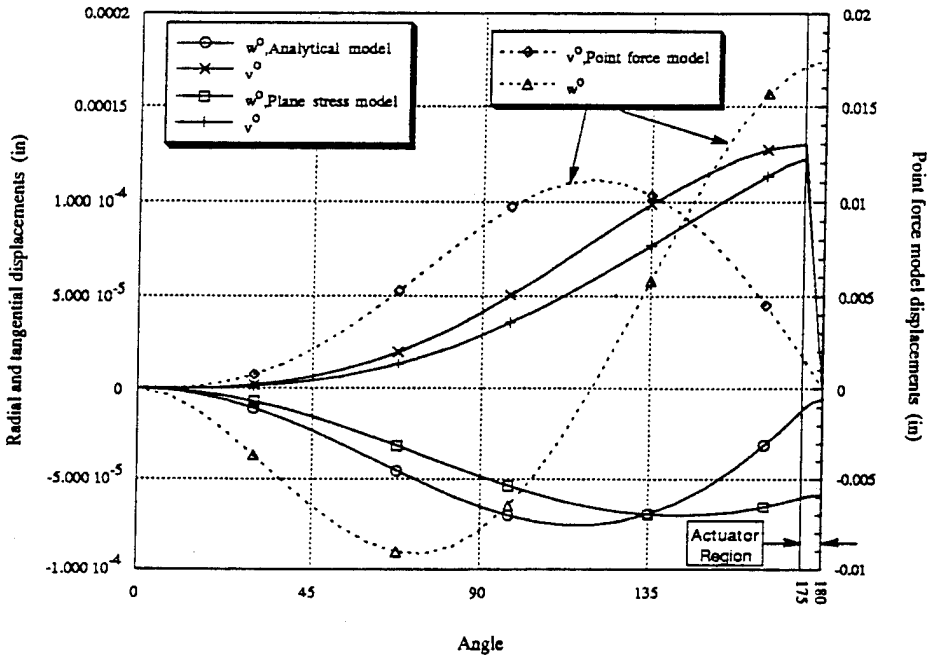

Figure 10. Match of displacements between the analytical model and the plane stress finite element model

Conclusion

In this paper, a deformation model for a circular ring subjected to in-phase actuation was derived. The actuator equivalent loading includes a uniform transverse pressure to maintain the self-equilibrium of the shell structure. The results of the in-phase actuation deformation model are in exact agreement with the finite element results the when actuator stiffness is neglected. If the actuator stiffness is considered, the analytical model gives a good approximation of the shell's deformed shape. If the self-equilibrium is not maintained (point-force model), the predicted deformed shape is completely different from the actual shell response to in-phase actuation. Thus, to obtain accurate results, a uniform transverse pressure should be applied to maintain the shell self-equilibrium.

Acknowledgments

The authors would like to acknowledge the funding support of the Office of Naval Research, Grant ONR N00014-92-J-1170, Dr. Kam Ng, Technical Monitor.

References

1) Chaudhry, Z., Lalande, F. and Rogers, C.A., 1994, "Modeling of Induced Strain Actuator Patches", Proceedings, *SPIE 1994 North American Conference on Smart Structures and Materials*, Orlando, FL, 13-18 February 1994; in press.

2) Crawley, E.F. and Anderson, E.H., 1990, "Detailed Models of Piezoceramic Actuation of Beams", *J. of Intel. Mater. Syst. and Struc.*, Vol. 1, pp. 4-25.

3) Crawley, E.F. and de Luis, J., 1987, "Use of Piezoelectric Actuators as Elements of Intelligent Structures", *AIAA Journal*, 25 (10), pp. 1373-1385.

4) Crawley, E.F. and Lazarus, K.B., 1989, "Induced Strain Actuation of Isotropic and Anisotropic Plates", *AIAA Journal*, Vol. 29, No. 6, pp. 944-951.

5) De Salvo, G.J. and Swanson, J.A., 1979, "ANSYS User's Manual", Swanson analysis systems, Houston, PA.

6) Dimitriadis, E.K., Fuller, C.R. and Rogers, C.A., 1991, "Piezoelectric Actuators for Distributed Vibration Excitation of Thin Plates", *J. of Vibration and Acoustics*, Vol. 113, pp. 100-107.

7) Fuller, C.R., Snyder, S., Hanson, C. and Silcox, R., 1990, "Active Control of Interior Noise in Model Aircraft Fuselages using Piezoceramic Actuators", *Proceedings, AIAA 13th Aeroacoustic Conference*, Vol. 90-3922, Tallahasse, FL, October 22-24 1990.

8) Flugge, W., 1973, "Stresses in shells", Springer-Verlag.

9) Larson, P.H., and Vinson, J.R., 1993, "The Use of Piezoelectric Materials in Curved Beams and rRngs", *Proceedings, ASME Winter Annual Meeting*, New Orleans, LA, 28 Nov-3 Dec 1993; pp. 277-285.

10) Lester, H.C. and Lefebvre, S., 1991, "Piezoelectric Actuator Models for Active Sound and Vibration Control of Cylinders, *Proceedings, Recent Advances in Active Noise and Vibration Control*, Blacksburg, VA, 15-17 April 1991; pp. 3 -26.

11) Liang, C., Sun, F.P., and Rogers, C.A., 1993c, "An Impedance Method for Dynamic Analysis of Active Material Systems", *Proceedings, 34th SDM Conference*, La Jolla, CA, 19-21 April 1993; pp.. 3587-3599.

12) Rossi, A., Liang, C. and Rogers, C.A., 1993, "Impedance Modeling of Piezoelectric Actuator-Driven Systems: an Application to Cylindrical Ring Structures", *Proceedings, 34th SDM Conference*, La Jolla, CA, 19-21 April 1993; pp. 3618-3624

13) Soedel, W., 1981, *Vibrations of Plates and Shells*, Marcel and Decker Inc, New-York.

14) Sonti, V.R. and Jones, J.D., 1991,"Active Vibration Control of Thin Cylindrical Shells using Piezo-electric Actuators", *Proceedings, Recent Advances in Active Noise and Vibration Control*, Blacksburg, VA, 15-17 April 1991; pp. 27-38.

15) Sonti, V.R., 1993, "Curved Piezo-Actuator Models for Active Vibration Control of Cylindrical Shells", *Proceedings, 125th meeting of the Acoustical Society of America*, Ottawa, Canada, 17-21 May .

16) Timoshenko, S. and Goodier, J.N., 1951, *Theory of Elasticity*, McGraw-Hill.

17) Wang, B.T. and Rogers, C.A., 1991, "Modeling of Finite-Length Spatially Distributed Induced Strain Actuators for Laminate Beams and Plates", *Proceedings, 32nd SDM Conference*, Baltimore, MD, 8-10 April 1991; pp. 1511-1520.

18) Zhou, S., Liang, C., and Rogers, C.A., 1993, "Impedance modeling of two dimensional piezoelectric actuators bonded on a cylinder", *Proceedings, 114th ASME Winter Annual Meeting*, New Orleans, LA, 28 Nov -3 Dec 1993, pp. 247-255.

19) Zhou, S., Liang, C. and Rogers, C.A., 1994, "A Dynamic Model of a Piezoelectric Actuator Driven Thin Plate", *Smart Structures and Materials '94, SPIE*, Orlando, FL, 13-18 February 1994; in press.

C-45 Control of Sound Radiation/Reflection with Adaptive Foams, C. R. Fuller, M. J. Bronzel, C. A. Gentry and D. E. Whittington, Proceedings of Noise-Con '94, pp. 429-436, Ft. Lauderdale, FL, May, 1994.

NOISE-CON 94
Ft. Lauderdale, Florida
1994 May 01–04

CONTROL OF SOUND RADIATION/REFLECTION WITH ADAPTIVE FOAMS

C.R. Fuller, M.J. Bronzel, C.A. Gentry and D.E. Whittington

Vibration and Acoustics Laboratories
Department of Mechanical Engineering
Virginia Polytechnic Institute and State University
Blacksburg, Virginia, 24061

INTRODUCTION

The objective of Active Structural Acoustic Control (ASAC) is to minimize the sound radiating from a vibrating structure with integrated actuators and sensors. The need for high performance, compact and lightweight noise control systems has motivated researchers to investigate the use of porous layers and piezoelectric materials for sound transmission and reflection control. Kang et al. [1] studied the effect of foam anisotropy and mounting on the normal incidence reflection coefficient offered by finite-depth polyimide foam layers. A porous layer can absorb a significant amount of acoustic energy only if its thickness is comparable to the wavelength of incident sound. It inevitably becomes a less effective sound absorber as the frequency is decreased. The use of active methods to extend the frequency range of sound absorbers to lower frequencies has been investigated by Guicking et al. [2] and Wenzel [3]. Similarly, Bolton et al. [4] presented a theory which allowed the required force, displacement and control power to be calculated for "smart foams" allowing active absorption of sound. They showed that at any angle of incidence, the solid phase of the foam may be forced so as to create a perfect impedance match with the incident plane wave, thus causing the sound to be completely absorbed. "Smart" acoustic control systems may be manufactured by incorporating piezoelectric materials. A high AC voltage applied to a piezoelectric material causes it to vibrate in response to the forces produced by the piezoelectrically induced expansion or contraction. Conversely, when an external force applied to the piezoelectric material results in a compressive or tensile strain, a proportional voltage is generated. This phenomena allows the material to be utilized as an actuator and a sensor. An active acoustic coating has been developed by Howarth et al [5,6] which prevents an incident sound wave from reflecting off a submerged object. The elastomer coating consists of a piezocomposite actuator and piezoelectric

polymer sensors. Lafleur et al. [7] were succesful in using a multi-layer piezoelectric composite of piezorubber to control reflected and transmitted sound in a fluid-filled tube.

Very little, if any work has been carried out to develop active foams for *radiation* control. In this study, Polyvinylidene fluoride (PVDF), a piezoelectric polymer film, is encapsulated in partially-reticulated polyurethane foam creating an "adaptive foam "element. The active foam element is driven in such a way as to minimize the radiated sound from a vibrating piston as well as reflection from its surface depending upon the application. The objective of this study is to investigate the potential of adaptive foam for radiation and reflection control.

ADAPTIVE FOAM ACTUATOR

The active foam element used in this study is comprised of a circular piece of partially reticulated polyurethane foam internally lined with PVDF as in Figure 1. To manufacture the active element, a sine wave is cut in a 50 mm by 150 mm (2 in by 6 in) circular piece of foam. A sheet of 28 μm Ag metalized PVDF is fabricated to fit the entire cross-sectional area of the foam. Approximately 2 mm of the silver electrodes are removed from the periphery of the PVDF to prevent arcing,. To facilitate the application of a voltage to the actuator, wires are soldered to the top and bottom surface of the PVDF using copper foil tape backed with conductive adhesive. This wire attachment is reinforced by applying Ag-epoxy around the copper foil/PVDF interface. Using silicon glue or spray adhesive, the PVDF actuator is bonded in between the two foam halves forming an active PVDF foam element. To investigate the feasability of a combined actuator and sensor arrangement, a circular piece of 28 μm Al metallized PVDF film, approximately 50 mm (2 in) in diameter, is mounted on top of the active foam surface using spray adhesive. This PVDF sensor measures the rate of surface strain induced by structural vibrations and acoustic radiation. The Al metallization provides a higher sensitivity and is well suited for sensing applications. Conversely the Ag metallization can sustain higher voltages needed for actuator applications.

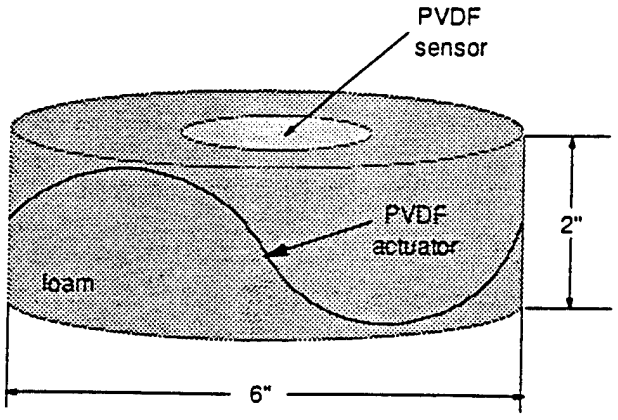

Figure 1. Adaptive foam element.

RADIATION CONTROL

Experimental Setup

The experimental arrangement is illustrated in Figure 2. The noise source is a metal piston enclosed in a casing which stands 0.76 m (2.5 ft) tall and has a 0.30 m (1.0 ft) circular cross section. On top of the casing is a 50 mm by 150 mm (2 in by 6 in) circular cavity which exposes the piston's head and determines the size of the active foam element to be used. During the experiment, the noise source is mounted inside a rigid baffle located in an anechoic chamber, while all auxiliary test equipment is placed outside this chamber. Pure tones from a Wavetek signal generator are used to drive a mechanical shaker located underneath the piston creating a radiation pattern that is comparable to a monopole radiating in half space at the test frequencies studied. A 1/2" B&K microphone is mounted on a stepper motor traverse at a 1.5 m (5 ft) distance from the noise source to measure the farfield acoustic directivity. The controller consists of a single channel filtered-x LMS control algorithm implemented on a Spectrum TMS320C30 DSP board resident in a personal computer. A B&K 2032 Spectrum Analyzer displays the sound pressure levels with and without control applied indicating the effectiveness of the passive and passive-active control treatment.

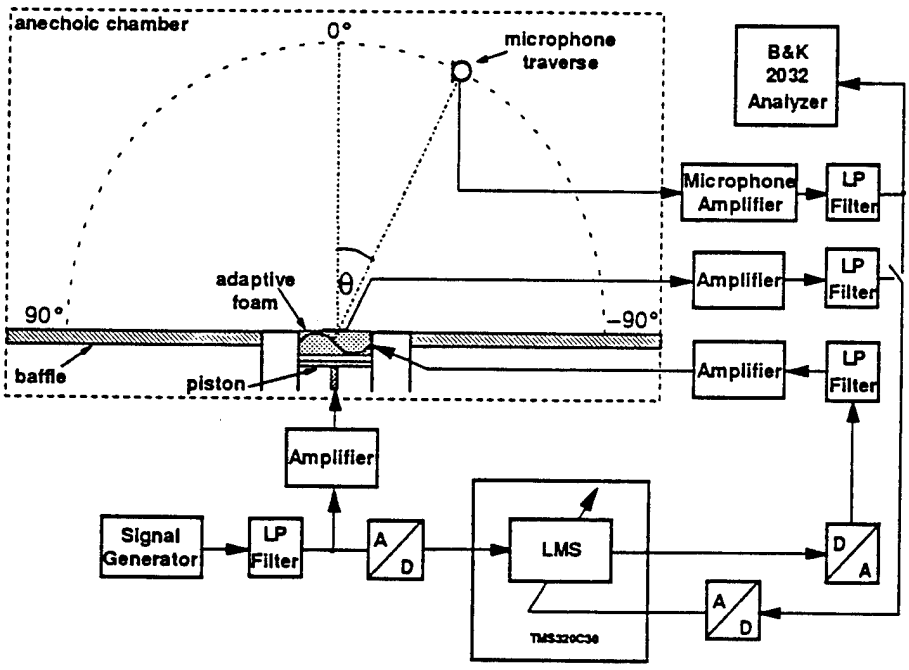

Figure 2. Radiation control experimental arrangement.

The experimental procedure consists of two parts. In the first part, the pressure response measured by the farfield traverse microphone, located at 0°, is the error to be minimized and is used in the system identification process. This

error signal is conditioned by an Ithaco filter and amplified prior to being incorporated in the filtered-x LMS algorithm along with a reference signal from the disturbance. The sampling rate is 1000 Hz. The resulting control signal is amplified and used to drive the PVDF actuator with AC voltage levels of up to 300 V producing a strain in the piezoelectric material and corresponding acoustic radiation. Once the farfield pressure is minimized at 0°, the coefficients of the adaptive filter are fixed and the directivity pattern is measured from -90° to 90° with and without control applied. The response of the surface mounted PVDF sensor is monitored while minimizing the pressure level at the farfield microphone location. In the second part of the experiment, the response from the PVDF sensor is now considered the error signal to be minimized. Again, the acoustic directivity pattern is measured -90° to 90° using the traverse microphone. Comparing the sound pressure level before and after control gives an indication of the acquired global sound attenuation.

Experimental Results

Several test frequencies between 70 Hz and 400 Hz have been studied. A typical result corresponding to a 340 Hz drive frequency is shown in Figure 3. The resulting sound pressure level dB(SPL) has been recorded at 21 discrete locations as the traverse microphone shifted from -90° to 90°.

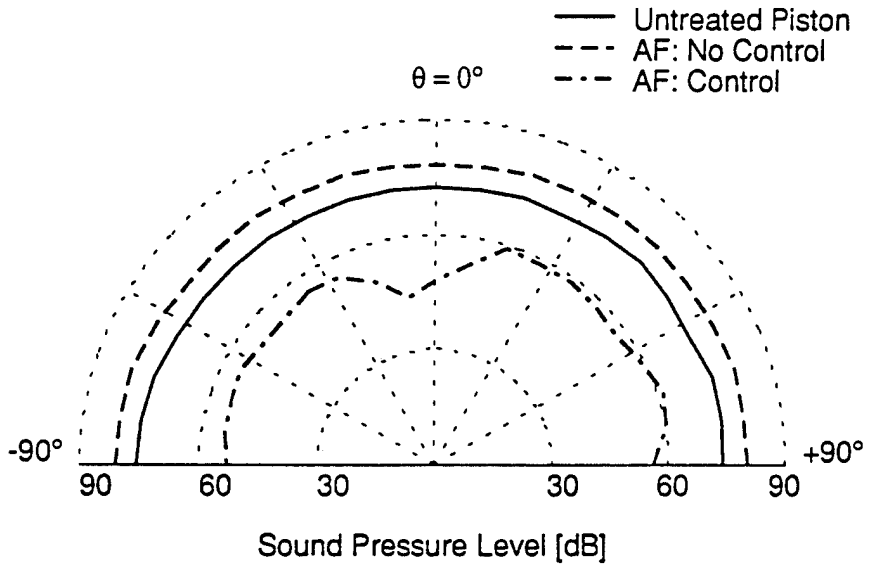

Figure 3. Radiation control using PVDF layered Adaptive Foam (AF) with microphone error sensor, f = 340 Hz.

The acoustic radiation efficiency of the piston noise source is significantly increased after placement of the unactivated adaptive foam. Reasons for the increase in sound pressure level are not fully understood at the moment but are

most likely due to the adaptive foam increasing the radiation coupling of the piston. The results do indicate that much care must be taken in designing active passive systems. However, minimizing the sound pressure level at 0° using the farfield microphone results in a global sound attenuation of approximately 20 dB, compared with the untreated noise source. The adaptive foam accomplishes the global noise cancellation by changing the radiation impedance seen by the piston. Experiments performed using the surface mounted PVDF film as an error sensor exhibit no farfield pressure reduction. In fact, farfield pressure minimization tends to increase the signal measured by the PVDF sensor. Conversely, the farfield sound pressure level detected with the traverse microphone is increased if the signal from the surface bonded PVDF sensor is minimized in the process of adaptation. However, using a microphone in the vicinity of the foam surface results in global farfield sound attenuation. Potential reasons for this phenomena are due to the complex dynamics between the PVDF actuator, the partially-reticulated polyurethane foam and the PVDF sensor. The sensor is mounted to the surface of the foam and is able to detect acoustic pressure fluctuations as well as structural vibrations generated by the piston and the PVDF actuator transmitted into the solid phase of the foam. Acoustical disturbances propagating within the liquid phase of the foam must follow tortuous passages. Tortuosity reduces the phase speed of airborne waves within the foam and increases the viscous and inertial coupling between the fluid and solid phases of the foam [1]. It is desired that the PVDF sensor bonded to the foam only detect pressure fluctuations in the nearfield of the complex secondary source, but the viscous and inertial coupling between the liquid and solid phase is prominent. Accordingly, the phase information of the desired acoustic error signal is distorted, which prevents farfield cancellation when using a surface mounted sensor.

During the process of system identification, which is essential for application of the filtered-x LMS algorithm, the output spectrum of the farfield error microphone is monitored yielding an indication of the actuator characteristics. The adaptive foam exhibits a nonlinear distortion in the frequency range investigated. A second harmonic of the excitation frequency is observed having a magnitude of approximately 20 dB below the fundamental drive frequency. The presence of this nonlinear distortion is influenced by the attachment of the PVDF actuator. This characteristic is not fully understood. However, these properties are currently being investigated.

REFLECTION CONTROL

Experimental Setup

The efficiency of "smart" adaptive foams has also been applied to minimize the reflected plane wave intensity of low frequency sound. A thin 28 μm Ag metallized PVDF layer is embedded in partially-reticulated foam, which has been used in the radiation control experiments. The adaptive foam has a circular cross section of 90 mm (3.5 in) and is 50 mm (2 in) thick and is positioned at one end of a B&K 4002 standing wave tube with a cutoff frequency of 1600 Hz as shown

in Figure 4. The two microphones for estimating the reflected intensity in accordance with the ASTM standard E 1050-90 [8] are positioned at a distance of 100 mm (4 in) and 150 mm (6 in) from the foam surface. A B&K 2032 Spectrum Analyzer provides the frequency domain estimates of the microphone spectra needed to calculate the reflected sound wave intensity, as well as the driving input signal to a loudspeaker which is located at the opposite end of the standing wave tube and acts as the primary noise source. An analog wave deconvolution circuit, which has been used by Elliott [9], provides a real time domain estimate of the reflected sound wave. This signal is used as an error input to modify the weights of an adaptive filter. The control is accomplished using the filtered-x LMS algorithm. The resulting control signal activates the embedded PVDF film after being lowpass filtered and amplified.

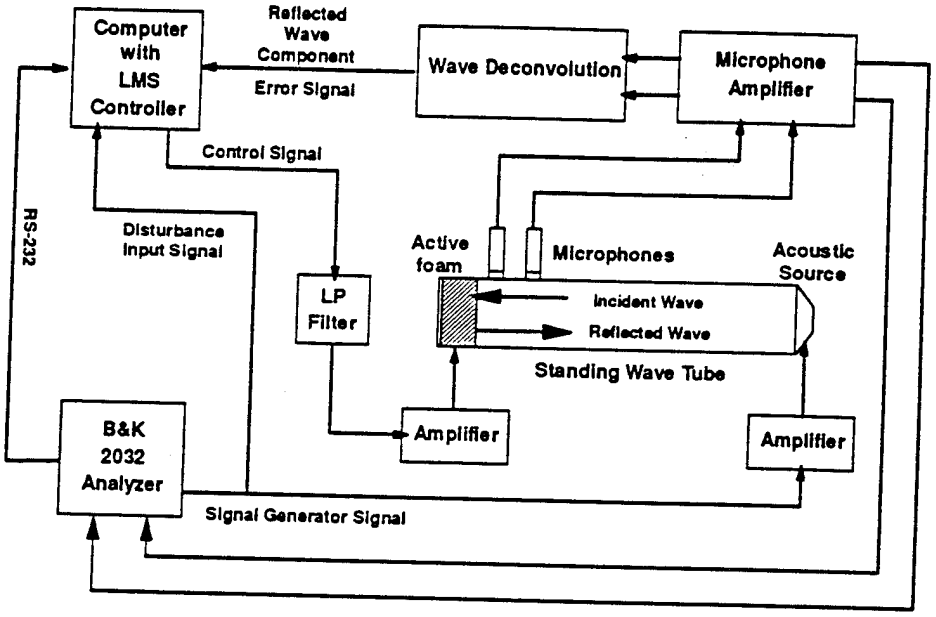

Figure 4. Reflection control experimental arrangement.

Experimental Results

The efficiency of a smart foam for minimizing the reflected sound intensity has been investigated using a sinusoidal tone for the frequency range of 100 Hz to 1000 Hz. The experimental results are summarized in Figure 5. Reflection control is based on the process of actively creating an impedance at the surface of the foam which matches the impedance seen by the incident plane wave propagating away from the source. This impedance match is generated by the embedded PVDF actuator. In Figure 5, the amount of passive attenuation is indicated by the difference between the "reflected wave" and "incident wave" amplitude and is negligible below 300 Hz. The attenuation achieved with the active foam (i.e.

both, active and passive) is given by the difference between "reflected wave under control" and the "incident wave." Up to 40 dB of attenuation is achieved at frequencies above 600 Hz with the adaptive foam. The attenuation efficiency is markedly improved in comparison to the passive attenuation of the pure foam. At low frequencies between 150 and 300 Hz, where the passive attenuation tends to be less efficient, the adaptive foam still provides about 10 dB attenuation.

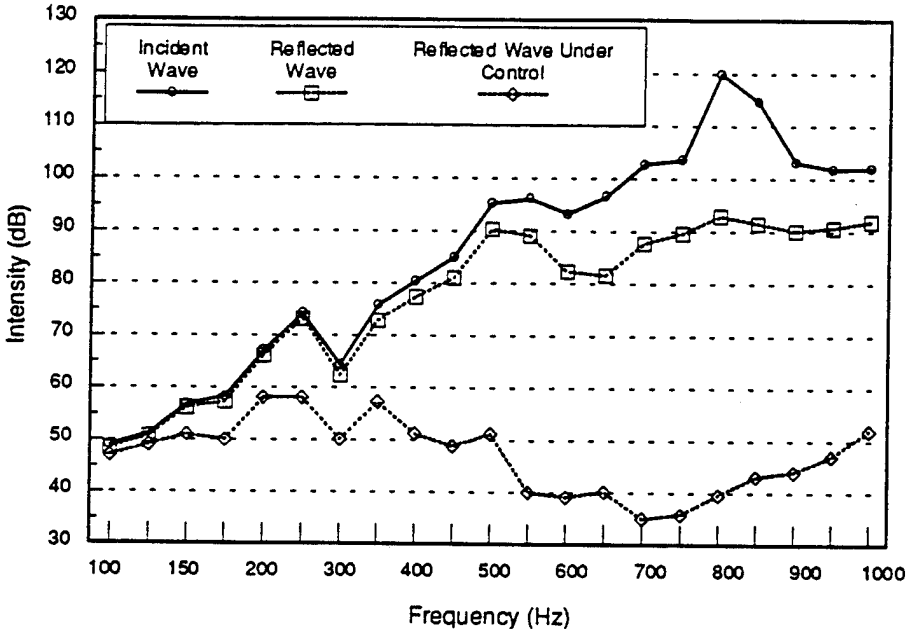

Figure 5. Minimization of the reflected sound intensity.

CONCLUSION

Our experiments prove the efficiency of composite active foam layers for controlling low frequency sound. These adaptive foams are effective in reducing reflected sound energy and also capable of reducing the radiated sound power of a vibrating structure. Standing wave tube experiments reveal that the reflected sound intensity of an incident plane wave can be minimized by as much as 55 dB for frequencies below 1 kHz. Experimental results prove that a 20 dB attenuation of the farfield sound pressure level can be achieved for a vibrating piston. These results are typical for drive frequencies below 400 Hz. The increase in radiation efficiency observed when investigating the passive properties of the adaptive foam element indicates the need for careful active-passive control design approaches. An attempt was made to monitor and cancel the nearfield sound pressure using a PVDF sensor mounted on the surface of the foam. This setup was unsuccessful and further research is needed.

ACKNOWLEDGEMENTS

The authors gratefully acknowledge the support of this work by the Office of Naval Research under grant N 00014-92-J-1170.

REFERENCES

[1] "The effect of mounting on the acoustical properties of finite-depth polyimide foam layers," Y.J. Kang, W. Tsoi, and J.S. Bolton, *Proceedings of NOISE-CON 93 (Williamsburg, VA)*, 285-290 (1993).

[2] "Coherent active methods for applications in room acoustics," D. Guicking, K. Karcher, and M. Rollwage, *J. Acoust. Soc. Am.*, **78** (4), 1426-4034 (1985).

[3] "Untersuchungen zur breitbandigen Messung und Regelung der akustischen Wandimpedanz an einer aktiven Schallwand mit adaptiven Filtern," M. Wenzel, PhD Thesis, Göttingen, 1992.

[4] "Smart foams for active absorption of sound," J.S. Bolton, and E.R Green, *Second Conference on Recent Advances in Active Control of Sound and Vibration (Blacksburg, VA)*, 139-149 (1993), Technomic Press, Lancaster, PA.

[5] "Digital time delay network for an active underwater acoustic coating," T.R. Howarth, X. Boa, R. Moser, and V.K. Varadan, *J. Acoust. Soc. Am.*, **93** (3), 1613-1619 (1993).

[6] "Piezocomposite coating for active underwater sound reduction," T.R. Howarth, V.K. Varadan, X. Boa, and V. Varadan, *J. Acoust. Soc. Am.*, **91** (2), 823-831 (1992).

[7] "Acoustically active surface using piezorubber," L.D. Lafleur, F.D. Shields, and J.E. Hendrix, *J. Acoust. Soc. Am.*, **90** (3), 1230-1237 (1991).

[8] "Standart Test Method for Impedance and Absorption of Acoustical Materials Using a Tube, Two Microphones, and a Digital Frequncy Analysis System," ASTM E 1050 -90, July 1990.

[9] "A simple two microphone method of measuring absorbtion coefficient," S.J. Elliott, *Acoustic Letters* , **5** (2), 39-44 (1981).

C-46 Experimental Modal Testing Using Piezoceramic Patches as Collocated Sensor-Actuators, F. P. Sun, C. Liang and C. A. Rogers, 1994 Spring Conference on Experimental Mechanics and Exhibits, Baltimore, MD, 6-8 June 1994.

EXPERIMENTAL MODAL TESTING USING PIEZOCERAMIC PATCHES AS COLLOCATED SENSOR-ACTUATORS

F. P. Sun, C. Liang and C. A. Rogers

Center for Intelligent Material Systems and Structures
Virginia Polytechnic Institute and State University
Blacksburg, Virginia 24061-0261
U.S.A.

ABSTRACT

A single piezoceramic (PZT) patch bonded to a structure may be used as a collocated actuator/sensor for structural modal analysis. The frequency response function (FRF) of the structure can be deduced from the electric admittance of PZT as a result of the electromechanical interaction. This paper presents a modal analysis technique based on the electric admittance measurement. A generic model governing the electromechanical interaction is used to extract FRF of structures from the measured electrical admittance. Two corresponding modal parameter extraction algorithms are presented. Both exclude the stiffening effect of PZT on the structure, yielding better estimations of natural frequencies and modal damping. A new approach is introduced of identifying structural modal shapes by measuring both the self-admittance of a single sensor and transfer-admittance between two sensors in parallel. The results show the advantages of this technique in modal test of light-weight and flexible structures whose modal parameters are extremely sensitive to the stiffening of the transducers and shaker.

1. INTRODUCTION

Experimental modal testing has now become a mature and standard technique in structure dynamic analysis. It usually consists of several independent stages: structure excitation, measurement of driving force and vibration response, formation of Frequency Response Function (FRF), and modal parameter extraction. The entire process needs a set of sophisticated equipment, such as a multi-channel signal analyzer, force and response transducers, shakers, and various types of signal conditioners. Typical transducers used in a modal test are piezoceramic force gauges, accelerometers and shakers. The attachment of conventional transducers onto a structure may result in considerable errors in the extracted modal parameters, especially with light-weight and flexible structures. The use of Laser Doppler Vibrometer and eddy current sensor provide a non-contact measurement technique, but they still need attachment of force gauge and shaker to the structure.

A piezoceramic patch, on the other hand, may serve as both sensor and actuator [1,2] at the same time as a result of piezoelectric effect and its converse. When bonded to a structure and driven by an alternating voltage, the PZT imposes a bending moment on the structure through its longitudinal expansion and contraction, causing the structure to vibrate. This vibration then in turn "modulates" the current flowing through the patch. Consequently, the electric admittance of the bonded patch, defined as the ratio of the current to the voltage, is physically in the same position as its mechanical counterparts, such as mobility, in representing the transfer characteristics of a structure between the excitation and the response. As an electric quantity, the admittance is much easier to measure than a mechanical transfer function. Because of the light weight and the low flexural stiffness of a PZT patch, the mass loading effect can usually be neglected and its stiffening effect can be easily compensated when necessary.

This paper presents a technique of structure modal testing using a surface-bonded piezoceramic patch as a collocated sensor-actuator. The electric admittance or impedance of the bonded piezoceramic patch versus frequency is measured with a sine-sweeping impedance analyzer. A generic model governing the electromechanical interaction of the actuator and the structure is derived and used to extract the frequency response function, or mobility of the structure at the position where the PZT is bonded.

Two algorithms of modal parameter extraction associated with the technique are presented. One uses electric

1994 Spring Conference on Experimental Mechanics and Exhibits

Baltimore, Maryland, 6-8 June, 1994

admittance match/half-power band width method, and the other employs revised Nyquist plane curve fitting. Both algorithms can extract the modal damping coefficients, natural frequencies and curvature mode shapes of the structure. The model has considered the stiffening effect of the actuator on the structure, yielding refined estimations of extracted structure natural frequencies. This is critically important when the test piece is flexible and small.

As identified in a previous paper, an inherent problem with this approach is that the modal shapes extracted from the admittance of collocated sensors will lose their spatial phase information because of the "point" nature of the collocated sensor-actuator. Introduced in this paper is a new method of identifying the phase of modal shapes by measuring "transfer-admittance" of two sensors in parallel with a single impedance analyzer. This results in a complete description of the modal shapes.

2. MODELING OF ELECTROMECHANICAL INTERACTION

A piezoceramic, most commonly known as PZT, short for Lead (Pb) Zirconate Titanate, exhibits a bi-directional "piezoelectric" effect. When motion in only one direction is considered and the stress T and the electric field E are chosen as the intensive variables, the electromechanical interaction between the stress, strain, the electric field and flux density is governed by the following constitutive equations:

$$S_2 = s_{22}^E T_2 + d_{32} E_3 \qquad (1)$$

$$D_3 = d_{32} T_2 + \varepsilon_{33}^T (1 - i\delta) E_3 \qquad (2)$$

where, as shown in Figure 1, S_2 is the strain and T_2 the stress in PZT along the y-axis, E_3 the electric field and D_3 electric flux density along the z-axis between two parallel surfaces. s_{22}^E the complex mechanical compliance at zero electric field, d_{32} the piezoelectric constant at zero stress, ε_{33}^T the dielectric constant at zero stress and δ the dielectric loss tangent of PZT. Assume that the PZT actuator is fixed at one end and the other end is connected to a structure represented by a mass-spring-damper, the velocity of the moving end under voltage V_3 may be expressed as

$$v = \frac{F_{2b}}{Z_a + Z_s} \qquad (3)$$

and the driving force on the mechanical system

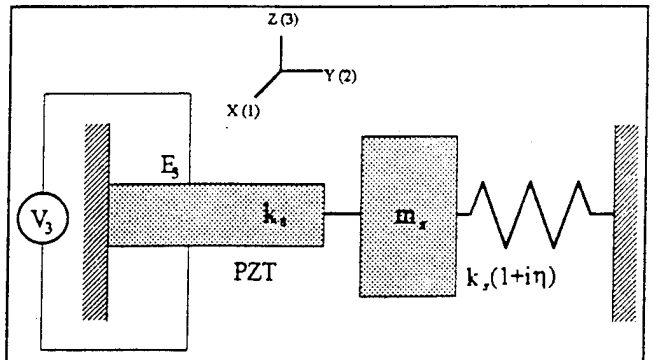

Figure 1 SDOF model of electromechanical interaction of PZT with structure

$$F_2 = Z_s v = \frac{Z_s}{Z_a + Z_s} F_{2b} \qquad (4)$$

where Z_S is the mechanical impedance of the structure and Z_a the short-circuit mechanical impedance of PZT actuator, respectively. F_{2b} is the force when PZT is blocked, which can be obtained from Eq. (1) by simply letting $S_2 = 0$ as

$$F_{2b} = -\frac{d_{32} E_3}{s_{22}^E} w_a h_a = -d_{32} E_3 Y_{22}^E w_a h_a \qquad (5)$$

where $Y_{22}^E = 1/s_{22}^E$ is the complex modulus of PZT, and w_a and h_a are the width and thickness of PZT, respectively. Differentiating the electric flux density with respect to time and integrating it over the electroded area yields the total electric current flowing through the PZT

$$I_3 = i\omega \iint_\sigma D_3 dx dy \qquad (6a)$$

Substituting Eqs.(2), (4) and (5) in it and using the relation $E_3 = V_3 / h_a$ and $T_2 = F_2 / (w_a h_a)$ results in

$$I_3 = i\omega \frac{w_a l_a}{h_a} [\varepsilon_{33}^T (1 - i\delta) - \frac{Z_s}{Z_s + Z_a} (d_{32})^2 Y_{22}^E] V_3 \qquad (6b)$$

or the coupled electric admittance of PZT

$$Y = \frac{I_3}{V_3} = i\omega a [\varepsilon_{33}^T (1 - i\delta) - \frac{Z_s}{Z_s + Z_a} (d_{32})^2 Y_{22}^E] \qquad (7a)$$

where l_a is the length of PZT, and $a = \frac{w_a l_a}{h_a}$. Note that a uniform distribution of electric flux density in PZT is assumed in the integration. It is obvious that the first term in Eq.(7a) is the capacitance admittance and the second

term is the result of the electromechanical interaction of PZT with the structure. The mechanical frequency response function of the structure, or the mobility, defined as the ratio of velocity response to excitation force may then be easily solved from Eq. (7a) as

$$H_S = \frac{1}{Z_s} = \frac{1}{Z_a}\left(\frac{d_{32}^2 Y_{22}^E}{\varepsilon_{33}^T (1-i\delta) - \frac{Y}{i\omega a}} - 1 \right) \qquad (7b)$$

The significance of Eq.(7b) lies in that the mechanical frequency response function of a structure can be determined from the electric admittance of the actuator/sensor bonded to the structure. This provides a convenient alternative to the shaker-impedance head approach for determining a frequency response function of a mechanical structure, which constitutes the basis of experimental modal analysis. Although most modal analysis approaches are applicable to Eq.(7b) in general, the extraction algorithms presented in this paper are different due to the involvement of the actuator impedance Z_a in the structure impedance expression and the "collocated" nature of the sensor.

3. MODAL PARAMETER EXTRACTION WITH SDOF MODEL

To demonstrate the application of this electromechanical approach to modal analysis, an SDOF model for extraction is developed. The mechanical impedance of the PZT element in Fig. 1 may be expressed as

$$Z_a = -\frac{i}{\omega} k_a \qquad (8)$$

where k_a is the short-circuit stiffness of PZT along the y-axis. The effect of PZT's mass along the y direction is neglected, assuming that the stress wavelength is much larger than PZT's characteristic dimension under normal operating frequency [3]. The mechanical impedance of an SDOF system with a structure damping is given by

$$Z_s = i(m_s\omega - \frac{k_s(1+i\eta)}{\omega}) \qquad (9)$$

where m_S is the modal mass, k_S the modal stiffness and η the modal damping. Substituting Eqs.(8) and (9) in Eq. (7) yields the electric admittance in term of the modal parameters

$$Y = \omega a[\varepsilon\delta + \frac{ck_a k_s \eta}{(k_s\eta)^2 + (k_s + k_a - m_s\omega^2)^2} + i(\varepsilon - c + \frac{ck_a(k_s + k_a - m_s\omega^2)}{(k_s\eta)^2 + (k_s + k_a - m_s\omega^2)^2})] \qquad (10)$$

where a = $w_a l_a / h_a$ and c = $(d_{32})^2 Y_{22}^T$. The real and imaginary parts of the mechanical mobility can then be deduced as:

$$H_r = (\frac{\mathrm{Re}(Y)}{\omega a} - \varepsilon\delta)/c = \frac{k_a k_s \eta}{(k_s\eta)^2 + (k_s + k_a - m_s\omega^2)^2} \qquad (11)$$

$$H_i = (\frac{\mathrm{Im}(Y)}{\omega a} - \varepsilon - c)/c = \frac{k_a(k_s + k_a - m_s\omega^2)}{(k_s\eta)^2 + (k_s + k_a - m_s\omega^2)^2} \qquad (12)$$

As a PZT actuator usually has a size much smaller than that of the host structure, its mechanical damping can be ignored. Equations.(11) and (12) traces out a non-closing circle in Nyquist plane as

$$(H_r - \frac{k_a}{2k_s\eta})^2 + H_i^2 = (\frac{k_a}{2k_s\eta})^2 \qquad (13)$$

This is the locus of the mechanical compliance of an SDOF system with proportional damping connected in parallel with a massless spring K_a.

3.1 Revised Nyquist plane curve fitting

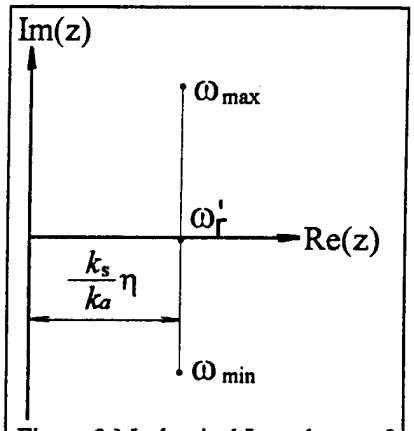

Figure 2 Mechanical Impedance of SDOF in inverse Nyquist plane

As Eqs. (11) and (12) are highly nonlinear functions of the modal parameters, it is much easier to conduct the curve fitting to the impedance plot in the Nyquist plane than to extract parameter from the mobility. The mechanical impedance of SDOF with structural damping takes the simple form [4] as

$$Z = \frac{1}{Y_{mr} + iY_{mi}} = \frac{k_s}{k_a}\eta - i\frac{k_s + k_a - m_s\omega^2}{k_a} \quad (14)$$

It traces out a straight line on the inverse Nyquist plane as shown in Fig. 2. Note that due to the stiffening effect of PZT on the structure, the intersection of the line with the real axis no longer defines the natural frequency of SDOF system alone but the natural frequency of the PZT-SODF joint structure. Curve fitting the measurement data to the imaginary part of Eq. (14) generates to two quantities, k_S/k_a and m_S/k_a. Note that they are the structure modal stiffness and modal mass normalized to the actuator modal stiffness, and none of them has a physical meaning. However, the natural frequency of the structure can be determined as

$$\omega_r = \sqrt{k_s / m_s} = \sqrt{(k_s / k_a)/(m_s / k_a)} \quad (15)$$

Another independent curve fitting to the real part of the measurement data yields a refined estimation of Re(Z), and from it the structural modal damping can be calculated

$$\eta = \frac{\mathrm{Re}(Z)}{k_s / k_a} \quad (16)$$

Equations (14), (15) and (16) constitute the revised Nyquist Plane Curve Fitting approach which will be referred to as NPCF later.

3.2. Admittance matching/half power bandwidth

Equation(12) and (7a) together provide a new approach to the determination of η and ω_r. Take the partial derivative of Eq.(12) with respect to ω and let it be zero

$$\frac{\partial(H_i)}{\partial\omega} = \frac{-2k_a m_s[(k_s\eta)^2 - (k_s + k_a - m_s\omega^2)]}{[(k_s\eta)^2 + (k_s + k_a - m_s\omega^2)^2]^2} = 0 \quad (17)$$

This leads to

$$k_s\eta = (k_s + k_a - m_s\omega_1^2) \quad (18)$$

$$k_s\eta = -(k_s + k_a - m_s\omega_2^2) \quad (19)$$

where ω_1 and ω_2 correspond to the peak and valley of Y_{mi} ,respectively. Addition of Eqs.(18) and (19) results in the structural modal damping

$$\eta = \frac{1}{2\omega_r^2}(\omega_2^2 - \omega_1^2) \quad (20)$$

where

$$\omega_r^2 = k_s / m_s$$
$$\omega_1^2 = (k_s(1-\eta) + k_a)m_s$$
$$\omega_2^2 = (k_s(1+\eta) + k_a)m_s \quad (21)$$

The natural frequency of the structure ω_r can be determined by the special point of the coupled electric admittance Y At resonance of the structure, the mechanical impedance Z_S decreases nearly to zero and Eq.(7) is deduced to the electric admittance of the "free" PZT actuator

$$Y_{ef} = \omega\alpha\varepsilon_{33}^T\ (\delta + i) \quad (22)$$

and similarly, the electric admittance of a blocked PZT actuator can be obtained by letting Z_S be ∞

$$Y_{eb} = \omega\alpha\ (\varepsilon_{33}^T\delta + i(\varepsilon_{33}^T - c)) \quad (23)$$

The imaginary parts of both admittance intersect with the imaginary part of the coupled admittance *Im(Y)*, as is

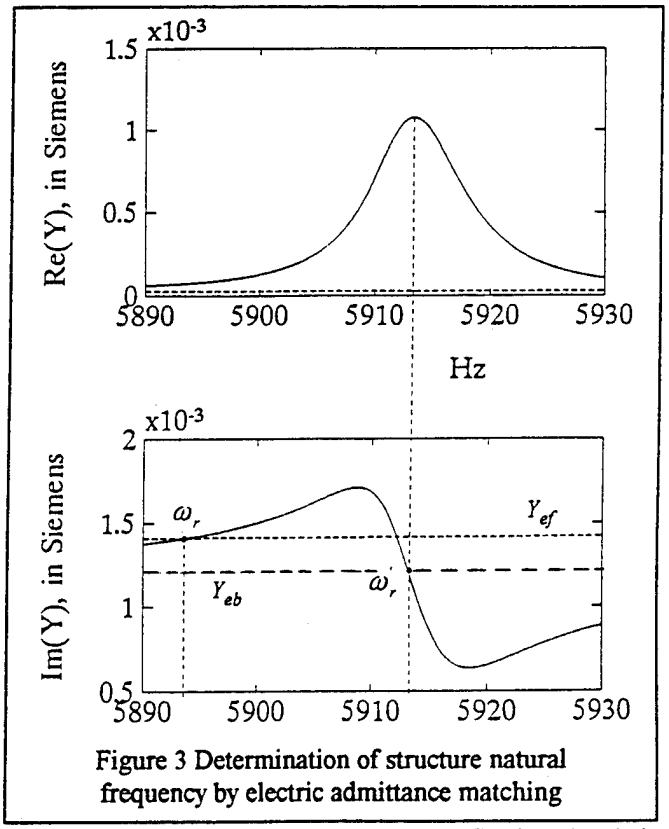

Figure 3 Determination of structure natural frequency by electric admittance matching

illustrated in Fig. 3. It is apparent by definition that it is

the intersection of *Im (Y_ef)* with *Im (Y)* that determines the natural frequency of the structure (impedance matching). By checking Eq.(10), it is not difficult to see that the intersection of *Im (Y_eb)* with *Im(Y)* happens to correspond to the natural frequency of the joint system of PZT and SDOF

$$\omega_r' = \sqrt{\frac{k_s + k_a}{m_s}} \tag{24}$$

at which *Re(Y)* peaks and *Im(Y)*'s interaction term vanishes. The difference between the two frequencies is, once again, caused by the stiffening of the PZT sensor. Note that in Eq.(20), ω_r is the characteristic of the structure alone and ω_1, ω_2 are those of the joint system. This distinguishes it from the conventional half power band method and it will be referred to as Admittance Matching / Half Power Band (AM/HPB) approach later.

3.3 Modal shapes extraction

From Eqs.(11) and (12), the modal response of the structure, or the modal shape when applied to a continuum system, can be determined. At the system resonance ω_r', $H_i = 0$ and

$$H_r = H_r^* = \frac{k_a}{k_s \eta} = \frac{k_a}{\eta} y \tag{25a}$$

where y is the modal response to a unit force excitation ($y = 1/k_s$). For a continuum structure, this modal response is a function of measurement coordinate and the mode. The modal stiffness of the sensor k_a and structure modal damping η for a particular mode is independent of the coordinate. When m measurements of H_r^* are made along the structure for each of its n modes, the mode shapes (eigenvectors) can be obtained and its element takes the form of

$$H_r^*(i,j) = \frac{k_a(i)}{\eta(i)} y(i,j) \tag{25b}$$

where i = 1,2,...m and j = 1,2...n. This can also be directly deduced from the fact that $k_a / k_s \eta$ is the diameter of the modal circle in Nyquist plane. It should be understood that the modal shapes thus obtained are also contaminated by the stiffening of the PZT as their are extracted at ω_r', rather than at ω_r. However, this approximation has a sufficient accuracy when the modal coupling is weak and the stiffening is not severe.

Equation (25a) reveals an inherent problem of this approach in determining the modal shape of a structure, as identified in a previous paper.[5] The collocated sensing-actuation results in a "point" frequency response function of the structure. Consequently, the modal response given by Eq.(25b) is always positive regardless of the measurement coordinates. The physical interpretation is straightforward that when in structural resonance, the response at excitation point has a constant phase with the driving force regardless of its spatial location (for mobility, this phase is always 0). To obtain complete modal shapes, auxiliary measurements are made of the transfer admittance of two PZT sensor in parallel. Figure 4 is the schematic diagram. When two bonded PZT patches are electrically connected in parallel, the total electric admittance can be expressed as

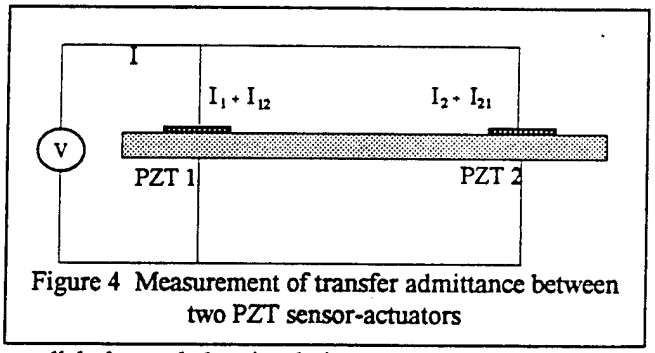

Figure 4 Measurement of transfer admittance between two PZT sensor-actuators

$$\begin{aligned} Y_p &= \frac{I_1}{V} + \frac{I_2}{V} + \frac{I_{12}}{V} + \frac{I_{21}}{V} \\ &= Y_{11} + Y_{22} + Y_{12} + Y_{21} \end{aligned} \tag{26}$$

where Y_{11} and Y_{22} are the admittance of the PZT sensors 1 and 2 measured individually, and Y_{12} is the additional admittance of sensor 1 induced by the excitation of actuator 2. As the mechanical transfer frequency response function of a structure between two locations is reversible, the transfer electric admittance Y_{12} and Y_{21} can also be considered as identical if the stiffening effect of the PZT sensor is ignored,[6] and therefore, it can be simply expressed as

$$Y_{12} = \frac{Y - (Y_{11} + Y_{22})}{2} \tag{27}$$

which differs from the mechanical transfer mobility H_{12} by only a real constant.[6] Equation (27) can be used to determine the phase of the modal response at each spatial location with respect to the excitation. Equations (25b) and Eq. (27) together yield a complete description of modal shape. For instance, a positive real part of Y_{12} indicates that the response at location 2 is in phase with the excitation at location 1, and a negative value corresponds to the out-of-phase.

4. MODAL TEST OF A FREE-FREE BEAM

System identification of a small and flexible structure is usually a challenge as the extracted structural modal parameters are extremely sensitive to the stiffening and mass loading of the attachment of sensor and actuator. By using surface-bonded PZT sensor-actuator, these effects can be minimized. As an example, a test of proof-of-concept-is conducted on a aluminum beam of 153.0 × 25.7 × 0.8 mm. A PZT patch of 32×19× 0.19 mm is bonded on the beam 52 mm from the end of the beam. The size of the PZT is considerable compared with that of the beam so that its stiffening effect to the beam can be fully demonstrated and the performance of the proposed algorithms be properly investigated. The beam is suspended in air by very thin wires to simulate a free-free boundary condition and to minimize the possibility of introducing external damping. The electric impedance of the PZT patch is measured over a broad frequency band by an HP 4194A Impedance Analyzer. Figure 5 is the schematic diagram of the experimental setup.

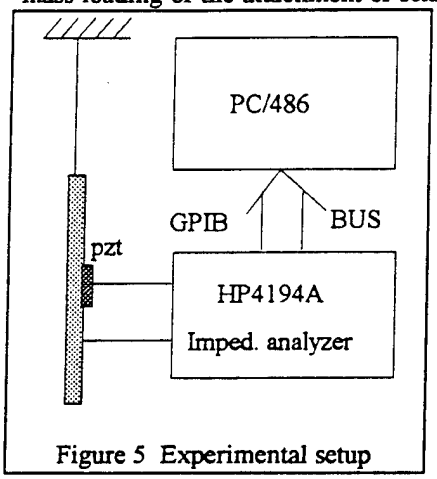

Figure 5 Experimental setup

Figure 6 is the electric admittance of the PZT patch from 100 Hz to 7000 Hz, in which the first 9 flexural vibration modes of the beam are clearly identifiable. Note that each mode is well separated from the others. This qualifies the application of the SDOF model to the data. For the actual parameter extraction, each mode is zoomed in to obtain a much higher frequency resolution and amplitude accuracy. Table 1 shows the natural frequencies and modal damping of the beam extracted respectively by the two algorithms previously discussed.

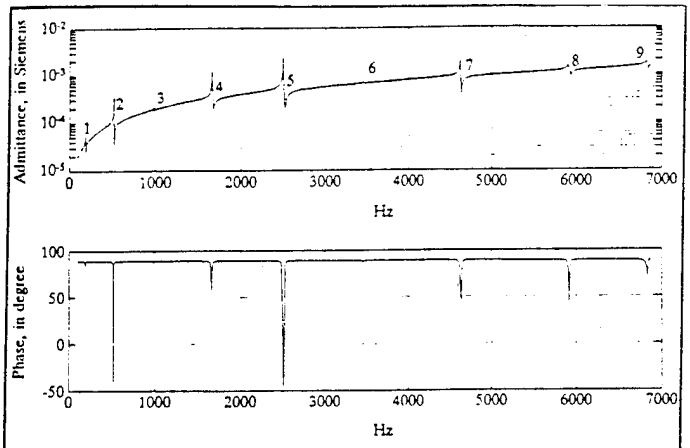

Figure 6 electric admittance of PZT bonded to the beam

To obtain the uncontaminated natural frequencies of the beam, the original PZT patch is replaced by a tiny one (4 × 6 × 0.19 mm) and its admittance is measured. It is assumed that the stiffening of this tiny PZT is negligible as its length is less than 1/6 of the original one. Therefore, the resonant peaks in its admittance may well represent the "true" natural frequencies of the beam.

Table 1

Mode	1	2	3 *	4
f_{r1}(Hz)	185.9	498.3	982.0	1628.4
η_1 (%)	0.37	0.37	0.15	0.20
f_{r2}(Hz)	187.6	497.2	982.2	1628.0
η_2 (%)	0.21	0.31	0.095	0.15

Mode	5	6 *	7	8
f_{r1}(Hz)	2437.5	3457.6	4588.5	5893.8
η_1 (%)	0.22	0.13	0.16	0.17
f_{r2}(Hz)	2439.9	3456.0	4588.2	5891.7
η_2 (%)	0.18	0.064	0.15	0.17

Subscript 1---AM/HPB and Subscript 2---- NPCF

Table 2 lists the natural frequencies of the beam thus obtained verses the resonant frequencies of the beam-PZT joint structure as well as their relative difference.

Table 2

Mode	1	2	3 *	4
f_{rj} (Hz)	189.3	516.7	983.0	1656.8
f_{rs}(Hz)	183.3	494.7	982.5	1621.8
E_{js} (%)	+3.2	+4.4	+0.05	+2.2

Mode	5	6 *	7	8
f_{rj} (Hz)	2493.1	3459.9	4622.5	5913.3
f_{rs}(Hz)	2437.5	3455.2	4580.6	5863.4
E_{js} (%)	+2.3	+0.14	+0.9	+0.85

f_{rj}---natural frequencies of PZT-beam joint structure
f_{rs}---natural frequencies of the beam

$E_{js} = (f_{rj} - f_{rs}) / f_{rs}$, E_{js} max. = 4.4 % and E_{js} average = 1.62 %.

To verify the algorithms' capability of correcting the natural frequencies for stiffening effect, the relative errors of the corrected natural frequencies with respect to the beam natural frequencies are calculated and listed in Table 3.

Table 3

Mode	1	2	3 *	4
E_1(%)	+1.40	+0.67	-0.05	+0.33
E_2(%)	+2.30	+0.51	+0.03	+0.38

Mode	5	6 *	7	8
E_1(%)	0	+0.07	+0.17	+0.51
E_2(%)	+0.10	+0.02	+0.17	+0.48

$E_1 = (f_{r1} - f_{rs}) / f_{rs}$, E_1max = +1.40 % and E_1average = 0.41 %

$E_2 = (f_{r2} - f_{rs}) / f_{rs}$, E_2max = +2.30 % and E_2average = 0.49 %

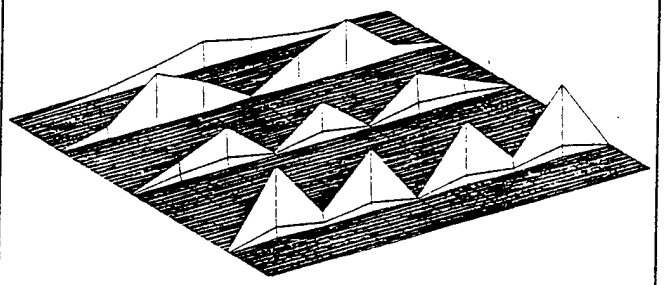

Figure 7 Mountain plot of first 4 curvature mode shapes

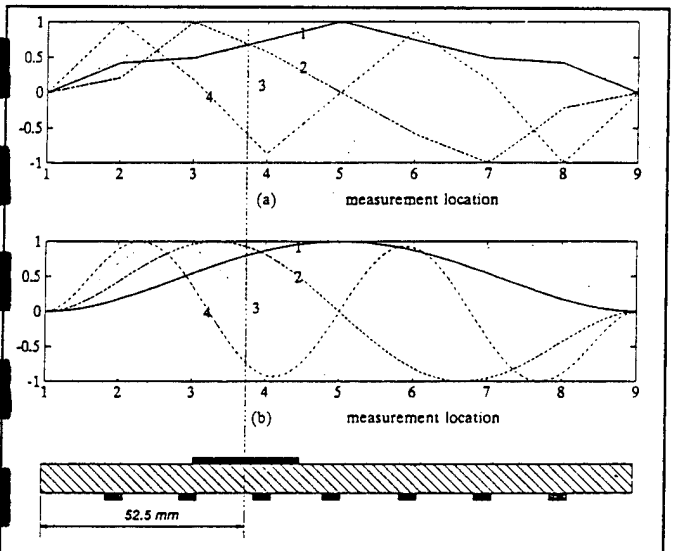

Figure 8 Curvature mode shapes of the beam
a. measured b. calculated

In order to obtain the curvature mode shape, 7 tiny (4 × 6× 0.19 mm) PZT were bonded to the beam at 7 locations uniformly spaced along the length of the beam (the two ends are ignored as their curvature are known to be zero, see Fig. 8). The admittance of each individual sensor as well as the transfer admittance between sensor 2 and 4, 3 and 4, and 3 and 5 are measured. The results are given in Appendix 1 and 2. Figure 7 is the first 4 curvature modal shapes of the beam extracted from the "point mobility" data in Appendix 1. Figure 8 is these modal shapes with their phase corrected by the transfer admittance given in Appendix 2. Due to the limited spatial resolution, only the first 4 mode shapes are meaningful. Table 4 is the material constants of PZT sensor used.

Table 4

d_{32}	y_{22}	ε_{33}^T	δ *
m/v	N/m^2	F/m	
-166e-12	6.30e10	1.50e-8	0.02

5. RESULT ANALYSIS

Although the electric admittance of the PZT gives approximate estimations of the natural frequencies of the beam, they are consistently higher than the "true values". As illustrated in Table 2, this bias can be up to 4.4 % with an average of 1.62 % for the first 8 flexural modes. Obviously, the stiffening, rather than the mass loading, of PZT to the beam dominates within this frequency range. This stiffening generally introduces more impact on low modes than high modes in term of the relative shift in natural frequencies. This demonstrates the need of correction for the stiffening effect when using surface-bonded PZT for a precision modal test of structure.

Table 3 lists the relative errors of the corrected natural frequencies with respect to the true natural frequencies of the beam. Note that the maximum errors reduce to 1.4 % and 2.3 % at the first mode, and average errors reduce to 0.41 % and 0.49 %, respectively. Although the results from two algorithms vary slightly, both of them produce better estimations of the true values of the natural frequencies in the sense that average error decreases by 75%.

The demand for this frequency correction varies with each mode at a particular PZT location. As one can see in Fig. 5, the strength of each mode varies significantly. Figure 8 lists four typical cases of different stiffening levels. For mode 1 and mode 2 (Fig. 9a and 9b), $Im(Y_{ej})$ intersects with $Im(Y)$ before the resonance of the joint structure,

which implies the in-plane vibration at this particular beam location is stronger than the free stroke of the PZT actuator. In other words, the PZT actuator is constraining the beam. There is substantial stiffening. For mode 3 (Fig. 9c), the two motions are completely compatible, neither of them imposes constraint on the other. This is indicated by the tangency of the two curves. As for Fig. 9d, mode 6 is marginally activated. The motion of PZT for this particular mode is nearly being blocked by the beam, or in other words, the PZT is "stiffened" by the beam rather than vice-

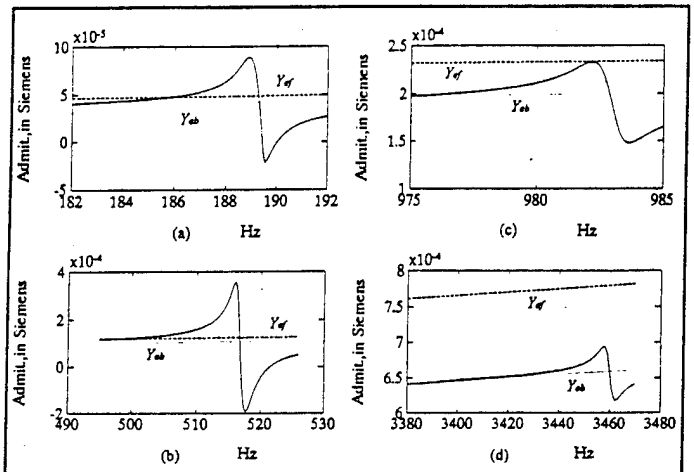

Figure 9 Four typical cases of the stiffening effect

versa. This variation of the stiffening with mode can also be seen from Table 2 where the relative frequency deviation for mode 3 and mode 6 are much smaller than that of the other modes. Obviously, there is little need for frequency correction for these two modes. Therefore, the application of frequency correction algorithms should be selective.

The phase correction for the mode shapes in Fig. 7 is fairly straightforward once the transfer admittance of proper pairs of sensors are available. As the first mode exhibits positive phase in Y_{24}, Y_{35} and Y_{36}, the modal response at 2, 3, 4 and 5 are all positive without doubt. For mode 2, Y_{36} shows a negative phase, therefore, the response at location 6 must be out of phase with location 2. The negative phase of mode 3 at location 5 is indicated by Y_{35}, the phase of mode 4 at location 4 and 6 can be determined by Y_{24} and Y_{36}, their are negative and positive respectively. Figure 8a is the normalized curvature shapes of the first 4 modes after phase correction. They are in good agreement with the analytical results in Fig. 8b obtained using transfer matrix method. It should be noted that both mode shape magnitude and phase can be extracted from the transfer admittance in theory. However, for some reasons which are still not clear, the extracted magnitudes are not as accurate as those from the point mobility. Practically, separate determination of amplitude and phase by point mobility and transfer admittance is necessary for rebuilding mode shapes.

Several issues must be addressed in order to have a comprehensive view of this approach. First of all, to obtain better estimation of mode shapes, a proper placement of PZT on a structure is critical. However, this requires some knowledge of the curvature mode shapes of the structure prior to the test. This is, unfortunately, not straight forward even with a simple structure. Second, because of the involvement of the modal stiffness of the actuator k_a in deduced mechanical mobility, the individual extraction of the modal stiffness k_s and mass m_s becomes very difficult. Finally, due to the limits of the energizing voltage of the impedance analyzer (typically 1 volt rms for HP 4194A) as well as the high electric impedance of PZT sensor, this approach may be less effective for a highly-damped structure than a lightly damped one, as for a high damping case, a much larger power is required to obtain H_r with an acceptable signal to noise ratio at each mode.

CONCLUSION

A complete modal analysis of structure can be conducted more conveniently, accurately and economically with surface-bonded piezoceramic patch as a collocated sensor-actuator. The measurement of electric admittance of the PZT sensor-actuator is proven to be an efficient and simpler method to acquire mechanical frequency response function of a structure. Applying the proposed extraction algorithms to the measurement data removes the stiffening of PZT actuator to structure, yielding refined estimations of modal damping and structure natural frequencies. With the assistance of the transfer admittance, both the magnitude and phase of curvature mode shapes of structure can be obtained. The beam example reveals the needs for natural frequency correction under some circumstances and demonstrates the effectiveness of the approaches in removal of the impact of PZT on the natural frequencies. These advantages make it an alternative approach to the noncontact modal test of small structure sensitive to the stiffening and mass loading of the transducers.

ACKNOWLEDGMENT

The authors would like to express their gratitude to the Office of Navy Research, Grant ONR N00014-92-J-1170.

REFERENCES

[1] Dosch, J.J., Inman, D.J., and Garcia, E., "A Self-Sensing Actuator for Collocated Control," *ADPA Intl. Symposium. on Active Materials and Adaptive Structures*, Alexandria, VA, Nov. 1991.

[2] Hagood, N.W. and Anderson, E.H., "Simultaneous Sensing and Actuation Using Piezoelectric Materials," *SPIE Conference on Active and Adaptive Optical Components*, July 1991, SPIE 1543-40.

[3] Liang, C, Sun, F.P. and Rogers, C.A., "Dynamic Output Characteristics of Piezoelectric Actuators", *Proceedings of SPIE Conference on Smart Structures and Materials*, February 1-4, 1993, Albuquerque, NM.

[4] Ewins, D.J, "*Modal Test: Theory and Practice*," Research Studies Press LTD., Letchworth, 1984, Hertfortshire, England.

[5] Sun, F. P., Liang, C. and Rogers, C. A., "Modal Analysis Using Collocated PZT Actuator/ Sensor—An Electromechanical Approach," *Proceedings of 1994 North American Conference on Smart Structures and Materials*, 13-18 February 1994, Orlando, Florida, in press

[6] Sun, F. P., Liang, C. and Rogers, C. A., "Structural Frequency Response Function Extraction from Measured Electric Admittance of PZT Sensor-Actuator", submitted to *The International Journal of Analytical and Experimental Modal Analysis.*

APPENDIX 1 point mechanical mobility (real part)

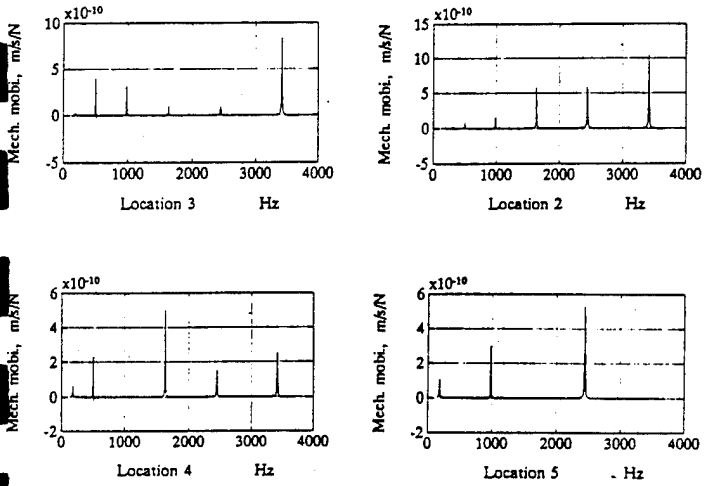

APPENDIX 2 transfer electric admittance

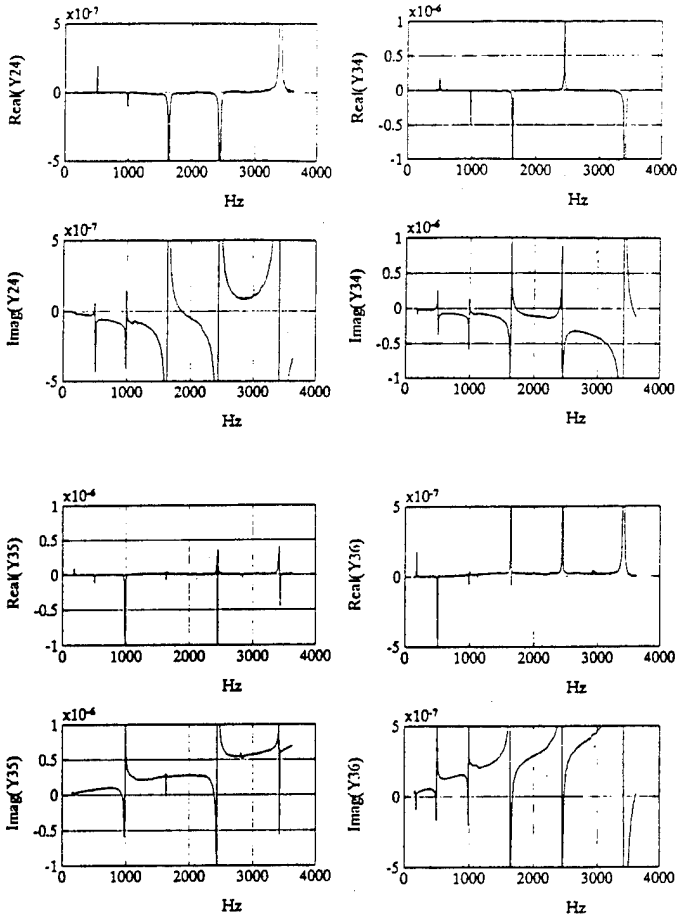

C-47 Design of Active Control Systems Using Eigenanalysis, C. R. Fuller and R. A. Burdisso, 3rd International Congress on Air- and Structure-Borne Sound and Vib., Montreal, Canada, 13-15 June 1994.

DESIGN OF ACTIVE CONTROL SYSTEMS USING EIGENANALYSIS

Chris R. Fuller
Ricardo A. Burdisso
Vibration and Acoustics Laboratories
Mechanical Engineering Department
Virginia Polytechnic Institute and State University
Blacksburg, VA 24061-0238
U.S.A.

ABSTRACT

A design procedure for the location and shape of the control transducers for feedforward controlled active systems is outlined. The procedure is based upon the relationship of the controlled eigenvalues and eigenfunctions of the controlled system to the control load and optimal compensator characteristics. The use of the design procedure is illustrated through modification of dynamics of a beam and radiation control from a plate. The extension of the method to complex structures using numerical techniques such as FEM/BEM and the impact of random broadband disturbances is briefly discussed. The method provides a basis by which feedforward controlled systems can be designed for specified performance requirements in contrast to the largely "ad hoc" methods presently used.

INTRODUCTION

Feedforward active control has shown much potential to alleviate problems in sound and vibration at audio frequencies [1,2]. The design of feedforward controllers is traditionally defined by an "ad hoc" selection of the number and location of actuators and sensors based upon a physical understanding of the behavior of uncontrolled and controlled systems. This empirical design contrasts with the large number of analytical tools available to designers of feedback controllers. Techniques such as pole allocation, various state space design methods, optimal control and so forth, are extensively used in feedback control applications [3]. The lack of mathematically based design formulations in feedforward control stems from the small amount of research carried out on understanding the behavior of feedforward controlled systems. The prevailing view in the feedforward control community is that the control "cancels" the disturbance an observation which is certainly true in a mathematical sense for steady state disturbances. However, it has been demonstrated in a number of different systems that, physically, the disturbance source "sees" a modified input or radiation impedance (see for example the work by Snyder and Hansen [4]).

Recent analytical work by the authors has demonstrated that this change in input impedance is a result of the feedforward controlled structure or system having new eigenvalues and eigenvectors [5,6]. It should be stressed here that these new eigen characteristics only appear for inputs which are coherent with the feedforward disturbance. In contrast to feedback control, the system will respond with

the uncontrolled eigenvalues to any other uncorrelated disturbance. The analysis outlined in reference 5 suggests a design approach for feedforward control systems. That is, given a desired set of modal properties, a feedforward controller can then be designed to force or adapt the controlled system to have those characteristics.

In this paper we summarize work in which a design formulation is developed for a single-input, single-output (SISO) feedforward controller to actively modify the dynamics of a distributed elastic system. Although the formulation is written in terms for a structural system, it is equally applicable to acoustic systems. The design formulation is applied to a problem in dynamics and then the extension to the control of sound radiation is outlined. The paper finishes with a brief discussion of the extension of the method to discretized complex systems, i.e. FEM/BEM analysis, and broadband disturbances.

The work described in this paper is largely a summary and combination of previous work by the authors published in a number of papers [5,7,8,9].

FEEDFORWARD CONTROLLED EIGENPROPERTIES

The structural system is assumed to be an undamped, linear, time invariant, distributed parameter system. Thus, the equations of motion can be written in the form of a partial differential equation as

$$L[W(D,t)] + m(D)\frac{\delta^2 W(D,t)}{\delta t^2} = f(D)\,F(t) + u(D)\,U(t) \tag{1}$$

where W(D,t) is the displacement in the domain D, L[.] is a self-adjoint linear differential operator, and m(D) is the mass distribution. The disturbance or "primary" input is defined by the time dependent amplitude F(t) and its spatial distribution f(D). The system is controlled by a coherent "secondary" control input defined by the amplitude U(t) and its spatial distribution u(D) as shown in Figure 1. Feedforward control approaches are used in applications where the disturbance excitation is stationary, i.e. single and multiple frequencies as well as random inputs. Then, the disturbance input F(t) is assumed stationary and thus W(D,t) and U(t) are also stationary variables. By taking the Fourier Transform, the analysis can be carried out on the frequency domain. That is,

$$L[W(D,\omega)] - \omega^2 m(D)\,W(D,\omega) = f(D)\,F(\omega) + u(D)\,U(\omega) \tag{2}$$

Solving for the eigenvalues and eigenfunctions of the homogeneous part of Eq. (2), the response of the system can be written in terms of the mode shape functions by using the expansion theorem as

$$W(D,\omega) = \sum_{n=1}^{N} q_n(\omega)\,\phi_n(D) \tag{3}$$

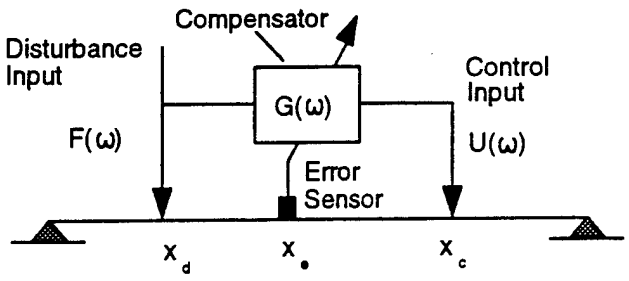

Figure 1--Schematic of a SISO feedforward control system

where $q_n(\omega)$ is the n^{th} generalized coordinate, $\phi_n(D)$ is the n^{th} eigenfunction, and N is the number of modes included in the analysis. The eigenfunctions satisfy the orthogonality conditions

$$\int_D \phi_n(D)\, m(D)\, \phi_m(D) dD = \delta_{nm} \quad ; \quad \int_D \phi_n(D)\, L[\phi_m(D)] dD = \delta_{nm}\, \omega_n^2 \qquad (4a,4b)$$

where δ_{nm} is the Kronecker delta function, and ω_n is the n^{th} natural frequency associated to the eigenfunction $\phi_n(D)$.

The generalized coordinate $q_n(\omega)$ is obtained by replacing Eq. (3) into (2), premultiplying by $\phi_m(D)$ and using the orthogonality conditions of Eq. (4). Then,

$$q_n(\omega) = [f_n F(\omega) + u_n U(\omega)]\, H_n(\omega) \qquad (5)$$

where $H_n(\omega)=(\omega_n^2-\omega^2+j2\beta_n\omega_n\omega)^{-1}$ is the n^{th} modal frequency response function, j is the imaginary number, β_n is the n^{th} modal damping ratio included here to bound the response at resonance, and f_n and u_n are the n^{th} modal disturbance and control forces defined by the inner products

$$f_n = \int_D \phi_n(D)\, f(D) dD \quad ; \quad u_n = \int_D \phi_n(D)\, u(D) dD \qquad (6a,6b)$$

In the SISO feedforward control system considered here, the optimum frequency component of the control input stems from driving to zero, a response of the system which is referred here as the error variable. The error variable can also be represented as the linear contribution of each modal response as follows

$$e(\omega) = \sum_{n=1}^{N} q_n(\omega)\, \xi_n \qquad (7)$$

where ξ_n is the n^{th} modal component of the error variable that is a function of the physical characteristics of the error transducer implemented. The modal error component indicates the relative importance assigned to each mode.

Replacing Eq. (5) into (7), the error signal can then be set to zero to solve for the optimum control input in terms of the modal quantities. That is

$$U(\omega) = -\sum_{n=1}^{N} \xi_n f_n H_n(\omega) \Big/ \sum_{n=1}^{N} \xi_n u_n H_n(\omega)\, F(\omega) = G(\omega)\, F(\omega) \qquad (8)$$

where $G(\omega)$ is the feedforward compensator. In this analysis the control system is assumed to be causal, and thus the compensator $G(\omega)$ is realizable [10]. For noncausal or non-minimum phase control systems, the ideal compensator is not implementable as discussed later. However, the approach presented here can still be used as a design tool. For single frequency and multiple frequencies disturbances, where causality is not an issue, the proposed design formulation is also applicable.

The feedforward compensator, $G(\omega)$, is the transfer function that relates the control input $U(\omega)$ to the disturbance input $F(\omega)$. The controller or compensator $G(\omega)$ in Eq. (8) is defined as the ratio of two transfer functions, where the numerator is the transfer function between the disturbance or "primary" input and the error variable $T_{de}(\omega)$, while the denominator is the transfer function between the "secondary" control input and the error variable $T_{ce}(\omega)$. The controller $G(\omega)$ can provide valuable information as to the performance of the control system. For example, the poles of $G(\omega)$ would indicate

the frequencies at which the control effort would be unbounded if no damping was present in the system.

The traditional view of feedforward control techniques is of "active cancellation" where the uncontrolled modes excited by the "primary" input are canceled by a "secondary" input of appropriate magnitude and phase driving the same uncontrolled modes. This view arises from the fact that the system response can be obtained by superimposing the response of the disturbance and control inputs as suggested by Eq. (2). The unwanted consequence of this view is that the design of feedforward controllers has become an empirical technique based largely on a physical understanding of the uncontrolled system. Recent work has shown that the mechanisms for acoustic control (for example) with stationary disturbances is that, in general, the active source modifies the radiation impedance of the disturbance source, thus leading to less power radiated [4]. For active vibration control (AVC) as well as active structural acoustic control (ASAC), the authors have recently demonstrated that feedforward controlled systems have new eigenvalues and eigenfunctions as in feedback control [6,11]. For the sake of brevity, only the main concepts of the controlled system eigen-analysis are presented here, while a complete description of this formulation can be found in Reference 5.

For this analysis the controlled system is assumed to be undamped. The dynamic behavior of the controlled system is governed by the characteristics of the controller $G(\omega)$. Multiplying and dividing Eq. (8) by the product of the modal frequency response functions $H_n(\omega)$, $G(\omega)$ can be written as the ratio of two polynomials as follows [5,6]

$$G(\omega) = -N(\omega)/P(\omega) \tag{9}$$

with

$$P(\omega) = \sum_{n=1}^{N} \xi_n u_n \prod_{\substack{m=1 \\ m \neq n}}^{N} (\omega_m^2 - \omega^2) \tag{10}$$

The polynomial $P(\omega)$ in the denominator can be shown to be the characteristic polynomial of the controlled system. Thus, the eigenvalues of the controlled system, $(\omega_\ell)^2$, are obtained by solving for the roots of $P(\omega)$, $P(\omega_\ell)=0$. It is not difficult to show that $P(\omega)$ is the numerator of the transfer function $T_{oc}(\omega)$ and, thus, the controlled system eigenvalues are the zeros of $T_{oc}(\omega)$ [6]. This implies that we are canceling the zeros of $T_{oc}(\omega)$ with the poles of $G(\omega)$. The order of the polynomial in Eq. (10) is (N-1) in the variable ω^2, and thus the controlled system has (N-1) new eigenvalues. It can be shown that the controller has reduced the dynamic-degree-of-freedom of the system by one through the constraint imposed on the structure by driving the error signal to zero. The controlled system eigenfunction $\phi_\ell(D)$ associated with the natural frequency ω_ℓ is easily computed once the controlled system eigenvalues have been determined. They are obtained as a linear combination of the uncontrolled modes, since they have been used as an expansion basis. Then,

$$\phi_\ell(D) = \sum_{n=1}^{N} \Gamma_{\ell n} \phi_n(D) \tag{11}$$

where the expansion coefficients are

$$\Gamma_{\ell n} = C_\ell u_n / (\omega_\ell^2 - \omega_n^2) \tag{12}$$

The constant C_ℓ in Eq. (12) is included since the controlled mode shapes are arbitrary to a constant multiplier, and it can be computed by requiring $\sum_n (\Gamma_{\ell n})^2 = 1$. It is worth while mentioning that Eq. (12) is identical to the relationship found in the computation of the modified eigenfunctions in dynamic local modification techniques [12]. Thus, feedforward control can also be used to actively modify the dynamics of a structure without the drawback of the unwanted increase in system mass

generally associated with structural modification methods [12]. Another important observation is that from Eqs. (11) and (12) it can be observed that the eigenproperties of the controlled system are a function of only the control input through u_n and of the error variable to be minimized through the modal error components ξ_n and they are independent of the disturbance input. This conclusions are again similar to those as found in feedback controlled systems.

EIGENVALUE ASSIGNMENT DESIGN APPROACH

The theory in the previous section shows that a system under feedforward control has different modal properties from the uncontrolled system with respect to the excitation $F(\omega)$. This implies that by proper control design a structure could be actively modified to behave with new dynamic properties as required by the analyst. The design of feedback control systems is related to the computation of the feedback gains, where techniques such as eigenvalue assignment, eigenvector assignment, linear optimal control, and others are extensively used to this end. On the other hand, the general design of a SISO feedforward control systems involves the selection of the control input distribution, determined by the modal components u_n, and of the error quantity to be minimized defined by the modal error components ξ_n. In contrast to feedback control where a substantial number of mathematical design formulations are available, analytical feedforward design approaches are effectively non-existent in the literature. In the following, a feedforward control design procedure based on the eigenvalue assignment technique will be presented. Here, it is assumed the control load is fixed and thus the modal control inputs u_n are known. The design approach will then focus on the selection of the proper error sensor, whose output will be minimized, in order to drive the closed loop behavior as required.

In the eigenvalue assignment technique, the controlled system eigenvalues are selected in advance and then the error sensor is designed so as to match the desired controlled system poles. This implies that the (N-1) controlled eigenvalues $(\omega_\ell)^2$ as well as the N modal control forces u_n are known quantities and the modal components of the error variable ξ_n are to be computed. Substituting the selected controlled system eigenvalues into the characteristic polynomial in Eq. (10), we can write

$$P(\omega_\ell) = \sum_{n=1}^{N} \xi_n \, u_n \prod_{\substack{m=1 \\ m \neq n}}^{N} (\omega_m^2 - \omega_\ell^2) = 0 \qquad \ell = 1, \cdots, (N-1) \tag{13}$$

which can also be written in matrix form as follows

$$\begin{bmatrix} S_{11} & S_{12} & \cdots & S_{1N} \\ S_{21} & S_{22} & \cdots & S_{2N} \\ \vdots & \vdots & \ddots & \vdots \\ S_{(N-1)1} & S_{(N-1)2} & \cdots & S_{(N-1)N} \end{bmatrix} \begin{Bmatrix} \xi_1 \\ \xi_2 \\ \vdots \\ \xi_N \end{Bmatrix} = \begin{Bmatrix} 0 \\ 0 \\ \vdots \\ 0 \end{Bmatrix} \quad \text{with} \quad S_{sn} = u_n \prod_{\substack{m=1 \\ m \neq n}}^{N} \left(\omega_m^2 - \omega_\ell^2 \right) \tag{14}$$

The dimension of the matrix in Eq. (14) is (N-1)xN. Careful observation of Eq. (14) shows that if one of the controlled eigenvalues is identical to one of the uncontrolled system eigenvalues, i.e. $\omega_s = \omega_\ell$ only the term S_{sn} in the s^{th} row in the above matrix does not vanish. Therefore, to satisfy the s^{th} equation ξ_n must also be zero. This implies that the s^{th} eigenfunction is unobservable by the error sensor and thus it can not be affected by the control input. The linear system in Eq. (14) is such that any multiple of the vector $\{\xi_1, \xi_2, \ldots, \xi_N\}^T$ is a solution, and therefore the only relevant information is the relative value between the modal error components. Assuming the N^{th} mode is observable, ξ_N is set to unity and by suitably partitioning the matrices in Eq. (14), the modal components can be obtained by solving the reduced linear system of equations

$$\begin{bmatrix} S_{11} & S_{12} & \cdots & S_{1(N-1)} \\ S_{21} & S_{22} & \cdots & S_{2(N-1)} \\ \vdots & \vdots & \ddots & \vdots \\ S_{(N-1)1} & S_{(N-1)2} & \cdots & S_{(N-1)(N-1)} \end{bmatrix} \begin{Bmatrix} \xi_1 \\ \xi_2 \\ \vdots \\ \xi_{N-1} \end{Bmatrix} = - \begin{Bmatrix} S_{1N} \\ S_{2N} \\ \vdots \\ S_{(N-1)N} \end{Bmatrix} \tag{15}$$

The vector $\{\xi_1,\xi_2,...,\xi_{N-1},1\}^T$ defines the error sensor in the modal domain. Thus, this modal information needs to be transformed into a physical sensor on the structure, and to this end two basic approaches can be implemented. One method utilizes an array of discrete point sensors, i.e. accelerometers, strain gages and so forth. The error variable is obtained by summing the weighted discrete sensor signals. Assuming N_s discrete point displacement sensors, the modal error component becomes

$$\xi_n = \int_D \sum_{i=1}^{N_s} b_i \, \delta(D_i - D) \, \phi_n(D) \, dD \tag{16}$$

where b_i is the weight of the i^{th} point sensor located at D_i, and $\delta(D_i-D)$ is the Dirac delta function. Then, Eq. (16) reduces to

$$\xi_n = \sum_{i=1}^{N_s} b_i \, \phi_n(D_i) \qquad n = 1,\cdots,N \tag{17}$$

Equation (17) can also be written in matrix form as

$$[A] \{b\} = \{\xi\} \tag{18}$$

where the components of matrix [A], which relates the error quantity in the physical domain to the modal domain, are $A_{ni}=\phi_n(D_i)$, and $\{b\}=\{b_1,b_2,...,b_N\}^T$ is the weighting vector. Assuming $N \geq N_s$ the solution of Eq. (18) can be obtained by the pseudo-inverse technique [13]. That is,

$$\{b\} = \left([A]^T [A]\right)^{-1} [A]^T \{\xi\} \tag{19}$$

The sum of the output of N_s discrete point sensors is a design approach applicable to any complex structure. However, implementation of this approach could result in considerable signal conditioning effort, particularly in "real-time" digital control where all calculation must be completed in one sampling period. The use of distributed sensors has recently gained acceptance in the control community for their inherent built in filtering capability of the system response. The flexibility, light weight and toughness properties of polyvinylidene fluoride polymer (PVDF) films have found application as distributed structural sensors in active control [14-18]. The PVDF film sensor is mounted on the surface of the structure and yields a response proportional to the integral of the strain over the surface of application. In particular, one dimensional problems are ideally suited for the use of PVDF distributed sensor because any desirable weighted response can be obtained by varying the width and polarity of the sensor as a function of the axial coordinate. The design of a physical PVDF sensor from the modal error components ξ_n will be presented for a beam problem. Thus, the domain D becomes the x coordinate in the following derivation.

Since PVDF film is a strain sensor, the modal error component becomes [7,14]

$$\xi_n = -\alpha h \int_0^L b(x) \frac{d^2\phi_n(x)}{dx^2} dx \tag{20}$$

where h is the distance of the upper beam surface to the neutral axis here assumed constant for the sake of clarity in the presentation; α is a constant of proportionality that relates the film electrical and mechanical properties to the surface strain; and b(x) is the function that weights the strain along the beam, and it is determined by the PVDF film's geometry. This function dictates the width of the film and can take either positive or negative values. The negative effective width can be implemented by segmenting the film with out-of-phase wiring of the negative segments, i.e. inverting the polarity of the sensors. In order to take advantage of the orthogonality conditions of the modes, the weight function b(x) is expanded as follows

$$b(x) = \sum_{m=1}^{N} b_m \, EI(x) \frac{d^2\phi_m(x)}{dx^2} \tag{21}$$

To solve for the unknown expansion coefficients b_m, Eq. (21) is replaced into Eq. (20) and using the orthogonality condition of Eq. (4b) gives

$$b_m = -\frac{\xi_m}{\alpha h \omega_m^2} \tag{22}$$

That yields the weight function in term of the computed modal error components as follows

$$b(x) = \sum_{n=1}^{N} \frac{\xi_n}{\omega_n^2} EI(x) \frac{d^2\phi_n(x)}{dx^2} \tag{23}$$

In this design formulation, the control input was assumed fixed and the error sensor is then configured to achieve the sought controlled system characteristics. However, inspection of the characteristic polynomial in Eq. (13) reveals that the design process could have also been stated as: assuming the error sensor fixed, the control input distribution is then designed to obtain the desired poles. This is simply accomplished by replacing ξ_n by u_n and vice versa in Eqs. (13) through (23). These two eigenvalue assignment design concepts differ only in that the associated controlled eigenfunctions are different since the expansion coefficients Γ_{en} in Eq. (12) are determined by u_n. Greater design flexibility is possible if both the control load distribution and the weighted error variable are designed simultaneously, as it will be discussed later.

Design Example: Control of motion of a simply supported beam

The applicability of the design formulation presented here is demonstrated for a uniform simply supported beam. The beam is made of steel and has bending stiffness EI=93 N.m^2, mass per unit length m=2.181 N.sec^2/m^2, and beam length L=0.38 m. To compute the response of the system, it is assumed a modal damping ratio of 0.1% in all modes (β_n=0.001), and only the first four modes are included in the analysis. The beam is excited by a concentrated force located at x_d=0.1L, and the response is controlled by another point force placed at x_c=0.65L. In this example, the error sensor, whose output is minimized, is a distributed PVDF shaped film mounted on the beam surface. This sensor is designed to induce the desired dynamic characteristics of the structure. Since the proposed design formulation is based on the modal representation of the system's response, the eigenproperties of the uncontrolled beam to be used in the analysis are given by

$$\omega_n = (n\pi/L)^2 \sqrt{EI/m} \quad ; \quad \phi_n(x) = \sqrt{2/m\,L}\ \mathrm{Sin}(n\pi\, x/L) \qquad (24a,24b)$$

In this example problem, we seek to arbitrarily shift the natural frequencies of the system in the frequency range of the first four modes. As mentioned before, the controlled system has one less dynamic degree of freedom due to the constraint imposed in the system as result of driving the error signal to zero. Thus, the number of controlled modes is three and the desired beam-control system natural frequencies, ω_f, (which are arbitrarily chosen) are shown in Table 1. The uncontrolled natural frequencies are also shown in the same table. These desired natural frequencies are replaced into Eq. (15) to compute the coefficients of the matrix and independent vector. Solving this linear system of equations for the modal error components ξ_n defines the error sensor in the modal space. To convert this into a PVDF distributed sensor, the modal components ξ_n are replaced into Eq. (23) where the weight function b(x) is computed. This function determines the width profile of the PVDF sensor which is shown in Figure 2.

Table 1--Uncontrolled and Controlled System Natural Frequencies

Mode	Natural Frequency [Hz]			
	Uncontrolled, $f_n=\omega_n/2\pi$		Controlled, $f_f=\omega_f/2\pi$	
	Analysis	Experimental	Analysis	Experimental
1	71.0	75	425	424
2	284.1	278	780	750
3	639.3	626	1000	1030
4	1136.5	1120		
5	1775.8	1450		

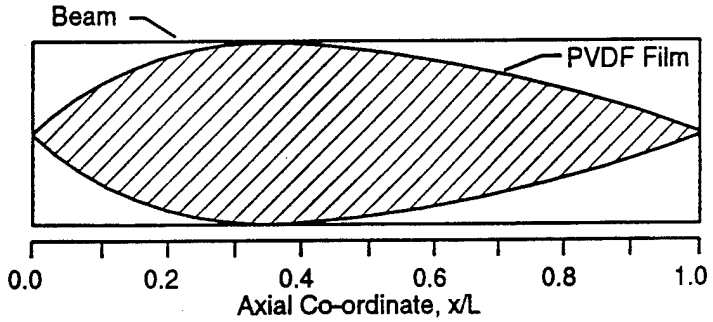

Figure 2--PVDF film sensor geometry

To illustrate the dynamic behavior of the beam before and after control, the acceleration response at the input force location was computed. The acceleration response is obtained by multiplying Eq. (3) by ω^2. Assuming a unit amplitude of the input force, the magnitude of the acceleration before and after control at x_q are shown in Figure 3 as function of the frequency ω. The dashed line is the analytical response of the uncontrolled beam obtained by using Eqs. (3) and (5) and setting $U(\omega)$ to zero. The continuous line corresponds to the controlled system calculated from Eqs. (3), (5) and (8) and shows resonance behavior at the preselected frequencies ω_f. Thus, upon driving the weighted response output from the PVDF sensor to zero, the beam-control system has the desired eigenvalues. Note that the results of Figure 3 were calculated in the frequency domain and the curves were obtained by

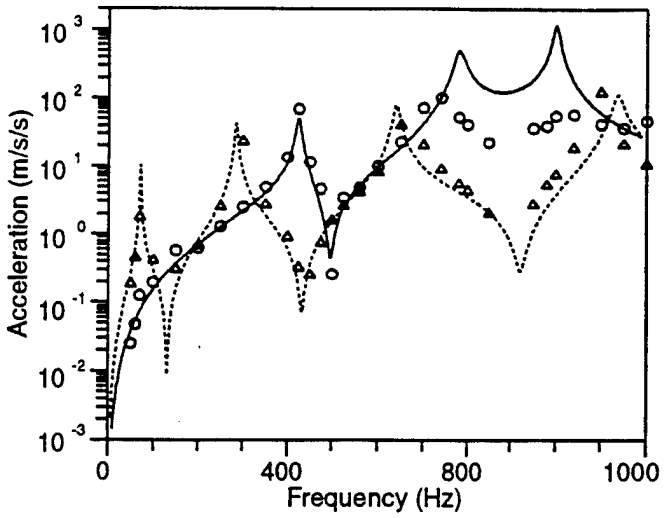

Figure 3--Acceleration at disturbance force location; Uncontrolled ---- Analytical, ΔΔΔ Experimental Controlled —— Analytical, OOO Experimental

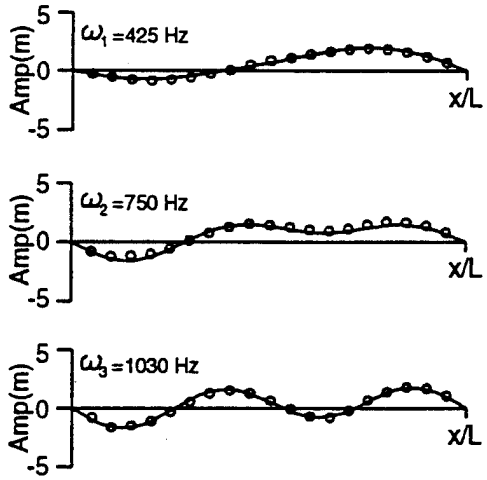

Figure 4--Controlled system eigenfunctions; —— Analytical, OOO Experimental.

evaluating at discrete frequencies. The results, thus, represente the best possible attenuation achievable over the bandwidth. Whether this is physically realizable depends upon the time domain response of the controlled system, i.e. wether it is causal, non-minimum phase etc. The associated controlled eigenfunctions, computed using Eqs. (11) and (12), are shown in Figure 4.

The above numerical example was also experimentally verified as described in reference 7. The experimentally determined values are plotted in Figures 3 and 4 and good agreement with the theory is seen. It should be noted that the computed mode shapes in Figure 5 were calculated from the individual eigenfunction expressions in eq.(11) and (12), rather than the total response of the system at the resonance points. A similar approach has demonstrated how it is possible to design the controller to cause a homogeneous beam to behave exactly as a beam (both eigenvalues and eigenvectors) with an attached mass-spring system [19].

EIGENVALUE-EIGENFUNCTION ASSIGNMENT DESIGN APPROACH

In this case, the controlled system eigenfunctions as well as the eigenvalues are preselected in advance using an eigenvalue-eigenfunction assignment technique. The main application of this approach would be in active structural acoustic control (ASAC) where the radiation efficiency of the controlled mode shapes are as important as the resonance conditions [20].

The main goal in ASAC is for the control system to render a controlled response that poorly couples with the acoustic medium, thus resulting in minimum radiated sound power. This objective can be accomplished if two conditions are met as follows:

(i) Firstly, the resonant frequencies of the controlled structure must lay away from the dominant part of the disturbance input spectrum. In other words, the controlled system resonances should be detuned from the excitation input.

(ii) Secondly and more important, the controlled or residual structural response should be dominated by a linear contribution of weak radiating modes, i.e. the new eigenfunctions.

As mentioned in the previous section, the controlled system has new resonant frequencies and associated eigenfunctions that are only a function of the selected actuator and sensor. Thus, this concept can be merged with the above conditions to yield an efficient design approach. The design formulation proposed here can be stated as to find the optimum actuator and sensor configuration that yields a controlled structure with eigenproperties that satisfied the above two conditions. The work summarized here is reported in detail in reference 9.

We thus seek the optimum expansion coefficients $\Gamma_{\ell n}$ that will render the controlled eigenfunctions $\phi_\ell(D)$ to have a minimum radiation efficiency. To achieve this requirement, we minimize the controlled modal radiation efficiency at frequency ω [9]

$$\sigma_\ell(\omega) = \frac{1}{A_r \rho c} \frac{\{\Gamma_\ell\}^T [\Pi(\omega)] \{\Gamma_\ell\}}{\{\Gamma_\ell\}^T [V(\omega)] \{\Gamma_\ell\}} \tag{25}$$

such that $\{\Gamma_\ell\}^T\{\Gamma_\ell\}=1$. In Eq. (25), $[\Pi(\omega)]$ is the uncontrolled power radiated matrix with the (n,m) element is given by

$$\Pi_{nm}(\omega) = \iint_A \frac{p_n p_m^*}{\rho c} dA \tag{26}$$

where p_n is the complex modal pressure computed over the hemisphere A; $[V(\omega)]$ is the uncontrolled mean square velocity matrix with the (n,m) element given by

$$V_{nm}(\omega) = \iint_{A_r} \phi_n(D)\, \phi_m(D)\, dD \tag{27}$$

where A_r is the area of the radiator; and ρc is the impedance of the acoustic medium.

The desired expansion coefficients that yield the lowest radiation efficiency for the controlled modes are obtained by minimizing $\sigma_\ell(\omega)$ in Eq. (25) with respect to the $\Gamma_{\ell n}$ with the constraint $\{\Gamma_\ell\}^T\{\Gamma_\ell\}=1$. This constraint minimization problem can be efficiently solved by recognizing that the stationary values of $\sigma_\ell(\omega)$ can be obtained by solving the eigenvalue problem

$$([\Pi(\omega)] - \sigma_\ell [V(\omega)] A \rho_0 c) \{\Gamma_\ell\}_d = \{0\} \qquad \ell=1,\cdots,N \tag{28}$$

The orthogonality condition

$$\{\Gamma_i\}^T [\Pi(\omega)] \{\Gamma_j\} = \sigma_i \delta_{ij} \tag{29}$$

implies that the controlled modes are uncoupled with each other with respect to the far-field radiation.

As depicted in Eq. (12), the expansion coefficients $\Gamma_{\ell n}$ are a function of the modal control forces and both the uncontrolled and controlled natural frequencies. Thus, once the optimum expansion coefficients $\Gamma_{\ell n}$ are obtained from the eigensolution in Eq. (28), the modal control forces and the controlled eigenvalues, $(\omega_\ell)^2$, can be determined by solving the least square constrained minimization problem

$$\text{Minimize} \quad F(u_n,\omega_\ell) = \sum_{\ell=1}^{N-1} \sum_{n=1}^{N} \left| (\Gamma_{\ell n})_{opt} - c_\ell \frac{u_n}{\omega_\ell^2 - \omega_n^2} \right|^2 \tag{30}$$

$$\text{such that} \quad \sum_{n=1}^{N} u_n^2 = 1$$

$$(\omega_\ell^2)_{lower} \le \omega_\ell^2 \le (\omega_\ell^2)_{upper}$$

where the equality constraint represents the normalization of the modal control forces since the relative controllability of the modes is the only relevant information. The upper and lower limits of the inequality constraints on the values for the controlled system eigenvalues $(\omega_\ell)^2$ are selected based on the characteristic of the spectrum of the disturbance input.

The error sensor modal components ξ_n are determined from the characteristic equation of the controlled system in Eq. (13). Again assuming ξ_N=1, the modal components ξ_n are obtained by solving the linear system of equations in Eq. (15).

The controlled system is completely defined in terms of the optimum modal parameters, u_n and ξ_n. It is then convenient to study the performance of the ASAC system before these modal parameters are translated in realizable actuators and sensors.

Design Example: Radiation control from a plate

As an example calculation, the design formulation is applied to control the sound radiation from a baffled simply supported steel plate of size L_x=0.38m x L_y=0.30m x h=2 mm thick. Thus, the domain D becomes the (x,y) coordinates in this example. The input disturbance is assumed to be a point force acting at the center of the plate with white noise in 0-600 Hz frequency band. In this example, the objective is to control the volumetric modes (1,1), (3,1) and (1,3) modes in the 0-600 Hz bandwidth with a SISO controller. The eigenproperties of the simply supported plate are given by

$$\omega_n = \sqrt{D_p/\rho_p h}\left(\gamma_x^2+\gamma_y^2\right) \quad ; \quad \phi_n(x,y) = (4/L_x L_y h \rho_p)^{1/2} \sin(\gamma_x x) \sin(\gamma_y y) \tag{31}$$

where $\gamma_x=\pi n_x/L_x$, $\gamma_y=\pi n_y/L_y$, $D=Eh/12(1-\nu^2)$ is the flexural rigidity, ρ_p is the plate density, and (n_x,n_y) are the modal indices traditionally used for rectangular panels that are associated to the n index in the theoretical analysis.

The first step in the design process is to find the desired controlled system eigenfunctions. The

single frequency of 300 Hz was selected to compute the matrices $[\Pi(\omega)]$ and $[V(\omega)]$ to form the eigenvalue problem of Eq. (28). The solution of the eigenvalue problem yielded three eigenvalues and associated eigenvectors. Since the SISO controller reduces the number of dynamic degree-of-freedoms by one, the desired expansion coefficients, $(\Gamma_m)_d$, are the first two eigenvectors. The radiation efficiency at 300 Hz, eigenvalues σ_p and associated expansion eigenvectors, $\{\Gamma_i\}_d$, of the desired controlled eigenfunctions are given in Table 2.

The optimum modal parameters, i.e. modal control and error components, can now be computed. The next step is to find the modal control forces, u_n, and controlled eigenvalues, $(\omega_i)^2$, that yield the desired expansion coefficients of Table 2. This is achieved by solving the minimization problem in Eq. (30) where the controlled eigenvalues $(\omega_i)^2$ are not constrained as in Eq. (30) because the spectrum of the excitation input is white noise. The minimization process was carried out by using the optimization IMSL routine DUNLSF (non-linear least squares problems) which yielded the optimum modal forces u_n shown in Table 3 and two controlled resonant frequencies at 399 and 700 Hz as shown in Table 4. These values yielded the expansion coefficients shown in columns 2 and 3 of Table 4. These coefficients are almost identical to the desired coefficients obtained from the solution of the eigenvalue problem in Eq. (28) and presented in Table 2. The modal control forces and controlled eigenvalues can now be used in the linear system of equations in Eq. (15) to solve for the modal error components, ξ_n, and they are given in Table 4. Note that this procedure could be used with any number of included modes; increasing the number of modes will simply increase the amount of computations required.

Table 2--Radiation efficiency and expansion coefficients of desired eigenfunctions

Radiation Efficiency, $\sigma_p x10^{-3}$		
	.239	1.13
Desired Coefficients, $\{\Gamma_i\}_d$		
(1,1)	-.367	0.128
(3,1)	0.361	-.893
(1,3)	0.857	0.431

Table 3--Modal control and error components.

Mode (n_x,n_y)	Modal Parameters	
	u_n	ξ_n
(1,1)	-.534	0.924
(3,1)	0.479	0.329
(1,3)	0.697	0.192

The resulting modal parameters listed in Table 3 define completely the control system. The controller has modified the eigenstructure of the system in such a way that the controlled structure will respond with two weak radiating modes. To illustrate this fact, the radiation efficiency for the three odd-odd uncontrolled eigenfunctions and the two new controlled eigenfunctions was computed and they are plotted in Figure 5. This figure shows clearly that the controlled modes have substantially lower radiation efficiency than the uncontrolled modes. It is also very interesting to note that, as calculated by numerical integration, the controlled eigenfunctions are nonvolumetric. Since the response is a linear expansion of the modes, this implies that the net volume displaced by the controlled plate is zero at all

frequencies. This same phenomenon was observed by the authors in studying the dynamic behavior of feedforward controlled systems using microphones in the far-field as error sensors [11]. This observation suggest an alternative control approach in which all the closed loop modes are chosen to be non-volumetric. Such a procedure would eliminate the lengthy radiation coupling equations and is the topic of present research.

The sensitivity of the controlled eigenfunctions to the selected frequency used in Eq. (28) is an important issue. Solving the eigenproblem in Eq. (28) for different values of the frequency within the excitation band, showed that the desired expansion coefficients did not vary substantially even though the design frequency and the excitation bandwidth limit is close to the plate critical frequency. This behavior is due to the new eigenvalues being independent of frequency as in all distributed elastic systems. Although this is not a general conclusion, the result suggests that in the proposed design approach the solution of the modal acoustic field could be efficiently carried out at a small number of frequencies. Since this analysis is the most computational intensive process, the proposed design approach has clear computational benefits over direct optimization methods for complex structures and excitations.

Table 4--Controlled system eigenproperties

Resonant Freq. $f_i=\omega_i/2\pi$ [Hz]		
	f_1=399	f_2=700
Expansion coefficients Γ_{in}		
(n_x,n_y)	Γ_{1n}	Γ_{2n}
(1,1)	0.224	-.314
(3,1)	-.877	0.371
(1,3)	0.424	0.874

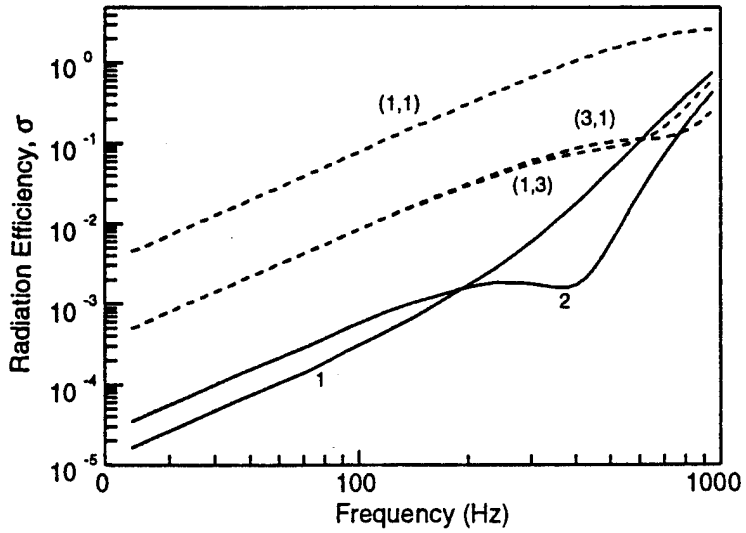

Figure 5--Radiation efficiency of ---- uncontrolled and —— controlled eigenfunctions.

The control system is completely defined in the modal domain in terms of the optimal modal parameters in Table 3. The performance of the controlled structure can be investigated with these basic modal parameters before physical transducers are devised. The effectiveness of the control system was evaluated for a disturbance input consisting of a point force located at $x=0.5L_x$ and $y=0.5L_y$. To illustrate the dynamic behavior of the plate before and after control, the acceleration response of the plate at the disturbance location was computed. The amplitude is shown in Figure 6 as a function of the frequency. The dashed line is the uncontrolled response and shows peaks at the resonant frequencies of the plate. On the other hand, when the control input is applied, the response shows resonance behavior at the two controlled resonant frequencies given in Table 4. The vibration levels of the controlled structure are slightly lower than the uncontrolled system, i.e. amplitude of the second controlled mode is the same as the (1,1) uncontrolled mode. The corresponding the before and after control far-field pressures at $r=(0°,0°,4.5L_x)$ was also computed. The sound pressure level in decibels (dB reference 20μPa) is shown in Fig. 7 as a function of the frequency. This figure shows that the sound levels produced by the

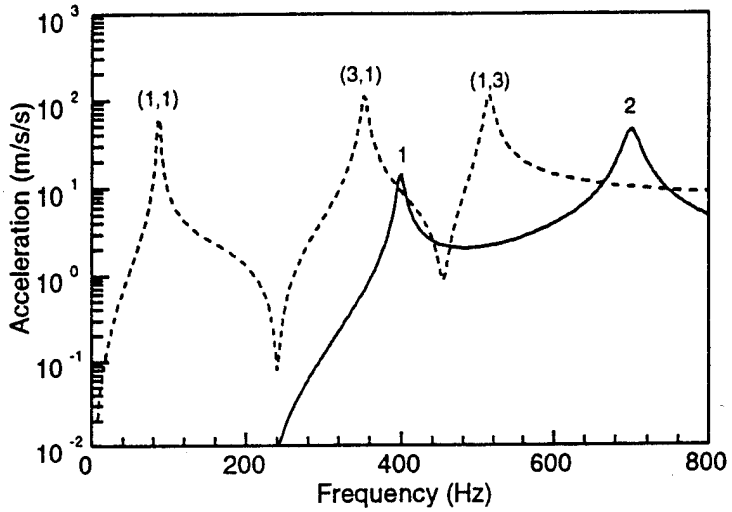

Figure 6--Acceleration at disturbance force location; --- uncontrolled and —— controlled.

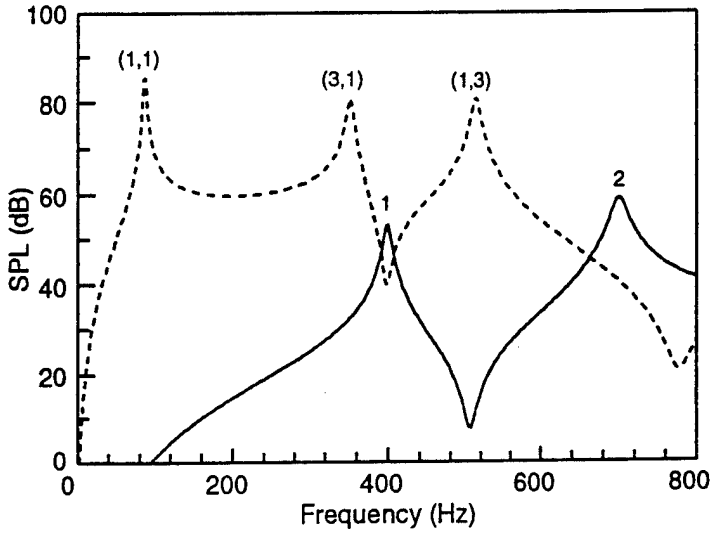

Figure 7--Far-field pressure at $r=(4.5L_x,0,0)$; --- uncontrolled and —— controlled.

controlled structure are well below the level generated by the uncontrolled one. This is due to the low radiation efficiency of the controlled modes that results in a weak coupling of the controlled response with the acoustic medium. This phenomenon takes place in spite of the plate vibration levels being comparable to the uncontrolled response levels.

The results demonstrate that the controller configuration gives good performance. The next step is to translate the optimum modal parameters, u_n and ξ_n, into realizable transducers. Here we assume the actuator and sensor will be rectangular piezoelectric distributed strain devices. Previous work [21] has shown that the modal control forces, u_n, are related to the location and configuration of the patches such that

$$u_n = \sum_{i=1}^{M} P_i \frac{\gamma_x^2+\gamma_y^2}{\gamma_x \gamma_y} \left[\mathrm{Cos}(\gamma_x(x_{ci}+p_x)) - \mathrm{Cos}(\gamma_x(x_{ci}-p_x))\right] \left[\mathrm{Cos}(\gamma_y(y_{ci}+p_y)) - \mathrm{Cos}(\gamma_y(y_{ci}-p_y))\right] \tag{32}$$

where $P_i=\pm 1$ is the relative polarity of the N_a patches, (x_{ci},y_{ci}) are the center coordinates of the patch, $2p_x$ and $2p_y$ are the patch dimensions. These can be determined by minimizing the cost function (for fixed sized actuators)

$$F(P_i,x_{ci},y_{ci}) = \sum_{n=1}^{N} \left| (u_n)_{opt} - u_n(P_i,x_{ci},y_{ci}) \right|^2 \tag{33}$$

A similar expression can be written for finding the configuration of the strain sensor [9].

Figure 8(a) shows the optimum PZT actuator which consists of four piezoelectric actuators driven in phase. Figure 8(b) shows the single optimum piezoelectric sensor. Note that these configurations are designed to be optimum across the complete bandwidth of $0 \le f \le 600$ Hz. Experimental testing of such system have recently validated the ASAC design approach and will be reported in the future.

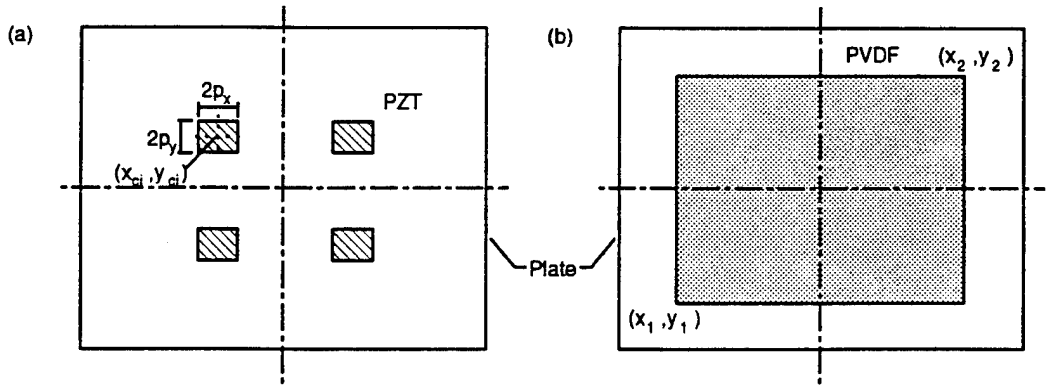

Figure 8--Optimum (a) PZT control actuator and (b) PVDF film error sensor.

EXTENSION TO DISCRETIZED SYSTEMS

The most computationally intensive process in the proposed eigenfunction design approach for

ASAC systems is the evaluation of the matrices $[\Pi(\omega)]$ and $[V(\omega)]$. These matrices will be computed at a few frequencies. A realistic structure will certainly required the numerical prediction of both the structural and the acoustic responses by FEM/BEM techniques. The computation of these matrices using numerical predictions is presented here.

A FEM/BEM model of the structure is first constructed and used to compute the structural eigenproperties, i.e. natural frequencies ω_n and mode shape vectors $\{\phi_n\}$. The (n,m) element of matrix $[V(\omega)]$ given in Eq. (27) can then be approximated as

$$V_{nm}(\omega) = \frac{\omega^2}{2A} \sum_{s=1}^{N_{FE}} \phi_n(s)\, \phi_m(s)\, A_s \tag{34}$$

where $\phi_n(s)$ is the s^{th} component of the mode shape vector; A_s is the area associated to the s^{th} node; A is the total area of the radiator ($A=\Sigma A_s$); and N_{FE} is the number of nodes in the FEM/BEM model.

The acoustic response can be computed by using the mode shape vectors, obtained from the FEM/BEM analysis, in conjunction with an acoustic FEM/BEM code. The velocity profile vector at frequency ω due to the n^{th} mode, $\{v_n(\omega)\}$, is first computed as

$$\{v_n\} = i\omega \{\phi_n\} \tag{35}$$

which in turn is input into an acoustic FEM/BEM code to compute the complex modal far-field radiated pressure over a surface enclosing the structure, i.e. a hemisphere.

The (n,m) component of matrix $[\Pi(\omega)]$ can then be computed using the modal far-field pressure distribution as follows

$$\Pi_{nm}(\omega) = \sum_{s=1}^{N_{BE}} \frac{p_n(s)\, p_m^*(s)}{\rho c} A_s \tag{36}$$

where $p_n(s)$, $s=1,...,N_{BE}$, is the complex pressure computed at the s^{th} node in the far-field; A_s now represents the area associated to $p_n(s)$; and the asterisk denotes the complex conjugate.

The matrices $[\Pi(\omega)]$ and $[V(\omega)]$, evaluated as in Eqs. (34) and (36), are then used to solve the eigenproblem in Eq. (28). From this eigenanalysis, the design process to find the optimum modal control parameters continuous in the same way as presented in the previous section. It is worth to mention that these matrices can also be estimated from experimental measurements carried out on the same system to be controlled.

BROADBAND DISTURBANCES

The previous analysis and design procedure has been based upon a frequency domain approach. This form is appropriate where the disturbance is narrow band, multiple frequencies or the response is dominated by behavior at discrete frequencies (i.e. system resonances). However, in many applications the disturbance is of a random broadband nature. Recently, Alberts and Pota [22] have investigated the broadband implementation of feedforward control to minimize the disturbance response at some point on a vibrating flexible structure. Alberts and Pota have shown that the optimal compensator for the problem of Figure 1 is

$$G(s) = -\frac{T_{de}(s)}{T_{oe}(s)} \tag{37}$$

where $T_{de}(s)$ is the transfer function from the disturbance input to the error point while $T_{ce}(s)$ is from the control to the error point and s is the Laplace variable. Alberts and Pota have extended the previous frequency domain results summarized in this paper and have shown that for broadband excitation (or time domain analysis) the controlled system will have as it's new eigenvalues (to the correlated disturbance force or forces), the zeros of T_{ce} and that all of the original eigenvalues are exactly canceled by the zeros of G(s).

However, many realistic systems have non-minimum phase zeros (for example control systems with non-collocated actuators and sensors) and this implies that the optimum compensator G(s) is unrealizable without leading to control instability. As discussed in the frequency domain approach of this paper, Alberts and Pota show that it is possible to arbitrarily assign the eigenvalues of the compensated system in the time domain and then derive the optimal controller to provide this required behavior. They developed a design technique by which the compensator nearly cancels the original system's poles and simultaneously minimizes the disturbance response at the error point while remaining stable over the complete bandwidth. Through simulations Alberts and Pota demonstrate that using the approach leads to only a slight reduction in control attenuation of the error signal over the bandwidth when compared to the performance calculated using the frequency domain approach (which predicts the maximum possible broadband attenuation).

CONCLUSIONS

A design technique based upon the eigen behavior of feedforward controlled systems has been developed. The technique has been applied to both vibration modification and radiation control of structures. The extension to complex bodies using numerical FEM/BEM techniques and broadband disturbances has been discussed. The method provides a very useful tool for designing the components of feedforward controlled systems based upon a required behavior.

ACKNOWLEDGMENTS

The authors gratefully acknowledge the financial support of a large portion of this work by the Office of Naval Research, Dr. Kam Ng Technical Monitor.

REFERENCES

[1] P.A. Nelson and S.J. Elliott, *Active Control of Sound*, Academic Press, London, 1992.

[2] C.R. Fuller, S.J. Elliott, and P.A. Nelson, *Active Control of Vibration*, Academic Press, London, (in-press).

[3] L. Meirovitch, Baruh, H. and Oz, H., "A Comparison of Control Techniques for Large Flexible Systems," AIAA *J. of Guidance and Control*, **6**(4), July-August 1983, pp. 302-310.

[4] S.D. Snyder and C.H. Hansen, "Active Noise Control in Ducts: Some Physical Insights," *J. Acoust. Soc. Am.* **86**, 1989, pp.184-194.

[5] R.A. Burdisso and C.R. Fuller, "Theory of Feedforward Controlled System Eigenproperties," *J. Sound Vib.* **153**(3), 1992, pp. 437-452.

[6] R.A. Burdisso and C. R. Fuller, "Theory of Feedforward Controlled System Eigenproperties," *J. Sound Vib.* (Letter to the Editor) **163**(2), 1993, pp. 366-371.

[7] R.A. Burdisso and C. R. Fuller, "Feedforward Controller Design by Eigenvalue Assignment," *AIAA J. of Guidance and Control*, 1994 (in press).

[8] R.A. Burdisso and C. R. Fuller, "Actuator and Sensor Design for Active Structural Acoustic Control: Part I - Analysis," *J. Acoust. Soc. Am.*, 1994 (submitted for publication).

[9] R.A. Burdisso and C. R. Fuller, "Optimum Actuator and Sensor Design for Feedforward Active Structural Acoustic Control," *Proceedings of the 1993 ASME Winter Annual Meeting*, Nov.28-Dec.3, New Orleans, pp. 363-370.

[10] R.A. Burdisso, J.S. Vipperman and C.R. Fuller ,"Causality Analysis of Feedforward Controlled Systems with Broadband Inputs," *J. Acoust. Soc. Am.*, **94**(1), 1993, pp. 234-242.

[11] R.A. Burdisso and C.R. Fuller, "Dynamic Behavior of Structural-acoustic Systems in Feedforward Control of Sound Radiation," *J. Acoust. Soc. Am.* **92**(1), 1992, pp. 277-286.

[12] J.T. Weissemburger, "The Effect of Local Modifications on the Vibration Characteristics of Linear Systems," *ASME J. Applied Mechanics*, 1968, pp. 327-332.

[13] T.N Greville, "Some Applications of the Pseudo-Inverse of a Matrix," *SIAM Review*, **2**, 1960, pp. 15-32.

[14] C.K. Lee and Moon F.C., "Modal Sensors / Actuators," *ASME J. of Applied Mechanics*, **57**, June 1990, pp. 434-441.

[15] T. Bailey and J.E. Hubbard, "Distributed Piezoelectric-Polymer Active Vibration Control of a Cantilevered Beam," *AIAA J. of Guidance and Control*, **6**(5), 1985, pp. 605-611.

[16] D.W. Miller, S.A. Collins and S.P. Peltzman, "Development of Spatially Convolving Sensors for Structural Control Applications," *AIAA Paper*, 90-1127-CP, 1990, pp. 2283-2297.

[17] R.L. Clark and C.R. Fuller, "Modal Sensing of Efficient Acoustic Radiators with PVDF Distributed Sensors in Active Structural Acoustic Approaches," *J. Acoust. Soc. Am.*, **91**(6), 1992, pp. 3321-3329.

[18] S.A. Collins, D.W. Miller and A.H. von Flotow, "Sensors for Structural Control Applications Using Piezoelectric Polymer Film," MIT Space Engineering Research Center, Cambridge, MA, SERC 12-90, Oct. 1990.

[19] R.A. Burdisso and C.R. Fuller, "Active Dynamic Modification of Flexible Structures," *Proceedings of the 10th International Modal Analysis Conference (IMAC)*, San Diego, California, Vol. II, Feb. 3-7, 1992, pp. 1159-1166.

[20] R.A. Burdisso and C.R. Fuller, "Design of Feedforward Active Structural Acoustic Control Systems by Eigenfunction Assignment," *126th Meeting of the Acoust. Soc. Am.*, 4-8 October 1993, Denver, Colorado (Abstract only).

[21] E. K. Dimitriadis, C. R. Fuller and C. R. Rogers, "Piezoelectric Actuators for Distributed Vibration Excitation of Thin Plates," *ASME J. Vib. Acoust.*, **113**, 100-107 (1989).

[22] T.E. Alberts and H.R. Pota, "Broadband Dynamic Modification Using Feedforward Control," 1994 (in preparation).

C-48 Detecting and Analyzing Collinearity in Simulations of Feedforward Active Noise Control, C. E. Ruckman and C. R. Fuller, 3rd International Congress on Air- and Structure-Borne Sound and Vibration, Montreal, Canada, 13-15 June 1994.

Presented at
Third International Contress on Air- and Structure-Borne Sound and Vibration
June 13-15, 1994
Montreal, Canada

DETECTING AND ANALYZING COLLINEARITY IN SIMULATIONS OF FEEDFORWARD ACTIVE NOISE CONTROL

Christopher E. Ruckman
Structural Acoustics and Hydroacoustics Research Branch
Carderock Division, Naval Surface Warfare Center
Bethesda, MD 20084-5000 USA

Chris R. Fuller
Vibration And Acoustics Laboratories
Virginia Polytechnic Institute & State University
Blacksburg, VA 24061 USA

ABSTRACT

In its most basic form, a frequency-domain simulation of feedforward active noise control can be described by a multiple linear regression in which the predictor variables are transfer functions and the data being modeled are the open-loop responses of the system being controlled. Linear least-squares regression may be used to find control inputs that minimize a radiation-related cost function, but the results are subject to a type of numerical ill-conditioning known as collinearity. This article explores how collinearity enters an active control system, and describes a basic set of numerical diagnostic procedures that can be used to detect and analyze collinearity problems. Techniques are adapted from existing diagnostics developed in the statistics literature. Numerical results are given for a simple active structural-acoustic control system in which radiation from an axisymmetric cylindrical shell is controlled by oscillating forces applied on the shell.

INTRODUCTION

Recent work by the authors [1,2] examines feedforward active noise control from a statistical viewpoint, using tools developed in the statistics literature for linear least-squares regression. Feedforward active noise control can be simulated the frequency domain using the same mathematical formulation used for regression. The primary difference is that in active noise control the regression variables are complex-valued transfer functions rather than real-valued sequences of observations; in other words, each predictor variable is a complex-valued frequency-domain transfer function between an control input (actuator) and a set of observations (error sensor outputs). Given this similarity, one might logically assume that numerical difficulties commonly associated with regression might also appear in active noise control simulations. Such is the case with collinearity, the topic of the present work. Collinearity is a type of numerical ill-conditioning that occurs when one or more transfer functions, which can be thought of as vectors in M-dimensional space, are not orthogonal to one another. For example, if each actuator excites only one mode of the system with no spillover into other modes, then all the transfer functions will be mutually orthogonal. Since it is unlikely that the transfer functions in a real dynamic system will all be mutually orthogonal, collinearity is usually present to some degree. In fact, control simulations are perhaps more prone to collinearity than other regressions.

This paper describes how collinearity enters an active control system and how it can affect a feedforward control simulation. Also given is a basic diagnostic procedure for detecting and analyzing collinearity. The diagnostic procedure is presented as a step-by-step outline. It is shown that when the goal is only to detect collinearity rather than provide a detailed analysis, the procedure simply examines the condition number of a special scaled design matrix. Two references that provide a comprehensive discussion of collinearity diagnostics for real-valued regressions are Belsley, Kuh, and Welsch [3] and by Belsley [4]. All of the concepts presented in the present work are based on [4]. The extensions to complex-valued regressions are given in Miller [5].

For purposes of illustration, results are presented for an active structural-acoustic control (ASAC) problem in which radiation from a cylindrical shell is reduced by applying time-harmonic control forces and moments on the structure itself. The shell, shown in Fig. 1, is a finite-length cylinder with clamped, rigid end caps, material properties are chosen to represent a steel shell submerged in water. The entire analysis is conducted in the frequency domain, and the time dependence $e^{i\omega t}$ is omitted for brevity of notation. Structural dynamic response information for the fully coupled structure-fluid system is incorporated as frequency-domain transfer functions that are obtained numerically using a finite-element/boundary-element computer program.

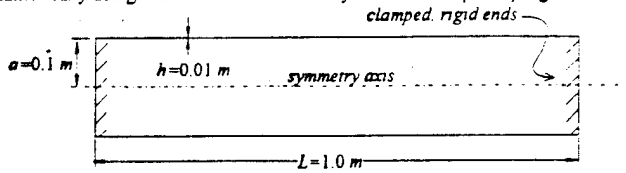

Figure 1: Example problem for collinearity diagnostics. Structure is a finite-length cylindrical shell with flat, rigid end caps that are clamped such that they cannot translate along the symmetry axis. Material properties are chosen to represent a steel shell submerged in water.

FEEDFORWARD CONTROL AS A MULTIPLE LINEAR REGRESSION

In multiple linear regression, one typically seeks a model $\hat{y}$ to approximate a dependent variable y. The model takes the form of a weighted sum of *predictor variables* X_i. Suppose the dependent and predictor variables contain a total of M observations written in vector form as $y=\{y_1 \;\; y_2 \;\; \ldots \;\; y_M\}^T$ and $X_i=\{X_{i1} \;\; X_{i2} \;\; \ldots \;\; X_{iM}\}^T$. We seek a set of *regression coefficients* b_i such that

$$\hat{y} = \sum_{i=1}^{N} b_i X_i \approx y. \tag{1}$$

Writing the regression coefficients as a vector $B=\{b_1 \;\; b_2 \;\; \ldots \;\; b_N\}^T$, we can define a *design matrix* $X=\{X_1 \;\; X_2 \;\; \ldots \;\; X_N\}$ and express the model as

$$\hat{y} = BX \approx y. \tag{2}$$

The most commonly used solution technique in statistical regressions is least squares, which seeks regression coefficients that minimize a weighted sum of the squared deviations between y and $\hat{y}$ at the M observation points. In other words, the regression coefficients must minimize a *cost function*

$$\chi^2 = \sum_{i=1}^{M} w_i |y_i - \hat{y}_i|^2 \tag{3}$$

where the w_i are weighting coefficients, usually set to unity. By defining a diagonal weighting matrix W containing the weighting coefficients w_i and requiring that the derivatives of χ^2 with respect to each of the b_i vanish, we obtain the $N \times N$ set of *normal equations* shown below, solution of which gives the desired regression coefficients B.

$$X^T W X B = X^T W y. \tag{4}$$

In feedforward control we know the *disturbance response* P, that is, the error sensor outputs from the disturbance acting alone. Also, we assume that the system is linear: the total response equals the disturbance response plus the *control response* $\hat{P}$, defined as the error sensor outputs from the actuators acting together but without the disturbance. The path between each individual actuator and the error sensor outputs is represented as a transfer function. The control response is a linear sum of all the transfer functions weighted by the associated actuator strengths or *control inputs*; we seek control inputs that minimize a radiation-related cost function. The direct analogies between feedforward control and multiple linear regression are as follows. The transfer functions between the actuators and error sensors are analogous to the predictor variables, X_i. The control inputs are analogous to the regression coefficients, and the desired control response is analogous to the model $\hat{y}$. Finally, dependent variable y equals the *negative* of the disturbance response. By choosing control forces such that $\hat{y}$ approximates $-y$, we cause the control response to "cancel" the disturbance.

Since most quantities of interest in vibrations and acoustics problems are complex-valued, we must formulate the regression using complex variables. It is straightforward to show [5] that the normal equations take the form

$$X^H W X B = X^H W y. \tag{5}$$

The physical significance of the cost function depends on how the variables and weighting coefficients are defined. If the error sensors measure farfield pressure, the cost function being minimized can be made to approximate the total radiated power by appropriate choice of sensor locations and weighting coefficients

Various statistical procedures used in statistical regressions have significance in simulating feedforward active control, for example, the F-test may be used to test the statistical significance of the simulation as a whole [1]. Of particular interest here is the idea that the variances of individual control input estimates may be calculated. If we assume the presence of Gaussian measurement noise in the error sensor data, we can calculate variances for each of the regression coefficients in the regression (which correspond to control inputs in an active control simulation.) The variance of the magnitude of the i^{th} control input is

$$\sigma_{b_i} = \sqrt{e_i} \tag{6}$$

where e_i is the i^{th} diagonal of the *variance-covariance matrix*

$$V(b) = \sigma_p^2 \left(X^H W X \right)^{-1} \tag{7}$$

and σ_p is the variance of the error sensor measurement noise. Note that a value for the error variance σ_p would be required to actually calculate the variances. For the present analysis it is not necessary to calculate variances directly, so the issue of choosing a value for σ_p is not addressed here.

COLLINEARITY IN FEEDFORWARD CONTROL

This section presents a brief example to show how collinearity can affect the results of an ASAC simulation, and discusses the role of approximate solution techniques in overcoming collinearity problems.

How collinearity enters a feedforward control problem

Suppose we apply two control forces at exactly the same location on the structure. Obviously their transfer functions are identical to each other, the normal equations are singular, and we have no unique solution for the control force magnitudes. Now suppose the two control forces are close together, but not quite collocated. Their transfer functions are similar, but not identical; the normal equation are ill-conditioned, but not quite singular. In fact, the possibility for such near-dependencies to cause ill-conditioning exists whenever the transfer functions are not all mutually orthogonal.

Suppose we plunge forward and solve the normal equation; what sort of solution can we expect? Often the adjacent (and partially redundant) control forces have opposite phases and very large magnitudes. In some circumstances this is purely a numerical artifact, the result of ill-conditioning of the normal equation. In other circumstances such results could be interpreted as a force couple approximating a concentrated moment, and there might be no indication of whether the solution was genuine or spurious. This disturbing ambiguity is the motivation for investigating collinearity diagnostics.

Control forces need not be located next to each other to produce collinearity. If the modal density is low and the structure is very lightly damped, there may be several locations at which applied forces would produce nearly the same response. Control forces applied at two or more such locations would produce collinearity even though they were distant from each other. Another source of collinearity arises when one control force can be replaced by a linear combination of other control forces in the system.

An example showing the effects of collinearity

A simple example shows how collinearity can affect even a relatively simple simulation. Consider the clamped cylinder (Fig. 1) with a disturbance force b_d, where b_d is a unit-magnitude, radially-directed, axisymmetric ring force applied near the left end cap. The disturbance excitation frequency is $k_o a$=0.95, where k_o is the acoustic wavenumber and a is the cylinder radius. Consider three control actuators b_1, b_2, and b_3, with locations to be discussed after performing a brief numerical experiment. The regression predicts that the control inputs reduce the radiated power by 23 dB. Since the F-test and t-test results appear reasonable, we accept as significant the following complex control inputs:

$$b_1 = (-18.1,-0.8) \quad b_2 = (-21.3,-2.2) \quad b_3 = (13.1.9,11.4) \tag{8}$$

where, for example, b_1=(-18.1,-0.8) means that $\mathrm{Re}\{b_1\}$=-18.1 N and $\mathrm{Im}\{b_1\}$=-0.8 N.

The purpose of the numerical experiment is to see how measurement noise in the error sensor data $Y=\{y_1, y_2, \ldots y_M\}$ affects the regression results. The method is to simulate the presence of measurement noise by artificially injecting various amounts of random noise into Y, recomputing the regression, and examining the control input magnitudes. The results are summarized in Table 1. The first pair of columns, labeled "No simulated noise," contains the original regression results given in Eq. (8). Next, each error sensor output y_i is perturbed with 0.5% simulated measurement noise, that is, a noise component with random phase and random magnitude up to 0.5% of the maximum value in Y, and the regression is recomputed using the perturbed Y. As shown in the second pair of columns in Table 1, 0.5% simulated measurement noise did not significantly change the predicted control inputs. Next we increase the simulated measurement noise to 5% and recompute the regression. As shown in the third pair of columns in Table 1, the control input magnitudes are changed by less than 2%. In fact, we can increase the simulated measurement noise to 25% or more before the control inputs change substantially. Thus the regression appears relatively insensitive to measurement noise.

Now consider another example in which we add a fourth control input b_4 to the configuration. (For the sake of illustration we choose a particularly bad location for b_4.) For the new configuration with no simulated measurement noise, we predict that the control inputs reduce the radiated power by 29 dB, an improvement of 6 dB over the previous case. Again the F-test and t-test results appear reasonable, so we accept as significant the control inputs shown in the first pair of columns in Table 2. As in the previous example, we add simulated measurement noise to Y and recompute the regression. But now, even with an error of only 0.5%, we see changes of up to 5% in the predicted control inputs. If we increase the simulated measurement noise to 5%, the control inputs are all but unrecognizable, although somehow the third input seems less drastically affected. Still, the F-test and t-test show no signs of trouble, and the subroutine used to solve the normal equation gives no warning or error messages. Why is the solution so sensitive to measurement noise? The reason, of course, is collinearity between the particular control forces we chose.

Table 1: Effect of simulated measurement noise without collinearity.

	No simulated noise		0.5% simulated noise		5.0% simulated noise	
	b_i	$\Delta\lvert b_i\rvert$	b_i	$\Delta\lvert b_i\rvert$	b_i	$\Delta\lvert b_i\rvert$
b_1	(-18.1,-0.8)	–	(-18.0,-0.8)	<0.5%	(-17.7,-0.8)	2%
b_2	(-21.3,-2.2)	–	(-21.3,-2.2)	<0.5%	(-21.0,-2.2)	1%
b_3	(131.9,11.4)	–	(131.9,11.4)	<0.5%	(131.8,11.3)	1%

Table 2: Effect of simulated measurement noise with collinearity.

	No simulated noise		0.5% simulated noise		5.0% simulated noise	
	b_i	$\Delta\lvert b_i\rvert$	b_i	$\Delta\lvert b_i\rvert$	b_i	$\Delta\lvert b_i\rvert$
b_1	(-627.7,-37.0)	–	(-604.5,-49.0)	5%	(-195.1,-78.9)	67%
b_2	(613.5,36.1)	–	(589.7,48.5)	2%	(164.9,78.2)	70%
b_3	(117.3,9.6)	–	(118.1,9.4)	1%	(128.2,9.6)	9%
b_4	(24.1,1.4)	–	(23.2,1.9)	2%	(7.0,3.1)	68%

If we now examine the locations of the control inputs, shown in Fig. 2, we can clearly see why we encounter numerical difficulties. The first two inputs, b_1 and b_2, are axisymmetric ring-forces at δ=0.17 and δ=0.31, respectively, while b_3 is a distributed axisymmetric ring-force. But the control input used in the second example, b_4, is an axisymmetric ring-moment applied at δ=0.25, exactly between b_1 and b_2. The two ring-forces, when combined with opposite phases, produce a force couple that has nearly the same effect as the ring-moment. The ring-moment is redundant, and in this simple example can easily be seen as the cause of the numerical problems. The collinearity diagnostics presented in the next section provide a general method that could be used to detect and analyze collinearities in more complicated systems where relations between actuators might not be so clear.

The role of approximate solution techniques

Generally some redundancy between the variables is unavoidable, and must be expected and planned for in one of several ways. One method, discussed in the next section, uses collinearity diagnostics to analyze sources of collinearity and suggest strategies for removing collinearity from the problem. Another method is to simply

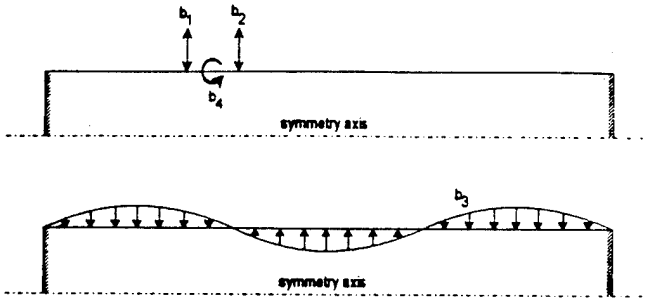

Figure 2: Locations of actuator forces. Axisymmetric ring-forces b_1 and b_2 are applied at δ=0.25 and δ=0.31. An axisymmetric distributed force b_3=cos(3$\pi\delta$) is distributed over the length of the cylinder. An axisymmetric ring moment b_4 is applied at δ=0.31.

circumvent the effects of collinearity by employing an approximate solution method to solve the normal equations. The former method appears to be the more appropriate: merely solving the normal equations does not eliminate the collinearity problem, and does nothing to illuminate its causes and possible solutions. However, if the situation at hand requires no more than workable solutions to the normal equations, the latter method may be used. Two examples exist in the literature, and are described below.

Rosenthal [6] finds approximate solutions to the normal equations by using singular-value decomposition (SVD). The SVD approach, described in [7], provides an approximate solution that minimizes the length of the solution vector. This has an interesting interpretation in the context of ASAC, since the length of the solution vector is a measure of the amount of control effort expended. The SVD method also provides convenient access to the covariances. A drawback of using SVD is that one must manually decide on a threshold beyond which singular values are discarded, and the threshold is somewhat problem-dependent. Nevertheless, the SVD provides a way to solve the normal equations in the presence of collinearity, and the singular vectors may have interesting physical interpretations as well.

Nelson and Elliott [8] discuss the use of iterative gradient descent techniques as an approximate solution technique for time-domain problems. Iterative techniques are able to find a reliable and stable solution to the normal equations even in the presence of collinearity. They are computationally efficient for practical applications, in which the problem parameters may be slowly varying in time. Also, they do not require the user to select a threshold value as in SVD, although the user must determine when to discontinue the iterations.

A COLLINEARITY DIAGNOSTIC

Rather than trying to present a comprehensive review of collinearity diagnostics and their possible applications in studying feedforward control, this section presents one diagnostic method with some basic example results. For more detail the reader is referred to Belsley [4].

Background discussion

Recall the normal equation for a feedforward control system with M sensors and N actuators,

$$\left(X^H W X\right) B = X^H W Y. \tag{9}$$

As the reader might expect, most collinearity diagnostics involve the condition number of $X^H W X$, the matrix product found in the left-hand side of Eq. (5). Clearly a large condition number announces the presence of ill-conditioning, but simply examining the condition number leaves unanswered three questions. First, how can we detect whether more than one near-dependency is present? Second, how large a condition number can we tolerate and still have confidence in the regression results? And third, how can we determine which variables (or, in the context of feedforward control, which control inputs) are involved in near-dependencies? We will briefly discuss these three questions before presenting the diagnostic method.

The first question, regarding the number of near-dependencies present, is answered by examining not just the condition number of $X^H W X$ but the eigenvalues of $X^H W X$. We accomplish this by examining the singular-value decomposition of $W^{1/2} X$, since the singular values of $W^{1/2} X$ are the positive square roots of the eigenvalues of $X^H W X$. A zero singular value indicates a perfect linear dependency in $W^{1/2} X$, a "small" singular value indicates a

near-dependency that may cause conditioning problems. Furthermore, as discussed below, the number of "small" singular values indicates how many near-dependencies are present in the problem. The second question seeks a way to make quantitative comparisons to determine whether the condition number is too large, or equivalently, whether a given singular value is too small. The answer lies in scaling the columns of $W^{1/2}X$ before computing the singular values; with proper scaling, the singular values may be interpreted in a way that permits quantitative comparisons. To answer the third question of determining which variables are involved in near-dependencies, we turn to a result from least-squares regression. As described above, standard regression procedures may be used to calculate the variances of the individual control inputs. One of the effects of collinearity is variance inflation when two or more actuators are involved in a near-dependency, their variances become large. The variances can be expressed in a form that illuminates their relationships with the singular values of $W^{1/2}X$. By examining these relationships, it is possible to determine which actuators are involved in near-dependencies.

The following sections describe the diagnostic method in somewhat of a cookbook fashion. The intent is not to present a detailed derivation, but rather to outline the method and show a simple numerical example related to feedforward control. The techniques of [4] are modified slightly to account for complex-valued variables and weighted least squares, which are not included in [4].

Step 1: Determine $W^{1/2}X$

Each column of $W^{1/2}X$ represents a transfer function between a given control input and the array of observation points (error sensor outputs). These may be obtained via analytical approximations, numerical calculations, or any other means available. For N actuators and M sensors, X has the form

$$X = \{X_1 \quad X_2 \quad \cdots \quad X_N\} \tag{10}$$

where X_j is a complex vector of length M containing the transfer function for the j^{th} actuator, and W is the weighting matrix. In our example the columns of X are transfer functions between the four control inputs and the farfield pressure at 25 sensor locations, thus N=4 and M=25. Transfer functions for the fluid-loaded cylindrical shell were obtained by numerical modeling of the structure-fluid system using a finite-element/boundary-element approach.

Step 2: Apply column-equilibration to $W^{1/2}X$

The purpose of column-equilibration is to produce a set of singular values that do not depend on the units of the problem. We scale each column in $W^{1/2}X$ to have unit vector length after scaling. This produces a new matrix Z, the scaled weighted design matrix:

$$Z = \Omega^{-1/2} W^{1/2} X, \tag{11}$$

where $\Omega^{-1/2}$ is a diagonal matrix whose diagonals are $\Omega_j^{-1/2} = \left\{X_j^H W X_j\right\}^{-1/2}$. The relation between Z and the original problem may be seen from

$$X^H W X = Z^H \Omega Z \tag{12}$$

Step 3: Obtain scaled condition indexes and variance-decomposition proportions

First we generate the singular-value decomposition of Z,

$$Z = UDV^H, \tag{13}$$

where U is column-orthogonal, V is column- and row-orthogonal, and D is non-negative and diagonal. (Note the distinction between the matrix V and the variance V). The elements of D are the singular values μ_k, k=1,2...N, which are real and non-negative since Z is Hermitian. The *scaled condition indexes* are then defined as

$$\tilde{\eta}_k = \frac{\mu_{max}}{\mu_k}, \quad k = 1,2...N. \tag{14}$$

If we express the elements of the matrix V as v_{kj}, we can write the variances in the following useful form.

$$V(b_k) = \sigma_p^2 \sum_{j=1}^{N} \frac{v_{kj}^2}{\mu_j^2} \tag{15}$$

The utility of Eq. (15) lies in the fact that each term in the summation is associated with only one scaled condition index $\tilde{\eta}_k$. By noting which of the "large" scaled condition indexes affect which variances, we can pick

out near-dependencies among the columns of $W^{1/2}X$. To this end, let us define *variance-decomposition proportions*,

$$\pi_{jk} \equiv \frac{\gamma_{kj}}{\gamma_k}, \quad k = 1,\ldots N., \tag{16}$$

where

$$\gamma_{kj} \equiv \frac{v_{kj}^2}{\mu_j^2} \quad \text{and} \quad \gamma_k \equiv \sum_{j=1}^{N} \gamma_{kj}, \quad k = 1,\ldots N. \tag{17}$$

The variance-decomposition proportions are interpreted as follows: π_{jk} is the portion of the variance for the k^{th} regression coefficient that is associated with the j^{th} scaled condition index.

Table 3 contains the scaled condition indexes and variance-decomposition proportions for the example problem of Fig. 2. The second column contains the scaled condition indexes ranked by size, with the largest shown in the last row. The remaining four columns contain the variance-decomposition proportions for each of the control forces b_1, b_2, b_3, and b_4. The next sections explain how to interpret Table 3.

Table 3: Variance decomposition proportions for example problem

j	$\tilde{\eta}_j$	π_{j1}	π_{j2}	π_{j3}	π_{j4}
1	1.0	.000	.000	.000	.000
2	1.1	.000	.000	.000	.000
3	6.3	.000	.000	.871	.000
4	11502.1	.999	.999	.129	.999

Step 4: Determine the number of near-dependencies.

The method for counting the number of near-dependencies involves choosing a threshold $\tilde{\eta}^*$ such that when $\tilde{\eta}_{max} < \tilde{\eta}^*$, the columns of $W^{1/2}X$ may be said to be free of collinearity. The value suggested by Belsley [4],

$$\tilde{\eta}^* = 30, \tag{18}$$

is used in the present work although slightly larger or smaller values could also be argued for. Having chosen a threshold value for $\tilde{\eta}^*$, we now have the most basic collinearity diagnostic: whenever $\tilde{\eta}_{max} < \tilde{\eta}^*$, at least one near-dependency is present and the regression should not be used without further examination of its collinearity properties. Thus, $\tilde{\eta}_{max}$ should be computed as a routine part of every regression. Note that the matrices involved are of order N, where N is usually small enough that negligible effort is required to compute $\tilde{\eta}_{max}$.

If more than one scaled condition index exceeds the threshold $\tilde{\eta}^*$, then multiple near-dependencies are present. The number of near-dependencies is determined according to the so-called "progression of 10/30": the first near-dependency corresponds to the first $\tilde{\eta}$ >30; the second near-dependency corresponds to $\tilde{\eta}$ >100, the third to $\tilde{\eta}$>300, the fourth to $\tilde{\eta}$>1000, and so forth. For example, the sequence of scaled condition indexes (1, 9, 33, 35) indicates only one near-dependency since there is at least one index greater than 30. On the other hand, the sequence (1, 9, 33, 105, 108) indicates two near-dependencies because there are indices greater than 30 and greater than 100.

Referring to the first column of Table 3, it is evident that only one scaled condition index exceeds $\tilde{\eta}^*$, so we conclude that only one near-dependency is present in the example.

Step 5: Determine actuator involvement

To determine which actuators are affected by a near-dependency, we examine the variance-decomposition proportions π_{jk}. Having associated a particular $\tilde{\eta}$ with a near-dependency, we examine the π_{jk} in that row of the table. If two or more actuators have π_{jk} in that row larger than some threshold value π^*, then those actuators are involved in the near-dependency. The value of π^* suggested by Belsley [4] and used in our example is

$$\pi^* = 0.5. \tag{19}$$

In Table 3 we examine the last row since that row is associated with a near-dependency. Noting that the π_{jk} for b_1, b_2, and b_4 are all well above π^*, it appears that these actuators are involved in the near-dependency.

(Recall that b_1 and b_2 are the ring-forces and b_4 is the ring-moment.) The third actuator b_3, with π_{j4}=0.129, is not involved in the near-dependency. When multiple near-dependencies are present, the rules for determining actuator involvement are somewhat more complicated and need not be discussed here to illustrate the basic technique. Again, the interested reader is invited to examine Belsley [4].

Step 6: Determine auxiliary regressions

Once it is known which actuators are involved in a near-dependency, the individual transfer functions can be regressed against each other to determine the relationships between them. Here the actuators b_1, b_2, and b_4 are involved in a near-dependency. Setting up a new regression using b_4 as the disturbance input with b_1 and b_2 as control inputs would show that b_1 and b_2 together can reproduce b_4 almost exactly (as is obvious from physical considerations.) Thus the control input b_4 could be removed to obtain a more stable regression result.

Step 7: Determine unaffected actuators

When an actuator associates most of its variance with "small" values of $\tilde{\eta}$, we can consider that actuator to be uninvolved with any near-dependency. To be more precise, when the total proportion of variance associated with "small" $\tilde{\eta}^*$ is less than π^*, that actuator is not involved with any near-dependency. In the example problem, the variance of b_3 is associated almost entirely with the first three small $\tilde{\eta}^*$, and therefore we conclude that it is not involved in any near-dependency. This is supported by the fact that b_3 was the least affected by the simulated measurement noise introduced in the example discussed earlier.

SUMMARY

The collinearity problems common in multiple linear regressions can occur when regression is used for a numerical simulation of feedforward active control in the frequency domain. Without proper collinearity diagnostics, numerical problems can go undetected and produce results that are very sensitive to measurement noise in the error sensors. Collinearity diagnostics can detect and analyze numerical ill-conditioning. Collinearity diagnostics for complex-valued regressions follow directly from their real-valued counterparts, which are developed in considerable detail in the statistics literature.

The primary collinearity diagnostic is the scaled condition number. Scaling allows for a quantitative comparison between the scaled condition number and a predetermined threshold value to determine whether or not collinearity is present. Even when no other collinearity diagnostics are performed, the analyst may compute the scaled condition number for each regression and compare it to the threshold value in a somewhat mechanical fashion. If the scaled condition number exceeds the threshold, the regression should be discarded because of collinearity. More detailed diagnostics are available for determining the number of near-dependencies and which control forces are involved. These diagnostics are less mechanical, requiring more interaction on the part of the analyst; however, they may provide insights when investigating complicated control systems.

ACKNOWLEDGMENTS

The authors gratefully acknowledge support from Carderock Division, Naval Surface Warfare Center and from the Office of Naval Research (Grant no. ONR-N00014-88-K-0721). The authors also thank Dr. Alan Miller (CSIRO) and Dr. Kenneth White (University of British Columbia) for generously providing advice concerning regression and general statistical considerations.

REFERENCES

[1] C.E. Ruckman, "A regression-based approach for simulating active noise control in the frequency domain, with application to fluid-structure interaction problems," Unpublished doctoral dissertation (expected March 1994).

[2] C.E. Ruckman and C.R. Fuller, "Optimizing actuator locations in feedforward control systems using subset selection," Proc. 2nd Conference on Recent Advances in Active Control of Sound and Vibration **Supplement**, pp.S122-S133 (1993).

[3] D.A. Belsley, E. Kuh and R.E. Welsch, *Regression diagnostics: Identifying influential data and sources of collinearity*, Wiley, New York (1980).

[4] D.A. Belsley, *Conditioning diagnostics: collinearity and weak data in regression*, John Wiley & Sons, Inc., New York (1991).

[5] K.S. Miller, "Complex linear least squares," SIAM Review, **15**(4), pp.707-726 (1975).

[6] F. Rosenthal, "A new technique for the active cancellation of wide-band noise using multiple sensors," Proc. 2nd International Congress on Recent Developments in Air- and Structure-borne Sound and Vibration, 1, pp.337-344 (March, 1992).

[7] W.H. Press, B.P. Flannery, S.A. Teukolsky and W.T. Vetterling, *Numerical Recipes: The Art of Scientific Computing, 2nd Ed.*, Cambridge University Press, Cambridge (1989).

[8] P.A. Nelson and S.J. Elliott, The Active Control of Sound, Academic Press, London (1992).

C-49 Optimum Design of Feedforward Active Structural Acoustic Control of Complex Structures, H. M. Rodriguez, R. A. Burdisso and C. R. Fuller, Proceedings of ACTIVE 95, The 1995 International Symposium on Active Control of Sound and Vibration, Newport Beach, CA, pp. 335-346, 6-8 July 1995.

Newport Beach, CA, USA
ACTIVE 95
1995 July 06–08

OPTIMUM DESIGN FOR FEEDFORWARD ACTIVE STRUCTURAL ACOUSTIC CONTROL OF COMPLEX STRUCTURES

Héctor M. Rodríguez
Ricardo A. Burdisso
Chris R. Fuller

Vibration and Acoustics Laboratories
Department of Mechanical Engineering
Virginia Polytechnic Institute and State University
Blacksburg, Virginia 24061-0238

INTRODUCTION

Active structural acoustic control (ASAC), where the acoustic response produced by a vibrating structure is minimized by applying the control inputs directly to the structure [1], has been demonstrated to be more effective than traditional active noise control (ANC) approaches for the abatement of structurally radiated noise [2]. The typical ASAC design approach, in particular for simple structures, consists in selecting the actuators and sensors based on some physical understanding of the uncontrolled system such as placing the control inputs at the antinodes of the most efficient modes [3-6]. More recent investigations have shown that using this simplistic design approach for the case of more complex structures could result in a inefficient control system with a large number of control inputs [7-8]. Wang et. al. investigated the optimum location of rectangular PZT actuators with fixed microphones as error sensors to minimize the radiation from a simply supported plate excited at a single tone [7]. It is demonstrated in this work that optimally located actuators provide a far better sound reduction, at both on and off resonance excitations, than actuators whose position are chosen based in some physical consideration. In the same way, Clark and Fuller studied the optimization of location of PZT actuators and both the size and location of Polyvilydene Fluoride (PVDF) structural sensors [8]. Analytical and experimental results confirm the previous results from Wang et. al. [7]. A single optimally located actuator/sensor pair rivals the sound reduction obtained with three arbitrarily located actuators and sensors and three error microphones. However it is clear from Clark's results using PVDF sensors that in order to implement structural sensors for ASAC applications an efficient design procedure is critical due to the inability of structural sensors to measure directly the acoustic response, which is the variable to minimize in structural acoustic applications.

There are several drawbacks in these optimization procedures that prevent the same approaches to be implemented in complex realistic structures. First, only simple systems, where analytical predictions for structural and acoustic response exist, have been used. Real industrial structures will require numerical approaches to obtain the necessary responses. Both Wang and Clark have used the mean square value of the sound pressure as a function of the physical characteristics of the transducers as a cost function and finite differences techniques in the sensitivity computation. Therefore, the acoustic response needed to be computed many times during the optimization process. The estimation of the acoustic response by numerical techniques represents a lengthy procedure, hence their approach resulted in an inefficient and impractical design formulation for complex structures and excitations.

In this paper, an efficient design formulation for feedforward ASAC of complex structures and disturbances is presented. The approach consists in a two-stage multi-level optimization scheme. The formulation takes advantage of the fact that both the structural response and the acoustic radiation from a controlled structure can be completely defined in terms of modal quantities. All the physical parameters that define the control inputs and the error sensors have their counterpart in the modal domain through the unit modal control forces and the modal error sensor components, respectively. Therefore, the upper level of the optimization is defined in the modal domain and solves for the optimum unit modal control forces and modal error sensor components that minimize the total radiated power, expressed in terms of modal quantities. Then, these optimum unit modal control forces and modal error components are used in a set of lower level optimization problems to determine the physical characteristics of the actuators and sensors to be implemented. A finite element model is used to obtain the natural frequencies, mode shapes and modal disturbance forces of the system. The computed mode shapes are used in turn in a boundary element model to provide the acoustic radiation due to each mode. This modal domain information, i.e. natural frequencies, mode shapes, modal disturbances and modal acoustic pressures, is the only input that is needed to formulate the problem in the upper level optimization and has to be computed only once during the design process. Therefore, the formulation permits that any complex structure could be analyzed in an efficient manner. The proposed approach is demonstrated for the case of a simply supported cylinder excited by a point force. Several different control system configurations are investigated. It is shown that the proposed approach represent an efficient way of designing ASAC systems.

FEEDFORWARD STRUCTURAL ACOUSTIC CONTROL

In feedforward structural-acoustic control, the response of a system due to an input disturbance $F(\omega)$ is reduced by applying secondary control inputs $U_k(\omega)$ as shown in figure 1. The control inputs are obtained by feeding forward a reference signal fully coherent to the input disturbance into the compensators $G(\omega)$. This reference signal is assumed to be obtained by tapping the disturbance input. The compensators are designed such that the output from the error sensors $E_s(\omega)$ is minimized. Assuming that the disturbance input is stationary, the analysis is performed in the frequency domain by taking the Fourier Transform (FT) of any time dependent variable.

Structural Response. The structural response can be obtained by modal superposition after solving the eigenvalue problem, i.e. natural frequencies and mode shapes. For the case of a complex system, these natural frequencies and mode shapes can be obtained by using numerical techniques such as the finite element method (FEM). For the case of sound radiation from structural systems submerged in light fluids (e.g. air), it is necessary to consider only the vibration in which the response normal to the radiating surface

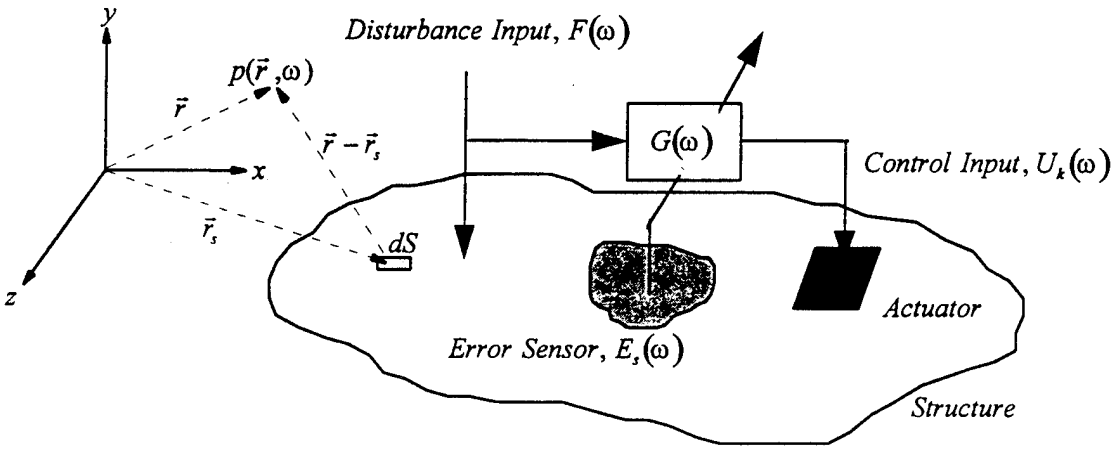

Figure 1. Feedforward structural-acoustic control arrangement.

is dominant [9]. After solving for the natural frequencies and mode shapes, the FT of the response in the normal direction at any location $\vec{r}_s$ over the structural domain can be obtained as a linear combination of the modes as

$$w(\vec{r}_s,\omega) = \sum_{n=1}^{N} q_n(\omega)\phi_n(\vec{r}_s) \tag{1}$$

where $\phi_n(\vec{r}_s)$ is the component normal to the surface of the n^{th} mass normalized mode shape, $q_n(\omega)$ is the FT of the n^{th} modal displacement, N is the total number of modes included in the analysis, and ω is the excitation frequency. The modal displacement $q_n(\omega)$ is expressed as

$$q_n(\omega) = \left(F(\omega)\cdot f_n + \sum_{k=1}^{N_c} U_k(\omega)\cdot u_{nk} \right) \cdot H_n(\omega) \tag{2}$$

where $F(\omega)\cdot f_n$ and $U_k(\omega)\cdot u_{nk}$ are the modal domain forces applied to the n^{th} mode due to the disturbance force and the k^{th} control input, respectively, and N_c is the total number of control inputs. The unit modal forces (f_n and u_{nk}) serve as weighting coefficients that dictate how much force is applied to each mode and are related to the physical implementation of the forces. For example, point forces will result in the unit modal forces to take the value of the mode shape at the force location. Similarly, distributed strain induced actuators will yield modal parameters related to the first derivative of the mode shapes [10]. Finally, $H_n(\omega)$ is the n^{th} modal frequency response function which is defined as

$$H_n(\omega) = \left(\omega_n^2 - \omega^2 + 2j\,\beta_n\omega_n\omega\right)^{-1} \tag{3}$$

where ω_n is the n^{th} natural frequency, β_n is the n^{th} modal damping ratio, and j is the imaginary number. Equation (1) represents the controlled response of a vibrating structure. The uncontrolled response is obtained by simply setting the control inputs $U_k(\omega)$ to zero in eq. (2).

Optimum Control Inputs. The complex amplitude of the control inputs $U_k(\omega)$ are obtained by minimizing a quadratic cost function of a measurable response quantity. This cost function, which is referred here as the *control cost function*, is defined as the sum of the mean-square-value (msv) of the error sensor outputs. That is

$$C = \sum_{s=1}^{N_s} \int_{-\infty}^{+\infty} E_s(\omega)E_s^*(\omega)d\omega \tag{4}$$

where $E_s(\omega)$ is the Fourier transform of the s^{th} error sensor output, N_s is the total number of error sensors, and (*) denotes the complex conjugate.

It is assumed that only structural error transducers are considered. Thus the error variable can always be expressed as a linear combination of modal terms as [11,12]

$$E_s(\omega) = \sum_{n=1}^{N} q_n(\omega)\xi_{ns} \tag{5}$$

where ξ_{ns} is the n^{th} modal error component of the s^{th} error sensor. Again, the modal error components are related to the physical implementation of the transducers. A discrete sensor such an accelerometer will yield a modal error component that is the value of the mode shape at the sensor's location.

As it is shown in the literature, the *control cost function* in eq. (4) is a positive definite function with respect to $U_k(\omega)$, and therefore there exists only one minimum [13]. By differentiating eq. (4) with respect to the real and imaginary part of the control forces $U_k(\omega)$ and setting them to zero, it can be shown that the set of the optimum control inputs at a single frequency is the solution of the following linear system of equations

$$[T(\omega)]\{U(\omega)\} = -F(\omega)\{B(\omega)\} \tag{6}$$

where matrix $[T(\omega)]$ contains the transfer functions between the control inputs and error outputs and has dimension N_sxN_c, and the elements of vector $\{B(\omega)\}$ are the transfer functions between the disturbance and the error outputs. The (s,k) element of matrix $[T(\omega)]$ and the s element of vector $\{B(\omega)\}$ are computed as

$$T(s,k) = \sum_{n=1}^{N} u_{nk}\xi_{ns}H_n(\omega)$$
$$B(s) = \sum_{n=1}^{N} f_n\xi_{ns}H_n(\omega) \tag{7a,b}$$

From eqs. (1) and (6), it is clear that the response of both the controlled and uncontrolled system can be expressed in terms of modal parameters where the control inputs and error sensors are defined in terms of the unit modal control forces u_{nk} and the modal error sensor components ξ_{ns}, respectively.

Acoustic Response. The acoustic radiation from a vibrating structure can be estimated after solving the boundary integral formulation of the Helmholtz wave equation. For the case of complex structures this equation is solved using numerical techniques. The Indirect Boundary Element Method (IBEM) estimates the acoustic radiation at any external field point of the vibrating structure after solving the modified integral equation [14]

$$p(\vec{r},\omega) = \int_S \mu(\vec{r}_s,\omega)\cdot\frac{\partial G(\vec{r}_s,\vec{r})}{\partial \vec{n}} - G(\vec{r}_s,\vec{r})\cdot\sigma(\vec{r}_s,\omega)\,dS \tag{8}$$

where $\mu(\vec{r}_s,\omega)$ and $\sigma(\vec{r}_s,\omega)$ represent the differences or "jumps" of the acoustic pressure and the normal velocities between the external part and the internal part of the structural surface S, respectively; $\vec{n}$ is an outward normal directional vector and $G(\vec{r}_s,\vec{r})$ is the 3-D Green's function that has the form

$$G(\vec{r}_s,\vec{r}) = \frac{e^{-jk|\vec{r}-\vec{r}_s|}}{4\pi\cdot|\vec{r}-\vec{r}_s|} \tag{9}$$

in which $k=\omega/c$ is the acoustic wave number, c is the phase speed in the fluid, and $|\vec{r}-\vec{r}_s|$ is the distance between the external field points and the points over surface. Equation (8) is usually solved in conjunction with the *Neumann* and *Sommerfeld* boundary conditions [14]. The *Neumann* condition relates the gradient of the acoustic pressure over the surface of the structure to the normal structural velocity as

$$\frac{\partial\, p(\vec{r}_s,\omega)}{\partial\, \vec{n}} = \rho\omega^2 w(\vec{r}_s,\omega) \tag{10}$$

where ρ is the fluid's density. The *Sommerfeld* boundary condition implies that energy can only flow from the vibrating structure towards infinity. In order to estimate the acoustic radiation at any field point $p(\vec{r},\omega)$, the formulation first compute the quantities $\mu(\vec{r}_s,\omega)$ and $\sigma(\vec{r}_s,\omega)$ on the basis of the known *Neumann* boundary condition.

By substituting the modal expansion solution of eq. (1) into the *Neumann* boundary condition in eq. (10), the acoustic pressure field can also be obtained as a linear contribution of the structural modes as

$$p(\vec{r},\omega) = \sum_{n=1}^{N} q_n(\omega)\,p_n(\vec{r},\omega) \tag{11}$$

where for a particular frequency ω the modal pressure $p_n(\vec{r},\omega)$ can be easily estimated from the BEM code considering the modal distribution $\phi_n(\vec{r}_s)$ as the surface normal response in eq. (10).

The total acoustic radiated power can be estimated by integrating the acoustic time average intensity over a sphere of area A that surrounds the structure as

$$\Pi(\omega) = \int_A \frac{|p(\vec{r},\omega)|^2}{2\rho c} dA \tag{12}$$

Replacing eq. (11) into (12) gives

$$\Pi(\omega) = \{q(\omega)\}^H [\mathrm{K}(\omega)]\{q(\omega)\} \tag{13}$$

where H implies conjugate transpose and the elements of matrix [K(ω)] are

$$\kappa_{mn}(\omega) = \int_A \frac{p_m(\vec{r}_f,\omega)p_n^*(\vec{r}_f,\omega)}{2\rho c} dA \tag{14}$$

The diagonal elements of the matrix [K(ω)] represent the power radiated by each one of the modes while the off-diagonal terms is the radiated power due to the coupling of the modes.

Equation (13) defines the total radiated power at a single frequency. The general case of multiple frequency excitations is expressed as a linear combination of the contributions due to each frequency as

$$\Pi_T = \sum_{i=1}^{NF} \left(\{q(\omega_i)\}^H [\mathrm{K}(\omega_i)]\{q(\omega_i)\} \right) = \sum_{i=1}^{NF} \Pi(\omega_i) \tag{15}$$

where NF is the total number of frequencies.

As can be seen from eqs. (11) and (13) the acoustic response is directly affected, through the modal displacements $q_n(\omega)$, by the vibration of the structure. This relationship between the structural and acoustical responses contains the essence of the ASAC technique, that is the acoustic radiation is controlled by modifying the vibration behavior of the structure. Therefore, the main task in the ASAC design is the proper selection of the type, size, number and location of the actuators and sensors that will modify the structural response in such way that the desired acoustic response is minimized. In the next section a multi-level optimization procedure is proposed for the optimum selection of these control system components.

DESIGN APPROACH: MULTI-LEVEL OPTIMIZATION

In multi-level optimization a complex problem is broken into a set of simpler problems that offers computational advantages. The process of decomposition consists of separating the optimization process in an upper level problem, in which a global cost function is minimized with respect to global design variables, and a set of lower level problems, in which a set of local design variables are related to each global design variable. From eqs. (1), (6), (11) and (15), it is clear that the structural and acoustic responses, both before and after control, can be computed without any knowledge of the physical characteristics of the transducers, i.e. only modal domain information is required. Based on this, a two-level optimization formulation is ideal for the design of feedforward control systems. Since the physical design variables of the control system can be completely defined as modal quantities it brings out the possibility of separating the design process into an upper level or modal domain optimization and a set of lower level or physical domain optimizations.

The total radiated acoustic power expressed in terms of the modal quantities u_{nk} and ξ_{ns} as in eq. (15), is selected as the *global cost function* to be minimized in the upper level or modal domain. The global design variables in the upper level are the unit modal control forces u_{nk} and the modal error sensor components ξ_{ns}. The physical parameters that define the actuators and sensors to be implemented, i.e. size, location, etc., are the local design variables in the lower level or physical domain problems. Each lower level problem will consist in finding the optimum physical parameters or local variables for each actuator and sensor that best match the optimum unit modal control forces u_{nk} and modal error sensor components ξ_{ns}, respectively.

Some of the advantages of this approach over the previous optimization attempts could be summarized as follows: (1) the design process is broken into two simpler problems; (2) since the upper level optimization is performed in the modal domain, the formulation is applicable to any structure modeled using FE/BE codes; (3) the highest computational cost in this upper level is related to the estimation of the matrices $[K(\omega_i)]$ in eq. (15) and is carried out only once; (4) the optimum modal control parameters are determined after solving a simple continuos optimization problem, therefore different arrangements in the number of control and error signals (control system configurations) can be investigated with a low computational cost; and finally (5) once these optimum modal quantities are obtained in the upper level, different types of actuators and error sensors can be investigated in the lower level optimization without the need of any further expensive computation. The focus of this paper is to present the upper level or modal domain design formulation. The lower level optimization will be addressed in future publications.

Modal Domain or Upper Level Optimization. As mentioned before, the modal domain or upper level optimization consists in solving for the optimum modal control forces u_{nk} and the modal error sensor components ξ_{ns} that will minimize the total radiated power. A straightforward approach to solve this problem could be to minimize the expression in eq. (15) as a function of the design variables u_{nk} and ξ_{ns}. This results in a continuous unconstrained optimization problem that could be solved by any gradient search technique such as a Newton or Quasi-Newton Method [15]. The major drawback of this approach is that it does not provide any bound in the amount of the required control input. It is most likely that the optimum solution of this unconstrained problem will be at the expense of a great amount of input energy through the control forces, which is an aspect of major concern if an optimum control system is desired.

The modal domain optimization problem is better expressed as

$$
\begin{aligned}
&Min\ \Pi_R = \frac{\Pi_{TC}}{\Pi_{TU}} \\
&such\ that: \sum_{n=1}^{N} \frac{\left|U_k(\omega_i)\cdot u_{nk}\right|^2}{\left|F(\omega_i)\cdot f_n\right|^2} \le \lambda_m \qquad k=1,..,N_c;\ i=1,..,NF \\
&\sum_{n=1}^{N} u_{nk}^2 = 1 \qquad\qquad k=1,..,N_c \\
&\sum_{n=1}^{N} \xi_{ns}^2 = 1 \qquad\qquad s=1,..,N_s
\end{aligned}
\tag{16}
$$

This formulation seeks to minimize the ratio Π_R of the total radiated power of the controlled system Π_{TC} to the total radiated power of the uncontrolled system Π_{TU}. The inequality constraints impose restrictions in the control effort in the modal domain. By having the penalty parameter λ with a value less than one it is implied that the modulus square of each one of the modal control forces $(U_k(\omega_i)\cdot u_{nk})$ will be, in average, less than the modulus square of the modal disturbances $(F(\omega_i)\cdot f_n)$. There is an inequality constraint of this type for each one of the N_c control inputs at each one of the NF frequencies ($m=N_c\times NF$). The equality constraints imply a normalization of the design variables since the only relevant information is their relative values, which defines the relative controllability and observability of the modes, respectively.

By minimizing the ratio Π_R in eq. (16), instead of minimizing directly the radiated power of the controlled system Π_{TC}, the cost function will always acquire a value between zero and one. In the same way, the equality constraints will keep the values of the design variables between -1 and 1. The reason for these normalizations is related to the implementation of numerical algorithms to solve optimization problems. Within optimization routines, convergence tolerances and other criteria are necessarily based

upon an implicit definition of "small" and "large", and thus variables with widely varying orders of magnitude may cause difficulties for some algorithms [15].

This upper level or modal domain optimization is solved using the Goal Attainment Method of Gembicky [16]. This method is a multi-objective optimization procedure in which the cost function and the constraints are both expressed as design objectives with individual goals to reach. The advantage of this method over other conventional nonlinear constrained optimization routines is that instead of having to satisfy hard constraints it allows the design goals to be under or over achieved. Therefore, it is always possible to obtain a solution even if the constraints are violated.

NUMERICAL EXAMPLE

The applicability of the formulation presented here is demonstrated for the ASAC of a simply supported cylinder driven by a multiple-frequency point disturbance as shown in figure 2. In order to keep the solution of the numerical acoustics problem simple, and avoid any irregular frequency [14], the cylinder is assumed to be open. The analysis of a cylindrical structure is interesting from the point of view that it represents a structure of involved complexity on its vibration and acoustic response that is not tractable under previous design approaches. The disturbance force is located at x=0.00m, y=0.30m and z=0.00m with frequency components at 180Hz, 240Hz and 300Hz. The amplitude of the disturbance force at the three frequencies is 10N, 15N and 2N respectively. This combination of disturbance frequencies and amplitudes has been chosen in order to have more than one mode producing significant contributions to the total radiated power in eq. (15). The analysis includes the first eight modes that will be excited by that force, i.e. symmetric with respect to the axial direction. The respective natural frequencies, mode shapes and modal disturbances are computed using the FE code IBM-CAEDS using 720 thin-shell quadrilateral linear elements. The results are presented in Table I where "a" and "b" are the modal indices in the circumferential and axial direction, respectively. A constant modal damping ratio of 0.05% (β_n=0.005) is assumed in all the modes.

The modal acoustic radiation at each one of the disturbance frequencies is obtained using the boundary element code SYSNOISE in conjunction with the same mesh used in the finite element analysis [14]. From the estimated modal acoustic pressures, the modal power matrices [$K(\omega_i)$] in eq. (15) are generated. The contribution of each one of the modes and the cross coupling between the modes, including the dynamics of the structure, to the total radiated power given by eq. (15) can be

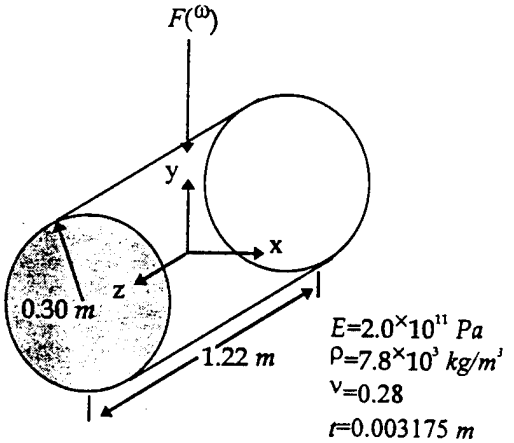

Figure 2. Simply-supported cylinder with disturbance.

Table I. FE modal data.

Mode	Index a	Index b	Nat. Freq. (Hz)	f_n
1	4	1	159	-0.256
2	3	1	174	0.249
3	5	1	213	-0.259
4	6	1	303	-0.263
5	2	1	314	0.230
6	7	1	416	0.261
7	6	3	484	-0.260
8	7	3	522	0.261

observed in figure 3. The dark and white bars represent positive and negative contributions (dB of the absolute values) to the total radiated power. It can be noticed that even though modes 2 and 4 are near on-resonance conditions, it is mode 5 who dominates the contributions to the total radiated power (75.7 dB). This result is of no surprise, since the radiation efficiency of this mode is the highest compared to the other modes included in the analysis. From figure 3, it is observed that most of the radiated power is due to the direct contributions of modes 2 and 5 and the coupling between modes 4 and 5.

The next step is to perform the upper level or modal domain optimization to investigate different control system configurations. In particular, we are interested in six different combinations: 1I1O, 1I2O, 1I3O, 2I2O, 2I3O and 3I3O where "I" and "O" denote control inputs and error sensor outputs, respectively. Therefore, we need to compute the optimum unit modal control forces u_{nk} and modal error sensor components ξ_{ns} related to each one of the control and error channels for each one of the mentioned configurations. These modal domain optimization problems are solved using Matlab's Goal Attainment subroutine [17], in conjunction to previously developed analytic sensitivity formulations [18], in a personal computer.

The reductions in the total radiated power, $\Delta\Pi=\Pi_{TC}-\Pi_{TU}$, due to each one of the optimum control configurations as a function of the control effort penalty parameter λ (the same value for all constraints) are presented in figure 4. Notice that, since at this stage all the formulations are expressed in terms of modal quantities, these results will be the same regardless of the type of transducer that is implemented. This represents one of the greatest advantages of this approach over previous optimum ASAC design formulations which require a different formulation for each different type of transducer [7,8]. From this information, the designer is allowed to decide which particular configuration is more suitable early in the design process with a relative low computational cost.

Inspection of figure 4 shows that the single control input cases seem to approach slowly an upper bound in the reduction of the total radiated power of around 8 dB. On the other hand, when the number of control inputs is equal or greater than two, there is a significant reduction in the total radiated power with less control effort, i.e. small λ. This result is due to the fact that there are two modes (2 and 5) responsible for

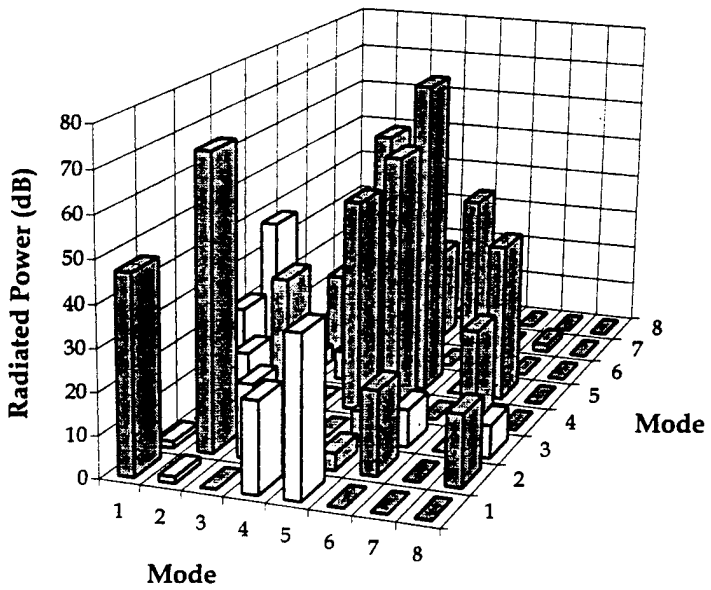

Figure 3. Modal contributions to total radiated power. Radiated power: 77.3 dB.

most of the total acoustic power and at least two control inputs are needed to effectively control their responses.

Another relevant aspect in the results in figure 4 is related to the number of error signals. According to the results, there is no apparent advantage in using more error channels than control inputs. As can be observed from the chart, for a particular number of control inputs, the reduction in the total radiated power will be the same regardless the number of error signals.

As can be noticed, there are thirty different control system configurations that were investigated in figure 4. For the sake of brevity the results for the case of 2I2O and λ=0.4 are presented. Table II contains the optimum unit modal control forces and modal error sensor components. As could be expected, the optimum unit modal control forces show that in order to reduce the total acoustic power, modes 2 and 5 must be controlled. On the other hand, the results show that the optimum modal error sensor components do not necessarily need to "observe" those modes that contribute more to the total radiated power. The outcome of this results is explained as follows. The contribution to the total radiated power in eq. (15) by a particular mode or its combination with any other mode (cross-coupling) is related to both the radiation efficiency of the involved mode(s), through the elements of matrices $[K(\omega_i)]$, and its (their) related modal displacements $q_n(\omega_i)$. In particular, the contribution due to modal cross-coupling could be either positive or negative. Thus, reduction in the total radiated power is achieved by either minimizing the modal displacements related to the highest contributors or increasing the values of the modal displacements related to negative cross terms. By inspecting eq. (2) it could be seen that if the values of the control inputs are fixed, as is the case when the inequality constraints in eq. (16) are active, the only parameters that change from mode to mode, besides the modal disturbances are the unit modal control forces. Therefore, the total radiated power is minimized by assigning values to the unit modal control forces that will allow to control the most effective modes. However, the relevance of the modal error sensor components stands in providing the allowed amplitudes for the control inputs in eq. (6) and not in observing a particular mode due to its radiation characteristics. This also explains why is that there is no improvement in the reduction in the

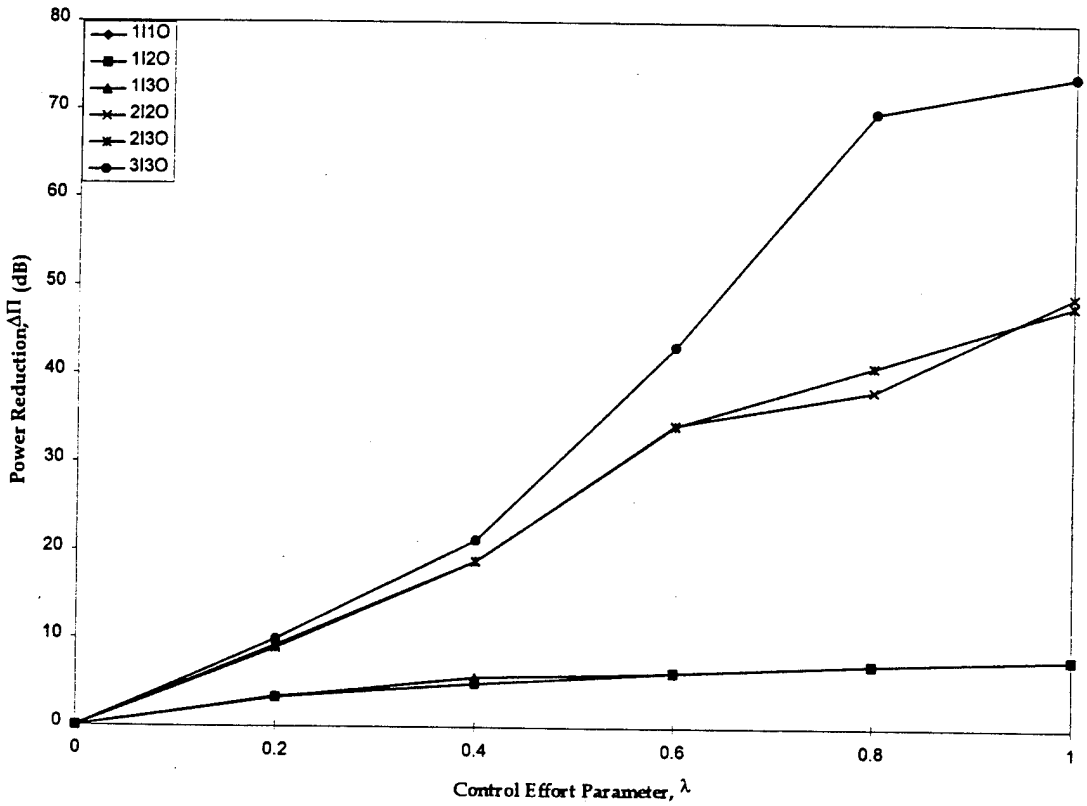

Figure 4. Reductions in total radiated power.

radiated power by increasing the number of error signals. This will only provide different means to obtain the required control inputs.

After applying the 2I2O-λ=0.40 control configuration the total radiated power is reduced by 18.8 dB. Figure 5 presents the modal contributions to the total radiated power of the controlled structure. When these results are compared to the ones in figure 3, it can be noticed that the direct contributions due to modes 2 and 5 were significantly reduced. In particular the radiated power due to modes 2 and 5 have been reduced by 14 dB and 31 dB, respectively.

Finally, it is also possible to investigate the reduction in the far-field pressure after applying the 2I2O-λ=0.40 control configuration. Figures 6 and 7 present the before and after control sound pressure levels (ref $20\mu Pa$) at $5.00m$ from the center of the structure. Figure 6 presents the radiation directivity in a plane parallel to the axial direction of the cylinder while figure 7 includes a plane perpendicular to the axial

Table II. Optimum modal parameters for 2I2O-λ=0.40.

Mode	Unit Modal Control Forces		Modal Error Sensor Components	
	u_{n1}	u_{n2}	ξ_{n1}	ξ_{n2}
1	-0.011	0.184	0.056	0.258
2	0.671	-0.658	0.023	0.378
3	-0.002	0.001	0.027	-0.037
4	-0.048	0.049	-0.005	-0.000
5	0.740	-0.751	0.753	0.101
6	-0.000	-0.000	-0.198	0.272
7	-0.003	-0.004	0.594	0.838
8	-0.000	-0.000	0.193	0.052

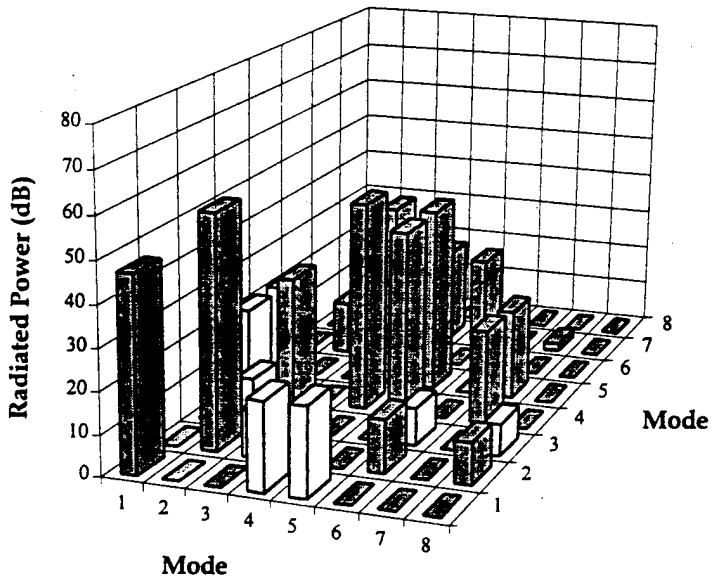

Figure 5. Modal contribution to radiated power after 2I2O-λ=0.40. Total radiated power: 58.5 dB.

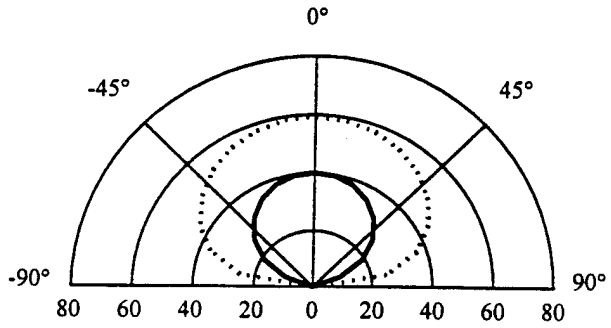

Figure 6. Radiation directivity on the z-y half plane; - - - uncontrolled — controlled.

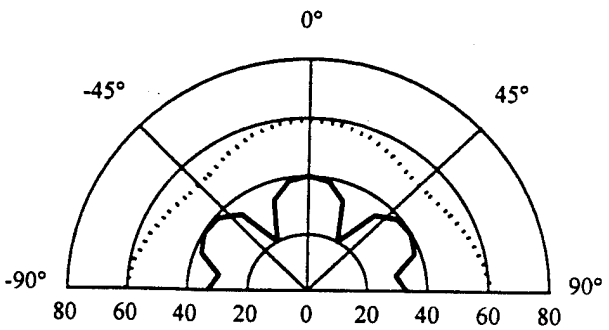

Figure 7. Radiation directivity on the x-y half plane; - - - uncontrolled — controlled.

direction at z=0.00m. The figures show that the controlled structure produce global sound reduction. Again these plots can be obtained using only the modal information of the system. The next step is to use the lower level design optimization to implement the transducers that will yield the modal parameters in Table II. This will be the topic of a future paper, however an example of this procedure for a planar radiator has been given by Burdisso and Fuller [19].

CONCLUSIONS

An efficient formulation for the optimum design of ASAC of complex structures has been presented. The approach is based in a multi-level optimization scheme that allows the implementation of numerical techniques, such as FE and BE, during the analysis. The utilization of such numerical techniques permits the applicability of the proposed approach to complex systems that are not tractable under previous optimum ASAC design formulations. The upper level optimization of the design approach has been demonstrated for the ASAC design of a simply supported cylinder under a multiple frequency excitation. Several different control system configurations were investigated in this upper level analysis. The results showed that an optimum control configuration consists of equal number of error signals and control inputs. In addition, the optimum values of the unit modal control forces show a preference for those modes that are related to the highest contributions to the total radiated power. On the other hand, the optimum modal error sensor components will tend to observe those modes that lead to the required amplitudes of the control inputs. A sample of one of the optimum configurations was presented in detail showing very good reductions in the total radiated power.

ACKNOWLEDGMENT

The authors gratefully acknowledge the support of this work by the Office of Naval Research Grant No. ONR-N00014-92-J-1170.

REFERENCES

1. "Apparatus and methods for global noise reduction", C.R. Fuller, U.S. Patent No.4,715,599 (1987)
2. "Active Control of Sound Radiation from a Rectangular Panel by Sound Sources and Vibration Inputs: an Experimental Comparison", C.R. Fuller, C.H. Hansen and S.D. Snyder, J. Sound Vib. **145**(2), 195-215 (1991)
3. "Active Control of Sound Transmission/Radiation from Elastic Plates by Vibrating Inputs-I Analysis", C.R. Fuller, J. Sound Vib. **136**(1), 1-15 (1990)

4. "Active Control of Sound Transmission/Radiation from Elastic Plates by Vibration Inputs-II Experiments", V.L. Metcalf,C. R. Fuller, R. J.Silcox and D. E. Brown, J. Sound Vib. **153**(3), 387-401 (1992)
5. "Experiments on Active Control of Sound Radiation from a Panel using a Piezoceramic Actuator", C.R.Fuller, C.H. Hansen and S.D. Snyder, J. Sound Vib. **150**(2), 179-190 (1991)
6. "Experiments on Active Control of Structurally Radiated Sound Using Multiple Piezoceramic Actuators", R.L. Clark and C. R. Fuller., J. Acoust. Soc. Am. **91**(6), 3313-3320 (1992)
7. "Optimal Placement of Piezoelectric Actuators for Active Control of Sound Radiation from Elastic Plates", B. T. Wang, R.A. Burdisso and C.R. Fuller, *Proceedings of Noise-Con 91*, 267- 275 (1991)
8. "Optimal Placement of Piezoelectric Actuators and Polyvinylidene Fluoride (PVDF) Error Sensors in Active Structural Acoustic Control Approaches", R.L. Clark and C.R. Fuller, J. Acoust. Soc. Am. **92**(3), 1521-1533 (1992)
9. F. Fahy, *Sound and Structural Vibration* (Academic Press, Orlando Fl.,1985)
10. "Piezoelectric Actuators for Distributed Vibration Excitation of Thin Plates", E.K. Dimitriadis, C.R. Fuller and C.R. Rogers, J. Vib. Acoust. **113**, 100-107 (1989)
11. "Theory of Feedforward Controlled System Eigenproperties," R.A. Burdisso and C.R. Fuller, J. Sound Vib. **153**(3), 437-452 (1992)
12. "Dynamic Behavior of Structural-Acoustic Systems in Feedforward Control of Sound Radiation", R.A. Burdisso and C.R. Fuller, J. Acoust. Soc. Am. **92**(1), 277-286(1992)
13. P.A. Nelson and S.J. Elliot, *Active Control of Sound* (Academic Press, San Diego ,CA., 1993)
14. Numerical Integration Technologies NV, *Sysnoise Rev. 5.1 User's Manual* (Leuven, August 1994)
15. P.E. Gill, W. Murray and M.H. Wright, *Practical Optimization* (Academic Press, San Diego, CA.,1981)
16. "Vector Optimization for Control with Performance and Parameter Sensitivity Indices," F.W. Gembicki, Ph.D. Dissertation, Case Western Univ., (1974)
17. The MathWorks, Inc., *Optimization Toolbox User's Guide* (Natick, Mass., 1992)
18. "Sensitivity Analysis for Feedforward Control System Design", H.M. Rodríguez and R.A. Burdisso, submitted for publication to J. Acoust. Soc. Am. (1994)
19. "Design of Active Structural Acoustic Control Systems by Eigenproperty Assignment", R.A. Burdisso and C.R. Fuller, to appear in J. Acoust. Soc. Am. **96**(3), 1582-1591 (1994)

C-50 Implementation of Fast Recursive Estimation Techniques for Active Control of Structural Sound Radiation, M. J. Bronzel and C. R. Fuller, Proceedings of ACTIVE 95, The 1995 International Symposium on Active Control of Sound and Vibration, Newport Beach, CA, pp. 359-368, 6-8 July 1995.

Newport Beach, CA, USA
ACTIVE 95
1995 July 06-08

IMPLEMENTATION OF FAST RECURSIVE ESTIMATION TECHNIQUES FOR ACTIVE CONTROL OF STRUCTURAL SOUND RADIATION

M. J. Bronzel, C. R. Fuller

Vibration and Acoustics Laboratories, Virginia Polytechnic Institute and State University
Blacksburg, VA 24061-0238, USA

INTRODUCTION

Recently, much research has been conducted in the area of active control of sound radiated from a vibrating structure. The minimization of the radiated sound can be accomplished using different approaches. Active Structural Acoustic Control (ASAC) changes the radiation characteristics of the vibrating structure by applying forces or moments directly to the structure. In contrast, Active Noise Control (ANC) involves additional noise sources usually by means of loudspeakers to superimpose a secondary sound field which attenuates the primary noise. The effectiveness of ASAC techniques has successfully been reported by Fuller using point actuators [1]. More recently, Smith [2] has demonstrated the potential attenuation of broadband sound radiation from a simply supported plate by means of piezoelectric actuators directly mounted on the vibrating structure. ASAC effectively reduces the control effort needed to minimize the sound radiation by forcing the structure to vibrate in non-volumetric modes which are inefficient radiators [3]. Structural time domain wavenumber sensing has successfully been demonstrated by Maillard and Fuller [4, 5]. They have developed a technique to estimate the sound radiated in the farfield using time domain structural wavenumber sensors based on out-of-plane acceleration signals measured directly on the structure. This eliminates the need of microphones in the farfield to obtain error signals needed to optimize the impulse response of a feedforward adaptive controller.

The implementation of an Active Noise Control System for controlling the sound radiation from a vibrating structure requires the selection of suitable reference signals. Causality and coherence considerations have to be taken into account with respect to the reference signal filtered through a representation of the control and error path. This filtering is inevitable to feedforward control implementations based on adaptive filtering. Sensing of the reference signals from the vibrating structure is inevitable for real applications since in most cases the original disturbance signal is either unknown or cannot be measured directly. This will effectively result in a structural filtering of the unknown noise source and limit the bandwidth of the measured reference signals. Most feedforward control algorithms used for adapting the coefficients of an FIR filter rely on certain assumptions concerning the statistical properties of the provided reference signals. However, these do not hold for real applications and results in non-optimal convergence properties of the implemented adaptation algorithm.

The deficiencies of stochastic gradient type algorithms for non-white input data have been overcome by exact recursive least squares type algorithms which converge independently of the statistical properties of the input or reference signal. In active noise control applications the secondary path transfer functions have to be taken into account within the update loop of the adaptive filter. The commonly used Filtered-X approach applies only to algorithms which convergence in a stochastic sense. This paper describes the modifications needed to make exact recursive least squares algorithms feasible for active noise control applications. Experiments for controlling the sound radiated from a vibrating plate have been carried out using a stabilized version of the Fast A-priori Error Sequential Technique (SFAEST) algorithm. This paper discusses design issues for development and implementation of an active noise control system based on fast feedforward control algorithms. It presents a method which effectively reduces the limitations imposed by bandlimited reference signals exhibiting a large eigenvalue spread of the associated covariance matrix. This paper will demonstrate the superior control authority of fast transversal filter algorithms in the context of an overall ASAC design approach. Experiments for control of sound radiation from a vibrating plate are carried out and results demonstrate the effectiveness of the proposed design method.

FAST RECURSIVE ESTIMATION

During the past decade fast adaptive algorithms have been developed and further refined in order to reduce their computational complexity and insure their stability under noisy or time-varying constraints. But only recently these algorithms have been applied to noise control problems. Alexander [6], Bronzel [7] and Carayannis [8] provide an overview of fast recursive estimation techniques. Recursive identification is based on optimizing a set of model parameters given the sampled signals rather than relying on assumptions concerning the statistical properties of the signals involved. The Recursive Least Squares (RLS) algorithm implements a sequential iterative procedure for inverting the sampled autocorrelation matrix based on the Sherman-Morrison Lemma [9] resulting in a computational complexity of $O(N^2)$ operations. Fast algorithms have been developed which further utilize the shift-invariance properties of the autocorrelation matrix. They usually circumvent the direct inversion of the covariance matrix by means of feedforward and feedbackward transversal filters to calculate the Kalman gain for updating the unknown parameters of the adaptive filter. These fast variants of RLS algorithms have a computational complexity down to O(7N) for the Fast A-posteriori Error Sequential Technique (FAEST) algorithm [10]. Hence these algorithms are becoming feasible for real-time applications. In our ASAC application we have implemented a numerically stabilized version (SFAEST) of this algorithm which has been developed by Moustakides [11]. The iterative adaptation loop of the SFAEST algorithm is summarized in the Appendix.

In order to apply adaptive filters in feedforward control applications, it is necessary to estimate the contribution of the filter output to the error signal. A common approach is to obtain a representation S of the control and error path and change the order of filter operations. This results in the standard Filtered-X algorithm, depicted schematically in Figure 1. Changing the order of filter operations is possible only for Linear Time-Invariant (LTI) systems. Adaptive filters are time-varying by definition and the corresponding filter operators do generally not commute. However, the errors resulting from a change of the filter operations are small in the limit of slow adaptation. This assumption is valid for stochastic gradient algorithms such as the LMS algorithm which is commonly used in feedforward adaptive control applications.

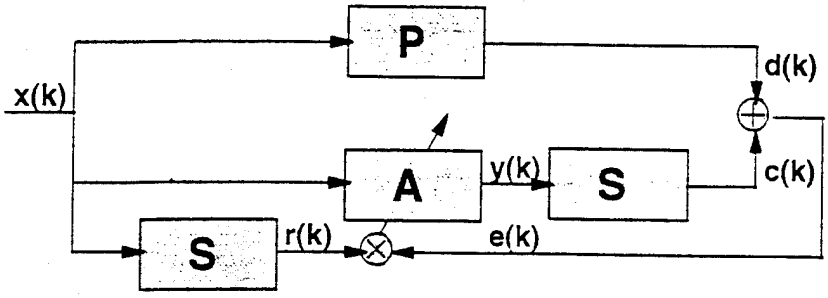

Figure 1: Filtered-X configuration for adaptive feedforward controllers based on stochastic gradient adaptation schemes.

The failure of the Filtered-X algorithm, when applied to fast recursive estimation schemes has been reported by Bronzel [7], who successfully introduced the Extended-Filtered-X algorithm which enables the implementation of fast recursive identification techniques for feedforward control applications. The basic scheme of this approach is shown in more details in Figure 2. The Extended-Filtered-X algorithm calculates an adjustment $\Delta e[k]$ which compensates the error introduced by exchanging the non-commuting filter operators in the standard Filtered-X algorithm. The output y[k] of the adaptive filter A is filtered through a representation S of the control and error path, yielding an estimate $c_\alpha[k]$ of the contribution from the control signal to the error signal e[k]. Exchanging the order of the corresponding filters yields another estimate $c_\beta[k]$. The necessary adjustment to the sampled error signal e[k] is given by the difference of these estimates:

$$\Delta e[k] = \sum_i a_i[k]\, r[k-i] - \sum_j s_j\, y[k-j].$$

Schirmacher [12] has reported the active control of airborne sound using the SFAEST algorithm with a slightly modified form of the Extended-Filtered-X configuration which has been developed by Bjarnason [13], who applied his Modified-Filtered-X scheme to the LMS algorithm. Although the Extended-Filtered-X technique could be applied to stochastic gradient algorithms it will generally yield no performance improvements and is furthermore not essential to ensure stability.

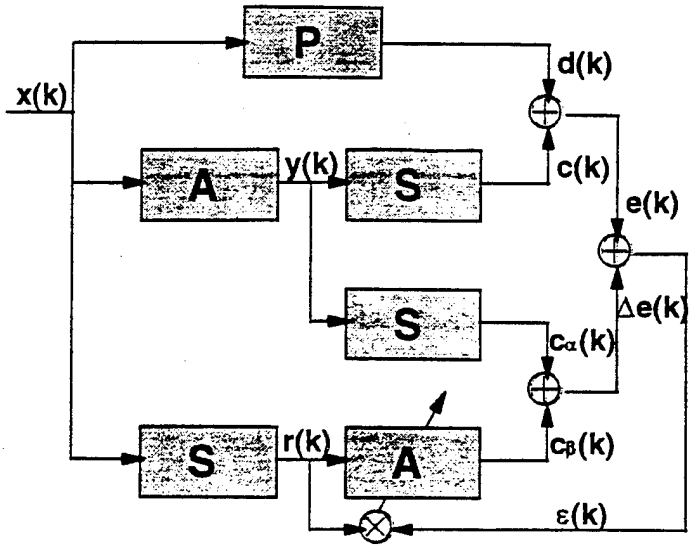

Figure 2: Extended-Filtered-X configuration for adaptive feedforward controllers based on fast recursive estimation techniques.

EXPERIMENTAL SET-UP

The experiments were performed on a simply supported plate made of plain carbon steel with dimensions 380 x 298 x 1.93 mm. Figure 3 shows a schematic display of the experimental arrangement. The simply supported boundary conditions were provided by thin flexible metal shims connecting the edges of the steel plate with a heavy support stand. The lower order resonance frequencies of this plate are presented Table 1.

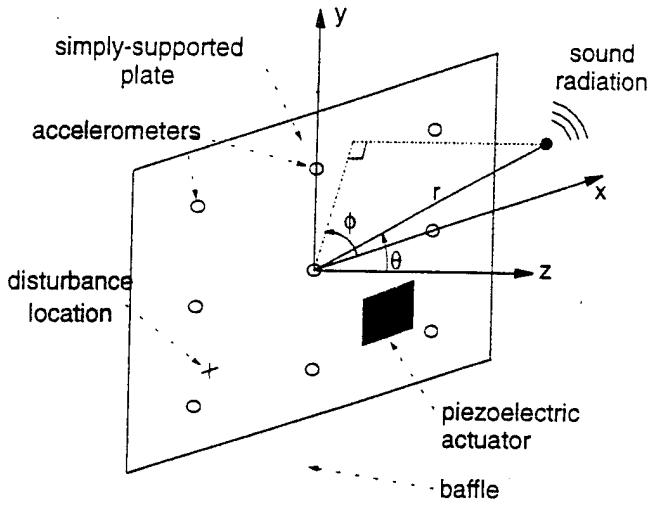

Figure 3: Experimental setup of simply supported plate with disturbance shaker, PZT control actuator and an array of 9 accelerometers for estimating the wavenumber components radiating in the farfield.

Nine accelerometers were mounted on the plate as depicted in Figure 3 to measure the structural vibration. The acceleration signals were sampled at 1 kHz and passed through a digital filter network to provide time domain estimates of 3 wave-number components. One of these is used as an error signal for the adaptive feedforward controller. The calculations are carried out in real-time on a TMS320C30 DSP board. A more detailed description of the wave-number sensor is given by Maillard and Fuller [5].

Table 1: Plate modal resonant frequencies.

Mode (m,n)	(1,1)	(2,1)	(1,2)	(2,2)	(3,1)	(3,2)
Frequency [Hz]	87	183	244	330	343	474

Two G1195 PZT piezoelectric actuators with dimensions 38 x 32 x 0.19 mm were mounted on each side of the plate and wired out of phase to provide bending moments as control inputs. The controller and a digital random noise signal generator were implemented an a separate TMS320C30 DSP board with 2 channel built-in analog I/O. The signal taken from the output of the built-in signal generator was filtered through a low-pass Butterworth filter with a cut-off frequency of 400 Hz to excite the disturbance shaker. While the reference signal for the adaptive feedforward controller is directly available from the random noise sequence, an adjustable delay was introduced in the disturbance path to investigate the effects of causality. The I/O data stream is sampled at 1 kHz. The adaptive controller uses 180 FIR filter coefficients which are updated

using the Extended-Filtered-X SFAEST algorithm as outlined in the Appendix. The control and error path is represented using a transversal filter with 180 coefficients. The windowing parameter λ in the SFAEST algorithm is set to 1.0 which resembles the stationarity of the disturbance signal and of the plate dynamics. Suitable values for the initialization parameter μ = 1.0 and for the stability parameter ρ = 1.0 were established during experimental testing. The coherence between the disturbance signal and the error signal as well as the auto-spectrum of the estimated wavenumber components were monitored using a portable B&K 2148 dual channel signal analyzer.

EXPERIMENTAL RESULTS

The estimate of the sound pressure based on structural time domain wavenumber sensing provides a signal related to the noise radiation from the vibrating simply supported plate coupling in the directions corresponding to $\theta = -30°$, $\theta = 0°$ and $\theta = 30°$ (see Figure 3). The implemented controller is currently designed for SISO systems. Therefore it is only possible to minimize the sound radiation in one direction using a single PZT actuator mounted on the vibrating plate. However, the estimated sound pressure corresponding to the other two directions was monitored. as well.

The following results present an optimal controller, where a 20 ms delay has been added to the disturbance path to make the system more causal. This enables the controller to adapt the coefficients necessary to compensate the non-minimum phase zeros of the control and error path. Figure 4 shows the auto-spectrum of the estimated error signal at $\theta = -30°$ for the uncontrolled (solid line) and controlled (dashed line) system after 5000 iterations using the Extended-Filtered-X SFAEST based controller. Significant reduction of the radiated sound is achieved with peak attenuation levels up to 28 dB for the entire bandwidth ranging from 50 Hz to 400 Hz. The total sound pressure level attenuation is 7.9 dB across that frequency range. Figure 5 displays the noise reduction being achieved. Large reductions in radiated sound level are obtained for on-resonance frequencies. Figure 6 and Figure 7 show the estimated sound pressure level before (solid line) and after (dashed line) control for the additional signals corresponding to pressure radiation in $\theta = 30°$ and $\theta = 0°$. Note that these signals were not included in the costfunction to be minimized using the adaptive feedforward controller. Cancellation occurs at resonant frequencies while the noise level off-resonance is increased in general.

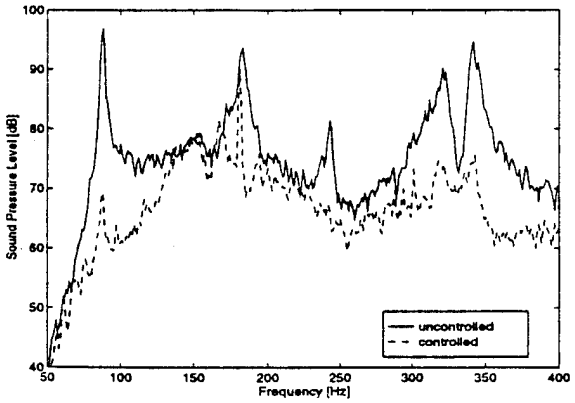

Figure 4: Auto-spectrum of the estimated error signal ($\theta = -30°$, $\phi = 0°$) before and after control.

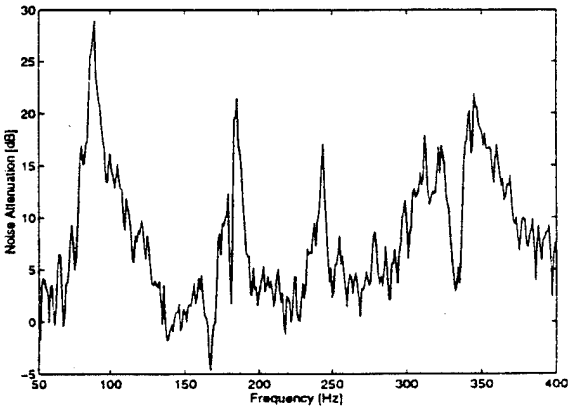

Figure 5: Noise attenuation of the estimated error signal ($\theta = -30°$, $\phi = 0°$) after 5000 iterations.

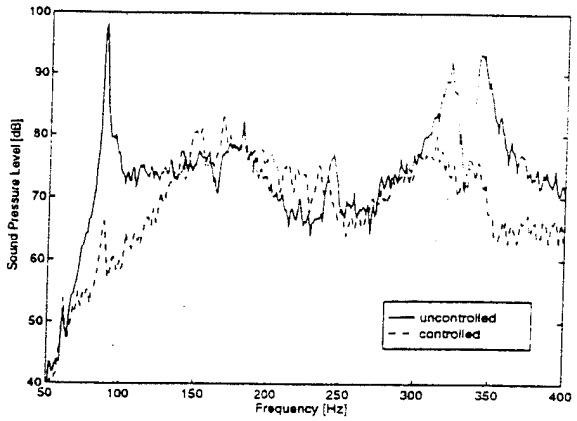

Figure 6: Auto-spectrum of the estimated signal corresponding to sound pressure radiation in second direction ($\theta = -30°$, $\phi = 0°$) before and after control.

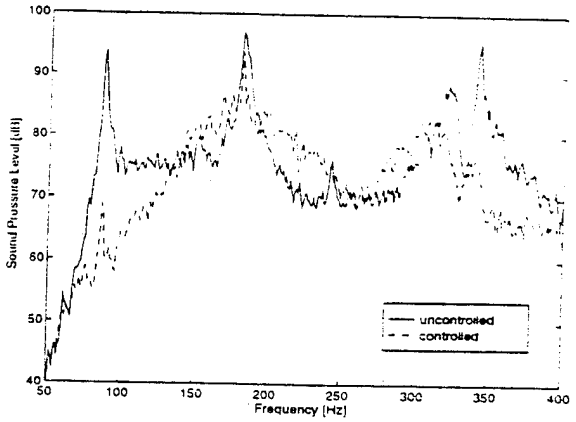

Figure 7: Auto-spectrum of the estimated signal corresponding to sound pressure radiation in third direction($\theta = 0°$, $\phi = 0°$) before and after control.

The previously presented results were obtained after 5000 iterations using the Extended-Filtered-X SFAEST algorithm. In order to demonstrate its effectiveness, the experiments were repeated using the common Filtered-X LMS algorithm. A convergence factor of μ = 2.0E−10 was chosen as the maximum possible value to maintain stability during the process of adaptation. Figure 8 and Figure 9 show respectively the auto-spectrum of the error signal before (solid line) and after (dashed line) control and the achievable noise attenuation after 20000 iterations. Although the radiated pressure associated with most dominant radiating modes has been reduced, the overall broadband performance of the Filtered-X LMS based controller has still not achieved that obtained using the Extended-Filtered-X SFAEST algorithm. The total sound pressure attenuation results in 4.0 dB in the frequency range between 50 and 400 Hz.

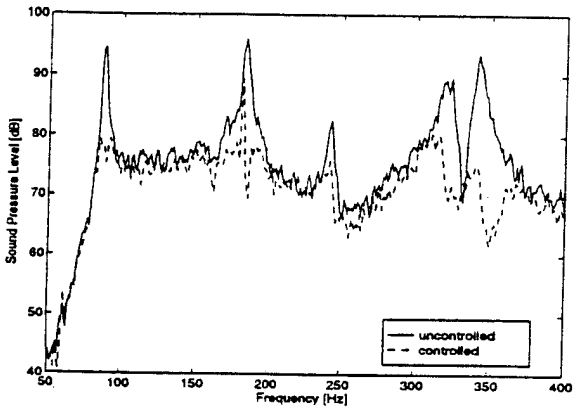

Figure 8: Auto-spectrum of the estimated error signal ($\theta = -30°$, $\phi = 0°$) before and after control.

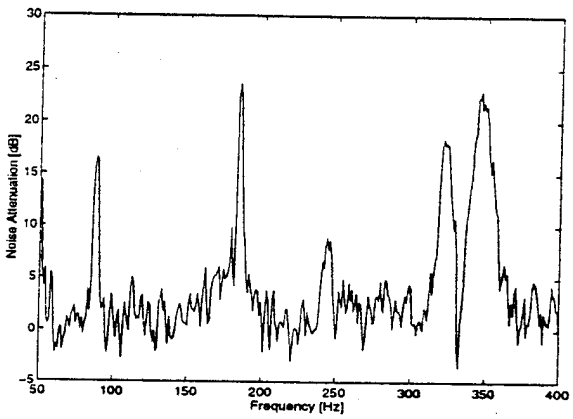

Figure 9: Noise attenuation of the estimated error signal ($\theta = -30°$, $\phi = 0°$) after 20000 iterations.

A direct comparison of the learning curves for the SFAEST and the LMS based controllers demonstrates the superior performance of the fast recursive least squares controller. The SFAEST algorithm converges very fast although the covariance matrix of the filtered reference signals exhibits an extremely high eigenvalue ratio of η = 4.42E+5. The residual error signals for the first 5000 iterations are shown in Figure 10 for the two different controllers. Note that the output of the SFAEST based controller was switched off during the first 1000 iterations. This results in better control performance since the SFAEST and other fast adaptation schemes tend to overshoot the residual error during the first iterations in a noisy environment.

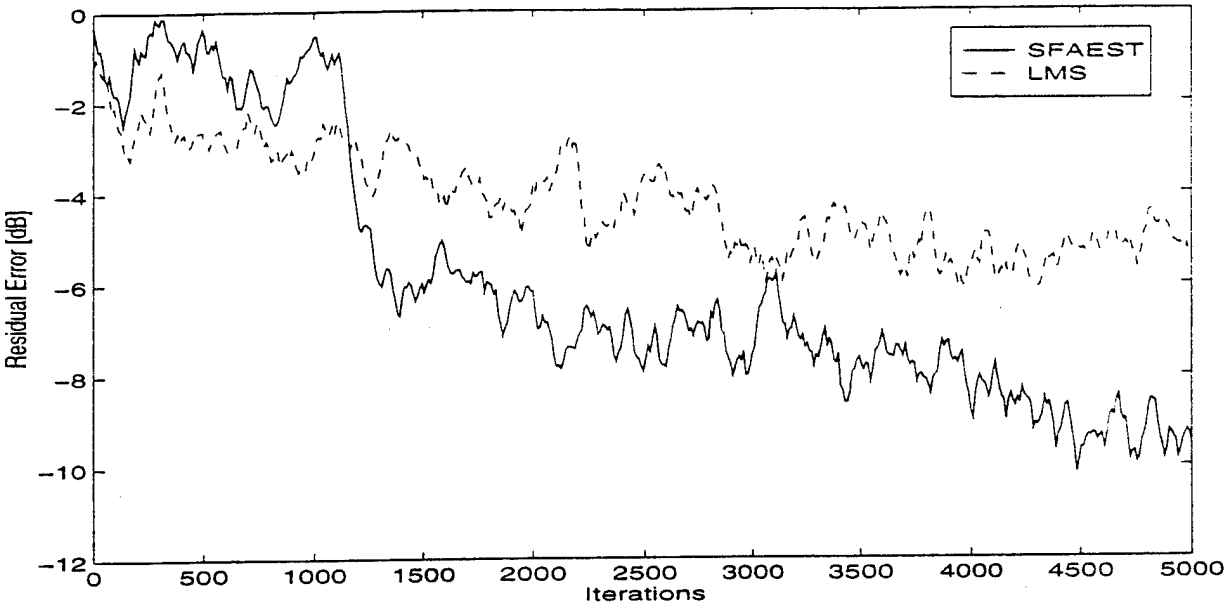

Figure 10: Residual adaptation error during the initial 5000 iterations for the SFAEST. The results are obtained as a smoothed ensemble average from 10 experiments.

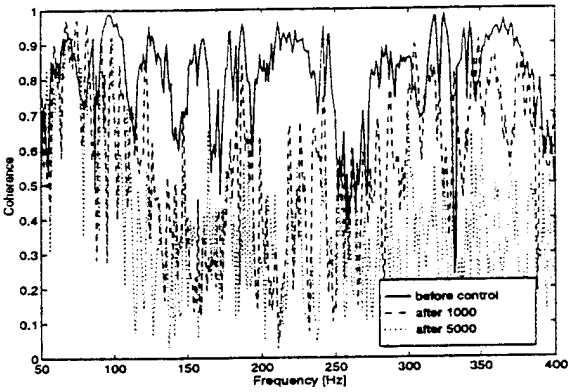

Figure 11: Coherence function γ_{xe}^2 before control and after 1000 and 5000 iterations using the SFAEST based controller.

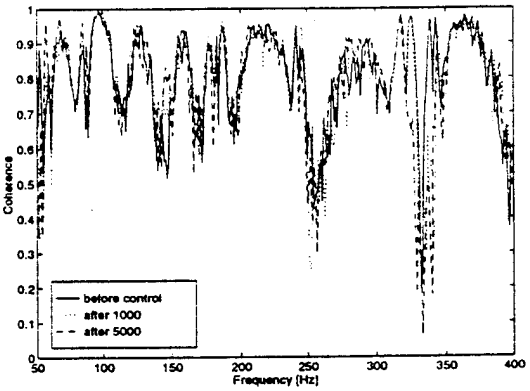

Figure 12: Coherence function γ_{xe}^2 before control and after 1000 and 5000 iterations using the LMS based controller.

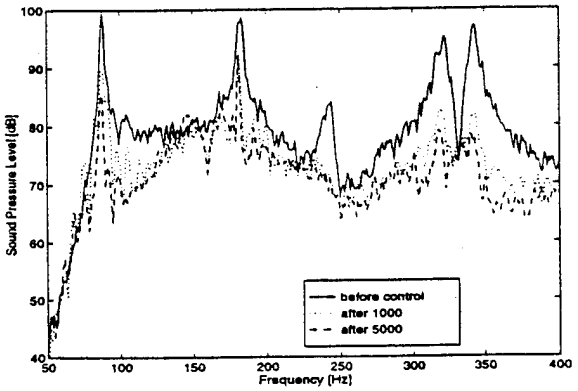

Figure 13: Control performance of the SFAEST based controller after 1000 and after 5000 iterations.

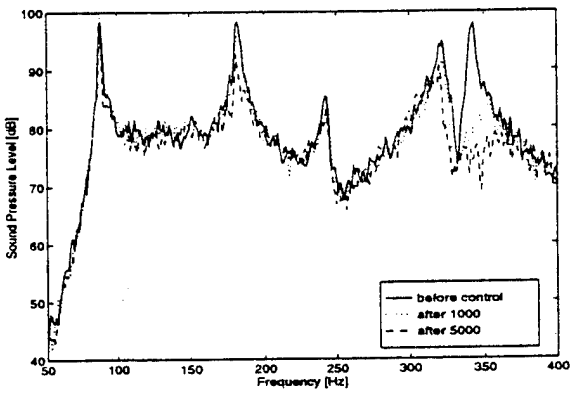

Figure 14: Control performance of the LMS based controller after 1000 and after 5000 iterations.

Figure 11 compares the coherence function between the reference signal and the error signal before and after 1000 and 5000 iterations for the SFAEST based controller. The significant decrease of the coherence indicates that most of the correlated content from the reference signal has already been removed from the error signal after 1000 iterations. The corresponding coherence functions for the LMS based controller are shown in Figure 12. The coherence has not remarkably decreased after 5000 iterations. Figure 13 and Figure 14 show respectively the effective noise attenuation for the SFAEST and for the LMS based controller before control and after 1000 and 5000 iterations. The attenuation of the radiated sound pressure corresponds to the decrease of the coherence between the reference and the error signal shown before.

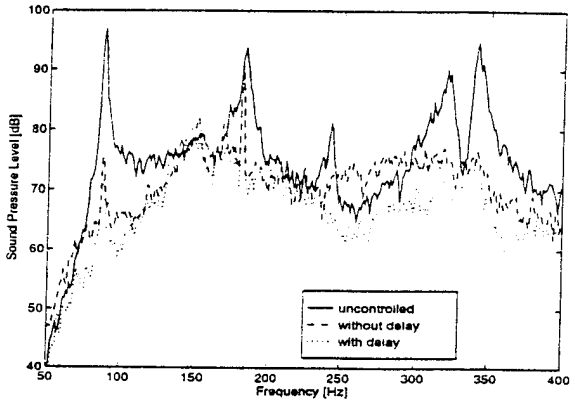

Figure 15: Auto-spectrum of the estimated error signal before and after control with 20 ms delay and without delay.

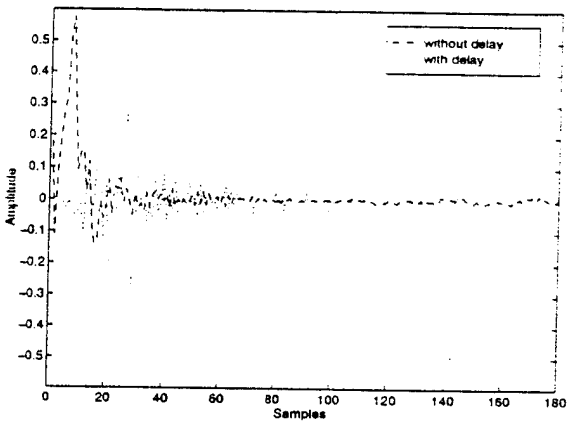

Figure 16: Comparison of the optimal controllers impulse response for an implementation with 20 ms delay and without delay.

In Figure 15, the previously obtained results (dotted line) are compared with that achieved with a controller implementation where no additional delay has been added in the disturbance path (dashed line). The corresponding optimal controller coefficients after 5000 iterations are shown in Figure 16. As expected, better attenuation over the frequency band is obtained with the delay being added, due to the non-minimum phase characteristics of the control and error path. The controller coefficients with smaller index than the number of additional delay taps in the disturbance path cannot be modeled in realistic applications. This results in some control spill-over for off-resonance frequencies which can be reduced using more than only one control actuator. However, significant attenuation was achieved at resonant frequencies using the control implementation without delay. The broadband overall sound pressure reduction is 4.2 dB across the entire bandwidth.

CONCLUSIONS

Active structural acoustic control of structure-born sound has been investigated using a fast RLS algorithm. Application of fast adaptation schemes has been made feasible using an Extended-Filtered-X algorithm which eliminates the inevitable errors associated with the standard Filtered-X approach. The presented results clearly demonstrate the superior control authority of the Extended-Filtered-X SFAEST algorithm over the Filtered-X LMS algorithm if the covariance matrix of the underlying filtered reference signals exhibits a large eigenvalue ratio. Broadband attenuation of the noise radiated from a simply supported plate in one direction has been demonstrated with peak attenuation levels up to 28 dB in the frequency range from 50 Hz to 400

Hz. Most of the reduction in the radiated sound pressure has been achieved after 1000 iterations. However, a significant number of FIR coefficients were necessary to provide attenuation of the levels achieved. Furthermore, results indicate, that a significant performance improvement could be expected from implementing fast IIR type adaptive filters based on recursive least squares estimation techniques.

REFERENCES

[1] "Active control of sound transmission/radiation from elastic plates by vibrational inputs. I. Analysis," C.R. Fuller, *Journal of Sound and Vibration*, **136**, 1-15, 1990.

[2] "Control of broadband radiated sound with adaptive structures," J.P. Smith, C.R. Fuller and R.A. Burdisso, *Proceedings of the SPIE 1993 North American Conference on Smart Structures and Materials, 31 Jan - 4 Feb, Albuquerque, New Mexico*, 1993.

[3] "Active control of sound by minimization of volume velocity on finite beams," C. Guigou, F. Charette and A. Berry, *Proceedings of Third International Conference on Air- and Structure--Borne Sound and Vibration, Montreal, Canada*, 1507-1514, June 1994.

[4] "Advanced time domain wave-number sensing for structural acoustic systems. I. Theory and design," J.P. Maillard and C.R. Fuller, *Journal of the Acoustical Society of America*, **95**(6), 3252-3272 (1994).

[5] "Advanced time domain wave-number sensing for structural acoustic systems. III. Experiments on active broadband radiation control of a simply supported plate," J.P. Maillard and C.R. Fuller, *Journal of the Acoustical Society of America*, submitted, 1994.

[6] S.T. Alexander, Adaptive signal processing. Theory and applications (Springer, New York, 1986).

[7] "Aktive Beeinflussung nicht-stationärer Schallfelder mit adaptiven Digitalfiltern," M.J. Bronzel, PhD thesis, Georg-August-Universität, Göttingen, 1993.

[8] "A unified view of parametric processing algorithms for prewindowed signals," G. Carayannis, N. Kalouptsidis and D. Manolakis, *Signal Processing*, **10**, 335-368, 1986.

[9] P. Strobach, Linear Prediction Theory, (Springer, New York, 1990).

[10] "A Fast Sequential Algorithm for Least Squares Filtering and Prediction", G. Carayannis, N. Kalouptsidis and D. Manolakis, *IEEE Transactions on Acoustics, Speech and Signal Processing*, ASSP-31,1394-1403, 1983.

[11] "Correcting the Instability due to Finite Precision of the Fast Kalman Identification Algorithms," G.V. Moustakides, *Signal Processing*, **18**, 33-42, 1989.

[12] "Fast Algorithms for Active Adaptive Control of Nonstationary Sound Fields," R. Schirmacher, T. Auspitzer and D. Guicking, *NAG Journaal Nr. 120: Anti-Geluid en Anti-Trillingen*, 41-55, 1939.

[13] "Active Noise cancellation using a modified Form of the Filtered-X LMS Algorithm," E. Bjarnason, *Proceedings of EUSIPCO*, 1053-1056, 1992.

ACKNOWLEDGMENTS

This work has been funded under ONR N00014-92-J-470. The authors are grateful to Rolf Schirmacher and Thomas Auspitzer from University of Göttingen for providing a C-code version of the SFAEST algorithm and to Julien Maillard for providing the time domain wavenumber sensor.

APPENDIX

Stabilized Fast A-posteriori Error Sequential Technique (SFAEST) algorithm. The following list summarizes the update equations for the Extended-Filtered-X SFAEST algorithm. The computational complexity of this algorithm counts 8n+41+2n+2m+1 Multiply-And-Add instructions including 5 divisions.

$$r[k+1] = \mathbf{s}_m^T \mathbf{x}_m[k+1]$$ filtered reference signal

$$e_n^f[k+1] = r[k+1] - \mathbf{f}_n^T[k]\,\mathbf{r}_n[k]$$ a priori forward predictor error

$$e_n^b[k+1] = r[k-n] - \mathbf{b}_n^T[k]\,\mathbf{r}_n[k+1]$$ a priori backward predictor error

$$\gamma_{n+1}[k+1] = \frac{\lambda\,\alpha_n^f[k]}{\lambda\,\alpha_n^f[k] + e_n^f[k+1]^2\,\gamma_n[k]}\,\gamma_n[k]$$ order recursion for angle update (step up)

$$\gamma_n[k+1] = \frac{\gamma_{n+1}[k+1]}{1 + e_n^b[k+1]\left(\kappa_n^n[k] + \frac{e_n^f[k+1]}{\lambda\,\alpha_n^f[k]}\,f_n[k]\right)\gamma_{n+1}[k+1]}$$ angle update (step down)

$$c_n[k] = \lambda^{-n}\,\gamma_n[k]\,f_n^n[k]$$ windowed angle parameter

$$\xi_n[k+1] = e_n^b[k+1] + \lambda\,\alpha_n^b[k]\,\kappa_n^n[k] + c_n[k]\,e_n^f[k+1]$$

$$\tilde{\xi}_n[k+1] = \frac{\xi_n[k+1]}{1 + \rho\left(1-\gamma_n[k+1]\right) + \rho\,c_n[k]^2\left(1-\gamma_n[k]\right)}$$ stabilization factor

$$\tilde{e}_n^f[k+1] = e_n^f[k+1] - \left(1-\gamma_n[k]\right)c_n[k]\,\rho\,\tilde{\xi}_n[k+1]$$ stabilized forward predictor error

$$\alpha_n^f[k+1] = \lambda\,\alpha_n^f[k] + \gamma_n[k]\,\tilde{e}_n^f[k+1]^2$$ forward angle update

$$\tilde{e}_n^b[k+1] = e_n^b[k+1] - \left(1-\gamma_n[k+1]\right)\rho\,\tilde{\xi}_n[k+1]$$ stabilized backward predictor error

$$\alpha_n^b[k+1] = \lambda\,\alpha_n^b[k] + \gamma_n[k+1]\,\tilde{e}_n^b[k+1]^2$$ backward angle update

$$\kappa_{n+1}[k+1] = \begin{Bmatrix} 0 \\ \kappa_n[k] \end{Bmatrix} - \frac{1}{\lambda}\begin{Bmatrix} 1 \\ -\mathbf{f}_n[k] \end{Bmatrix}\frac{\tilde{e}_n^f[k+1]}{\alpha_n^f[k]}$$ alternative Kalman gain update

$$\mathbf{f}_n[k+1] = \mathbf{f}_n[k] - \gamma_n[k]\left(e_n^f[k+1] + \rho\,\tilde{\xi}_n[k+1]\,c_n[k]\right)\kappa_n[k]$$ forward predictor update

$$\begin{Bmatrix} \kappa_n[k+1] \\ 0 \end{Bmatrix} = \kappa_{n+1}[k+1] - \kappa_{n+1}^{n+1}[k+1]\begin{Bmatrix} -\mathbf{b}_n[k] \\ 1 \end{Bmatrix}$$ partitioning of alternative Kalman gain

$$\mathbf{b}_n[k+1] = \mathbf{b}_n[k] - \gamma_n[k+1]\left(e_n^b[k+1] + \rho\,\tilde{\xi}_n[k+1]\right)\kappa_n[k+1]$$ backward predictor update

$$y[k+1] = \mathbf{a}_n^T[k]\,\mathbf{x}_n[k+1]$$ FIR filter output

$$\Delta e[k+1] = \mathbf{a}_n^T[k]\,\mathbf{r}_n[k+1] - \mathbf{s}_n^T\,\mathbf{y}_n[k+1]$$ a priori error adjustment

$$\varepsilon_n[k+1] = \gamma_n[k+1]\left(e_n[k+1] + \Delta e[k+1]\right)$$ modified a posteriori error

$$\mathbf{a}_n^T[k+1] = \mathbf{a}_n^T[k] - \varepsilon_n[k+1]\,\kappa_n[k+1]$$ FIR filter update